Chengmin Liu   *Editor*

Proceedings of the 23rd Pacific Basin Nuclear Conference, Volume 1

PBNC 2022, 1–4 November, Beijing & Chengdu, China

Springer

Springer Proceedings in Physics   **283**

Indexed by Scopus

The series Springer Proceedings in Physics, founded in 1984, is devoted to timely reports of state-of-the-art developments in physics and related sciences. Typically based on material presented at conferences, workshops and similar scientific meetings, volumes published in this series will constitute a comprehensive up-to-date source of reference on a field or subfield of relevance in contemporary physics. Proposals must include the following:

– Name, place and date of the scientific meeting
– A link to the committees (local organization, international advisors etc.)
– Scientific description of the meeting
– List of invited/plenary speakers
– An estimate of the planned proceedings book parameters (number of pages/articles, requested number of bulk copies, submission deadline).

Please contact:

For Americas and Europe: Dr. Zachary Evenson; zachary.evenson@springer.com
For Asia, Australia and New Zealand: Dr. Loyola DSilva; loyola.dsilva@springer.com

Chengmin Liu
Editor

Proceedings of the 23rd Pacific Basin Nuclear Conference, Volume 1

PBNC 2022, 1–4 November, Beijing & Chengdu, China

Springer

Editor
Chengmin Liu
Nuclear Power Institute of China
Chengdu, China

Acknowledgment

Thanks to all the members of the PBNC 2022 Conference Committees

COMMITTEES

Title	Name
Conference Chairman	Jianfeng YU Shoujun WANG
Steering Committee	
Chairs	Qi LUO
Co-Chairs	Yanfeng SHEN Tao ZHANG Hongzao LU Gang WAN Zhi WANG Corey McDaniel
Members	Fengxue WANG、Kamal Verma、Mimi Holland Limbach、Jorge Spitalnik、Vladimir Kuchinov、Benhamin Rouben、George Christidis、Kazuaki Matsui、Masahito Kinoshita、Armando Gomez、Ozemoyah Peter、Javier Palacios Javier、John Harries、Tomofumi Yamamoto、Faridah Idris
Organizing Committee	
Chairs	Jianqiao LIU Conglin WANG
Co-Chairs	Dazhu YANG Jiashu TIAN Keli GAO Yongjin FENG
Members	Fengxue WANG、Lixin SHEN、Xiaoguang LIU 、Ning SHEN、Laisheng YANG、Hong TANG、Aubrey Whittington
Chair Assistant	Ruoshan XU、Yanyan ZHU、Siyan LIU、Dan DENG、Li YANG、Yan QUAN
Technical Program Committee	
Chairs	Chengmin LIU
Executive Chair	Hongxing YU
Members	Danrong SONG、Zhou ZHOU、Wei SHI、Hangzhou ZHANG、Tao ZHANG、Wei YI、Guanghui SU、Yizhe LIU、Xiaoyong WU、Yue ZUO、Jiang HU、Yaming LI、Suyuan YU
Technical Secretariat	Wenjie LI、Bowen QIU

Contents

Research on the Public Participation of Nuclear Safety Based on Social Psychology

Guanghui Li, Gang Bai, Xiaoding Li, Yunhuan Qu, and Yu Gong[✉]

Nuclear and Radiation Safety Center, Ministry of Ecology and Environment of the People's Republic of China, Beijing, China
`gongyu322@qq.com`

Abstract. Nuclear safety concerns the development of the cause of putting nuclear energy and technology to good use, environmental safety, and the public interest. The public participation of nuclear safety is an important means of popularizing safety knowledge and eliminating public concerns. Social psychology is a branch of psychology that studies the social phenomena of individuals and groups. In fact, the public participation of nuclear safety is a collective activity for citizens to integrate into nuclear safety and participate in nuclear safety. The theoretical root of public participation is social psychology. Using social psychology to analyze the behavior and ideas of various stakeholders in public participation can effectively enhance the relevance and effectiveness of public participation. Therefore, it is very important to carry out public safety research based on social psychology. This paper investigates the present situation of public participation of nuclear safety, and analyze the misunderstandings of current public participation based on social psychology: Public participation requires a high level of knowledge because more knowledgeable people are more supportive of nuclear energy; The public must either support or oppose nuclear energy, without a third option; Public opposition to nuclear energy is attributed to insufficient public participation; Wrong views should be downplayed and will disappear over time; Public participation is only the responsibility of dedicated staff. For these misunderstandings, this paper proposes a follow-up to the recommendations of public participation: Understand the conformity among individuals; Apply various measures to engage people from different groups to improve the effectiveness of public participation; Encourage extensive participation to create synergy; Step up international cooperation to promote public participation.

Keywords: Public · Participation · Nuclear Safety · Social · Psychology

1 Introduction

Along with the development of China's economy and society and the improvement of people's livelihood, the public has enhanced their awareness of the environment and safety, and paid increasing attention to nuclear safety. Especially in the wake of the Fukushima Daiichi nuclear disaster, public attention to nuclear safety has reached an unprecedented level. Many people have demanded that nuclear power development

should be slowed down or suspended. There are two main reasons for it. On the one hand, the public have suffered psychological trauma from major nuclear accidents in history, fearing that similar accidents will occur in nearby nuclear power plants. On the other hand, they have little knowledge about nuclear or the safety of using nuclear energy and technology, which remains mysterious. The anti-nuclear campaigns in places such as Pengze County, Jiangmen City and Lianyungang City have fully demonstrated that public acceptance instead of technology will hinder the further utilization of nuclear energy and technology. Public participation is an efficient means to meet people's right to know and protect their legitimate rights and interests as well as an essential way to supervise nuclear safety, thus playing a critical role in promoting the safe, efficient, and sustainable utilization of nuclear energy and technology.

2 Relationship Between Public Participation in Nuclear Safety and Social Psychology

Public participation in nuclear safety refers to a serious of systems and mechanisms for stakeholders and the general public to participate in the decision-making process by providing information, voicing opinions, making comments and expressing appeals on major issues related to personal or public interests during the site selection, design, construction, commissioning, operation and decommissioning of nuclear facilities to make decisions more fair, legitimate and reasonable.

Social psychology, a branch of psychology for social psychological phenomena of individuals and groups, studies psychological problems related to society. Based on the interactions between individuals and society, social psychology studies the law of development and change of individuals' psychological activities in a certain social context. Social psychology focuses on the interactions between society and individuals, the explorations into social situations, and the internal psychological factors.

Overall, with the theoretical source of social psychology, public participation in nuclear safety is an collective activity that involves the public in nuclear safety. It stresses that ill-founded prohibition will further ignite people's desire to explore the truth. Therefore, it is important to plan public participation in nuclear safety in steps, particularly when a nuclear project is approved and a nuclear accident occurs. Through the sound communication between the government, operators of nuclear facilities and the public, conflicts among them can be effectively prevented and resolved.

3 Current Situation and Problems of Public Participation in Nuclear Safety

The utilization of nuclear energy and technology started relatively late in China. Though public participation in nuclear safety had a even later start, it has been developing rapidly and made certain achievements. For example, the Qinshan nuclear base in Haiyan County and Tianwan nuclear power plant in Lianyungang City were listed as "demonstration sites of industrial tourism". As a result of several major nuclear accidents, including the Three Mile Island accident, the Chernobyl disaster, especially the Fukushima Daiichi nuclear disaster, public participation in nuclear safety has received growing attention and played an increasingly important role.

3.1   Current Situation of Public Participation in Nuclear Safety in China

In China, active participation is the primary form of public participation throughout the overall life cycle of nuclear facilities from site selection to decommissioning. The content of participation varies by the stage of nuclear facilities. In the stage of site selection, the public can provide their opinions and suggestions according to the environmental impact assessment report on nuclear facilities released by the government and operators. In the stage of construction, they can learn about and advise on the preliminary design scheme for environmental protection of nuclear facilities. During the operation period, they can offer their inputs based on an understanding of the environmental impact of final design and construction of nuclear facilities, the operation of environmental protection facilities, and the implementation of environmental protection measures. In the decommissioning phase, the public can also advise on the time and method of decommissioning, in addition to the usage and final disposal of decommissioned nuclear facilities.

The main organizations for public participation in nuclear safety in China include government agencies, operators, societies and associations. Government agencies include the Ministry of Environmental Protection (National Nuclear Safety Administration), the National Energy Administration, the State Administration of Science, Technology and Industry for National Defence and local governments involved in nuclear energy. China National Nuclear Corporation, China General Nuclear Power Corporation, State Power Investment Corporation, and China National Nuclear Corporation are among the nuclear operators, while China Nuclear Energy Association and Chinese Nuclear Society are examples of societies and associations.

The public can participate in nuclear safety through ways of telephone, fax, letter, email, website, exhibition, lecture, open day and questionnaire. Government departments will also hold press conferences, hearings and symposiums, which enable the public to feed back their concerns to the government or operators and demand a response. Currently, nuclear power enterprises have done a good job of public participation, some government agencies and operators have set up a special team for public participation, some have even established a committee for handling relations with the people living around the plant site.

However, there is a lack of laws that support public participation in nuclear safety. Existing laws only include the Environmental Impact Assessment Law of the People's Republic of China and the newly revised Environmental Protection Law of the People's Republic of China. The former provided that "The state encourages relevant entities, experts and the general public to participate in the appraisal of the environmental impacts in appropriate ways." The latter stated that "The competent environmental protection administrations of the people's governments at various levels and other departments with environmental supervision responsibilities shall disclose environmental information pursuant to the law, improve public participation procedures, and facilitate citizens, legal persons and other organizations to participate in, and supervise, environmental protection work."

In 2008, the Ministry of Environmental Protection (National Nuclear Safety Administration) issued the Implementation Measures for Public Participation in the Environmental Impact Assessment of Nuclear Power Plants (Draft for Comment), which emphasized public participation in the site approval, construction and operation of nuclear

power plants. It also clarified the relevant work of such plants concerning public participation, including ways of participation, main content of participation, organizational forms of participation, time requirements of participation, and principles of selecting people for comment. In addition, it made clear that project construction units are the subjects for engaging the public in environmental impact assessment activities of nuclear power plants.

3.2 Problems of Public Participation in Nuclear Safety

After years of development, China has made certain achievements in encouraging public participation in nuclear safety, but there are some misunderstandings as well. It is critical to use the theory of social psychology to identify the shortcomings in public participation and analyze causes of those misunderstandings. Based on analysis, the misunderstandings about public participation in nuclear safety are as follows:

Misunderstanding 1: Public participation requires a high level of knowledge because more knowledgeable people are more supportive of nuclear energy. Almost all staff working on public participation are committed to the view that the public generally lack the knowledge about nuclear energy, and see it as a main reason why they do not support or even oppose nuclear energy. That's not true, because more knowledge does not necessarily result in greater support. A poll by Electricite De France (EDF) showed that support for nuclear energy is not related to educational level. See Table 1 for more details.

Table 1. Public knowledge level and attitude toward nuclear power

Knowledge level	Oppose	Support
Low	38%	31%
Relatively high	53%	53%
High	9%	16%
Total	100%	100%

This is a widespread phenomenon in social psychology. Social psychologists argue that those who have a higher knowledge level and social status are more likely to act on their independent values instead of the alleged authority. The values, once formed, are stable and enduring, so nuclear knowledge should be imparted during the time when values are informed rather than after they are developed.

Misunderstanding 2: The public must either support or oppose nuclear energy, without a third option. Almost all people believe that they can only support or oppose nuclear energy instead of staying neutral. However, according to the poll by EDF, 32% strongly opposed the development of nuclear energy, 23% were highly supportive of nuclear, and the remaining 45% stayed neutral. Those who neither support nor oppose nuclear energy are critical for public support, and should be the target group for efforts to increase public participation.

Actually this is the so-called conformity in social psychology. It means that in unknown and mysterious fields, the public have no idea of how to make a choice because their information for judgment is vague. They'd rather wait for government decisions and answers from authorities, and popularization of new knowledge.

Misunderstanding 3: Public opposition to nuclear energy is attributed to insufficient public participation. Many practitioners in the nuclear industry consider insufficient public participation as the reason for public opposition, and think that enhanced participation can lead to public support. In fact, stakeholders who are most sensitive to nuclear energy pay much more attention to their own economic interests than nuclear safety. The majority of opponents are not the people within the relocation area of or faraway from the nuclear project, but rather those close to the project but outside the relocation area. They generally believe that nuclear projects are acceptable only if "they are not in my backyard". It a tough issue in the public participation work to properly address the effect of not-in-my-backyard (NIMBY).

It is the prevailing rational decision-making theory in social psychology. This theory emphasizes that when making a choice, people will estimate different interests and their costs, and choose the behaviors with minimum risks and maximum benefits. For this reason, the top priority of public participation should be finding the balance of interest between the public and operators that is accepted by the people.

Misunderstanding 4: Wrong views should be downplayed and will disappear over time. Today, personnel in some government agencies and operators still have a fluke mind that downplaying is the best solution to wrong views in reality or on the Internet, which will disappear over a period of time. However, the opposite is true. Murphy's laws in social psychology indicate that: nothing is as easy as it looks; everything takes longer than you think; anything that can go wrong will go wrong; if you worry about something happening, it is more likely to happen. When you choose to downplay the wrong views, instead of disappearing with time, they will be long-lasting and be repeatedly mentioned, thus exerting a greater influence. Then it will be much more difficult to deal with them. Social psychology suggests that early persuasion is more effective, and bringing out the facts and reasons when things occur only plays a fairly limited role.

Misunderstanding 5: Public participation is only the responsibility of dedicated staff. Some staff of nuclear operators think they only need to their part to ensure the safety of nuclear facilities, and public participation is the responsibility of the government. This is actually one-sided thinking. Social psychology holds the opinion that when there is a larger group of people who agree with some idea or take certain action, they will exert greater pressure on individuals, the group will become more cohesive with more consensus among its members, and individuals are more likely to follow the crowd. Just as the saying goes, "Birds of a feather flock together." Those who are of the same gender with similar educational level, economic income, native place, occupation, social status, social value and qualifications will more easily become attractive to each other. Only when nuclear practitioners are involved to affect more people from the similar background will public participation be further improved.

4   Conclusions

Social psychology can help identify and avoid the misunderstandings about public participation, improve the pertinence and effectiveness of public participation, and better utilize nuclear energy and technology in China. Hence, the following suggestions are provided:

4.1   Understand the Conformity Among Individuals

Social psychology stresses that conformity is more obvious in a more mysterious field for two reasons: individuals want to be accepted by the group; individuals have limited access to information. For some historical reasons, nuclear remains a mysterious field for the public. Since many people are fairly ignorant about nuclear, conformity is quite commonly seen. To deal with this problem, the two measures below can be helpful:

First, use the authority of the government. In countries with a credible government, government decisions tend to exert huge influences on public opinions. Therefore, it is imperative to enhance government credibility and timely issue authoritative opinions in case of rumors or negative public sentiments to minimize their adverse effects.

Second, cultivate role models and opinion leaders. Efforts should to made to cultivate role models and authority figures to guide the conformity behavior. Opinion leaders, especially those on new media, should be fostered to guide the people's acquisition of correct nuclear knowledge.

4.2   Apply Various Measures to Engage People from Different Groups to Improve the Effectiveness of Public Participation

People with a high level of knowledge and a high social status can make full use of their resources to obtain related knowledge and make independent judgments. Given this situation, nuclear knowledge can be imparted by integrating media, especially new media, with lectures to persuade them with actual data. For student groups who are forming values, science popularization can be adopted to help students master correct nuclear knowledge and spread such knowledge among their family members. For the general public with limited nuclear knowledge, government authority should be used to provide the guidance they need. More often, government decision is exactly what their attitude is.

Different measures should be adopted for people in various areas. For people within the relocation area of nuclear projects, relocation grants should be reasonable. For those outside the area but close to such projects, the NIMBY effect should be avoided through two ways: improving the transparency of operators and providing the public with more nuclear information to reduce information asymmetry; increasing material compensation to bring surrounding residents real benefits while enhancing mental compensation through psychological guidance to ease their anxiety.

4.3   Encourage Extensive Participation to Create Synergy

Nuclear safety is a common issue which cannot be managed by any institution or company alone. In this context, the work for public participation requires concerted efforts

from the whole industry as well as enhanced coordination between government agencies and operators to create synergy for sustained progress. Meanwhile, social forces should be fully engaged to help create a favorable public opinion atmosphere and improve people's nuclear knowledge so as to minimize public resistance.

4.4 Step up International Cooperation to Promote Public Participation

Nuclear safety transcends national boundaries. China should work with countries with a high level of public participation in nuclear safety, pay attention to their problems and avoid our previous misunderstandings. As a major country in the utilization of nuclear energy and technology, France has developed its nuclear energy by virtue of advanced technology, sound management and a transparent mechanism of public participation. In the future, China should step up cooperation with other countries to jointly promote public participation.

References

1. Xi-zi, W.: System Practice of Public Participation in Administration. China Legal Publishing House, Beijing (2008)
2. Myers, D.G.: Social Psychology. Translated by Hou Yubo. et al. Posts & Telecom Press, Beijing (2006)
3. Xian, C.: Preliminary Reflections on Nuclear Safety Publicity in the New Situation [EB/OL], 12 March 2012
4. Witkowski, D.: French Nuclear Energy Poll and Public Opinion Analysis [R]. EDFT (2014)
5. Mian, Q.: Talking about the Causes and Countermeasures of the Adjacent Avoidance Effect of Nuclear and Radiation Projects [EB/OL], 31 May 2018

Development Prospect and Application of Nuclear District Heating in China

Yifan Zhang[(✉)], Wenan Li, and Qian Yu

China Nuclear Power Engineering Corporation, Beijing, China
mszhangyifan@126.com

Abstract. With the increase of heating demand, in order to further expand the heat source channels and promote China's clean heating work, this paper investigates the development status of nuclear regional heating at home and abroad, explores the development prospect of China's nuclear heating industry, and discusses the difficulties encountered in the future application and the corresponding solutions. The research results show that China's nuclear heating has broad development prospects, but there are some problems in the construction of regional heating network and the safety, reliability and economy of nuclear power plant operation, and put forward targeted solutions, so as to promote the wide application of nuclear regional heating and realize the sustainable development of economy.

Keywords: Nuclear energy · District heating · Clean heating · Advantages

1 Introduction

The heating area in northern China has reached more than 13 billion square meters, increasing at a rate of 5%–10% per year, resulting in an increasing heating gap in many cities [1]. At present, the main heat sources used are cogeneration units and regional boiler rooms. The fuels used are still mainly fossil fuels such as coal and natural gas, which has brought great pressure to the atmospheric environment and resource supply. As a clean and efficient energy, nuclear energy is a major component of China's energy structure. At present, it has been widely used in power production. From January to June 2022, the cumulative power generation of the nuclear power generating units in operation nationwide was 1989.99 billion kWh, an increase of 2.00% over the same period in 2021 [2], but it is rarely used in the field of regional heating. From the perspective of energy utilization and green development, it is necessary to explore the prospect and application path of nuclear energy in the field of regional heating, which is of great significance to the sustainable development of central cities in heating regions in northern China.

Therefore, from the perspective of sustainable development, this paper explores the development prospect of China's nuclear energy heating industry on the basis of investigating the application experience of nuclear energy district heating at home and abroad, and discusses the difficulties encountered in the future application and the corresponding solutions, so as to further expand the heat source channel, and make contributions to improving the effective utilization rate of energy and building an environment-friendly and resource-saving society.

2 Development Status of Nuclear District Heating at Home and Abroad

Nuclear heating is not a new concept. As early as half a century ago, there were nuclear reactors for civil nuclear heating in Europe, mainly deployed in Russia, Ukraine and Bulgaria, Georgia, Czech Republic and other countries. Due to the climate, the demand for heat supply is large and widely distributed, and the heating network is relatively developed, which provides a prerequisite for the development of central heating [3]. With the peaceful application of nuclear energy in power production, Switzerland, Bulgaria, Hungary, Finland and other countries have conducted research on nuclear heating reactors to meet the demand of urban central heating. For example, two 365 MWe pressurized water reactor nuclear power plants of Beznau nuclear power plant in Switzerland began to provide district heating for 11 surrounding cities in 1983 and 1984; The Kozloduy nuclear power plant in Bulgaria has supplied heat to the city of Kozloduy since 1990; There are four VVER-440 units in Paksh nuclear power plant in Hungary to supply heat to Paksh city [4–8]; Finland provided a comprehensive district heating application scheme for the first time in the project design stage [9]; The Bohunic nuclear power station in Slovakia not only generates electricity, but also supplies heat and industrial steam to the city of Ternava. The former Soviet Union, Canada, France and other countries developed district heating as an important part of the energy system, conducted fruitful research and development on the special low-temperature heating nuclear heating reactor, and successively built a series of verification and demonstration reactors [10]. SAFA's research shows that the nuclear reactors currently in operation can effectively realize large-scale district heating through transformation, which opens up a new path for the efficient utilization of energy in the future [11].

By 2022, there are 438 nuclear reactors in operation in the world, with a total installed capacity of 393.3 GWe, of which 56 units support regional heating, more than 10% of the total, mainly distributed in cold European regions [12]. Heating reactor types include pressurized water reactor, heavy water reactor, graphite water cooled reactor, fast reactor, etc., with thermal power output between 5–240 MW. The total distributed thermal power is about 5000 MW, and the average energy recovery rate is less than 5% [13]. In many cases, heat is used to supply nearby cities several kilometers away from the nuclear power plant.

In China, the history of research and development of nuclear heating reactor can be traced back to the 1980s. In 1983, Tsinghua University realized the first nuclear low-temperature heating experiment in China on the pool research reactor; In 1984, the State Science and Technology Commission approved the construction of a 5 MW nuclear heating test reactor [14] in the Nuclear Energy Institute of Tsinghua University; Since 1986, low-temperature nuclear heating has been officially listed as the national "Seventh Five Year Plan" science and technology project; In 1989, the 5 MW low-temperature nuclear heating reactor was officially started up, and then the 72 h full power continuous operation experiment was successfully completed [15]; In 2017, CNNC took the lead in making a breakthrough in nuclear heating and released the "Yanlong" reactor with a thermal power of 400 MW [16]. "Yanlong" is a safe, economic, green and environment-friendly reactor product developed by CNNC for the heating needs of northern cities on the basis of the safe and stable operation of the pool type research reactor for more than

50 years; In 2019, the first commercial nuclear heating project in China, the first phase of the first phase of Shandong Haiyang nuclear heating project of State Power Investment Group Co., Ltd., was officially put into use, covering an area of 700000 m^2. The heating range is the staff dormitory and more than 30 surrounding residential areas; In 2020, the National Nuclear demonstration organization held the feasibility study review of CAP1400. The maximum extraction capacity of the nuclear heating project is 800 t/h, which is designed in combination with the future heating planning of Weihai City, and is expected to be the main heat source of central heating.

Through the research on the development status of nuclear district heating at home and abroad, it is found that the development of nuclear district heating in foreign countries started earlier and the related technologies are relatively mature, and large-scale district heating has been realized. Its technology and development strategy have certain reference significance for China; Domestic nuclear heating started late and has not been widely used nationwide. However, the theoretical foundation has been established through the research of test reactor. Various enterprises are also actively promoting nuclear heating projects and continuously accumulating practical experience to provide a solid foundation for the promotion and application of nuclear heating. Therefore, nuclear district heating has a broad development prospect in China.

3   Advantages of Nuclear District Heating

At present, there are two ways of nuclear district heating in China. One is the single heating mode. The reactor in this mode does not need to generate electricity, and can be designed with smaller power and lower parameters. Generally, the heating capacity of a single module is about 200 MW, which is suitable for cities or counties with small heating area and small population [17]; The other is the nuclear power cogeneration mode, which extracts part of the heat from the steam turbines of large nuclear power plants and provides heat while generating electricity. It is suitable for cities with large population. Compared with traditional coal-fired and gas-fired heating, nuclear heating has significant social and environmental benefits, without any smoke, ash, carbide, sulfide and nitrogen oxide emissions. It is a truly "zero emission" energy technology. Nuclear district heating has advantages in technology, environment and energy utilization, which are mainly divided into the following points.

3.1   Technical Advantages

For the single heating mode, the technical advantages of nuclear heating are mainly manifested in low-temperature heating. In traditional boiler heating, the fuel combustion must maintain the high temperature of the furnace, even if the supply of low-temperature heat cannot be reduced. The nuclear fission reaction reacts at any temperature. If only low-temperature heat is required, the reactor can work at low temperature and low pressure, which can simplify the reactor structure, improve safety and reduce cost. In addition, nuclear power is transformed from nuclear power, which will release a lot of heat during the reaction process, and the direct utilization of reactor heat energy can be fully realized.

Due to the technical characteristics of low-temperature heating, the nuclear heating reactor has the characteristics of low operation cost, convenient maintenance, long service life, high safety, strong adaptability to the plant site, technically canceling off-site emergency, etc. it can be close to users and built in the plant site areas around the city and in remote inland areas, thus making it possible to supply electricity, heat, water and cold energy. After the batch and modular construction, the construction and deployment time of the nuclear heating reactor will be greatly shortened. It can be completed in only 2–3 years, and its economy will be improved.

3.2 Environmental Protection Advantages

Compared with fossil energy heating, nuclear heating has significant environmental benefits. It is estimated that a 200 MW nuclear heating reactor can meet the winter central heating demand of about 7.5 million square meters, and can replace 160000 t of coal or 80 million m^3 of gas every year. Compared with coal, it can reduce the emission of 1600 t of smoke, 50000 t of ash, 260000 t of carbon dioxide, 3000 t of sulfur dioxide and 1000 tons of nitrogen oxides. Compared with natural gas, it can reduce carbon dioxide emissions by 130000 t and nitrogen oxides by 500 t. The emission of radioactive substances is only about 2% of that of coal [16].

At present, the heat source of heating in China is still cogeneration and regional boiler room, and the fuel used is still coal. The emission of coal is the main cause of winter haze in northern China. If nuclear heating is used to undertake the basic urban heat load, it can not only solve the shortage of heat sources, but also achieve clean heating, so as to alleviate the winter haze in northern cities, which is of great significance for urban development and environmental protection.

3.3 Energy Utilization Advantages

For the nuclear district heating mode of cogeneration, any heat extracted from the secondary circuit will reduce the power output of the nuclear power plant, but the increase of thermal power will compensate for the power loss. According to the energy and exergy analysis, under the cogeneration mode, the performance of the nuclear power plant can be improved by 5–10%. Improving the energy utilization is a major achievement of nuclear cogeneration [18–20]. For the single heating mode, reactor heat can be directly used for heating. Compared with the conversion of heat energy into electric energy, the efficiency of direct heat utilization will be higher. Based on the two methods, district heating can improve the energy efficiency of nuclear power plants and realize low-cost heating network.

To sum up, nuclear district heating has advantages in technology, environmental protection and energy utilization. Compared with traditional coal-fired heating, the pool type low-temperature heating reactor reactor has a service life of 60 years, and the construction investment is about 2 to 3 times that of coal-fired boilers of the same scale. However, the operating cost is much lower than that of coal-fired boilers, and the service life reaches 60 years, which is 2 to 4 times that of coal-fired boilers. It is economically feasible [21].

Therefore, from the aspects of technology, environmental protection and energy utilization, nuclear heating is the development direction of regional heating in China in the future, and has broad development prospects.

4   Problems and Solutions of Nuclear District Heating

Based on the above analysis of the advantages of nuclear district heating, nuclear district heating is an effective means to achieve green development and efficient operation, and has a good development prospect. However, the progress of nuclear heating with many advantages is very slow, and there are many difficulties in its application in China at present. Through the study of the domestic status quo, this paper discusses the specific problems existing in the field of nuclear district heating in China, and draws lessons from foreign experience, puts forward practical and feasible solutions to promote the clean heating work in China and promote the popularization and application of nuclear district heating.

4.1   Selection of Reactor Type Scheme

In terms of reactor type selection for district heating, the heat sources of nuclear district heating in Eastern European countries are large-scale commercial reactors with mature technology, which have a large heating range, form economies of scale, and adapt to the cold climate and intensive heating demand in Eastern Europe. However, the application of large-scale reactors in regional heating in China is very limited, mainly for two reasons: first, China's nuclear safety regulations require that the radius of the planned restricted area of large-scale nuclear power units should be at least 5000 m. When nuclear power plants are used for heating urban residents, they should be at least 10 km away from the development boundary of cities and towns with a population of more than 100000 and at least 25 km away from the development boundary of cities and towns with a population of more than 1 million, Thus, the number of heating residents around large nuclear power plants is limited; Secondly, in terms of the scale of heat sources, the current power of China's main heating units is between 200 MW and 300 MW, and the power of large-scale commercial reactors is about 1000 MW, which is too large for regional heating capacity.

In recent years, the concept of small reactor has been put forward internationally. The small reactor is a 330 MW integrated pressurized water reactor developed by KAERI (Korea Atomic Energy Research Institute) together with domestic users and suppliers for power generation, seawater desalination or district heating [22, 23]. Different from the traditional large-scale pressurized water reactor, the small-scale reactor installs the core, steam generator, pressurizer, control element drive mechanism, main coolant pump and other main components in a steel pressure vessel. This innovative and progressiveness overall arrangement enhances the safety, reliability, performance and operability of small reactors, and has been fully proved in the commercial operation of foreign power reactors.

Although small reactors lack the economies of scale of large reactors, due to their system simplification, reactor system modularization, component standardization, factory manufacturing and easy on-site installation, the installation cost of large pipelines

and valves is reduced, and their small floor space also reduces the construction cost and improves the economy of the reactor to a certain extent. On the other hand, small-scale reactors have small thermal energy storage and less decay heat after shutdown. Moreover, passive safety systems are widely used, with high safety performance. Theoretically, they can be built around densely populated areas such as large cities. Small-scale reactors are more suitable as heating sources in urban areas.

The modular small reactor ACP100, modular high temperature gas cooled reactor HTP-PM and 200 MW low temperature heating reactor currently being developed in China belong to the category of small reactors and have the potential to be applied to urban heating. As for the heating mode, the longest heating period in northern cities of China is only 6 months. If the simple heating mode is adopted, the economic competitiveness is poor, and the domestic thermal power cogeneration mode is more suitable. Therefore, it is relatively reasonable for China's nuclear power district heating to adopt the scheme of small-scale reactor cogeneration with high safety.

4.2   Construction of District Heating Network

At present, nuclear power plants are mainly used for power production. For safety reasons, their location is far away from residential areas, so they need a long district heating network. China has not yet developed a heating network, but there is a mature heating network in the cold northern region of Europe. Considering the climate, population density, energy price and other factors, the proportion of citizens for district heating increases from south to north, and the heating network is mostly distributed in areas with high population density and low energy availability.

The operation mode of heat supply network is similar to that of power grid. A large thermal transmission line is transmitted to the secondary pipeline and finally to the local distribution network at the customer's end. The district heating network sector benefits from improved communication, control and regulatory systems. For example, sensors that detect leaks or hot spots can relay this information to the control room to improve maintenance. However, the construction cost of heat transmission trunk line is high, which will determine the economic feasibility of the project. However, with the rise of energy prices, the demand for heating in the region is also rising. The combination of cogeneration plant and district heating is an efficient heating method, which can keep the heating price of users at a reasonable level.

According to the characteristics of heat supply areas in China, the cold regions in the north have a large population and dense urban buildings, which are suitable for the development of central district heating. The heating network can start from small and scattered, and then gradually grow and connect with each other over time, thus avoiding the need for a large amount of initial investment.

4.3   Operation and Coupling of Nuclear Power Plant

The nuclear district heating technology has not yet had mature commercial operation experience in China. The coupling technology between the reactor type itself and the heat supply network is one of the difficulties. The main challenge is to prevent radioactive substances from entering the heat supply network. Referring to the experience of foreign

district heating, the nuclear power plant can be coupled to the district heating system by referring to the mode of cogeneration power plant. First, multiple closed loops are set between the primary loop of the reactor core and the end user to prevent the risk of radioactive contamination. Secondly, a specific loop is set to separate the user from the main heat transfer loop. Thirdly, an isolation valve is set on the main transmission circuit to prevent any material exchange between the reactor and the local power distribution network. Finally, ensure that the water pressure in the main transmission circuit is higher than the steam pressure, so as to prevent the secondary steam from entering the heat transmission circuit in case of accidental leakage of the hot water heat exchanger pipe.

By taking the above defensive measures, even if the reactor steam generator and water heat exchanger leak at the same time, the reliable operation of the nuclear power district heating system can be ensured.

4.4   Safety of Nuclear Power Plant

Although the safety of nuclear district heating is basically the same as that of nuclear facilities, there are some specific safety problems in the coupling between nuclear power plants and district heating systems. In the cogeneration mode, unlike nuclear power generation, which uses seawater, rivers or cooling towers as cooling, the heat transfer network system also plays a major role in cooling. Any failure, such as pipe rupture or heat exchanger defect, will affect the cooling performance of nuclear components. On the other hand, due to its huge heat capacity, the heat transmission line also provides an alternative radiator for the nuclear power plant. In this sense, the district heating cogeneration facility can even improve the safety level of the nuclear power plant. In addition, small reactors are in the initial stage in China and around the world. Although most of the current small reactor schemes apply the passive concept, simplified system design and mature equipment, and the theoretical core melting probability is very low, the safety still needs to be verified by demonstration projects.

At present, Liaoning, Shandong and other provinces in China have begun to build large-scale nuclear power projects, which can be used as the transition of small-scale reactor district heating. Nuclear power plants under construction or to be built in the north can be selected as the pilot of cogeneration, and relevant mature technologies in the world can be used for reference to heat the living quarters in the plant area or small towns around the power station. Through the pilot, the safety of the coupling technology between the nuclear power plant and the thermal pipe network can be verified, and the nuclear engineering experience can be accumulated for the subsequent gradual promotion of the coastal small reactor project.

4.5   Economy of Nuclear Power Plant

According to relevant foreign studies, the total cost of district heating system can be divided into design cost, investment cost and operation cost [24]. Design cost refers to the expenses that must be paid before the construction stage, such as market research, safety analysis, public acceptance survey, etc. The investment cost refers to the construction and installation cost of infrastructure, such as the transformation of the secondary circuit of the power plant, the laying of the heat transmission pipeline, the connection

of the distribution network, etc. Operation and maintenance costs refer to the expenses related to the operation and maintenance of the project, such as the salaries of operation and maintenance personnel, maintenance expenses, etc. Different from nuclear power generation, district heating needs to lay a thermal network, so the construction cost of thermal transmission pipeline is a part that needs to be paid attention to in the future, and the economic benefit can be improved by controlling its cost. At the same time, the preliminary planning and design should be connected and coordinated with the built heating pipelines to lay the foundation for the systematic and large-scale development of the municipal heating network and improve social benefits to a certain extent.

The nuclear district heating technology has little commercial operation experience in China. At present, there are no relevant regulations and technical regulations. If the technical specifications of nuclear power generation reactor are simply applied, it will have an impact on the economy. Relevant departments can improve the laws, regulations and standard system of nuclear heating reactors through scientific evaluation of small-scale reactor demonstration projects, large-scale reactor cogeneration, large-scale nuclear power generation and other projects. In addition, compared with large reactors, if small reactors are used for district heating, the unit construction cost will rise due to the decline of reactor scale, and the economy will face greater challenges. Therefore, in the early stage of the development of nuclear district heating, it needs the strong support of the state and the government to increase subsidies, so as to make nuclear district heating competitive in the market.

5 Conclusions

As a safe and efficient clean energy, nuclear energy has multiple advantages of low-carbon and clean heating, simple system and high energy utilization rate, which can effectively alleviate the increasingly severe atmospheric environment problems caused by the burning of fossil energy. Exploring nuclear regional heating is of great significance for the sustainable development of central cities in North China's heating regions. From the large number of operating experience of nuclear heating units in the world, nuclear district heating, especially cogeneration, is technically mature and safe. Therefore, China has the conditions and technologies for urban nuclear district heating, which can be transformed into scientific and technological achievements suitable for domestic development on the basis of existing nuclear technology and international experience. Nuclear district heating has broad development prospects.

The small-scale reactor under development in China has the characteristics of systematic modularization and small scale. It is likely to be arranged around large cities as a regional heating source. It is a promising heating reactor type. The scheme of small-scale reactor cogeneration for nuclear district heating in China is relatively reasonable, but it still faces great challenges in terms of safety, economy and reliability, which brings difficulties to the application of nuclear district heating.

In order to effectively deal with the difficulties faced by the development of small-scale reactor combined heat and power supply and promote the application and popularization of nuclear heating, this paper puts forward practical suggestions: a) reasonably plan the heating pipeline according to the needs of users, change from small scattered

to interconnected, and gradually improve the construction of regional heating network; b) The multi loop loop circuit is designed to realize the coupling between the nuclear reactor and the heat supply network and improve the reliability of the operation of the nuclear power plant; c) Select large-scale nuclear power projects as the pilot of cogeneration, gradually promote the small reactor type heat supply project, accumulate engineering experience, and improve the safety of nuclear power plants; d) Select reasonable pipeline materials and laying methods, control the cost of thermal transport pipelines, and improve the economy of nuclear power district heating system. Through the above measures, promote the popularization and application of nuclear district heating, and realize low-carbon economy and green sustainable development.

References

1. Zhang, Z.: Development and application of urban nuclear heating. In: Proceedings of the 2019 Symposium on Heating Engineering Construction and Efficient Operation (Part 2) (2019)
2. China Nuclear Energy Industry Association: National nuclear power operation from January to June 2022 http://www.china-nea.cn/site/content/41232.html
3. Dong, Z., Pan, Y.: A lumped-parameter dynamical model of a nuclear heating reactor cogeneration plant. Energy **145**, 638–656 (2018)
4. Wahlroos, M., Pärssinen, M., Manner, J., et al.: Utilizing data center waste heat in district heating–Impacts on energy efficiency and prospects for low-temperature district heating networks. Energy **140**, 1228–1238 (2017)
5. Leurent, M., Da Costa, P., Jasserand, F., et al.: Cost and climate savings through nuclear district heating in a French urban area. Energy Policy **115**, 616–630 (2018)
6. Rämä, M., Leurent, M., de Lavergne, J.G.D.: Flexible nuclear co-generation plant combined with district heating and a large-scale heat storage. Energy **193**, 116728 (2020)
7. Persson, U., Münster, M.: Current and future prospects for heat recovery from waste in European district heating systems: a literature and data review. Energy **110**, 116–128 (2016)
8. Bach, B., Werling, J., Ommen, T., et al.: Integration of large-scale heat pumps in the district heating systems of Greater Copenhagen. Energy **107**, 321–334 (2016)
9. Värri, K., Syri, S.: The possible role of modular nuclear reactors in district heating: case Helsinki region. Energies **12**(11), 2195 (2019)
10. Khosravi, A., Olkkonen, V., Farsaei, A., et al.: Replacing hard coal with wind and nuclear power in Finland-impacts on electricity and district heating markets. Energy, 117884 (2020)
11. Safa, H.: Heat recovery from nuclear power plants. J. Electr. Power Energy Syst. **42**, 553–559 (2012)
12. IAEA : The database on nuclear power reactors, 02 April 2020. https://pris.iaea.org/pris/
13. Leurent, M., Da Costa, P., Rämä, M., et al.: Cost-benefit analysis of district heating systems using heat from nuclear plants in seven European countries. Energy **149**, 454–472 (2018)
14. Zhang, Y., Zheng, W., Dong, D.: Historical review and Prospect of nuclear heating reactor technology development in China. J. Tsinghua Univ. **40**(S3), 192–196 (2000)
15. You, Z.: Birth of the first integrated shell type low temperature nuclear heating reactor. Science **68**(5), 39–44 (2016)
16. Zuo, Z.: Development history and advantages of urban nuclear heating. Res. Urban Constr. Theor. (electronic version) **10**, 131 (2018)
17. Chen, H., Xiang, Y.: A new star of nuclear heating – introduction to pool type low temperature reactor. District Heating **1**, 19–23 (2018)
18. Carlsson, J., Shropshire, D.E., van Heek, A., et al.: Economic viability of small nuclear reactors in future European cogeneration markets. Energy Policy **43**, 396–406 (2012)

19. Wang, H.: Opportunities and challenges faced by nuclear power district heating in China. Energy Energy Conserv. **4**, 36–38 (2013)
20. Unternährer, J., Moret, S., Joost, S., et al.: Spatial clustering for district heating integration in urban energy systems: application to geothermal energy. Appl. Energy **190**, 749–763 (2017)
21. Wang, N.: Low temperature nuclear heating reactor: alternative to coal-fired boiler. China Nuclear Industr. **7**, 24–24 (2017)
22. International Atomic Energy Agency: Status of Design Concepts of Nuclear Desalination Plants, IAEA-TECDOC-1326, IAEA, Vienna (2002)
23. International Atomic Energy Agency: Safety Aspects of Nuclear Plants Coupled with Seawater Desalination Units, IAEA-TECDOC-1235, IAEA, Vienna (2001)
24. Jasserand, F., de Lavergne, J.G.D.: Initial economic appraisal of nuclear district heating in France. In: GLOBAL 2015–21st International Conference & Exhibition: "Nuclear Fuel Cycle for a Low-Carbon Future" (2015).

Application of MC-MC Coupled Method in Neutron Shielding Analysis of Reactor Pit in Reactor Building

Guanghao Zeng[✉], Qianqian Huang, Shouhai Yang, Yonghai Zhou, and Jun Xiong

Shenzhen CGN Engineering Design Co., Ltd., Shenzhen, Guangdong, China
15820586851@163.com

Abstract. As one of the areas with highest radiation risk in nuclear power plant with neutron and gamma ray radiation emitted from the reactor core, the reactor pit in reactor building has great radiation impact on personnel radiation safety by neutron. In order to further improve the shielding design effort of reactor pit, the MC-MC coupled method is developed. By applying the MCNP code and SuperMC code, the variance of the effective dose rate and thermal neutron flux inside the reactor pit is lower than 5% by consuming 6.7 h. The result shows that the MC-MC coupled method can effectively solve neutron shielding problem in large scale or in complex space.

Keywords: Neutron design · Reactor pit · Monte carlo · MCNP · MC-MC coupled method

1 Introduction

The reactor pit in reactor building, as one of the area with highest radiation risk of neutron radiation in reactor building, is a neutron shielding design object with main focus [1, 2] Accurate neutron shielding analysis is carried out in order to minimize the neutron radiation risk and meet the requirements for personnel access to reactor pit. Hence, in order to analyze neutron shielding design problem of large-scale model accurately, a new analysis methodology that meets shielding design requirements should be established.

2 Development of Neutron Shielding Design for Reactor Pit

2.1 Methodology Development of Neutron Shielding Analysis

At present, two neutron shielding analysis method is widely used in the field of nuclear engineering: the deterministic method represented by the discrete ordinate method and the Monte Carlo (MC) non-deterministic method [3]. The discrete ordinate method is mostly used to deal with engineering problems that can be simplified to one-dimensional or two-dimensional problem, while Monte Carlo method is for stochastic simulation of neutron behavior by computer. Although Monte Carlo method can simulate complex

geometry with high accuracy, slow convergence speed greatly influences its engineering application.

Due to the structural complexity and large-scale characteristics in nuclear power plant (NPP), neutron shielding problems with large and complex geometric is usually solved by coupled multi-dimensional calculation method [4–6]. Therefore, the MC-MC coupled method, which can decompose one model into continuous parts, is established to solve this type of problem. The MC-MC coupled method not only has high reliability on calculation results, but also has low accuracy loss during continuous calculation. Hence, MC-MC coupled method has been widely used to solve neutron shielding problem of large nuclear facilities due to the above advantages.

2.2 Development of Neutron Shielding in Reactor Pit

In order to shield the neutron generated by the reactor core, different NPPs adopt different structural design and shielding design to establish a sufficient shielding effect.

As shown in Fig. 1, the reactor pit and its passage in EPR NPP is built up by concrete wall with a watertight door at the egress of the reactor pit passage. Since the egress is on the second floor above the reactor pit passage, the access process of personnel includes stair climbing activity.
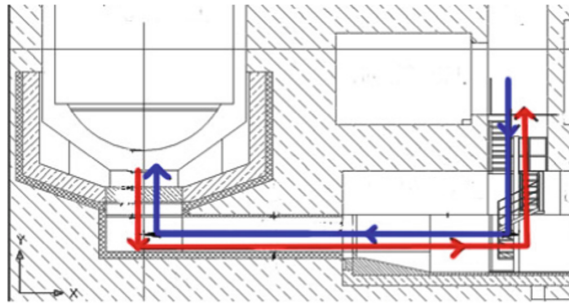
Fig. 1. Access Process of Reactor Pit in EPR NPP

Similar to EPR NPP, the access process in AP1000 NPP which is shown in Fig. 2 also includes stair climbing.

As for CPR NPP, an iron-made shielding door with 7 cm thick is installed at the egress of the reactor pit passage. Furthermore, unlike the reactor pit in other types of NPP, the egress and the passage of CPR is on the same floor (Fig. 3).

For the reactor pit in HPR1000 NPP, the design experience of EPR has been referred and a airtight door instead of watertight door is installed at the egress of the reactor pit passage (Fig. 4).
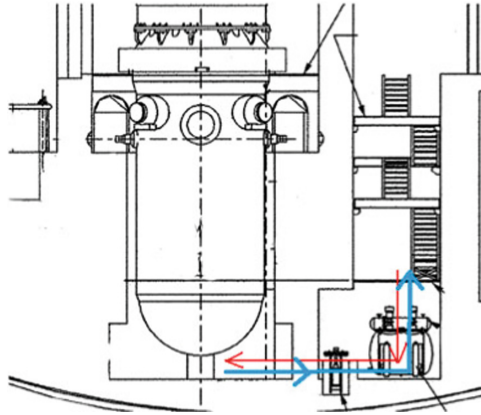
Fig. 2. Access Process of Reactor Pit in AP1000 NPP
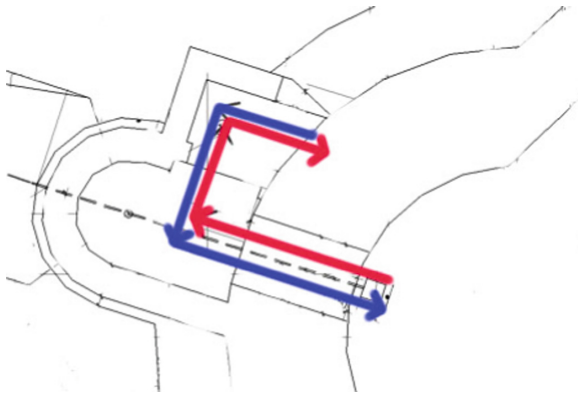
Fig. 3. Access Process of Reactor Pit in CPR NPP
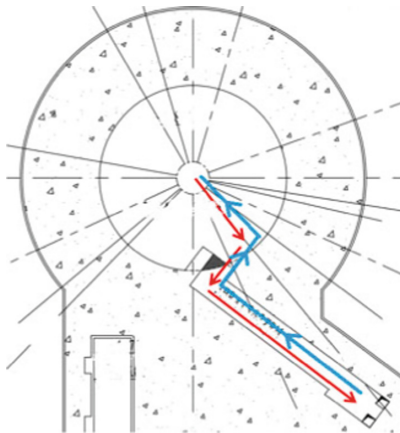
Fig. 4. Access Process of Reactor Pit in HPR1000 NPP

3 Establishment of MC-MC Coupled Method

3.1 Process of MC-MC Coupled Method

The current simulation program capable with MC-MC coupled method are MCNP code and SuperMC code developed based on Monte Carlo algorithm. These two programs can not only read and write standard surface source, but can also record accurately the particle trajectory information passing through the continuous surface as source distribution input for the continuous calculation. The MC-MC coupled method can greatly reduce calculation time and save computing hardware on the premise of ensuring result accuracy. Hence, these two programs are both suitable for solving large-scale neutron shielding problems such as reactor pit in NPP. The process of MC-MC coupled method is shown in Fig. 5.
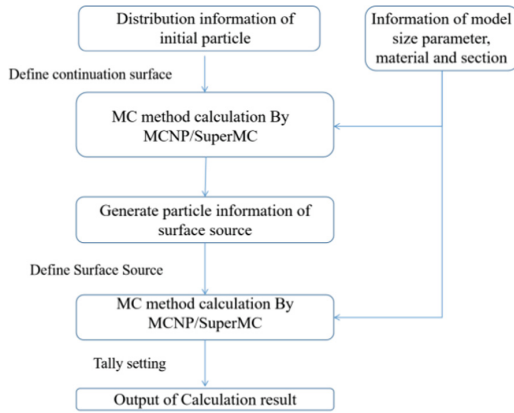
Fig. 5. The Process of MC-MC Coupled Method

3.2 Selection Principle of Continuation Surface

The reliability of the calculation result by MCNP or SuperMC code depends on its statistical error. In addition, as the statistical error is transitive in the process of MC-MC coupled method, the statistical error of the surface flux density should be controlled to ensure that the influence of statistical error transfer is acceptable on the reliability of the results when selecting the continuation surface.

The integral calculation is taken as an example to briefly describe the calculation process of the Monte Carlo sampling calculation method. The integral to be computed is treated as the mathematical expectation of a random variable $f(x)$ obeying the distribution density function $p(x)$:

$$F = \int f(x)dx \qquad (1)$$

With

$$\int p(x)dx = 1 \tag{2}$$

Through sampling experiments, sub-samples $x_1, x_2 \ldots x_n$ can be drawn from the distribution density function $p(x)$, and the arithmetic mean $\bar{f}$ of the corresponding random variables $f(x_i)$ is the Monte Carlo estimation of the integral value F of the values:

$$\bar{f} = \frac{1}{n} \sum_{i=1}^{n} f(x_i) \tag{3}$$

The unbiased estimate of statistical error σ^2 is calculated by formula (4):

$$\sigma^2 = \frac{1}{n} \sum_{i=1}^{n} [f(x_i) - \bar{f})]^2 \tag{4}$$

As statistical error is transitive in formula (3), the total value of the statistical error after n times of consecutive calculation is approximately as formula (5):

$$\sigma = \prod_{i=1}^{n} (1 + \sigma_i) - 1 \approx \sigma_1 + \sigma_2 + \cdots + \sigma_n \tag{5}$$

Hence, the calculation results by MCNP code or SuperMC code is reliable only when the statistical error of calculation result is within 10%. According to the above analysis, for a two-step connection problem, the area with the statistical error of the surface flux density less than 5% should be selected as the spatial connection surface to ensure that the final result of the connection calculation is reliable.

4   Application of MC-MC Coupled Method for Reactor Pit Shielding Design

Take one Chinese NPP as an example. By applying MC-MC coupled method, the neutron shielding design problem of reactor pit can be evaluated accurately with less time consumed.

The general shielding design objectives for the NPP during normal operation is to ensure that the radiation exposure to personnel is ALARP and within the limits of radiation regulations. As the neutron radiation emitted from the reactor core is one of the predominant contributors to the reactor pit and its passage, specific shielding design objectives of reactor pit egress are as follows:

1. the area dose rate should not exceed 1 mSv/h;
2. the thermal neutron flux should not exceed $1.00E + 05$ n/(cm^2.s).

4.1   Calculation Assumption and Modeling

As the reactor pit is complex and is in large scale, the MC-MC coupled method is suitable to solve the neutron shielding problem of this area. Based on conservative assumption, the neutron passing through the continuation surface are assumed to be all reflected into the reactor pit passage. By referring the actual structure of the reactor pit, the calculation model is established in Fig. 6 by SuperMC code.
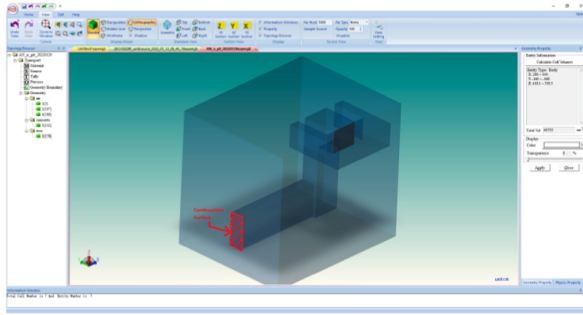
Fig. 6. Three-Dimensional View of Reactor Pit Passage Model

4.2 Calculation Process and Result Analysis

Based on the calculation assumption and modeling analysis in Sect. 4.1, the environmental effective dose rate and neutron flux are analyzed by MC-MC coupled method. The advantage of the methodology would be found through the calculation process.

A) Neutron Energy Distribution by First Continuation Calculation
As the continuation surface is selected in the red flame in Fig. 6, by applying MCNP code, the neutron energy distribution on continuation surface is calculated and is shown in Fig. 7.
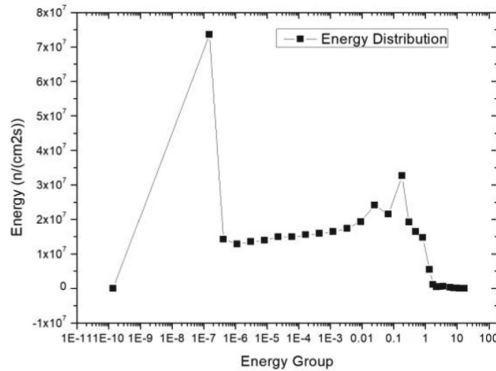
Fig. 7. Neutron Energy on Continuation Surface

B) Effective Dose Rate by Secondary Continuation Calculation
The environmental effective dose rate and neutron flux in reactor pit passage are analyzed by applying the neutron energy distribution on continuation surface in the secondary continuation calculation as calculation input. Neutron particle with a number of 1.00E + 06 is simulated in calculation with about 101 h consumed.

As shown in Fig. 8 and Fig. 9, the effective dose rate and neutron flux at the egress of reactor pit could not meet the radiation protection requirement if no shielding door is
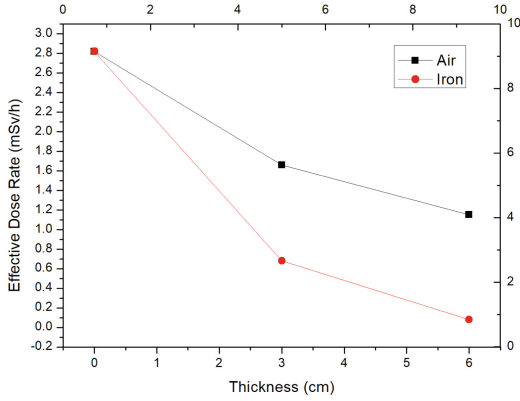
Fig. 8. Effective Dose Rate at the Egress of Reactor Pit
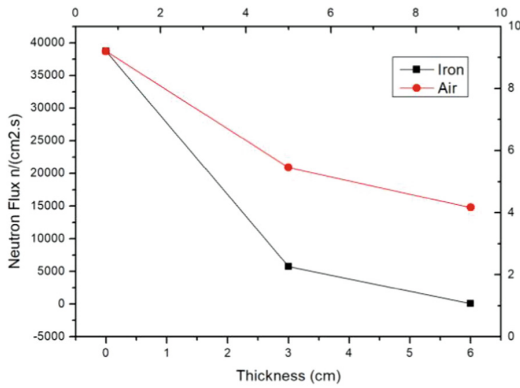
Fig. 9. Neutron Flux at the Egress of Reactor Pit

installed. An iron shielding door with thickness of 3 cm at the egress of reactor pit could ensure that the effective dose rate and neutron flux meets the design objective.

C) Three-Dimensional View of Environmental Effective Dose Rate and Neutron Flux

In order to evaluate the three-dimensional dose rate field and neutron flux field as well as for the process acceleration, SuperMC code is applied to optimize the calculation.

SuperMC code is a computer aided design (CAD)-based Monte Carlo program for integrated simulation of nuclear system developed by Chinese FDS team [7–9]. Compared with MCNP code, SuperMC code can generate global mesh weight window to speed up the three dimensional dose rate field calculation, which is practical to analyze the environmental effective dose rate variance tendency [10].

By using 64 CPU in parallel calculation, the global mesh weight window is generated with 1.0E + 13 neutron after consuming 2.8 h. The effective dose rate and neutron flux are then calculated with the help of generated global mesh weight window by consuming 6.8 h with 1.00E + 09 neutron. The three-dimensional view of neutron effective dose rate field and neutron flux field are shown in Fig. 10, Fig. 11 and Fig. 13.
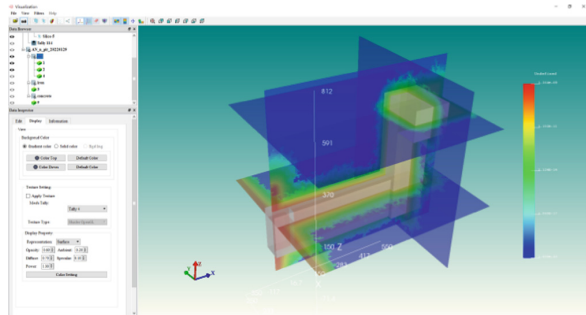
Fig. 10. Effective Dose Rate Field of Reactor Pit Passage Contributed by Neutron
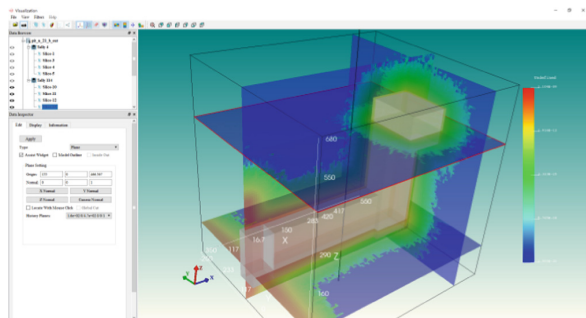
Fig. 11. Effective Dose Rate Field of Reactor Pit Passage Contributed by Secondary Photon

As shown in Fig. 12, the effective dose rate is calculated alongside the exit direction of reactor pit egress. As the origin point is set at the inner surface of shielding door, the neutron area dose rate decrease to 1 mSv/h at the reactor pit egress shielded by the iron in the airtight door.

Meanwhile, the three-dimensional view of neutron flux is shown in Fig. 13. Similar to the variance tendency of effective dose rate, the neutron flux decrease to 1.00E + 05 n/(cm^2.s) at the reactor pit egress which is presented in Fig. 14.
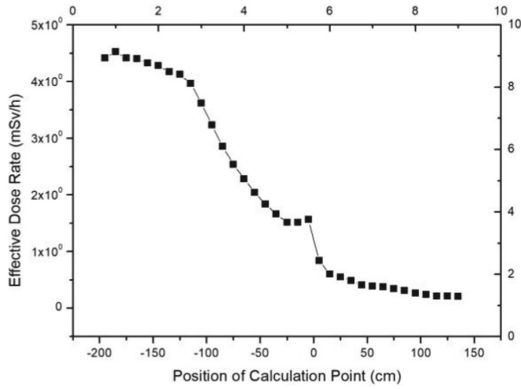
Fig. 12. Effective Dose Rate Variance Tendency of Reactor Pit Contributed by Neutron
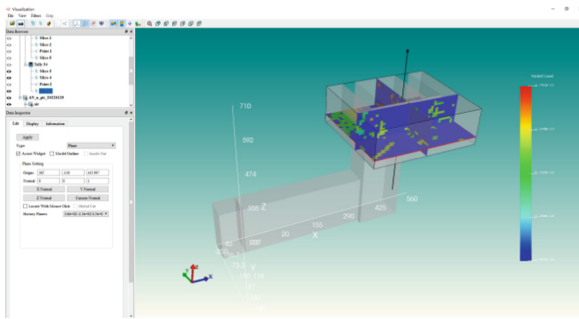
Fig. 13. Neutron Flux Field of Reactor Pit
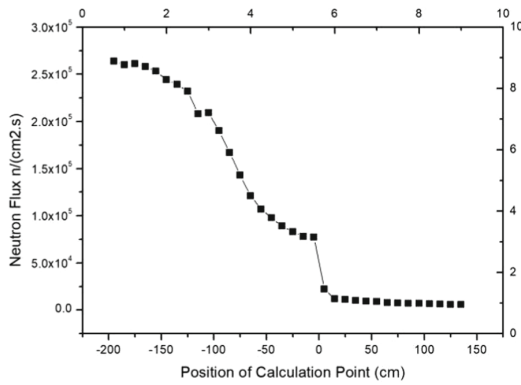
Fig. 14. Neutron Flux Variance Tendency of Reactor Pit

5   Conclusion

By applying the MC-MC coupled method, the neutron shielding problem in large scale can be effectively analyzed. In addition, the superiority of this methodology is proved in the application of reactor pit neutron shielding analysis. Furthermore, by applying SuperMC code, the calculation process of neutron shielding problem in large-scale model can be further optimized by ensuring the calculation accuracy with less time consumed.

References

1. Liu, G.: Radiation flux calculation of reactor pit bottom in Qinshan phase II nuclear power project. Nucl. Power Eng. **19**(4), 375–379 (1998)
2. Brovchenko, M., Dechenaux, B., Burn, K.W., et al.: Neutron-gamma flux and dose calculations in a Pressurized Water Reactor (PWR). EPJ Web Conf. EDP Sci. **153**, 05008 (2017)
3. Piotrowski, T., Tefelski, D., Polański, A., Skubalski, J.: Monte Carlo simulations for optimization of neutron shielding concrete. Open Eng. **2**(2),(2012). https://doi.org/10.2478/s13531-011-0063-0
4. Han, J., Chen, Y., Yuan, L., et al.: Particle fluence rate calculation of reactor pit based on MC-SN bidirectional coupled method. Atomic Energy Sci. Technol. **48**(9), 1621 (2014)
5. Wu, Y.: Multifunctional neutronics calculation methodology and program for nuclear design and radiation safety evaluation. Fusion Sci. Technol. **74**(4), 321–329 (2018)
6. Chen, Z.P., Zheng, H.Q., Sun, G.Y., et al.: Preliminary study on CAD-based method of characteristics for neutron transport calculation. Chin. Phys. C **38**(5), 08201 (2014)
7. Wu, Y., Song, J., Zheng, H., et al.: CAD-based Monte-Carlo program for integrated simulation of nuclear system SuperMC. Ann. Nucl. Energy **82**, 161–168 (2015)
8. Song, J., Sun, G., Chen, Z., et al.: Benchmarking of CAD-based SuperMC with ITER benchmark model. Fusion Eng. Des. **89**(11), 2499–2503 (2014)
9. Jing, S., Liqin, H., Pengcheng, L., et al.: Monte Carlo Simulation Software SuperMC 2.3 for Fusion and Fission Application.
10. He, P., Wu, B., Hao, L., et al.: Performance study of global weight window generator based on particle density uniformity. EPJ Web Conf. EDP Sci. **247**, 18005 (2021)

Study on the Effects from Spacer Wires on Coolant Flow Within a Fuel Assembly Used in the CiADS Core

Yunxiang Li[1], Lu Meng[1], Song Li[1], Bo Liu[1], Disi Wang[1], Youpeng Zhang[1(✉)], Lu Zhang[2], and Wei Jiang[2]

[1] Institute of Modern Physics, Fudan University, Shanghai 200433, China
`zhangyp@fudan.edu.cn`

[2] Institute of Modern Physics, Chinese Academy of Sciences, Lanzhou 730000, China

Abstract. Spacer wires are frequently applied as the positioning components of fuel bundles in lead-based fast reactor fuel assemblies. It is extremely important to carry out the research of the impacts from spacer wires on coolant flow within fuel assemblies, and therefore the safety performances of reactor core. In this paper, the open source CFD calculation software OpenFOAM was adopted to perform the refined numerical simulation on the multi-pitch assembly model of 61 bundles and analyze the distribution of flow characteristics such as pressure, velocity, and temperature. The results show that: there is a pressure difference on both sides of the wires, which may cause the coolant to mix laterally; the mixing effect incurred by the wires may cause the uneven distribution of coolant velocity. There are obvious high-speed and low-speed zones, and the high-speed zone is located at the same position as the low-pressure zone. Due to the high flow rate in the peripheral sub-channel, the coolant temperature is lower. The maximum temperature difference at the outlet of the fuel assembly can reach 20K, which may cause local overheating and therefore cladding rupture under accidental conditions. The simulation can provide a reference for the correction of the calculation results of the 1D single-channel program and lay the foundation for the development of the subsequent two-phase flow model for fuel assemblies containing wire spacers.

Keywords: Spacer Wire · CiADS · Fuel Assembly · OpenFOAM · CFD Simulations

1 Introduction

Nuclear energy is a clean and efficient energy source that can also facilitate the reduction of carbon emissions for power generation in countries worldwide, thereby providing essential solutions toward sustainable human development. In 2002, the American Nuclear Society proposed six Generation IV advanced nuclear reactor types [1]. Compared with other fast reactors, the structure of lead-cooled fast reactors has been significantly simplified [2]. Moreover, many countries are trying to implement lead-cooled

fast reactors as they have attracted considerable attention due to their good nuclear fuel transmutation capability, excellent economics, and inherent safety [3].

Lead-cooled fast reactors mostly use spacer wires for positioning to maintain the fuel rods at the same pitch. A reasonable thermal-hydraulic design inside the core enables the safe operation of fuel assemblies and other components in a reactor. Therefore, it is imperative to elucidate the flow characteristics of fuel assemblies with spacer wires. The thermal-hydraulic properties of heavy metals greatly differ from those of conventional media; thus, the radiation shielding of lead critically hampers experimental analysis, and the internal flow characteristics cannot be studied using devices such as X-rays [4]. Given this limitation, most previous studies have used numerical simulations to obtain the thermal-hydraulic parameters.

Ahmad performed numerical simulations of a 7-rod bundle assembly and found that the transverse gradient induced by spacer wires exhibited certain periodic pattern among the sub-channels [5]. Gajapathy performed numerical simulations of the flow field inside various rod bundle assemblies containing spacer wires and found that increasing the diameter of the spacer wires while decreasing the pitch increased the friction coefficient and Nussle number [6]. Hamman revealed a 10–15% error in pressure drop calculations compared to empirical formulations; this error was affected by the factors such as turbulence and geometric models [7]. Merzari performed numerical calculations using various RANS models for a 7-rod bundle assembly containing spacer wires and demonstrated that the k–ω SST model better simulated the velocity field near the spacer wires [8]. Zhao performed numerical calculations using OpenFOAM for a single-pitch model of a 7-rod bundle assembly of sodium-cooled and analyzed the distribution of transverse velocities in different gaps [9]. Overall, a significant corpus of previous studies about spacer wires was focused on full-size calculations based on coarser large-size grids. In this way, they determined the outcomes for larger-size models and calculations using commercial software for 7-rod bundle and 19-rod bundle assembly models.

Given the complexity of spacer wires, the effect of multi-pitch axial height, and the subsequent two-phase flow model development, this study investigated the flow characteristics of lead-bismuth coolant in a lead-based fast reactor within a fuel assembly containing spacer wires. Methodologically, we used the open-source OpenFOAM software to refine the calculation of multi-pitch wire-wrapped bundle assemblies in CiADS [10] and provide interface parameters for two-phase flow model development under accident conditions.

2 Models and Methods

2.1 Geometric Model

For advanced reactors with a conventional design of lead/lead-bismuth alloy as coolant, the fuel rods are usually arranged in a triangular fashion to form a hexagonal assembly, as shown in Fig. 1. The sub-channels of the assembly are divided into three types, namely internal, edge, and corner channels.
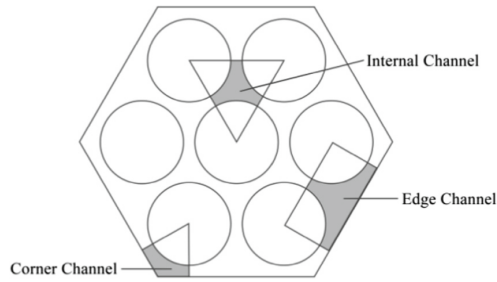
Fig. 1. Sub-channel division method of the fuel assembly

In this study, we referred to the fuel assembly parameters in CiADS [11] for the simulations. The regular hexagonal fuel assembly contained 60 fuel rods and one stainless steel rod located in the center. The stainless-steel rod represented a locking device designed to prevent the assembly from floating in the liquid lead/lead-bismuth alloy. The simulation area was part of the active area of the fuel assembly. The spacer wires were placed in the clockwise direction. The geometric parameters of the fuel assemblies are summarized in Table 1.

Table 1. The geometry parameters of the fuel assembly

Parameter Name	Parameter	Unit
Number of fuel rods	60	Number
Arrangement method	Equilateral triangle	–
Rod length	180	mm
Apothem	61.25	mm
Rod diameter	13.1	mm
Pitch	15.1	mm
Helical pitch	144	mm
Helical wire diameter	2	mm

The spacer wires and fuel rods were aligned tangentially to each other, thus signifying a line contact and forming sharp angles at the contact location where the points and lines affected the quality of the grids. The model simplification used in this study was based on the Natesan [12] approach, as shown in Fig. 2. To this end, the diameters of fuel rods and spacer wires were kept constant, and indent spacer wires were placed toward the center of fuel rods by 0.1 mm. To improve the quality of the generated grids, a 0.25 mm chamfering process was performed at the location where the spacer wires and fuel rods were in contact. Figure 3 shows the geometric model of the fuel assembly.
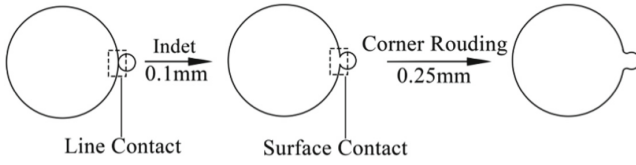
Fig. 2. Simplified model approach

(a)   (b)
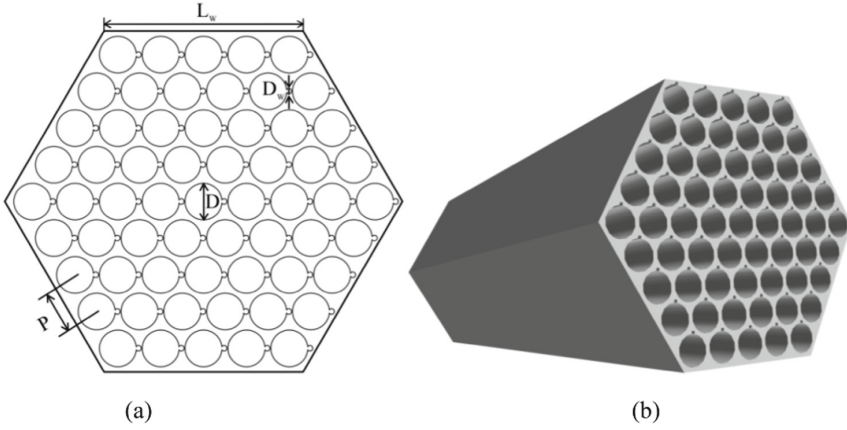
Fig. 3. 61 wire-wrapped rod bundle assembly (a) top view (b) 3D view

2.2 Grid Division

It is challenging to delineate the structured grids for complex geometric features, such as many large-curvature spacer wire surfaces in the fuel assembly. This simulation was used to delineate the polyhedral grids for spacer wires. The grid encryption process is described in Table 2, while the grid division in the Z-plane is shown in Fig. 4. The quality of grids was evaluated by the "checkMesh" method in OpenFOAM. The evaluation demonstrated that the grids satisfied the computational requirements.

Table 2. Method of grid encryption

	Number of boundary layer and grid layers	Total thickness of prismatic layer	Grid growth rate	Expected y+
The area near the wall	4 layers	0.03 mm	1.2	<1
The area near the assembly box	4 layers	0.09 mm	1.2	<1
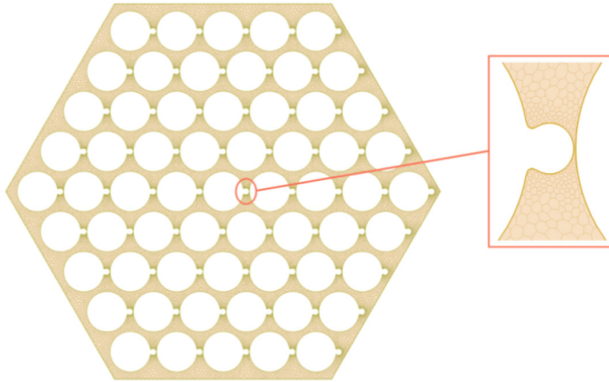
Fig. 4. Section of grid in Z direction

2.3   Boundary Condition Setting

For numerical simulation problems, suitable boundary conditions must be provided for each boundary, according to the actual working conditions. Table 3 lists the established boundary conditions based on the CiADS [10, 11] method.

Table 3. Boundary conditions for the fuel assembly

Boundary	Boundary conditions
Inlet	Average temperature of the inlet is 553.15K The mass flow rate of the inlet is 17.07 kg/s
Outlet	Pressure outlet with a gauge pressure of 0 Pa [13]
60 fuel rods	The line power density [11] is set in the way shown in Fig. 5
One stainless steel rod	Adiabatic and no-slip surface
Spacer wires	Adiabatic and no-slip surface [14]
Assembly box	Adiabatic and no-slip surface

2.4   Coolant Thermal Physical Parameters and Turbulence Model

Due to the special thermal properties of lead-bismuth, it will show different phenomena from the conventional coolant in the calculation process, and according to the recommendation of OECD/NEA [15], the expression of the thermal property parameter was selected as follows.

Density, kg/m^3:

$$\rho_{\text{LBE}} = 11096 - 1.3236T \tag{1}$$
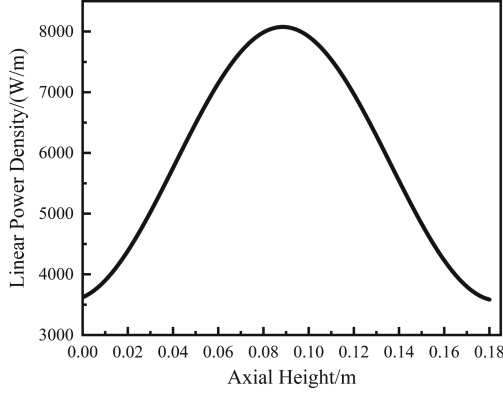
Fig. 5. Axial linear power density distribution of fuel rods

Constant pressure specific heat capacity, J/(kg · K):

$$C_{p,\text{LBE}} = 159.0 - 0.0272T + 7.12 \times 10^{-6}T^2 \tag{2}$$

Power viscosity, Pa · s:

$$\mu_{\text{LBE}} = 0.00456 - 7.03 \times 10^{-6}T + 3.61 \times 10^{-9}T^2 \tag{3}$$

Thermal conductivity, W/(m · K):

$$\lambda_{\text{LBE}} = 3.61 + 1.517 \times 10^{-2}T - 1.741 \times 10^{-6}T^2 \tag{4}$$

The comparison with the LES calculation results of Merzari [8] shows that the k-ω SST model calculations agree better compared to the k-ε turbulence model, so the k-ω SST turbulence model was used in this calculation. The k-ω SST turbulence model can be described by the following five equations:

$$\frac{D(\rho\omega)}{Dt} = \frac{\partial}{\partial x_i}\left((\mu + \sigma_k\mu_t)\frac{\partial k}{\partial x_i}\right) + G_\omega - \rho\beta^*\omega k \tag{5}$$

$$\frac{D(\rho\omega)}{Dt} = \frac{\partial}{\partial x_i}\left((\mu + \sigma_\omega\mu_t)\frac{\partial k}{\partial x_i}\right) + G_k - \rho\beta\omega^2 + 2(1 - F_1)\rho\sigma_{\omega^2}\frac{1}{\omega}\frac{\partial k}{\partial x_i}\frac{\partial \omega}{\partial x_i} \tag{6}$$

$$G_k = \rho\gamma S^2 - \frac{2}{3}\rho k\frac{\partial U_i}{\partial x_i} - \frac{2}{3}\mu_t\left(\frac{\partial U_i}{\partial x_i}\right)^2 \tag{7}$$

$$G_\omega = \rho\gamma\left(S^2 - \frac{2}{3}\left(\frac{\partial U_i}{\partial x_i}\right)^2 - \frac{2}{3}\omega\frac{\partial U_i}{\partial x_i}\right) \tag{8}$$

$$F_1 = \tanh\left(\min\left(\max\left(\frac{\sqrt{k}}{0.09\omega y}, \frac{500v}{\omega y^2}\right), \frac{2k}{y^2 CD_{k\omega}}\right)^4\right) \tag{9}$$

In these equations, ρ is the density (kg/m^3). G_k is the generating term of turbulent kinetic energy k. G_ω is the generating term of the specific dissipation rate ω. t is the time term (s). x is the Cartesian coordinate system direction. μ is the kinetic viscosity (Pa·s). $\mu_t = \rho kT$, and T is the turbulence time scale. The parameters σ_k, σ_{ω^2}, β^*, β are solved by the mixing function. γ is the cross-mixing factor. S is the mode of the mean stress tensor of the fluid. U is the fluid velocity (m/s). y is the distance from the wall. v is the fluid kinematic viscosity. $CD_{k\omega}$ is the term associated with the lateral diffusion term of the fluid.

2.5 Grid Independence Analysis

According to the 61-rod bundle assembly model, grids were classified into three groups with different degrees of sparseness. The grid-independence analysis was carried out by comparing the variation in temperature along the axial direction near the central rod bundle. The number of grids and the calculated y+ for the three cases are summarized in Table 4. As seen, all three cases yielded the average value of y+ less than 1. Figure 6 shows a comparison of the calculated results for the three temperature groups. As observed, the calculated results for the grid number of 16.9 million were very close to the calculated results for the grid number of 26.7 million. Furthermore, the accuracy of the calculation and the length of the calculation time were taken into account, and Case 2 was selected as the grid division scheme for the subsequent calculation.

Table 4. Grids for independence studies

	The number of grids (million)	Min y+	Max y+	Average y+
Case 1	13.1	0.0219	2.3263	0.4517
Case 2	16.9	0.0429	3.7309	0.4736
Case 3	26.7	0.0133	2.0685	0.5047

2.6 Solver Validation

buoyantSimpleFoam is a finite-volume method-based solver for solving the N-S equation for a steady-state compressible Newtonian fluid in OpenFOAM. The SIMPLE/SIMPLEC algorithm was used in this study for the pressure-velocity coupling in this solver. The simulation was validated using the uniform heating of the coolant to evaluate the accuracy of this solver in the simulation of lead-based fast reactors. The calculated results were further compared with those of the experimentally calibrated SACOS-PB sub-channel program [16] under the same conditions. The model geometry parameters used to evaluate the accuracy of the solver were as follows: the fuel rod diameter was 8.2 mm. The pitch was 10.49 mm. The helical wire diameter was 2.2 mm. The
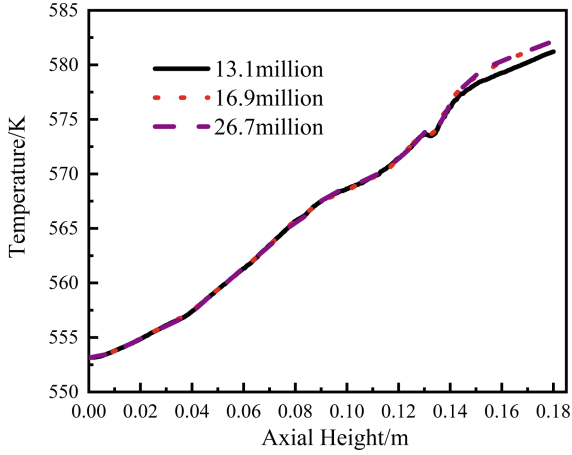
Fig. 6. Grid independence analysis
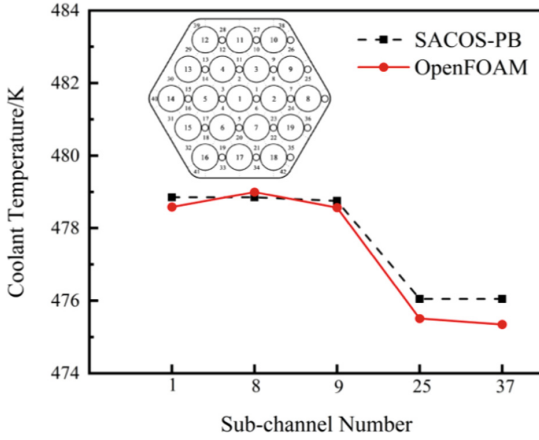
Fig. 7. Coolant temperature distribution at the axial height of 54.6 mm in the active zone

helical pitch was 328 mm. A comparison of the calculated coolant temperature results for an axial height of 54.6 mm in the active zone is shown in Fig. 7.

Figure 7 shows the differences in the coolant temperature within different sub.channels on the same cross.section. As seen, the inner channel coolant temperature was higher than the outer channel coolant temperature. The coolant temperature within different sub.channels on the same cross.section under the same calculation conditions for both programs matched well, with the maximum relative error of <1%. Therefore, the results of OpenFOAM were deemed to be accurate, based on which the additional 61.rod bundle assembly calculations were performed.

3 Results and Discussion

3.1 Pressure Distribution Characteristics

Besides the coolant flow in the sub-channels along the axial direction, a complex transverse flow is also present. The drivers behind the transverse flow can be divided into natural and forced mixing; these transverse effects strengthen the resistance pressure drop of the flow. The cross-sectional pressure distributions at the axial heights of 60, 90, 120, and 150 mm within the 61-rod bundle fuel assembly are shown in Fig. 8, with the arrow direction reflecting the spin-in direction of the spacer wires. The pressure cloud contours at different axial heights exhibited similar distributions, while a clear difference between the high-pressure zone, low-pressure zone, and both sides of the spacer wires was identified. The low-pressure zone was generally distributed upstream of the spacer wires in the spin-in direction and downstream of the high-pressure zone. When the spacer wires rotated past the nearby fuel rods, the pressure inside the gaps between the fuel rod and spacer wires was low. Moreover, a pressure difference between the two sides of the spacer wire was identified.
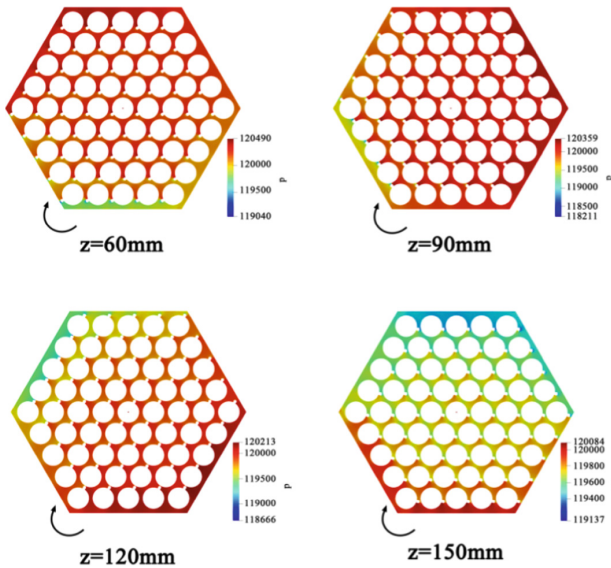
Fig. 8. Pressure distribution at different axial heights

Spacer wires force the coolant to mix, thereby making the transverse pressure distribution uneven. In general, a high-pressure zone is an area with a strong cross-flow effect. The pressure cloud contours for different axial heights revealed that the axial pressure tended to decrease as the Z-axis coordinate increased. Figure 9 shows the pressure cloud contours for each 1/6H interval of the axial height within a pitch. As seen, for each 1/6H increase in the axial height, the direction of the pressure cloud contours was rotated 60° clockwise, and the value of the pressure distribution decreased along the axial fluctuation.
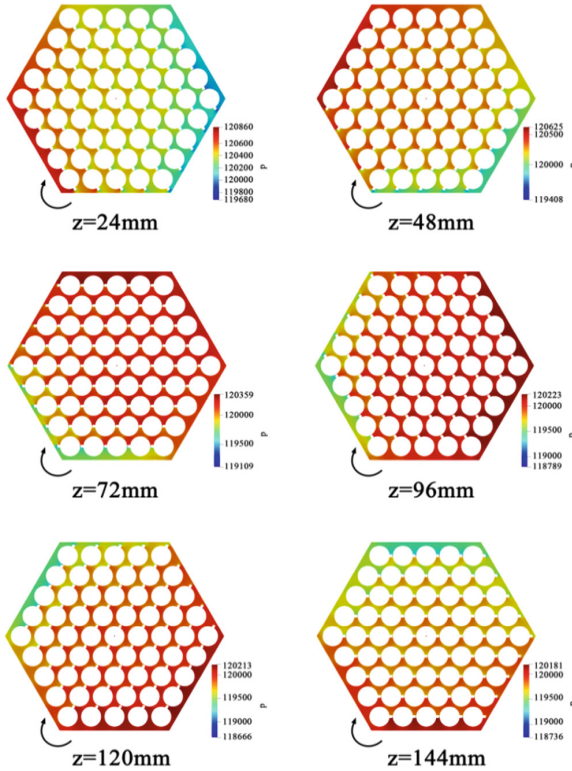
Fig. 9. Pressure distribution at 1/6H intervals within a pitch

3.2 Velocity Distribution Characteristics

The velocity distributions at different axial heights are shown in Fig. 10. Given the effects of the spacer wires, the velocity in the cross-section exhibited heterogeneity. The cloud contours indicate that the high-speed zone was generally dispersed around the assembly box upstream of the spin-in direction of the spacer wires. The fundamental driver of the variable coolant flow rates in the different sub-channels was the variance in the sub-channel flow area. The flow area of the channel near the assembly box was large, while the frictional resistance was relatively small, thus suggesting that the peripheral channel could obtain a larger velocity distribution. The inner sub-channels exhibited a more uniform velocity distribution due to the mixing of the spacer wires.

The velocity cloud contours for each 1/6H interval of the axial height within the pitch are shown in Fig. 11. For every 1/6H increase in axial height, the direction of the velocity cloud contours rotated 60° clockwise, and the velocity distribution period was 1H. The position of the maximum velocity also rotated periodically, and within a pitch, the maximum velocity distribution seemingly rotated by 360°. The maximum velocity decreased at the higher axial heights along the flow direction. Moreover, as the axial height increased, the lateral mixing introduced by the spacer wires caused the
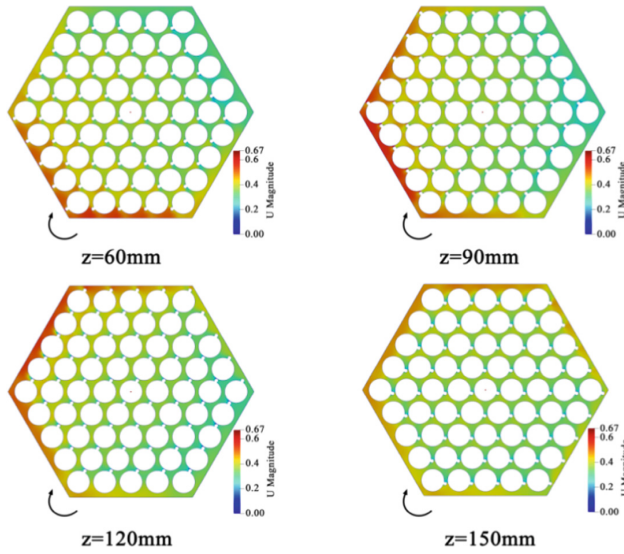
Fig. 10. Velocity distribution at different axial heights

coolant momentum exchange in different channel positions, thereby making the velocity distribution continuously uniform with the flow.

3.3 Temperature Distribution Characteristics

The temperature cloud contours at different axial heights are shown in Fig. 12, where the high- and low-temperature zones are reflected in the cross-section. The high-temperature zone was identified at the same position and rotated continuously along the spin direction of the spacer wires. The temperature of the central sub-channel was higher than that of the peripheral sub-channel because of the difference in the velocity distribution between the inner and outer channels. The coolant flow rate near the assembly box was high and the coolant was not sufficiently heated. Due to the mixing effect of the spacer wires, the velocity distribution of the inner sub-channels was uniform, the flow rate was low, the coolant was fully heated, and the high-temperature zones emerged.

The temperature distribution in the cross-section was also not hexagonally symmetric, thereby yielding some bias according to the relative position of the spacer wires. The temperature of the sub-channels near the center stainless-steel rod was lower. Although the average velocity of the sub-channels in the presence of spacer wires exceeded the average velocity of the sub-channels without spacer wires, the overall mass flow rate was smaller, and the average temperature was higher. Figure 13 shows the average and maximum temperatures of the surfaces at the different axial heights. As seen, the average temperature exhibited a linear increase along the axial direction, while the maximum temperature varied along the axial direction. The maximum difference between the maximum and average temperatures in the axial direction was 16.86K. Moreover, the
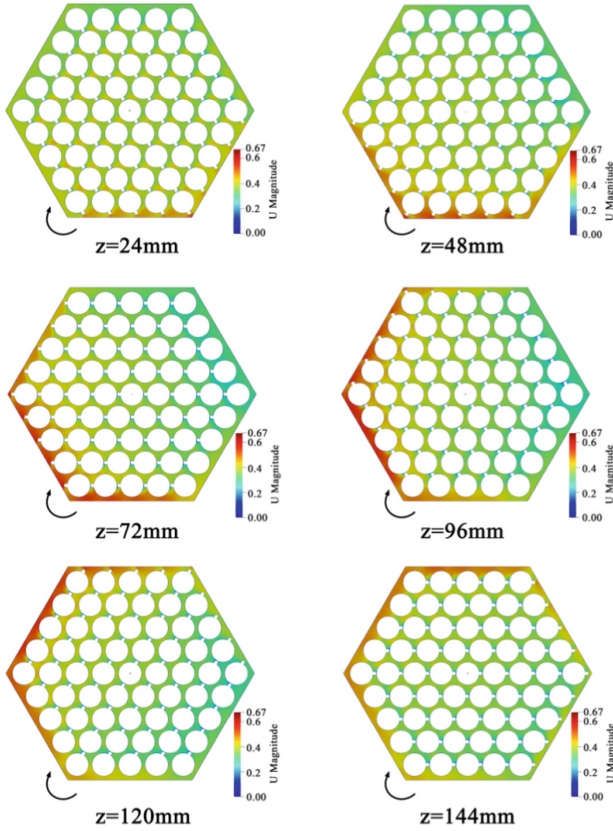
Fig. 11. Velocity distribution per 1/6H interval within a pitch

maximum temperature difference between the average temperatures of the two cross-sections of the inlet and outlet could reach 25K. Given the linear power density peaks at 0.09 m axial height, the temperature growth reached its highest levels here.

The temperature cloud contour of the fuel assembly with an axial height of 180 mm is shown in Fig. 14. As seen, the temperature of the inner sub-channels located in the central region was generally higher than that of the peripheral side sub-channels and corner sub-channels. The calculation demonstrated that the maximum temperature difference in the radial direction at $Z = 180$ mm could be up to 28.23K. Moreover, the spacer wires strongly affected the temperature distribution, thereby strengthening the heat transfer of coolant between sub-channels but also inducing local overheating. With the increase in axial height, the maximum temperature difference in the radial direction of the cross-section seemingly exhibited a gradual increase, and the flow field temperature near some fuel rods was excessively high. The uneven thermal expansion of the fuel rods near the flow field with a higher temperature was greater. Thus, the uneven thermal expansion of the fuel rods would result in the narrowing of the flow sub-channels, thus potentially causing a sub-channel block accident. Different helical pitches, pitch ratios, and winding methods of spacer wires can all affect the thermal-hydraulic behavior of
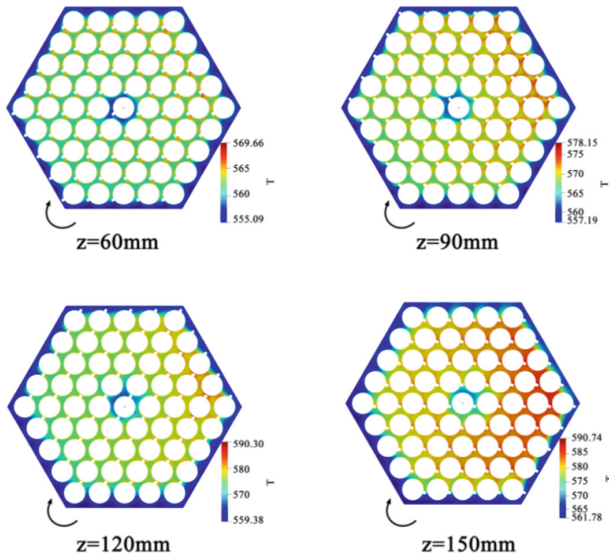
Fig. 12. Temperature distribution at different axial heights
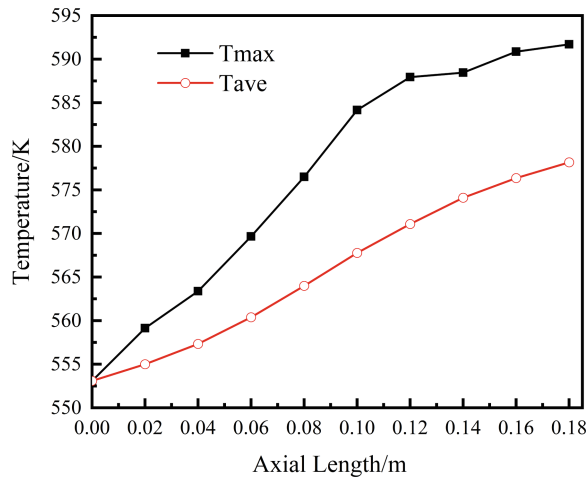
Fig. 13. Average and maximum temperature of cross.sections at different axial heights

the assembly. Future studies should elucidate the effects of the structural parameters of the fuel assembly on the flow heat transfer of the coolant within the fuel assemblies in CiADS.
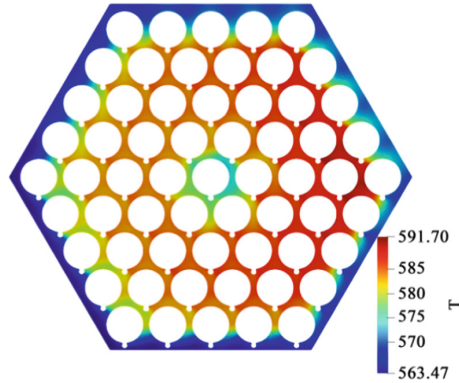
Fig. 14. The temperature cloud contour of Z = 180 mm

4 Conclusion

In this study, the flow characteristics of lead-bismuth coolant in a lead-based fast reactor within a fuel assembly containing spacer wires were elucidated using the open-source CFD software OpenFOAM and the buoyantSimpleFoam solver. To this end, the 61-rod bundle assembly was finely modeled, the polyhedral grids were delineated, and the physical parameters of the lead-bismuth coolant were implanted in OpenFOAM. The k–ω SST turbulence model was applied, the boundary conditions were set, and the solver was validated using a sub-channel procedure. The analysis of the physical field characteristics, such as pressure, velocity, and temperature inside the assembly demonstrated the following results:

(1) A significant pressure difference on both sides of the spacer wires was identified, which forced the transverse mixing of the coolant inside the assembly. Given the mixing effect, the transverse pressure distribution in the module was not uniform, while prominent high-pressure and low-pressure zones were formed. The high-pressure zone was generally located downstream of the spin in the direction of the spacer wires. Within a pitch (H), for every 1/6H increase in axial height, the direction of the pressure cloud contours rotated 60° clockwise, thereby weakening the pressure distribution variability.
(2) The velocity on the cross-section was not uniform. The inner sub-channels inside the assembly exhibited low-velocity zones, and the velocity distribution of the central sub-channels was more uniform due to the effect of mixing. The flow area of the sub-channels near the assembly box was large, while the friction resistance was relatively small, and the coolant flow rate in the peripheral channel was larger. For every 1/6H increase in axial height, the velocity cloud contours rotated 60° clockwise, and the velocity distribution period was 1H.
(3) Under the action of spacer wires, the temperature distribution of the internal sub-channels of the fuel assembly was more uniform. Given the uniform velocity distribution and low flow rate of the inner channel, the coolant was fully heated, and a high-temperature zone appeared. Although the temperature distribution in the

cross-section was not hexagonally symmetrical, some bias was revealed according to the relative position of the spacer wires. At the outlet, the temperature difference between the internal and side sub-channels near the assembly box was large. Moreover, the temperature of the flow field near some fuel rods was excessively high, thereby being conductive for the burning of the cladding under accident conditions.

References

1. Lake, J.A.: The fourth generation of nuclear power. Prog. Nucl. Energy **40**(3–4), 301–307 (2002)
2. Wang, J., Tian, W.X., Tian, Y.H., Su, G.H., Qiu, H.Z.: Thermal-hydraulic primary numerical analysis for pb-bi fast reactor sub-channel. Atomic Energy Sci. Technol. **47**(01), 38–42 (2013)
3. Alemberti, A., Smirnov, V., Smith, C.F., et al.: Overview of lead-cooled fast reactor activities. Prog. Nucl. Energy **77**, 300–307 (2014)
4. Yang, S., Zhang, Y.P.: Study on two-phase flow in fluid channel of lead-based fast reactor based on OpenFOAM. Atomic Energy Sci. Technol. **54**(09), 1582–1588 (2020)
5. Ahmad, I., Kim, K.Y.: Flow and convective heat transfer analysis using RANS for a wire-wrapped fuel assembly. J. Mech. Sci. Technol. **20**(9), 1514–1524 (2006)
6. Gajapathy, R., Velusamy, K., Selvaraj, P., et al.: CFD investigation of helical wire-wrapped 7-pin fuel bundle and the challenges in modeling full scale 217 pin bundle. Nucl. Eng. Des. **237**(24), 2332–2342 (2007)
7. Hamman, K.D., Berry, R.A.: A CFD simulation process for fast reactor fuel assemblies. Nucl. Eng. Des. **240**(9), 2304–2312 (2010)
8. Merzari, E., Fischer, P., Yuan, H., et al.: Benchmark exercise for fluid flow simulations in a liquid metal fast reactor fuel assembly. Nucl. Eng. Des. **298**, 218–228 (2016)
9. Zhao, P., Liu, J., Ge, Z., et al.: CFD analysis of transverse flow in a wire-wrapped hexagonal seven-pin bundle. Nucl. Eng. Des. **317**, 146–157 (2017)
10. Peng, T.G., Gu, L., Wang, D.W., Li, J.Y., Zhu, Y.L., Qin, C.P.: Conceptual design of subcritical reactor for China initiative accelerator driven system. Atomic Energy Sci. Technol. **51**(12), 2235–2241 (2017)
11. Liu, J.Q.: Research on Subchannel Analysis Method of Lead-Based Fast Reactor Fuel Assembly with Wire Spacers for CiADS. University of Chinese Academy of Sciences (Institute of Modern Physics, Chinese Academy of Sciences) (2021)
12. Natesan, K., Sundararajan, T., Narasimhan, A., et al.: Turbulent flow simulation in a wire-wrap rod bundle of an LMFBR. Nucl. Eng. Des. **240**(5), 1063–1072 (2010)
13. Ge, Z.F., Zhou, T., Bai, Y.Q., Song, Y.: Thermal-hydraulic analysis in wire-wrapped fuel assembly for China lead-based research reactor. Atomic Energy Sci. Technol. **49**(S1), 167–173 (2015)
14. Zhou, Z.W.: Numerical Study of Flow Behavior of Lead-Bismuth in Fuel Assembly with Wire Spacer. University of Science and Technology of China (2014)
15. OECD. Handbook on lead-bismuth eutectic alloy and lead properties, materials compatibility, thermal hydraulics and technologies. OECD, France (2007)
16. Deng, J., Lu, Q., Wu, D., et al.: Sub-channel code development of lead-bismuth eutectic fast reactor available for multiple fuel assembly structures. Ann. Nucl. Energy **149**, 107769 (2020)

Research of Corrosion Products Migration Behavior in PWR Primary Circuit Under Extended Low Power Operation Mode

Changying Li, Shuqi Meng[(✉)], Tianming Ruan, and Yalun Yan

China Nuclear Power Technology Research Institute, Shenzhen, Guangdong, China
13902664284@163.com

Abstract. In order to improve the flexibility of response to power grid demand, both newly built and in-service nuclear power units need to demonstrate the feasibility of ELPO (Extended Low Power Operation) and design schemes. During ELPO, the change of local thermal hydraulic conditions caused by the change of core power will have a great impact on the migration behavior of corrosion products in the primary circuit of PWR (Pressurized Water Reactor). Corrosion products deposited in the core will affect the heat transfer of fuel cladding, axial power distribution and critical heat flux. Corrosion products deposited outside the reactor, such as the main tubes, will affect the dose rate of personnel and pose challenges to radiation protection. A model for simulating the migration of corrosion products in the primary circuit of a PWR was established. The variation trends of the total amount of fuel CRUD (Chalk Rivers Unidentified Deposit), the total amount of fouling outside the reactor, the removal amount of corrosion products, the coolant source term and the main tubes deposition source term of a PWR before and after ELPO were compared. The results show that ELPO mode can inhibit the deposition of corrosion products in the core, and make more corrosion products deposit outside the core or be removed by CVCS (Chemical and Volume Control System). Because ELPO mode accelerates the migration of activated corrosion products to other regions, the coolant source term increases slightly. For the source term of main tubes sediment, ELPO model can reduce its total activity, thus reducing the personnel dose rate.

Keywords: ELPO · PWR · Corrosion products · CRUD · Migration

1 Introduction

In order to meet the demand of peak shaving of power grid, nuclear power units will adopt load tracking operation or power reduction operation [1]. The reduced power operation mode [2], in which all the gray rods are extracted and the PWR(Pressurized Water Reactor) is reduced from full power to a specific power platform by boronization, and the low power platform runs continuously for more than 12 h, is called ELPO (Extended Low Power Operation). During ELPO, the core axial power distribution, enthalpy rise

factor and power peak factor will change [3, 4], which will affect the whole core and local thermal hydraulic parameters.

The corrosion products in the primary circuit circulate with the coolant, some of which are removed by the CVCS (Chemical and Volume Control System), and the other part is deposited in the inner and outer areas of the core. The corrosion products deposited on the fuel surface are commonly known as CRUD (Chalk Rivers Unidentified Deposit). With the increase of CRUD, the heat transfer capability of fuel may decrease, and the risk of axial offset anomaly and local corrosion caused by scale will increase [5]; After irradiation, some CRUD will generate radioisotope, and these isotopes will migrate and redeposit in the primary loop after dissolving or shedding, forming coolant source term and shutdown deposition source term [6, 7].

The results of CRUD measurement data [5, 8] and mechanism study [9, 10] show that the rate of SNB (Subcooled Nucleate Boiling) on the fuel surface and the coolant temperature are the key parameters affecting the deposition and migration of corrosion products in the core. ELPO mode may have a great influence on local SNB rate and coolant temperature, which may change the distribution of corrosion products in the primary loop and change the migration of radioisotope. Therefore, it is necessary to study the migration behavior of corrosion products in the primary loop of PWR during ELPO, and evaluate the safety and economy of ELPO mode in reactor from the perspective of hydrochemistry and radiation protection.

2   Theoretical Model

2.1   Migration Model of Corrosion Products

The PWR primary loop is divided into the control volume shown in Fig. 1, in which only Fuel assembly is considered in the core, and it is finely divided along the axial direction, which is used to accurately characterize the influence of local SNB rate and coolant temperature on CRUD deposition.

The primary corrosion products are mainly composed of Ni, Fe, Cr complexes and a small amount of Co, Mn [5, 11]. For each element, the mass conservation equation in the PWR primary circuit can be listed as follows:

$$
\begin{aligned}
M_{RCS} \frac{dC}{dt} \cdot 10^9 \\
= R_{release} - R_{CVCS} - \frac{dM_c}{dt} - \frac{dM_{oc}}{dt}
\end{aligned}
\tag{1}
$$

Where: M_{RCS} represents water loading capacity, in g; $R_{release}$ represents the release rate of corrosion products, in g/s; R_{CVCS} represents the removal rate of corrosion products by CVCS, in ppb/s; $\frac{dC}{dt}$ indicates the change rate of corrosion products concentration, in ppb/s; $\frac{dM_c}{dt}$ and $\frac{dM_{oc}}{dt}$ respectively represent the deposition rate of corrosion products inside and outside the core, in g/s; t denotes time, in s.

The calculation formula of the items to the right of the equal sign of Eq. (1) is as follows:

$$
R_{release} = \sum_i v_i \cdot A_i
\tag{2}
$$
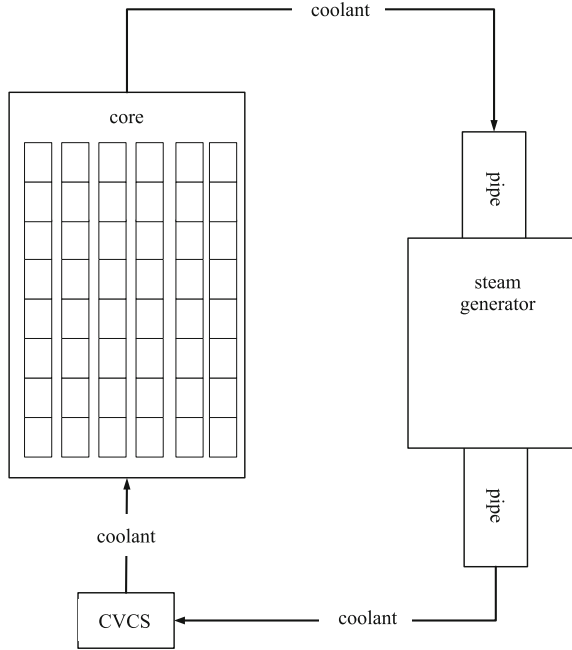
Fig. 1. Schematic Diagram of Corrosion Products Migration

$$R_{CVCS} = C \cdot \eta \cdot w_{CVCS} \tag{3}$$

$$\frac{dM_c}{dt} = \sum_j \left(\frac{dm_j}{dt} \cdot A_j \right)$$

$$= \sum_j \left[\dot{m}_{e,j} \cdot C_j + k_j \cdot (C_j - C_{j,0}) \right] \cdot A_j \tag{4}$$

$$\frac{dM_{oc}}{dt} = \sum_k \left(\frac{dm_k}{dt} \cdot A_k \right)$$

$$= \sum_k \left[k_k \cdot (C_k - C_{k,0}) \right] \cdot A_k \tag{5}$$

Where: v_i represents corrosion rate, in $g/(cm^2 \cdot s)$; A_i represents the infiltration area of the corroded material, in cm^2; C denotes the concentration of corrosion products in mainstream, in g/g; η represents the removal efficiency of corrosion products by CVCS; W_{CVCS} represents circulating water traffic, in g/s; m_j and m_k respectively represent the deposition amount of corrosion products in the inner and outer areas of the core, in g; A_j and A_k represent the infiltration area inside and outside the core respectively, in cm^2; $\dot{m}_{e,j}$ represents SNB rate, in $g/(cm^2 \cdot s)$; k_j and k_k represent the deposition coefficients in the inner and outer regions of the core respectively, which can be calculated according

to the coolant temperature [12], in g/(cm^2 · s); C_j and C_k respectively represent the concentration of corrosion products in the mainstream in the inner and outer regions of the core, which is greatly affected by the local coolant temperature [13], in g/g; $C_{j,0}$ and $C_{k,0}$ respectively represent the concentration of corrosion products on the deposited surface inside and outside the core, in g/g.

2.2 Source Term Model

According to the PWR operation experience, consider the radioisotope produced by Ni, Fe, Cr and Co, as shown in Table 1 [14, 15].

Table 1. Generation of Some PWR Radioactive Nuclides

Element	Mother nucleus	Reaction	Sub nucleus
Ni	^{62}Ni	(n,γ)	^{63}Ni
Fe	^{54}Fe	(n,γ)	^{55}Fe
Fe	^{54}Fe	(n,p)	^{54}Mn
Fe	^{58}Fe	(n,γ)	^{59}Fe
Cr	^{50}Cr	(n,γ)	^{51}Cr
Co	^{58}Ni	(n,p)	^{58}Co
Co	^{59}Co	(n,γ)	^{60}Co
Mn	^{55}Mn	(n,γ)	^{56}Mn

The migration process of radioisotope can be general as follows: corrosion products are deposited in the core and irradiated to form isotopes and attach to the fuel surface, part of isotopes is dissolved into coolant to form coolant source term, and isotopes migrating with coolant is deposited outside the core to form shutdown deposition source term. In conjunction with Eqs. (1) to (5), the deposition mass of corrosion products on the fuel surface in dt time period can be obtained, and then the coolant source term and dose rate level can be calculated as follows:

$$\frac{d\varphi_c}{dt} = \sum_j \left[P_j - \lambda \cdot n_j \cdot \left(1 - e^{-\lambda t} \right) \right] \tag{6}$$

$$\frac{d\varphi_w}{dt} = P_w - \lambda \cdot n_w \tag{7}$$

$$\frac{d\varphi_{oc}}{dt} = \sum_k \left(P_k - \lambda \cdot n_k \right) \tag{8}$$

Where: $\frac{d\varphi_c}{dt}$, $\frac{d\varphi_w}{dt}$ and $\frac{d\varphi_{oc}}{dt}$ represent the radioisotope change rate on the fuel surface, coolant and outside the core respectively, in Bq/s; P_j, P_w and P_k represent the radioisotope generation rates on the fuel surface, coolant and outside the core respectively, in Bq/s;

N_J, N_W and N_K denote the radioisotope activity on the fuel surface, coolant and outside the core respectively, calculated from the amount of corrosion products deposited and the nuclear reactions shown in Table 1, in Bq; λ represents decay constant, in s^{-1}.

3   Calculation Results and Analysis

3.1   Analytical Methods

Using LINDEN software [16] and CAMPSIS software [17] independently developed by CGN (China General Nuclear power group), the migration behavior of corrosion products of a million kilowatt PWR during one cycle running on 75% power and 50% power platforms was evaluated. Among them, LINDEN is used to calculate the thermal hydraulic parameters of each control body in the primary loop, including SNB rate and coolant temperature; CAMPSIS based on LINDEN calculations, analog corrosion products in the various control body deposition, dissolution, activation and redeposition migration process.

3.2   Migration of Corrosion Products

Figure 2 shows the migration of corrosion products in the primary loop under ELPO mode. The calculation results show that:

1) Compared with full power operation, when ELPO is carried out with 75% power and 50% power platform, the total amount of CRUD is significantly reduced, and more corrosion products will be deposited outside the core or removed by CVCS. From Eq. (4), it can be seen that this is because ELPO reduces SNB rate, thus inhibiting the deposition of corrosion products on the fuel surface;
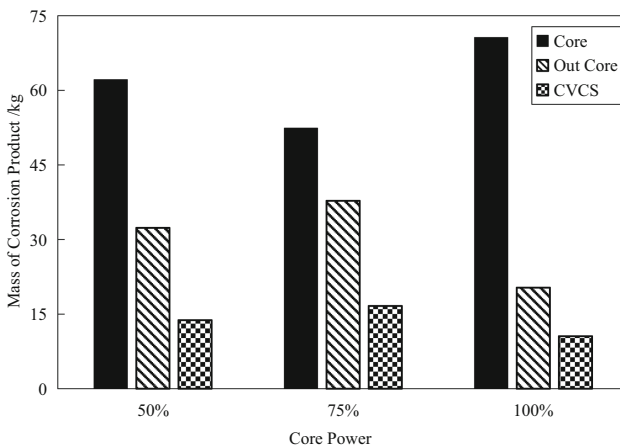
Fig. 2. Calculation Results of Corrosion Product Migration

2) The total CRUD of 50% power platform is higher than the total CRUD of 75% power platform. The reason for this phenomenon is that although the SNB rate decreases at lower power platform, the local coolant temperature of fuel also decreases, the concentration of corrosion products increases, and the CRUD deposition rate increases instead.

3.3 Distribution of Primary Loop Source Terms

Figure 3 shows the distribution of primary loop source terms in ELPO mode. The calculation results show that:

1) With the decrease of core power, the coolant source term gradually increases. This is because the decrease of core power causes the radioisotope deposited on the fuel surface to dissolve into the coolant, thus increasing the coolant source term;
2) Compared with full power operation, the dose rate decreases slightly in ELPO mode. The main reason is that ELPO reduces the total amount of CRUD and inhibits the formation of radioisotope under the premise of constant irradiation level;
3) The dose rate of the 50% power platform is slightly higher than that of the 75% power platform. The reason for this phenomenon is the same as the migration trend of corrosion products. The superposition of the effects of lower power platform on SNB rate and corrosion product concentration may lead to the increase of CRUD total, radioisotope and dose rate.
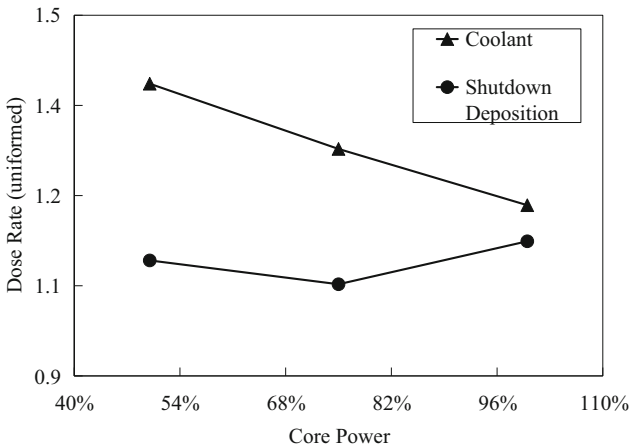
Fig. 3. Calculation Results of Source Term Distribution in Primary Loop

4   Conclusions

In this paper, a model of corrosion product migration and radioisotope formation in the primary circuit of Analog PWR is established, and the migration behavior of corrosion products during ELPO mode of a PWR is evaluated. The main conclusions are as follows:

1) ELPO can restrain CRUD deposition and alleviate the influence of CRUD on fuel capability by reducing SNB rate and changing local coolant temperature;
2) Compared with full power operation, ELPO will cause the coolant source term to rise, and the radioisotope deposited on the fuel surface will enter the coolant and be gradually removed by CVCS;
3) The total amount of CRUD, coolant source term and dose rate increased slightly when the power platform was reduced from 75% to 50%, which indicated that the ELPO power platform had a great influence on the migration behavior of corrosion products in the primary circuit.

References

1. Wang, J.: Research on Optimal Dispatching Model of Power System Considering Peak-shaving Operation of Nuclear Power. Wuhan University (2018). (in Chinese)
2. Liao, Y., Xiao, M., Li, X., et al.: Axial power difference control strategy and computer simulation for GNPS during stretch-out and power decrease. Nuclear Power Eng. **25**(4), 297–300 (2004). (in Chinese)
3. Liu, G., Xiao, W., Bie, Y., et al.: Study on influence factor and control strategy of axial power difference in peak load operation of CNP600 core. Atomic Energy Sci. Technol. **50**(7), 1256–1263 (2016). (in Chinese)
4. Xiao, H., Liu, G., Yao, H., et al.: Influence of extended low power operation on neutronics parameters of CNP600. Nucl. Tech. **39**(11), 74–80 (2016). (in Chinese)
5. Deshon, J.: PWR Axial Offset Anomaly (AOA) guidelines [R]. EPRI Technical Report, 1008102 (2004)
6. Tian, C., Xia, M., Huang, B., et al.: Effect analysis of zinc injection on corrosion product in primary circuit. Atomic Energy Sci. Technol. **55**(11), 2107–2112 (2021). (in Chinese)
7. Li, L.: Study on Activation and Migration Model of Corrosion Products in Main Loop of Water-Cooled Reactor. North China Electric Power University (2017). (in Chinese)
8. Riess, R.: Chemistry experience in the primary heat transfer circuit of kraftwerk union pressurized water reactors. Nucl. Technol. **29**(2), 153–159 (2017)
9. Jiao, C., Han, X., Hou, H., et al.: Model development of the deposition process of chalk river unidentified deposit on the fuel cladding surface of PWR. J. Harbin Eng. Univ. **42**(6), 915–920 (2021). (in Chinese)
10. Henshaw, J., Gibson, C., Mcgurk, J., et al.: Zinc chemistry in PWR fuel crud. In: Nuclear Plant Chemistry Conference 2016, Brighton, United Kingdom (2016)
11. Lyu, W., Chen, M., Huang, Q., et al.: Development on calculation code CPAP for radioactive activation product of pressurized water reactor nuclear power plant. Nucl. Tech. **43**(4), 25–32 (2020). (in Chinese)
12. Manacorda, A., Schehr, G., Zamponi, F.: Numerical solution of the dynamical mean field theory of infinite-dimensional equilibrium liquids. J. Chem. Phys. **152**(16), 164506 (2020)

13. Deshon, J.: Modeling PWR fuel corrosion product deposition and growth processes. EPRI, 1009734 (2004)
14. Lundgren, K.: ANTIOXI- Development of Oxide Model for Activity Build-up in LWRs-PWR and WWER Plant Data Analysis [R]. VTT, No VTT-R-03907-08 (2008)
15. Yi, Y., Xu, B., Jia, M.: Study of radiation impact on a nuclear power plant and its countermeasures. Environ. Sci. Manage. **45**(6), 142–146 (2020). (in Chinese)
16. China General Power Technology Research Institute, China General Nuclear Power Group, CGN Power. Sub-channel Analysis Code for Reactor Core [Abbreviation: LINDEN]V1.4 [CP]. China: 2018SR517526 (2017)
17. China General Power Technology Research Institute, China General Nuclear Power Group, CGN Power. PWR Fuel Crud Behavior Analysis Code [Abbreviation: CAMPSIS]V1.0 [CP]. China: 2021SR0623899 (2021)

Structure Design and Optimization of the Mass Flow Distribution Device of Downcomer for Fluoride-Salt-Cooled High-Temperature Advanced Reactor – FuSTAR

Xinyu Li, Dalin Zhang$^{(\boxtimes)}$, Xingguang Zhou, Wenxi Tian, and Suizheng Qiu

Xi'an Jiaotong University, Xi'an, Shaanxi, China
dlzhang@mail.xjtu.edu.cn

Abstract. The new generation of water-free cooling reactors: the FuSTAR system (Fluoride-Salt-cooled high-Temperature Advanced Reactor), mainly proposed by Xi'an Jiaotong University, is at the design stage. So far, the overall parameters of the heat transport system of FuSTAR have been obtained, and there is a pressing need to design and optimize the mass flow distribution device of Downcomer. In this paper, to obtain the specific parameters of structure matching the design values of mass flow rate, the finite element analysis was adopted, combined with the Nelder-Mead algorithm in the nonlinear programming. The results show that the mass flow distribution device with a multiple-port plate structure can achieve the purpose of the values of mass flow rate. Moreover, the mass flow rate is not so sensitive to the geometric parameters of these structures, which means more engineering margin. Based on this research, the detailed structural parameters and physical information about the distribution device were obtained, and the data from numerical tests can be used to build the proxy models to speed up transient analysis programs of FuSTAR.

Keywords: Mass Flow · Distribution · Downcomer · FuSTAR · Finite Element Analysis

1 Introduction

Small Modular Fluoride salt-cooled High-temperature Reactor (SMFHR) equipped with solid fuel and liquid-salt coolant, has the advantages of inherent safety, compact structure, high temperature, and modularity, which can be built in remote areas and inland water shortage, underground mines, industrial park facilities, military bases, etc., to provide the solutions of multi-purpose integrated energy [1]. Fluoride-Salt-cooled high-Temperature Advanced Reactor (FuSTAR) is a new generation of water-free reactor technology proposed by Xi'an Jiaotong University, which uses the integrated SMFHR as the heat source, modular molten salt pool as the energy storage device, and closed Brayton power cycle as energy conversion system. At present, the design of the core neutronics-thermohydraulics-power cycle system has been completed, and a safety analysis is needed to verify the inherent safety. The integrated structure is adopted in FuSTAR

and shown in Fig. 1. The coolant is FLiBe salt, which is heated from the core and enters the riser, then flows down into the Primary Heat Exchanger (PHE) to release the heat. The Cold salt is then pressured by the pump and split into two paths: one is along the Downcomer and returns into the core, and the other flow across the Downcomer and flows up into the Direct heat Exchanger (DHE) to constitute the steady loop of Passive Residual Heat Removal System (PRHRS).
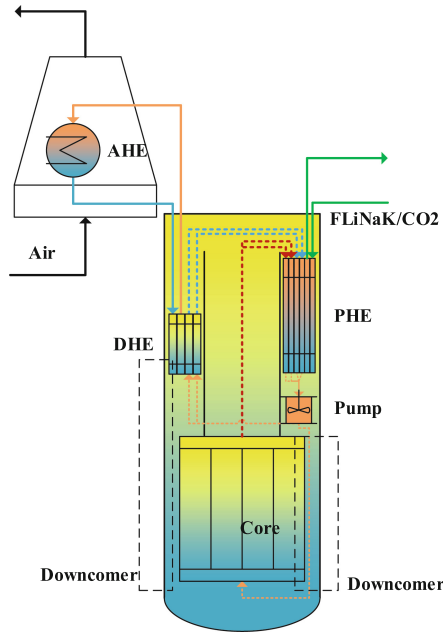
Fig. 1. Integrated interior structure of FuSTAR
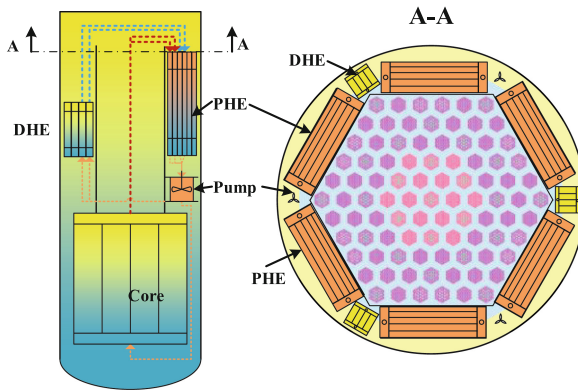
Fig. 2. Cross-section of heat exchangers and reactor

Figure 2 shows the layout scheme of the heat exchangers and reactor, with a total of 6 PHEs and 3 DHEs installed alternately around the riser. After neutronics and burnup calculations [2], the decay heat accounts for 1% of the total power thermal heat from the core, which must be removed by three DHEs of PRHRS.

However, the structure mentioned above has an obvious backflow region of Downcomer, which is difficult to be described by one-dimensional thermal-hydraulics equations. Therefore, detailed structural design and analysis are required. In this paper, the computational fluid dynamics method (CFD) is used to design the detailed structure of the Downcomer to ensure the flow distribution is as same as that of the design value. At the same time, the results of flow distribution are less sensitive to the structure, which is feasible in engineering processing. In addition, the numerical results or experimental results of the structure can provide equivalent resistance coefficients for the one-dimensional thermal-hydraulics and safety analysis programs.

2 Methodologies

2.1 Thermodynamic and Geometry Boundaries

The flow distribution and thermodynamic boundary were calculated by the energy balance method, and the thermophysical properties were referred to TRACE and CoolProp [3, 4]. 1/6 axisymmetric initial geometric structure was used for modeling, and Fig. 3 shows the boundary conditions and complete structure of the fluid domain with streamlines. The uniform velocity at the inlet boundary, the zero gradient outlet boundary at the outlet to DHEs, and the zero gauge pressure at the bottom annular outlet were used.

2.2 Design and Optimization Method

In this paper, the processes of design and optimization are shown in Fig. 4, which are mainly divided into two parts: preliminary analysis and secondary analysis. The Finite Element Method (FEM) was used to discretize space [5] based on COMSOL software.

In the preliminary analysis, to realize automation, the grid sequence should be established first for automatic generation. Subsequently, the robust and simple turbulence model was used to directly calculate the flow distribution and the optimization algorithms are adopted to change the structural parameters, minimizing the deviation between the calculated flow distribution and the design value. The sensitivity of structural parameters was analyzed based on the optimal solution to check if there are parameters that significantly affect the distribution. If the structure sensitivities are too strong, the structure needs to be changed and re-analyzed.

In the secondary analysis, suitable turbulence models for specific structures were selected, and optimization and sensitivity analyses were performed again for the optimal structures in the preliminary analysis. To ensure accuracy, the second-order element is used in the optimization stage. While to ensure efficiency, the first-order element is used in the sensitivity analysis stage.

The standard k-ε turbulence model was used in the preliminary analysis because of its robustness [6]. In the secondary analysis, as there are phenomenons of boundary layer
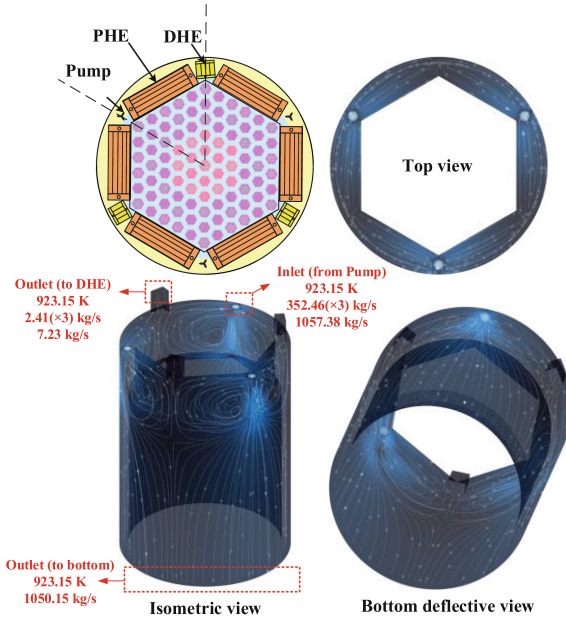
Fig. 3. Boundary conditions and complete structure of the fluid domain with streamlines.
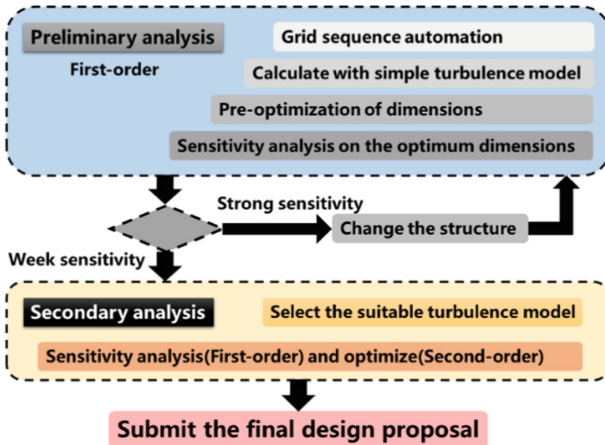
Fig. 4. The processes of design and optimization on Downcomer

separation and mainstream impact on the wall in the geometric structure in Fig. 3, the Spalart-Allmaras model with the anisotropic transport effect of turbulent viscosity [7], and the v2f model with the anisotropy of pulsation velocity [8], both of which have been applied.

In the solving process, the linear equations are calculated by PARDISO direct solver [9], the nonlinear part is separated and iterated by the Newton method, and the original

variables of the NS equation and turbulent variables are calculated successively. In the process of optimization, the Nelder-Mead algorithm was adopted [10]. The decision variables are the dimensions of the structure, and the objective function is the deviation between the calculated value and the designed value of flow distribution. When the deviation is zero, the optimization is completed.

3   Results and Discussion

3.1   Preliminary Analysis

The parameters initially involved in the optimization calculation are inlet-diameter and riser-height. After 37 times of optimization calculations, the final dimensions and velocity field are shown in Fig. 5, where the flow deviation at the outlet to DHE is only 0.09 kg/s. It is obvious that once the fluid enters the Downcomer, it will undergo sudden separation, accompanied by a large adverse pressure gradient. Subsequently, part of the large vortex impacts the riser region at the bottom, introducing pulsating velocity anisotropy. Then in the ring section, the vortex and mass flow rate separate. One-dimensional and two-dimensional safety analysis programs cannot capture this process, so they need to be developed again and introduce empirical relations.
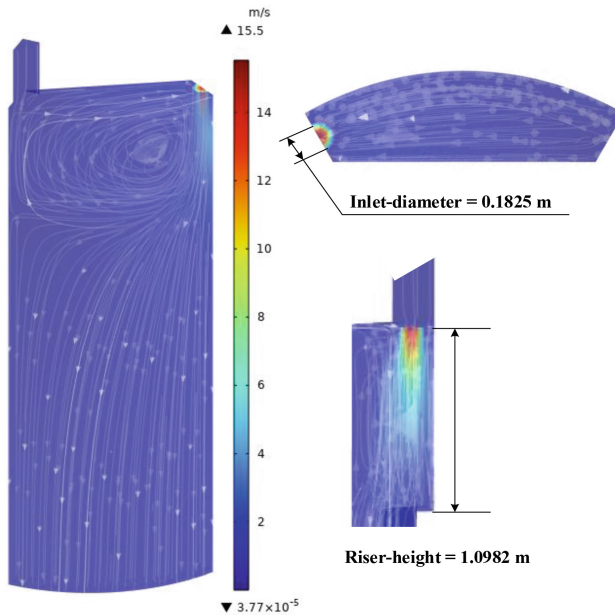
Fig. 5. Optimal dimensions and velocity in preliminary analysis

Based on the preliminary optimal dimensions above, dimension sensitivity analysis is carried out to judge the feasibility of the structure in engineering.

The influence on the mass flow rate of DHE by inlet-diameter under different riser-heights is shown in Fig. 6. The inlet-diameter has a great influence on the mass flow rate of DHE. For every 1 mm increase in inlet-diameter, the flow rate increases by 1 kg/s, which is difficult to control in engineering because the rated mass flow rate of DHE is only 7.23 kg/s.
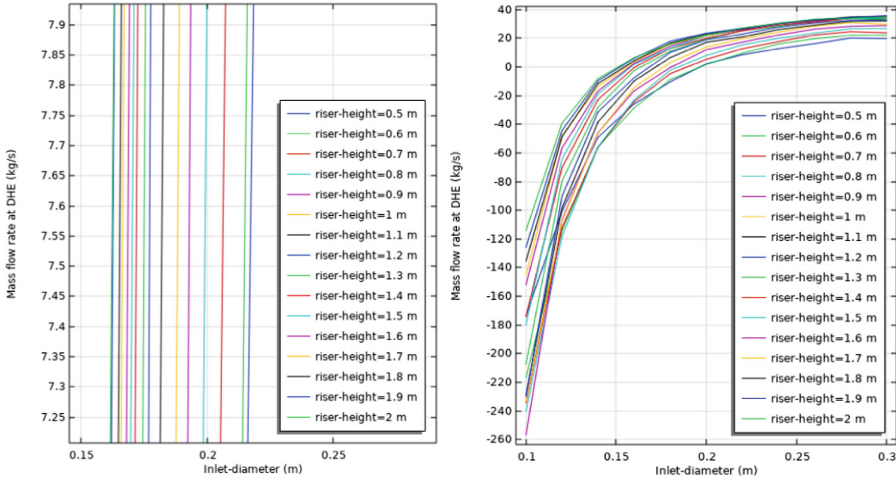
Fig. 6. The influence on the mass flow rate of DHE by inlet-diameter

The influence on the mass flow rate of DHE by riser-height under different inlet-diameters shown in Fig. 7. The sensitivities on riser-height are really weak, so the machining accuracy of riser-height can be appropriately relaxed in engineering.

To sum up, the flow distribution ratio of DHE in the preliminary structure is greatly affected by the inlet-diameter, which is unstable to rely on a split of the large vortex. Therefore, it is necessary to improve the geometry structure to weaken the sensitivities of dimensions. In addition, the stability in the calculation process is very well, so the Spalart-Allmaras model was used later to better describe the boundary layer and anisotropic effect. Finally, the optimal scheme is calculated and compared with the v2f model.

3.2   Sensitivity Weakening and Structural Optimization

The improved structure design is shown in Fig. 8. Relying only on a large vortex for flow distribution would be difficult to control, so consider a separator plate in the vortex area on the riser. The plate divides the upstream fluid into two parts, one flowing laterally to the outlet at the DHE, and the other flowing downstream to the bottom of the Downcomer. In addition, to better control the outlet flow at the DHE, this outlet is also assembled in a single hole plate, through the size of the hole to obtain a different flow distribution. Therefore, the structural variables are updated as new decision variables in optimization, which are: **split-height, Theta, inlet-diameter, Outlet-diameter**, and **riser-height**.

Split-height represents the distance between the separator plate and the top, of which range is constrained as 0.05–0.15m. The initial value is 0.06 m.
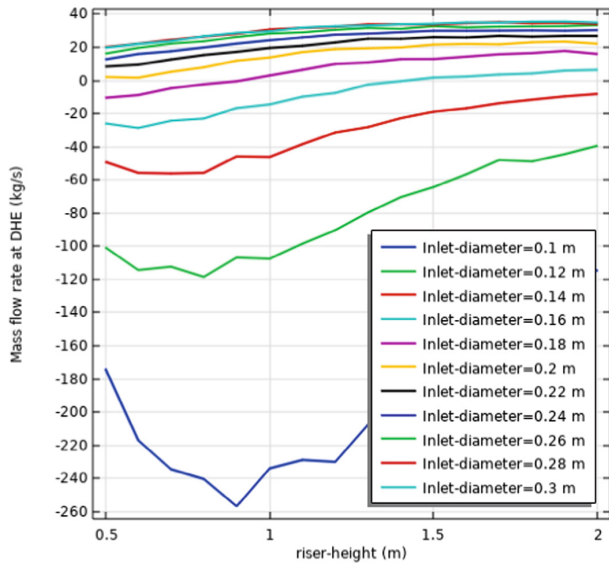
Fig. 7. The influence on the mass flow rate of DHE by riser-height
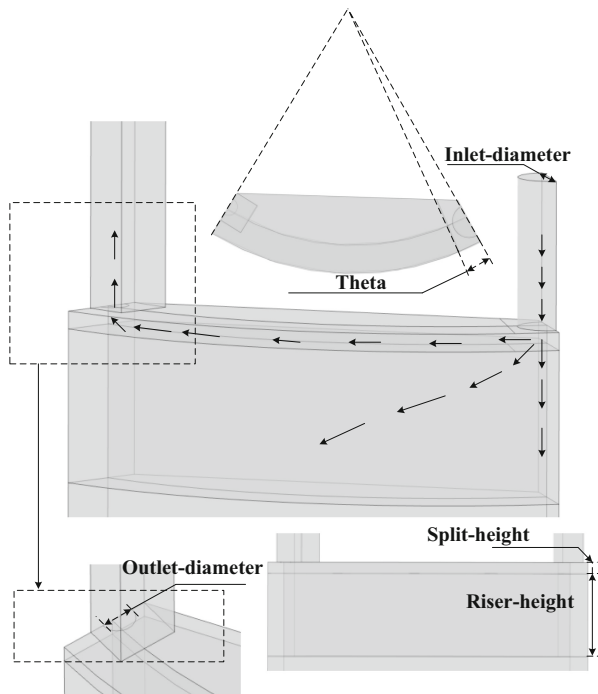
Fig. 8. Improved structure design and updated new decision variables

Theta represents the opening angle of the separator plate, which is calibrated based on the central axis of the reactor and its variation range is constrained as 5–50°. The initial value is 5°.

Inlet-diameter still represents the diameter at the inlet, upstream of which is the fluid at the pump outlet. Due to the constrained size of the container, its range is limited to 0.1–0.25 m. The initial value is 0.21 m.

Outlet-diameter represents the hole diameter of the hole plate at the outlet, and its downstream is the entrance of the DHE. Limited by the size of the outlet channel, its range is limited to 0.05–0.15 m. The initial value is 0.11 m.

Riser-height still represents the height of the riser in the flow domain, which does not include the split-height. The range of riser-height is constrained to 0.2–2 m. The initial value is 0.5 m.

Considering the more complex structures, the separation and attachment of boundary layer become more complicated, so the Spalart-Allmaras model was used for calculation. For the final scheme, the v2f model was also used to compare.

Stepwise Sensitivity Analysis and Selection of Stability Region

The stepwise sensitivity analysis parameters were scanned to find the stability region of each parameter. To save time on calculation, the first-order element was used to discretize the space. The higher-order elements only have some quantitative differences compared to the first-order element, but do not affect the qualitative results of sensitivity analysis.

First, the sensitivities of the split-height and the theta on the flow distribution ratio of DHE in their range were analyzed when other parameters were set to their initial values, as shown in Fig. 9. With the increase of the theta and the split-height, the mass flow rate increases gradually but the slope decreases. The stable slope can be controlled well only when both the theta and the split-height are small. Therefore, the theta $= 5°$ and the split-height $= 0.06$ m are selected within the stable ranges of low slope. The structural sensitivities decreased from 1(mm/(kg/s)) to about 4(mm/(kg/s), split-height) and 60(mm/(kg/s), theta), which are 1/4 and 1/60 of the original.

Then, based on the above parameters selected, the sensitivities analysis of the inlet-diameter and the outlet-diameter on the flow distribution ratio of DHE were carried out. The analysis results are shown in Fig. 10. When the inlet-diameter is about 0.2 m and the outlet-diameter is about 0.1 m, the slope is the lowest with weak sensitivity. Therefore, the inlet-diameter $= 0.21$ m and the outlet-diameter $= 0.11$ m. The structural sensitivities decreased from 1(mm/(kg/s)) to about 13(mm/(kg/s), inlet-diameter) and 15(mm/(kg/s), outlet-diameter), which are 1/13 and 1/15 of the original.

Finally, the above parameters were fixed and the sensitivity analysis of the riser-height on the flow distribution ratio of DHE was conducted. The results are shown in Fig. 11. The mass flow rate is not affected significantly by the riser-height. Therefore, the values in all the range of riser-height can be used. The structural sensitivity decreased from 1(mm/(kg/s)) to about 800(mm/(kg/s)), which is 1/800 of the original.

Structural Optimization in the Stability Region

Structural parameters optimization was carried out based on the stability region above. To ensure accuracy, the second-order element was used to discretize the space. The riser-height has the lowest sensitivity to mass flow rate, so only it was used as the decision
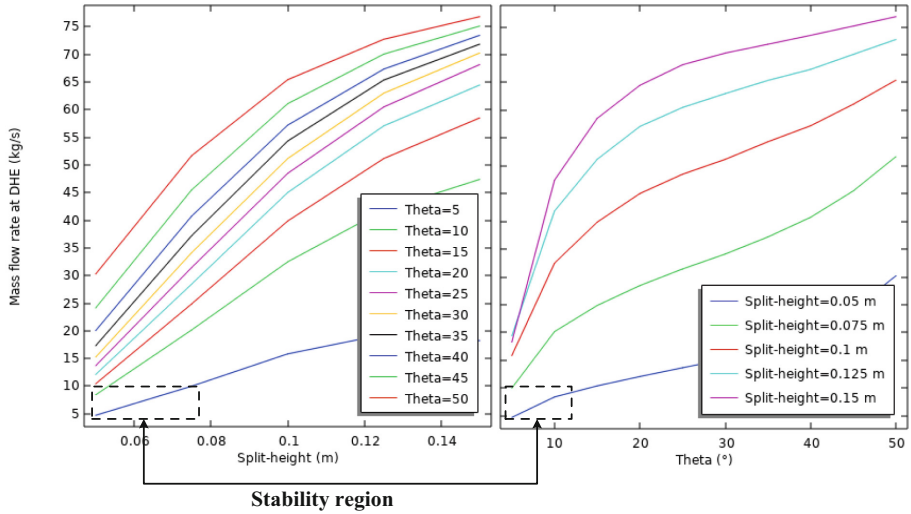
Fig. 9. The sensitivities of split-height and theta
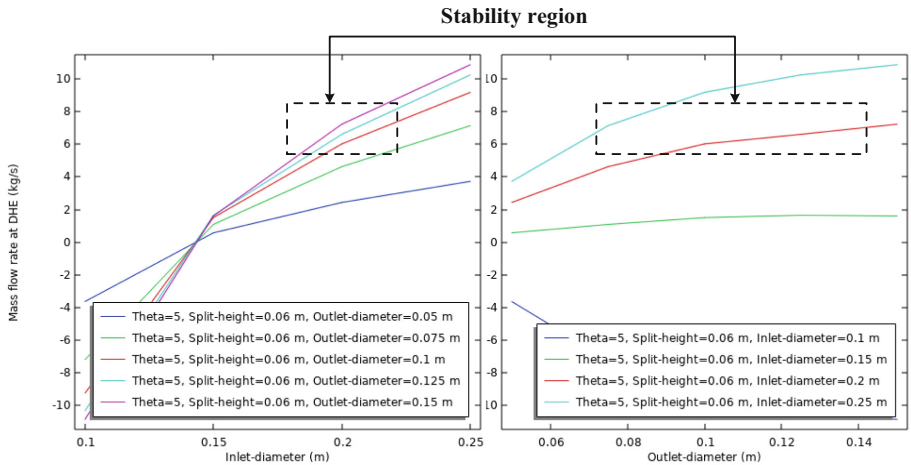
Fig. 10. The sensitivities of inlet-diameter and outlet-diameter

variable, and other variables are not optimized to avoid shifting out of the stability domain. The objective function is the deviation of the outlet mass flow rate at the DHE from the design value – 7.23 kg/s. The Nelder-Mead algorithm was selected and the process of optimization is shown in Fig. 12. Finally, the value of riser-height stabilized at 1.3375 m, where the deviation between the calculated mass flow rate and the designed value was minimum to zero, and the optimization was completed.

The distribution of y+ and the global velocity field of the optimal solution are shown in Fig. 13. The global maximum value of y+ is 3.76 at the inlet due to the uniform boundary of velocity, while it of other parts is about 1, which meets the requirements
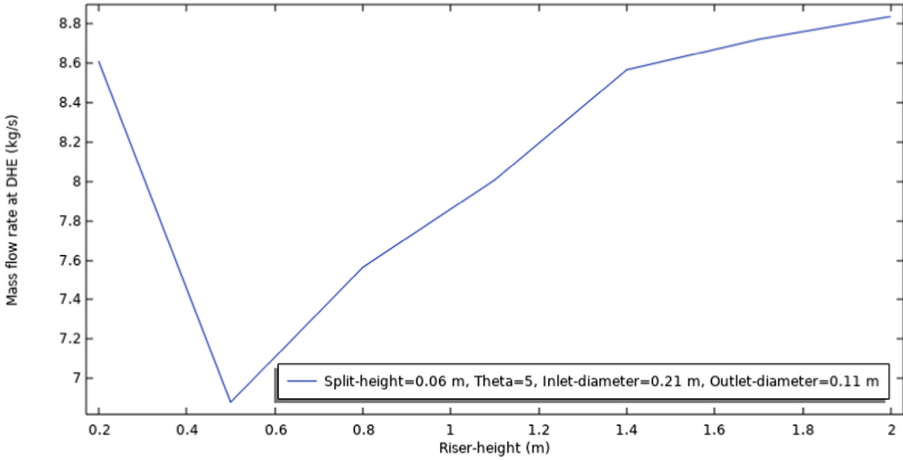
Fig. 11. The sensitivities of riser-height
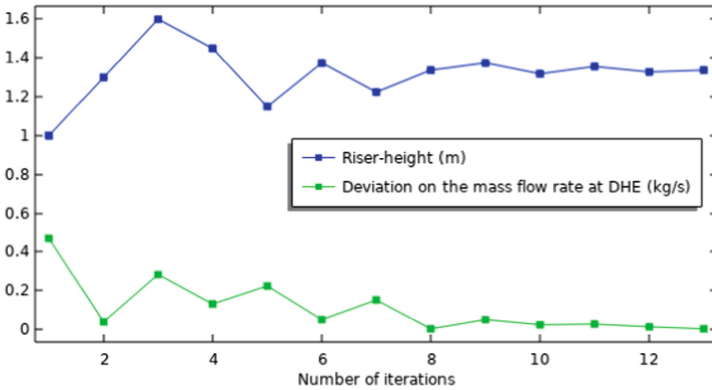
Fig. 12. Optimization of the riser-height with minimal deviation

of boundary layer analysis of the Spalart-Allmaras model. According to the streamline, most of the flow forms a stagnant vortex in the riser region, and a small part of the fluid flows horizontally along with the separator plate to the outlet at DHE. As can be seen from the sensitivity analysis above, this structure of flow separation has low geometric sensitivity and is suitable for engineering processing (Fig. 14).

Figure 15 shows the velocity field at the longitudinal section of the inlet. With the riser-height of 1.3375 m, the mainstream flow velocity at the riser bottom has attenuated from 10 m/s to 4 m/s, which weakens the anisotropic impact effect and is also an important reason why the wall y+ always keeps a low level. Lower impact momentum results in less vibration and direct pressure, which also improves the long-term operating life of the structure.

Figure 16 shows the velocity field of the outlet at DHE and the mesh diagram. The second-order element only needs the thicker mesh to be able to resolve the streamline of
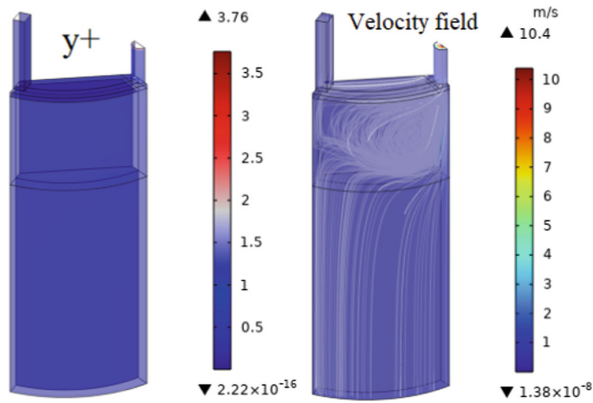
Fig. 13. The y+ and global velocity field of the optimal solution
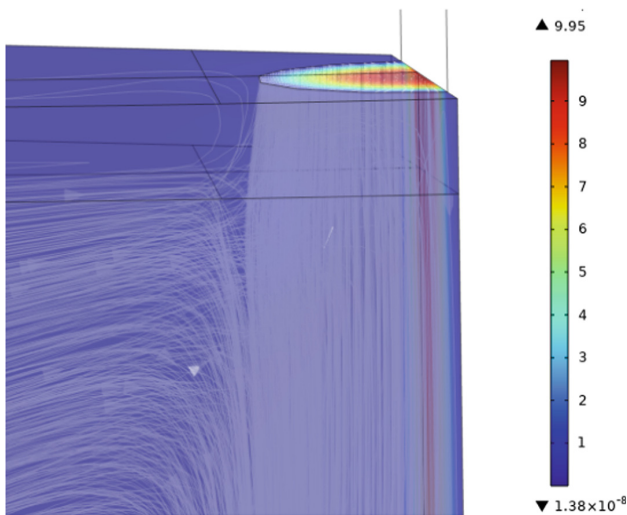
Fig. 14. Velocity field and streamline at the inlet of the separator plate

the curve well. By changing the diameter of the hole plate, the sensitivity of the structure is lower, which is about 15 times that of the original scheme, and is more beneficial to engineering processing.

Finally, the v2f model with the same parameters was used to verify the results of the Spalart-Allmaras model. The comparison of overall results is shown in Table 1. The results show that the error of the Spalart-Allmaras model and v2f model is really small, the maximum error of pressure drop is less than 1.5%, and that of the mass flow rate is at the magnitude of $10-5$. Therefore, to get the macro parameter of mass flow rate and pressure drop, the Spalart-Allmaras model with faster speed and stronger stability can be considered in the design work. The final dimensions based on Fig. 8 are summarized in Table 2.
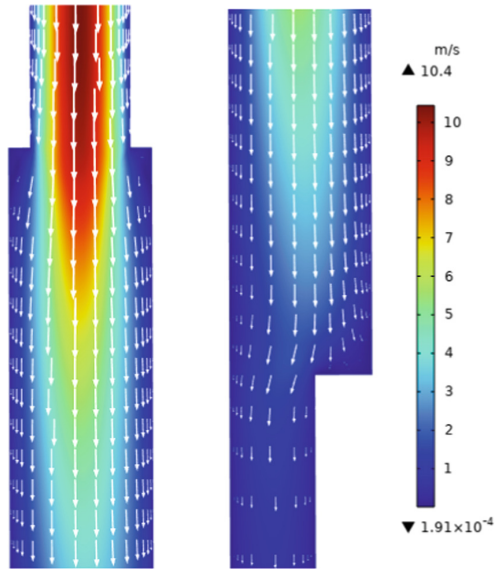
Fig. 15. Velocity field at the longitudinal section of the inlet (The top of the right image continues at the bottom of the left)
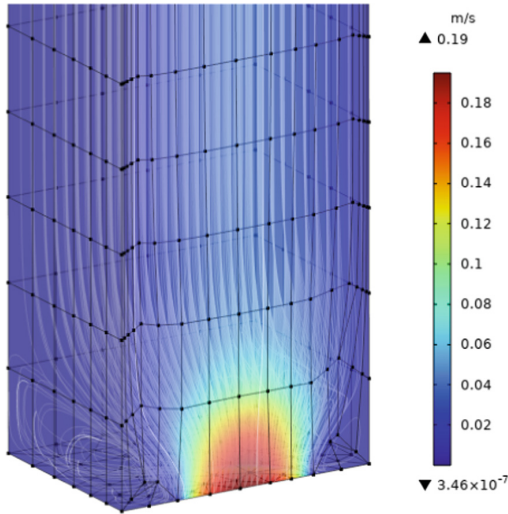
Fig. 16. Velocity field of the outlet at DHE and the mesh diagram

Table 1. Comparison of overall results with Spalart-Allmaras and v2f turbulence model

Turbulence model	Spalart – Allmaras	v2f	Deviation(based on v2f)
Mass flow rate at bottom of Downcomer	1050.14648 kg/s	1050.14598 kg/s	4.76E-07
Pressure drop from inlet to bottom of Downcomer	10651.14 Pa	10522.64 Pa	1.22%
Mass flow rate of outlet at DHE	7.2435 kg/s	7.2440 kg/s	-6.90E-05
Pressure drop from inlet to outlet at DHE	92066.58 Pa	92195.09 Pa	-0.14%

Table 2. The final dimensions based on Fig. 8

Parameters	Values	Units
Split-height	60	mm
Theta	5	°
Inlet-diameter	210	mm
Outlet-diameter	110	mm
Riser-height	1.3375	m

4 Conclusions

In this paper, the CFD method was used to design the detailed structure of the Downcomer to ensure the flow distribution is as same as that of the design value. 1/6 axisymmetric initial geometric structure was used for modeling, and the processes of design and optimization are divided into two parts: preliminary analysis and secondary analysis. The standard k-ε model, Spalart-Allmaras model, and v2f model were used and compared respectively, and the Nelder-Mead algorithm was used for the optimization.

The results of the preliminary analysis showed that in the ring section, the vortex and mass flow rate separate. One-dimensional and two-dimensional safety analysis programs cannot capture this process, so they need to be developed again and introduce empirical relations. However, the flow distribution ratio of DHE in the preliminary structure is greatly affected by the inlet-diameter, which is unstable to rely on a split of the large vortex.

The results of the secondary analysis showed a hole plate at the outlet and a separator plate in the vortex area on the riser will reduce structural sensitivity by 1/4 to 1/800. Most of the flow forms a stagnant vortex in the riser region, and a small part of the fluid flows horizontally along with the separator plate to the outlet at DHE. Lower impact momentum at the bottom of the riser results in less vibration and direct pressure, which also improves the long-term operating life of the structure. Finally, the results show

that the error of the Spalart-Allmaras model and v2f model is really small. The Spalart-Allmaras model with faster speed and stronger stability can be considered in the design work.

References

1. Jiang, D., et al.: Fluoride-salt-cooled high-temperature reactors: review of historical milestones, research status, challenges, and outlook. Renew. Sustain. Energy Rev. **161**, 112345 (2022). https://doi.org/10.1016/j.rser.2022.112345
2. Zhou, X., et al.: A coupling analysis method of the thermal hydraulics and neutronics based on inverse distance weighted method, p. 12
3. Bell, I.H., Wronski, J., Quoilin, S., Lemort, V.: Pure and pseudo-pure fluid thermophysical property evaluation and the open-source thermophysical property library CoolProp. Ind. Eng. Chem. Res. **53**(6), 2498–2508 (2014). https://doi.org/10.1021/ie4033999
4. Richard, J., et al.: Implementation of liquid salt working fluids into TRACE, p. 11 (2014)
5. Hughes, T.J.R., Mallet, M.: A new finite element formulation for computational fluid dynamics: III. The generalized streamline operator for multidimensional advective-diffusive systems. Comput. Meth. Appl. Mech. Eng. **58**(3), 305–328 (1986). https://doi.org/10.1016/0045-7825(86)90152-0
6. Wilcox, D.: Turbulence Modeling for CFD, 3rd edn. (Hardcover) (2006)
7. Dacles-Mariani, J., Bradshaw, P., Chow, J.S., Zilliac, G.: Numerical/experimental study of a Wingtip Vortex in the near field. AIAA J. **33**, 1561–1568 (2012)
8. Laurence, D., Uribe, J., Utyuzhnikov, S.: A robust formulation of the v2-f model. Flow Turbul. Combust. **73**, 169–185 (2005). https://doi.org/10.1007/s10494-005-1974-8
9. Alappat, C., et al.: A recursive algebraic coloring technique for hardware-efficient symmetric sparse matrix-vector multiplication. ACM Trans. Parallel Comput. **7**(3), 1–37 (2020). https://doi.org/10.1145/3399732
10. Conn, A.R., Scheinberg, K., Vicente, L.N.: Introduction to derivative-free optimization. Society for Industrial and Applied Mathematics/Mathematical Programming Society, Philadelphia (2009)

Study on the Influence of Stretch-Out Operation on the Deposition of Corrosion Products and Source Term Level in the Primary Circuit of Pressurized Water Reactor

Tianming Ruan[✉] and Yulong Mao

China Nuclear Power Technology Research Institute, Shenzhen, Guangdong, China
ruantianming@cgnpc.com.cn

Abstract. Corrosion products in the primary circuit of Pressurized Water Reactor (PWR) during operation will cause Chalk Rivers Unidentified Deposit (CRUD), increase the level of coolant source term and deposition source term outside the core, and then affect the normal operation of PWR and the radiation field during the shutdown overhaul. Stretch-Out (SO) operation is a flexible mode of reactor, which can improve the economy of reactor. In this paper, the theoretical model of CRUD and source term analysis for PWR is introduced, and the influence of SO operation on CRUD and source term level of PWR is studied. The calculation results show that SO operation can reduce the total amount of CRUD in PWR. However, the level of coolant source term rises at the initial stage of SO operation, and the level of coolant source term can be reduced by double discharge pumps running in this case. The deposition source term outside the reactor show a gradual increasing trend. The research results provide theoretical basis and data reference for CRUD and source term level control during SO operation in PWR.

Keywords: PWR · Stretch-out · CRUD · Coolant source term · Deposition source term

1 Introduction

Stretch-Out (SO) operation of nuclear power plants refers to an operation mode in which positive reactivity is introduced by reducing primary coolant temperature and reactor power at the end of fuel cycle life when all control rods are at the top of the reactor and boron concentration in the primary loop is close to 0 ppm (1 ppm = 10^{-6}), thus prolonging reactor operation time. The SO operation of nuclear power plants can not only improve the flexibility of overhaul schedule, meet the needs of refueling overhaul of group reactor units, but also increase the depth of burnup and improve the economy of plants [1].

Metallic materials in the primary circuit of Pressurized Water Reactor (PWR) will corrode and release corrosion products in the high temperature and high pressure environment, the main components of which are Ni, Fe, Cr, etc. [2, 3]. After entering the

primary circuit, corrosion products migrate to all parts of the primary circuit with coolant, and deposit on the surface of fuel cladding mainly through subcooled nucleate boiling (SNB), thus forming Chalk Rivers Unidentified Deposit (CRUD) [4].

On the one hand, CRUD will adsorb boron in coolant, forming local boron enrichment on fuel assemblies, which will increase the risk of Crud Induced Power Shift (CIPS); On the other hand, the continuous increase of CRUD thickness will affect the heat transfer capacity of fuel assemblies, causing local corrosion and increasing the risk of fuel cladding failure. At the same time, metal materials will be activated under neutron irradiation to form Activated Corrosion Products (ACPs), among which the main radionuclide are 58-Co, 60-Co, 51-Cr, 54-Mn, 59-Fe, etc. ACPs are deposited on the surface of metallic material inside and outside the core, which directly affects the total radiation dose during shutdown overhaul [5]. According to statistics, about 85% of the radiation field outside the core is caused by ACPs [6]. Therefore, it is necessary to analyze the CRUD and the source terms of PWR.

In this paper, the key theoretical models of CRUD analysis and source term calculation in PWR are introduced around the main corrosion product elements (i.e. Ni, Fe, Cr) and radionuclide (i.e. 58-Co, 60-Co, 51-Cr, 54-Mn, 59-Fe). The effects of SO conditions on CRUD and source term of a PWR are obtained by analyzing and calculating under normal operating conditions and SO conditions, which provides guidance for CRUD and radiation field control under SO operation.

2 Theoretical Model

2.1 Hydrochemical Model

The hydrochemical model is used to calculate the saturated solubility of Ni, Fe and Cr in primary coolant. According to the main chemical reaction equations of these three elements in the primary circuit hydrochemical environment [7], the formulas for calculating the saturated solubility of Ni, Fe and Cr can be obtained as follows:

$$C_{Ni} = \log K_{NiFe_2O_4} + \log K_{NiO} + \log K_{Ni} \\ - \frac{2}{3}\log K_{Fe_3O_4} + 6[H^+] - \frac{5}{3}[H_2] \tag{1}$$

$$C_{Fe} = \frac{1}{3}\log K_{Fe_3O_4} + 2[H^+] + \frac{1}{3}[H_2] \tag{2}$$

$$C_{Cr} = \frac{1}{2}\log K_{FeCr_2O_4} - \frac{1}{6}\log K_{Fe_3O_4} + 2[H^+] \\ + \frac{1}{3}[H_2] \tag{3}$$

where: C_{NI}, C_{FE} and C_{CR} represent the saturated solubility of Ni, Fe and Cr, in mol/kg; $[H_2]$ represents the concentration of dissolved hydrogen, in mol/kg; $[H^+]$ represents the concentration of hydrogen ion, in mol/kg; K_i represents the chemical equilibrium constant, which can be written as a function of temperature T, and the subscript i corresponds to different metal oxides.

2.2   CRUD Deposition Model

CRUD deposition model is used to calculate CRUD deposition inside and outside the core. CRUD deposition is the result of turbulent mixing and SNB mechanism, and its process can be explained based on the classical diffusion layer model [8]. Figure 1 is a schematic diagram of the diffusion layer model, and primary coolant can be divided into the bulk coolant domain and the near-wall layer near the surface of metal materials.
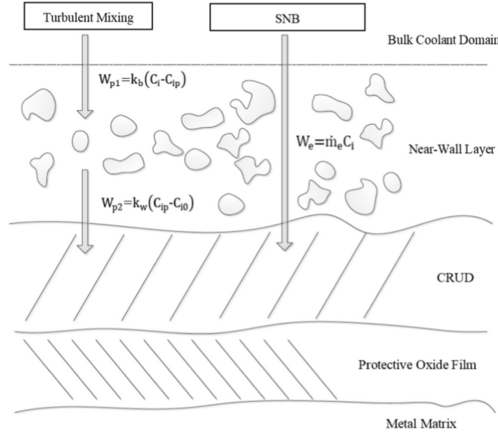
Fig. 1.   Schematic Diagram of Diffusion Layer Model

After the primary circuit metal material is corroded, a part of the corrosion products will form the protective oxide film, and the remaining corrosion products will be released into the coolant in the form of ion and particulate, and then enter the near-wall layer from the bulk coolant domain by diffusion. After reaching a certain concentration in the near-wall layer, they will deposit on the surface of the protective oxide film, and form CRUD in a turbulent way. At the same time, SNB will occur on the surface of fuel rods, forming a stable steam channel, and corrosion products will deposit around the steam channel, finally forming CRUD with dense bottom and loose porous in the near-wall layer. The mass transfer process is shown in Fig. 1.

Based on the above mechanism, the deposition of corrosion products in the coolant can be regarded as the result of turbulent mixing and SNB, so the deposition rate per unit area of CRUD is:

$$w_i = \frac{k_b \cdot \dot{m}_e}{k_b + k_w} \cdot C_i + \frac{k_b \cdot k_w}{k_b + k_w} \cdot (C_i - C_{i0}) \qquad (4)$$

where: w_i represents the deposition rate, in $g/(cm^2 \cdot s)$; $\dot{m}_e$ represents the SNB rate, in $g/(cm^2 \cdot s)$; k_b and k_w represents the deposition coefficients from the bulk coolant domain to the near-wall layer and from the near-wall layer to the fuel surface, respectively, which can be calculated by Chilton-Colburn [9] formula, in $g/(cm^2 \cdot s)$; C_i and C_{i0} represent the solubility of corrosion products in the bulk coolant domain and fuel surface respectively,

which need to be obtained according to Gibbs' law and data fitting of solubility experiment in the primary circuit environment of PWR [10–16], in g/g; i corresponds to three elements: Ni, Fe and Cr.

2.3 Source Term Model

The source term model is used to calculate the radioactivity level distribution of coolant and nuclide inside and outside the reactor.

The corrosion product particles and ion released from the base metal in the primary circuit circulate with the coolant. When the corrosion products flow through the core area, some of them will be irradiated by neutron to become activated corrosion products, forming coolant source term. On the other hand, corrosion products may be deposited when they flow in the circuit, and the CRUD deposition on the fuel surface forms the deposition source term inside the core, while the deposition outside the core forms the deposition source term outside the core.

The formula of activity concentration of activated corrosion products in primary coolant is as follows:

$$\frac{dC_i(t) \cdot m_w}{dt} = P_i - \lambda_i \cdot C_i(t) \cdot m_w \tag{5}$$

where: $C_i(t)$ represents the specific activity mass of radionuclide i in coolant, in Bq/t; m_w represents the mass of primary coolant, in t; λ_i represents the decay constant of nuclide, in s^{-1}; P_i represents the generation rate of nuclide i, in Bq/s. $C_i(t)$ and P_i are related to decay constant of nuclide, nucleon neutron of parent core in coolant, neutron neutron rate in core area, microscopic reaction cross section, ratio of fluid flow time in core to total flow time inside and outside the core, and axial power share of control body.

The deposition source term inside the core mainly considers the surface of fuel assemblies, and the formula of activity concentration of the deposition source term inside the core is as follows:

$$\frac{dC_i(t)_{in} \cdot A_d}{dt} = P_i' - \lambda_i \cdot C_i(t)_{in} \cdot A_d \tag{6}$$

where: $C_i(t)_{in}$ represents the area specific activity of nuclide i inside the core, in Bq/cm²; A_d represents the deposition area, in cm²; λ_i represents the decay constant of nuclide, in s^{-1}; P'_i represents the formation rate of nuclide i in CRUD inside the core, in Bq/s; $C_i(t)_{in}$ and P'_i are related to decay constant in nuclide, nucleon neutron in the parent core of CRUD inside the core, neutron rate in the core area, microscopic reaction cross section, axial power share of control body, CRUD thickness inside the core and deposition area.

The deposition of corrosion products outside the core is mainly considered in the main pipeline, Steam Generator (SG) heat transfer tube, lower chamber, and primary pumps. The deposition rate is different at positions with different fluid velocity and temperature. The formula of activity concentration of the deposition source term outside the core is as follows:

$$\frac{dC_i(t)_{out}}{dt} = D_i(t) - \lambda_i \cdot C_i(t)_{out} \tag{7}$$

where: $C_i(t)_{out}$ represents the area specific activity of nuclide i outside the core, in Bq/cm^2; $D_i(t)$ represents the radioactivity generation rate caused by CRUD deposition outside the core, in $Bq/(cm^2 \cdot s)$; λ_i represents the decay constant of nuclide, in s^{-1}; $C_i(t)_{out}$ and $D_i(t)$ are related to the decay constant in nuclide, the deposition rate of corrosion products, and the proportion of nuclide isotopes in all isotopes.

2.4 Mass Conservation of Corrosion Products in Primary Circuit

Regardless of the element changes caused by activation, the corrosion products of metal materials are released into the coolant, and the following mass transfer processes will occur:

1) CRUD inside and outside the core is deposited on the fuel surface and the surface of the primary circuit structural material;
2) CRUD inside and outside the core will be slowly released after deposition and return to the primary coolant again;
3) Some of the corrosion products that have not been deposited are purified by the chemistry and volume control system, and some remain in the coolant.

Based on the mass conservation equation:

$$M_{bulk} \cdot \Delta C = -\Delta m_{IC} - \Delta m_{OC} - \Delta m_{CVCS} + \Delta m_{REL} \tag{8}$$

where: M_{bulk} represents the water loading capacity of the primary circuit; C represents the concentration change rate of corrosion products in the primary circuit; Δm_{IC} represents the rate of mass change of CRUD inside the core; Δm_{OC} represents the rate of mass change of CRUD outside the core; Δm_{CVCS} represents the rate of mass change of corrosion products purified by the chemical and volume control system; Δm_{REL} represents the rate of mass change of CRUD release.

3 Calculation Results and Analysis

3.1 Input Parameters

Based on the above model, CAMPSIS software independently developed by China Nuclear Power Technology Research Institute [17] is used to analyze the normal operation and SO conditions of a PWR continuous fuel cycle. The letdown system can purify primary coolant, reduce CRUD deposition inside and outside the core, and reduce coolant source term and deposition source term. There is only one letdown pump in normal operation. In the analysis, by increasing flow rate, the influence of double letdown pumps operation on CRUD and source term is obtained. Thermal hydraulic parameters for calculations are provided by sub-channel software LINDEN [18].

3.2   Discussion on Calculation Results

Figure 2 shows the total CRUD in different operation modes of the PWR, and Fig. 3 shows the CRUD mass distribution in each operation mode in the primary circuit. The calculation results show that:

1) Under normal operating conditions, the total amount of CRUD deposition is gradually increased with the operating time in a fuel cycle; However, during SO, the total amount of CRUD decreases, which is due to the decrease of the output power and temperature of the primary circuit, the decrease of SNB rate reduces the total amount of CRUD deposition caused by boiling. However, with the increase of fuel cycle, the oxide film on the surface of the primary circuit structure materials becomes more and more stable, and the corrosion products released into the primary circuit become less and less, and the total amount of CRUD shows a gradual downward trend.

2) In the primary circuit, the total amount of CRUD inside the core is more than half of the total amount of CRUD in primary circuit and the mass removed by letdown. Under the condition of double letdown pumps operation, the total amount of CRUD removed by letdown accounts for about 23% of the total CRUD mass while under normal operation conditions, it is only about 14%, which efficiently reduces the total amount of CRUD deposited inside and outside the core.

3) Under the double letdown pumps operation condition, because of the increase of letdown flow rate, the purification efficiency is improved, and the total amount of corrosion products in the primary circuit is reduced, so the total amount of CRUD deposition is also reduced. With the increase of fuel cycle, the total CRUD of double letdown pumps decreased continuously. Compared with single letdown pump operation condition, the CRUD decreased by about 18% at the end of the fourth fuel cycle.
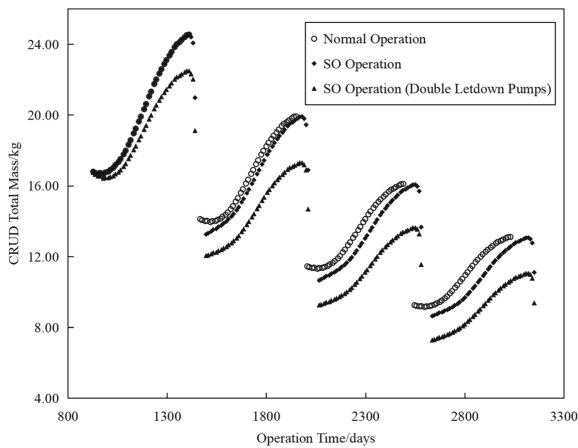
Fig. 2. CRUD Amount
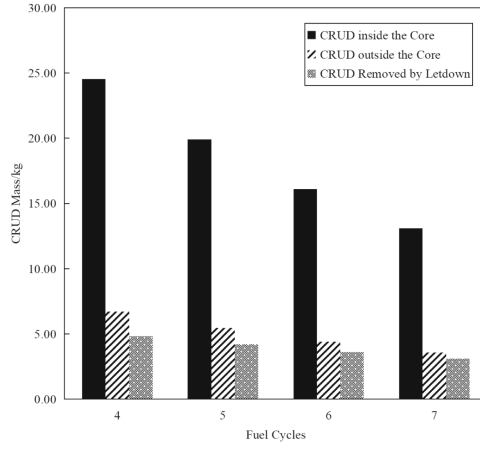
(a) Normal Operation
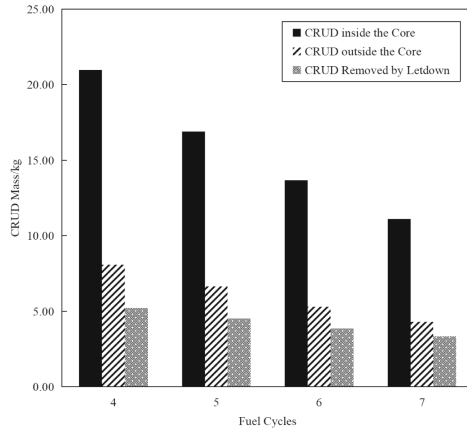
(b) SO Operation-Single Letdown Pump
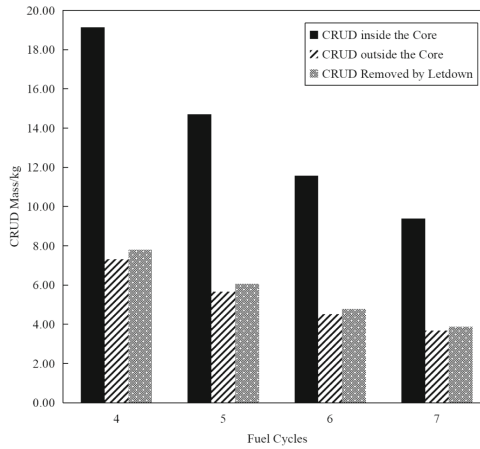
(c) SO Operation-Double Letdown Pumps

Fig. 3. Distribution of CRUD Mass in Primary Circuit

Figure 4 and Fig. 5 show the coolant source term levels of 58-Co and 60-Co respectively, and 51-Cr, 54-Mn and 59-Fe have similar trends, which are not listed here. Figure 6 shows the deposition source term level at the main pipeline outside the reactor. The calculation results show that:

1) The source term level of radionuclide is determined by its generation rate and disintegration rate, and the disintegration rate is related to the half-life time of nuclide. The coolant source terms of 58-Co and 60-Co generally show a decreasing trend with the fuel cycle. However, during SO, the source term level of coolant rises, which is due to the fact that part of CRUD returns to the primary circuit due to temperature drop at this stage, resulting in an increase in the source term level of coolant. At this time, the source term level of coolant can be reduced by running the double letdown pumps.

2) With the fuel cycle, the deposition source term of the main pipeline outside the reactor gradually increases, which is due to the fact that some radionuclide with long half-life, such as 60-Co, form a relatively stable CRUD structure after deposition on the main pipeline, which is difficult to return to the primary circuit, so the deposition source term will become larger and larger. According to the operation experience, the radioactivity such as 58-Co and 60-Co can be replaced from the CRUD by adding Zinc in the primary circuit, and then the deposition source term level can be reduced by letdown purification circuit [2, 19].
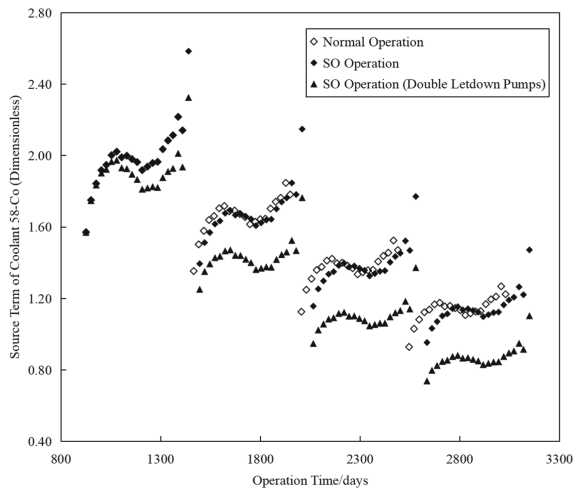
Fig. 4. Source Term of Coolant 58-Co
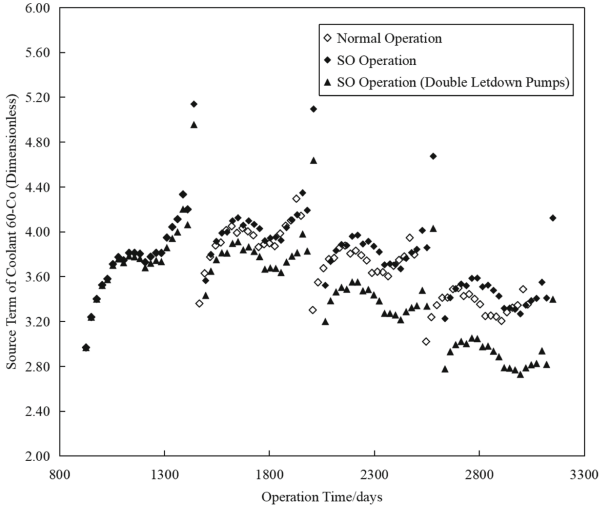
Fig. 5. Source Term of Coolant 60-Co
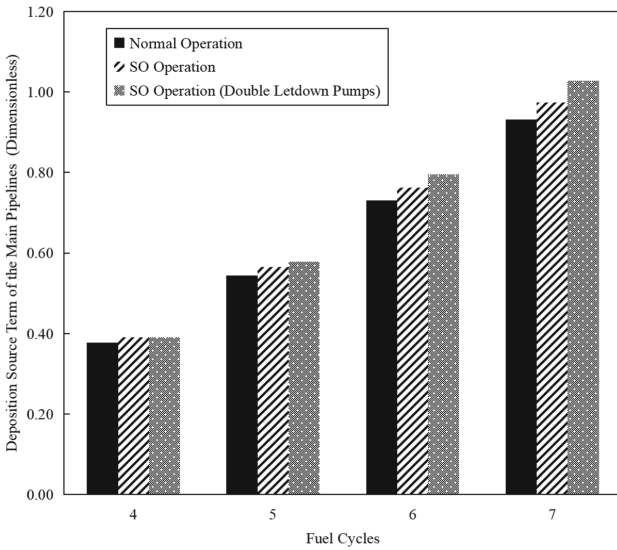
Fig. 6. Deposition Source Term of the Main Pipeline

4   Conclusion

In this paper, the effects of SO conditions on CRUD, coolant source term and deposition source term of a PWR are analyzed. The main conclusions are as follows:

1) During SO, the total amount of CRUD can be reduced while the economy is improved, and the total amount of CRUD inside and outside the core can be further reduced by double letdown pumps operation;
2) At the initial stage of SO, the coolant source term level will increase, and at this time, the coolant source term level can be reduced by running double letdown pumps;
3) The deposition source term level of the main pipeline outside the core increases with the running time.

References

1. Yin, L., Wu, D., Shen, Z.X., et al.: Special study on stretch-out operation of M310 PWR. Sci. Technol. Innovat. Herald **8**, 47–48, 50 (2020). (in Chinese)
2. Deshon, J.: PWR Axial Offset Anomaly (AOA) Guidelines. EPRI Technical Report, 1008102 (2004)
3. Riess, R.: Chemistry Experience in the Primary Heat Transfer Circuit of Kraftwerk Union Pressurized Water Reactors. Nuclear Technology, Taylor & Francis Group, pp. 153–159 (2017)
4. Meng, S.Q., Hu, Y.S., Li, C.Y., et al.: A CIPS risk evaluation methodology applicable for PWR. Nucl. Techniq. **44**(09), 86–91 (2021). (in Chinese)
5. Li, L.: Research on model of activation and migration of corrosion products in the primary loop of water-cooled reactor. School Nucl. Sci. Eng. (2017). (in Chinese)
6. Xu, M.X.: Primary coolant activation corrosion products cobalt/silver/antimony in PWR. Nucl. Safety **1**, 1–9 (2012). (in Chinese)
7. Meng, S.Q., Hu, Y.S., Yan, Y.L., et al.: Research of thermal hydraulic conditions effect on PWR CIPS risk. Front. Energy Res. Nucl. Energy (2022)
8. Kang, S., Sejvar, J.: The CORA-II Model of PWR Corrosion-Product Transport. EPRI Technical Report (1985)
9. Bird, R.B., Stewart, W.E., Lightfoot, E.N.: Transport Pheomena, 2nd Edn. Department of Chemical Engineering, University of Wisconsin (2002)
10. Speight, J.G.: Lange's Handbook of Chemistry, 16th edn. The McGraw-Hill Companies (2005)
11. Rummery, T.E., Macdonald, D.D.: Prediction of corrosion product stability in high temperature aqueous systems. J. Nucl. Mater. **55**(1), 23–32 (1975)
12. Chen, C.M., Aral, K., Theus, G.J.: Computer-Calculated Potential pH Diagrams to 300 °C. EPRI Technical Report, EPRI-NP--3137-Vol. 3 (1983)
13. Beverskog, B., Puigdomenech, I.: Revised pourbaix diagrams for chromium at 25–300 °C. Corros. Sci. **39**(1), 43–57 (1997)
14. Beverskog, B., Puigdomenech, I.: Revised pourbaix diagrams for iron at 25–300 °C. Corros. Sci. **38**(12), 2121–2135 (1996)
15. Beverskog, B., Puigdomenech, I.: Revised pourbaix diagrams for nickel at 25–300 °C. Corros. Sci. **39**(5), 969–980 (1997)

16. Huang, J., Wu, X., Han, E.H.: Influence of pH on electrochemical properties of passive films formed on alloy 690 in high temperature aqueous environments. Corros. Sci. **51**(12), 2976–2982 (2009)
17. China General Power Technology Research Institute. China General Nuclear Power Group, CGN Power. PWR Fuel Crud Behavior Analysis Code [Abbreviation: CAMPSIS]V1.0. China: 2021SR0623899 (2021)
18. China General Power Technology Research Institute. China General Nuclear Power Group, CGN Power. Sub-channel Analysis Code for Reactor Core [Abbreviation: LINDEN]V1.4. China: 2018SR517526 (2017)
19. Haas, C.: Pressurized water reactor zinc application: 2010 industry zinc update report. EPRI Technical Report, 1021184 (2010)

Study and Resolution of Pressurizer Pressure Great Fluctuation Problem in CRP1000 RGL04 Test

Kai Wang[(✉)], Bing-wen Li, Ming-jia Zhou, You-sen Hu, and Yu-long Mao

China Nuclear Power Technology Research Institute, Shenzhen, Guangdong, China
`wangkai8554@163.com`

Abstract. RGL04 Test is the highest risky test during CPR1000 power operation,which is difficult to control the state and easily results in house load, turbine trip and reactor trip. Pressurizer pressure great fluctuation problem has occurred in some of CPR1000 units, and the pressure exceeds the allowed operation range during test transient. The paper discusses the reason of the problem and the resolution is given: according to the different overheating degree of core, groups of on-off heater are actuated, or the proper power reduction rate is chosen to satisfy the operation requirement.

Keywords: RGL04 · Pressure control · Overheating · CPR1000 · Power reduction

1 Introduction

Power control bank-turbine load test (RGL04 test) [1] is to be performed to verify the accuracy of calibration G9 curve by quickly reducing the power before nuclear power plant connecting to power grid. G9 curve represents the corresponding relationship between power control rod position and steam turbine load. For the reactor with load following operation mode, it is necessary to calibrate the G9 curve periodically in order to accurately control the reactor power, and Rod Position Indication and Rod Control System (RGL) can precisely regulating the power according to the turbine load demand.

According to RGL04 test feedback of CPR1000 nuclear power plants, Pressurizer pressure of some units fluctuated greatly, and the lowest value exceeded the operating limit of ±0.1 MPa. This paper analyzes the causes of this problem and gives solutions through simulation: according to different core overheating degree, groups of on-off heater are started to increase pressure during the test, or appropriate power reduction rate is adopted to meet the requirements of operating limits. This method is reasonable and verified by current plants, and can be applied to solve the same problems.

2 Description of RGL04 Test

The initial state of RGL04 test for CPR1000 unit is as follows:

– The reactor power is maintained at 100% FP for at least 48 h, and xenon density is balanced;
– Turbine control is in automatic mode;
– Power control rod groups are all draw at 225 steps;
– Temperature control rod R is placed in automatic mode;
– The axial power deviation change rate is less than 1% FP/hour;
– The average reactor temperature is maintained within ±0.5 °C of the reference value;
– Pressurizer pressure control is in automatic mode, and on-off heater is in operation;
– Chemistry and Volume Control System is in automatic mode.

During the test, the unit power firstly reduces 100 MWe from full power (from 100% FP to around 90% FP) at 30 MWe/min; Then the power was reduced to 550 MWe (from 90% FP to 50% FP) at 50 MWe/min. In the process, R rod is manually operated and maintained at its original position, and the power control rod follows the load change automatically. Before power reduction, the dead zone of power control rod movement will be set to one step and the rod movement speed will be 72 steps/minute. During the test, the relationship between the turbine load and rod position was recorded, and a new G9 curve was determined.

3   The Problem of Pressurizer Pressure Greatly Fluctuation

When CPR1000 turbine load decreases normally, the power decrease speed is 0.5% FP/min (5 MWe/min), and the fluctuation range of system pressure does not exceed the operating limit. In RGL04 test, because the load drops rapidly, the shrinkage of primary coolant volume is obvious, and the pressure easily goes out of the operating limit.

Based on CAITA2 code simulation, when the power is linearly reduced from 100% FP to 50FP% at 5% FP/min (50 MWe/min), the changes of nuclear power and Pressurizer pressure (Figs. 1 and 2) show that the minimum pressure is 15.3 MPa, which exceeds the operating limit. Therefore, it is difficult to avoid the pressure from exceeding the limit at 50 MWe/min.

In the situation, if the pressure is required to meet the steady-state fluctuation limit, it can only be achieved by increasing the system pressure or changing the speed of power reduction.

4   Solution

4.1   Increasing System Pressure in Test

The problem of large pressure fluctuation in RGL04 test can be alleviated by manually opening two or four groups of on-off heater in advance. Pressurizer on-off heater, as a booster actuator with power non-adjustable, has four groups and it is closed at rated full power operation [2].

The influence of different on-off heater groups on Pressurizer pressure in test was analyzed by CAITA2 code at 0 °C overheating degree at 30 MWe/min (Fig. 3). At 3000s, the power was reduced from 100% FP to 50% FP at a rate of 30 MWe/min (3% FP/min).
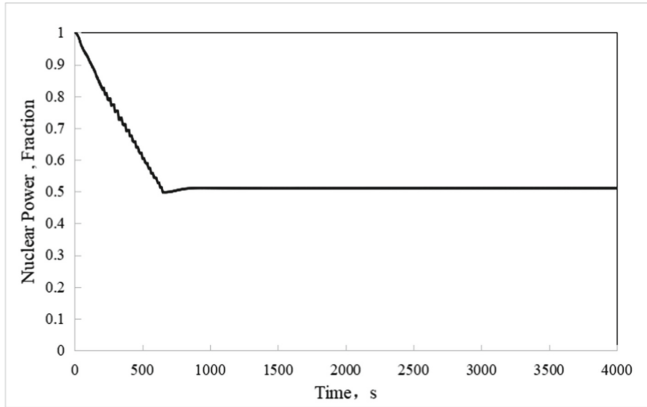
Fig. 1. Nuclear power variation in load ramp from 100%FP to 50%FP with gradient of 5%FP/min
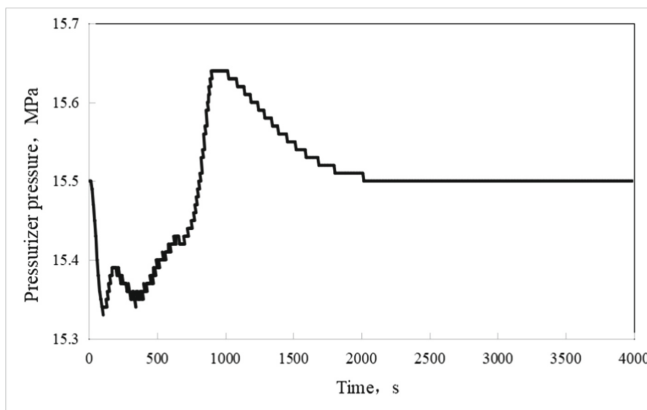
Fig. 2. Pressurizer pressure variation in load ramp from 100%FP to 50%FP with gradient of 5%FP/min

Shown from the Fig. 3, the Pressurizer pressure can be controlled within ± 0.1 MPa by actuating four groups of heater. Due to the insufficient heat provided, opening two groups of on-off heater is not enough to alleviate the pressure drop caused by power reduction. So heaters will continue to open until all the groups are started.

When no heaters work, the initial value of pressure controller PID output is 0. The on-off heater opening threshold is triggered quickly in transient, and the system pressure begins to rise until the power reduction process ends (Fig. 4). When two groups of on-off heater working, the initial value of PID output is greater than 0 and the opening threshold of all heaters is not triggered until 4000s. The pressure fluctuation is the largest on the contrary. When four groups of Heater are turned on, the PID output fluctuation is minimal, and the pressure is relatively stable.
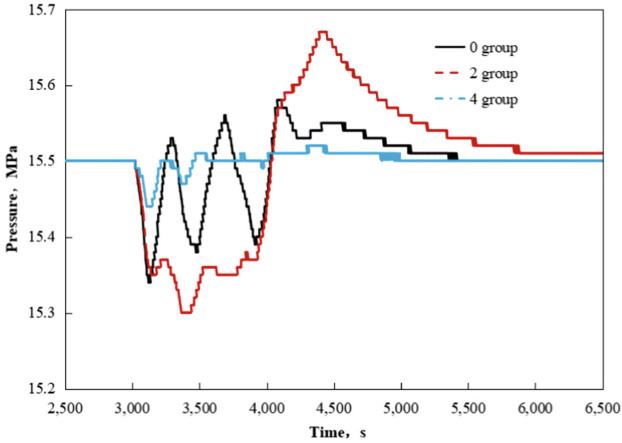
Fig. 3. Pressurizer pressure variation at different groups of on-off heater started during load ramp with gradient of 30 MWe/min
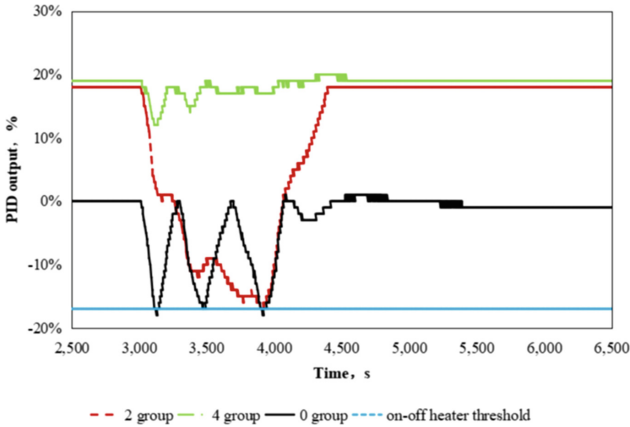
Fig. 4. Pressurizer controller PID output at different groups of on-off heater started during load ramp with gradient of 30 MWe/min

4.2   Decreasing Power Reduction Rate in Test

Under different power reduction rates, the fluctuation of Pressurizer pressure in test is different. Under 0 °C overheating and without heaters opening, the test is simulated at different reduction rates (Fig. 5). The greater the power reduction rate is, the more drastic the pressure changes. The pressure fluctuation of 50 MWe/min and 30 MWe/min are more than ± 0.1 MPa. Therefore, the appropriate power reduction rate can reduce the fluctuation degree of pressure.
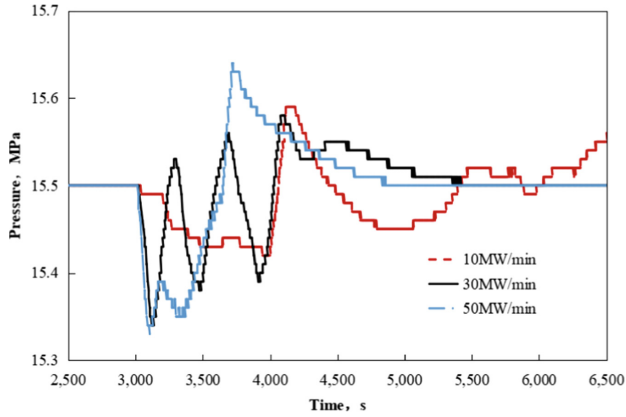
Fig. 5. Pressurizer pressure variation with different power reduction rate during load ramp

4.3 The Influence of Core Overheating

Accurate G9 curve enables the power control rod to exactly compensate power changes and ensure that the average coolant temperature is consistent with the reference value. However, due to the change rate of turbine load faster than that of core power, the power effect cannot be completely compensated by the power control rod. So the core will overheat (the average core temperature is higher than the reference temperature) in the test [3]. In the process of rapid power reduction, due to R rod manually operated, the change of average core temperature lags behind the change of power, which leads to the temperature deviation. The temperature overheating degree is accumulating. At present, core overheating phenomenon in RGL04 test is commonly existed in CPR1000 unit, and the average temperature overheating is about 3–5 °C (the test will be terminated if the overheating exceeds 6 °C) (Fig. 6). This core overheating problem is related to the operation mode of the CPR1000 unit and is the inherent characteristic.
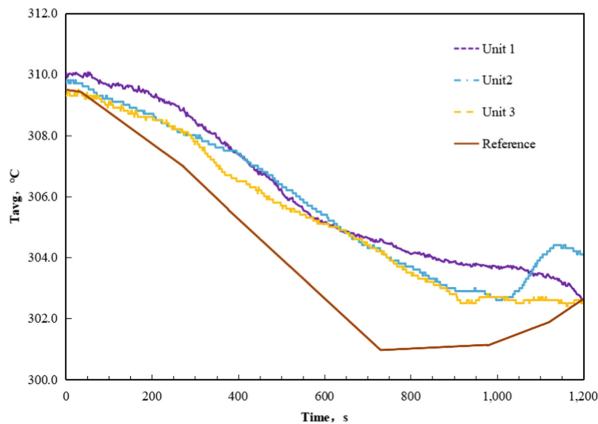
Fig. 6. Overheating degree of core average temperature in RGL04 test of different CPR1000 unit

In the process of load reduction, the existence of core overheating alleviates the problem of large pressure fluctuation in test to a certain extent, but it is still impossible to avoid the pressure from exceeding the operation limit. Without heaters opening and at a rate of 30 MWe/min, the test is simulated and Pressurizer pressure under different overheating shows that the greater the core overheating is, the smaller the pressure fluctuates (Fig. 7). Therefore, the overheating of the core is helpful to alleviate the fluctuation problem.
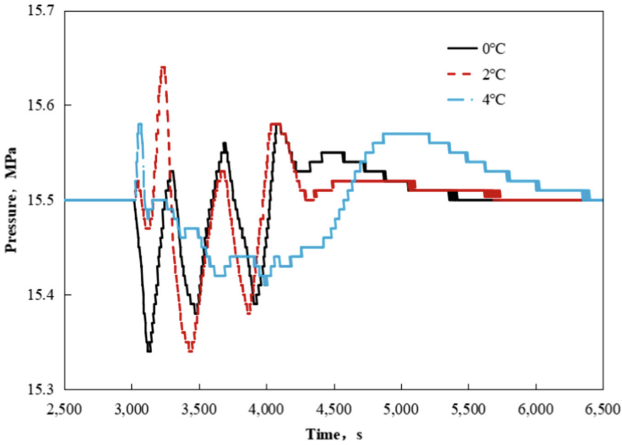
Fig. 7. Pressurizer pressure without heaters started during load ramp with gradient of 30 MWe/min

4.4 Strategy

According to the different core overheating degree, the combination of the groups of on-off heater actuated in advance and different power reduction rates is designed as shown in Table 1. The operator can choose the appropriate power reduction rate and groups of heater started based on the actual unit state. In the table, the condition of two groups of heater opened is not considered because the heat generated by the two groups of heater is insufficient to compensate for the system pressure reduction. Because the initial value of PID output is greater than 0, it spend much more time to start all the on-off heaters, which will induce large pressure fluctuation reversely.

It should be noted that when the power reduction rate is 50 MWe/min and the over-heating degree is less than 2 °C, the Pressurizer pressure cannot be maintained within ± 0.1 MPa even if opening four groups of heaters. So it should be avoided.

Table 1. The groups of on-off heater opened in advance in RGL04 test at different conditions

Overheating degree (°C)	Power reduction rate (MWe/min)				
	10	20	30	40	50
0	0	4	4	4	NA①
1	0	0	4	4	NA①
2	0	0	4	4	4
3	0	0	4	4	4
4	0	0	0	4	4
5	0	0	0	0	4

Note: ①the Pressurizer pressure cannot be maintained within ±0.1 MPa even if opening four groups。

5 Conclusion

The problem of Pressurizer pressure greatly fluctuation in RGL04 test of CPR1000 unit is discussed and the solution is given that: the operator can choose the appropriate power reduction rate and start the corresponding on-off heater groups in advance based on the different core overheating conditions to maintain the pressure within operation limit, and reduce the risk of occurrence of load rejection and reactor tripping in the test.

References

1. Zhen, Z., Liu, J.: Risk control of CPR1000 PWR RGL04 test. SME Manag. Technol. **27**, 151–152 (2018)
2. GUANGDONG Nuclear Power Training Center: 900MW PWR Nuclear Power Plant System and Equipment (I), vol. 1. Atomic Energy Press, Beijing (2007)
3. Wang, X., Fu, X., Zhang, M.: Core overheating study in power plant control rod bank calibration test. High Power Laser Particle Beams **29**(3), 56–59 (2017)

Group Constants Generation Based on NECP-MCX Monte Carlo Code

Shuai Qin[✉], Qingming He, Jiahe Bai, Wenchang Dong, Liangzhi Cao, and Hongchun Wu

School of Nuclear Science and Technology, Xi'an Jiaotong University, Xi'an 710049, Shaanxi, China
qinshuai@stu.xjtu.edu.cn

Abstract. The reliability of few-group constants generated by lattice physics calculation is significant for the accuracy of the conventional two-step method in neutronics calculation. The deterministic method is preferred in the lattice calculation due to its efficiency. However, it is difficult for the deterministic method to treat the resonance self-shielding effect accurately and handle complex geometries. Compared to the deterministic method, the Monte Carlo method has the characteristics of using continuous-energy cross section and the powerful capability of geometric modeling. Therefore, the Monte Carlo particle transport code NECP-MCX is extended in this study to generate assembly-homogenized few-group constants. The cumulative migration method is adopted to generate the accurate diffusion coefficient and the leakage correction is performed using the homogeneous fundamental mode approximation. For the verification of the generated few-group constants, a code sequence named MCX-SPARK is built based on NECP-MCX and a core analysis code SPARK to perform the two-step calculation. The physics start-up test of the HPR1000 reactor is simulated using the MCX-SPARK sequence. The results from MCX-SPARK agree well with the results from the design report and a deterministic two-step code Bamboo-C. It is concluded that the NECP-MCX has the ability to generate accurate few-group constants.

Keywords: Few-group constant · Monte Carlo · Two-step · NECP-MCX · HPR1000

1 Introduction

The two-step method [1] is the most popular approach for the practical application of neutronics calculations. During the two-step calculation, a series of lattice physics calculations are performed to evaluate the spatial and spectral flux of fuel assemblies under different state-points, and these fluxes are homogenized and collapsed to generate the assembly-homogenized few-group constants. These few-group constants are then parameterized and inputted into the nodal diffusion code to obtain the interested quantities for reactor design or analysis. Conventionally, the deterministic method like the collision probability method [1] or the method of characteristics [2] is preferred in the stage of lattice physics calculation since its efficiency, and many applications have

proven its validity. However, two main drawbacks still exist in the deterministic lattice physics codes in spite of their success, which will limit their further application. The first drawback is that the resonance self-shielding calculation like the subgroup calculation [3] must be performed to evaluate a set of problem-dependent cross-sections before the transport calculation. Some modifications or extensions must be added to the conventional resonance self-shielding methods and adopted in a deterministic lattice physics code to obtain accurate self-shielded cross-sections. And these treatments are only specific to their target problem. The second drawback is that the range of a deterministic lattice physics code for geometric modeling is limited, and the problem with complicated geometry is often replaced by an approximated model in a deterministic lattice physics model.

In order to overcome the drawbacks in the deterministic lattice physics calculation, the Monte Carlo (MC) method for the generation of the few-group constants has drawn some attention [4–7]. MC is an approach that tracks a large number of neutrons in a stochastic way and obtains the interested quantities by calculating the expected value from repeated tallies. Compared to the deterministic method, the neutron is tracked under the detailed geometric model and continuous-energy cross-section information. In addition, the neutron under MC tracking is simulated through real physical details if it interacts with a nuclide. These characteristics of the MC method make it a more rigorous and generalized method than the deterministic method. The main drawback of the MC method is that its calculation efficiency is far below the deterministic method, but the MC method is suitable to be calculated in parallel, and the improvement of the parallel computational technique and super-computer permit the MC method to be a more efficient method.

In this paper, we extend the MC code NECP-MCX [8] to generate assembly-homogenized few-group constants, and the physical start-up test of HPR1000 [9] is simulated for verification. The detailed methodology is introduced in Sect. 2, the method for verification and the numerical results are given in Sect. 3, and Sect. 4 gives the conclusion and discussion.

2 Methodology

2.1 Homogenization Method

During homogenization, three important physical quantities including the integrated reaction rates, the integrated net current, and the eigenvalue must be conserved for the homogenized assembly [10]. The equations below represent these conservation conditions in sequence:

$$\int_V \Sigma_{x,g}^{\text{hom}} \phi_g^{\text{hom}}(\vec{r}) d\vec{r} = \int_{E_g}^{E_{g-1}} \int_V \Sigma_x^{\text{het}}(\vec{r}, E) \phi^{\text{het}}(\vec{r}, E) d\vec{r} dE \tag{1}$$

where $\Sigma_{x,g}$ represents the cross-section for reaction type x and group g, ϕ is the scalar flux. The superscript "hom" and "het" represents the homogenized and heterogeneous assembly, respectively.

$$-\int_{S_k} D_g^{\text{hom}} \nabla \phi_g^{\text{hom}}(\vec{r}) ds = \int_{E_g}^{E_{g-1}} \int_{S_k} J^{\text{het}}(\vec{r}, E) ds dE \tag{2}$$

where k represents the k-th surface of assembly, J is the net-current, and D_g is the diffusion coefficient.

$$
-\sum_{k=1}^{K} \int_{S_k} D_g^{\text{hom}} \nabla \phi_g^{\text{hom}}(\vec{r}) ds + \int_V \Sigma_{t,g}^{\text{hom}} \phi_g^{\text{hom}}(\vec{r}) d\vec{r}
$$
$$
= \sum_{g'=1}^{G} \int_V \Sigma_{s,g' \to g}^{\text{hom}} \phi_{g'}^{\text{hom}}(\vec{r}) d\vec{r} \tag{3}
$$
$$
+ \frac{1}{k_{eff}^{\text{het}}} \sum_{g'=1}^{G} \int_V \chi_g^{\text{hom}} \nu \Sigma_{f,g'}^{\text{hom}} \phi_{g'}^{\text{hom}}(\vec{r}) d\vec{r}
$$

where k_{eff}^{het} is the eigenvalue before homogenization. Equation (3) is conserved if the first two conditions are satisfied.

It is impractical to perform the homogenization based on the above equation strictly, therefore, in the conventional homogenization process, the heterogeneous assembly flux is approximated by the lattice physics calculation of a 2D assembly with zero net current, then the homogenized cross-sections are be calculated as:

$$
\Sigma_{x,g}^{\text{hom}} = \frac{\int_{E_g}^{E_{g-1}} \int_V \Sigma_x^A(\vec{r}, E) \phi^A(\vec{r}, E) d\vec{r} dE}{\int_{E_g}^{E_{g-1}} \int_V \phi^A(\vec{r}, E) d\vec{r} dE} \tag{4}
$$

where the superscript A represents the assembly with net zero current.

The diffusion coefficient is approximated by:

$$
D_g^{\text{hom}} = \frac{\int_{E_g}^{E_{g-1}} \int_V D(\vec{r}, E) \phi^A(\vec{r}, E) d\vec{r} dE}{\int_{E_g}^{E_{g-1}} \int_V \phi^A(\vec{r}, E) d\vec{r} dE} \tag{5}
$$

Equations (4) and (5) cannot guarantee the conservations described before, therefore, an additional set of quantities, called the assembly discontinuous factors (ADFs) [10], are calculated and delivered to the downstream nodal diffusion code to conserve the integrated reaction rates and net currents. The ADFs are defined as:

$$
f_{g,k} = \frac{\phi_{g,k}^{\text{het}}}{\phi_{g,k}^{\text{hom}}} \tag{6}
$$

where $f_{g,k}$ is the ADF in the group g and k-th surface. $\phi_{g,k}^{\text{het}}$ and $\phi_{g,k}^{\text{hom}}$ are the surface flux of the assembly in the heterogeneous and homogeneous condition, respectively.

In addition, the assembly with zero net current differs from the assembly in a critical core, therefore, the leakage correction process is adopted by deterministic lattice physics code to evaluate the critical spectrum under its multigroup structure. This spectrum is then used to collapse multigroup cross-sections. In order to make this approach embedded in the MC homogenization, the original tally during MC simulation is based on a multigroup structure to calculate a critical spectrum for further treatments.

As described before, the basic process for MC homogenization in NECP-MCX follows:

a) MC reaction rate tallies with appropriate estimators (analog estimator for scattering matrix and fission spectrum, track-length estimator for others) are performed in the multigroup structure;
b) Flux-volume weighting are performed to calculate the multigroup cross-section. Then the leakage correction is performed based on the multigroup cross-sections to obtain a critical spectrum;
c) The critical spectrum from b) is used to calculate final few-group constants;
d) Evaluate the ADFs.

Some details must be determined from the procedures above: The tally of the diffusion coefficient in MC code, the methodology for leakage correction, and the calculation of ADFs. And these details are described below.

2.2 Generation of Diffusion Coefficient

Derived from P1 equation and Fick's law, the diffusion coefficient can be defined as:

$$D(\vec{r}, E) = \cfrac{1}{3 \left[\cfrac{\Sigma_t(\vec{r}, E) - \int_0^\infty dE' \Sigma_{s,1}(\vec{r}, E' \to E) J(\vec{r}, E')}{J(\vec{r}, E)} \right]} \tag{7}$$

where $\Sigma_{s,1}$ denotes the 1-order scattering matrix, and $J(\vec{r}, E)$ is the magnitude of current at $\vec{r}$.

However, it is impractical to tally the volume-integrated current from MC calculation since the cancellation of neutron tracks at different directions will lead to an unacceptable statistic error. Therefore, a cumulative migration method [11] is adopted in this study to generate the diffusion coefficient.

In the one-group diffusion theory, the migration area is defined as [12]:

$$M^2 = \frac{D}{\Sigma_a} = \frac{1}{6}\overline{r_m^2} \tag{8}$$

where M^2 is the migration area, D is the diffusion coefficient, Σ_a is the absorption cross-section, and $\overline{r_m^2}$ is the average square flight length of a neutron that starts from its born site to the absorbed site.

The multigroup extension for the Eq. (8) can be realized by replacing the one-group absorption cross-section with the multigroup removal cross-section:

$$M_g^2 = \frac{D_g}{\Sigma_{r,g}} = \frac{1}{6}\overline{r_{m,g}^2} \tag{9}$$

According to Eq. (9), the calculation of diffusion coefficient is given as follows:

a) During MC calculation, tally the $\overline{r_{m,g}^2}$, and notates its raw summation as T_g;
b) The multigroup migration area M_g^2 is calculated by averaging T_g by removal reaction rate;

c) The multigroup diffusion coefficient is finally calculated by:

$$D_g = M_g^2 \Sigma_{r,g} = \frac{T_g}{\Sigma_{r,g}\phi_g}\Sigma_{r,g} = \frac{T_g}{\phi_g} \tag{10}$$

However, the application of cumulative migration method is limited with infinite problems like assemblies with reflective boundaries. Therefore, an alternative method from [13] is used for homogenization of reflectors.

The P1 equation of the first moment for the 1D geometry is written as:

$$\frac{1}{3}\frac{\partial \phi_g(z)}{\partial z} + \Sigma_{t,g} J_g(z) = \sum_{g'=1}^{G} \Sigma_{s,1,g'\to g} J_{g'}(z) \tag{11}$$

Using Fick's law, Eq. (11) can be rewritten as:

$$\frac{1}{3}\frac{\partial \phi_g(z)}{\partial z} - \Sigma_{t,g} D_g \frac{\partial \phi_g(z)}{\partial z} = -\sum_{g'=1}^{G} \Sigma_{s,1,g'\to g} D_{g'}\frac{\partial \phi_{g'}(z)}{\partial z} \tag{12}$$

The integration of Eq. (12) can obtain:

$$\frac{1}{3}\phi_g - \Sigma_{t,g} D_g \phi_g = -\sum_{g'=1}^{G} \Sigma_{s,1,g'\to g} D_{g'}\phi_{g'} \tag{13}$$

After MC calculation, the quantities except for the diffusion coefficient are known, so we can solve the linear equation of Eq. (13) to calculate diffusion coefficient.

2.3 Leakage Correction

As described before, the leakage correction is necessary for homogenization since the infinite assembly differs from its actual condition in the critical core. In spite of it that some approaches like the buckling-search [14] and the albedo-search method [15] have been developed for MC, the leakage correction in NECP-MCX follows the homogeneous fundamental mode approximation [1] in the deterministic lattice physics code since its efficiency and successful application.

Using the modal expansion method, the flux in a 1D system can be expanded using its fundamental approximation which assumes that space- and energy-dependence can be separated:

$$\phi(z, E, \mu) = \psi(z)\varphi(E, \mu) \tag{14}$$

where $\psi(z)$ describes the spatial dependence, and is the spectrum.

The spatial term $\psi(z)$ satisfies the wave equation:

$$\nabla^2 \psi(z) + B^2 \psi(z) = 0 \tag{15}$$

where $B^2\varphi(E, \mu)$ is the buckling.

Then we can obtain:

$$\psi(z) = \psi_0 e^{\pm iBz} \tag{16}$$

Based on Eq. (14), Eq. (16), the 1-order expansion of anisotropic scattering, and the 1D neutron transport equation, we can obtain the B1/P1 equations:

$$
\begin{aligned}
&\Sigma_t(E)\varphi(E) \pm iBJ(E) = \\
&\int_0^\infty dE' \Sigma_{s,0}(E' \to E)\varphi(E') + \chi(E) \\
&\pm iB\varphi(E) + 3\alpha[B, \Sigma_t(E)]\Sigma_t(E)J(E) = \\
&3 \int_0^\infty dE' \Sigma_{s,1}(E' \to E)J(E')
\end{aligned}
\tag{17}
$$

The difference of B1 and P1 equations is $\alpha[B, \Sigma_t(E)]$. For B1 equation:

$$
\alpha[B, \Sigma_t(E)] =
\begin{cases}
\dfrac{1}{3}x^2\left(\dfrac{\arctan(x)}{x - \arctan(x)}\right), & x^2 = (B/\Sigma_t(E))^2 > 0 \\[2ex]
\dfrac{1}{3}x^2\left(\dfrac{\ln\left(\frac{1+x}{1-x}\right)}{\ln\left(\frac{1+x}{1-x}\right) - 2x}\right), & x^2 = -(B/\Sigma_t(E))^2 > 0
\end{cases}
\tag{18}
$$

For P1 equation:

$$\alpha[B, \Sigma_t(E)] = 1 \tag{19}$$

The critical spectrum can be calculated by solving Eq. (17) with changing buckling iteratively until the eigenvalue converges to 1. Then, the multigroup flux is corrected by the critical spectrum for further treatments.

2.4 Assembly Discontinuous Factor

The strict definition for ADF is as Eq. (6), but approximated calculations must be performed for Eq. (6) since the surface flux of the assembly in neither the heterogeneous nor the homogeneous core is unknown.

For the homogenization of infinite assembly, the heterogeneous surface flux is approximated by the surface flux from the infinite assembly transport calculation, and the homogenized surface flux is approximated by the volume-averaged flux from the infinite assembly transport calculation since the flux in the homogenized region is constant under zero net current. The ADF is calculated as:

$$f_{g,k} = \frac{\phi_{g,k}^A}{\overline{\phi}_g^A} \tag{20}$$

For the homogenization of problems without zero net current, the approximation of heterogeneous surface flux follows Eq. (20), but the approximation of homogenized surface flux in Eq. (20) fails since the flux in such a homogenized region is inconstant. Therefore, it is important to calculate a homogenized diffusion flux using the same diffusion calculation method as the downstream nodal diffusion code.

2.5 Overall Calculation Flow

The overall calculation flow for the MC homogenization is given below (Fig. 1).
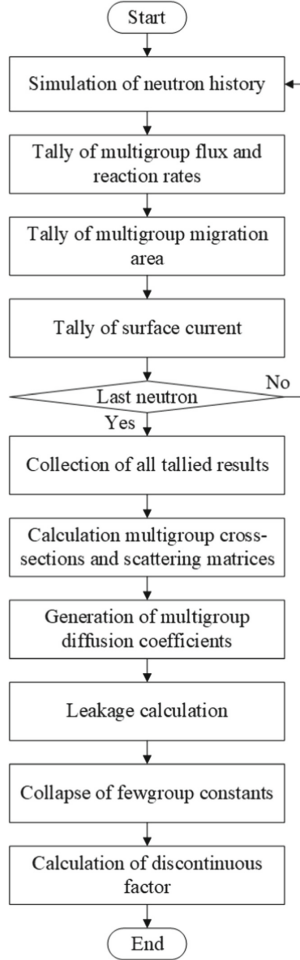
Fig. 1. Overall calculation flow for the MC homogenization

3 Verification

The validity of few-group constants generated by NECP-MCX is verified in this section. A code sequence called MCX-SPARK, where NECP-MCX generates the few-group constants and SPARK [16] performs the nodal diffusion calculation, is built for the two-step calculation. The reference results are from the design report and Bamboo-C [16]. Bamboo-C is a home-developed PWR fuel management software and has undergone the engineering validations of commercial PWR for over 100 reactor years.

The physics start-up test of HPR1000 [9] is simulated using MCX-SPARK for verification. HPR1000 is a Chinese design of the third-generation commercial PWR. There are five control rod banks in the HPR1000 notated by G1, G2, N1, N2, R, and three shutdown banks notated by SA, SB, and SC. Several tests including the critical boron concentration and the isothermal temperature coefficient under insertion of different control rods are simulated. Different control rod bank worths are also calculated.

For MC homogenization of the fuel assemblies, the quarter models of different fuel assemblies, which are classified by the fuel enrichment, the burnable absorber, the control rods, and the grid spacer, are built. A total 500 cycles including 100 inactive cycles with 200 000 particles per cycle are adopted. For the homogenization of the reflectors, the one-dimensional reflector models are built with two models for the top and bottom reflectors and nine models for the radial reflectors according to their positions. A total 500 cycles including 100 inactive cycles with 500 000 particles per cycle are adopted for the homogenization of reflectors.

3.1 Critical Boron Concentration

The tests for critical boron concentration under 11 different states are simulated and Table 1 gives the comparison of critical boron concentrations calculated by MCX-SPARK to the reference results.

Table 1. Comparison of critical boron concentration

State	Bias with the design report (ppm)	Basic with Bamboo-C (ppm)
All rods out (ARO)	−31.256	−6.473
R in	−30.635	−5.996
R, G1 in	−31.854	−6.272
G1 in	−31.411	−6.487
G1, G2 in	−33.72	−6.450
G1, G2, N1 in	−38.147	−7.501
G1, G2, N1, N2 in	−30.488	−3.165
R, G1, G2, N1, N2 in	−28.136	−0.761
R, G1, G2, N1, N2, SC in	−31.025	−1.950
R, G1, G2, N1, N2, SC, SB in	−34.483	−4.344
All rods in (ARI) with the R rod at B08 out	−45.415	−7.959

It can be seen from Table 1 that the bias between the MCX-SPARK and the design report is −45 to −28 ppm, which satisfies the limit of 50 ppm. The bias between the MCX-SPARK and Bamboo-C is −8 to −1 ppm, which has a good agreement.

3.2 Isothermal Temperature Coefficient

The isothermal temperature coefficient is a reflector of both the moderator temperature coefficient and the fuel Doppler temperature coefficient, and it is an important content in the physics start-up test. Three states are calculated and compared. Table 2 gives the results.

Table 2. Comparison of isothermal temperature coefficient

State	Bias with the design report (pcm/°C)	Bias with Bamboo-C (pcm/°C)
ARO	−0.337	0.048
R in	−1.035	0.008
R, G1 in	−1.069	−0.037

The bias between the MCX-SPARK sequence and the design report is −1.069 to −0.337 pcm/°C, which satisfies the limit of 3.6 pcm/°C. The bias of three isothermal temperature coefficients between MCX-SPARK and Bamboo-C is less than 0.1 pcm/°C.

3.3 Control Rod Bank Worth

Different control rod banks worth values measurement by boron dilution method or rod swap method in the physics start-up test are also simulated using MCX-SPARK sequence, and the comparison of the results are given in Table 3.

Table 3. Comparison of control rod bank

Test item	Bias with the design report (%)	Bias with Bamboo-C (%)
Worth of R by boron dilution	0.2	−0.3
Worth of G1 by boron dilution with R in	4.7	0.9
Worth of SB by boron dilution	−0.7	−0.4
Worth of SA by rod swap	0.1	−0.8
Worth of N2 by rod swap	−1.8	−1.7
Worth of N1 by rod swap	1.6	0.5
Worth of G2 by rod swap	0.1	−0.1
Worth of SC by rod swap	1.9	1.3
Worth of G1 by rod swap	−0.2	0.2
Worth of SB rods by rod swap at G03 and J13	0.9	−0.1

Table 3. (*continued*)

Test item	Bias with the design report (%)	Bias with Bamboo-C (%)
Worth of SB rods at G13 by rod swap	1.5	0.4
Worth of G1 by boron dilution	3.2	0.2
Worth of G2 by boron dilution with G1 in	2.9	0.1
Worth of N1 by boron dilution with G1, G2 in	6.4	1.6
Worth of N2 by boron dilution with G1, G2, N1 in	−3.0	−2.1
Worth of R by boron dilution with G1, G2, N1, N2 in	−1.2	−1.1
Worth of SC by boron dilution with R, G1, G2, N1, N2 in	4.4	1.6
Worth of SB by boron dilution with R, G1, G2, N1, N2, SC in	2.3	2.0

The range of bias for the MCX-SPARK and design report is −2.989 to 6.442%, with the RMS bias of 1.692%, which satisfies the limit of 10%. The results of the MCX-SPARK agree well with Bamboo-C, with the bias being −2.084 to 1.981%, and the RMS bias being 0.521%.

4   Conclusion and Discussion

In this study, the Monte Carlo code NECP-MCX is extended to generate the assembly-homogenized few-group constants. The cumulative migration method is used to generate the diffusion coefficient with minimum approximation and the leakage correction is performed using the fundamental mode approximation. A two-step code sequence named MCX-SPARK is built based on MC homogenization. The physics start-up test of HPR1000 is simulated by this code sequence. The results are compared with the design report and a deterministic PWR fuel management software Bamboo-C. It is observed that the biases of all test items between the MCX-SPARK and the design report satisfy the limit value. In addition, MCX-SPARK also agrees well with Bamboo-C.

The capability of NECP-MCX for the generation of few-group constants is developed and verified. But it should be noted that the application of this capability in this study is PWR two-step calculation, which poses almost no particular difficulty for current deterministic lattice physics code. In spite of it, this study, which shows the validity of MC homogenization for the practical application, gives a perspective of MC homogenization for further practical application of reactors where many approximations must be made for deterministic lattice physics calculation.

References

1. Stammler, R.J., Abbate, M.J.: Methods of Steady-State Reactor Physics in Nuclear Design (1983)
2. Askew, J.R.: A Characteristics Formulation of the Neutron Transport Equation in Complicated Geometries (No. AEEW-M--1108). United Kingdom Atomic Energy Authority (1972)
3. Cullen, D.E.: Application of the probability table method to multigroup calculations of neutron transport. Nucl. Sci. Eng. **55**(4), 387–400 (1974)
4. Tohjoh, M., Watanabe, M., Yamamoto, A.: Application of continuous-energy Monte Carlo code as a cross-section generator of BWR core calculations. Ann. Nucl. Energy **32**(8), 857–875 (2005)
5. Fridman, E., Leppänen, J.: On the use of the Serpent Monte Carlo code for few-group cross section generation. Ann. Nucl. Energy **38**(6), 1399–1405 (2011)
6. Park, H.J., Shim, H.J., Joo, H.G., Kim, C.H.: Generation of few-group diffusion theory constants by Monte Carlo code McCARD. Nucl. Sci. Eng. **172**(1), 66–77 (2012)
7. Shchurovskaya, M.V., Geraskin, N.I., Kruglikov, A.E.: Comparison of research reactor full-core diffusion calculations with few-group cross sections generated using Serpent and MCU-PTR. Ann. Nucl. Energy **141**, 107361 (2020)
8. He, Q., et al.: NECP-MCX: a hybrid Monte-Carlo-deterministic particle-transport code for the simulation of deep-penetration problems. Ann. Nucl. Energy **151**, 107978 (2021)
9. Xing, J., Song, D., Wu, Y.: HPR1000: Advanced pressurized water reactor with active and passive safety. Engineering **2**(1), 79–87 (2016)
10. Smith, K.S.: Assembly homogenization techniques for light water reactor analysis. Prog. Nucl. Energy **17**(3), 303–335 (1986)
11. Liu, Z.: Cumulative Migration Method for Computing Multi-group Transport Cross Sections and Diffusion Coefficients with Monte Carlo Calculations (Doctoral Dissertation, Massachusetts Institute of Technology) (2020)
12. Lamarsh, J.R., Baratta, A.J.: Introduction to Nuclear Engineering, vol. 3, p. 783. Prentice Hall, Upper Saddle River (2001)
13. Ryu, M., Jung, Y.S., Lim, C.H., Joo, H.G.: Incorporation of anisotropic scattering in nTRACER. In: Transactions of the Korean Nuclear Society Autumn Meeting, Pyeongchang, Korea (2014)
14. Yamamoto, T.: Monte Carlo method with complex weights for neutron leakage-corrected calculations and anisotropic diffusion coefficient generations. Ann. Nucl. Energy **50**, 141–149 (2012)
15. Yun, S.H., Cho, N.Z.: Monte Carlo depletion under leakage-corrected critical spectrum via albedo search. Nucl. Eng. Technol. **42**(3), 271–278 (2010)
16. Wan, C., et al.: Code development and engineering validation of PWR fuel management software Bamboo-C. Nucl. Power Eng. **42**(5), 15–22 (2021)

Preliminary Application of CT Technology in Non-destructive Testing of Nuclear Fuel Elements

Xiaoliang Yang[✉], Xuequan Wang, Zhe Pan, Jie Liu, and Jiandong Luo

Science and Technology Reactor Fuel and Materials Laboratory, Nuclear Power Institute of China, Chengdu, Sichuan, China
a020602@qq.com

Abstract. With the emergence of various novel fuel elements, traditional X-ray test technologies refer to national standards that have gradually been unable to meet the non-destructive testing (NDT) requirements for these novel fuel elements. As a new NDT technology, industrial computed tomography (CT) has great potential for NDT of nuclear fuel elements. In this paper, through a personalized transformation of self-developed X-ray equipment, we carried out CT scanning imaging experiments up to more than 400 kV on pellet-shell gap in rod-shaped fuel elements, a high-density annular component, and a tungsten-based workpiece. Not only that, after three-dimensional reconstruction and image analysis, it was found that sub-millimeter internal void defects could be detected. Furthermore, size measurements were carried out through image analysis which achieved a relative error of 5%. A conservative conclusion can be drawn from this research: industrial CT, including but not limited to micro-CT, high-energy X-ray CT, etc., has an optimistic future in testing internal defects and measuring internal dimensions of novel fuel elements.

Keywords: Nuclear fuel element · NDT · CT system · Measure dimensions

1 Introduction

Computed tomography technology can obtain tomography images of tested objects by calculating the attenuation information of the X-ray. It is capable of displaying the internal structure of the tested objects in an intuitive manner in the form of two-dimensional or three-dimensional images without destroying the tested objects. CT is featured with the fast speed of scanning, high resolution of image, and efficient utilization rate of radiation. Currently, X-ray CT technology has been comprehensively applied in various fields, including aerospace, aviation, military, and national defense, providing an important NDT method for the development of spaceflight rockets and spacecraft, aero-engines, and weapon system inspection.

Research institutes and universities all over the world have adopted CT technology to perform researches on nuclear fuels and nuclear materials. Argonne National Laboratory developed an XRD-CT NDT apparatus in 2017. Argonne Lab performed material

analysis and morphology observation of uranium molybdenum granular nuclear fuel. XRD-CT technology is of great significance in the preparation of nuclear fuels [1]. Purdue University and Los Alamos National Laboratory completed the experimental study of synchronous X-ray CT for the first time in 2020. They could compute the porosity and phase volume of U10Zr after neutron irradiation [2]. Argonne National Laboratory and Los Alamos National Laboratory applied near-field high-energy X-ray diffraction microscope (NF-HEDM) and μ-CT technology to non-destructively characterize the relationship between microstructure and fuel performance of sintered UO_2 in 2017 [3–5]. Germany Aachen University applied the combination of μ-CT and FIB-SEM technology to study the 3D inter-space network transportation properties of materials of the highly radioactive disposal experimental site in 2016 [6].

To meet the needs of scientific research and production, improve the testing efficiency and enhance the professional technical capability, the NDT center has performed the transformation research from X-ray Digital Radiography system (DR) to CT device. The original DR system has been transformed into a CT imaging system by hardware addition and software development, reaching a spatial resolution of 41 p/mm and a density resolution of 1%. Based on the confirmed resolution and sensitivity of the CT system, the imaging experiments of the gap in rod element, an annular components, and a tungsten-based sample are conducted. Meanwhile, artifacts generation and elimination measures of CT images are preliminarily discussed.

2 DR and CT Systems

2.1 Overview of DR Imaging System

DR imaging equipment (HS-XY-450, Dandong Huari Company) is capable of realizing a long-thin type of welding DR imaging. The device has consisted of an X-ray source, an X-ray digital imaging detector plate, a mechanical motion rack, and a necessary software system. The X-rays source emits X-rays, the detector plate receives signals in real-time, and the software system determines the automatic testing program after driving the mechanical rack to position the workpiece ROI as Fig. 1 shown. Influenced by the particularity of customization, the original DR system suffered from a poor testing range, inadequate testing efficiency, insufficient resolution, and weak testing capability. To improve the testing efficiency, increase the testing range, and enhance the testing technology capability, the research work on system transformation is implemented.

2.2 CT Transformation

The transformed system is deemed as a spiral scanning CT device, which is mainly composed of subsystems, including of X-ray source, detector system, mechanical system, high-precision motion control system, image data collection and transmission system, image processing system, radiation safety protection system. Through CT transformation, and reserving the original function capabilities, the new apparatus can realize DR two-dimensional imaging, CT tomography imaging, and CT three-dimensional imaging.

A new high voltage generator (450 kV) and auxiliary cables in the X-ray source were replaced for a stronger penetration ability. After replacement, the maximum voltage of
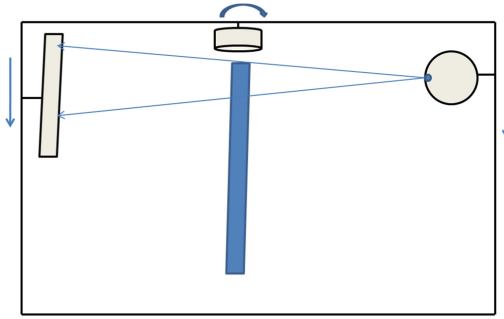
Fig. 1. Structure diagram of main components in the DR system

a high-voltage generator can reach 450 kV and the maximum power can reach 1,500 W. By adding a high precision turntable on a removable countertop at the vertically below cantilever, the samples could achieve 360-degree rotation and adjust the imaging magnification. New moving functions can be realized through the coordinated controlling of the motion control system. Figure 2 shows the pictures of the newly-added precision turntable and the high voltage generator.
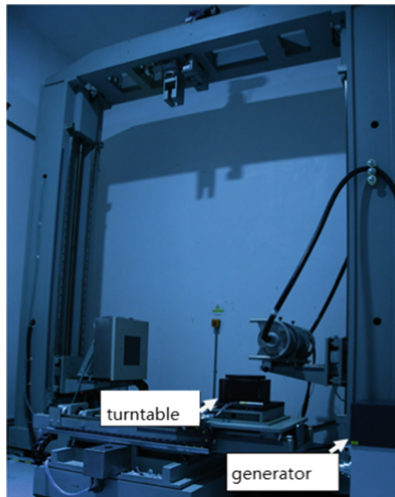
Fig. 2. Precision turntable and high voltage generator for ct imaging

The main technical indicators of the turntable include: a bearing capacity of 100 kg, maximum torque of 179 N*m, positioning accuracy of $\pm 30''$, the flatness of 5 μm, and axial deflection of 8 microns. There is no need to change the original multiple motion axes of the detector and X-ray source tube in the mechanical motion system.

The newly added turntable uses a three-claw chunk to install and fix various workpiece. When conducting CT scanning, the claws shall be fixed on the workpiece. Meanwhile, the turntable shall be disassembled quickly to ensure that the transformation has

no influence on the original function of DR. The newly added turntable is equipped with an independent electrical controlling card, which can be operated through the controlling software of the system. Other multi-axis's motion still adopts the original electrical controlling system. To realize the application needs of the CT system, the transformation system is equipped with original system controlling software, CT scanning controlling software, image reconstruction software, and image processing software. CT scanning controlling software is capable of realizing different working modes, including circular track scanning, spiral scanning, comprehensive view field scanning, and bias scanning. The image reconstruction software is capable of correcting the scanned data in real-time and repairing the image deviation caused by mechanical systems and geometric errors. Image processing software is capable of realizing CT data visualization and analysis, applying functions of data measurement, image processing, data output, animation, and other necessary features.

3   CT Imaging Experiments

3.1   CT Imaging and Artifacts

During the process of CT data collection, the initial X-ray passes through the object and occurs the attenuation after the X-ray source emitting a certain energy ray. As being absorbed by the object, partial rays come from transmission rays, and other partial rays come from scattering rays. Through the receiving by the detector plate, both transmission rays and scattering rays form a ray image, and finally impact the digital image processing and displaying system. The process is prone to be influenced by various factors, resulting in data deviation from the expected value, which seriously influences the image reconstruction results.

Various artifacts from detector outputting information cause an influence on the reconstruction results, seriously polluting the attenuation information of X-rays. Artifact on CT images is caused by equipment or sample and does not belong to the image of the scanned object, which shows that different shapes in the image will affect the accuracy of diagnosis. Generally, there are commonly two kinds of artifacts, which are artifacts caused by samples and artifacts caused by equipment. The causes of artifacts are complex and the typical artifacts include geometric artifacts, hardening artifacts, scattering artifacts, motion artifacts, and metal artifacts, which are shown in Fig. 3.
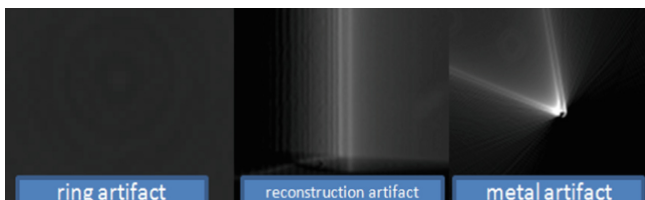
Fig. 3. Various artifacts during CT imaging

The removal of artifacts is mainly through various hardware corrections or software algorithms compensation. Based on generally suppressing most artifacts and stable

operation this equipment, we optimized the CT imaging system parameters. Finally, the spatial resolution of CT imaging system can reach 4 LP/mm, the density resolution can reach 1%, and the sensitivity is higher than 0.4 mm. The imaging of the line pair card and round hole card of the CT imaging system is shown in Fig. 4, where the resolution and sensitivity can be clearly observed. Based on this, the CT imaging research of some fuel simulators are implemented.
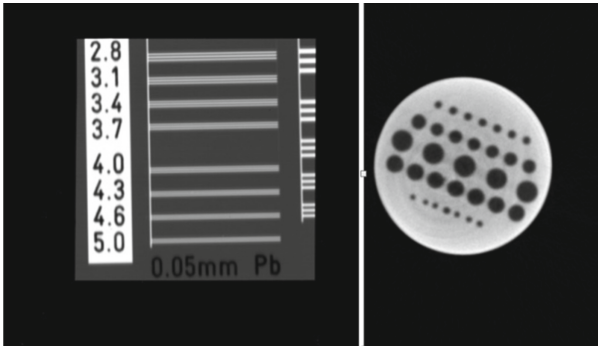
Fig. 4. Imaging of line pair test and round hole card CT

3.2 CT Imaging of Typical Work Piece

During the ray testing of the gap between shells and pellets in fuel rods, the X-ray energy selected shall be capable of penetrating the thickest place of 360° rotation of the workpiece. To obtain a high image resolution, scanning imaging is usually implemented in the range of small focus ($\leq$0.3 mm) and large focal length (1300 mm). This is because to combine the reduced size of the light source and enlarged geometric projection, a higher spatial resolution can be obtained. However, reducing the light source means reducing the luminous flux and prolonging the exposure time. To obtain the maximum testing efficiency, the core issue lies in the balance between the light source diameter and the luminous flux. The imaging of the pellet-shell gap in a simulation fuel rod are shown in Fig. 5. The gap within a certain range of different simulators can be effectively measured. In addition, it can be clearly seen that the internal assembly size is less than 0.1 mm, but it is unavailable to confirm the size obtained from the destructive test. The size exceeds the spatial resolution of the transformation system. This imaging experiment can qualitatively judge that there is a gap between pellets and the shell with a size less than 100 μm.

In the CT imaging of high-density annular components, the X-ray energy will not capable of penetrating completely until it rises to 430 kV. The reconstruction and analysis process is similar to that of fuel rod simulators. The CT images of the annular workpiece are shown in Fig. 6. Three views show the slice projection in three directions respectively. It can be observed obviously that the position with poor X-ray attenuation shows black. The X-ray intensity becomes weak after the absorption of solid substances.
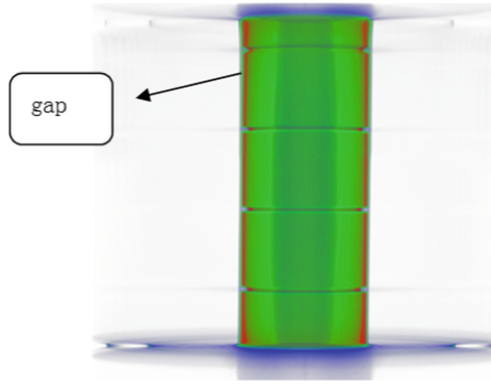
Fig. 5. CT imaging of pellet-shell gap

There are certain ray artifacts in the peripheral area of the components, and there are also reconstruction artifacts brought by the equipment or sample in the inner hole area. After selecting various imaging parameters, the ring structure can be observed in the three-dimensional image. After analyzing and measuring the image, the error between the measured size from images and the actual verification tool is about $\pm(3\text{--}5)\%$.
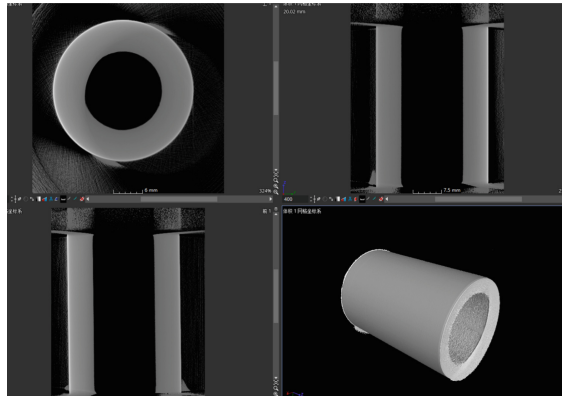
Fig. 6. CT imaging of a high density annular component

Influenced by the complex internal structure of additive manufacturing, it is difficult to be directly tested by the traditional ray or ultrasonic testing methods. Therefore, three-dimensional imaging technology represented by X-ray CT has strong application potential in nondestructive testing or online monitoring. Regarding the research on CT imaging of a triangular prism tungsten workpiece manufactured by 3-D printing, the sample size was 28 mm, the height was 100 mm, and there were 6 holes with a diameter of 2 mm and one hole with a diameter of 0.1 mm on a certain end face. When performing CT imaging for this sample, the ray energy is capable of completely penetrating only when it rises up to 445 kV. The specific experimental conditions are as follows: voltage

445 kV, current 1.2 mA, small focus 0.3 mm, exposure 0.1 s, image merging number 3, focal length 1,400 mm. Through Fig. 7, we can learn that circular holes with regular sizes are distributed on the triangular prism, but there are some non-eliminative artifacts in the triangular boundary region. Through the resolution calculation after physical calibration, the blind hole diameter is about 2.1 mm, the length is 96.5 mm, and the blind hole section length is 3.5 mm. Influenced by the decrease of sensitivity under high voltage, the seventh through-hole with a diameter of 0.1 mm (not shown in the image, but exists in the real object) is unavailable to be identified.
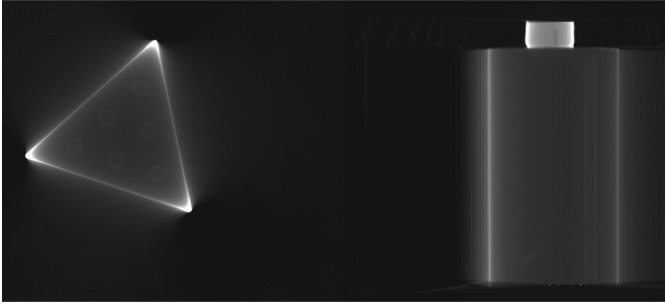
Fig. 7. Scanning reconstruction of triangular prism model

3.3   Key Factor Analysis of CT Imaging

The main factors influencing the data collection during the experiment include that dead pixels of the X-ray detector will cause the point to be unresponsive to X-rays (the dead pixels will only be displayed in the scanning stage), thus making it impossible for the pixel to collect projection data. Invalid data caused by mechanical error, program running time difference, air ambient temperature, and humidity would also bring negative effects. Furthermore, from the imaging process, we can find the installation and motion accuracy of the scanning mechanism, projection collection density, reconstruction algorithm accuracy, and the experiment factors which include exposure parameters, quantum noise, ray beam hardening, scattered ray influence, tester dynamic response, dark field noise influencing CT imaging quality.

The complex artifacts problem was caused by equipment, involving all aspects, including the data collection system, the high-voltage system, and the reconstruction process. There are several situations that will result in fringe artifacts, including the distortion of filter window, unstable rotation of scanning frame, and contamination of x-ray window. A poor detector channel will cause a clear ring artifact, and the dead pixel will also cause the same artifacts. If the temperature of the detector is too high or too low, the nonlinear response from the detector and the different performance of the integral amplifier, there will be the fuzzy ring artifacts. Data collection system: the components are also capable of generating artifacts. The development of CT imaging technology is closely connected with the development of ray sources, high-resolution X-ray detectors and various artifacts elimination algorithms. On the one hand, based

on the traditional absorption of single energy spectrum X-ray CT imaging, different substances may correspond to similar or identical CT values, resulting in the incapability to effectively distinguish target information through CT images. On the other hand, the spatial resolution is limited by the focus size of the X-ray source, the size of the detector pixel unit, the size of the measured objects, and the object image magnification ratio. There is a direct method to develop and improve the spatial resolution, including directly reducing the size of radiation source or detector pixel, and directly obtaining the resolved projection data through the magnification ratio of the object image. Besides, there is an indirect method to develop and improve spatial resolution. For instance, the current nano-CT or μ-CT imaging produces the focal depth fine beam to form an enlarged projection image on the detector through the X-ray lens.

4   Conclusions

This paper implements CT system transformation from DR imaging equipment. Through the overall planning of the X-ray source, X-ray detector, mechanical controlling, projection data collection, image reconstruction, and three-dimensional display, our team realizes the integrated operation interface, which not only improves the work efficiency, simplifies the operation process, and stabilizes the system, but also provides a more convenient and efficient inspection imaging for the nondestructive testing of nuclear fuels and nuclear materials. Through the necessary CT imaging technology conditioned experiment, the paper explores the suitable CT three-dimensional imaging parameters for the specific workpiece. The newly transformed apparatus is capable of realizing a spatial resolution of 41 p/mm and a density resolution of 1%. Through three processes of CT scanning, data reconstruction and image analysis, the volumetric defects within the sensitivity range (0.4 mm) and the dimension measurement (3–5)% error can be identified. Through analyzing and discussing the key factors in the imaging process, the paper proposes the core issues and development goals of developing high-quality CT imaging technology, providing a reference for related research in the future.

References

1. Palancher, H.: 2D and 3DX-ray Difffraction and Imaging of Nuclear Fuels (2017)
2. Thomas, J., Bengoa, A.F., Nori, S.T., et al.: The application of synchrotron micro-computed tomography to characterize the three-dimensional microstructure in irradiated nuclear fuel. J. Nucl. Mater. **537**, 152161 (2020)
3. Pokharel, R., Brown, D.W., Clausen, B., et al.: Non-destructive characterization of UO2 nuclear fuels. Microsc. Today **25**(6), 42–47 (2017)
4. Jailin, C., Bouterf, A., Poncelet, M., et al.: In situ μ-CT scan mechanical tests: Fast 4D mechanical identification. Exp. Mechan. **57**(8) (2017)
5. Jin, S.C., Hsieh, C.J., Chen, J.C., et al.: Development of limited-angle iterative reconstruction algorithms with context encoder-based sinogram completion for micro-CT applications. Sensors **18**(12) (2018)
6. Yu, W., Jie, P., Lwa, B., et al.: Characterization of typical 3D pore networks of Jiulaodong formation shale using nano transmission X-ray microscopy. Fuel **170**, 84–91 (2016)

The Investigation of Overpower ΔT Triggered Mechanism and Optimizing Strategy During Reactor Trip Experiment

Zhaojun Yuan[✉], Yuting Wu, Yanhua Cheng, Chaohao Shang, Yulong Mao, and Yalun Yan

China Nuclear Power Technology Research Institute, Shenzhen, China
545914521@qq.com

Abstract. In some nuclear power plants, the overpower ΔT protection signal may be triggered during the reactor trip test unexpectedly, which may guide operators' unexpected operations. A reactor trip protection control logic model is established to simulate the response of overpower ΔT protection channel and the onsite data in the period of reactor trip test, such as nuclear power, ΔI, etc., are used as inputs for this model. The results show that protection signals simulated by the model are almost consistent with the process of triggering protection signal in plant. According to the simulation, the drastic change of core ΔI during the reactor trip process is the main cause of triggering overpower ΔT protection signal. In order to reveal the mechanism of ΔI change in the process of reactor trip and develop corresponding strategies, a two-group three-dimensional transient neutron code (SMART) is adopted to study the physical process of reactor trip test. The effects of initial core state parameters on ΔI evolution during reactor trip are studied. And it is concluded that the initial ΔI and R bank position are the main factors affecting the extreme value of ΔI in the process of reactor trip. To avoid unnecessary overpower ΔT triggering in reactor trip test, a xenon oscillation method is proposed and proved to be effective according to SMART's simulation results.

Keywords: Reactor Trip Test · Three Dimensional Transient Simulation · Overpower ΔT Protection · Xenon Oscillation Method

1 Introduction

The reactor trip test is a normal and necessary operation in nuclear power plant to verify the reactor ability of recovering to stable conditions after triggering reactor trip without starting the emergency feedwater system and safety injection system. The test is usually conducted in the first cycle of CPR1000 PWR and all the control rod banks drop after the manual shutdown. Recently, it was found that in the process of reactor trip, the overpower ΔT protection signal is triggered, and then the process is directly guided into the emergency operation criterion (ECP1) according to the criterion "Boron Dilution Alarm shutdown" of SOP program. After that, the unit is switch to the fuel pool cooling and treatment system (PTR) to fetch water, which is inconsistent with the expected

shutdown DOS program to stabilize the unit. After analyzing the onsite data, it is found that the fundamental reason for triggering the protection signal is the drastic change of axial power difference (ΔI) which caused by the insertion of control banks during the reactor trip process.

ΔI is a parameter characterizing the axial power distribution, which is defined as follow:

$$\Delta I = P_H - P_B;$$

where P_H and P_B are relative power of the upper and lower part of the core respectively.

To verify if the protection systems work properly and the reason why the ΔI change so drastically in the reactor trip process, two major works are conducted in this paper. Firstly, a reactor trip protection control logic model is established exactly the same as the plant to simulate the response of overpower ΔT protection channel and the onsite data in the period of reactor trip test, such as nuclear power, ΔI, etc., are used as inputs for this model. The results show that protection signal will be triggered too. Secondly, the two group three-dimensional transient neutron code (SMART) is used to study the physical process of reactor trip test, and the accuracy of the model is verified by comparing the simulation results with multiple plants' experimental data. Afterwards, based on the model, the key factors affecting ΔI in the process of reactor trip is analyzed under different initial state parameters of the core. Based on the results, a theoretically feasible method with constructing core xenon oscillation is proposed to improve the reactor trip test. The simulation results show that this method can avoid triggering overpower ΔT protection signal in the process of reactor trip test by using short-term axial xenon oscillation of the core.

2   Reason Analysis of Triggering Overpower ΔT Protection Signal

The overpower ΔT protection channel [1] provides necessary protection in case of overtemperature and overpower transient of the reactor, and ensures that there is enough operating margin during normal operation transient to avoid triggering shutdown. During the operation of the unit, the ΔT measured on-line is compared with the ΔT protection setting value to judge whether the protection action is triggered or not. The setting value of overpower ΔT protection channel is a function of the average temperature of reactor coolant (measured by the temperature of cold pipe section and hot pipe section), the speed of primary pump and the axial power deviation (measured by the external detector of reactor).

The formula for calculating the setting value of overpower ΔT protection channel is as follows:

$$
\begin{aligned}
\Delta T_{o.p} = \Delta T_{nom} \times \bigg[& K_4 - K_5\left(\frac{\tau_5 s}{1+\tau_5 s} \times\right)\frac{1}{1+\tau_1 s}\overline{T} - K_6\left(\frac{1}{1+\tau_1 s}\overline{T} - \overline{T}_{nom}\right) \\
& - K_8\left(\frac{1}{1+\tau_7 s}\right)\left(\frac{\Omega}{\Omega_{nom}} - 1\right) - F_{o.p}(\Delta I) \bigg]
\end{aligned}
\tag{1}
$$

Among them:

$\Delta T_{o.p}$:   Setting value of overpower ΔT protection;

ΔT_{nom}:   Temperature difference between heat pipe section and cold pipe section under nominal working conditions;

Ω_{nom}:   Nominal speed of primary pump;

Ω: Actual speed of primary pump;

$\overline{T}_{nom}$:   Nominal average temperature of core pressure vessel;

$\overline{T}$:   Measured average coolant temperature of primary loop;

s: Laplace variable;

K_i: ΔT protection channel coefficient (if $\overline{T} \leq \overline{T}_{nom}$, K6 = 0; if $\overline{T}_{reduce}$, K5 = 0);

τ_i: Constant of control module time;

$F_{o.p}(\Delta I)$:   Penalty function of overpower ΔT protection

The reactor trip when the measured temperature difference between cold and heat pipe sections exceeds the setting value of protection channel.

The reactor trip test process only lasts for a few seconds, so the coolant temperature in the primary loop can be considered unchanged because of the heat transfer delay. In the process of reactor trip, the control rod banks drop from the reactor top to the bottom, which will lead to the rapid reduction of core power. Besides, the core axial power distortion occurs because of the rapid movement of control banks in the core vertical direction which will lead to drastic change in core axial power offset. Therefore, the last term in overpower ΔT protection channel named ΔI penalty function has great influence on the setting value of overpower ΔT protection. For the first cycle in CPR1000 plant, the function is shown in Table 1.

Table 1. ΔI penalty function of overpower ΔT protection signal

	Onsite data	
Overpower ΔT $F_{O.P.}(\Delta I)$	$\Delta I \leq 0.48$	$F_{o.p.}(\Delta I) = 0.61$
	$-0.48 < \Delta I \leq -0.23$	$F_{o.p.}(\Delta I) = -2.44 \times (\Delta I + 0.23)$
	$-0.23 < \Delta I \leq 0.28$	$F_{o.p.}(\Delta I) = 0.0$
	$0.28 < \Delta I \leq 0.62$	$F_{o.p.}(\Delta I) = 1.50 \times (\Delta I - 0.28)$
	$\Delta I > 0.62$	$F_{o.p.}(\Delta I) = 0.51$

The overpower ΔT protection channel is simulated and the onsite ΔI data in the reactor trip test are used as inputs for this model to analyze (see Fig. 1). It can be seen that the drastic change of ΔI in the reactor trip process is the direct cause of triggering the overpower ΔT protection signal.
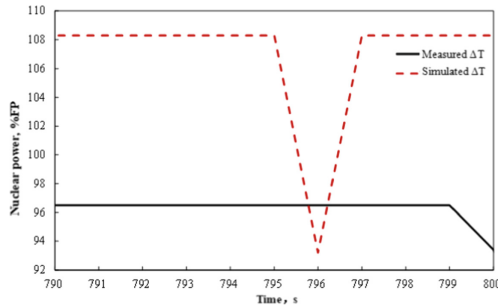
Fig. 1. The simulation of overpower ΔT signal triggered

3 Modeling the Physics Process of Reactor Trip Test

The transient duration of the reactor trip test is about 2s from the beginning of the control banks dropping to the bottom of the reactor. During this period, the average coolant temperature in the primary loop is almost constant. The core power is mainly affected by the control banks value and doppler feedback, and the moderator feedback can be regarded as almost zero. Therefore, the influence of thermal hydraulic parameters can be ignored when considering the model. In this paper, a three-dimensional two-group transient neutronic codes named SMART, is used to simulate the physical process of reactor trip test with the same initial conditions as the target unit.

3.1 SMART Model

SMART is a three-dimensional neutronic code developed by Framatome and used in the PWR fuel management and accident analysis for decades. It can simulate some reactivity insertion transient such as control rod drop and withdraw. Also, it can predict the core xenon oscillation trend and the axial power distribution in the process.

In this simulation, the analysis is mainly divided into five parts, and the overall flow chart is shown in Fig. 2:

1) Refer to the three-dimensional fuel management model. Simulation of reactor trip test is carried out based on this fuel loading scheme.
2) Simulation of xenon transient. Because the main cause of triggering the overpower ΔT protection signal is ΔI, the initial core power distribution (initial ΔI) must be adjusted by xenon transient.
3) Initial state adjustment. Adjust the initial nuclear power and coolant temperature in the core to the onsite initial state.
4) Core geometry and mesh adjustment. To capture the details of axial power distribution, the core axial mesh is refined, and the geometry is expanded to full model instead of one quarter.
5) Transient simulation of rod drop. The control banks insertion step vs time is defined here.
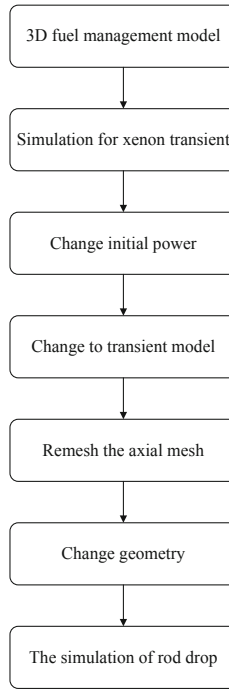
Fig. 2. SMART analysis process

3.2 Detector Influence

The core power detectors are mainly used to detect the axial power offset and radial power inclination of the reactor. The location of detector in core is shown in Fig. 3. Because the mechanism of power detection is the thermal neutron fission, the signal strength is mainly affected by the peripheral fuel assemblies neutron diffusion nearby the detector. The proportion of each assembly is defined in advance according to the Monte Carlo simulation. The radial power redistribution factor FRR is defined as the ratio of the detector power after rod drop to that before rod drop at the same average power:

$$FRR\mathrm{i} \; = \; \frac{\sum\limits_{j=1}^{n} a_j * P_j(\text{Roddrop})}{\sum\limits_{j=1}^{n} a_j * P_j(\text{ARO})}, \quad \mathrm{i} = 1, 2, 3, 4$$

a_j is the balance factor of peripheral components calculated by simulation, that is, the weight of detector response to the average power of peripheral fuel assembly. P_j(Rod drop) and P_j(ARO) are average assembly power for each component after and before rod drop.

The onsite detectors' responses are mainly affected by the peripheral components power of the core, while the simulation by SMART calculates axial power distribution

base on the power of the whole core. There may be some difference between the real detector response and theoretic calculation. In order to assess the difference in the process of rod drop, the detector response is calculated by algorithm described below. The specific method is as follows:

Calculate the axial power offset of peripheral components at time i:

$$AO_{ij} = \frac{P_{ij-up} - P_{ij-down}}{P_{ij}}$$

Calculate the measured power of detector at time i:

$$P_d = \frac{P_i * \sum_{j=1}^{n} a_j * P_{ij}}{P_0 * \sum_{j=1}^{n} a_j * P_{0j}} * P_0$$

Calculation of axial power distribution measured by detector at time i:

$$\Delta I_d = P_d * \sum_{j=1}^{n} a_j * AO_{ij}$$

P_0:   Total core power at initial time;
P_i: Total core power at time i;
P_{0j}:   Peripheral component power at initial time;
P_{ij}:   Peripheral component power at time i;
P_{ij-up}:   Peripheral component upper power at time i;
$P_{ij-down}$: Peripheral component down power at time i;
AO_{ij}:   Axial power offset of peripheral components at time i;
P_d: Detector measured power at time i;
AO_d: Detector measured axial power offset at time i;
ΔI_d: Detector measured ΔI at time i

Because the initial detector is calibrated, the initial power of the detection response is consistent with the initial power of the programmed simulation, both of which are P_0.

Based on the method defined above, the ΔI change in the rod drop transient is simulated. Figure 4 shows the ΔI comparison between theoretical detector's response and core average value. It can be seen that the difference of ΔI between detector response and core average axial power distribution during rod drop is only about 1%FP, which means we can use the core average ΔI to replace the detector response ΔI.

3.3 Control Banks Drop Curve

The control rod drop curve has a great influence on the reactivity insertion and axial power distribution. The ideal way to obtain the rod drop curve is the data from control bank step detector. Unfortunately, the accuracy of data acquisition is far from enough in
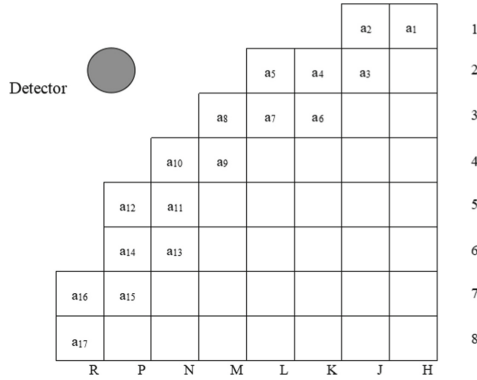
Fig. 3. Detector location

(a) AO

(b) ΔI
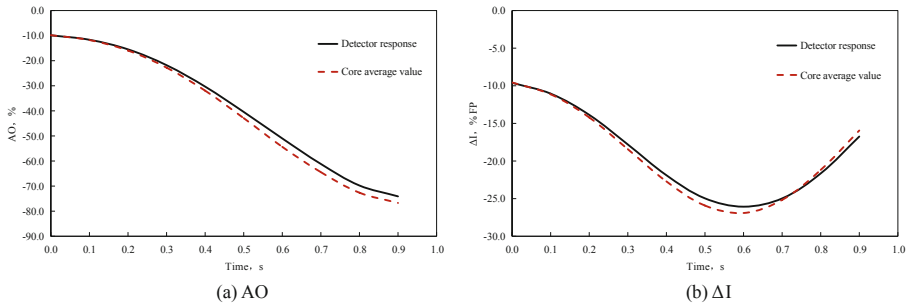
Fig. 4. Comparison of AO and ΔI between detectors response and core average value

2 s. Therefore, a few control banks drop curve coming from different rod drop tests and a curve calculated by the rod drop codes [2–4] are selected as the inputs of the transient calculation model. Under the test conditions, the other control banks drop from the top of the reactor, while the Regulation banks(R banks) drop at the upper part of the reactor core. Because there is no rod drop test data with R banks, a compromised way by fitting drop curve of original test is proposed. According to the test data dropping from top as shown in Fig. 5, the rod drop process can be divided into three phases: acceleration phase, uniform phase and deceleration phase. The main difference between dropping from top and in the upper part is the uniform phase time. The acceleration phase and deceleration phase can be considered the same. Because the initial R banks withdraw step is known, a R banks drop curve is constructed in Fig. 5 based on the theory above.

The simulation results of different rod drop curves are shown in Fig. 6. It can be seen that the simulation results with Unit 1 has better agreement with nuclear power and ΔI test data, so the Unit 1 rod drop curve is chosen in the next analysis. Based on this model, this paper also simulates the reactor trip test process of other PWR units, and compares their ΔI extreme values achieved in the test process. The comparison results are shown in Table 2. It can be seen from the results in the table that the simulation results are in good agreement with the test data.
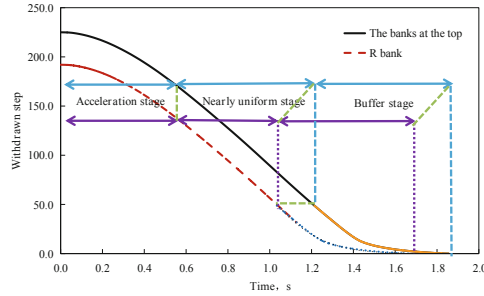
Fig. 5. The rod drop curve of Outside banks and R bank
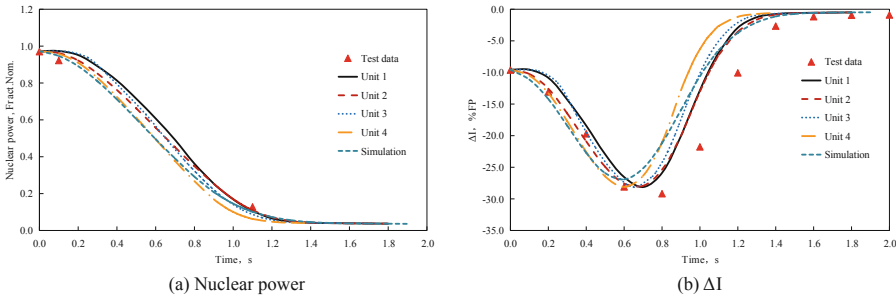
(a) Nuclear power   (b) ΔI

Fig. 6. Comparison of nuclear power and ΔI with different rod drop curve

Table 2. The comparison results between tests and simulation in different nuclear power station

Unit	Initial power (%)	Withdrawn step of R bank	Onsite ΔI (%FP)		Simulating ΔI (%FP)		Whether to trigger ΔT signal	
			Initial value	Extreme value	Initial value	Extreme value	Onsite	simulation
A	96.40	190	−9.24	−26.17	−9.21	−27.11	N	N
B	97.80	190	−13.77	−29.50	−13.76	−30.11	Y	Y
C	97.30	192	−9.61	−29.18	−9.56	−27.94	Y	Y
D	98.87	184	−9.40	−27.56	−9.37	−27.00	Y	Y
E	98.60	192	−12.30	NA	−12.14	−29.02	Y	Y
F	98.60	192	−11.10	NA	−11.14	−27.95	Y	Y

4 Investigation on Influence Factors of ΔI Change in Reactor Trip Test

Because the initial state of the core has a great influence on ΔI in the process of reactor trip, the initial axial power distribution, initial position of R bank and burnup of the reactor core are analyzed in this paper.

4.1 Initial Axial Power Distribution

The initial axial power distribution will affect the differential value during the rod drop process, thus affecting the power decreasing rate and the change of ΔI. Therefore, the influence of core power distribution (initial ΔI) is evaluated. The method is to keep the R bank position unchanged, adjust the initial ΔI of the core to different values, and then simulate the control banks drop. The analysis results are shown in Fig. 7. It can be seen that the more negative the initial ΔI is, the slower the core power decreases, and the more negative value of ΔI reached during rod drop.
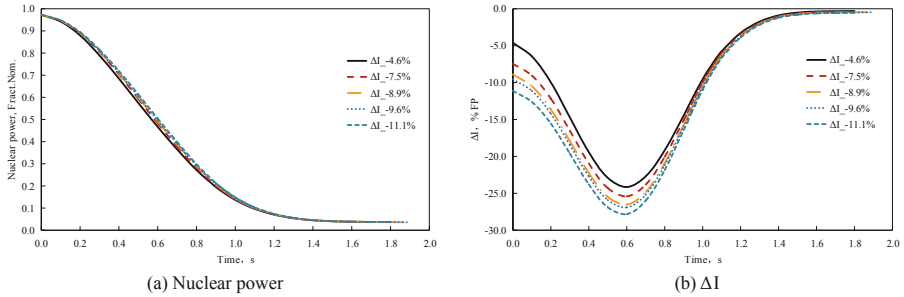
(a) Nuclear power   (b) ΔI

Fig. 7. Comparison of nuclear power and ΔI at different initial core ΔI

4.2 R Bank Position

R banks is mainly used as coolant temperature regulation, so its initial step is adjustable. Because the reactivity value of R bank is relatively large, the initial position of R banks determines the integral and differential reactivity value of R bank during the rod drop process, thus affecting the power change during the reactor trip. Therefore, this section evaluates the influence of the initial position of R bank. The evaluation method is that keeping the initial ΔI unchanged and adjusting the R bank to different initial positions. The analysis results are shown in Fig. 8. It can be seen that the larger the R bank withdrawn step, the slower the power decreasing rate, and the more drastic of ΔI change. From the withdraw steps (210 steps) to the R bank insertion limit (179 steps), the influence of R bank position on ΔI exceeds 5%FP.
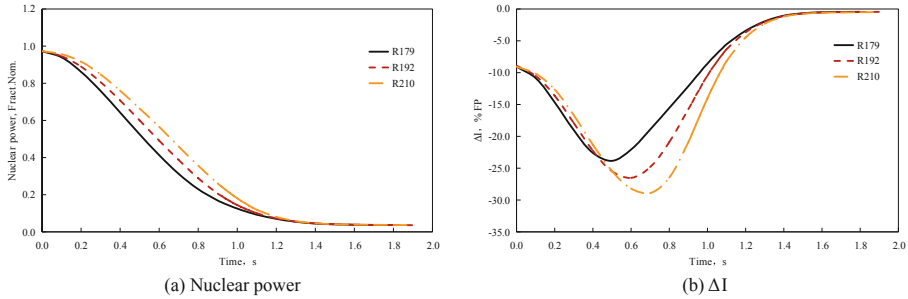
(a) Nuclear power   (b) ΔI

Fig. 8. Comparison of nuclear power and ΔI between different R bank withdrawn step

4.3 Influence of Burnup

Different burnup may affect the rod worth and core reactivity feedback character. This section analysis five burnups from 150MWd/tU to 750MWd/tU in xenon equilibrium state with the R bank adjusted to different positions. The calculation results are shown in Fig. 9. From the analysis in the figure, it can be seen that in the range of 150MWd/tU to 750MWd/tU, burnup has little influence on ΔI in the process of reactor trip. Besides, under xenon equilibrium condition, no matter where the initial position the R bank is, there is no obvious difference in the extreme value of ΔI, which will trigger the overpower ΔT signal without doubt.

According to the above analysis, the following conclusions can be drawn:

1) The change of ΔI in the reactor trip process is an important factor affecting the triggering of the overpower ΔT signal. The extreme value of ΔI determines whether the overpower ΔT signal can be triggered or not.
2) The main factor affecting the ΔI extreme value in the reactor trip process is the initial ΔI and R bank positions of core. The more negative the initial ΔI is, the easier the overpower ΔT signal is trigged. When the initial ΔI is the same, the larger the R bank withdrawn step is, the easier the overpower ΔT signal is triggered.
3) In the burnup range analyzed in this paper, no matter what position the R bank is in the regulation band under xenon equilibrium condition, the difference of ΔI extreme value is small, and the overpower ΔT signal will be triggered.

(1) 150MWd/tU

(2) 300MWd/tU

(3) 450MWd/tU

(4) 600MWd/tU

(5) 750MWd/tU
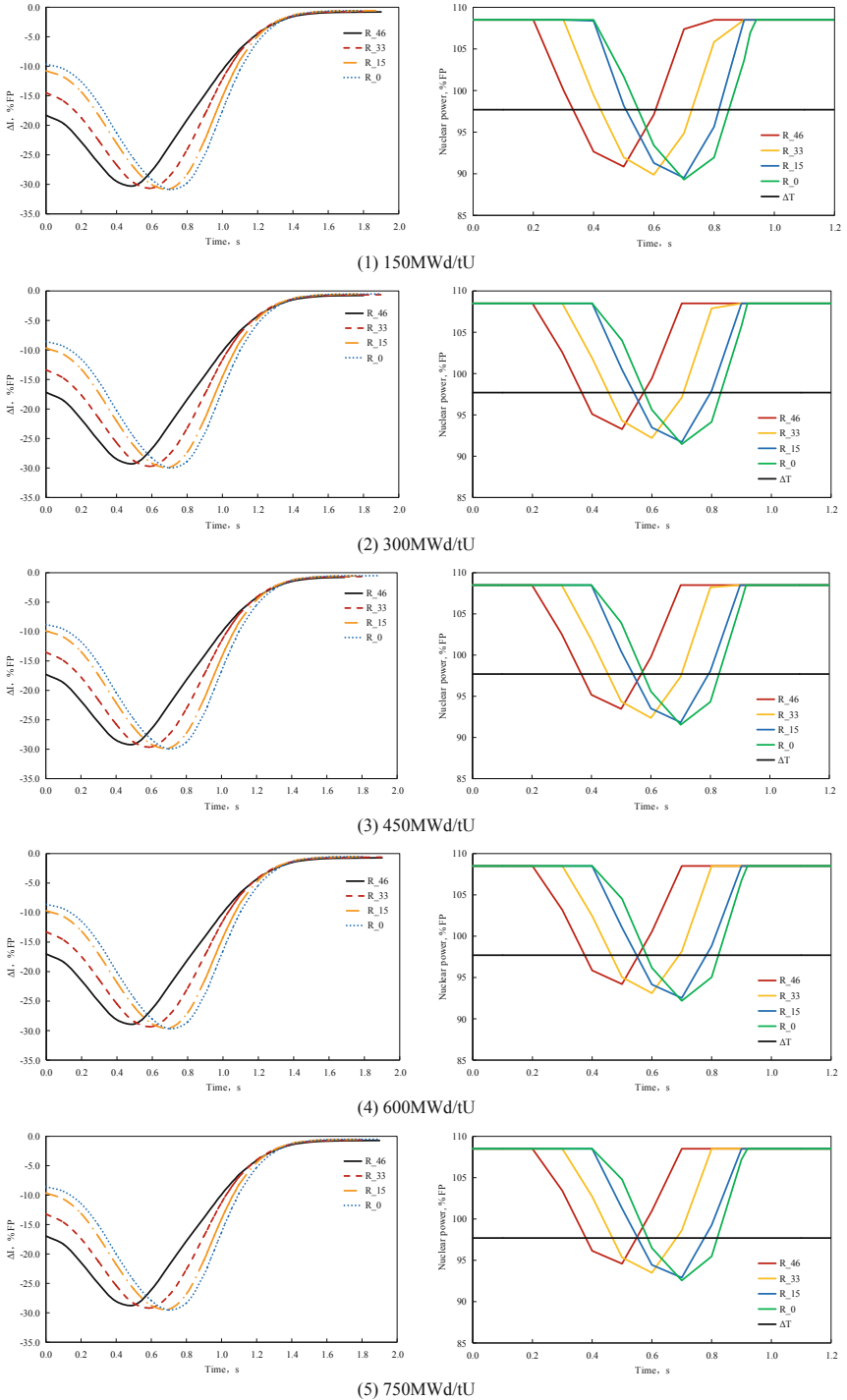
Fig. 9. Comparison of ΔI and overpower ΔT trip signal in different burnup

5   Improvement Method

Based on the above conclusions, the overpower ΔT signal is triggerd undoubtedly under xenon equilibrium condition. Under xenon disequilibrium condition, different ΔI extremes can be obtained by adjusting ΔI and R bank positions before rector trip test. Therefore, in this paper, a method of boronizing and withdrawing R banks together is proposed to cause a xenon oscillation in the core (xenon strategy is shown in Table 3). The xenon oscillation process is simulated by SMART codes and the simulation results are shown in Fig. 10. In this xenon oscillation process, the ΔI continuously moves towards in the positive direction within 7 h, so a more positive value of initial ΔI can be obtained in this period compared with the xenon equilibrium condition (under the same R bank position).

The ΔI, R banks position and boron concentration in different xenon oscillation moments are selected as the initial states of the reactor trip test. The ΔI curve of the reactor trip process is shown in Fig. 11-(a). The simulation is carried out based on the protection logic of overpower ΔT signal. As shown in Fig. 11-(b), the reactor trip test conducted after 1.9 h will not trigger the overpower ΔT protection signal. It can be seen that the improved method can avoid triggering the overpower ΔT signal in the process of reactor trip test.

Table 3. The strategy of xenon oscillation

Time (h)	Power (fract.nom.)	R bank position (insertion step)	Boron concentration (ppm)
0	1	46	735.46
0.1	1	36	739.19
0.3	1	26	742.73
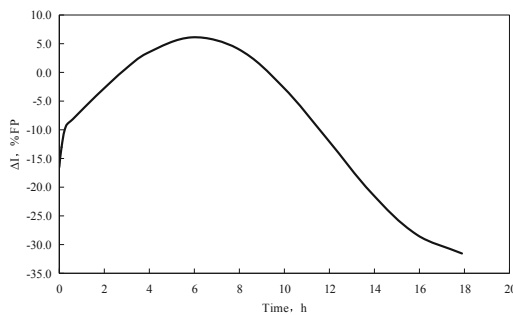
Fig. 10. Evolution of ΔI under xenon transient
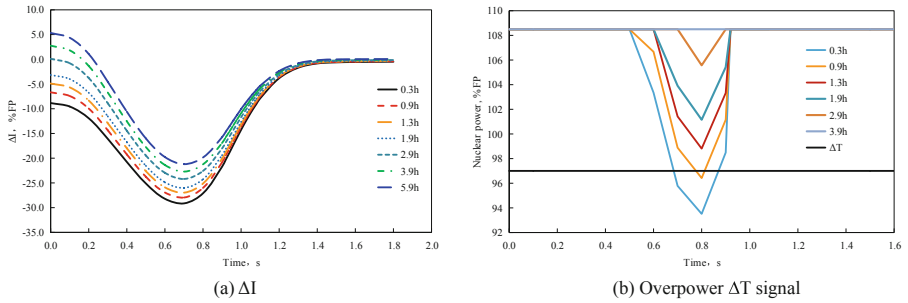
Fig. 11. Comparison of ΔI and overpower ΔT signal in different xenon oscillation moments

6 Conclusion

In this paper, the reason of overpower ΔT protection signal triggered is revealed, and a three-dimensional transient analysis model is established to reveal the mechanism of triggering the overpower ΔT protection signal in the reactor trip test. The comparison with the test data shows the rationality of the model selection. Based on the model, various factors affecting the change of ΔI during the reactor trip test are analyzed. The analysis results show that the initial axial power distribution of the core and the position of R bank have great influence on ΔI during the reactor trip, while the influence on burnup is relatively small. Based on these results, this paper presents an improved xenon oscillation method for reactor trip test. The results of simulation show that this method can effectively avoid the trigger of overpower ΔT protection signal during reactor trip test, which can be used as a reference for test of new reactor.

References

1. Li, J.: Overtemperature ΔT and overpower ΔT protection setpoint design for qinshan phase II NPP project. Nucl. Power Eng. **24**, 20–23 (2003)
2. Zhao, L.: Numerical simulation and analysis of control rod dropping of Qingshan 600MWe nuclear reactor. Nucl. Power Eng. **24**, 211–214 (2003)

3. Li, G.: Monitoring and early warning of control rod state in rod drop test. Nucl. Sci. Eng. (1) (2012)
4. Zhong, Y.: Drop performance testing of Qinshan phase II NPP project. Nucl. Power Eng. **6**, 221–222 (2003)

Analysis of Nuclear Power Economy and Its Influencing Factors

Liming Nie[1(✉)], Sa Liu[2], Xiukun Wu[2], and Zhe Li[1]

[1] Shanghai Nuclear Engineering Research and Design Institute Co., Ltd., Shanghai, China
nieliming@snerdi.com.cn
[2] China Nuclear Energy Development Center, Beijing, China

Abstract. The improvement of nuclear power economy is indispensable to the safe and efficient development of nuclear power. This paper explores the scope of economic evaluation of nuclear power based on literature and actual project operation. The evaluation scope includes power plant level, grid level and external level and this paper proposes a corresponding evaluation indicators based on the above analysis. This paper qualitatively analyzes the characteristics and influencing factors of nuclear power economy based on the current situation of nuclear power economy in China. Considering the difference between economic evaluation standard and actual operation, the typical influencing factors of economic evaluation indicators of power plant level are quantitatively evaluated. The economy of grid level and external level is analyzed by referring to foreign literature. Finally, suggestions on improving the economic efficiency of nuclear power are put forward from the aspects of economic evaluation standards and policies.

Keywords: Nuclear power economy · Evaluation scope · Evaluation indicators · Influencing factors

1 Introduction

Nuclear power is clean, low-carbon, safe and efficient high-quality energy. It plays an important role in constructing modern energy system, realizing energy transformation, protecting ecological environment, realizing carbon peaking and carbon neutrality goals, promoting scientific and technological progress, improving national comprehensive strength and guaranteeing national security.

However, in the context of the improved safety standards, the market-oriented reform of electricity, and the gradual cost reduction brought about by the large-scale development of wind power, photovoltaic and other new energy sources, the economics of nuclear power are also controversial. What is the prospect and the way out of nuclear power?

In this paper, combined with the current economic status of nuclear power, the scope and indicator system of economic evaluation will be explored, the characteristics and influencing factors of nuclear power economy will be analyzed from qualitative and quantitative perspectives, and suggestions for improving nuclear power economy will be put forward based on economic evaluation standards and policy levels.

2   The Connotation of Nuclear Power Economics

2.1   Scope of Nuclear Power Economic Evaluation

The economic evaluation of nuclear power has cost dimension and value dimension. The core is to bring more value to investors and society with competitive cost. The level of evaluation is progressive from micro level, medium level to macro level. As shown in Fig. 1 [1], micro level refers to power plant-level assessment, medium level includes grid-level assessment, and macro-level level includes environmental and social impacts. From the perspective of cost, the micro is mainly the internal cost, while the medium and macro are used to evaluate external cost. As a clean energy that can provide stable baseload power, the external cost of nuclear power is very small, but in the market competition, only the micro internal cost is usually measured.
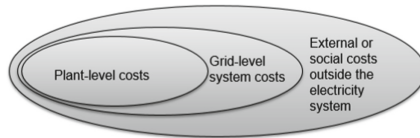
Fig. 1. Scope of nuclear power cost evaluation

2.2   Nuclear Power Economic Evaluation Indicators

Internationally, the economics of nuclear power projects are often compared and analyzed by calculating the levelized cost of electricity (LCOE) and overnight cost per kilowatt electric power. In China, the economics of nuclear power projects is evaluated by calculating the total capital cost per kilowatt electric power, the average generation cost and the on-grid electricity price during the period of operation.

The nuclear power economic evaluation indicator system corresponding to different evaluation scopes is shown in the Fig. 2 below.
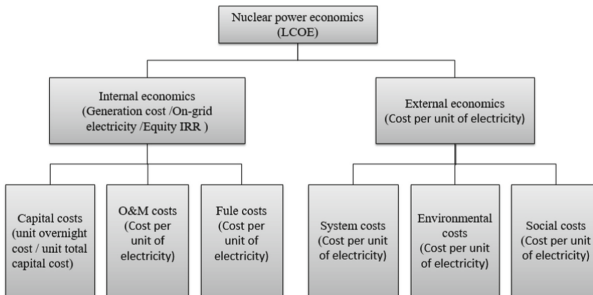
Fig. 2. Nuclear power economic evaluation indicator system diagram

3 The State of Nuclear Power Economics

Most of the Nuclear Power Plants (NPPs) in operation in China are Gen-II, and the total capital cost per kilowatt electric power is usually 11,000–14,000 yuan. Due to factors such as delays, the unit total capital cost of Gen-III First-of-A-Kind (FOAK) nuclear power units is 20,000–25,000 yuan, while the unit total capital cost of the subsequent Gen-III nuclear power units is expected to be less than 16,000 yuan.

NPPs used to adopt the "One price for one plant" electricity policy, no matter how much the cost, can always ensure a certain internal rate of return on capital. Later, the benchmark electricity price policy was adopted. The upper limit of the electricity price is 0.43 yuan/kWh or the local coal-fired benchmark electricity price (including desulfurization and denitrification price), and the return on capital depends on the cost of nuclear power. This is also the main reason why the economic efficiency of the Gen-III nuclear power plant decreases after the investment cost increases. In the future, with the continuous advancement of electricity market reform, the proportion of nuclear power participating in market-oriented transactions will gradually increase, which will further squeeze the economics of nuclear power.

4 Factors Affecting the Economics of Nuclear Power

4.1 Overview of Influencing Factors

There are many factors that affect the economics of nuclear power. The most basic factor is the technical and economic characteristics of the power plant itself. In addition, construction duration, load factor, economic life, discount rate, scale effect and learning effect will all affect the economics of nuclear power to varying degrees [2].

(1) The technical and economic characteristics of NPPs are the most important and basic factors affecting the economics of nuclear power. The constructability, operability and maintainability of the plant will affect the cost of nuclear power. The complexity, safety level, reliability requirements, achievable power plant construction period, and the power plant capacity, efficiency, availability, fuel cycle (such as UOX cycle, MOX cycle), as well as discharge fuel consumption depth, etc., will have an impact on the composition and cost of nuclear power costs as well.

(2) Nuclear power construction requires huge investment, a long construction period and a large proportion of capital cost. It is a typical capital-intensive project. Any delay in the construction of nuclear power will seriously affect the economics, such as the increased loans and the gradual rise of material costs and wages.

(3) The capital cost of NPPs is high, accounting for about 40%–60% of the generation cost. The cost related to power output is mainly fuel cycle cost, which accounts for a relatively low proportion of power generation cost, about 20%–30%, while the fuel cost of coal power and natural gas power plants accounts for more than 60%. Therefore, the economics of nuclear power is greatly affected by the load factor. The higher the annual operating rate of nuclear power, the lower the unit power generation cost.

(4) Economic life refers to the life of a nuclear power plant when it is scrapped for economic reasons, which will never be greater than its design life. The current design life of NPPs is 40–60 years. Affected by the time value of money, the benefits after 30–40 years have shrunk significantly to the present value when discounting is considered. Therefore, for the purpose of economic evaluation, the economic life of NPPs is usually set as 30 years. However, there is still a lot of profit in the later stage of actual nuclear power operation.

(5) The discount rate is an interest rate that reflects the time value of money, and is used to convert the benefits and expenses that occurred at different times into the equivalent value at the same time. It is expressed as the opportunity cost of the country or region where the power plant is built and operated. The discount rate has a great influence on the economic analysis results of NPPs with high initial investment and long life. The economic comparison of nuclear power and other power plants under different discount rates may draw diametrically opposite conclusions.

(6) The unit capital cost of nuclear power is calculated by electric power, and it is an important indicator for evaluating the economics of nuclear power. Since the proportion of unit capital cost of nuclear power in the generation cost is much higher than that of conventional thermal power, reducing unit capital cost is of great significance to improving the economics of nuclear power. When the reactor type, technical conditions and external factors are basically the same, a power plant with a smaller electric power capacity has a higher unit capital cost than those with larger power capacity, that is, NPPs have capacity scale effect, and cluster reactor construction at the same site also contributes to the total scale effect. The average unit capital cost of a series of standardized units is lower than that of a single unit with the same characteristics but designed and built separately, mainly because of the first reactor effect and the learning effect from serialized, standardized manufacturing and construction.

4.2 Analysis of Typical Influencing Factors on Internal Economy

In addition to the impact of technical solutions on the work amount, the engineering economic standard system also has a great effect on the parameters of consumption, other expenses, operation and maintenance and fuel cost, electricity price and rate of return. The following will select several typical evaluation standard parameters for detailed analysis.

(1) Impact during the economic evaluation period

At present, the principle of Gen-II plus is generally continued to be used, and the "economic evaluation period" is also considered as 30 years during the economic evaluation of the Gen-III nuclear power project. However, as the design life of the Gen-III nuclear power plant (60 years) has been significantly extended compared with that of the Gen-II plus (40 years), and most of the new domestic projects in the future are Gen-III nuclear power projects, the industry has raised the appeal of appropriately extending the economic evaluation period of the third generation nuclear power project.

Taking a domestic Gen-III reactor as an example, it is roughly estimated (according to Equity IRR (EIRR) of 9%, the electricity price of 0.430 yuan/kWh, and the total investment cost of 17,000 yuan/kW). The independent impact results of the changes in the project economic evaluation period on electricity price and total investment cost are roughly shown in the Table 1 below.

Table 1. The economic impact of nuclear power under different economic evaluation periods

No.	Economic evaluation periods (years)	Marginal change of electricity price (RMB cents /kWh)	Cumulative change of electricity price (RMB cents /kWh)
1	35	−0.72	−0.72
2	40	−0.46	−1.18
3	45	−0.32	−1.5
4	50	−0.21	−1.71
5	55	−0.14	−1.85
6	60	−0.1	−1.95

It can be seen from the above calculation that when the requirement of 9% internal rate of return on capital is met, with the extension of the project economic evaluation period, the estimated electricity price will be reduced to a certain extent, and the economy of the nuclear power plant will be further improved, but the marginal effect of extension is diminishing.

(2) The impact of loan repayment period

In the economic evaluation, the "domestic loan repayment period" refers to the past experience of operating power plants, and is generally considered as 15 years. However, with the implementation of the benchmark electricity price policy for nuclear power and the promotion of electricity market-oriented reforms, the operating income of newly-commissioned nuclear power units in my country has been affected to a certain extent, and the pressure on enterprises to repay loans has also increased relatively. In particular, the nuclear power projects to be built in the future are mainly based on the Gen-III technology route, and their economic pressure is even greater. According to the actual internal operation of the enterprise, after stress analysis and testing, the enterprise generally needs at least 25 years to complete the full repayment of the principal and interest of the domestic loan.

At present, some nuclear power projects have signed 20-year loan repayment agreements with lending banks. After communication, if there are relevant documents in the industry to support 25-year loan repayment, the bank agrees to sign an agreement with the enterprise for 25-year loan repayment.

Taking a domestic third-generation reactor as an example, it is roughly estimated (the construction price is 16,000 yuan/kW, and the capital return rate is 9% to calculate

the electricity price inversely), the general situation of the on-grid electricity price under
different loan repayment years is as follows (Table 2).

Table 2. The economic impact of nuclear power under different loan repayment periods

No.	Loan repayment period (years)	Electricity price (yuan/kWh)	Marginal change of electricity price (RMB cents /kWh)	Average generation cost (yuan/kWh)	Marginal change of average generation cost (RMB cents /kWh)
1	15	0.425	/	0.26	/
2	20	0.414	−1.13	0.27	1
3	25	0.406	−0.81	0.279	0.9

It can be seen from the above that with the extension of the loan repayment period,
the increase in the interest repaid by the project leads to a certain increase in the average
power generation cost. However, due to the reduction in the amount of loan repayment
amortized to each year, and the improvement of the project's operating conditions and
cash flow, the on-grid electricity price calculated at a fixed rate of return has declined to
a certain extent, and the economy has improved.

(3) Impact of equity internal rate of return

At present, the reference value given in "Methods and Parameters of Economic Eval-
uation of Construction Projects" (Third Edition) and "Methods of Economic Evaluation
of Nuclear Power Plant Construction Projects" is 9%, which is not a mandatory parame-
ter. The value usually reflects the requirements and expectations of investors on the return
of capital, which can be different due to the different requirements and expectations of
investors on the return of capital. The "Standard for economic evaluation of wind farm
projects" (NB/T 31085-2016) stipulates that the EIRR of wind power projects is 8%,
and the EIRR when the benchmark electricity price of Gen-II nuclear power is approved
is 8%. The National Development and Reform Commission estimates thermal power
and other benchmark electricity price capital returns are considered by 8%.

Judging from the current overall situation of the power industry, in the context of
supply-side reform, power generation enterprises can appropriately reduce the return on
capital, but at the same time should reflect the basic income level. The current 10-year
treasury bond interest rate (risk-free yield) is about 3.3%, while the SASAC's standard
for assessing the cost of capital for central SOEs is usually 5.5%.

Taking a third-generation reactor type as an example, it is roughly estimated (the
construction price is 16,000 yuan/kW, and the fixed capital rate of return calculates
the electricity price inversely), the electricity price under different yields is roughly as
follows (Table 3).

Table 3. The economic impact of nuclear power under different EIRR

No.	EIRR (%)	Electricity price (yuan/kWh)	Marginal change of electricity price (10^{-2} yuan /kWh)
1	9	0.425	/
2	8	0.4115	-1.35
3	7	0.3989	-1.26
4	6	0.3868	-1.21
5	5	0.3756	-1.12

It can be seen from the above that with the decline in the expectation of capital return, the electricity price level of the inverse calculation of the return on fixed capital is also declining, and the marginal effect is diminishing.

(4)   Impact of lending rates

Long-term loan interest rate for nuclear power projects in our base case is implemented at 4.9% (effective interest rate 4.99%). If certain preferential loan policies are considered, such as a decrease of 5%, 10%, 15%, and 20%, take a third-generation nuclear power reactor as an example to make a rough calculation (the total capital cost is 16,000 yuan/kW, and the EIRR is 9%). The electricity price under different loan interest rates is roughly as follows (Table 4).

Table 4. The economic impact of nuclear power under different loan interest rates

No.	Effective interest rate (%)	Electricity price (yuan/kWh)	Marginal change of electricity price (10^{-2} yuan/kWh)
1	4.99	0.425	/
2	4.74	0.4212	-0.38
3	4.48	0.4172	-0.4
4	4.23	0.4134	-0.38
5	3.98	0.4096	-0.38

It can be seen from the above that based on the assumed loan interest rate, for every 5% decrease in the interest rate level, the electricity price with a fixed capital yield of 9% decreases by about 0.4 cents/kWh, that is, the preferential loan policy has a certain effect on the improvement of nuclear power economy.

(5) Impact of market power

Due to the gradual increase in the proportion of nuclear power participating in market-oriented transactions, some power plants have already been between 30% and 46%.

Taking a domestic Gen-III nuclear power reactor as an example, it is roughly estimated (the total capital cost is 16,000 yuan/kW, and the annual utilization is 7,000 h), of which the benchmark electricity price of nuclear power (0.43 yuan/kWh) is used for 5,000 h, and the remaining 2,000 h are based on market bidding (considering 0.43 yuan, down 5%, 10%, 15%, 20%, 25%, 30%), the EIRR is as follows.

Table 5. Indications of the impact of market electricity prices

No.	Planned power (h)	benchmark electricity price (yuan/kWh)	Market power (h)	market electricity price (yuan/kWh)	EIRR (%)	Marginal change of EIRR (%)
1	5000	0.430	2000	0.430	10.44	–
2	5000	0.430	2000	0.409	9.97	−0.47
3	5000	0.430	2000	0.387	9.51	−0.46
4	5000	0.430	2000	0.366	9.02	−0.49
5	5000	0.430	2000	0.344	8.57	−0.45
6	5000	0.430	2000	0.323	8.09	−0.48
7	5000	0.430	2000	0.301	7.58	−0.51

As can be seen from the above table, every 5% drop in the market electricity price for 2000 h will affect the internal rate of return of the project capital by about 0.47%, and the decline rate is about 5%, which has a greater impact on the economics of nuclear power. Due to the high cost of nuclear power construction, it is necessary to ensure a certain number of annual utilization hours and electricity prices to recover fixed costs.

(6) Impact of batch

The international experience of nuclear power development shows that in the process of standardization and batch construction of nuclear power units, due to various factors such as proficiency in skills, accumulation of experience, and improvement of management, the productivity will increase, and the unit total capital cost of nuclear power units will gradually decline. This phenomenon is called the learning effect. The cost reduction due to the learning effect can be described by a learning curve. Different product series have different learning curves and learning rates. For nuclear power, the construction frequency, the number of constructions on a single site, the construction market conditions, the degree of standardization and the level of construction management will all have a certain impact on the learning rate.

Due to the scheme effect of nuclear power, that is, the development surcharge involved in the FOAK project. This is necessary to complete the design, development, qualification, testing of new systems, new equipment, and obtain manufacturing, construction licenses and authorizations. It varies with technological progress and the degree of standardization and procurement policies, but it has nothing to do with the number of units in the standardized series and is relatively fixed, which is a one-time cost.

If it is expected that a certain model can be developed in batches, such as about 8 units, then the additional one-time cost of FOAK can be shared among the series of units, thereby improving the overall economy of the model. For recurring costs, it can be reduced by learning effects, with a learning rate of 3%–10%. Even if it is a recurring cost, if considering the construction of multiple reactors at a single site, the site-related costs can be allocated within a small area. If the multi-site group reactors are located in the same area, the shared off-site emergency facilities costs can also be shared, so that there is a possibility of further economic improvement.

4.3 External Cost and System Cost

4.3.1 External Cost

The external cost of nuclear power is relatively small. According to "synthesis on the economics of nuclear energy WPEN2013-14", the external cost of nuclear power in the case of no nuclear accident is compared with other forms of power generation as in Fig. 3 [3].
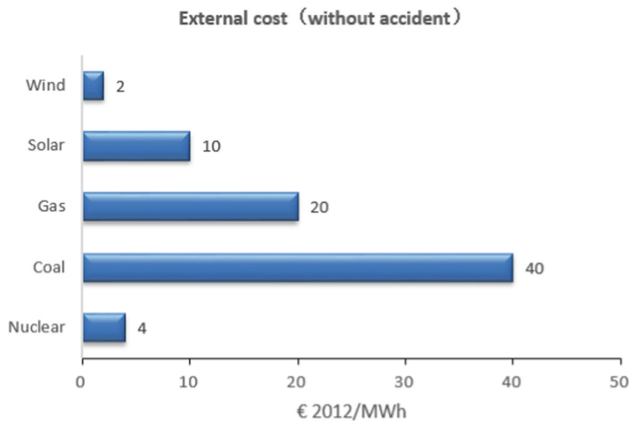
Fig. 3. Different energy external costs

After considering a certain risk of nuclear accident, the added value of the external cost of nuclear power is about 0.1–3 EUR/MWh (EUR 2012).

As the internal cost of nuclear power has taken into account the cost of post-treatment of spent fuel, the cost of treatment and disposal of medium and low radioactive waste,

decommissioning fund and insurance, etc., that is, some external costs have been internalized and not all countries include costs such as greenhouse gas emissions in the internal costs of power plants.

The external costs of nuclear power are still significantly better than those of fossil fuel power plants.

4.3.2 System Cost

The so-called system cost in foreign literature mainly refers to backup, balancing cost, grid connection, grid strengthening and extension, etc. Domestic auxiliary services refer to the services needed to maintain the safe and stable operation of the power system or restore system security, ensure the safe, high-quality, and economical operation of the power system, maintain the legitimate rights and interests of power companies, and ensure the supply of electrical energy and meet the requirements of voltage, frequency, and quality. It includes basic auxiliary services and paid auxiliary services (basic auxiliary services include primary frequency regulation, basic peak regulation, and basic reactive power regulation. Paid auxiliary services include automatic generation control (AGC), paid peak regulation, paid reactive power regulation, and automatic voltage control. (AVC), spinning reserve, hot spare, black start). The connotation of foreign system cost is greater than that of domestic auxiliary services.

Although nuclear power usually operates at base load for economic reasons, it has a certain load-following capability from a technical point of view, which gives it an advantage in system cost compared with new energy sources such as wind power and photovoltaics. Please see Table 6 [3] for details.

As shown in Table 7 [3] and Table 8 [3], nuclear power has a smaller system cost, higher than coal and gas-fired power plants, but much lower than wind and photovoltaics. At the same time, with the increase in the proportion of power sources, the system costs of nuclear power, coal-fired and gas-fired power plants remained unchanged or slightly decreased, while the system costs of wind power and photovoltaics increased significantly.

Table 6. Load tracking capabilities of different energy sources

	Start-up time	Maximal change in 30 s	Maximum ramp rate
Open cycle gas turbine (OCGT)	10–20 min	20–30%	20%/min
Combined cycle gas turbine (CCGT)	30–60 min	10–20%	5–10%/min
Coal plant	1–10 h	5–10%	1–5%/min
Nuclear power plant	2 h–2 days	up to 5%	1–5%/min

Table 7. Comparison of system costs of different energy sources in Germany1 (2011 USD/MWh)

Technology	Nuclear		Coal		Gas	
Penetration level	10%	30%	10%	30%	10%	30%
Back-up costs (adequacy)	0.00	0.00	0.04	0.04	0.00	0.00
Balancing costs	0.52	0.35	0.00	0.00	0.00	0.00
Grid connection	1.90	1.90	0.93	0.93	0.54	0.54
Grid reinforcement and extension	0.00	0.00	0.00	0.00	0.00	0.00
Total grid-level system costs	2.42	2.25	0.97	0.97	0.54	0.54

Table 8. Comparison of system costs of different energy sources in Germany2 (2011 USD/MWh)

Technology	Onshore wind		Offshore wind		Solar	
Penetration level	10%	30%	10%	30%	10%	30%
Back-up costs (adequacy)	7.96	8.84	7.96	8.84	19.22	19.71
Balancing costs	3.30	6.41	3.30	6.41	3.30	6.41
Grid connection	6.37	6.37	15.71	15.71	9.44	9.44
Grid reinforcement and extension	1.73	22.23	0.92	11.89	3.69	47.40
Total grid-level system costs	19.36	43.85	27.89	42.85	35.65	82.96

5   Conclusions

In order to cope with climate change, it is necessary to establish a clean and efficient energy supply mix. Nuclear power, which is clean, safe, stable and flexible, will be an important option in the energy mix. At present, economy seems to be the factor restricting its development.

The current cost of Gen-III nuclear power is relatively high, but its inherent technical and economic characteristics show a good economic potential. In addition, with the breakthrough of advanced fuel and material technologies, as well as the application of digital and intelligent technologies, nuclear power will achieve an effective balance between technology and economy and have a better economic prospect.

From the perspective of the full range of costs, nuclear power has a certain economic advantage, but the current economic evaluation focuses on internal costs, and the internal cost advantage is not prominent. Therefore, to improve the economy of nuclear power, one solution is to better control the internal cost, the other solution is to internalize the external cost, reflecting the comprehensive cost advantage.

Based on the above analysis, it is suggested to improve the economy of nuclear power:

(1) Appropriately extend the economic evaluation period of Gen-III advanced nuclear power. It is recommended to be clearly stated in the standard specification that the

economic evaluation period of the Gen-II plus project is still considered as 30 years, while that of the Gen-III project is considered as 40 years.

(2) Provide low-interest loans or discount policies for NPPs, explicitly support appropriate extension of loan repayment terms, but the longest term should not exceed 25 years which may better match the depreciation life.

(3) Nuclear power investors appropriately reduce the EIRR. It is specified in the standard specification that each unit can choose the EIRR by itself based on its own capital cost and investment expectation.

(4) Create a good policy and regulatory environment to promote the sustainable and stable development of nuclear power and moderate mass production, so as to obtain a better learning effect and reduce the cost of subsequent units.

(5) In the context of electricity marketization, research and introduce carbon pricing strategies to take advantage of the lower external cost of nuclear power.

(6) Internalize grid system costs when feasible and necessary.

References

1. OECD-NEA: The full costs of electricity provision. OECD 2018 NEA No. 7298
2. Zheng, M., Yan, J.: Large-scale Advanced Passive Dynamic Pressurized Water Reactor CAP1400 (Volume 1 and 2). Shanghai Jiaotong University Press, Shanghai (2018)
3. D'haeseleer, W.D.: Synthesis on the economics of nuclear energy. Study for the European Commission, DG Energy (2013)
4. Huang, G., Guo, Q.: Economic Analysis of Advanced Nuclear Power Technology. Tsinghua University Press, Beijing (2014)
5. Cao, S., Zou, S., Liu, W., et al.: Research progress and review of economic evaluation of nuclear power in my country. Beijing Sci. Technol. Ind. (2), 58–62 (2014)
6. Ren, D., Xiao, D.: Nuclear Energy Economics. Harbin Engineering University Press, Harbin (2014)
7. Qirui, G., Hanhong, S., Pingdong, C.: Philosophy towards success: From Qinshan to Chashma to AP1000. China Electric Power Press, Beijing (2012)
8. OECD-NEA: The Costs of Decarbonisation: System Costs with High Shares of Nuclear and Renewables. OECD 2019 NEA No. 7299

Local- and Small-Scale Atmospheric Dispersion Modeling Towards Complex Terrain and Building Layout Scenario Using Micro-Swift-Spray

Xinwen Dong, Shuhan Zhuang, and Sheng Fang[✉]

Institute of Nuclear and New Energy Technology, Tsinghua University, Beijing, China
fangsheng@tsinghua.edu.cn

Abstract. Atmospheric dispersion models (ADMs) have been widely used in simulating the contamination from released pollutants, which supports the emergency response and assist the inverse modeling for unknown source, due to its balance between accuracy and speed of calculation. The Micro-SWIFT-SPRAY modeling system (MSS) is one of the candidates that are able to accurately reproduce the wind and concentration fields with inputs of meteorology, topography, and source information. The obstacle treatments benefit its performance over dense buildings. Applying the optimal parameters to MSS, both the local and small-scale simulations were carried out in the vicinity of the same nuclear power plant (NPP) site with dense buildings and surrounded by mountains and sea. In these scenarios, the airflows came from the NE direction and cross over the sea and buildings to mountains. Both the wind and concentration results were evaluated against the measurements of two wind tunnel experiments. The results demonstrate that MSS can reproduce the variations of wind and concentration towards the changes in terrain elevation or building layout. The local-scale simulation well matches the measurements in the mountain area, whereas the small-scale one better reconstructs those around the buildings. The clusters of wind direction and speed are found that result from the topography of monitoring networks. The high concentration area around the release position is successfully reproduced, which indicates the turbulence is sufficient facing complex obstacles. Besides, MSS outperforms the concentration simulations in the local-scale scenario with a FAC5 of 0.710 and a FB of -0.010. However, the VG of the local-scale scenario reaches 15.510 meaning many extremes are introduced. The small-scale scenario obtains a lower VG of 2.303. Considering different performance dominances of two scales, nesting grids may bring improvement in the case both the simulations in the mountain and building areas are meant for the emergency response.

Keywords: Atmospheric dispersion · Wind field reproduction · Concentration simulation · Wind tunnel data validation

1 Introduction

Atmospheric dispersion models are designed to simulate the behaviors of ambient pollutants when released into the atmosphere, involving the wind-driven advection, turbulent

diffusion, deposition, material transformation, and decay if considering radionuclides [1–5]. They can provide the spatiotemporal distribution of the contamination, with the input of source information, meteorological data, terrain, and land use data. In the early phase of emergency response, the impact of unplanned release into the atmosphere can be predicted with ADMs, which support the decision-making of appropriate counter-measures for public protection and monitoring arrangements. Besides, the ADMS is also an indispensable tool for inverse modeling in the case of unknown sources [6].

To ensure the required speed of response, many Gaussian plume models are developed which assumes point-wise source released in the homogenous and stationary wind and turbulence intensity, e.g., ADMS [7] and AERMOD [8]. In local-scale modeling, physical turbulence parameterizations replaced the empirical stability classes to improve model accuracy [9]. Gaussian puff dispersion models have been also developed which hybrid the Gaussian plume modeling with Lagrangian modeling, e.g., RIMPUFF [10]. The appropriate scale of cases using such Gaussian-based is the local scale of 1–10 km and may oversimplify some dispersion patterns, even the urbanized ADMS-Urban model [9, 11]. In contrast, the computational fluid dynamics method (CFD) provides solutions for reproducing complicated dispersion patterns, especially the scenarios with a built-up area like buildings [12]. But CFD method requires quite more computational time compared to Gaussian-based models, due to handling with the Navier-Stokes equations. Considering the limited resources in operational platforms, a compromise between the accuracy and the response time is unavoidable.

The Micro-SWIFT-SPRAY (MSS) is a promising system for fast airflow and dispersion modeling that ensembles a trade-off approach for the obstacle parameterizations using Röckle's method [13]. Both modules of MSS, i.e., SWIFT and SPRAY, are able to consider the presence of obstacles. Among them, SWIFT provides the derived diagnostic turbulence around an obstacle area, and SPRAY, therefore, treats bouncing against obstacles and computes deposition on walls or roofs [11]. The applicate scenarios of MSS refer to both the local and the small scale in the vicinity of heterogeneous terrain and complex obstacles. Many efforts have been made to evaluate the performance of MSS (or one of its modules) in different scenarios, including the field experiments with complex terrain e.g. WSMR [14], DP26 [15], and OLAD [16], or with buildings e.g. MUST [17] and Jack Rabbit II [18], or referring to real cities as Oklahoma [19], Rome [20], and Paris [21]. Besides, there are also many evaluations of MSS based on wind tunnel experiments, e.g., RUSHIL [22], a case with a replicated urban area [23], and cases with a replicated nuclear power plant (NPP) site [24–27].

In practice, the NPP sites are commonly located with complex layouts and are surrounded by mountains and rivers. The sensitivity analysis of MSS applied to such scenarios in the local scale [25] and small scale [27] guides the parameter optimization as the number of particles, the horizontal and vertical resolutions, and the lower bound of turbulence intensity. The comparison of MSS performance in the same NPP site but with different scales remains to carry out for demonstrating the differences in dispersion behaviors and serving as a reference for scale selections in the operational application. Herein, two atmospheric dispersion scenarios of local and small scales have been applied in an NPP site featured with the aforementioned topography with the corresponding optimal parameters. These scenarios are all with NE direction airflow incoming, across over

buildings to mountains. The simulation involves wind and concentration fields, which are further compared to measurements from wind tunnel experiments qualitatively and quantitatively.

2 Materials and Methods

2.1 MSS Modeling

MSS is a 3D flow and dispersion modeling system that works well in both local and small-scale simulations. It is constituted by two individual modules, i.e., the SWIFT and the SPRAY [5]. This system has a parallelization version called PMSS [3].

SWIFT is a diagnostic wind field generator featured with mass-consistent and terrain-following over complex terrain, which was derived from the MINERVE wind model [16]. This module can ultimately provide the wind, turbulence, pressure, temperature, humidity, and other variables with the input of topography data over the entire calculation domain and meteorological data from sparse monitoring sites. The main steps of SWIFT operation involve the determination of an initial field by interpolation of raw data, the modification of previous fields considering the presence of obstacles, and the adjustment of the final non-divergent field that satisfies the boundary conditions, atmospheric stability, and consistency equation. This mass-consistency is achieved via Eq. (1) which minimizes the difference between the modified and initial wind vectors $\mathbf{U}$ and $\mathbf{U}_0$ over the calculation volume V under the mass conservation constraint [11].

$$\min_{\mathbf{U}} \int (\mathbf{U} - \mathbf{U}_0)^2 \, \mathrm{dV} \text{ with div} (\mathbf{U}) = 0 \tag{1}$$

SPRAY is a Lagrangian particle dispersion calculator, which can reproduce the physical and chemical behaviors of airborne pollutants released in various atmospheric conditions, with the input of emission information, meteorological fields, and obstacle descriptions if required.

In this module, pollutants are treated as a certain number of fictitious particles. These particles can be considered as the indivisible unit of pollutants, and their 3D distribution represents the spatial pattern of the pollutant. The velocity of one particle is the time-integrated of a transport component that defines by the averaged wind, and a stochastic component that stands for the influence of turbulence. The concentration field is therefore determined by calculating the density of particles on each grid. The motion of one particle P at the location $\mathbf{X}_p$ and time t is formulated as Eq. (2), which is the aggregate of the average wind and a stochastic component.

$$\mathrm{d}\mathbf{X}_p(t)/\mathrm{dt} = \mathbf{U}_p(t) \tag{2}$$

$$\mathrm{d}\mathbf{U}_p(t) = a(\mathbf{X}, \mathbf{U})\mathrm{dt} + \sqrt{B(\mathbf{X}, t)\mathrm{dt}}\mathrm{d}\mu \tag{3}$$

where a and B are generally functions of position and time, while $\mathrm{d}\mu$ is a stochastic standardized Gaussian term.

2.2 Wind Tunnel Experiment

Two wind tunnel experiments under a neutral stratification situation were conducted by China Institute for Radiation Protection (CIRP), with incoming airflows of 3.8 m/s (in a real-world scale) from the NE direction. Both the surface topographic models of experiments replicated the heterogeneous topography and dense buildings at a nuclear power plant site in China, but with different scales of 1:2000 and 1:600 that represent local and small scenarios (Fig. 1). Among them, the release location of tracers is in the domain center (the star in Fig. 1), in the vicinity of many buildings placed. Besides, there is mainly flat terrain of sea area in the upwind direction of the release position and continuous mountains in the downwind direction. In the experiments, the airflow or concentration is sampled and measured when the mass reaches a steady state. The numerical conversion of measurements is based on the similarity theory.
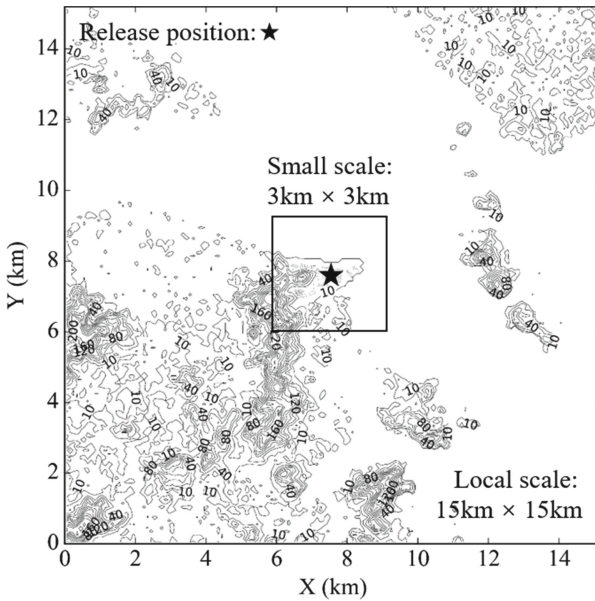
Fig. 1. Topography of wind tunnel experiments.

The measurement networks of wind fields are presented in Fig. 2, where the left and right panels represent local and small scales respectively. These sites are located around the release position and are distributed along with the NE direction. The local scale scenario places more sites in the mountain area, while the small scale one owns dense sites around the building area. The total number of measurement sites is 50 in two scenarios.

As for the measurement networks of concentration fields, the amount of sites is varying in different scenarios. The local scale scenario owns 244 sites whereas the small scale scenario takes 179 sites, due to the consideration of network density and measure accuracy. These sites are placed from near the release position to the downwind area,
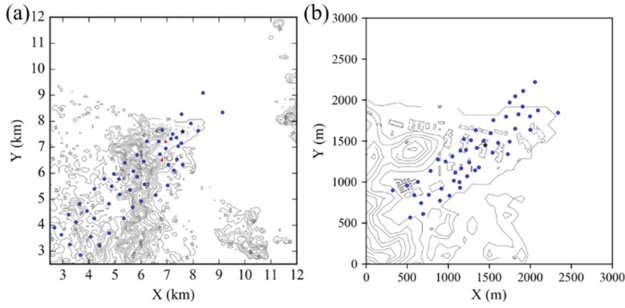
Fig. 2. Networks of wind measurements.

and the density of the sites is generally sparser with the distance further away. Similar to the placements of the sites for wind measurement, the arrangement of sites in the local scale scenario deep extends to the mountain area, whereas the small scale scenario covers more areas around the buildings (Fig. 3).
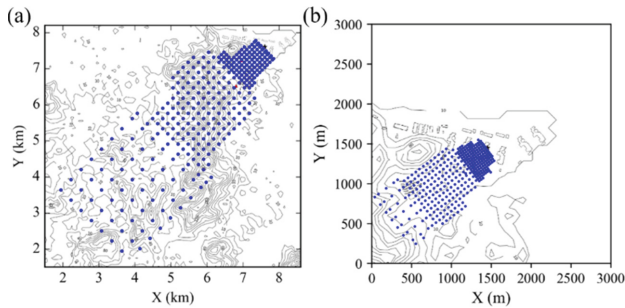
Fig. 3. Networks of concentration measurements.

2.3   Model Parameter Settings

The parameter settings of MSS used to simulate in different scales are according to previous sensitivity analysis [25, 27]. Essential inputs were collected to drive the simulations, e.g., the annual meteorological observations from monitoring stations, terrain elevation, and building information, which obey the relevant relationship of the wind tunnel experiments. The calculation domain of the local scale scenario is 15 km × 15 km, whereas that of the small scale is 3 km × 3 km. For both scenarios, the emission time step was set to 10 s, and the averaging period was 600 s. Besides, the dispersion duration was all set to 4 h to ensure that the airflow and concentration reach a steady state. The turbulence calculation follows the Louis model [28]. Other key parameters are listed in Table 1, including the grid size, the number of particles released per time step, and the lower bound of turbulence intensity.

Table 1. Key parameters of MSS simulations.

Parameters	Local scale	Small scale
Horizontal grid size	100 m	5 m
vertical grid size	10 m	5 m
Particle number (per time step)	10,000	10,000
Low bound of turbulence intensity (m/s) SUMIN, SVMIN, SWMIN	0.9, 0.9, 0.3	0.3, 0.3, 0.3

2.4 Statistical Evaluation Methodology

Quantitative evaluation of MSS modeling in the aspect of model-to-measurement discrepancies of concentration fields. The used statistical metrics include the fraction of predictions within a factor of 2 (FAC2) and 5 (FAC5), fractional bias (FB), and geometric variance (VG). FAC2/5 can provide robust access over outliers. And FB measures the mean bias of pairs of data, whereas VG works well for indicating differences across orders of magnitude. These two metrics are defined as follows:

$$\text{FAC2} = \text{fraction of data for which } 0.5 \ \leq \ \frac{C_p}{C_o} \ \leq \ 2.0 \tag{4}$$

$$\text{FAC5} = \text{fraction of data for which } 0.2 \ \leq \ \frac{C_p}{C_o} \ \leq \ 5.0 \tag{5}$$

$$\text{FB} = 2\left(\frac{\overline{C_p} - \overline{C_o}}{\overline{C_p} + \overline{C_o}}\right) \tag{6}$$

$$\text{VG} = \exp\left(\frac{1}{N}\sum_i \ln\left(\frac{C_p}{c_o}\right)^2\right) \tag{7}$$

where C_p and C_o are the predicted and observed values of concentration respectively. $\overline{C}$ denotes the average values of simulations or measurements.

3 Results and Discussion

3.1 Wind Field

Figure 4 exhibits the simulated wind field of two scenarios compared with the measurements obtained from sites in Fig. 2. For the local-scale simulation, the calculation domain is featured with many mountains (Fig. 1), most of which are located in downwind places. The airflows show a consistent tendency with terrain changes when passing over mountains, which is manifested by their increased speed and deflected direction (red arrows in Fig. 4a). The spatial distribution of measurements confirms the accuracy of the trend (blue arrows in Fig. 4a). Due to the length of buildings varies from 5.2 m to 225 m, a horizontal grid size of 100 m may smooth out some details of the airflows

in the building area. For the small-scale simulation with a grid size of 5 m, it allows a comparison of wind changes in the building area that occupies most of the domain center. As shown in Fig. 4b, the speed of airflows in the gaps between buildings is noticeably low, whereas those across the sides of buildings show overestimated speed. Although biased speed, the wind direction there was adjusted according to the building layout and reaches a high consistency.

The scatterplots in Fig. 5 compare the direction and speed of airflows that are simulated and measured at the monitoring sites. For the local-scale scenario, the clusters of simulated direction and speed are around 42 and 3 m/s respectively. This phenomenon represents the evolution change of airflows along with the mountains where the lower altitude exists. The accuracy in simulating the wind direction is high than the speed, as shown in Fig. 5a and 5b that the variation range of direction is much narrower. However, there are extremes out of 2 fold lines in both the direction and speed simulations. As for the small-scale scenario, the clusters of around 62 and 2.3 m/s of simulation demonstrate the behaviors of airflows around the buildings. The simulated direction is normally overestimated when compared with the measurements (Fig. 5c). And there appears an extreme of about 115, of which the site locates in the narrow gap between two buildings. Some of the simulated wind speed is below 2 m/s but exist many overestimations (Fig. 5d) which are consistent with the visual airflows in Fig. 4b.

3.2 Concentration Field

The simulated concentration fields are compared with the measurements in Fig. 6. Both two scenarios show an overall satisfactory consistency between the simulations and the measurements (Fig. 6a and 6c). For the local-scale scenario, some points in the middle of the plume are overestimated (the arrow in Fig. 6a), but the MSS succeeded in reproducing the high concentration area ($>10^{-11}$ s/m^3) in the center of the plume and the upwind of release position (the arrow in Fig. 6b). This phenomenon is absent in the previous study using RIMPUFF mode [24], which demonstrates the importance of turbulence for dispersion modeling in complex terrain and building layout.

Figure 6b also shows that the simulations are consistent with the measurements in front of central mountains, but significantly overestimate the downwind direction of the mountains. For the small-scale scenario, Fig. 6c shows that the model-to-measurement discrepancies at the edge of the plume are within an acceptable range for those far away from the release position (0 m < x < 1000 m), while the simulation at the central axis of the plume is underestimated by one order of magnitude. Besides, the simulations around the release position match the measurements well (Fig. 6d). However, the simulations show underestimation at the rear of a building compared with the measurements (the circle in Fig. 6d), for that the plume is affected by the building effects.

Table 2 summarizes the quantitative metrics of MSS modeling in two scenarios with different spatial scales. For the local-scale scenario, the FB of −0.010 indicates a significant low model-to-measurement discrepancy but the large VG of 15.510 reminds us of the presence of many extremes. In contrast, MSS achieves a large FB while accompanied by a small VG. It demonstrates that the concentration varies by several orders of magnitude, but the discrepancies between pairs of simulation and measurement are not noticeable in logarithm. Comparing the FAC2/5, MSS outperforms in the local-scale
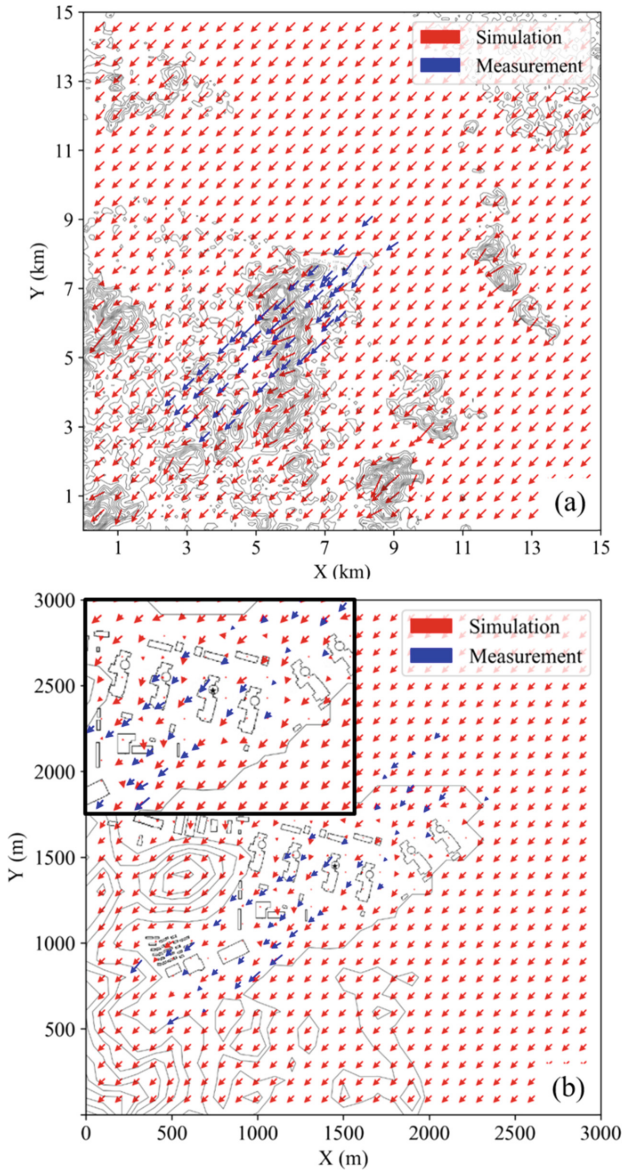
Fig. 4. Comparison of simulated horizontal wind fields with measurements in the local (a) and small (b) scales.

scenario, of which the simulations in the mountain area improve the overall scores. The biased airflows on the sides of the buildings result in underestimated concentration, which accounts for the worse FAC2/5.
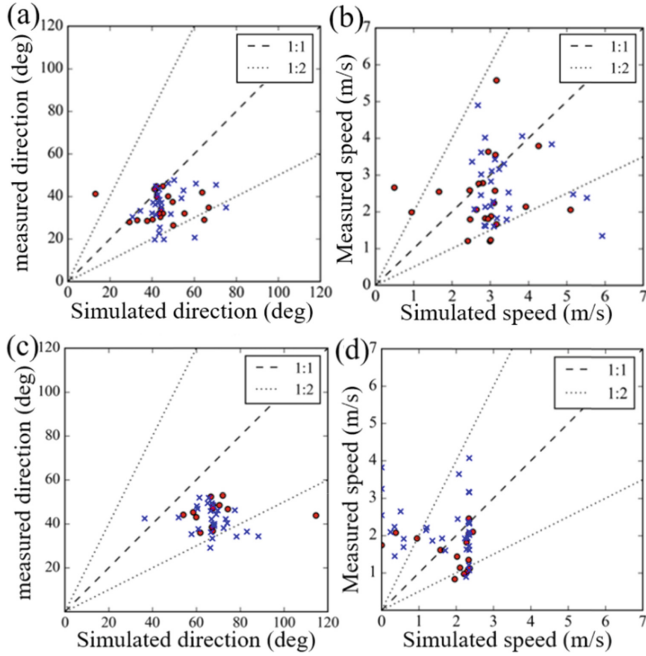
Fig. 5. Comparison of simulated and measured direction and speed in the local (a, b) and small (c, d) scales. The red dots and blue crosses represent the sites near the buildings and mountains respectively.
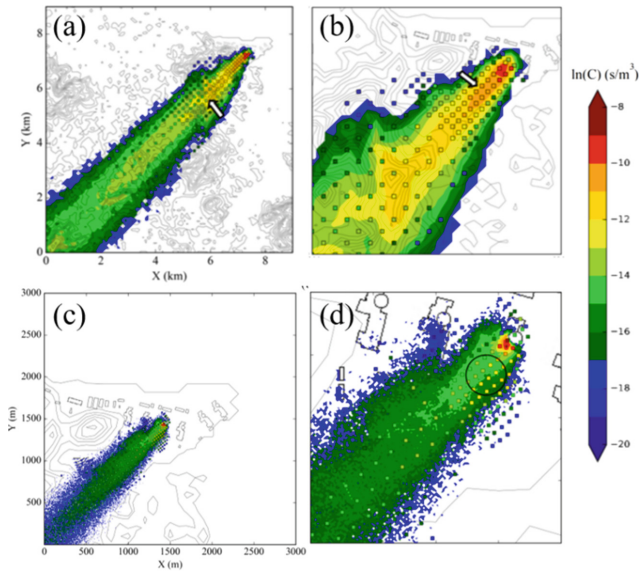
Fig. 6. Comparison of simulated concentration fields with measurements (colored squares) in the local (a, b) and small (c, d) scales. (b) and (d) are the zoom-in plots for (a) and (c) respectively.

Table 2. Performance metrics of concentration fields in sites of different scenarios.

Scenario	FAC2	FAC5	FB	VG
Local scale	0.370	0.710	−0.010	15.510
Small scale	0.239	0.543	−1.530	2.303

4   Conclusions

Fast and accurate support for public protection and arrangement of sampling is essential in case of a nuclear emergency. ADMs are widely welcomed in such a situation rather than the CFD method, thanks to a trade-off between accuracy and execution speed. They can provide forward simulations of the movements of airborne pollutants released into the atmosphere, which serve as a part of emergency response systems and assist the source inversion. Among them, the MSS has been extensively evaluated and feedback with benefit performances, which includes a modified mass consistent wind interpolator and a Lagrangian particle dispersion model. The presence of an independent component for obstacle treatments inside MSS enables it to fine model the atmospheric dispersion around dense buildings.

In practice, the nuclear power plant (NPP) sites usually are surrounded by various topography, e.g., the mountains and sea or rivers, and lies dense building layout. Both local-scale and small-scale evaluations of MSS in the vicinity of such an NPP site have been published, which provide suites of optimal parameters in these two scenarios including the number of particles per time step, the horizontal and vertical grid sizes, and the lower bound of turbulence intensity. But the comprehensive comparison of MSS's performance in the same topography but in different scales has not been demonstrated using the recommended settings. Thus, two such scenarios were selected for MSS evaluation with incoming airflows from the NE direction airflow incoming, across over buildings to mountains. The simulations of MSS involve the wind and concentration fields, which are further compared to measurements from wind tunnel experiments qualitatively and quantitatively.

The results demonstrate the MSS reproduces acceptably accurate ground wind and concentration. Due to separate processes for buildings, airflows display sharp changes in building area, while those over mountain reserve details as well. The simulated wind results show clusters of wind and speed in the monitoring sites, in which 42 and 3 m/s for the local-scale scenario and 62 and 2.3 m/s for the small-scale one. These differences are related to the measurement networks of the wind and represent the influences of nearby topography. Many local-scale sites are located in the mountain area, whereas the small-scale sites are placed more in the building area.

For the concentration fields, the high concentration area around the release position and its upwind area is well reproduced, due to the optimal lower bound of turbulence intensity. MSS outperforms the concentration simulations in the local-scale scenario, in which the FAC5 metric reaches 0.710 when comparing the simulations in monitoring sites with measurements, whereas the small-scale scores 0.543 of FAC5. The negative FBs in two scenarios indicate the frequent underestimations, which are −0.010 and

−1.530 for local and small scales respectively. The VG of 15.510 in the local-scale simulation shows many extremes are introduced. And the model-to-measurement discrepancies in an algorithm are acceptable in the small-scale simulation, due to a VG of 2.303 although a large FB exists. The local-scale simulation of MSS benefits the performance in the mountain area while that of the small-scale one is in the building area. A nesting calculation domain may be required if both the mountain and building areas are weighted equally to the emergency response.

References

1. Ehrhardt, J., Päsler-Sauer, J., Schüle, O., Benz, G., Rafat, M., Richter (Invited), J.: Development of RODOS-a comprehensive decision support system for nuclear emergencies in Europe-an overview. Radiat. Prot. Dosimetry **50**, 195–203 (1993). https://doi.org/10.1093/oxfordjournals.rpd.a082089

2. Brioude, J., et al.: The Lagrangian particle dispersion model FLEXPART-WRF version 3.1. Geosci. Model Dev. **6**, 1889–1904 (2013). https://doi.org/10.5194/gmd-6-1889-2013

3. Oldrini, O., Olry, C., Moussafir, J., Armand, P., Duchenne, C.: Development of PMSS, the parallel version of Micro-swift-spray. In: HARMO 2011 - Proceedings 14th International Conference on Harmonisation within Atmospheric Dispersion Modelling for Regulatory Purposes (2011)

4. Draxler, R.R., Hess, G.D.: An overview of the HYSPLIT_4 modelling system for trajectories, dispersion and deposition. Aust. Meteorol. Mag. **47**, 295–308 (1998)

5. Tinarelli, G., Brusasca, G., Oldrini, O., Anfossi, D., Castelli, S.T., Moussafir, J.: Micro-Swift-Spray (MSS): a new modelling system for the simulation of dispersion at microscale. General description and validation. In: Borrego, C., Norman, A.L. (eds.) Air Pollution Modeling Its Application, vol. 17, pp. 449–458 (2007). https://doi.org/10.1007/978-0-387-68854-1_49

6. Seibert, P., Frank, A.: Atmospheric chemistry and physics source-receptor matrix calculation with a Lagrangian particle dispersion model in backward mode. Atmos. Chem. Phys. **4**, 51–63 (2004). http://www.forst.tu-muenchen.de/EXT/. Accessed 14 June 2022

7. CERC, ADMS 5 Atmospheric Dispersion Modelling System User Guide (2016)

8. Cimorelli, A.J., et al.: AERMOD: a dispersion model for industrial source applications. Part I: general model formulation and boundary layer characterization, J. Appl. Meteorol. **44**, 682–693 (2005). https://doi.org/10.1175/JAM2227.1

9. Leelőssy, Á., Lagzi, I., Kovács, A., Mészáros, R.: A review of numerical models to predict the atmospheric dispersion of radionuclides. J. Environ. Radioact. **182**, 20–33 (2018). https://doi.org/10.1016/j.jenvrad.2017.11.009

10. Thykier-Nielsen, S., Deme, S., Mikkelsen, T.: Description of the atmospheric dispersion module RIMPUFF (1999)

11. Oldrini, O., Armand, P., Duchenne, C., Olry, C., Moussafir, J., Tinarelli, G.: Description and preliminary validation of the PMSS fast response parallel atmospheric flow and dispersion solver in complex built-up areas. Environ. Fluid Mech. **17**(5), 997–1014 (2017). https://doi.org/10.1007/s10652-017-9532-1

12. Labovský, J., Jelemenský, L.: CFD-based atmospheric dispersion modeling in real urban environments. Chem. Pap. **67**(12), 1495–1503 (2013). https://doi.org/10.2478/S11696-013-0388-7

13. Röckle, R.: Bestimmung der Strömungsverhältnisse im Bereich komplexer Bebauungsstrukturen. der Technischen Hochschule Darmstadt, Germany (1990)

14. Cox, R.M., Cogan, J., Sontowski, J., Dougherty, C.M., Fry, R.N., Smith, T.J.: Comparison of atmospheric transport calculations over complex terrain using a mobile profiling system and rawinsondes. Meteorol. Appl. **7**, 285–295 (2000). https://doi.org/10.1017/S135048270000 01651

15. Chang, J.C., Franzese, P., Chayantrakom, K., Hanna, S.R.: Evaluations of CALPUFF, HPAC, and VLSTRACK with two mesoscale field datasets. J. Appl. Meteorol. **42**, 453–466 (2003). https://doi.org/10.1175/1520-0450(2003)042%3c0453:EOCHAV%3e2.0.CO;2

16. Cox, R.M., Sontowski, J., Dougherty, C.M.: An evaluation of three diagnostic wind models (CALMET, MCSCIPUF, and SWIFT) with wind data from the Dipole Pride 26 field experiments. Meteorol. Appl. **12**, 329–341 (2005). https://doi.org/10.1017/S135048270500 01908

17. Tinarelli, G., et al.: Review and validation of MicroSpray, a Lagrangian particle model of turbulent dispersion. Lagrangian Model. Atmos. **15**, 8041 (2013)

18. Gomez, F., Ribstein, B., Makké, L., Armand, P., Moussafir, J., Nibart, M.: Simulation of a dense gas chlorine release with a Lagrangian particle dispersion model (LPDM). Atmos. Environ. **244**, 117791 (2021). https://doi.org/10.1016/J.ATMOSENV.2020.117791

19. Hanna, S., et al.: Comparisons of JU2003 observations with four diagnostic urban wind flow and Lagrangian particle dispersion models. Atmos. Environ. **45**, 4073–4081 (2011). https://doi.org/10.1016/j.atmosenv.2011.03.058

20. Barbero, D., et al.: A microscale hybrid modelling system to assess the air quality over a large portion of a large European city. Atmos. Environ. **264**, 118656 (2021). https://doi.org/10.1016/J.ATMOSENV.2021.118656

21. Oldrini, O., Armand, P., Duchenne, C., Perdriel, S.: Parallelization Performances of PMSS flow and dispersion modeling system over a huge urban area. Atmosphere (Basel) **10**, 404 (2019). https://doi.org/10.3390/ATMOS10070404

22. Finardi, S., Brusasca, G., Morselli, M.G., Trombetti, F., Tampieri, F.: Boundary-layer flow over analytical two-dimensional hills: a systematic comparison of different models with wind tunnel data. Boundary-Layer Meteorol. **63**, 259–291 (1993). https://doi.org/10.1007/BF0071 0462

23. Trini Castelli, S., Armand, P., Tinarelli, G., Duchenne, C., Nibart, M.: Validation of a Lagrangian particle dispersion model with wind tunnel and field experiments in urban environment. Atmos. Environ. **193**, 273–289 (2019). https://doi.org/10.1016/j.atmosenv.2018.08.045

24. Liu, Y., Li, H., Sun, S., Fang, S.: Enhanced air dispersion modelling at a typical Chinese nuclear power plant site: coupling RIMPUFF with two advanced diagnostic wind models. J. Environ. Radioact. **175–176**, 94–104 (2017). https://doi.org/10.1016/j.jenvrad.2017.04.016

25. Wang, S., et al.: Validation and sensitivity study of Micro-SWIFT SPRAY against wind tunnel experiments for air dispersion modeling with both heterogeneous topography and complex building layouts. J. Environ. Radioact. **222**, 106341 (2020). https://doi.org/10.1016/j.jenvrad.2020.106341

26. Dong, X., Fang, S., Zhuang, S.: SWIFT-RIMPUFF modeling of air dispersion at a nuclear powerplant site with heterogeneous upwind topography. In: 2021 28th International Conference on Nuclear Engineering, American Society of Mechanical Engineers Digital Collection (2021). https://doi.org/10.1115/icone28-64608

27. Dong, X., Zhuang, S., Fang, S., Li, X., Wang, S., Li, H.: Validation and sensitivity study of Micro-SWIFT SPRAY against wind tunnel experiments for small-scale air dispersion modeling between mountains and dense building at a nuclear power plant site. Prog. Nucl. Energy. **142**, 104007 (2021). https://doi.org/10.1016/j.pnucene.2021.104007
28. Louis, J.F., Weill, A.: Dissipation length in stable layers. Boundary-Layer Meterol. **25**, 229–243 (1983)

Discussion on the Reporting of Nuclear Safety Incident from the Perspective of Media Ecology

Yang Li[✉] and Li Jie Yao

Hualong International Nuclear Power Technology Co., Ltd., Shenzhen, Guangdong, China
393263138@qq.com

Abstract. Nuclear safety events report is an important part of news reports related to nuclear power. Correct and appropriate reporting is very important for the positive development of public opinion and the emotional guidance of the public in China, and it also directly reflects the overall level of China's nuclear safety culture construction. Based on the media ecology, this paper studies the evolution of the concept and way of accident reporting in China, and taking the recent report of Taishan nuclear power incident in 2021 as an example, discusses the differences and changes in several public opinions in the brand-new media ecology mode, such as the report way, the report idea and narrative subject, and puts forward a new perspective and thinking, and holds that we should seek truth from facts, be scientific and rigorous, use appropriate reporting and public communication methods, and take advantage of news language and different narrative subjects to make the real situation. I hope the new perspective of this paper can provide reference for future related work, and maintain the healthy and upward development of our nuclear safety culture atmosphere.

Keywords: Nuclear Power · Report · Event · Accident · Media · Ecology · Digital New Media · People Oriented

1 Introduction

Media ecology view [1] is the news cognition and rational thinking made by contemporary media ecology in order to establish the harmonious relationship among people, media and society system and realize the virtuous circle of media ecosystem under the condition of market economy. Aiming at the report of "nuclear safety Event" in nuclear power industry, it is of great significance and function to learn the correct concept of media ecology and establish the report concept and direction under the brand-new mode of joint reporting by mainstream media (including TV stations, radio, newspapers and magazines, etc.) and self-(new) media after 2008, so as to meet the test of market economy, launch all-round competition with western media giants, resolve the public opinion crisis and establish a good nuclear safety culture atmosphere of sustainable development in.

2 Relationship Between Nuclear Safety-Related Events (Accident) and Other Events (Accident)

2.1 Nuclear Safety Incident/Accident

Nuclear power plants and all facilities related to the civil nuclear industry, transportation of materials in radioactivity and any incidents related to materials (or radiation) in radioactivity are classified into seven levels: the higher Grade (4–7 levels) is classified as an "accident"; The lower Grade (grade 1–3) is "event". Events that do not have safety significance are classified as zero level and designated as "deviation". Incidents not related to security are classified as "off-Classification" (Fig. 1).
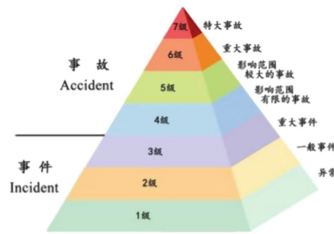
Fig. 1. Classification of accidents and incidents

In the operation of civil nuclear power plants in China, there was a Class 1 incident (abnormal, the operation of nuclear power plants deviated from the specified functional scope), but this Grade had no impact on the outside, only the internal operation violated safety standards, or minor problems that might involve safe operation occurred). The rest are Class 0 events (deviation will not affect the nuclear safety of nuclear power plants). There are only two major accidents of Grade 7 (radioactivity materials released by nuclear power plants outside the plant, resulting in extensive health and environmental impacts) in history, namely Chernobyl nuclear accident in 1986 and Fukushima Daiichi nuclear power plant nuclear leakage accident in 2011.

The international atomic energy agencies require member states to promptly rate nuclear incidents of Level 2 and above and those that cause media and public concern and notify the international atomic energy agencies within 24 h [4].

2.2 Safety Incidents (Accidents)

Safety accidents refer to accidents that suddenly occur in production and business operations (including activities related to production and business operations), harm personal safety and health, damage equipment and facilities, or cause economic losses, resulting in temporary suspension or permanent termination of original production and business operations (including activities related to production and business operations). According to the Regulations of the People's Republic of China on Reporting, Investigation and Handling of Production Safety Accidents promulgated by State Administration of Work Safety Decree No.13 in July 2007, accidents are generally divided into the following Class according to casualties or direct economic losses:

(1) Special Major Accident refers to accidents that cause more than 30 deaths, or more than 100 serious injuries (including acute industrial poisoning, the same below), or direct economic losses of more than 100 million yuan;

(2) Major Accident refers to accidents that cause more than 10 deaths and less than 30 deaths, or more than 50 serious injuries and less than 100 serious injuries, or direct economic losses of more than 50 million yuan and less than 100 million yuan;

(3) Major accidents refer to accidents that cause more than 3 deaths and less than 10 deaths, or more than 10 serious injuries and less than 50 serious injuries, or direct economic losses of more than 10 million yuan and less than 50 million yuan;

(4) General accidents refer to accidents that cause less than 3 deaths, or serious injuries to less than 10 people, or direct economic losses of less than 10 million yuan.

According to the Opinions of the Office of the Security Committee of the State Council on Strengthening the Information Disclosure of Production Safety Accidents issued in 2012, all regions and relevant departments are required to inform the public of the information on the response and disposal of production safety accidents in a more comprehensive, timely and detailed manner in accordance with the requirements of "active disclosure". First, it is necessary to timely and accurately release the information of production safety accidents, especially accidents with great social impact and high attention, so as to eliminate the space for false rumors and suspicions to spread. Second, it is necessary to timely and accurately release the accident handling measures taken by the government and the progress information of emergency rescue, grasp the trend of social public opinion in real time, actively respond to social concerns, and eliminate public doubts. And promote the investigation and accountability of production safety accidents and information disclosure, and take the initiative to accept social supervision.

2.3 Public Emergencies and Disasters

Public emergencies [5] generally refer to "public emergencies involving public safety that occur suddenly, pose or may pose major threats and damages to national security and legal system, social security and public order, citizens' lives and property safety in the whole country or some areas, and cause huge casualties, property losses and social impacts. For example, SARS in 2003 and COVID-19 in 2019.

Disaster refers to the phenomenon that great productivity and means of production are destroyed to human society due to sudden natural disasters and disasters. Such as Wenchuan earthquake in 2003.

2.4 Potential Relationship Between Incidents (Accidents)

Nuclear safety incidents (accidents) have many similarities with "accidents", public emergencies and disasters, all of which are sudden and urgent, which lead to rapid changes in the social environment. The response to the regulatory authorities also requires urgency, and the consequences are highly uncertain in the short term, that is, the environmental changes cannot be accurately judged at the beginning of the events, which may have a huge impact on society, that is, it has a serious impact on the normal ecology and code of conduct of the social system, and even threatens the harmony and security

of the country. In addition to the above characteristics, nuclear accidents have their own particularities: Firstly, the diffusion is relatively concentrated, and radioactivity materials are mainly concentrated in the location of nuclear power plants and surrounding areas, so there will be no similar epidemic spread in a wide area, but the early warning time is short, and the early warning time of Validity is usually only a few hours, and the nuclear accident process is fast and the impact is lasting. Radioactive element's half-life is very long, and some radioactive element and half-life even last for tens of thousands of years; Radiation damage to human health is difficult to detect in a short time, long-term and hereditary, and its medical effect is very limited. These characteristics are also the root cause of the widespread and high attention of the society and the public to the nuclear safety accident, even the "nuclear safety", and it is easy to cause rejection and fear emotionally!

3 Media Ecology and Characteristics of Accident Reports in China

3.1 Media Ecology

Media ecology refers to a science that explores and reveals the relationship between man, media, society and nature, and the essence and law of development and change with ecological viewpoints and methods [1]. Media ecology refers to a subsystem of social ecosystem, which emphasizes the interaction between media system and social system. Under the mutual checks and balances, the internal and external ecological environment of the media promotes the development of the media and promotes the virtuous circle of the media itself. The development of China's media ecology has gone through three stages: politicization stage, marketization stage and digitalization stage [2].

The following data [6] cannot be ignored: According to the 48th Statistical Report on Internet Development in China, as of June 2021, the number of Internet users in China reached 1.011 billion, and the Internet penetration rate reached 71.6%; As of June 2021, the number of mobile Internet users in China reached 1.007 billion; The number of online video (including short video) users in China reached 944 million; The number of online payment users in China reached 872 million; The number of online news users in China has reached 760 million; The Internet penetration rate reached 71.6%, exceeding the global average (65.6% 21) by 6 percentage points. One billion users access the Internet, forming the largest and vibrant digital society in the world.

3.2 Evolution of the Concept of Accident Reporting

It is an important part of news report and an object of great news value. Since the founding of the People's Republic of China, most scholars take 1978 and 2003 as the demarcation points, and divide accident reports into several stages. Before 1978, the reporting mode emphasized "the government's care and guidance" and pursued strong political propaganda, while relatively ignoring the relevant information of the accident itself, especially the human factors and consequences. From 1978 to 2003, when SARS happened, news reports gradually involved the information level of the event

itself, and changed from political weight to "matter-based". The national level gave correct guidance, but some local governments treated news reports conservatively or even controlled when it involved local interests. After 2003, the news reports of events (accidents) repeatedly broke the forbidden zone, and constantly pursued the accuracy and transparency of information. Especially after the Wenchuan earthquake in 2008, the main channels of reporting gradually formed a brand-new mode of joint reporting by mainstream media and self-media from the original mainstream media (including TV stations, radio, newspapers and magazines, etc.), so the media also pursued the attention of participants (including witnesses, witnesses, victims, investigators, responsible persons, etc.) besides the events themselves, and the event reports changed from "event-based" to "people-based". Although there are many problems at this stage, such as over-reporting, ethical disputes, lack of news literacy of new media and so on. However, with the rapid development of Internet technology, the public's demand for information under the new situation of unprecedented diversification of communication subjects and contents, and has a series of social impacts.

Several stages of accident reporting are corresponding, closely related and closely related to several stages of media ecological development. Establishing a correct concept of media ecology is of great significance and function for meeting the test of market economy, launching all-round competition with western media giants, resolving news crisis and establishing a harmonious society with sustainable development.

3.3 Reporting Basis and Present Situation of Nuclear Safety Event

The report of nuclear safety incident in China was officially released in October 2017 according to the Nuclear Safety Law of the People's Republic of China. The fifth chapter, "Information Disclosure and Public Participation", clarifies that relevant departments should disclose nuclear safety-related information to the competent or regulatory authorities, the society and the public, and there is Article 65, "nuclear safety in that is disclosed according to law should be disclosed to the public in a timely manner through government announcements, websites and other ways that are convenient for the public to know." This provision clarifies the legality of reprinting and interpreting by new media such as "websites and other ways that are access for the public to know". In addition, it also stipulates that "citizens, legal persons and other organizations shall not fabricate or disseminate false information about nuclear safety rights."

In June 1995, National Nuclear Safety Administration promulgated the Reporting System for Nuclear Power Plant Operating Units (HAF001/02/01), which clarified the relevant guidelines and format requirements for nuclear power plant operating units to report National Nuclear Safety Administration incidents and operational incident reports to the, as well as the requirements for periodic reports, important activity notices and nuclear accident emergency reports. Through years of practice, in order to improve the shortcomings in the implementation process. To further implement the relevant requirements of the Law, the Nuclear Power Safety Supervision Department organized and formed the Regulations on Reporting Nuclear nuclear safety of Nuclear Power Plant Operating Units, which was reviewed and approved by the Ministry of Ecology and Environment on November 5, 2020 and implemented on January 1, 2021. There are seven chapters and thirty-four clauses, which mainly specify the reporting requirements

such as periodic report, important activity report, construction phase incident report, operation phase incident report and nuclear accident emergency report. The reporting criteria for operational events have been expanded from the original 9 to 12, which makes it clear that events such as shutdown, exceeding safety limits or safety system setting values, violating operation limits and conditions, serious deterioration of main physical barriers, and real threats to the safety of nuclear power plants should be reported as operational events, and relevant provisions on common cause events, cyber attacks and fraud events have been added..

It can be seen here that the regulatory authorities have been improving the reporting requirements of various incidents and accidents, and realism, objectivity and openness have always been their basic attitude and starting point. At present, the report of civil nuclear safety related events is basically the mode of official notification and media report, and the content of the report is basically the event itself and related concepts. Different media reports are basically reprinted, and there is no difference.

4   Examples of Nuclear Safety Incident Reports

In this paper, the report of an operation event of Taishan Nuclear Power Plant in 2021 and related public opinion are taken as cases for discussion.

April 9, 2021 National Nuclear Safety Administration website news: "At 13:58:14 on April 5, 2021, the radioactivity of dose of chimney gas dropped below the alarm threshold of high 1, and the incident ended. During the whole event, the unit is in a stable state and there is no other abnormality. After the incident, the operating unit carried out inspection and Validation, and preliminarily analyzed that the alarm reason was that after the initial water seal was filled with water, a small amount of radioactivity gas unexpectedly entered the water seal pipeline, and during the re-water seal filling process, the gas remaining in the water seal pipeline was discharged to the chimney through the ventilation pipeline; After calculation, the total amount of inert gas emitted in radioactivity this time accounts for 0.00044% of the annual emission limit. According to Article 22 (9) radioactivity and radiation exposure events in "of nuclear safety Reporting Regulations for Operating Units of Nuclear Power Plants, this event is defined as a Class 0 operation event."

On June 13, CNN reported that the US government was evaluating a report last week about the "leakage incident" of Taishan nuclear power plant in China. He said that before that, China's security department was raising the acceptable limit of radiation detection outside the plant to avoid the fate of nuclear power plants facing closure. French Famatong Company, which participated in the operation of Taishan Nuclear Power Plant in Guangdong Province, contacted the US government and asked the US for technical support to correct the problem, "warning" that an "imminent nuclear radiation threat" was about to occur in China. After CNN hype, keywords such as "nuclear radiation" and "leakage" appeared on the Internet very quickly, and the first round of public opinion aroused public concern.

On June 13th, CGNPC announced that the surrounding environmental indicators of Taishan Nuclear Power Station were normal. On June 16, the relevant person in charge of the Ministry of Ecology and Environment (National Nuclear Safety Administration) responded to the situation of Taishan Nuclear Power Plant in detail by asking questions at

a press conference, saying that the radioactivity level radioactivity of the primary circuit of Unit 1 of the nuclear power plant has been monitored at present, but it is still within the scope of allowing stable operation, and the operation safety of the nuclear power plant is guaranteed, and stressed that this is "completely different from radioactivity leaking radioactivity". On the same day, the International atomic energy Agency (IAEA) indicated that it had received the latest information provided by the Chinese National atomic energy Agency on the above issues. Zhongqian Nuclear Power Plant is in normal condition, safe and secure operation, and there is no concern about radioactivity leakage or environmental pollution. The IAEA said it would continue to maintain communication with Chinese national atomic energy institutions. Global Times, the mainstream media, published an article on June 15th: "CNN refreshes the lower limit again! This time, they came to spread rumors about Taishan Nuclear Power Plant in Guangdong, China." Reviewed and clarified the relevant facts in detail. It is pointed out that "CNN is writing according to the potential risks of Class like Fukushima nuclear accident"; The United States' own restrictions on nuclear technology exports laid the groundwork for this hype. In August 2019, CGN and its affiliated enterprises were listed by the United States as "entities" in export control (Famatong needs to apply to the United States for exemption if it wants to apply American technology to Taishan Nuclear Power Plant), so Famatong contacted the United States to seek exemption for technology sharing. Of course, the United States finally decided that the situation at Taishan nuclear power plant was not critical, and rejected Famatong's application to maintain export control to CGN.

Less than a month later, there was a second round of public opinion. On July 23rd, EDF, the French shareholder of Taishan Nuclear Power, suddenly issued a statement, which mainly meant that if the fuel damage was put in France, SHUTDOWN would be overhauled, but whether China's SHUTDOWN in depends on China's opinions. The statement may be highly technical. Nearly two hours after EDF official website issued the press release, there were only five reprints and seven praises within one hour after EDF official Twitter was reprinted. It did not cause social media shock. However, a CGN statement on July 30th (the content is that Taishan Nuclear Power stopped to operate SHUTDOWN from the perspective of conservative decision-making according to relevant requirements, and just took advantage of this minor repair opportunity to check and repair this fuel rod damage problem in advance), which triggered the third round of secondary public opinion. Some media began to jointly ferment the second round of public opinion and this statement. It was even rumored that 75 fuel rods were damaged this time (the actual number was 5, accounting for 0.01% of the total).

On August 21-02-02, WeChat official account of nuclear energy industry published "Talk Together: The Story Behind Taishan Nuclear Power's shutdown", which explained in detail the causes, probability, maintenance difficulty and acceptability of fuel rod damage in shutdown, which is equivalent to a deep nuclear culture popularization and clarifies the facts. Tencent. Com, Sohu. Com and Beijing Business Today also reprinted some information.

So far, there have been no follow-up new reports from the mainstream media, but there are still many comments, inquiries and controversies about this incident on the Internet until December. The public has only seen some of the above facts due to factors such as education, industry, age and Internet habits, which is easy to take them out of

context. This article also specially consulted most of the media public information, only to sort out the causes and consequences.

At the same time, looking at CNN's operation techniques, we have to admit that it skillfully uses news language in reporting, expands risks in an empathetic way, avoids the important points, frequently uses sensitive words, and makes full use of the network to achieve the purpose of hype, which adds troubles to the already complicated international relations and affects the establishment of China's peace and safety culture atmosphere.

5 Thinking

Nuclear facility operating units are fully responsible for nuclear safety. When nuclear facility operating units adjust operational restrictions and conditions and report them to the administrative department of nuclear safety under the State Council for approval, they need multi-party participation and follow-up. This incident reflects the lack of mutual communication and cooperation among all parties, and the powers and responsibilities of Supplier, operating units and nuclear safety supervision departments should be further clarified.

News discourse [3] is a set of rhetorical discourse that pays attention to universality, concreteness and innovation, in order to achieve a certain purpose of public opinion. Media ecology holds that when the discourse shared by the knowledge interpretation community enters the discourse context of news production, it must face the problem of re-contextualization. It is not simply the transfer of meaning, but also pays more attention to the coupling relationship between science and media, actively participates in public expression, and especially achieves the expected reporting effect with the help of the communication power of the new media platform. In the process of reporting nuclear power events, story rhetoric can be introduced and used on the basis of scientific background. On the basis of seeking truth from facts, describing narration with scenes and sincere atmosphere can highlight the hardships and rigor behind scientific decision-making. Emphasizing the role of "experts" is also an effective way. The news media facing the public needs the scientific discourse of experts, while the knowledge community represented by experts needs the media to speak out to the society. Qiao Sukai (fuel rod maintenance expert) and David Fishman (Chinese name: Yu Dewei; Researchers in China's energy field and energy supervision have received good results.

6 Conclusions

1) It is considered that the media literacy of nuclear power journalists should be continuously improved, journalism professionalism suitable for nuclear safety should be established, the correct concept of event reporting should be cultivated, the emergency reporting mechanism should be established and improved, and the shortcoming of "individual narrative" should be remedied. The follow-up influence of reporting should be continuously paid attention to, and in-depth reporting should be carried out when necessary. Learn from the more and more in-depth "people-oriented" characteristics of accident reports in other industries. Nowadays, under the brand-new media ecological mode of joint reporting by mainstream media and self-media. In addition to the incident

itself, in-depth reporting and dealing with public opinion should also pay more attention to relevant people, such as involved operators, construction engineers, surrounding residents, etc., which is easy to arouse people's resonance and empathy. Contribute to the popularization of nuclear safety culture outside the nuclear industry [8].

2) Since the outbreak of pneumonia in COVID-19 in 2019 [7], the press release work as an important means of risk communication [8] has basically achieved normalization and institutionalization, and has played a role in meeting public information needs, curbing the widespread spread of rumors, appeasing social panic, ensuring social stability. Operation, boosting public confidence in anti-epidemic and other multiple functions, nuclear safety incident reporting and press release can also learn from this form, in the process, we can gain insight into public psychology, respond to public concerns, and enhance social communication.

3) It is also a continuous task to improve the effect of press release by strengthening the professional level and public orientation of press release internally. Information release should be more timely, standardized and consistent in caliber to achieve more accurate information push; The release of different information should be classified. Classification should answer questions according to the public's questions in public opinion, and use vivid ways such as diagrams, tables or dynamic evolution diagrams to popularize basic nuclear power knowledge, so that the public can understand the specific situation of events, eliminate unknown panic and relieve anxiety and panic.

4) In Taishan case, the incident report was issued by the official media, the clarification article was issued by different mainstream media, and the final overall incident review report was issued by WeChat official account in the nuclear industry. Different types of media have different audiences. Although the time response is timely, there is no continuity, and the general public cannot get in touch with the complete public opinion process of events. It is suggested to cultivate mainstream media neighborhoods and new media with a wide audience that can track, timely and continuously report the "nuclear safety" events. Nuclear power has developed rapidly in recent years, and international and domestic public opinion is unknown and changeable, which is also an inevitable choice to do a good job in public communication of nuclear power under the existing media ecology.

As early as more than 2,000 years ago, Shi Bo of Zhou Taishi put forward the famous proposition of "harmony with real creatures, but not continuity with the same" and "Guoyu Zheng Yu", which pointed out the systematic harmony, difference and diversity. At present, China has the largest scale of nuclear power under construction in the world, and its completed nuclear power operation performance is almost excellent. In the domestic and international media ecosystem, we should take seeking truth from facts as the basis, use appropriate reporting and public communication methods, make good use of news language and different narrative subjects to maintain our nuclear safety culture atmosphere, and nuclear safety's news in China is dominated by itself.

References

1. Shao, P.: Basic principles of media ecology research. Journalism Writ. **1**, 25–26 (2008)
2. Huang, R., Wang, Y.: On the three stages of ecological change in China. Today Media **1**, 16–17 (2013)

3. Shao, P.: On five concepts of media ecology. Journalism Univ. 20–21 (2001)
4. Anonymous. Decision of the State Council on Approving the Convention on Early Notification of a Nuclear Accident and the Convention on Assistance in a Nuclear Accident or Radiological Emergency
5. Xue, L., Zhong, K.: Classification, Classification and stages of public emergencies: the management basis of emergency system. China Adm. **2**, 102–107 (2005)
6. The 48th Statistical Report on Internet Development in China of China Internet Network Information Center, August 2021
7. Public media literacy in post-epidemic era_Wang Jue
8. Research on China's public support for nuclear power development in the post-Fukushima era_Alina Zhang
9. Risk Communication Paradox and Balanced Reporting Pursuit–An Investigation from the Perspective of Media Ecology_Du Jianhua

Economic Analysis of the One Through Fuel Cycle Based on Equilibrium Mass Flow

Zhiyong Li[(✉)], Jiang Hu, Mei Rong, Xin Shang, and Yifan Zhang

China Nuclear Power Engineering Corporation, Beijing, China
`lizhiyong893@163.com`

Abstract. In order to evaluate the cost of each stage of the one through fuel cycle (OTC), the uranium required for each stage of the OTC is calculated in detail based on the equilibrium mass flow. According to the material flow analysis, front-end cost and back-end cost of the nuclear fuel cycle under different discount rates are analyzed according to the material flow. The results show that the front-end cost increases with the discount rate, while the back-end cost decreases with the discount rate, and the front-end cost is higher than the back-end cost. The three stages of natural uranium, uranium enrichment and fuel manufacturing not only account for a large proportion of the total cost, but also have a strong sensitivity. Among them, the cost of uranium enrichment has the greatest impact on LCOE, followed by the cost of natural uranium.

Keywords: Nuclear fuel cycle · Balanced material flow · LCOE · Economic evaluation · Sensitivity analysis

1 Introduction

According to the latest statistics of the world nuclear association, about 11% of the world's electricity comes from about 450 nuclear power reactors. At present, more than 60 reactors are under construction, equivalent to 16% of the existing capacity. It is estimated that China's uranium demand will be about 18500tU in 2025, and about 130 reactors will operate to 24000tU in 2030 [1]. By the end of 2021, 53 commercial units in mainland China have been used for an average of 3546.6 h, and the utilization rate of units has reached 81.6% on average.

At present, there are three main types of nuclear fuel cycle strategies implemented by countries around the world. The first type is one cycle, which is characterized by the direct geological treatment of spent fuel unloaded from the reactor after cooling. This cycle method is widely used because of its simple process and no risk of nuclear proliferation; The second type is the recycling of uranium and plutonium, which is mainly represented by MOX fuel. This cycle method cools the UOX spent fuel discharged from the thermal reactor and extracts uranium and plutonium, and then mixes Pu and UO_2 to make MOX fuel. Compared with one cycle, the recovery of uranium and plutonium improves the utilization rate of uranium resources; The third type is to introduce fast reactor to realize the utilization of transuranium elements. This cycle truly realizes the

effective utilization of uranium resources, but it is seldom implemented at present due to the lack of commercial technology and complex process. In the foreseeable future, China will mainly focus on primary recycling, uranium and plutonium recycling and the utilization of transuranium elements through fast reactors.

The large-scale use of nuclear power has also brought another focus of attention, that is, the economy of nuclear power. In the economic analysis of nuclear power, the cost required by the fuel cycle is an important part. The cost analysis of each stage of the fuel cycle can not only find the part that has a greater impact on the total cost, but also control the cost of each stage according to the sensitivity to realize the economy of nuclear power. To intuitively understand the cost of each stage of the nuclear fuel cycle, this paper calculates the material flow of each stage in the typical PWR Fuel one-time pass scheme, and calculates the relevant levelized cost according to the material flow.

2 Characteristics and Material Flow Analysis of Nuclear Fuel Cycle

2.1 One Through Fuel Cycle Feature

Nuclear fuel cycle refers to the whole process from uranium ore mining, uranium conversion and enrichment to fuel production and fuel recycling or geological disposal after irradiation in the reactor. Generally, uranium ore mining and processing, uranium conversion to UF_6, UF_6 enrichment and fuel element manufacturing are divided into the front end of the cycle. The irradiation of fuel elements in the reactor is called the irradiation stage, the spent fuel discharged from the reactor is temporarily cooled and finally disposed of in geology or extracted from uranium and plutonium, which is called the back end of the cycle [2].

The irradiated nuclear fuel in the reactor is usually called spent fuel. There are two main ways to treat it after cooling: one is conventional geological treatment, and the other is the separation and recycling of actinides [3]. In the first way, the radioactivity of spent fuel will continue to exist for more than hundreds of thousands of years after storage. Therefore, not only a special repository is required, but also it must be ensured that the radioactive and/or toxic elements in spent fuel will not leak for such a long time, causing harm to the surrounding environment and public safety. At the same time, various problems faced by the public acceptance must be considered.

The nuclear fuel cycle is divided into different cycle types according to the treatment methods of spent fuel. At present, many countries adopt the one through fuel cycle (OTC) scheme, and its cycle flow is shown in Fig. 1. The OTC scheme has a simple and short process, but the utilization rate of uranium resources is relatively low, and the amount of waste for subsequent treatment is relatively large.

Another popular cycle scheme is to recover uranium and plutonium from spent fuel and make it into MOX fuel. This cycle scheme is also known as the twice through fuel cycle (TTC). In addition to conventional UOX fuel, the reactor can also be loaded with MOX fuel. The preparation, application and post-treatment of MOX fuel is one of the key technologies of the closed fuel cycle. The utilization of uranium resources can be significantly improved by recycling uranium and plutonium in UOX spent fuel.
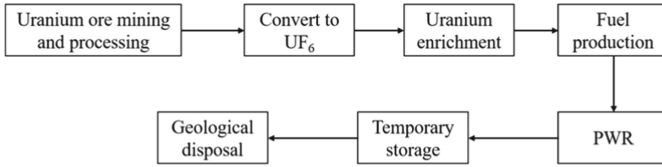
Fig. 1. One through fuel cycle route

Research shows that using MOX fuel in thermal reactor can improve the utilization rate by 20%–30%. If it is used in fast reactor, the utilization rate can be increased by 20 times.

The separation of uranium and plutonium in spent fuel is conducive to reducing the radioactivity, volume of spent fuel and the time required for radioactivity to return to the natural level, and minimizing the harm to the environment and human health caused by long-term storage of radioactive substances. Compared with the TTC scheme, the OTC scheme is not a true fuel cycle in the sense of geological disposal of spent fuel directly.

2.2 Equilibrium Material Flow Analysis

Material flow is the basis for calculating the levelized power generation cost. In this paper, assuming that the nuclear fuel meets the mass conservation during the cycle, the annual reactor loading M can be calculated according to the following formula [4]:

$$M = \frac{P_e \times CF \times 365}{\varepsilon \times B_d}$$

where: M is the annual fuel quantity required by the nuclear power plant (tHM/a); P_e is the electric power of reactor (GWe); CF is the capacity factor or load factor of the reactor; ε is the thermal efficiency of the reactor (%); B_d is burnup depth (GWd/tHM).

By calculating the amount of fuel required by the nuclear power plant each year, the mass of natural uranium required and the required separation work can be calculated according to the following two formulas.

$$M_{nat} = \frac{F}{R} = P \frac{X_p - X_t}{X_{nat} - X_t} \frac{1}{R} = M \frac{X_p - X_t}{X_{nat} - X_t} \frac{1}{R^3}$$

$$\text{Definition } f_1 = \frac{X_p - X_{nat}}{X_{nat} - X_t} \quad f_2 = \frac{X_p - X_t}{X_{nat} - X_t} :$$

$$S = \frac{M}{r^2} \left((2X_p - 1)ln(\frac{X_p}{1 - X_p}) + f_1(2X_t - 1)ln(\frac{X_t}{1 - X_t}) - f_2(2X_{nat} - 1)ln(\frac{X_{nat}}{1 - X_{nat}}) \right)$$

where: M_{nat} is the annual natural uranium demand of the reactor (tHM/a); F is the mass of natural uranium in the enrichment feed (tHM/a); P is the quality of uranium enrichment product (tHM/a); X_p is the concentration of U_{235} in enriched uranium products (%); X_{nat} is the concentration of U_{235} in natural uranium (%); X_t is the concentration of U_{235} in depleted uranium tailings (%); R is the utilization rate of uranium at each stage (%);
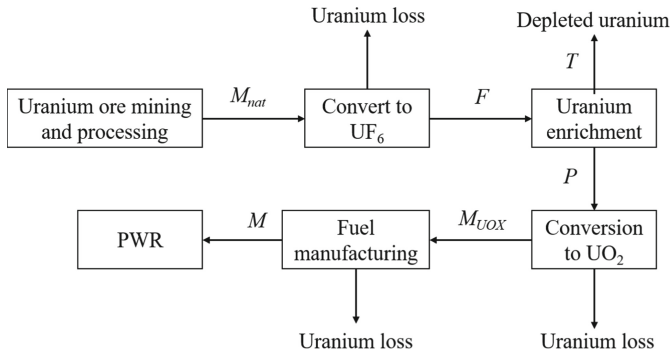
Fig. 2. Schematic diagram of material flow calculation

S is the separation work (SWU). The mass inflow and outflow diagram of each stage of material flow calculation is shown in Fig. 2.

At present, the mainstream commercial reactor types in China not only consider the Fukushima nuclear power accident, but also integrate the international advanced three generation nuclear power idea. They shoulder an important mission both at home and abroad. Therefore, this paper selects the design parameters of the mainstream nuclear power reactor types at this stage for calculation, as shown in Table 1 below.

Table 1. Calculation Parameters

Parameter	Value	Parameter	Value
P_e (GWe)	1.2	X_p (%)	4.45
B_d (GWd/tHM)	47.9	X_{nat} (%)	0.711
CF (%)	81.0	X_t (%)	0.25
ε (%)	38	R (%)	99.5

To calculate the cost of each phase of the fuel cycle, the mass of each part of the cycle must be provided. According to the above introduction, the balance materials of each cycle component can be calculated as shown in Table 2 below:

Table 2. Material flows of each part

Cycle part	Mass (t/a)
Natural uranium	180.27
Uranium conversion (natural uranium)	180.27
SWU required for uranium enrichment	133.22
Reactor fuel quality	19.49
Spent fuel	19.49

3   Calculation Results and Discussion

Price information is not only a necessary condition for levelized cost calculation in each cycle stage, but also a judgment standard for accuracy in economic calculation and analysis. However, because different countries have different policies and different calculation methods, some costs, such as the price of natural uranium, will change with the passage of time and the relationship between countries, so it is difficult to accurately calculate the absolute value of each stage. The unit cost used in this paper is the average value in recent years. At the same time, the upper limit and lower limit are taken as the upper and lower limit according to the 20% fluctuation of the average value.

3.1   Levelized Cost Analysis

The total cost of a simple nuclear fuel cycle can be calculated by multiplying the fuel required at each stage of the cycle by the unit cost. However, as the whole cycle of nuclear fuel is long, reaching several decades, the time factor needs to be considered. Levelized cost is a commonly used method for economic analysis of energy and power industries. Considering the technical differences, the evaluation of different energy costs is particularly appropriate. In this paper, the levelized cost of energy (LCOE) is used to evaluate the economic benefits of each stage. The calculation method is as follows:

$$LCOE = \frac{\sum_{t=1}^{T} \frac{\text{Fuel cost}_t}{(1+r)^t}}{\sum_{t=1}^{T} \frac{\text{Generating capacity}_t}{(1+r)^t}}$$

where: T is the annual score, and r is the discount rate.

The concentration of natural uranium (0.711%) is far less than that of U in fuel elements of nuclear power plants (4.45%), so it is necessary to enrich natural uranium and convert it into UF_6. The price of natural uranium is affected by the military strategy and trade between countries and the global inventory, and often shows an irregular change trend, so it is difficult to accurately quantify it. Therefore, this paper selects the average price of UxC company in recent months of 57.3 USD/kg, the price of uranium conversion is 9.5 USD/kg, and the unit price of uranium enrichment is 140 USD/SWU. According to the OECD/NEA 2006 report, the production price of fuel elements is 285 USD/kg.

The cost of temporary storage and final geological disposal of spent fuel includes overnight cost, operation and maintenance cost and decommissioning cost. These costs are difficult to estimate, mainly due to the lack of reference information for commercial operation. Cameron R [5] has calculated the cost of each part in detail and made corresponding analysis. Therefore, this paper has made corresponding fitting for the temporary storage and geological disposal of spent fuel according to the results of Cameron R. finally, the unit price of spent fuel cooling and temporary storage is 200 USD/kg, and the unit price of spent fuel transportation and geological disposal is 412 USD/kg. The fitting results are basically consistent with the research results of MIT [6].

Table 3. Nuclear fuel cycle interval

Cycle part	Interval from reference year (a)
Natural uranium	−4.5
Uranium conversion	−3.5
Enriched and depleted uranium	−2.5
Fuel manufacturing	−1
Reference year, reactor loading	0
Spent fuel cooling and temporary storage	9
Geological disposal	50

According to the above relevant parameter analysis and OTC cycle time interval Table 3, the cost of each part of the nuclear fuel cycle can be calculated when the discount rate is 0%, 2% and 4%, as shown in Table 4.

Table 4. Cost of nuclear fuel cycle corresponding to different discount rates

Cycle part	Levelized fuel cost (USD/MWh), $r = 0\%/2\%/4\%$		
	Lower limit value	Normal value	Upper limit value
Natural uranium	0.97/1.06/1.16	1.21/1.33/1.45	1.46/1.59/1.74
Uranium conversion	0.16/0.17/0.18	0.20/0.22/0.23	0.24/0.26/0.28
Uranium enrichment	1.75/1.84/1.93	2.19/2.30/2.42	2.63/2.76/2.90
Fuel manufacturing	0.52/0.53/0.54	0.65/0.67/0.68	0.78/0.80/0.81
Cooling and temporary storage	0.37/0.31/0.26	0.46/0.38/0.32	0.55/0.46/0.39
Geological disposal	0.75/0.28/0.11	0.94/0.35/0.13	1.13/0.42/0.16
Total	4.52/4.19/4.18	5.65/5.25/5.23	6.79/6.29/6.28

It can be seen from Table 4 that the selection of discount rate affects not only the total levelized cost, but also the cost of each stage. For OTC fuel cycle of nuclear power plant, the front levelized fuel cost increases with the increase of discount rate, and the back levelized fuel cost decreases with the increase of discount rate. In addition, it can be seen from Table 4 that the front-end levelized cost of the nuclear fuel cycle is greater than the rear end levelized cost. Among the total costs, the purchase of natural uranium, uranium enrichment and fuel production account for the largest proportion. When the discount rate is 4%, the purchase of natural uranium accounts for 28%, uranium enrichment accounts for 46% and fuel production accounts for 13%.

Figure 3 shows the cost accumulation diagram of the nuclear fuel cycle corresponding to different discount rates. It can be clearly seen from Fig. 3 that with the increase of the discount rate, the total cost of the nuclear fuel cycle gradually decreases. In particular,

the cost required for geological disposal decreases significantly, and the cost required for fuel production and uranium conversion does not change significantly.
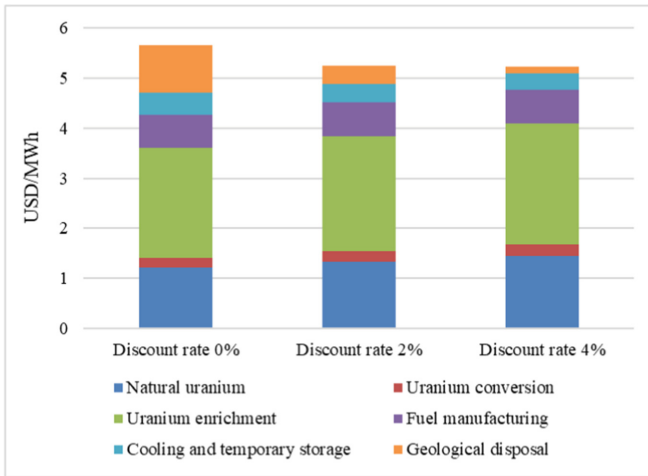
Fig. 3. Cost accumulation map with different discount rates

3.2 Sensitivity Analysis

In order to further analyze the impact of each stage of the nuclear fuel cycle on the total LCOE, this paper selects the impact of 20% of each unit price change on the total cost when the discount rate is 2%, as shown in Fig. 4 below.
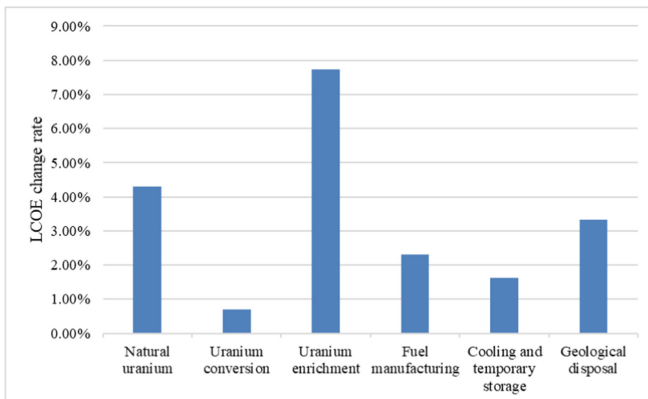
Fig. 4. Effect of 20% change in each price on LCOE

As can be seen from Fig. 4, the four factors that have a greater impact on LCOE are the cost of enriched uranium, the cost of natural uranium, the cost of spent fuel

disposal and the cost of fuel production. Among them, the cost of uranium enrichment has the greatest impact on LCOE, followed by the cost of natural uranium, which shows that the cost of uranium enrichment and natural uranium play an important role in the nuclear fuel cycle. As the price of natural uranium is greatly affected by the strategies of various countries, with the extensive use of nuclear energy in China's energy layout, the economy of nuclear power can be better guaranteed only when the supply of uranium resources is stable.

In addition, 95% of the spent fuel is composed of uranium and plutonium, so these elements can be separated and converted into MOX fuel for recycling. The separation and transmutation of spent fuel can not only increase the service life of nuclear elements, but also greatly reduce the risk caused by long-term storage, reduce the impact of radioactive elements on the environment and public health, and alleviate the supply of natural uranium to a certain extent.

4   Conclusions

Based on the material flow and economic analysis, this paper makes a detailed calculation on the cost of nuclear fuel passing through each stage at one time, and mainly draws the following conclusions:

Although the OTC scheme of the nuclear fuel cycle is simple and easy to operate, the utilization rate of uranium in the fuel is low. In terms of the cost of the cycle, the front-end cost is greater than the back-end cost, and the front-end cost increases with the increase of the discount rate, while the back-end cost decreases with the increase of the discount rate. The sensitivity analysis further shows that the cost of uranium enrichment, the cost of natural uranium and the manufacturing cost of fuel not only account for a large proportion of the total cost, but also have strong sensitivity.

To further reduce the total cost of the nuclear fuel cycle, it is necessary not only to reduce a large proportion of the cost of the cycle, but also to improve uranium enrichment and fuel production technology through technological innovation. In the future, when optimizing the fuel cycle, designers can improve the enrichment of fuel, increase fuel consumption, and reduce the enrichment of tailings. For the cost control of fuel assembly production process, it is necessary to focus on the cost of fuel assembly production and natural uranium procurement. At the same time, it should also focus on the recycling of spent fuel. The separation of uranium and plutonium at the back end of the nuclear fuel cycle can not only control and minimize the harm to the environment and human health caused by long-term storage of radioactive substances, it can also improve the sustainability of nuclear energy. Finally, as the recovery of spent fuel involves the recovery of plutonium, we should also pay attention to the impact of technical, environmental and political factors on the nuclear fuel cycle strategy while considering the economy.

References

1. World Nuclear Association, Nuclear Power in the World Today (Updated May 2021). http://www.world-nuclear.org/information-library/country-profiles/countries-a-f/china-nuclear-fuel-cycle.aspx

2. Wu, Y., Wu, J., Mu, Q., et al.: Study on nuclear fuel cycle model of PWR in China before 2050. Nucl. Sci. Eng. **32**(4), 371–378 (2012)
3. Hu, W., Jing, J., Pan X., et al.: Transmutation characteristics of secondary actinides in large advanced pressurized water reactor. Intense Laser Particle Beam **29**(03), 29036016 (2017)
4. Ko, W.I., Gao, F.: Economic analysis of different nuclear fuel cycle options. Sci. Technol. Nucl. Installations **2012**, 1–10 (2012)
5. Cameron, R., Urso, M.E., Lokhov, A.: The economics of the back end of the nuclear fuel cycle (2014)
6. Kazimi, M., Moniz, E.J., Forsberg, C.W., et al.: The Future of the Nuclear Fuel Cycle. Massachusetts Institute of Technology, Cambridge (2011)

Analysis of Fast Power Reduction System for CPR1000 Nuclear Power Plants

Yanhua Cheng[✉], Kai Wang, Xingxing Xu, Yulong Mao, and Yousen Hu

China Nuclear Power Technology Research Institute, Shenzhen, China
chengyanhua_1983@163.com

Abstract. CPR1000 nuclear power plants have the risk of reactor trip during the house load and turbine trip transients. Rapid power reduction system of AP1000 nuclear power plants and fast power setback system for VVER nuclear power plants are designed respectively, which can avoid this problem and thus provide more availability of units. It is necessary to introduce the Fast Power Reduction system to CPR1000 units to get more economy and flexibility. Based on the core control mode of CPR1000 units, the rod control assembly banks are regrouped to realize the fast power reduction function. Besides, the impact of fast power reduction system on the normal transients are evaluated. The results show that more operational margin can be released, and also the capacity of turbine bypass system can be reduced. Finally, more availability and economy can be obtained for CPR1000 units.

Keywords: CPR1000 NPP · Fast Power Reduction · Bank Regroup · Economy · Flexibility

1 Introduction

In the power range from 15% FP to 100% FP, the CPR1000 nuclear power plant is adaptable to the linear change rate of $\pm 5\%$ FP/min and to the step change of $\pm 10\%$ FP, without resulting in reactor trip and/or the open of pressurizer safety relief valve (PSV) and/or turbine bypass system. However, in case of large and fast load decrease, such as turbine trip and house load from 100% FP, the capacity of turbine bypass system (GCT) needs to be large enough to match the bypass steam flow. Generally the turbine bypass system capacity is set as 85% of the nominal steam flow, so as to ensure the operation of the reactor under such large and fast transients. However, as the core power decrease lags behind the turbine load, there is still the risk of reactor trip during the house load and turbine trip transients. Besides, loss of a reactor coolant pump (RCP) at full power will cause a reactor trip actuated by low-low RCP speed signal, which is not in accordance to the new UTILITY REQUIREMENT DOCUMENT (URD), requiring the unit to remain operation in case of loss of a RCP.

The Rapid Power Reduction (RPR) system in the AP1000 nuclear power plants is designed to reduce the reactor power rapidly to the capability of turbine bypass dump system in the turbine load rejection event [1]. There is no risk of reactor trip, or no opening of safety valves of pressurizer and steam generators.

In the operation of VVER-1200 which permits one or two RCPs to be switched off, the reactor control is equipped with Fast power setback (FPS) system [2]. It automatically reduces reactor power by insertion of automatic control banks and prohibits reactor power rise by prohibiting withdrawal of the control protection system rods, so that it can avoid the reactor trip and prevent violation of safety limits and conditions.

On one hand, the fast power reduction or setback system can improve the ability of the unit to deal with large and fast load transients, and improve the availability of the unit without triggering the emergency reactor trip. On the other hand, it can also reduce the design capacity of GCT system (the capacity of AP1000 GCT system is 40% of nominal steam flow), and thus save the unit cost. In order to improve the economy and flexibility of unit operation, and also to meet the new URD to enhance the advanced nature of the unit, it is necessary to introduce a fast power reduction system for CPR1000 units.

2 Function Introduction

The main function of the fast power reduction system is to realize the fast power reduction by releasing a pre-selected control rod groups, which will drop into the bottom of the core in several seconds, during the rapid and large-scale load rejection of the turbine, thus to avoid triggering the emergency reactor trip and the open of any safety valve.

In the process of releasing the pre-selected control rod groups in the fast power reduction system, an interlock logic is set to prohibit the lifting of other power control banks, which would lift in case of power reduction during normal operation. During the rapid power reduction, the average temperature control system (ACT) is assumed in an automatic state. At the same time, the RT signal of high (negative) change rate of neutron flux is blocked, so as to avoid the unexpected reactor trip during the dropping process of the pre-selected control rod groups.

After the power reduction process, the position structure of the Rod Cluster Control Assembly (RCCA) is different from that after power reduction during normal core control, which is named as calibration curve. It is necessary to adjust the RCCA position to the calibration curve to be ready for the return to full power operation afterwards. Thus, after a delay, the power control banks are operated manually to move toward the target rod position corresponding to the calibration curve, while the temperature control banks (R banks) are in automatic mode to maintain the power near the target value.

The fast power reduction system is mainly used to prevent triggering reactor trip during deviation from normal operation, and it is classified as non-safety function.

3 Rod-Drop Strategy

In order to realize the power reduction process in the fast power reduction function, the existing control rod banks are re-grouped, and the new rod-drop groups are analyzed and calculated.

3.1 RCCA Re-group Mode

The main consideration of control rod re-grouping used for fast power reduction function is the value of control rod group and the flattening of core power. Thus the control rod group releasing for the fast power reduction function is not an random combination of control rods. In order to ensure the symmetry of power distribution and avoid unacceptable power peaks after the drop of the re-grouping control rods, the re-grouped control rods used for fast power reduction function are symmetrically arranged in the core.

The control rods arranged in CPR1000 core are divided into control rod banks and shutdown rod banks [3]. The shutdown rod banks are all black rods. The control rod banks are divided into power control banks (G1, G2, N1, N2) and temperature control banks (R), among which 12 bundles of control rods such as G1 and G2 are gray rods, and the remaining 56 bundles of control rods are black rods.

As the value of shutdown rod banks is larger than power control banks, a smaller power reduction interval can be obtained by releasing power control rod groups comparing with shutdown control rod groups, which is beneficial for power control. Furthermore, the power control rods need to be adjusted to the rod position of calibration curve with corresponding power (30% FP to 60% FP for example) after a delay of the fast power reduction process, so it is easier to restore to the target rod position by using power control rod banks.

The R control banks are not only used for regulating average temperature, but also used for axial power distribution control. Besides the R banks position will change during the plant normal operation, so R control banks are not considered for the fast power reduction function.

The general principle for re-grouping is that two RCCAs symmetrically distributed on the diagonals are classified as a new group. As the value of G1 banks is small, there is no need to divide G1 banks. The original G2 banks are divided into four groups, which are G2a, G2b, G2c and G2d respectively. The original N1 banks are divided into four groups, of which two groups are in the outer ring named as N1a and N1b respectively, and two groups in the inner ring named as N1c and N1d respectively. The original N2 banks does not need to be grouped. The re-grouping mode of power control banks is shown in Fig. 1.

3.2 Rod-Drop Group Pre-selection

The value of control rods varies with the burnup and cycle. In the algorithm of fast power reduction system, it is necessary to calculate the value of control rods at different burnups, so as to select the control rod group to be released. Taking the equilibrium cycle of a CPR1000 unit as an example, the control rod groups to be released for fast power reduction system are analyzed. Both the beginning of cycle (BOL) and the end of life (EOL) are calculated.

The calculation results of the power control rod groups to be released for the fast power reduction function are summarized in Table 1. The power control rod groups are assumed to be released in the order of G1→G2a→G2b→G2c→G2d→N1a→N1b→N1c→N1d→N2. In BOL, the power can be reduced to 47% FP when power control rod groups from G1 to G2c are released,

	R	P	N	M	L	K	J	H	G	F	E	D	C	B	A
1															
2						N2				N2					
3															
4				N1a		G2a		G1		G2d		N1b			
5															
6		N2		G2c				N1c				G2b		N2	
7															
8				G1		N1d				N1d		G1			
9															
10		N2		G2b				N1c				G2c		N2	
11															
12				N1b		G2d		G1		G2a		N1a			
13															
14						N2				N2					
15															
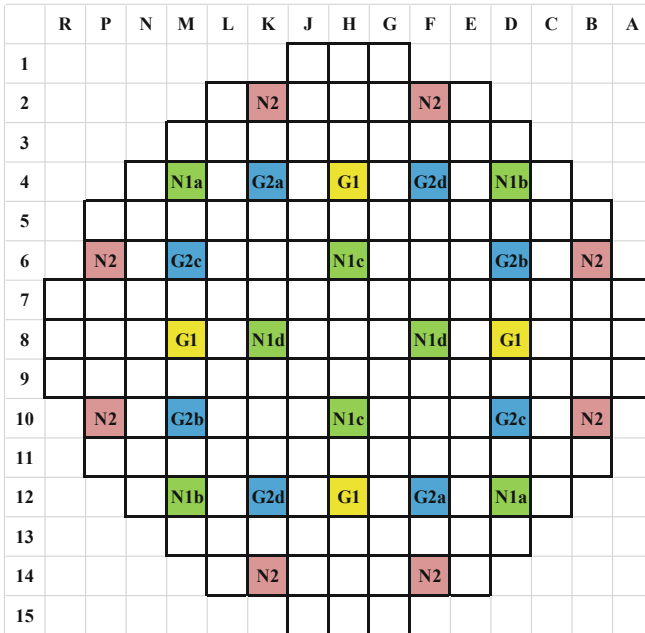
Fig. 1. Re-group Mode of Power Control RCCAs

and 33% FP when G1 to G2d are released. As can be seen in Table 1, the nuclear enthalpy rise hot channel factor ($F_{\Delta H}$) after the drop of some control rod groups exceeds the limit slightly. However, as the fast power reduction is a short-term process, and the peak linear power density and the maximum outlet temperature decrease monotonously with the power reduction, the safety of the core will not be threatened. In EOL, when power control rod groups G1 to G2d are released, the power decreases only to 60% FP, which is due to the large feedback coefficient (in absolute value) in EOL. More positive reactivity is introduced when the power is reduced, so more power control rod groups are needed to be released comparing with that in BOL. When power control rod groups G1 to N1a are released, the power can be reduced to 49% FP, and 36% FP when G1 to N1b are released. The outer ring N1a and N1b control rod groups was selected instead of the inner ring N1c and N1d because the power peak factor was lower when N1a and N1b are released.

To sum up, it is recommended to select power control rod groups to perform the fast power reduction function. Taking equilibrium cycle as an example, the pre-selected rod-drop groups for fast power reduction are G1G2aG2bG2c with target power at 50% FP and G1G2aG2bG2cG2d with target power at 30% FP at BOL, and G1G2aG2bG2cG2dN1a with target power at 50% FP and G1G2aG2bG2cG2dN1aN1b with target power at 30% FP at EOL, respectively.

Table 1. Main Parameters for the Selected Power Control Groups during Fast Power Reduction Process

Burn-up	Selected Groups	Power (%FP)	Power Variation (%FP)	$F_{\Delta H}/F_{\Delta H limit}$
	ARO	100		0.976
	G1	77	23	0.949
	G1G2a	71	6	0.987
BOL	G1 to G2b	59	12	*1.034***
	G1 to G2c	47*	12	*1.023***
	G1 to G2d	33*	14	*1.052***
	G1 to N1a	18	15	0.974
	G1 to N1b	4	14	*1.111***
	ARO	100		0.935
	G1	86	14	0.944
	G1G2a	80	6	0.976
	G1 to G2b	74	6	0.947
	G1 to G2c	67	7	0.990
	G1 to G2d	60	7	0.893
EOL	G1 to N1a	49*	11	0.998
	G1 to N1b	36*	13	0.944
	G1 to N1c	24	12	0.958
	G1 to N1d	14	10	0.998

Note: * means the possible target power level for fast power reduction function.

       ** means $F_{\Delta H}$ exceeds the limit.

4 Nuclear Design Analysis

The effects of fast power reduction on nuclear design parameters are analyzed, including xenon toxicity, radial power distribution, axial power distribution, and $F_{\Delta H}$. Two typical burn-ups, BLX and EOL, are analyzed. The rod-drop groups are selected according to the analysis in Sect. 3.

(1) The negative reactivity induced by xenon accumulation can be compensated by boron concentration regulation or power control banks lifting. In BOL, due to the high boron concentration, the boron concentration regulation is completely able to compensate the negative reactivity induced by xenon accumulation. In EOL, as the boron concentration is nearly zero, the power control banks are considered to compensate the negative reactivity, which will produce a penalizing axial power distribution. Furthermore, this will also impact the power lifting hereafter. In order

to facilitate control and subsequent power lifting, it is suggested to limit the core burnup for implementation of fast power reduction function.

(2) In the process of fast power reduction, the radial power distribution of the core will be affected when the rods are dropped. Taking BLX of the equilibrium cycle as an example, the radial power distribution during the implementation of fast power reduction is analyzed, and the calculation results are shown in Fig. 2. The radial power distribution is very uniform before the rods are dropped. The radial power distribution deteriorates after the pre-selected rod groups drop. The maximum relative power is 1.158, and the minimum relative power is 0.860. When the power control rods are fully lifted and restored to full power, the radial power distribution is further improved, and the maximum relative power is 1.014 and the minimum relative power is 0.989. The maximum deviation of radial power distribution is only 1.4%, which is basically uniform.

(a) before rod-drop   (b) after rod-drop

(c) back to full power
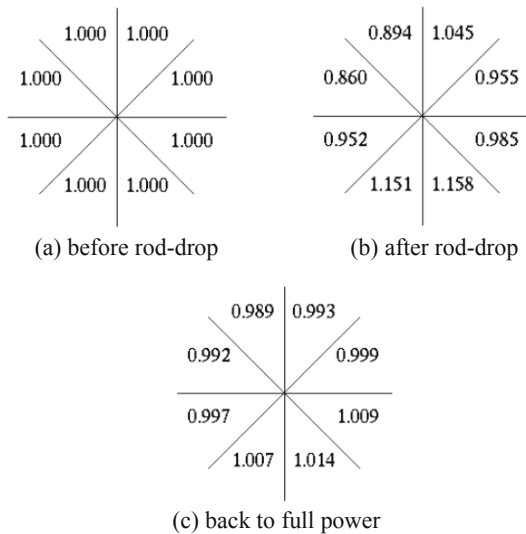
Fig. 2. Radial Power Distribution Change

(3) The action of control rods will lead to the change of ΔI of the core. The point of worse axial power distribution appears in the rod dropping process at EOL. It can be seen in Table 2 that, if R banks are placed in the position out of core (ARO) or in the middle of regulating belt (RMBM) before rod dropping, ΔI will exceed the right boundary of operation diagram after rod dropping. If the R rod is placed at 190 insertion steps in advance, ΔI can be controlled in the operation diagram, but the implementation of rapid power reduction will be delayed. Therefore, it is necessary to limit the burnup of rapid power reduction.

Table 2. ΔI after Fast Power Reduction at EOL

R Position (insertion steps)	Power (%FP)	ΔI (%)	ΔI_{limit} (%)
ARO	48	20.07	**15**
RMBM	47.5	18.08	
190	48.5	9.75	

(4) The action of control rods will also lead to the increase of $F_{\Delta H}$. Taking BOL as an example, Fig. 3 shows that $F_{\Delta H}$ is worse in the process of rod dropping, and the value for some low power level exceeds the limit. So it is necessary to analyze and perform the safety evaluation under the new $F_{\Delta H}$ limit, which will be discussed in Sect. 6.
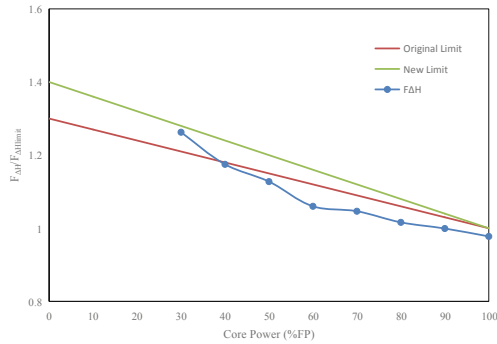
Fig. 3. $F_{\Delta H}$ during Fast Power Reduction for BOL

Thus it is found that the impact of fast power reduction on nuclear design mainly comes from rod-dropping process, and all parameters will be improved after the power control rod banks are adjusted back to the corresponding position of the calibration curve corresponding to the target power level.

5   Normal Transients Analysis

The fast power reduction function is mainly used for rapid and large-scale load decrease transients. House load from 100% FP to auxiliary power supply is one of the typical transients of this kind, which will trigger the fast power reduction function [4].

Taking BOL of equilibrium cycle as an example, the normal transient house load from 100% FP is analyzed considering the fast power reduction function. The target power level after fast power reduction function is considered as 30% FP and 50% FP respectively.

(a) Nuclear Power

(b) Over-Temperature ΔT Margin

(c) GCT Flowrate
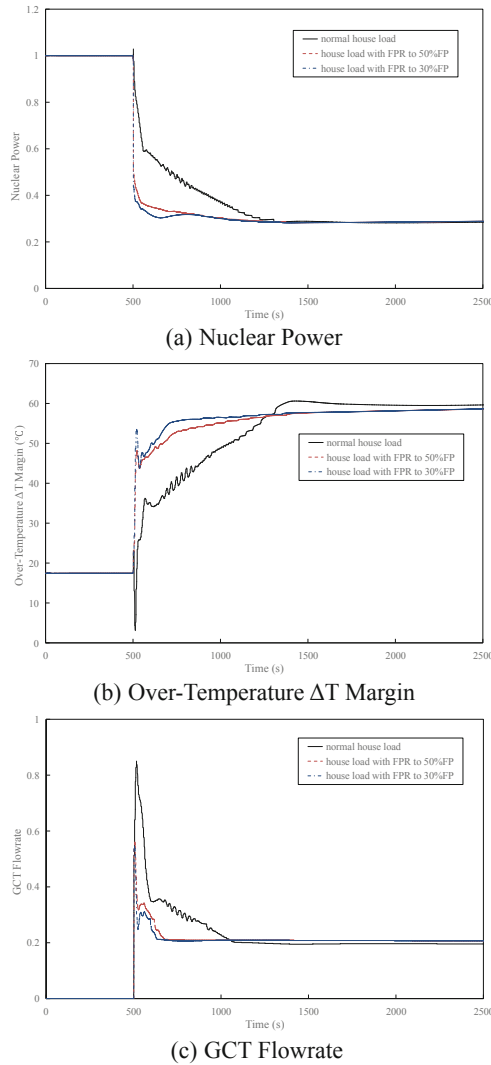
Fig. 4. House Load from 100% FP

Figure 4 shows the changes of key parameters in the transient process of house load from 100% FP. It can be seen that after the introduction of the fast power reduction function, the power balance time of the primary and secondary circuits is shortened (Fig. 4a). The over-temperature ΔT margin means the difference between the real ΔT and the over-temperature ΔT reactor trip channel setpoint. The results in Fig. 4b shows that the over-temperature ΔT margin is significantly improved after the introduction of the fast power reduction function, which means the operational margin is improved. At the same time, the total capacity requirement of GCT can be reduced to 60% of the nominal steam flow (Fig. 4c), which can improve the flexibility and economy of the unit.

6 Safety Analysis

The function of fast power reduction system belongs to non-safety class, so its mitigation effect on accidents is not considered in the analysis. However, during rod-drop process of fast power reduction system, the $F_{\Delta H}$ will exceed the limit under some low power levels. Therefore a new $F_{\Delta H}$ limit is established when the power is lower than full power level (100% FP). The affected events or accidents are evaluated with the new $F_{\Delta H}$ limit [5].

For incidents of moderate frequency, which is defined as condition II events, the events affected by the new $F_{\Delta H}$ limit for low power levels include loss of off-site power, partial loss of forced reactor coolant flow and rod drop. The affected infrequent incident (condition III event) is the total loss of forced coolant flow accident. The affected postulated incident (condition IV event) is the RCP shaft seizure (locked rotor) accident.

For the rod drop event, the thermal power at the time of minimum DNBR in the transient process is close to 100% FP, and the new envelope has little influence on the results. The analysis results show that the minimum DNBR does not change in the transient process with the new $F_{\Delta H}$ limit.

Among other affected condition II events, the minimum DNBR appears in the loss of off-site power supply event. For the loss of power supply, the minimum thermal power at the time of minimum DNBR is 96.2% FP. If the new $F_{\Delta H}$ limit is adopted, the DNBR margin in the transient process will be reduced from 27.7% to 26.3%, which still meets the safety criteria.

For total loss of forced coolant flow accident, if the new $F_{\Delta H}$ envelope is adopted, the minimum DNBR margin in transient process is reduced to 11.0%, which still meets the limit requirements. For the RCP shaft seizure (locked rotor) accident, the new $F_{\Delta H}$ envelope has no effect on the result.

Table 3. Safety Evaluation with the New $F_{\Delta H}$ limit

Events	Minimum DNBR Margin	
	Original	New $F_{\Delta H}$ Limit
Rod Drop (II)	8.9%	8.9%
Loss of Offsite Power (II)	27.7%	26.3%
Total Loss of Forced Coolant Flow (III)	13.1%	11.0%

To sum up, with the new $F_{\Delta H}$ limit (see Table 3), the DNBR margin decreases, but the consequences of all the events still meet the safety criteria.

7 Conclusion

The function of fast power reduction can be realized for CPR1000 unit by regrouping the existing power control rod banks. At the same time, the effect of implementing fast power reduction system is analyzed from the aspects of nuclear design, normal transient operation, and safety analysis. The analysis results show that the fast power reduction system can improve the unit ability to cope with large and fast load drop, and improve the availability of the unit. Meantime it can also reduce the design capacity of GCT system and save the cost of the unit.

References

1. Zhang, X., Liu, L.: Analysis of AP1000 reactor power control system. Nucl. Power Eng. **32**(4) (2011)
2. Le, D.D., Do, N.D.: Verification of VVER-1200 NPP simulator in normal operation and reactor coolant pump coast-down transient. World J. Eng. Technol. **5**, 507–519 (2017)
3. Zhang, Y.: Comparative analysis of the control strategies for CPR1000 and AP1000 reactor power control system. Process Autom. Instrum. **36**(7) (2016)
4. Zhang, B., Shi, J.: Transient analysis of house load from 100% FP for Nuclear Power Plant. Nucl. Power Eng. **22**(5) (2001)
5. Xiao, M.: Primary study on core concept design and safety margin of CPR1000. Nucl. Power Eng. **26**(6), (S1) (2005)

Calculation and Analysis of Polonium-210 Source Term in Primary Coolant System of Lead-Bismuth Fast Reactor

Haixia Wan[✉]

China Institute of Atomic Energy, Beijing, China
why_1022@163.com

Abstract. After the lead-bismuth coolant flows through the core area of the lead-bismuth fast reactor and is irradiated by neutrons, the radionuclide Polonium-210 will be produced. Polonium-210 has a half-life of 138 days and releases alpha particles during decay. With certain volatility, Polonium-210 will pose a potential threat to the environment. Therefore, Polonium-210 is one of the key contents of radiation environmental impact assessment of lead-bismuth reactor. The calculation model of Polonium-210 is established according to the metabolic mechanism of Polonium-210 in the coolant. According to the Polonium-210 calculation model, the generation, decay and migration laws of Polonium-210 in the whole life were analyzed, and the influence of extraction rate on the saturation of Polonium-210 was calculated. The results show that, taking a 20MW$_{th}$ lead-bismuth reactor as an example, in the case of no extraction, Polonium-210 reaches saturation in the fifth year of reactor operation, with a saturation activity of 3.15E + 15Bq. With an extraction efficiency of 90%, Polonium-210 will reach saturation on the 60th day after the reactor starts operating, with a saturation activity of 3.83E + 10Bq. The calculation results can provide a reference for the research on the distribution of Polonium-210 in the coolant.

Keywords: Lead-Bismuth Fast Reactor · Coolant · Polonium-210 · Radioactivity · Activity

1 Introduction

Lead-bismuth fast reactor uses lead-bismuth alloy as coolant. Lead-bismuth coolant has the following natural characteristics: high melting point, inactive chemical properties, vacuolar reactivity is negative, etc. Lead-bismuth alloy is chemically inert with fuel, low alloy steel, water and air. In addition, lead-bismuth has higher boiling point, Therefore, compared with pressurized water reactor and sodium-cooled fast reactor, the safety has the potential to improve, and it is expected to simplify the reactor structure and improve the economic model. Based on the inherent safety of lead-bismuth alloys, the Fourth Generation Nuclear Forum (GIF) lists the lead-based fast reactor as one of the six advanced nuclear systems with the most potential for development.

The biggest problem with the lead-bismuth alloy as a coolant is the activation of Polonium-210, a volatile alpha emitter, during reactor operation. In the case of loss of integrity of primary circuit boundary and leakage of coolant, Polonium-210 will quickly adsorb on aerosols or dust in the external air, and then settle into soil and surface water from the air, causing internal exposure to the human body through breathing, drinking, or wound infection. Therefore, the yield of Polonium-210 is one of the important contents of Lead-bismuth reactor nuclear power.

With regard to Polonium-210, in the occupational exposure regulations of the Russian NRB-99, for professional personnel, annual inhalation activity less than 6.7E+3Bq/year, and inter-process air activity concentration less than 2.7 Bq/m^3. For the public, the annual inhalation activity is less than 2.5E+2Bq/year, and the activity concentration in the air is less than 3.4E–2Bq/m^3. Therefore, accurate calculation of Polonium-210 yield is very important. Based on the mechanism of Polonium-210 generation, migration and decay in lead-bismuth fast reactor, an equilibrium equation was established for Polonium-210 metabolism in coolant. The yield of Polonium-210 was calculated and analyzed, and the effect of extraction efficiency on the saturation of Polonium-210 was analyzed.

2   The Production of Polonium

In the operation process of the lead-bismuth reactor, the lead-bismuth coolant is irradiated by neutrons, and the nuclide Bismuth-209 first generates Bismuth-210, which then decays into Polonium-210 by β. Polonium-210, is highly toxic, highly volatile, and has a half-life of 138.4 days. It decays to form a stable nuclide Polonium-206 and releases 5.35 meV energy, while emitting low-intensity gamma rays.

$$^{209}_{83}\mathrm{Bi} + \mathrm{n} \rightarrow {}^{210}_{83}Bi \xrightarrow{\beta^-} {}^{210}_{84}Po \xrightarrow{\alpha} {}^{206}_{82}\mathrm{Po}$$
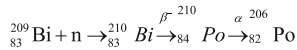
It is found that Polonium-210 mainly exists in pure Polonium-210 and Lead polonium, with the proportion of 0.2% and 99.8%. When lead-bismuth comes into contact with air, it reacts with water vapor in the air to form radioactive aerosols and hydrides of volatile Po. As a result, protective gas is usually placed on top of the reactor lead bismuth coolant to insulate the lead bismuth coolant from the air. Argon is generally
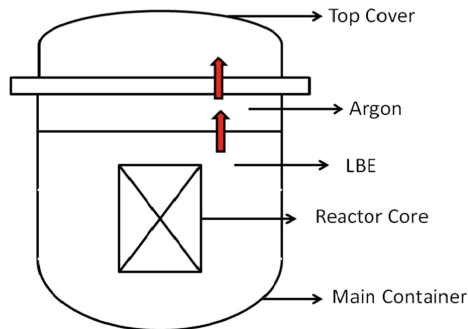
Fig. 1. Release path of Polonium-210 in lead-bismuth fast reactor

used as a protective gas. During operation of the reactor, Polonium-210, the activation product of the coolant lead and bismuth, migrates to the protective gas. When the gas tightness of the reactor cap occurs, Polonium-210 and the protective gas will leak out to the outer space (Fig. 1).

3   Calculation

3.1   Model

The Polonium-210 in the lead-bismuth coolant, produced by the decay of Bismuth-210 generated by Bismuth-209 activation, disappears in its own decay, extraction and evaporation. Therefore, the equilibrium equations for Bismuth-210 and Polonium-210 in lead-bismuth are as follows:

$$\frac{dN_{Bi}}{dt} = \sigma \emptyset N_{Bi} - \lambda_{Bi} N_{Bi} \tag{1}$$

$$\frac{dN_{Po}}{dt} = \lambda_{Bi} N_{Bi} - \lambda_{Po} N_{Po} - \varepsilon v \frac{N_{Po}}{M_{PbBi}} - \Gamma \tag{2}$$

In the formula above, σ is the microscopic reaction cross section of Bismuth-209 (n, γ) Bismuth-210, ϕ is neutron flux rate, N_{Bi} is the nucleon density of bismuth in the coolant, λ is the decay constant of Polonium-210, N_{Po} is the nuclear density of Polonium-210, ε is the extraction efficiency, v is the mass flow rate of lead and bismuth in the coolant, M_{PbBi} is the total mass of lead and bismuth, Γ is the evaporation rate of Polonium-210 from lead and bismuth into protective gas.

According to Formula 1, the radioactive activity of Bismuth-210 in lead-bismuth is derived as:

$$A_{Bi}(t) = \sigma \emptyset N_{Bi} \left(1 - e^{-\lambda_{Bi} t} \right) \tag{3}$$

If it is not extracted during the process, then f is 0, Polonium-210 and its radioactivity is:

$$A_{Po}(t) = \sigma \emptyset N_{B1} + \frac{\sigma \emptyset N_{Bi}}{\lambda_{Po}(\lambda_{Po} - \lambda_{Bi})} \left(\lambda_{Bi} e^{-\lambda_{Po} t} - \lambda_{Po} e^{-\lambda_{Bi} t} \right) \tag{4}$$

If extraction is set in the process, the radioactive activity of Polonium-210 is:

$$A_{Po}(t) = \frac{\lambda_{Po} \sigma \emptyset N_{Bi}}{\lambda'_{Po}} + \frac{\sigma \emptyset N_{Bi}}{\lambda'_{Po}(\lambda'_{Po} - \lambda_{Bi})} \left(\lambda_{Bi} e^{-\lambda'_{Po} t} - \lambda'_{Po} e^{-\lambda_{Bi} t} \right)$$

$$\lambda'_{P_o} = \lambda_{P_o} + \varepsilon v \frac{N_{Po}}{M_{PbBi}} \tag{5}$$

Because lead-bismuth is covered with protective gas argon, Polonium-210, the activation product of the coolant lead-bismuth, will evaporate into the covering gas during reactor operation. According to the experimental results of the Russian Institute of Physics

and Power Engineering (IPPE), the evaporation rate is only related to temperature. Then the evaporation rate equation of Polonium-210 is:

$$\lg \omega_{pbpo} = -\frac{4793}{T} + 2.476 \tag{6}$$

$$\lg \omega_{po} = -\frac{2929}{T} + 2.664 \tag{7}$$

3.2 Sample

According to the Polonium-210 calculation model, a 20 MW_{th} lead-bismuth stack is taken as an example to calculate the Polonium-210 source term, and analyze the Polonium-210 production, diffusion to argon gas, and leakage to outer space. Table 1 lists the relevant parameters used in the calculation process.

Table 1. Parameters of lead-bismuth reactor

Parameter	Numerical	Unit
Power	20	MW_{th}
Lifetime	30	years
Coolant Temperature Range	280–485	°C
Cover Gas Leakage Rate	0.5%	/day
Coolant Flow Rate	660	Kg/s

3.3 Results Analysis

Considering the distribution of lead and bismuth and in order to accurately calculate the exposure of Polonium-210, the coolant location was divided into 15 zones inside the main container. The MCNP program was used to calculate the maximum neutron injection rate and microscopic reaction cross section of the zones respectively (Table 2).

By putting the data in the table into formula (3), it can be obtained that Bismuth-210 reaches saturation after the 50th day of full power operation, and the saturation activity is 3.15E+15Bq. If extraction is not set in lead-bismuth coolant, according to formula (4), it can be deduced that Polonium-210 reaches saturation in the fifth year of full power operation, with a saturation activity of 3.15E+15Bq and a specific activity of 4.81E+10Bq/kg. If extraction is set in lead-bismuth coolant and extraction efficiency is assumed to be 90%, $(\lambda_{Po})' = \lambda_{Po} + 4.26E{-}03$ can be calculated according to formula (5) to achieve saturation on the 60th day of full power operation with saturation activity of 4.28E+10Bq, which is 5 orders of magnitude lower than that without extraction.

Table 2. Neutron flux rate and microscopic reaction cross section of the detection point

Area	Volumes	Maximum neutron flux rate n/(cm^{2}s)	The reaction cross section barn
1	200368	2.84E+14	5.17766E−05
2	634229.5	1.63E+13	5.56735E−05
3	3891251	1.40E+13	5.61781E−05
4	2056206	1.50E+10	5.31242E−05
5	1468921	1.43E+12	6.01188E−05
6	577780.6	1.61E+12	6.16246E−05
7	547454.2	7.55E+06	4.52382E−05
8	16091693	2.77E+06	5.66097E−05
9	478702.7	9.91E+12	5.86544E−05
10	521491.8	2.87E+12	5.40462E−05
11	1997715	1.44E+11	5.10215E−05
12	1157979	6.25E+07	4.6703E−05
13	6765525	3.71E+11	5.15931E−05
14	876741.8	4.11E+11	5.34095E−05
15	6828060	6.01E+07	4.79719E−05

The evaporation rate of Polonium-210, the activated product of coolant lead and bismuth, into the covering gas can be obtained by formulas (6) and (7). ω_{PBPO} is about 3.21E−04 kg/(m^2•s), ω_{PO} is about 1.07E−01 kg/(m^2•s). Considering evaporation area and Po concentration, the evaporation activity of Polonium-210 in the pool is:

$$A_{\text{PbPo}_0} = \omega_{\text{PbPo}}/1000 \times \alpha_{\text{Po}} \times 0.998 \times S \tag{8}$$

$$A_{\text{Po}} = \omega_{\text{Po}}/1000 \times \alpha_{\text{Po}} \times 0.002 \times S \tag{9}$$

$$A = A_{PbPo} + A_{Po} \tag{10}$$

Of these, 1000 are caused by the pressure of the protective gas. ω is the evaporation rate, kg/(m^2·s); a is the specific activity of Polonium-210 in lead-bismuth coolant, Bq/kg; S is evaporation surface, m^2;

If the leakage rate of the reactor top shield is calculated as 0.5%/day and the external space is calculated as 200 m^3, the leakage amount of Polonium-210 is about 5.45E+02 Bq/(m^3·a) without extraction, Which cannot meet the limit requirements. In the case of extraction, the leakage amount is about 7.45E−03 Bq/(m^3·a), which meets the limit requirements. The calculation results are shown in Table 3:

Table 3. Comparison of results

	Not extract	Extract
Activity, Bq	1.09E+05	1.49E+00
Average activity, Bq/l	6.36E+01	8.66E−04
Leak amount, Bq/(m^3·a)	5.45E+02	7.45E−03

4 Conclusion

In this paper, a calculation model is established for the metabolic mechanism of Polonium-210, the coolant activation product of lead-bismuth fast reactor, and an example is used to calculate the Bismuth-210 and Polonium-210 production, migration to protective gas and leakage to outer space under the condition of extraction or not.

Through calculation, it is found that in the early stage of reactor operation, the activity of Bismuth-210 increases gradually, and about 50 days later, the activity of Bismuth-210 reaches saturation. If Polonium-210 is not extracted, after 5 years of operation, the radioactive activity of Polonium-210 in lead-bismuth gradually reaches saturation, the saturation activity is 3.15E+15Bq, and the amount of leakage into the air is about 5.45E+02Bq/(m^3·a), which does not meet the limit requirements. If Polonium-210 is extracted and the extraction rate is assumed to be 90%, the Polonium-210 in the coolant can reach saturation after 60 days of operation of the reactor, and the total activity of saturated radioactivity is 4.28E+10Bq. The activity of Polonium-210 was about 5 orders of magnitude lower than that without extraction, and the amount leaked into the air was about 7.45E−03Bq/(m^3·a), less than the limit of 2.7Bq/(m^3·a).

To sum up, setting Polonium-210 extraction device in the reactor can not only significantly reduce the radioactive activity of Polonium-210, but also the radioactive activity of Polonium-210 can reach saturation faster, and only setting extraction can ensure that the leakage rate of Polonium-210 does not exceed the limit. The analysis in this report can provide reference for waste assessment, safety analysis and environmental impact analysis of lead-bismuth reactor.

References

1. Mao, L.: Preliminary analysis of polonium 210 behavior in lead reactor. University of Science and Technology of China (2014)
2. Dang, T.: Study on radioactive source term calculation and dose evaluation of lead-bismuth reactor. University of Science and Technology of China (2013)
3. Li, N., Yefimov, E., Pankratov, D.: Polonium Release from an ATW Burner System with Liquid Lead-Bismuth Cooland, LA: UR-98-1995 (1995)
4. Jolkkonen, M.: Volatilisation of Polonium-210.EUROTRAN 1.5 Safety Meeting, Stockholm, 22–23 May 2007. http://neutron.kth.se/EUROTRANS/Stockholm

Study on Resuspension Models Based on Force Balance

Liwen He, Lili Tong[✉], and Xuewu Cao

Shanghai Jiao Tong University, Minhang, Shanghai 200240, China
lltong@sjtu.edu.cn

Abstract. During the severe accident of the nuclear power plant, the resuspension of the aerosol particles deposited in the containment would occur, due to some disturbance, resulting in the increase of radioactive aerosols released into the environment. Therefore, aerosol resuspension should be considered for the radiological consequence assessment. Accurate aerosol resuspension prediction model is very important.

In this paper, three typical aerosol resuspension models considering force balance, named Wichner model, Michael model and ECART model, are investigated. These models follow the principle that resuspension occurs when the aerodynamic disturbing force is greater than the hindering force and differ in the consideration of the forces acting on particles. Wichner model proposes the aerodynamic disturbing force includes lift force, while Michael model considers it composed of lift and drag force, hindering effect of adhesive force is considered in the two models. ECART model considers the hindering force includes gravity, cohesive and adhesive force, the aerodynamic disturbing force is composed of drag, and burst force. Considering the aerosol characteristics and thermal hydraulic conditions during nuclear reactor severe accidents, the simulation for STORM and ART experiments with the three models is carried out. Finally, via comparing and analyzing the prediction results and experimental results, the applicability of these models is evaluated. Wichner model could reflect the rapid change of resuspension with the disturbing gas velocity and is in agreement with the experimental results for different particle sizes under different disturbing gas velocities, which is recommended for predicting aerosol resuspension behavior during nuclear reactor severe accidents.

Keywords: Aerosol Resuspension · Force Balance · Aerodynamic Disturbing Force · Hindering Force

1 Introduction

The phenomenon of aerosol particle resuspension is the deposited particles on the surface are resuspended under the action of disturbance [1]. Resuspension may occur in many scenarios, such as pesticide resuspension from soil, biological particle resuspension, outdoor industrial product resuspension, indoor dust resuspension, etc. [1]. During the severe accident of the nuclear power plant, the resuspension of the aerosol particles deposited in the containment would occur due to some disturbance, resulting

in the increase of radioactive aerosols released into the environment [2, 3]. Therefore, aerosol resuspension should be considered for the radiological consequence assessment. Accurate aerosol resuspension prediction model plays a vital role.

Since the beginning of last century, research about resuspension has been carried out. University of Kansas and other organizations carried out resuspension experiments on glass surfaces with relatively large particles [4], whose mean diameters ranged from 18 to 34 microns. In 1998, the Joint Research Centre of the European Commission conducted STORM (Simplified Test Of Resuspension Mechanism) experiment, the SR11 condition of it is in accordance with the ISP-40 standard [5]. Then Reeks and Hall [6] used alumina particles, graphite particles and polished stainless steel flat plate performed resuspension experiment. Oak Ridge National Laboratory (ORNL) conducted the ART (Aerosol Resuspension Tests) experiment with micron-sized particles and horizontal tube [7]. From 2003 to 2007, the experiment of resuspension after hydrogen deflagration was carried out in the THAI (Thermal-hydraulics, Hydrogen, Aerosol, and Iodine) experimental facility, however, there is a discrepancy between the experimental measured aerosol particle diameter distribution and the fast deposition velocity after resuspension [8, 9]. Overall, most resuspension experiments could provide parameters affecting aerosol resuspension such as particle size distribution and density, disturbing airflow velocity and physical properties, and corresponding resuspension fraction, etc., but lack of refined measurement about the deposition surface and aerosol particle, which may not be sufficient to support verification of complicated model [10]. Considering the aerosol characteristics and thermal hydraulic conditions during nuclear reactor severe accidents and data availability, the STORM experiment and the ART experiment are screened out as validation experiments for model applicability analysis.

With the development of resuspension experimental research and the cognition of resuspension mechanism, research on resuspension models has also been carried out. Particle resuspension models are generally divided into two categories: models based on force balance and models based on energy conservation [11]. Resuspension models based on energy conservation include RRH [12], VZFG [13], and Rock'n'Roll [6] models, which assumes that the particle vibrate and accumulate energy until it has enough energy to overcome the adhesion from the surface, and resuspend. Resuspension models based on force balance consider that resuspension occurs when the aerodynamic disturbing force is greater than the hindering force [14], including Wichner [15], Michael [10], ECART [16] models, etc., which differ in their consideration for the forces acting on the particle.

With the effect of resuspension on radiological assessment is recognized, aerosol resuspension models are gradually applied to the severe accident analysis codes and particle tracking code, such as ASTEC code [17], ECART code [18], Melcor2.2 code [15] and a 2D lagrangian particle tracking code–CAESAR code [19], all of which apply the models based on the force balance theory. While the resuspension behavior is closely related to the particle characteristics, deposited surface characteristics and disturbed airflow characteristics. Therefore, it is essential to study and evaluate the applicability of this type of aerosol particle resuspension model under severe accident in nuclear power plant.

In this paper, three typical aerosol resuspension models considering force balance, named Wichner model, Michael model and ECART model, are investigated. Considering the aerosol characteristics and thermal hydraulic conditions during nuclear reactor severe accidents, the simulation for STORM and ART experiments with the three models is carried out. Finally, by comparing and analyzing the prediction results and experimental results, the applicability of these models is evaluated. The research in this paper can support the subsequent codes improvements.

2   Models for Resuspension

Michael and Wichner resuspension models believe that when the criterion of aerodynamic disturbing force is greater than the hindering force is met, the particle will resuspend, regardless of time [10, 15]. ECART model considers the particle resuspension rate is an exponential function of the resultant force on particles [16].

Michael model proposes that aerodynamic disturbing force is composed of lift and drag forces [10], both acting at the center of the particle. Only the hindering effect of adhesive force on resuspension is considered. There are two contact points between the particle and deposited surface, the distance between two contact points is 'A'. The adhesive force F_A (N) between the deposited surface and particles is determined by the ratio of the particle diameter d_p (μm) to the surface roughness ε (μm).

$$F_R = \frac{1}{2}F_L + \frac{r}{A}F_D \tag{1}$$

$$\langle F_L \rangle \approx 20.9\rho v^2 \left(\frac{ru^*}{v}\right)^{2.31} \tag{2}$$

$$\langle F_D \rangle \approx 32\rho v^2 \left(\frac{ru^*}{v}\right)^{2} \tag{3}$$

$$u^* = \sqrt{\tau_w / \rho} \tag{4}$$

$$\tau_w = \frac{1}{2}f\rho U^2 \tag{5}$$

$$F_A = 5.0 \times 10^{-10}d_p / \varepsilon \tag{6}$$

where F_R is the aerodynamic disturbing force (N), F_L is lift force (N), F_D is drag force (N), *and r* is particle radius (m). The average lift force is related to gas kinematic viscosity v (m^2/s), gas density ρ (kg/m^3), friction velocity u^* (m/s). Friction velocity equals to square root of the ratio of turbulent shear stress to air density, which characterizes the turbulent shear stress property and has a velocity dimension. τ_w is wall shear stress (N/m^2), f is the friction factor, and U is gas velocity (m/s).

Wichner model [15] suggests that the aerodynamic disturbing force acting on particles is related to gas density, aerosol particle radius, friction velocity and the aerodynamic

disturbing force coefficient α. The assumption about hindering force is the same as in the Michael model.

$$F_R = \alpha\pi\rho\left(ru^*\right)^2 \tag{7}$$

ECART force balance model considers [16] that hindering force mainly includes gravity of aerosol particle F_G (N), cohesive force F_C (N) and adhesive force F_A (N), the aerodynamic disturbing force is composed of drag force F_D (N) and burst force F_B (N) which are generated by disturbing air flow.

$$N(r) = \begin{cases} 0.4037 \cdot [F(r)]^{0.6003} & 0 < F(r) \le 3.065 \cdot 10^{-4}\,\mu N \\ 90.28 \cdot [F(r)]^{1.269} & F(r) \ge 3.065 \cdot 10^{-4}\,\mu N \end{cases} \tag{8}$$

$$F_G = \frac{4\pi r^3}{3}\rho_p g \tag{9}$$

$$F_C = 2Hr\gamma \tag{10}$$

$$F_A = 0.2 \cdot (F_g\gamma^3 + F_c) \tag{11}$$

$$F_D = \tau_w\pi r^2\chi^{2}/3 \tag{12}$$

$$F_B = 4.21\rho_g\chi v^2\left(\frac{2r\rho_g u^*}{v}\right)^{2.31} \tag{13}$$

where, $N(r)$ refers to resuspension rate (1/s), $F(r)$ refers to resultant force acts on the particle (μN), ρ_p refers to density of aerosol particle (kg/m^3), g refers to acceleration of gravity (m^2/s), H refers to empirical coefficient related to the number of deposition layers, γ refers to collision shape factor, χ is the aerodynamic shape factor.

3   Evaluation for Resuspension Models Application

3.1   Verification Experiments

In the process of the resuspension experiments, the aerosol particles are deposited firstly, then the airflow passing through the deposited area is supplied to resuspend the particles. Considering the aerosol conditions, thermal hydraulic conditions during nuclear reactor severe accidents and data availability, the STORM SR11 experiment [5] and the ART 05 experiment [7] are screened out as validation experiments. The particle diameters of the experiments conform to log-normal distribution, and the particle diameter ranges from a few tenths of a micron to a few microns, which is consistent with the size of most aerosol particles in the containment under severe accidents. And the experimental disturbing airflow velocity scope is broad, in the range of 11.9 m/s to 127 m/s. The key aerosol and thermal hydraulic parameters are shown in Table 1 [5, 7, 20, 21], where GMD is geometric mean diameter of aerosol particle and GSD refers to geometric mean deviation.

Table 1. Aerosol and thermal hydraulic conditions.

Experiment	GMD (μm)	GSD	Airflow velocity (m/s)	Reynolds number
STORM SR11	0.434	1.7	58.0–127.0	68000–150000
ART 05	1.68	3.3	11.9–59.6	5900–88000

3.2 Comparison with Experiments

In these force balance models, the parameters such as the gas velocity, density and viscosity, particles size distribution can all be determined from the experimental measurement. Apart from these factors, the distance between two contact points of particle and deposited surface 'A' in Michael model, the coefficient of aerodynamic disturbing force 'α' in Wichner model, the empirical coefficient related to the number of deposition layers 'H' will also affect the models' prediction results. However, experimental measurements do not provide the accurate values. Therefore, different values are adopted in the simulations to conduct sensitivity analysis.

Table 2. The ratio of models' prediction and STORM SR11 experimental resuspension fraction

Friction velocity (m/s)	Wichner model			Michael model			ECART model		
	$\alpha = 3$	$\alpha = 5$	$\alpha = 7$	A = 1	A = 2	A = 4	H = 1E-6	H = 1E-5	H = 5E-5
2.9	0.00	0.00	0.25	3.53	0.17	0.00	3.61	2.86	0.12
3.6	0.00	0.79	3.62	4.48	1.69	0.09	7.54	6.69	1.65
4.3	0.00	1.06	2.20	1.97	1.03	0.39	2.99	2.77	1.14
4.9	0.22	1.09	1.73	1.40	0.87	0.45	2.02	1.93	1.11
5.4	0.39	1.07	1.44	1.15	0.80	0.49	1.57	1.53	1.14
6.1	0.52	1.02	1.21	1.00	0.76	0.53	1.22	1.19	0.91

Table 2 shows the comparison between the Wichner model's predictions and STORM SR11 experiment measurements [5]. The prediction results agree well with experimental results when 'α' values 5. Comparing the model's prediction results when 'α' takes different values, the resuspension fraction is positive proportional to 'α'. The greater the disturbing force coefficient, the greater the aerodynamic disturbing force, particles are more prone to resuspension.

Comparison between Michael force balance model's predictions and measurements for STORM SR11 experiment [5] is shown in Table 2. The prediction when 'A' takes different values is conducted to analyze the effect. The model considers the aerodynamic disturbing force equal to the sum of 0.5 times the lift force and r/A times the drag force, the larger the A, the smaller the r/A, the smaller the aerodynamic disturbing force, and the harder it is for the particles to resuspend. Overall, the prediction results satisfy experimental results better when 'A' values 2.

In ECART force balance model, the empirical coefficient about the number of deposition layers ('H') is related to the experimental conditions. Meanwhile, the prediction for STORM SR11 experiment [5] is taken when 'H' values 1E−6, 1E−5, 5E−5 to analyze the effect. As shown in Table 2, under the same friction velocity, the aerosol resuspension fraction predicted by the model decreases with the increase of 'H'. The prediction result fits well with the experimental measurement when 'H' takes 5E−5, overall. The deviation is obvious only when the friction velocity is 5.4 m/s and 6.1 m/s, which are 13.79% and 9.21%.

However, both Wichner, Michael and ECART model underestimate resuspension under low velocity disturbing airflow when the models accurately predict the resuspension under higher velocity airflow. The force driving aerosol resuspension are related to the physical properties of the disturbing airflow, the diameter of aerosol particles, and the friction velocity. When the friction velocity is low, the force to drive the resuspension calculated by these models is not enough to overcome the adhesive force. This may be related to the heterogeneity of the deposited surface in experiments. The adhesive force acting on the deposited particles is related to their state on the surface, and there exists fraction particles subjected to smaller adhesive force that can be resuspended at lower disturbing airflow velocities, as shown in Fig. 1. These three models adopt relationships can characterize the adhesive force of most particles with key parameters such as particle size and surface roughness, and ignores the adhesive force difference caused by the heterogeneity.
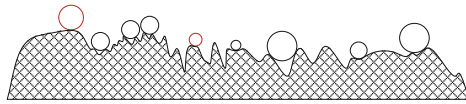
Fig. 1. Schematic diagram of particle deposition on the surface

These changes of the disturbing gas velocity and resuspension fraction with time under STROM SR11 [5] condition demonstrates most particle resuspension will complete in a very short time after the disturbing gas velocity changes in STORM SR11 experiment. Wichner and Michael force balance model are steady state model, its resuspension fraction predicted is independent of time and could reflect the rapid change of resuspension with disturbing gas velocity. However, ECART model considers the influence of time, which needs to estimate the action time of the force and consider their change with time. When obtaining resuspension fraction with ECART model, the rapid increase in resuspension fraction when the disturbing gas velocity disturbing changes suddenly could not be accurately predicted.

Figures 2, 3 and 4 shows the comparison between the measurements of ART 05 experiment [20, 21] and the prediction of Wichner, Michael and ECART force balance model respectively. The disturbing airflow's friction velocity of the ART 05 experiment ranges from 0.7 m/s to 2.9 m/s. Michael and Wichner models could not capture the resuspension of aerosols when the friction velocity is 0.7 m/s and could predict resuspension under higher velocity airflow, which is similar to the simulation of the STORM experiment. ECART model obviously overestimates the resuspension of the ART 05 experiment when the friction velocity is over 0.7 m/s. It's probably because the model

considers that the force driving the aerosol resuspension includes the burst force, which is greater than the force that hinders the aerosol resuspension under this condition. For the simulation of the ART experiment, simulation deviation of Wichner model is minimal when 'α' values 5, while the Michael model fit the experiment best when 'A' is 4. The resuspension fraction predicted by ECART model shows a drop trend with the increase of 'H' and this change is not obvious.
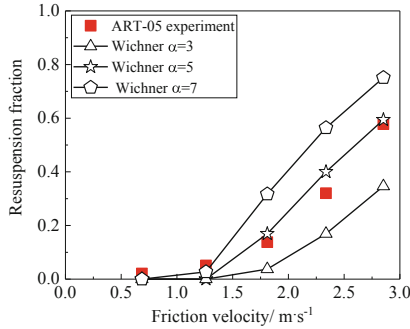
Fig. 2. Comparison between ART 05 experiment and predictions of Wichner model
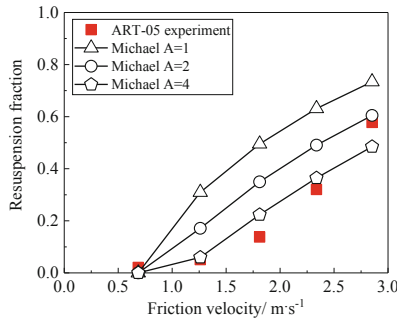
Fig. 3. Comparison between ART 05 experiment and predictions of Michael model
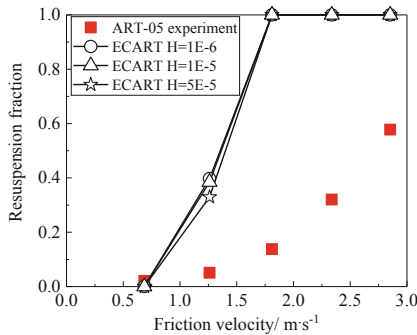
Fig. 4. Comparison between ART 05 experiment and predictions of ECART model

3.3 Discussion

Above all, it comes to summarize the comparison between these typical force balance models' simulations and selected experiments. When the coefficients take appropriate values, Wichner and Michael model are in better agreement with the experimental results.

The main difference between Wichner and Michael models is assumption about force acting on particle [10, 15]. Wichner model considers particle only contacts the deposition surface through a single point and determines whether the particles are resuspended by comparing the aerodynamic disturbing force and adhesive force in the vertical direction, as shown in Fig. 5. Michael model considers the particle is in contact with deposition surface at two points, and takes into account the forces on the particles in vertical and horizontal directions, as shown in Fig. 6.
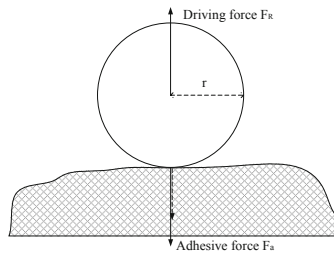
Fig. 5. Assumption about force acting on particle of Wichner model
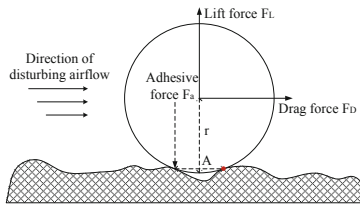
Fig. 6. Assumption about force acting on particle of Michael model

From the force assumption of the model, Michael model actually determines whether the particle could resuspend by comparing the torques. The resuspension judgment criteria of the Michael model is shown in Eq. (14), which can be expressed in the form of Eq. (15),

$$F_R = \frac{1}{2}F_L + \frac{r}{A}F_D > F_A \tag{14}$$

$$F_R \cdot A = \frac{1}{2}AF_L + rF_D > F_A \cdot A \tag{15}$$

where $0.5A$, r, A are the torque arms of lift, drag, and adhesive force respectively. The force assumption is valid only when the particle diameter is greater than 'A'. However,

according to the prediction results of Michael model, it fits well with the STORM SR11 experiment when 'A' values 2 μm, while the GMD of aerosol particles in this experiment is 0.434 μm, and diameter of most particles is less than 2 μm. Similarly, the particles' GMD in ART 05 experiment is 1.68 μm, which is smaller than the value of 'A' (4 μm) when the fit is best. Overall, by comparing and analyzing the prediction results and experiment measurements, and considering the valid condition of models, Wichner force balance model is recommended for predicting aerosol resuspension behavior during nuclear reactor severe accidents.

4 Conclusions

By comparing the experiment measurements with the predictions of the models, the applicability of Wichner, Michael and ECART force balance model to predict the resuspension phenomenon is evaluated and sensitivity analysis about the aerodynamic disturbing force coefficient, the distance between the two contact points of particle and deposited surface and empirical coefficient related to the number of deposition layers are conducted. The conclusions obtained in this paper are as follows.

When the aerodynamic disturbing force coefficient values 5, Wichner model agrees with the STORM SR11 and ART 05 experimental results, the predicted resuspension fraction is positive proportional to the coefficient. Michael model could predict STORM SR11 and ART experiments well when the distance between the two contact points values 2 μm and 4 μm separately, which is larger than most experimental particle diameters. And the assumption about force acting on particle of Michael model is not valid in the circumstance, the distance is negatively correlated with the predicted resuspension fraction. ECART model could not accurately predicted the rapid increase in resuspension fraction when the disturbing gas velocity disturbing changes suddenly of STORM SR11 experiment and overestimates the resuspension of the ART 05 experiment at friction velocity greater than 0.7 m/s when different values of the empirical coefficient related to the number of deposition layers are adopted. Wichner force balance model is recommended for predicting aerosol resuspension behavior during nuclear reactor severe accidents.

References

1. Henry, C., Minier, J.P.: Progress in particle resuspension from rough surfaces by turbulent flows. Prog. Energy Combust. Sci. **45**, 1–53 (2014)
2. Herranz, L., Ball, J., Auvinen, A., et al.: Progress in understanding key aerosol issues. Prog. Nucl. Energy **52**(1), 120–127 (2010)
3. Ardey, N., Mayinger, F.: Aerosol resuspension by highly transient containment flow-insights by means of laser optical methods. Kerntechnik-Bilingual Edition **63**, 68–75 (1998)
4. Braaten, D.: Wind tunnel experiments of large particle reentrainment-deposition and development of large particle scaling parameters. Aerosol Sci. Technol. **21**(2), 157–169 (1994)
5. Dilara, P., Krasenbrink, A., Hummel, R.: STORM TEST SR11–ISP40, deposition of SnO2 in partially insulated pipes with steam and resuspension of SnO_2 from partially insulated pipes with N2. Joint Research Centre of the European Commission, Brussels BEL (1998)

6. Reeks, M., Hall, D.: Kinetic models for particle resuspension in turbulent flows: theory and measurement. J. Aerosol Sci. **32**(1), 1–31 (2001)
7. Wright, A.L.: Primary system fission product release and transport: a state-of-the-art report to the Committee on the Safety of Nuclear Installations. Organisation for Economic Co-operation and Development-Nuclear Energy Agency, Washington USA (1994)
8. Gupta, S., Schmidt, E., Von Laufenberg, B., et al.: THAI test facility for experimental research on hydrogen and fission product behaviour in light water reactor containments. Nucl. Eng. Des. **294**, 183–201 (2015)
9. Nowack, H., Allelein, H. J.: Dry aerosol resuspension after a hydrogen deflagration in the containment. In: Nuclear Energy on New European 2007, pp. 401.1–401.8 (2007)
10. Young, M.F.: Liftoff Model for MELCOR. Sandia National Laboratories, Albuquerque USA (2015)
11. Stempniewicz, M., Komen, E., With, A.: Model of particle resuspension in turbulent flows. Nucl. Eng. Des. **238**(11), 2943–2959 (2008)
12. Reeks, M., Reed, J., Hall, D.: On the resuspension of small particles by a turbulent flow. J. Phys. D-applied Phys. **21**, 574–589 (1988)
13. Vainshtein, P., Ziskind, G., Fichman, M., et al.: Kinetic model of particle resuspension by drag force. Phys. Rev. Lett. **78**(3), 551–554 (1997)
14. Nasr, B., Dhaniyala, S., Ahmadi, G., et al.: Developments in Surface Contamination and Cleaning: Types of Contamination and Contamination Resources, 1st edn. William Andrew Publishing, Oxford (2017)
15. Humphries, L., Beeny, B., Gelbard, F., et al.: MELCOR Computer Code Manuals, vol. 2. Reference Manual. Version 2.2.9541. Sandia National Laboratories, Albuquerque USA (2017)
16. Morandi, S., Parozzi, F., Auvinen, A.: Possible improvements of the aerosol resuspension model of ECART in the light of VTT tests. In: 8th International Aerosol Conference (2010)
17. Chatelard, P., Reinke, N., Arndt, S., et al.: ASTEC V2 severe accident integral code main features, current V2.0 modelling status, perspectives. Nucl. Eng. Des. **272**, 119–135 (2014)
18. Paci, S., Parozzi, F., Porfiri, M.T.: Validation of the ECART code for the safety analysis of fusion reactors. Fusion Eng. Des. **75**, 1243–1246 (2005)
19. Hontanon, E., De los Reyes, A., Areia Capitão, J.: The CAESAR code for aerosol resuspension in turbulent pipe flows. Assessment against the STORM experiments. J. Aerosol Sci. **31**(9), 1061–1076 (2000)
20. Biasi, L., De Los Reyes, A., Reeks, M.W., et al.: Use of a simple model for the interpretation of experimental data on particle resuspension in turbulent flows. J. Aerosol Sci. **32**(10), 1175–1200 (2001)
21. Gonfiotti, B., Paci, S.: Implementation and validation of a resuspension model in MELCOR 1.8.6 for fusion applications. Fusion Eng. Des. **122**, 64–85 (2017)

Application of BIM Technology in Nuclear Power Construction Schedule Management

Jiafu Yan[1(✉)], Yonghui Xie[2], and Zhigang Zhou[1]

[1] State Key Laboratory of Nuclear Power Safety Monitoring Technology and Equipment, Design Institute, China Nuclear Power Engineering Company, Ltd., Shenzhen 518172, Guangdong, China
`281844101@qq.com`

[2] Construction Management Division, China Nuclear Power Engineering Co., Ltd., Shenzhen, Guangdong, China

Abstract. Schedule management is one of the important contents of nuclear power project management, which often leads to the lack of theoretical system due to the lack of sufficient information support. BIM technology provides a new solution for nuclear power project schedule management, ensures the effective linkage of all levels of schedule, reduces project delay and saves construction time. Combined with the theoretical basis of BIM and the characteristics of nuclear power project schedule management, this paper summarizes the application advantages of BIM technology in nuclear power construction schedule management.

Keywords: BIM · 4D · Nuclear power construction · Schedule management

1 Introduction

In the traditional domestic nuclear power construction schedule management, the progress work is carried out according to the hierarchical classification, and each project will form its own six-level schedule plan. The preparation and control of the schedule plan often depends on the professional level and engineering experience of the personnel. The construction progress is still managed based on two-dimensional drawing information, which is not effectively combined with the actual materials, equipment, manpower and other factors, it is difficult to track and analyze the progress, and it is impossible to effectively find the potential conflicts in the schedule plan. There is a lack of integrity in dealing with the deviation of the construction schedule, and it is difficult to coordinate and manage the participants, so it is difficult to achieve the goal balance of project duration, quality and cost.

The application of BIM technology can better interact and share engineering information, and reduce the communication obstacles and information loss caused by using two-dimensional drawings as information transmission medium [1]. Secondly, after many times of live process simulation, the connection of processes can be guaranteed to the optimal plan, and the amount of manpower, materials and equipment required can be accurately calculated to ensure the minimum error between experience estimation and

actual operation, and to ensure the accuracy and schedule of the project. To ensure the rationalization of resource allocation.

2 Nuclear Power Schedule Management Process Based on BIM Technology

The construction of domestic nuclear power general contracting projects generally adopts a six-level schedule system, which is decomposed and refined layer by layer from the first level of the project to the six levels of schedule, and the next layer of the schedule needs to undertake and respond to the target requirements of the upper level of the schedule. The traditional nuclear power construction schedule management includes the loading of enterprise resource information, schedule planning, progress monitoring and early warning, etc. The nuclear power progress management process based on BIM technology increases the requirements for the model and how the schedule plan is loaded on the model, as shown in the following Fig. 1.
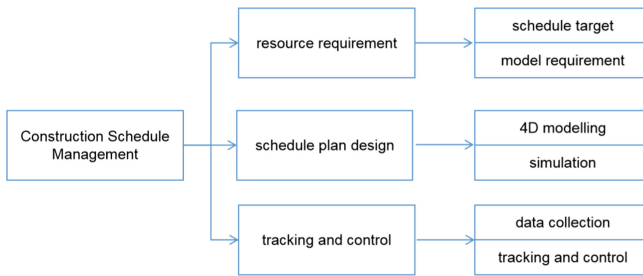
Fig. 1. Construction management process based on BIM

In the traditional construction schedule management, the loading of enterprise resource information needs to collect the data and basis for compiling the nuclear power construction schedule, and ensure the accuracy and validity of the data [2]. According to the collected resource information, the nuclear power construction activities are decomposed according to the WBS work task structure requirements, and the main objectives and activity contents of each level of progress plan are listed respectively. Determine each construction process and logical relationship according to the construction plan, and formulate a preliminary construction schedule, as shown in the following Fig. 2:

The nuclear power schedule management process based on BIM technology increases the requirements for the model and how the schedule plan is loaded on the model, and the construction schedule simulation model is generated through the correlation between the construction schedule plan and the construction drawing deepening design model. The loading of resource information also includes the standards or requirements of the construction drawing deepening design model, as well as the schedule and accuracy of each participant for the construction drawing deepening design model, and so on.
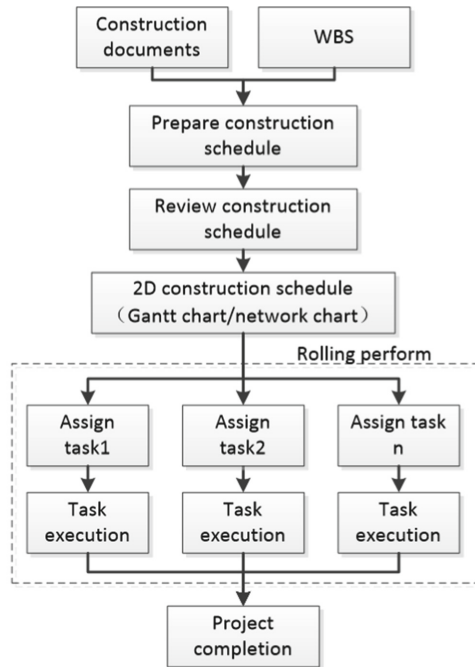
The traditional process of construction schedule management

Fig. 2. Traditional construction schedule management process

The virtual construction simulation is carried out by using the construction schedule simulation model to check whether each level of construction schedule is self-consistent, whether it meets the schedule target, whether it meets the constraints, the balance of quality and cost, and so on. If it is not met, it will be optimized and simulated repeatedly. After the optimized schedule is approved and accepted by all participants, it can be used to guide the construction of the project. This is shown in the following Fig. 3.

The construction schedule management based on BIM closely combines the project schedule with the three-dimensional visualization model, simulates the scene of the construction site in advance, corrects the problems existing in the construction process in time, and through repeated construction process simulation, the schedule plan and construction plan are the best, and the construction guidance obtained in this way is all reflected in the construction schedule model, which is simple and intuitive, and is easy for all participants to understand and implement.

Because the construction schedule management based on BIM is a virtual construction process, it is more convenient and economical than the traditional management mode, but it still needs a relatively complete BIM model. The scope and schedule of the model should be matched with the actual project. Different levels of schedule simulation can use different precision models, but the models must be consistent, which need to be considered in schedule planning.
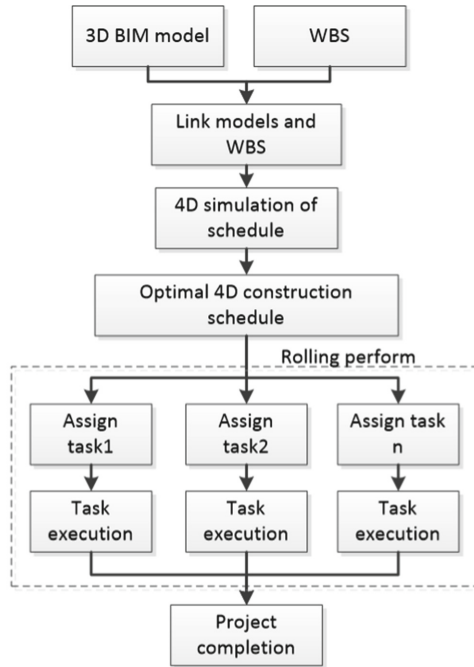
Project construction schedule management based on BIM

Fig. 3. BIM-based construction schedule management process

3   Preparation of Technical Schedule Based on BIM

In the six-level schedule system of domestic nuclear power project construction, the first three levels of progress plan are mainly to meet the milestone nodes and the interfaces and main activities with design, procurement and commissioning at all stages of the project, as well as the logical relationship and mutual constraints among various activities. The four to six levels of progress plan is to further decompose the construction activities on the basis of the first three levels of progress plan.

According to the plant, work package, elevation, region, system transfer and other professional work steps and processes are detailed, but also in six months, three months, two weeks as a cycle to develop rolling plans for tracking.

The target time limit of the subordinate progress plan shall be consistent with the superior schedule plan, and when the superior schedule plan has been adjusted, the subordinate schedule plan shall be adjusted accordingly.

The traditional construction schedule mainly includes work breakdown structure (WBS), time limit estimation method and work compilation process.

The WBS of the project is the basic work of the project planning, implementation and control. In principle, the project schedule should be compiled according to the organization of the project WBS. The complex construction process is combed and decomposed

through WBS, so as to facilitate the organization and arrangement of various construction operations, so as to constantly adjust the schedule according to the implementation of the project, and successfully achieve the project schedule management objectives.

With the introduction of BIM technology, the project WBS decomposition should include the engineering entity work and non-entity work content in the construction stage, and the BIM model is linked to the engineering entity, that is to say, when making the construction schedule according to WBS, the model should be incorporated into it.

In order to associate the model with the plan, in addition to establishing the WBS coding system of the project and the logical relationship with each WBS work package, we also need to establish a schedule model that matches this WBS, as well as the data classification of the model and the delivery standards of each phase.

To realize the schedule planning based on BIM, a perfect BIM model must be established, and at the same time, the WBS work package of the project should be associated with the BIM model components, and each work unit of the construction should correspond to the model components. Work unit schedule information, including task name, code, plan start time, plan completion time, project period and corresponding resource arrangement, can be completed in planning software such as Microsoft Project, and then work unit schedule information and model information are combined to be simulated in construction simulation software, as shown in the following Fig. 4.
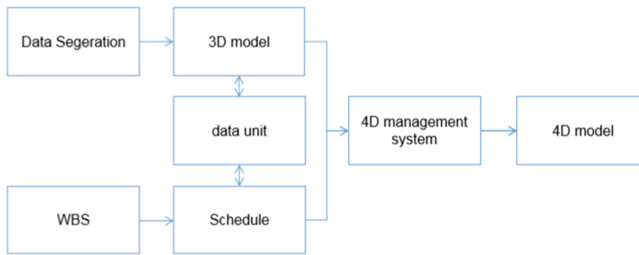
Fig. 4. Scheduling based on BIM technology

By associating the BIM model with the planned task, users are allowed to simulate the construction progress, construction process, construction scene and so on. The project team can collaborate to explore methods, solutions, and optimize results after schedule simulation. Through the visual simulation of the construction process, the construction schedule is arranged reasonably.

4 Progress Tracking and Control Based on BIM Technology

The key of progress tracking based on BIM technology is to collect and process the progress of the construction site in time, integrate the progress information, construction situation and 3D model, supervise and control the construction through 4D model, update dynamically and record the construction situation in real time [3]. The project should establish a 4D model synchronized with the construction progress, and each model component should belong to a construction work package, with work plan start time,

planned completion time, actual start time, actual completion time, the amount of work completed, the amount of resources, and so on. With the change of planning time and completion time, the system can automatically readjust and calculate, revise the target plan and update the corresponding resource data.

In the process of construction implementation, according to the actual project, the actual start time and actual completion time of each construction process need to be input in time in the 4D model, compared with the target plan, and analyzed whether the construction work is ahead of schedule or lagging behind [4]. Then carry on the follow-up schedule change adjustment to achieve the controllability of the schedule plan.

The general schedule management system will automatically check whether the progress of the schedule is in line with the compilation basis, and if it is found that it does not comply with its rules, it will enter the automatic correction and judgment procedure, and prompt the manager to continue the implementation only after the manager has made adjustments to the schedule. When the real-time progress of the automatic comparison of the schedule management information system lags behind the planned schedule, the system will actively prompt the manager whether to take rush measures according to the degree of lag, and revise the schedule plan and count the key lines. Modify the time limit and resource allocation plan, maintain continuous tracking and feedback on the implementation of the progress, and achieve dynamic management of the schedule.

5 4D Display and Application

There are two ways to associate WBS and model objects as the maturity of the BIM model advances. Under the current mode of low maturity of nuclear power BIM model, P6 and other planning software are used to compile the planning WBS structure, analyze the key duration and path, and then plan the WBS to be associated with the model object for 4D simulation and analysis. The title and custom properties of the WBS contain information that identifies the WBS, such as spatial location, such as the xx floor xx room of the xx factory building, system information, such as the 3RCV1 system, and category information, such as pipe bracket installation. The same information is contained in the name and properties of the model object, and the WBS can be automatically associated
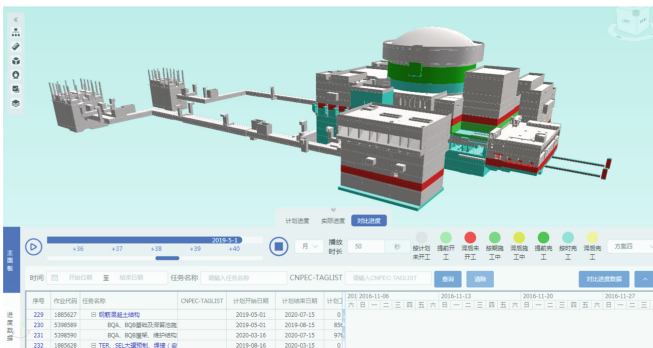
Fig. 5. 4D scheduling management platform

to the corresponding model object by configuring association rules on the platform, as shown in the following Fig. 5.

Construction schedule management using BIM technology is more and more used in nuclear power construction. Taking the construction of a factory building as an example, the schedule planning is more quantitative and intuitive after adopting BIM technology, which can make managers understand the logic between construction processes more clearly, so as to arrange resources reasonably, and can make construction personnel aware of their own work contents and improve work efficiency. It is predicted that the critical path construction period can be reduced by 10% after adopting BIM technology. After the maturity of the BIM model reaches certain conditions in the future, the WBS can be created by dividing the model objects directly in the 4D planning software, so that the WBS and the model objects are naturally associated, which will make the automation of schedule scheduling more efficient and more efficient and convenient.

6 Conclusions

It can be seen from this paper that through the 4D dynamic Analog construction technology combined with BIM platform, the whole project implementation process is modeled by scientific methods, and the dynamic Analog analysis is carried out by combining the project plan and comprehensively considering the dynamic relations among the factors such as schedule, resources and site in the construction process, which can reflect the dynamics and relevance of various factors in the construction process.

Schedule management based on BIM technology can also predict the possible problems in the process of nuclear power construction, check, compare and optimize the construction schemes, and finally maximize the overall income of the project.

References

1. Xi, Z.: Research on construction schedule management of engineering project based on BIM technology. Lanzhou Jiaotong University (2019)
2. Lu, G.: Research on the application of BIM technology in construction project schedule management, HuaZhong Keji University (2016)
3. PAS1192-2:2013: Specification for information management for the capital/delivery phase of assets using building information modeling. British Standards Institution, London (2014)
4. Weldu, Y.W., Knapp, G.M.: Automated generation of 4D building information models through spatial reasoning. Constr. Res. Congress, 612–621 (2012)

Research on Calculation Method and Additionality of Carbon Emission Reduction of Nuclear Energy Heating Based on Project Perspective

Chunhua Lu, Changle An[✉], Quantuo Sun, and Zhe Li

Shanghai Nuclear Engineering Research and Design Institute Co., Ltd., Shanghai, China
`ncepuacl@126.com`

Abstract. Nuclear energy has broad prospects for development driven by the goal of achieving peak carbon emissions and carbon neutrality, but the independent contribution of nuclear energy in low-carbon development has not obtained corresponding economic benefits. Studying the so-called "economic dilemma" problem of nuclear energy heating projects in the face of carbon trading market will reveal the influencing factors of this problem, and provide a method and paradigm reference for nuclear energy heating projects, that is, through active participation Carbon emissions trading to improve economics. This paper establishes a project-based calculation method for carbon emission reductions of nuclear energy heating, and conducts a systematic additionality analysis by taking a nuclear heating project in Shandong, China as an example. The method follows the principles of the Clean Development Mechanism (CDM) and the Chinese Certified Emission Reduction (CCER). The findings show that: (1) The carbon emission reduction of nuclear energy extraction and heating projects in Shandong region of China is about 274,100 tons/year, and its order of magnitude is highly suitable for carbon market demand. (2) The levelized heating cost of the case is about 49.20 yuan/GJ. Through the analysis of the change of coal price in the calculation parameters of the alternative scheme, it is found that the economics of the nuclear energy heating project is seriously affected by the "baseline" and the results of parameter selection. It is very easy to create the illusion that the levelized heating cost of the nuclear extraction steam heating project is higher than the "uneconomical" illusion of the alternative. (3) The empirical analysis results show that the nuclear energy heating project has the additionality of obtaining carbon emission reduction benefits, but when the economics of the nuclear energy project has no obvious disadvantage compared with the alternative, its demonstration should focus on analyzing its advanced technology, barriers to marketing. As the emission reductions of CCER projects are consumed year by year in a stagnant state, nuclear energy heating projects will have the opportunity to provide a stable supply of voluntary certified emission reductions for China's carbon market. Finally, based on this research, some suggestions are put forward, such as building a data monitoring and statistical system for carbon emission reduction of nuclear energy projects, and a pilot project for the transformation of economic benefits of carbon emission reduction in nuclear energy projects.

1 Introduction

The real impact of global climate change will be more severe than predicted, which means that the energy sector still needs major structural changes. The World Meteorological Organization (WMO) noted that the concentration of greenhouse gases in the atmosphere has neither slowed down nor declined in its 16th WMO Greenhouse Gas Bulletin. Countries must translate climate change commitments into action. The Intergovernmental Panel on Climate Change (IPCC) also holds a similar view. In its "Special Report on Global Warming of 1.5 °C", it pointed out that the past greenhouse gas reduction targets cannot effectively avoid the worst effects of climate change, which means that addressing climate change requires stronger carbon mitigation constraints and actions [1]. But pinning all hopes of tackling climate change on renewable energy would be a risky path. Some scholars have raised warnings. For example, the large-scale deployment of wind and solar power with intermittent characteristics on multiple time scales will have an incalculable impact on the existing power system architecture, and generate additional investment in power grid flexibility transformation or construction of supporting energy storage facilities [2, 3]. Climate change will also cause changes in climate variables such as wind and water vapor, resulting in increased uncertainty in the power generation potential of renewable energy sources such as wind power and solar energy [4].

In 2021, for the first time in many years, the Chinese government's work report changed its expression of nuclear power development, referring to the "active and orderly development of nuclear power". Although there has been a broad consensus on the emission reduction potential of nuclear energy and efforts to promote the deployment of nuclear energy development projects, the development of nuclear energy projects still faces many challenges. For the public, in addition to the safety factors that limit the large-scale deployment of nuclear energy, the economics of nuclear energy projects is also one of the core challenges. In addition to the inherent factors such as huge investment, high project risk cost, and long payback period, we have found an interesting phenomenon, that is, nuclear energy projects around the world have not been compensated for their environmental benefits as effectively as wind power, solar energy or even gas heating projects, but in fact carbon trading, clean fund concessional loans and other methods should also be gradually introduced.

Since nuclear power plants do not produce carbon dioxide emissions, policies that set explicit or shadow prices for carbon dioxide emissions can also affect their economic attractiveness compared with fossil fuel alternatives [5]. The difference between different energy forms puts nuclear energy projects at a disadvantage in energy market competition. Incorporating the carbon emission reduction contribution of nuclear energy projects into the carbon trading system can increase the source of income and improve the economics of nuclear energy projects, which seems to be a simple and feasible way to solve the "dilemma". However, there is no accurate measurement method for carbon

emission reduction during the operation period of nuclear energy projects. In China, the methodology to support its further development into Chinese Certified Emission Reduction (CCER) is also blank. The above situation is the real research gap.

In order to achieve the purpose of filling up the above research gap, this paper constructs a set of calculation and analysis framework for nuclear energy carbon emission reduction by sorting out the registered CCER development methodology in China. This paper also refers to the "Project Additionality Demonstration Tool" in the standard process of the Clean Development Mechanism (CDM) and CCER project development, and conducts a comparative analysis of the carbon emission reduction of nuclear energy heating projects in Shandong, China based on the alternative baseline scheme.

2   Literature Review

This study analyzes the literature in the fields of nuclear carbon emission reduction contribution, carbon emission reduction calculation method, role of additionality and demonstration method.

Nuclear energy is a clean energy source, which is generally considered to not generate CO2 during the operation period and will play a huge role in global carbon reduction efforts. This view has been widely accepted by the whole society.

Under a climate change regulatory regime that limits carbon dioxide emissions, nuclear energy is economically more attractive than fossil fuels, and nuclear energy is being favored by some environmental groups as a carbon-free energy source [5]. The recognition by governments and international organizations of the value of nuclear energy and its contribution to decarbonizing the world's energy system will encourage policymakers to explicitly include nuclear energy in their long-term energy plans and nationally determined contributions under the Paris Climate Agreement, the International Energy Agency (IEA) noted in its Global Nuclear Energy Development Report. At the same time, the EU's mid- and long-term energy strategy "Vision 2050 for an integrated energy system" also clearly states that nuclear energy and renewable energy will become the pillars of the EU's power system [6, 7], and will achieve carbon balance in 2050. However, in discussions on the eligibility of nuclear power generation for sustainable funding, the EU also stressed that the current recognition of nuclear energy's environmental and climate contribution still needs to be improved. In addition to qualitative analysis, quantitative analysis of some studies points out that nuclear energy has certain comparative advantages among many clean energy sources, which provides strong support for measuring the contribution of nuclear energy to carbon emission reduction. The research on the carbon emission coefficient of different energy forms based on the life cycle method shows that the average carbon emission of nuclear power LCA is 65 g CO_2/kWh, which is higher than that of wind power and lower than that of solar power [8]. More data support the nuclear power LCA carbon emission coefficient between 1.8–20.9gCO2/Kwh [8–10]. The greenhouse gas emission coefficient of China's nuclear power chain has been reduced from 13.71g CO2/Kwh in the mid-1990s to 11.9gCO2/Kwh, which is significantly lower than coal and other fossil energy sources, and most of them are concentrated in the nuclear power construction period [11–13]. Empirical studies in China, the United States, Japan and France show that the long-term

carbon emission coefficient of nuclear energy is lower than that of renewable energy, but current nuclear energy reduction effect in China is relatively limited compared to other countries [14].

Accurate calculation of carbon emissions/emission reductions is the basis for emission reduction policy formulation, mechanism design, and market transactions. It is particularly important to study and master calculation methods. The IPCC guidance manual provides a common method for calculating carbon emissions by multiplying activity level data by emission coefficients. This method is suitable for the compilation of national greenhouse gas inventories [15], but for specific projects, the use of default values usually leads to large deviations in the calculation results. Fine metering also includes the CO2 emission data of power plants obtained by the European Environment Agency (EEA) by monitoring the waste emissions and emission density of thermal power projects. This method requires the power plant to have complete flue gas monitoring equipment, and the cost is relatively high [16]. Chinese scholars have also conducted further research on project-based energy carbon emissions using mature methods. For example, explore modeling based on combustion mechanism analysis and statistical law to predict greenhouse gas emissions from coal-fired power plants [17]. This model is based on the analysis of the influencing factors of CO2 emission factors, and the calculation of comprehensive emission factors considering fuel combustion and process factors [18] However, in order to meet the balance between the actual measurement cost and the calculation accuracy, it is still practical to use the emission factor measurement method [19].

In order to deal with the problem of global warming, IPCC has led the development of calculation methods for emission reductions of CDM projects. The method development must explain basic issues such as project scope, emission sources, and baselines. Among them, the baseline directly determines the carbon reduction and environmental benefits of CDM projects [20]. Before China suspended the methodological review and project approval of the CCER project in 2017, as many as 200 corresponding CDM methodologies had been translated and transformed. In fact, most of China's current carbon emission reduction calculation standards are also derived from the project development methodology under the CDM mechanism. During the pilot period, the methods and principles in the calculation regulations for carbon emissions/emission reductions in each regional market are basically the same. They are all based on the emission factor method, the material balance method and the actual measurement method. The main difference is the selection of some default values [21].

Scholars at home and abroad have conducted in-depth research on the role of additionality, the method of demonstration and its effectiveness. Additionality determines the supply and quality of offset credits in the carbon market [22], which is essential for the environmental integrity of offset mechanisms and clean development mechanisms [23]. The most common way to demonstrate additionality is through barrier analysis and investment analysis. This means that if the project is not registered as a CDM activity, there are obstacles to its realization and the proposed project is less financially attractive than at least one other credible alternative. Finally, consider whether the proposed project type has been widely deployed in the relevant department or region through practical analysis [24]. Most views hold that the emission reduction mechanism based

on additionality is generally effective or at least in the progress of being perfected, and can achieve greenhouse gas emission reduction [25, 26], but attention should be paid to the problems in the development process [27]. The technical and economic evaluation of wind power, hydropower and other projects that do not consider CDM benefits finds that their internal rate of return is high and the possibility of additionality is low. Similar results provide evidence for this view [28]. In addition to the shortcomings of the rules, additionality descriptions and assessment tools also have problems such as overly complex assessment procedures [29]. In the process of project methodology, additionality is also an important issue to be discussed. The methodology development research in China's energy field has covered wind power, hydropower and other clean energy forms.

Through literature analysis, we found that the current research in the field of nuclear carbon emission reduction focuses on the macro-level such as industry and industry, which also verifies the realistic dilemma mentioned in the introduction of this study. In addition, the results of literature analysis help us determine the calculation method of carbon emission reduction of nuclear energy projects, and clarify the importance and method of additionality demonstration of nuclear energy projects.

3   Methodology

This chapter uses CDM methodology, EU carbon Emission reduction Trading system and carbon emission reduction quantification methods in China's voluntary emission reduction methodology to calculate carbon emission reduction. According to GB/T33760-2017 "Based on General Requirements for Technical Specifications for Assessment of Greenhouse Gas Emission Reductions of Projects" and GB/T32150-2015 "General Rules for Accounting and Reporting of Greenhouse Gas Emissions of Industrial Enterprises", this chapter studies the boundary range, emission source identification, baseline, emission factor, and activity level data of the calculation method of carbon emission reduction of nuclear energy projects.

3.1   Nuclear Energy Carbon Emission Reduction Calculation Method

The calculation method of carbon emission reduction of nuclear energy projects adheres to the following basic principles: (1) Select appropriate GHG emission sources, data and methods. (2) Include all greenhouse gas emissions adapted to the project needs. (3) Adopt the same criteria, procedures and calculation period. (4) Minimize uncertainty and deviation. (5) Release fully transparent information in accordance with national policies and trade secrets ensuring that assumptions, values and methods used do not overestimate emission reductions.

The evaluation procedure that should be adhered to for project-based carbon emission reduction calculations is shown in the Fig. 1.

3.1.1   Determine the Type of Accounting Gas

The types of GHGs to be assessed should be determined according to project needs. Combined with the current focus of carbon market trading, nuclear energy projects should focus on calculating CO_2, but should not ignore CH_4, N_2O, fluoride, etc. that may exist in the production process of the project.
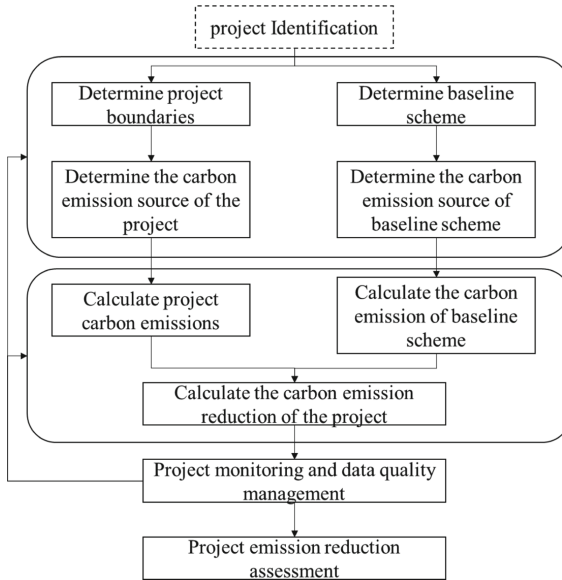
Fig. 1. Project based carbon emission reduction assessment procedure

3.1.2   Determine Project Boundaries

The project boundary refers to the spatial extent covered by project activities and emissions-related matters in the baseline scenario. It includes the considered emissions from all sources of greenhouse gases that are within the control of project participants and that are appreciable and reasonably attributable to the project. Since the scope of production activities of a nuclear energy project is relatively clear, the boundary of a nuclear energy project should include project-related equipment, facilities (systems) or organizations that are affected by the project. The emission source of the project points to the physical unit or process that emits greenhouse gases into the atmosphere. The nuclear energy project should identify the emission source separately according to Table 1, and should not be omitted due to the actual calculation process.

3.1.3   Determine Baseline Scheme

Different types of projects should choose different baseline Schemes. For new projects, the baseline Schemes should be based on the mainstream technologies adopted in the industry or in the region or the technologies required by national policies. For reconstruction and expansion projects, the baseline Schemes should be determined according to the needs of target users, which can be compared with the technology before reconstruction or with reference to new projects. The emission source of the baseline shall be identified according to the method of GB/T 32150 or by referring to other related methods. The argument for additionality is relative to the baseline of alternatives. Common central heating methods in northern China include: coal-fired thermal power plants,

Table 1. Potential carbon emission sources of nuclear energy projects

Accounting entries	Type of greenhouse gas source	Emission source	Gas species	Note
Fuel combustion emissions	Fixed source	All kinds of boilers and gas turbines	CO_2	Daily
	Mobile source	Transport vehicles	CO_2	Daily
Process emissions	The production process	Main process system	-	The designers believe there are no greenhouse gas emissions
	Waste treatment and disposal process	Waste gas and waste water treatment system	-	The designers believe there are no greenhouse gas emissions
	The dissipation process	Voltage converter	SF_6	Studies show that there may be gas leakage in the high voltage transformer, about 15%
Emissions from outsourced electricity and heat	Consumption sources of power, heat and steam input from outside the main body of the project	All kinds of motor, pump, fan, voltage converter, lighting equipment	CO_2 SF_6	-

coal-fired boiler rooms, gas-fired thermal power plants, gas-fired boiler rooms, gas-fired distributed cooling, heating and power supply stations and other heating sources [30].

3.1.4 Carbon Emission Reduction Calculation Method

According to the project, the emissions of each greenhouse gas in each greenhouse gas source under the project and baseline scenarios in a certain period are calculated respectively, and the project emissions and baseline emissions are obtained by summarizing. The emission factor calculation method is adopted, and the general formula is shown in (1)–(2):

$$ER = BE - PE - LE \tag{1}$$

where: *ER* refers to project emission reduction, *BE* refers to baseline emissions, *PE* refers to project emissions, and *LE* refers to emissions caused by gas leakage during project operation. The units are all tons of carbon dioxide (tCO_2).

The baseline emissions, project emissions and leakage emissions can all be calculated by multiplying activity level data and corresponding emission factors. As shown in formula (2):

$$E = AD \times EF \times GWP \tag{2}$$

where: E refers to baseline emissions, project emissions or leakage emissions. Units are tons of carbon dioxide equivalent (tCO2e). AD refers to activity level data, determined according to the emission source. EF is the emission factor matching the activity level data. GWP is the greenhouse gas potential value, which should refer to the data provided by the IPCC.

For nuclear energy heating projects, whether it is a small reactor heating mode or an extraction heating mode relying on large-scale nuclear power, the loss of heat transmission should be considered.

$$BE = HS_{BL} \times EF_{CO2}/\eta_L \tag{3}$$

$$HS_{BL} = HS_{PJ} - LOSS_{PJ} + LOSS_{BL} \tag{4}$$

where: HS_{BL} refers to the heat supply of the baseline scheme. HS_{PJ} refers to the heat supply of the project. $LOSS_{BL}$ refers to the heat loss of the heat transfer link of the baseline scheme. $LOSS_{PJ}$ refers to the loss of the heat transfer link of the project Heat. EF_{CO2} refers to the heating carbon dioxide emission factor of the baseline scheme. This variable is obtained by converting the carbon dioxide emission factor per unit of standard coal and the conversion coefficient of standard coal per unit of heat. η_L refers to the net thermal efficiency of the coal-fired boiler.

For nuclear energy heating projects in the small reactor heating mode, since electricity is purchased from outside in the operation process, it is necessary to take into account the carbon emissions caused by the additional electricity consumption of the project. At the same time, it also adheres to the principle of conservatively estimating emission reductions. In addition, the project considers carbon emissions from sporadic fossil fuel use during the operating period.

$$PE = PE_{EC} + PE_{FF} \tag{5}$$

$$PE_{EC} = EC \times EF_{PE} \tag{6}$$

Among them: PE_{EC} refers to the carbon emissions caused by the project's additional electricity consumption. PE_{FF} refers to the carbon emissions caused by the project's direct use of fossil fuels. EC is the annual extra power consumption of the project, and EF_{PE} is the average power emission factor of the power grid where the project is located.

3.2 Key Points of Nuclear Additionality Demonstration

3.2.1 Investment Analysis

After identifying the baseline scheme, the project applicant should screen out at least one suitable alternative and make an investment analysis. The so-called investment analysis is

to prove that the proposed project, in the absence of CER income: (1) is not economically or financially optimal; (2) is not economically or financially feasible. If the proposed project, without CER revenue, emits less GHGs, but because the economic benefits are not optimal, the investor will choose an alternative with higher emissions but higher economic benefits.

Common methods include: (1) simple cost analysis, which is used for projects that will not generate any income; (2) comparative investment analysis, which is used for projects that will generate income, usually it is necessary to select a certain economic indicator and the alternative selected in the first step. For nuclear energy projects, optional indicators include internal rate of return, net present value, levelized kWh (heating) cost, etc.; (3) Baseline analysis, which is also used for projects that generate income, but requires Note that this baseline analysis is not related to the baseline in 3.1.3. It refers to selecting a specific indicator to compare with a baseline. Optional indicators include return on capital, long-term loan interest rates, and officially released investment decision indicators. Etc., nuclear energy projects can choose the average yield of the power industry as the baseline. Therefore, when conducting investment analysis of nuclear energy projects, it is not necessary to strictly demonstrate its economic infeasibility, but only to prove that it is not the optimal choice economically.

3.2.2   Barrier Analysis

This step can be skipped if it has been demonstrated in the investment analysis that the proposed project is not "economically or financially optimal" or "economically or financially infeasible". However, if similar results cannot be obtained, a barrier analysis method must be used to demonstrate that (1) the proposed project cannot be implemented due to some barriers; and (2) the barriers do not affect at least one of the alternatives. In other words, although the proposed project is economically optimal (or feasible), it is not feasible for other reasons, and at least one alternative is not affected by those reasons.

The so-called "barriers" include (1) other investment barriers other than the economic/financial barriers in the second step (e.g. the proposed project does not allow any private capital entry by law); (2) technical barriers (e.g. the ability to operate and maintain Technicians for this project cannot be found in the proposed project implementation area/adjacent areas, thus creating obstacles to the operation and management of the project).

To sum up, if a nuclear energy project is economically feasible, it is difficult to advance the project due to obvious obstacles such as public safety concerns, technical verification of the first reactor, demonstration construction, and scientific research purposes, and even there are laws that strictly restrict the entry of private capital into a nuclear energy project. At the same time, in the case of encouraging investment in other clean energy fields such as wind power and photovoltaics, it is a feasible option to focus on the additionality argument on the analysis of obstacles.

3.2.3   Universal Analysis

Generality analysis is usually used as a supplementary verification after the preceding arguments have been completed. Including: (1) Analysis of whether there are similar

projects for the proposed project; (2) Analysis of the difference between similar projects and the proposed project. To be considered similar, two projects need to meet the following conditions: (1) are located in the same country or region and/or rely on similar science and technology; (2) have a similar scale; (3) have a similar legal environment, Investment climate, available technologies, size of capital, etc. For nuclear energy projects, its technical specificity determines that there are no other forms of energy similar to it. Therefore, the universal analysis of nuclear energy projects will not be a hindrance to project applications.

From the analysis of the additionality demonstration methods combined with the characteristics of nuclear energy projects, it shows that the focus and path of additionality demonstration of nuclear energy projects of different types, stages and application scenarios are also different. The actual case finds the argumentation method that suits its own demands.

4   Emprical Results and Analysis

4.1   Case Study Regions and Data Sources

Haiyang Nuclear Energy Pumping and Heating Project is located in Haiyang, Shandong Province, relying on Haiyang Nuclear Power Unit No. 1. The main technical feature is the intermediate stage extraction of conventional island steam turbines of nuclear power units. Public information shows that after the project is put into operation, the heating area of the second phase of the project is 4.5 million m^2, and 100,000 t of raw coal can be saved in each heating season, reducing the heat emission to the environment by 1.3 million GJ. The average heating index in this area is 45 W/m^2.

The case project data are all taken from the approved project feasibility study report. Through the project feasibility study report, environmental impact assessment report and other documents, it is confirmed that the implementation of this project can contribute to local sustainable development in terms of reducing greenhouse gas emissions and reducing pollutant emissions.

The power system emission factor is taken from the baseline emission factor of China's regional power grid of the emission reduction project in 2019.

4.2   Carbon Emission Reduction Calculation Results

The type of greenhouse gas calculated by the project is CO2. The project boundary is the nuclear energy extraction heating production boundary and all users connected to the heating pipe network. The project has no fossil energy combustion emission sources, and the electricity required for its production can be supplied by the Haiyang Nuclear Power Station, and there is no externally purchased electricity emission source. The waste treatment process is not considered as a process emission source due to lack of monitoring data. Therefore, the project has no emission sources as a whole.

Baseline options (Table 2) are identified based on the heating services available in the Shandong region where the project is located, capable of providing the same level of heating as the proposed nuclear energy project activity.

For the nuclear extraction heating project, the coal-fired boiler is the most convenient way to realize central heating in combination with the resource endowment and economic development level of the project location and Shandong region. Therefore, the alternative scheme for the nuclear heating project is proposed as follows:

(1) Implement the project activities without the benefit of emission reduction;
(2) The project activities that provide the same heating capacity by means of centralized heating with coal-fired boilers.

The annual assumed carbon emission reduction calculation results of the nuclear heating project are shown in Table 3. From the calculation results, it can be seen that the estimated value of annual carbon emission reduction is about 274100 tons of CO2. Since many default values are used in the calculation, the accuracy of the results needs to be further improved. In addition, compared with the publicly reported data of 180000 tons of emission reduction, the comparative analysis shows that the potential error factor is the net thermal efficiency of fossil fuel boilers. The value calculated in this study is conservative, and the publicly reported data may not consider the impact of this factor.

4.3 Carbon Emission Reduction Calculation Results

On the basis of identifying the baseline scheme, the economic attractiveness between the nuclear heating project and the alternative scheme is compared with the investment comparison analysis method given in the CDM project joint tool for baseline identification and additionality demonstration (v05.0.0). The commonly used levelized heating cost is selected as the financial index, which is derived from the "Projected Costs of Generating Electricity, 2020 Edition" published by the International Energy Agency.

The formula for calculating the cost of standardized heating is as follows:

$$LCOH = \sum_t \frac{I_t + M_t + F_t}{(1+r)^t} / \sum_t \frac{H_t}{(1+r)^t} \tag{7}$$

where: $LCOH$ refers to the levelized heating cost (yuan/GJ). I_t is the investment amount in the year t. M_t is the operating cost in the year t. M_t F_t is the fuel cost in the year t. H_t is the total amount of heat supply in year t. r is the discount rate.

Table 4 shows the main calculation parameters and results of levelized heating cost for nuclear extraction heating and coal-fired boiler heating. When the internal rate of return is required to be 8%, the levelized heating cost of the proposed project is 49.20 yuan/gj, which is slightly higher than that of the alternative scheme, which is 47.86 yuan/gj. Only from the cost point of view, the project needs to expand revenue channels to make up for the cost disadvantage. Therefore, since the construction of the project has good demonstration benefits for nuclear heating and emission reduction, carbon emission reduction benefits or subsidies can be obtained. This is consistent with the statement in the project feasibility study report.

In terms of Barrier Analysis, nuclear heating technology is advanced and faces technical and investment risks, and has not been commercialized in China. At the same time, the project complies with the requirements of current laws and regulations, and

Table 2. Potential baseline alternatives for nuclear extraction heating

Potential Baseline Alternatives		Analysis conclusion
1. Implement the project activities without the benefit of emission reductions		Feasible
2. Access to the heating system connected to the main network		The project feasibility study report indicates that there is no large-scale heating system in the target area
3. Connect to local heating network (in operation / newly built) to provide heat	Coal fired boiler	Feasible
	Gas fired boiler	The heating cost is much higher than that of coal-fired boilers, and the acceptance of residents is poor
	Oil fired boiler	
	Scattered small thermal power plants	There is no thermal power plant in the project area, and relevant policies do not allow the construction of scattered small thermal power plants
	Renewable energy	The area has not been popularized, the cost is high, and the residents' acceptance is poor
4. Continue to use or build a separate heating scheme	Single family coal fired boiler	New bulk coal burning stoves are being phased out in northern China
	Single family gas stove	The cost is much higher than that of coal-fired boilers, and the residents' acceptance is poor
	Single family oil stove	
	Electric energy	There are coal-fired boilers for central heating in the project area, which do not meet the conditions of "coal to electricity"
	Single household renewable energy	The area has not been popularized, the cost is high, and the residents' acceptance is poor

is not an object of enforcement by existing laws and regulations. Nuclear energy heating projects are not included in any policies and regulations that are conducive to the development of clean energy, such as subsidies, tax reductions, concessions, and quota systems. Therefore, it can be considered that there are certain obstacles in the project.

Table 3. Annual carbon emission reduction of nuclear energy extraction heating project

NO	Paraphrase	Value	Unit	Basis
1	Emission reduction (ER)	27.41	10k tCO$_2$	2-3-4
2	Baseline Emissions (BE)	27.41	10k tCO$_2$	2.1 × 2.2/2.3
2.1	Base line scheme heating capacity (HS$_{BL}$)	188.35	10k GJ/Year	2.1.1-2.1.2 + 2.1.3
2.1.1	Heat produced by nuclear Heating Projects (HS)	188.35	10k GJ/Year	According to public information, the calculation of heat load is obtained. Design heat load index 44.04 W/m2, heating season 110 days, an area of 4.5 million m^2
2.1.2	Heat loss from baseline scheme (LOSS$_{PJ}$)	0	10k GJ/Year	Based on the calculation of monitoring statistics, the heat loss of distribution network segment accounts for about 1.5% of the total heat production for the convenience of 0
2.1.3	Heat loss from baseline schemes (LOSS$_{BL}$)	0	10k GJ/Year	Collated according to public information
2.2	Carbon dioxide emission factor of base line scheme heating capacity (EF$_{CO2}$)	0.0946	tCO$_2$/GJ	2.2.1 × 44/12, The default oxidation value is 1
2.2.1	Carbon content of fuel used for base-line power generation (EF$_{coal}$)	25.8	kgCO$_2$/GJ	IPCC2006 Standard coal is classified as typical coal
2.3	Net thermal efficiency of fossil fuel boilers (η$_L$)	65	%	Default value, 2010 (in operation) efficiency of coal-fired industrial boilers, China Medium and Long Term Energy Conservation Plan, November 25, 2004, National Development and Reform Commission
3	Project emissions (PE)	0	tCO2	Monitoring statistics, none yet
4	Leakage emission (LE)	0	tCO$_2$	Monitoring statistics, none yet

For Universal Analysis, we refer to the CCER "Guidelines for Universal Analysis (v3.1)" to identify geographic scope, scale, technology, fuel source and project attributes one by one. The project is located within the geographical scope of Shandong Province, with a thermal load scale of 31.5MW. It is a nuclear energy heating project that utilizes gas extraction from the steam turbine of a nuclear power plant. After on-site investigation

and online inquiry, there is no heating project with similar scale and the same technology and fuel source within the geographical scope of the project. Therefore, this project is not universally implemented in Shandong Province and is not universal.

Table 4. Investment analysis of nuclear heating projects and alternatives

Parameter	Scheme 1 (Nuclear heating projects)	Scheme 2 (Coal fired boiler for central heating)	Value description
I_t (10k Yuan)	3479.00	1260.00	The data of Scheme 1 is taken from the project feasibility study report. The data of Scheme 2 is calculated according to the literature [31], and the heating investment per unit area is 18 yuan/m2
M_t (10k Yuan)	995.30	1168.49	The data of Scheme 1 are obtained from the feasibility study report of the project, and the data of Scheme 2 are calculated according to the literature [32]. The annual operating cost is 1669.24 yuan/year/household, and the average household area is 100m2
F_t (10k Yuan)	0	925.00	The data of Scheme 1 are taken from the feasibility study report of the project. There is no fossil fuel consumption in the thermal production of nuclear heating. According to the research data, the coal price is 609 yuan/ton, which is the integrated standard coal price of the thermal power plant in the neighboring area from January to April

(*continued*)

Table 4. (*continued*)

Parameter	Scheme 1 (Nuclear heating projects)	Scheme 2 (Coal fired boiler for central heating)	Value description
H_t (10k Yuan)	26.9	26.9	Project feasibility study report
r (%)	8	8	"Construction project economic evaluation method and Parameters (third edition)" heating industry standard
$LCOH$ (Yuan/GJ)	49.20	47.86	-

5   Conclusions

The calculation framework of carbon emission reduction of nuclear energy projects established by this research reveals that the accurate calculation of carbon emission reduction of nuclear energy projects is feasible from the calculation logic and method, and there is no particularity in the design and parameter selection of calculation methods and verification methods. At the same time, through the comparative analysis of the levelized heating cost in the additionality demonstration, it is preliminarily verified that when the coal price is about 650 yuan/t, the economics of the nuclear energy heating project in Shandong is not significant, and the carbon emission reduction brought by nuclear energy heating The so-called inadequacy of "economics" will be further improved. In fact, the "economics" of nuclear energy heating projects is seriously affected by the "baseline" and the results of parameter selection. In addition, this also provides a method and paradigm reference for nuclear-armed countries around the world to explore the economic improvement path of nuclear energy projects.

Through the analysis of the carbon emission reduction calculation method and the results of the case study, the specific conclusions can be drawn as follows:

(1) The carbon emission reduction of the nuclear energy extraction and heating project in the case study is about 274,100 t, which is in the order of magnitude as the emission reduction of large-scale emission reduction projects in the market. From the perspective of the project, the market adaptation of the nuclear energy extraction and heating project higher degree. However, the emission reduction of a single unit of nuclear power projects generally reaches millions of tons of CO2, which is much higher than that of nuclear energy heating projects.

(2) The carbon emission reduction of nuclear energy projects is affected by factors such as regional energy consumption structure, application scenarios, and project scale. Among these factors, the regional energy consumption structure determines the value of the grid emission factor, which has a fundamental impact on the emission reduction of the project. For example, the carbon emission factors of power grids in North China and Northeast China are relatively large because of the high proportion

of fossil energy in the power grid energy structure in these regions. This makes the potential carbon emission reduction benefits of deploying nuclear energy projects in the above regions even greater. This idea also provides another strong support for the deployment of nuclear energy projects in northern and inland regions.

(3) In the case study, the levelized heating cost of the nuclear steam extraction heating project is slightly higher than that of the alternative, which creates an illusion. When we increase the coal price by 100 yuan/t, the *LCOH* of the alternative scheme becomes 52.99 yuan/t. At this time, the nuclear energy extraction steam heating project is more economical. Therefore, the carbon emission reduction calculation and additionality demonstration of nuclear energy projects should carefully select the baseline. This suggests that our nuclear energy projects will give full play to their advantages in the energy situation with high coal prices. When there is no obvious disadvantage in the economics of nuclear energy projects compared with other alternatives, the demonstration of the additionality of nuclear energy projects should focus on analyzing the obstacles such as technological advancement and market promotion.

In China, the CCER mechanism is currently in a stagnant state, but during the research process, we found that the expectation of the restart of the CCER market is becoming clearer. In the future, the development of project-based carbon emission reduction calculation methods should show a trend of broader application fields and more accurate parameters. In order to promote the incorporation of nuclear energy projects into the carbon emission reduction market mechanism, it is also necessary to proceed from the perspective of engineering practice. The first task is to fully learn from mature experience and conduct research on project-based carbon emission reduction measurement methods. In fact, as the emission reductions of CCER projects are consumed year by year in a stagnant state, and new energy projects such as wind power and photovoltaics gradually achieve grid parity, nuclear energy heating projects will have the opportunity to provide stable voluntary certified emission reductions for China's carbon market supply.

Finally, the prospect of further research is proposed:

(1) In order to meet the data accuracy requirements of emission reduction project development, nuclear energy projects should establish a perfect data monitoring and statistical system, and optimize the calculation parameters through field research.

(2) Promote the transformation of economic benefits of carbon emission reduction of nuclear energy projects, and select projects with appropriate emission reduction scale and high urgency for economic improvement to carry out pilot projects.

(3) In the face of a wider range of nuclear energy applications, it is necessary to do reserve research on the calculation method of nuclear energy carbon emission reduction based on the project caliber in more scenarios.

References

1. IPCC: SPECIAL REPORT: Global Warming of 1.5 °C (2018)

2. Bo, Z., Kankan, B., Zhicheng, X., Youbing, Z.: Optimal sizing for grid-connected PV-and-storage microgrid considering demand response. Proc. CSEE **35**, 10 (2015)
3. Chang, L., et al.: A review on the utilization of energy storage system for the flexible and safe operation of renewable energy microgrids. Proc. CSEE **40**, 19 (2020)
4. Schaeffera, R., et al.: Energy sector vulnerability to climate change: a review. Energy **38**, 12 (2012)
5. Joskow, P.L., Parsons, J.E.: The economic future of nuclear power. Daedalus **138**(4), 45–59 (2009)
6. Rinaldi, R., et al.: ETIP-SNET vision 2050–integrating smart networks for the energy transition. In: 25th International Conference and Exhibition on Electricity Distribution, CIRED 2019, p. 0175 (2019)
7. Zhiqin, Z.: The future trend of EU energy policy. Global Technol. Econ. Outlook **30**, 7 (2015)
8. Lenzen, M.: Consumer and producer environmental responsibility: a reply. Ecol. Econ. **66**(2–3), 547–550 (2008)
9. Tokimatsu, K., et al.: Energy analysis and carbon dioxide emission of Tokamak fusion power reactors **48**(3–4), 483–498 (2000)
10. Voorspools, K.R., Brouwers, E.A., D'haeseleer, W.D.: Energy content and indirect greenhouse gas emissions embedded in 'emission-free' power plants: results for the low countries **67**(3), 307–330 (2000)
11. Ziying, J., Ziqiang, P., Jiang, X.: Life-cycle greenhouse gas emissions of China's nuclear power energy chain. China Environ. Sci. **35**, 9 (2015)
12. Zhonghai, M., Ziqiang, P., Jianlun, X.: Life-cycle greenhouse gas emissions of China's nuclear power energy chain. Radiat. Prot. **21**, 6 (2001)
13. Zhonghai, M.: Comparative evaluation of greenhouse gas emission coefficients of main energy sources. China Institute of Atomic Energy, Beijing (2002)
14. Minmin, Z.: Nuclear energy, renewable energy and low-carbon growth: an empirical comparison from China, the United States, France and Japan, Dalian University of Technology, Dalian (2017)
15. Bofeng, C., Songli, Z., Shengmin, Y.: Interpretation of "IPCC 2006 national greenhouse gas inventory guidelines 2019 revised edition." Environ. Eng. **8**, 1–11 (2019)
16. Rui, L., Xiangbin, Z.: Calculation and analysis of carbon emissions from coal-fired power plants in China. J. Ecol. Environ. **7**, 9 (2014)
17. Huanzhang, L., Taihua, C., Jizhen, L.: Calculation of greenhouse gas emissions from power plant boilers. Therm. Power Eng. **6**, 665–668 (2007)
18. Xiaowei, W., Fahua, Z., Jintian, Y.: Calculation of greenhouse gas emission factors in thermal power generation industry. Environ. Sci. Res. **2**, 6 (2010)
19. Xin, W., Xiaowei, W., Ying, H.: Research on calculation method of main gaseous pollutant emissions in thermal power industry. Environ. Monit. Manag. Technol. **6**, 4 (2010)
20. Bing, H., Lianlian, A.: CDM baseline determination method based on combustion theory. China Electr. Power **8**, 58–60 (2009)
21. Jiren, Z., Zhihui, J., Hui, Z.: Comparative analysis of carbon emission accounting methods in chemical industry in my country's carbon trading pilot areas. Environ. Sustain. Dev. **2**, 31–36 (2018)
22. Gillenwater, M.: Redefining RECs—Part 1: untangling attributes and offsets. Energy Policy **36**, 2109–2119 (2008)
23. Paulsson, E.: A review of the CDM literature: from fine-tuning to critical scrutiny? Int. Environ. Agreements Law Econ. **9**, 63–80 (2009)
24. Schneider, L.: Assessing the additionality of CDM projects: practical experiences and lessons learned. Clim. Policy **9**, 242–254 (2009)
25. Barrera, J., Schwarze, R.: Does the CDM contribute to sustainable development? Evidence from the AIJ Pilot Phase **7**(4), 353–368 (2004)

26. Timilsina, G.R., Shrestha, R.M.: General equilibrium effects of a supply side GHG mitigation option under the clean development mechanism **80**(4), 327–341 (2006)
27. De-shun, L.: Introduction to CDM project development both abroad and in china and analysis to its typical cases. China Water Power Electrification **69**, 15–23 (2010)
28. Alexeew, J., et al.: An analysis of the relationship between the additionality of CDM projects and their contribution to sustainable development **10**(3), 233–248 (2010)
29. Mendis, M., Openshaw, K.: The clean development mechanism: making it operational. Environ. Dev. Sustain. **6**(1), 183–211 (2004)
30. Kang, H., Sun, B., Li, R.: Probe into the problem of clean heating in China. Energy China **39**, 7–10 (2017)
31. Jitai, Z.: Economic and technical analysis on heating and air conditioning modes of urban residences in northern China. Presented at the Excellent Papers of Shandong Architectural Society in 2005, Shandong (2005)
32. Jinlu, F.: Economic evaluation of clean heating technology based on user's affordability. Coal Econ. Res. **39**, 39–44 (2019)

Effect of β-Phase Heat Treatment
on Microstructure of Zr-Sn-Nb-Fe Alloy

Yiran Cui, Zhongbo Yang[✉], Wei Zhang, and Hong Liu

National Key Laboratory for Nuclear Fuel and Material, Nuclear Power Institute of China,
Chengdu 610213, China
yangzhongb@mails.ucas.ac.cn

Abstract. Zirconium alloys are extensively used in nuclear fuel element cladding tube, guide tube and positioning spacer grid and other reactor core structural materials because of their excellent nuclear properties. The preparation of these profiles includes ingot forging, β-phase heat treatment, hot and cold deformation processing and other processes. Among them, The β-phase heat treatment process significantly affects the microstructure and processability of zirconium alloys forging billets. OM, SEM and TEM were used to study the microstructure of Zr-0.85Sn-1Nb-0.3Fe alloy forging ingot samples after β-phase heat treatment at (950–1150 °C)/(15 min–2 h), and water quenching. The results indicated that under different heat treatment conditions, typical acicular shape martensitic microstructure appears in Zr-Sn-Nb-Fe alloy after water quenching. The size of martensitic laths increased with the extension of holding time, which showed that the length and width of the small part of the acicular martensite away from the forging plane both increased significantly; on this basis, the effects of β-phase heat treatment temperature and holding time on the phase transformation behavior of the alloy were analyzed.

Keywords: Nuclear reactor · Core structural material · Zr-Sn-Nb-Fe alloy · β-phase heat treatment · Microstructure

1 Introduction

Zirconium alloys, because of their low thermal neutron absorption cross-section, excellent mechanical behavior under high temperature, and corrosion resistance, are extensively used as fuel cladding, pressure tube, fuel assembly spacer grids, and other structural materials in nuclear reactors, which are also the only material used as fuel cladding in PWRs at present. Compared with the Zr-Sn (Zr-2, Zr-4) and Zr-Nb (E110, M5) alloys developed in the last century, Zr-Sn-Nb alloys have gradually become one of the important directions in the research and development of new zirconium alloys under the requirements of high fuel consumption and long life of fuel assemblies, such as ZIRLO in the United States, E635 in Russia, M-MDA in Japan, HANA-4 in Korea and N36 in China, which have been proved to have better comprehensive properties inside and outside the reactor than Zr-4 [1].

During the preparation of zirconium alloy profiles for fuel assemblies, zirconium alloy ingots obtained by vacuum arc melting are usually subjected to β-phase heat treatment after forging, which will promote alloy element in zirconium alloy to a more homogeneous state and re-dissolve the precipitated second phase into the β-phase, followed by quenching. In the above process, the α-phase of the Close-packed hexagonal (HCP) structure transforms into the β-phase of the Body-centered cubic (BCC) structure with the increase of temperature, and the second phase particles from ingot gradually dissolve completely in the β-phase region [2]. The microstructure and properties of zirconium alloys will be affected by the different parameters of β-phase quenching treatment. It has been shown that zirconium alloys under slow cooling rate have better corrosion resistance, but different microstructure formation mechanisms of zirconium alloys with various alloy elements have been reported. Massih et al. [2] attributes the improved corrosion resistance of Zr-2 alloy to the presence of large-sized second phases with a low density resulting from quenching with a slow cooling rate. While for Nb-containing zirconium alloys, if the Nb content is between 1.0 and 5.0 wt%, the formation of β-phase will reduce the supersaturated Nb content, and the β-Nb in the sample will retard the transformation of oxide film from tetragonal Zr dioxide to a monoclinic Zr dioxide subsequently, which will stabilize the oxide film structure, and result in slowing corrosion down [3–5]. From this, the microstructure of zirconium alloys can be controlled by adjusting the heat treatment parameters in order to obtain better mechanical behavior and corrosion properties.

During cooling and β → α transformation of zirconium alloys, with the increase of cooling rate, performs with different microstructure patterns: lenticular α → parallel plate α → basketweave α → martensitic α [6, 7]. It has been reported that the quenched Zr-4 shows martensitic-α structure only when the cooling rate exceeds 1500 °C/s. But in fact, the existence of O will reduce the critical cooling rate of the martensite transformation and the existence of Nb will reduce the temperature of the β → α phase transformation meanwhile. The microstructures of many Zr-Sn-Nb-Fe alloys subjected to β-phase homogenization and water quenching showed martensitic-α [3, 8], where both the increase in O content and the decrease in cooling rate will increase the width of α [9].

It is obvious that a series of microstructural variations will take place with adjusting quenching parameters, which will ultimately affect the mechanical and corrosion properties of zirconium alloys. Especially for Nb-containing zirconium alloys, where both the Nb content and the size and distribution of the second-phase particles will lead to an increase or decrease in corrosion resistance, while these characteristics can be controlled by heat treatment. Most of the current studies on quenching of zirconium alloys have focused on the effect of cooling rate on β → α martensite transformation, and fewer studies have been conducted for β-phase heat treatment temperature and time in the quenching process. In this paper, domestic Zr-Sn-Nb-Fe alloy forging ingots prepared on an industrial scale are selected, to analyze parameters' influences on the phase transformation behavior of zirconium alloys according to setting a series of β-phase heat treatment temperature and time.

2 Experimental

The nominal composition of the domestic Zr-Sn-Nb-Fe alloy selected in this paper is given in Table 1. The alloy forging billet plate specimens were obtained from 3000 kg grade ingots with the size of φ720 mm prepared by State Nuclear Baoti Zirconium Industry Company by secondary forging to form ingot billets with thickness δ60 mm. A tubular resistance furnace of model SK2-4-12 was taken to carry out the β-phase heat treatment of the alloy forging billet plate specimens and the parameters of heat treatment are shown in Table 2. Zirconium alloy was quickly transferred to water cooling whose rate is about 1000 °C/s after heat treatment. The samples of rolling direction-normal direction (RD-ND) were prepared after quenching. The Leica MeF3A optical microscope, the FEI Nova Nano SEM 400 field emission scanning electron microscope, and the FEI TECNAI G2 F20 Field emission transmission electron microscope were used to observe and analyze samples' microstructure characteristics.

Table 1. The nominal composition of Zr-Sn-Nb-Fe alloy (wt%).

Sn	Nb	Fe	Zr
0.85	1.00	0.30	bal

Table 2. β-phase heat treatment parameters setting.

Trial No	1	2	3	4	5	6	7
Temperature (°C)	950	1050	1050	1050	1050	1150	1150
Times (h)	0.5	0.25	0.5	1	2	0.25	1

3 Results and Discussion

3.1 Microstructure Analysis

Figure 1 shows the microstructure of the Zr-Sn-Nb-Fe alloy after quenching under each parameter, with the sampling position at the middle of the ingot away from the forging plane. As can be seen from the figure, due to the fast water cooling rate, the alloy almost all underwent β → α martensite transformation, in the set quenching parameters, there appears irregular small acicular martensitic formation, acicular martensitic clusters in a certain range of parallel row within the micro-zone, the shades of color in the polarized photo represents the martensitic laths of different orientation distribution, the original β grain boundary can be distinguished, where the Martensite nucleation takes place during phase transformation. In addition, martensitic nucleation can also occur in the subgrain boundaries and dislocations of the parent phase [10].

The conclusion that the β-phase heat treatment temperature has little effect on the morphology of martensitic after phase transformation at the same holding time can be confirmed preliminarily. This is in agreement with the results given by Kim et al. [3]. That the β-phase heat treatment temperature doesn't affect the corrosion resistance of zirconium alloys. However, when the β-phase heat treatment temperature was constant, the post-phase transformation microstructure showed some differences with the extension of the holding time. At the temperature of 1050 °C, the acicular martensite has a tendency to increase in size with the extension of the holding time from 0.25 h to 0.5 h and even 1 h (Fig. 1b, c, d), but the discrepancy is not obvious, while when the holding time is extended to 2 h, in addition to the acicular martensite, thick lens-like microstructure distributed vertically to each other appear in the crystal whose length (Fig. 1e, Fig. 2a). This discrepancy also shows regional variability, thick lenticular microstructure only exists in the middle of the ingot away from the forging plane. While in the region near the forging plane, Only a few plates with a similar orientation at the grain boundary of the parent phase appear (Fig. 2b), which is the result of parallel plates' nucleation in the grain boundary and growth into the crystal. This kind of microstructure will show lower ductility in mechanical properties.

Further observation of the SEM photographs of the zirconium alloy ingot in the original forged state and after different quenching processes (Fig. 3) showed that the original forged zirconium alloy plates were organized as coarse plate bundles with different dislocations and plate widths of about 4 μm, with the skeleton structure formed by the precipitation of second-phase particles at the boundary. After water quenching, the alloying elements in the zirconium alloy were re-dissolved into the matrix under water cooling conditions and underwent martensite transformation to different degrees, and most of the areas formed acicular martensite with a dislocation difference of about 60° between the laths and similar dimensions, representing the usual direction of martensite growth during the β → α transformation, which is similar to the water quenched organization of the Zr-Sn-Nb-Fe alloy characterized by CHAI et al. [9]. There are also a few coarser long plate-shaped martensites.

Under the heat treatment conditions set in this study, the change in heat treatment temperature hardly affected the dimensions of acicular martensite and plate-shaped martensite. Regarding the effect of holding time on the β → α phase transformation, a comparison of SEM photographs of samples observed under 1050 °C/2 h heat treatment conditions in Fig. 1e and Fig. 2a reveals that the coarse lenticular microstructure exhibits closely spaced clusters of parallel laths, and although this microstructure has the structural characteristics of basket-weave widmanstatten (Fig. 2a, c, Fig. 3f), this kind of widmanstatten mostly appears in the case of zirconium alloys with the low cooling rate after β-phase heat treatment, such as furnace cooling. Okvist et al. [11] suggested that the basket-weave widmanstatten is formed by the quenching and cooling process in which the β-phase provides a large number of nucleation sites for the α-phase (precipitated second-phase particles, etc.), and the symmetry of the BCC structure β-Zr makes the α plates grow simultaneously on multiple inertial surfaces and truncate each other, but the second phase is mostly redissolved into the β-phase during the β-phase heat treatment, and then the α plates grow from the grain boundary. In addition, the ZrC particles in the Zr-C alloy can also induce the nucleation of α plates. At a lower cooling rate, the
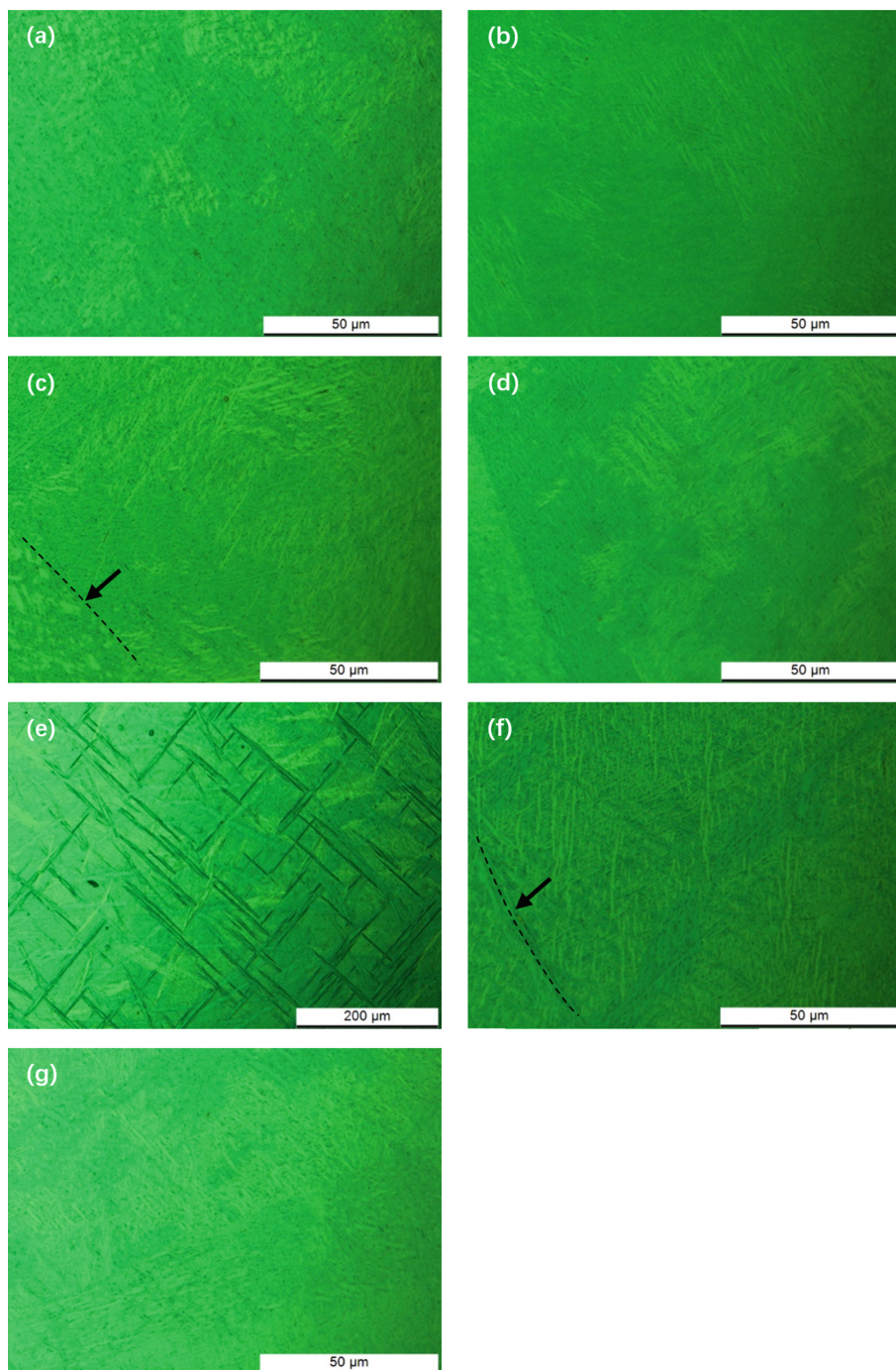
Fig. 1. RD-ND surface metallographic microstructure of Zr-Sn-Nb-Fe billet sheet specimens under different quenching processes (a) 950 °C/0.5 h (b) 1050 °C/0.25 h (c) 1050 °C/0.5 h (d) 1050 °C/1 h (e) 1050 °C/2 h (f) 1150 °C/0.25 h (g) 1150 °C/1 h
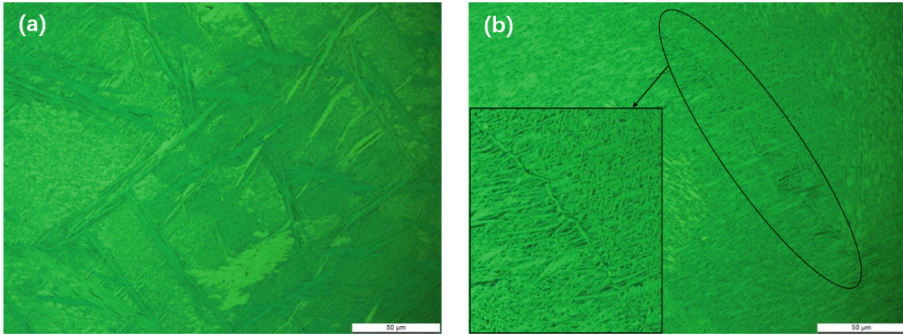
Fig. 2. Zr-Sn-Nb-Fe ingot billet sheet specimens RD-ND surface metallographic microstructure after 1050 °C/2 h heat treatment (a) away from the forging plane (b) near the forging plane

second phase will form to provide nucleation points for the basket-weave widmanstatten due to the diffusion of alloy elements. However, no second phase particle are found in Fig. 2f, so the phase transformation is judged to be still carried out in a tangential mechanism, which proved the non-diffusivity of phase transformation and the existence of martensitic microstructure. It can be seen that the width of martensitic laths will increase significantly when the holding time is extended to a certain value under a certain temperature, which is consistent with the phenomenon observed in M5 zirconium alloy by Xu [12]. O.T. WOO et al. [6] found that an increase in oxygen content leads to an increase in the width of lath as well under certain conditions of cooling rate. Because of the condition of non-vacuum heat treatment in this experiment, the oxygen content will increase with the extension of holding time, the starting temperature of martensite transformation increase, which expands the β + α region, and the time for oxygen diffusion from β grains to α grains increases, a series of changes mentioned above will enhance the diffusion-controlled phase transformation mechanism to some extent, resulting in the increase of martensite width.

In summary, the forged domestic Zr-Sn-Nb-Fe alloy under the β-phase heat treatment and subsequently water quenching, its microstructure transformed from the coarse β plates to some acicular and a few plate-shaped martensites, whose orientations have a certain relationship with parent phase, the latter is more coarse and long. Under the set quenching condition, the heat treatment temperature basically hardly affect the martensitic characteristics, but under the heat treatment condition of 1050 °C, with the extension of the holding time from 0.25 h to 2 h, part of the martensite width increased significantly, and a cluster laths appeared in parallel, a possible reason is that under the non-vacuum heat treatment conditions, the oxygen content increases with the extension of the holding time probably, more promote the growth of the nucleated laths rather than the nucleation of new laths, and finally lead to martensite Widening.

3.2 Component and Structure Analysis

The bright-field images of the samples under transmission electron microscopy for the four parameters 1, 2, 5, and 6 are shown in Fig. 4. A large number of martensitic

Fig. 3. RD-ND surface SEM images of Zr-Sn-Nb-Fe billet sheet specimens under different quenching processes (a) as forged (b) 950 °C/0.5 h (c) 1050 °C/0.25 h (d) 1050 °C/0.5 h (e) 1050 °C/1 h (f) 1050 °C/2 h (g) 1150 °C/0.25 h (h) 1150 °C/1 h

laths with different widths were found in the matrix of the zirconium alloy ingot plate specimens under four different quenching conditions, most of them were around several hundred nanometers, and there were obvious twinning and parallel dislocation lines in the tissue, the existence of a large number of dislocations provided nucleation sites for the transformation and promoted the formation of acicular martensite, the twinning was related to the starting temperature of martensite transformation, and when this temperature was reduced to a certain value, the twinning opens. The diffraction spots were calibrated for the black stripes present at the boundaries of the martensitic laths. It showed that most of them are β-Zr with BCC, which satisfies the burgers orientation relationship with the α-Zr matrix, while the existence of other diffraction spots indicated that the alloy contains a few ω-Zr with HCP. The $\alpha \rightarrow \omega$ phase transformation generally occurs under high pressure. It has been reported that the above transformation can occur in zirconium alloys with high Nb content or high pressure during quenching or aging treatment [13, 14]. And as the enrichment area of oxygen, the ω-phase also proves the hypothesis in Sect. 3.1 that the oxygen content in zirconium alloy increases under 1050 °C/2 h quenching condition. It indicates that even in zirconium alloys with low Nb content and no high pressure, quenching with high cooling rate will also promote the process of $\alpha \rightarrow \omega$ transformation and increase the thermal stability of ω-Zr phase. No second-phase particle was detected in transmission electron microscopy, which also proves that the phase transformation under the water-cooled quenching condition is of the tangential type due to the high cooling rate.

The alloys were further scanned by surface scanning energy spectroscopy mode, as shown in Fig. 5. The quantitative analysis of the alloy composition at the martensitic laths boundary was shown in Table 3. Different degrees of Fe partial gather were found at the martensitic lath boundaries for each condition, which had the highest value at 1050 °C/2 h quenching condition, this phenomenon is consistent with the highest Fe content of more than 5 wt% at the same parameter in the quantitative elemental analysis. In addition to Fe elements, the alloying elements Sn and Nb are diffusely distributed in the alloy.

Usually, the second phase particles are re-dissolved into the zirconium alloy matrix during the β-phase heat treatment stage to form a supersaturated solid solution, and the shear martensite transformation process doesn't have the diffusion phenomenon, while the phenomena of Fe partial gather and its increase with the extension of the holding time mentioned above are inconsistent with it. It proved that the actual quenching process is accompanied by a weak diffusion phase transformation, which also explains the existence of parallel-plate of widmanstatten in Fig. 2b. Thus, when the β-phase heat treatment temperature is certain, the extension of the holding time enhances the diffusion-controlled phase transformation mechanism, and this diffusion process transports the solute elements in the alloy into the β-Zr that is not transformed timely between the α martensitic laths due to cooling after high-temperature and makes the diffusion of alloying element Fe to the α lath boundaries more significant. But the weak diffusion process is not sufficient to transport Sn and Nb with larger atomic radius, which leads to the discrepancy in the degree of segregation of the three alloying elements. The segregation of the Fe element and the gradually increasing content of oxygen in the
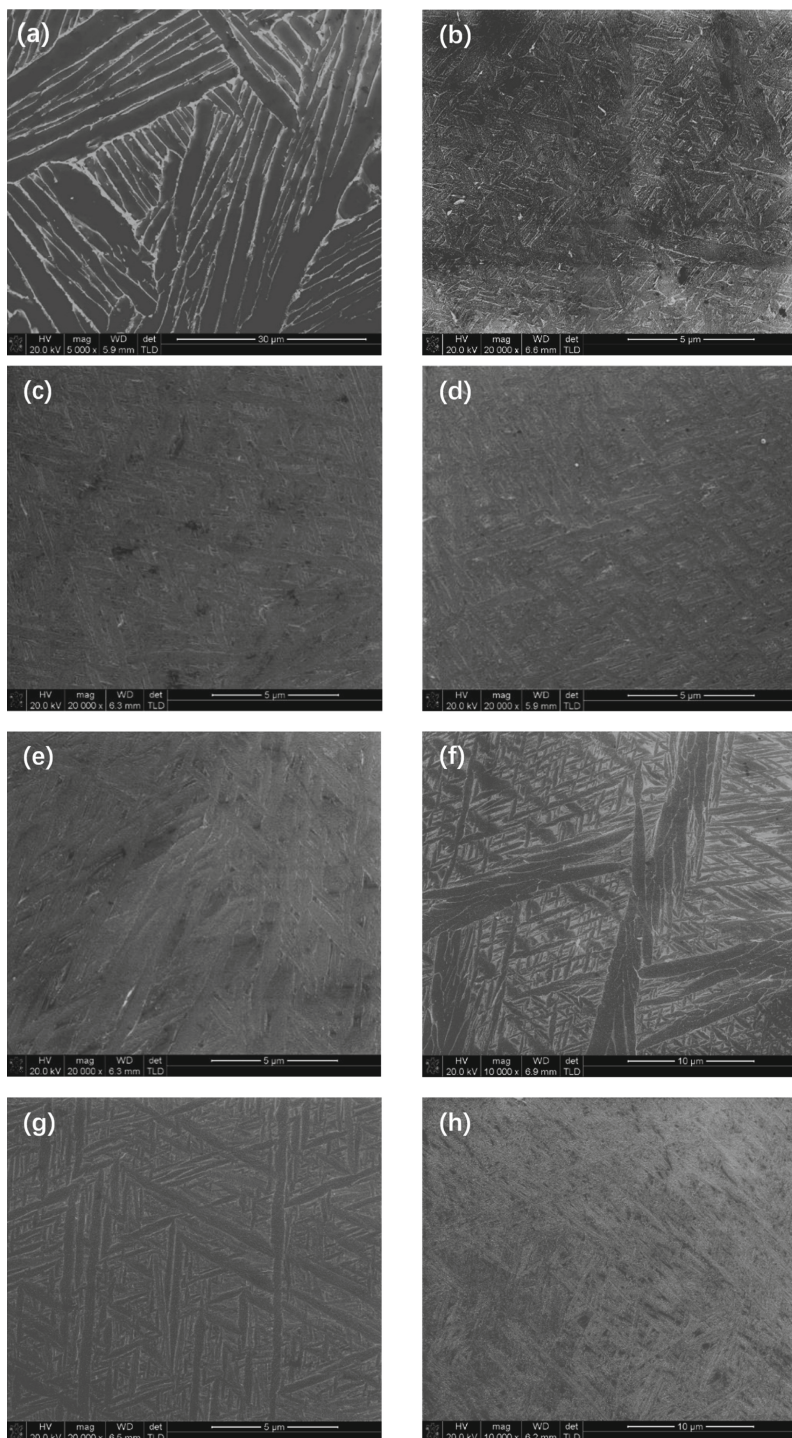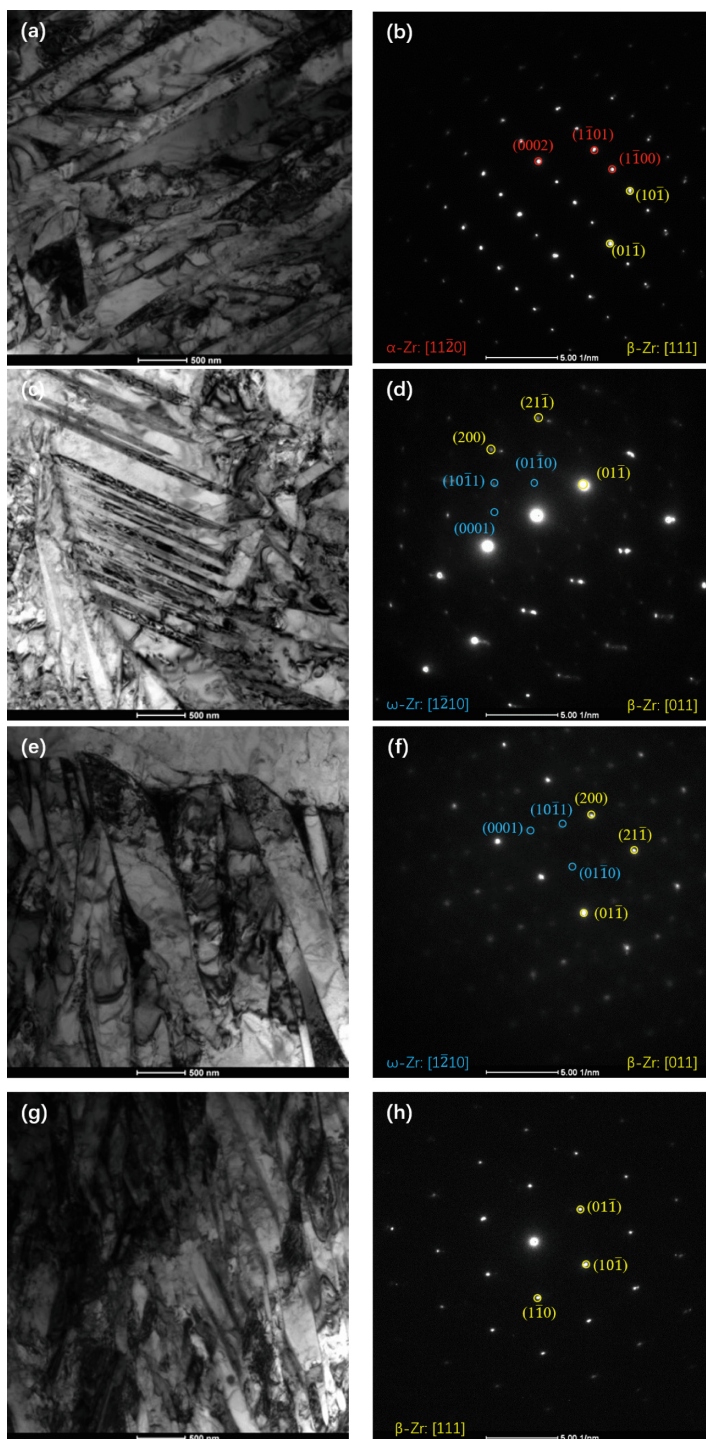
Fig. 4. RD-ND surface TEM images of Zr-Sn-Nb-Fe billet sheet specimens under different quenching processes (a) (b) 950 °C/0.5 h (c) (d) 1050 °C/0.25 h (e) (f) 1050 °C/2 h (g) (h) 1150 °C/0.25 h

process will lead to an increase in the martensitic laths width, while the increase in the heat treatment temperature had essentially no effect on the martensitic phase transformation.
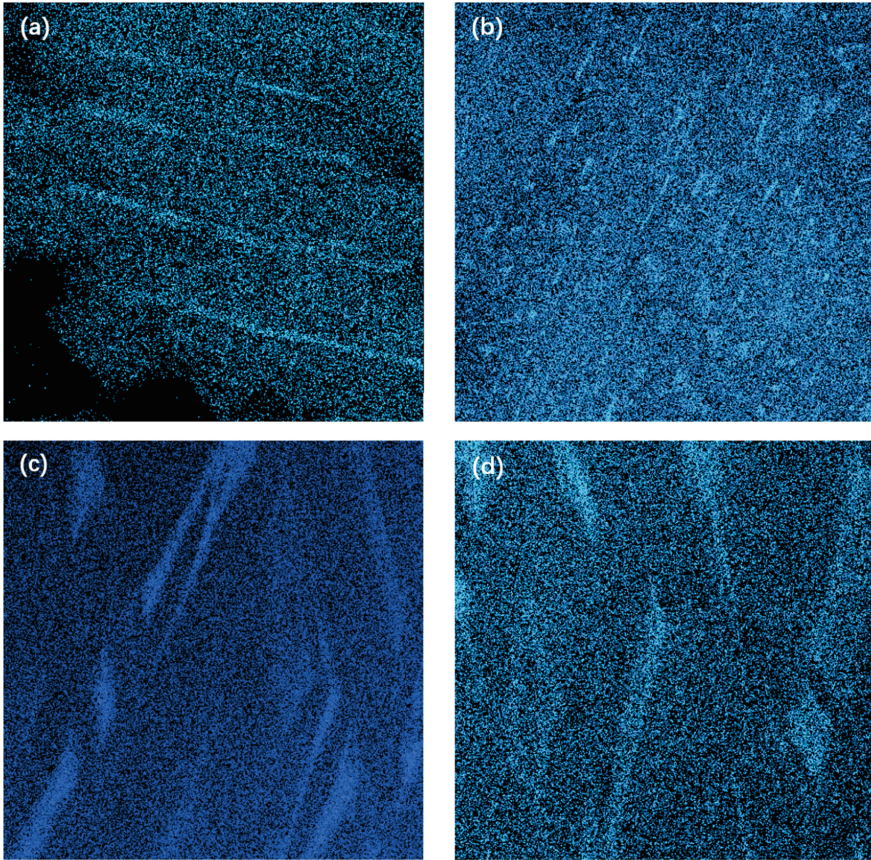
Fig. 5. Signal spectra of Fe elements at the martensite boundary of Zr-Sn-Nb-Fe alloys under different quenching processes (a) 950 °C/0.5 h (b) 1050 °C/0.25 h (c) 1050 °C/2 h (d) 1150 °C/0.25 h

Comprehensive analysis of the above TEM bright-field images, diffraction spots and elemental signal spectra shows that the water-cooled quenched zirconium alloy undergoes β → α incomplete martensitic phase transformation after β-phase heat treatment, and both β-Zr and ω-Zr exist in the matrix of the transformed zirconium alloy, but the content is small, which proves that there is some elemental diffusion at the same time of the phase transformation process. As a result of diffusion, alloying elements such as Fe, Sn, and Nb enter the martensitic slat boundary, where Fe elements undergo obvious segregation at the boundary, and the degree of segregation increases in a certain range with the extension of holding time, which is also one of the reasons for the increase of martensitic laths width.

Table 3. Content of alloying elements at the martensite boundary (wt%) 1–950 °C/0.5 h; 2–1050 °C/0.25 h; 5–1050 °C/2 h; 6–1150 °C/0.25 h

No	Zr	Sn	Nb	Fe
1	92.03	3.67	0.7	3.60
2	93.05	1.09	1.74	4.12
5	90.40	1.93	2.40	5.27
6	91.28	2.44	2.03	4.25

4   Conclusions

The results of studying the microstructure of Zr-Sn-Nb-Fe alloy under different β-phase heat treatment and following water quenching showed:

(1) Zr-Sn-Nb-Fe alloy in the forged state has a coarse plate microstructure, while the microstructure of water-cooled quenching after β-phase heat treatment is mostly acicular martensite and a few long plate-shaped martensite with a width of several hundred nanometers; the β-phase heat treatment temperature has little effect on the microstructure of alloy, but at a certain temperature, the extension of holding time will increase the martensitic lath width, and this phenomenon only occurs far from the forging plane of the ingot.

(2) Both BCC structure of β-Zr and HCP structure of ω-Zr exists in α-Zr matrix after β → α phase transformation under Water-cooled quenching condition. At the time all the alloy elements Fe, Sn, and Nb are solidly dissolved in the matrix, with Sn and Nb diffusely distributed and Fe gathered at the martensitic boundaries. β-phase heat treatment temperature has little effect on the composition and the structure, but the degree of segregation at a certain temperature increases with the extension of the holding time.

(3) The domestic Zr-Sn-Nb-Fe alloy undergoes shear-controlled martensitic phase transformation during β-phase heat treatment and water-cooled quenching, but the extension of the holding time will enhance the diffusion-controlled phase transformation by increasing the O content in the alloy, and the diffusion process transports the alloy elements to the martensitic boundary and leads to the partial gathering of Fe element with small atomic radius.

References

1. Zhao, W.J., et al.: Development of Chinese advanced zirconium alloy. Atomic Energy Sci. Technol. (S1), 3–2+4–9 (2005). (赵文金,周邦新,苗志,彭倩,蒋有荣,蒋宏曼,庞华.我国高性能锆合金的发展.原子能科学技术, 2005(S1):3–2+4–9.)
2. Massih, A.R., Dahlbäck, M., Limbäck, M., et al.: Effect of beta-to-alpha phase transition rate on corrosion behaviour of Zircaloy. Corros. Sci. **48**(5), 1154–1181 (2006)

 3. Kim H G, Baek J H, Kim S D, et al. Microstructure and corrosion characteristics of Zr–1.5 Nb–0.4 Sn–0.2 Fe–0.1 Cr alloy with a β-annealing[J]. Journal of nuclear materials, 2008, 372(2–3): 304–311

 4. Zhao, W., Liu, Y., Jiang, H., et al.: Effect of heat treatment and Nb and H contents on the phase transformation of N18 and N36 zirconium alloys. J. Alloy. Compd. **462**(1–2), 103–108 (2008)

 5. Chen, L., Song, X., Pang, H., et al.: Influence of second phase particles on corrosion resistance of N36 alloy in superheated steam. Prog. Nucl. Energy **93**, 84–88 (2016)

 6. Woo, O.T., Tangri, K.: Transformation characteristics of rapidly heated and quenched zircaloy-4-oxygen alloys. J. Nucl. Mater. **79**(1), 83–94 (1979)

 7. Holt, R.A.: The beta to alpha phase transformation in Zircaloy-4. J. Nucl. Mater. **35**(3), 322–334 (1970)

 8. Srivastava, D., Mukhopadhyay, P., Banerjee, S., et al.: Morphology and substructure of lath martensites in dilute Zr- Nb alloys. Mater. Sci. Eng. A **288**(1), 101–110 (2000)

 9. Chai, L.J., Luan, B.F., Chen, J.W., et al.: Effect of cooling rate on β→α transformation during quenching of a Zr-0.85 Sn-0.4 Nb-0.4 Fe-0.1 Cr-0.05 Cu alloy. Sci. China Technol. Sci. **55**(10), 2960–2964 (2012)

10. Tao, J., Yao, Z.J., Xue, F.: Fundamentals of Materials Science, vol. 319. Chemical Industry Press, Beijing (2006). (陶杰，姚正军，薛烽.材料科学基础. 北京：化学工业出版社,, 2006:319.)

11. Ökvist, G., Källström, K.: The effect of zirconium carbide on the β→α transformation structur in zircaloy. J. Nucl. Mater. **35**(3), 316–321 (1970)

12. Xu, Y.: Study on martensite structure of M5 zirconium alloy. Xi'an Technological University (2014). (徐悠. M5 锆合金马氏体亚结构研究.西安工业大学, 2014.)

13. Rogachev, S.O., Sundeev, R.V., Nikulin, S.A.: Effect of severe plastic deformation by high-pressure torsion at different temperatures and subsequent annealing on structural and phase transformations in Zr-2.5% Nb alloy. J. Alloys Compd. **865**, 158874 (2021)

14. Zhilyaev, A.P., Sabirov, I., González-Doncel, G., et al.: Effect of Nb additions on the microstructure, thermal stability and mechanical behavior of high pressure Zr phases under ambient conditions. Mater. Sci. Eng. A **528**(9), 3496–3505 (2011)

The Main Reason of SG Thermal Power Imbalance Between Each Loop in CPR1000 Nuclear Power Plants

Chao-hao Shang[1,3]([✉]), You-sen Hu[1], Yuan-xiong Guo[2], Chang-ying Li[1], and Jun Chen[1]

[1] China Nuclear Power Technology Research Institute, Shenzhen 518038, Guangdong, China
shangchaohao@126.com
[2] Daya Bay Nuclear Power Operation and Management Co., Ltd., Shenzhen 518124, Guangdong, China
[3] Research on Reactor Thermal Hydraulic, Safety Analysis and Technical Support for PWR Operation, China Nuclear Power Technology Research Institute, Shenzhen, Guangdong, China

Abstract. The SG thermal power imbalance between each loop exists in some CPR1000 nuclear power plants. In this paper, the authors trying to figure out the chief reasons of SG power imbalance between each loop by analyzing the measurement data from the Nuclear Power Plants. The main thermal parameters from the nuclear power plants are analyzed. By analyzing factors affecting the SG thermal power, the main factors affecting the SG thermal power are loop flowrate and hot leg temperature. The loop flowrate depends on the pump characteristic curve and the loop resistance coefficient. The hot leg temperature depends on RPV structure and core power distribution. A CPR1000 SG model was established and the sensitivity analysis of the coefficients which affect SG heat transfer is performed. The analysis results show that the deviation of the hot leg temperature between loops has the most significant effect on the SG thermal power imbalance. Hence, the SG thermal power imbalance between each loop mainly due to the RPV structure, the core power distribution and the flowrate deviation.

Keywords: CPR1000 nuclear power plants · Power imbalance · RPV structure · Core power distribution · Asymmetric primary flowrate

1 Introduction

The alarm of 'Loop 1 SG Thermal Power Greater than 102%FP' was occurred in one CPR1000 Nuclear Power Plant during operation. The total reactor power is less than 100% FP when the alarm occurs. The core flowrate and each loop flowrate are both between the thermal design flow rate and the mechanical design flow rate, which means the flowrate does not exceed the criteria. The power measurement results show that there is a large deviation (almost 50MW) of SG thermal power between loops. Further investigation found that the SG thermal power imbalance between each loop exists in some CPR1000 nuclear power plants, especially when these power plants are operated

in the transition cycles (from 12-month fuel management change to 18-month fuel management). This paper extracts a large number of measurement data from 13 CPR1000 nuclear power plants within total 27 cycles. The data mainly include SG thermal power, feedwater temperature, feedwater flowrate, SG steam pressure, primary loop flowrate, hot leg temperature, cold leg temperature etc. The trends of SG thermal power for two typical SG thermal power imbalance cycles in CPR1000 nuclear power plants are showed in Fig. 1 and Fig. 2.

The research in China mainly focuses on the flowrate imbalance between loops. ZHAO De-yuan [1] has analyzed the flow measurement deviation of the primary loop of Unit 2 in Ling'ao Nuclear Power plant, and provided the treatment measures. Wang Chuang [2] concluded that the single loop flowrate deviation mostly is caused by the measurement factors and nuclear power stations can carry out the fault analysis and confirmed by test and measurement data during the unit overhaul. LI Hua-sheng [3] concluded that loop flowrate deviation mostly is caused by resistance characteristics and pump characteristics. Liu Jianquan [4] made an analog study on the influence of loop flow deviation on enthalpy rise characteristics of the units. Some research on the influence of pipe blockage on safety analysis in Steam generator also has been carried out [5, 6].

This paper trying to figure out the main reason of SG power imbalance between loops in CPR1000 Nuclear Power Plants by measuring data analysis and quantitative calculation.
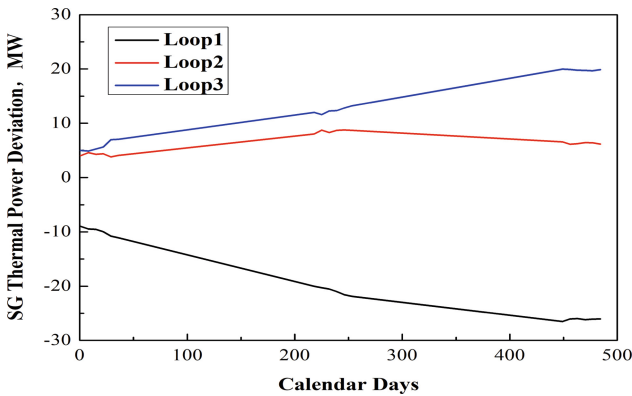
Fig. 1. Relationship between thermal power deviation and calendar days in typical cycle 1

2 Root Cause Analysis

According to the source of the deviation, the reason of SG thermal power imbalance can be divided into measurement factors and actual deviation. The analysis flow chart is shown in Fig. 3.
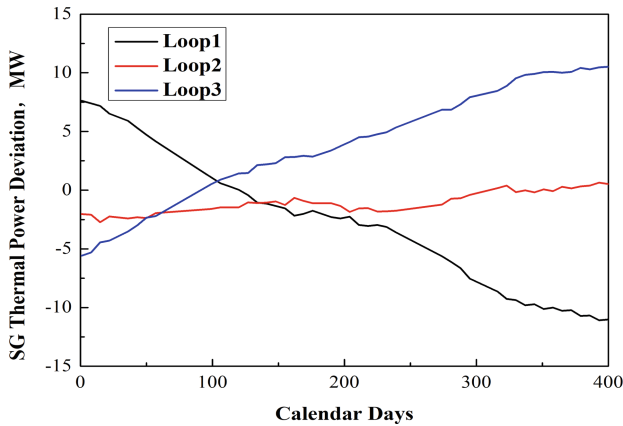
Fig. 2. Relationship between thermal power deviation and calendar days in typical cycle 2
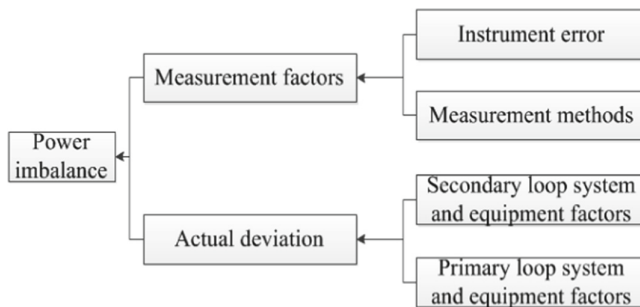
Fig. 3. The source of the SG thermal power imbalance

2.1 Measurement Factors

The measurement factors consist of the following two parts:

(1) Measurement uncertainty. Mainly refers to the uncertainty during the parameter measurement process. The uncertainty of each SG thermal power measurement is about 0.87% in CPR1000. So the maximum uncertainty of the thermal power deviation between loops is about 1.23% (nearly 12 MW). If the SG thermal power imbalance between each loop is less than 12 MW, the SG thermal power imbalance is considered to be within the measurement uncertainty.

(2) Measurement method. Due to instrument limitations, the blowdown flowrate of each SG can't be measured separately in CPR1000. The calculation of SG thermal power assumes that the three SG blowdown flowrate are equal. In fact, the blowdown flowrate between three SG can't be consistent. This may introduce some error. However, the blowdown flowrate is only 1% of the feedwater flowrate. So the error caused by the measurement method is very small.

Taking into account that the CPR1000 units are using the same measurement system, each unit shall be calibrated regularly according to the regulations, the measured SG power is credible.

Hence, the power deviation is realistic. The root cause analysis are performed based on the data from two typical cycles. Additional measured data in these two cycles are provided in Fig. 4 and Fig. 5.

2.2 Actual Deviation

Power deviation can be classified into two parts: primary circuit deviation and secondary circuit deviation.

2.2.1 Secondary Circuit Factors

The thermal power of the secondary circuit is calculated by the following formulas:

$$W_{SG} = Q_s \cdot x \cdot H_s + Q_s \cdot (1 - x) \cdot H_{sat} + Q_b \cdot H_{sat} - Q_{fw} \cdot H_{fw}$$
$$Q_s + Q_b = Q_{fw}$$

where:
W_{SG}: SG thermal power.
Q_s: SG steam flowrate.
x: Steam quality.
Q_b: blowdown flowrate.
Q_{fw}: feedwater flowrate.
H_s: Steam enthalpy.
H_{sat}: blowdown enthalpy.
H_{fw}: feedwater enthalpy.

(1) Feedwater Temperature

The difference in feedwater temperature between loops is small. The deviation of the feedwater temperature between each loop is generally within 0.1 °C. The main causes of feed water temperature difference are heat dissipation, flow resistance and other factors. The slight difference of feed water temperature has little effect on SG thermal power imbalance.

(2) Steam Pressure

There is little difference in steam pressure between loops, because steam from each loop will converge into the steam header. The deviation of the steam pressure between each loop is generally within 0.01 MPa. Assuming that the steam pressure deviation is 0.05 MPa, the change of steam enthalpy is less than 0.025%. This deviation leads to the imbalance of SG thermal power less than 0.23 MW. Therefore, the influence of steam pressure deviation on thermal power imbalance between circuits can be ignored.
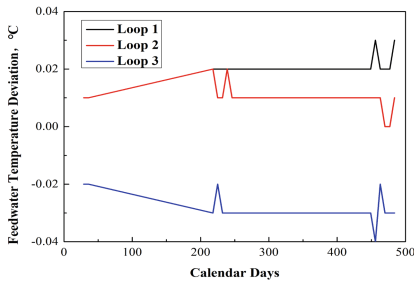
a) Feedwater Flowrate
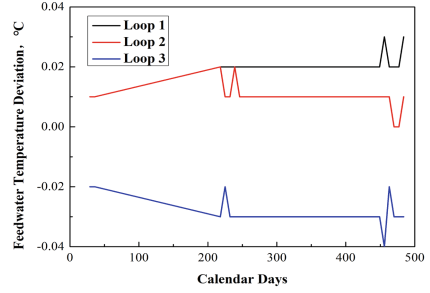
b) Feedwater Temperature
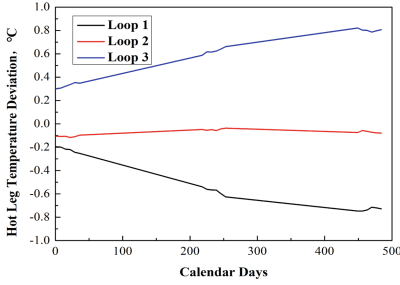
c) Hot Leg Temperature
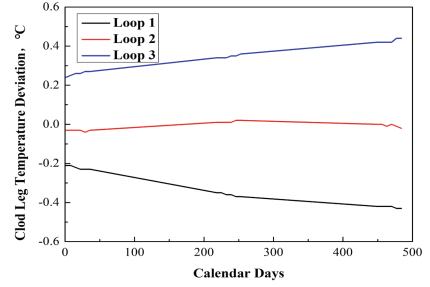
d) Clod Leg Temperature

Fig. 4. Main thermal parameters in typical cycle 1
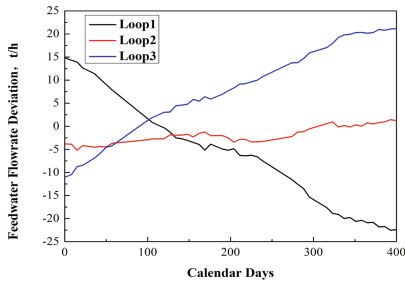
a) Feedwater Flowrate
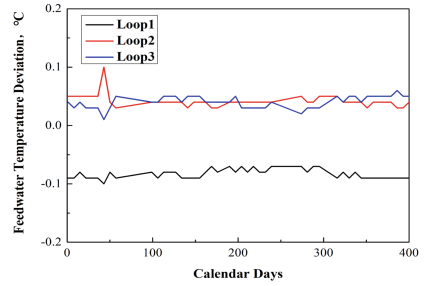
b) Feedwater Temperature
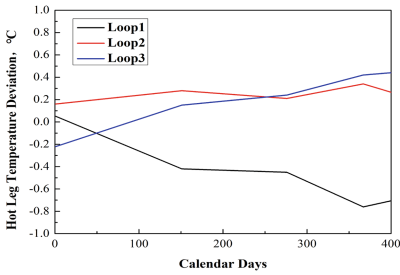
c) Hot Leg Temperature
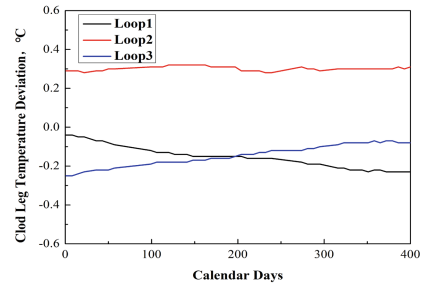
d) Clod Leg Temperature

Fig. 5. Main thermal parameters in typical cycle 2

(3) Steam Quality

According to experience feedback, there is no obvious change in steam quality. If the steam humidity deviation between each loop is 0.1%, the steam enthalpy difference caused by steam humidity deviation is about 0.55%, and the influence on SG thermal power imbalance is about 0.54 MW. Therefore, the influence of steam quality deviation on thermal power imbalance between circuits can be ignored.

(4) Feedwater Flowrate (Steam Flowrate)

It can be seen from the variation trend of SG thermal power and feedwater flowrate that the variation trend of these parameters is highly consistent. This is because there is little difference in other parameters affecting thermal power among circuits. Therefore, the SG thermal power is substantially linearly related to the feedwater flowrate (steam flow rate). According to the characteristics of the Steam generator, the steam flowrate depends on the heat transfer in the primary circuit. Feedwater flowrate control program is applied to regulating flow rate to match with steam flowrate and keep SG water level stable. Therefore, the feedwater flowrate (steam flow rate) is affected by SG heat transfer. The influencing factors of SG heat transfer performance and primary circuit need further analysis.

(5) SG heat Transfer Performance

At present, no direct data can prove the heat transfer capability between Steam generators. Considering that CPR1000 nuclear power plant has not been in operation for a long time, and there is no pipe blockage in SGs, the heat transfer capability of SG is expected to be sufficient. Therefore, it is considered that the difference of heat transfer capability of SG is not the main factor causing the thermal power imbalance between loops.

(6) Summary

According to the previous analysis, the influence of feed water temperature deviation, steam pressure deviation and steam quality deviation on SG thermal power imbalance can be ignored. The deviation of feedwater flowrate is caused by SG heat transfer imbalance. The heat transfer of SG is directly affected by the state parameters of the primary circuit, so it is necessary to analyze the state parameters of the primary circuit.

2.2.2 Primary Circuit Factors

The thermal power of the primary circuit is calculated by the following formula:

$$W_{SG} = Q_{loop} \cdot (H_h - H_c) + W_o$$

where:
W_{SG}: SG thermal power.

Q_{loop}: loop flowrate.

H_h: hot leg enthalpy.

H_c: cold leg enthalpy.

W_o: Other heat sources except the core transfer to RCP.

(1) Loop Flowrate

The difference of loop flowrate will directly affect the SG heat transfer capability. The results of loop flow measurement test (RCP64) show that there are differences in loop flowrate. The flow rate of each loop is determined by the characteristics of the pump and the resistance characteristics of the primary circuit. For the resistance characteristics of the primary loop, the core and upper chamber in the Reactor pressure vessel are not strictly symmetrical relative to three loops. Thus, the resistance characteristics of the three loops are different. For the characteristics of the pump, the design is the same, but it may be slightly different in manufacture and installation. In the base load operation condition, the output of Primary pump remains basically unchanged. Therefore, the loop flowrate contributes to the initial deviation of thermal power between loops, but it is not the cause of the change of thermal power deviation between loops during operation.

(2) Primary Circuit Temperature

The measurement data shows that there are significant differences in the hot leg temperature and the old leg temperature among different loops. The temperature deviation of hot legs is about 0.8°C, and the maximum is more than 1.6 °C. The temperature deviation of cold legs is within 0.5 °C, and the maximum is less than 0.8 °C. Because the temperature deviation of cold leg is smaller than that of hot leg. The deviation of hot leg temperature will lead to the deviation of average temperature between loops, which will change the heat transfer of each SG and further lead to the deviation of SG thermal power.

(3) Hot Leg Temperature

From the direction of coolant flow, the coolant is heated by the core and then flows to SG for heat transfer. Hot leg temperature is mainly affected by core power distribution and mixing capacity in the upper plenum. In the RPV structure design, the core and the upper plenum are 1/4 symmetrical, and the loops are 1/3 symmetrical. The asymmetry of this structure will cause the difference of core area corresponding to each loop. Meanwhile, the time of the coolant flows through the upper plenum is very short, the mixing effect of the upper plenum is limited. The coolant at the different assembly's outlet will directly flow to the loop which the assembly is closer to. This phenomenon makes it difficult for coolant to mix in the upper plenum area, which leads to the difference of temperature in the hot leg of each loop. Therefore, due to the asymmetry of core power distribution corresponding to the three loops, the core outlet temperature corresponding to the three loops is different. The coolant does not mix well in the upper plenum area, which leads to the hot leg temperature deviation between the loops. During power operation, the change

of core power distribution will further lead to the change of hot section temperature during the cycle.

(4)   Summary

The flow deviation of the three loops caused by RPV structure factors (resistance characteristic difference between loops) and primary pump output will bring the initial thermal power deviation of the unit, but the deviation generally remains stable during operation. The core power distribution (asymmetry corresponding to the three loops) and RPV structure factors (asymmetry between the loops and the core, uneven mixing in the upper plenum area) lead to the hot leg temperature difference between the loops. These are the main factors that affects thermal power imbalance in primary loop.

2.3   The Influence of Core Power Distribution on Hot Leg Temperature

In order to analyze the influence of core power distribution on hot leg temperature, a core sub-channel model and an upper plenum CFD model are established to calculate hot leg temperature. The analysis model is shown in Fig. 6.
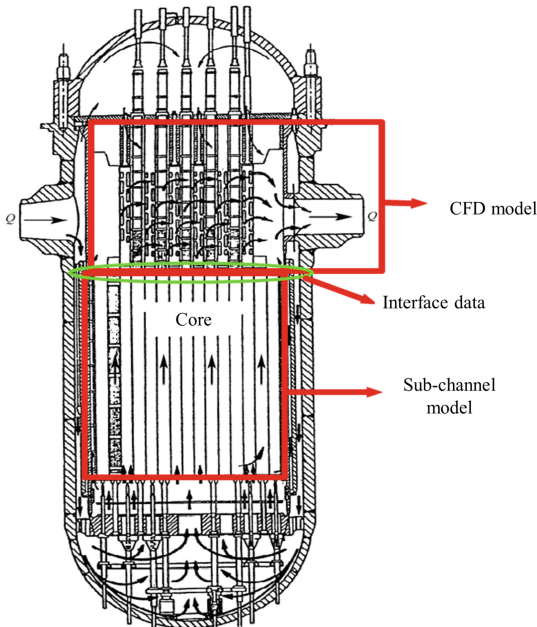
Fig. 6. Schematic diagram of analysis model

2.3.1   Core Sub-channel Model

The core sub-channel model consists of 157 sub-channels. Each channel corresponds to one Fuel assembly. The core power distribution and thermal parameters are used

as inputs of the model. The flow rate and temperature of each Fuel assembly can be calculated by changing the core power distribution under different Burn-ups. The results are provided as interface parameters to the upper plenum CFD model to carry out the hot leg temperature calculation.

2.3.2 The Upper Plenum CFD Model

A lot of research have been carried out on the upper plenum CFD model [7–9]. In this paper, the structure of the upper plenum is modeled in detail with reference to the relevant analysis experience. The STAR CCM + code is used for the analysis. The area of the CFD model is shown in Fig. 7, and the CFD meshing result is shown in Fig. 8. The total grid of the whole CFD model is 28.48 million. The inlet boundary conditions of the model are core outlet velocity and temperature, and the hot leg outlet boundary condition is set to the pressure boundary.
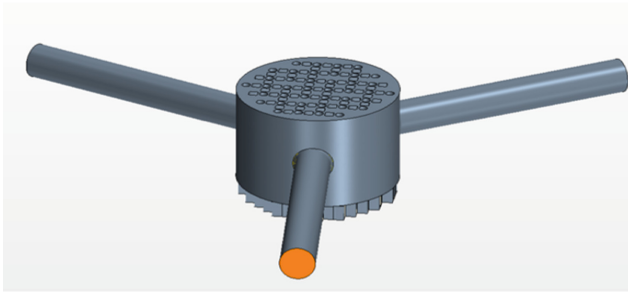
Fig. 7. CFD model domain
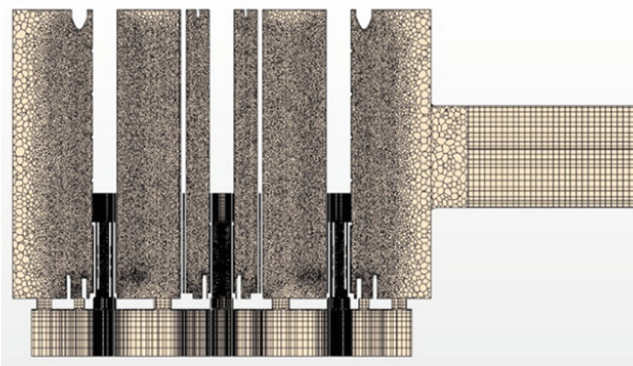
Fig. 8. Mesh generation

2.3.3 The Hot Leg Temperature Analysis Result

Based on the power distribution of two typical cycles, the hot leg temperature is calculated by analysis model, the calculated results are shown in Fig. 9 and Fig. 10. It can be seen

from the calculation results that the variation trend of hot leg temperature is in good agreement with the actual variation trend. This further proves that the variation of hot leg temperature during the cycle is caused by the variation of core power distribution.
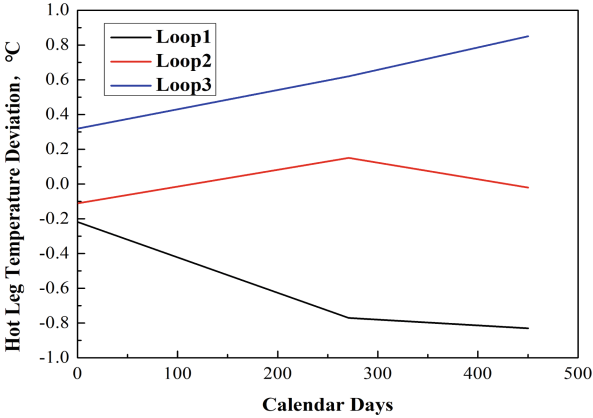
Fig. 9. Hot leg temperature result of typical cycle 1
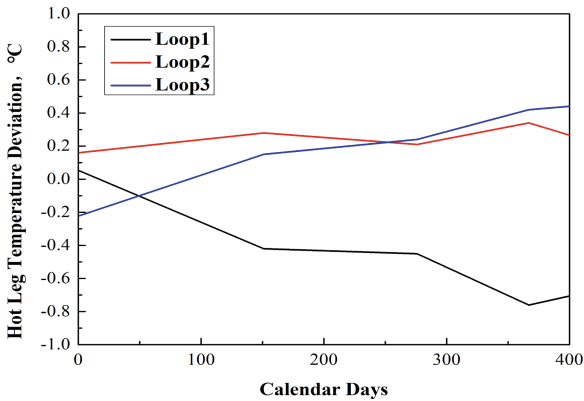
Fig. 10. Hot leg temperature result of typical cycle 2

3   Weight Sensitivity Analysis

The sensitivity analysis of the main factors affecting the thermal power imbalance between loops is carried out in this chapter. These analyses try to find out the weight of each influencing factor. Through the analysis, the main factors affecting SG thermal power imbalance are: hot leg temperature and loop flow rate. The CPR1000 SG model was established by CGN in house code LOCUST. Sensitivity analysis of hot leg temperature and loop flowrate was carried out respectively.

The influence of these parameter changes on SG thermal power is shown in Fig. 11. It can be seen from the calculation results that the influence of each parameter on SG thermal power is different. The influence of hot leg temperature on SG thermal power is more significant.
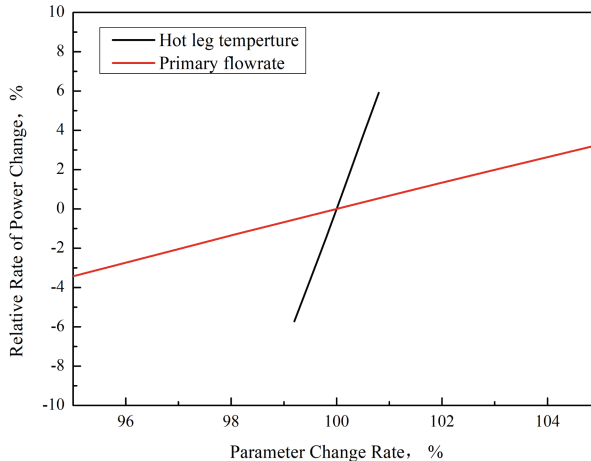
Fig. 11. The corresponding relationship between parameters and SG thermal power

4 Conclusion

Based on the measured data and a core sub-channel coupled with CFD analysis model, this paper analyzes the causes of thermal power deviation between loops, and deduces that the main reasons affecting the power deviation between loops are the difference of loop flow and hot leg temperature. Weight sensitivity analysis shows that hot leg temperature deviation has more significant effect on thermal power deviation.

The flow deviation of the three loops are caused by RPV structure factors (resistance characteristic difference between loops) and primary pump output, which will bring the initial thermal power deviation of the unit, but the deviation generally remains stable during operation. The core power distribution (asymmetry corresponding to the three loops) and RPV structure factors (asymmetry between the loops and the core, uneven mixing in the upper plenum area) lead to the hot leg temperature difference between the loops. The main factor that causes the increase of thermal power deviation between loops during operation is the change of core power distribution.

References

1. Zhao, D..-y.: Analysis of the discrepancies of reactor coolant flowrate measurement in unit 2 of Ling'ao nuclear power plant. Nucl. Power Eng. **25**(4), 373–376 (2004)

2. Wang, C., et al.: Fault mechanism analysis of single loop flow deviation in PWR nuclear power plants. Nucl. Power Eng. **35**(5), 117–119 (2014)
3. Li, H., et al.: Proposed solutions and root cause of the M310 type PWR licensee event on RCP loop flow and core total flow over the mechanical design flow limit. Nucl. Saf. **14**(4), 30–35 (2015)
4. Liu, J., et al.: Simulation study of enthalpy gain characteristics on nuclear power 1 000 MW unit pressurized water reactor loop flow deviation. Proc. CSEE **35**(16) (2015)
5. Pla, P., Reventos, F., Ramos, M.M., et al.: Simulation of steam generator plugging tubes in a PWR to analyze the operating impact. Nucl. Eng. Des. **30515**, 132–145 (2016)
6. Zhao, X., et al.: Three-dimensional study on the hydraulic characteristics under the steam generator (SG) tube plugging operations for AP1000. Prog. Nucl. Energy **112**, 63–74 (2019)
7. Li, X.-b., et al. : Analysis of coolant temperature fluctuating in upper plenum of PWR. Atomic Energy Sci. Technol. **46**(11) (2012)
8. Yu, P.-a., et al.: The experimental study on steady flow in PWR upper plenum. Chin. J. Nucl. Sci. Eng. **16**(1) (1996)
9. Wana, L., et al.: Numerical simulation of temperature heterogeneity inside the AP1000 upper plenum and hot leg. Nucl. Eng. Des. **362**, 110525 (2020)

Mechanical and Numerical Simulation Analysis for the Insertion Section Sampling of Irradiation Charpy Specimen Reconstitution

Yunpeng Tang[1], Muran Qi[1], Huiping Zhu[1(✉)], Zhenfeng Tong[1], and Chenglong Wang[2]

[1] North China Electric Power University, Beijing, China
zhuhuiping@ncepu.edu.cn
[2] China Institute of Atomic Energy, Beijing, China

Abstract. The reactor pressure vessel (RPV) is one of the most critical equipment in the pressurized water reactor, and its structural integrity is the key factor that determines the operational safety and service life of the reactor. In practical applications, the aging degree of RPV can be evaluated through the ductile-brittle transition temperature (DBTT) curve of the Charpy impact specimen pre-placed in RPV. However, due to the space limitation inside the reactor core, the available irradiation surveillance specimens are limited for mechanical testing. Especially, most reactors have faced the problem of life extension in recent years, and the impact data of the irradiation surveillance specimen is an important basis for the life extension of the reactor. One of the solutions is to reconstitute new Charpy specimens from the impacted ones to obtain more impact data. In this paper, the basic methods for the reconstitution of RPV material Ni-Cr-Mo-V steel are studied. By testing the hardness change of the Charpy impact broken specimen along the length direction, the maximum value of the plastic deformation zone of the impact fracture is obtained. Besides, based on the Gurson-Tvergaard-Needleman (GTN) model, the impact process of the material in the upper shelf temperature region is calculated by ABAQUS numerical simulation. Compared with the tested microhardness results of the material, the maximum length of the insert section of Charpy impact specimen reconstitution is confirmed. It shows that for Ni-Cr-Mo-V steel, the maximum length of the plastic deformation zone at the upper shelf temperature region is about 7 mm, and the insert length of the reconstituted specimens can be selected to 20 mm. The results can be used as an important reference for establishing the fabrication standard of the reconstituted Charpy specimen of the reactor pressure vessel.

Keywords: Pressure vessel steel · Charpy impact · Specimen reconstitution · Insert length · GTN model

1 Introduction

As the core component of a nuclear reactor, the nuclear reactor pressure vessel (RPV) contains the active zone of the core, holds the primary circuit coolant, supports all components of the reactor, and stabilizes the operating pressure in the reactor [1]. The RPV

structural integrity affects the service life of nuclear power plants. Structural materials subjecte to high energy neutron irradiation during the service life in a nuclear power plant, resulting in irradiation aging and deterioration of the mechanical properties [2, 3]. The aging degree of structural materials affects the safety and economy of the reactor, which can be evaluated through the ductile-brittle transition temperature (DBTT) curve of the pre-placed irradiation surveillance specimen in the reactor [4–7].

In recent years, the early service nuclear power plants are facing the problem of life extension. Considering the conservative design of nuclear power plants, the service life is primarily based on the economic life of construction costs, rather than the aging degree of the structural materials. Therefore, many nuclear power plants approaching the end of the service life need to be evaluated for life-extending. Actually, due to the space limitation inside the reactor cores, the available irradiation surveillance specimens are limited for mechanical testing. The specimen reconstitution technique is considered the most promising solution to the problem of insufficient samples. As shown in Fig. 1, the Charpy specimen reconstitution technique [8–11] removes the plastic deformation zone of the broken specimen and welds the materials with similar properties at both ends of the retaining elastic zone. The reconstituted specimen is eventually processed into the standard specimen. The reconstitution technique enables the reuse of irradiation surveillance specimens to provide more material property data. With the development of the specimen reconstitution technique, many countries have established relevant technical specifications to guide the reconstituted specimen, such as the enhanced irradiation surveillance program in Belgium [12], the specimen reconstitution technique implementation standard ASTM E1253 in the United States [8], and the formulated technical specifications of JEAC 4201-2007 for irradiation surveillance specimens in Japan [13], etc.
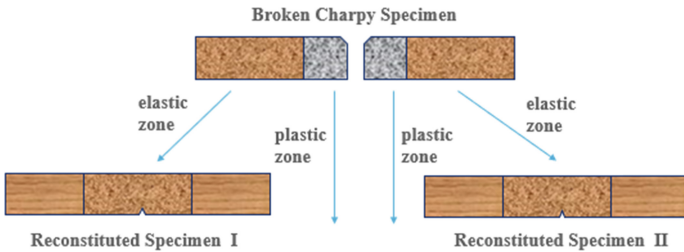
Fig. 1. The specimen reconstitution technique.

The central insertion section of the reconstituted specimen should avoid the plastic deformation zone to prevent affecting the results of the reconstituted specimen. Measurement of Stress distribution and the plastic zone for the broken specimen is a necessary step to determine the insertion size in the specimen reconstitution technique. In previous studies, the hardness test was often performed on impact fractures to determine the plastic deformation zone. The place where the hardness test value increases sharply is determined as the edge of the plastic zone. In recent years, finite element numerical simulation has been widely used in the field of engineering science due to the high agreement between the simulation results and the experimental results. The plastic zone can

be determined by the simulation graph of the fracture model. Therefore, the hardness test results and simulation results are usually combined to determine the plastic deformation zone of the broken specimen. The reasonable insert length of the reconstituted specimen was determined.

The Ni-Cr-Mo-V steel is studied in this paper. The different temperature impact tests were selected to confirm the ductile-brittle transition temperature. The impact fracture at different temperatures was obtained. And the maximum plastic deformation zone of Ni-Cr-Mo-V steel through the hardness test was determined. In addition, the numerical model of the upper shelf temperature region of Ni-Cr-Mo-V steel was established based on the reverse finite element method. The simulation results were combined with the microhardness test results to accurately determine the reasonable size of the insertion section in the reconstituted specimen. The results provide a theoretical basis for establishing the insertion section sampling specification for the Charpy impact reconstitution technique of the Ni-Cr-Mo-V steel.

2 Experimental Procedure and Materials

2.1 Experiment

The material used in the test is the Ni-Cr-Mo-V steel for RPV. The Charpy impact test is carried out to obtain the DBTT curve of the Ni-Cr-Mo-V steel. And the impact fracture in the different temperature regions was obtained. The absorbed energies are recorded during the impact tests at different temperatures. The RPV steel taken from the base material was processed into a standard Charpy impact specimen, referring to the Russian GOST-9454-1978 standard. The size of the specimen is shown in Fig. 2. The Charpy impact test machine spans 40 mm at both ends of the anvil. The radius of the hammer tup is R = 2 mm. And the theoretical impact speed is 5.2 m/s. The test temperature range is from −120 °C to 100 °C with a temperature control accuracy of ± 1 °C.
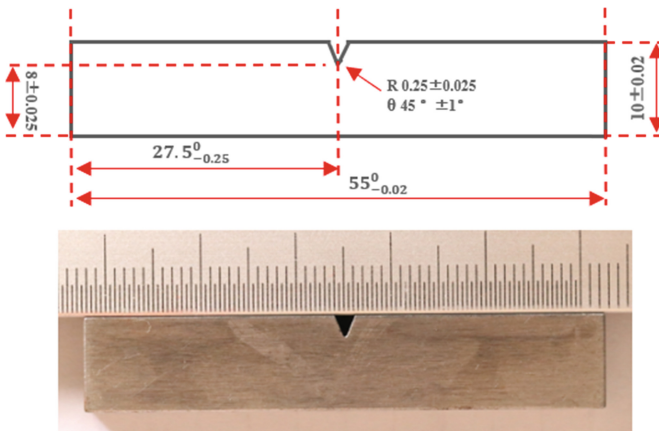
Fig. 2. The size of Charpy impact specimens.

Vickers hardness is used in the experiment to obtain the hardness distribution in the impact fracture because of its accurate and reliable measurement. The impact fractures that are not broken should be cut from the V-notch as shown in Fig. 3. Before the test started, the impact fracture was polished with sandpaper, 600#, 1000#, 1200# and 1500# respectively. Then polish the specimen with 0.9μm polishing liquid in the microcre polishing. Finally the polished specimens were washed with anhydrous ethanol. The treated specimens were tested by the FALCON-500 automatic micro-Vickers hardness tester. The hardness test was carried out at an interval of 2 mm at the same position from the broken end. Based on the results, the hardness distribution graph was drawn. And the average value of the distance from the same position of the broken end was obtained to draw the hardness trend graph.

Fig. 3. The impact fracture.

2.2   Numerical Simulation

In the process of numerical simulation, an accurate and reasonable intrinsic constitutive relationship is the premise for the success of a numerical simulation. Damage to metallic materials is usually characterized by ductile damage, which is based on the nucleation, growth, and aggregation of micro-voids within the material [14–16]. In this case, Gurson [17] developed a set of damage constitutive equations based on introducing the void volume fraction in the mesoscopic damage mechanics. The Gurson model establishes the relationship between plastic deformation and the evolution of microcavities. Since then Tvergaard [18, 19] and Needleman [19, 20] further modified the Gurson model to obtain a more accurate Gurson-Tvergaard-Needleman model (GTN) [21–23].

The Charpy impact process was simulated using ABAQUS/Explicit based on the reverse finite element method. The model adopts the GTN intrinsic equation with element type C3D8R and local refinement of the mesh at the contact of the specimen. The mechanical property parameters of the Ni-Cr-Mo-V steel required for the simulations were obtained by tensile experiments. The tensile test was carried out on a ZWICK tester using the videoXtens2-120 HP video extensometer. The tensile test refers to GB/T 229.

3 Results and Discussion

3.1 Experiment

3.1.1 Charpy Impact Test

According to the Charpy impact results, the upper and lower shelf energy of the Ni-Cr-Mo-V steel was determined according to the experimental temperature and the absorbed energy. And the ductile-brittle transition temperature curves for Ni-Cr-Mo-V steel were obtained through the hyperbolic tangent function (1):

$$U = \frac{E_p + E_l}{2} + \frac{E_p - E_l}{2} \tanh \frac{T - D}{C} \tag{1}$$

where: E_p – the upper shelf energy, J;

E_l – the lower shelf energy, J;

T – Temperature, °C;

C, D – the fitted value.

According to Eq. (1), the ductile-brittle transition temperature curves are fitted for Ni-Cr-Mo-V steel, which is shown in Fig. 4. It shows that the overall temperature curve presents an "S" shape. The absorbed energy is basically around the fitted curve. The Charpy impact data shows good stability. On the curve, the upper shelf energy (USE) of the steel is 238J and the lower shelf energy (LSE) is 2.7J. Figure 4 shows that when the temperature rises to 70 °C, the absorbed energy value of the Ni-Cr-Mo-V steel tends to 238J. When the specimen is cooled to −105 °C, the material also has a similar change trend. The absorbed energy in the energy transition temperature (ETT) is relatively discrete. The phenomenon is caused by unstable material properties in the ETT region. According to the РДЭО.0598–2004 specification, the temperature corresponding to the absorbed energy of 47J is used as the DBTT $T_k = T_{47J} \approx -72$ °C.

3.1.2 Hardness Test

After the Charpy impact test, the impact fracture at different temperatures was obtained. Based on the hardness test results, the hardness distribution graph at different temperatures was drawn.

Figure 5 shows the hardness distribution along the length of the impact fracture at the lower shelf. It is found that the hardness of the specimen at the lower shelf does not change significantly. There is almost no plastic deformation in the lower shelf of the Ni-Cr-Mo-V steel. Figure 6 shows the hardness distribution of the impact fracture at −55 °C. There is an abrupt change near the broken end, especially at the location of the hammer tup impact where the hardness is highest. This is due to the high strain rate strengthening causing plastic deformation of the material during the impact. The conclusion is that the upper shelf fracture should have a similar deformation in Fig. 7. Comparing Fig. 6 with Fig. 7, it was found that the specimen has a larger hardness abrupt change region on the upper shelf. The width of the plastic deformation zone is the largest in the hardness distribution graph of the upper shelf fracture.

According to the hardness distribution of the material, the location where the hardness value steep increases would be the edge of the plastic deformation zone of the broken
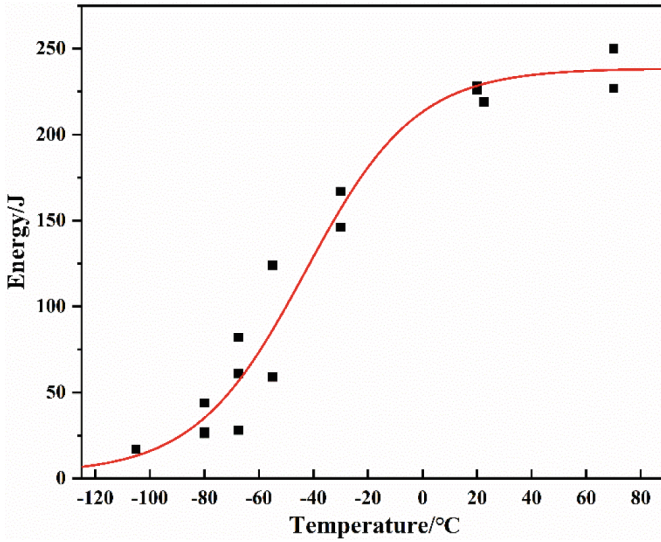
Fig. 4. The ductile-brittle transition temperature curves for Ni-Cr-Mo-V steel.

specimen. To accurately measure the size of the plastic deformation zone, the hardness trend graph is shown in Fig. 8. The hardness value of the lower shelf fracture remains largely unchanged at 232 $HV_{0.3}$. The impact fracture of the ETT region shows that the hardness value is relatively stable in the elastic zone away from the fracture. And the hardness value has a large change in the plastic zone. The hardness of the specimen in the transformation zone changes from $232HV_{0.3}$ to 241 $HV_{0.3}$ at 4.5 mm from the fracture. The upper shelf fracture has a similar phenomenon, except that the length of the plastic deformation zone changes from 4.5 mm to 7.0 mm. Figure 8 shows that the plastic deformation zone of the specimen becomes increases with the temperature increases. The largest plastic deformation zone at the upper shelf with a length of approximately 7 mm. The hardness test results match the prediction of the ductile-brittle transition temperature curve for Ni-Cr-Mo-V steel, which with the largest plastic deformation zone in the upper shelf region.

3.2 Numerical Simulation

The GTN model is widely used to simulate ductile damage fracture of metals, and it is one of the most classic models in damage dynamics. The complete GTN model with the following Eqs. (2):

$$\Phi = (\frac{\sigma_{eq}}{\sigma_m})^2 + 2\,q_1 f^* \cosh(q_2\,\frac{3}{2}\frac{\sigma_h}{\sigma_m}) - (1 + q_3 f^{*2}) = 0 \tag{2}$$

where q_1, q_2, q_3, f^* are the correction parameters. The void volume fraction f^* affects the growth, nucleation and coalescence of the material. The functional relationship is as
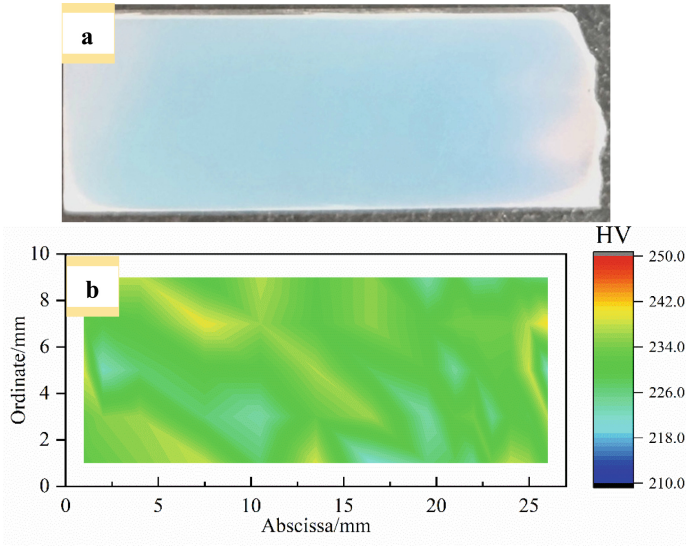
Fig. 5. The hardness distribution of the impact fracture at the lower shelf. a) impact fracture, b) The hardness distribution graph.
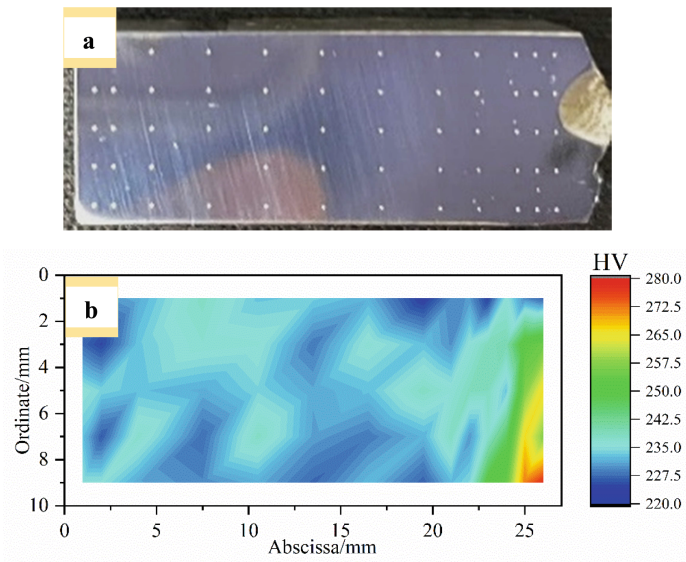
Fig. 6. The hardness distribution of the impact fracture at −55 °C. a) impact fracture, b) The hardness distribution graph.
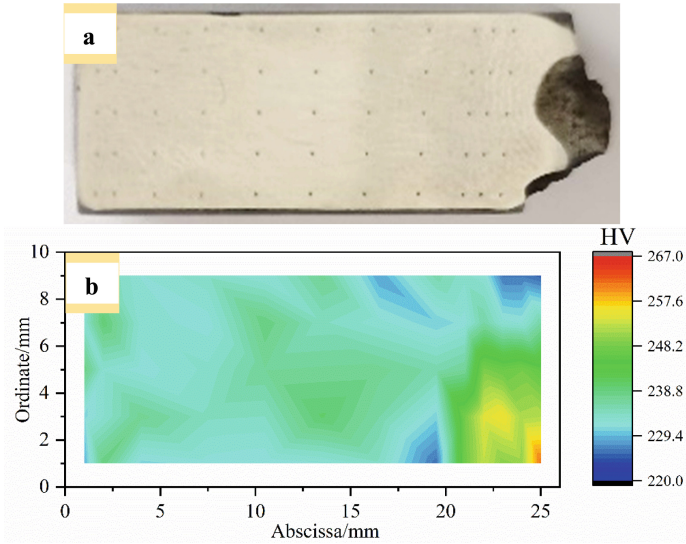
Fig. 7. The hardness distribution of the impact fracture at the upper shelf. a) impact fracture, b) The hardness distribution graph.

follows (3):

$$f^* = \begin{cases} f & f_0 \leq f \leq f_c \\ f_c + \frac{(f_u^* - f_c)}{(f_F - f_c)}(f - f_c) & f_c < f \leq f_F \end{cases} \tag{3}$$

where f_u^* is the ultimate value of the damage parameter, f_0 is the initial void volume fraction, f_c is the critical void volume fraction, f_F is the final void volume fraction. The equation shows that the material has certain microvoids in the GTN model. With the increase of plastic deformation, the void volume fraction reaches the critical value f_c, at which time the microvoids coalesce. When the void volume fraction further coalescence to f_F, the material will fracture. At this time, the material appears a lost load-bearing capacity. The failure element will be deleted.

The damage evolution of the material in the GTN model exists mainly in two forms, the growth of the initial voids f_g and the nucleation of new voids f_{nu}. Therefore, the change of the void volume fraction of the material is also dominated by these two components, as shown in (4):

$$df = df_g + df_{nu} \tag{4}$$

$$df_g = (1 - f) d\varepsilon^p : I \tag{5}$$

$$df_{nu} = \frac{f_N}{S_N \sqrt{2\pi}} \exp\left[-\frac{1}{2}\left(\frac{\varepsilon^p - \varepsilon_n}{S_N}\right)^2\right] d\varepsilon^p \tag{6}$$
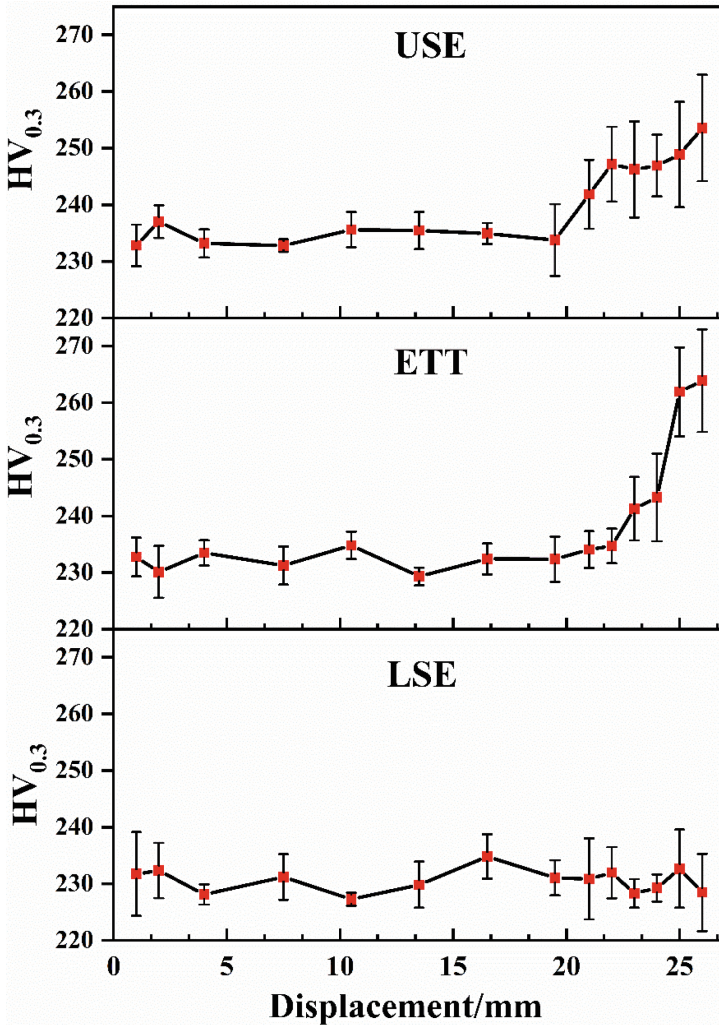
Fig. 8. The hardness trend of the impact fracture at different temperatures region.

where ε^p is the equivalent plastic strain of the material, f_N is the volume fraction of void nucleation, ε_n is the mean strain for void nucleation, S_N is the corresponding standard deviation of void nucleation.

The requirements of the GTN model include the inherent material parameters. There are nine undetermined parameters to be determined which are q_1, q_2, q_3, f_0, f_N, f_c, f_F, ε_n, S_N. Considering the symmetry of the Charpy impact specimen structure and load, the model is established with 1/2 of the thickness direction of the Charpy impact specimen. The symmetry constraint boundary conditions were given at the cross-section. The impact results have shown that Ni-Cr-Mo-V steel has the largest absorbed energy and the greatest plastic deformation zone of the fracture in the upper shelf. To ensure that

the size of the insertion section of the reconstituted specimen satisfies the reconstitution technique. The numerical simulations should be carried out for the upper shelf. The load-displacement curve obtained from the simulation was compared with the experimental curve. The two curves should be matched to accurately reproduce the impact process of the Ni-Cr-Mo-V steel. The GTN damage model parameters were finally determined, as shown in Table 1. The hammer tup and anvil of the model are set as rigid structures with a material density is 7.8×10^3 kg/m^3, Young's modulus is 210 GPa and the Poisson's ratio is 0.3. The parameters obtained from the tensile test and the required for the impact model are shown in Table 2.
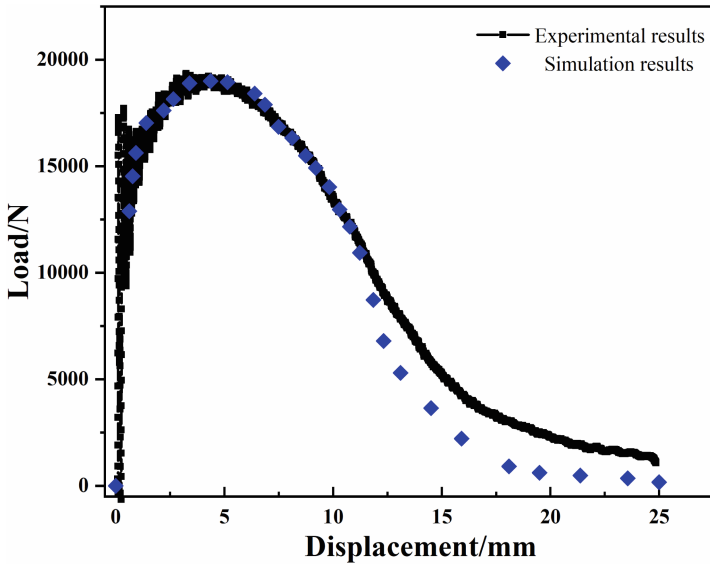
Fig. 9. The load-displacement graph of the Charpy impact and simulation results on the upper shelf.

At the end of the simulation of the impact process, the load-displacement graph was obtained. Figure 9 shows that the simulation results are consistent with the overall trend of the impact test. The simulation model better reproduces the impact of the Ni-Cr-Mo-V steel on the upper shelf. The cloud diagram of the plastic deformation zone of the upper shelf fracture is shown in Fig. 10. The figure shows that the plastic deformation of the broken specimens on both sides of the notch is symmetrically distributed, which is consistent with the theoretical reasoning of fracture mechanics. The cloud has a similar deformation distribution to the hardness distribution shown in Fig. 7b. The graph shows that the greatest plastic deformation where the hammer tup touches. There is no plastic deformation in the region of the V-notch, which the stresses from the impact are released near the V-notch. The maximum plastic deformation size of the upper shelf fracture can be determined from the outermost contours of the plastic cloud in the numerical simulation. Figure 10 shows that the maximum length of the plastic deformation zone at the upper shelf is approximately 7 mm, which also corresponds to the hardness results.
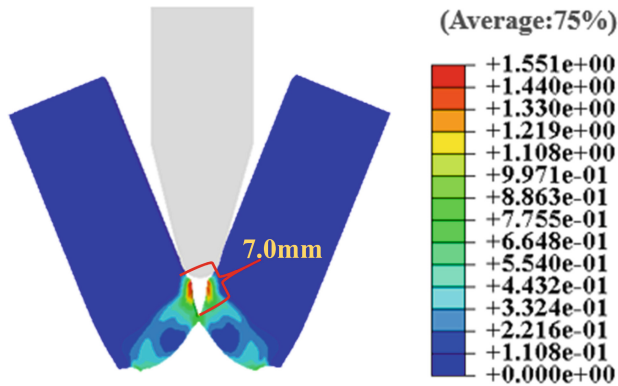
Fig. 10. The cloud diagram of the plastic deformation on the upper shelf.

Table 1. GTN model parameters.

Parameters	q_1	q_2	q_3	ε_n	S_N	f_0	f_N	f_c	f_F
Value	1.5	1.0	2.25	0.3	0.1	0.0002	0.0011	0.10	0.12

Table 2. The impact model parameters.

Parameters	Material density	Young's modulus	The Poisson's ratio	Yield Strength	The initial velocity of the tup	Friction coefficient	Time
Value	7.8×10^3 Kg/m^3	128GPa	0.28	498 MPa	5.2 m/s	0.2	0.006 s

3.3 Insert Length

To accurately measure the mechanical properties of the reconstituted specimen, the reconstituted specimen should reflect the properties of the virgin specimen, which requires that the central portion should avoid the plastic deformation zone. Finally, the broken specimen on the upper shelf was selected for the simulation. The hardness test results are consistent with the simulation results. The plastic deformation zone of the Ni-Cr-Mo-V steel in the upper shelf region is about 7.0 mm. Ultimately, the insert length of the Charpy reconstituted specimen of the Ni-Cr-Mo-V steel was determined to be 20 mm, which conforms to the technical specification for reconstituted specimens, as shown in Fig. 11.
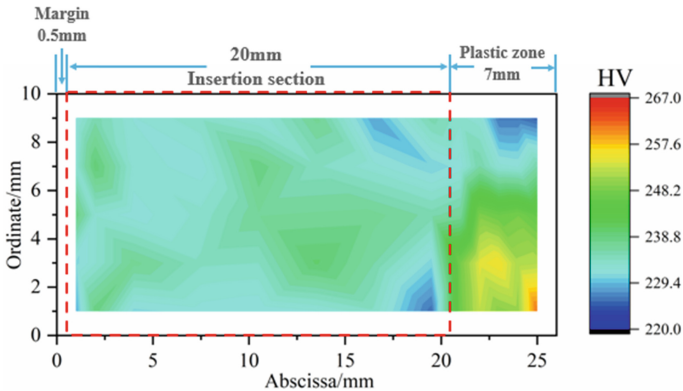
Fig. 11. The insertion section sampling specification of the Charpy reconstituted specimen.

4   Conclusions

The main purpose of the paper is the reconstituted specimens of Ni-Cr-Mo-V steel to obtain more specimen data in response to the scarcity of irradiation surveillance specimens. After obtaining the DBTT curve, the impact fractures at different temperatures are also obtained. The DBTT of the Ni-Cr-Mo-V steel is $-72\,°C$. The conclusion shows that the Ni-Cr-Mo-V steel has better ductility. The hardness test is carried out on the impact fractures of the different temperature regions. The length of the plastic deformation zone in the ETT region is 4.5 mm. But the length of the plastic deformation zone in the USE region is 7.0 mm. The hardness test results show that the plastic deformation zone of the Ni-Cr-Mo-V steel becomes increases with the temperature increases. In addition, the finite element numerical simulation of the impact process in the upper shelf was carried out by ABAQUS. The GTN (Gurson-Tvergaard-Needleman) fine damage model was established based on the reverse finite element method. The numerical simulation results compared with Charpy impact results to determine the GTN model parameters. The maximum plastic deformation zone of the simulation results is approximately 7.0 mm, which is consistent with the hardness test results. The insertion section size of the Ni-Cr-Mo-V steel reconstituted specimen was determined to be 20 mm, which provided data basis for the insertion section sampling specification of the Charpy reconstituted specimen.

References

1. Odette, G.R., Lucas, G.E.: Embrittlement of nuclear reactor pressure vessels. J. Miner. **53**(7), 18–22 (2001)

2. Luigi, D., Filippo, S.: Integrity of reactor pressure vessels in nuclear power plants: assessment of irradiation embrittlement effects in reactor pressure vessel steels. Int. At. Energy Agency (2009)

3. Margolin, B., Etsova, V.S.: Radiation embrittlement modeling in multi-scale approach to brittle fracture of RPV steels. Int. J. Fract. **179**, 87–108 (2013)

4. Sun, X., Yao, J., Chai, G., et al.: Thickness effects of base wall and inlet pipe on the structural integrity of reactor pressure vessels considering ductile-to-brittle transition. Eng. Fail. Anal. **105**, 1032–1044 (2019)

5. Odette, G.R., Yamamoto, T., Williams, T.J., et al.: On the history and status of reactor pressure vessel steel ductile to brittle transition temperature shift prediction models. J. Nucl. Mater. **526**, 151863 (2019)

6. Bezdikian, G.: Nuclear PWR plants life management reactor pressure vessel strategy evaluation for fluence in relation with integrity assessment. In: ASME 2008 Pressure Vessels and Piping Conference (2008)

7. Xing, R., Yu, D., Xie, G., et al.: Effect of thermal aging on mechanical properties of a bainitic forging steel for reactor pressure vessel. Mater. Sci. Eng. A **720**(21), 169–175 (2018)

8. ASTM E1253-07: Standard Guide for Reconstitution of Irradiated Charpy-Sized Specimens

9. Backer, F.D., Gutierrez-Solana, F.: Influence of the specimen configuration and the insert material on fracture toughness characterisation with reconstituted specimens. Nucl. Eng. Des. **188**(2), 231–240 (1999)

10. May, J., Rouden, J., Efsing, P., et al.: Extended mechanical testing of RPV surveillance materials using reconstitution technique for small sized specimen to assist Long Term Operation Extended mechanical testing of RPV surveillance materials using reconstitution technique for small sized specimen (2015)

11. Walle, E.V., Scibetta, M., Valo, M.J., et al.: Reconstitution techniques qualification and evaluation to study ageing phenomena of nuclear pressure vessel materials (RESQUE). Nucl. Eng. Des. **209**, 67–77 (2001)

12. Gérard, R., Chaouadi, R.: Reactor pressure vessel surveillance programs in Belgium (2018)

13. Yamashita, N., Iwasaki, R., Dozaki, R., et al.: Industry practice for the neutron irradiation embrittlement of reactor pressure vessels in Japan. J. Eng. Gas Turbines Power **132**(10), 102919.1–102919.8 (2010)

14. Mcclintock, F.A.: Challenges in fracture mechanics. Dev. Mech. **5**, 905–919 (1969)

15. Yildiz, R.A., Yilmaz, S.: Experimental investigation of GTN model parameters of 6061 Al alloy. Eur. J. Mech. A. Solids **83**, 104040 (2020)

16. Pirondi, A., Bonora, N.: Modeling ductile damage under fully reversed cycling. Comput. Mater. Sci. **26**, 129–141 (2003)

17. Gurson, A.L.: Continuum theory of ductile rupture by void nucleation and growth: part I-yield criteria and flow rules for porous ductile media. J. Eng. Mater. Technol. **99**(1), 297–300 (1977)

18. Tvergaard, V.: On localization in ductile materials containing spherical voids. Int. J. Fract. **18**(4), 237–252 (1982)

19. Tvergaard, V., Needleman, A.: Analysis of the cup-cone fracture in a round tensile bar. Acta Metall. **32**(1), 157–169 (1984)

20. Chu, C.C., Needleman, A.: Void Nucleation effects in biaxially stretched sheets. J. Eng. Mater. Technol. **102**(3), 249–256 (1980)

21. Marouani, H., Aguir, H.: Identification of material parameters of the Gurson-Tvergaard-Needleman damage law by combined experimental, numerical sheet metal blanking techniques and artificial neural networks approach. Int. J. Mater. Form. **5**(2), 147–155 (2012)

22. Zhang, Y., Jar, P.B., Xue, S., et al.: Numerical simulation of ductile fracture in polyethylene pipe with continuum damage mechanics and Gurson-Tvergaard-Needleman damage models. Proc. Inst. Mech. Eng. Part L J. Mater. Des. Appl. **233**(12), 2455–2468 (2019)
23. Bambach, M., Imran, M.: Extended Gurson-Tvergaard-Needleman model for damage modeling and control in hot forming. CIRP Ann. Manuf. Technol. **68**(1), 249–252 (2019)

Research on Atmospheric Dispersion Factor Used in the Calculation of Emergency Planning Zone

Qun Cao[1] and Lin Qiu[2(✉)]

[1] Nuclear Science and Technology, China Nuclear Power Engineering Co. Ltd., Beijing, China
[2] Radiation Protection and Nuclear Emergency, China Nuclear Power Engineering Co. Ltd., Beijing, China
qiulin@cnpe.cc

Abstract. Reasonable division of emergency planning zones is an important technical basis for emergency preparedness and responses. In order to evaluate the size of the emergency planning zone, it's important to determine the appropriate atmospheric dispersion factor based on the realistic site conditions to calculate the dose consequences caused by the accident through the radioactive plume. This paper introduces the current progress in the calculation of emergency planning zoning for different reactor nuclear power plant sites, the general method of determining the emergency planning zone in China and puts forward the method for optimizing the calculation of the atmospheric dispersion factor used in the emergency planning zoning for HPR1000 nuclear power plant site. Based on the theoretical analysis and comparison of the current main calculation models of atmospheric dispersion factor, this paper is devoted to the feasibility analysis of use of Gaussian puff models in the EPZ calculation considering the light wind and the calm wind condition, which can obtain the convergence results. This model can fully consider the dispersion process, spatial variation of meteorological fields, topographic effects and accumulation of pollutants and greatly improve the calculation accuracy. To solve the problems of low calculation speed brought by Gaussian puff models used in the EPZ calculation, the paper makes a theoretical analysis of the current main weather sampling methods and puts forward the stratified random sampling method to improve the speed of EPZ calculation. This method can select representative weather samples from the annual weather sequences to represent the annual situation so as to speed up the calculation without affecting the calculation accuracy.

Keywords: Emergency Planning Zone · Atmospheric Dispersion Factor · Weather Sampling · Stratified Sampling · Weather Classification

1 Introduction

Emergency planning zone refers to the area around the nuclear power plant which has emergency plans and emergency preparedness so as to take effective protective actions to protect the public in case of a nuclear accident. The aim of establishing emergency

planning zone is to divide the zone that requires protection measures in advance and make emergency preparedness in this zone so as to take intervention actions in the event of an accident at the nuclear power plant, protect the public and reduce the harm to the public and the environment [1]. Reasonable division of emergency planning zone is an important technical basis for making emergency plans.

HPR1000 is the third generation nuclear reactor researched and developed by CNPE (China Nuclear Power Engineering Company) independently, which has active and passive safety features. The research on the division of emergency planning zone for HPR1000 nuclear power plant site is helpful to the subsequent optimization work for HPR1000. Based on the current main calculation models of atmospheric dispersion factor and the current main weather sampling methods, this paper puts forward the optimization method of emergency planning zones for HPR1000 nuclear power plant site.

2 Calculation and Division of Emergency Planning Zones at Home and Abroad

2.1 Calculation of Emergency Planning Zones Abroad

D. W. Hummel et al. [2] calculate atmospheric dispersion factors, dose consequences and the reasonable size of emergency planning zone of small modular reactors including high temperature gas-cooled reactor, molten salt reactor, lead cooled fast reactor and small pressurized water reactor using ADDAM and compare the calculation results with the calculation results of emergency planning zones for CANDU 6 under the USBO accident. The calculation results show that the dose consequences of small modular reactors are much smaller than that of CANDU 6. A relatively smaller emergency planning zone can be chosen for small modular reactors. Mazzammal Hussain et al. [3] calculate dose consequences of 10 MW nuclear research reactor using InterRAS developed by IAEA. The calculation considers accidents of 61 m high reactor source release and ground release and selects constant weather conditions. The calculation results are consistent with the dose consequences of PARR-1 calculated by Hotspot and meet the standard for emergency planning zone of IAEA and PAK/914.

2.2 Calculation of Emergency Planning Zones at Home

Luo Haiying et al. [4] calculate dose consequences of emergency planning zone of Taishan Nuclear Power Plant which adopts the third generation EPR using MACCS2. The calculation considers three design basis accidents including large loss of coolant accident, steam generator tube rupture and fuel operation accident and selects the hourly weather data. The calculation results show that the radius of the emergency planning zone of Taishan Nuclear Power Plant is less than 0.5 km, which is consistent with the design goal of EPR. Considering social conditions and the public psychology near Taishan Nuclear Power Plant, the inner radius of the emergency planning zone of Taishan Nuclear Power Plant is recommended to be 4 km and the outer radius is recommended to be 7 km. Huang Ting et al. [5] select some coastal nuclear power plant site which adopts AP1000, calculate the atmospheric dispersion factor using PAVAN and calculate the dose

consequences using MACCS. The calculation considers large loss of coolant accident and core melt release accident and selects the hourly weather data. The calculation results show that the inner radius of the emergency planning zone of the AP1000 nuclear power plant site is recommended to be 3 km and the outer radius is recommended to be 7 km. Yu Fei et al. [6] select some underground nuclear power plant site, consider large loss of coolant accident and calculate the atmospheric dispersion factor using Hotspot. The calculation results are compared with the intervention level in GB18871-2002. The results show that the dose level at any distance outside the underground nuclear power plant is far less than the standard value.

2.3 Size of Emergency Planning Zones of Operating Nuclear Facilities at Home

Size of plume emergency planning zone is generally determined within a radius of 10 km with the reactor as the center according to the thermal power of the reactor, the inner zone of the plume emergency planning zone is generally determined within a radius of 5 km with the reactor as the center. Size of ingestion emergency planning zone should be determined according to the radiation consequences of the accident and can be determined according to the actual radiation monitoring results during emergency response. Sizes of emergency planning zones of current nuclear power plants in China are shown in Table 1 [1, 7].

Table 1. Sizes of Emergency Planning Zones for operating Nuclear Power Plants in China

Name of nuclear power plant	Radius of plume emergency planning zone/km	Radius of ingestion emergency planning zone/km
Guangdong Daya Bay/Ling'ao Nuclear Power Plant	Inner: 5 Outer: 10 Preventive protective action zone: 3	50
Zhejiang Qinshan Nuclear Power Plant	Inner: 3 Outer: 7	30
Jiangsu Tianwan Nuclear Power Plant	Inner: 4 Outer: 8	30

The data in Table 1 can be used as a reference for the subsequent calculation and optimization of the emergency planning zone of HPR1000 nuclear power plant site. The general method of determining the emergency planning zone and the optimization method of HPR1000 nuclear power plant site are introduced below.

3 General Method for Determining Emergency Planning Zone [8]

The process of determining emergency planning zone of nuclear power plant is shown in Fig. 1:

(1) Determine the accident type and source type, weather data, weather sampling methods and atmospheric dispersion factors.

(2) Calculate the expected dose that the accident may cause to the public through the passing plume and the dose that can be prevented after taking specific protective actions and estimate the contamination level of contaminated food and drinking water.

(3) Compare the calculated dose level and contamination level with the general optimization intervention level or action level in GB18871-2002 [9] and determine the size of the emergency planning zone. Ensure that the public dose and contamination level of contaminated food and drinking water caused by the accident are lower than the corresponding general optimization intervention level and action level.

When calculating the dose consequences caused by the accident through passing plume, it is necessary to determine the appropriate atmospheric dispersion factor according to the actual working conditions and evaluation purposes. Based on the determination of atmospheric dispersion factor, the optimization method of emergency planning zone for HPR1000 nuclear power plant site is put forward below.
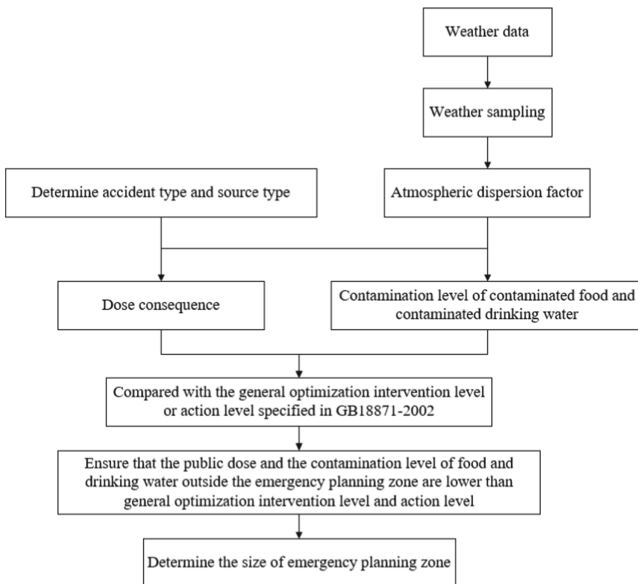
Fig. 1. Process of determining emergency planning zone

4 Introduction and Comparison of Different Calculation Models of Atmospheric Dispersion Factors

In the evaluation of consequence of nuclear power plant accidents, the calculation mode of atmospheric dispersion factor depends on the evaluation purpose. In this section,

the current main calculation models of atmospheric dispersion factor are introduced and analyzed. The optimization idea of emergency planning zone of HPR1000 nuclear power plant site under the light wind and the calm wind condition is put forward.

4.1 RG1.145 Model

RG1.145 model is based on Gaussian plume model, that is, the radioactive material is normally distributed about the plume axis in the atmosphere, it is assumed that the plume between the release point and points at all distances where the X/Q value needs to be calculated is flat.

RG1.145 model realizes the transformation of atmospheric dispersion estimation from RG1.4 determinism to probability theory and introduces the important idea that dispersion conditions are related to orientation. At the same time, it considers building wake effect and plume wind vibration effect. It can make calculations under the ground source release and elevated release conditions. The model takes the joint frequency data of wind direction, wind speed and atmospheric stability of nuclear power plant site as input and calculates the atmospheric dispersion factor X/Q values of radioactive materials at the boundary of exclusion area boundary (EAB) and the outer boundary of the low population zone (LPZ) in different time periods and different locations under the design base accident conditions.

4.2 NUREG/CR-6331 Model

NUREG/CR-6331 model adopts linear Gaussian plume dispersion model, assuming that the release rate of contaminants is uniform and constant in the whole period, which is convenient for users to evaluate the accident consequences without fully understanding the accident release sequence.

ARCON96 based on NUREG/CR-6631 model can make calculations in the case of ground release, mixed release and elevated release and consider the influence of building wake effect on atmospheric dispersion factor in the case of ground release. The calculation result of mixed release is a simple superposition of that of ground release and elevated release and their respective proportions are determined by the ratio of the vertical outflow velocity of pollutants to the wind speed at the release height. The calculation result of elevated release will consider the downwash effect of the building and the influence of the height difference of the control room.

ARCON96 uses hourly weather data to calculate atmospheric dispersion factors and uses hourly results to calculate atmospheric dispersion factors in different periods from 2 h to 30 days to obtain cumulative percentage distribution, from which the value of 95% probability level is selected as the atmospheric dispersion factor value in each period.

4.3 NUREG/CR-4691 Model [10, 11]

NUREG/CR-4691 model adopts one-dimensional Gaussian linear plume model to simulate atmospheric transport, dispersion and deposition of radioactive materials, considers physical and chemical phenomena including building wake effect, plume rise, dry/wet

deposition, radioactive decay and resuspension and finally obtains the atmospheric dispersion factor X/Q values of different probability levels on the downwind axis of plume at different distances from the center of the nuclear power plant site (such as mean, 50th, 90th, 95th, 99.5th, etc.).

Gaussian linear plume model regards the release of radionuclide as a continuous point source and assumes that the contaminant concentration is normally distributed in the vertical and horizontal directions when weather conditions (such as wind direction, wind speed, stability, etc.) do not change with time and distances, as shown in Formula (1):

$$C(x, y, z) = \frac{Q}{2\pi \bar{u}\sigma_y \sigma_z} \cdot \exp\left[-\frac{y^2}{2\sigma_y^2}\right] \cdot \exp\left[\frac{-(z-h)^2}{2\sigma_z^2}\right] \tag{1}$$

where:

$C(x, y, z)$: the time integrated air concentration (Bq $\cdot$ s/m^3);
Q: the quantity of radionuclides released (Bq);
$\bar{u}$: average wind speed (m/s);
h: release height (m);
σ_y, σ_z: horizontal and vertical dispersion parameters (m).

4.4 Lagrange Gaussian Puff Model [12, 13]

Lagrange Gaussian puff model is used widely in CALPUFF, which is based on unsteady Lagrange Gaussian puff dispersion model and simulates the dispersion, transformation and removal of puff on the moving path by tracking the movement of discrete puff released from the emission source until the puff leaves the simulation area. In addition, changes in time and space of weather conditions are considered in the process of puff dispersion. An important role of unsteady dispersion is that puff can change its moving path with the change of wind direction. In the process of movement, the puff responds to the surface characteristics changing with space, such as surface roughness, soil moisture content, etc.

The CALPUFF Modeling System includes three main modules: CALMET, CALPUFF and CALPOST. CALMET is a meteorological model, which develops wind and temperature fields on a three-dimensional gridded modeling domain and simultaneously develops two-dimensional fields including mixing height, surface characteristics and dispersion properties. CALPUFF is a transport and dispersion model which advects puffs of material emitted from sources and simulates dispersion and transformation processes along the way. CALPUFF uses fields changing with time and space generated by CALMET. The primary output files from CALPUFF include concentration fields or deposition fluxs. CALPOST is used to process postprocess modules of output files, produces time series files, count the maximum value of concentration and the exceeding rate of some certain threshold concentration, etc.

CALPUFF has two kinds of puffs: the Gaussian puff with isotropic distribution and the puff stretched along the wind direction. CALPUFF can choose either puff or the mixed simulation method to make full use of the advantages of the two puffs.

The unsteady process of the puff model is based on the theory that the contaminant concentration at a certain point in space is the superposition result of dispersion contributed by the continuously released puffs. Formulas describing the concentration contribution of a certain puff at a certain receptor point are shown in Formula (2) and Formula (3):

$$C = \frac{Q}{2\pi\,\sigma_x\sigma_y} g \exp\left[-d_a^2/\left(2\sigma_x^2\right)\right]\exp\left[-d_c^2/\left(2\sigma_y^2\right)\right] \tag{2}$$

$$g = \frac{2}{(2\pi)^{1/2}\sigma_z}\sum_{n=-\infty}^{\infty}\exp\left[-(H_e+2nh)^2/\left(2\sigma_z^2\right)\right] \tag{3}$$

where:

C: ground concentration (g/m^3);

Q: the quantity of contaminant (g);

$\sigma_x, \sigma_y, \sigma_z$: dispersion parameters (m) in longitudinal horizontal, transverse horizontal and vertical directions;

d_a, d_c: the distance (m) between the longitudinal puff center and the transverse puff center and the receptor;

g: the vertical term (m) in the Gaussian equation;

H_e: the effective height (m) from the center of the puff to the ground;

h: mixing height (m);

The sum term in g represents multiple reflections between the top of the mixed layer and the ground. When $\sigma_z > 1.6\ h$, the mixed layer is nearly uniform in the vertical direction.

In the medium distance scale transmission, the piecewise change of the puff volume in the sampling step is small and the integral puff can meet the calculation requirements. When dealing with local scale problems, the integrated puff may not meet the requirement because some puffs may grow very fast.

Stretched puffs can be used to deal with local scale air contamination because stretched puffs can reflect the influence of contamination source on the near field. Stretched puffs can be regarded as a group of overlapping puffs with small separation distances. The concentration contribution of a stretched puff is shown in Formula (4) and Formula (5):

$$C(t) = \frac{Fq}{\sqrt{2\pi}\,u'\sigma_y} g \exp\left[\frac{-d_c^2}{2\sigma_y^2}\frac{u^2}{u'^2}\right] \tag{4}$$

$$F = \frac{1}{2}\left\{erf\left[\frac{d_{a2}}{\sqrt{2}\sigma_{y2}}\right] - erf\left[\frac{-d_{a1}}{\sqrt{2}\sigma_{y1}}\right]\right\} \tag{5}$$

where:

u: vector average wind speed (m/s);

u': scalar wind speed ($u' = \left(u^2+\sigma_v^2\right)^{1/2}$, σ_v is the standard deviation of the wind speed);

q: source emission rate (g/s);

F: causal effect function;

g: the vertical term of the Gaussian equation;

d_c, d_a: the distance to the receptor from the position perpendicular to the axis of the stretched puff and the position along the direction of the stretched puff, footmarks 1 and 2 represent the old release point and the new release point, the footmarks without numbers represent the values defined on the receptor.

4.5   Comparisons of Atmospheric Dispersion Factor Models

RG1.145 and NUREG/CR-4691 are both based on Gaussian plume models while CALPUFF is based on Gaussian puff models, the comparison between them are shown in Table 2. When calculating atmospheric dispersion factors, Gaussian puff model will consider the dispersion process while Gaussian plume model assumes that the plume forms instantly at every point in the space without considering the dispersion process. Under the low wind speed conditions, the Gaussian plume model is still suitable while the calculation results of Gaussian plume model tend to be infinite when the wind speed approaches zero. Gaussian plume model will dynamically consider the spatial change of meteorological field and topographic effect while Gaussian plume model ignores them. Gaussian puff model will consider the accumulation of calculation results at every time point while the calculation results of Gaussian plume model at each time point are independent of each other.

Therefore, compared with the Gaussian plume model, CALPUFF based on Gaussian puff model is more suitable for the calculation of atmospheric dispersion factor under the light wind and the calm wind condition. When calculating the emergency planning zone of HPR1000 nuclear power plant site under the light wind and the calm wind condition, it is more appropriate to choose CALPUFF based on Gaussian puff model.

Table 2. Comparisons between Gaussian plume model and Gaussian puff model

	Gaussian puff model	Gauss plume model
Whether the dispersion process is considered	Yes	No
Whether the models is suitable under the low wind speed conditions	Yes	No
Whether the spatial change of meteorological field is considered	Yes	No
Whether the contaminant accumulation is considered	Yes	No

5   Weather Sampling

When calculating the atmospheric dispersion factor, it is necessary to consider the weather conditions according to the actual working conditions and determine the atmospheric stability, the wind speed, the wind direction and the rainfall intensity when an

accident occurs. According to the discussion in the previous section, it is appropriate to choose CALPUFF to calculate the atmospheric dispersion factor under the light wind and the calm wind condition. In order to consider the weather conditions throughout the year, CALPUFF uses the annual weather data to calculate hourly which can ensure the accuracy, but it takes a long time to calculate.

We can consider appropriate weather sampling methods which select representative weather data from the annual weather data to reduce the number of hours to be calculated. This part of weather data should represent the annual weather data: the error between the atomspheric dispersion factor value calculated by using this part of weather data and that calculated by using the annual weather data must be within a reasonable range. Therefore, by choosing the appropriate weather sampling methods, we can reduce the calculation time to optimize the calculation of atmospheric dispersion factor and the emergency planning zone of HPR1000.

5.1   Introduction to Different Weather Sampling Methods [14]

Weather sampling methods include the following three types: systematic sampling, simple random sampling and stratified random sampling [15]. Systematic sampling: determine the sampling starting point, the sampling interval and the sampling number, choose samples from the population in turn. Simple random sampling: the characteristics of the sampling population are completely ignored and the weather data are randomly selected with equal probability as the representative of the annual weather data. Stratified random sampling: divide the whole weather data into several subpopulations named layers, samples are chosen from each layer.

Compared with systematic sampling and simple random sampling, stratified sampling can fully consider various weather conditions, including those with low frequency but possibly causing serious accident consequences. For example, according to the actual working conditions and specific weather conditions, we can separate layers for those weather conditions that have a low frequency but may cause serious accident consequences so as to ensure that the weather conditions will be sampled during sampling. While simple random sampling and systematic sampling cannot do this. Therefore, maybe it is feasible to select stratified random sampling to optimize the calculation of the emergency planning zone of HPR1000 nuclear power plant site. Take the following typical stratified random sampling method of weather data as an example to briefly explain the stratified random sampling method.

5.2   Stratified Random Sampling of Weather Data

The current typical stratified sampling process of weather data is shown in Fig. 2.

(1) Determine the standard of stratifying weather data and the characteristics of weather data of each layer. A typical weather classification standard is shown in Table 3. The weather stratification standard includes 32 weather bins according to the influence of weather conditions on the accident consequences.

(2) According to the characteristics of weather data at each moment, divide the annual weather data into the corresponding weather bins. For example, the weather data of the first hour of the year, the atmospheric stability is A, the wind speed is 3 m/s, no rainfall, then the weather data at that moment should be put into weather bin 1.

(3) Sample weather data from each weather bin. The weather data chosen are used as weather input for calculating the atmospheric dispersion factor. If four weather data are sampled from each weather bin, 128 weather data are finally sampled. For the sake of simplification, simple random sampling can be adopted to sample weather data from weather bins.

The final calculated atmospheric dispersion factor value is the sum of the atmospheric dispersion factor values calculated under different weather conditions multiplied by the corresponding weights. For the weather data sampled from the ith weather bin, its weight is shown in Formula (6):

$$\frac{1}{K_i} \cdot \frac{N_i}{\sum\limits_{i=1}^{32} N_i} \tag{6}$$

where:

K_i: the number of weather data sampled from the N_ith weather bin, which is 4 in this example;

N_i: The total number of weather data contained in the ith weather bin.
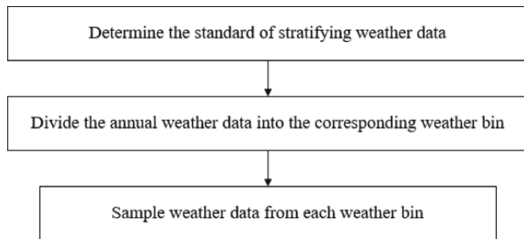
Fig. 2. The flow chart of stratified weather sampling

In addition, Hu et al. [15–17] improve the typical weather stratification standard and put forward the weather stratification standards applicable to China coastal nuclear power plant sites. For the optimization of the emergency planning zone of HPR100 nuclear power plant site, when adopting stratified random sampling to sample weather data as the weather input of CALPUFF, two problems need to be considered, which are to be solved in the follow-up research:

(1) Weather conditions of different nuclear power plant sites are different, so it's necessary to determine appropriate weather stratification standards according to the actual weather conditions of nuclear power plant sites.

Table 3. A typical weather classification standard

Weather bin number	Weather characteristics	Weather bin number	Weather characteristics
1	A-B, $u \leq 3$	17	The rainfall intensity in the interval (0, 10) is 1
2	A-B, $u > 3$	18	The rainfall intensity in the interval (10, 16) is 1
3	C-D, $u \leq 1$	19	The rainfall intensity in the interval (16, 24) is 1
4	C-D, $1 < u \leq 2$	20	The rainfall intensity in the interval (24, 32) is 1
5	C-D, $2 < u \leq 3$	21	The rainfall intensity in the interval (0, 10) is 2
6	C-D, $3 < u \leq 5$	22	The rainfall intensity in the interval (10, 16) is 2
7	C-D, $5 < u \leq 7$	23	The rainfall intensity in the interval (16, 24) is 2
8	C-D, $u > 7$	24	The rainfall intensity in the interval (24, 32) is 2
9	E, $u \leq 1$	25	The rainfall intensity in the interval (0, 10) is 3
10	E, $1 < u \leq 2$	26	The rainfall intensity in the interval (10, 16) is 3
11	E, $2 < u \leq 3$	27	The rainfall intensity in the interval (16, 24) is 3
12	E, $u > 3$	28	The rainfall intensity in the interval (24, 32) is 3
13	F, $u \leq 1$	29	The rainfall intensity in the interval (0, 10) is 4
14	F, $1 < u \leq 2$	30	The rainfall intensity in the interval (10, 16) is 4
15	F, $2 < u \leq 3$	31	The rainfall intensity in the interval (16, 24) is 4
16	F, $u > 3$	32	The rainfall intensity in the interval (24, 32) is 4

u: the initial wind speed (m/s)
The interval unit is km.
The unit of rainfall intensity is mm/h and the three breakpoints of rainfall intensity are 0.5, 2.5 and 15 mm/h.

(2) The weather input of CALPUFF is not the weather data at a certain moment, but a weather sequence containing the weather data changing with time and space. It is impossible to directly use the weather stratification standard to stratify the weather

sequences, feature extraction of weather sequences may be needed to meet the weather stratification standard.

6   Conclusion

(1)   This paper puts forward the optimization method of HPR1000 emergency planning zone calculation. Based on different calculation models of atmospheric dispersion factors, it is suggested that CALPUFF based on Gaussian puff model is appropriate under the light wind and the calm wind conditions. Based on different weather sampling methods, it is proposed to select stratified random sampling to sample weather data from the annual weather data as the weather input for calculating atmospheric dispersion factor, which can reduce the calculation time and ensure the calculation accuracy.

(2)   There are two problems needed to be solved in the follow-up research: how to determine appropriate weather stratification standards to reflect the actual weather conditions of the nuclear power plant site and how to extract the features of CALPUFF weather sequences to meet the weather stratification standards.

References

1.   Yue, H.: Nuclear Accident Emergency Preparedness and Response Manual. China Environmental Science Press (2012)
2.   Hummel, D.W., Chouhan, S., Lebel, L.: Radiation dose consequences of postulated limiting accidents in small modular reactors to inform emergency planning zone size requirements. Ann. Nucl. Energy **137**, 107062 (2020)
3.   Syed, W.A.A., Hussain, M.: Estimation of emergency planning zones (EPZs) for nuclear research using plume dispersion code. In: International Conference on Nuclear Engineering & the Asme Power Conference (2012)
4.   Luo, H., Wang, J., Li, W., et al.: Evaluation of emergency planning zone for EPR nuclear power unit in TSNPP. Nucl. Power Eng. **6**, 117–121 (2010)
5.   Huang, T., Qu, J., Hong, L., et al.: Preliminary study on plume emergency planning zone for AP1000. Atomic Energy Sci. Technol. **45**(12), 1472–1477 (2011)
6.   Fei, Y., Shun, Z.: Preliminary study on classification of plume emergency planning zone for underground nuclear power plant. Yangtze River **52**(S01), 219–221 (2021)
7.   GB/T 17680.1-17680.12, Criteria for Emergency Planning and Preparedness for Nuclear Power Plants
8.   Xia, Y.: Advanced Ionizing Radiation Protection Course. Harbin Engineering University Press (2010)
9.   GB18871-2002, Basic standards for protection against ionizing radiation and for the safety of radiation sources
10.   Alpert, D.J., Chanin, D.I., Helton, J.C., et al.: MELCOR accident consequence code system (MACCS) (1985)
11.   Code manual for MACCS2:Volume1, user's guide
12.   Zhang, Y.: Atmosphere dispersion research of accident source terms in nuclear power plant on CALPUFF. Shanghai Jiao Tong University (2010)

13. Hao, Z.: Experiments and Modelling of Atmospheric Dispersion over Complex Terrain. Peking University
14. Jin, Y., et al.: Sampling Technique. China Renmin University Press (2015)
15. Erbang, H., et al.: Candidates of weather sampling criterion suitable for meteorological condition in China. Radiat. Prot. Bull. **24**(2), 7 (2004)
16. Erbang, H., et al.: Comparative study of weather sampling schemes based on measuring meteorological data of Tianwan nuclear power plant. Radiat. Prot. **25**(3), 10 (2005)
17. Hu, E., et al.: Screening and comparison of weather sampling criteria in China using the least squares method. Radiat. Prot. Bull. **24**(6), 8 (2004)

Effects of Eluting Volumes to Isolation Efficiencies in Manual Synthesis of Ga-68 Labelled FAPI-04

Fei Jiang, Naiguo Xing, Taiyong Lv, Zhanliang Sun[✉], and Yan Zhao

Department of Nuclear Medicine, The Affiliated Hospital of Southwest Medical University, Luzhou, Sichuan, China
zsun@swmu.edu.cn

Abstract. Among different FAPIs (fibroblast activation protein inhibitors) developed for PET imaging, ^{68}Ga-FAPI-04 has demonstrated the most impressive properties with low nanomolar affinity to FAP, near-complete internalization of radioactivity bound to FAP, and rapid blood clearance. The application of ^{68}Ga-FAPI-04 has been extended to 28 different kinds of clinical cancer detection. The manual synthesis of ^{68}Ga-FAPI-04 is like other ^{68}Ga-labeling peptides, such as PSMA-11 and DOTATATE. However, because the radiochemical conversion (RCC) is about 90%, it is required to conduct a purification and isolation process to meet the required standard for clinical application. The purpose of this work is to characterize the increase of isolation efficiency (IE) by increasing the volume of eluting liquid applied to C18 columns and sterile filters. We designed an experiment and measured the residual activity distribution on both C18 columns and sterile filters for different eluting volumes. We characterized the change of activity residuals and isolation efficiencies with different eluting volumes in the process of purification and isolation. As a result, it was found that there were more activity leftovers on sterile filters than on C18 columns. By increasing the eluting volume from 6 mL to 12 mL, we measured the average IE being improved from 62.4% to 87.4%, which is greatly beneficial to clinical applications. In addition, the fluctuation of IE which might come from the different radiolabeling operators or materials used in the experiment, was also obviously decreased from 11.3% to 4.5%. This method has been proven to be efficient in the production of ^{68}Ga-FAPI-04.

Keywords: Radiopharmaceutical · FAPI-04 · Isolation efficiency · Quality control · Gallium-68

1 Introduction

In cancer-associated fibroblasts, one of overexpressed proteins is called fibroblast activation protein (FAP), which was applied by researchers to develop new PET tracers for various cancers. Among different FAP inhibitors developed for PET imaging, ^{68}Ga-FAPI-04 has demonstrated the most impressive properties with low nanomolar affinity to FAP, near-complete internalization of radioactivity bound to FAP, and rapid blood clearance.

Its first PET/CT demonstration in breast cancer patients was accomplished by Lindner et al. [1], whose work in the same group was prized the image of the year on 2019 Annual Meeting of the Society of Nuclear Medicine and Molecular Imaging (SNMMI).[2] The application of ^{68}Ga-FAPI-04 has been extended to 28 different kinds of clinical cancer detection [3, 4]. All these exciting achievements quickly triggered a clinical research wave on FAPI-04 imaging and therapy globally [5–7].

The work on ^{68}Ga-FAPI-04 clinical research has started since 2020 in Luzhou. There have been multiple works published on ^{68}Ga-FAPI-04 PET imaging, which ranges from case studies to systematic research [8–11].

The manual synthesis of ^{68}Ga-FAPI-04 is like other ^{68}Ga-labeling peptides, such as PSMA-11 and DOTATATE.[12] However, because the radiochemical conversion (RCC) is about 90%, it is required to conduct a purification and isolation process to meet the required standard for clinical application.

To the best of our knowledge, there has been no previous study on quantitively characterizing the effect of eluting volumes to isolation efficiency (IE) in the manual synthesis of ^{68}Ga-FAPI-04. The purpose of this work is to quantitively characterize the increase of IE by increasing the volume of formation liquid applied to elute the C18 column and the sterile filter.

We designed an experiment and measured the residual activity distribution on both C18 columns and sterile filters for different eluting volumes. From the measurements, we calculated IE with different eluting volumes. In addition, we characterized the change of activity residuals in the process of purification and isolation.

2 Materials and Methods

Ga-68 eluates were obtained from a ^{68}Ge/^{68}Ga generator with nominal activity 1850 MBq (ITG GmbH Germany) using 4 mL of 0.05 M HCl. FAPI-04 (60 µg, MedChemExpress LLC, China) was dissolved in 1 mL NaAc/HAc buffer (pH 4.0–5.0). The reaction mixture was incubated for 10 min at 95 °C (LAWSON DHS-100).

After the completion of radiolabeling, the reaction mixture passed over a C18 column (Sep-Pak Plus C18 Cartridge) and washed with 10 mL saline. The purified product was eluted with 1 mL 50-vol% ethanol followed by 5 mL saline and sterile filtered (Millex-GS, 0.22 µm) to get the final formulation. The activities of product, waste, and residuals on the C18 column and the sterile filter were measured with a dose calibrator (Capintec, CRC-55tR).

In order to study the effect of eluting volumes to IE, another 1 mL 50-vol% ethanol followed by 5 mL saline was applied to the C18 column and the sterile filter. For comparison, the activities of product, and residuals on the C18 column and the sterile filter were measured again by the dose calibrator.

The radiochemical purity (RCP) were determined by a radio-HPLC (LabAlliance). A C18 column (Agilent, ZORBAX Eclipse C18 Plus, 4.6 mm × 250 mm, 5 µm) was installed on the radio-HPLC. The gradient used mobile phase A and mobile phase B. Flow rate was 1 mL/min starting with 90% A to 10% A within 15 min.

This experiment was repeated by three different sophistic radio-labeling operators to suppress the effects caused by operators.

3   Results
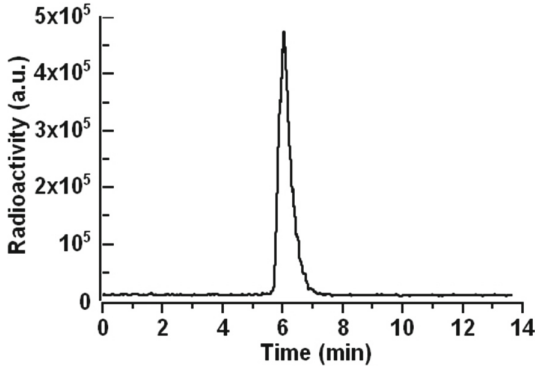
Fig. 1. The radio-HPLC results of purified ^{68}Ga-FAPI-04 product.

The radio-HPLC results of the purified product are shown in Fig. 1 with an RCP of 99.4%. The free ^{68}Ga peak appear near 2–4 min, which is not visible in the figure as a result of purification. The labeled ^{68}Ga-FAPI04 peak appears near 5–7 min.

In the process of purification and separation, the labeled ^{68}Ga-FAPI-04 normally could leave some percentages on C18 column and sterile filter. IE is calculated by,

$$IE = \frac{A_{product}}{A_{product} + A_{C18} + A_{filter}} \times 100\%$$

where $A_{product}$ is the activity of the product, A_{C18} is the residual activity on C18 column, and A_{filter} is the residual activity on sterile filter.

Similarly, the ratio of the C18 column residual over the labeled ^{68}Ga-FAPI-04, R_{C18}, and the ratio of sterile filter residual over the labeled ^{68}Ga-FAPI-04, R_{sf}, are also calculated for each eluting volume case. The results are listed in Table 1.

Table 1. The calculated IE, R_{C18} and R_{sf} based on 3 different experiments, in which the average value and the standard deviation are shown.

V(mL)	6	12
IE (%)	62.4 ± 11.3	87.4 ± 4.5
R_{C18} (%)	9.5 ± 4.5	3.4 ± 1.8
R_{sf} (%)	28.1 ± 7.9	9.3 ± 2.7

4   Discussion

From IE results, it was found that an obvious improvement was achieved by eluting the C18 column and the sterile filter twice. Although the volume of the product was

increased as two times, the ratio of the radioactivity over the eluting volume is dropped only to 70% because of more product eluted off the C18 column and the sterile filter. In general, it is preferable to achieve more product activity in the production of ^{68}Ga-FAPI-04, which means that more patients and better imaging results could be accomplished with one dose of production.

In addition, the standard deviation of IE representing the fluctuations was decreased by a factor of 2.5, from 11.3% to 4.5%. The fluctuations might come from the factor of different radiolabeling operators or the materials used in the experiment. In radiopharmaceutical production, the fluctuation should be reduced, which was also achieved by increasing the eluting volume.

In summary, the increase of eluting volume from 6 mL (1 mL 50-vol% ethanol followed by 5 mL saline) to 12 mL is more beneficial for clinical applications.

From the measurements, it was also found that more percentage of activity residual stays with the sterile filter than with the C18 column. There was about 3.0 times of ^{68}Ga-FAPI-04 activity left on the sterile filter as much as on the C18 column after the first eluting. This factor was changed to 2.7 after the second eluting, which was not much with the consideration of the standard deviations.
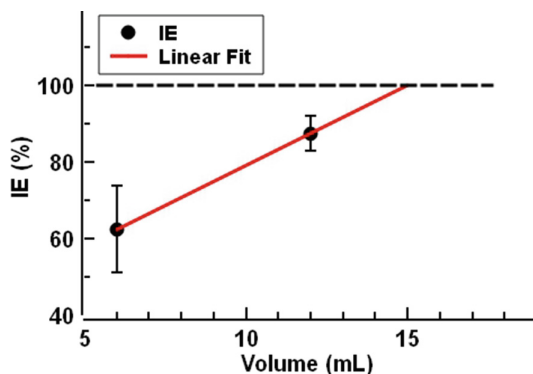
Fig. 2. IE changes with eluting volume.

Assuming a linear extrapolation (see Fig. 2), 100% of IE could be obtained at V = 15.0 mL, which might not be perfectly realized in practice, but would give a guidance on how much more one need to increase the eluting volume to gain more IE. For sure, the ratio of the radioactivity over the eluting volume will drop further down with the increase of the eluting volume.

5   Conclusion

In this work, we designed an experiment to quantitively characterize the change of manually labeled ^{68}Ga-FAPI-04 IE by enlarging the eluting volume from 6 mL (1 mL 50-vol% ethanol followed by 5 mL saline) to 12 mL. It was found that the average IE was increase from 62.4% to 87.4%, with the standard deviation dropped from 11.3% to

4.5%, which are beneficial to clinical applications in general. In addition, it was found that there was 3.0 times activity left on the sterile filter as much as on the C18 column. Assuming a linear extrapolation, the highest IE could be expected with a third eluting on the C18 column and sterile filter.

References

1. Lindner, T., Loktev, A., Altmann, A., et al.: Development of quinoline-based theranostic ligands for the targeting of fibroblast activation protein. J. Nucl. Med. **59**(9), 1415–1422 (2018). https://doi.org/10.2967/jnumed.118.210443
2. SNMMI Image of the Year: Novel radiotracer detects 28 cancer types. (2019) https://medicalxpress.com/news/2019-06-snmmi-image-year-radiotracer-cancer.html. Accessed 01 June 2022
3. Giesel, F.L., Kratochwil, C., Lindner, T., et al.: ^{68}Ga-FAPI PET/CT: biodistribution and preliminary dosimetry estimate of 2 DOTA-containing FAP-targeting agents in patients with various cancers. J. Nucl. Med. **60**(3), 386–392 (2019). https://doi.org/10.2967/jnumed.118.215913
4. Kratochwil, C., Flechsig, P., Lindner, T., et al.: ^{68}Ga-FAPI PET/CT: tracer uptake in 28 different kinds of cancer. J. Nucl. Med. **60**(6), 801–805 (2019). https://doi.org/10.2967/jnumed.119.227967
5. Calais, J.: FAP: the next billion dollar nuclear theranostics target? J. Nucl. Med. **61**(2), 163–165 (2020). https://doi.org/10.2967/jnumed.119.241232
6. Wang, S., Zhou, X., Xu, X., et al.: Dynamic PET/CT imaging of ^{68}Ga-FAPI-04 in Chinese subjects. Front. Oncol. **11**, 651005 (2021). https://doi.org/10.3389/fonc.2021.651005
7. Wang, J., Yang, W., Wang, J.: Research progress of new tumor imaging agent ^{68}Ga-FAPIs. Chin. J. Nucl. Med. Mol Imaging **41**(06), 374–377 (2021). https://doi.org/10.3760/cma.j.cn321828-20200313-00100
8. Liu, H., Wang, Y., Zhang, W., et al.: Elevated ^{68}Ga-FAPI activity in Splenic hemangioma and pneumonia. Clin. Nucl. Med. **46**(8), 694–696 (2021). https://doi.org/10.1097/RLU.0000000000003638
9. Zhou, Y., et al.: Value of [^{68}Ga] Ga-FAPI-04 imaging in the diagnosis of renal fibrosis. Eur. J. Nucl. Med. Mol. Imaging **48**(11), 3493–3501 (2021). https://doi.org/10.1007/s00259-021-05343-x
10. Deng, M., Chen, Y., Cai, L.: Comparison of ^{68}Ga-FAPI and ^{18}F-FDG PET/CT in the imaging of pancreatic cancer with liver metastases. Clin Nucl Med **46**(7), 589–591 (2021). https://doi.org/10.1097/RLU.0000000000003561

11. Wu, J., Wang, Y., Liao, T., et al.: Comparison of the relative diagnostic performance of [^{68}Ga]Ga-DOTA-FAPI-04 and [^{18}F]FDG PET/CT for the detection of bone metastasis in patients with different cancers. Front Oncol **11**, 737827 (2021). https://doi.org/10.3389/fonc.2021.737827

12. Zhao, Y., Sun, Z., Jiang, F., et al.: Study of problem checking in the radiosynthesis of ^{68}Ga-DOTATATE. J. Southwest Med. Univ. **44**(5), 576–583 (2021). https://doi.org/10.3969/j.issn.2096-3351.2021.05.024

Visualized Numerical Analysis of Fustar Reactor Based on Modelica Language

Xuan'ang He[1,2], Dalin Zhang[1] , and Xiang Wang[2(✉)]

[1] College of Nuclear Science and Technology, Xi'an Jiaotong University, Xi'an 710049, China
[2] College of Nuclear Science and Technology, Harbin Engineering University, Harbin 150001, China
xiang.wang@hrbeu.edu.cn

Abstract. FuSTAR is a new small fluoride-salt-cooled high-temperature reactor designed for the energy needs of remote western regions. The TRISO fuel and helical cruciform fuel elements used in FuSTAR and the integrated core design enables inherent safety. Modelica is a process description language based on object equations. It has key features such as non-causal expression and model reuse, which achieve repeatable visual modeling by connecting components. By modeling and simulating FuSTAR using the Modelica, studies were carried out under steady-state as well as multiple transients to understand the primary loop system response of FuSTAR under accident scenarios. The results show that the parameters of the primary loop system cannot exceed the safety limit with the insertion of step reactivity and after changing the size of the temperature coefficient of reactivity, the model can give a reasonable response.

Keywords: FuSTAR · Modelica · Transient Analysis · Inherent Safety

1 Introduction

FuSTAR, the integral inherently safe Fluoride-Salt-cooled high-Temperature Advanced Reactor, is a kind of molten salt reactor using the solid fuel, which belongs to Gen-IV reactor concepts. It is jointly designed by Xi'an Jiaotong University and Shanghai Nuclear Engineering Research and Design Institute, aiming to effectively meet the multi-purpose energy needs of industrial facilities in remote western China.

FuSTAR has a core power of 125 MW and uses TRISO pellet fuel in the core. In this fuel, the granular nuclear fuel is wrapped in graphite. The very high melting point of the graphite layer enhances the failure temperature of the fuel to a high level, which is considered inherent safe to the reactor. During the operation of the reactor, the first loop molten salt coolant (FLiBe) flushes the core with a certain flow rate to take away the heat generated by fission in the core. After flowing out from the upper chamber of the core, the coolant passes through three heat exchangers between the first loop and the second loop to transfer heat to the molten salt (FLiNaK) in the second loop. Next, after being pressurized by three main pumps installed inside the core, most of the FLiBe flows back into the core again, and a small part passes through the passive residual heat

removal system and then joins with the main flow of molten salt flowing out of the core, thus a closed cycle of the primary circuit is completed [1].

FLiNaK flows from the heat exchangers with obtained heat into the high-temperature molten salt pool to give heat to the energy conversion system, which converts the energy from heat to other forms of energy through the supercritical carbon dioxide cycle (Fig. 1).
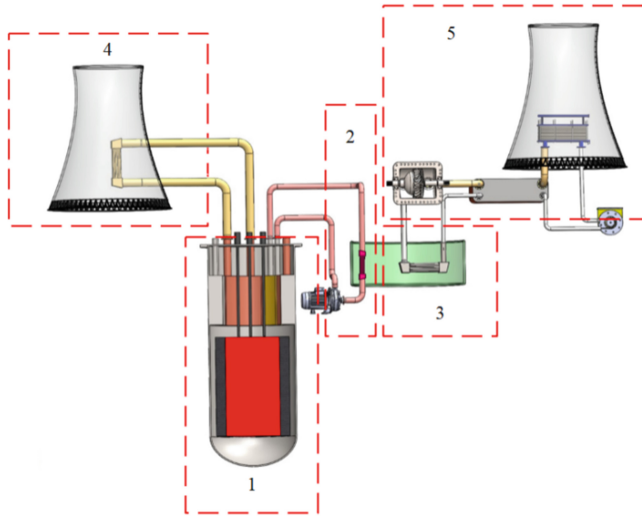
Fig. 1. The FuSTAR system (1- Reactor (the first loop); 2- The second loop; 3- Molten salt pool; 4- Passive residual heat removal system; 5- Energy conversion system).

2   Method and Modelling

The main purpose of this paper is to study the response characteristics of the first loop of FuSTAR. Therefore, the parts other than the primary loop system are simplified.

The energy conversion system and passive residual heat removal system are ignored. The flow of molten salt in the second loop is assumed to be constant, and it is assumed to flow into a node with constant pressure from a node with a constant temperature.

In the calculation of the core, using the point kinetics model, which is of 6 groups of delayed neutrons precursors (DNP) are as follows [2] (Table 1):

The equations involved are as follows:

$$\frac{dn(t)}{dt} = \frac{\rho(t) - \beta}{\Lambda} n(t) + \sum_{i=1} \lambda_i C_i(t) \tag{1}$$

$$\frac{dC_i(t)}{dt} = \frac{\beta_i}{\Lambda} n(t) - \lambda_i C_i(t) \cdots \cdots i = 1, 2, \cdots, 6 \tag{2}$$

The above does not consider as the reflector, the radial distribution of core power, etc.

Table 1. Kinetics Data of DNPs.

Precursor Group	Precursor Fractions β_{eff}	Decay Constant λ (s^{-1})
1	0.000221570	0.0124906
2	0.00114377	0.0317961
3	0.00110754	0.109529
4	0.00316699	0.317445
5	0.000949597	1.35253
6	0.000320846	8.67551

Modelica programming language is developed by Linköping University and it is a modern, strongly typed, declarative, and object-oriented language [5]. Modelica language is characterized by component-oriented and multi-disciplinary, making it able to simulate complex and dynamic systems. OpenModelica [6] is a free and open-source environment for Modelica language, and it provides facilities including debugging, optimization, visualization and plotting for Modelica program. In this paper, the DynamicPipe component in the Fluid library in OpenModelica is used to simulate each molten salt flow channel in the first loop of FuSTAR (among which, the Pipe component of the core part of FuSTAR is divided into ten nodes according to the axial direction); the valve component is used to integrate the local pressure loss in each flow channel of FuSTAR so that the simulation results of OpenModelica can be as close to the design parameters of FuSTAR as possible; the tank component is to simulate the pressurizer in FuSTAR; the pump component is to simulate the main pump; and in order to make the model more in line with the actual needs, the point kinetics model components and the axial distribution of the core power, the temperature feedback part, and the heat exchanger part of each Pipe component are added [3]. Finally, a schematic diagram of the model is shown in Fig. 2.

The physical property parameters are obtained by using OpenModelica.Media. Incompressible. Table Based to generate interpolation functions. The temperature coefficient of reactivity and the physical parameters of the related materials are shown in Table 2 and Table 3.

Table 2. Temperature coefficient of reactivity.

Medium	Temperature coefficient of reactivity (pcm/°C)
Fuel	−0.41
Molten salt coolant	−4.76

Table 3. Physical property parameters.

Physical parameters	Molten salt coolant
Density (kg/m^3)	2413.3–0.4884T
Specific heat capacity [J/(kg · K)]	2380.6
Viscosity (Pa · s)	0.000116exp(3755/T)
Thermal Conductivity [W/(m · K)]	1.1
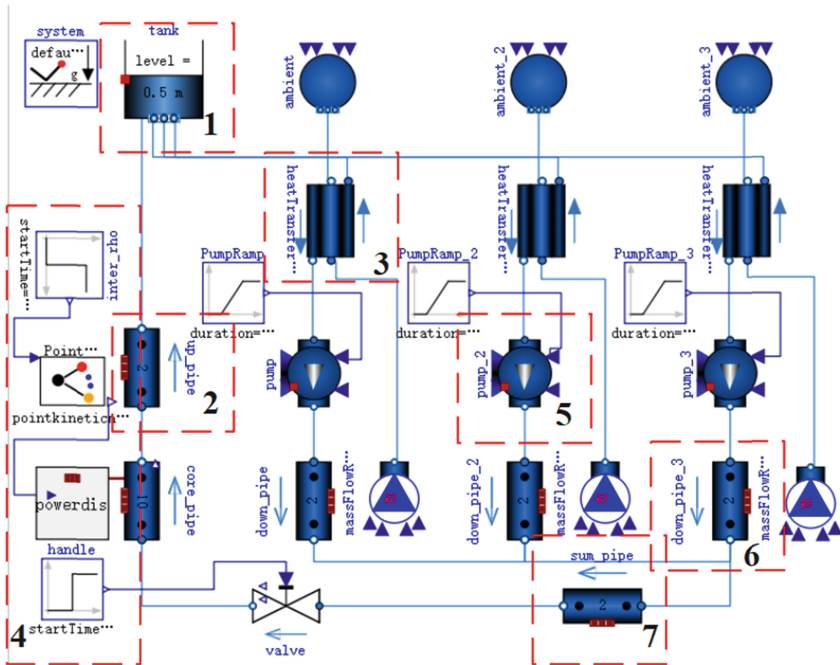
Fig. 2. Model diagrams in OpenModelica (1- Pressurizer; 2- Upper chamber; 3- Heat exchanger; 4- The point reactor model; 5- Pump; 6- Downpipe; 7- The lower chamber).

3 Results and Discussion

3.1 Steady-State Calculation

The steady-state model is simulated under the core power of 125 MW, and the calculated results are compared with the design parameters in Table 4. It shows that the steady-state results are in good agreement with the design parameters, and the transient calculation can be carried out based on this model and dataset.

Table 4. Comparison between calculated results and design parameters.

Parameter	Designed value	Calculated value	Relative deviation (%)
Core Power (MW)	125.00	124.79	0.168
Core inlet temperature (K)	923.15	924.87	0.186
Core outlet temperature (K)	973.15	974.93	0.183
Main circuit flow (kg/s)	1050.15	1041.18	0.854

3.2 Step Reactivity Insertion Transient Analysis

In the case that the steady-state results are verified, this paper gets the results under inserting 10 pcm, 50 pcm, and 100 pcm [4] of step reactivity into the core at t = 650 s. The temperature change in the molten salt coolant at the core exit, the change in the average temperature of the fuel, and the change in the core power after the insertion of the step reactivity are shown in Figs. 3, 4 and 5. Figure 6 is an image of changes in Core Power and Heat removed from the second loop under the insertion of 100 pcm step reactivity, and Fig. 7 is the temperature of the molten salt of the second loop at the outlet of the heat exchanger. Figure 8 shows the temperature change in the fuel center at the node with the highest power in the core (the hottest spot).
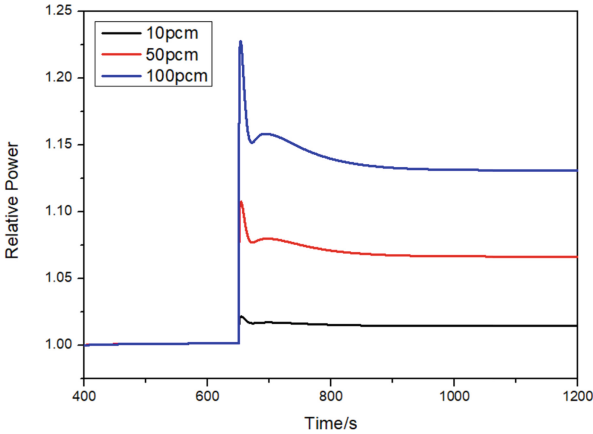
Fig. 3. Transient change in relative power.

As can be seen in Fig. 3, after the step reactivity is inserted, the change in the core power can be divided into three stages: In the first stage, the power increases rapidly and then decreases rapidly; in the second stage, there is an increasing process for a short period; in the third stage, the system reaches a steady state again. For other images, there are three such processes. For example, the temperature change of the molten salt coolant at the core exit shown in Fig. 5, it can be seen that the coolant temperature first increased rapidly, then decreased with a very small amplitude, and finally increased slowly to reach the final steady state.
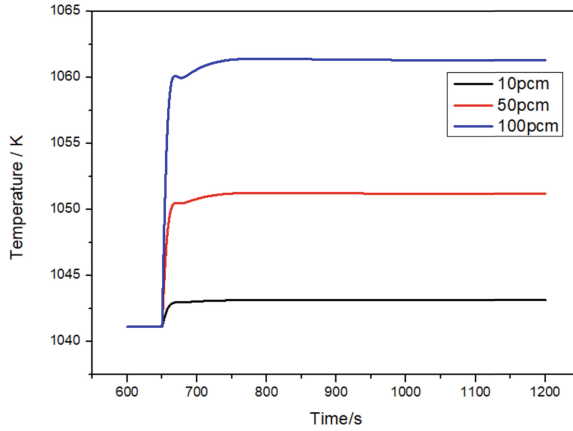
Fig. 4. Transient change in the average temperature of the fuel.
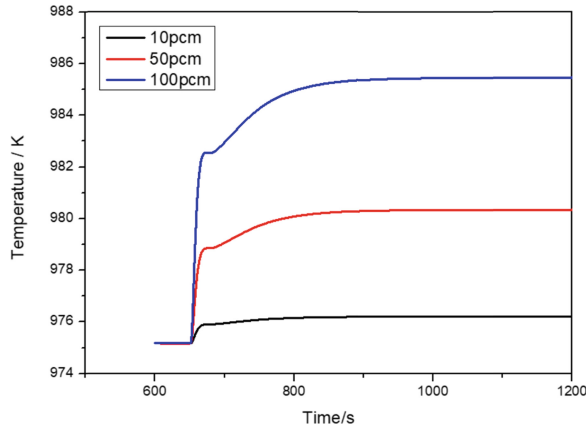
Fig. 5. Coolant salt temperature change at the core outlet.

For such a changing image, it is necessary to analyze the characteristics of the system and how the step input influence on the system. The following analysis is performed in the order of the three stages of parameter change.

In the first stage, the core power is increased sharply due to the insertion of a step reactivity to the reactor. At the same time, the molten salt coolant and fuel temperature will also increase. The increase in both adds negative reactivity to the reactor through the temperature feedback, so the power peaks quickly and starts to drop. During this process, the temperature rise of the molten salt in the core also increases rapidly in response to the power change.

In the second stage, due to the temperature feedback, the core power rapidly drops from peak, and the molten salt cannot maintain the temperature rise at high power. Therefore, both the molten salt and the fuel will have a temperature drop at this time, and these changes are reflected in Fig. 4 and Fig. 5. It adds positive reactivity to the
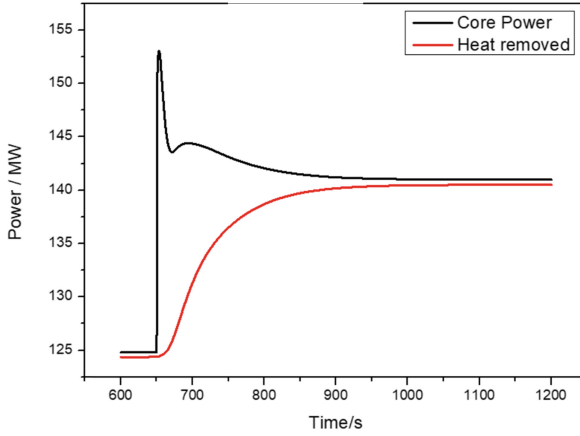
Fig. 6. Changes in core power and Heat removed from the second loop at 100 pcm insertion.
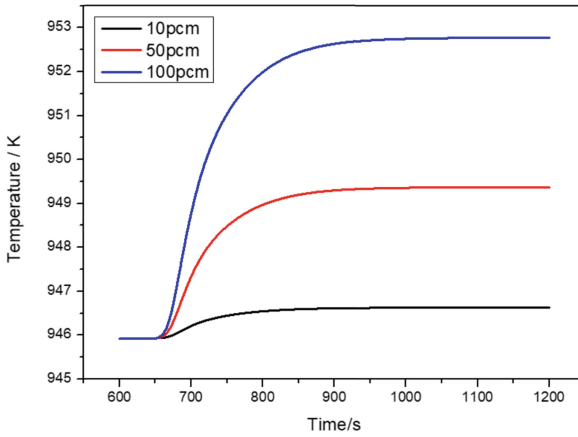
Fig. 7. The temperature change in the molten salt of the second loop at the outlet of the heat exchanger.

core through the temperature feedback, which leads to a second increase in core power between 670 s and 700 s.

In the third stage, such a temperature drop will not last too long, and the core power will return to the increasing trend immediately due to the temperature feedback, thus, the system has entered the third stage of change. It can be seen in Fig. 6 that the heat removed by the second loop does not keep up with the rapidly change in core power, it is a slowly increasing process that eventually equals the heat generated by the core, allowing the system to achieve a new steady state. Therefore, during the whole process, the temperature of the molten salt in the second loop is always increasing, and this change can be seen in Fig. 7. For a long period, the second loop cannot remove all the heat generated by the primary loop, which leads to a slow increase in the temperature
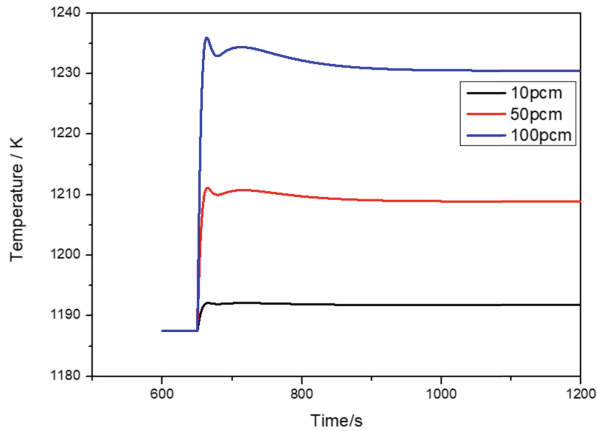
Fig. 8. Transient change in the hottest spot.

of the molten salt in the third stage. Eventually, the system will reach a new steady state around 850 s.

From the point of view of safety analysis, it can be seen that even if 100 pcm of reactivity is inserted, the molten salt temperature is still lower than 986 K, and the peak temperature of the hottest spot of nuclear fuel will be lower than 1240 K. The design safety limit of FuSTAR is: the hottest spot temperature needs to be lower than 1873 K, and the temperature of the fluorine salt coolant needs to be lower than 1089 K, both temperatures are well below the limit with the insertion of 100 pcm of reactivity. Without adding any safety facilities, the FuSTAR system is still safe under the insertion of 100 pcm reactivity only by the temperature feedback.

3.3   Increasing the Outlet Pressure of the Pump

At t = 800 s, the outlet pressure of the three main pumps are simultaneously increased from 2.15 MPa to 2.16 MPa within 50 s. Figure 9 shows the change in the pump outlet pressure and the total flow of molten salt coolant under this condition. Figure 10, 11 and 12 show the change in the core power, the change in temperature of the molten salt coolant at the core outlet, and changes in the hottest temperature of nuclear fuel under the transient. And in this transient, the size of the temperature coefficient of reactivity is artificially changed. Multiply its value by 5 or divide it by 5, and the obtained parameter changes are also put into Figs. 10, 11 and 12.

It can be seen from Fig. 9 that under the operation of the pump changing the outlet pressure value, the total mass flow value of molten salt in the circuit will increase with the increase of pressure, which is determined by the momentum conservation equation in the Pipe component. When the pressure of the fluid is increased, there must be a concomitant increase in its flow. When the pump outlet pressure increases by 0.01 Mpa, it can be seen that the flow value will increase by 90 kg/s.

Analyzing Figs. 9, 10, 11 and 12, it can be found that when the flow rate of molten salt increases, its temperature rises in the core becomes smaller, which increases the heat
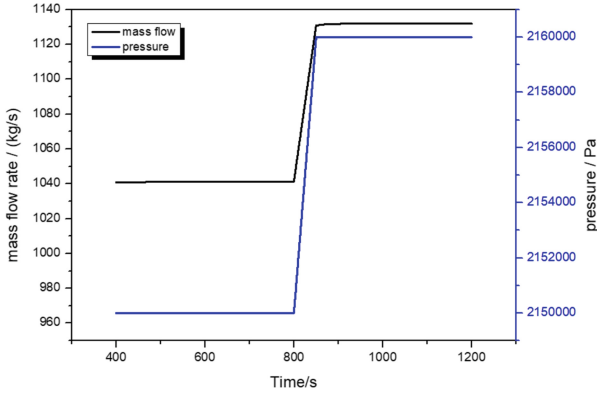
Fig. 9. Changes in pump outlet pressure and molten salt mass flow.
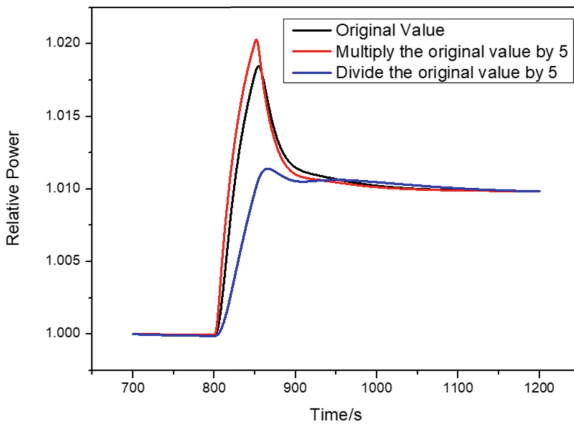
Fig. 10. Change in core power.

taken away by the coolant from the core at the same time. Therefore, the coolant temperature at the core exit will decrease and the fuel temperature will decrease accordingly. At the same time, due to the existence of the temperature feedback, the change in both will add a positive reactivity to the core. Then it can be seen from Fig. 10 that the total power of the reactor will be increased accordingly.

In the process of increasing power due to the existence of a negative feedback, the hottest temperature of nuclear fuel will change from decreasing to increasing at a certain time (Fig. 11, Fig. 12). However, the temperature of the molten salt coolant will always decrease due to the operation of increasing the flow rate for 50 s. After the pump pressurization process is over, the excessive power will cause the coolant that is no longer increasing its flow to start to heat up, which will add a positive reactivity to the core, and the power will also start to decrease at this time. Then the system re-establishes a new equilibrium, the temperature of the coolant will rise again, and the power of the reactor will reach a new steady state value with the presence of temperature feedback.
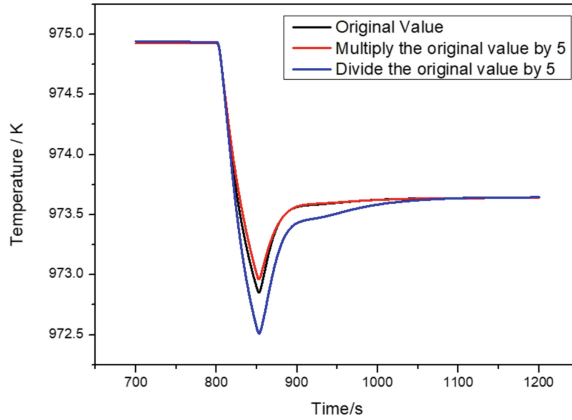
Fig. 11. Coolant salt temperature change at the core outlet.
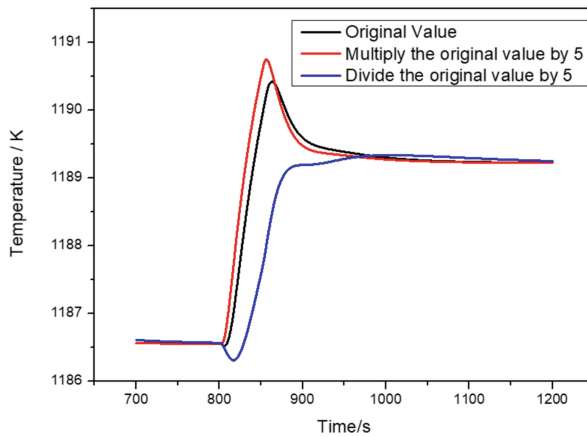
Fig. 12. Change of the hottest temperature of the fuel.

Figure 10, 11 and 12 do a sensitivity analysis on the temperature coefficient of reactivity. Figure 10 shows that a system with a larger temperature coefficient of reactivity will have a greater rate of power boost during this transient and a shorter time for the system to establish a new steady state. Because such system feedback is stronger. As can be seen in Fig. 11, the strong negative feedback will cause the change in molten salt coolant temperature to be smaller than in other systems. In systems with smaller temperature coefficients of reactivity, the results are reversed, with lower power peaks, larger changes in molten salt temperature, and a longer time to establish a new steady state.

4   Conclusion

In this paper, a model of the primary loop system of FuSTAR is established. After the steady state results are verified, two transients are considered: adding step reactivity and increasing pumps outlet pressure. Then, reasonable analysis of parameters changes images obtained under the transient is carried out. Finally, the following conclusions are drawn:

After the insertion of positive reactivity in the core, the fuel temperature and nuclear power of the core will quickly reach a peak value due to the existence of the temperature feedback after a brief increase, followed by a new steady state establishment process of the order of 200 s;

Under the transient state of inserting 10 pcm, 50 pcm, and 100 pcm of positive reactivity, FuSTAR can still operate under the safety limit without taking any action and only relying on temperature feedback;

During the transient of the pump pressurization, the flow of molten salt coolant is increased and pictures of the system response due to the temperature feedback are obtained;

A system with a larger temperature coefficient of reactivity (absolute value) will have a stronger power response and weaker changes in molten salt temperature during pump pressurization transients.

References

1. Zhang, D.L., Qin, H., Li, X.Y., et al.: Conceptual design of integral inherently safe fluoride salt-cooled high-temperature advanced reactor FuSTAR. China Basic Sci. **23**(04) (2021)
2. Duderstadt, J.J., Hamilton, L.J.: Nuclear Reactor Analysis, pp. 244–259. Wiley, Hoboken (1976)
3. Fritzson, P.: Principles of Object-Oriented Modeling and Simulation with Modelica 3.3, Wiley-IEEE Press, Hoboken (2015)
4. He, F., Cai, X. Z., Guo, W., He, L., Cui, L.: The transient analysis of molten salt reactor reactivity insertion based on RELAP5/ FLUENT coupled program. Nucl. Tech. **44**(03) (2021)
5. Fritzson, P.: The modelica object-oriented equation-based language and its openmodelica environment with metamodeling, interoperability, and parallel execution. In: Ando, N., Balakirsky, S., Hemker, T., Reggiani, M., von Stryk, O. (eds.) SIMPAR 2010. LNCS (LNAI), vol. 6472, pp. 5–14. Springer, Heidelberg (2010). https://doi.org/10.1007/978-3-642-17319-6_4
6. Fritzson, P., et al.: The OpenModelica integrated modeling, simulation and optimization environment. In: Proceedings of the 1st American Modelica Conference. Modelica Association Linköping, Sweden (2018)

The Potential Force Interface Tension Model in MPS Method for Stratification Simulation

Lijun Jian[1,2], Xiao Zeng[2], and Jie Pei[2(✉)]

[1] Tsinghua University, Beijing 100084, China
[2] China Nuclear Power Engineering Co. LTD., Beijing 100840, China
peijiepku@163.com

Abstract. In the analysis of phenomenology of serious accident, stratification behavior is important in the late in-vessel stage of core melt. Traditional numerical methods have difficulties in analyzing stratification process accompanying with free surface, which need extra processes such as empirical correlations. The Moving Particle Semi-implicit (MPS) method has a natural advantage in calculating multiphase flows with free surface. In this paper, we apply the potential force surface tension model to the MPS program and extend the original surface tension model to the interface tension calculation of multiple flows. The improved MPS method is verified by a classical dam break problem. The surface tension model is verified by the cases of droplet oscillation, droplet on solid wall and floating droplet. Finally, the two-dimensional dam-break stratification experiment of silicone oil and salt water is simulated, and the simulation results agree with the experiment.

Keywords: MPS Method · Surface Tensional Model · Severe Accident · Density Stratification · Contact Angle

1 Introduction

Different fluids will be stratified by gravity. In the late in-vessel stage of core melt severe accident, stratification behavior is an important phenomenon. Like in the TIM accident [1], due to the decay heat of fission products, the molten corium is formed and collected in the lower head. And the molten corium may be separated into immiscible layers, usually thought of as two or three layers. For example, MASCA [2] experiment, which uses the prototypic core materials, indicate that the molten pool, initially a uniform mixture of components, separates into two layers with different densities. The process of melt stratification can influence the distribution of thermal load across the vessel wall and affect the process of severe accident [3].

Some system program, such as MAAP [4], MELCOR [5] and PECM [6], can calculate the thermo-hydraulics of the molten pool in lower head assuming stratified configuration with empirical correlations employed. For numerical simulation which does not rely on empirical correlations, the large deformation of interface and the interface tracking of stratification process is a challenging task. To model the interfaces between phases,

some methods, like the Front Tracking Method, Level Set Method [7], or Immersed Boundary Method [8] are applied in CFD. These mesh methods have difficult in the simulation of large topology deformation, such as unphysical total mass change.

Except for grid methods, particle methods have natural advantages in dealing with free surface flow and large deformation of fluids. The Moving Particle Semi-implicit (MPS) method [9] is one of particle methods for incompressible flow with free surface flow. This method is widely applied in nuclear engineering [10]. In Lagrange system of particle methods, two major approaches have been adopted to model the surface tension, the continuum surface force (CSF) model [11] and the potential force (PF) model [12]. And the potential force model is much simpler and more stable compared to the continuum surface force model.

In this study, the potential force model is added to the original MPS method and extended to simulate the interface between different fluids for stratification calculation. The surface tension model and contact angle are verified by some droplet cases. And the modified method is validated by a two-dimensional dam-break stratification experiment.

2 Numerical Methods

2.1 The Basis MPS Method

The governing equations of MPS are the mass conservation equations and the momentum conservation equations for incompressible flow:

$$\frac{D\rho}{Dt} + \rho\nabla \cdot \boldsymbol{u} = 0 \tag{1}$$

$$\frac{D\boldsymbol{u}}{Dt} = -\frac{1}{\rho}\nabla p + \upsilon\nabla^2\boldsymbol{u} + \frac{\boldsymbol{f}}{\rho} + \boldsymbol{F} \tag{2}$$

where the vectors $\boldsymbol{u}, \boldsymbol{f}$ and $\boldsymbol{F}$ respectively are velocity, surface tension, and external force (gravity), t, ρ, p and υ respectively are time, density, pressure, and kinematic viscosity. For different fluids, the fluid properties of each particle don't change.

Particle interactions are based on the kernel function:

$$w(r) = \begin{cases} \frac{r_e}{r} - 1 & (r < r_e) \\ 0 & (r \geq r_e) \end{cases} \tag{3}$$

where r is the distance between particle i and particle j. The cut-off radius r_e, which determines the range of interaction, is usually set as $3.1d_p$, where d_p is the initial particle diameter.

The particle number density is defined as the summation of neighboring kernel function:

$$n_i = \sum_{j \neq i} w\left(|\vec{r}_{ij}|\right) \tag{4}$$

where n_i is the particle number density of particle i. For impressible fluid, the mass conservation is ensured by keeping the n_i as a constant.

The gradient and Laplacian terms could be discretized based on the weighted average of neighboring particles:

$$\nabla \phi_i = \frac{d}{n^0} \sum_{j \neq i} \left[\frac{\phi_j - \phi_i}{|r_j - r_i|^2} (r_j - r_i) w(|r_j - r_i|) \right] \tag{5}$$

$$\nabla^2 \phi_i = \frac{2d}{n^0 \lambda} \sum_{j \neq i} \left[(\phi_j - \phi_i) w(|r_j - r_i|) \right] \tag{6}$$

$$\lambda = \frac{\sum_{j \neq i} |r_j - r_i|^2 w(|r_j - r_i|)}{\sum_{j \neq i} w(|r_j - r_i|)} \tag{7}$$

where ϕ_i and ϕ_j is represent scalar, n^0 is the constant particle density calculated in the initial state, d is the spatial dimension.

2.2 Boundary Condition

To preserve incompressible condition, the particle number density is kept constant in each time step. While for particles on the free surface, the number density will decrease. Using this property, the particles on free surface can be identified with a threshold value of particle number density. Then the Dirichlet boundary condition on free surface is applied in the pressure calculation. The threshold is set as follows:

$$n_i < \beta n^0 \tag{8}$$

where β is a constant value less than 1.0 and usually set as 0.97.

The wall boundary condition is the Norman boundary condition. The wall particles and dummy particles are arranged along the boundary. The wall particles are included in the pressure calculation and density calculation and the dummy particles are only included in density calculation. Then non-slip boundary condition is utilized for wall boundary.

2.3 The Potential Force Surface Tension Model

The potential function [13] is set similar to the molecular forces

$$P(r) = \begin{cases} \frac{C\_sur}{3} \left(r - \frac{3}{2} r_0 + \frac{1}{2} r_e \right) (r - r_e)^2 & (r < r_e) \\ 0 & (r \geq r_e) \end{cases} \tag{9}$$

where r, r_0 and r_e respectively are the distance between particles, the distance between initial particles and the effective radius, which is generally set r_e as 3.2 r_0.

C_sur is a coefficient related to surface tension, which can be obtained by the surface energy between fluids:

$$C_f = \frac{3 \times 2\sigma r_0^2}{\sum_{i \in A, j \in B, |r_{ij}| < r_e} \left(r - \frac{3}{2} r_0 + \frac{1}{2} r_e \right) (r - r_e)^2} \tag{10}$$
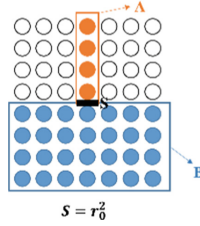
Fig. 1. Schematic diagram of calculation of surface

where σ is the coefficient of surface tension. The distribution of region A and B is shown in Fig. 1.

The coefficient C_sur between fluid particles and solid particles can be derived from C_f:

$$C_{fs} = \frac{C_f}{2}(1 + \cos\theta) \tag{11}$$

where θ is the contact angle.

The coefficient C_sur between different fluid particles can be derived in a similar way to a single fluid

$$C_{f,AB} = \frac{3(\sigma_{f,A} + \sigma_{f,B} - \sigma_{f,AB})r_0^2}{\sum_{i\in A, j\in B}(r - \frac{3}{2}r_0 + \frac{1}{2}r_e)(r - r_e)^2} \tag{12}$$

where $\sigma_{f,AB}$ indicates the miscibility of fluid A and B, and θ_{AB} is defined as the hypothetical interface contact angle.

The interface tension coefficient can be calculated in a similar way to the coefficient between fluid particles and solid particles. Since the fluid A floats on the fluid B, $\rho_{f,A} < \rho_{f,B}$ is presumed.

$$C_{f,AB} = \frac{C_{f,A}}{2}(1 + \cos\theta_{AB}) \tag{13}$$

3 Model Verification

3.1 Dam Break

The dam break case has been widely used for liquid computing in CFD. In a rectangular container, the water column stands still on the left side of the container originally, and takes up 1/4 of the width of the container. Within 1s of the barrier being dropped, the water column is flowing rapidly due to gravity.

With the initial particle distance r_0 of 0.008 m and time step Δt of 0.001 s, the process in 1s is simulated. The fluid front position was compared with the experiment [14] in Fig. 2. The trend of fluid front changing with time in MPS calculation is consistent with the experimental results, but the front motion changes slightly faster in simulation. Such a difference is reasonable considering that it takes time for the water column barrier to be extracted in the experiment. The simulation results of other scholars also reflected this difference.
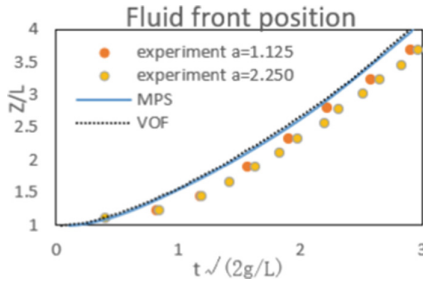
Fig. 2. Comparison of different fluid front positions

3.2 Droplet Oscillation

A square droplet is released in two-dimensional space in vacuo. The droplet oscillates periodically due to surface tension and the theoretical solution of the oscillation period can be calculated according to the physical properties. In this case, the droplet oscillation period is about 1.3 s and the numerical results are shown in Fig. 3.
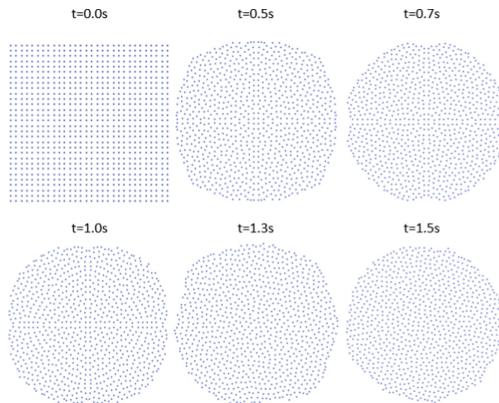
Fig. 3. Numerical results of droplet oscillation

The simulated oscillation period is close to the analytical result. The droplet shape rotates 45° at 0.7 s, and is close to the initial shape at 1.3 s. As numerical dissipation inhibits oscillation, eventually the droplet will approach the equilibrium sphere.

3.3 Droplet on Solid Wall

The droplet contacts the solid wall in initial state and is released. Figure 4 shows droplet morphology after 10.0s, when droplet movement almost stops and approaches steady state.

In Fig. 4, the larger potential force between fluid particles is, the smaller contact angle appears. The simulated solid-liquid contact angle is consistent with the set contact
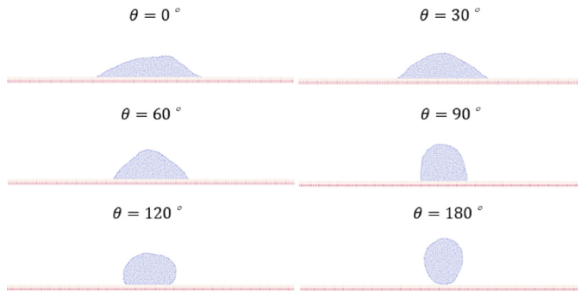
Fig. 4. Numerical results of droplet behavior on solid wall

angle. When the contact angle is 180°, there is no attractive potential force between fluid and wall and the droplet separates from the wall.

3.4 Floating Droplet

For the case of two fluid interfaces, a case similar to the solid-liquid contact angle is selected. Fluid A and fluid B have the same physical properties and are immiscible. Fluid A is a droplet floating on fluid B. Figure 5 shows the calculation of different interface contact angles. It is considered that the calculated state is close to steady state after 10 s and the gravity is not calculated.

It can be seen from Fig. 5 that the contact angle θ_{AB} has a significant influence on the droplet interface shape. The contact area between fluid A and fluid B decreases as the contact angle increases. The principle is similar to the solid-liquid contact angle.

4   Model Validation

To validate the simulation of stratification process, Li et al. [15] carried out experiments similar to the dam break case. Two immiscible fluids, silicone oil and salt water, were chosen, and the density and viscosity of the two fluids could be adjusted. At the initial time, the baffle plate of the two liquids was removed and then the stratified flow process of the two liquids over time was recorded. The experimental schematic diagram is shown in Fig. 6.

The comparison between the results simulated by MPS method and the experimental results under the same conditions is shown in Fig 7.

It shows that the silicon oil with a lighter density flowed to the top of the salt water. The fluids flow quickly in the first 5s, because the pressure gradient of the fluid interface is larger. During the time after the fifth second, the fluid shape varied slowly and gradually reached steady state at 30 s. The density difference between fluids is the essential reason of stratification and the viscosity affects the time to steady state. The addition of the surface tension model makes the fluid interface smoother and more consistent with the actual situation.
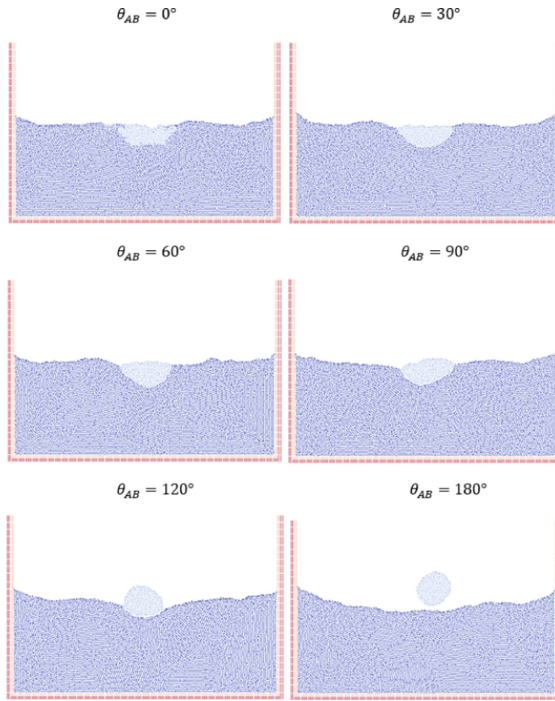
Fig. 5. Numerical results of droplet behavior with different fluid-to-fluid interface angle
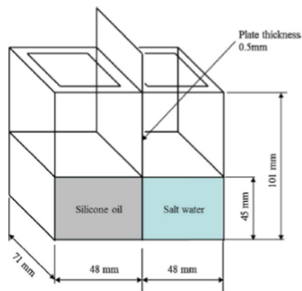
Fig. 6. Experiment container for stratification of two fluid columns
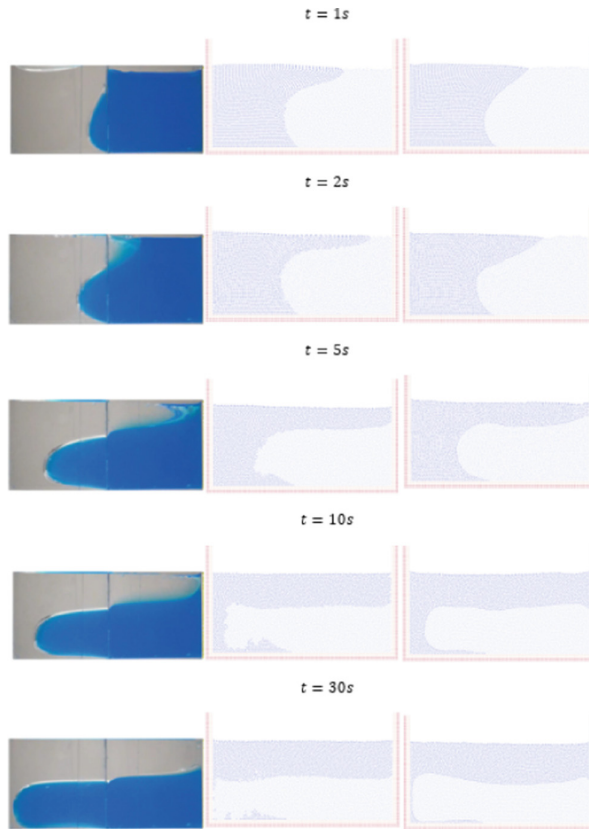
Fig. 7. Side views of experiment (left), MPS without surface tension (middle) and MPS with surface tension (right)

5 Conclusions

The surface tension model based on potential function is added to the original MPS method and is extended to calculate the liquid-liquid interface in a way similar to solid-liquid contact angle. The new program is verified by a dam break case, and the surface tension model is verified by the cases of droplet oscillation, droplet on solid wall and floating droplet. Finally, the ability of the improved program is validated by a stratification experiment similar to the dam break experiment.

Density stratification is an important process of molten pool formation in severe accident analysis. The research in this paper can lay a foundation for the analysis of molten pool process in future.

References

1. TEPCO, Fukushima Daiichi Nuclear Power Station Unit 2 Primary Containment Vessel Internal Investigation (2018). Accessed 14 Dec 2020

2. Tsurikov, D.F., Strizhov, V.F., Bechta, S.V., Zagriazkin, V.N., Kiselev, N.P.: MainResults of the MASCA1 and 2 Projects. RRC Kurchatov Institute (2007)

3. Li, G., Wen, P., et al.: Study on melt stratification and migration in debris bed using the moving particle semi-implicit method. Nucl. Eng. Des. **360**, 110459 (2020)

4. Suh, K.Y., Henry, R.E.: Debris interactions in reactor vessel lower plena duringa severe accident I. Predictive model. Nucl. Eng. Des. **166**, 147–163 (1996)

5. Gauntt, R.O., et al.: MELCOR Computer Code Manuals. Version 1.8.6. SandiaNational Laboratories, Albuquerque (2005)

6. Tran, C.T., Dinh, T.N.: Theeffectiveconvectivity model for simulation of meltpool heat transfer in a light water reactor pressure vessel lower head. Part I:physical processes, modeling and model implementation. Prog. Nucl. Energy **51**, 849–859 (2009)

7. Mancilla, E., Palacios-Muñoz, A., Salinas-Vázquez, M., Vicente, W., Ascanio, G.: A Level Set method for capturing interface deformation in immiscible stratified fluids. Int. J. Heat Fluid Flow **76**, 170–186 (2019)

8. O'Brien, A., Bussmann, M.: A moving immersed boundary method for simulating particle interactions at fluid-fluid interfaces. J. Comput. Phys. **402**, 109089 (2020)

9. Koshizuka, S., Oka, Y.: Moving particle semi-implicit method for fragmentation of incompressible fluid. Nucl. Sci. Eng. **123**, 421–434 (1996)

10. Li, G., Gao, J., et al.: A review on MPS method developments and applications in nuclear engineering. Comput. Methods Appl. Mech. Eng. **367**, 113166 (2020)

11. Brackbill, J.U., Kothe, D.B., Zemach, C.: A continuum method for modeling surface tension. J. Comput. Phys. **100**(2), 335–354 (1992)

12. Shirakawa, N., Horie, H., Yamamoto, Y., Okano, Y., Yamaguchi, A.: Analysis of jet flows with the two-fluid particle interaction method. J. Nucl. Sci. Technol. **38**(9), 729–738 (2001)

13. Kondo, M., Koshizuka, S.: Improvement of stability in moving particle semiimplicit method. Int. J. Numer. Meth. Fluids **65**(6), 638–654 (2011)

14. Martin, J.C., Moyce, W.J.: Part IV: an experimental study of the collapse of liquid columns on a rigid horizontal plane. Phil. Trans. Roy. Soc. A Math. Phys. Eng. Sci. **244**(882), 312–324 (1952)

15. Li, G., Oka, Y., Furuya, M., et al.: Experiments and MPS analysis of stratification behavior of two immiscible fluids. Nucl. Eng. Des. **265**, 210–221 (2013)

A Multi-state Degradation Model for Reliability Assessment of Multi-component Nuclear Safety Systems Considering Degradation Dependency and Random Shocks

Qingzhu Liang[1], Changhong Peng[1(✉)], Hang Zhang[2], and Jianchao Lu[2]

[1] University of the Science and Technology of China, Hefei, Anhui, China
pb142140@mail.ustc.edu.cn, pengch@ustc.edu.cn
[2] Nuclear Power Institute of China, Chengdu, Sichuan, China

Abstract. The degradation (e.g., wear, stress corrosion cracking, and fatigue) of nuclear safety systems is an inherently irreversible process, which will lead to system failure when the accumulated damage reaches a threshold level, resulting in catastrophic consequences. Therefore, it is essential to understand and model the degradation behavior of nuclear safety systems to predict and prevent potential failures and thus effectively avoid subsequent losses. This paper proposes a multi-state degradation model for multi-component nuclear safety systems, considering the dependency among the degradation processes and the effect of random shocks. The degradation processes of the system were modeled by the Semi-Markov process. The arrival of random shocks obeys a Poisson process. The transfer kernel function of the holistic model was derived, based on which the Monte Carlo algorithm for estimation of the system reliability was developed. Based on a simple case, the correctness of the proposed model is verified. The model is applied to the reliability analysis of one sub-system of the residual heat removal system of a nuclear power plant.

Keywords: Degradation Modeling · Semi-Markov Process · Multi-component Systems · Monte Carlo Simulation

1 Introduction

For nuclear safety systems that are typically designed for high reliability, traditional approaches based on time-to-failure data may be inapplicable, and degradation models that can take advantage of the wealth of the infrastructure health information have received widespread attention and impetus in several decades [1].

The multi-state models (MSMs) have been widely used in degradation modeling, including the Markov process and its extended version Semi-Markov process. Fleming et al. [2] developed a generalized 4-state Markov model for nuclear power plant (NPP) piping systems applicable to different degradation mechanisms such as wall thickness thinning and weld defect growth. Unwin et al. [3] proposed a multi-state physic model

(MSPM) for a dissimilar metal weld in a primary coolant system of an NPP. Giorgio et al. [4] presented an age- and state-dependent Markov model to describe the cylinder liner wear process in a marine heavy-duty diesel engine. Moghaddass and Zuo [5] studied a nonhomogeneous continuous-time hidden Semi-Markov process for holistic modeling of the degradation and observation processes.

Random shocks may influence degradation evolution and require to be accounted for. For example, the impacts of thermal and mechanical shocks (e.g., internal thermal shock and water hammer) [6–8] on power plant components can result in increases in temperature and stress, which could accelerate component degradation. In the literature, random shocks are generally modeled by Poisson processes [8–11], mainly divided into two categories, extreme shocks that directly lead the system to fail and cumulative shocks that cause an additional instantaneous increase in the degradation degree of the system cumulatively. Lin et al. [8, 9] analyzed the effect of the random shocks on the transition rates of MSMs and the possibility that the component degrades instantaneously from the current state to a more "deteriorated" state. Similar considerations can be found in the performance analysis by Srivastav et al. [10] for subsea safety valves, where the device degradation was modeled as a Markov chain, and the device demand was considered as random shocks. Yang et al. [11] assumed that the shock arrival rate is dependent on the current state of the system, and a shock would result in a sudden change in the system state. Eryilmaz [12] suggested that a shock is extreme when its load exceeds the threshold level and considered the randomness of the number of system states induced by random shocks.

Most of these models mentioned above, however, are based on a single degradation process. Nuclear safety systems are usually complex collections of different kinds of constituent units, exhibiting the phenomenon of multiple degradation processes that may be correlated and have competitive/non-competitive relationships. In addition, few studies have considered both dependency among multiple degradation processes and dependency between degradation processes and random shocks. In this paper, we develop a holistic multi-state degradation model for nuclear safety systems with considering degradation dependency and random shocks. The Monte Carlo (MC) algorithm for estimating the system reliability indexes was presented. The validity and applicability of the models were demonstrated by a numerical example. The remainder of the paper is structured as follows, Sect. 2 presents the framework of the model, Sect. 3 gives the model validation, Sect. 4 provides the application of the model, and Sect. 5 gives some conclusions.

2   Model Framwork

2.1   Assumptions

– The system has L components, each of which may subject multiple degradation processes/mechanisms. Denote by $\boldsymbol{M} = \{1, \cdots, M\}$ the degradation processes of the system.
– The degradation process $n \in \boldsymbol{M}$ can be modeled by a time-homogeneous Semi-Markov process (SMP) $\{X_n(t); t \geq 0\}$ on a discrete state space $S_{X_n} = \{0, 1, \cdots, s_n\}$, where s_n is the perfect functioning state and 0 is the failure state. The transition rate $\lambda_{i_n, j_n}\left(\tau_{i_n}\right)$

of $X_n(t)$ from state i_n to state j_n is a function of the sojourn time in the current state i_n since the last transition of the process, i.e.,

$$
\begin{aligned}
&\lambda_{i_n,j_n}\left(\tau_{i_n}\right) \\
&= \lim_{\Delta t \to 0} \mathbb{P}\big(X_{n,k+1} = j_n, T_{n,k+1} \in \left[T_{n,k}, T_{n,k} + \tau_{i_n} + \Delta t\right] \\
&\quad | \{X_{n,l}, T_{n,l}\}_{l=0}^{k-1}, \left(X_{n,k} = i_n, T_{n,k}\right)\big) / \Delta t \\
&= \mathbb{P}\big(X_{n,k+1} = j_n, T_{n,k+1} \in \left[T_{n,k}, T_{n,k} + \tau_{i_n}\right] | \left(X_{n,k} = i_n, T_{n,k}\right)\big) / \Delta t
\end{aligned}
\tag{1}
$$

where $T_{n,k}$ and $X_{n,k}$ are the time and the arrival state of the kth jump of $X_n(t)$.

- The arrival of random shocks is governed by a homogeneous Poisson process $\{N(t); t \geq 0\}$ with parameter μ.
- A shock could cause the degradation process $X_n(t)$ to transfer instantaneously with probability p_{i_n,j_n} from the current state i_n to the state $j_n \leq i_n$. Note $p_{i_n,0}$ that denotes the probability of the extreme shock.
- Considering repair, the system can recover from a "worse" to a "better" state except from the failed state.

2.2 Multi-state Model Considering Multiple Dependent Degradation Processes and Random shocks

Let $X(t) = (X_1(t), \cdots, X_M(t))$, then $X(t)$ is a stochastic process on an n-dimensional discrete state space $S_X = S_{X_1} \times \cdots \times S_{X_M}$, whose failure space $\mathcal{F}_X$ is dependent on the structure of the system and can be determined with the help of fault tree analysis or reliability block diagram. The correlation among degradation processes will have an impact on the evolution of $X_n(t)$, $n \in M$. Assume that the transition rate of $X_n(t)$ from the current state i_n is correlated with the state of $X(t)$ during the sojourn time of $X_n(t)$ in the current state i_n. It may be hypothesized that $X_n(t)$ jumps to state j_n at time t after sojourning τ_{i_n} in the current state i_n since the last transition, then the transition rate can be expressed as

$$
\lambda_{i_n,j_n}\left(\tau_{i_n} | \{X(\tau)\}_{\tau=t-\tau_{i_n}}^{t}\right)
\tag{2}
$$

The state transition diagram of the system is shown in Fig. 1. We assume no simultaneous state mutation of any two degradation processes will occur. Given that the kth transfer of $X(t)$ occurs at time t to reach state $x_i = (i_1, \cdots, i_n, \cdots, i_M)$ and the sojourn times of $X_1(t), \cdots, X_M(t)$ in states $i_1, \cdots, i_M$ at time t are $\tau_{i_1}^t, \cdots, \tau_{i_M}^t$ and the states of $X(t)$ on the time interval $\left[t - \tau_{max}^t, t\right]$ ($\tau_{max}^t = max\{\tau_{i_1}^t, \cdots, \tau_{i_M}^t\}$) are $\{X(\tau)\}_{\tau=t-\tau_{max}^t}^{t}$, and let, the transition rate of the process $X(t)$ from the current state x_i to $x_j = (i_1, \cdots, j_n, \cdots, i_M)$ is

$$
\begin{aligned}
&\lambda_{x_i,x_j}\left(\tau_{x_i} | \boldsymbol{\theta}(t)\right) = \\
&= \lambda_{i_n,j_n}\left(\tau_{n_i}^t + \tau_{x_i} | \{X(\tau)\}_{\tau=t-\tau_{i_n}}^{t}\right) \\
&\boldsymbol{\theta}(t) = \left(\tau_{i_1}^t, \cdots, \tau_{i_M}^t, \{X(\tau)\}_{\tau=t-\tau_{max}^t}^{t}\right)
\end{aligned}
\tag{3}
$$

where τ_{x_i} is the sojourn time of $X(t)$ in current state x_i.
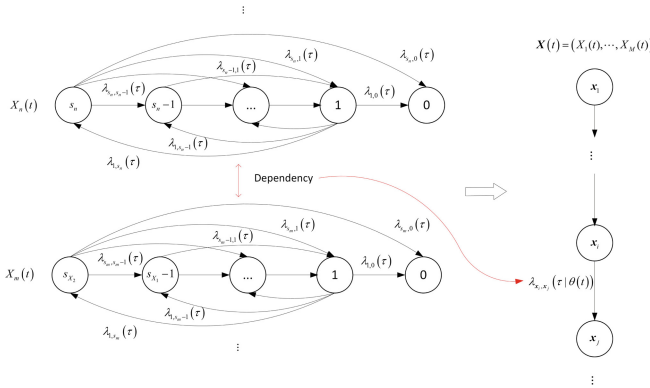
Fig. 1. The state transition diagram of the system
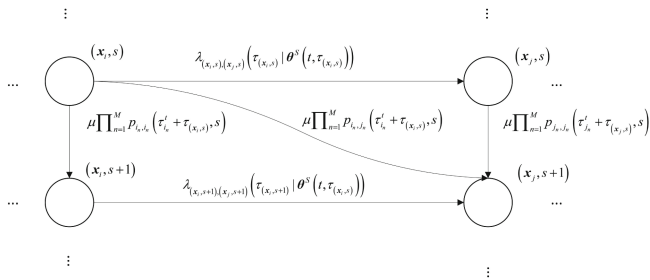
Fig. 2. The multi-state model of the system considering random shocks

Construct the stochastic process. $X^S(t) = (X(t), N(t))$., the state space and failure space of $X^S(t)$. Are $S_{X^S} = S_X \times \mathbb{N}$ and, respectively. The multi-state model considering multiple dependent degradation processes and random shocks is shown in Fig. 2.

Given that the kth transfer of $XS(t)$. Occurs at time t to reach state $(x_i = (i_1, \cdots, i_n, \cdots, i_M), s)$ and the sojourn times of $X_1(t), \cdots, X_M(t)$ in states $i_1, \cdots, i_M$ at time t are $\tau_{1_i}^t, \cdots, \tau_{M_i}^t$ and the states of $X(t)$ on the time interval $\left[t - \tau_{max}^t, t\right]$ are $\{X(\tau)\}_{\tau=t-\tau_{max}^t}^t$, the possible transition rates of the process from the current state (x_i, s) include

$$\lambda_{(x_i,s),(x_j,s)}\left(\tau_{(x_i,s)}|\theta(t)\right) = \lambda_{i_n,j_n}\left(\tau_{n_i}^t + \tau_{(x_i,s)}|\theta(t)\right) \qquad (4)$$

the rate of occurrence of $X(t)$ jumping to state $x_j = (i_1, \cdots, j_n, \cdots, i_M)$;

$$\lambda_{(x_i,s),(x_i,s+1)}\left(\tau_{(x_i,s)}|\theta(t)\right) = \mu \prod_{n=1}^{M} p_{i_n,i_n} \qquad (5)$$

the rate of occurrence of a shock which doesn't cause the state change of $X(t)$;

$$\lambda_{(x_i,s),(x_j,s+1)}\big(\tau_{(x_i,m)}|\theta(t)\big) = \mu \prod_{n=1}^{M} p_{i_n,j_n} \tag{6}$$

the rate of occurrence of a shock which causes $X(t)$ to go to state $x_j = (i_1,\cdots,j_n,\cdots,i_M) \neq x_i$.

Obtaining analytical solutions of the Semi-Markov process $X^S(t)$ with complex state transition rates related to the state of the process at some time in the past and the sojourn time in the current state is a complicated task. The integral/differential equations describing the evolution of the system states over time for multi-component systems with dependent degradation processes may be challenging to develop. The number of the equations is usually extensive, which demands high computational resource requirements. Monte Carlo (MC) simulation is an effective way to overcome the above challenges and has been widely used in system reliability analysis studies [13–15].

In the following we derive the transfer kernel function of $X^S(t)$ for MC simulation, which is denoted by $Q^S_{(x_i,s),(x_j,m)}\big(\tau_{(x_i,s)}|\theta(t)\big)$ and represents the probability of that $X^S(t)$ go to state (x_j, m) during infinitesimal time interval $\big[t + \tau_{(x_i,s)}, t + \tau_{(x_i,s)} + d\tau_{x_i}\big]$, given that the kth transfer of $X^S(t)$ occurs at time t to reach state $(x_i = (i_1,\cdots,i_n,\cdots,i_M), s)$ and the condition $\theta(t)$. Satisfies:

$$Q^S_{(x_i,s),(x_j,m)}\big(\tau_{(x_i,s)}|\theta(t)\big)d\tau_{(x_i,s)} = P_{(x_i,s)}\big(\tau_{(x_i,s)}|\theta(t)\big) \cdot \lambda_{(x_i,s),(x_j,m)}\big(\tau_{(x_i,s)}|\theta(t)\big)d\tau_{(x_i,s)} \tag{7}$$

where $P_{(x_i,s)}\big(\tau_{(x_i,s)}|\theta(t)\big)$ is the probability of that there is no transition of $X^S(t)$ during time interval $\big[t + \tau_{(x_i,s)}, t + \tau_{(x_i,s)}\big]$, given that the kth transfer of $X^S(t)$ occurs at time t to reach state $(x_i = (i_1,\cdots,i_n,\cdots,i_M), s)$ and the condition $\theta(t)$. $P_{(x_i,s)}\big(\tau_{(x_i,s)}|\theta(t)\big)$ satisfies

$$P_{(x_i,s)}\big(\tau_{(x_i,s)} + d\tau_{(x_i,s)}|\theta(t)\big) = P_{(x_i,s)}\big(\tau_{(x_i,s)}|\theta(t)\big) \cdot \big(1 - \lambda_{(x_i,s)}\big(\tau_{(x_i,s)}|\theta(t)\big)\big)d\tau_{(x_i,m)} \tag{8}$$

$$\lambda_{(x_i,s)}\big(\tau_{(x_i,s)}|\theta(t)\big) = \sum_{x_j} \lambda_{(x_i,s),(x_j,m)}\big(\tau_{(x_i,s)}|\theta(t)\big) \tag{9}$$

The solution of Eq. (9) is

$$P_{(x_i,s)}\big(\tau_{(x_i,s)}|\theta(t)\big) = exp\left(-\int_0^{\tau_{(x_j,s)}} \lambda_{(x_i,s)}\big(\tau_{(x_i,m)}|\theta(t)\big)du\right) \tag{10}$$

Then, we have

$$Q^S_{(x_i,s),(x_j,m)}\big(\tau_{(x_i,s)}|\theta(t)\big) = \pi_{(x_i,s),(x_j,m)}\big(\tau_{(x_i,s)}|\theta(t)\big) \cdot \psi_{\tau_{(x_i,s)}}\big(\tau_{(x_i,s)}|\theta(t)\big) \tag{11}$$

$$\pi_{(x_i,s),(x_j,m)}\big(\tau_{(x_i,s)}|\theta(t)\big) = \frac{\lambda_{(x_i,s),(x_j,m)}\big(\tau_{(x_i,s)}|\theta(t)\big)}{\lambda_{(x_i,s)}\big(\tau_{(x_i,s)}|\theta(t)\big)} \tag{12}$$

$$\psi_{\tau_{(x_i,s)}}\left(\tau_{(x_i,s)}|\boldsymbol{\theta}(t)\right) = \lambda_{(x_i,s)}\left(\tau_{(x_i,s)}|\boldsymbol{\theta}(t)\right) \cdot exp\left(-\int_0^{\tau_{(x_i,s)}}\lambda_{(x_i,s)}(u|\boldsymbol{\theta}(t))du\right) \qquad (13)$$

According to Eq. (11) to Eq. (13), we can implement the MC simulation procedure for the system as follows: repeatedly using $\psi_{\tau_{(x_i,s)}}\left(\tau_{(x_i,s)}|\boldsymbol{\theta}(t)\right)$ and $\pi_{(x_i,s),(x_j,m)}\left(\tau_{(x_i,s)}|\boldsymbol{\theta}(t)\right)$ to sample the sojourn time $\tau_{(x_i,s)}$ and the arrival state (x_j, m), until the cumulative sojourn time reaches the preset task time or the system enters the failure space. **Algorithm 2.1** provides the procedure to sample $\tau_{(x_i,s)}$ and (x_j, m). **Algorithm 2.2** presents the MC simulation procedure for the system.

Algorithm 2.1 Procedure for sampling $\tau_{(x_i,s)}$ and (x_j, m)

Step1: Generate two uniformly distributed random numbers r_1 and r_2 in interval [0,1].

Step2: If $\ln(1/r_1) < \int_0^\infty \lambda_{(x_i,s)}(u|\boldsymbol{\theta}(t))du$, go to Step3, otherwise $\left(\tau_{(x_i,s)}, (x_j, m)\right) = (\infty, (x_i, s))$.

Step3: Choose $\tau_{(x_i,s)}$ satisfying $\int_0^{\tau_{(x_i,s)}}\lambda_{(x_i,s)}(u|\boldsymbol{\theta}(t))du = \ln(1/r_1)$.

Step4: Construct a state indexing scheme $k = 1,2, ...,$ for all possible outgoing states from (x_i, s) and choose the arrival state (x_j, m) with index k_j satisfying $\sum_{k=1}^{k_j-1}\lambda_{(x_i,s),k}\left(\tau_{(x_i,s)}|\boldsymbol{\theta}(t)\right) < r_2\lambda_{(x_i,s)}\left(\tau_{(x_i,s)}|\boldsymbol{\theta}(t)\right) \le \sum_{k=1}^{k_j}\lambda_{(x_i,s),k}\left(\tau_{(x_i,s)}|\boldsymbol{\theta}(t)\right)$.

Algorithm 2.2 MC simulation procedure for the system

Step1: **Set** N_{max} (the maximum number of replications), $n=0$ and T (the mission time).

Step2: While $n < N_{max}$, do the following.

Initialize the state of $X_t^S = (X(0), 0)$ (initial state), time $t=0$ (initial time), the condition $\boldsymbol{\theta}(t) = (0, \cdots, 0, \{X(0)\})$.

While $t < T$, do the following.

Sample $\tau_{(x_i,s)}$ and (x_j, m) by **Algorithm 2.1**.

Update $t = t + \tau_{(x_i,s)}$, $X_t^S = (x_j, l)$, and $\boldsymbol{\theta}(t)$.

End if.

If $X_t^S \in \mathcal{F}_{X^S}$, then break.

End if.

End While.

Set $n=n+1$.

End While.

Then, the estimation of the state probability vector $\hat{\boldsymbol{P}}(t) = \left(\hat{p}_1(t), \ldots, \hat{p}_N(t)\right)$ at time t is

$$\hat{\boldsymbol{P}}(t) = \frac{1}{N_{max}}\left(n_{1,t}, \ldots, n_{N_X,t}\right) \qquad (14)$$

where $\{n_{i,t}|i = 1, \ldots, N_X, t \le T\}$ is the total number of visits to state $x_j \in S_X$ by time t, N_X is the total number of states in S_X. The sample variance of $\hat{p}_i(t)$ is defined as

$$var_{\hat{p}_i(t)} = \frac{1}{N_{max} - 1}\hat{p}_i(t)\left(1 - \hat{p}_i(t)\right) \qquad (15)$$

Then, the reliability function of the system is

$$R(t) = 1 - \sum_{i \in \mathcal{F}_X} \hat{p}_i(t) \tag{16}$$

3   Model Validation Based on a Simple Case

(a) Degradation process $X_1(t)$

(b) Degradation process $X_2(t)$
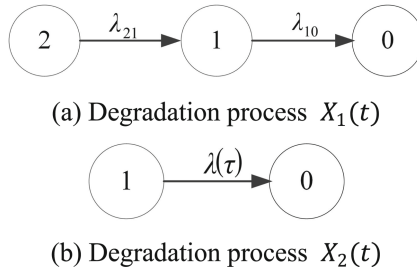
Fig. 3. Degradation models for validation calculation

We selected a simple system with 2 degradation processes (as shown in Fig. 3) for model validation. The correctness of the model is verified by comparing the computational results of the model with the results estimated using the analytic formulations of the functioning states of the system derived subsequently.

We assume that sojourn times in the functioning state of $X_1(t)$ and $X_2(t)$ obey exponential and Weibull distributions, respectively. The transition rate λ_{ij} of $X_1(t)$ is constant. The degenerate evolution of $X_2(t)$ is influenced by the state of $X_1(t)$. Suppose $X_2(t)$ jumps to state j at time t after a sojourn of τ in state i, and the parameters of the distribution of the state sojourn time of $X_2(t)$ under the state k of $X_1(t)$ are $\left(\alpha^k, \beta^k\right)$. Given the state set of $X_1(t)$ on time interval $(t - \tau, t)$ is $\left\{k; k \in S'_{X_1} \subset S_{X_1}\right\}$, the transition rate of $X_2(t)$ is assumed as

$$\bar{\lambda}_{ij}^2(\tau) = \bar{\alpha}^2 \left(\bar{\beta}_{ij}^2\right)^{\bar{\alpha}^2} \tau^{\bar{\alpha}^2 - 1} \tag{17}$$

$$\bar{\alpha}^2 = \sum_{k \in S'_{X_1}} \frac{\alpha^k}{N_k}, \bar{\beta}_{ij}^2 = \sum_{k \in S'_{X_1}} \frac{\beta^k}{N_k} \tag{18}$$

where N_k is the state number of S'_{X_1}.

The probability model [9, 10] for a shock leading to a sudden transition in the state of $X_1(t)$ or $X_2(t)$ is

$$p_{ij}^x = \frac{9 \times 0.1^{(i-j+1)}}{1 - 0.1^{(i+1)}}, i \geq j, x = 1, 2 \tag{19}$$

The model satisfies $\sum_{j=i}^{0} p_{ij}^x = 1$.

Given that $X_1(t)$ state i_1 and $X_2(t)$ state i_2 at time s, the probability that $X_1(t)$ and $X_1(t)$ do not experience a sudden state change caused by random shocks on the time interval $[s, s + u]$ is

$$\varphi_{(i_1,i_2)}(u) = \sum_{n=0}^{\infty} \left(p_{i_1,i_1}^1\right)^n \left(p_{i_2,i_2}^2\right)^n \frac{(\mu u)^n}{n!} e^{-\mu u} = e^{-\mu u \left(1 - p_{i_1,i_1}^1 p_{i_2,i_2}^2\right)} \tag{20}$$

Suppose $X_1(0) = 2$ and $X_2(0) = 1$, and use $P_{(i_1,i_2)}(t)$ to denote the probability that the system is in state (i_1, i_2) at time t. For $X_1(t)$ and $X_2(t)$ to be in the initial state at time t, the 2 degradation processes should be free of state transfers due to degradation or random shocks, then we have

$$P_{(2,1)}(t) = e^{-\lambda_{21}t} e^{-(\beta^2 t)^{\alpha^2}} \varphi_{(2,1)}(t) \tag{21}$$

Define $\eta_2 = min\{\delta_2, \tau_1\}$, where δ_2 is the sojourn time of $X_1(t)$ in state 2 considering the effect of random shocks, and τ_1 is the time interval from $t = 0$ when no transfer of $X_2(t)$ from the initial state 1 caused by random shocks occurs. The probability density function (PDF) of η_2 is

$$g(u) = \lambda_{21} e^{-\lambda_{21}u} \varphi_{(2,1)}(u)$$
$$+ e^{-\lambda_{21}u} \sum_{n=1}^{\infty} \left(p_{22}^1\right)^{n-1} p_{21}^1 \left(p_{11}^2\right)^n \frac{(\mu u)^{n-1}}{(n-1)!} \mu e^{-\mu u} = \left(\lambda_{21} + \mu p_{21}^1 p_{11}^2\right) \tag{22}$$
$$\cdot e^{-\left(\mu\left(1 - p_{22}^1 p_{11}^2\right) + \lambda_{21}\right)u}$$

Assume that $X_1(t)$ transfers from state 2 to state 1 at time u and $X_2(t)$ is in initial state 1 at this time, let $\rho^u = min\{\delta_{u,1}, \delta_{u,2}\}$, where $\delta_{u,1}$ and $\delta_{u,2}$ denote the sojourn times in the current states since time u for $X_1(t)$ and $X_2(t)$, respectively. Without considering the effect of random shocks, ρ^u has the cumulative distribution function (CDF)

$$F_{\rho^u}(x) = 1 - exp\left(-\int_0^x \left(\lambda_{10} + \overline{\alpha}(\overline{\beta})^{\overline{\alpha}}(v + u)^{\overline{\alpha}-1}\right) dv\right) \tag{23}$$

where $\overline{\alpha} = (\alpha^2 + \alpha^1)/2$, $\overline{\beta} = (\beta^2 + \beta^1)/2$.

Then we have

$$P_{(1,1)}(t) = \int_0^t g(u) e^{-(\beta^2 u)^{\alpha^2}} \cdot \left(1 - F_{\rho^u}(t - u)\right) \varphi_{(1,1)}(t - u) du \tag{24}$$

Based on the parameters in Table 1, the functioning state probabilities of the system calculated using the model are shown in Fig. 4, where the results calculated using Eqs. (21) and (24) are also presented. A quantitative comparison of the results shows a high degree of agreement between the results using the model and the analytical formulas, with relative errors below 6%, indicating the correctness of the model.

Table 1. Parameters for model validation

Parameter	Value
λ_{21}	1.0E–3/h
λ_{10}	1.0E–3/h
β^0	1.0E–4/h
β^1	1.0E–4/h
β^2	1.0E–4/h
α^k	2.0
μ	1.0E–4/h
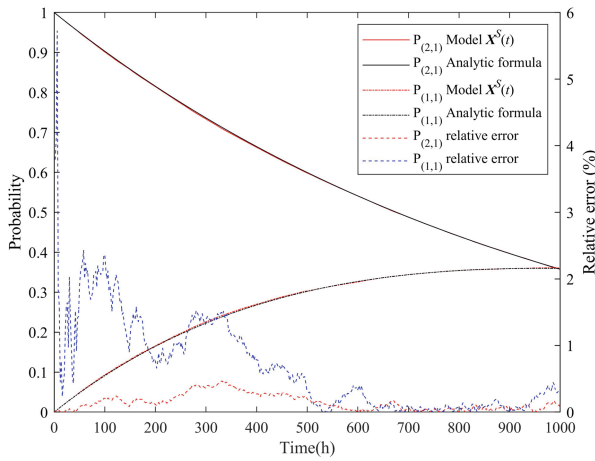
Fig. 4. Probabilities of functioning states estimated with different methods

4   Numerical Example

The model is applied to one sub-system of the residual heat removal system (RHRS) of a nuclear power plant [9]. The system consists of a centrifugal pump and a pneumatic valve in series, as shown in Fig. 5.

Valve   Pump
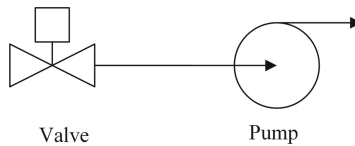
Fig. 5. A Subsystem of RHRS, consisting of a centrifugal pump and a pneumatic valve

4.1 Degradation Modeling

Table 2. Model parameters

Parameter	Value
β_{32}^1	5.0E–3/h
β_{21}^1	5.0E–4/h
β_{10}^1	5.0E–5/h
α^1	2.0
$\beta_{21}^{2,3}$	1.0E–4/h
$\beta_{21}^{2,2}$	1.5E–4/h
$\beta_{21}^{2,1}$	3.0E–4/h
$\beta_{21}^{2,0}$	1.0E–4/h
$\beta_{10}^{2,3}$	1.0E–5/h
$\beta_{10}^{2,2}$	1.5E–5/h
$\beta_{10}^{2,1}$	3.0E–5/h
$\beta_{10}^{2,0}$	1.0E–5/h
α^{2k}	2.0
μ	1.0E–4/h

The pump's performance will deteriorate if wear, corrosion, or erosion occurs to the parts that comprise the pump. The primary degradation mechanism of the valve is the external leakage due to corrosion at the actuator and bottom pneumatic port connection. We assumed that the pump's performance could be divided into four mutually exclusive levels, and there are three states for the valve. Let $X_1(t)$ denote the degradation level of the pump by time t, with a state space $S_{X_1} = \{0, 1, 2, 3\}$ where 3 is the perfect functioning state and 0 is the failure state. Let $X_2(t)$ denote the degradation level of the valve by time t, with a state space $S_{X_2} = \{0, 1, 2\}$ where 2 is the perfect functioning state and 0 is the failure state. The multi-state models describing the degradation process of the pump and valve are shown in Fig. 6, where $\lambda_{ij}^1(\tau)$ and $\lambda_{ij}^1(\tau)$ denote the derogation transition rates of the pump and valve associated with the sojourn time τ in the current state, respectively.

The state space of the process $X(t) = (X_1(t), X_2(t))$ is $S_X = \{(0, 0), (1, 0), (2, 0), (3, 0), (0, 1), (1, 1), (2, 1), (3, 1), (0, 2), (1, 2), (2, 2), (3, 2)\}$. The failure state space is $\mathcal{F}_X = \{(0, 0), (1, 0), (2, 0), (3, 0), (0, 1), (0, 2)\}$.

We assumed that the sojourn time τ in the current state i of $X_n(t)$, $n = 1, 2$ before the process jumps to state i-1 follows the Weibull distribution. We take the shape parameter $\alpha > 1$ to consider the increase of the component degradation transition rate with

(a) Pump degradation process

(b) Valve degradation process
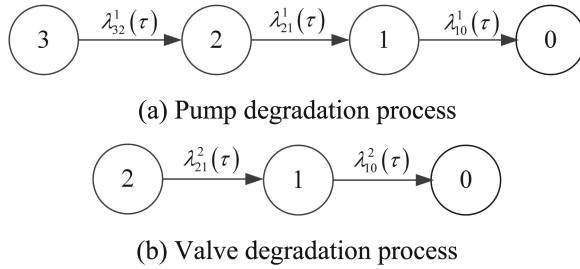
Fig. 6. Degradation models for the pump and valve

the growth of the sojourn time, namely, the aging effect. Then the transition rates of $X_n(t), n = 1, 2$ are

$$\lambda_i^x(\tau) = \alpha^x \left(\beta_{ii-1}^x\right)^{\alpha^x} \tau^{\alpha^x - 1}, x = 1, 2 \tag{25}$$

The dependency of the two degradation processes is that the pump degradation will vibrate, causing the valve to vibrate, which accelerates the external leakage process of the valve. The assumption on the transition rate of (Eq. (17)) is used again. Furthermore, the shock impact model (Eq. (19)) in Sect. 3 is applied.

The degradation transition rates could be evaluated from degradation/failure data from historical field collection. The transition rates associated with maintenance tasks could be estimated from the data on maintenance activities. For example, for the pump, the parameters of the postulated distribution of state transition times can be estimated by statistics of the state transition times of numerous identical or similar pumps using the method of maximum likelihood or Bayesian estimation. The optimal distribution could be selected by the goodness-of-fit hypothesis test. Correspondingly, the state transition rates of the pump are obtained. Due to the lack of data, we assumed the model parameters as presented in Table 2 for the illustrative calculations.

4.2 Results and Analysis

Let the number of simulations be taken as 1E4, 1E5, and 1E6, respectively, and we estimate the reliability of the system over [0, 13176 h] (18 months, a typical nuclear plant refueling cycle), as shown in Fig. 7, which tends to stabilize when reaches 1E5.

The time-dependent probabilities of functioning states of the system are shown in Fig. 8. In many trials, the system jumps out of the initial state (3, 2) in a very short time, so the probability of this state drops quickly (at about $t = 52$ h) to 0. Due to the degradation of the pump and valve, the probabilities of the other functioning states go through an increasing phase and then a decreasing phase.

The reliability of the system, the pump, and the valve with/without random shocks are estimated, as shown in Fig. 9. Furthermore, the numerical comparisons on the reliabilities at t = 13176 h are provided in Table 3. The results reveal that ignoring random shocks will lead to an overestimation of the reliability of the system and the components.
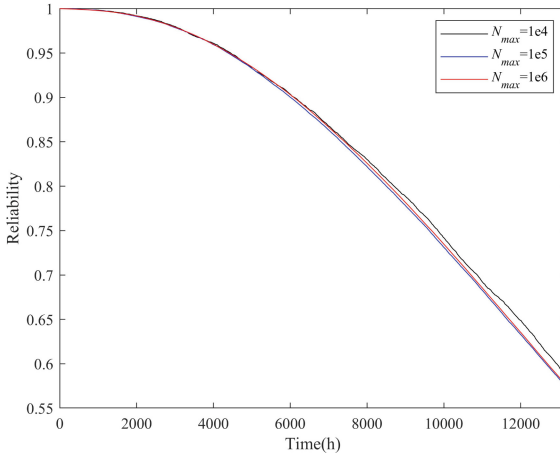
Fig. 7. System reliability estimated with different Nmax
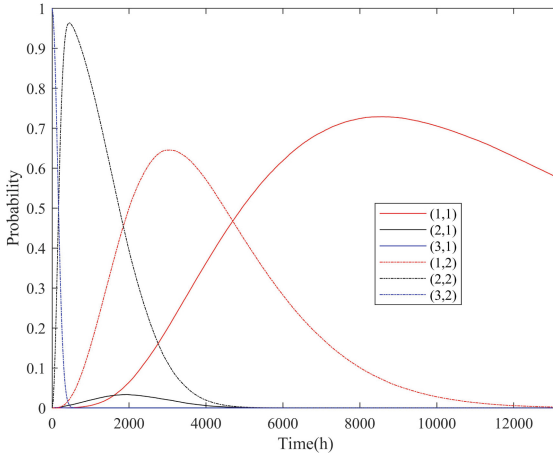
Fig. 8. Probabilities of functioning states of the system

Figure 10 presents the reliability of the system, the pump, and the valve with/without degradation dependency. Table 4 gives the numerical comparisons on the reliabilities at $t = 13176$ h. Neglecting degradation dependency will result in an overestimation of the reliability of the system and the valve. Since the degradation process of the pump is independent of the degradation level of the valve, the reliabilities of the pump with/without degradation dependency are equal.
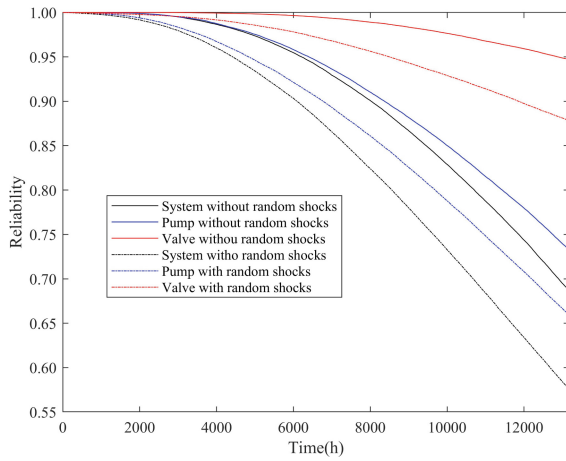
Fig. 9. The reliability of the system, the pump, and the valve without/with random shocks

Table 3. Reliability with/without random shocks at $t = 13176$ h

	Without random shocks	With random shocks	Relative change
System	0.6869	0.5758	16.17%
Pump	0.7325	0.6557	10.48%
Valve	0.9470	0.8778	7.31%
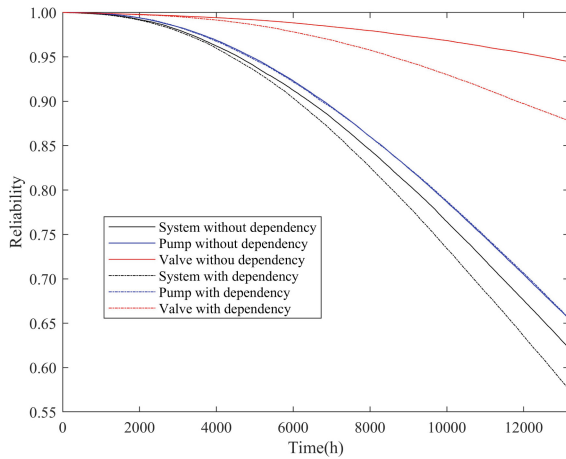
Fig. 10. The reliability of the system, the pump, and the valve without/with dependency

Table 4. Reliability with/without dependency at $t = 13176h$

	Without dependency	With dependency	Relative change
System	0.6222	0.5758	7.46%
Pump	0.6557	0.6557	0%
Valve	0.9447	0.8778	7.08%

5   Conclusions

In this paper, a multi-state degradation model for reliability assessment of multi-component nuclear safety systems is proposed, accounting for the dependency between degradation processes and random shocks. The degradation process of the system is modeled by the Semi-Markov process, and the random shocks are modeled by the Poisson process. Degradation dependency is modeled explicitly in the transition rates of the integrated degradation process of the system. The transfer kernel function of the holistic model for Monte Carlo simulation is derived. Based on a simple case, the correctness of the proposed model is verified by comparing the system state probabilities estimated using the proposed model and the analytical solution, respectively. The model is applied to the reliability analysis of one sub-system of the RHRS of a nuclear power plant.

The present model uses relatively simple models for the effects of random shocks and maintenance. In future work, more realistic and complex models for the effects of random shocks and maintenance will be investigated.

References

1. Zio, E.: Some challenges and opportunities in reliability engineering. IEEE Trans. Reliab. **65**(4), 1769–1782 (2016)
2. Fleming, K.N.: Markov models for evaluating risk-informed in-service inspection strategies for nuclear power plant piping systems. Reliab. Eng. Syst. Saf. **83**(1), 27–45 (2004)
3. Unwin, S.D., Lowry, P.P., Layton, R.F., Heasler, P.G., Toloczko, M.B.: Multi-state physics models of aging passive components in probabilistic risk assessment. In: Proceedings of International Topical Meeting Probabilistic Safety Assessment and Anal. (PSA 2011), Wilmington, NC, USA, 13–17 March 2011, vol. 1, pp. 161–172 (2011)
4. Giorgio, M., Guida, M., Pulcini, G.: An age-and state-dependent Markov model for degradation processes. IIE Trans. **43**(9), 621–632 (2011)
5. Moghaddass, R., Zuo, M.J.: Multistate degradation and supervised estimation methods for a condition-monitored device. IIE Trans. **46**(2), 131–148 (2014)
6. Lin, Y.-H., Li, Y.-F., Zio, E.: Integrating random shocks into multi-state physics models of degradation processes for component reliability assessment. IEEE Trans. Reliab. **64**(1), 154–166 (2014)
7. Fleming, K.N., Unwin, D. Kelly, et al. Treatment of Passive Component Reliability in Risk-Informed Safety Margin Characterization (FY 2010 Report NL/EXT-10–20013). Idaho National Laboratory (INL) Idaho Falls, ID (2010)
8. Salonen, J., Auerkari, P., Lehtinen, O., et al.: Experience on in-service damage in power plant components. Eng. Fail. Anal. **14**(6), 970–977 (2007)

9. Lin, Y.-H., Li, Y.-F., Zio, E.: Reliability assessment of systems subject to dependent degradation processes and random shocks. IIE Trans. **48**(11), 1072–1085 (2016)
10. Srivastav, H., Lundteigen, M.A., Barros, A.: Introduction of degradation modeling in qualification of the novel subsea technology. Reliab. Eng. Syst. Saf. **216**, 107956 (2021)
11. Yang, W.S., Lim, D.E., Chae, K.C.: Maintenance of multi-state production systems deteriorated by random shocks and production. J. Syst. Sci. Syst. Eng. **20**(1), 110–118 (2011)
12. Eryilmaz, S.: Assessment of a multi-state system under a shock model. Appl. Math. Comput. **269**, 1–8 (2015)
13. Gillespie, D.T.: Monte Carlo simulation of random walks with residence time dependent transition probability rates. J. Comput. Phys. **28**(3), 395–407 (1978)
14. Zio, E.: The Monte Carlo Simulation Method for System Reliability and Risk Analysis. Springer, Heidelberg (2014)
15. Lin, Y.-H., Li, Y.-F., Zio, E.: A comparison between Monte Carlo simulation and finite-volume scheme for reliability assessment of multi-state physics systems. Reliab. Eng. Syst. Saf. **174**, 1–11 (2018)

Heat Pipe Temperature Oscillation Effects on Solid-State Reactor Operation

Yugao Ma[1], Yicheng Zhao[2], Hongxing Yu[1], Shanfang Huang[2(✉)], Jian Deng[1], and Xiaoming Chai[1]

[1] Nuclear Power Institute of China, Chengdu, China
[2] Tsinghua University, Beijing, China
sfhuang@tsinghua.edu.cn

Abstract. The alkali metal heat pipes are the critical heat transfer elements in heat pipe cooled reactors. However, there are instabilities in heat pipes such as geyser boiling, resulting in temperature oscillation and even threatening the reactor safety. This work developed a coupled neutronic and thermal-mechanical analysis method to analyze the effects of geyser boiling and heat pipe temperature oscillations on the critical parameters, e.g., temperature and stress, during reactor operation. The megawatt heat pipe reactor MegaPower was chosen as an application case. The simulations show that the heat pipe temperature oscillation leads to the same frequency oscillation of the temperature and stress in the solid-state core. Besides, the temperature amplitudes are significantly reduced by shortening the oscillation period. Reducing the oscillation period from 60 s to 15 s reduced the temperature amplitude of the fuel pellet center from 22°C to 5°C. Furthermore, the stress oscillation in the core may lead to material fatigue or even failure for a long period of operation, which is highly undesired. This work can provide valuable data and references for the safety design of heat pipe reactors.

Keywords: heat pipe cooled reactor · geyser boiling · temperature oscillation

1 Introduction

The heat pipe cooled reactor is characterized by a simple system, high reliability, passive heat transfer, and a high operating temperature. There is a wide range of potential application scenarios in the field of micro-nuclear power in extreme environments such as deep space, deep sea, and deep earth [1–4]. In heat pipe reactors, alkali metal heat pipes are the critical heat transfer elements. Heat is transferred efficiently through these heat transfer elements based on latent heat. Additionally, capillary force drives the internal medium into continuous phase transitions. Therefore, heat pipes have high heat transfer performance [5], isothermal performance [6], and thermal response speed [7]. Due to their excellent heat transfer capabilities, heat pipes have been widely used in waste heat recovery [8–10], nuclear reactor power [11–14], and residual heat removal [15, 16].

In general, heat pipes provide a high level of robustness and repeatability. Many steady-state and transient analyses have demonstrated the high level of safety and reliability of the heat pipe reactor. For example, Poston et al. [17] described the design and analysis of the SAFE-400 reactor. They analyzed heat pipe failure scenarios and pointed out that the SAFE-400 was designed with a considerable thermal margin under nominal operating conditions. Li et al.[18] developed a transient analysis code SNPS-FTASR to study the transient response of HP-STMCs core on reactivity-insertion accident transient and a heat pipe failed transient. The simulation showed that the HP-STMCs core was safe at transient states including reactivity-insertion accidents and a heat pipe failure. Ma et al. [12] also conducted the transient heat pipe failure accident analysis of the MegaPower reactor. Their results showed that the operating conditions far from the failure area were little affected.

However, heat pipes can experience a particular unstable phenomenon, known as geyser boiling, which leads to temperature oscillations in heat pipes. Murphy [19] described the geyser boiling phenomenon as the rapid expulsion of a boiling liquid and its vapor from a vertical heat pipe and mentioned that geyser boiling behavior can be affected by many factors. Lin et al. [20] experimentally studied the influence of heating power, condenser temperature, liquid charge ratio, and evaporator length on water and ethanol geyser boiling. Ma et al. [21] mainly considered the geyser boiling in sodium heat pipes at near-horizontal inclination angles. They found that the evaporation pulsation was up to 80 °C in the operating temperature range of 600 °C–700 °C.

In a heat pipe cooled reactor, alkali metal heat pipes are closely related to the reactor operation. During geyser boiling, the heat pipe's temperature oscillates, which inevitably affects the core's operation status. However, previous studies of reactor safety have barely considered the instability of heat pipe temperature oscillations. Meanwhile, in reactor design, safety is an absolute priority and extremely strict. Therefore, further investigations on the effects of heat pipe temperature oscillations are essential.

In the present work, a coupled neutronic and thermal-mechanical model was developed to study the effects of geyser boiling and temperature oscillations on the thermal-mechanical performance of the reactor core. The sensitivity analysis of the oscillation period was also conducted.

2   Methodology

Figure 1 shows the model relationship, developed in this work, which mainly includes the heat pipe heat transfer model, neutronic point kinetics model, neutron transport model, and core zonal multi-channel thermal-mechanical model. The neutronic point kinetics model determines the total power with the neutron transport simulation to obtain the relative power distribution. The power is transferred as a volumetric heat source to the core zonal multi-channel thermal-mechanical model to determine the temperature field and force field of the heat pipe, fuel, monolith, and other components, and fed back to the neutronic point kinetics model via reactivity feedback.

These models are discussed in detail in the following sections.
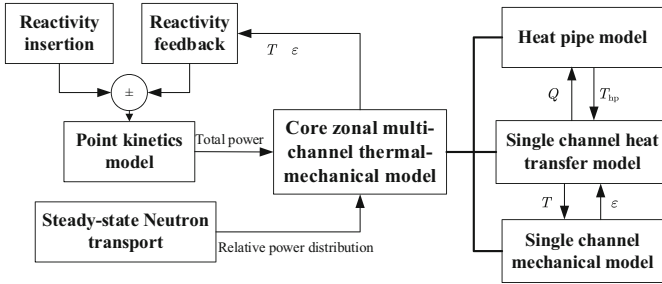
Fig. 1. Coupled neutronic and thermal-mechanical model

2.1 Point Kinetics Model

A point kinetics model is used to determine the fission power. The standard point kinetics model is used with six groups of delayed neutrons to calculate the core fission power as:

$$\frac{\mathrm{d}N(t)}{\mathrm{d}t} = \frac{\rho(t) - \overline{\beta}(t)}{\Lambda(t)} N(t) + \sum_{i=1}^{d} \lambda_i C_i(t)$$

$$\frac{\partial C_i(t)}{\partial t} = \frac{\overline{\beta}_i(t)}{\Lambda(t)} N(t) - \lambda_i C_i(t) \tag{1}$$

where $N(t)$ is the approximate neutron density of each energy group, t is the time, ρ is the reactivity, β_i is the fraction of effective delayed neutrons, Λ is the neutron generation time, λ_i is the decay constant of the delayed neutrons, and C_i is the delayed neutron precursor concentration. The Monte Carlo program RMC is used to determine the dynamics parameters in Eq. (1).

2.2 Reactivity Feedback Model

The Doppler effect and thermal expansion are the primary mechanisms for reactivity feedback. Besides, in the heat pipe cooled reactor, the heat pipe two-phase working fluid is impacted by the operating temperature, introducing a reactivity temperature coefficient. Therefore, the reactivity feedback equation can be written as:

$$\rho(t) = \rho_{\mathrm{ext}} + \rho_{\mathrm{feedback}}$$
$$= \rho_{\mathrm{ext}} + \alpha_{\mathrm{f,D}} \ln\left(\overline{T_{\mathrm{f}}}/T_{\mathrm{f}}^0\right) + \alpha_{\mathrm{f,G}}\left(\overline{T_{\mathrm{f}}} - T_{\mathrm{f}}^0\right)$$
$$+ \alpha_{\mathrm{M,D}} \ln\left(\overline{T_{\mathrm{M}}}/T_{\mathrm{M}}^0\right) + \alpha_{\mathrm{M,G}}\left(\overline{T_{\mathrm{M}}} - T_{\mathrm{M}}^0\right)$$
$$+ \alpha_{\mathrm{R,D}} \ln\left(\overline{T_{\mathrm{R}}}/T_{\mathrm{R}}^0\right) + \alpha_{\mathrm{R,G}}\left(\overline{T_{\mathrm{R}}} - T_{\mathrm{R}}^0\right)$$

$$+ \alpha_{HP}\left(\overline{T_{HP}} - T_{HP}^0\right) \tag{2}$$

where $\overline{T}$ and T^0 are the average temperature and the reference temperature. Subscripts f, M, R and HP refer to the fuel, the monolith, the reflector, and the heat pipe, respectively. Subscripts D and G refer to the Doppler reactivity coefficient and geometric reactivity coefficient.

2.3 Zonal Multi-channel Thermal-Mechanical Model

Temperature changes can lead to changes in geometric parameters such as radius and air gap thickness and material properties such as density. These changes, in turn, affect the temperature distribution in the core. Therefore, thermal-mechanical coupled analyses are essential for heat pipe cooled reactors. To simplify this coupling problem, the core is divided into several zones, and each zone is further divided into several channels. Each channel's thermal and mechanical models are constructed and then coupled.

2.3.1 Heat Transfer Model in a Single Channel

A hexagonal single heat transfer unit, as illustrated in Fig. 2, can be extracted from a typical heat pipe cooled reactor and contains a heat pipe, its adjacent monolith, and fuel rods. Each unit is then modeled as a single channel based on volume equivalence. Figure 2 depicts the modeled single channel with control volumes separated axially. The heat pipe is in the middle with layers for the heat pipe wall, monolith, helium gap, and fuel. The heat conduction equation in the radial direction in cylindrical coordinates is:

$$\rho_i c_i \frac{\partial T_i}{\partial t} = \frac{1}{r}\frac{\partial}{\partial r}\left(\lambda_i r \frac{\partial T_i}{\partial r}\right) + \dot{\phi}_i \tag{3}$$

where the subscript i represents the various structures such as the monolith, helium gas gap, fuel, or heat pipe wall; ρ is the density; c is the specific heat; λ is the thermal conductivity; T is the material temperature, and $\dot{\phi}$ is the power density including the fission heat source and the radial thermal conduction between components.

The boundary conditions have continuity of the temperature and heat flux at the contact surfaces of the walls. The outer channel wall, which corresponds to the fuel pellet center, is assumed to be adiabatic due to symmetry.
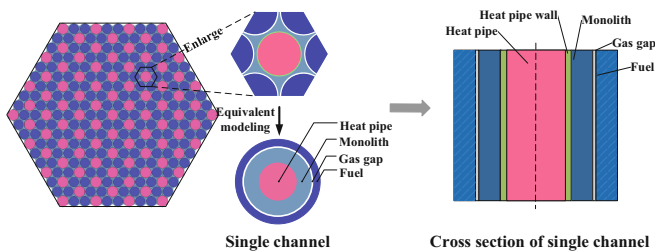
Fig. 2. A fuel assembly and its single-channel model

This modeling changes the geometry of the air gap and the fuel, which affects the thermal resistance and temperature distribution. Therefore, according to the conservation conditions of heat flow and the principle of equivalence with thermal resistance, a thermal conductivity correction is introduced to correct the heat transfer results:

$$
\begin{cases}
\lambda'_f = k_f \lambda_f = \dfrac{\frac{\dot{\phi}}{4}\left(r_{f,o}^2 - r_{f,i}^2\right) - \frac{\dot{\phi}}{2} r_{f,i}^2 \ln\left(\frac{r_{f,o}}{r_{f,i}}\right)}{\frac{\dot{\phi}}{4\lambda_f} r_f^2} = \dfrac{\left(r_{f,o}^2 - r_{f,i}^2\right) - 2 r_{f,o}^2 \ln\left(\frac{r_{f,o}}{r_{f,i}}\right)}{r_f^2} \lambda_f \\[4mm]
\lambda'_g = k_g \lambda_g = \dfrac{6 \ln(r_{g,o}/r_{g,i})/(2\pi L)}{3 \ln((r_f + 2 r_g)/r_f)/(2\pi L \lambda_g)} = \dfrac{2 \ln(r_{g,o}/r_{g,i})}{\ln((r_f + 2 r_g)/r_f)} \lambda_g
\end{cases}
\tag{4}
$$

where λ is the thermal conductivity, and k is the correction factor. Subscripts f and g refer to the fuel and gas gap. L is the axial height. r is the radius. Subscripts o and i refer to the outer and inner radius, respectively.

2.3.2 Mechanical Model in a Single Channel

The mechanical model unit is extracted according to the repeating geometric layout of the heat pipe reactor, which differs from the heat transfer model in that the fuel is located in the center and the monolith surrounds it, as shown in Fig. 3.
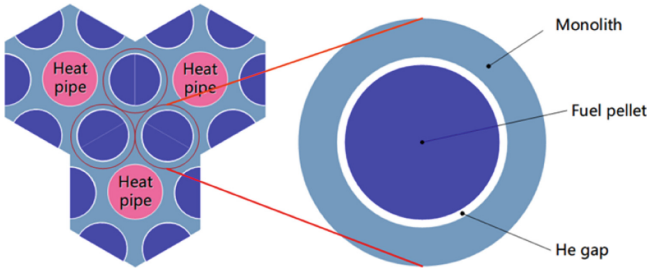
Fig. 3. Mechanical model

Basic assumptions such as generalized plane strain assumption, continuity assumption, and quasi-static assumption are introduced [22], then the balance equation, geometric equation, and constitutive equation are as follows:

$$
\frac{\partial \sigma_r}{\partial r} + \frac{\sigma_r - \sigma_\theta}{r} = 0
\tag{5}
$$

$$
\begin{cases}
\varepsilon_r = \frac{\partial u}{\partial r} \\[2mm]
\varepsilon_\theta = \frac{u}{r} \\[2mm]
\varepsilon_z = \frac{\partial w}{\partial z} = \text{const}
\end{cases}
\tag{6}
$$

$$
\begin{cases}
\varepsilon_r = \varepsilon_r^e + \varepsilon_r^\alpha + \varepsilon_r^{ie} = \frac{1}{E}(\sigma_r - \mu(\sigma_\theta + \sigma_z)) + \varepsilon_r^\alpha + \varepsilon_r^{ie} \\[2mm]
\varepsilon_\theta = \varepsilon_\theta^e + \varepsilon_\theta^\alpha + \varepsilon_\theta^{ie} = \frac{1}{E}(\sigma_\theta - \mu(\sigma_r + \sigma_z)) + \varepsilon_\theta^\alpha + \varepsilon_\theta^{ie} \\[2mm]
\varepsilon_z = \varepsilon_z^e + \varepsilon_x^\alpha + \varepsilon_z^{ie} = \frac{1}{E}(\sigma_z - \mu(\sigma_r + \sigma_\theta)) + \varepsilon_z^\alpha + \varepsilon_z^{ie}
\end{cases}
\tag{7}
$$

where σ is principal stress and ε represents the strain. Subscripts r, θ and z refer to the radial, circumferential, and axial terms, respectively. ε^e, ε^α and ε^{ie} are the elastic strain,

thermal expansion strain, and other inelastic strains. u and w are the radial and axial displacements, respectively; μ is Poisson's ratio, and E is the elastic modulus.

The boundary conditions of the fuel pellet center, the outer side of the fuel, and the inner side of the monolith are as follows:

$$\sigma_{r,\,in}^{pellet} = \sigma_{\theta,\,in}^{pellet}$$

$$\sigma_{r,\,in}^{monolith} = \sigma_{r,\,out}^{pellet} = \begin{cases} -P_g, \, d_g > 0 \\ -P_{con}, \, d_g = 0 \end{cases} \tag{8}$$

where d_g is the air gap thickness. When the fuel and the monolith contact with each other, $d_g = 0$ and the radial stress is the contact stress of the fuel and the monolith(P_{con}). Otherwise, $d_g > 0$ and the radial stress is the gas pressure (P_g).

2.3.3   Thermal and Mechanical Coupling

The thermal and mechanical results for the reactor are then coupled via variable transfer, as illustrated in Fig. 4. The core temperature field calculated by the heat transfer model is transferred to the mechanical model as a thermal load, and the core stress and strain calculated by the mechanical model will update the fuel radius, air gap thickness, and material density in the heat transfer model.
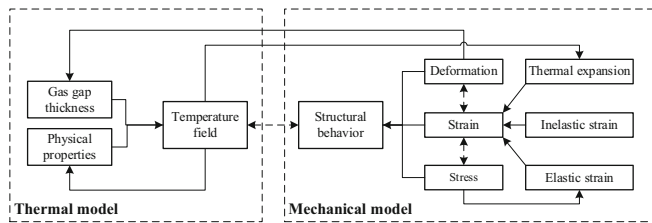
Fig. 4. Relationship between the thermal and mechanical analyses

2.3.4   Core Zonal Multi-channel Thermal-Mechanical Model

The core zonal multi-channel thermal-mechanical model is used to reflect the radial heat transfer between channels. In a typical heat pipe reactor, the fuel rods and heat pipes are organized within the monolith in a regular, compact way that may be separated into hexagonal zones, as shown in Fig. 5a. Figure 5b illustrates the extraction of a single channel for transient thermal analysis within each hexagonal zone. The operational statuses of all channels within a zone are assumed to be identical due to symmetry. The heat transfer between channels inside a zone is thus not taken into account; only the heat transfer between zones is.

The different zones are modeled using the equal volume method as:

$$SN_i = \pi \left(r_i^2 - r_{i-1}^2 \right) \tag{9}$$

where S is the area of one fuel unit, and N is the number of units contained in the zone. r is the outer wall radius corresponding to the zone, and i represents different zones.

The total heat source is the sum of the fuel fission power inside the zone and the conduction heat with adjacent zones:

$$\phi_{i,j} = \phi_{i,j}^{\text{fuel}} + \phi_{i,j}^{\text{con}} = \phi_{i,j}^{\text{fuel}} + \sum_{k=1}^{m} \lambda_{k,i} A_{k,i} \frac{\overline{T_{k,j}} - \overline{T_{i,j}}}{\Delta \overline{r_{i,k}}} \qquad (10)$$

where ϕ is net heat flux, T is volume average temperature, and A is the heat transfer area. λ is the conductivity, which is temperature-dependent and determined by the volume equivalence. Subscripts i and j refer to the zone number and the axial position. Subscript k represents the zone around the zone i.
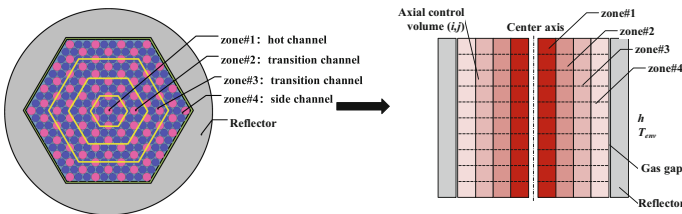
(a) Zones partitioning
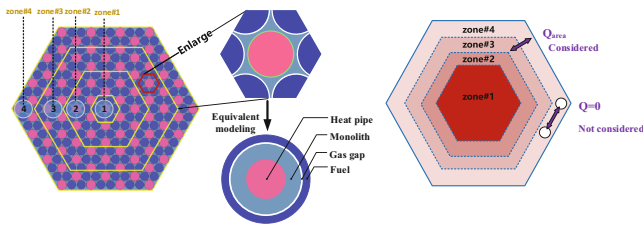
(b) Single channel

Fig. 5. Multi-channel heat transfer model

The heat source term of a unit is:

$$\phi_{i,j,\text{single}} = \phi_{i,j}/N_i \qquad (11)$$

where $\phi_{i,j,\text{single}}$ represents the power of axial control volume j in the single channel of the zone i, and N_i is the number of single channels in the zone i.

Through the helium gap, heat is transferred from the side channel into the reflector and then to the environment via convection.

3 Simulations and Analyses

The MegaPower reactor is a heat pipe cooled reactor designed by Los Alamos National Laboratory to meet off-grid areas' specialized energy demands [23]. Numerous calculations have been published on the neutron physics and thermal engineering of the MegaPower reactor [23, 24]. The above models and methods will be applied to the MegaPower to analyze the effects of heat pipe temperature oscillations on the reactor core.

As shown in Fig. 6, the core is divided into 16 zones with zone #1 as the hot channel, zone #2 to zone #15 as the transition channels, and zone #16 at the edge. The reactor heat is removed by solid heat conduction to the environment through the outer reflector wall by natural air convection to the ambient temperature at 300 K with a convection heat transfer coefficient of 20 $W/(m^2 \cdot k)$.

3.1 Heat Pipe Temperature Oscillation

Figure 7 illustrates the heat pipe temperature oscillation behavior. Table 1 lists the temperature oscillation parameters for the case of a 30° inclination angle [21]. The temperature oscillation in this work is described using a power function as follows:

$$A_1(h) = \begin{cases} A_{1,\max} \frac{h}{H} \left(\frac{t}{\alpha T}\right)^{\beta}, t < \alpha T \\ A_{1,\max} \frac{h}{H} \left(\frac{T-t}{(1-\alpha)T}\right)^{\gamma}, t > \alpha T \end{cases}$$

$$A_v = \begin{cases} A_{v,\max} \left(\frac{t}{\alpha T}\right)^{\beta}, t < \alpha T \\ A_{v,\max} \left(\frac{T-t}{(1-\alpha)T}\right)^{\gamma}, t > \alpha T \end{cases} \tag{12}$$

where $A_1(h)$ is the temperature amplitude at height h in the liquid pool, H is the maximum height of the liquid pool. A_v is the temperature amplitude in the vapor area. $A_{1,\max}$ and $A_{v,\max}$ represent the corresponding maximum temperature amplitudes, respectively. α represents the ratio of rise time in a single cycle. β and γ are power function coefficients of 0.5 and 1, respectively, determined by the experimental results. T is the period of geyser boiling, and $t \in [0, T]$.
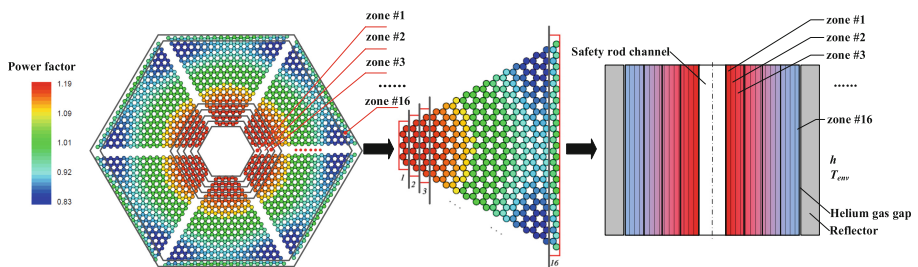
Fig. 6. Core zones partitioning

Table 1. Oscillation parameters for a 30° inclination angle

Heating rate (W)	Period (s)	Temperature (°C)		Amplitude (°C)		Fall time (s)		Rise time (s)	
		T_1^*	T_2^*	T_1	T_2	T_1	T_2	T_1	T_2
330	63	580	525	32	11	8	58	55	5
420	43	590	540	29	12	8	38	35	5
530	38	630	570	31	9	9	34	29	4
670	34	685	625	34	6	7	30	27	4
770	41	740	670	42	8	9	35	32	6
900	46	790	710	52	12	13	34	33	12

*T_1 and T_2 are the temperature of the liquid pool and the vapor area, respectively.
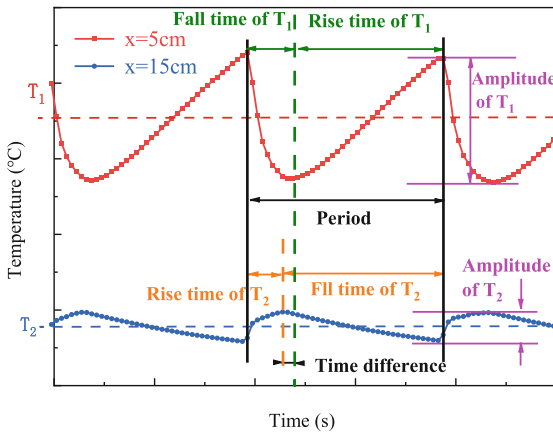
Fig. 7. Temperature oscillation of heat pipes

3.2 Effect of Heat Pipe Temperature Oscillation on the Core

The heat pipe reactor uses the heat pipe as the heat transmission element. The changes in heat pipe temperature will inevitably cause the core temperature and the core power to fluctuate. Besides, the changes will also affect the stress in the core. Therefore, this paper simulates the thermal and mechanical effects of heat pipe temperature oscillations on the core separately. The simulation parameters are determined by the above experimental results with an oscillation period of 60 s, a liquid pool height of 1/4 of the evaporator, and vapor area and liquid pool amplitudes of 10 °C and 70 °C, respectively. Finally, a sensitivity analysis of the period in the oscillation parameters is performed.
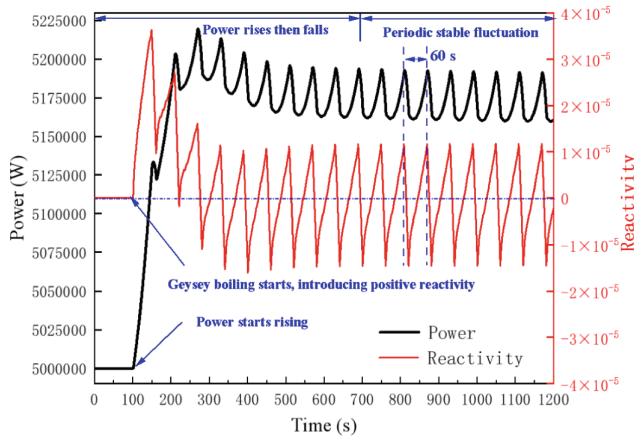
Fig. 8. The effect of temperature oscillation on the core

3.2.1 Thermal Effect

Figure 8 shows the effect of heat pipe temperature oscillation on the core power and reactivity. At 100 s, the geyser boiling starts, which introduce a small positive reactivity and thus increase the core power. However, negative feedback, such as the Doppler effect, causes the core to return to the critical gradually. Then, the heat pipe temperature oscillation still affects the core, resulting in a steady fluctuation in core power with a period of 60 s and an amplitude of 25 kW.

Figure 9a shows the temperature fluctuation of the heat pipe's outer wall. As height rises, the amplitude decreases. The temperature amplitude is 60 °C at a height of 0.15 m from the bottom of the evaporator and falls to 10 °C at a height of 0.375 m.

Figure 9b shows the temperature fluctuation of the monolith wall near the fuel. It can be seen that the effect of heat pipe temperature oscillation is slightly suppressed. The wall's temperature amplitude drops to 47 °C (at 0.15 m) and 9 °C (at 0.375 m or higher). Figure 9c and Fig. 9d show the temperature fluctuation of the fuel outer wall and the fuel pellet center, respectively. The influence is further attenuated. At a height of 0.15 m, the fuel outer wall temperature amplitude falls to 30 °C and the center temperature amplitude falls to 22 °C.

(a) heat pipe outer wall

(b) monolith wall near fuel

(c) fuel outer wall

(d) fuel pellet center
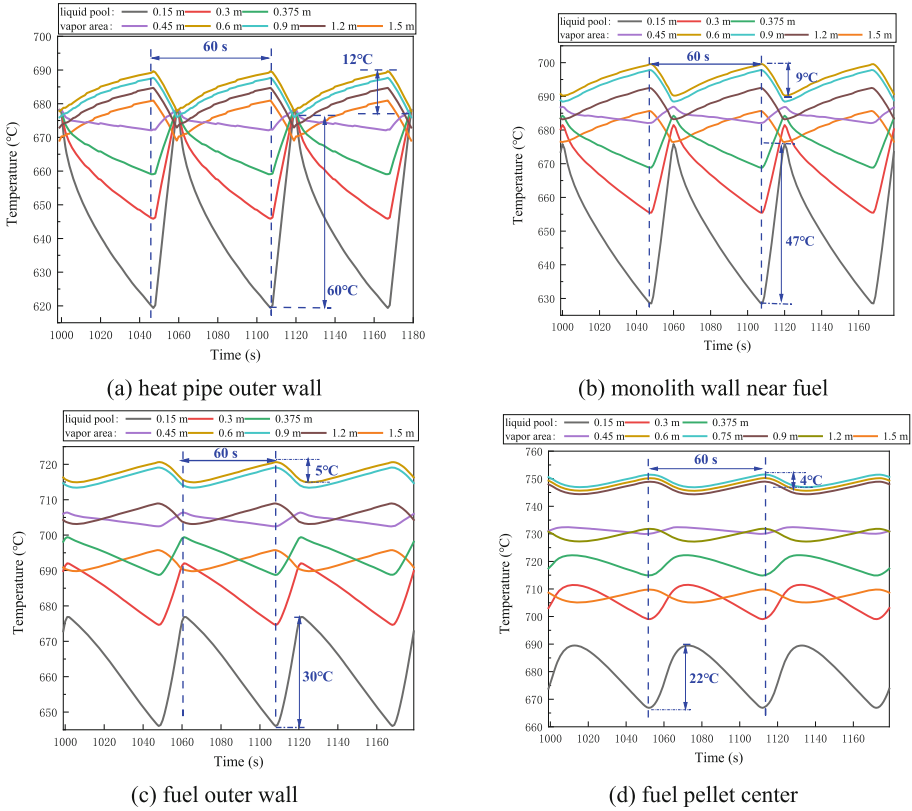
Fig. 9. Core temperature oscillation for geyser boiling condition (zone #1)

3.2.2 Mechanical Effect

Figure 10 shows the effect of heat pipe temperature oscillation on the stress in the core. With an amplitude of about 6 MPa, the peak stress oscillates at the same frequency as the temperature for both the fuel and the monolith. Although the oscillation range remains within the safety limit, the oscillation may aggravate the material thermal fatigue and cause structural failure during the long life of heat pipe reactors, which threatens the core safety. Therefore, temperature oscillations should be avoided in heat pipe reactors.
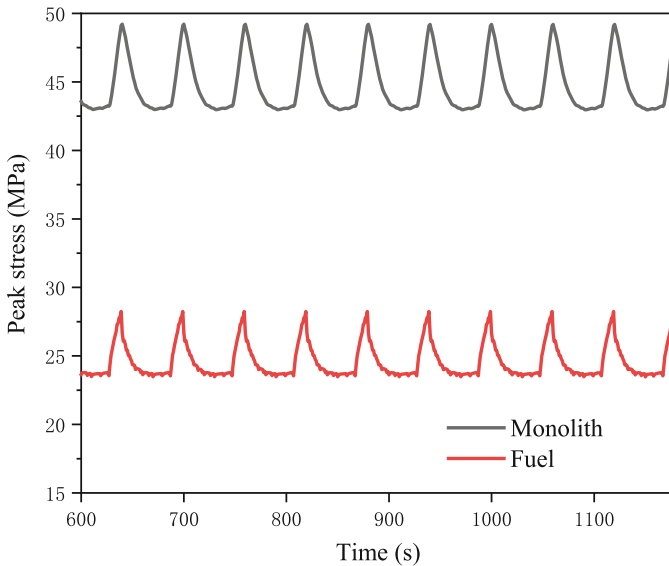
Fig. 10. Stress oscillation for geyser boiling condition (zone #1)

3.2.3 Sensitivity Analysis of the Period

For sensitivity analysis, the oscillation period is adjusted to 1/4 of the original, that is, 15 s. The results are shown in Fig. 11. The temperature oscillation amplitude of the fuel and the monolith is significantly reduced as the period decreases. When the period is reduced from 60 s to 15 s, the temperature amplitude of the fuel pellet center at a height of 0.15 m decreases from 22 °C to 5 °C. Similar trends are seen in the other areas. Therefore, long-period heat pipe temperature oscillations are more likely to transmit temperature fluctuations to the core, and high-frequency heat pipe temperature oscillations can be absorbed by the core heat capacity and their effects are mitigated.
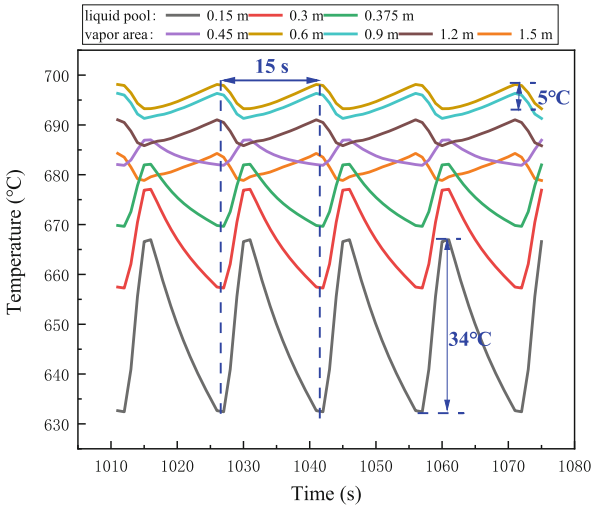
(a) monolith wall near fuel
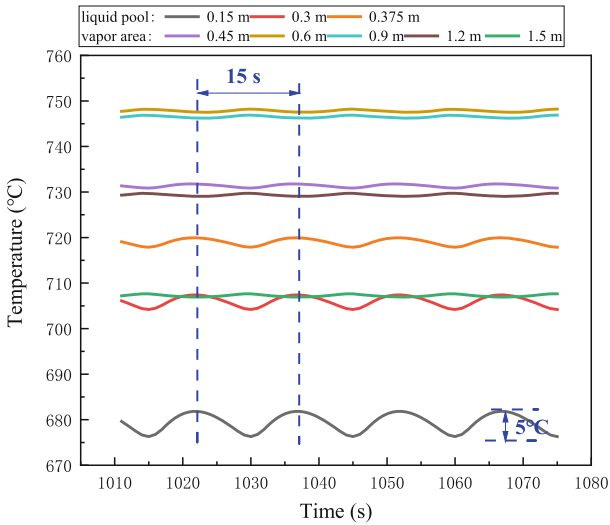
(b) fuel pellet center

Fig. 11. Temperature oscillation of monolith and fuel with a period of 15 s

4   Conclusions

This work introduces a coupled neutronic and thermal-mechanical analysis method of heat pipe reactors. The megawatt heat pipe reactor, MegaPower, was chosen as an application case to study the influence of heat pipe temperature oscillations caused by geyser boiling on the critical parameters during reactor operation, such as temperature and stress. The calculations show that:

(1) The heat pipe temperature oscillation has a thermal effect on the core, causing the monolith temperature and fuel temperature to oscillate at the same frequency. Besides, as the oscillation period decreases, the temperature amplitude also decreases due to the heat capacity of the core. The core temperature amplitudes are 22 °C and 5 °C, respectively, for oscillation periods of 60 s and 15 s, which indicates that the effects will be mitigated for low-period heat pipe temperature oscillations.

(2) Due to the temperature oscillation in the core, the peak stresses in the monolith and the fuel oscillate at the same frequency. The oscillation amplitude is about 6 MPa at a period of 60 s. Although the fluctuation range remains within the safety limit, this fluctuation may aggravate thermal fatigue, which may result in structural failure for a long period of operation. Therefore, the geyser boiling must be avoided during the steady-state operation of a heat pipe cooled reactor.

References

1. Cai, F., et al.: Engineering fronts in 2018. Engineering **4**, 748–753 (2019)
2. Sun, H., Ma, P., Liu, X., Tian, W., Qiu, S., Su, G.: Conceptual design and analysis of a multipurpose micro nuclear reactor power source. Ann. Nucl. Energy **121**, 118–127 (2018)
3. Poston, D.I., Gibson, M.A., Godfroy, T., McClure, P.R.: KRUSTY reactor design. Nucl. Technol. **206**, S13–S30 (2020)
4. Choi, Y.J., et al.: Conceptual design of reactor system for hybrid micro modular reactor (H-MMR) using potassium heat pipe. Nucl. Eng. Des. **370**, 110886 (2020)
5. Panda, K.K., Dulera, I.V., Basak, A.: Numerical simulation of high temperature sodium heat pipe for passive heat removal in nuclear reactors. Nucl. Eng. Des. **323**, 376–385 (2017)
6. Kusuma, M.H., et al.: Passive cooling system in a nuclear spent fuel pool using a vertical straight wickless-heat pipe. Int. J. Therm. Sci. **126**, 162–171 (2018)
7. Yan, X.K., Duan, Y.N., Ma, C.F., Lv, Z.F.: Construction of Sodium Heat-Pipe Furnaces and the Isothermal Characteristics of the Furnaces. Int. J. Thermophys. **32**, 494–504 (2011)
8. Chaudhry, H.N., Hughes, B.R., Ghani, S.A.: A review of heat pipe systems for heat recovery and renewable energy applications. Renew. Sustain. Energy Rev. **16**, 2249–2259 (2012)
9. Wang, C., Tang, S., Liu, X., Su, G.H., Tian, W., Qiu, S.: Experimental study on heat pipe thermoelectric generator for industrial high temperature waste heat recovery. Appl. Therm. Eng. **175**, 115299 (2020)
10. Tang, S., et al.: Experimental investigation of a novel heat pipe thermoelectric generator for waste heat recovery and electricity generation. Int. J. Energy Res. **44**, 7450–7463 (2020)
11. Ma, Y., et al.: Neutronic and thermal-mechanical coupling analyses in a solid-state reactor using Monte Carlo and finite element methods. Ann. Nucl. Energy **151**, 107923 (2021)
12. Ma, Y., et al.: Heat pipe failure accident analysis in megawatt heat pipe cooled reactor. Ann. Nucl. Energy **149**, 107755 (2020)
13. Ma, Y., et al.: Transient heat pipe failure accident analysis of a megawatt heat pipe cooled reactor. Prog. Nucl. Energy **140**, 103904 (2021)
14. Hernandez, R., Todosow, M., Brown, N.R.: Micro heat pipe nuclear reactor concepts: Analysis of fuel cycle performance and environmental impacts. Ann. Nucl. Energy **126**, 419–426 (2019)
15. Wang, C., et al.: Code development and analysis of heat pipe cooled passive residual heat removal system of Molten salt reactor. Ann. Nucl. Energy **144**, 107527 (2020)
16. Nezam, Z.Z., Zohuri, B.: Heat pipe as a passive cooling system driving new generation of nuclear power plants. Edelweiss Chem. Sci. J. **3**, 9 (2020)

17. Poston, D.I., Kapernick, R.J., Guffee, R.M.: Design and analysis of the SAFE-400 space fission reactor, in: AIP Conference Proceedings, AIP, Albuquerque, New Mexico (USA), pp. 578–588 (2002)
18. Huaqi, L., et al.: Transient thermohydraulic characteristics of HP-STMCs space reactor core. Nucl. Power Eng. **36**, 36–40 (2015)
19. Murphy, D.W.: An experimental investigation of geysering in vertical tubes. In: Timmerhaus, K.D. (ed.) Advances in Cryogenic Engineering, pp. 353–359. Springer US, Boston, MA (1965). https://doi.org/10.1007/978-1-4684-3108-7_42
20. Lin, T.F., Lin, W.T., Tsay, Y.L., Wu, J.C., Shyu, R.J.: Experimental investigation of geyser boiling in an annular two-phase closed thermosyphon. Int. J. Heat Mass Transf. **38**, 295–307 (1995)
21. Ma, Y., et al.: Effect of inclination angle on the startup of a frozen sodium heat pipe. Appl. Therm. Eng. **201**, 117625 (2022)
22. Qi, F.: Development and application of performance analysis procedures for liquid metal-cooled fast reactor fuel elements, in, University of Science and Technology of China (2018). (in Chinese)
23. Sterbentz, J.W., et al.: Special purpose nuclear reactor (5 MW) for reliable power at remote sites assessment report, in, Idaho National Lab.(INL), Idaho Falls, ID (United States) (2017)
24. Mcclure, P.R., Poston, D.I., Dasari, V.R., Reid, R.S.: Design of Megawatt Power Level Heat Pipe Reactors. Report of Los Alamos National Laboratory, USA (2015)

Uncertainty Analysis and Sensitivity Evaluation of a Main Steam Line Break Accident on an Advanced PWR

Xueyan Zhang, Yixuan Zhang, Ye Yang, Chengcheng Deng, and Jun Yang[✉]

Huazhong University of Science and Technology, Wuhan, Hubei, China
{xueyanzhang,yang_jun}@hust.edu.cn

Abstract. A RELAP5 input model was established for a scaled-up facility simulating China's Advanced Passive Water Reactor with passive safety features. The simulation was performed to reproduce a Main Steam Line Break (MSLB) scenario at steam line connected to one Steam Generator. The figure of merit selected in this accident scenario includes the maximum containment pressure, mass and energy release to containment. Driving factors of this response function include Passive Residue Heat Removal material thermal conductivity, Pressurizer temperature, and broken steam line temperature.

To achieve an adequately justified safety margin using a Best Estimate Plus Uncertainty analysis, dominant phenomena were selected from a reference Phenomenon Identification and Ranking Table. The calculation results were compared with the available reference data of similar Generation III Passive Water Reactor to assess the code's capability to predict the MSLB phenomena. The DAKOTA toolkit is used to drive both parameter sensitivity analysis and uncertainty propagation. The 95/95 uncertainty bands of key output parameters were obtained using the Wilks' statistical methods.

Compared with the reference data, the simulation results partially confirmed the stability and repeatability of the code model for initial and boundary condition perturbations. The uncertainty bands of important output parameters were demonstrated. The results indicated that the maximum containment pressure value was below the safety limit, and the passive safety system can mitigate the consequence of the MSLB. The mass and energy released into the containment were assessed according to the containment design.

The parameter sensitivity analysis was performed with 34 input parameters, and the results were evaluated by Spearman's Simple Rank Correlation Coefficients.

Keywords: China's Advanced PWR · MSLB · Uncertainty · Passive Safety · PIRT

1 Introduction

China's Advanced Passive Water Reactor (PWR) is an advanced Generation III (G-III) reactor with passive safety features, developed through the introduction and absorption

of AP1000 technology (Zheng et al. 2016) to meet the growing electricity demand and to take advantage of the economies of large reactors (Bodansky 2007). The AP1000 developed by Westinghouse is a passive safety pressurized water reactor (Schulz 2006). It is a G-III+ reactor (Saha et al. 2013) that received the design certification from the U.S. Nuclear Regulatory Commission in 2008 (Matzie 2008).

China's National Nuclear Safety Administration illustrated the study requirements for mass and energy release in the case of Design Basic Accident (such as Loss Of Coolant Accident (LOCA) or Main Steam Line Break (MSLB) accidents) in nuclear safety guideline HAD 102/06–2020, *The Design of Reactor Containment and Related Systems for Nuclear Power Plant* (NNSA 2020). When the MSLB accident happens, the break of the main steam pipe will cause a large amount of high-enthalpy flow to inject into the containment. This large mass and energy leakage would result in a significant increase of pressure in the containment. Then the Passive Core Cooling System (PCCS) works to remove the heat by natural circulation. In order to find the key parameters influencing the transient response of China's large advanced PWR containment and mass- and energy-release into the containment during an MSLB accident, the sensitivity analysis of the MSLB accident with a thermal-hydraulic model is necessary.

Several studies have been performed on uncertainty quantification and sensitivity analysis of the passive safety system of China's advanced PWR or MSLB accident in PWR with passive safety features. Yang Ye et al. performed the Best Estimate Plus Uncertainty (BEPU) analysis in a postulated 2-in. Small Break LOCA (Yang et al. 2020a). Deng Chengcheng et al. carried out best-estimate calculations using RELAP5/MOD3.4 code plus uncertainty quantification and sensitivity analysis of the Small Break LOCA transient for a scaled-down facility-the Advanced Core-cooling Mechanism Experiment (ACME) test facility (Deng et al. 2019). Chang Yuhao et al. performed a BEPU analysis of China's advanced large-scale PWR under the conditions of Large Break LOCA scenarios by employing the RELAP5 code (Chang et al. 2020). Sun Qiuteng et al. performed global sensitivity analysis of the MSLB accident in AP1000 by using sampling methods and surrogate models (Sun et al. 2021). Angelo Lo Nigro et al. performed MSLB coupled 3D NEU-TH sensitivity analysis of the AP1000 plant using RELAP5-3D (Lo Nigro et al. 2002). Yang Ye et al. performed a simulation and uncertainty analysis of MSLB accident on PUMA integral test facility (Yang et al. 2020b).

The sketch of China's Advanced PWR is shown in Fig. 1. In this study, best-estimate calculations using RELAP5 code plus uncertainty quantification and sensitivity analysis of the MSLB transient were carried out for China's Advanced PWR. The important thermal-hydraulic phenomena under MSLB transient were investigated by comparing calculations between China's Advanced PWR and AP1000. Thereafter, the uncertainty quantification process based on Code Scaling, Applicability and Uncertainty (CSAU) methodology was demonstrated, including the selection of input uncertain parameters, the application of Wilks' statistic method and the uncertainty propagation using the SNAP interface. Lastly, the results of uncertainty quantification and sensitivity analysis were discussed.
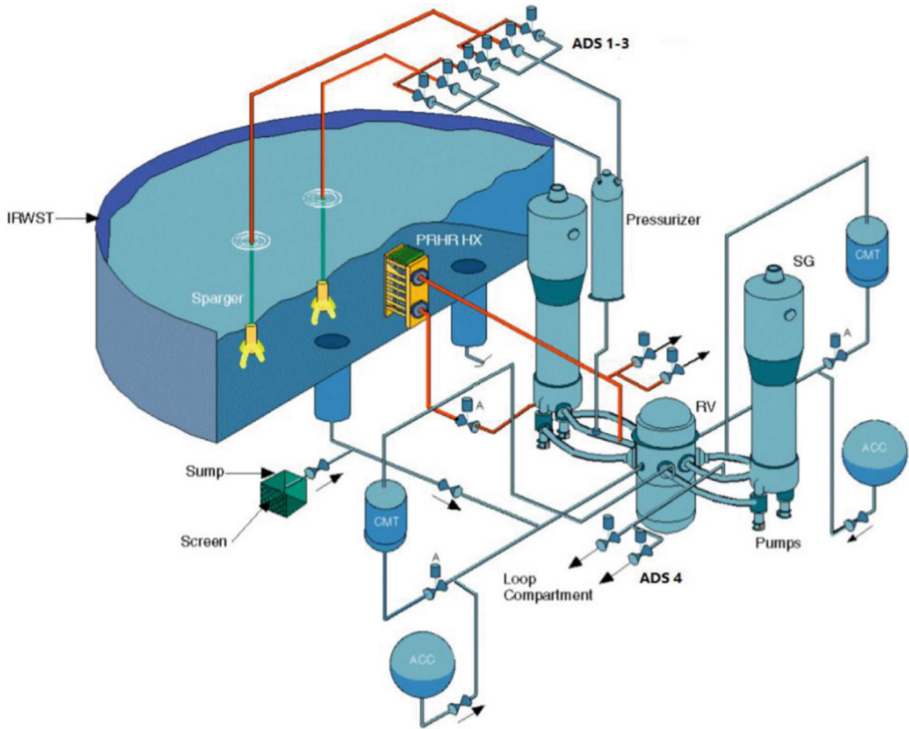
Fig. 1. The Sketch of China's Advanced PWR (Shi et al. 2021)

2   RELAP5 Nodalization

The RELAP5 input model for the selected reactor was established based on the technical information obtained from the open literature and design information (Yang et al. 2020a). The selected transient condition is the break of main steam line inside the containment vessel, and the main steam isolation valve is closed within 5s after the break open. In order to simulate the amount of mass and energy released from the break of the secondary loop to the containment, the containment node was set up in the RELAP5 model and connected with the upper cell of In-Containment Refueling Water Storage Tank (IRWST) to form the internal control volume of the containment.

As shown in Fig. 2, the model mainly focuses on the Reactor Coolant System (RCS), including a Reactor Pressure Vessel (RPV), 4 Cold Legs, 2 Hot Legs, 4 Coolant Pumps, 2 Direct Vessel Injection (DVI) pipes, 2 Steam Generators (SGs) and 1 Pressurizer (PZR). The passive safety system consists of 2 Accumulators (ACCs), 2 Core Makeup Tanks (CMTs), Passive Residue Heat Removal (PRHR) system, Automatic Depressurization System (ADS) and an IRWST. The RPV downcomer is composed of a pair of eight vertical channels, which is connected to 4 cold legs, 2 hot legs, and 2 DVI lines.

330 X. Zhang et al.
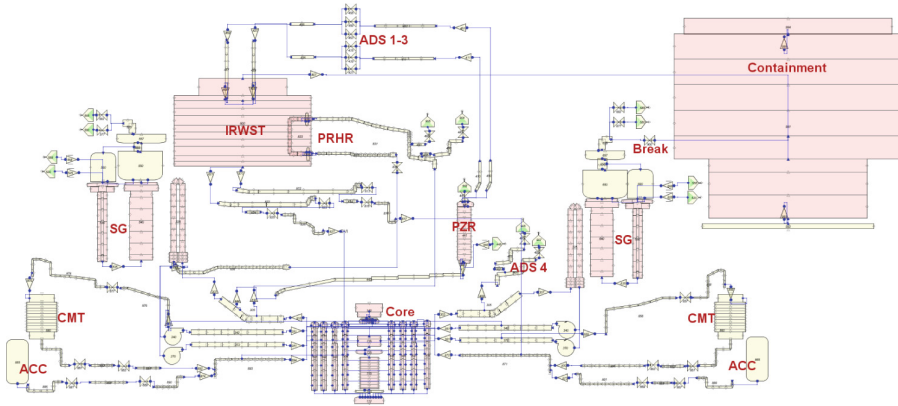
Fig. 2. RELAP5 Nodalization of MSLB in China's Advanced PWR

2.1 Steady-State Results

The MSLB accident is hypothetical, so its initial conditions are set to the normal steady-state operating conditions of the nuclear power plant. After the RELAP5 node modeling is completed, the steady-state calculation of the code is carried out firstly. According to the output file of the RELAP5 code, the model reaches steady-state at about 150 s. The steady-state results are shown in Table 1. Therefore, in the subsequent transient calculation, the steady-state operation phase of 300 s was first set before the opening of the break valve.

2.2 Transient Sequence and Results

The sequence of accidents in the hypothetical scenario is shown in Table 2. In the MSLB accident, there was no coolant leakage in the primary side, and the low setting value of RCS cold leg temperature (T_{cl}) is triggered to generate the "S" signal, then the reactor is shut down. Therefore, CMT is always in recirculation mode and does not switch to drainage mode. Therefore, ADS1–4 is not enabled. The total amount of mass and energy released depends on the water inventory of SG secondary side and the condensing tank storage of the start-up feed water system.

As shown in Fig. 3 and Fig. 4, compared with the MSLB accident of AP1000 (Westinghouse 2011) (partial data of 600 s after the accident began), APR1400 (Ekariansyah and Sunaryo, 2018), ATLAS (Ha et al. 2014), the PZR pressure (i.e., system pressure) was in good agreement with AP1000 during the blowdown phase. In the passive decay heat removal phase, the pressure of China's Advanced PWR decreases slowly but keeps a downward trend. The CMT maintains a recirculation mode, injecting cooling water into the core in natural circulation. At about 1700 s, the core pressure drops to the ACC injection pressure of 4.83 MPa, and the pressurized nitrogen in ACC injects coolant into the core passively (Fig. 6). Because there was steam loss on the secondary loop in MSLB accident, the RCS integrity was maintained during the accident. Hence, the RPV liquid level remains constant. CMT injection flow rate is lower, but the injection time is logically consistent (Fig. 5).

Table 1. Steady-State Simulation Confirmation (Zheng et al. 2016; Yang et al. 2020a)

Main Design Parameters	China's Advanced PWR	RELAP5 Simulation
Core thermal power (MW)	4040	4037.73
RCP flow rate (m^3/h)	21642	21642.00
RCS pressure (MPa)	15.5	15.55
Vessel inlet temperature (K)	557.45	557.58
Vessel outlet temperature (K)	596.85	597.01
Steam pressure at SG exit (MPa)	6.02	6.01
Steam flow per SG (kg/s)	1123.4	1123.11
CMT volume (m^3)	85	84.98
ACC volume (m^3)	78.3	78.68
IRWST volume (m^3)	2730	2730

Table 2. Main safety system set points in accident analysis (Deng et al. 2019; Li et al. 2016)

Event sequence	Set point assumed in accident analysis	Simulate Time (s)
Safety signal	T_{cl} low	20.01791
Reactor SCRAM	13.2 MPa	20.01791
SG main feed water valves start to close	After 'Safety' signal	25.01532
SG main steam valves start to close	After low PZR pressure signal	49.01773
RCPs trip	After 'S' signal	27.01532
PRHRS isolation valve starts to open	After 'S' signal	42.01712
CMT injection starts	After 'S' signal	42.01712
ACC injection starts	4.83 MPa	1676.0046
ADS1 valves start to open	30 s after 67.5% liquid volume in any CMT	–
ADS2 valves start to open	48 s after ADS1 actuation	–
ADS3 valves start to open	120 s after ADS2 actuation	–
ADS4a valves start to open	120 s after ADS3 & CMT low-low level	–
ADS4b valves start to open	60 s after ADS4a actuation	–
IRWST injection valve starts to open	RCS pressure less than 0.5 MPa	–

According to the accident logic, the primary side pressure did not drop to 0.5 MPa, so IRWST was not injected in the MSLB accident. The steel containment vessel has a design pressure of 0.443 MPa and a safety margin of 10%. As shown in Fig. 7, the pressure of the containment vessel rises rapidly when the break is opened in the process of a transient accident. Then the pressure decreases without overpressure due to the cooling of the containment vessel by the thermal components outside the containment vessel (imitating the passive containment cooling system and spray system).

The integral of mass and energy release integral is shown in Fig. 8. Later, as the auxiliary water supply system injected water into the damaged steam generator, steam was continuously released into the containment vessel through the break of main steam line, as shown in the break flow (Fig. 7).
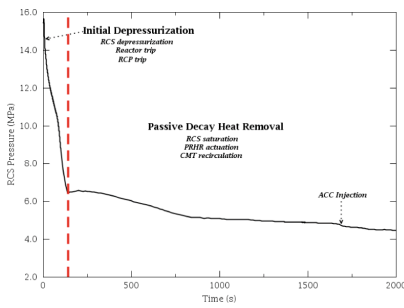
Fig. 3. RCS Pressure
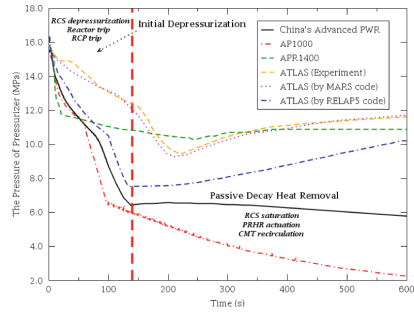
Fig. 4. Pressurizer Pressure
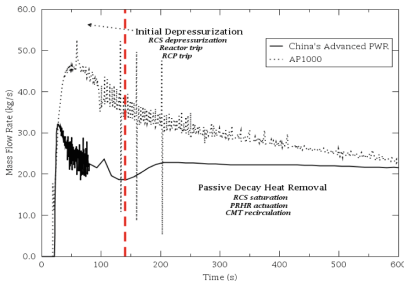
Fig. 5. CMT Injection Mass Flow Rate
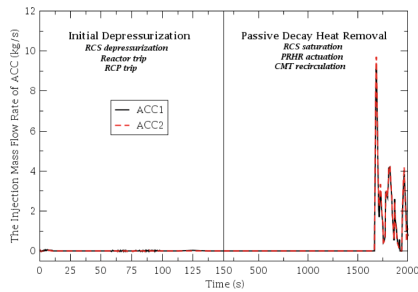
Fig. 6. ACC Injection Mass Flow Rate
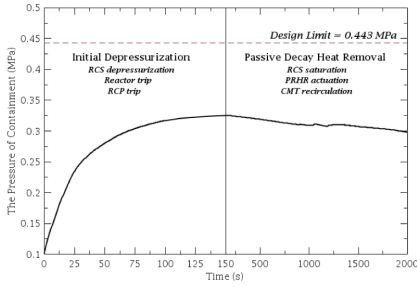
Fig. 7. Containment Pressure
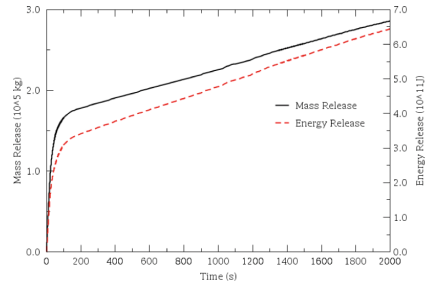
Fig. 8. Mass and Energy Release Amount

3 Uncertainty and Sensitivity Analysis

Referring to AP600 and AP1000, the MSLB accident scenario is divided into five phases (see Fig. 9): Initial Depressurization, Passive Decay Heat Removal, CMT Draining to ADS Actuation, ADS Blowdown, and IRWST & Sump Injection phase (Wilson et al. 1997). However, in this simulation, only the MSLB accident was set, with no superimposed failure of other systems. Therefore, in the later transient process, it can be seen that there are only Initial Depressurization and Passive Decay Heat Removal phases.

The well-known Wilks' formula for the one-side tolerance interval is expressed as follows (Wilks 1941):

$$\beta = 1 - \gamma^N \tag{1}$$

To achieve 95% tolerance with 95% confidence (95%/95%), 59 sets of input variables would be sampled according to the Wilks' formula. The input sets were automatically generated by Design Analysis Kit for Optimization and Terascale Applications (DAKOTA) toolkit using simple random sampling (Adams et al. 2015).

3.1 Phenomena Identification and Ranking Tables

The initial decompression phase begins at the time of the pipe break and continues until the secondary side of the affected SG (i.e., the SG connected to the steam line of the break) is decompressed to the containment pressure. The reactor is shut down at this stage. The steam line is arranged, so the broken SG initially loss steam through a double-ended pipe break. However, a steam line isolation signal is generated relatively early in this phase to prevent the steam from losing from the turbine side. The behavior at this phase is mainly the discharge of the affected SG into the containment vessel, resulting in supercooling of the RCS due to heat discharge through the pipes of the affected steam generator. It is important to note that this process is asymmetric, with significant differences in heat load and fluid temperature between the affected and unaffected coolant cycles. The primary and secondary side heat transfer of SG plays a dominant role in RCS cooling and is therefore considered to be the primary parameter in this stage. Dominant processes are break flow, SG secondary behavior, RCS loop flow, and asymmetric loop cooldown (Table 3).

Phase	Initial Depressurization	Passive Decay Heat Removal	CMT Draining to ADS Actuation	ADS Blowdown	IRWST & Sump Injection
TRANSIENT DURATION:					
MSLB, no failure					
MSLB, failure					
SIGNIFICANT PHASE FEATURES	RCS depressurization Reactor trip RCP trip	RCS saturation PRHR actuation CMT recirculation	Interruption of CMT recirculation Asymmetric loop response if unequal CMT draining PRHR cooling	Completion of CMT draining, Including potential flashing Accumulator injection PRHR cooling Transition to stage 4 ADS subsonic flow	Intermittent IRWST injection Intermittent Sump injection
SIGNAL RELATED ELEMENTS		End of SG blowdown	PBL voiding	CMT Level at 67.5% (ADS actuation)	RCS pressure minus containment pressure less than 28 ft. of water (initiation of IRWST injection) — Initiation of sump injection

Fig. 9. MSLB Transient Scenario (Wilson et al. 1997)

When the affected steam generator depresses to containment pressure, the passive residual heat removal phase begins and continues until the CMT recirculation stops (due to the presence of two-phase liquid in the CMT or its inlet line). This stage is characterized by primary path, CMT and PRHR flow driven by natural circulation. The temperature distribution of RCS is asymmetric. The RCS heat source is decay heat and reverses heat transfer generated by an unaffected steam generator. CMT recirculation and PRHR systems are heat traps for RCS. The RCS energy distribution determines the decay heat emission and is therefore considered the most important parameter. Processes important for accurate modeling of this phase are loop asymmetry effects, core heat transfer, SG heat transfer, PRHR heat transfer, and containment shell heat transfer.

3.2 Input Parameters Selection

According to the Phenomena Identification and Ranking Table investigation, the main input parameters related to containment pressure in the MSLB accident can be determined. Under ideal conditions, the distribution of uncertain input parameters is shown in Table 4. Due to the limitation of the RELAP5 model initial conditions, part of the temperature needs to be specified in the form of internal vapor and liquid energy. The final input parameters and their distribution are shown in Table 5.

3.3 Uncertainty Results

Figure 10 shows the uncertainty results of the containment pressure, which is also the figure of merit. The uncertainty of the outside temperature of PCCS heat structure directly causes different heat removal from the steel containment shell, which leads to the difference of the pressure and temperature inside the containment. Due to the changes in

Table 3. Ranking criteria for the MSLB

Parameters/Processes	Initial Depressurization	Passive Decay Heat Removal
Important Parameters	SG Primary-to-Secondary Heat Transfer	RCS Energy Distribution
Dominant Processes	Break flow SG secondary behavior (level swelland depletion,liquid carryover,flashing, and entrainment) RCS loop flow Asymmetric loop cooldown	Loop assymetry effects Core heat transfer SG heat transfer PRHR heat transfer Containment shell heat transfer

Table 4. Input Parameters under Ideal Condition

Position	Penomenen	Parameter
Fuel Rod	Power/Decay Power	Decay Power
	Critical Heat Flux	–
Break	Flow Rate	Hydraulic Diameter
		Discharge Coefficient
		Flow Area
	Energy Release	Temperature
	Choking Flow	Pressure
Core	Two-Phase Swell Level	Void Fraction
	Core Chanal	Cross Flow
	Subcooling	Temperature
	Flashing	Pressure
ADS	Mass Flow Rate	ADS1–3 valve lift
		ADS4 valve lift
		ADS1–3 Discharge Coefficient
		ADS4 Discharge Coefficient
	Energy Release	Temperature
CMT	Water Level	Pressure
	Density Difference between CMT & RCS	Temperature
	Flow Resistance	Pipe Wall Friction

Table 4. (*continued*)

Position		Penomenen	Parameter
SG	1st/2nd Side	Heat Transfer from 1st Side to 2nd Side	Thermal Conductivity of Material 8
	Seperator	Liquid Entrainment	Open Entrainment Model
	1st Side	Optimal Circulation Loop	–
	2nd Side	Entrainment	Open Entrainment Model
		Flashing	Pressure
		Feedwater Line Draining	Temperature
		Level Swell	Water Level (As Result)
IRWST		Liquid Entrainment	Pipe Wall Friction
		Water Level	Water Level (As Result)
		Thermal Stratification	Temperature
PZR		Flashing	Temperature
		Water Level	Water Level (As Result)
		Steam Space Behavior	Gas Space Pressure
Sump		Fluid Temperature	Temperature
		Water Level	Water Level (As Result)
Hot Leg		Phase Separation in Tee	Open Entrainment Model
Downcomer/Lower Plenum		Water Level	Water Level (As Result)
Upper Head/Upper Plenum		Two-Phase Ratio in Upper Plenum	Void Fraction
		Entrainment/De-Entrainment	Open Entrainment Model
Containment		Heat transfer from the outside to the environment	Thermal Conductivity of Material 11
		Heat transfer from the interior to the wall	Heat Capacity of Material 11
Pump		Stopping Behavior	–
PRHR		Heat transfer between PRHR and IRWST	Thermal Conductivity of Material 5

Table 5. Input Parameters with Uncertainty Distribution in RELAP5 Model

No.	Parameter	Reference Value	Unit	Factor Range
1	Decay Power	Curve Table	–	[0.95, 1.05]
2	Break Area	0.5944	m^2	[0.98, 1.0]
3	Break Discharge Coefficient	1.0	–	[1.0, 1.4]
4	RPV Pressure	15.5	MPa	[0.98, 1.02]
5	Thermal Conductivity of SG Material	Thermal Conductivity Table	W/m*K	[0.95, 1.05]
6	ADS4 Valve Opening Rate	2.0	s^{-1}	[0.95, 1.05]
7	CMT Wall Friction	5.0×10^{-5}	m	[0.95, 1.05]
8	ADS1 Valve Opening Rate	0.033	s^{-1}	[0.95, 1.05]
9	ADS2 Valve Opening Rate	0.0125	s^{-1}	[0.95, 1.05]
10	ADS3 Valve Opening Rate	0.0125	s^{-1}	[0.95, 1.05]
11	ADS4 Discharge Coefficient	0.92	–	[1.0, 1.4]
12	ADS1–3 Discharge Coefficient	0.92	–	[1.0, 1.4]
13	CMT Pressure	15.5	MPa	[0.98, 1.02]
14	IRWST Temperature	322.0	K	[0.95, 1.05]
15	PZR Vapor Space Pressure	15.5	MPa	[0.98, 1.02]
16	Thermal Conductivity of PRHR Material	Thermal Conductivity Table	W/m*K	[0.95, 1.05]
17	Break Pipe Pressure	6.067	MPa	[0.98, 1.02]
18	CMT Liquid Internal Energy	2.02312×10^5	J/kg	[0.98, 1.02]
19	CMT Vapor Internal Energy	2.44414×10^6	J/kg	[0.98, 1.02]
20	PZR Liquid Internal Energy	~ 1.60×10^6	J/kg	[0.98, 1.02]
21	PZR Vapor Internal Energy	2.44414×10^6	J/kg	[0.98, 1.02]
22	Main Sump Liquid Internal Energy	3.622×10^5	J/kg	[0.98, 1.02]
23	Main Sump Vapor Internal Energy	3.64×10^5	J/kg	[0.98, 1.02]
24	IRWST Wall Friction	5.0×10^{-5}	m	[0.95, 1.05]
25	ADS1–3 Liquid Internal Energy	1.603772×10^6	J/kg	[0.98, 1.02]
26	ADS1–3 Vapor Internal Energy	2.44414×10^6	J/kg	[0.98, 1.02]
27	IRWST Liquid Internal Energy	2.10925×10^5	J/kg	[0.98, 1.02]
28	IRWST Vapor Internal Energy	5.50466×10^5	J/kg	[0.98, 1.02]
29	Intact SG 2nd Side Pressure	6.136	MPa	[0.98, 1.02]
30	Intact SG 2nd Side Temperature	539.09	K	[0.95, 1.05]

Table 5. (*continued*)

No.	Parameter	Reference Value	Unit	Factor Range
31	Broken SG 2nd Side Pressure	6.136	MPa	[0.98, 1.02]
32	Broken SG 2nd Side Temperature	539.09	K	[0.95, 1.05]
33	Containment Outside Temperature	298.15	K	[0.92, 1.25]
34	Start-up Feedwater Flow Rate	61.1	Kg/s	[0.95, 1.05]

various input parameters (will be discussed in Sect. 3.4), the maximum containment pressure is 0.3362 MPa, which does not exceed the safety limit-0.443 MPa.

The variation of break mass and energy release is shown in Fig. 11. In the initial depressurization phase, the uncertainty of the break mass and energy release is mainly caused by the uncertainty of the break mass flow. In the passive decay heat removal phase, the uncertainty of the break mass flow, CMT heat removal capacity and PRHR heat removal contributes to the uncertainty of the break mass and energy release. Meanwhile, the maximum mass released to the containment vessel is 4.16×10^5 kg, and the maximum energy released to the containment vessel is 9.74×10^8 kJ.

These maximum values could be referred to new reactor containment design with proper scaling analysis.

3.4 Sensitivity Analysis

The importance of the input variables to the safety parameters can be quantified by the spearman rank correlation coefficient:

$$Spearman = r_s = \frac{\sum_{i=1}^{n}\left[\left(R_i - \frac{1}{n}\sum_{i=1}^{n}R_i\right)\left(Q_i - \frac{1}{n}\sum_{i=1}^{n}Q_i\right)\right]}{\sqrt{\sum_{i=1}^{n}\left(R_i - \frac{1}{n}\sum_{i=1}^{n}R_i\right)^2}\sqrt{\sum_{i=1}^{n}\left(Q_i - \frac{1}{n}\sum_{i=1}^{n}Q_i\right)^2}} \tag{2}$$

The correlation coefficient ranges from −1 to + 1. Positive and negative signs indicate positive and negative correlations, and the magnitude of the value indicates the strength of the correlation. Figure 12 shows the spearman rank correlation coefficients. The statistical significance of parameters is taken into account when its absolute value is greater than 0.2.

The main findings are given below:

1. Thermal Conductivity of PRHR Material: The thermal conductivity of PRHR material is negatively correlated with the containment pressure. With the thermal conductivity of PRHR material increasing, the heat is removed more, then the containment pressure decreases to a lower value. In the accident transient, the thermal conductivity of PRHR material determines the heat removed from the RCS.
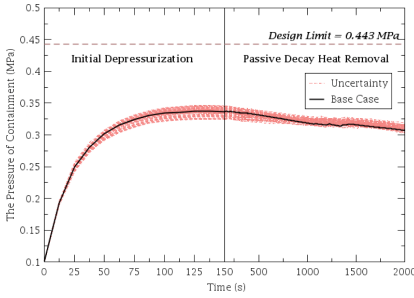
Fig. 10. Uncertainty Results of Containment Pressure
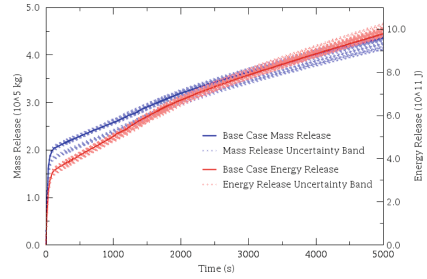
Fig. 11. Uncertainty Results of Break Mass and Energy Release
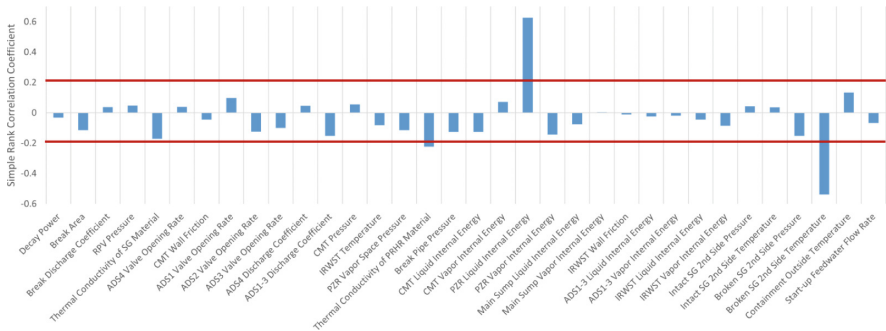
Fig. 12. Sensitivity Analysis Results: 34 Input Parameters to Containment Pressure

2. PZR Liquid Internal Energy: The PZR liquid internal energy has a positive correlation with the containment pressure. With the PZR liquid internal energy increases, the more heat is removed, the higher the containment pressure would be. The PZR is connected to the RCS hot leg, and its temperature will affect the coolant temperature of the whole primary system. After the MSLB accident occurred, due to the instantaneous increase of the secondary side flow and the supercooling of the primary side, the low setting value of RCS cold leg temperature (T_{cl}) is triggered to generate "S" signal. When the primary coolant temperature increases, the "S" signal would be delayed, resulting in more core heat being released to the primary coolant, then to the heat sink (SG), and finally to the containment, resulting in increasing containment pressure.

3. Broken SG 2nd Side Temperature: The broken SG 2nd side temperature negatively correlates with the containment pressure. With the broken SG 2nd side temperature increases, the SG water is flashing earlier and remove RCS heat earlier, tripped the "S" signal earlier. Therefore, the core generates less decay power, and the containment pressure decreases.

4 Conclusions

The simulation and analyzation of China's Advanced PWR MSLB accident were conducted by RELAP5 code. The uncertainty and sensitivity analysis were performed, and the spearman rank correlation coefficient evaluated the importance of each input parameter on the object safety parameter, i.e., the figure of merit.

By comparing the code simulation results and the available test results, it is observed that the code can reasonably predict the important thermal-hydraulic phenomenon for China's Advanced PWR MSLB accident. The maximum containment pressure did not reach the design limit pressure during the overall uncertainty analysis. This indicates the passive safety system was put into operation by pre-set logic during the entire accident transient, ensuring effective heat removal from the core. The passive safety system can assure the safety of the core and containment in the MSLB accident.

According to the spearman rank correlation coefficient, the most influential variable for the maximum containment pressure is the RCS temperature. It means that the RCS temperature has an essential effect on the initial energy stored in RCS coolant. The uncertainty of parameters such as thermal conductivity of PRHR material and broken SG 2nd side temperature also significantly impact the maximum containment pressure.

References

1. Zheng, M., Yan, J., Jun, S., Tian, L., Wang, X., Qiu, Z.: The General design and technology innovations of CAP1400. Engineering **2**, 97–102 (2016)
2. Bodansky, D.: Nuclear Energy: Principles, Practices, and Prospects. Springer, Heidelberg (2007)
3. Schulz, T.L.: Westinghouse AP1000 advanced passive plant. Nucl. Eng. Des. **236**, 1547–1557 (2006)
4. Saha, P., et al.: Issues and future direction of thermal-hydraulics research and development in nuclear power reactors. Nucl. Eng. Des. **264**, 3–23 (2013)
5. Matzie, R.A.: AP1000 will meet the challenges of near-term deployment. Nucl. Eng. Des. **238**, 1856–1862 (2008)
6. NNSA. The Design of Reactor Containment and Related Systems for Nuclear Power Plant. National Nuclear Safety Administration, Beijing, pp. 3–82 (2020)
7. Shi, G., et al.: CAP1400 passive core cooling integral testing and application in code validation. Ann. Nucl. Energy **154**, 107997 (2021)
8. Yang, Y., Deng, C., Yang, J.: Best estimate plus uncertainty analysis of a small-break LOCA on an advanced Generation-III pressurized water reactor. Int. J. Energy Res. **45**, 11916–11929 (2020)
9. Deng, C., Chen, L., Yang, J., Wu, Q.: Best-estimate calculation plus uncertainty analysis of SBLOCA transient for the scale-down passive test facility. Prog. Nucl. Energy **112**, 191–201 (2019)
10. Chang, Y., Wang, M., Zhang, J., Tian, W., Qiu, S., Su, G.H.: Best estimate plus uncertainty analysis of the China advanced large-scale PWR during LBLOCA scenarios. Int. J. Adv. Nucl. Reactor Des. Technol. **2**, 34–42 (2020)
11. Sun, Q., et al.: Global sensitivity analysis of the main steam line break accident by using sampling methods and surrogate models. Ann. Nucl. Energy **150**, 107787 (2021)

12. Lo Nigro, A., Spadoni, A., D'Auria, F., Frogheri, M., Saiu, G.: MSLB (Main Steam Line Break) coupled 3D NEU-TH sensitivity analysis of the AP1000 plant using RELAP5–3D (2002)
13. Yang, Y., Yang, J., Deng, C., Ishii, M.: Simulation and uncertainty analysis of main steam line break accident on an integral test facility. Ann. Nucl. Energy **144**, 107565 (2020)
14. Li, Y.Q., et al.: Analyses of ACME integral test results on CAP1400 small-break loss-of-coolant-accident transient. Prog. Nucl. Energy **88**, 375–397 (2016)
15. Westinghouse, L.: Westinghouse AP1000 Design Control Document Rev. 19. Westinghouse Electirc Company LLC (2011)
16. Ekariansyah, A., Sunaryo, G.R.: Main steam line break accident simulation of APR1400 using the model of ATLAS facility. J. Phys. Conf. Ser., 012037 (2018)
17. Ha, T.W., Yun, B.J., Jeong, J.J.: The MARS simulation of the ATLAS main steam line break experiment. J. Energy Eng. **23**, 112–122 (2014)
18. Wilson, G.E., Fletcher, C.D., Davis, C.B., Buttt, J.D., Bowher, T.J.: PIRTs for Westinghouse AP600 SBLOCA, MSLB and SGTR Scenarios. In: Commission, U.S.N.R. (Ed.). Idaho National Engineering and Environmental Laboratory, Lockheed Idaho Technologies Company, Washington, DC (1997)
19. Wilks, S.S.: Determination of sample sizes for setting tolerance limits. Ann. Math. Stat. **12**(91–96), 96 (1941)
20. Adams, B.M., et al.: Dakota: a multilevel parallel object-oriented framework for design optimization, parameter estimation, uncertainty quantification, and sensitivity analysis. Version 6.2 User's Manual. Sandia National Laboratories (2015)

Hysteresis Behaviors of a Bump-Type Foil Bearing Structure with Amended LuGre Friction Model

Runeng Zhou, Yongpeng Gu, Gexue Ren[✉], and Suyuan Yu[✉]

Tsinghua University, Beijing, China
zhourn19@mails.tsinghua.edu.cn, {guyp,rengx,
suyuan}@tsinghua.edu.cn

Abstract. The gas foil bearing (GFB) has the prospect of application in the nuclear field because of its oil-free lubrication and high-speed as well as high-temperature performance. In this paper, the hysteresis behaviors of the bump foil structure of bump-type gas foil bearings are investigated. The bump foil is modeled by beam elements and reduced by Guyan reduction method. The amended LuGre friction model is adopted and all the state variables are solved simultaneously in the fully coupled scheme. It is found that, along with the decrease of the friction stiffness per normal force, the presliding behavior is enhanced and it is more and more difficult to distinguish the stick and slip states, which results a decrease of the energy dissipation of hysteresis curves. Besides, the differences of high-slope and low-slope hysteresis curves are caused by the changes of stick and slip states of partial contact nodes close to the free end of the bump foil. Finally, the simulation results considering the Stribeck effect indicate that the high-slope and low-slope parts of hysteresis curves are dominated by maximum static friction coefficient and kinetic friction coefficient, respectively. Moreover, the comparisons of simulation and experimental hysteresis curves prove that the presliding behavior and Stribeck effect are prevalent phenomena in bump foil structure and should be taken into account in the modeling of the GFB system.

Keywords: Gas bearing · Bump foil · Hysteresis · LuGre · Presliding · Stribeck

1 Introduction

Gas foil bearings (GFBs) are increasingly used in oil-free and high-speed as well as high-temperature fields and show great potential in the nuclear field [1, 2]. The bump-type GFB, as shown in Fig. 1, is the most studied and widely used type of GFBs [3]. Its top foil is supported by one or more compliant corrugated foil strips, and the end of the top foil and bump foil are welded to the bearing sleeve. The hydrodynamic pressure generated between the rotor and top foil acts on the foil structure while suspending the rotor. The hydrodynamic pressure deforms the foil structure, and the relative motion between the bump foil and top foil as well as the bearing sleeve is generated. Then, the friction force arises to prevent the relative motion. The friction provides energy dissipation for the system and stiffens the foil structure, thus significantly affecting the mechanical characteristics of the GFB system [4, 5].
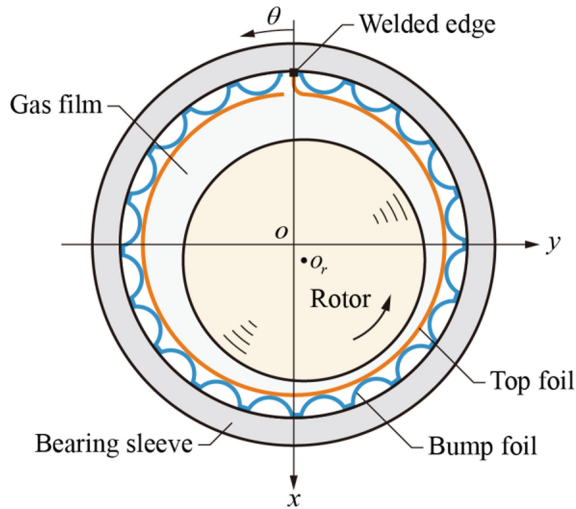
Fig. 1. The configuration of the bump-type GFB system.

The early numerical investigation on the friction inside the foil structure was carried out by Ku and Heshmat [6]. They found that the bumps near the welded end have a much higher static stiffness, and a higher friction coefficient could increase the static stiffness. Then experimental results of hysteresis curves for bump strips pressed between two parallel surfaces were presented in [7]. It was found that the local stiffness is higher than the global stiffness, and the local stiffness and damping are dependent on the excitation amplitude and static load. Following their previous work, Ku and Heshmat [8, 9] developed a theoretical model to calculate the equivalent viscous damping coefficient and structural stiffness for nonrotating journal acting on bump foil strips. Then, the experiments were carried out to investigate the dynamic characteristics of the bump foil, and the results were compared to the theoretical model with good agreement [10, 11]. The results showed that along with the increase of excitation amplitude or decrease of the static load, the local structural stiffness and equivalent viscous damping coefficient decrease, and an increase of the excitation frequency was found to increase the local structural stiffness while decrease the equivalent viscous damping coefficient. Subsequently, similar experiments were performed by many authors to investigate the structural stiffness and equivalent viscous damping coefficient [12–16].

The understanding of hysteresis behaviors of the bump foil structure was improved by Lez et al. [17, 18]. The simulation results evidenced the presence of stick and slip states in the foil structure, and then, the variations of the equivalent stiffness and damping coefficients could be explained by stick-slip behaviors of contact nodes. During the loading and unloading processes, the high-slope and low-slope curves correspond to stick states and slip states of most contact nodes, respectively. Besides, only the few bumps close to the free end of the bump foil structure participate in the change of stick and slip states, while the other bumps keep stuck all the time.

Larsen et al. [19] investigated the mechanical behaviors of bump foil strips pressed between two parallel surfaces, and experimental results showed complex dynamic phenomena which cannot be fully captured by classical friction model. Feng et al. [20] first introduced the original LuGre friction model into the modeling of bump foil structure. This model is capable of capturing the presliding behavior, Stirbeck effect and associated stick-slip motion [21]. The original LuGre friction model was then adopted by Zhou et al. [5] to develop a fully coupled dynamic model of the GFB system. However, this friction model was developed for cases of fixed normal contact force and may give nonphysical results under variable normal contact force conditions, which is caused by the implicit expression of normal contact force in the calculation of the friction force.

Therefore, in this paper, to further investigate the hysteresis behaviors of the bump-type foil bearing structure, the amended LuGre friction model was adopted to couple with the bump foil structure. The modeling and solution were validated by experimental data. Then, the presilding behavior, the stick-slip states during loading-unloading process and the Stribeck effect were investigated in sequence.

2   Modeling and Solution

The purpose of this work is to investigate the hysteresis behaviors of the bump foil structure. So, the system is modeled as a flexible bump foil strip pressed between two parallel rigid surfaces, as shown in Fig. 2(a). The reduction of the bump foil structure and the frictional contact between the bump foil and two surfaces are implemented, and finally, the system is solved in a fully coupled manner.
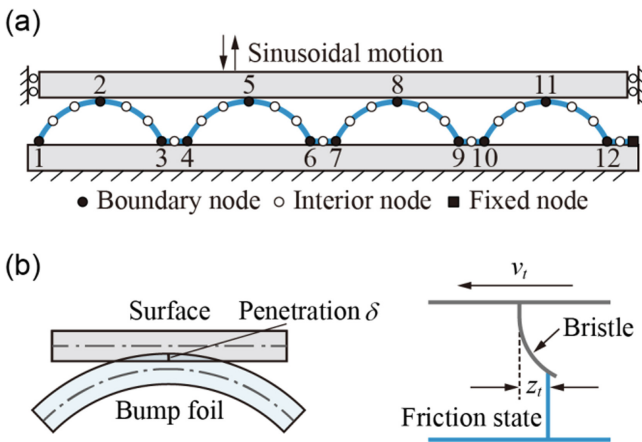
Fig. 2. Modeling of the system: (a) the schematic of the system and the reduction scheme of the bump foil and (b) the diagram of the frictional contact.

2.1 Modeling of the Bump Foil Structure

The standard two-node Euler beam elements are used to model the bump foil structure. The governing equation for an element e is expressed as.

$$\mathbf{M}^e \ddot{\mathbf{q}}^e + \mathbf{C}^e \dot{\mathbf{q}}^e + \mathbf{K}^e \mathbf{q}^e = \mathbf{F}^e, \tag{1}$$

where $\mathbf{q}^e$ is the nodal deflection vector of the element, $\mathbf{M}^e$, $\mathbf{C}^e$ and $\mathbf{K}^e$ are the element mass matrix, damping matrix and stiffness matrix, respectively, and $\mathbf{F}^e$ is the element external force vector. The proportional damping $\mathbf{C}^e = \beta \mathbf{K}^e$ is adopted in which β is the proportional damping coefficient. Besides, a correction of the Young's modulus is implemented due to the plane stress assumption.

In view of that the natural frequency of the bump foil structure is much higher than the excitation frequency in this work, the dynamic characteristics of the bump foil can be ignored. Besides, most of the nodes of the bump foil elements are unloaded. Therefore, the Guyan reduction method [22] can be adopted to improve the computational efficiency while still guarantee the accuracy. Based on the geometric configuration of the bump foil, only the highest nodes and corner nodes of the bumps are assumed to be potentially loaded. These potentially loaded nodes are defined as boundary nodes of substructures and the left over nodes are interior nodes, as shown in Fig. 2(a).

By assembling the corresponding elements, the governing equation of a substructure can be obtained as

$$\mathbf{M}_s \ddot{\mathbf{q}}_s + \mathbf{C}_s \dot{\mathbf{q}}_s + \mathbf{K}_s \mathbf{q}_s = \mathbf{F}_s, \tag{2}$$

where $\mathbf{q}_s$ is the nodal deflection vector of the substructure, $\mathbf{M}_s$, $\mathbf{C}_s$ and $\mathbf{K}_s$ are the mass matrix, damping matrix and stiffness matrix of the substructure, respectively, and $\mathbf{F}_s$ is the external force vector of the substructure. Based on the mechanical characteristics of the bump foil, the governing equation of a substructure can be approximated as a static equilibrium equation

$$\mathbf{K}_s \mathbf{q}_s = \mathbf{F}_s. \tag{3}$$

By partitioning the degrees of freedom (DOFs) of the substructure into the boundary DOFs $\mathbf{q}_{s,b}$ and interior DOFs $\mathbf{q}_{s,i}$, the static equilibrium equation can be rewritten as

$$\begin{bmatrix} \mathbf{K}_{bb} & \mathbf{K}_{bi} \\ \mathbf{K}_{ib} & \mathbf{K}_{ii} \end{bmatrix} \begin{bmatrix} \mathbf{q}_{s,b} \\ \mathbf{q}_{s,i} \end{bmatrix} = \begin{bmatrix} \mathbf{F}_{s,b} \\ \mathbf{0} \end{bmatrix}, \tag{4}$$

where the subscripts b and i denote the boundary and interior, respectively. The second row of Eq. (4) can be reformulated as

$$\mathbf{q}_{s,i} = -\mathbf{K}_{ii}^{-1} \mathbf{K}_{ib} \mathbf{q}_{s,b}. \tag{5}$$

Then, the substructure DOFs $\mathbf{q}_s$ can be represented by the boundary DOFs $\mathbf{q}_{s,b}$ as

$$\mathbf{q}_s = \begin{bmatrix} \mathbf{I} \\ -\mathbf{K}_{ii}^{-1} \mathbf{K}_{ib} \end{bmatrix} \mathbf{q}_{s,b} = \Phi \mathbf{q}_{s,b}, \tag{6}$$

where Φ is the transformation matrix. Substituting Eq. (6) into Eq. (3) and premultiplying both sides by Φ^{T}, the static equilibrium equation is reduced to

$$\tilde{\mathbf{K}}_s \mathbf{q}_{s,b} = \tilde{\mathbf{F}}_s, \tag{7}$$

where $\tilde{\mathbf{K}}_s$ and $\tilde{\mathbf{F}}_s$ are reduced substructure stiffness matrix and external force vector, respectively. Note that, considering the dynamic friction model, although the dynamic characteristics of the bump foil is negligible, the mass matrix and damping matrix of the bump foil are needed to be incorporated to avoid a fully implicit solution strategy which greatly reduces the computational efficiency. The mass matrix and damping matrix of the substructure are reduced to the subspace using the same base as the stiffness matrix; that is

$$\tilde{\mathbf{M}}_s = \Phi^{\mathrm{T}} \mathbf{M}_s \Phi, \tag{8}$$

$$\tilde{\mathbf{C}}_s = \Phi^{\mathrm{T}} \mathbf{C}_s \Phi. \tag{9}$$

Then, the reduced substructure can be viewed as a super element and is governed by

$$\tilde{\mathbf{M}}_s \ddot{\mathbf{q}}_{s,b} + \tilde{\mathbf{C}}_s \dot{\mathbf{q}}_{s,b} + \tilde{\mathbf{K}}_s \mathbf{q}_{s,b} = \tilde{\mathbf{F}}_s. \tag{10}$$

By assembling all the substructure equations, the governing equation of the reduced bump foil structure can be organized as

$$\mathbf{M}_f \ddot{\mathbf{q}} + \mathbf{C}_f \dot{\mathbf{q}} + \mathbf{K}_f \mathbf{q} = \mathbf{F}_c(\mathbf{q}, \dot{\mathbf{q}}, \mathbf{z}), \tag{11}$$

where $\mathbf{q}$ is the generalized nodal deflection vector of the reduced bump foil structure, $\mathbf{M}_f$, $\mathbf{C}_f$ and $\mathbf{K}_f$ are the generalized mass matrix, damping matrix and stiffness matrix of the reduced bump foil structure, respectively. $\mathbf{F}_c(\mathbf{q}, \dot{\mathbf{q}}, \mathbf{z})$ is the generalized force due to the frictional contact, in which $\mathbf{z}$ is the generalized coordinate vector of the internal friction states of contacts.

2.2 Modeling of the Frictional Contact

In view of the reduction scheme of the bump foil, a general node-to-element contact framework is adopted in this work to model the frictional contact behavior between the bump foil and two parallel surfaces. The boundary nodes of the reduced bump foil are chosen to be the slave nodes of the contacts, and the two parallel surfaces are the master segments. For a contact pair, the contact force is composed of the normal contact force f_n and tangential friction force f_t.

The normal contact force f_n is governed by the Hertz contact model as

$$f_n = k\delta + c\dot{\delta}, \tag{12}$$

where δ is the penetration depth, as shown in Fig. 2(b), k and c are the normal contact stiffness and damping, respectively.

The tangential friction force f_t is governed by the amended LuGre dynamic friction model [23]. This model is capable of capturing the Stribeck effect and dealing with

conditions of significant variations in the normal contact force [24]. A typical form of the amended LuGre friction model is given as

$$f_t = (\sigma_0 z_t + \overline{\sigma}_1 \dot{z}_t + \sigma_2 v_t) f_n, \tag{13}$$

$$\dot{z}_t = v_t - \sigma_0 \frac{|v_t|}{g(v_t)} z_t, \tag{14}$$

where z_t is the internal friction state of the contact point, which can be seen as the average microscopic deflection of the contact surface, while v_t is the macroscopical tangential velocity of the contact point, as illustrated in Fig. 2(b). The function

$$\overline{\sigma}_1 = \sigma_1 e^{-(v_t/v_c)^2}, \tag{15}$$

with a sufficiently small transition velocity v_c is applied to make the friction model passive and well micro-damped [25]. σ_0, σ_1 and σ_2 are the friction stiffness, micro damping and viscous damping coefficients per unit of normal force, respectively. $g(v_t)$ is a function that captures the Stribeck effect and is expressed as

$$g(v_t) = \mu_k + (\mu_s - \mu_k) e^{-(v_t/v_s)^2}, \tag{16}$$

where μ_k and μ_s are the kinetic friction coefficient and maximum static friction coefficient, respectively, and v_s is called the Stribeck velocity. For a constant velocity, the steady-state friction force $f_{t,s}$ is written as

$$f_{t,s} = (g(v_t)\text{sgn}(v_t) + \sigma_2 v_t) f_n. \tag{17}$$

Denoting the generalized coordinate vector of all the internal friction states as $\mathbf{z}$, the governing equation of the dynamic friction is established as

$$\dot{\mathbf{z}} = \mathbf{R}(\mathbf{q}, \dot{\mathbf{q}}, \mathbf{z}). \tag{18}$$

2.3 System Coupling and Solution

Eventually, the governing equations of the system comprise Eq. (11) and Eq. (18). Denoting the state vector of the system as

$$\mathbf{y} = \begin{bmatrix} \mathbf{q} \\ \dot{\mathbf{q}} \\ \mathbf{z} \end{bmatrix}, \tag{19}$$

the governing equations of the system can be arranged in a fully coupled form as

$$\mathbf{M}(\mathbf{y})\dot{\mathbf{y}} = \mathbf{F}(\mathbf{y}). \tag{20}$$

All the state variables are solved simultaneously by the variable-step and variable-order implicit integrator ode15s in MATLAB [26], and the analytical Jacobian matrix $\partial \mathbf{F}/\partial \mathbf{y}$ is implemented to improve the computation efficiency.

3   Results and Discussions

In this section, the hysteresis behaviors of the bump foil are investigated. The parameters of the bump foil are listed in Table 1 and the parameters of the friction and simulation are listed in Table 2.

Table 1. Parameters of the bump foil.

Parameters	Values
Bump foil thickness, t_b	0.127 mm
Bump half length, l_b	3.30 mm
Bump pitch length, s_b	7.00 mm
Bump height, h_b	0.9 mm
Bump foil width, w_b	18 mm
Number of bumps, N_b	4
Density, ρ	7,800 kg/m^3
Young's modulus, E	207 GPa
Poisson's ratio, ν	0.3

Table 2. Parameters of the friction and simulation.

Parameters	Values
Micro damping per normal force, σ_1	0.01 s/mm
Viscous damping per normal force, σ_2	0 s/mm
Transition velocity, v_c	1×10^{-8} mm/s
Stribeck velocity, v_s	1 mm/s
Normal contact stiffness, k	1×10^6 N/mm
Normal contact damping, c	1×10^2 N·s/mm
Proportional damping coefficient, β	1×10^{-4} s
Relative tolerance of ode15s, ε	1×10^{-6}

3.1   Modeling Verification

The modeling of the bump foil structure and the solution strategy are verified in this subsection by comparing with the test results under dynamic excitation in Ref. [19]. The excitation is implemented through the sinusoidal amplitude perturbation of the upper surface. The kinetic and maximum static friction coefficients are both set as 0.2 and
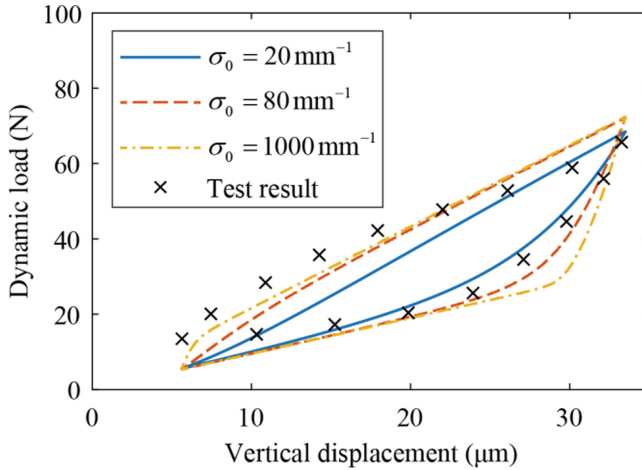
Fig. 3. Comparison of hysteresis curves under different friction stiffness per normal force with test result.

the excitation frequency is 1 Hz. The simulation is carried out with different friction stiffness per normal force σ_0, and the results are given in Fig. 3.

As can be seen, with a high friction stiffness per normal force, the hysteresis curve obviously possesses four stages during one loading-unloading process. Along with the decrease of the friction stiffness per normal force, the boundaries between the two stages in loading and unloading processes are increasingly blurred, and the dissipation of energy (the area of the hysteresis curve) is accordingly decreased. Besides, the simulation results are in good agreement with the test data, especially for the case of $\sigma_0 = 80 \, \mathrm{mm}^{-1}$.

3.2 Presliding Behavior

To explain the variation trend of hysteresis curves in Fig. 3, the details of the friction are illustrated in Fig. 4 in the form of normalized friction and velocity of node 2 with the first half period being the loading process and the second half period being the unloading process. The friction force is normalized by the maximum static friction force (equal to the kinetic friction force in this case), and the tangential velocity is normalized by the product of excitation amplitude and excitation angular frequency.

As can be seen, for a high friction stiffness per normal force, the stick and slip states are quite distinguishable; that is, when the friction force is less than the maximum static friction force, the tangential velocity stays low to approximate the stick state. Along with the decrease of the friction stiffness per normal force, it is more and more difficult to distinguish the stick and slip states, as there is a considerable tangential velocity even though the friction force is less than the maximum static friction force. This phenomenon is physical and is due to the presliding behavior of the contact point. Therefore, the friction stiffness per normal force σ_0 should be chosen based on the experimental data to capture reasonable presliding behavior.
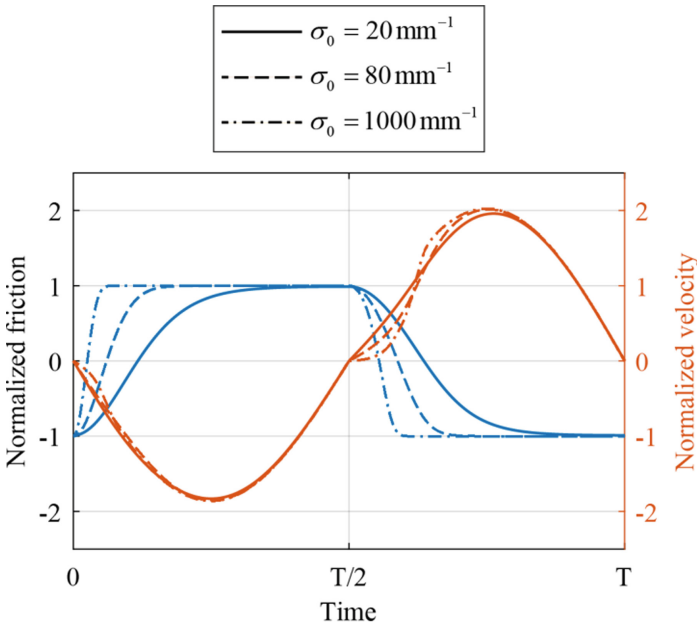
Fig. 4. Normalized friction force and tangential velocity of node 2 during loading-unloading process under different friction stiffness per normal force.

3.3 Stick-Slip States During Loading-Unloading Process

As indicated in Fig. 4, a low friction stiffness per normal force would make it difficult to distinguish the stick and slip states. So, to investigate the changes in friction states of contact nodes, a high friction stiffness per normal force $\sigma_0 = 1000\,\mathrm{mm}^{-1}$ is adopted in this subsection. The stick state is recognized when the normalized friction force is higher than 0.99, and the results are plotted in Fig. 5 with four key points.

As can be seen, the high-slope loading curve from key point 1 to 2 is caused by the stick states of all contact nodes, while the low-slope loading curve from key point 2 to 3 corresponds to slip states of almost all contact nodes. The unloading process is similar to the loading one except for a longer stick stage. Around key point 2 and 4, the contact nodes change from the stick state to slip state in sequence, beginning at the free end of the bump foil. Note that, there would be one or more nodes close to the welded end of the bump foil that are always stuck.

3.4 Stribeck Effect

In this subsection, the influence of the Stribeck effect on the hysteresis curves is investigated with $\sigma_0 = 80\,\mathrm{mm}^{-1}$, $\mu_k = 0.1$ and $\mu_s = 0.2$. The simulation is carried out with different excitation amplitudes under an excitation frequency of 10 Hz. The results are given in Fig. 6.

(a)

(b)
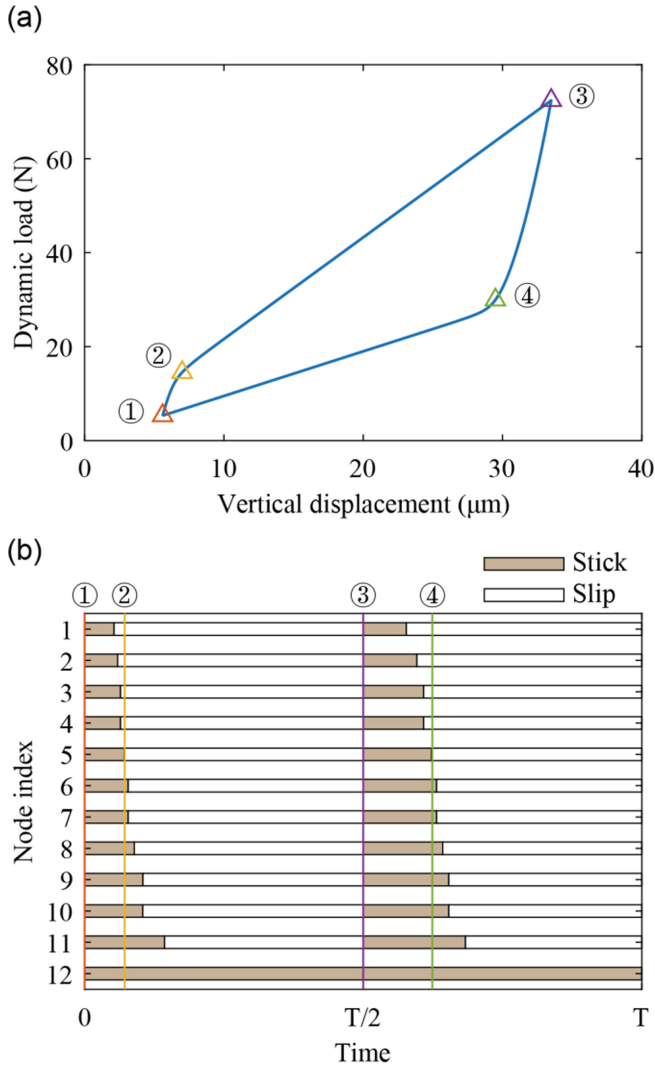
Fig. 5. Changes in stick-slip states of all the contact nodes during loading-unloading process.

As can be seen, when taking into account the Stribeck effect, the hysteresis curves are dominated by different friction coefficients in different stages. The low-slope loading and unloading curves are obviously dominated by the kinetic friction coefficient as most of the nodes are sliding, while the high-slop loading and unloading curves are governed by the maximum static friction coefficient in the form of extended length. Near the end of the loading and unloading processes, the tangential velocities of contact nodes decrease and the friction forces increase, resulting an increasing slope of the curve. This phenomenon is observed in [19], which means that the Stribeck effect is a prevalent phenomenon in bump foil structure.
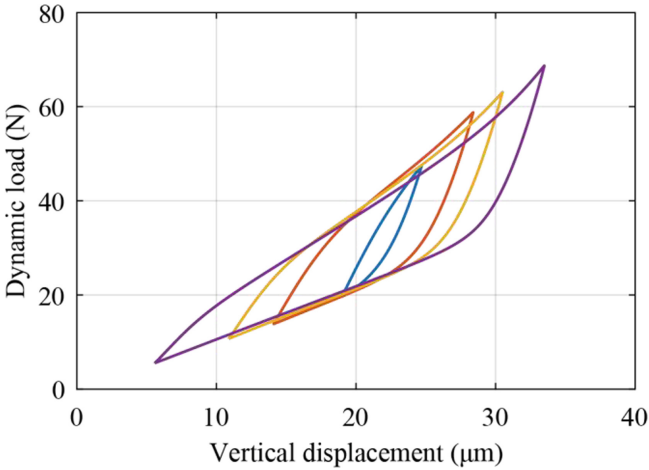
Fig. 6. Influence of the Stribeck effect on the hysteresis curves with different excitation amplitudes.

4　Conclusions

The hysteresis behaviors of a bump-type foil bearing structure were investigated in this paper. The bump foil was modeled by two-node Euler beam elements and reduced by Guyan reduction method. The amended LuGre friction model was adopted to deal with the cases of variable normal contact force. All the state variables were solved simultaneously in the fully coupled scheme, and the modeling and solution were validated by experimental data.

It was found that the friction stiffness per normal force controls the presliding behavior of the contact point. Along with the decrease of the friction stiffness per normal force, the presliding behavior is enhanced and it is more and more difficult to distinguish the stick and slip states, finally resulting a decrease of the energy dissipation of hysteresis curves. Besides, the high-slope loading and unloading curves correspond to the stick states of all contact nodes, while the low-slope ones correspond to the slip states of partial contact nodes close to the free end of the bump foil. Finally, the Stribeck effect was taken into account and the results showed that the high-slope and low-slope parts of hysteresis curves are dominated by maximum static friction coefficient and kinetic friction coefficient, respectively. Moreover, the comparisons of simulation and experimental hysteresis curves indicated that the presliding behavior and Stribeck effect are prevalent in bump foil structure and should be taken into account in the modeling of the GFB system.

References

1. Agrawal, G.L.: Foil air/gas bearing technology-an overview. In: ASME 1997 international gas turbine and aeroengine congress and exhibition. American Society of Mechanical Engineers Digital Collection, pp. 1–11 (1997)
2. DellaCorte, C.: Oil-Free shaft support system rotordynamics: Past, present and future challenges and opportunities. Mech. Syst. Signal Process. **29**, 67–76 (2012)
3. Samanta, P., Murmu, N.C., Khonsari, M.M.: The evolution of foil bearing technology. Tribol. Int. **135**, 305–323 (2019)
4. Zhou, R., Gu, Y., Cui, J., et al.: Nonlinear dynamic analysis of supercritical and subcritical Hopf bifurcations in gas foil bearing-rotor systems. Nonlinear Dyn. **103**(3), 2241–2256 (2021)
5. Zhou, R., Gu, Y., Ren, G., et al.: Modeling and stability characteristics of bump-type gas foil bearing rotor systems considering stick–slip friction. Int. J. Mech. Sci. **219,** 107091 (2022)
6. Ku, C.P.R., Heshmat, H.: Compliant foil bearing structural stiffness analysis: part I—theoretical model including strip and variable bump foil geometry. J. Tribol. **114**(2), 394–400 (1992)
7. Ku, C.P.R., Heshmat, H.: Compliant foil bearing structural stiffness analysis—part II: experimental investigation. J. Tribol. **115**(3), 364–369 (1993)
8. Ku, C.P.R., Heshmat, H.: Structural stiffness and coulomb damping in compliant foil journal bearings: theoretical considerations. Tribol. Trans. **37**(3), 525–533 (1994)
9. Ku, C.P.R., Heshmat, H.: Structural stiffness and coulomb damping in compliant foil journal bearings: parametric studies. Tribol. Trans. **37**(3), 455–462 (1994)
10. Heshmat, H., Ku, C.P.R.: Structural damping of self-acting compliant foil journal bearings. J. Tribol. **116**(1), 76–82 (1994)
11. Ku, C.P.R., Heshmat, H.: Effects of static load on dynamic structural properties in a flexible supported foil journal bearing. J. Vib. Acoust. **116**(3), 257–262 (1994)
12. Salehi, M., Heshmat, H., Walton, J.F.: On the frictional damping characterization of compliant bump foils. J. Tribol. **125**(4), 503–514 (2003)
13. Rubio, D., Andrés, L.S.: Bump-type foil bearing structural stiffness: experiments and predictions. J. Eng. Gas Turbines Power **128**(3), 653–660 (2006)
14. Rubio, D., San, A.L.: Structural stiffness, dry friction coefficient, and equivalent viscous damping in a bump-type foil gas bearing. J. Eng. Gas Turbines Power **129**(2), 494–502 (2007)
15. Zywica, G., Baginski, P., Bogulicz, M.: Experimental and numerical evaluation of the damping properties of a foil bearing structure taking into account the static and kinetic dry friction. J. Braz. Soc. Mech. Sci. Eng. **43**(1), 1–23 (2021)
16. Zywica, G., Baginski, P., Bogulicz, M., et al.: Numerical identification of the dynamic characteristics of a nonlinear foil bearing structure: Effect of the excitation force amplitude and the assembly preload. J. Sound Vib. **520**, 116663 (2022)
17. Le Lez, S., Arghir, M., Frene, J.: Static and dynamic characterisation of a bump-type foil bearing structure. J. Tribol. **129**(1), 75–83 (2007)
18. Le Lez, S., Arghir, M., Frene, J.: A dynamic model for dissipative structures used in bump-type foil bearings. Tribol. Trans. **52**(1), 36–46 (2008)
19. Larsen, J.S., Varela, A.C., Santos, I.F.: Numerical and experimental investigation of bump foil mechanical behaviour. Tribol. Int. **74**, 46–56 (2014)
20. Feng, K., Guo, Z.: Prediction of dynamic characteristics of a bump-type foil bearing structure with consideration of dynamic friction. Tribol. Trans. **57**(2), 230–241 (2014)
21. De Wit, C.C., Olsson, H., Astrom, K.J., et al.: A new model for control of systems with friction. IEEE Trans. Autom. Control **40**(3), 419–425 (1995)
22. Guyan, R.J.: Reduction of stiffness and mass matrices. AIAA J. **3**(2), 380 (1965)

23. De Wit C C, Tsiotras P. Dynamic tire friction models for vehicle traction control[C]. Proceedings of the 38th IEEE Conference on Decision and Control, 1999, 4: 3746–3751
24. Marques, F., Woliński, Ł, Wojtyra, M., et al.: An investigation of a novel LuGre-based friction force model. Mech. Mach. Theory **166**, 104493 (2021)
25. Johanastrom, K., Canudas-De-Wit, C.: Revisiting the LuGre friction model. IEEE Control Syst. Mag. **28**(6), 101–114 (2008)
26. Shampine, L.F., Reichelt, M.W.: The matlab ode suite. SIAM J. Sci. Comput. **18**(1), 1–22 (1997)

Research on Re-extraction Technology for Uranium Refining Based on Fractionation Extraction

Zhiquan Zhou, Yan Ren, Kaikai Ye, Yuqing Niu[✉], Jiayu Zhang, Shu Meng, Shaohui Kang, Xiaohao Cao, and Dabing Li

Beijing Research Institute of Chemical Engineering and Metallurgy, No. 145, Jiukeshu, Tongzhou District, Beijing, China
nyq@bricem.com.cn

Abstract. TBP extraction in nitric acid system is the core purification process of the wet method for uranium refining and conversion. Reextraction for uranium refining based on fractionation extraction was proposed, according to the characteristics and requirements of uranium refining extraction. The operation line and step line of reextraction were obtained through mathematical model, and the control law is explained. The reextraction bench test was carried out to investigate the stable operation and the concentration variation of the related components. The study shows that the reextraction process can run stably. After extraction, the concentration of uranium in organic phase can reach 120g/L, the extraction saturation can reach 96.7%, the concentration of uranium in raffinate is less than 10mg/L, and the concentration of impurity components is greatly reduced. Reextraction technology can facility the control of uranium refining extraction, which maintains the state of high saturation vs. low raffinate concentration.

Keywords: Uranium refining · Reextraction · Fractionation extraction · Solvent extraction · Extraction

1 Introduction

Uranium refining and conversion is the process of further removing impurities and neutron poisons from natural uranium ore concentrate and making uranium fluoride reach nuclear grade. Wet uranium refining and conversion process were used in the majority of countries in the world. First, the uranium concentrate is dissolved by nitric acid, and then TBP-kerosene extraction method is used in uranium refining, the loaded solvent can be stripped by hot water (trace nitric acid) or ammonium carbonate solution. Finally, the loaded strip is prepared into uranium fluoride. The core purification process of wet uranium refining and conversion is TBP-kerosene/$UO_2(NO_3)$-HNO_3 extraction.

Compared with other extraction processes, uranium refining extraction has its own characteristics: high concentration of target components and especially low concentration of impurities. In order to to reduce the extraction of impurities and achieve a better purification effect, maintaining a higher extraction saturation of uranium is necessary

in industry. However, it is difficult to stabilize the operation for negative correlation between high extraction saturation and low uranium concentration in raffinate. In this paper, a saturated re-extraction technology based on fractionation extraction is proposed to solve this problem.

Fractionation extraction is an important extraction technology. Compared with the conventional multistage countercurrent (or continuous countercurrent) solvent extraction, fractionation extraction add one or more inlet or outlet. This method is suitable for the extraction of two or more components which is difficult to separate. Lots of research of fractionation extraction were shown in other industries [6–12]. Scrub process with loaded organic phase is necessary for further improving the effect of refining in uranium refining extraction. Extraction – scrub can also be regarded as fractionation extraction if scrub raffinate is incorporated into the feed solution. Only extraction process is discussed in this paper, not including scrub.

2 Theory of Fractionation Extraction

The saturated re-extraction process proposed in this paper is as follows: after extracted and reextracted through N-level (or continuous) counter-current operation successively, the stripped solvent become the loaded organic phase of re-extraction, and then the loaded solvent is recycled by scrubbing and stripping. A certain concentration of feed solution is prepared for the first stage of extraction and re-extraction respectively. The reextracted raffinate (N' raffinate) is returned to prepare the feed solution. The process is shown in Fig. 1.

The symbols of each part are as follows:

Q_O——Flow rate of organic phase

Q_A——Flow rate of the extraction feed solution

$Q_A{}'$——Flow rate of the reextraction feed solution

Q_{F0}——Flow rate of new feed fluid (or imaginary new feed fluid)

x_0——Concentration of the new feed solution (or imaginary new feed solution)

x_F——Concentration of the extraction and reextraction feed solution

y_0——Concentration of stripped solvent

y_1——Concentration of loaded solvent after extraction

$y_1{}'$——Concentration of loaded solvent after reextraction

ξ——Saturation of loaded solvent after extraction

ξ'——Saturation of loaded solvent after reextraction

N——Stage of extraction

N'——Stage of reextraction

x_i——Concentration of $i^\#$ grade aqueous in extraction

y_i——Concentration of $i^\#$ grade organic phase in extraction

$x_j{}'$——Concentration of $j^\#$ grade aqueous phase in extraction

$y_j{}'$——Concentration of $j^\#$ grade aqueous phase in reextraction

x_N——Concentration of extraction raffinate

$x_N{}'$——Concentration of reextraction raffinate

n——Extraction flow ratio, $n = Q_O / Q_A$

n'——Reextraction flow ratio, $n' = Q_O / Q_A{}'$
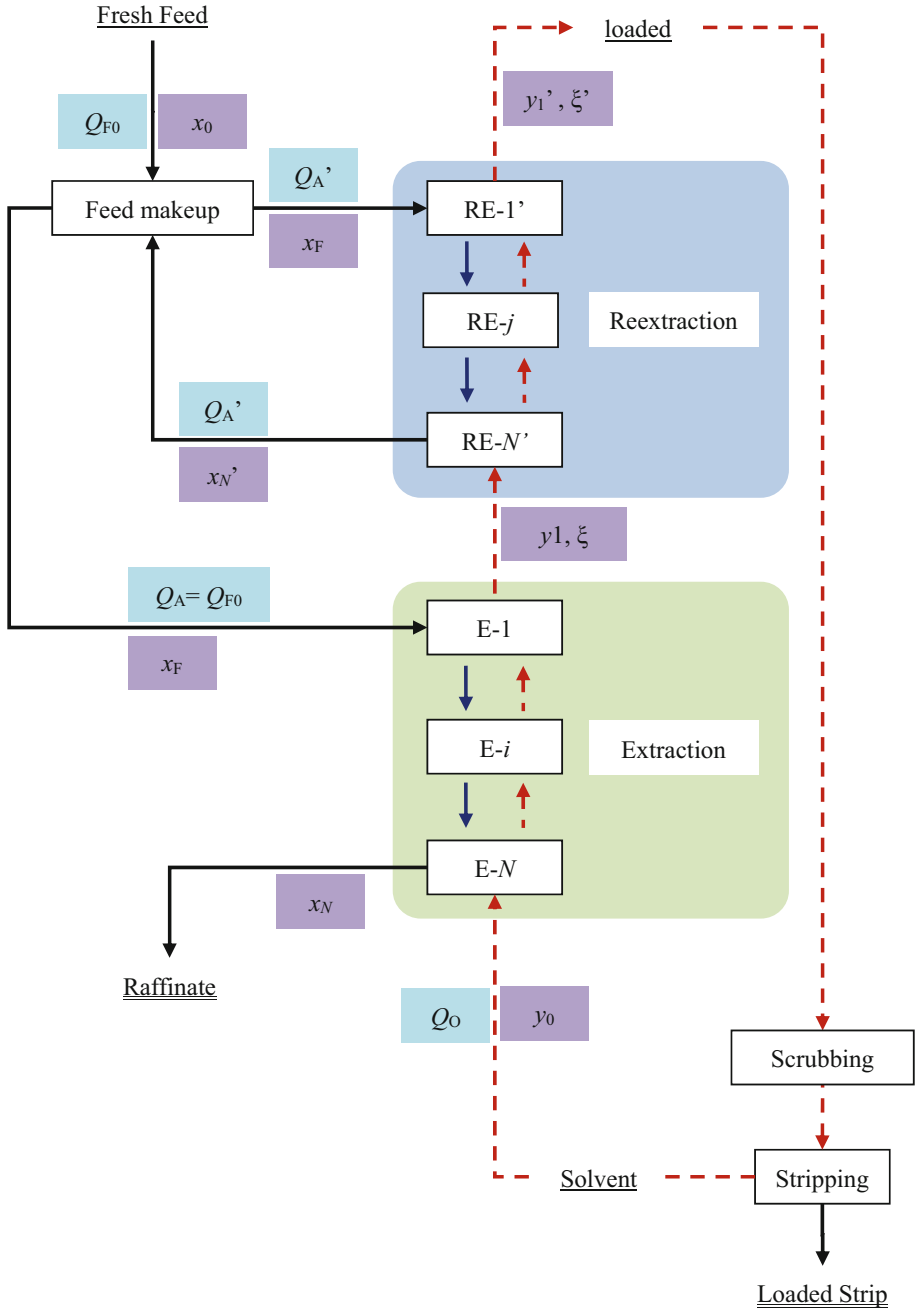
Fig. 1. Process flow chart

The flow rate of reextraction aqueous phase is greater than that of extraction, that means $Q_A{}' > Q_A$, or $n' < n$. n takes a relatively large parameter so that the uranium concentration of raffinate can easily reach a lower standard in the extraction part. While, n' tend to be taken as a relatively small parameter to improve the saturation of the loaded solvent in the reextraction part.

3   Results and Discussion

3.1   Extraction Equilibrium Isotherms

Uranium refining extraction is a double-component extraction of nitric acid and uranyl nitrate from the point of view of constant concentration, and extraction equations are as follows:

$$UO_2{}^2{}_{(w)} + 2NO_2{}^-{}_{(w)} + 2TBP_o \rightleftharpoons UO_2(NO_3)_2 \cdot 2TBP_o$$

$$H^+_{(w)} + NO_3{}^-{}_{(w)} + TBP_{(o)} \rightleftharpoons HNO_3 \cdot TBP_{(o)}$$

The equations for the equilibrium constants are as follows:

$$K_U = \frac{\{UO_2(NO_3)_2 \cdot 2TBP\}}{\left\{UO_2^{2+}\right\} \cdot \{NO_3^-\}^2 \cdot \{TBP\}^2} = \frac{y_U \gamma_U}{x_U \cdot (NO_3^-)^2 \cdot \gamma_\pm^3 \cdot T^2 \cdot \gamma_T^2}$$

$$K_H = \frac{\{HNO_3 \cdot TBP\}}{\{H^+\}\{NO_3^-\}\{TBP\}} = \frac{y_H y_H'}{x_H \cdot (NO_3^-) \cdot \gamma_\pm'^2 \cdot T \cdot \gamma_T}$$

The activity coefficient can be calculated:

$$\begin{aligned}
y_U &= \overline{K_U} x_U \left(NO_3^-\right)^2 T^2 \gamma_\pm^3 \\
y_H &= \widetilde{K_H}\, x_H \left(NO_3^-\right) T \\
F &= \frac{f_U}{(1+f_H)^2} \\
f_U &= \overline{K_U} x_U (2x_U + x_H)^2 \gamma_\pm^3 \\
f_H &= \widetilde{K_H}\, x_H (2x_U + x_H) \\
y_U &= \tfrac{1}{2}\left[T_0 - \tfrac{1}{4F}\left(\sqrt{1 + 8FT_0} - 1\right)\right.
\end{aligned} \tag{1}$$

$$y_H = \frac{f_H}{1 + f_H}(T_0 - 2y_U) \tag{2}$$

y_U— Concentration of $UO_2(NO_3)_2$. 2TBP in organic phase at equilibrium (mol/L)

x_U— Concentration of UO_2^{2+} in aqueous phase at equilibrium (mol/L)

y_H— Concentration of HNO_3.TBP in organic phase at equilibrium (mol/L).

x_H— Concentration of HNO_3 in aqueous phase at equilibrium (mol/L).

T— Concentration of free TBP at equilibrium (mol/L).

T_0— Concentration of total TBP (mol/L).

$\gamma_\pm$— Activity ionic activity coefficients of UO_2^{2+} and NO_3^- in aqueous phase.

γ_U— Activity coefficient of $UO_2(NO_3)_2$. 2TBP in organic phase.

$\gamma'_\pm$— Average ionic activity coefficients of H^+ and NO_3^- in aqueous phase.

γ'_H— Activity coefficient of HNO_3. TBP in organic phase.

γ_T— Activity coefficient of TBP.

$\overline{K_U} = 63$— The equivalent equilibrium constant of uranium.

$\widetilde{K_H} = 0.19$— The apparent equilibrium constant of hydrogen ions.

A.M.Pozeh calculated the effect on $\gamma_\pm$ according to Harend rule in the presence of nitric acid and other nitrates in aqueous solution. In uranyl nitrate and nitric acid system, $x_{EQ} = (x_U + x_H/3)$. According to the data fitting in Fig. 2 the relationship can be obtained as Eq. (3). According to Eq. (1), (2) and (3), the extraction equilibrium line for uranium with different nitric acid concentration can be calculated under the condition that 30%TBP- kerosene is used as extraction agent (Fig. 3).
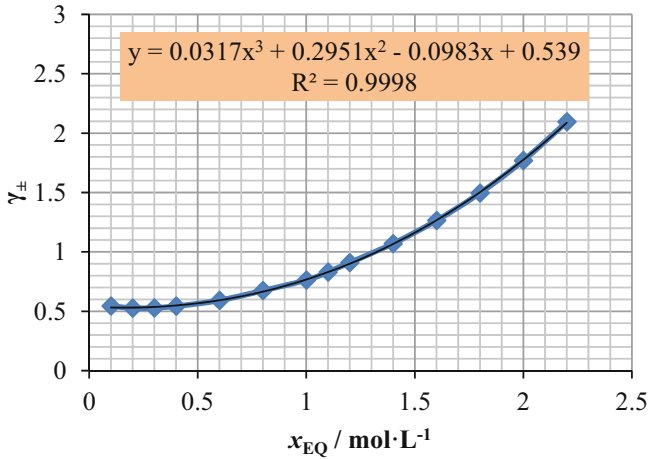
Fig. 2. The relationship between average ionic activity coefficients $\gamma_\pm$ and component concentration

$$\gamma_\pm = 0.0317x_{EQ}^3 + 0.2951x_{EQ}^2 - 0.0983x_{EQ} + 0.539 \tag{3}$$
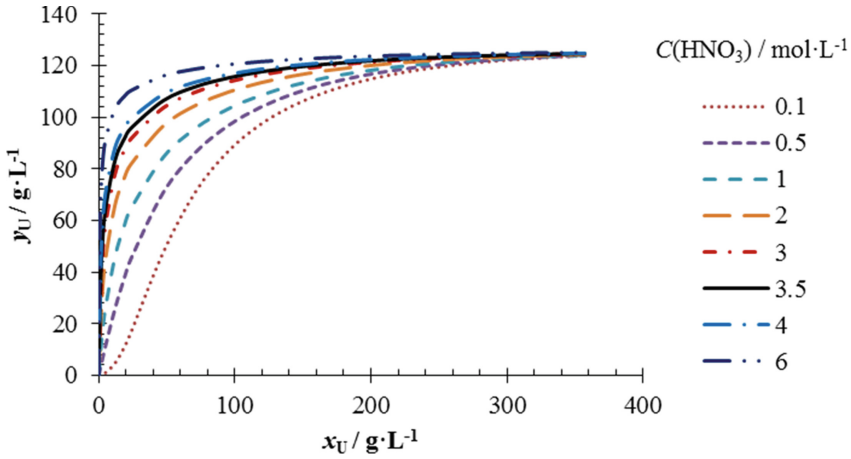
Fig. 3. Isotherms of uranium extraction at different nitric acid concentrations

3.2 Discussion of Operation Step Line

Operation line of reextraction process is shown in Fig. 4.
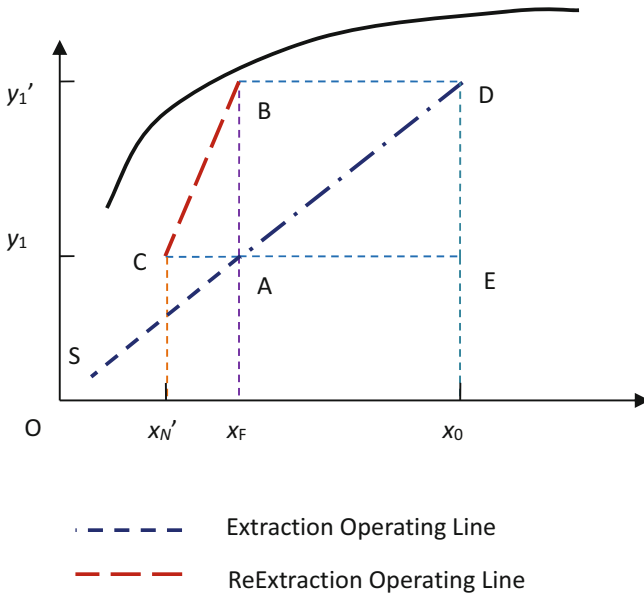
Fig. 4. Operation line of reextraction process

In the figure, SA is the extraction line and CB is the reextraction line. The organic phase is extracted from point S to point A, and then reextracted from point C to point B. The reextraction feed solution is reextracted from point B to point C and becomes

reextraction raffinate. The extraction feed solution is extracted from point A to point S and becomes raffinate. SD is an imaginary operating line when extraction-reextraction is considered as a whole. The operating line does not represent the actual internal state of the actual operation, but can represent the state of the feed solution in the import and export. The operating line is very useful for the research of reextraction process. The relationship between the length of segment and flow ratio in in reextraction n', flow ratio in extraction n, component concentration and flow rate in the Fig. 4 is shown as follows.

$$\overline{CA} = x_F - x_N' = \frac{Q_O}{Q_{A'}}(y_1' - y_1) = \frac{Q_O}{Q_{A'}}\overline{BA}$$
$$\overline{EA} = x_0 - x_F = \frac{Q_O}{Q_A}(y_1' - y_1) = \frac{Q_O}{Q_A}\overline{DE} \tag{4}$$
$$\frac{\overline{CA}}{\overline{EA}} = \frac{x_F - x_N'}{x_0 - x_F} = \frac{Q_A}{Q_{A'}} = \frac{n'}{n}$$

Formula (4) shows the internal relationship between concentration and flow rate caused by the solid-liquid cycle of extraction-reextraction, and it is an important basis for regulating flow ratio and concentration of extract feed solution. The feed solution with 3.5 mol/L nitric acid and 300 g/L uranium is generally used in uranium refining extraction in industry for better effect. Uranium refining extraction is a double-component extraction of nitric acid and uranyl nitrate from the point of view of constant concentration, and the concentrations of acid and uranium at all stages of the multistage countercurrent process are changed. In this study, the uranium extraction equilibrium line with 3.5mol/L nitric acid was used as the basis of the operation line research. Operation line and step diagram are shown in Fig. 5 and Table 1 according to different operating conditions.

Figure 5 shows that using extraction-reextraction with N' = 1–2 can improve extraction saturation greatly. Reextraction technology hardly increase the extraction stages compared with the common countercurrent extraction technology. The equipment stage efficiency has a great impact on extraction stage compared with the change of concentration conditions. The inverse of the flow ratio of uranium refining is equal to the slope of the operation line $k \approx y_1/x_F$. Only if the slope of the operation line controls within the range of (124–120) /120 = 3% can the concentration of the organic phase reach to 120–124 g/L. Otherwise, the concentration of the organic phase cannot meet the requirements, or the concentration of raffinate exceeds the standard. The operating conditions are extremely rigor. This problem does not exist in reextraction technology. The control accuracy range of the extraction section can be preset at about 20%, such as (124–100) /100 = 24% or (124–108) /108 = 15%, and then the reextraction operation without special control accuracy can be carried out.

3.3 Continuous Operation and Stability Control Investigation

The feed solution was prepared as 240g/L for extraction-reextraction experiment. Extraction-reextraction operation line and step diagram are shown in Fig. 6. $x_F = 240$g/L, $y_1' = 120$ g/L, $x_N < 0.05$ g/L, $y_0 = 0$ g/L, extraction flow ratio $n = 3$, reextraction flow ratio $n' = 1$, stage efficiency is 80%. The figure clarifies that N = 6, N' = 2.

6-stage extraction and 2-stage reextraction operation was used in the experiment which was run continuously for 81h. After stable operation, the concentration of uranium in extraction loaded solvent (y_1), the concentration of uranium in reextraction loaded
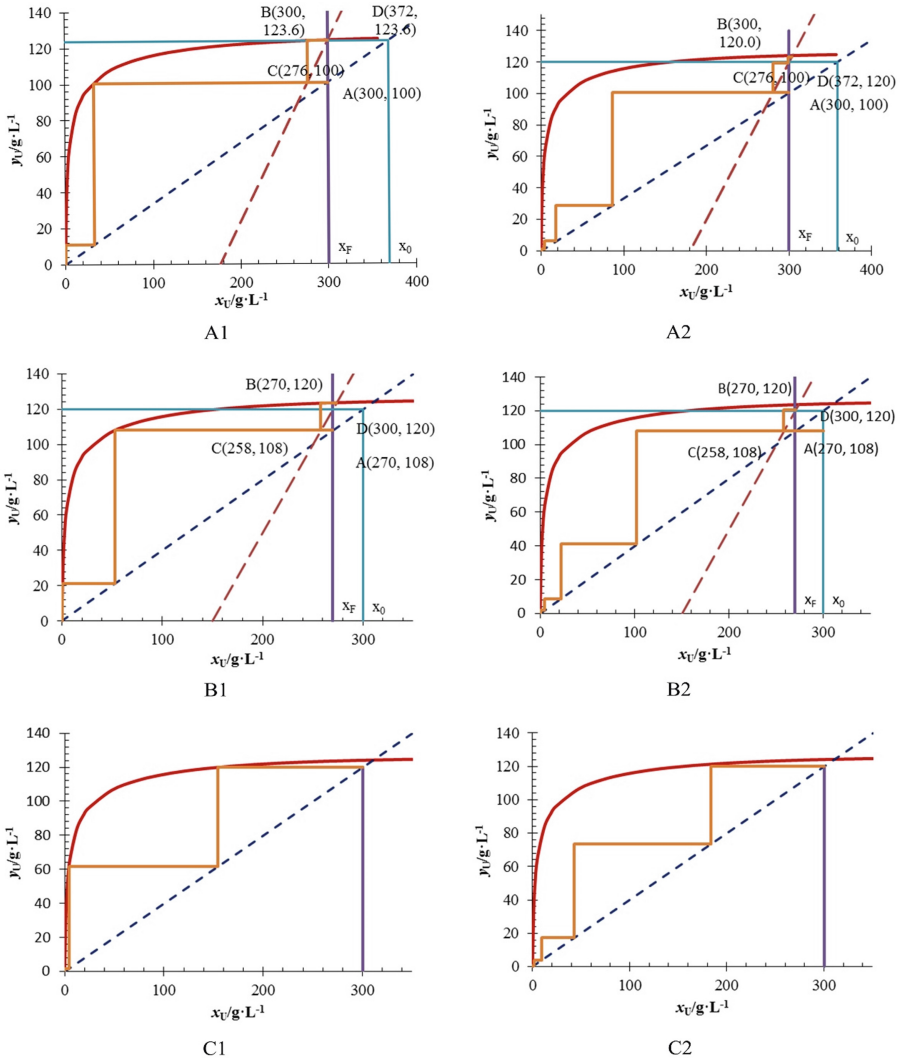
Fig. 5. Operation line and step diagram under different conditions

solvent (y_1') and the concentration of uranium in raffinate (x_N) at different times were obtained. The result is shown in Fig. 7.

Figure 7 clarifies that saturation reextraction technique had a good performance in the stable operation control of uranium refining. The concentration of uranium in raffinate keeps low during the whole extraction process, x_N is lower than 10 mg/L. the saturated and reextraction organic phase concentration The average of y_1' was 124 g/L, which was greater than 120 g/L. The saturation of reextraction loaded solvent ξ' reached more than 96.7%. The concentration of uranium in export is stable. In addition, the concentration of uranium in extraction loaded solvent fluctuates between 80 and 100 g/L, which indicate

Table 1. Countercurrent progression required under different operating conditions

Condition 2 / Condition 1		stage efficiency 100%	stage efficiency 80%
x_F=300 g/L,	y_1'=120 g/L;	N=3, N'=1	N=6, N'=2
x_N<0.05 g/L,	y_0=0 g/L		
x_0=300 g/L,	y_1'=120 g/L;	N=3, N'=1	N=6, N'=1
x_N<0.05 g/L,	y_0=0 g/L		
x_F=300 g/L,	y_1=120 g/L;	N=4	N=7
x_N<0.05 g/L,	y_0=0 g/L		
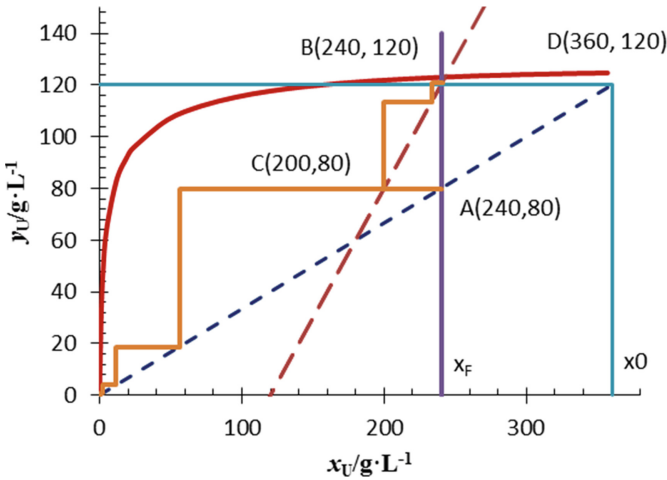
Fig. 6. Operating line and step diagram under test conditions

that the control conditions of extraction part was not accurate. However, the concentration of export organic phase can be rapidly increased and kept stable by using saturation reextraction.

3.4 Purification Effect

The concentration of uranium and impurity components before and after extraction are shown in Table 2. It indicates that the impurity content of the loaded solvent was greatly reduced compared with the feed solution, and a good purification effect was achieved after saturation reextraction.
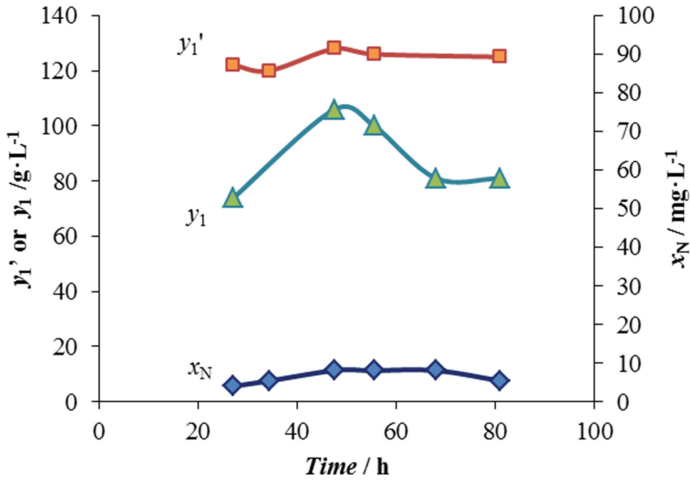
Fig. 7. The concentration of uranium at different times

Table 2. Concentration of uranium and impurity components before and after extraction

Experiment 1				Experiment 2	
Elements	Units	x_F	y_1'	x_F	y_1'
U	g/L	237.59	125.28	241.35	127.03
Ti	mg/L	1.84	0.3	1.97	<0.1
Mo	mg/L	34.02	0.54	41.85	<0.1
W	mg/L	0.64	0.63	0.83	0.42
V	mg/L	14.37	0.24	18.37	0.24
Cr	mg/L	1.59	1	1.85	0.5
Sb	mg/L	<1.0	<0.1	0.624	0.8
Nb	mg/L	<1.0	<0.1	0.305	<0.1
Ru	mg/L	8.2	<0.1	4.434	<0.1
Ta	mg/L	<1.0	<0.1	<0.01	<0.1
B	mg/L	1.4	<0.1	1.8	<0.1
Si	mg/L	<10.0	–	<10.0	–
P	mg/L	55.9	–	66.5	–
Cl	mg/L	6.72	–	5.81	–
Al	mg/L	526.9	5.72	539.8	2.7
Ba	mg/L	<1.0	<0.1	0.318	<0.1
Be	mg/L	<1.0	<0.1	<0.01	<0.1

(*continued*)

Table 2. (*continued*)

Experiment 1				Experiment 2	
Elements	Units	x_F	y_1'	x_F	y_1'
Bi	mg/L	<1.0	<0.1	<0.01	<0.1
Cd	mg/L	<1.0	<0.1	0.168	<0.1
Ca	mg/L	234.7	163.65	2204.9	17.8
Cu	mg/L	<1.0	<0.1	0.604	<0.1
Fe	mg/L	653.7	7.99	622.8	4.52
Pb	mg/L	1.1	<0.1	1.556	<0.1
Li	mg/L	1.3	0.47	1.3	0.48
Mg	mg/L	132.9	14	126.4	0.7
Mn	mg/L	24.3	0.24	23.86	0.24
Ni	mg/L	4.8	<0.1	4.1	0.11
K	mg/L	82.1	6.98	82	3.34
Na	mg/L	9391	61.49	8953	44.13
Ag	mg/L	<1.0	0.24	<0.1	0.71
Sr	mg/L	17.2	0.19	16.5	<0.1
Th	mg/L	–	6.85		22.42
Sn	mg/L	<1.0	0.31	<0.01	0.27
Zn	mg/L	9	11.3	10.3	1.83
Zr	mg/L	64.3	<0.1	33.28	14.56

4   Conclusion

TBP extraction is the core purification process of the wet method for uranium refining and conversion. In order to achieve better refining results, saturation of uranium extraction usually keeps high in refining. However, high extraction saturation is not easy to achieve. High extraction saturation may lead to the excess concentration of uranium in raffinate. In this study, reextraction for uranium refining based on fractionation extraction was proposed according to the characteristics and requirements of uranium refining extraction. The law of reextraction is obtained. 1 ~ 2 stages reextraction operation after extraction are generally used to achieve higher extraction saturation. Reextraction technology hardly increase the extraction stages compared with the common countercurrent extraction technology. The re-extraction bench test shows that the re-extraction process can run stably. After extraction, the concentration of uranium in organic phase can reach 120g/L, the extraction saturation can reach 96.7%, the concentration of uranium in raffinate is less than 10mg/L, and the concentration of impurity components is greatly reduced. Reextraction technology can facility the control of uranium refining extraction, which maintains the state of high saturation vs. low raffinate concentration.

References

1. Singh, H., Gupta, C.K.: Solvent extraction in production and processing of uranium and thorium. Mineral Process. Extractive Metallurgy Rev. **21**(1–5), 307–349 (2000)
2. Shikerun, T.G., et al.: Refining of uranium solutions in centrifugal extractors. Radiochemistry **56**(2), 173–176 (2014)
3. Ostrovskii, Y., et al.: Extractive refining of uranium concentrates using urea nitrate. Radiochemistry **51**(1), 34–37 (2009)
4. Deng, Z., Zhung, H., Huang, L.: Development and present situation of natural uranium purification technical research in China. Uranium Mining Metallurgy **04**, 231–238 (1998). https://doi.org/10.13426/j.cnki.yky.1998.04.004
5. Huang, Z., Gong, D., Wang, Y.: Analysis of purification capacity of vanadium by the combined TBP extraction-ADU-AUC purification process. Uranium Mining Metallurgy **35**(02), 94–96 (2016). https://doi.org/10.13426/j.cnki.yky.2016.02.004
6. Xia, D.: Characteristics of combined TBP extraction and AUC process. Uranium Mining Metallurgy **30**(01), 14–17 (2011). https://doi.org/10.13426/j.cnki.yky.2011.01.017
7. Zhong, X., Li, Y., Xu, Y., et al.: Study on theory of AB/BC fractional extraction for rare earth separation. Chin. J. Nonferrous Metals **30**(03), 657–665 (2020)
8. Zhong, X.: Preliminary study on the influence of main factors on the product purity of rare earth by fractional extraction. Chinese Rare Earths **37**(06), 114–120 (2016). https://doi.org/10.16533/J.CNKI.15-1099/TF.201606020
9. Chen, T., Jia, X., Huang, Y., et al.: Fractional extraction separation of Uranium and Vanadium in sulfuric acid system. Hydrometallurgy China (2018)
10. Zhong, X., Fu, M., Qin, Y., et al.: Theoretical study on mole fraction distribution of fractional extraction through dynamic simulation (2013)
11. Zhong, S., Wang, X., Lv, Y., et al.: Study on separation of cobalt and nickel by fractionation and extraction with P507. China Nonferrous Metallurgy **41**(01), 69–71 (2012)
12. Zhong, X., Zeng, H., Wu, S.: The principle and advantages of fractional extraction system with two inlets for separating rare earths from two kinds of material liquid. In: The 8th International Rare Earth Development and Application Symposium and the 3rd China Rare Earth Summit (2016)

Hazard Identification on the Process of High-Level Liquid Waste Concentration and Denitration in Spent Fuel Reprocessing by HAZOP

Weishuai Wang, Xuegang Liu[✉], Qian-ge He, and Xinghai Wang

Tsinghua University, Beijing, China
`liu-xg@mail.tsinghua.edu.cn`

Abstract. To develop China's spent nuclear fuel reprocessing, safety analysis of reprocessing facility is of great importance and high priority. Any methodology of safety analysis, no matter whether it is in a kind of deterministic analysis, probabilistic assessment or so-called Integrated Safety Analysis, is beginning with the identification and systematic analysis of hazards as the very first essential step. Recognizing that reprocessing facilities are, to a large extent, chemical processing plants, HAZard and OPerability analysis (HAZOP) was introduced firstly in the US. It is featured as one of the most suitable methods for performing detailed identification of a wide range of hazards.

In this paper, our work on part of the concentration and denitration process (C/D process) of high-level liquid waste (HLLW) was revealed to exemplify the procedure of hazard identification and analysis for a typical reprocessing process, as the C/D process of HLLW has many symbolic features of spent fuel reprocessing, such as high radiation, various chemicals, complex chemical reactions and operation stages. The purpose of this paper was to test the applicability of HAZOP for a typical process in reprocessing.

The HAZOP approach was starting with the identifications of process, reactions, equipment, and system borders. Base on the features of the given system (part), specific elements and guidewords were selected and combined to generate deviations for different operation stages. The possible causes and consequences of deviation as well as existing safeguards were taken into consideration. To make the workflow of HAZOP complete and underscore its significance, a 4-by-5 risk matrix was established to evaluate the risk levels of all consequences resulted from deviations, based on the severity of consequence and associated likelihood of occurrence.

The final results were shown in a HAZOP analysis worksheet, in which twenty-two deviations were presented, revealing the potential hazards found in the C/D part. After a preliminary risk assessment using a risk matrix, eight of them were recognized as undesirable risks (only accepted when risk reduction is impracticable). The results verified that the HAZOP analysis was suitable for the processes or parts involved with high radiation and complex chemical reactions in reprocessing facilities.

Keywords: Concentration and denitration · Hazop · Risk analysis · High-level liquid waste

1 Introduction

With the development of nuclear power, more and more spent fuels have been produced from nuclear power plants. China's policy is to have a closed fuel cycle, where spent fuels are reprocessed for recycling of uranium and plutonium into fresh nuclear fuel and optimizing the management of radioactive waste [1]. In particular, there has been an intensive domestic effort in construction and operation of a commercial reprocessing facility in recent years. Therefore, the safety analysis of reprocessing facility becomes an issue of high priority in the national program to develop spent fuel reprocessing.

Generally, the recognized methods of deterministic analysis are required to be used for safety analysis of reprocessing facilities [2]. In parallel, varying degrees of probabilistic assessments for reprocessing facilities have been carried out in several countries [3–6]. In addition, an Integrated Safety Analysis (ISA) method was developed and applied in the US reprocessing plants (Idaho Chemical Processing Plant and Barnwell plant) [7]. And since 2000, the ISA has been authorized to be an indispensable part of safety analysis for NRC reprocessing facilities [8].

Whatever method of safety analysis is conducted, an identification and systematic analysis of hazard is always the first essential step. Compared with other hazard identification methods such as failure mode and effects analysis (FMEA) and safety checklist (SC), HAZard and OPerability analysis (HAZOP) is suitable to analyze the hazards of complex chemical processes or facilities [5]. It is featured as one of the most suitable methods for performing detailed identification of a wide range of hazards. Recognizing that reprocessing facilities are, to a large extent, chemical processing plants, HAZOP has been logically extended to address radiological and nuclear criticality hazards.

In our research, the HAZOP methodology was introduced to identify and analyze the hazards of a reprocessing facility. Given the limited space available, only part of work on the concentration and denitration process (C/D process) of high-level liquid waste (HLLW) was revealed in this paper, since the C/D process of HLLW has many symbolic features of spent fuel reprocessing, such as high radiation, various chemicals, complex chemical reactions and operation conditions. The purpose of this paper was to test the applicability of HAZOP for a typical process in reprocessing.

Therefore, according to the HAZOP application guide [9], HAZOP analysis was conducted and described in this paper. By a risk matrix, the consequences listed in the HAZOP analysis worksheet were evaluated and categorized into different risk levels.

2 Description of the C/D Process

2.1 Reprocessing and HLLW Management

All over the world, uranium and plutonium in the spent fuel are recovered by a version of the PUREX reprocessing process. The term High Level Liquid Waste (HLLW), generally implies the raffinate (liquid effluent) from the first extraction cycle of reprocessing operations. It contains nitric acid at moderate acidity and greater than 99% of the nonvolatile fission products, almost all minor actinides, together with impurities from cladding materials, corrosion products, several tenths of a percent of originally dissolved plutonium and uranium. Around 5–10 m^3 of HLLW is produced per tonne of

fuel reprocessed. The HLLW is treated to remove any remaining organic solvents and then concentrated by evaporation to reduce its volume for interim storage in specially designed waste tanks prior to vitrification. Free nitric acid in HLLW is destroyed by reaction with formaldehyde during the concentration process (so-call concentration and denitration process) [10].

2.2 C/D Process

The target concentration after evaporation is corresponding to the equivalent of 110 g/L of fission products oxide in the concentrated HLLW (concentration factor of 6–20 approximately). The final acidity of HLLW is roughly reduced and stabilized to 2–3 mol/L [11].

Generally, the C/D process consists of three major parts as (1) receiving and feeding, (2) concentration and denitration, and (3) off-gas treatment, which are shown in Fig. 1. The first receiving and feeding part is designed to collect HLLW from the first extraction cycle of reprocessing operations, and to transfer HLLW to evaporator. The off-gas treatment part is designed for off-gas decontamination and nitric acid recombination.

In our research, the HAZOP analysis had been done to identify and analyze the hazards of the above three parts. But only the work on the C/D part would be illustrated later.

The major equipment in the C/D part is the evaporator (R-01) which is mainly composed of a kettle type boiler and a bubble-cap-tray decontamination column. The kettle type boiler is heated by superheated water. The stream evaporated from the top of column is condensed through the heat exchanger (E-01). A part of the condensate water is refluxed back to the column to enhance the decontamination performance.

2.2.1 Chemical Reactions

The chemical reactions for denitration between formaldehyde and nitric acid may occur according to three possible reactions as followed [11]:

At high acidity ([HNO_3] > 8 mol/L):

$$HNO_3 + HCHO \rightarrow 4NO_2 + CO_2 + 3H_2O \tag{1}$$

At low acidity (0.5 mol/L < [HNO_3] < 8 mol/L):

$$4HNO_3 + 2HCHO \rightarrow 2NO_2 + 2NO + 2CO_2 + 4H_2O \tag{2}$$

$$4HNO_3 + 3HCHO \rightarrow 4NO + 3CO_2 + 5H_2O \tag{3}$$

Actually, the mechanism of denitration reactions is more complex than the above reactions since the existence of the induction period [12], which refers to the time span needed for nitrous acid to be autocatalytically generated in the mixture to reach a threshold concentration [13]. Because the reactant formaldehyde is added consistently in the induction period without observable reactions with nitric acid, the accumulated formaldehyde may result in uncontrolled runaway reactions later, implying an explosive

boiling in the evaporator and accidental release of radioactivity. Research shows that the induction period can be reduced to a few seconds when the concentration of nitrous ions reaching a threshold concentration of about 10^{-1}-10^{-2} mol/L and by operating at boiling temperature [12].

2.2.2 Three Operation Stages

HLLW is concentrated in the evaporator operated at constant level in a semi-continuous mode which means continuous feeding and batch discharging. The complete sequence of the concentration and denitration procedure is listed below:

a. Start-up stage:

1) Feed HLLW into the evaporator (R-01) through L-01 from the receiving tank (V-01).
2) Heat HLLW to the boiling point to start evaporation.
3) Add NaNO$_2$ into the evaporator to reach the concentration of 10^{-1}-10^{-2} mol/L through L-04.
4) Add formaldehyde into the evaporator through L-05 to start the denitration reaction.

b. Normal operation stage:

5) Simultaneously feed HLLW (through L-03) and formaldehyde (through L-05) into the evaporator at a suitable flowrate, keeping the liquid level at constant level. During this stage, the concentration of HLLW increases consistently.

c. Shut-down stage:

6) Stop HLLW and formaldehyde feeding when reaching the target concentration of HLLW.
7) Keep heating HLLW with total reflux for a few hours to ensure that formaldehyde has been destroyed.
8) Stop heating HLLW and cool down the evaporator.
9) Transfer the concentrated HLLW to storage tanks.

2.2.3 Potential Difficulties and Monitoring

One major challenge for C/D process is the corrosion risk associated with the acidic solution and high temperature. In addition, the HLLW contains a wide variety of constituents, some of which can promote attack on the stainless steel commonly used for evaporator construction in high acidity. The corrosion risk should be controlled because no direct maintenance operation will ever be possible after the active commissioning.

Reliable monitoring devices are also essentially required for safe operations of the C/D part. The monitor parameters in this part are listed below [11]. The monitoring devices are regarded as a sort of safeguard measurements in hazard analysis.

1) Flowrate of the HCHO and HLLW in L-05 and L-03 respectively.
2) Acidity of the HLLW: acidity of HLLW is measured twice a day by sampling.
3) Liquid level and temperature, pressure inside of the evaporator.
4) Flowrate of the $NaNO_2$.
5) Flowrate of the superheated water and temperature of the superheated water.
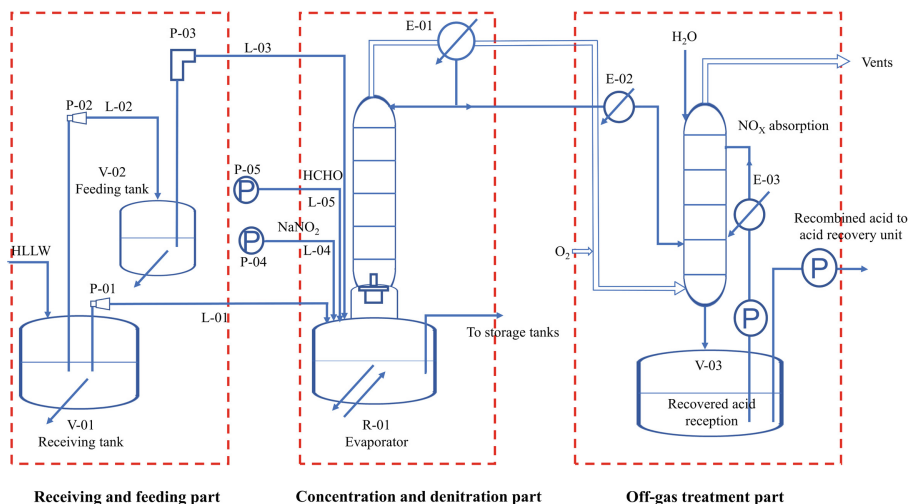
Fig. 1. General flow diagram of a HLLW concentration and denitration system [11]

3 Methodology and Framework

3.1 HAZOP Methodology

3.1.1 HAZOP Analytical Procedures

HAZOP is a structured and systematic technique for hazard identification. As an inductive tool, HAZOP is often used for identifying a broad range of potential hazards in a system and operability problems likely resulting in nonconforming products.

Generally, the HAZOP analysis process is executed in four phases: (1) definition, (2) preparation, (3) examination, and (4) documentation and follow-up. As the core part of the entire task, the examination phase consists of several major steps as followed.

1) Divide a system into parts, select a part and define design intent.
2) Identify deviation by using guidewords on each element.
3) Identify possible causes and consequences.
4) Identify existing safeguards or protections.

In contrast to HAZOP application guide [9], the step "identify whether a significant problem exists" was excluded from the examination phase. Instead, a risk matrix was established to assess the risks resulted from each consequence/deviation. In addition, some recommendations were proposed for further risk reduction when necessary based on the results of risk assessment.

3.1.2 Elements and Deviations

The selection of elements to be examined is to some extent a subjective decision. For material transferring parts, materials, activities, sources, and destinations can be viewed as elements of the part. For procedural sequence parts, elements may be selected from discrete steps or stages.

The guideword is a specific word or phrase in the HAZOP method used to describe the deviation from design intent. The standard HAZOP guidewords in the process industry include "no", "more", "less", "as well as", "part of", "other than" and etc.

Each deviation is then proposed by combining the guideword with the element. Not all combinations will generate credible deviations when all guide word/element combinations are considered. If a credible deviation is identified, it is examined for possible causes and consequences. In our research, causes are only examined in the same part and the consequences can be found in all parts. Then, existing safeguards are also taken into consideration.

3.2 Risk Assessment

In our research, risk is defined as the combination of the likelihood of occurrence of consequence and the severity of that consequence. Risk matrix is a matrix that is used during risk assessment to define the level of risk by considering the category of likelihood against the category of consequence severity. The categories of likelihood of occurrence and severity of consequence were listed in Table 1 and Table 2.

Table 1. Qualitative likelihood classification [14]

Description	Likelihood Range(/year)	Definition
L4	$>10^{-2}$	Events that may occur several times during the lifetime of the facility
L3	$10^{-4}-10^{-2}$	Events that are not anticipated to occur during the lifetime of the facility
L2	10^{-6}-10^{-4}	Events that will probably not occur during the lifetime of the facility
L1	$<10^{-6}$	Events are so unlikely that they generally do not require special controls

Table 2. Severity classification [15]

Description	Definition
C1 Negligible	Negligible effect on the safety operation, but deserves close attention, but no safety concerns for the facility workers, as well as no environmental effect
C2 Minor	Potential effects on the safety operation of the facility, but no safety concerns for the facility workers, as well as no environmental effect
C3 Moderate	Potential significant damage of the evaporator, partial loss of function or negligible safety concerns for the facility workers, and no significant environmental effect outside the facility confinement systems
C4 Serious	The loss of use of the evaporator or low radiological exposure dose consequences to the facility workers, and limited environmental discharge of hazardous material outside the facility
C5 Critical	The integrity of the evaporator has been damaged with potential significant radiological dose consequences to on-site workers located outside the facility, and large environmental discharge of hazardous material within or outside the plant site boundary

A 4 by 5 risk matrix was showed in Fig. 2. There are four different colors – green, yellow, orange, and red – to distinguish the risks according to the likelihood that they will happen and the extent of the damage they would cause. As shown in Table 3, the green zone denotes that the risk is reasonably acceptable, the yellow zone denotes risk that is acceptable with control, and the orange and red zones denote undesirable risk and intolerable risk, respectively [16].

By application of risk matrix, the hazards identified by HAZOP analysis can be further classified. Based on the classified risk, some recommendations were proposed for further risk reduction when necessary.

Fig. 2. Risk matrix [16]

Table 3. Risk matrix [16]

Risk level	Risk description	Risk qualitative description
Red	Intolerable	Risk must be mitigated; either decreases the probability or relieves the consequences
Orange	Undesirable	Undesirable and only accepted when risk reduction is impracticable
Yellow	Acceptable with control	Acceptable after review, and regular safety assurance measurement shall be imposed
Green	Reasonably acceptable	Risk reduction not needed

4   Results and Discussions

Table 4. Deviations of the concentration and denitration part

Stage	No.	Guideword	Element/Characteristic	Deviation
Start-up	1	Less	Add HLLW into the evaporator	Too little HLLW added into the evaporator
	2	More	Add HLLW into the evaporator	Too much HLLW added into the evaporator
	3	More	Heat the HLLW	High heating power
	4	Less	Heat the HLLW	Low Heating power
	5	More	Add $NaNO_2$ into the evaporator	Too much $NaNO_2$ added into the evaporator
	6	Less	Add $NaNO_2$ into the evaporator	Too little $NaNO_2$ added into the evaporator
	7	More	Add HCHO into the evaporator	Too much HCHO added into the evaporator
	8	Less	Add HCHO into the evaporator	Too little HCHO added into the evaporator
	9	Other than	Add HCHO into the evaporator	HCHO added before $NaNO_2$ into the evaporator
Normal operation	10	More	Feed HLLW into the evaporator	Increased flowrate of HLLW
	11	Less	Feed HLLW into the evaporator	Reduced flowrate of HLLW
	12	More	Feed HCHO into the evaporator	Increased flowrate of HCHO

(*continued*)

Table 4. (*continued*)

Stage	No.	Guideword	Element/Characteristic	Deviation
	13	Less	Feed HCHO into the evaporator	Reduced flowrate of HCHO
	14	More	Heat the HLLW	High heating power
	15	Less	Heat the HLLW	Low heating power
	16	More	A part of the condensate water is refluxed to the column	Too much condensate water refluxed to the column
	17	Less	A part of the condensate water is refluxed to the column	Too little condensate water refluxed to the column
Shut-down	18	Other than	Stop HLLW and formaldehyde feeding into the evaporator	Continue feeding HLLW into the evaporator
	19	Other than	Stop HLLW and formaldehyde feeding into the evaporator	Continue feeding HCHO into the evaporator
	20	More	Keep heating with total reflux for a few hours	Keep heating HLLW longer than designed time
	21	Less	Keep heating with total reflux for a few hours	Keep heating HLLW shorter than designed time
	22	Other than	Transfer concentrated HLLW and insoluble matter to storage tanks	Insoluble matter deposited at the bottom of the evaporator (R-01)

Table 4 listed the deviations in the concentration and denitration part. The results of the HAZOP analysis and risk assessment by risk matrix were recorded in the HAZOP analysis worksheet shown in Table 5.

Table 5. HAZOP analysis worksheet of the C/D part

Stage	Deviation	Possible causes	Consequences	Safeguards	P	S	R	Recommendations
Start-up	1. Too little HLLW added into the evaporator	1.1 L–01 partially blocked, or pump (P–01) under-performing	① Failed to start-up	①Flowrate monitoring in L–01; ②Liquid level monitoring in evaporator (R–01)	L2	C1	G	
		1.2 L–01 leakage	① Same as above; ② Possibly radioactivity release	①, ②Same as above	L2	C3	Y	
	2. Too much HLLW added into the evaporator	2.1 Wrong pump (P–01) fitted	① The liquid level in the evaporator continued to rise; evaporator (R–01) is topped with HLLW; ② Possibly radioactivity release	①Flowrate monitoring in L–01; ②Liquid level monitoring in evaporator (R–01)	L2	C4	Y	
	3. High heating power	3.1 Temperature or flowrate of superheated water is too high	①Explosive boiling of HLLW; ②Possibly radioactivity release; ③Corrosion of the evaporator (R–01)	① Temperature and flowrate monitoring of superheated water; ②Temperature monitoring in evaporator(R–01)	L2	C4	Y	
	4. Low Heating power	4.1 Temperature or flowrate of superheated water is too low	①Time of start-up stage extended; ② Extended induction period, resulting explosive boiling of HLLW, possibly excessive radioactivity release to off-gas treatment part	① Temperature and flowrate monitoring of superheated water; ②Temperature monitoring in evaporator(R–01)	L2	C4	Y	
	5. Too much NaNO$_2$ added into the evaporator	5.1 Wrong pump (P–04) fitted	①Increasing salt content in HLLW	①Flowrate monitoring in L–04; ②Nitrite ion concentration monitoring	L2	C2	G	
	6. Too little NaNO$_2$ added into the evaporator	6.1 L–04 partially blocked, or pump (P–01) under-performing; 6.2 L–04 leakage	① Extended induction period, resulting explosive boiling of HLLW, possibly excessive radioactivity release to off-gas treatment part	①Flowrate monitoring in L–04; ②Nitrite ion concentration monitoring	L2	C4	Y	
	7. Too much HCHO added into the evaporator	7.1 Wrong pump (P–05) fitted	① Violent reaction; damage to the stability of equipment; a danger of dumping of evaporator; ② Explosive boiling of HLLW, possibly excessive radioactivity release to off-gas treatment part, possible radioactivity release into the environment	①Flowrate monitoring in L–05; ②Temperature and liquid-level monitoring in evaporator(R–01)	L2	C5	O	Reinforcement of the evaporator (R–01)
	8. Too little HCHO added into the evaporator	8.1 L–05 partially blocked, or pump (P–01) under-performing; 8.2 L–05 leakage	①Time of start-up stage extended	①Flowrate monitoring in L–05; ②Temperature and liquid-level monitoring in evaporator(R–01)	L2	C2	G	
	9. HCHO added before the NaNO$_2$ into the evaporator	9.1 Operating procedure error	① Extended induction period, resulting explosive boiling of HLLW, possibly excessive radioactivity release to off-gas treatment part	①Flowrate monitoring in L–04; ②Nitrite ion concentration monitoring	L2	C4	Y	
Normal operation	10. Increased flowrate of HLLW	10.1 Wrong pump (P–03) fitted	① The liquid level in the evaporator continued to rise; evaporator (R–01) is topped with HLLW; ②The gas entrained radionuclides increased, resulting possible radioactivity release into the environment	①Flowrate monitoring in L–02 and L–03; ②Liquid level and temperature monitoring in evaporator (R–01); ③Liquid level monitoring in feeding tank (V–02)	L2	C5	O	A high/high-level trip to stop pump (P–03) and evaporator (R–01)

Table 5. (*continued*)

Stage	Deviation	Possible causes	Consequences	Safeguards	P	S	R	Recommendations
	11. Reduced flowrate of HLLW	11.1 L-03 partially blocked, or pump (P-03) under-performing; 11.2 L-03 leakage	① The liquid level continues to decrease and the amount of insoluble matter increases ② Evaporator may explode because of excessive evaporation of HLLW thus resulting possible radioactivity release into the environment	① Flowrate monitoring in L-02 and L-03 ② Liquid level and temperature monitoring in evaporator (R-01)	L2	C5	O	Continuous γ-ray monitoring device in L-02 and L-03
	12. Increased flowrate of HCHO	12.1 Wrong pump (P-05) fitted	① Violent reaction; damage to the stability of equipment; a danger of dumping of evaporator ② Explosive boiling of HLLW, possibly excessive radioactivity release to off-gas treatment part, possible radioactivity release into the environment ③ The amount of insoluble matter increases	① Flowrate monitoring in L-05 ② Temperature and liquid-level monitoring in evaporator(R-01)	L2	C5	O	Reinforcement of the evaporator (R-01)
	13. Reduced flowrate of HCHO	13.1 L-05 partially blocked, or pump (P-05) under-performing; 13.2 L-05 leakage	①Insufficient denitration of HLLW leading to high final acidity, aggravating corrosion of evaporator	① Flowrate monitoring in L-05 ② Liquid level and temperature monitoring in evaporator (R-01)	L2	C3	Y	
	14. High heating power	14.1 Temperature or flowrate of superheated water is too high	① Violent reaction; the liquid level continues to decrease, and the amount of insoluble matter increases ② Evaporator may explode because of excessive evaporation of HLLW thus resulting possible radioactivity release into the environment	① Temperature and flowrate monitoring of superheated water ②Temperature monitoring in evaporator(R-01)	L2	C5	O	A high/high-temperature trip to stop evaporator (R-01)
	15. Low heating power	15.1 Temperature or flowrate of superheated water is too low	①Insufficient denitration of HLLW ②The liquid level in the evaporator continued to rise; evaporator (R-01) is topped with HLLW ③ The gas entrained radionuclides increased, resulting possible radioactivity release into the environment	① Temperature and flowrate monitoring of superheated water ②Temperature monitoring in evaporator(R-01)	L2	C5	O	A high/high-level trip to stop pump (P-03) and evaporator (R-01)
	16. Too much condensate water refluxed to the column	16.1 Excessive heat exchange in heat exchanger (E-01)	①The liquid level in the evaporator continues to rise, and the daily processing capacity of evaporator(R-01) decreases	① Liquid level and temperature monitoring in evaporator (R-01) ② Temperature monitoring in heat exchanger(E-01)	L2	C2	G	
	17. Too little condensate water refluxed to the column	17.1 Insufficient heat exchange in heat exchanger (E-01)	①The amount of evaporation in the evaporator(R-01) is large, possibly excessive radioactivity release to off-gas treatment part	① Liquid level and temperature monitoring in evaporator (R-01) ② Temperature monitoring in heat exchanger(E-01)	L2	C4	Y	
Shut-down	18.Continue feeding HLLW into the evaporator	18.1 Pump (P-03) is not properly closed	① The concentration ratio of HLLW is decreased ②The liquid level in the evaporator continued to rise; evaporator (R-01) is topped with HLLW	① Flowrate monitoring in L-02 and L-03 ② Liquid level and temperature monitoring in evaporator (E-01)	L2	C5	O	Add a special stop valve to L-03

Table 5. (*continued*)

Stage	Deviation	Possible causes	Consequences	Safeguards	P	S	R	Recommendations
	19. Continue feeding HCHO into the evaporator	19.1 Pump (P-05) is not properly closed	①The liquid level in the evaporator (R-01) continues to rise, and there is a danger of radioactive release ② The accumulation of HCHO increases the heating time of the evaporator (R-01), and the daily processing capacity decreases	① Flowrate monitoring in L-05 ② Liquid level and temperature monitoring in evaporator (R-01)	L2	C4	Y	
	20. Keep heating HLLW longer than designed time	20.1 The superheated water supply time is too long	①The concentration ratio is too large, and the content of insoluble substances increases ② The residence time is too long, aggravating corrosion ③ The daily processing capacity decreases	① Liquid level and temperature monitoring in evaporator (R-01) ②Superheated water flowrate monitoring	L2	C4	Y	
	21. Keep heating HLLW shorter than designed time	21.1 The superheated water supply time is too short	①HCHO accumulates in the concentrate HLLW, and there is a danger of explosion in long-term storage	① Liquid level and temperature monitoring in evaporator (R-01) ②Superheated water flowrate monitoring	L2	C5	O	Set up a backup heating circuit
	22. Insoluble matter deposited at the bottom of the evaporator (R-01)	22.1 Insufficient stirring 22.2 Insoluble matter hardening	①Aggravating the corrosion of the evaporator (R-01) ②The daily processing capacity decreases	① Liquid level and temperature monitoring in evaporator (R-01)	L3	C3	Y	

*G denotes that the risk level is Green; Y denotes that the risk level is Yellow; O denotes that the risk level is Orange;

5 Conclusions

The concentration and denitrition process has some symbolic features of spent fuel reprocessing, such as high radiation, various chemicals, complex chemical reactions and operation stages. The HAZOP analysis method was applied in the C/D process. Twenty-two deviations, which were generated by combining elements with guidewords, revealed some potential hazards in the C/D part. After a preliminary risk assessment with the risk matrix, eight of them were recognized as undesirable risks (only accepted when risk reduction is impracticable). The results verified that the HAZOP analysis were suitable for the processes or parts involved with high radiation and complex chemical reactions in reprocessing facilities. More and deeper efforts will be needed in the future to improve the performance of HAZOP for identification and analysis of the hazards in a spent fuel reprocessing facility.

References

1. Liang, F., Liu, X.: Analysis on the characteristics of geologic disposal waste arising from various partitioning and conditioning options. Ann. Nucl. Energy **85**, 371–379 (2015)
2. International atomic energy agency, IAEA Safety Standards Series No. SSR-4: Safety of Nuclear Fuel Cycle Facilities, Vienna, Austria (2017)
3. Perkins, W.C.: Application of probabilistic risk assessment to reprocessing. United States (1984)
4. Sullivan, L.H., MacFarlane, D.R., Stack, D.W.: Probabilistic Safety Assessment for High-Level Waste Tanks at Hanford, Los Alamos National Laboratory, United States (1996)
5. International Atomic Energy Agency, IAEA-TECDOC-1267: Procedures for Conducting Probabilistic Safety Assessment for Non-Reactor Nuclear Facilities. Austria, Vienna (2002)
6. Ishida, M., Nakano, T., Morimoto, K., Nojiri, I.: PSA application on the Tokai reprocessing plant. In: 11th International Conference on Nuclear Engineering, ICONE11–36526, Tokyo, Japan (2003)
7. NEI Letter. Integrated Safety Analysis: Why It Is Appropriate for Fuel Recycling Facilities. United States (2010)
8. U.S. Nuclear Regulatory Commission, NUREG-1513: Integrated safety analysis guidance document. Washington DC, U.S (2001)
9. International Electrotechnical Commission: IEC 61882:2016 Hazard and operability studies (HAZOP studies)–application guide. Switzerland, Geneva (2016)
10. Upson, P.C.: Highly active waste management at Sellafield. Process Nuclear Energy **13**, 31–47 (1984)
11. Schneider, J., Bretault, P.: Highly active liquid waste concentration using the formaldehyde denitration process in the French reprocessing plants. In: Proceedings of Global, pp. 244–249 (2009)
12. Cecille, L. Kelm, M.: Chemical reactions involved in the denitration process with HCOOH and HCHO. In: Cecille, L., Halaszovich. S., (eds.) Denitration of Radioactive Liquid Waste, p. 6 (1986). ISBN 0 86010 854
13. Ando, M., Fujita, M., Izato, Y., Miyake, A.: A kinetic model for the autocatalytic behavior of nitric acid/formic acid mixtures to predict induction period. Process Saf. Environ. Prot. **151**, 182–187 (2021)
14. U.S. Department of Energy, DOE-STD-3009–2014: Preparation of nonreactor nuclear facility documented safety analysis. Washington DC, U.S (2014)

15. U.S. Department of Energy, HNF-6527 Revision 0: Hazard Evaluation for Storage of Spent Nuclear Fuel Sludge at the Solid Waste Treatment Facility. Washington DC, U.S (2000)
16. Zou, S., Kuang, Y., Tang, D., Guo, Z., Xu, S.: Risk analysis of high-level radioactive waste storage tank based on HAZOP. Ann. Nucl. Energy **119**, 106–116 (2018)

Development of Subchannel Code for Plate-Type Fuel Plus Verification

Bo Zhang[✉], Gefan Jiang, Peichao Zhai, and JianQiang Shan

Xi'an Jiaotong University, Xi'an, Shannxi, China
`bzhang_nss@mail.xjtu.edu.cn`

Abstract. The fuel shape and flow path structure of the plate-type fuel reactor are different from those of the conventional rod-bundle reactor, which leads to the difference between the thermal-hydraulic phenomenon and thermal conduction in the rod bundle assembly. Therefore, in this thesis, the subchannel analysis model and code applied to the plate-type fuel reactor are developed. The calculation results of the code are compared with the simulation results of FLUENT and MATRA and the experimental results of the flow and heat transfer of the rectangular channel, so that the code is verified.

This thesis first fully investigated the thermal-hydraulic and friction models applicable to rectangular flow channels, and developed the plate-type fuel heat conduction model and flow redistribution model. On the basis of the existing two-fluid three-field subchannel code, the subchannel analysis software for the plate type fuel reactor was developed. The comparison with the rectangular channel heat transfer experiment shows that the code can accurately predict the heat transfer coefficient under the rectangular channel. The comparison and verification with the simulation calculation results of the MTR reactor under steady-state conditions with the FLUENT and MATRA codes show that the developed subchannel code can simulate the thermal-hydraulic phenomena of the plate fuel assembly. Finally, according to the calculation results of the MTR reactor by the code, the thermal-hydraulic characteristics of the plate fuel reactor are analyzed, and the safety of the plate fuel is evaluated.

Keywords: Plate-type fuel · Multi-field subchannel model · Rectangular channel

1 Introduction

Compared with the traditional rod-type fuel, the plate-type fuel has obvious advantages, which is mainly achieved in the higher heat flux under the same volume, which also means that the plate-type fuel reactor has higher power under the same volume. From the perspective of thermal-hydraulics, the flow channel of plate-type fuel is a narrow rectangular channel, its size is usually between 1 mm and 3 mm, which has a certain strengthening effect on convective heat transfer, and its heat transfer efficiency is higher than that of rod-type channel. In addition, plate-type fuel can obtain higher burn up depth than rod fuel. In conclusion, the application of plate fuel improves the economy of the reactor.

The earliest use of plate-type fuel is MTR reactor [1] (material test reactor), which uses U-Al alloy plate-type fuel. After that, MIT built MITR reactor for the purpose of research and education [2], and Indonesia built the reactor RSG-GAS for material testing and radioisotope production [3]. China advanced research reactor (CARR) is a pool reactor, which is cooled by light water and moderated by heavy water. These reactors have the same characteristics, that is, to increase the heat transfer area between the fuel plate and the coolant as much as possible by arranging ribs on the fuel plate and using curved fuel plate.

From the above application of plate-type fuel, it can be seen that the use of plate-type fuel as reactor fuel is mainly due to the compact core structure and high power density of plate-type fuel. Therefore, the research on thermal-hydraulics of plate-type fuel mainly focuses on how to take more heat away. Generally, the coolant channel in plate-type fuel is rectangular channel, which belongs to narrow channel. Therefore, a lot of research work has been done on the flow and heat transfer characteristics of narrow rectangular channel.

1.1 Research Status of Flow and Heat Transfer in Rectangular Channel

The flow and heat transfer characteristics of narrow rectangular channel is one of the concerns of plate-type fuel research. The research on it can provide reference and verification for the design of plate-type fuel element. Generally, for plate-type fuel elements, the channel shape is narrow rectangular channel, and the channel gap is generally 2–3 mm, some even less than 2 mm.

In terms of flow resistance, Ha Taesung of McMaster University studied the velocity distribution and friction resistance characteristics in the flow passage when coolant enters the fuel assembly from the upper part [4]. The experimental results show that the inlet flow distribution is uniform in different channels, and the maximum difference is less than 5%; In a single channel, the velocity in the middle of the channel is the largest, and then slowly attenuates, and rapidly attenuates to 0 near the outside of the channel. Through the calculation of pressure drop in the channel, the results show that the conventional friction resistance relationship is also suitable for rectangular channel.

In terms of flow pattern, Chang of Shandong University measured the gas-liquid two-phase flow pattern on the heating experimental bench with rectangular channel width of 0.5 mm to 2.0 mm respectively. The results show that the void fraction is about 0.7 in the transition from isolated or confined bubble to plug flow and about 0.9 in the transition from plug flow to annular flow. Wang observed the flow pattern characteristics of hydrodynamic boiling in vertical narrow rectangular channel under the conditions of low pressure and inlet temperature supercooling. Four flow patterns were observed: diffuse bubble flow, combined bubble flow, agitated flow and annular flow. The experimental data were compared with the existing typical flow pattern diagrams. The results show that the flow pattern of heating steam-water and its transformation law are obviously different from that of adiabatic air-water.

In terms of heat transfer, Sudo used JRR-3 reactor fuel elements to carry out experimental research on single-phase heat transfer in rectangular channel [5]. By comparing the experimental results, it can be seen that the Dittus-Bolter, Sider-Tate and Colburn

relations are suitable for single-phase heat transfer in rectangular channel, but the relations used in laminar flow are different from those used in circular tube, and the Nusselt numbers of upflow and downflow are also different. Qiu of Xi'an Jiaotong University studied the characteristics of saturated boiling heat transfer in horizontal rectangular channel. The experimental results show that the heat transfer coefficient of rectangular channel is significantly higher than that of circular tube in laminar and turbulent regions. When the gap size is less than 1.5 mm, the heat transfer effect is obviously weakened, while when the gap size is more than 1.5 mm, the gap size has no obvious effect on the heat transfer effect. Tian studied the heat transfer characteristics of rectangular channel under natural convection. The results show that in the case of natural circulation convective heat transfer, the decrease of inlet subcooling has a weakening effect on heat transfer, and the heat transfer capacity will be improved with the increase of heating power. Moreover, the experimental results show that the Gnielinski relation [6] can be used to predict the heat transfer coefficient under natural circulation.

Through the investigation of the flow and heat transfer characteristics of rectangular channel, it can be concluded that the flow and heat transfer in rectangular channel is different from the traditional round tube and rod bundle, mainly in the enhancement of heat transfer in narrow channel.

1.2 Research Status of Plate-Type Fuel Code Development

In the reactor design stage, the design parameters often need to be calculated with the help of thermal-hydraulic analysis code, and the simulation code can also verify the existing design. The thermal hydraulic code can also be used to study specific phenomena and provide direction for experimental research, Therefore, the development of thermal analysis code for plate-type fuel reactor plays an important role in reactor construction and academic research. In the world, many countries, including China, have independently developed codes suitable for plate-type fuel. The developed codes are shown in Table 1.

In the design stage, the thermal-hydraulic analysis code is used to obtain the design parameters and predict the state of the reactor, so as to verify, evaluate and modify the existing design. The commonly used thermal-hydraulic analysis methods include computational fluid dynamics method, single-channel analysis method and subchannel analysis method. Although computational fluid dynamics (CFD) can obtain fine parameter distribution, it is difficult to simulate the reactor scale, and the two-phase calculation needs to be strengthened; Although the single-channel analysis method has a small amount of calculation, it is unable to obtain the distribution of core thermal parameters; The subchannel analysis method considers that there are transverse momentum, mass and heat mixing in the process of coolant flow between adjacent channels. Therefore, compared with the single-channel model, the calculation results are closer to the real parameters, and the thermal parameters of the core can be obtained with less calculation.

According to the literature research, at present, most of the international plate-type fuel analysis codes use single-channel models to verify and analyze accident conditions. For the subchannel model, there is only the MATRA-h subchannel analysis code developed by South Korea on the basis of MATRA, and there is no subchannel analysis code for plate-type fuel in China. However, under the requirements of refined analysis and

Table 1. The existing thermal hydraulic analysis code for plate-type fuel

Name	Country	Model
PARET-ANL	America	Single-channel
RELAP5	America	Single-channel
MERSAT	Syria	Single-channel
TMAP	South Korea	Single-channel
COOLOD	Japan	Single-channel
MATRA-h	South Korea	Subchannel
RETRAC-PC	Italy	Single-channel
FOR-CONV	Egypt	Single-channel
SAC-RIT	India	Single-channel
THAS-PRR	China	Single-channel

under the background of nuclear power software autonomy, the development of sub-channel analysis code suitable for plate-type fuel can obtain more accurate and refined thermal hydraulics than single-channel models. The results of the analysis are also helpful for the verification and analysis of the experimental research reactors that have been built and are in the design stage in China. For the above purposes, it is necessary to develop the best estimation code for the analysis of plate-type fuel subchannels with independent property rights.

2 Development of Plate-Type Fuel Subchannel Code

The code reads in the geometric structure information, boundary conditions, control information and other parameters needed for the calculation in the form of an input card. In the initialization phase, the read-in data is used to construct a geometric model and set boundary conditions. After the initialization is completed, the solution process of the code starts. First, use the initial input mass flow to perform transient calculations, and then redistribute the inlet flow after the transient calculations are completed, until the pressure drop of each subchannel is in a balanced state. In each transient calculation, the calculation is ended by judging whether the steady-state convergence condition is reached or the calculation time is reached. In transient calculations, discrete conservation equations are solved by the SIMPLE algorithm. After the transient calculation is completed and the pressure drop of the subchannel is balanced, the calculation result will be output. The calculation process of the code is shown in Fig. 1.

2.1 Basic Conservative Equations

The conservation equations coded are presented in this section. The basic equations of the mathematical model are derived by applying the general equations of continuity, energy, and momentum. The equations are:

Mass:

$$\frac{\partial}{\partial t}(\alpha_k \rho_k) + \nabla \cdot \left(\alpha_k \rho_k \overrightarrow{V}_k\right) = L_k + M_k^T \tag{1}$$

The first term at left is the change in mass of each phase in the control body over time, and the second term at left is the convection term.

Momentum:

$$\frac{\partial}{\partial t}\left(\alpha_k \rho_k \overrightarrow{V}_k\right) + \frac{\partial}{\partial x}\left(\alpha_k \rho_k u_k \overrightarrow{V}_k\right) + \frac{\partial}{\partial y}\left(\alpha_k \rho_k v_k \overrightarrow{V}_k\right) +$$
$$\frac{\partial}{\partial z}\left(\alpha_k \rho_k w_k \overrightarrow{V}_k\right) = \alpha_k \rho_k g + \nabla \cdot \left[\alpha_k (\tau_k + T_k)\right] - \tag{2}$$
$$\alpha_k \nabla P + \overrightarrow{M}_k^L + \overrightarrow{M}_k^d + \overrightarrow{M}_k^T$$

The first term at left is the change of momentum in the control body over time, the second, third, and fourth terms are momentum convection; the first term at right is gravity, the second is pressure, and the third is viscous force and turbulent shear force.

Energy:

$$\frac{\partial}{\partial t}(\alpha_k \rho_k h_k) + \nabla \cdot \left(\alpha_k \rho_k h_k \overrightarrow{V}_k\right) =$$
$$-\nabla \cdot \left[\alpha_k \left(\overrightarrow{Q}_k + \overrightarrow{q}_k^T\right)\right] + \Gamma_k h_k + q_{wk} + \alpha_k \frac{\partial P}{\partial t} \tag{3}$$

The first term at left is the change of energy in the control body over time; the second term is the energy convection term. The first term at right side of the equation is the heat exchange caused by heat conduction between phases, turbulence mixing and cavitation drift, the second term is the energy change caused by the phase change; the third term is the energy entering the fluid due to wall heating; The fourth item is pressure doing work.

2.2 Constitutive Models

The wall heat transfer model determines the heat transfer coefficient between fluid and fuel, and directly affects the temperature distribution in the whole core. According to the relationship of void fraction, enthalpy and temperature, the heat transfer modes can be divided into single-phase liquid heat transfer, subcooled boiling, saturated boiling, transitional boiling, annular boiling, dispersed flow and single-phase steam heat transfer.

For single-phase fluid heat transfer, the relationship proposed by Dittus-Boelter [2, 7] is used:

$$Nu = 0.023 \mathrm{Re}^{0.8} \Pr^{0.4} \tag{4}$$

For subcooling and saturated nucleate boiling, use the relationship proposed by Chen [8]:
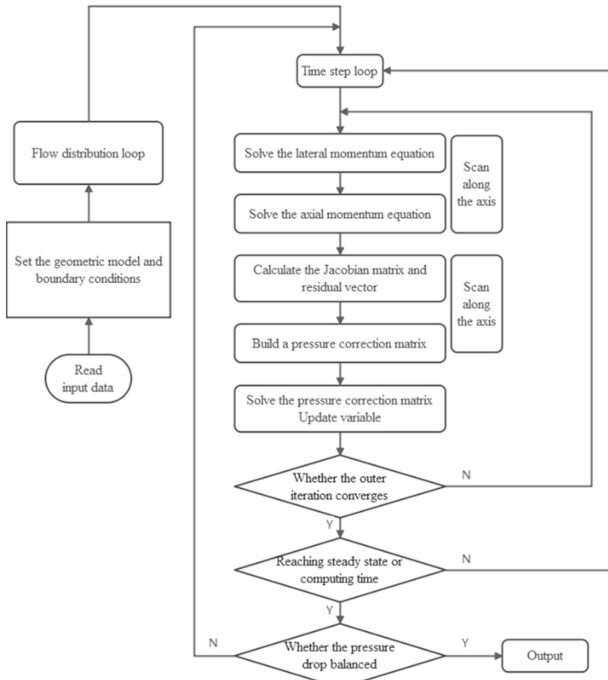
$$h_{Chen} = h_{fc} + h_{nb} \tag{5}$$

Fig. 1. Evaluation scheme of the subchannel code

$$h_{fc} = 0.023 \mathrm{Re}^{0.8} \, \mathrm{Pr}^{\,0.4} \left(\frac{k_l}{D_e} \right) F \tag{6}$$

$$h_{nb} = 0.00122 \left(\frac{k_l^{0.79} C_{pl}^{0.45} \rho_f^{0.49}}{\sigma_l^{0.5} \mu_f^{0.29} H_{fg}^{0.24} \rho_g^{0.24}} \right) \Delta T_{sat}^{0.24} \Delta P_{sat}^{0.75} S \tag{7}$$

For the heat transfer coefficient after transitional boiling, the heat transfer effect of four parts should be considered: convective heat transfer on the wall q_{wv}, boiling heat transfer on the liquid q_{wb}, radiative heat transfer on the wall q_{rwl} and radiative heat transfer on the wall q_{rwv}.

$$q = q_{wv} + q_{wb} + q_{rwv} + q_{rwl} \tag{8}$$

In particular, under the annular flow, the modified Bromley relationship is used to calculate the heat flux [9]

$$q = 0.62 \left(\frac{D_e}{\lambda} \right)^{0.172} \left[\frac{k_g^3 \rho_g (\rho_f - \rho_g) H_{fg} G}{D_e \mu_g (T_w - T_{sat})} \right]^{0.25} (T_w - T_{sat}) \tag{9}$$

In forced convection heat transfer, when the heat flux density is so high that it is difficult for the liquid phase to wet the heating surface, the peak heat flux density at this

time is called the Critical Heat Flux (CHF). This paper uses the Sudo relationship [10] to determine the occurrence of CHF.

$$q^*_{CHF1} = 0.005 |G^*|^{0.611} \tag{10}$$

$$q^*_{CHF2} = \left(\frac{A}{A_H}\right) \Delta T^*_{sub,in} |G^*| \tag{11}$$

$$q^*_{CHF3} = 0.7\left(\frac{A}{A_H}\right) \frac{(w/\lambda)^{0.5}}{\left(1 + \left(\frac{\rho_g}{\rho_f}\right)^{0.25}\right)^2} \tag{12}$$

$$q^*_{CHF4} = 0.005 |G^*|^{0.611} \left(1 + \frac{5000}{|G^*|} \Delta T^*_{sub,ex}\right) \tag{13}$$

For ascending flow, if $q_{CHF1} <= q_{CHF3}$, then $q_{CHF} = q_{CHF3}$. If $q_{CHF1} <= q_{CHF2}$, then $q_{CHF} = q_{CHF4}$. In other cases, $q_{CHF} = q_{CHF1}$.

For descending flow, if $q_{CHF2} <= q_{CHF3}$, then $q_{CHF} = q_{CHF3}$. If $q_{CHF1} <= q_{CHF2}$, then $q_{CHF} = q_{CHF4}$. In other cases, $q_{CHF} = q_{CHF2}$.

For the flow pattern before CHF, since it is assumed that the vapor phase does not contact the wall surface, the friction force between the vapor phase and the wall surface is set to zero. After CHF, the Darcy friction resistance coefficient can be calculated using the following formula:

$$f_{w,k} = \max \begin{cases} (96.0/\text{Re}) (\mu_w/\mu_k)^{0.14} \\ 0.316 \text{Re}^{-0.25} \end{cases} \tag{14}$$

2.3 Flow Distribution Model

The traditional flow distribution method using fixed step iterations judges whether the balance is reached by the difference between the maximum pressure drop and the average pressure drop in the subchannels. If the balance is not reached, the flow needs to be redistributed. This method requires multiple iterations, which greatly increases the calculation time.

Therefore, a new flow distribution method is proposed to distribute the flow of each subchannel. This method regards the subchannel pressure drop as a linear function of the flow rate, and predicts the subchannel inlet mass flow rate for the next flow iteration by means of a fitting relationship. The function is as follows.

$$\Delta P^n_i = a^n + b^n W^n_i \tag{15}$$

In the calculation, the linear function of the iteration step is solved for each subchannel, and a new mass flow rate is obtained from the average pressure drop, as follows:

$$W^{n+1}_i = \frac{P^n_{ave} - a^n}{b^n} \tag{16}$$

2.4   Special Heat Conduction Treatment of Side Cladding

Since the plate-type fuel has a cladding on the side, as shown in Fig. 2, if the closed subchannel is calculated, the heat conduction of this part of the cladding does not need to be considered. If the opened subchannel is calculated, the heat conduction of the side shell for the subchannel needs to be calculated, otherwise the energy will not be conserved.

The gray part in Fig. 2 is the side cladding. For the side cladding, after solving the heat conduction of the pellets (using the additional source term method), the heat entering the side cladding is obtained explicitly.
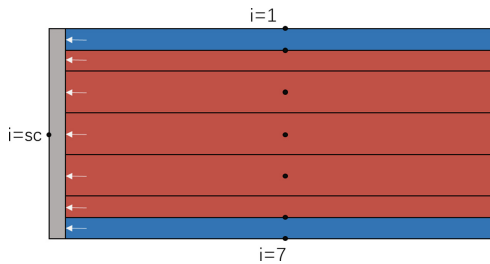
Fig. 2. Diagram of side cladding

$$T_{sc} = \frac{\sum\limits_{i=1}^{n} b_i R_i + q_{chn}}{\sum\limits_{i=1}^{n} R_i + h_{chn}} \qquad (17)$$

For the nodes in the core block that are in contact with the side bread shell, use the additional source term method to subtract the heat derived from the side bread shell. The source term is as follows:

$$b = q\Delta x + a(T_{sc} - T_i) \qquad (18)$$

3   Verification of Plate-Type Fuel Subchannel Code

The State Key Laboratory of Multiphase Flow at Xi'an Jiaotong University carried out experiments on the flow resistance and heat transfer performance of the double rectangular narrow slits between the plate-type fuels. The overall length of the narrow slit part of the test piece is 1200 mm, the effective heating section length is 900 mm, and the effective pressure measurement length is 1000 mm; the entrance has a stable section of 150 mm, the exit has a stable section of 50 mm, and the plate thickness is 0.7 mm. The cross-sectional size of the circulation channel is 50 mm × 1.8 mm; the processed test piece is measured by a spiral micrometer, and its average gap width is 1.806 mm, which

does not exceed 0.4% of the design value. Use the developed plate-type fuel subchannel code to simulate the above experiment.

In order to verify the influence of the mass flow rate on the heat transfer coefficient, the method of variable-controlling is adopted. The experimental conditions are shown in Table 2. The mass flow rates are 600, 800, and 1000 $\text{kg·m}^{-2}\text{·s}^{-1}$.

Table 2. Boundary condition

Boundary condition	Value
Heat Flux / kW·m^{-2}	320
Inlet temperature / °C	60
Pressure / MPa	0.1

The developed plate-type fuel subchannel code is used to calculate the heat transfer coefficient, which is divided into 90 nodes along the axial direction. The comparison between the heat transfer coefficient along the axial position and the experimental results is shown in Fig. 3.
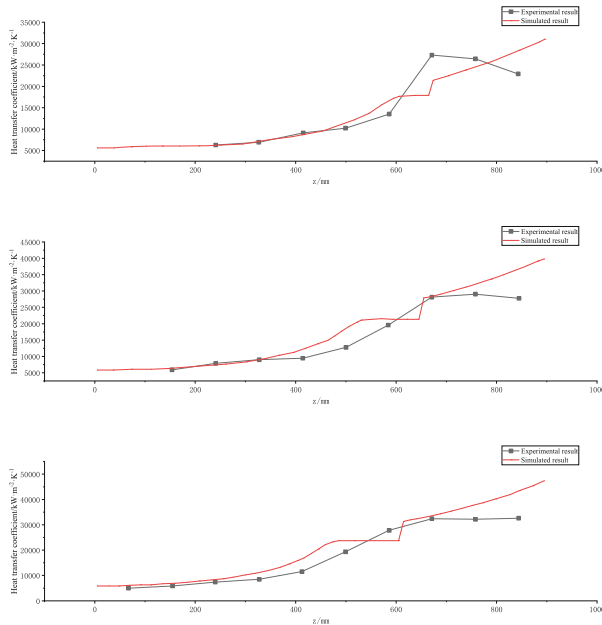
Fig. 3. Comparison between calculated and experimental values of heat transfer coefficient under the influence of mass flow rate

The heat transfer area calculated in Fig. 3 includes the stages from single-phase heat transfer, subcooled boiling to saturated boiling. There is a sudden jump in the calculated

value of the subchannel code, which is caused by the switch of the heat transfer relationship from subcooled boiling to saturated boiling. In the single-phase liquid heat transfer phase, the heat transfer coefficient calculated by the code is in good agreement with the experimental data; in the subcooled boiling and saturated boiling phases, although the heat transfer coefficient calculated by the code has a certain difference with the experimental data, the trend is still in good agreement. It can be seen from Fig. 3 that as the mass flow rate increases, the position where the saturation point appears gradually moves upward.

4   Subchannel Analysis of a MTR Bundle

In this section, the MTR reactor is used as a steady-state analysis and verification model. The schematic diagram of the fuel assembly is shown in Fig. 4.

There are 25 fuel assemblies in the MTR core, each of which contains 23 fuel plates placed at equal intervals; there are 4 control body assemblies, each of which contains 17 fuel plates.

Figure 4 shows part of the structure of the standard assembly. The geometric parameters of the flow channel and fuel plate are shown in Table 3. The physical parameters used in the calculation are shown in Table 4.
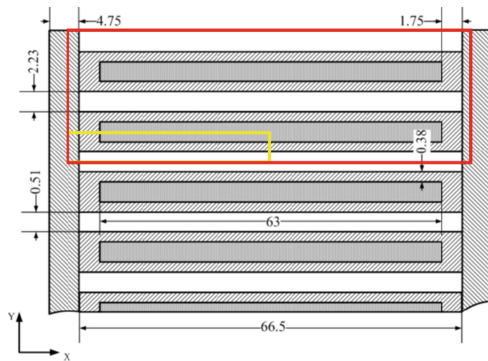

Fig. 4. The structure of the plate-type fuel in MTR reactor

In the calculation, it is assumed that the body heat sources in the fuel plate are uniformly distributed, and the power along the axial direction is considered to be a cosine distribution.

Song from Harbin Engineering University calculated the outlet temperature of MTR reactor assembly by FLUENT. The calculation area used is shown in red area in Fig. 4. In the red area, there are two fuel plates and three subchannels from top to bottom. The calculation results of the developed subchannel code are compared with the calculation results of FLUENT, and the results are shown in Table 5.

Table 3. Geometry of the fuel

Parameter	Value
Total length/mm	80.0
Total width/mm	76.0
Total height/mm	600.0
Number of fuel plates in fuel assembly	23/17
Thickness of single fuel plate /mm	0.51
Width of single fuel plate /mm Active region / Full region	63.0/66.5
Height of single fuel plate /mm	600.0
Coolant flow path thickness /mm	2.23
Cladding thickness of fuel plate /mm	0.38

Table 5 shows that under the same conditions, the relative error between the results of the developed subchannel code and that of FLUENT is less than 0.05%, which is in good agreement with each other. The difference between the results of the subchannel code and that of the CFD is mainly due to the fact that the heat conduction of the fuel plate is not considered in the CFD, so there is a little difference in the heat distribution, but the total energy is conserved.

Table 4. Parameters related to MTR

Parameter	Value	
Fuel thermal conductivity /W·m^{-1}·K^{-1}	158 High enriched uranium	50 Low enriched uranium
Enthalpy of fuel /kJ·kg^{-1}·K^{-1}	0.728 High enriched uranium	0.34 Low enriched uranium
Fuel density /kg·m^{-3}	680 High enriched uranium	445 Low enriched uranium
Cladding thermal conductivity /W·m^{-1}·K^{-1}	180	
Enthalpy of cladding /kJ·kg^{-1}·K^{-1}	0.892	
Cladding density /kg·m^{-3}	2700	
Coolant inlet temperature /°C	38.0	
Operating pressure /MPa	0.17	

Table 5. Outlet temperature of the channel calculated by CFD and subchannel code

	CFD			Subchannel code		
Subchannel	1	2	3	1	2	3
Inlet temperature /K	311.15	311.15	311.15	311.15	311.15	311.15
Outlet temperature /K	324	323.81	317.94	324.17	324.18	317.62
Temperature difference /K	12.85	12.66	6.79	13.02	13.03	6.47

Amgad Salama [11] of South Korea used the subchannel code MATRA to calculate the axial variation of coolant and cladding temperature in MTR reactor under steady-state conditions. The calculation area used by Salama is the yellow area in Fig. 4, which is a quarter of the flow channel.

The calculation model used in the developed code is shown in Fig. 5. It contains a complete fuel plate and two flow channels. The width of the flow channel is half of the actual width, which is equivalent to four times of the calculation area of Amgad Salama. During the modeling process, the single channel is divided into three subchannels, as shown in Fig. 5.

The results of cladding temperature distribution and coolant temperature distribution are shown in Fig. 6. The results of coolant temperature and fuel cladding temperature are the same due to the same heating conditions and flow rate of the three subchannels divided by the same channel, so the calculation results of subchannel 2 were used.
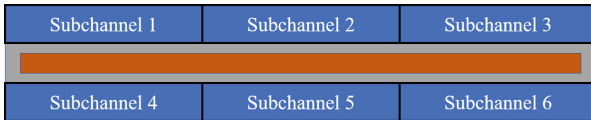

Fig. 5. Diagram of subchannel code modeling

Figure 6 shows that the temperature distribution of the cladding is very close between MATRA and the developed subchannel code under the approximate operating conditions. In Fig. 6, the coolant temperature predicted by Matra is slightly lower than the developed subchannel code, which may be due to the difference in the calculation of total power estimation. In this example, because the pressure difference between the subchannels is the same, there is almost no transverse flow between the subchannels. In conclusion, the developed subchannel code can be used for thermal hydraulic analysis of plate-type fuel reactor.
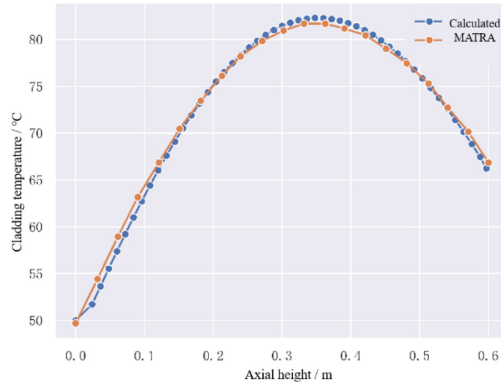
(a)   Distribution of cladding temperature
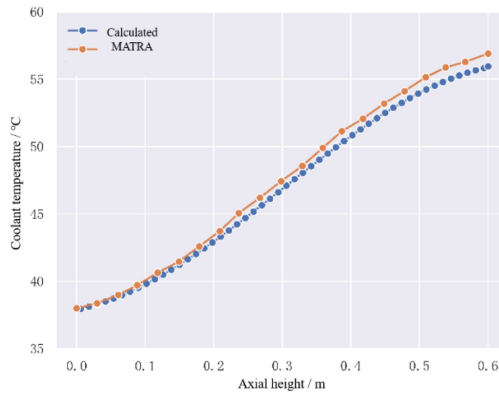
(b)   Distribution of coolant temperature

Fig. 6. Temperature distribution along the axis

5   Results

Plate-type fuel is widely used in different reactors due to its high heat transfer efficiency. Its fuel shape and flow path structure are different from those of traditional pressurized water reactor, which leads to different thermal hydraulic phenomena and temperature field distribution in fuel. In order to obtain the thermal-hydraulic characteristics in the rectangular channel, this paper conducts related research on the thermal-hydraulic characteristics in the rectangular channel, and develops a subchannel analysis model and code suitable for plate-type fuel reactors.

This article first fully investigated the flow heat transfer, friction model, plate-type fuel heat conduction model and flow distribution model suitable for rectangular flow channels. Based on the existing two-fluid three-flow field subchannel code, a subchannel analysis code suitable for plate-type fuel reactors has been developed. After that, the comparison with the flow and heat transfer experiment in the rectangular channel shows that the code can accurately predict the heat transfer coefficient under the rectangular channel. The comparison and verification with the simulation calculation results of

the MTR reactor show that the developed subchannel code can simulate the thermal-hydraulic phenomena of the plate-type fuel assembly.

According to previous studies, the parametric uncertainty such as theoretical and experimental analysis uncertainties, instrumentation and control inaccuracies, manufacturing tolerances, material properties and correlation uncertainties have effect on the hot channel, so in the further study, the parametric uncertainty will be analyzed to make the analysis more realistic.

References

1. IAEA. Research Reactor Core Conversion from the Use of Highly Enriched Uranium to the Use of Low Enriched Uranium Fuels Guidebook. Vienna, Austria: International Atomic Energy Agency (1980)
2. Chiang, Y.: Thermal Hydraulic Limits Analysis for the MIT Research Reactor Low Enrichment Uranium Core Conversion Using Statistical Propagation of Parametric Uncertainties. Massachusetts Institute of Technology, Boston, USA (2012)
3. Abdelrazek, D., Naguib, M., Badawi, A., et al.: Benchmarking RSG-GAS reactor thermal hydraulic data using RELAP5 code. Ann. Nucl. Energy **70**, 36–43 (2014)
4. Ha, T., Garland, J.: Hydraulic study of turbulent flow in MTR-type nuclear fuel assembly. Nucl. Eng. Des. **236**(9), 975–984 (2006)
5. Sudo, Y., Miyata, K., Ikawa, H., et al.: Experimental study of differences in DNB heat flux between upflow and downflow in vertical rectangular channel. J. Nucl. Sci. Technol. **22**(8), 604–618 (1985)
6. Gnielinski, V.: New equations for heat and mass transfer in turbulent pipe and channel flow. Int. Chem. Eng. **16**(2), 359–367 (1976)
7. Singh, T., Kumar, J., Mazumdar, T., et al.: Development of neutronics and thermal hydraulics coupled code–SAC-RIT for plate type fuel and its application to reactivity initiated transient analysis. Ann. Nucl. Energy **62**, 61–80 (2013)
8. Chen, J.: Correlation for boiling heat transfer to saturated fluids in convective flow. IEC Process Design Developm. **5**(3), 322–329 (1966)
9. Bromley, L.: Heat transfer in stable film boiling. Chem. Eng. Prog. **46**, 226–230 (1950)
10. Sudo, Y., Kaminaga, M.: A New CHF Correlation Scheme Proposed for Vertical Rectangular Channels Heated from Both Sides in Nuclear Research Reactors[J]. J. Heat Transfer **115**(2), 426–434 (1993)
11. Salama, A., El-, S.E.: CFD Simulation of the IAEA 10MW Generic MTR Reactor Under Loss of Flow Transient[J]. Ann. Nucl. Energy **38**(2), 564–577 (2011)

Multi-Physics Coupling Model for Thermal Hydraulics and Solute Transport in CRUD Deposits

Yan Liu[1], Xiaojing Liu[1(✉)], Sijia Du[2], Jiageng Wang[2], and Hui He[1]

[1] Shanghai Jiao Tong University, Shanghai, China
`xiaojingliu@sjtu.edu.cn`
[2] Nuclear Power Institute of China, Chengdu, Sichuan, China

Abstract. The porous Chalk River Unidentified Deposit (CRUD) depositions on the fuel cladding have a great impact on the heat transfer and power distribution of the reactor, resulting in a decrease in reactor safety and economy. In current paper, a multi-physics model is developed to simulate thermal hydraulics and boron hideout within the CRUD depositions. Processes including heat transfer, pressure drop, capillary flow, solute transport, chemical reactions and radiolysis reactions are fully coupled. The coolant flows through the capillary tubes in the porous medium and evaporates into steam at the surface of chimneys. The solute diffuses into the porous medium by capillary flow and maintains its chemical equilibrium. Chemistry and thermal hydraulics are coupled by saturation temperature that varies with solute concentrations. The new model can reasonably predict the distributions of temperature, pressure, Darcy velocity and chemical concentrations. This model shows the effect of evaporation at the chimney surface on CRUD temperature and boric acid concentration. In addition, the results show that boron hideout is caused by the accumulation of boric acid and the precipitation of $Li_2B_4O_7$ at the bottom of CRUD. The influence of morphology parameters such as porosity, thickness, and chimney geometry on heat transfer and solute transport within CRUD depositions is also evaluated.

Keywords: CURD · Boron hideout · Cips · Multi-Physics coupling

1 Introduction

The pressurized water reactor (PWR) core has been in a harsh environment of high temperature, high pressure and high radioactivity. The fuel performance of PWR core is a key factor affecting the safety and economy of the reactor. During the operation of nuclear reactors, the steam generator heat transfer tubes, the largest heat transfer area in the primary coolant circuit, are continuously scoured and eroded by the high-pressure subcooled coolant, producing a large number of oxidation corrosion products. Driven by subcooled boiling, metal ions and corrosion products in the primary coolant circuit deposit on the surface of the fuel cladding at the upper part of the reactor core, forming

a thin and porous scale layer, named as Chalk River Unidentified Deposit (CRUD) [1], shown in Fig. 1.

On the one hand, the thermal resistance of the fuel rods increases and the heat transfer deteriorates as a result of the deposition of corrosion products. On the other hand, the loose and porous CRUD depositions can strengthen local boiling, and the boric acid is continuously concentrated until precipitated and adsorbed by the depositions, resulting in the uneven distribution of boron in the axial direction of the fuel rods. Since ^{10}B has obvious neutron absorption capacity, the boron hideout within the CRUD depositions will distort the axial power distribution and cause the core power shift, known as CRUD-Induced Power Shift (CIPS) [2].

In order to evaluate the thermal hydraulics and solute transport within CRUD depositions, many previous studies [3–11] have developed a series of methods to simulate the heat and mass transfer in CRUD under PWR operating conditions, such as Boron-induced Offset Anomaly (BOA) [12] developed by EPRI and MAMBA-3D [13] developed by CASL. However, there are still relatively few studies on the impact of chimney boiling and morphology structure in CRUD.

In this paper, a thermal hydraulics and solute transport model is developed to realize the coupling of heat transfer, pressure drop, capillary flow, solute transport, chemical reactions and radiolysis reactions within the CRUD depositions. The influence of the evaporation at the chimneys surface on thermal hydraulics and solute transport is obtained. Additionally, the impact of CRUD morphology parameters such as porosity, thickness, chimney radius and chimney diameter is evaluated.
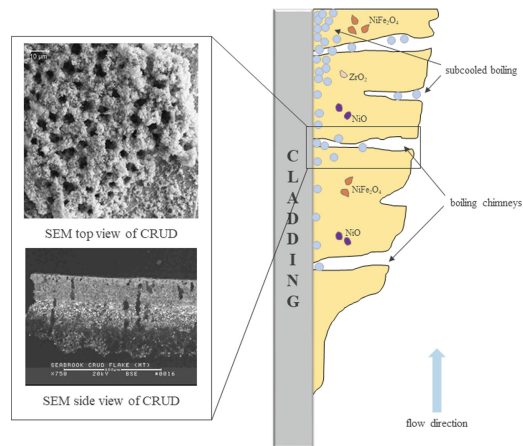

Fig. 1. The formation mechanism and microstructure schematic diagram of CRUD depositions

2 Model

The heat transfer, capillary flow, pressure drop, chemical reactions and radiolysis reactions within the CRUD depositions are tightly coupled. The coolant enters the capillary

tubes under the action of capillary force, evaporates into steam at the surface of the chimneys and escapes through the chimneys into the bulk coolant [7]. In this process, the solutes are concentrated and maintain the chemical equilibrium between other solutes, such as H_3BO_3, Li^+ and $B(OH)_4{}^-$. Boiling on the chimney surface enhances the concentration of solute, and the continuously concentrated solute in turn affects the saturation temperature of the coolant and chemical equilibrium between solutes within the CRUD depositions. In order to establish the multi-physics coupling model, a chimney and its surrounding porous structure (also called shell) are selected for research. The coordinates and boundary conditions are shown in Fig. 2.
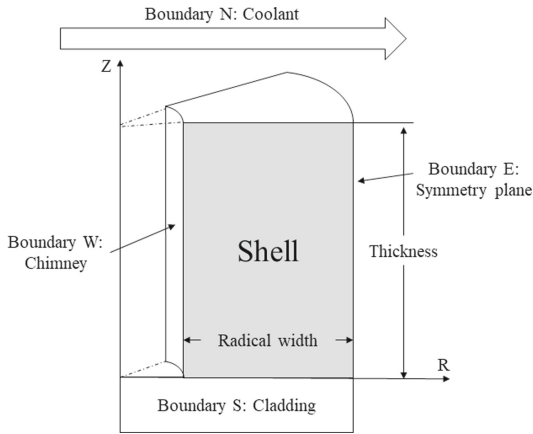

Fig. 2. Schematic diagram of coordinates and boundary conditions

2.1 Thermal Model

The coolant flows through the capillary tubes in the porous medium and evaporates into steam at the surface of chimneys. Based on the energy conservation, the governing equation of heat transfer within the CRUD depositions is derived as Eq. (1). Equations (2)–(5) represent the entrance of heat from cladding, its removal through the coolant interface, its removal through the chimney surface and its conduction on the symmetric plane, respectively.

$$\nabla(k_{CRUD}\nabla T) = 0 \tag{1}$$

$$-k_{CRUD}\left.\frac{\partial T}{\partial z}\right|_{z=0} = Q_{clad} \tag{2}$$

$$-k_{CRUD}\left.\frac{\partial T}{\partial z}\right|_{z=d} = h_c\left(T - T_f\right) \tag{3}$$

$$-k_{CRUD}\left.\frac{\partial T}{\partial r}\right|_{r=r_c} = -h_e\left(T - T_{sat}\right) \tag{4}$$

$$-k_{CRUD}\left.\frac{\partial T}{\partial r}\right|_{r=r_R} = 0 \tag{5}$$

where T is temperature; k_{CRUD} is the heat conductivity of the CRUD depositions; Q_{clad} is heat flux from the cladding surface; d is the CRUD thickness; h_c is conductive heat transfer coefficient at the CRUD and coolant interface, which usually takes the typical value 12000 W/(m × K) [9]; T_f is the bulk coolant temperature; r_c is chimney radius; h_e is conductive heat transfer coefficient at the chimney surface, which can be calculated as Eq. (6) suggested by Pan [8] et al.; T_{sat} is the saturation temperature, which is a function of solute concentration, and is usually described by the activity of water, a_w, which is also a function of solute concentration, shown as Eqs. (7)–(8) [14, 15]; r_R is the distance from the chimney center to the porous shell center (symmetric boundary), and it should be noted that the value is determined by the chimney density.

$$h_e = \left(\frac{2E}{2-E}\right)\left(\frac{M_{H_2O}}{2\pi R}\right)^{1/2} \frac{h_{fg}^2}{T^{3/2}\left(V_g - V_l\right)} \tag{6}$$

where E is the evaporation coefficient; M_{H2O} is the molecular weight of H_2O; R is the gas constant; h_{fg} is the vaporization enthalpy; V_g and V_l are the molecular volume of steam and water.

$$a_w = \frac{m_w}{m_w + \sum m_c} \tag{7}$$

$$\begin{aligned} T_{sat} = {} & 618.09 + 199.01(1-a_w) - 952.74(1-a_w)^2 \\ & + 26013.91(1-a_w)^3 - 262916.0(1-a_w)^4 \\ & + 997166.1(1-a_w)^5 \end{aligned} \tag{8}$$

where m_w is the mass molar concentration of water, equal to 55.509 mol/kg; m_c is the molar concentration of boric acid and other solutes.

2.2 Capillary Flow Model

The capillary flow with low fluid velocity within the porous CRUD depositions follows Darcy's low. The governing equation and boundary conditions are shown as Eqs. (9)–(13).

$$\nabla \cdot \left(-\varepsilon\rho_w \frac{\kappa}{\mu_w}\nabla P\right) = 0 \tag{9}$$

$$-\frac{\kappa}{\mu_w}\left.\frac{\partial P}{\partial z}\right|_{z=0} = 0 \tag{10}$$

$$P|_{z=d} = P_f \tag{11}$$

$$-\frac{\kappa}{\mu_w}\left.\frac{\partial P}{\partial r}\right|_{r=r_c} = -\frac{k_{CRUD}}{\rho_w h_{fg}}\frac{\partial T}{\partial r} \tag{12}$$

$$-\frac{\kappa}{\mu_w}\frac{\partial P}{\partial r}\bigg|_{r=r_R} = 0 \tag{13}$$

where P is pressure; ε is the porosity; ρ_w is the water density; κ is the permeability; μ_w is the water kinetic viscosity changing with temperature as Eq. (14) [16]; P_f is the pressure of bulk coolant.

$$\mu_w = \frac{25.3}{-8.58 \times 10^4 + 91 \cdot T + T^2} \tag{14}$$

In Darcy's law, the capillary flow velocity in the porous CRUD depositions is proportional to the pressure gradient as Eq. (15).

$$u_l = -\frac{\kappa}{\mu_w}\nabla P \tag{15}$$

where u_l, a vector with r and z directions, is the Darcy velocity of water within the CRUD depositions.

2.3 Solute Transport and Reaction Model

The governing equation of solute transport considers solute diffusion, convection, chemical reaction and radiolysis reaction, shown as Eq. (16). Due to the rapidity of reaction, solute transport and reaction within the CRUD depositions maintain in the quasi-steady state, so each item on the r.h.s of Eq. (16) can be considered zero. The boundary conditions are as Eqs. (17)–(20).

$$\frac{\partial C_i}{\partial t} = RC_i + RR_i - \nabla \cdot J_i \tag{16}$$

$$\frac{\partial C_i}{\partial z}\bigg|_{z=0} = 0 \tag{17}$$

$$C_i|_{z=d} = C_{f_i} \tag{18}$$

$$\left(-D_i\frac{\partial C_i}{\partial r} + u_{l_r}C_i\right)\bigg|_{r=r_c} = 0 \tag{19}$$

$$\frac{\partial C_i}{\partial r}\bigg|_{r=r_R} = 0 \tag{20}$$

where C is concentration; i represents the number of the solute; t is time; RC is the concentration changed by chemical reactions; RR is the concentration changed by radiolysis reactions; J is molar flux calculated as Eq. (21); D is diffusion coefficient, which is modified according to fractal theory as Eq. (22) [6].

$$J = -D\nabla C - DC\frac{zD\nabla\phi}{RT} + u_lC \tag{21}$$

$$D = \frac{\varepsilon}{\tau} D_w \tag{22}$$

where z is the solute's charge number; ϕ is the potential; τ is the tortuosity, which is a function of porosity as Eq. (23) [17]; D_w is the diffusion coefficient in pure water, and for boric acid, the value is 1.07×10^{-9} m^2/s in 298.15 K water, and at other temperatures the diffusion coefficient of boric acid satisfies the Stokes-Einstein relation [18] as Eq. (24).

$$\tau = \frac{1}{2}\left[1 + \frac{1}{2}\sqrt{1-\varepsilon} + \sqrt{1-\varepsilon} \frac{\sqrt{\left(\frac{1}{\sqrt{1-\varepsilon}} - 1\right)^2 + \frac{1}{4}}}{1 - \sqrt{1-\varepsilon}} \right] \tag{23}$$

$$D_w = 1.07 \times 10^{-9} \cdot \frac{T}{298.15} \cdot \frac{\mu_{w,T=298.15}}{\mu_w(T)} \tag{24}$$

The chemical reactions within the CRUD depositions considered include ionization of water, interactions of boric acid and water, and precipitation of boron. For a generalized chemical reaction as Eq. (25), the concentration changed by chemical reactions can be described as Eq. (26).

$$aA + bB \leftrightarrow cC + dD \tag{25}$$

$$RC = -k_f C_A^a C_B^b + k_r C_C^c C_D^d \tag{26}$$

where uppercase letters represent participants in the chemical reaction and lowercase letters represent stoichiometric coefficients; k_f and k_r are forward and reverse reaction rate constants.

At equilibrium or quasi-steady state, $RC = 0$, so the ratio of the forward and reverse reaction rate constant is given by Eq. (27). The thermodynamic equilibrium expression[19] for the reaction is given by Eq. (28).
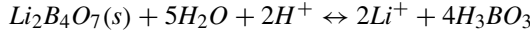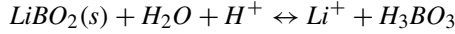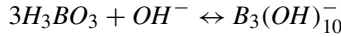
$$\frac{k_f}{k_r} = \frac{C_C^c C_D^d}{C_A^a C_B^b} \tag{27}$$

$$K = \frac{m_C^c m_D^d}{m_A^a m_B^b} \frac{\gamma_C^c \gamma_D^d}{\gamma_A^a \gamma_B^b} = \frac{k_f}{k_r} \frac{\gamma_C^c \gamma_D^d}{\gamma_A^a \gamma_B^b} (\zeta \rho_w)^{-a-b+c+d} \tag{28}$$

where K, the thermodynamic equilibrium expression, is a function of temperature corresponding to each chemical reaction; m is mass molar concentration; γ is the solute's activity coefficient; ζ is the correction of volume considering the solute volume.

The chemical reactions within the CRUD depositions considered in this paper include:

$$H_2O \leftrightarrow H^+ + OH^-$$

$$H_3BO_3 + OH^- \leftrightarrow B(OH)_4^-$$

$$2H_3BO_3 + OH^- \leftrightarrow B_2(OH)_7^-$$

$$3H_3BO_3 + OH^- \leftrightarrow B_3(OH)_{10}^-$$

$$LiBO_2(s) + H_2O + H^+ \leftrightarrow Li^+ + H_3BO_3$$

$$Li_2B_4O_7(s) + 5H_2O + 2H^+ \leftrightarrow 2Li^+ + 4H_3BO_3$$

The alpha dose within the CRUD depositions is raised by the concentrating boron via ^{10}B(n,α)^{7}Li reaction. The solute concentration changed by radiolysis reactions can be considered as production RR_1, consumption and reproduction RR_2 two parts, which can be calculated by Eqs. (29) and (30) [20], respectively.

$$RR_1 = \left(\frac{G_\alpha \Gamma_\alpha + G_\alpha \Gamma_\alpha + G_\alpha \Gamma_\alpha}{100 N_A} \right) f \rho_w \tag{29}$$

$$RR_2 = \sum \sum k_{AB} C_A C_B - C_C \sum k_D C_D \tag{30}$$

$$RR = RR_1 + RR_2 \tag{31}$$

where G is the number of molecules produced from the irradiation of 100 eV into a solution; Γ is dose rate; N_A is Avogadro's constant; f is a conversion factor from rad/sec to eV/(kg $\times$ sec); k is radiolysis reaction rate constant defined by Arrhenius law.

The radiolysis reactions within the CRUD depositions considered in this paper include:

$$H_2 + OH \leftrightarrow H + H_2O$$

$$H + H_2O_2 \leftrightarrow OH + H_2O$$
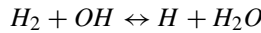
2.4 Numerical Approach and Coupling Scheme

The finite volume method is used to discrete in the two-dimensional cylindrical coordinates. The maximum relative error of temperature, pressure and solute concentration is used as the convergence condition, and the allowable maximum relative error is less than 10^{-7}. The thermal model, capillary flow model and solute transport and reaction model affect each other, and feedback each other in the coupling calculation process until the final calculation results converge. The whole calculation process is shown in Fig. 3.

The thermal model obtains temperature distribution and updates physical properties for capillary flow model and solute transport and reaction model. The pressure and Darcy velocity calculated by capillary flow model are used to determine the velocity of solute transport. The concentrations obtained by the solute diffusion and chemical reaction module update the saturation temperature, which has a significant influence on physical properties and then affects the temperature and pressure distribution.
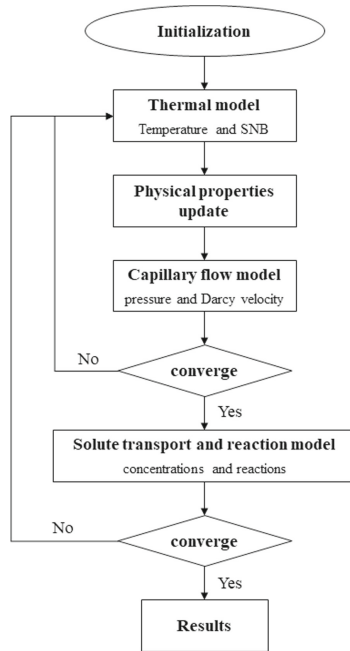
Fig. 3. Flow chart of the simulation process of CRUD heat and mass transfer

3   Results

In order to evaluate the thermal hydraulics and solute transport within the CRUD depositions, typical PWR thermal and hydrochemical conditions are selected for the analysis. Also the CRUD geometric parameters are chosen to evaluate the influence of CRUD morphology on the thermal hydraulics and solute transport. The overall input parameters are listed in Table 1.

Figure 4 shows the calculation results for the distributions of temperature, pressure, Darcy velocity, boric acid concentration, lithium concentration and pH within the CRUD depositions. The temperature reaches the maximum value of 642.42 K at the interface between the cladding and the symmetry plane. The maximum temperature difference is 26.53 K. The maximum subcooled boiling heat flux occurs at the interface between the cladding and the chimney, reaching 0.455 MW/m^2. At the same time, this region is also the position where the maximum pressure drop occurs reaching 2.8 kPa, making the capillary flow velocity of 0.78 mm/s in the R direction. The heat taken away by subcooled boiling at the chimney surface accounts for 61% of the total heat transfer through the CRUD depositions.

Table 1. Overall input parameters and analysis variables

Parameters	Units	Values	Variable quantity
System pressure	MPa	15.5	–
Coolant temperature	K	600	–
Heat flux	MW/m^2	1.50	–
Boric acid concentration	ppm	1200	–
Lithium concentration	ppm	2	–
Hydrogen concentration	cc(STP)/kg	25.3	–
Gamma dose rate	Mrad/h	1200	–
Neutron dose rate	Mrad/h	2400	–
Neutron flux	#/(cm^2 × s)	3.6×10^{14}	–
CRUD porosity	–	0.8	0.4, 0.5, 0.6, 0.7, 0.8
CRUD thickness	μm	60	20, 40, 60, 80
CRUD chimney radius	μm	2.5	1.5, 2.0, 2.5, 3.0
CRUD chimney density	× 10^3/mm^2	3	1, 2, 3, 4

Boric acid concentration and lithium concentration are closely related to capillary flow within the CRUD depositions, which are affected by subcooled boiling at the chimney surface. The solutes reach the area near the chimney under the action of capillary flow. Since most of the solutes do not evaporate like water but get concentrated, so the concentrations in the area near the chimney are usually higher. At the interface between the cladding and the chimney, the boric acid concentration and lithium concentration reach the maximum values of 0.60 mol/L and 1.5 mmol/L, respectively. Although theoretically for chemical reactions, the more boric acid, the more reaction with OH-, due to the chemical equilibrium by temperature and other chemical reactions, even though the trend is roughly the same, the concentration ratio is different. Compared with the concentration in the bulk coolant, the maximum concentration ratios of $B(OH)_4^-$, $B_2(OH)_7^-$, $B_3(OH)_{10}^-$ are 4.04, 32.06 and 248.26, respectively. After H^+ enters the CRUD depositions with the coolant, its concentration decreases, because OH^- concentration increases accordingly to maintain the chemical equilibrium of boric acid and other boron elements. In the area near the interface between the chimney and the cladding, H^+ concentration increases because the reaction of boron precipitation produces H^+. As for boron precipitation, it is found that $Li_2B_4O_7$ always reaches the required concentration condition for precipitation before $LiBO_2$, so it is considered that boron is more inclined to precipitate in the form of $Li_2B_4O_7$.
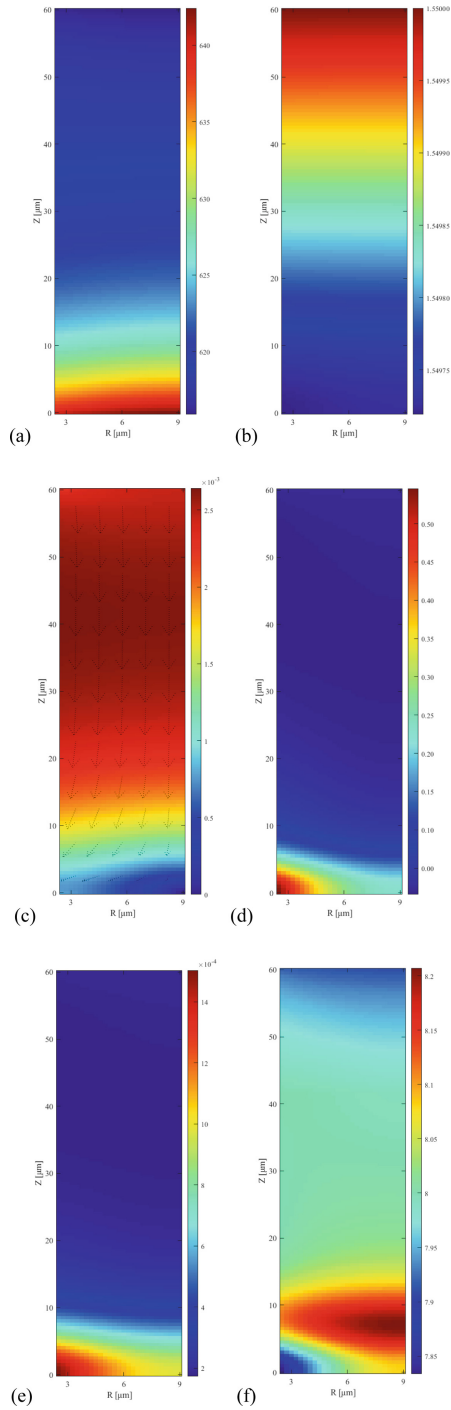
Fig. 4. The distributions of (a)temperature [K], (b)pressure [Pa], (c)Darcy velocity [m/s], (d)boric acid concentration [mol/L], (e)lithium concentration [mol/L], (f)pH within the CRUD depositions

4   Discussion

4.1   Influence of CRUD Porosity

Figure 5 plots the axial temperature difference, SNB heat removal ratio and boron mass through the CRUD depositions according to the CRUD porosity. Because the thermal conductivity of water is smaller than that of metal oxides constituting the CRUD porous structure, the higher the porosity is, the lower the CRUD thermal conductivity is, and the larger the temperature difference is. SNB heat removal ratio is approximately linear with the porosity, but the increase is not large. The diffusion coefficient corrected by fractal theory increase with the increase of the porosity. Because the capillary flow velocity is small and has little change, solutes with larger diffusion coefficients only need a smaller diffusion gradient to establish a balance with the convection. Therefore, the higher the porosity, the lower the solute concentration. But considering the volume fraction of coolant in the porous depositions, boron mass increases with the increase of porosity. The boron mass per unit area of CRUD is obtained by multiplying the boron mass of a chimney-centered calculation area by the chimney density.

(a)   (b)

(c)
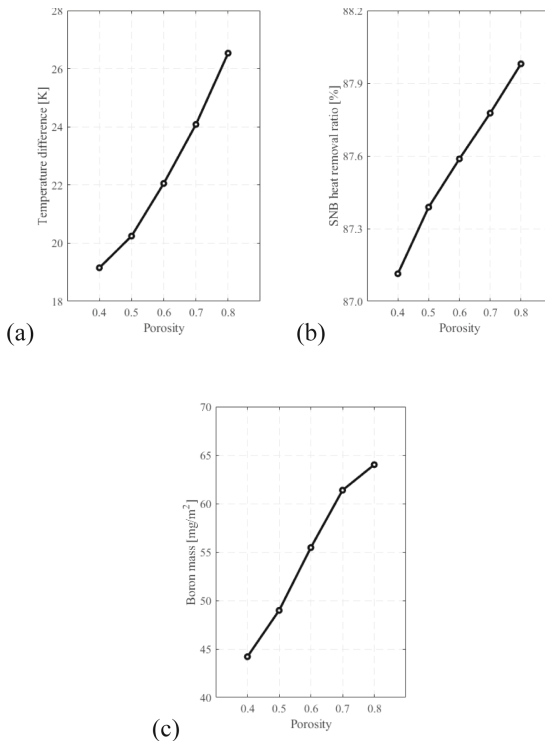
Fig. 5. (a) Axial temperature difference at the chimney surface, (b) SNB surface heat removal ratio, (c) boron mass per square meter CRUD along with the CRUD porosity
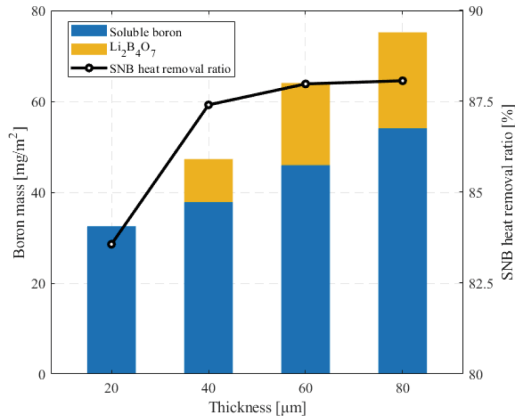
4.2 Influence of CRUD Thickness

Fig. 6. Boron hideout and SNB heat removal ratio along with the CRUD thickness

Figure 6 shows the boron hideout and SNB heat removal ratio within the CRUD depositions according to the CRUD thickness. With the increase of CRUD thickness, boron is also accumulated and the mass increases. $Li_2B_4O_7$ has been precipitated a lot when the CRUD thickness reaches 40 μm, which is quite different from the characteristics reported by EPRI [2] that precipitation $LiBO_2$ begins to precipitate between 35–42 μm CRUD thickness. This also indicates that $Li_2B_4O_7$ reaches the precipitation condition earlier than $LiBO_2$. After the beginning of boron precipitation, the increasing trend of soluble boron mass slows down, and more boron is precipitated in the form of precipitation $Li_2B_4O_7$. At the same time, SNB heat removal ratio increases slightly after the thickness reaches 40 μm.

4.3 Influence of CRUD Chimney Radius

Figure 7 plots the axial temperature difference, pressure drop maximum and boric acid concentration maximum through the CRUD depositions according to the CRUD chimney radius. For a certain chimney density, the increase of chimney radius means the decrease of the shell area and the increase of the phase change area at the surface of the chimney. Therefore, with the increase of the chimney radius, more subcooled boiling occurs at the surface of the chimney, and less heat is removed by heat conduction, leading to smaller temperature difference and greater pressure drop. But larger chimney radius also means that the solutes are easier to reach the surface of the chimney and more difficult to diffuse to the interface between the cladding and the CRUD, and the maximum boric acid concentration decreases accordingly.
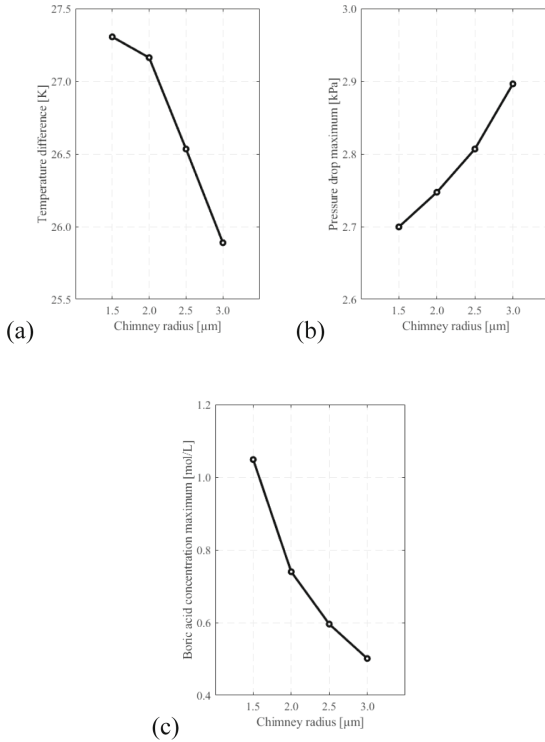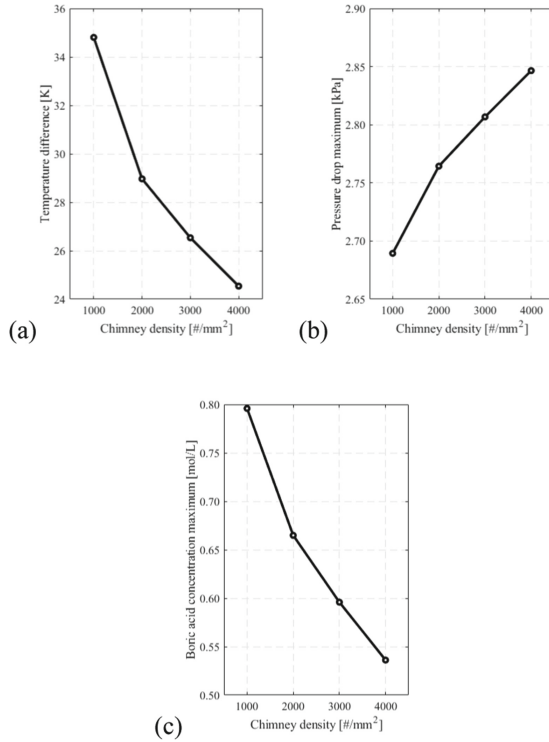
Fig. 7. (a) Axial temperature difference at the chimney surface, (b) pressure drop maximum, (c) boric acid concentration maximum along with the CRUD chimney radius

4.4 Influence of CRUD Chimney Density

Figure 8 plots the axial temperature difference, pressure drop maximum and boric acid concentration maximum through the CRUD depositions according to the CRUD chimney density. Similar to the effect of increasing the chimney radius, the increased chimney density also squeezes the area share of the CRUD porous shell and reduces the radial length (the distance from the chimney surface to the symmetric plane). Therefore, with the increase of chimney density, the temperature difference decreases, the pressure drop increases, and the maximum concentration of boric acid decreases.

Fig. 8. (a) Axial temperature difference at the chimney surface, (b) pressure drop maximum, (c) boric acid concentration maximum along with the CRUD chimney density

5 Conclusion

The multi-physics coupling model is developed to predict the thermal hydraulics and solute transport within the porous CRUD depositions. Processes including heat transfer, pressure drop, capillary flow, solute transport, chemical reactions and radiolysis reactions are fully coupled. This model reasonably predicts the distributions of the temperature, pressure, Darcy velocity and solute concentrations within the CRUD depositions. The subcooled boiling at the surface of the chimney has an important influence on the thermal hydraulics and solute transport within the CRUD depositions. Temperature, pressure, SNB heat removal ratio, solute concentrations and boron mass are evaluated under different CRUD morphology parameters. With the increase of thickness, more boron exists in the form of precipitated $Li_2B_4O_7$. The porosity, chimney radius and chimney density have positive correlations with subcooled boiling and negative correlation with boron concentration. The thermal hydraulics and solute transport analysis by this model can provide technical support for the prediction of the CIPS phenomenon.

References

1. Li, S., Liu, X.: Development of boron tracking and boron hideout (CRUD) model based on subchannel approach. Nucl. Eng. Des. **338**, 166–175 (2018)
2. Deshon, J.: PWR axial offset anomaly (AOA) guidelines, revision 1," EPRI, Palo Alto, CA, 1008102(3) (2004)
3. Jaiswal, A.: A numerical study on parameters affecting boric acid transport and chemistry within fuel corrosion deposits during crud induced power shift (2013)
4. Park, B.G., Seo, S., Kim, S.J., Kim, J.H., Choi, S.: Meso-scale multi-physics full coupling within porous CRUD deposits on nuclear fuel. J. Nucl. Mater. **512**, 100–117 (2018)
5. Pan, C., Jones, B.G., Machiels, A.J.: Concentration levels of solutes in porous deposits with chimneys under wick boiling conditions. Nucl. Eng. Des. **99**, 317–327 (1987)
6. Short, M., Hussey, D., Kendrick, B., Besmann, T., Stanek, C., Yip, S.: Multiphysics modeling of porous CRUD deposits in nuclear reactors. J. Nucl. Mater. **443**(1–3), 579–587 (2013)
7. Macbeth, R.: Boiling on surfaces overlayed with a porous deposit: heat transfer rates obtainable by capillary action. Atomic Energy Establishment, Winfrith (England) (1971)
8. Pan, C., Jones, B., Machiels, A.: Wick boiling performance in porous deposits with chimneys. In: Proceedings of 23rd National Heat Transfer Conference, American Society of Mechanical Engineers (ASME), pp. 15–24
9. Haq, U.: Heat and mass transfer analysis for crud coated PWR fuel. Imperial College London (2011)
10. Zou, L., Zhang, H., Gehin, J., Kochunas, B.: A coupled TH/Neutronics/CRUD framework in prediction of cips phenomenon, Idaho National Lab.(INL), Idaho Falls, ID (United States) (2012)
11. Cohen, P.: Heat and mass transfer for boiling in porous deposits with chimneys
12. Deshon, J., Hussey, D., Kendrick, B., McGurk, J., Secker, J., Short, M.: Pressurized water reactor fuel crud and corrosion modeling. JoM **63**(8), 64–72 (2011)
13. Kendrick, B., Petrov, V., Walker, D., Manera, A.: CILC studies with comparative analysis to existing plants," CASL-U-2013–0224–000, Los Alamos National Laboratory (2013)
14. Pitzer, K., Brewer, L.: Thermodynamics. International Student Edition. McGraw-Hill, New York, NY (1961)
15. Deshon, J.: Modeling PWR fuel corrosion product deposition and growth processes, EPRI, Palo Alto, CA, 1009734 (2004)
16. Gierszowski, P., Mikic, B., Todreas, N.: Property correlations for lithium, sodium, helium, flibe and water in fusion reactor applications (1980)
17. Yu, B., Li, J.: Some fractal characters of porous media. Fractals **9**(03), 365–372 (2001)
18. Cappelezzo, M., Capellari, C., Pezzin, S., Coelho, L.: Stokes-Einstein relation for pure simple fluids. J. Chem. Phys. **126**(22), 224516 (2007)
19. Marshall, W.L., Franck, E.: Ion product of water substance, 0–1000°C, 1–10,000 bars New International Formulation and its background. J. Phys. Chem. Ref. Data **10**(2), 295–304 (1981)
20. Christensen, H.: Fundamental aspects of water coolant radiolysis, Swedish Nuclear Power Inspectorate (2006)

Study on Composition Design of Enamel Coating and Its Resistance to Active Metal Vapor Corrosion

Y. F. Jiang[(✉)], H. Y. Li, J. Chen, X. Q. Shi, and Y. X. Zhu

The 404 Company Limited, China National Nuclear Corporation, Lanzhou 732850, China
jiangyfd@mail.ustc.edu.cn

Abstract. After evaporation of cerium metal (simulated radioactive substance) in a stainless steel plate in a production process, Ce and Fe elements are inter-diffused at the bonding interface and Ce-Fe solid solution is formed. There are problems such as incomplete recovery of attached materials and increased surface roughness at the interface, which cannot be reused. In order to reduce radioactive iste generation, metallic enamel coating is prepared on stainless steel substrate with SiO_2, Al_2O_3, Na_2O, K_2O, CaF_2 and CoO and its resistance to active metal vapor corrosion at high temperature is studied. The results show that the enamel coating is closely bonded to the substrate, forming a chemical bond of Fe-Co rich phase. The enamel coating can stably form a film with cerium metal atoms, and the evaporation coating does not fall off. The microstructure results show that cerium oxide is formed at the bonding interface between the enamel coating and cerium metal, forming a stable chemical bond. Compared with stainless steel substrate, there is no interfacial corrosion caused by mutual diffusion between enamel coating and cerium metal at the bonding interface, so it can only desorb cerium metal without damaging the coating and realize multiple reuse.

Keywords: Enamel coating · Evaporation · Corrosion · Diffusion

1 Introduction

In the process of metal evaporation recovery and stainless steel plate reuse, problems such as incomplete recovery and large amount of iron impurities are encountered. As a result, stainless steel plate can only be used once and cannot be reused for many times due to the residue of radioactive materials. Although in the verification phase, it also caused a large accumulation of radioactive material. Therefore, it is necessary to research on the reuse technology to realize the complete recovery of the metal and multiple reuse of the plate [1]. The active metal atoms have high thermal conductivity, high specific heat capacity, low vapor pressure and other characteristics. The metal atoms and the substrate are very easy to diffuse in the process of evaporation, resulting in the coating metal is difficult to completely desorption. Therefore, the development and preparation of high temperature corrosion resistant coating against active metal atomic steam is the factor to restrict the reuse of plate [2, 3]. The traditional high temperature anti-corrosion protective coating

can be generally divided into ceramic coating [4, 5] and metal coating [6, 7]. According to the composition, mainly includes metal oxide coating and other coating. Through the composition design of ceramic, enamel coating can significantly reduce the corrosion rate. Multiple service will not affect the surface state after passivation. So in various professional fields have broad application prospects.

Enamel coating is a kind of amorphous glass coating. In the process of high temperature firing, it is easy to form strong combination with metal or alloy to improve the corrosion resistance of the whole plate [8–10]. Chen et al. [11] prepared 0.6 (mass fraction) borosilicate ratio enamel coating. The softening temperature of the enamel is higher than 750 °C. Thermal shock results show that the performance of metal enamel composite coating with nickel particles is significantly improved. Zhu et al. [4] coated Ti60 with enamel coating to study its high temperature oxidation and sulfate hot corrosion behavior at 700 °C for 1000 h. The enamel coating forms a thin oxide layer composed of α-Al_2O_3, TiO_2, Al_2SiO_5 and Al_2TiO_5, thus providing high temperature stability and avoiding high temperature corrosion.

Most of the existing research focuses on the high temperature oxidation corrosion resistance of enamel coating. In view of the high requirement of coating recovery on substrate surface state in atomic vapor laser technology [12–16], the resistance of enamel coating to active metal vapor corrosion in high-temperature evaporation is studied.

2   Enamel Coating Composition Design

Based on the actual service situation, SiO_2, Al_2O_3, Na_2O, K_2O, CaF_2 and CoO are chosen as the main components of special enamel coating. The composition ensure that free oxygen makes all Al_2O_3 intermediate in the form of four coordination into the silica oxide grid. Enamel coating with high temperature resistance, acid corrosion resistance and strong bonding force with stainless steel is prepared. The addition of CoO mainly considers that the Fe-Co-rich phase generated by firing can self-repair cracks in the service process and improve the thermal shock performance of enamel coating [17]. The composition of enamel coating directly affects the compactness, adhesion, acid resistance, hardness and other properties of the coating, and then affects its service behavior.

2.1   Preparation Technology of Enamel Coating

In this study, 316L stainless steel is used as the base material. Metal flakes of 50 mm $\times$ 50 mm $\times$ 1 mm are cut by electric discharge wire. In order to ensure more physical and mechanical teeth forming between enamel powder and stainless steel substrate during firing, sand blasting is required to increase roughness. The sand blasting device used is shown in Fig. 1.

Choose 200–220 mesh corundum sand, sand blasting pressure control is less than 1 kg/cm^2, the smooth surface with matte surface state is obtained, as shown in Fig. 2.
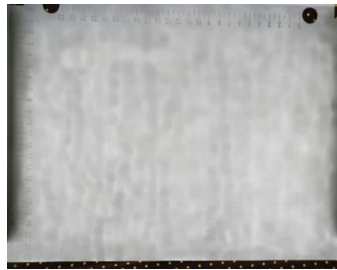
Fig. 1. Sandblasting equipment.

Fig. 2. Macro appearance of sandblasting stainless steel plate.

Main components of enamel glaze (wt%) is 64.6 SiO_2, 14.2 Al_2O_3, 9.61 Na_2O, 4.65 K_2O, 4.96 CaF_2, 1.98 CoO. The raw material with 500 g weight is placed in the agate tank and agate balls are added. Then mechanical mixing is carried out in the planetary ball mill with the speed controlled at 300 r /min and the mixing time about 30 min. After the mixing, the raw material is put into a corundum crucible into a muffle furnace and heated to 1300 °C for 4 h. All the enamel melts are quenched at room temperature to obtain the enamel glaze. A planetary ball mill is used for dry ball grinding of enamel glaze and agate ball again. The rotating speed is set at 300 r/min, and the ball grinding time is about 120 h. Finally, the standard sieve (200 mesh) is used to screen the enamel powder ground by the ball to remove the large particles that are not ground.

The method of preparing special enamel coating on the surface of stainless steel substrate is to mix alcohol and enamel powder into suspension solution at a ratio of 2 g per 30 ml, and then vibrate with high frequency ultrasound until dispersing into slurry. The slurry is sprayed onto the surface of stainless steel by atmospheric spraying. The spraying pressure is about 0.3 MPa, and the distance between the nozzle and the stainless steel plate is controlled to 200 mm. From left to right and top to bottom, repeated spraying sequence to ensure uniform and smooth enamel coating. Each spray is about 2 μm thick as a spray cycle. Control about 20 passes to finish spraying. The coated stainless steel plate is put into the oven and adjusted to 70 °C for 10 min to obtain the powder. Then it

is adjusted to about 900 °C in the muffle furnace for firing, and the firing is completed about 3 min later.

2.2 Interface Between Enamel Coating and Stainless Steel

Figure 3 shows the SEM morphology at the interface between enamel coating and stainless steel matrix.
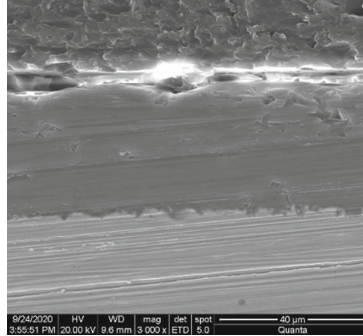

Fig. 3. SEM morphology of enamel coating/matrix interface.

The thickness of the enamel coating formed by firing is about 40 μm, and the coating is dense without holes (Fig. 3). The enamel coating is closely bonded to the substrate, and the interface is serrated. The presence of these serrated interfaces increases the physical bonding between the coating and the substrate on the one hand. The reaction area is between the coating and the substrate on the other hand, which promotes the chemical bonding and makes the coating and the substrate bond well. In order to further analyze the bonding mode between enamel coating and matrix, EDS line scanning analysis is carried out on the interface (Fig. 4).
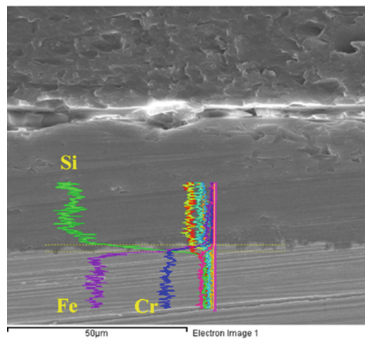

Fig. 4. EDS line scan of enamel coating/matrix interface

As shown in the Fig. 4, the main component of enamel coating is Si. Through the observation of the interface, it is found that there is a transition layer at the interface, as shown in the middle of the two yellow dotted lines. In this transition layer, Fe element decreases gradually from substrate to coating, indicating that Fe atom diffusion occurs during the preparation of coating. Cobalt is also found in the transition layer, which confirmed the diffusion of Co from the coating to the interface.

3 Enamel Coating Properties

3.1 Phase Characterization of Enamel Coating

The phase composition of enamel coating is analyzed by X-ray diffraction (XRD) with a sample of 10×10 mm cut by linear cutting method. The radiation used is Cu Kα ($\lambda = 0.1548$ nm), the working voltage is 50 kV, and the scanning speed is 2°/min. XRD results are analyzed with Jade 6.0 software.
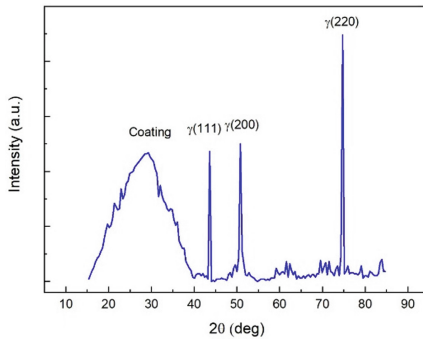

Fig. 5. XRD pattern of enamel coating.

As can be seen in the Fig. 5, steamed bun peak appears in the XRD pattern at 25°, which is a typical morphology of amorphous structure. Therefore, the enamel coating is mainly composed of short-range ordered and long-range disordered glassy phase. The peak of substrate austenite can also be seen.

3.2 Hardness of Enamel Coating

The hardness of enamel coating and substrate is measured by automatic micro hardness tester. The test pressure is 50 g and the holding time is 10 s. The average measured results are 874.8 HV for enamel coating and 195.7 HV for stainless steel substrate. The hardness of enamel coating on stainless steel surface is about 4.5 times that of stainless steel substrate. The improvement of hardness can greatly improve the wear resistance of the surface. So as to ensure that the surface of the work piece is not damaged when it is scratched externally, and maintain a smooth surface.

4   High Temperature Evaporation Performance

Self-designed vacuum chamber evaporation device is adopted, and its limit vacuum is 3 $\times$ 10^{-4} Pa. The water-cooled copper crucible is selected as the electron beam evaporation vessel. The purity of 99.5% cerium metal is used as raw material, and the smooth 316 stainless steel plate of 360 mm $\times$ 240 mm $\times$ 1 mm and the same stainless steel plate with enamel coating are used as the substrate respectively. The power of the electron gun is 30 kW, and the heating temperature of the material plate is 360 °C. When the vacuum degree is better than 5 $\times$ 10^{-3}, the cerium metal is vaporized by electron beam to form metal atom vapor and the stable evaporation begins. After evaporation, the microstructure and phase composition of the bonding interface between cerium metal and substrate are analyzed by means of SEM and EDS.

4.1   Interface Between Cerium Metal and Stainless Steel After Evaporation

The bonding interface between cerium metal and stainless steel after evaporation is shown in the Fig. 6.
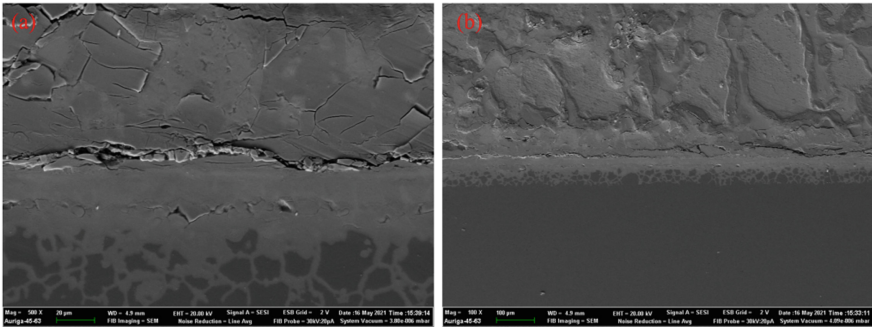

Fig. 6.   SEM morphology at the bonding interface with (a) 500X and (b) 100X

The bonding interface between Ce metal coating and stainless steel can be clearly seen from Fig. 6a. The bonding interface is slightly cracked, and the diffusion of Ce metal to stainless steel can be observed on the surface of stainless steel. As the diffusion deepens, the diffusion of Ce metal layer is patterned. The results show that Ce metal diffused first on the surface of stainless steel along the grain boundary of 316L stainless steel. The Ce metal atoms at the grain boundary gradually diffused into the crystal to form a solid solution under the thermodynamic action, and finally formed metal compounds of $CeFe_2$, which is consistent with the XRD analysis results. In the relatively deep region of 316L stainless steel, the diffusion ability of Ce metal atoms is weakened, so Ce metal atoms only diffuse along the grain boundary and rarely diffuse into the crystal interior, resulting in patterned diffusion [21]. As can be seen from Fig. 6b, the diffusion distribution of Ce metal coating is relatively uniform. The distribution of elements at the cerium-stainless steel bonding interface is shown in the Fig. 7.
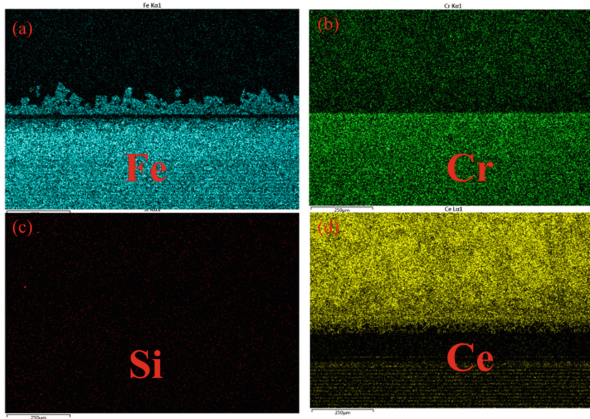
Fig. 7. Surface scanning spectrum at the interface.

It can be seen from Fig. 7a that Fe diffuses inside Ce metal. Different from the diffusion of Ce metal, Fe expands into a zigzag shape, which may be related to the crystal structure of Ce metal and the radius of Fe element. In addition, the distribution cross section of Cr element is linear. It indicates that Cr element has not diffused inside Ce metal to form a solid solution. The solid solution is divided into intergap solid solution and replacement solid solution. For intergap solid solution, its formation factors are determined by lattice gap, atomic radius and electronegativity of elements. For replacement solid solutions, the formation factors are only related to atomic radius and electronegativity. According to the table element radius, Fe atomic radius is 64.5 pm, Cr atomic radius to 52 pm, Ce atomic radius of 103.4 pm. This result indicates that the solid solution formed by Ce metal and Fe element at the interface of the coating is substitution solid solution.
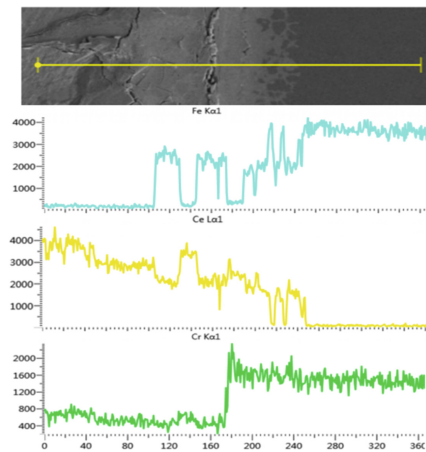

Fig. 8. Element line scan analysis at interface

Figure 8 shows the linear scanning analysis results of Ce metal and stainless steel substrate surface. It can be seen from the figure that the composition of Fe and Ce elements changed significantly with the change of scanning area. In the area about 40 µm left and right of the interface, Fe and Ce is a zigzag. This result further proves that Fe and Ce diffused each other rather than one way. The content of Cr element shows a cliff-like change, indicating that Cr element did not participate in diffusion. The above test results show that the stainless steel plate is corroded by cerium atoms after long time evaporation, forming a diffusion layer of tens of microns. Because of the diffusion effect between Ce metal and stainless steel layer, the bonding force between the two is strong, and the Ce metal atoms in the inner layer of stainless steel are difficult to be desorbed by means of steam oxidation treatment, which is the root cause of the material plate can not be reused.

4.2   Interface Between Cerium Metal and Enamel Coating After Evaporation

The macro morphology of cerium metal and stainless steel plate with enamel coating after evaporation is shown in the Fig. 9.
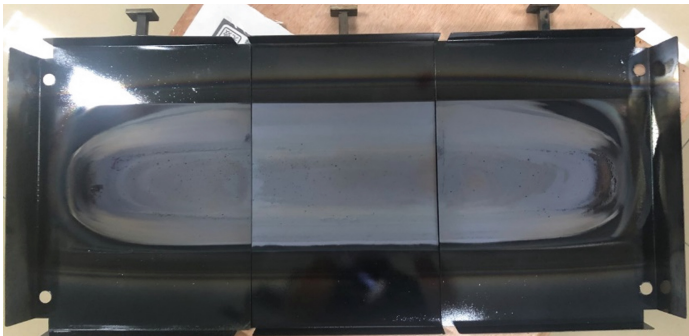

Fig. 9. Macromorphology of enamel coated stainless steel plate after evaporation.

As can be seen from the Fig. 9, the enamel coating combines well with cerium vapor. After weighing, the deposition capacity of left plate, middle plate and right plate is equivalent to that of stainless steel plate. The microstructure of stainless steel plate with enamel coating at the bonding interface after steam plating is shown in the Fig. 10.

SEM observations show that a layer of metal is evaporated above the enamel coating in the service process, and the main component is Ce after EDS analysis. The interface between the enamel coating and the matrix is still well combined, there is no obvious change compared with that before service. The thickness of the enamel coating is basically unchanged, proving that the enamel coating can serve stably in the target environment. In order to further analyse the bonding between enamel coating and autoclaves at the interface layer, EDS line scanning analysis is carried out on the interface layer of enamel coating/autoclaves, and the results are shown in the Fig. 11.
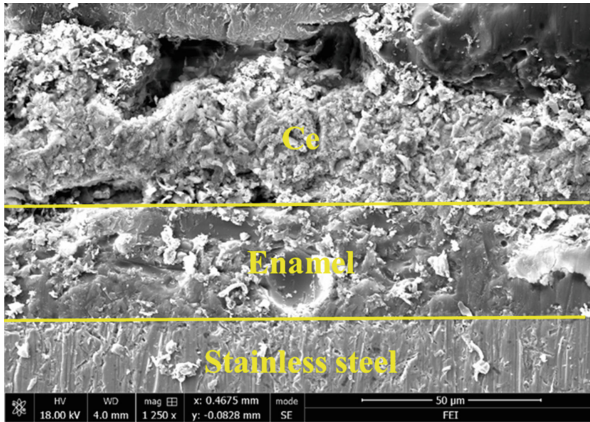
Fig. 10. SEM morphology of enamel coated stainless steel plate after evaporation
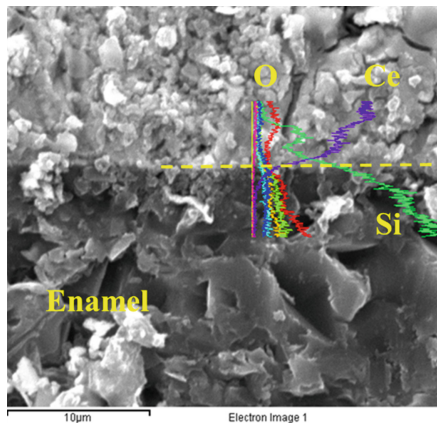

Fig. 11. EDS line scanning map of enamel coating/steam plating interface

EDS line scanning map shows that, a transition region is formed at the interface between Ce and enamel coating. The thickness of this region is about $2\,\mu$m surrounded by the double yellow curve in the Fig. 11. In this transition region, the content of Si decreases and the content of Ce increases, and Si increases with the direction of steam gold plating. This phenomenon indicates that chemical reactions took place in the transition region, and the following reactions can be inferred from the distribution results of elements.

$$Sio_2 + Ce \xrightarrow{500^{\circ c}} Ceo_2 + Si \tag{1}$$

The Gibbs free energy change of the reaction is -158.3 kJ/mol less than -40 kJ/mol, it can be spontaneous. The reduced Si atoms diffused into the Ce metal with low Si content, resulting in the enrichment of Si elements towards the Ce metal layer. However, once CeO_2 is formed at the transition layer, the CeO_2 layer can hinder the further diffusion of Ce to the enamel coating, thus preventing the further reaction between Ce and the

enamel coating, resulting in the termination of the reaction. Due to chemical reaction, make the enamel coating and steamed metallized caused by van der Waals force not only the physical union. It is a chemical reaction to form the Si, O and Ce chemical combination. So the enamel coating can well with steamed metallized combination.

4.3   Enamel Coated Stainless Steel Plate Reuse

The method of pickling is used to verify that enamel coated stainless steel plate can be reused. Through the study on the acid resistance of enamel coating, it can be concluded that the enamel coating has a high acid resistance, so pickling has no effect on the enamel coating while removing the steam gold plating.
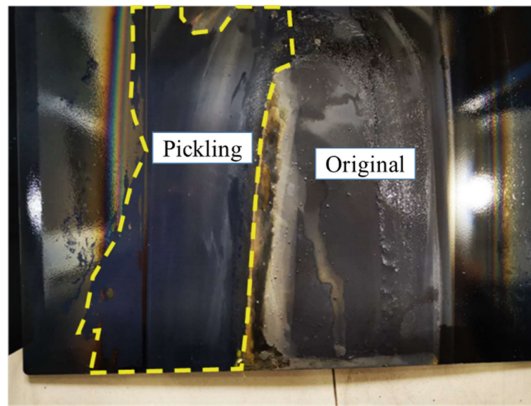

Fig. 12. Macromorphology of stainless steel plate with enamel coating before and after pickling.

In order to compare the morphology of enamel stainless steel plate with evaporation before and after pickling, only part of pickling is carried out. The pickling part is surrounded by yellow dotted line in the Fig. 12. Seen from the figure, pickling parts show that the smooth surface of the enamel coating, and no local corrosion phenomenon, found that pickling in good remove steaming and plated at the same time, does not damage to enamel basement. The rainbow-like fringe on the left of the pickling part should be different elements or oxides with different valence states of the same element. The specific chemical composition has not been further analyzed here, but the results of local experimental cleaning by dilute hydrochloric acid show that the oxides here can also be removed by pickling. Therefore, the enamel coated material plate has the ability of reuse in theory.

5   Conclusions

By characterizing the phase composition, composition, hardness and microstructure of enamel coating at the interface between coating and substrate, the following conclusions are obtained.

(1) The enamel coating is closely bonded to the substrate, and the coating itself has high density and low roughness. The enamel coating is closely bonded with the substrate due to the chemical bonding of Fe-rich Co phase and mechanical tooth bonding;

(2) Ce and Fe in stainless steel will interact with each other to form a solid solution, resulting in greater roughness of stainless steel plate, cannot be reused;

(3) Enamel coating can be stable in high temperature service. Silicon and cerium metal form a good chemical bond, so that the steam metal does not fall off;

Enamel coating has the ability of acid, alkali and high temperature oxidation corrosion. The bonding mode with cerium metal is non-diffusive and no corrosion occurs at the bonding interface. Therefore, pickling or high temperature oxidation can be used to remove cerium metal without damaging the enamel coating, so as to achieve multiple reuse of the material plate.

References

1. Brinkmann, U., Hartig, W., Telle, H., et al.: Isotope selective photoionization of Calcium using two-step laser excitation. Appl. Phys. **5**, 109–115 (1974)
2. Fromm, C.: Theory. In: Spectral Evolution in Blazars. ST, pp. 11–36. Springer, Cham (2015). https://doi.org/10.1007/978-3-319-10768-4_2
3. Tang, Z.L., Wang, F.H., Wu, W.T.: Effect of a sputtered TiAlCr coating on the oxidation resistance of TiAl intermetallic compound. Oxid. Met. **48**, 511 (1997)
4. Xiong, Y.M., Zhu, S.L., Wang, F.H.: Effect of ultra-fine enamel coating on the oxidation and mechanicalproperty of Ti60 alloy. Acta Metall. Sin. **40**(7), 768 (2004)
5. Liao, Y.M., Feng, M., Chen, M.H., et al.: Comparative study of hot corrosion behavior of the enamel based composite coatings and the arc ion plating NiCrAlY on TiAl alloy. Acta Metall. Sin. **55**(2), 61–69 (2019)
6. Guo, C.A., Chen, M.H., Liao, Y.M., et al.: Protection mechanism study of enamel-based composite coatings under the simulated combusting gas shock. Acta Metall. Sin. **54**(12), 113–120 (2018)
7. Ni, Y.R., Lu, C.H., Zhang, Y.: Effect of rare earth on glass formation and thermal expansion of boroaluminasilicate glass. Chinese Rare Earths **27**(1), 83–86 (2006)
8. An, Z.B., Zhang, P.Y., Shen, X.J., et al.: Effect of CeO_2 on microstructure and thermal shock resistance of W-2 high temperature enamel coating. Hot Working Technol. **20**(45), 140–142 (2016)
9. Han, T., Wang, Y., Chen, Y.H., et al.: Effect of cerium oxide on the adhesiveness of glass coating and base metal. J. Univ. Petroleum **26**(5), 68–70 (2002)
10. Zhu, Y.M., Wang, D.W.: Studies of heat-transfer in the crucible pool with the heat of the electron gun. Atomic Energy Sci. Technol. **34**(3), 238–243 (2000)
11. Li, F.J., Chen, M.H., Zhang, Z.M., et al.: Preparation and thermal shock behavior of a metal-enamel high-temperature protective coating. J. Chin. Soc. Corrosion Protection **39**(5), 411–416 (2019)
12. Xiao, J.X., Wang, D.W.: Study of heat transfer of molten cavity with solid-liquid interface heated by electron beam in crucible. J. Tsinghua Univ. (Sci. & Tech.) **39**(10), 56–59 (1999)
13. Xiao, J.X., Wang, D.W.: Numerical simulation dynamic process of 2-D metal evaporation. J. Tsinghua. Univ. (Sci. & Tech.) **39**(10), 52–55 (1999)

14. Xiao, J.X., Wang, D.W.: Research on metal atom evaporation with 2-D steady flows. Atomic Energy Sci. Technol. **34**(3), 244–251 (2000)
15. Xie, G.F., Wang, D.W., Ying, C.T.: The collector plate's influence on 2-D metal evaporation. J. Tsinghua Univ. (Sci, & Tech.) **42**(5), 584–586 (2002)
16. Yuan, K.X., Xu, P.F., Yu, P.Z., et al.: Investigation of ion extraction in laser isotope separation. J. At. Mol. Phys. **10**(3), 2839–2843 (1993)
17. Shao, G.X., Gou, W.B., Wen, R.C., et al.: Enamal. Light Industry Press, Beijing (1983)
18. Li, W., Chen, M., Wu, M., et al.: Microstructure and oxidation behavior of a SiC-Al$_2$O$_3$-glass composite coating on Ti-47Al-2Cr-2Nb alloy. Corros. Sci. **87**, 179–186 (2014)
19. Wang, X., Chen, M., Zhu, S., et al.: Oxidation behavior of glass-based composite thermal barrier coating on K417G superalloy with a NiCoCrAlY bond coat at 1000 °C. Surf. Coat. Technol. **270**, 314–323 (2015)
20. Yu, Z.D., Chen, M.H., Chen, K., et al.: Corrosion of enamel with and without CaF$_2$ in molten aluminum at 750 °C. Corros. Sci. **148**, 228–236 (2019)
21. Chen, K., Chen, M.H., Yu, Z.D., et al.: Exploring the hindering mechanism of element Ti on the adherence of CoO-bearing one-coat enamel/steel. Int. J. Appl. Ceram. Technol. **16**, 185–194 (2019)

Discussion on Common Bolt Scuffing Factors and Control Measures in the Installation and Maintenance Stage of Nuclear Power Plant

Xuefeng Gong[✉], Xiaohan Feng, Xue Liu, Lianjun Mu, and Jianxiang Lu

China Nuclear Industry 23 Construction Co., Ltd., Liaoning, Huludao, China
903837621@qq.com, {liuxue,mulianjun,lujianxiang}@cni23.com

Abstract. Because of its high control precision, high efficiency, easy operation and safe to threads, bolt tensioning is widely used in many mainstream reactor types of nuclear power plants at home and abroad, such as M310, EPR, VVER, AP/CAP and HPR 1000. It plays an indispensable role in the installation and removal of foundation fixing bolts and flange connecting bolts of dynamic and static mechanical equipment in the construction and maintenance stage of domestic nuclear power plants. With the development and upgrading of bolt tensioner, the technology of bolt tensioning has become more and more mature. At present, it has become an irreplaceable means of bolt pre tightening.

However, in the installation and maintenance stage of nuclear power plant, the fixing bolts and flange connecting bolts of mechanical equipment will still be jammed, damaged or even be scuffed. This situation may cause damage to bolts and bolt holes, which requires additional repair and rework costs and the construction period would delayed, or it may cause scrapping of bolts and bolt holes, and even affect the main functions of equipment and flanges, cause more serious economic losses and even nuclear safety accidents.

This paper analyzes the common bolt scuffing factors in the installation and maintenance stage of nuclear power plant through the experience of actual disposal means on site of bolt tensioning and scuffing, and defines the corresponding control means pertinently, so as to reduce the bolt scuffing probability, and then reduce the additional cost in the installation and maintenance stage and even the probability of nuclear safety accident.

Mainly analyze from the aspects of thread material, working environment, manufacturing tolerance, thread cleaning, bolt assembly, bolt tensioning and bolt fastening, and formulate standard and effective work plans for thread material inspection, working environment isolation, manufacturing tolerance inspection, thread cleaning, bolt assembly, bolt tensioning and bolt fastening in combination with the actual situation of the construction site, so as to ensure the reduction or even elimination of nuclear power plant installation The probability of bolt scuffing in the maintenance stage can enhance the quality of nuclear power installation and maintenance at the construction site of the nuclear power plant and improve the operation safety probability of the nuclear power plant.

Keywords: Bolt tensioning · Scuffing · Nuclear power plant

1 Introduction

1.1 Research Background

1.1.1 Application Situation of Bolt Tension in Nuclear Power Plant During Installation and Maintenance at Home and Abroad

The pre tightening method of bolt tension is widely used in the installation and maintenance stages of many mainstream pressurized water reactor types of nuclear power plants in operation and under construction, such as M310/EPR, VVER, AP/CAP, Hualong 1, and other fourth-generation mainstream nuclear power plants in the future, such as high temperature gas cooled reactor, molten salt cooled reactor, sodium cooled reactor, etc., which are in the stage of experimental construction.

The pre tightening method of bolt tensioning is easy to operate, has high tensioning precision, does not damage the thread, and is not affected by the operation space and environment. Bolt tensioners can be used individually or in groups. Multiple tensioners can be used in parallel, which can not only improve work efficiency, but also ensure the uniformity of force on multiple bolts, which is particularly important in the flange connection of high-pressure seal. For example, the main bolts connecting the pressurized water reactor pressure vessel and the head cover, the primary and secondary side manholes of the steam generator of the pressurized water reactor cooling system, and the flange connecting bolts of the primary circuit helium pipe of the high temperature gas cooled reactor all need to be tensioned and locked with a paralleling bolt tensioner.

1.1.2 Hazard of "Scuffing" of Bolt Tensioner, Bolt and Nut

Due to its simple structure, easy to carry and connect, convenient operation and simple introduction for operators, the hidden safety hazards of the bolt tensioner are easy to be ignored. On the one hand, during the bolt tensioning process, the bolt tensioner is blocked with the flange, nut and bolt, which is not easy to be found, especially during the use of the parallel bolt tensioner. Once the bolt tensioner is jammed with a bolt, nut or flange surface, due to its ultra-high pressure and ultra-high tensioning force, it is very easy to cause oil pipe cracking, thread fracture or even bolt fracture, and then cause the bolt tensioner to slip off. The operators and supervisors are easy to be hit by objects and mechanical injuries because they can't avoid them; On the other hand, due to the influence of the material, cleanliness, operating environment, manufacturing tolerance and many other factors of bolt, nut and bolt hole, after one or more times of tensioning, the thread is damaged or even glued and broken, resulting in the bolt being stuck in the bolt hole or the nut being stuck on the bolt, which is often a disastrous accident in the flange connection of high-pressure seal. The bolt and threaded hole thread will be damaged and need to be reworked and repaired, which will affect the construction period; In serious cases, the bolts, nuts and bolt holes will be scrapped, which will seriously affect the construction period and leave serious potential safety hazards.

For example, in the maintenance stage of a nuclear power plant, it was found that the main bolt connecting the reactor pressure vessel and the top cover was stuck in the main bolt hole of the reactor pressure vessel, the thread was glued and broken, and the main bolt was removed after the bolt was broken. It involves the breaking and re

manufacturing of the main bolts and the repair of the main bolt holes of the reactor pressure vessel, resulting in great economic losses; In the installation stage of a nuclear power plant, due to improper operation by the construction personnel, the thread of the steam generator anchor bolt of the reactor cooling system was jammed with the edge of the bolt hole after tensioning, which was not found and handled in time, resulting in the fracture of the anchor bolt at the thread, springing up and impacting the steel structure beam between the steam generators. Fortunately, no personal injury was caused.

1.2 Research Purpose and Method

1.2.1 Research Purpose

By discussing the standard operation and precautions of bolt tensioning in the installation and maintenance stage of nuclear power plant, this paper provides normative reference for the bolt tensioning operation in the installation and maintenance stage of nuclear power plant, ensures the safety and reliability of the bolt tensioning operation in the installation and maintenance stage of nuclear power plant, ensures the personal safety of construction personnel, improves the construction quality, and builds a strong nuclear safety defense line.

1.2.2 Research Methods

Step 1: case analysis of bolt tension during installation and maintenance of nuclear power plant;
Step 2: standardized operation process of bolt tension during installation and maintenance of nuclear power plant.

2 Detailed Description

2.1 Case Analysis of Bolt Tension During Installation and Maintenance of Nuclear Power Plant

2.1.1 The "Scuffing" of Anchor Bolts and Nuts for Lateral Support of Reactor Coolant Pump in a Nuclear Power Plant

During the installation of M310 pressurized water reactor unit in a nuclear power plant, the anchor bolts of the lateral support 3# hydraulic damper anchor seat of the reactor coolant pump were tensioned. It was found that after the fractional tensioning (three times of tensioning locking at 20%, 60% and 100% of the maximum tensioning torque + one-time tensioning verification at 100% of the maximum tensioning torque, and the tensioning torque was converted by the reading of the hydraulic pressure gauge), after the maximum tensioning torque reached 60%, the tightening resistance of some anchor nuts became larger, and when the maximum tensioning torque reached about 69%, the nuts could not rotate. Immediately, tensile verification was carried out on all the anchor bolts of the hydraulic damper anchor seats supporting the lateral support of the three

loop reactor coolant pumps on site, and it was found that the anchor nuts of most of the anchor bolts "bite" after reaching about 69% of the maximum tensile torque.

Through analysis and demonstration, the cause of "scuffing" of the anchor bolt and nut is analyzed on site and verified step by step.

Firstly, it is assumed that the stroke of the bolt tensioner does not meet the installation of the anchor bolt on site, the anchor nut interferes with the inner wall of the bolt tensioner, and the friction is too large to rotate the nut. On site verification was carried out immediately. After the anchor nut was coated with grease, it was still "locked" after being tensioned again, and after the bolt tensioner was removed, the inner wall was not adhered with grease. Therefore, the conjecture that the anchor nut interfered with the inner wall of the bolt tensioner was denied, and the problem of the bolt and nut itself was considered.

Then, consult the manufacturer's completion documents, and arrange the manufacturer's personnel to recheck the go no go gauges on the anchor bolts and nuts. The manufacturer's personnel used ring thread go no go gauges with a tolerance code of 6h for anchor bolts and cylindrical thread go no go gauges with a tolerance code of 6h for anchor nuts. Due to the phosphate coating on the surface of anchor bolts and nuts, some of the go no go gauge inspection results were unqualified. At the same time, by comparing with the design documents, it is found that the tolerance zone used by anchor bolts and nuts does not meet the matching requirements of anchor bolts 6h and nuts 7h in the design documents.

Therefore, it is determined that the main cause of the "scuffing" of the anchor bolts and nuts of the lateral support of the reactor coolant pump this time is the manufacturer's wrong use of the anchor bolts and nut tolerance zone. At the same time, the manufacturer's inspection time of the go no go gauge is before the phosphating of the anchor bolts and nuts, and the go no go gauge of the anchor bolts and nuts is not rechecked after the phosphating. Afterwards, the anchor bolts and nuts were returned to the factory according to the process, and finally the tensile work of the anchor bolts of the lateral support of the reactor coolant pump was successfully completed.

2.1.2 Other Common Bolt and Nut "Bite" Cases in the Installation and Maintenance Stage of a Nuclear Power Plant

In the process of anchor bolt tensioning of steam generator primary and secondary side inspection holes and pressurizer inspection holes during the installation and maintenance of M310 pressurized water reactor unit in a nuclear power plant, it is summarized that the main aspects affecting the tension safety of anchor bolts are as follows:

First, cleanliness control. If there are burrs, iron filings, rust or small slag inclusions on the internal thread of the anchor bolt hole on the flange surface, the external thread of the anchor bolt or the internal thread surface of the nut, they will be involved in the thread connection pair during the thread tightening process, and then squeezed into the internal and external thread connection thread, increasing the relative friction between the local internal and external threads, and causing local thread jamming under the influence of the force between the threads, high temperature, vibration and other conditions, Even glued, resulting in "bite" of anchor bolts and nuts.

Second, the control of relative cooperation relationship. The anchor bolt holes, anchor bolts and nuts used for the inspection holes on the primary and secondary sides of the steam generator and the inspection holes of the pressurizer are sealed with steel seal inscriptions to ensure that the anchor bolt holes, anchor bolts and nuts are used together during the disassembly and assembly process during the installation and commissioning stages. After many times of connection, coordination and tension, and under the high temperature conditions during the test and operation stages, the anchor bolt holes The internal and external threads of the anchor bolt and nut squeeze and run in with each other, and the connection pair is stable, avoiding the "scuffing" of the anchor bolt and nut caused by the matching relationship between the internal and external threads.

Third, prevent the misuse of "bite dead" agents. In order to prevent the anchor bolts and nuts from seizing, anti "seizing" agents such as molybdenum disulfide and N5000 will be used during the installation and commissioning of the nuclear power plant. The correct use of anti seize agent reduces the risk of "seizing" of anchor bolts and nuts to a certain extent. However, due to the characteristics of high temperature and high pressure of internal medium during the experiment and operation of steam generator and pressurizer, the wrong use of anti seize agent that is not resistant to high temperature will cause "seizing" of anchor bolts and nuts.

Fourth, improper operation methods. The correct installation method of anchor bolts and nuts is to manually install and tighten the anchor bolts and nuts. If manual tightening fails, immediately stop tightening and remove the anchor bolts and nuts for inspection. During the installation and commissioning of nuclear power plants, in order to pursue progress, many construction personnel will tighten the anchor bolts and nuts by increasing the torque, especially when the anchor bolts and nuts are tightened and jammed, increase the tightening force and lengthen the force arm, which will greatly increase the risk of "bite" of the anchor bolts and nuts.

Fifth, improper selection of tensioning tools. Bolt tensioning tools are divided into single type and parallel type, which should be paid special attention when using parallel bolt tensioning machine. The deviation of the relative position of the bolt hole on the flange surface and the manufacturing error of the parallel bolt tensioner will cause the parallel bolt tensioner to jam with the anchor bolt and nut, and then cause the anchor bolt to tilt in the bolt hole, and the anchor bolt to jam with the inspection hole on the primary and secondary sides of the steam generator or the sealing cover plate of the inspection hole of the pressurizer. If the operator fails to check in place, continue to complete the tensioning, the anchor bolt The risk of nut "seizing" is high.

2.2 Specification and Operation Process of Bolt Tensioning During Installation and Maintenance of Nuclear Power Plant

First of all, in order to prevent the design deviation of bolt tensioning in the installation and maintenance stage of nuclear power plant, it is necessary to carefully identify the upstream documents when technicians prepare the scheme. For the anchor bolts and nuts that need to be tensioned, especially the bolts and nuts with large diameter, it is necessary to check the tolerance zone selected by the designer to avoid the "bite" event of anchor bolts and nuts caused by design deviation.

Secondly, during the installation and maintenance stage of the nuclear power plant, the compliance acceptance of threaded holes, anchor bolts and nuts should be carried out before the on-site construction. If serious manufacturing deviations of threaded holes, anchor bolts and nuts are found, they should be reported in time, and repaired, reworked or scrapped according to the relevant procedures. At the same time, the material of threaded holes, anchor bolts and nuts shall be inspected. If there is a risk of "seizing", the corresponding process shall be opened in time for treatment.

Finally, it is mainly necessary to control the operation specifications of construction personnel:

First, control the cleanliness, carefully clean the threaded holes, anchor bolts and nuts, remove foreign matters, and protect against foreign matters;

Second, control the relative cooperation relationship, code and record the threaded holes, anchor bolts and nuts, and check them many times after installation to prevent misuse;

Third, before the installation of anchor bolts and nuts, apply an appropriate amount of anti seize agent according to the bolt material, control the dosage and use model, and ensure that the use of anti seize agent conforms to the corresponding working environment of anchor bolts and nuts;

Fourth, the selection of tensioning tools and operation methods are standardized. Single or parallel bolt tensioners are correctly selected and used in strict accordance with the operation requirements of bolt tensioners. The following is a detailed description of the tensioning of anchor bolts and nuts at the primary and secondary inspection holes of steam generators during the installation and maintenance of M310 PWR units in a nuclear power plant:

1. During the installation of anchor bolts and nuts, install and tighten them manually, check whether there is obvious jamming during the installation of anchor bolts and nuts, and return half a circle to one circle after tightening;
2. Install the bolt tensioner. During the installation process, check whether there is jam between the bolt tensioner and the anchor bolt and nut, and tighten the fixing nut of the bolt tensioner evenly. Check that the bolt tensioner can move relatively and all anchor bolts are tightened evenly;
3. Install the dial gauge base and dial gauge, ensure that the dial gauge base is tightened evenly, there is no jam with the bolt tensioner, and the dial gauge reading is normal;
4. Establish a control area and set up a warning line. Non operators are not allowed to enter the bolt tensioner operation area;
5. Start the bolt tensioner, tighten and tighten the nuts according to the three-time tension locking of 20%, 60% and 100% of the maximum tension torque + one-time tension verification of 100% of the maximum tension torque, and ensure that all nuts are tightened evenly;
6. Check whether the maximum elongation and residual elongation of the bolt meet the operating requirements of the anchor bolt and nut; Remove the bolt tensioner, remove the fixing nut of the bolt tensioner evenly, remove the bolt tensioner, and adjust the position of the bolt tensioner and nut in case of jamming;
7. Clean and protect anchor bolts and nuts.

3 Conclusions

After eliminating the two uncontrollable "bite" factors of design deviation and manufacturing deviation at the site during the installation and maintenance of the nuclear power plant, we should mainly start with the standardized operation of the construction personnel to ensure that the probability of "bite" of anchor bolts and nuts caused by human factors during the installation and maintenance of the nuclear power plant is reduced.

It is necessary to carry out necessary pre job training and pre job disclosure for the construction personnel who carry out the tensioning operation of anchor bolts and nuts, and carry out necessary inspections during the tensioning process of anchor bolts and nuts, so as to reduce the "bite" of anchor bolts and nuts caused by human factors during the installation and maintenance of nuclear power plants.

References

1. Jian, W.: Cause analysis and solution of bolt scuffing of main steam isolation valve of a nuclear power unit [c] Zhejiang University of technology (2020)
2. Xie, J.: Analysis on the causes of bolt scuffing and preventive measures. Sci. Technol. Innov. **13**,173–174 (2019)
3. Shi, Y.: Study on the treatment of bolt scuffing of reactor pressure vessel flange in a nuclear power plant Manage. Technol. Small Medium-sized Enterprises (issue of mid ten day) **07**, 172–173 (2018)
4. Sangf, G.: Application of drilling technology in the treatment of reactor bolt scuffing. Equipment Manage. Maintenance **(01)**, 36–37 (2018)
5. Hu, M., Wei, Z., Luo, K., Li, Wangf: Cause analysis of bolt "scuffing" of main steam isolation valve in secondary circuit of nuclear power unit. China Nuclear Power. **8**(01), 75–78 (2015)

Study on Unstructured-Mesh-Based Importance Sampling Method of Monte Carlo Simulation

Hanlin Shu, Liangzhi Cao$^{(\boxtimes)}$, Qingming He, Tao Dai, Zhangpeng Huang, and Hongchun Wu

School of Nuclear Science and Technology, Xi'an Jiaotong University, Xi'an, Shaanxi, People's Republic of China
caolz@xjtu.edu.cn

Abstract. Monte Carlo (MC) method is widely adopted in radiation transport calculation due to its high accuracy, but suffers from high variance in deep-penetration problems. To obtain reasonable results, variance reduction techniques are necessary and thus be widely studied worldwide. The Consistent Adjoint Driven Importance Sampling (CADIS) method is proved to be an effective variance reduction technique, which generally employs finite-difference discrete ordinate (S_N) code to obtain the adjoint flux, and generates parameters of source biasing and weight window for MC code. However, the finite-difference method, which models through structural meshes, will introduce considerable geometric approximations in complex geometry. The finite element method (FEM) performs calculations with lower truncation error and can employ unstructured meshes, which are capable of modeling complex geometry with relatively lower geometric approximations. Therefore, the adjoint flux calculated by unstructured-mesh FEM is able to generate more appropriate parameters of source biasing and weight window which will further reduce the variance of forward MC calculation. A fully automatic unstructured-mesh CADIS method is studied and implemented in this paper, parallel three-dimensional unstructured-mesh neutron-photon coupled transport calculation code NECP-SUN based on the S_N method and discontinuous FEM is developed and embedded into the MC code NECP-MCX to calculate the adjoint flux with unstructured meshes. The updated code is applied to the HBR-2 benchmark, the numerical results show that the relative statistic error is reduced by up to 22% compared to the traditional CADIS method while the calculation results are closer to the measurements and the figure of merit (FOM) is increased by 3–4 orders comparing to direct MC simulation.

Keywords: Neutron transport calculation · Monte Carlo method · Variance reduction techniques · CADIS method · Unstructured mesh

1 Introduction

In order to improve the efficiency of the Monte Carlo (MC) method, various variance reduction techniques have been proposed, such as geometrical importance, weight window, source biasing, etc. [1]. These methods perform well in most scenarios but require

the users to set relevant parameters (such as geometrical importance, weight window boundary, and source sampling probability) which are strongly related to the problem. Therefore, high demands are put forward for the user's experience and ability to analyze problems. For the purpose of optimizing the selection of parameters and reducing the burden on users, a variety of automated methods which generate parameters for weight window and source biasing based on the importance distribution obtained by forward or adjoint transport calculation have been proposed. Among the above methods, the Consistent Adjoint Driven Importance Sampling (CADIS) method, which is proposed by Wagner [2] can automatically generate the parameters of weight window and source biasing for MC simulation based on the adjoint flux calculated by the discrete ordinate (S_N) method. The CADIS method is proved to be effective in practical applications and is applied to the ADVANTG [3] and the MAVRIC [4], which is the shielding analysis tool of SCALE.

Most traditional CADIS implementations depend on the adjoint flux calculated by finite-difference S_N code which can only model geometry with structural meshes. The structural meshes can only approximate the curve surfaces by reducing the mesh size thus considerable approximations will be introduced when modeling complex geometry through finite-difference code. Unstructured meshes are capable of modeling complex geometry with relatively lower approximations. Therefore, the adjoint flux obtained through unstructured meshes is more accurate, and can better describe the distribution of the importance of particles in space and energy, resulting in a more reasonable source biasing and weight window. The theoretical research and practical application of the traditional CADIS method based on structural mesh have been relatively mature [5], but the research on the unstructured-mesh CADIS method is rarely reported. The Finite Element method (FEM) can utilize unstructured meshes to perform transport calculations and the truncation error is inherently lower than the finite-difference method. Numerous researches on FEM have been carried out, including solving the second-order neutron transport equation through the continuous finite element method [6], solving the first-order neutron transport equation through stabilized finite element method [7], and solving the first-order neutron transport equation through discontinuous finite element method [8]. Among them, the numerical method which combines the S_N method and the discontinuous FEM to discretize the first-order neutron transport equation in space and angle respectively shows strong stability in solving the problem with the internal vacuum region, and can effectively realize high-order angular expansion calculation, which makes it well applicable to the strong angular anisotropy problems such as shielding calculation.

In this paper, the parallel three-dimensional unstructured-mesh neutron-photon coupling transport calculation code NECP-SUN based on the discrete ordinate method and discontinuous finite element method is developed. Furtherly, the fully automatic unstructured-mesh CADIS method is implemented by embedding NECP-SUN into MC code NECP-MCX [9] and is applied to calculate the specific activity of the radiometric monitor in the cavity of the HBR-2 benchmark. The numerical results show that, compared with the traditional CADIS method, the unstructured-mesh CADIS method can obtain results that are closer to measurements with a lower relative statistical error, and its figure of merit (FOM) raised 3–4 orders compared to direct MC simulation.

2   Method and Implementation

2.1   Description of Unstructured-Mesh CADIS Method

The theoretical basis of the unstructured-mesh CADIS method includes the S_N method and discontinuous FEM, as well as the source bias and weight window of the CADIS method. In this section, the local weighted residual form and global variational form of adjoint neutron transport equation are derived firstly, and then the basic theory of source biasing and weight window is briefly illustrated.

2.1.1   The Discretization of Aadjoint Transport Equation Through S_N Method and FEM

The steady-state linear Boltzmann transport equation without fissile materials is:

$$\boldsymbol{\Omega}\nabla\phi(\boldsymbol{r}, E, \boldsymbol{\Omega}) + \Sigma_t(\boldsymbol{r}, E)\phi(\boldsymbol{r}, E, \boldsymbol{\Omega})$$
$$= \iint \Sigma_s(\boldsymbol{r}, E', \boldsymbol{\Omega}' \to E, \boldsymbol{\Omega})\phi(\boldsymbol{r}, E', \boldsymbol{\Omega}')dE'd\boldsymbol{\Omega}' + S(\boldsymbol{r}, E, \boldsymbol{\Omega}) \tag{1}$$

where $\boldsymbol{r}$ is space, E is energy, $\boldsymbol{\Omega}$ is direction, Σt is total macro-cross section, cm^{-1}, ϕ is forward flux, Σs is scattering macro-cross section, S is the forward source, particle $\cdot$ $cm^{-3} \cdot s^{-1}$.

The adjoint equation of Eq. (1) can be constructed as Eq. (2):

$$- \boldsymbol{\Omega}\nabla\phi^*(\boldsymbol{r}, E, \boldsymbol{\Omega}) + \Sigma_t(\boldsymbol{r}, E)\phi^*(\boldsymbol{r}, E, \boldsymbol{\Omega})$$
$$= \iint \Sigma_s(\boldsymbol{r}, E, \boldsymbol{\Omega} \to E', \boldsymbol{\Omega}')\phi^*(\boldsymbol{r}, E', \boldsymbol{\Omega}')dE'd\boldsymbol{\Omega}' + S^*(\boldsymbol{r}, E, \boldsymbol{\Omega}) \tag{2}$$

where ϕ^* is adjoint flux, S^* is adjoint source.

The multi-group form adjoint transport equation can be obtained by integrating both sides of Eq. (2) over the energy interval $[E_g, E_{g-1}]$:

$$- \boldsymbol{\Omega}\nabla\phi_g^*(\boldsymbol{r}, \boldsymbol{\Omega}) + \Sigma_t^g(\boldsymbol{r})\phi_g^*(\boldsymbol{r}, \boldsymbol{\Omega})$$
$$= \sum_{g'=g}^{1} \int \Sigma_s^{g \to g'}(\boldsymbol{r}, \boldsymbol{\Omega} \to \boldsymbol{\Omega}')\phi_{g'}^*(\boldsymbol{r}, \boldsymbol{\Omega}')d\boldsymbol{\Omega}' + S_g^*(\boldsymbol{r}, \boldsymbol{\Omega}) \tag{3}$$

The S_N method can be introduced by integrating Eq. (3) on the region $\Delta\boldsymbol{\Omega}_m$ near the selected discrete direction $\boldsymbol{\Omega}_m(\mu_m, \eta_m, \xi_m), m = 1, \cdots, M$:

$$- \boldsymbol{\Omega}_m\nabla\phi_g^*(\boldsymbol{r}, \boldsymbol{\Omega}_m) + \Sigma_t^g(\boldsymbol{r})\phi_g^*(\boldsymbol{r}, \boldsymbol{\Omega}_m)$$
$$= \sum_{g'=g}^{1} \Sigma_s^{g \to g'}(\boldsymbol{r}, \boldsymbol{\Omega}_m \to \boldsymbol{\Omega}'_m)\phi_{g'}^*(\boldsymbol{r}, \boldsymbol{\Omega}'_m) + S_g^*(\boldsymbol{r}, \boldsymbol{\Omega}_m) \tag{4}$$

Expanding the scattering term with the spherical harmonics function and expressing the angular discretization as a subscript, the discrete ordinate form of the steady-state

multi-group adjoint neutron transport equation without fissile materials can be described by Eq. (5):

$$-\boldsymbol{\Omega}_m \nabla \phi_{g,m}^*(\boldsymbol{r}) + \Sigma_t^g(\boldsymbol{r})\phi_{g,m}^*(\boldsymbol{r})$$

$$= \sum_{g'=g}^{1} \sum_{l=0}^{\infty} \Sigma_{s,1}^{g \to g'}(\boldsymbol{r}) \sum_{n=-l}^{l} Y_l^n(\boldsymbol{\Omega}_m) \sum_{m'=0}^{M} w_{m'} Y_l^n(\boldsymbol{\Omega}_{m'})\phi_{g',m'}^*(\boldsymbol{r}) + S_{g,m}^*(\boldsymbol{r}) \qquad (5)$$

Equation (5) only contains spatial-related unknown variables, which can be discretized in the spatial dimension by the discontinuous Galerkin method. Since the right-hand side of Eq. (5) can be regarded as a known function in S_N calculation, it can be combined into a spatially related known function $Q_{g,m}^*(\boldsymbol{r})$:

$$-\boldsymbol{\Omega}_m \nabla \phi_{g,m}^*(\boldsymbol{r}) + \Sigma_t^g(\boldsymbol{r})\phi_{g,m}^*(\boldsymbol{r}) = Q_{g,m}^*(\boldsymbol{r}) \qquad (6)$$

The solution area can be divided into non-overlapping mesh elements and the dimensional approximation functions can be defined on them. Integrating the Eq. (6) on D^k ($k = 1,\ldots, K$) with each term multiplied by the verification function $\phi_{g,m}^t$ which is arbitrarily selected from the aforementioned dimensional approximation functions:

$$\int_{D^k} -\phi_{g,m}^t(\boldsymbol{r})\boldsymbol{\Omega}_m \nabla \phi_{g,m}^*(\boldsymbol{r})\mathrm{d}\boldsymbol{r}$$

$$+ \int_{D^k} \phi_{g,m}^t(\boldsymbol{r})\Sigma_t^g(\boldsymbol{r})\phi_{g,m}^*(\boldsymbol{r})\mathrm{d}\boldsymbol{r}$$

$$= \int_{D^k} \phi_{g,m}^t(\boldsymbol{r})Q_{g,m}^*(\boldsymbol{r})\mathrm{d}\boldsymbol{r} \qquad (7)$$

After integrating the first term at the left-hand side of Eq. (7) by parts and applying the divergence theorem:

$$\int_{D^k} -\phi_{g,m}^t(\boldsymbol{r})\boldsymbol{\Omega}_m \nabla \phi_{g,m}^*(\boldsymbol{r})\mathrm{d}\boldsymbol{r}$$

$$= -\int_{\partial D^k} (\boldsymbol{\Omega}_m \cdot \boldsymbol{n})\phi_{g,m}^t(\boldsymbol{r})\phi_{g,m}^*(\boldsymbol{r})\mathrm{d}s$$

$$+ \int_{D^k} \phi_{g,m}^*(\boldsymbol{r})\boldsymbol{\Omega}_m \nabla \phi_{g,m}^t(\boldsymbol{r})\mathrm{d}\boldsymbol{r} \qquad (8)$$

The local Galerkin weighted residual form of Eq. (6) can be obtained by substituting Eq. (8) into Eq. (7) and adopting the upwind flux, which is, finding the function $\phi_{g,m}^*$ to make sure Eq. (9) is satisfied for any testing function $\phi_{g,m}^t$ in $V(D^k)$:

$$(\phi_{g,m}^*, (\boldsymbol{\Omega}_m \cdot \nabla + \Sigma_t^g)\phi_{g,m}^t) - \left\langle \phi_{g,m}^{*-}, \phi_{g,m}^{t-} \right\rangle_{\partial D^{k+}}$$

$$+ \left\langle \phi_{g,m}^{*-}, \phi_{g,m}^{t+} \right\rangle_{\partial D^{k-}} = (\phi_{g,m}^t, Q_{g,m}^*) \qquad (9)$$

where,

$$(f, g)_{D^k} := \int_{D^k} f \cdot g \, \mathrm{d}\boldsymbol{r} \qquad (10)$$

$$\langle f, g \rangle_{\partial D^k} := \int_{\partial D^k} |\boldsymbol{\Omega} \cdot \boldsymbol{n}| f \cdot g \, \mathrm{d}s \tag{11}$$

$$\begin{cases} \phi_{g,m}^{+} = \lim_{\varepsilon \to 0^{+}} \phi_{g,m}(\boldsymbol{r} + \varepsilon \boldsymbol{\Omega}_m) \\ \phi_{g,m}^{-} = \lim_{\varepsilon \to 0^{-}} \phi_{g,m}(\boldsymbol{r} + \varepsilon \boldsymbol{\Omega}_m) \end{cases} \tag{12}$$

$$\begin{cases} \partial D^{k+} = \left\{ \boldsymbol{r} \in \partial D^k : \boldsymbol{\Omega} \cdot \boldsymbol{n} \geq 0 \right\} \\ \partial D^{k-} = \left\{ \boldsymbol{r} \in \partial D^k : \boldsymbol{\Omega} \cdot \boldsymbol{n} < 0 \right\} \end{cases} \tag{13}$$

The global variational form of the steady-state S_N adjoint transport equation in the direction of a single discrete angle of a single group can be obtained by summarizing the Eq. (9) over all elements, that is, finding $\phi_{g,m}^{*}$ in V_{D_h} to make sure Eq. (14) is satisfied for any testing function $\phi_{g,m}^{*}$ in V_{D_h}:

$$\begin{aligned} &(\phi_{g,m}^{*}, (\boldsymbol{\Omega}_m \cdot \nabla + \Sigma_t^g)\phi_{g,m}^t)_{D_k} + \left\langle \left[\!\left[\phi_{g,m}^t \right]\!\right], \phi_{g,m}^{\mathrm{upwind}} \right\rangle_{E_k} \\ &+ \left\langle \phi_{g,m}^{t+}, \phi_{g,m}^{*+} \right\rangle_{\partial D_k^{+}} = \left(\sum_{g'=g}^{1} \sum_{l=0}^{\infty} \Sigma_{s,l}^{g \to g}(\boldsymbol{r}) \sum_{n=-l}^{l} Y_l^n(\boldsymbol{\Omega}_m) \right) \\ &\sum_{m'=1}^{M} w_{m'} Y_l^n(\boldsymbol{\Omega}_{m'}) \phi_{g',m'}^{*}(\boldsymbol{r}), \psi_{g,m}^t)_{D_k} \\ &+ \left\langle \phi_{g,m}^{t-}, \phi_{g,m}^{inc} \right\rangle_{\partial D_k^{-}} \\ &V_{D_k} := \{ v \in L^2(D) \ : \ v|_{D^k} \in V(D^k), \forall D^k \in D_h \} \\ &E_k := \bigcup_{D^k \subset D_k} \partial D^k / \partial D \end{aligned} \tag{14}$$

where, $\phi_{g,m}^{\mathrm{upwind}}$ is the value of upwind flux on the mesh interface, E_h is the set of mesh interfaces, and $\phi_{g,m}^{inc}$ is the boundary condition.

2.1.2 Source Biasing and Weight Window

Based on the adjoint theory, the response of the target region can be determined by Eq. (15):

$$\begin{aligned} R &= \int_{V_d} \mathrm{d}\boldsymbol{r} \int_0^{\infty} \mathrm{dE} \int_{4p} \phi(\boldsymbol{r}, \mathrm{E}, \boldsymbol{\Omega}) \sigma_d(\boldsymbol{r}, \mathrm{E}, \boldsymbol{\Omega}) \mathrm{d}\boldsymbol{\Omega} \\ &= \int_{V_s} \mathrm{d}\boldsymbol{r} \int_0^{\infty} \mathrm{dE} \int_{4p} \phi^{*}(\boldsymbol{r}, \mathrm{E}, \boldsymbol{\Omega}) \mathrm{S}(\boldsymbol{r}, \mathrm{E}, \boldsymbol{\Omega}) \mathrm{d}\boldsymbol{\Omega} \end{aligned} \tag{15}$$

where R is the response, V_d is the volume of the target region, cm^3, σ_d is the response function, and V_s is the volume of the forward source, cm^3.

It can be seen from Eq. (15) that the adjoint flux stands for the contribution of particles at a specific position, energy, and direction to the response of the target region. This is the theoretical basis for the CADIS method to generate parameters of source biasing and weight window based on adjoint flux.

With an appropriate bias function, the source biasing is able to sample more low-weight source particles in important space, energy, and angle ranges. The reducing factor

of initial weight is determined by the increasing factor of source particles to ensure the result is unbiased. To minimize the variance of the response of the target region, the bias function shown in Eq. (16) is recommended:

$$
\begin{aligned}
\widehat{S}(\boldsymbol{r}, E, \boldsymbol{\Omega}) &= \frac{\phi^*(\boldsymbol{r}, \mathrm{E}, \boldsymbol{\Omega})S(\boldsymbol{r}, \mathrm{E}, \boldsymbol{\Omega})}{R} \\
&= \frac{\phi^*(\boldsymbol{r}, \mathrm{E}, \boldsymbol{\Omega})S(\boldsymbol{r}, \mathrm{E}, \boldsymbol{\Omega})}{\int_{V_s} d\boldsymbol{r} \int_0^\infty dE \int_{4\pi} \phi^*(\boldsymbol{r}, \mathrm{E}, \boldsymbol{\Omega})S(\boldsymbol{r}, \mathrm{E}, \boldsymbol{\Omega})d\boldsymbol{\Omega}}
\end{aligned}
\tag{16}
$$

The initial weight of the corresponding source particle should be determined by Eq. (17):

$$
w = w_0 \frac{S(\boldsymbol{r}, E, \boldsymbol{\Omega})}{\widehat{S}(\boldsymbol{r}, E, \boldsymbol{\Omega})} = w_0 \frac{R}{\phi^*(\boldsymbol{r}, \mathrm{E}, \boldsymbol{\Omega})}
\tag{17}
$$

where w and w_0 are the initial weight of source particles with and without an unbiased source, respectively.

Weight window is a synergistic application of split and Russian roulette, which can be applied separately or simultaneously to the dimensions of space, energy, and angle. The upper and lower bounds of the weight window are used as a trigger of split and Russian roulette to ensure that the population and weight of particles maintain at a reasonable level. To minimize the variance of the response of the target region, the weight of the particles generated by the weight window should be consistent with Eq. (17). Thus, the mean value of the weight window can be determined by Eq. (18):

$$
\frac{w_t + w_b}{2} = w_0 \frac{R}{\phi^*(\boldsymbol{r}, \mathrm{E}, \boldsymbol{\Omega})}
\tag{18}
$$

where w_t and w_b are the upper and lower bound of the weight window, respectively. Practical experience indicates that to ensure the validity and applicability of the weight window, the gap between its upper and lower bounds should neither be too large nor too small. Therefore, most MC codes provide a default upper and lower bound ratio for the weight window and recommend users to generate a weight window with the default ratio. Thus, the lower bound of the weight window in Eq. (18) can be determined by Eq. (19) with the aforementioned upper and lower bound ratio c_u:

$$
w_b = w_0 \frac{2R}{(c_u + 1)\phi^*(\boldsymbol{r}, \mathrm{E}, \boldsymbol{\Omega})}
\tag{19}
$$

2.2 Implementation

Based on the theoretical model in Sect. 2.1, the parallel three-dimensional unstructured-mesh neutron-photon coupled transport calculation code NECP-SUN, which is capable of performing adjoint transport calculation based on the unstructured mesh is developed independently. NECP-MCX [10] is a MC particle transport simulation code with independent intellectual property rights developed by the Nuclear Engineering Computational Physics (NECP) laboratory of Xi'an Jiaotong University. The traditional structural-mesh-based CADIS method has already been fulfilled by coupling the NECP-MCX with
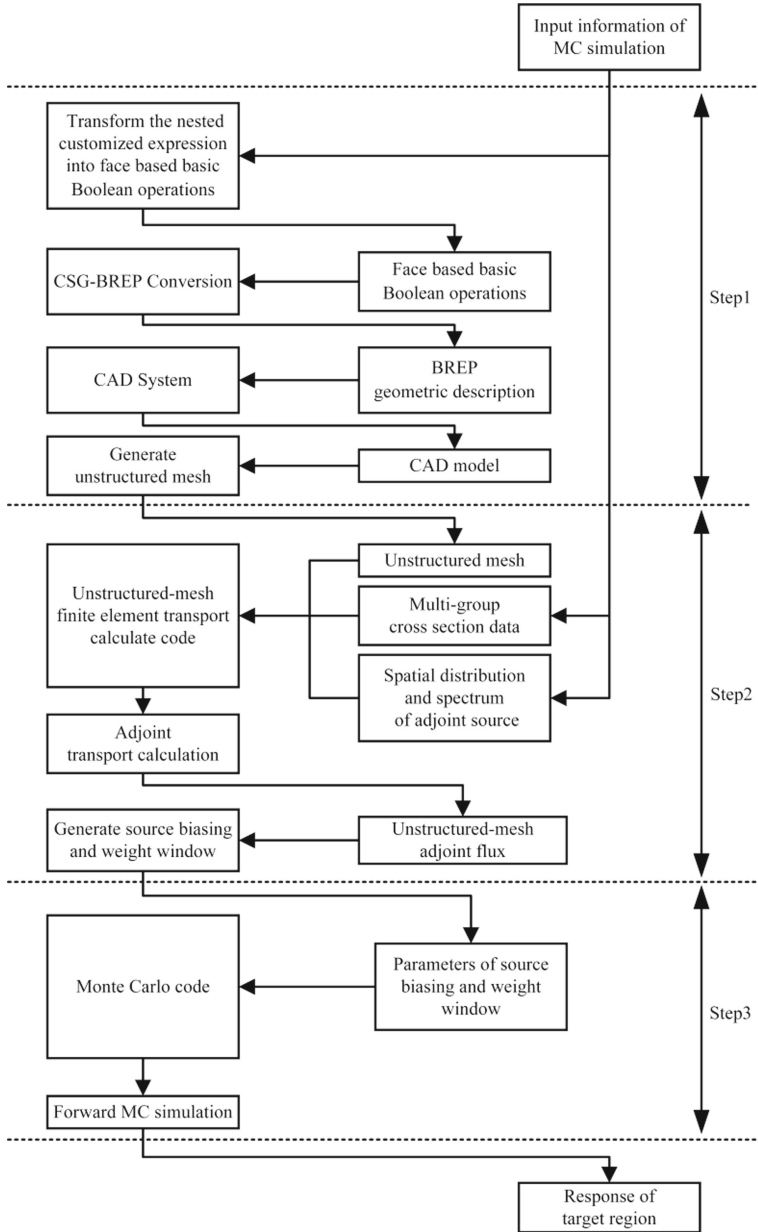
Fig. 1. Flowchart of unstructured-mesh CADIS method

the finite-difference S_N code NECP-Hydra [10]. To verify the method proposed in this paper, a coupling code based on unstructured-mesh CADIS is developed by embedding NECP-SUN into NECP-MCX as an adjoint transport solver. Figure 1 shows the flowchart of the unstructured-mesh CADIS method, which mainly consists of the following steps:

Step 1: Generate the unstructured mesh, the multi-group cross-section data, and the adjoint source which are required by FEM code based on the Constructive Solid Geometry (CSG) model, the continuous energy cross-section data, and the response characteristics of the tallied variable used in MC simulation, respectively.

Step 2: Obtain the distribution of adjoint flux on energy groups and unstructured meshes by performing the adjoint transport calculation based on the unstructured mesh, the multi-group cross-section data, and the adjoint source information generated in step 1.

Step 3: Perform forward MC simulation with the source biasing and weight window generated based on the distribution of adjoint flux provided by step 2 to obtain the response of the target region.

To implement the above processes, the following three problems need to be properly solved:

1) Building the computer-aided design (CAD) model corresponding to the CSG model,
2) Generating unstructured meshes,
3) Obtaining the adjoint source and cross-section data.

2.2.1   CSG-CAD Model Conversion

The unstructured mesh is generally generated based on the CAD model, thus it's necessary to build a CAD model corresponding to the CSG model used in MC simulation. Boundary representation (BREP) is a relatively mature solid geometric representation method and is widely used in commercial CAD systems. A series of CSG-BREP conversion tools have been developed to generate CAD models based on the uniform surface-based basic Boolean operation. However, the geometric information for MC codes is often described by text, and complex nested customized expressions such as universe and lattice are added to effectively describe the complex characteristics of nuclear facilities. Moreover, the geometric description texts of different Monte Carlo codes are quite different in format. Therefore, to generate a CAD model utilizing the CSG-BREP conversion tools, it's necessary to develop the analytic code for specific MC codes. The analytic code should be capable of parsing the geometric description text and translating the complex nested customized expression into uniform surface-based basic Boolean operations. The CSG-CAD conversion tool for NECP-MCX is developed and the specific processes are depicted in Fig. 2.

2.2.2   Unstructured Mesh Generation and the Local Mesh Refinement in the Target Region

The efficiency and accuracy of FEM calculation are determined by the quality of meshes. Many automatic mesh generation tools such as Gmsh and ICEM have been developed, which complete unstructured mesh generation within the global mesh size inputted by users. However, the following problems will occur when the automatically generated unstructured mesh is adopted in adjoint transport calculation: the size of the mesh in a specific region is determined by its geometric characteristics such as curvature and proximity. Unfortunately, the geometric characteristics are hardly irrelevant to the importance

of particles, which will lead to serious memory waste and reduce the efficiency and accuracy of adjoint transport calculation. To solve this problem, the local mesh refinement for the target region based on face meshing control is implemented. After the global face meshing is completed, the face mesh in the target region will be regenerated with a smaller size, and then the volume mesh generation will be performed based on the updated face mesh. The above process is shown in Fig. 3, in which the size of global meshes and meshes in the target region is automatically determined based on CSG model information.
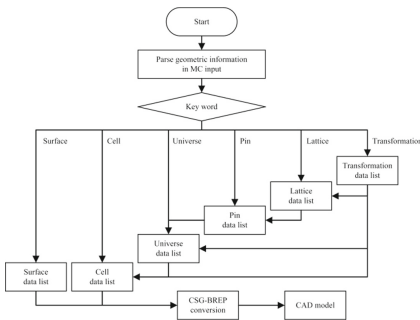
Fig. 2. Flowchart of CSG-CAD conversion
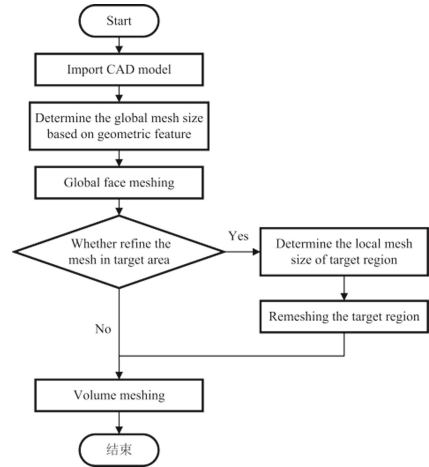
Fig. 3. Flowchart of unstructured mesh generation

2.2.3 Determination of Adjoint Source and Generation of Multi-group Cross-section Data

Multi-group macro-cross section data are essential to carry out adjoint transport calculations with deterministic code. The coupling code automatically parses the nucleon density of nuclides in MC input and generates corresponding macro-cross sections based on the prefabricated bugle96 database.

The spatial and energetic distribution of the adjoint source is dependent on the location of the tallied region and the response function of the tallied variable. The coupling code automatically parses the tally information in MC input and then sets the adjoint source in deterministic code.

3 Numerical Results

To verify the variance-reduction capability of the update code, it is applied to calculate the specific activity of the radiometric monitor in the cavity of the HBR-2 benchmark

problem. The CAD model of the HBR-2 benchmark is depicted in Fig. 4. The unstructured mesh generated automatically based on the CAD model and the structural mesh established by the finite difference discrete ordinate code are shown in Fig. 5 respectively.

To demonstrate the advantages of the unstructured-mesh CADIS method over the traditional CADIS method and illustrate the significant effect of local mesh refinement on improving the computational efficiency of unstructured-mesh CADIS, several cases are performed as follows:

(1) Case1 performs MC simulation through NECP-MCX with unbiased source and energy cutoff, which is the base case.
(2) Case2 obtains results through the traditional CADIS method which MC simulation is performed with source biasing and weight window generated based on adjoint flux calculated by finite-difference S_N code NECP-Hydra.
(3) Case3 obtains results through the unstructured-mesh CADIS method which MC simulation is performed with source biasing and weight window generated based on adjoint flux calculated by S_N-FEM code NECP-SUN.
(4) Case4 obtains results through the same method in case 3 with local mesh refinement for the target region implemented. The parameters of meshing control which are determined automatically are shown in Table 1 and the meshes of the radiometric monitor in case3 and case4 are shown in Fig. 6.

radiometric monitor in cavity
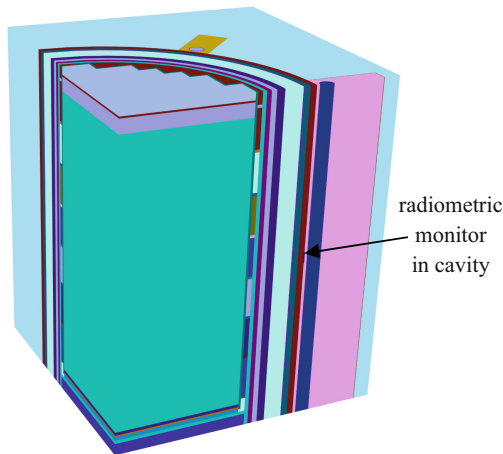
Fig. 4. CAD model of HBR-2 benchmark

To ensure the comparability of the results, all 4 cases simulate 2×10^9 particles through 256 cores paralleled. For case2–4, the modeling and computing time of deterministic code is considered.

The dose rates of the radiometric monitor in the cavity and its ratio to measurements in all cases are shown in Table 2. From Table 2 we can conclude that the calculation of dose rates of the radiometric monitor in the cavity is a typical deep-penetration problem.
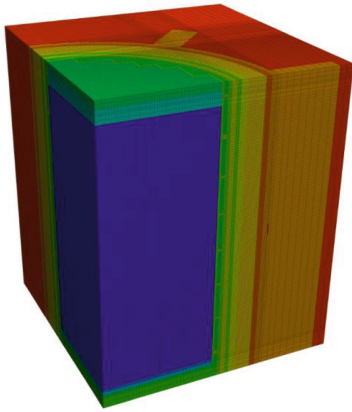
(a)   Structural-mesh model   (b)   Unstructured mesh model
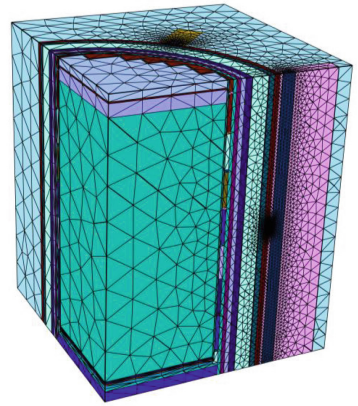
Fig. 5. Structural-mesh and unstructured-mesh models for HBR-2 benchmark

Table 1. Parameters for meshing control

Meshing control	Global meshing	Local mesh refinement
Minimum size	0.5 cm	2 cm
Maximum size	48 cm	48 cm
Hard size	/	0.5 cm
Mesh numbers	1113428	246357
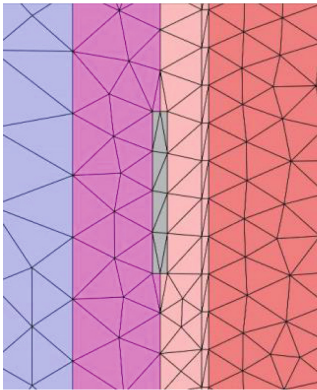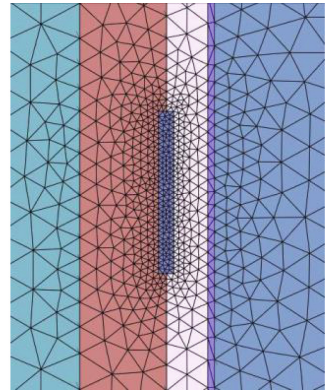
(a)   Global meshing   (b)   Local mesh refinement

Fig. 6. Meshes of the radiometric monitor in case3 and case4

Table 2. Dose rates and their C/E for different cases

Case	Item	^{237}Np(n,f) ^{137}Cs	^{238}U(n,f) ^{137}Cs	^{58}Ni(n,p) ^{58}Co	^{54}Fe(n,p) ^{54}Mn	^{46}Ti(n,p) ^{46}Sc	^{63}Cu(n,α) ^{60}Co
Measurement	Dose rate	2.24E+01	8.51E-01	1.96E+02	8.71E+00	3.31E+00	2.65E-01
1	Dose rate	2.00E+01	9.24E-01	6.86E+01	7.89E-01	/	/
	C/E	0.89	1.09	0.35	0.09	/	/
2	Dose rate	1.64E+01	6.63E-01	2.29E+02	1,00E+01	4.63E+00	3.25E-01
	C/E	0.73	0.78	1.17	1.15	1.40	1.23
3	Dose rate	1.60E+01	6.40E-01	2.20E+02	9.65E+00	4.27E+00	2.87E-01
	C/E	0.71	0.75	1.12	1.11	1.29	1.08
4	Dose rate	1.60E+01	6.39E-01	2.17E+02	9.51E+00	4.26E+00	2.84E-01
	C/E	0.71	0.75	1.11	1.09	1.29	1.07

Table 3. Relative statistic error and FOM for different cases

Case	Item	^{237}Np(n,f) ^{137}Cs	^{238}U(n,f)1 ^{37}Cs	^{58}Ni(n,p) ^{58}Co	^{54}Fe(n,p) ^{54}Mn	^{46}Ti(n,p) ^{46}Sc	^{63}Cu(n,α) ^{60}Co
1	Relative statistical error	37.86%	97.97%	85.49%	99.99%	100%	100%
	FOM	1.57E-03	2.35E-03	3.08E-03	2.25E-03	/	/
2	Relative statistical error	0.21%	0.74%	1.04%	1.18%	2.23%	4.05%
	FOM	4.97E+01	4.09E+00	2.08E+00	1.60E+00	4.52E-01	1.36E-01
3	Relative statistical error	0.49%	1.05%	1.48%	1.73%	1.57%	2.47%
	FOM	5.14E+00	1.13E+00	5.65E-01	4.14E-01	5.02E-01	2.03E-01
4	Relative statistical error	0.32%	0.74%	0.86%	0.98%	1.74%	3.25%
	FOM	1.37E+01	2.52E+00	1.89E+00	1.43E+00	4.59E-01	1.31E-01

Case1 can barely obtain reasonable results because of the dramatically low tally rate caused by the strong shielding effect between cavity and source. On the contrary, owing to the applications of the CADIS method, case2–4 obtain dose rates with acceptable error. Among them, cases in which unstructured-mesh CADIS is applied give out dose rates closer to measurements on the whole than in case2 the traditional CADIS method is applied. Furthermore, the C/E of all reaction channels in case4 is closer to 1 than in case3 because of the local mesh refinement in the radiometric monitor.

The relative statistical error and figure of merit (FOM) are listed in Table 3. It can be drawn from the results of the case1 that conventional MC simulation is incompetent since the unacceptable high variance. In certain reaction channels, the relative statistical error reaches 100% because of the zero tally rate, resulting in terrible FOM. By contrast, the relative statistical error is significantly reduced and the FOM is raised by 3–4 orders in case2–4 the CADIS method is implemented. Case2 and case4 demonstrate that the application of the unstructured-mesh CADIS method can further reduce the relative statistical error by up to 22% compared to the traditional CADIS method. Besides, case3 and case4 indicate that the local mesh refinement for the target region effectively improves the computational efficiency of the unstructured-mesh CADIS method, which is reflected in the reduction of relative statistical error and the boost of FOM.

4 Conclusions

The parallel three-dimensional unstructured-mesh neutron-photon coupled transport calculation code NECP-SUN based on the S_N method and discontinuous FEM is developed and coupled with MC code NECP-MCX to study and implement the unstructured-mesh CADIS method. The coupled code automatically generates unstructured mesh based on the CSG model in MC input and performs adjoint transport calculation through the unstructured-mesh FEM, the adjoint flux obtained is utilized to generate the parameters of source bias and weight window for forward MC simulation. The numerical results of the HBR-2 benchmark obtained by the coupled code show that for deep-penetration problems, the unstructured-mesh CADIS method can obtain more accurate results with less relative statistical error (up to 22% reduction) than the traditional CADIS method, and the FOM is increased by up to 3–4 orders comparing to conventional MC simulation. Moreover, the efficiency and accuracy of the unstructured-mesh CADIS method can be further improved by applying the refinement of meshes in target regions.

References

1. Evans, T.M., Hendricks, J.S.: An enhanced geometry-independent mesh weight window generator for MCNP[R]. Los Alamos National Lab (LANL), Los Alamos, NM (United States) (1997)

2. Wagner, J.C., Haghighat, A.: Automated Variance Reduction of Monte Carlo Shielding Calculations Using the Discrete Ordinates Adjoint Function. Nucl. Sci. Eng. **128**(2), 186–208 (1998)
3. Mosher, S.W., Bevill, A.M., Johnson, S.R., et al.: ADVANTG-An Automated Variance Reduction Parameter Generator, Rev. 1. Oak Ridge National Lab. (ORNL), Oak Ridge, TN (United States) (2015)
4. Peplow, D.E.: Monte Carlo shielding analysis capabilities with MAVRIC[J]. Nucl. Technol. **174**(2), 289–313 (2011)
5. Munk, M., Slaybaugh, R.N.: Review of hybrid methods for deep-penetration neutron transport[J]. Nuclear Science and Engineering (2019)
6. deOliveira, C.R.E., Goddard, A.J.H.: EVENT-A multidimensional finite element-spherical harmonics radiation transport code[M]//3-D deterministic radiation transport computer programs. Features, applications and perspectives (1997)
7. Miao, J., Fang, C., Wan, C., et al.: Development and preliminary application of deterministic code NECP-FISH for neutronics analysis of fusion-reactor blanket. Ann. Nucl. Energy **169**, 108943 (2022)
8. Wareing, T.A., McGhee, J.M., Morel, J.E.: ATTILA. A 3-D unstructured tetrahedral-mesh Sn code[M]//3-D deterministic radiation transport computer programs. Features, applications and perspectives (1997)
9. He, Q., Zheng, Q., Li, J., et al.: NECP-MCX: A hybrid Monte-Carlo-Deterministic particle-transport code for the simulation of deep-penetration problems[J]. Ann. Nucl. Energy **151**, 107978 (2021)
10. Remec, I., Kam, F.B.K.: H.B. Robinson-2 pressure vessel benchmark[R]. US Nuclear Regulatory Commission (NRC), Washington, DC (United States). Div. of Engineering Technology; Oak Ridge National Lab.(ORNL), Oak Ridge, TN (United States) (1998)
11. Xu, L., Cao, L., Zheng, Y., et al.: Development of a new parallel SN code for neutron-photon transport calculation in 3-D cylindrical geometry. Progress in Nuclear Energy (2017)
12. El-Mehalawi, M., Miller, R.A.: A database system of mechanical components based on geometric and topological similarity. Part I: representation. Comput.-Aided Design **35**(1), 83–94 (2003)

Research on Parameter Sensitivity for Deeply Embedment SSI Analysis Based on Sub-structuring Method

Ziqiao Liu[1(✉)], Dongyang Wang[1], Xiaoying Sun[1,2], and Yingying Gan[1]

[1] China Nuclear Power Engineering Co., Ltd., Beijing, China
2193282646@qq.com
[2] Institute of Engineering Mechanics, China Earthquake Administration, Key Laboratory of Earthquake Engineering and Engineering Vibration, China Earthquake Administration, Harbin, China

Abstract. This paper carried out a seismic analysis of a nuclear island structure under the site of a soft soil foundation, based on the spatial sub-structuring analysis method. In order to fully consider the influence of embedment effect in the analysis, the embedded part is modeled independently in the model. Then, the sensitivity effects from the number of interaction nodes and the radius of the cylindrical central area on the calculation time and results is studied. The research show that: (1) Selecting the nodes only at the boundary of the embedded part as the interaction points can significantly reduce the calculation time on the premise of ensuring the accuracy of the results. (2) The value of cylindrical radius in finite element model does not affect the calculation time and accuracy significantly, but has a certain effect on the spectrum value. It is suggested to determine the radius using the average value of the elements which are a large proportion in the model for an non-uniform mesh. In this paper, the suggested values for two parameters are provided based on the sensitivity analysis. The conclusions provide technical reference for the seismic analysis of the deeply embedded nuclear buildings.

Keywords: Nuclear power plant · Soil-structure interaction · Embedment effect · Sub-structuring method

1 Introduction

The safe design of nuclear power plant structure and reasonable safety assessment provide important guarantee for the high efficient development of nuclear energy. In the seismic design of nuclear power structures, the nuclear building is usually buried below the ground surface in order to obtain higher seismic performance [1]. However, the seismic analysis of the building are usually performed without considering embedment effect for simplification. In this case, the support effect from the lateral backfill soil on the structure is ignored. Also, the stiffness of the whole SSI system is therefore reduced which further affect the dynamic characteristic of the system and its response. Additionally, the ground motion for seismic design is usually inputted at the bottom of

the baseslab. The ground motion in a certain depth in the site is normally smaller than the motion on the ground surface. In other words, the assumption without considering embedment effect leads to a smaller seismic excitation. Hence, the results obtained from analysis without embedment tend to be conservative [2].

However, non-bedrock sites or soil sites are becoming the potential construction sites for nuclear power plant (NPP) in recent year due to the rapid development of nuclear power and scarce hard rock sites. Therefore, the soil-structure interaction (SSI) gradually draw the attention of nuclear structural engineers. For a soft site, non-uniform distribution of the foundation bearing capacity and the dynamic soil pressure caused by the embedment effect will affect the seismic response of the superstructure. Hence, the embedment effect shall be considered in the seismic design and seismic in-structure response spectra (ISRS) analysis for a nuclear building.

Many scholars have summarized the research on SSI effect [3]. Two widely-used methods are: direct method and sub-structuring method. The sub-structuring method is a frequency domain solution method. Its basic principle is to decompose the soil-structure interaction system into three parts: the super structure, the foundation and the excavated soil, and solve respectively. The load acting on the structure is obtained under the condition of displacement coordination at the interface between soil and structure. Compared with the direct method, the sub-structuring method has less degree of freedom due to that the soil layer is assumed to be an analytical model. In addition, the damping adopted by the sub-structuring method remains unchanged in the entire frequency range and is more stable. The sub-structuring method [4] is based on the superposition principle and is suitable only for linear analysis systems. Therefore, sub-structuring method is widely used in the field of nuclear engineering because the nuclear structure is required to maintain a linear state under the safe shutdown earthquake.

The ACS SASSI software used in this study is based on the sub-structuring method. The sensitivity analysis is conducted for two key parameters in the embedded effect analysis such as: the selection principle of the interaction node and the radius of the cylindrical central area. The conclusions provided technical reference for the seismic analysis and ISRS calculation of the deeply embedded nuclear buildings.

2   Analysis Model

2.1   Finite Element Model of the Superstructure

To avoid the influence from the adjacent buildings on the analysis results, a separate reactor building (including the internal structure and containment) in a Small Modular Reactor was selected as the analysis object in this analysis. The key information of the model of the reactor building is shown in Table 1, and the finite element model established in ANSYS is shown in Fig. 1.

In the model, the embedded part of the structure and the excavated volume are modeled separately but have common nodes at their interface. The characteristics of the excavated volume are consistent with the surrounding soil. And the vertical height of the element of the backfill soil is same to the thickness of the soil.

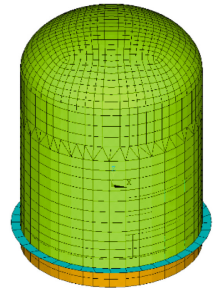**Table 1.** Key information of the finite element model

Part	Size (m)	Element type
Containment	Φ16.50 × 37.20	Shell element
Internal structure	—	Shell element /beam element /mass element
Embedded part	Φ19.00 × 12.50	Solid element
Backfill soil	Φ19.00 × 2.50 × 12.50	Solid element
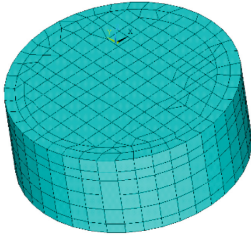
(a) Embedded part model   (b) Backfill soil model   (c) Superstructure model
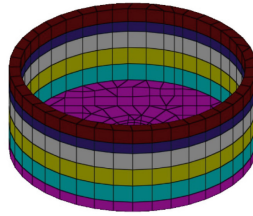
Fig. 1. Finite element model for sensitivity analysis of deep embedded SSI parameters

2.2 Parameters of the Site

According to the geological survey report, the target site in this study is a kind of soft soil site. The building is located on silty clay. The detailed parameters of silty clay are shown in Table 2.

Table 2. Key information of the finite element model

Parameters(unit)	Value
Density (kg/m^3)	1980
Dynamic shear modulus (GPa)	0.19
Dynamic elastic modulus (GPa)	0.55
Compression wave velocity (m/s)	1510
Shear wave velocity (m/s)	313
Damping ratio (%)	3.2
Dynamic Poisson's ratio	0.48

2.3 Seismic Input

According to the safety assessment report of the site, the standard spectra RG1.60 is adopted in the sensitivity analysis. Although the target site of this paper is soft soil, the site amplification effect is not the focus this study. Therefore, the input position of the RG1.60 spectra is assumed to be at the bottom of the building.

A single group of seismic acceleration time histories(shown in Fig. 2(a) –c)) compatible to RG1.60 spectra are used in ACS SASSI. The duration of the time history is 40 s and the time interval is 0.005 s. Both the peak ground accelerations (PGA) for horizontal direction and the vertical direction are 0.30 g.

(a)Horizontal X direction

(b)Horizontal Y direction

(c)Vertical Y direction
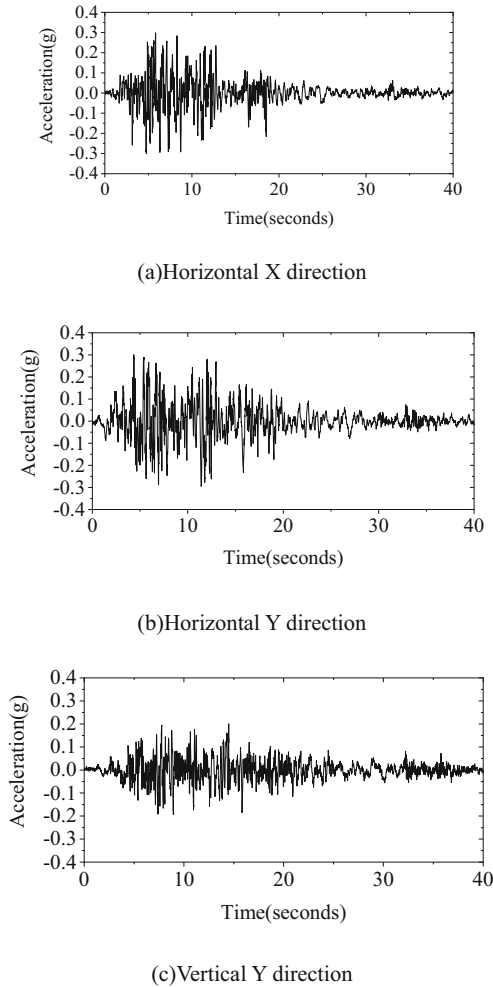
Fig. 2. The input acceleration time history curves

2.4 Observation Nodes at Key Positions

In order to observe the influence of changing parameter on the ISRS, nodes at two key positions of the superstructure (elevations of 16 m and 6 m, respectively) were selected for output and comparison. The positions and numbers of the observation nodes are described in Table 3 and illustrated in Fig. 3.

Table 3. Observation nodes at key positions

Elevation	Node number	Detailed position
16m	a(6339), b(6340), c(6347), d(6436)	See Fig. 3-(a)
6m	e(5698), f(5780), g(5869)	See Fig. 3-(b)
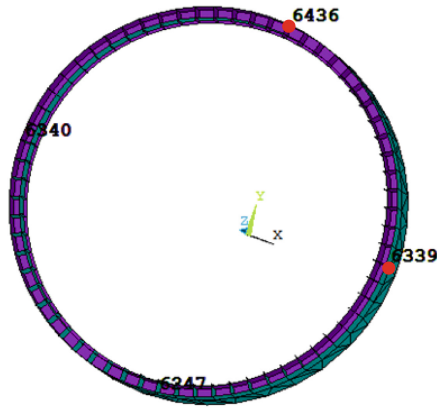
(a)Observation nodes on the elevation of 16m
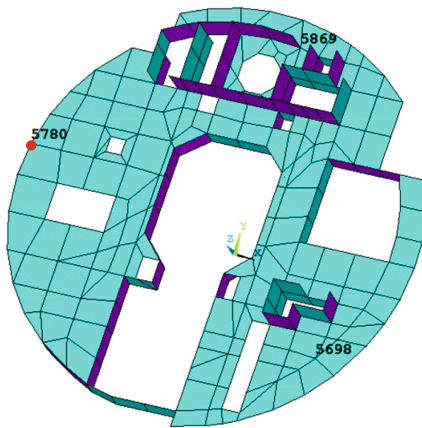
(b)Observation nodes on the elevation of 6m

Fig. 3. The positions and numbers of the observation nodes

3 Sensitivity Analysis Results

3.1 Selection of the Interaction Nodes

The solution of foundation impedance is the most time-consuming procedure in SSI analysis by using the sub-structuring method, and it is depended to the number of interaction nodes. According to the statistical data in Fig. 4, the time-consuming increases exponentially with the increase of the number of interaction nodes.
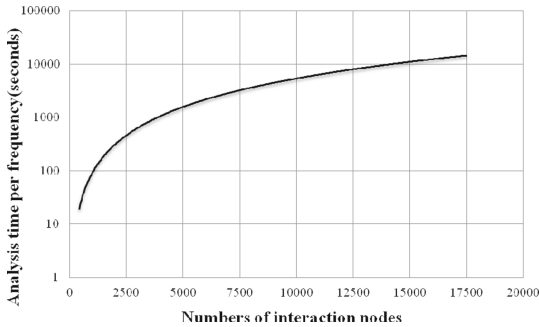
Fig. 4. Relationship between number of interaction nodes and calculation time

For an SSI analysis with deeply embedment, if all nodes in the embedded part are specified as interaction nodes, it can be predicted that there will be a large amount of the interaction nodes when the embedded depth is large. Therefore, the calculation time cannot meet the requirement of the construction period. To provide an appropriate selection method for the interaction nodes, three interaction node selection methods (as shown in Fig. 5 (a) –c)) were tested: method A is to define all nodes in the embedded part as the interaction node; method B is to select the nodes around the embedded part; method C is based on the method B, but several layers of nodes in the embedded part are also defined as interaction nodes. According to these three interaction node selection methods, the SSI analyses for the deeply embedded reactor building using above-mentioned three methods are carried out respectively.

In method C, two different selection are made. The first conditions is to add one intermediate layer of nodes on the basis of method B, namely working condition 1–2. The second condition is to add two intermediate layers of nodes, namely working condition 1–3.

Table 4 showed the relationship between the number of interaction nodes and the calculation time.
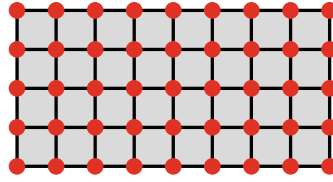
(a) Methods A
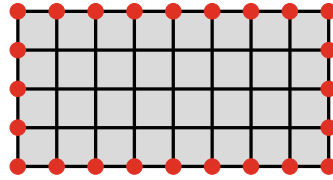
(b) Methods B
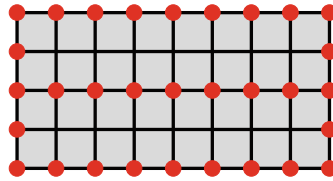
(c) Methods C

Fig. 5. Schematic diagram of selection method for interaction nodes

Table 4. The interaction nodes and the calculation time of different methods

Condition number	Selection methods	Number of interaction nodes	Calculation time per frequency
1–1	B	822	13.765 s
1–2	C	1093	22.365 s
1–3	C	1364	36.230 s
1–4	A	2177	94.500 s

Figure 6 and Fig. 7 showed the comparison of the ISRS from different working conditions. It can be found that the ISRS from four methods are nearly the same. The maximum relative error of the ISRS between methods is only about 3.75%. In other words, for the sensitivity analysis model, all the methods can provide stable and accurate analysis results. Hence, method B has the highest computational efficiency and the time consumption is only 15% of that of method A.
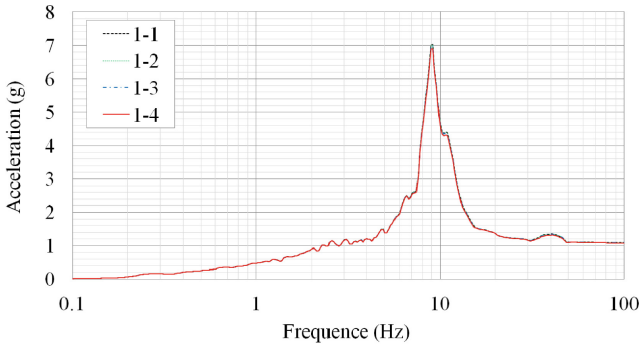
(a) ISRS of X direction
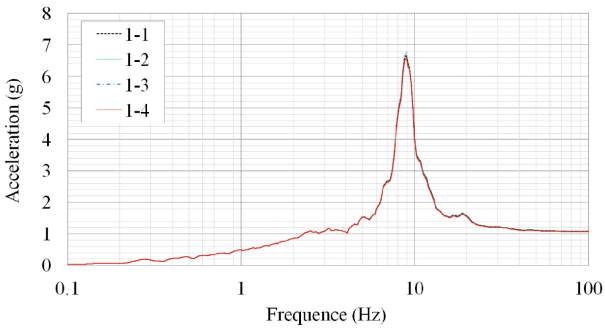
(b)ISRS of Y direction
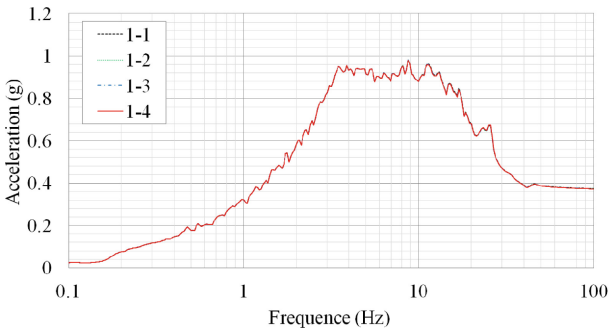
(c)ISRS of Z direction

Fig. 6. Comparison of the ISRS of node A on the elevation of 16 m
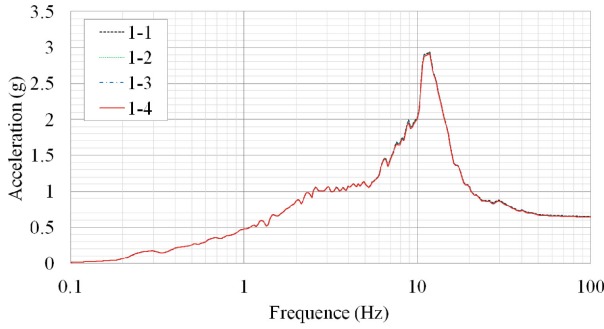
(a) ISRS of X direction
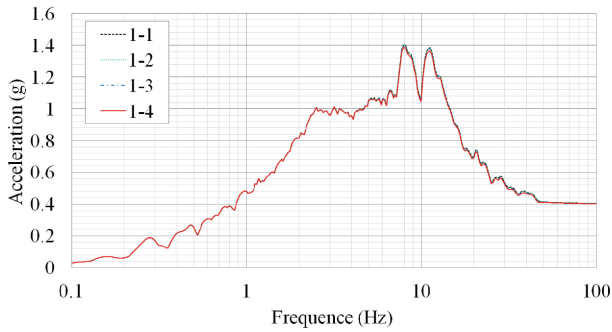
(b)ISRS of Y direction
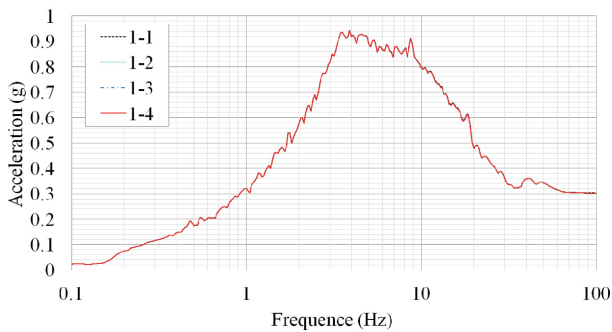
(c)ISRS of Z direction

Fig. 7. Comparison of the ISRS of node F on the elevation of 6 m

3.2   Radius of the Cylindrical Central Area

According to the basic principle of the sub-structuring method, the impedance matrix is obtained by inverting the flexibility matrix. For the three-dimensional SSI analysis of the nuclear island, the solution of the flexibility matrix $[F_f]$ of the three-dimensional problem is the most time-consuming problem, and the solution of the flexibility matrix of the three-dimensional problem is to determine the displacement response of the horizontal

layered system under the element simple harmonic point load, which can be solved by the axisymmetric model in Fig. 8.
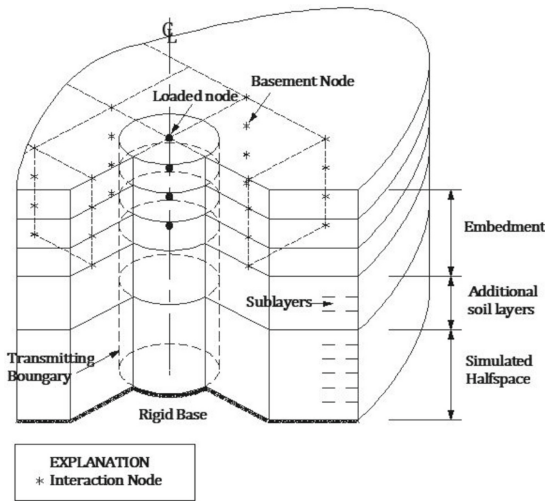
Fig. 8. Axisymmetric model for impedance analysis [5]

The model contains two areas, one is a cylindrical central area with a radius of R, which is composed of axisymmetric elements, and an axisymmetric transmission boundary outside the simulated central area. The bottom can be a fixed boundary, or a viscoelastic half space approximated by a variable thickness and a viscous boundary.

When solving the flexibility matrix, it is not necessary to apply the element harmonic load to all the interaction points to solve the dynamic displacement, but only to apply the load to a row of nodes on the soil interface covering the buried depth of the foundation in turn, and the element width is taken as the minimum transverse distance between the interaction nodes. The response of load on other nodes can be obtained simply by horizontal coordinate translation The radius R of the central area is taken as the smallest lateral distance between the interaction nodes. Changing R affects the flexibility matrix $[F_f]$, and then affects the impedance matrix $[S(\omega)]$ of the SSI system, and finally changes the response of the whole system.

If the mesh of the embedded part or the base slab are relatively uniform, the value of R can be determined by the average value of the mesh size. However, in most practical projects, it is difficult to get an uniform mesh for the base slab. Figure 9 shows the mesh of the reactor building model.

To determine a relative reasonable value of R, five radius values of 1.80, 1.98, 1.56, 1.00, and 0.66 were selected in the analysis. Table 5 shows the selection principle for different radius R.

Figures 10 and 11 show the comparison results of the ISRS in the horizontal X direction, the horizontal Y direction and the vertical Z direction, respectively.

For both the horizontal X and Y direction, it can be seen that the change of R has slight effect on the shape of the ISRS. When R is taken as 1.80, 1.98 and 1.56 respectively,
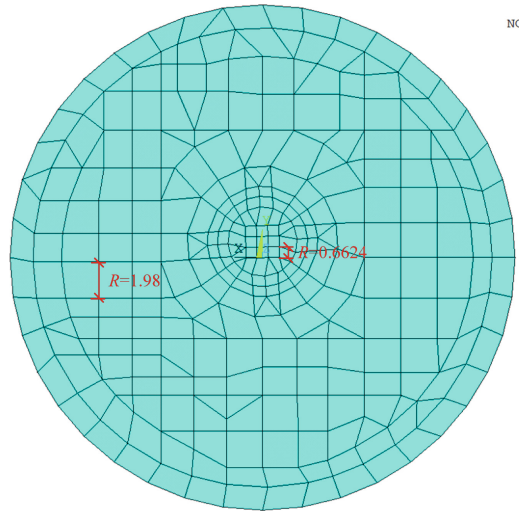
Fig. 9. Mesh generation of base plate for trial model

Table 5. Selection principle for different radius R

Condition number	Value of R	Selection principle
2–1	1.80	Based on the relatively uniform grid size outside the core
2–2	1.98	Based on the maximum grid size at the bottom of the core
2–3	1.56	Based on the weighted average value of bottom plate grid size
2–4	1.00	Based on the engineer's experience
2–5	0.66	Based on the size of dense grid at the bottom

the ISRS are nearly the same. When R is taken as 1.00, the acceleration response of the containment and the internal structure increases. When R is taken as 0.66, the ISRS of the containment and the internal structure is slightly reduced. However, the response of the backfill soil in Y direction increases.

For Z direction, it can be seen that the ISRS from different radius are nearly the same. When R is taken as 0.66, the value of ISRS at the frequency higher than 20 Hz is amplified.

In general, the change of the radius R within a reasonable range has negligible effect on the shape and value of the ISRS. However, it can also be seen that radius of 1.80, 1.98 and 1.56 provided a relative stable results compared to radius of 1.00 and 0.66.

It is suggested that for non-uniform mesh, the value of the radius R can be estimated by weighted averaging, or take the grid sizes that accounts for a large proportion in the model. Deviation. It is not reasonable to estimate based using the grid sizes of a small percentage in the model or take the maximum or minimum grid size.
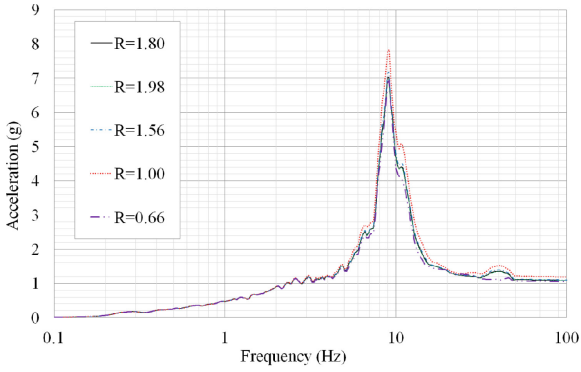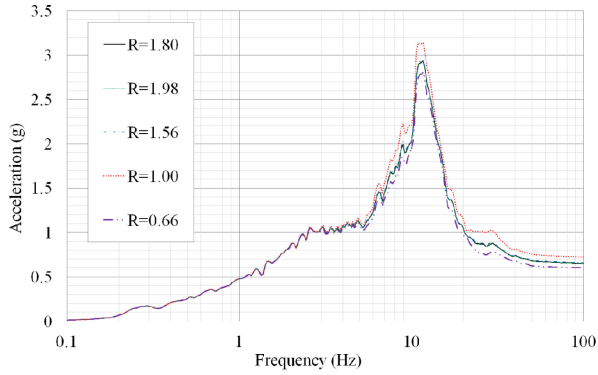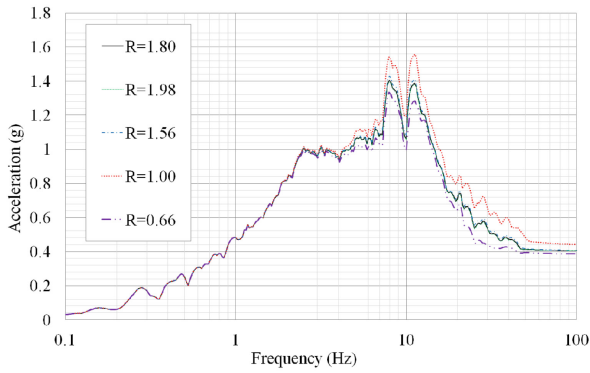
(a)Response spectrum-X
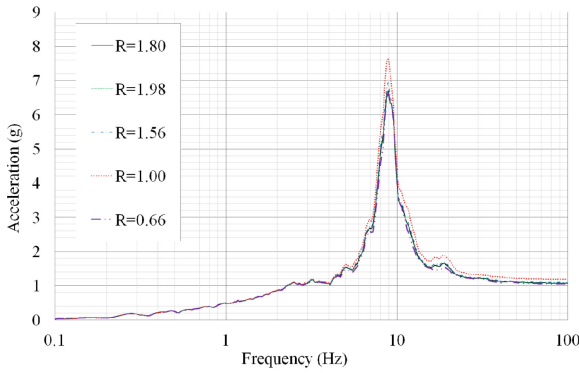
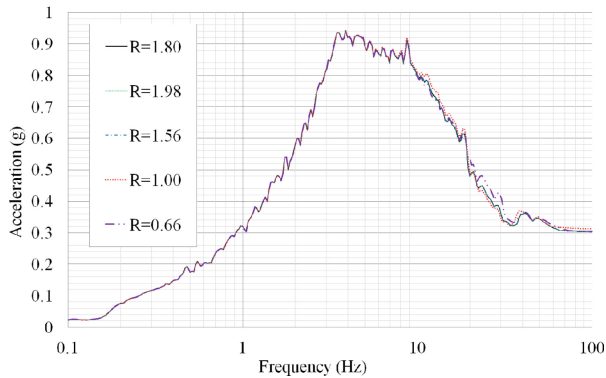(b)ISRS of Y direction
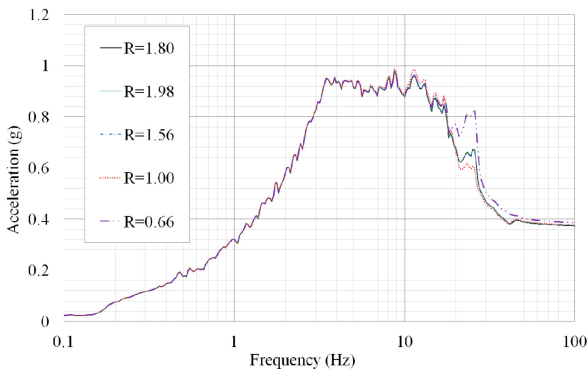
(c)ISRS of Z direction

Fig. 10. Comparison of ISRS of node A for different radius R

(a)Response spectrum-X

(b)ISRS of Y direction

(c)ISRS of Z direction

Fig. 11. Comparison of ISRS of node F for different radius R

4 Conclusions

In this paper, sensitivity analysis for a deeply embedded reactor building is carried out. The sensitivity of changing selection method of the interaction nodes and the radius of the cylindrical central area are studied. The conclusion is as follows:

Three interaction node selection methods used in this study are all applicable. However, the calculation time of method B is much less than other two methods on the premise of enough accuracy. It is suggested to perform similar sensitivity analysis for selection interaction nodes before starting SSI analysis to determine an optimum interaction node number.

The central radius R has little effect on the shape and value of the ISRS. The value of the radius R obtained by weighted averaging, or taking the grid sizes that accounts for a large proportion in the model provides a relative stable response.

Apart from the two parameters studied in this paper, there are other ley influence parameters in deeply embedment analysis that might affect the result and calculation effectiveness of the SSI analysis, such as the thickness of the top layer and the element size of the superstructure. Further sensitivity analysis related to them shall be carried out to establish a suggestion principle guideline for each key parameters in deeply embedment analysis, ensuring the stability and rationality of the SSI analysis.

References

1. Ding, J., Li, J., Zhong, H.: Influence of foundation embedment on seismic response of power house for nuclear power station. Water Resources Power, **28**(10), 70–73 2010
2. Wang, F.: Study on the effect of non-rock site on seismic behavior of safety-related nuclear structure. Institute of Geophysics,China Earthquake Administration (2021)
3. Lin, G.: Soil-structure dynamic interaction. World Earthquake Eng. (01), 4–21+36 (1991)
4. Wang, J., Zhou, D.: A systematic review of semi-analytical sub-structuring method applied in soil-structure dynamic interaction. World Earthquake Eng. **35**(2), 96–106 (2019)
5. Mansour, T.-R.: The Flexible Volume Method for Dynamic Soil-Structure Interaction Analysis. San Francisco: University of California, Berkeley

Study on the Cause and Solution of Quadrant Power Tilt Rate Alarm in a PWR Plant

Desheng Jin, Qiubai Li, Yulong Mao[(✉)], Wei Zhang, and Yousen Hu

China Nuclear Power Technology Research Institute Co., Ltd., Shenzhen, Guangdong, China
{jindesheng,maoyulong}@cgnpc.com.cn

Abstract. During the normal operation of a pressurized water reactor plant, RPN430KA (quadrant power tilt rate over 3%) alarms were issued several times, and the alarm frequency increased with the increase of burnup, which affected the normal operation of the unit. The original signal of this alarm is from four power range channels (RPN). After the process of signal filtering, if the difference between the maximum and minimum nuclear power is still greater than 3%, the alarm will be triggered. In this paper, the root cause of the quadrant power tilt rate alarm phenomenon is studied, and targeted solutions are given. The research shows that the main factor affecting the alarm is the inconsistency between the filtering sampling time during the discretization process and the physical sampling time of the alarm signal, and the induced reason is that the fluctuation of nuclear power gradually increases with the deepening of burnup. The nuclear power fluctuation is a noise signal with too many complex factors but existed objectively. Therefore, in the case of large fluctuation of nuclear power, if the actual filtering effect is not achieved, it is easy to appear alarm phenomenon, which can be solved by modifying the sampling time of signal processing. The results of this paper can be used as reference for plant operation.

Keywords: Quadrant power tilt rate · Alarm · Nuclear power fluctuation · Discretization · Filtering sampling time

1 Introduction

The core quadrant power tilt ratio (QPTR) is defined as the ratio of the average power of a certain quadrant of the core to the average power of the whole reactor, which is an index to measure the asymmetry of radial power distribution of the core (referring to 1/4 symmetry). In the actual core, except some accident conditions, due to manufacturing tolerance, installation tolerance, loop asymmetry, operation history effect and other reasons, the physical quantities affecting power distribution in the core can not be completely symmetrical in practice, that is, there is a phenomenon of core quadrant power tilt.

In the PWR nuclear power plant, there are many quadrant power tilt related alarm signals. One of the alarm signal is the quadrant power tilt rate which is defined as the difference between the maximum and minimum nuclear power displayed in four RPN power range channels, and is set in LOCA monitoring system (LSS) after filtering

process. The alarm signal variable is defined as RPN430KA, and the alarm logic diagram is shown in Fig. 1. The alarm threshold is set to 3%. When the RPN430KA signal is greater than 3%, the alarm will be triggered.
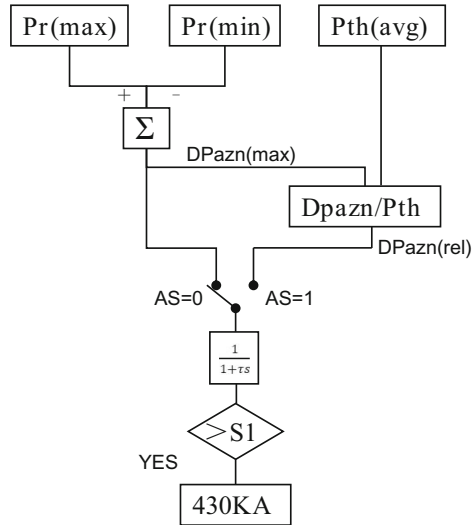

Fig. 1. Logical figure of RPN430KA alarm signal

In which:

- Pr(max): Maximum power of four power range channels
- Pr(min): Minimum power of four power range channels
- Pth(avg): Average thermal power in LSS system
- AS = 1: the alarm is triggered with DPazn (rel) parameter which equals to the ratio of maximum quadrant tilt rate to relative average thermal power
- AS = 0: the alarm is triggered with DPazn (max) parameter which equals to the difference of maximum nuclear power and minimum nuclear power.

Unit X (AS is set to 0) of a PWR nuclear power plant has flashed RPN430KA alarm several times during normal operation in the middle and late life of a certain cycle. When the cycle burnup reaches to 65%, the alarm trigger frequency is about once in month. After burnup of 80% EOL, the trigger frequency increases, and the alarm trigger frequency has reached once a day or even many times a day.

2 Root Cause Analysis

According to Fig. 1, the triggering of RPN430KA is mainly affected by several aspects. First, the nuclear power signal measured by RPN will trigger an alarm if the nuclear power deviation in different quadrants is large. Second, the process of filtering can reduce the number of alarm triggering if the filtering effect is good. This paper analyzed the cause from these two aspects.

2.1 RPN Measurement Data Analysis

Theoretically, the nuclear power of the four power range channels are all the same, but due to quadrant power tilt, neutron noise and other factors, the nuclear power mean values of the RPN four channels are different and fluctuate in a certain extent. So data analysis of RPN power of X unit in different cycles and different burnups is needed.

Figure 2 shows the standard deviation comparison of nuclear power fluctuation under the burnup of about 17000MWd/tU at the end of cycle life of X unit with different RPN measurement channels in different cycles.

It can be found that the fluctuation of nuclear power in cycle C02 is similar to that in cycle C03, and the fluctuation in cycle C04 is slightly larger, which is consistent with the phenomenon that RPN430KA alarm phenomenon is more frequent at the end of cycle C04 1.

Marcus Seidl studied the neutron noise phenomenon of nuclear power fluctuation [2, 3]. The research showed that the fluctuation amplitude of nuclear power increases with the increase of the absolute value of moderator temperature coefficient, Generally speaking, the absolute value of moderator temperature coefficient is larger at the end of cycle life, so the fluctuation amplitude of nuclear power is larger than that of beginning of cycle.

Figure 3 shows the variation of the absolute value of moderator temperature coefficient in different cycles of X unit with burnup. It can be seen from the figure that the absolute value of moderator temperature coefficient in cycle C04 is larger than that in cycle C03 at the same burnup. In the same cycle, the absolute value of temperature coefficient of moderator at the end of life is larger than that of beginning of cycle. This is consistent with the fact that the nuclear power fluctuation of cycle C04 is larger than that of cycle C03 and the nuclear power fluctuation of cycle C04 is larger at the end of cycle than that of beginning of cycle.

Nuclear power fluctuation or neutron noise fluctuation is a very complex phenomenon, which has been studied in the world and is still being further studied [4, 5].

Therefore, from the data analysis of RPN measurement, it can be seen that the large fluctuation of nuclear power at the end of cycle C04 is a promoting factor for the alarm of quadrant power tilt rate signal (RPN430KA).

2.2 Filtering Effect Analysis

According to the logic diagram of RPN430KA alarm, the difference between the maximum value and the minimum value of nuclear power signal is processed by a filter. The transfer function of the first-order filter is $1/(1 + \tau s)$, in which τ is the filter time constant. After discretization, the transfer function can be written as follows:

$$\text{tNewOutput} = a \times \text{tLastOutput} + b \times \text{tLastInput} + c \times \text{tNewInput} \qquad (1)$$
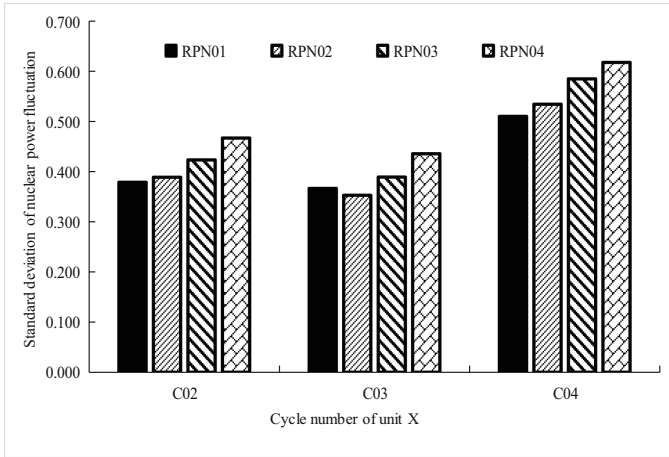
Fig. 2. Neutral flux fluctuation amplitude under different cycles at EOL
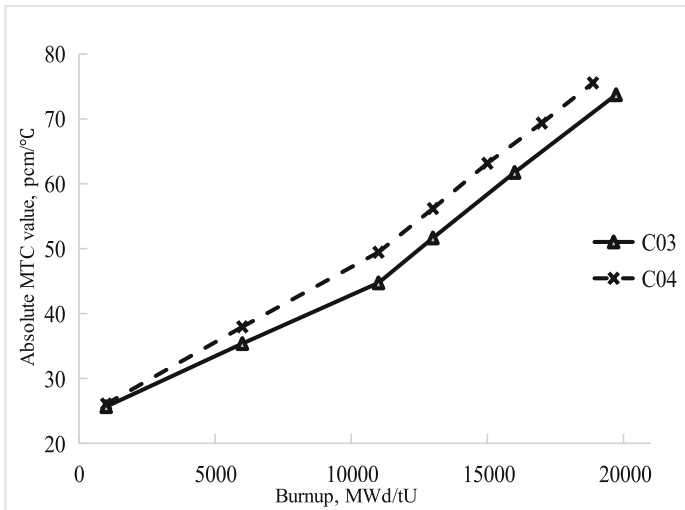

Fig. 3. Change of absolute value of MTC with burnup

in which:

tNewOutput: output result of current time step after filtering;

tLastOutput: output result of last time step after filtering;

tLastInput: input data of last time step;

tNewInput: input data of current time step.

Where a, b and c are weight coefficients. Through proper weighting processing of the original signal at current and last time step and the filtered signal at the last time step, the current filtered output result is finally obtained. The choice of weight coefficient greatly affects the filtering effect, which is defined as follows:

a = 1.0−(SampleTime/d);
b = −a + (Tau/d);
c = 1.0−(Tau/d);
d = Tau + (SampleTime/2.0) + (SampleTime/(12.0 × Tau × Tau)).

Where Tau is the time constant (τ), and its initial design value is 20 s, SampleTime is the time of sampling.

The filtering time constant and SampleTime jointly determine the weight coefficient. In principle, the SampleTime depends entirely on the frequency at which the original signal is collected. If the sampling frequency of a system is determined, the filtering effect can only be modified by time constant.

Assuming a group of input signals, the deviation signal DPazn (max) between the maximum value and the minimum value of RPN core power changes as the input signal in Fig. 4 (note that this input signal amplitude is larger than the actual value onsite, and it is only assumed for the convenience of observing the filtering effect). In order to monitor the effect of filtering, the time interval of the input signal is 50 ms, and the values of Tau are 20s and 0.5s. The input signal and output effect at different SampleTime are shown in Fig. 4 below.

It can be seen from the comparison that when the filtering time constant Tau is 20s, the setting of SampleTime has a great influence on the filtering effect. When the SampleTime setting is consistent with the time interval of the input signal (both are 50 ms), the filtering effect is better, while when the SampleTime setting is larger, the filtering effect is worse.
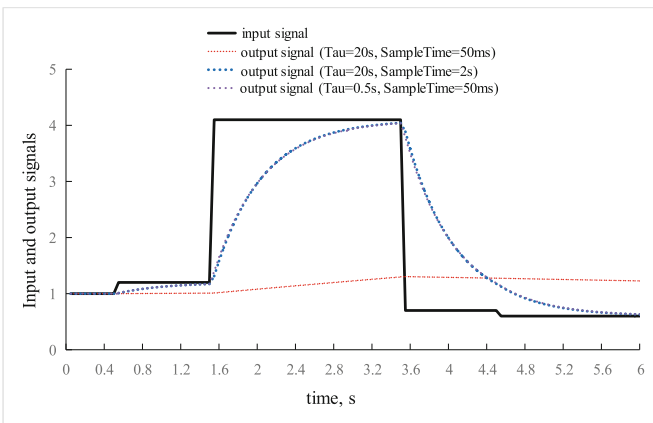

Fig. 4. Output of filter with different Tau and SampleTime

When SampleTime is set to 50 ms and the filtering time constant is 0.5 s, the filtering effect is basically the same as that when Tau is set to 20 s and SampleTime is set to 2 s.

After onsite inspection, in order to shorten the response time of the system, the SampleTime for calculating the weight coefficient was modified in the design of Unit X, which was inconsistent with the physical sampling frequency of the system. Its effect on the weight coefficient is equivalent to changing the filtering time constant without changing the SampleTime.

Therefore, the main reason for the RPN430KA alarm is that the SampleTime in the discretization calculation of LSS system of Unit X is inconsistent with the physical sampling time, and a larger SampleTime is set.

3   Research in Solution

The purpose of setting RPN430KA alarm in LSS system is to monitor the power tilt of core quadrant and the operation state of core during normal operation. For noise signals, effective filtering means should be used. According to the cause analysis, it can be solved from two aspects for the alarm:

One method is the effective filtering setting. This method includes setting a suitable filtering time constant Tau and setting a sampling time (SampleTime) which is the same as the physical sampling frequency during discrete processing. Tau = 20s and SampleTime = 50 ms are recommended for unit X.

The second method is to reduce the fluctuation amplitude of nuclear power as much as possible. The reason of nuclear power fluctuation is complex, and it is closely related to the temperature coefficient of moderator from the phenomenon. Therefore it can be considered to optimize the temperature coefficient of moderator as much as possible in the design of fuel management, especially for the end of life. From the reason analysis of current research, the fluctuation of nuclear power is closely related to the fluctuation of core inlet flowrate. So in the design of a new reactor type, it is necessary to optimize the flow distribution device as much as possible to reduce the flow fluctuation of core inlet flowrate. For the in-service unit, because its flow distribution device has been finalized, it needs to be considered from other aspects.

In view of the first solution, this paper investigates the RPN430KA alarm of Y unit. For the same cycle, under almost similar fuel management strategies, the nuclear power fluctuation standard deviations of Unit X and Unit Y under the same burnup at the end of cycle are shown in Fig. 5. It can be seen that the fluctuation amplitude of cycle C03 of Unit X is equivalent to that of Unit Y, and the fluctuation range of cycle C04 of Unit X is slightly larger at the end of life. According to RPN430KA alarm statistics, the SampleTime of Unit Y is consistent with the physical sampling time, and there is no alarm during normal operation, but there is a certain alarm phenomenon of Unit X. It can be seen that this scheme has a good effect on solving the alarm of quadrant power tilt rate RPN430KA in normal operation.
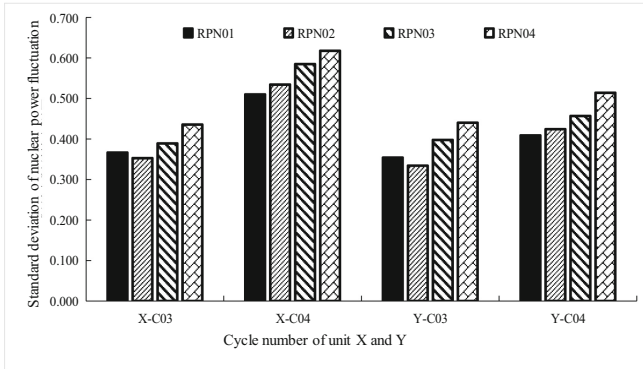
Fig. 5. Comparison of neutral flux fluctuation amplitude

4   Conclusions

In this paper, the quadrant power tilt rate alarm phenomenon of a PWR nuclear power plant is studied. Based on its alarm logic, the root cause is analyzed, and the solution is determined. Research shows that:

(1) The main reason of the quadrant power tilt rate alarm is that the sampling time (SampleTime) is not consistent with the physical sampling time when the LSS system discretizes the filter link. The contributing factor is that the nuclear power of the unit fluctuates greatly at the end of the cycle.

(2) In terms of solution, the abnormal alarm phenomenon of the unit can be well solved by optimizing the setting of SampleTime. At the same time, in order to reduce the fluctuation amplitude of nuclear power, for in-service units, the temperature coefficient of moderator can be optimized by optimizing fuel management scheme, and for new units, the flow distribution device should also be optimized to reduce the fluctuation of inlet flow.

The research results of this paper can also be used as relevant good experience (RGP) of a new reactor design. Appropriate alarm setting is of great significance for monitoring quadrant power tilt and ensuring stable operation of the unit.

References

1. Zenghua, Y.: Study on quadrant power tilt of pressurized water reactor. Nucl. Sci. Eng. **19**(1), 27–38 (1999)
2. Marcus, S., Kai, K., Uwe, S., et al.: Review of the historic neutron noise behavior in German KWU built PWRs.Progress in Nuclear Energy, **85** 668–675 (2015)
3. Grondey, G., Harms, R., Kumpf, H., et al.: Low frequency noise in a PWR and its influence on the normal operational characteristics of the plant

4. Bermejo, J.A., Montalvo, C., Ortego, A.: On the possible effects contributing to neutron noise variations in KWU-PWR reactor: Modelling with S3K. Prog. Nucl. Energy **95**, 1–7 (2017)
5. Viebach, M., Lange, C., Bernt, N.: Simulation of low-frequency PWR neutron flux fluctuations. Progress Nuclear Energy **117** 103039 (2019)

Wetting Behavior of LBE on 316L and T91 Surfaces with Different Roughness

Tingxu Yan, Huiping Zhu[✉], Xudong Liu, Xu Tu, Muran Qi, Yifeng Wang, and Xiaobo Li

North China Electric Power University, Beijing 102206, China
{zhuhuiping,wangyifeng,lixiaobo}@ncepu.edu.cn

Abstract. In this paper, two typical candidate structural materials of 316L and T91 with different surface roughnesses were studied at temperatures from 200–500 °C. The surface with different roughness was prepared by mechanical polishing on the sandpapers with particle sizes from 400 to 2000 mesh. The wetting test was carried out in a smart contact angle measuring device by using the sessile-drop method. Meanwhile, the microstructure of the liquid-solid surface was analyzed by scanning electron microscope (SEM). The results show that the surfaces of both materials are non-wetting to LBE in the tested temperature range. The contact angles of LBE drop on material surfaces decrease with increasing temperature in general. However, it appears to increase significantly at 400 °C for both two materials. Besides, the decrease of surface roughness can effectively inhibit the wettability of LBE on the material surface. In addition, compared with 316L, the wetting of the LBE to T91 surface is better, indicating the higher tendency of LME for T91 in practical application. These results can provide references for the prediction of the LME behavior of structural materials.

Keywords: Structural materials · LBE · Wettability · Surface roughness

1 Introduction

Liquid lead-bismuth alloy (Pb44.5%, Bi55.5%, LBE) as the coolant of LFR, possesses favorable thermophysical property, neutron radiation-resistant, and chemical stability [1–4]. However, the working environment of LBE is easy to cause the problem of liquid metal embrittlement (LME) of stressed structural materials. The phenomenon of LME occurring under specific load or environmental conditions may lead to rapid and uncontrollable crack growth, which cause the transition of liquid metal from ductile fracture mode to brittle fracture mode under plastic deformation [5, 6]. There are many complicate factors affecting the LME. The "adsorption theory" of the solid-liquid two-phase interface is widely used for explaining the phenomenon of LME [7]. It is considered that the liquid metal atoms adsorbed on the steel surface reduce the binding energy between the main alloy elements (such as Fe, Cr, Ni, etc.) of the steel, thereby reducing the fracture toughness of the steel and leading to early fracture [7, 8]. The wetting behavior between liquid metal and structural materials can qualitatively reflect the adsorption

capacity of the steel to liquid metal atoms and has guiding significance for the prediction and mechanism study of brittle fracture of structural materials in liquid metal [9].

At present, there are a large amount of data on the wettability between liquid metals and materials. However, the research data about the wettability between LBE and structural materials are limited. Among them, D. Giuranno et al. [10] studied the wetting behavior of LBE and lead on AISI 316L at different temperatures. They found that the contact angle of LBE on the sample was smaller than that of pure lead. Liu Jing et al. [11] conducted real-time contact home test of liquid lead and LBE at different temperatures on T91 steel surface. It is concluded that the contact angle of T91 in both systems is greater than 90°, indicating that liquid lead and LBE are in a nonwetting state with T91 steel. And the contact angle of the two systems decreased with the increase of temperature. Besides, Zhen Qi et al. [12] studied the contact angle of liquid lead on alumina substrates with different roughness at temperature range from 923K to 1123K. With the increase of surface roughness, the increase of the actual surface area of the substrate leads to the increase of surface free energy, which increases the contact angle. However, there is little research on the influence of different surface roughness of LBE and structural materials on wettability.

In this work, T91 and 316L steels with different roughness were prepared. The surface roughness values and three-dimensional surface morphology were measured. The contact angles of LBE on different samples were measured systematically at temperatures ranging from 200 to 500 °C. The reasons for the difference of wettability were analyzed by observing the micro morphology of boundary between LBE and sample surfaces.

2 Experimental

2.1 Samples Preparation

Two typical candidate structural materials 316L and T91 are selected. The nominal composition of commercial 316L and T91 steels is shown in Table 1. Before the experiment, the two materials were cut into small pieces of $15 \times 5 \times 1.5$ mm^3 in size. To make different surface roughness, the UNIPOL-802 automatic precision grinding and polishing machine of Shenyang Kejing Auto-instrument Co, LTD. (Fig. 1-a) was used to perform surface treatment on the surfaces of the two materials. Four samples are selected for each material, and the treatment method is shown in Table 2. The polishing time on each type of sandpaper was 20 min. The mirror polishing time was 30 min. All the samples were stored in vacuum before the experiment. For the polished samples, the roughness and three-dimensional morphology were measured by atomic force microscope (AFM).

2.2 Wetting Test

The wetting test was carried out on the contact angle measuring device by using static drop method. The device is shown in Fig. 2.
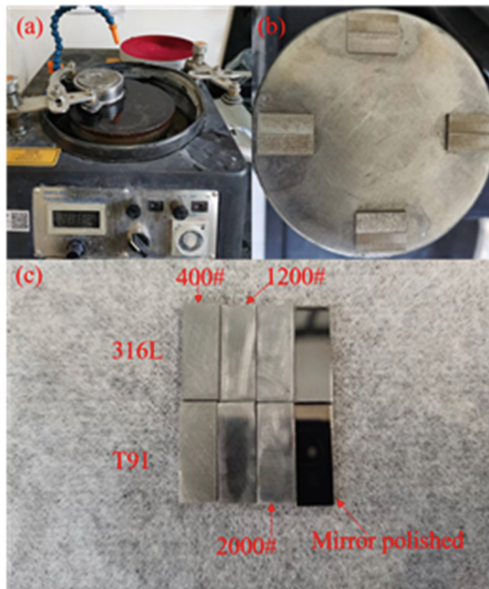
The LBE droplet was 0.25 g in weight with an error of $\pm$ 0.005 g. Before experiments, LBE droplets were heated and melted in glycerol at 300 °C and quickly stirred to

Table 1. Chemical composition of experimental steel (in wt. %).

	Fe	Cr	C	Si	Ni	V	Mn	N	P	S	Mo	Nb	Al	Ti
316L	Bal	16	0.022	0.51	10.1	-	1.58	-	0.029	0.016	2.2	-	-	-
T91	Bal	8.2	0.09	0.31	0.06	0.2	0.39	0.44	0.1	0.02	0.93	0.07	0.05	0.02

Table 2. Sample preparation method.

Samples	Label	400#polished	1200#polished	2000#polished	Mirror polished	Alcohol ultrasonic cleaning	Acetone ultrasonic cleaning
316L	1#	✓	-	-	-	✓	✓
	2#	✓	✓	-	-	✓	✓
	3#	✓	-	✓	-	✓	✓
	4#	✓	-	✓	✓	✓	✓
T91	5#	✓	-	-	-	✓	✓
	6#	✓	✓	-	-	✓	✓
	7#	✓	-	✓	-	✓	✓
	8#	✓	-	✓	✓	✓	✓

Fig. 1. Polishing process: (a) UNIPOL-802 automatic precision grinding and polishing machine, (b) Sample loading platform, (c) Prepared sample.

discharge air after reaching the preset temperature. The purpose is to make the droplet shape more regular. Then cooled in glycerin. Put the cooled sample into acetone for 2 min, removed the residual glycerol on the sample surface, and then stored it in vacuum.

Before the experiment, the test bench was leveled to ensure that the sample was in a horizontal state. When the test began, one sample was placed on the metal ceramics heater (MCH), and the prepared LBE droplet was placed on the center of the sample surface. Then, high-purity argon was introduced to remove the air in the chamber, and the argon atmosphere in the chamber was maintained during the experiment. The test temperature was from 200 °C to 500 °C, and every 50 °C was a test recording point. When the temperature reached the set temperature point, the image of the sessile droplet was taken by the camera after 0.75h. In order to explore the influence of contact time on contact angle, the contact angle of four samples (1#, 4#, 5# and 8#) were tested after keeping the temperature at 500 °C for 6 h. The cross-section of the boundary between droplet and sample surface were analyzed by SEM.

Graphical analysis software JC2000 was used to analyze the droplet photos. Contact angles value was measured by the five-point fitting method, as shown in Fig. 3.
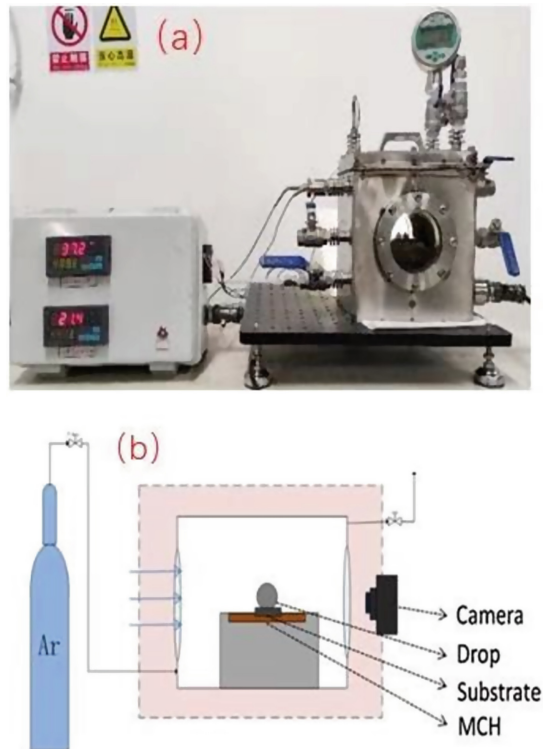
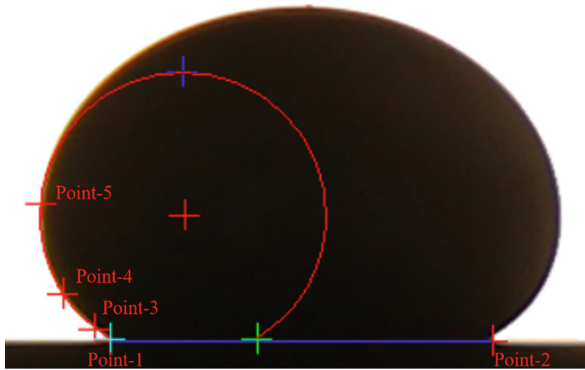**Fig. 2.** Contact angle measuring device: (a) Device picture, (b) Schematic diagram.

Fig. 3. Five-point fitting example.

3   Results and Discussions

3.1   Surface Morphology Analysis

Figure 4 shows the 3D morphology of the surface roughness of eight samples by AFM. There are obvious differences between samples polished with different sandpapers. Different colors in the figure represent different heights. The surface roughness characterizing in Sa is shown in the figure. The larger the Sa value, the rougher the sample surface. As the mesh number of sanding paper increases, the Sa value decrease and the sample surface becomes more flat. After mirror polishing, almost no bulge exists on the surface of the sample. The surface roughness of the two steels is different when they are polished under same conditions, which may be caused by the difference of steel hardness.

3.2   Contact Angle

The contact angle measured by the five-point measurement method refers to the angle θc between the tangents of the gas-liquid interface as shown in Fig. 5. The relationship between contact angle and liquid surface tension can be obtained from Young's equation [13].

$$\cos \theta_c = \frac{\gamma_{SG} - \gamma_{SL}}{\gamma_{LG}} \tag{1}$$

In the above formula, γ_{SG}, γ_{SL} and γ_{LG} represents the free energy of solid-gas, solid-liquid and liquid-solid interfaces respectively. When the surface roughness of the sample increases, it will cause obstacles to the liquid paving, the solid-liquid free energy γ_{SL} decreases, the contact angle increases, and the wettability becomes worse. When $\theta c = 0°$, define that the liquid completely wets the solid surface. When $0 < \theta c \leq 90°$, solid surfaces are defined as wetted surfaces. When $90° < \theta c \leq 150°$, solid surfaces are defined as nonwetting surfaces. When $\theta c \geq 150°$, Solid surfaces are defined as super nonwetting surfaces.

The contact angles of LBE droplet on 316L sample surface with different roughness are shown in Fig. 6.
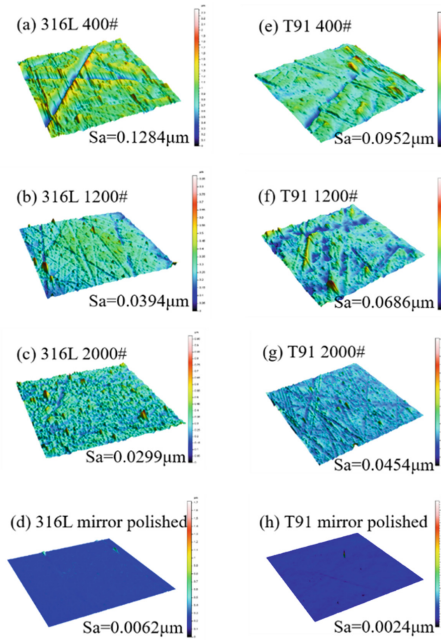
Fig. 4. 3D topography of AFM on different surfaces. (a) 316L 400#, (b) 316L 1200#, (c) 316L 2000#, (d) 316L mirror polished, (e) T91 400#, (f) T91 1200#, (g) T91 2000#, (h) T91 mirror polished.
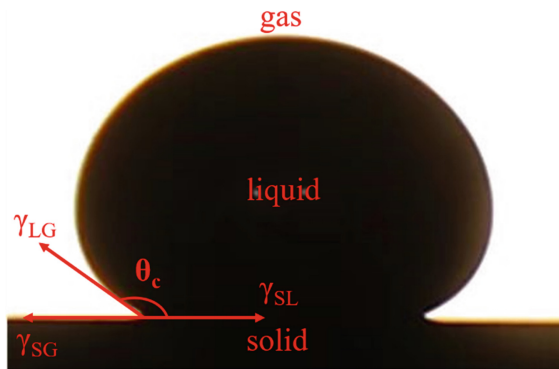

Fig. 5. The contact angle of a liquid drop on the solid surface.

As shown in Fig. 6 (a). All the contact angles of LBE on 316L samples surfaces are greater than 149°, indicating that they are nonwetting to LBE. With the increase of temperature, the contact angle shows an increasing trend as a whole. For example, when the temperature is 200 °C, the contact angle of the sample surface polished by 400# sandpaper is 158.32°. With the increase of temperature, the contact angle decreases to 153.36° at 350 °C. When the temperature rises to 500 °C, the contact angle continues
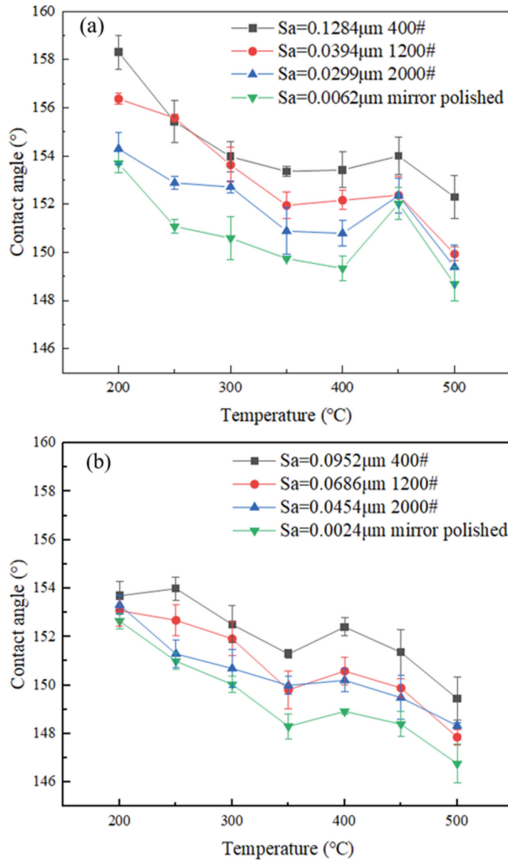
Fig. 6. Contact angle with different roughness. (a) 316L, (b) T91.

to decrease to 152.29°. A special temperature point can be seen from the overall trend. When the temperature rises to 450 °C, the contact angle of the four samples increases. This may be caused by the change of surface morphology caused by carbide precipitation of austenitic stainless steel. Besides, with the decrease of surface roughness, the surface contact angle reduces significantly. This means that the increase in surface roughness helps to reduce the wettability of LBE on 316L surfaces.

As shown in Fig. 6 (b). The contact angle of LBE on T91 samples surfaces is greater than 145°.which is also nonwetting to LBE. The change trend of contact angle with temperature and roughness is the same as that of 316L steel.

Figure 7 compares the contact angle of LBE on two stainless steels with same roughness. The contact angle of 316L is greater than that of T91 on each surface roughness. The difference of surface contact angle between the two steels after mirror polishing is the smallest. As the surface becomes rougher, the difference of contact angle between the two steels becomes larger. This indicates that the wettability of LBE to 316L steel is worse under the same temperature and surface roughness. It can be inferred that T91 steel has a higher tendency of LME under the actual operating conditions of the reactor.

The influence of contact time on contact angle is shown in the Fig. 8. With the increase of holding time, the surface contact angle between smooth surface and rough surface shows obvious difference. For the smooth surface obtained by mirror polishing, with the increase of holding time, the contact angle of 316L steel decreases from 148.69° to 136.04°, and that of T91 steel decreases from 146.76° to 143.82°. For the rough surface obtained by grinding with 400# sandpaper, with the increase of holding time, the contact angle of 316L steel increases from 152.29° to 158.22° and that of T91 steel decreases from 149.45° to 151.68°. In the change of contact angle between the two surfaces, the change degree of 316L steel is much greater than that of T91 steel. At high temperature, the mutual diffusion of elements intensifies, which accelerates the interaction between liquid metal and material surface, which leads to the enhancement of wettability. This phenomenon can be effectively suppressed by using only rough surface treatment. In contrast, the surface roughening treatment has a better inhibition effect on the infiltration behavior of LBE on the surface of austenitic stainless steel.
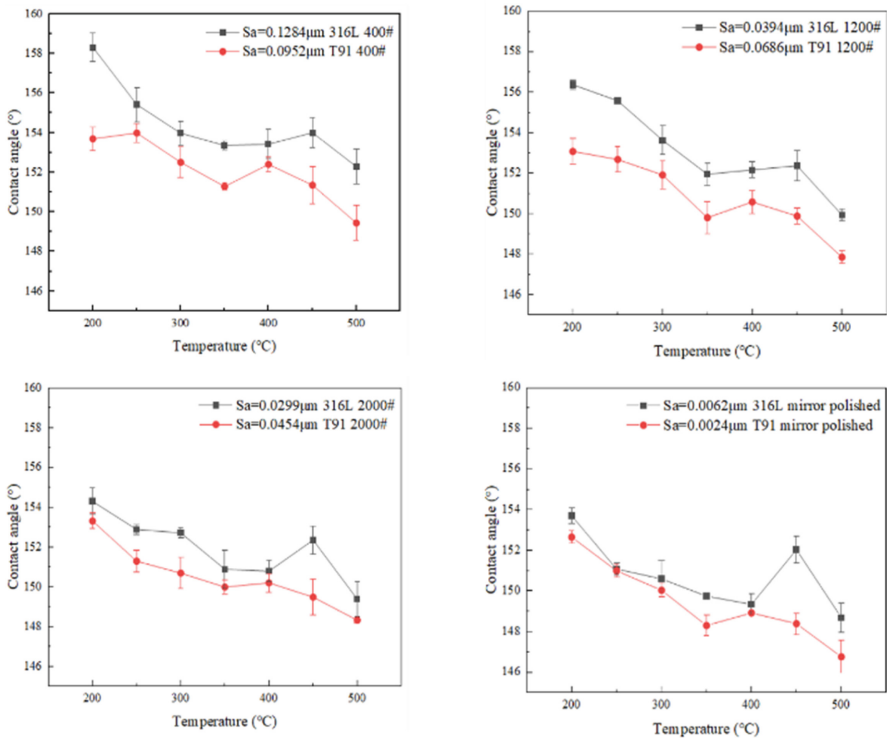
Fig. 7. Comparison of contact angle between 316L and T91 steel at the same roughness.
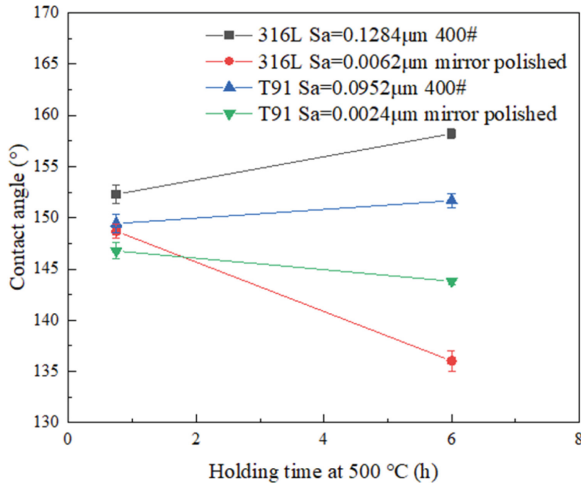
Fig. 8. Influence of contact time on contact angle.

3.3　Contact Time Affects

As mentioned above, with the increase of contact time, the change of contact angle of high and low roughness surfaces shows an opposite trend. In order to further analyze the influence of holding time on the infiltration degree of LBE on the surface of the material, SEM was used to analyze the morphology of 316L interface of LBE under different polishing degree and holding time. The cross-sectional morphology is shown in Fig. 9. It can be seen that when the holding time is 0.75h, LBE at the surface of materials with different polishing conditions is incomplete infiltration, and there are certain gaps at the interface. With the increase of contact time, LBE infiltrates into the surface gap. For rough polished samples, the surface gap is completely penetrated by LBE, and the material surface is in close contact with LBE. For the fine polished samples, in addition to the complete penetration of LBE at the surface, the original flat surface was also found to become rough. The matrix elements of the material diffuse to the LBE, and the combination between the two is closer. Combined with the analysis results of contact angle, it can be seen that with the increase of holding time, the existence of initial rough surface increases the time of complete contact of LBE on the material surface, effectively delaying the dissolution of matrix elements to LBE. The smooth surface is more prone to lead bismuth alloy infiltration, which is not conducive to inhibiting the dissolution of matrix elements in LBE. Therefore, in practical engineering applications, rough polishing of the surface of structural materials is more conducive to the inhibition of LME.
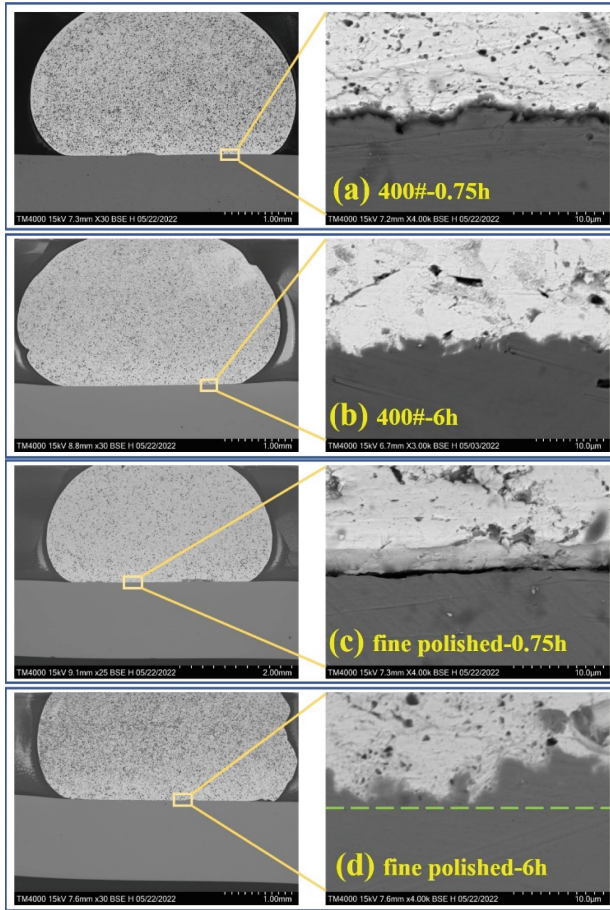
Fig. 9. Cross-section morphology of (a) 316L 400#-0.75h, (b) 316L 400#-6h, (c) 316L mirror polished-0.75h, (d) 316L mirror polished-6h, The green dashed line indicates the location of the original surface of the material.

4   Summary

This paper mainly studied the LBE contact angle of 316L and T91 steels with different surface roughness at 200 ~ 500 °C to analyze the change of wettability, combined with the SEM analysis results. The conclusion can be drawn as follows.

(1) With the increase of temperature, the contact angle of two kinds of stainless steels on different roughness surfaces decreases gradually.
(2) With the increase of roughness, the surface contact angle of the two stainless steels decreases at any temperature.
(3) With the increase of holding time, the contact angle of the two steels on the smooth surfaces decreases, while increases on the rough surfaces.

(4) In contrast, LBE has better wettability to T91 than 316L, indicating that 316L has a lower tendency of LME in practical applications.

References

1. Smith, C.F., Cinotti, L.: 6 - Lead-cooled fast ,kreactor, Editor(s): Igor L. Pioro, In Woodhead Publishing Series in Energy, Handbook of Generation IV Nuclear Reactors, Woodhead Publishing, pp. 119–155, (2016) ISBN 9780081001493,
2. Sobolev, V.: Database of Thermophysical Properties of Liquid Metal Coolants for GEN-IV (2011)
3. Murty, K.L., Charit, I.: Structural materials for Gen-IV nuclear reactors: challenges and opportunities, J. Nucl. Mater. **383,** 189e195 (2008)
4. Shen, X., Yamamoto, T., Han, X., Hibiki, T.: Interfacial area concentration in gas-liquid metal two-phase flow Experimental Comput. Multiphase Flow **5**, 84–98 (2021)https://doi.org/10.1007/s42757-021-0110-x
5. Auger, T., Serre, I., Lorang, G., Hamouche, Z., Gorse, D., Vogt, J.-B.: Role of oxidation on LME of T91 steel studied by small punch test. J. Nucl. Mater. **376**(3), 336–340 (2008)
6. Hojna, A., Di Gabriele, F.: On the kinetics of LME for the ferritic–martensitic steel T91 immersed in liquid PbBi eutectic J. Nuclear Mater. **413**(1), 21–29 (2011) ISSN 0022–3115
7. DiGiovanni, C., Ghatei Kalashami, A., Biro, E., Zhou, N.Y.: Liquid metal embrittlement transport mechanism in the Fe/Zn system: Stress-assisted diffusion, Materialia, **18** (2021) 101153, ISSN 2589–1529
8. Monchoux, J.P., Rabkin, E.: Microstructure evolution and interfacial properties in the Fe-Pb system. Acta Mater. **50**, 3159 (2002)
9. Zhao, Z.-Y., Li, T., Duan, Y., Wang, Z., Li, H.: Wetting and coalescence of the liquid metal on the metal substrate. Chinese Phys. B, **26**(08), 144–150 (2017)
10. Giuranno, D., Gnecco, F., Ricci, E., et al.: Surface tension and wetting behaviour of molten Bi–Pb alloys. Intermetallics **11**, 1313–1317 (2003)
11. Liu, J., Jiang, Z., Tian, S., et al.: Wetting of T91 by Molten Pb and PbBi alloy. Atomic Energy Sci. Technol. **49**, 194–199 (2015)
12. Zhen, Q., Liang, L., Rong-yue, W., Yan-gang, Z., Zhang-fu, Y.: Roughness-dependent wetting and surface tension of molten lead on alumina, Trans. Nonferrous Metals Society China, **31**(8), 2511–2521, (2021) ISSN 1003-6326.
13. Young, T.: An essay on the cohesion of fluids. Philos. Trans. R. Soc. Lond. **95**, 65–87 (1805)

Solid-Liquid Equilibria of Ternary Systems UO$_2$(NO$_3$)$_2$ + HNO$_3$ + H$_2$O and UF$_4$ + HF + H$_2$O at 298 K

Wang Lin$^{(\boxtimes)}$, Xu Dan, Feng Jianxin, Cui Hanlong, Wang Wenhui, and Zhu Yingxi

The 404 Company Limited, CNNC, Lanzhou, Gansu Prov, China
wanglinc413@126.com

Abstract. UO$_2$(NO$_3$)$_2$ and UF$_4$ are significant intermediates that connect different chemical unit operations (such as dissolution, evaporation, concentration, extraction and etc.) in uranium chemical industry. Commonly, there is a basic physicochemical question about phase equilibrium of ternary systems UO$_2$(NO$_3$)$_2$ + HNO$_3$ + H$_2$O and UF$_4$ + HF + H$_2$O, it is crucial to understand the phase behavior and thermodynamic properties of them with the continuous development of uranium chemical industry. In this study, solid-liquid phase equilibria of ternary systems UO$_2$(NO$_3$)$_2$ + HNO$_3$ + H$_2$O and UF$_4$ + HF + H$_2$O at 298 K were studied by means of isothermal dissolution method, the solubilities and densities of equilibria liquid phase were investigated experimentally for two systems, the composition of equilibria solid phase of system UO$_2$(NO$_3$)$_2$ + HNO$_3$ + H$_2$O at 298 K were determined by Scherinemakers' wet residue method, and the method of X-ray diffraction was used to determine the composition of equilibria solid phase for system UF$_4$ + HF + H$_2$O at 298 K. Phase diagrams and diagrams of density-composition were constructed for systems UO$_2$(NO$_3$)$_2$ + HNO$_3$ + H$_2$O and UF$_4$ + HF + H$_2$O at 298 K. Results show that there are unique isothermal dissolution curve for two ternary systems, and corresponding crystallization zone are UO$_2$(NO$_3$)$_2$·6H$_2$O and UF$_4$·2.5H$_2$O, respectively.

Keywords: Solid-liquid Equilibria · Uranium Nitrate · Uranium Tetrafluoride

1 Introduction

UO$_2$(NO$_3$)$_2$ and UF$_4$ are significant intermediates that connect different chemical unit operations in uranium chemical industry, such as dissolution, evaporation, concentration, extraction and etc. Commonly, HNO$_3$ was widely used to dissolve U$_3$O$_8$, UO$_3$, UO$_2$, or UF$_4$, and HF was used to produce UF$_4$ in uranium chemical industry. Herein, a ternary system UO$_2$(NO$_3$)$_2$ + HNO$_3$ + H$_2$O widely existed in unit operations of the former mentioned, and ternary system UF$_4$ + HF + H$_2$O can be simplified in the unit process of the latter mentioned. There is a basic physicochemical question about phase equilibrium of two ternary systems mentioned above, it is crucial to understand the phase behavior and thermodynamic properties of them with the continuous development of uranium chemical industry.

For ternary system $UO_2(NO_3)_2 + HNO_3 + H_2O$, research temperature mainly was focused on 298 K – 357 K, in literature [1], three crystalline phase regions can be found for ternary system $UO_2(NO_3)_2 + HNO_3 + H_2O$, which corresponding to $UO_2(NO_3)_2 \cdot 6H_2O$, $UO_2(NO_3)_2 \cdot 3H_2O$ and $UO_2(NO_3)_2 \cdot 2H_2O$, respectively. It was suggested that the crystalline form of $UO_2(NO_3)_2$ is not only related to temperature, but also to co-existing ion in aqueous solution. Recently, Maliutin et al. [2] adopted Pitzer-Simonson-Clegg model to simulate the solubility of quaternary system $UO_2(NO_3)_2 + Ca(NO_3)_2 + HNO_3 + H_2O$ at 263 K, 298 K, and 323 K, and corresponding model parameters were presented. In our precious study [3], the Pitzer thermodynamic model was used to simulate the solubility of ternary system $UO_2(NO_3)_2 + + HNO_3 + H_2O$ with HNO_3 concentration range of $0 - 8.5$ mol·kg^{-1} at 298 K. For solid-liquid phase equilibrium of ternary system $UF_4 + HF + H_2O$, there are very few reports in the literatures [4, 5]. Meanwhile, there are relatively large differences in the only data available, for instance, the solubility of UF_4 in pure water is 0.005% from literature [4], but it is 0.028% in literature [5]. Indeed, it is difficult to evaluate their reliability.

Based on this, ternary systems $UO_2(NO_3)_2 + HNO_3 + H_2O$ and $UF_4 + HF + H_2O$ at 298 K were investigated in this work, experimental thermodynamic data of density and solubility were measured for two systems at 298 K. These thermodynamic data acquired by this work can provide theoretical basis for comprehensive utilization and treatment of wastewater resources produced by uranium chemical industry.

2 Experimental Section

2.1 Reagents

Double-deionized water ($\kappa \leq 5.5 \times 10^{-6}$ S·m^{-1}) obtained from UPT water purification system was used in the experiments. Nitric acid with mass fraction 65% – 68% and hydrofluoric acid with mass fraction 40% were purchased from the Shandong Zibo Haofeng Chemical Co., Ltd., which were used directly as received without further purification. Uranyl nitrate hexahydrate and uranium tetrafluoride obtained by laboratory synthesis were used in the experiments. The detailed information of all chemicals used in this work is listed in Table 1.

Table 1. The source and purity of the chemicals used in this experiments

chemical name	CAS No	mass fraction purity	source
nitric acid	7697-37-2	65%–68%	Shandong Zibo Haofeng Chemical Co., Ltd., China
hydrofluoric acid	7664-39-3	40%	Shandong Zibo Haofeng Chemical Co., Ltd., China
Uranyl nitrate hexahydrate	13520-83-7	> 99.5%	Sinopharm laboratory synthesis
uranium tetrafluoride	10049-14-6	> 90%	laboratory synthesis

2.2 Apparatus

An analytical balance (Sartorius, Germany) with a precision of 0.0001 g was used to determine the weight of solution. The thermostat (GDJS-1009, China) with the temperature kept at 298 ± 0.2 K was used for the phase equilibrium experiments. The densities of the sample of the equilibrium liquid phase were determined by weighing bottle method with an uncertainty of 5.0×10^{-4} g·cm^{-3}.

2.3 Experimental Method

Isothermal dissolution method was used to determine the solubilities of systems $UO_2(NO_3)_2 + HNO_3 + H_2O$ and $UF_4 + HF + H_2O$ at 298 K. The specific experimental steps are as follows: 1) a series of stock solutions of HNO_3 with the mass fraction of HNO_3 0% – 65% in glass bottles (approximately 20 mL) were prepared, and teflon bottles were used to prepare the stock solution of HF (approximately 20 mL) with the mass fraction of HF 0% – 40% because of its' strong corrosion. 2) Excess uranyl nitrate hexahydrate and uranium tetrafluoride were added to the stock solutions acquired by step 1), respectively. 3) the samples were placed in the thermostat at 298 ± 0.2 K with a 120 rpm stirring speed to promote equilibration. 4) When the equilibrium point of solution was reached (approximately 12 to 15 days), the samples were kept a static condition at working temperature for an additional 24 h, and then the clear liquid of each solution at equilibrium was collected by filtering to determine density, and composition.

2.4 Analysis Method

The mass fraction of $UO_2(NO_3)_2$ and UF_4 in equilibrium solution was acquired by determining the concentration of UO_2^{2+} and U^{4+}, which can be obtained by the methods of dichromate titration and ammonium thiocyanate spectrophotometric with an uncertainty of 0.5%, respectively. The mass fraction of HNO_3 and HF in equilibrium solution was acquired by determining the concentration of H^+, which can be obtained by the method of sodium hydroxide titrate with an uncertainty of 0.5%. Schreinemakers' wet residue method [6] and X-ray diffraction were used to determine the compositions of equilibrium solid phase for two systems.

3 Results and Discussion

3.1 Synthesis of $UO_2(NO_3)_2 \cdot 6H_2O$ and UF_4

Synthesis of $UO_2(NO_3)_2 \cdot 6H_2O$. Take U_3O_8 and HNO_3 with the concentration 6.0 mol·L^{-1} as raw material. First, adding 100 g U_3O_8 into 130 mL HNO_3 solution and keep stirring with a 120 rpm stirring speed to make U_3O_8 dissolve sufficiently at 333 K – 363 K, the stirring was stopped after the solution was clarified, uranyl nitrate solution was obtained by filtration. Then, $UO_2(NO_3)_2$ solution was evaporated until the volume of the solution was reduced to half of the original, and the heating was stopped and slowly cooled to room temperature to crystallize out $UO_2(NO_3)_2 \cdot 6H_2O$ crystals, After filtration, $UO_2(NO_3)_2 \cdot 6H_2O$ crystal with purity meeting the requirements of this experiment can be obtained.

Synthesis of UF$_4$. Taking the UO$_3$ and NH$_4$HF$_2$ as raw material, according to the mass ratio of 1:1.5, UO$_3$ and NH$_4$HF$_2$ were mixed evenly in a self-made fluorination reactor, which was then placed in muffle furnace. Setting temperature of muffle furnace at 723 K for 6 h, UF$_4$ with purity meeting the experimental requirements can be obtained.

3.2 Phase Equilibrium for Ternary System UO$_2$(NO$_3$)$_2$ + HNO$_3$ + H$_2$O at 298 K

The composition of saturation point measured by this work was compared with literatures for binary system UO$_2$(NO$_3$)$_2$ + H$_2$O at 298 K as shown in Fig. 1, the solubility of UO$_2$(NO$_3$)$_2$ in pure water obtained by this work is 56.15%, and the solubility of UO$_2$(NO$_3$)$_2$ in pure water obtained by literatures [7, 8] are 56.15% and 55.85%, respectively. The relative deviation below 0.005, which suggests that the experimental method is reliable.
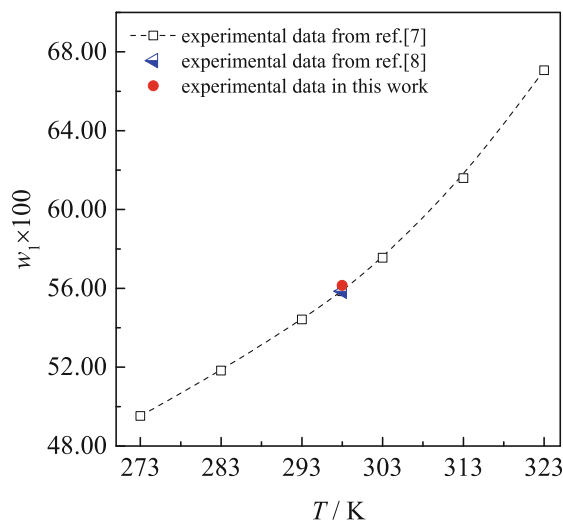

Fig. 1. Solubilities of UO$_2$(NO$_3$)$_2$ in pure water at 298 K

The data of densities, compositions of equilibrium liquid phase and the compositions of wet-solid phase for ternary system UO$_2$(NO$_3$)$_2$ + HNO$_3$ + H$_2$O at 298 K were presented in Table 2.

According to the experimental phase equilibrium data of system UO$_2$(NO$_3$)$_2$ + HNO$_3$ + H$_2$O at 298 K, the diagrams of solubility and density-compositions were plotted, and presented in Fig. 2. As shown in Fig. 2(a), the equilibrium phase diagram was composed of one univariant isothermals and one crystalline phase zone corresponding UO$_2$(NO$_3$)$_2$·6H$_2$O for ternary system UO$_2$(NO$_3$)$_2$ + HNO$_3$ + H$_2$O at 298 K. In univariant isothermals, the solubilities of UO$_2$(NO$_3$)$_2$ present a trend that decreases first and then increases with the increase of mass percentage of HNO$_3$ in equilibrium liquid phase. This phenomenon may be due to 1) when the mass fraction of HNO$_3$ in equilibrium solution is low, the dissociation of HNO$_3$ molecules is relatively complete, it exists as H$^+$ and

Table 2. Experimental phase equilibrium data for ternary system $UO_2(NO_3)_2(1) + HNO_3(2) + H_2O(3)$ at 298 Ka

No	Density /g·cm^{-3}	Composition of equilibrated solution/%		Composition of wet solid phase/%		Equilibrated solid phase
		w_1	w_2	w_1	w_2	
1	1.7690	56.15	0.00	-b	-b	UNHc
2	1.7378	51.11	1.94	63.83	1.18	UNH^c
3	1.7323	50.99	3.18	-b	-b	UNH^c
4	1.7244	47.07	5.00	64.25	2.04	UNH^c
5	1.6368	42.05	8.50	61.89	4.09	UNH^c
6	1.6547	40.84	10.55	60.56	5.29	UNH^c
7	1.6589	38.82	12.71	61.31	5.98	UNH^c
8	1.6060	37.13	13.64	60.02	5.98	UNH^c
9	1.6158	38.67	15.34	65.40	5.11	UNH^c
10	1.5737	34.42	18.22	58.60	8.55	UNH^c
11	1.5652	31.77	21.18	57.99	9.84	UNH^c
12	1.5432	32.11	23.20	62.03	8.07	UNH^c
13	1.6032	33.25	25.34	68.88	6.04	UNH^c
14	1.6538	35.54	29.98	64.52	10.11	UNH^c

Note: ^{a} Standard uncertainties u are $u(T) = 0.20$ K; $u_r(\rho) = 5.0 \cdot 10^{-4}$ g·cm^{-3}; $u_r (1) = 0.0050$; $u_r (2) = 0.0050$; ^{b} Not determined; ^{c} UNH represents $UO_2(NO_3)_2 \cdot 6H_2O$

NO_3^-, the common-ion effect of NO_3^- cause the solubility of $UO_2(NO_3)_2$ decreases. 2) However, with the increase of mass fraction of HNO_3 in solution, the common-ion effect get more weaker because of the lower degree of dissociation of HNO_3 molecules, thus the solubility of $UO_2(NO_3)_2$ increases slightly. Meanwhile, comparing the solubility of $UO_2(NO_3)_2$ in mixed solution HNO_3-H_2O with literatures [3, 9], it can be shown from Fig. 2(a) that the experimental solubility measured by this work are in good agreement with literatures.

As shown in Fig. 2(b), the change trend of densities of equilibrium liquid phase has a same regulation that the densities of equilibrium solution decreases first and then increases with the increase of mass fraction of HNO_3 for ternary system $UO_2(NO_3)_2 + HNO_3 + H_2O$ at 298 K.

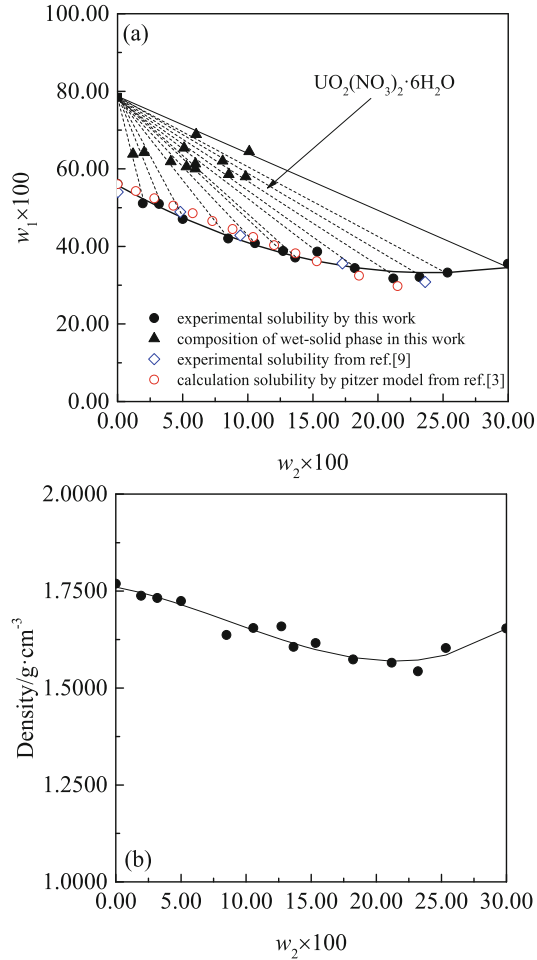**Fig. 2.** Equilibrium phase diagram(a) and diagram of density-composition(b) for ternary system $UO_2(NO_3)_2 + NO_3\ H_2O$ at 298 K

3.3 Phase Equilibrium for Ternary System $UF_4(1) + HF(2) + H_2O(3)$ at 298 K

The data of densities, compositions of equilibrium liquid phase for ternary system UF_4 + HF + H_2O at 298 K were presented in Table 3.

The diagrams of solubility and density-compositions were plotted according to the experimental phase equilibrium data of system UF_4 + HF + H_2O at 298 K and presented in Fig. 3. As shown in Fig. 3(a), the solubility of UF_4 in pure water is 0.31%, and it decreases sharply with the increase of mass fraction of HF when the mass fraction of HF

is between 0% - 10.5%. However, the solubility of UF_4 presents a trend of slow increase with the increase of mass fraction of HF when the mass fraction of HF beyond 10.5%. Likewise, this change trend is same as that in ternary system $UO_2(NO_3)_2 + HNO_3 + H_2O$ at 298 K, which is also due to the co-ionic effect caused by partial dissociation of HF in aqueous solution. Meanwhile, the solubility of UF_4 in water at 298 K was compared with literatures [3, 4] in this work, it can be shown that there are tremendous difference for the solubility of UF_4 in water at 298 K, which is 0.005% measured by lit. [3], 0.028% obtained by lit [4]. and 0.31% acquired by this work. And from Fig. 3(a), the solubility of UF_4 in HF + H_2O at 298 K obtained by lit [3]. is slightly higher than the experimental value measured by this wok. It may be due to the low purity of UF_4 synthesized by this work, where a small amount of UO_2F_2 existing in UF_4. However, these thermodynamic data is still of great value for guiding the comprehensive utilization of waste liquid resources from the process of UF_4 production.

Table 3. Experimental phase equilibrium data for ternary system $UF_4(1) + HF(2) + H_2O(3)$ at 298 K[a]

No	Density /g·cm^{-3}	Composition of equilibrated solution/%		Composition of wet solid phase/%		Equilibrated solid phase
		w_1	w_2	w_1	w_2	
1	0.9986	0.3100	0.0000	$-c$	$-c$	UFH[b]
2	1.0012	0.2600	0.8087	$-c$	$-c$	UFH[b]
3	1.0089	0.0334	3.8185	$-c$	$-c$	UFH[b]
4	1.0270	0.0128	8.1103	$-c$	$-c$	UFH[b]
5	1.0408	0.0070	10.5036	$-c$	$-c$	UFH[b]
6	1.0520	0.0079	12.3714	$-c$	$-c$	UFH[b]
7	1.0640	0.0102	15.1684	$-c$	$-c$	UFH[b]
8	1.0807	0.0155	17.3424	$-c$	$-c$	UFH[b]
9	1.0920	0.0136	20.5006	$-c$	$-c$	UFH[b]
10	1.1020	0.0149	23.6198	$-c$	$-c$	UFH[b]
11	1.1184	0.0169	24.2049	$-c$	$-c$	UFH[b]
12	1.1331	0.0259	29.4052	$-c$	$-c$	UFH[b]

Note: [a] Standard uncertainties u are $u(T) = 0.20$ K; $u_r(\rho) = 5.0 \cdot 10^{-4}$ g·cm^{-3}; $u_r(1) = 0.0050$; $u_r(2) = 0.0050$; [b] UFH represents $UF_4 \cdot 2.5H_2O$, determined by the method of X-ray diffraction; [c] Not determined
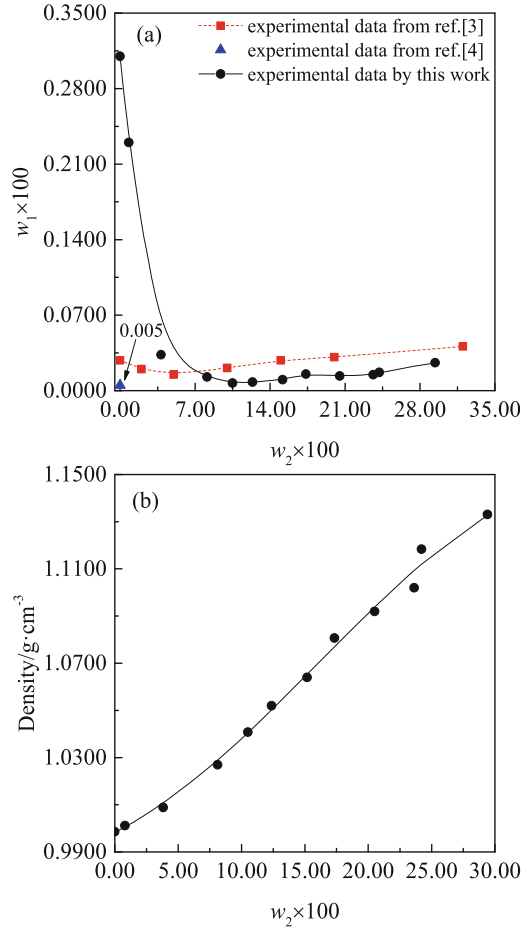
Fig. 3. Equilibrium phase diagram(a) and diagram of density-composition(b) for ternary system $UF_4 + HF + H_2O$ at 298 K

From Fig. 3(b), it is shown that the density of equilibrium solution increases with the mass fraction of HF for ternary system $UF_4 + HF + H_2O$ at 298 K, which suggests that the density of equilibrium solution is dominated by HF.

For ternary system $UF_4 + HF + H_2O$ at 298 K, the composition of wet-solid phase was not given in this work because of its low solubility of UF_4 in pure water. Thus, the X-ray diffraction method was used to identify the equilibrium solid phase for this system. As shown in Fig. 4, the X-ray diffraction of wet-solid phase of point 12 for system $UF_4 + HF + H_2O$ at 298 K can be consistent well with the characteristic peak of the standard card of PDF#11–0623, which suggests that the equilibrium solid phase is $UF_4 \cdot 2.5H_2O$.

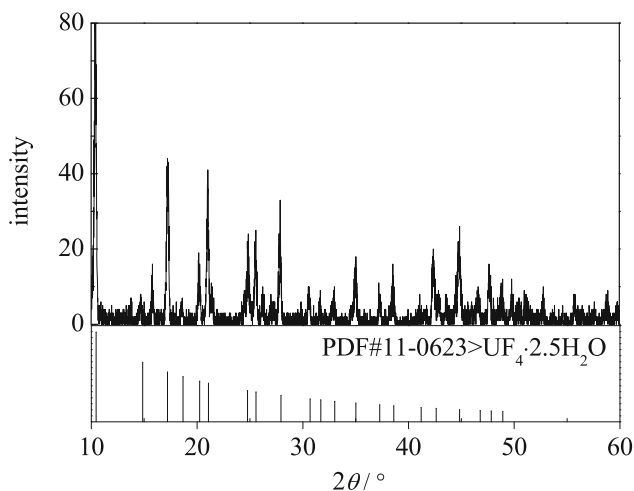**Fig. 4.** X-ray diffraction pattern of equilibrium solid phase of point 12 for ternary system UF_4 + HF + H_2O at 298 K

4   Conclusions

In this paper, solid-liquid phase equilibria of ternary systems $UO_2(NO_3)_2$ + HNO_3 + H_2O and UF_4 + HF + H_2O at 298 K were investigated by isothermal dissolution method, the compositions and densities of equilibria liquid phase were measured experimentally. Phase diagrams and diagrams of density-composition were constructed for systems $UO_2(NO_3)_2$ + HNO_3 + H_2O and UF_4 + HF + H_2O at 298 K. There are unique isothermal dissolution curve for two ternary systems, and corresponding crystallization zone are $UO_2(NO_3)_2 \cdot 6H_2O$ and $UF_4 \cdot 2.5H_2O$, respectively. In univariant isothermals, the solubilities of $UO_2(NO_3)_2$ or UF_4 present a trend that decreases first and then increases slightly with the increase of mass percentage of HNO_3 or HF in equilibrium liquid phase.

References

1. William, L.M., Ruth, S.: J. Inorg. Nucl. Chem. **25**(3), 283–290 (1963)
2. Maliutin, A.S., Kovalenko, N.A., Uspenskaya, I.A.: J. Chem. Eng. Data **66**(4), 984–993 (2022)
3. Wang, L., Wang, J.C., Yue, X.Y., et al.: Progress Report on China Nuclear Science & Technology. **7**, 1–6 (2021)
4. Lukyanicev, Y.A., Nikolaev, N.S.: Atomnaya Energia. **15**, 423 (1964)
5. Tananaev, I.V., Savchenko, G.S.: Atomnaya Energia. **12**, 399 (1962)
6. Fosbol, P.L., Thomsen, K., Stenby, E.H.: J. Solution Chem. **38**(1), 1–14 (2009)
7. Haynes, W.M.: CRC Handbook of chemistry and physics [M], 97th edn., pp. 8–177. CRC Press/Taylor & Francis, Boca Raton, FL (2016)

8. Cohen-Adad, R., Lorimer, J.W., Phillips, S.L., Salomon, M.: J. Chem. Inf. Model. **35**(4), 675–696 (2002)
9. Davis, W., Lawson, P.S., deBruin, H.J., et al.: J. Phys. Chem. **69**, 1904–1914 (1965)

A Moose-Based Neutron Diffusion Code with Application to a LMFR Benchmark

Weixiang Wang, WenPei Feng, KeFan Zhang, Guangliang Yang, Tao Ding, and Hongli Chen$^{(\boxtimes)}$

University of Science and Technology of China, Hefei, Anhui, China
`hlchen1@ustc.edu.cn`

Abstract. MOOSE (Multiphysics Object-Oriented Simulation Environment) is a powerful finite element multi-physics coupling framework, whose object-oriented, extensive system is conducive to the development of various simulation tools. In this work, a full-core MOOSE-based Neutron Diffusion application is developed, and a 3D PWR benchmark 3D-IAEA with given group constants is applied for code verification. Then the MOOSE-based Neutron Diffusion application is applied to the calculation of a Sodium-cooled Fast Reactor (SFR) benchmark, together with the research on homogenized few-group constants generation based on Monte Carlo method. The calculation adopts a 33-group cross section sets, which is generated using Monte Carlo code OpenMC. Considering the long neutron free path and strong global neutron spectrum coupling of liquid metal cooled reactor (LMFR), a full-core homogeneous model is used in OpenMC to generate the homogenized few-group constants. In addition, transport correction is used in the process of cross section generation, considering the prominent anisotropic scattering of fast reactor. The calculated results, including effective multiplication factor (k_{eff}) and assembly power distributions, are in good agreement with the reference values and the calculation results of OpenMC, which proves the accuracy of the neutron diffusion application, and also shows that the Monte Carlo method can be applied to generation of homogenized few-group constants for LMFR analysis.

Keywords: MOOSE · OpenMC · Neutron diffusion · Few-group constants generation · LMFR

1 Introduction

Neutron diffusion equation is a great simplification of Boltzmann transport equation, while it can obtain sufficient accuracy with less requirements for computer resources, so neutron diffusion theory is still a main method to solve the neutron flux at full-core scale. Nodal method is widely used in most neutron diffusion codes like DIF3D [1], DYN3D [2], and SIMULATE-4 [3], while which is different from the numerical methods of common Thermal-Hydraulic code, so coupling between neutronics and thermal-hydraulics is usually in manner of "code to code", which often requires a lot of modifications to the original codes, and such kind of coupling is usually "loosely". An alternative

coupling method, called multi-physics modeling approach, can solve variables of each system simultaneously, which promotes the research on the solution of neutron diffusion problem based on multi-physics platform. Neutronic modeling based on multi-physics platform like COMSOL [4, 5], OpenFOAM [6, 7], NURESIM [8, 9] has been widely researched. In this work, a full-core neutron diffusion application is developed based on MOOSE, a powerful Finite Element Method (FEM) multi-physics coupling framework. 3D-IAEA Benchmark with given few-group constants is applied for code verification.

In addition, solutions of neutron diffusion equation in conventional deterministic neutronic codes are generally based on fixed assembly shape and arrangement (such as rectangular or hexagonal assemblies). While with the trend of modularization and miniaturization of Generation IV nuclear reactors, the core structure is becoming more and more complex. Therefore, deterministic neutronics needs a more convenient modeling method. The MOOSE-based neutron diffusion application in this paper can achieve a free manner of reactor core modeling.

Full-core diffusion calculation need few-group constants as input. Traditionally, complicated procedure of self-shielding and lattice transport calculation was adopted to generate few-group constants, while problem of accuracy exists because of simplifications made in this procedure. Recent years, generation of few-group constants using Monte Carlo method has been widely researched, aim to improve accuracy. Monte Carlo code like Serpent [10], McCARD [11], cosRMC [12] already has the ability to generate homogenized few-group constants. In order to realize the practicability of the developed MOOSE-based diffusion program, the problem of the giving of few-group constants must be solved. Therefore, this work research on few-group constants generation using MC code OpenMC. The homogenized few-group constants of a Sodium-cooled Fast Reactor (SFR) benchmark is generated in this work, and the MOOSE-based diffusion application is applied on this benchmark.

Rest of this paper is organized as follows. Section 2 gives a brief introduction of codes and computational methods used in this paper. Section 3 & 4 presents the diffusion calculation of 3D-IAEA (with given few-group constants) and ABR-MOX (with few-group constants generated by OpenMC) respectively. Section 5 summarizes the conclusions.

2 Code and Method Introduction

2.1 MOOSE Introduction

MOOSE [13] (Multiphysics Object-Oriented Simulation Environment) is an open-source FEM computational framework developed by Idaho National Laboratory (INL), aims at solution of coupled physics systems. JFNK algorithm and physics-based preconditioning of MOOSE framework enable it to solve multi-physics systems in a "fully coupled" manner. The layered coupling structure makes the development of MOOSE-based application relatively easy, developers only need to pay attention to the definition of the top-level physical field or "kernels", rather than the solution of algebraic equations and data transmission. Well-known nuclear fuel performance code BISON [14], general purpose reactor physics code MAMMOTH [15] are all developed based on MOOSE.

Solution of steady-state neutron diffusion equation is an eigenvalue problem, and the equation is written as:

$$-\nabla \cdot D_g \nabla \phi_g + \Sigma_{t,g} \phi_g = \sum_{g'=1}^{G} \Sigma_{g' \to g} \phi_{g'} + \frac{\chi_g}{k_{eff}} \sum_{g'=1}^{G} \left(\nu \Sigma_f \right)_{g'} \phi_{g'} \tag{1}$$

$$g = 1, 2, \cdots, G$$

Where $\Sigma_{t,g}$ is macroscopic total cross section, D_g is neutron diffusion coefficient, ϕ_g is scalar neutron flux, χ_g is normalized fission spectrum, and k_{eff} is effective multiplication factor. The first step of using FEM to solve a partial difference equation (PDE) is forming it into Weak form, the weak form of diffusion equation can be written as:

$$\boldsymbol{F}_{\phi_g}(\boldsymbol{U}) = \left(\nabla \boldsymbol{B}, D_g \nabla \phi_g \right) - \langle \boldsymbol{B}, D_g \nabla \phi_g \cdot \boldsymbol{n} \rangle + \left(\boldsymbol{B}, \Sigma_{\mathrm{r},g} \phi_g \right)$$
$$- \left(\boldsymbol{B}, \sum_{g'=1}^{G} \Sigma_{g' \to g} \phi_{g'} \right) - \frac{1}{k_{eff}} (B, \chi_g \sum_{g'=1}^{G} \left(\nu \Sigma_f \right)_{g'} \phi_{g'}) \tag{2}$$

Five terms at the right end of the equation are leakage term, boundary condition, removal term, scattering source term and fission source term, the parentheses term represent the volume integral term, and the angle brackets term represent the surface integral term (boundary condition) of the calculation domain. Because neutronics is export controlled physics, MOOSE itself has no modules related to neutronic calculation. Therefore, for the MOOSE-based diffusion application of this work, the kernels corresponding to each term of Eq. (2) are developed. As mentioned before, steady-state neutron diffusion equation is an eigenvalue problem, and the built-in Eigenvalue Executioner of MOOSE can be used to solve such kind of problem.

2.2   MC-Based Few-Group Constants Generation

OpenMC [16] is a Monte Carlo neutron and photon transport simulation code, developed by Massachusetts Institute of Technology (MIT). It is capable of performing fixed source, k-eigenvalue, and subcritical multiplication calculations like usual MC code, and has many unique features like its rich, extensible Python and C/C++ programming interfaces, depletion calculation ability and so on. Energy condensation and spatial homogenization in a few-group constants generation process can be accomplished in OpenMC by its tally system, which process is based on the principle of reaction rate conservation, as:

$$\Sigma_{x,g,k} = \frac{\int_{E_g}^{E_{g-1}} dE' \int_{V_k} d\boldsymbol{r} \Sigma_x(\boldsymbol{r}, E') \phi(\boldsymbol{r}, E')}{\int_{E_g}^{E_{g-1}} dE' \int_{V_k} d\boldsymbol{r} \phi(\boldsymbol{r}, E')} \tag{3}$$

Where $\Sigma_{x,g,k}$ is the homogenized few-group cross section of reaction x in energy group g and region k, which can be used directly in neutron diffusion code. The generated group constants for diffusion calculation include total cross section, scattering cross section, diffusion coefficient and fission cross section (multiplied by normalized fission

spectrum and average fission neutrons produced per fission). Considering the prominent anisotropic scattering of fast reactor, transport correction is used in the process of scattering cross section generation, as:

$$\Sigma_{s,g'\to g} = \frac{\left\langle \Sigma_{s,0,g'\to g}\phi \right\rangle - \delta_{gg'}\sum_{g''}\left\langle \Sigma_{s,1,g''\to g}\phi \right\rangle}{\langle\phi\rangle} \tag{4}$$

Where $\Sigma_{s,g'\to g}$ is transport-correction cross section. In addition, (n, xn) reactions are negligible for the hard neutron spectrum of fast reactor [17]. The effect of neutron multiplication from (n, xn) reactions is incorporated into the transport-correction cross section.

Most MC-based few-group constants generation methods are somewhat similar to the traditional 2-step method, i.e., cell or assembly level transport calculation with leakage-corrected model is applied in few-group constants generation [18]. While in this work, considering the long neutron free path and strong global neutron spectrum coupling of LMFR, an approach of using a full-core homogeneous MC model to generate the homogenized few-group constants is researched, which can directly model the neutronic coupling between fuel assemblies and reflectors.

The overview Technique Route of the OpenMC-based few-group constants generation and full-core neutronic diffusion calculation by MOOSE-based diffusion application is depicted in Fig. 1. In which process, an in-house tool to automatically write the input file of MOOSE is developed, which can read the output of OpenMC and automatically write the few-group constants into the format of MOOSE input file; And an in-house post-processing tool, which can process the output of MOOSE and output the normalized assembly power factor.
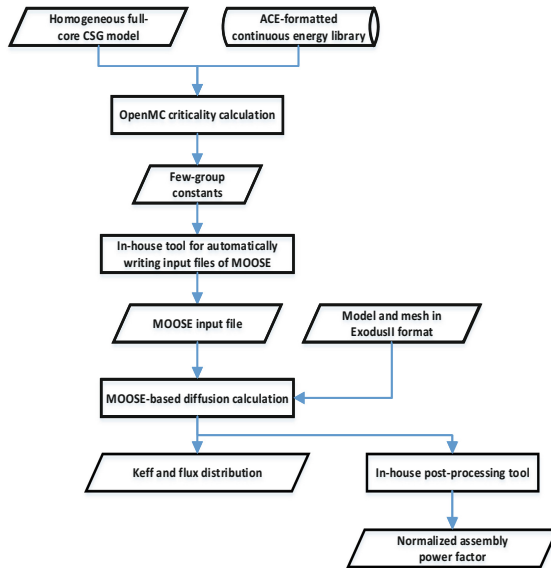

Fig. 1. Overview of Technique Route

3   Code Verification

3.1   Benchmark Modeling Description

A 3D PWR full-core benchmark 3D-IAEA [19] is calculated by the diffusion application for code verification. 3D-IAEA is a full-core steady-state two group neutron diffusion problem, there are 177 fuel assemblies and 64 reflector assemblies, and there are 9 fully inserted and 4 partially inserted control rods, the total height of the core is 380 cm. The core structure is shown in Fig. 2. And the 2-group constants set is given as Table 1. Considering the symmetry structure of the core, a 1/4 geometry is constructed for calculation, the geometry and unstructured mesh used in the calculation is shown in Fig. 3. The number of elements and DOF is 4.94 million and 1.71 million respectively. The high-performance computer used in the calculation procedure has dual Intel Core i9-7900X ten-core CPU (3.30 GHz) and contains 64 GB of RAM. The total run time of this problem was 93.3 min using 16 processors with MPI.
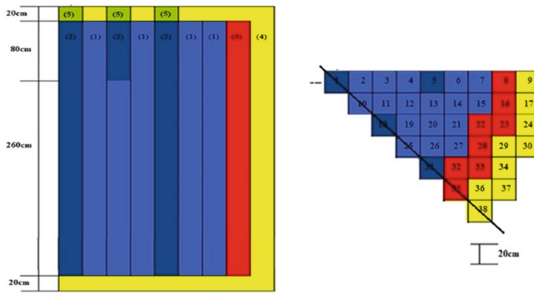
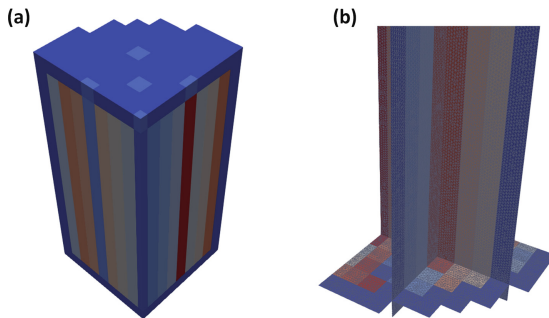

Fig. 2.   Core structure of 3D-IAEA

Fig. 3.   (a) Quarter-Core geometry and (b) slice of unstructured mesh of 3D-IAEA

Table 1. 2-group constants of 3D-IAEA

Region	Group	D_g	$\Sigma_{a,g}$	$\upsilon\Sigma_{f,g}$	$\Sigma_{s,1\rightarrow 2}$
1	1	1.500	0.010	0.000	0.020
	2	0.400	0.080	0.135	–
2	1	1.500	0.010	0.000	0.020
	2	0.400	0.130	0.135	–
3	1	1.500	0.010	0.000	0.020
	2	0.400	0.085	0.135	–
4	1	2.000	0.000	0.000	0.040
	2	0.300	0.010	0.000	–
5	1	2.000	0.000	0.000	0.040
	2	0.300	0.010	0.000	–

3.2 Computation and Results

The calculation results of the MOOSE-based diffusion application are listed below. Table 2 shows the comparison of effective multiplication factor (k_{eff}) between calculation and reference. The calculated k_{eff} is 1.02900, and the relative error with the reference value of 1.02903 is only 3 pcm. The calculated peak-to-average power density is 2.429, which is 3.2% different from the reference value of 2.354. Figure 4 shows the comparison between the calculated normalized assembly power factor distribution and the reference value. The maximum relative error is 1.91%, and the average relative error is 0.52%, which is in good agreement with the reference value, which proves the accuracy of the diffusion application. The distributions of fast and thermal neutron flux are depicted in Fig. 5.

Table 2. Comparison of calculated results and reference

	Calculated	Reference	Error
k_{eff}	1.02900	1.02903	3 pcm
Peak-to-average Power Density	2.429	2.354	3.2%

It could be concluded from above calculation that the MOOSE-based neutron diffusion application is valid and accurate, the solution of neutron diffusion problem based on unstructured mesh is realized, which can handle complex geometry. The benchmark verified in this section is a given few-group constants problem, while as mentioned before, most practical problems can not directly obtain few-group constants. Therefore, the content of the next section is to research the generation of few-group constants based on MC, to solve the input-given problem of the developed diffusion application.

					0.597 0.6084 1.91%		
				0.476 0.4813 1.12%	0.7 0.7038 0.55%	0.611 0.6206 1.57%	
Ref Cal error			1.178 1.1804 0.21%	0.972 0.9739 0.20%	0.923 0.9285 0.60%	0.866 0.8772 1.30%	
		1.369 1.3701 0.08%	1.311 1.3128 0.14%	1.181 1.1841 0.26%	1.089 1.0944 0.49%	0.999 1.0061 0.71%	0.711 0.7207 1.37%
	1.397 1.3961 0.06%	1.432 1.4316 0.03%	1.291 1.2913 0.02%	1.072 1.0723 0.03%	1.055 1.0587 0.35%	0.976 0.9810 0.52%	0.757 0.7627 0.75%
0.73 0.7330 0.42%	1.282 1.2789 0.24%	1.423 1.4222 0.05%	1.194 1.1928 0.10%	0.611 0.6154 0.71%	0.954 0.9553 0.13%	0.96 0.9643 0.45%	0.777 0.7821 0.66%

Fig. 4. Comparison of calculated assembly power distributions with reference of 3D-IAEA
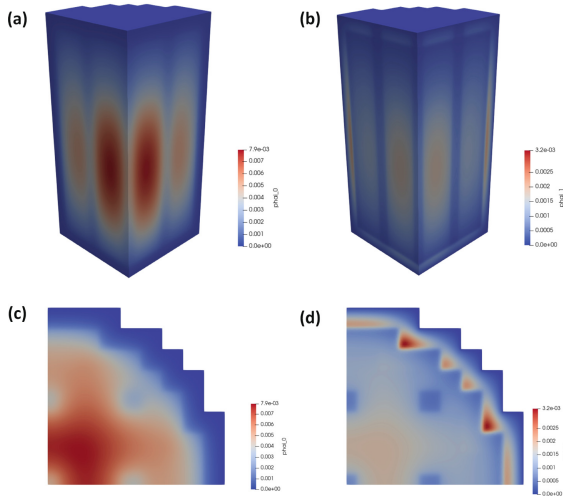
Fig. 5. (a) (c) Fast flux and (b) (d) Thermal flux distribution of 3D-IAEA problem

4 LMFR Application

4.1 Homogenized Few-Group Constants Generation

The developed MOOSE-based neutron diffusion application is used to calculate the benchmark problem of a sodium cooled fast reactor [20]. The benchmark set gives two large size core designs and two medium size core designs with different fuel types. In this work, the design of 1000 MW$_{th}$ medium size core loaded with MOX fuel is selected for verification, and the layout is shown in Fig. 6.
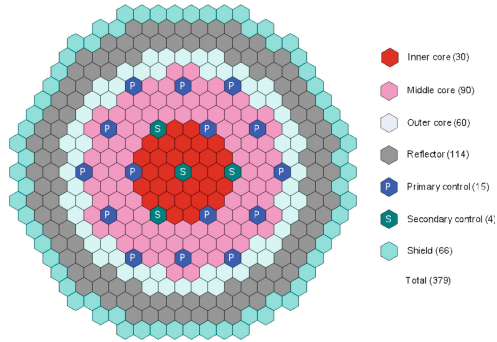
Fig. 6. Radial layout of ABR-MOX-1000

According to the core layout and material density given by the benchmark problem, a full core assembly-wise homogenization model is constructed using OpenMC to generate the group constants, as shown in Fig. 7. A widely-used equal-lethargy 33-group cross sections structure [21] is used for fast reactor analysis, as presented in Table 3. A total number of 1 billion particles (500000 particles per batch, with 100 inactive batches and 1900 active batches) was used in the criticality MC problem to reduce the variance of the output.
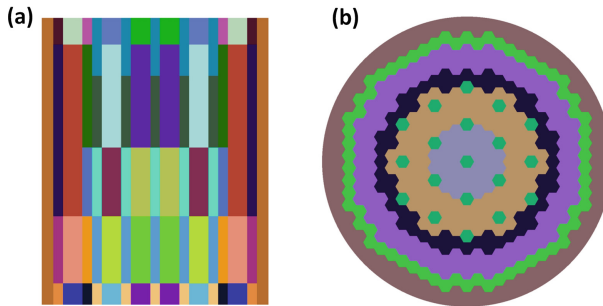
Fig. 7. (a) Aixal and (b) Radial view of OpenMC calculation model

A 1/6 full-core model with unstructured mesh is constructed for deterministic diffusion calculation, as shown in Fig. 8. The number of elements and DOF is 1.49 million and 8.5 million respectively. The fuel assemblies, reflector assemblies, coolant and other structural components are distinguished as different blocks, and the 33-group few-group constants of each block are generated by OpenMC. The ACE formatted continuous energy cross section library used in OpenMC calculation is generated by ENDF/B-VIII.0 evaluated nuclear data library.

Table 3. 33-group structure for fast reactor analysis.

Group	Upper bound (eV)	Group	Upper bound (eV)
1	1.42E+07	18	3.36E+03
2	1.00E+07	19	2.04E+03
3	6.07E+06	20	1.23E+03
4	3.68E+06	21	7.49E+02
5	2.23E+06	22	4.54E+02
6	1.35E+06	23	2.75E+02
7	8.21E+05	24	1.67E+02
8	4.98E+05	25	1.01E+02
9	3.02E+05	26	6.14E+01
10	1.83E+05	27	3.73E+01
11	1.11E+05	28	2.26E+01
12	6.74E+04	29	1.37E+01
13	4.09E+04	30	8.32E+00
14	2.48E+04	31	3.93E+00
15	1.50E+04	32	5.32E−01
16	9.12E+03	33	4.18E−01
17	5.53E+03		

4.2   Computation and Results

The calculation results of the diffusion application are compared with those calculated directly by OpenMC. The effective multiplication factor calculated by MOOSE is 1.01951, which is only 12 pcm different from the OpenMC calculated value of 1.01963. The comparison of assembly power factors is shown in Fig. 9. The maximum relative error is 1.98%, and the average relative error is 0.56%. Figure 10 shows the results of neutron spectrum calculated by MOOSE-based diffusion application and OpenMC respectively, and they are almost identical. It can be seen that the peak of neutron spectrum appears in the tenth group, i.e. neutron energy between 111 keV and 183 keV, which indicating the hard neutron spectrum of LMFR (Table 4).

The calculated neutron flux distribution is shown in Fig. 11. It can be seen that fast neutrons are generated in the fuel assemblies with higher energy. Since the fission and absorption cross sections are relatively low at higher energy, the neutron flux of the fuel assembly is relatively high at this energy, as shown in Fig. 11(a); And also because the fission and absorption cross sections are relatively low at higher energy, neutrons gradually diffuse and slow down, and the neutron flux distribution in the core is almost uniform at the order of hundreds keV, as shown in Fig. 11(b). As the moderation continues, the resonance absorption effect of the fuel assemblies appears, the fission cross section increases, the neutron flux inside the assembly decreases, and the coolant
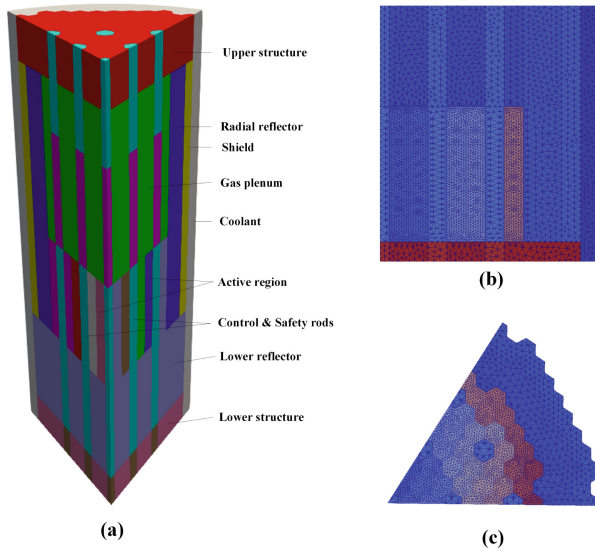
Fig. 8. (a) Geometry and (b) Axial & (c) Radial view of unstructured mesh of ABR-MOX-1000

Table 4. Comparison of calculated results between MOOSE-based diffusion application and OpenMC

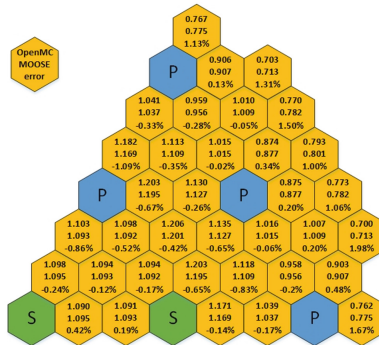|	MOOSE	OpenMC	Error
k_{eff}	1.01951	1.01963	12 pcm

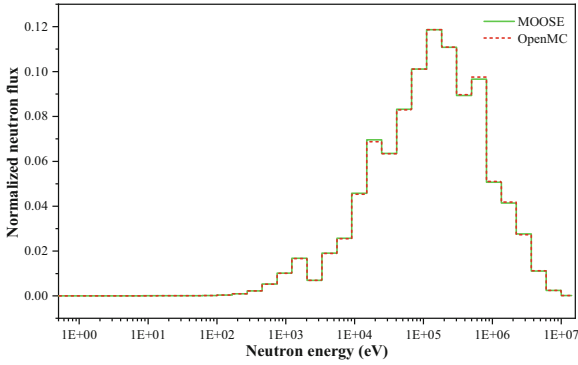**Fig. 9.** Comparison of calculated assembly power distributions with reference of ABR-MOX-1000

Fig. 10. Comparison of calculated neutron spectrum of ABR-MOX-1000

neutron flux is higher than that inside the fuel assembly, as shown in Fig. 11(c). However, it can also be seen that the neutron moderation of fast reactors is relatively weak, and the overall neutron flux is very low at the order of several keV. This is also the reason why fast reactor needs higher fissile enrichment than light water reactor to maintain criticality.

(a)   **(b)**

(c)   **(d)**
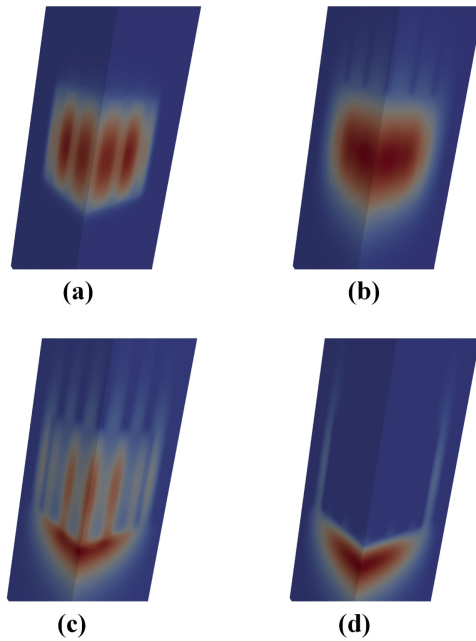
Fig. 11. Relative distribution of neutron flux of (a) group-1 (b) group-10 (c) group-20 (d) group-30

The calculation results above show that the approach of MC-based few-group constants generating by full-core modeling is feasible for LMFR analysis, the accuracy of

the neutron MOOSE-based diffusion application is also further verified. It can be seen that the neutron diffusion theory could achieve the acceptable accuracy compared with MC method in the calculation of homogenized full-core scale, while some calculations can be carried out better through deterministic codes than MC method, such as neutron diffusion kinetics analysis, sensitivity and uncertainty analysis, etc., which is the significance of developing deterministic diffusion code. At the same time should also see, in the more detailed pin-by-pin neutronic calculations, some assumptions of the diffusion theory itself do not hold, and more accurate neutron transport codes are required, which is also our next research direction.

5   Conclusion

In this paper, a neutron diffusion application is developed based on the multi-physics framework MOOSE, which realizes the FEM solution of neutron diffusion problems and a free manner of core modeling. A LWR benchmark 3D-IAEA with given few-group constants is calculated using the diffusion application, the calculation result shows the accuracy of it. In addition, the research on the few-group constants generation based on MC code OpenMC is carried out, using a full-core homogeneous model, and is applied to a LMFR full-core benchmark diffusion calculation, the result shows the feasibility of this approach, which solves the problem of the few-group constants given of the developed application. The above verification shows that the developed diffusion application is universal and accurate, which can be further applied to the coupling between neutronic and thermal-hydraulic calculation in our future work.

It can be seen from this work that the neutron diffusion theory has good accuracy in the full-core scale calculation with homogenized assemblies. While at the same time, it should be noted that with the development of computing power, the requirements of neutron calculations are more refined, and a more precise neutron flux distribution with the resolution of pin level is pursued. At this scale, the neutron diffusion theory itself has the problem of accuracy, so a more accurate neutron transport theory is needed. And it is generally deemed that diffusion approximation is inadequate for fast reactor calculations due to the strong neutron leakage and heterogeneity. Therefore, the development of a neutron transport program based on MOOSE and the corresponding multi-physics coupling research is our further research directions.

References

1. Lawrence, R.D.: DIF3D nodal neutronics option for two- and three-dimensional diffusion theory calculations in hexagonal geometry. [LMFBR]. Argonne National Laboratory (1983)
2. Grundmann, U., Rohde, U., Mittag, S.: DYN3D-three dimensional core model for steady-state and transient analysis of thermal reactors (2000)
3. Bahadir, T., Palmtag, S.P.: Simulate-4 Multigroup Nodal Code with Microscopic Depletion Model (2005)
4. Chandler, D., Maldonado, G.I., Iii, R., et al.: Neutronics modeling of the High Flux Isotope Reactor using COMSOL. Ann. Nucl. Energy **38**(11), 2594–2605 (2011)
5. Xoubi, N., Soliman, A.Y.: Neutronic modeling and calculations of the ETRR-2 MTR reactor using COMSOL multiphysics code. Ann. Nucl. Energy **109**, 667–674 (2017)

6. Hu, T., Wu, H., Cao, L., et al.: Finite volume method based neutronics solvers for steady and transient-state analysis of nuclear reactors. Energy Procedia **127**, 275–283 (2017)
7. Fiorina, C., Clifford, I., Aufiero, M., Mikityuk, K.: GeN-Foam: a novel OpenFOAM® based multi-physics solver for 2D/3D transient analysis of nuclear reactors. Nucl. Eng. Des. **294**, 24–37 (2015)
8. Chauliac, C., Aragonés, J.M., Bestion, D., et al.: NURESIM – a European simulation platform for nuclear reactor safety: multi-scale and multi-physics calculations, sensitivity and uncertainty analysis. Nucl. Eng. Des. **241**(9), 3416–3426 (2011)
9. Calleja, M., Jimenez, J., Sanchez, V., Imke, U., Stieglitz, R., Macián, R.: Investigations of boron transport in a PWR core with COBAYA3/SUBCHANFLOW inside the NURESIM platform. Ann. Nucl. Energy **66**, 74–84 (2014)
10. Fridman, E., Leppanen, J.: On the use of the Serpent Monte Carlo code for few-group cross section generation. Ann. Nucl. Energy **38**(6), 1399–1405 (2011)
11. Park, H.J., Shim, H.J., Joo, H.G., et al.: Generation of few-group diffusion theory constants by Monte Carlo Code McCARD. Nucl. Sci. Eng. J. Am. Nucl. Soc. **172**(1), 66–77 (2012)
12. Zheng, Yu., Quan, G., Liu, S., Chen, Y.: Generation of few-group constants by Monte Carlo code cosRMC. Progress Nucl. Energy **109**, 264–269 (2018)
13. Gaston, D., Newman, C., Hansen, G., et al.: MOOSE: a parallel computational framework for coupled systems of nonlinear equations. Nucl. Eng. Des. **239**(10), 1768–1778 (2009)
14. Williamson, R.L., Hales, J.D., Novascone, S.R., et al.: Multidimensional multiphysics simulation of nuclear fuel behavior. J. Nucl. Mater. **423**(1–3), 149–163 (2012)
15. Gaston, D.R., Permann, C.J., Peterson, J.W., et al.: Physics-based multiscale coupling for full core nuclear reactor simulation. Ann. Nucl. Energy **84**, 45–54 (2015)
16. Paul, K.R., Nicholas, E.H., Bryan, R.H., et al.: OpenMC: a state-of-the-art Monte Carlo code for research and development. Ann. Nucl. Energy **82**, 90–97 (2015)
17. Yang, W.S.: Fast reactor physics and computational methods. Nucl. Eng. Technol. **44**(2), 177–198 (2012)
18. Boyd, W., Forget, B., Smith, K.: A single-step framework to generate spatially self-shielded multi-group cross sections from Monte Carlo transport simulations. Ann. Nucl. Energy **125**, 261–271 (2019)
19. Arogonne Code Center. Benchmark problem book. ANL-7416, 1977, 437 (1977)
20. Bernnat, W., Blanchet, D., Brun, E., et al.: Benchmark for neutronic analysis of sodium-cooled fast reactor cores with various fuel types and core sizes (2016)
21. Ruggieri, J.M., Tommasi, J., Lebrat, J.F., et al.: ERANOS 2.1: international code system for GEN IV fast reactor analysis. Design (2006)

Research on High-Performance Concrete for Volute Region of PX Combined Pump Room in Hualong Nuclear Power Plant

Xiangkun Liu[1(✉)], Chongxu Zhou[2], Dehua Hu[1], and Wei Zhang[1]

[1] Chinese Nuclear Construction Concrete Co., Ltd., Xi'an, Shanxi, China
lxkedu111@126.com
[2] Chinese Nuclear Huachen Construction Engineering Co., Ltd., Xi'an, Shanxi, China

Abstract. Aiming at the volute area concrete structure design requirements for PX combined pump room of HUALONG, the high performance concrete with wonderful property resistance to harmful ion erosion was made by optimization design. The strength grade of the concrete is CF50. Based on experimental result, its slump was 195 mm, its compressive strength was 60.9 MPa with the chloride ion permeability coefficient was 3.6×10^{-12} m^2/s at twenty-eight days, and the restrained expansion rate was 2.7×10^{-4} with the dry shrinkage rate was 1.3×10^{-4}. All the technical indexes conform to the design and construction requirements. Verified by engineering application, concrete compressive strength during continuous production period was according to the evaluation criteria of GB/T 50107-2010. And the standard deviations were only 1.64 MPa. It indicates that the concrete quality is stable and controlled.

Keywords: high-performance concrete · PX combined pump room · HUALONG nuclear power plant

1 Introduction

PX combined pump room in HUALONG nuclear power plant is a special concrete structure with extremely complex shape. The concrete construction at the bottom and inner wall of the structure is extremely difficult, and the designed service life of the project is 50 years. It is a permanent concrete structure that is not repairable during the operation life of the nuclear power plant, which is directly related to nuclear safety [1–3].

In addition, because of the volute pump in water environment, the lining concrete structure to withstand erosion and corrosion of sea water for a long time, the presence of cracks or other defects in concrete structure will lead to corrosion of the internal reinforcement, significantly reduce the overall durability of the concrete structure, in turn, affects the safe operation of nuclear power unit [4–6].

Therefore, it is required that the construction concrete has excellent working performance, crack resistance, chloride ion penetration resistance and steel corrosion resistance, in order to ensure the high durability of the concrete structure in the seawater

corrosion environment. According to the above reasons, the high-performance concrete with wonderful property resistance to harmful ion erosion was made by optimization design. The workability, mechanical property, long-term behavior and durability were test. Furthermore, the technical feasibility of the concrete was evaluated.

2   Experiment Design and Method

2.1   Raw Materials Selection

Fly ash: Grade I class fly ash, fineness shall not be more than 12% (45 μm hole sieve residue), firing loss shall not be more than 5%, water requirement ratio shall not be more than 95%, sulfur trioxide content shall not be more than 3%.

Silicon powder: The dosage is 5%–10% of the cementing material, the specific surface area is more than 15000 m^2/kg, and the silica content is more than 85%. The dosage should be determined by test according to the degree of grinding and application requirements.

Cement: Ordinary Portland cement with strength grade of cement is 42.5 mpa. Do not mix different varieties or strength grades of cement. It is required to use cement with low hydration heat. The 3d hydration heat shall be no more than 251 kJ/Kg, and the 7d hydration heat shall be no more than 293 kJ/Kg. Cement fineness (specific surface area) should not exceed 350 m^2/kg. And cement with relatively high dicalcium silicate content should be used.

Coarse aggregate: The maximum particle size of concrete stones should not be greater than 25 mm, the water absorption rate should not be greater than 1.5%. The alkali active aggregate shall not be used. The other requirements should comply with the provisions of JGJ 52-2006.

Fine aggregate: The medium sand should be used for concrete sand, and marine sand should not be used. Its requirements should meet the provisions of JGJ 52-2006.

Polypropylene fibers: The fiber must own the function of increasing anti-crack, anti-seepage and wear resistance. Its size is 6D. Density is 0.91 g/cm^3 with length of 19 mm. Its elastic modulus is no less than 3900 MPa, tensile strength is no less than 550 MPa, and tensile limit is no less than 15%. In addition, its anti-crack efficiency should be grade one.

2.2   Design of Mix Proportion

In order to approve the workability, mechanical property, long-term behavior and durability, the following technical measures have been taken:

The co-mixing of low-alkali cement with silica fume, fly ash and expansion agent gives full play to the superposition effect of cementing materials. At the same time, the polypropylene fiber and composite amino alcohol reinforcement rust inhibitor are added to jointly realize the protection of reinforcement in concrete structures [7].

The co-mixing of silica fume, fly ash and anti-crack and water-proof agent can reduce the auto shrinkage of concrete to a certain extent, give full play to the advantages of the electric flux of concrete doped with silica fume significantly reduced and the early

strength increased quickly, and better inhibit the early shrinkage crack of concrete after the addition of silica fume.

Silica fume, polypropylene fiber and polycarboxylates high performance water-reducing admixture used in combination, can give full play to reduce and restrain plastic stage sedimentation and shrinkage crack, and reduce the affection of the internal capillary porosity of concrete structure. The water reducing effect is used to maintain the good fluidity of concrete mixture, which is conducive to construction [8].

Based on above design conception, the main design parameters of the concrete mix proportion are determined: the water-binder ration is 0.36, the binder content is 478 kg/m^3, the reasonable sand ratio is 37.5% and water content is 172 kg/m^3. Polypropylene fibers content is 0.9 kg/m^3. The binder consists of cement, 19.9% fly ash, 6.3% silica fume and 8.4% expansion agent. The rebar inhibitor admixture is 12 kg/m^3.

2.3 Test Method

The slump of fresh concrete was tested according to GB/T 50080-2016. The compressive strength (3d, 7d, 28d and 60d) of concrete was tested in accordance with GB/T 50081-2019. Chloride permeability coefficient and shrinkage rate were test according to GB/T 50082-2009.

3 Results and Discussion

3.1 Workability

Based on the experimental results, Fig. 1 gives the line chart of the slump.
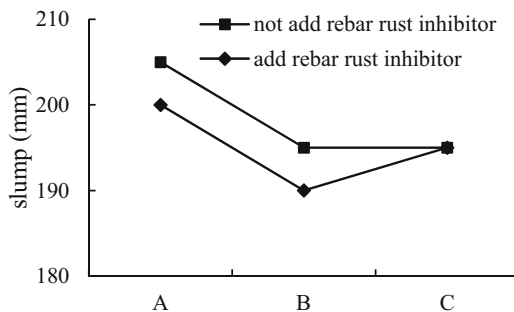
Fig. 1. Slump of the concrete

From Fig. 1, the following observations can be made:

i)   The high-performance concrete for volute region of PX combined pump room has wonderful workability. The slump was both no less than 190 mm, and it can well meet the technical requirements for construction.

ii)   Large flowing ability of the concrete can significantly improve the efficiency of
      construction and reduce the probability of concrete quality defects.
iii) Adding rebar rust inhibitor in the concrete can effectively improves the steel
      corrosion-resistance. And compared with concrete without rebar rust inhibitor, it
      also owns fine workability.

3.2   Compressive Strength

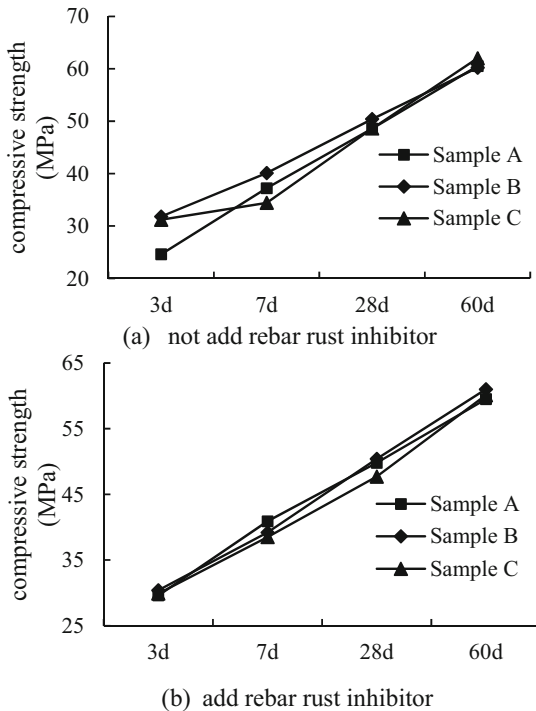Based on the experimental results, Fig. 2 gives the line chart of the compressive strength
(3d, 7d, 28d and 60d).

(a)   not add rebar rust inhibitor

(b)   add rebar rust inhibitor

Fig. 2. Compressive strength of the concrete

   From Fig. 2, the following observations can be made:

i)   With increasing of the test age, the compressive strength shows growth trend. The 7d
     compressive strength can reach 74.5% of the design strength. But the 28d compres-
     sive strength below the design strength. Large percentage of the mineral admix-
     ture results in the compressive strength of early-age increases slowly [9]. It is
     recommended to check and accept according to 60d strength.
ii) The compressive strength with 60d test age were both above 50 MPa, and the
     maximum strength can reach 124% of the design.

iii) Compared with concrete without rebar rust inhibitor, adding rebar rust inhibitor don't affect the compressive strength. And the 60d compressive strength is basically the same. Meanwhile, rebar rust inhibitor can significantly improve the rust resistance of rebar in concrete matrix.

3.3 Chloride Permeability Coefficient and Shrinkage Rate

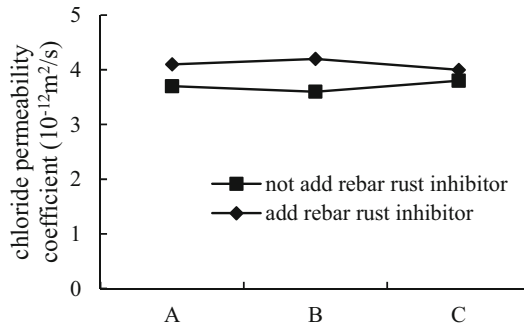Based on the experimental results, Fig. 3 gives the line chart of the chloride permeability coefficient. Figure 4 gives the line chart of the shrinkage rate.

Fig. 3. Chloride permeability coefficient of the concrete

From Fig. 3 and Fig. 4, the following observations can be made:

i) The high-performance concrete for volute region of PX combined pump room has wonderful resistance to chloride penetration. The 28d chloride permeability coefficient is both below 4.5×10^{-12} m^2/s. It can well meet the requirements of design which is no more than 5×10^{-12} m^2/s. It is because that the mineral admixture can effectively improve the capillary structure of concrete and increase the compactness [10].

ii) The concrete without rebar rust inhibitor has more lower chloride permeability coefficient, and the minimum is only 3.6×10^{-12} m^2/s. According to the GB/T 50476-2019, the high-performance concrete for volute region of PX combined pump room can meet the requirement of 100 years design working life.

iii) The shrinkage rate (14d in water) of the concrete is both more than 0.02%, and the shrinkage rate (14d in water and 28d in air) of the concrete is both less than 0.02%. They are both meet the requirement of design that shrinkage rate (14d in water) is more than 0.015% and shrinkage rate (14d in water and 28d in air) is less than 0.03%.

3.4 Evaluation of Concrete Compressive Strength Design Organization

Based on the engineering application of concrete, Fig. 5 gives the compressive strength of hardened concrete. And Fig. 6 gives the normal distribution curve of compressive strength.
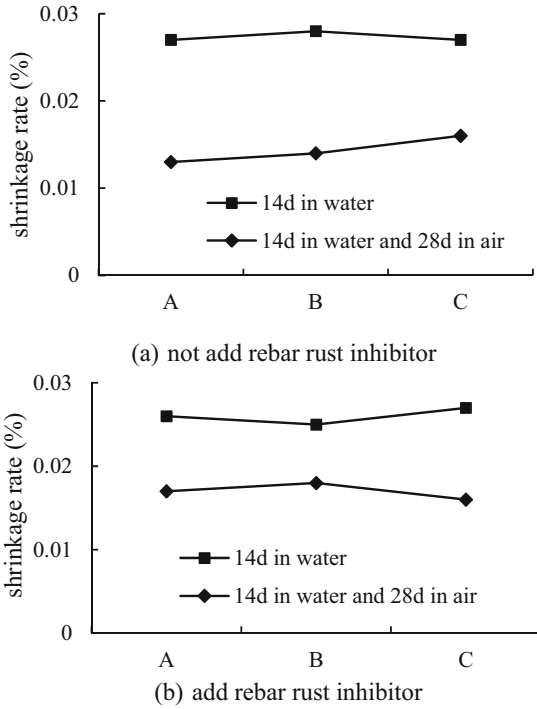
(a) not add rebar rust inhibitor

(b) add rebar rust inhibitor
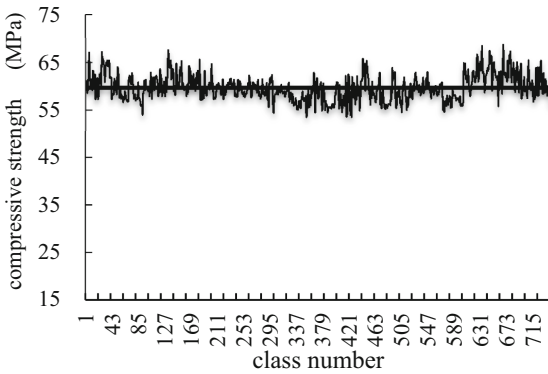
Fig. 4. Shrinkage rate of the concrete

Fig. 5. Compressive strength of hardened concrete

From Fig. 5 and Fig. 6, the following observations can be made:

i) The mean compressive strength of concrete is 58.24 MPa which is 116.8% of the designed strength. The standard deviation of strength is 1.63 that shows the strength fluctuation is relatively stable. Base on the results, $m_{fcu} > f_{cu,k} + \lambda_1 \times S_{fcu} = 50$
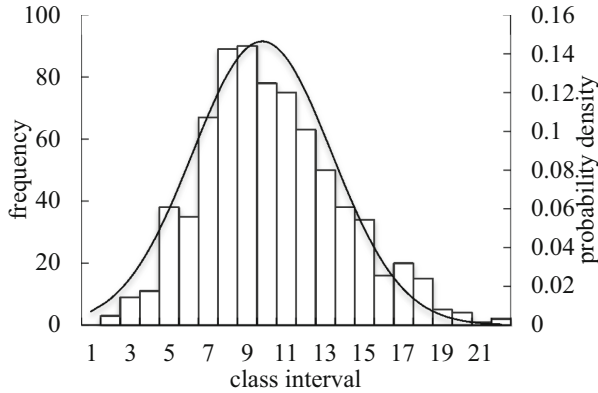
Fig. 6. Normal distribution curve of compressive strength

+ 0.95 × 1.63 = 51.54 MPa, in line with the "concrete strength Inspection and Evaluation Standard" (GBT 50107-2010) related control requirements.

ii) The number of samples located in $[m_{\text{fcu}} - S_{\text{fcu}}, m_{\text{fcu}} + S_{\text{fcu}}]$ was 40, accounting for 65.6% of the total sample, and the number of samples located in $[m_{\text{fcu}} - 2S_{\text{fcu}}, m_{\text{fcu}} + 2S_{\text{fcu}}]$ was 61, accounting for 100% of the total sample. The results show that the concrete mix design method for PX pump house volute area conforms to the design requirements of "Ordinary Concrete Mix Design Regulations" (JGJ55-2011), and the measured compressive strength is well in accordance with normal distribution.

4   Conclusions

i)   The high-performance concrete for volute region of PX combined pump room has wonderful workability. The slump was both no less than 190 mm, and it can well meet the technical requirements for construction.

ii) The compressive strength with 60d test age were both above 50 MPa, and the maximum strength can reach 124% of the design. It conforms to the design requirements of the design organization.

iii) The high-performance concrete for volute region of PX combined pump room has wonderful resistance to chloride penetration. And the minimum chloride permeability coefficient is only 3.6×10^{-12} m²/s that indicates meeting the requirement of 100 years design working life.

iv) The shrinkage rate (14d in water) of the concrete is both more than 0.02%, and the shrinkage rate (14d in water and 28d in air) of the concrete is both less than 0.02%. It shows the concrete owns wonderfully volume stability.

References

1. Giaccio, G., et al.: Use of small beams to obtain design parame-ters of fiber reinforced concrete. Cem. Concr. Compos. **30**, 297–306 (2008)

2. Xia, D., Liu, X., Zhou, B.: Flexural toughness of hybrid fiber reinforced high-performance concrete under three-point bending. Appl. Mech. Mater. **357**, 1110–1114 (2013)
3. Wang, H., Liu, J.: The experiment of bending tension performance on the hybrid fiber reinforced concrete with higher toughness. China Concr. Cem. Prod. **4**, 46–49 (2011)
4. Deng, Z., Li, J., Liu, G.: Experimental study on mechanical properties of hybrid macro-fiber reinforced concrete. Concrete **8**, 50–55 (2006)
5. Zhao, L.-P., Gan, D.-Y., Zhu, H.-T. : Effect of the steel fiber on the strength and toughness on the concrete. J. China Univ. Water Resour. Electr. Power **33**(6), 29–32 (2012)
6. Mei, G., Li, J., Liu, X.-F. : Hybrid fiber reinforced concrete flexural behavior and hybrid effects. Concrete **2**, 21–24 (2013)
7. Wang, Z.-J., Meng, X.-L., Wang, Q.: Study on the flexural toughness of the steel fiber reinforced concrete. Concrete **3**, 71–74 (2014)
8. China Association for Engineering Construction. Standard test methods for fiber reinforced concrete. China Planning Press, Beijing (2010)
9. Xia, D., Liu, X., Xia, G.: Research on the flexural toughness of hybrid fiber reinforced high-performance concrete. J. Huazhong Univ. Sci. Technol. (Nat. Sci. Edn.) **41**(6), 108–112 (2013)
10. Gao, D.-Y., Zhao, L.-P., Feng, H.: Study on the flexural toughness and evaluating method of the steel fiber reinforced concrete. J. Build. Mater. **17**(5), 783–789 (2014)

Thermo-Physical Property Database of Fusion Materials and Thermo-Hydraulic Database of Breeder Blankets for CFETR

Wen Ding, Kui Zhang$^{(\boxtimes)}$, Ronghua Chen, Wenxi Tian, Jing Zhang, Suizheng Qiu, and G. H. Su

Xi'an Jiaotong University, Xi'an 710049, China
`zhangkui101@xjtu.edu.cn`

Abstract. The Chinese Fusion Engineering Test Reactor (CFETR) is a fusion engineering reactor independently designed and developed by China, and the design of the blanket is one of the key points during the design of CFETR. The configurations of CFETR, the detailed designs of the three types of blankets and typical blanket module, and the coolant flowing schemes in blanket module are introduced in paper. Besides, the work about Thermo-physical Property Database of Fusion Material and Thermo-hydraulic Database of Models established for the three types of blankets is presented. The fusion material involves Plasma Facing Materials (PFM), structural materials, coolant and breeding materials, and the peak temperature and the peak pressure in both steady-state and transient conditions are covered for property of materials. The thermo-hydraulic database includes the heat transfer models, the pressure drop models, and some special models for the fluid flow in blanket. In addition, the tests and verification for the database are performed, and the shortages and deficiencies of current database are analyzed.

Keywords: Fusion Reactor · CFETR Database · Blanket · Property · Material · Thermo-hydraulic

1 Introduction

Nuclear fusion energy is a kind of ideal new energy, and the reaction product is pollution-free and easy to emit, which is conducive to promoting a zero-carbon future. In 1985, the International Thermonuclear Experimental Reactor (ITER) project was established with the goal of building a thermonuclear fusion test reactor for self-sustaining combustion. The China Fusion Engineering Test Reactor (CFETR) is an independently designed fusion reactor in China and is a transition reactor from the ITER experimental reactor to the Demonstration Fusion Reactor (DEMO), designed to bridge the technology gap between the experimental reactor and the demonstration reactor. The devices in CFETR mainly consist of an external superconducting magnet system (containing toroidal field (TF) coils, central solenoid (CS) coils, and CS model coils), an internal vacuum vessel, and blankets in the vacuum vessel. The fusion reactor blanket is the focus of the CFETR design difficulties, which is divided into shielding blanket and breeder blanket. The

shielding blanket is used to prevent neutron leakage, and the breeder blanket plays the roles of tritium breeding, neutron multiplier, and heat conversion. The study in this paper focuses on the breeder blankets.

Many feasible blanket concepts have been proposed in ITER projects, such as HCPB [1] and HCLL [2] in European Union (EU), SWCB [3] and WCCB [4] in Japan, HCSB [5] and HCCR [6] in Korea, HCCB [7] and DFLL [8] in China, etc., while for the CFETR project, three types of blankets are proposed, as: Helium Cooled Solid Breeder blanket (HCSB) [9], Water Cooled Ceramic Breeder blanket (WCCB) [10], and liquid lead-lithium blanket [11], and the design of these three types of blankets is currently being refined.

The development of fusion design requires a large number of material databases with mechanical, physical, and thermodynamic properties, and many countries have long established relatively well-developed material databases. For example, the Japanese Atomic Energy Agency (JAEA) has established the HFIR/ORR irradiated/non-irradiated experimental database [12], the Data-Free-Way database [13], the European Fusion Material properties database [14], the Fusion component failure rate database (FCFR-DB) [15], the EUROfusion RAFM steel database for EUROFER97 steel developed by the European Fusion Center [16], an international fusion materials database established by the International Energy Agency (IEA) [17], a database for nuclear materials management software (FUMDS) established by the FDS team at the Institute of Plasma Physics, Chinese Academy of Sciences (ASIPP) [18], the Nuclear Reactor Material Database (NRMD) [19] by the Chinese Academy of Sciences, and a database for fusion reactor tritium breeder material properties established by the Institute of Physics, Chinese Academy of Sciences.

The fusion reactor blanket is the carrier of the energy conversion function. In order for the coolant to heat the nucleus inside the blanket and transfer the heat to the outside of the blanket, it is necessary to perform flow heat exchange with various materials. The most basic of them is the thermal-hydraulic heat transfer model of coolant and structure, the distribution of neutron nuclear heat, etc. The special model involving thermal-hydraulic phenomena is also important to judge whether the blanket can operate safely during the transient conditions. Therefore, a thermo-hydraulic database was established to provide data and model support for the thermal hydraulic analysis of the CFETR blanket.

Compared with the previous databases for fusion, the thermo-physical property database and the thermo-hydraulic database for CFETR with both thermo-physical property of fusion materials and thermo-hydraulic models are not yet established. Besides, the above databases are not publicly available and the involved datasets are not targeted, so their data applicability does not cover the steady-state and transient conditions in the three types of blankets.

In this work, the thermo-physical property database of fusion material and the thermo-hydraulic database of blankets for CFETR were established as part of the development of the nuclear design and safety analysis code for the blanket system.

2 Introduction of Blankets

Several research teams in China have carried out corresponding blanket design and analysis work for CFETR based on ITER projects, and there are three main types of

blanket concept schemes: helium-cooled solid breeder blanket, water-cooled ceramic breeder blanket, and liquid lithium-lead blanket. For CFETR phase I, University of Science and Technology of China (USTC) proposed the HCSB blanket [9], ASIPP proposed the HCCB blanket [20] and WCCB blanket [21, 22], and Southwestern Institute of Physics (SWIP) proposed the HCSB blanket. For the CFETR Phase II, which has much greater power and size than Phase I, SWIP updates the HCCB blanket and ASIPP proposes a new design for WCCB blanket [23]. In this subsection, the structure and coolant flow scheme will be introduced for the HCSB blanket from USTC, the WCCB blanket from ASIPP, and the DFLL blanket proposed by the Institute of Nuclear Energy Safety Technology (INEST-CAS) [24].

2.1 Helium Cooled Solid Breeder Blanket (HCSB)

The structural design of the HCSB blanket proposed by the University of Science and Technology of China is presented. The blanket, as a whole, is divided into 32 equal sectors along the annulus. The angle of each equal division is 11.25°. Each part has 15 groups of blanket modules along the toroidal direction, of which 7 modules from No. 1 to No. 7 are inner blanket modules and 8 modules from No. 8 to No. 15 are outer blanket modules. The radial-polar cross section of the inner blanket is rectangular, while the circumferential-radial cross section is trapezoidal. Due to the different locations, the neutron wall loads of different modules within the blanket vary greatly, and the maximum thermal load is calculated to appear on the inner side of the first wall of module No. 12, which is about 0.473 MW/m^2. The structural schematic of this blanket module could refer to reference [9].
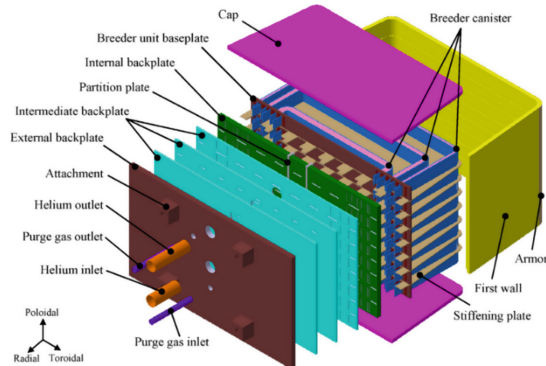

Fig. 1. Schematic of the typical blanket module[9] of HCSB

This typical blanket module is rectangular in shape with the following main components along the radial direction from inside to outside: tungsten tile, first wall, stiffening plate, breeder unit backplate, breeder canister, partition plate, top and bottom caps, backplates, helium inlet and outlet, purge gas inlet and outlet, and four mechanical attachments. A 2 mm thick tungsten plate covers the first wall and protects the inner

components from plasma heat flow. The outer backplate has four mechanical attachments to secure the module to the shield blanket and also has an inlet and an outlet for helium gas, an inlet and an outlet for purge gas. The outer backplate and the remaining five backplates, as well as the top and bottom caps and the first wall, enclose the three chambers for the distribution of helium and purge gas (He $+ 0.1\%$ H$_2$, 0.1 MPa) for tritium. The gas chambers are connected to the breeder zone, which has U-shaped breeder units packed with breeder pebbles of Li$_4$SiO$_4$ for tritium breeder and pebbles of Be for neutron multiplier. The pump pumps the cold helium into the inlet and then into the gas channels in FW. Afterwards, the helium absorbs part of the nuclear heat and enters the pipes in caps as well as the stiffening plates. After absorbing the internal heat of all the plates, it flows into the channels in the backplates, and finally all the helium is gathered and flows out through the outlet, which can take away most of the heat from the structural material.

2.2   Water Cooled Ceramic Breeder Blanket (WCCB)

ASIPP, in collaboration with European Nuclear Energy Agency (ENEA), has proposed a design for a water-cooled ceramic breeder blanket based on the latest design parameters of CFETR Phase II. Similar to the helium-cooled solid blanket, the WCCB can be divided into 16 toroidal sectors.

In each sector, modules from 1# to 6# are the outer blanket area, and modules from 7# to 11# are the inner blanket area. The inner blanket area has 2 identical sub-blankets along the toroidal, and the outer blanket area has 3 identical sub- blankets.

This section describes the structural design of blanket module 3# in WCCB for CFETR-2018 [23]. The outer shell of the blanket is a closed steel box with FW, top and bottom cover plates, and back plates. The first wall is fitted with tungsten tiles on the outside, and the interior is a U-shaped plate bent along the radial-annular direction. 95 square coolant channels are contained inside this plate, each with a cross-sectional area of 8×8 mm^2 and a pitch of 22 mm between two adjacent channels. Each module contains three stiffening plates (SPs), which separate a blanket module into four sub-modules. Each SP contains 81 U-shaped channels inside, each with a cross-sectional area of 5×5 mm^2. The cover plate contains 12 U-shaped channels with a square cross-section for removing heat from the module, and the upper and lower cover plates have a total of 16 purge gas channels for gas collection and gas distribution. Each module also has 23 cooling tube assemblies (CTAs) in the breeder zone for heat dissipation. Each assembly contains three coolant channels, toroidal and radial ribs, where the coolant flows and exits at the outlet. The ribs connect the cooling tubes to each other and fix the SPs to the sidewalls, which improves the structural stability and heat transfer performance of the module. The cooling system of the blanket could refer to reference [23]. It can be seen that three independent cooling systems are used in this blanket design scheme: cooling system 1 is mainly responsible for taking away the heat from the structural components such as the FW, CPs, and SPs, while cooling systems 2 and 3 mainly take away the heat from the pebble bed area of the blanket.

2.3 Dual-Functional Lithium-Lead (DFLL)

The dual-functional lithium-lead blanket (DFLL) is designed by the Institute of Nuclear Energy Safety Technology, Chinese Academy of Sciences, with helium and liquid Li-Pb as the coolant and liquid Li-Pb eutectic as the tritium breeder material. The whole blanket is divided into 16 sectors along the toroidal, the inner blanket module is divided into two sub-modules along the toroidal, and the outer blanket module can be divided into three sub-modules. A 2 mm thick tungsten protective layer is set on the surface of the blanket, followed by the first wall (FW), tritium breeder zone (TBZ), helium header (HH), back plate (BP), and shielding blanket (SB).

 The structure design of the liquid lithium-lead blanket was shown in reference [24]. It is shaped like a rectangular box, consisting of the first wall (FW, U-shape, 15 mm in thickness), the upper and lower cover plates, and the back plate, with dimensions of 1280 mm (poloidal direction) × 1200 mm (radial direction) × 1300 mm (toroidal direction). Considering the structural stability and internal heat extraction, the toroidal-radial, radial-poloidal, toroidal-poloidal stiffening plates are welded together to form a U-shape and two sets of "7" shaped tritium breeder zones. Square-shaped helium coolant channels (cross-sectional area of 15×15 mm^2, 20 mm in pitch) are uniformly arranged inside the CPs, the FW and the SPs, and several guide tubes (GTs) with 35 mm in diameter, 5 mm in thickness, 750 mm in length are arranged radially in the U-shaped breeder zones through the FWs and BPs. On the fourth backplate, there are several mechanical attachments, helium inlet and outlet pipes, and liquid Li-Pb inlet and outlet pipes, etc. The backplate is connected to the shielding blanket, which is connected by mechanical attachments, and the thickness of the shielding blanket is 250 mm.

 The liquid Li-Pb enters the module at the inlet and is distributed among three sub-channels before flowing into the TBZs. Li-Pb enters the module, flows along the U-shaped channel, and then exits at outlet. At the same time, Li-Pb enters the "7" shaped TBZs from two sub-channels. In reference [24], the Li-Pb enters the module and flows upwards in two parts at the bottom, then converges at the same exit and exits the module at the outlet. The helium enters the first helium stage directly from the inlet tube, flows simultaneously into the FW and GTs, and exits through the FW helium outlet into the second helium stage. Afterwards, the helium flows simultaneously into the coolant channels of the radial-poloidal stiffening plates, the toroidal-poloidal stiffening plates, the toroidal-radial stiffening plates (rpSP, tpSP, trSP) and the cover plates. Finally, the helium is collected in the third stage helium manifold and flows out of the module through the outlet.

3 Databases

3.1 Thermo-Physical Property Database of Blanket Material

The thermo-physical properties for coolant and material are important elements of the fusion reactor database, and the various materials in the normal operating conditions of the blanket and in accident conditions need to be in a safe state, so before analyzing the safety of the blankets it is necessary to establish a material database that meets the temperature and pressure range in fusion reactor. In this section, we introduce the

thermo-physical property database of materials under normal and transient conditions for CFETR blanket, mainly introducing the thermal properties of coolant materials, structural materials, breeder materials and PFM materials, as shown in the following Table 1.

Table 1. The materials in thermo-physical property database

Functional materials	Chemical formulas or name of materials
Coolant materials	H_2O, He, Li, LiPb, Flibe, HTO, T_2
Structural materials	RAFM steel (EUROFER97,F82H, JLF-1, CLF-1, CLAM), oxygen-free copper, CuCrZr alloy, 316L stainless steel, ODS steel
Breeder materials	Tritium breeder: Li_4SiO_4, Li_2TiO_3, LiPb, Flibe Neutron multiplier: Be, $Be_{12}Ti$
PFM material	W

The coolant materials mainly involve H_2O, He, and Li-Pb, and in some liquid metal blankets, Li and Flibe are used as coolant or breeder materials. Under special conditions, the first wall ruptures and causes the coolant water to be sprayed into the vacuum vessel, where the coolant reacts with hydrogen to become deuterated water (HTO) or tritium gas (T_2), so it is also necessary to consider the thermal properties of HTO and T_2. The thermal properties of coolant materials in the database involve density, specific heat capacity, thermal conductivity, kinematic viscosity, Prandtl number, specific enthalpy, latent heat of vaporization, specific entropy, surface tension, isothermal compressibility, etc.

The International Association for the Properties of Water and Steam (IAPWS) introduced the formula for the thermal properties of water and steam in 1997 [25], referred to as the IAWPS-IF97 formula. This formula can be calculated to obtain the thermal properties of water and steam in the range of pressure from 611.153 Pa to 100 MPa and temperature from 273.15 K to 1073.5 K. However, considering that the pressure in the vacuum vessel is close to 0 Pa, the thermal properties of water less than 611.153 Pa will be supplemented by referring to Gothic's theoretical manual [26], from which the thermal property data from 0 to 611.153 Pa can be obtained. Helium is a single phase within the blanket and does not undergo phase changes, and its physical properties are obtained from the National Institute of Standards and Technology (NIST), the International Atomic Energy Agency (IAEA) [27] and other journal supplemental data [28–32]. The current pressure range of helium is from 0 to 15 MPa and the temperature range is from 273.15 to 1273.15 K. The pressure in the liquid metal blanket is relatively low, with the thermal properties of Li-Pb ranging from 273.15K to 1473.15 K and 0 to 1 MPa [27, 33–35], and the thermal properties of Li ranging from 473.15 to 1673.15 K and 0.1 to 1 MPa [30, 36]. The melting point of Flibi is 732.15 K, so the current database contains its properties at a temperature greater than 732.15 K [30, 37]. The properties of water (H_2O) and HTO are almost identical, and the thermal properties of water can be

used directly in the calculations of HTO [38]. Tritium has properties similar to hydrogen except for density [39], and the hydrogen properties can be directly used in the calculations.

The structural material is the basis to ensure the structural stability of the blanket and efficient energy conversion. The structural material of FW in HCSB, WCCB, and DFLL is chosen from Reduced Activation Ferritic/Martensitic steel (RAFM). RAFM steel has higher thermal conductivity and smaller thermal expansion compared with other types of steel, and is the preferred steel type for fusion reactor structural materials in the prospect of better physical and mechanical properties. Among the RAFM steels [40], EUROFER97 steel, F82H steel, JLF1 steel, 9Cr-2WVTa steel and CLAM steel are currently well developed, among which CLAM steel and CLF-1 steel are researched and manufactured in China, while the rest of the steel types come from Europe, Japan and the United States. The current database contains the thermal properties of EUROFER97 [41], F82H [42], JLF-1 [42], CLF-1, and CLAM [43]. The oxygen-free copper wire as reinforcement material mainly serves to strengthen the mechanical properties of the sub-cable and increase the stability of the conductor. Due to their excellent thermal conductivity, the copper alloys are used as heat sinks in the high heat flow region of ITER. The CuCrZr-IG alloy has good thermal conductivity and is generally used as a structural and heat conduction material for divertors. Oxide dispersion-strengthened alloy (ODS) is a material formed on the basis of martensitic and ferritic steels that can withstand high neutron fluxes and has high temperature creep resistance. While conventional ferritic/martensitic steels can only reach a maximum working temperature of 550–600 °C, ODS steels can increase the working temperature to 700 °C and are therefore one of the candidates for fusion blanket structure materials. The vacuum vessel design uses ultra-low carbon austenitic stainless steel 316L as the primary material. The database mainly contains the thermal property data of the above materials.

The fusion blanket is equipped with a breeder zone containing tritium breeder materials and neutron multiplier materials, which serve to maintain the fusion reaction by tritium breed and neutron multiplication [44–46]. The tritium breeder materials in the solid blanket are mainly Li_2TiO_3, $LiAlO_2$, Li_4SiO_2, $LiZrO_3$, and the required neutron multiplier is metallic lead or metallic beryllium, while the tritium breeder materials in liquid blankets are mainly Li, Li-Pb, molten salt, etc., and the required neutron multiplier is Pb. Among the three types of blankets, the breeder zone of HCSB is filled with Li_4SiO_4 and Be pebble beds, the breeder zone in WCCB is filled with Li_2TiO_3 and $Be_{12}Ti$ pebble beds, and the DFLL uses liquid Li-Pb eutectic as the breeder material only.

Tungsten is the material for the first wall protection layer facing the plasma in the current fusion blanket. The tungsten could protect the internal components from plasma heat flow and ensure the integrity of the blanket. The physical properties data can be referred to Structural Design Criteria for ITER In-vessel Components (SDC-IC).

3.2 Thermo-Hydraulic Database for Blankets

This chapter introduces thermal hydraulic models and special models for three types of blankets, which mainly deals with the models under steady state and transient accidents involved in HCSB, WCCB, and DFLL. The heat transfer models for the single phase

Table 2. The models in thermo-hydraulic database

Structure/working conditions	Models
Steady-state operating conditions in blanket and divertors	Single-phase heat transfer correlation, single-phase pressure drop model, liquid metal MHD model, metal heat transfer correlation, metal pressure drop model
Transient conditions in blanket and divertors	Two-phase boiling heat transfer correlation, inter-phase heat transfer correlation, two-phase pressure drop model, critical flow model
Vacuum vessel	critical flow model in high pressure drop, hydrogen production model, flash vaporization model, HT and HTO conversion model

of different coolants are presented first, followed by the two-phase boiling heat transfer models. The models in thermo-hydraulic database are listed briefly in Table 2.

Theoretical analysis of the full development of convective heat transfer by laminar flow in pipes is relatively well done and many results have been publicly available [47]. For forced convective heat transfer within a pipe, the longest and most commonly applied correlations are the D-B correlation and its modifications [48], the Gnielinski correlation [49], and the heat transfer formulas for liquid metals [36]. The steady-state conditions in fusion reactor mainly involve single-phase heat transfer, but in some special conditions the pressure in the channel changes, leading to the boiling of the liquid, when the phenomenon of boiling in the tube should be analyzed. Bergles and Rohsenow [50] derived a criterion for the onset of subcooled boiling based on experimental data obtained from several industrial smooth tubes. A more general model to determine the onset of subcooled boiling is Jens-Lottes formula [51], jointly with the single-phase forced convection equation. For nucleation boiling of different liquids, Rohsenow [52] proposed the correlations for calculation of heat flux or boiling temperature difference. Chen correlation [53], with a mechanism that considers both saturated boiling heat transfer and convective heat transfer, is applicable to the whole saturated boiling before DNB. In 1961, Kutateladze [54] proposed the calculation of the two-phase flow heat transfer coefficient for flow boiling by the asymptotic method, and another class of empirical correlations considers the total heat transfer coefficient as consisting of two components, such as the correlations used by Mattson [55]. Such correlations are applicable to both transition boiling and film boiling. There are also some empirical correlations with limited applicability, such as the McDonough correlation [56], the empirical correlations obtained by fitting experimental data of flow boiling proposed by Tran [57] and Lazarek-Black [58], etc. In particular,, for a single-sided heated pipe, Luan Zhenbo [59] proposed the heat transfer correlation for subcooled boiling.

The pressure drop of single-phase liquid between two sections can be calculated by the following equation:

$$\Delta P = p_1 - p_2 = \Delta P_{el} + \Delta P_a + \Delta P_f + \Delta P_c \tag{1}$$

where, p is the static pressure of the fluid at the given cross-section. ΔP_{el} is the elevation pressure drop caused by the change in height of fluid. ΔP_a is the acceleration pressure drop caused by the change in fluid velocity. ΔP_f is the pressure loss caused by frictional resistance. ΔP_c is the local pressure drop, which should be calculated at the corner of the FW, bent pipe in CPs where the shape of the flow channel changes. The pressure drop model for two-phase flow is as follows:

$$\Delta p = \Delta p_{E,TP} + \Delta p_{AD,TP} + \Delta p_{F,TP} \tag{2}$$

The terms on the right side are elevation pressure drop, acceleration pressure drop, and friction pressure drop, respectively.

For the two-fluid model of two-phase flow, there are interphase exchanges of mass, momentum, and energy in the boiling condition. In the six-equation model, the interphase mass transfer equation is the key, however, the equations are different in each flow pattern. The interphase heat exchange model in the database is from RELAP [60].

The transient conditions in the fusion blanket involve some special models. The critical flow model of coolant is involved in the break accident of a vacuum vessel, such as the single-phase critical flow model [61, 62] and the two-phase critical flow model [61, 62]. The calculation of the coolant leakage to the vacuum vessel is referred to the GETTHEM code [63]. The reaction rate of the oxidation reaction in the blanket cooling system, which involves the reaction between beryllium metal and water vapor and oxygen, and the oxidation reaction between tungsten metal and water vapor, can be calculated by the model [64–66]. The tritium extraction system (TES) is an auxiliary system whose function is to extract tritium from the blanket using the purge gas, and the exchange reaction of HT and HTO is considered as one of the important chemical reactions to obtain tritium from the purge gas, and the reaction rate constant can be calculated by [67, 68]. Flashing occurs at the break of the fusion blanket where the coolant flows from the high pressure region to the low pressure region. GETTHEM considers the special case of high pressure drop model for flashing phenomenon, which could refer to reference [63]. Cheng et al. [69] proposed an effective conduction coefficient model for flash evaporation of droplets by a diffusion-controlled evaporation model with convective heat transfer inside the droplet. Elias and Chambre [70] proposed a phenomenological model for predicting the flash evaporation of fluids during static or flow transients. Assuming that the water jet inside the vacuum vessel begins to evaporate in large quantities after contact with the FW and that the heat flux is distributed equally over the surface of the FW, the pressure of the vacuum vessel can be calculated using the equation [71].

4 The Testings of Database

The data presented above was organized into the database, which needs to be tested to ensure the accuracy of the data. The data or model will be calculated using a code written

in Fortran language, and the results will be compared and analyzed with experimental or simulation results.

4.1   Testing of Material Database

Numerical simulations of convective heat transfer for uniform heating tubes were performed in the reference [72] to obtain the heat transfer coefficient of the wall. In this paper, the heat transfer coefficients at the same conditions are derived from the code with data in database, and compared with the reference.
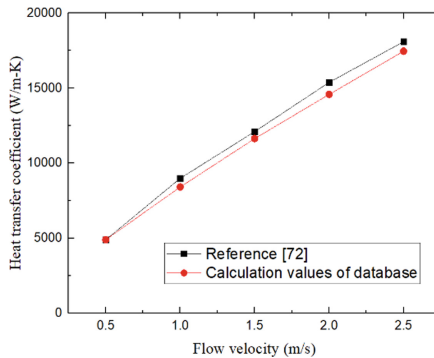

Fig. 2. Comparison of calculated results and values in [72]

The diameter of the circular tube is 11 mm, the wall is uniformly heated, the pressure is 10 MPa, and the inlet temperature of water is 373.15 K. The heat transfer coefficient between fluid and wall can be calculated for different flow velocities. The dimensions of the circular tube, pressure, and inlet temperature are written into the code, the thermal properties are read and the D-B correlation is selected as the heat transfer model for the calculation of the heat transfer coefficient. The obtained calculation results and results in reference are shown in Fig. 1, where the maximum error is within 6.2%.

4.2   Testing for Thermo-Hydraulic Database

In the reference [73], a thermal analysis of WCCB was carried out, and the RELAP5 code was applied to simplify the typical blanket and perform steady-state calculations to obtain the inlet and outlet temperatures, mass flow rate, and distributions of wall temperature. In this paper, based on the database data and the thermo-hydraulic models, a code was written in Fortran to perform steady-state calculations on the node diagram shown in Fig. 2, and the results were compared and analyzed with the results in reference [73].

The inlet and outlet temperatures of the flow channel, such as nodes 106, 207, 211, 215, 219, etc. in Fig. 3, are calculated by reading the thermal properties of fluid and structure based on the nuclear heat of each part and the fluid temperature at each location obtained from the neutronics analysis. Subsequently, the heat transfer coefficients are

calculated based on the temperature distribution of the coolant along the axial height, the heat of the component, the size of the channel, and the mass flow rate, based on empirical correlations to obtain the wall temperature. The calculated results of temperatures on the left of the 2080 component and the left of the 2010 component are compared with the reference [73] as follows.
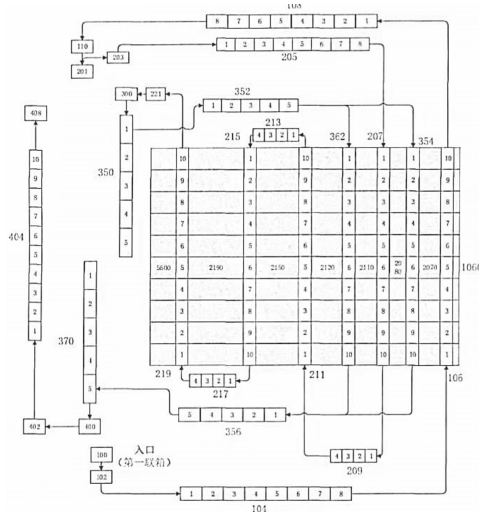
Fig. 3. The node diagram of WCCB [73]
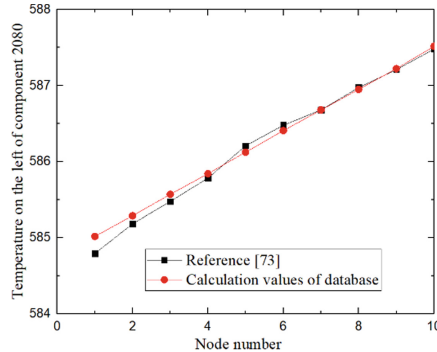
Fig. 4. Comparison of temperatures on the left of the 2080 component

The comparison results are shown in Fig. 4 and Fig. 5. It can be seen that the overall data is relatively in good agreement, and the error may be caused by the heat flux of wall not being completely uniform.
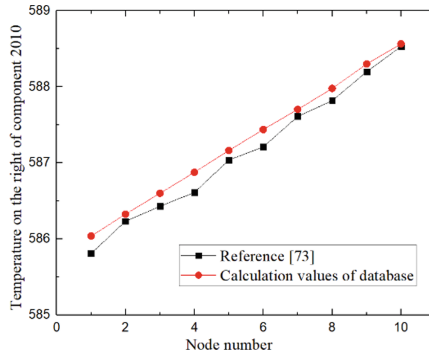
Fig. 5. Comparison of temperatures on the right of the 2010 component

5   Conclusions

The object of this paper is the three types of CFETR blanket: HCSB, WCCB, and DFLL. The thermal properties of coolant, structural materials, PFM materials, tritium breeder and neutron multiplier materials, the structural characteristics, and the coolant flow scheme in the three types of blanket are introduced, and the thermal hydraulic models and special models are summarized. Finally, based on the database, the data is tested and verified with different cases. The preliminary database has been built and briefly tested. However, the current data is not directly available to the system code without validation, and the data has not been integrated into the subroutines for code. For the thermo-hydraulic models, the applicability for CFETR blankets still needs to be further analyzed. In the future, we will use the system code and the physical property package of a database for testing as well as application evaluation for CFETR blankets.

References

1. Zmitko, M., et al.: Development and qualification of functional materials for the European HCPB TBM. Fusion Eng. Des. **136**(PTB), 1376–1385 (2018)
2. Aiello, G., et al.: HCLL TBM design status and development. Fusion Eng. Des. **86**(9), 2129–2134 (2011)
3. Enoeda, M., et al.: Design and technology development of solid breeder blanket cooled by supercritical water in Japan. Nucl. Fusion **43**(12), 1837 (2003)
4. Enoeda, M., et al.: Development of the Water Cooled Ceramic Breeder Test Blanket Module in Japan. Fusion Eng. Des. **87**(7–8), 1363–1369 (2012)
5. Ann, M.Y., et al.: Thermo-hydraulic and thermo- mechanical analysis of Korean helium cooled solid breeder TBM. Fusion Eng. Des. **85**(7–9), 1664–1669 (2010)
6. Ahn, M.Y., et al.: Design change of Korean HCCR TBM to vertical configuration. Fusion Eng. Des. **88**(9–10), 2284–2288 (2013)

7. Feng, K.M., et al.: Progress on design and R&D for helium-cooled ceramic breeder TBM in China. Fusion Eng. Des. **87**(7–8), 1138–1145 (2012)

8. Wu, Y.: Design analysis of the China dual-functional lithium lead (DFLL) test blanket module in ITER. Fusion Eng. Des. **82**(15–24), 1893–1903 (2007)

9. Chen, H., et al.: Conceptual design and analysis of the helium cooled solid breeder blanket for CFETR. Fusion Eng. Des. **96–97**, 89–94 (2015)

10. Liu, S., et al.: Conceptual design of a water cooled breeder blanket for CFETR. Fusion Eng. Des. **89**(7), 1380–1385 (2014)

11. Ni, M., et al.: Structural design and preliminary analysis of liquid lead–lithium blanket for China fusion engineering test reactor. Fusion Eng. Des. **94**, 61–66 (2015)

12. Jitsukawa, S., et al.: Development of an extensive database of mechanical and physical properties for reduced-activation martensitic steel F82H. J. Nucl. Mater. **307**(1), 179–186 (2002)

13. Ueno, F., et al.: Development of '"Data-Free-Way"' distributed database system for advanced nuclear materials. J. Nucl. Sci. Technol. **31**(12), 1314–1324 (1994)

14. Karditsas, P.J., et al.: The European fusion material properties database. Fusion Eng. Des. **81**, 1225–1229 (2006)

15. Pinna, T., et al.: Fusion component failure rate database (FCFR-DB). Fusion Eng. Des. **81**(8/14), 1391–1395 (2006)

16. Ermile, G., et al.: Development of EUROFER97 database and material property handbook. Fusion Eng. Des. **135**, 9–14 (2018)

17. Davis, J.W.: Development of an international fusion materials database. J. Nucl. Mater. **179–181**, 1139–1143 (1991)

18. Wu, Y.: Conceptual design activities of FDS series fusion power plants in China. Fusion Eng. Des. **81**(23), 2713–2718 (2006)

19. Shen, L.F., et al.: Design and implementation of nuclear reactor material database. Nucl. Sci. Eng. **35**, 639–644 (2015)

20. Lei, M., et al.: Design and thermal-hydraulic evaluation of helium-cooled ceramic breeder blanket for China fusion engineering test reactor. Int. J. Energy Res. **42**, 1657–1663 (2017)

21. Liu, S., et al.: Conceptual design of a water cooled breeder blanket for CFETR. Fusion Eng. Des. **89**(7–8), 1380–1385 (2014)

22. Liu, S., et al.: Conceptual design of the water cooled ceramic breeder blanket for CFETR based on pressurized water cooled reactor technology. Fusion Eng. Des. **124**, 865–870 (2017)

23. Liu, S., et al.: Updated design of water-cooled breeder blanket for CFETR. Fusion Eng. Des. **146**, 1716–1720 (2019)

24. Zeng, Z., et al.: Preliminary neutronics analyses of China Dual-Functional Lithium-Lead (DFLL) test blanket module for CFETR. Fusion Eng. Des. **152**, 111414 (2020)

25. Cooper, J.R., Dooley, R.B. : Revised release on the IAPWS industrial formulation 1997 for the thermodynamic properties of water and steam (2007)

26. EPRI, GOTHIC Thermal Hydraulic Analysis Package Technical Manual, Version 8.0 (QA) (2012)

27. IAEA. Thermophysical Properties of Materials For Nuclear Engineering: A Tutorial and Collection of Data (2008)

28. Mccarty, R.D., Arp, V.D.: A new wide range equation of state for helium. Adv. Cryog. Eng. **35**, 1465–1475 (1990)

29. Petersen, H.: The properties of helium: Density, specific heats, viscosity, and thermal conductivity at pressures from 1 to 100 bar and from room temperature to about 1800 K (1970)

30. Gierszowski, P., Mikic, B., Todreas, N. : Property correlations for lithium, sodium, helium, flibe and water in fusion reactor applications. 80rr (2015)

31. 居怀明, 载热质热物性计算程序及数据手册. 载热质热物性计算程序及数据手册 (1990)

32. Mccarty, R.D.: Thermophysical properties of helium-4 from 4 to 3000 R with pressures to 15000 psia (1972)

33. Valls, E., et al.: Lead–lithium eutectic material database for nuclear fusion technology. J. Nucl. Mater. **376**(3), 353–357 (2008)

34. Abanades, A., et al.: Conceptual design of the liquid metal laboratory of the TECHNOFUSION facility. Fusion Eng. Des. **87**(2), 161–166 (2012)

35. Martelli, D., Venturini, A., Utili, M.: Literature review of lead-lithium thermophysical properties. Fusion Eng. Des. **138**, 183–195 (2019)

36. 杨世铭 and 陶文铨, 传热学(第4版) [Heat Transfer]. 传热学 (第4版) [Heat Transfer] (2006)

37. Liu, L., et al.: Modification and application of Relap5 Mod3 code to several types of nonwater-cooled advanced nuclear reactors. Int. J. Energy Res. **42**, 221–235 (2018)

38. 黎清, 辐射诱导聚合制备氚化水防护材料及其性能研究. 苏州大学

39. Frenkel′, M.L.V.: Thermodynamics of Organic Compounds in the Gas State, vol. 1. CRC Press, Boca Raton (1994)

40. 黄群英, et al.: 聚变堆低活化马氏体钢的发展. In: 反应堆数值计算和粒子输运学术会议暨反应堆物理会议 (2008)

41. Tavassoli, A.A., et al.: Materials design data for reduced activation martensitic steel type EUROFER. J. Nucl. Mater. **329**, 257–262 (2004)

42. 黄群英, et al.: 中国低活化马氏体钢CLAM研究进展. 第十二届反应堆数值计算与粒子输运学术会议论文集 (2008)

43. 雷玉成, et al.: CLAM钢TIG焊有限元模拟. 焊接技术 **038**(003), 16–19 (2009)

44. Löbbecke, B., et al.: Thermal conductivity of sintered lithium orthosilicate compacts. J. Nucl. Mater. **386**, 1068–1070 (2009)

45. Uchida, M., Ishitsuka, E., Kawamura, H.: Thermal conductivity of neutron irradiated Be 12Ti. Fusion Eng. Des. **69**(1/4), 499–503 (2003)

46. Reimann, J., et al.: Thermomechanics of solid breeder and Be pebble bed materials. Fusion Eng. Des. **61**, 319–331 (2002)

47. Shah, K.R.: Laminar Flow Forced Convection in Ducts, pp. 366–384 (1978)

48. Babus'Haq, R.F.: Sforced-convection heat transfer from a pipe to air flowing turbulently inside it. Exp. Heat Transf. **5**(3), 161–173 (1992)

49. Gnielinski, V.: New equations for heat and mass transfer in turbulent pipe and channel flows. Int. Chem. Eng. **16**, 359–368 (1976)

50. Bergles, A.E., Rohsenow, W.M.: The determination of forced-convection surface-boiling heat transfer. Asme Ser. C. **86**(3), 372 (1964)

51. Jens, W.H., Lottes, P.A.: Analysis of heat transfer, burnout, pressure drop and density date for high- pressure water. United States (1951)

52. Fagerholm, N.E., Ghazanfari, A.R., Kivioja, K.: Boiling heat transfer in a vertical tube with freon 114. Wärme - und Stoffübertragung **17**(4), 221–232 (1983)

53. Chen, C.J.: A correlation for boiling heat transfer to saturated fluids in convective flow. Ind. Eng. Chem. Proc. Des. Dev. **5**(3), 322–329 (1966)

54. Kutateladze, S.S.: Boiling heat transfer. Int. J. Heat Mass Transf. **4**(9), 31–45 (1961)

55. Mattson, R.J., et al.: Regression analysis of post-CHF flow boiling data. scripta book co washington dc (1974)

56. Mcdonough, J.B., Milich, W.: An experimental study of partial film boiling region with water at elevated pressures in a round vertical tube. Technical Report 71 (1961)

57. Tran, T.N., et al.: A correlation for nucleate flow boiling in small channels. phase change materials (1997)

58. Lazarek, G.M., Black, S.H.: Evaporative heat transfer, pressure drop and critical heat flux in a small vertical tube with R-113. Int. J. Heat Mass Transf. **25**(7), 945–960 (1982)

59. 栾振博, 管内水过冷流动沸腾传热系数关联式研究. 中国科学技术大学 (2020)
60. Co, L. : RELAP5/MOD3 code manual. Volume 4, Models and correlations. Office of Scientific & Technical Information Technical Reports (1995)
61. 于平安, 朱瑞安, 喻真烷. 核反应堆热工分析. 北京: 原子能出版社 (1986)
62. The RELAP5–3D Code Development Team. RELAP5- 3D Code Manual Volume IV: Models and Correlations. INEEL-EXT-98–00834 (2005)
63. Froio, A., et al.: Modelling an in-vessel loss of coolant accident in the EU DEMO WCLL breeding blanket with the GETTHEM code. Fusion Eng. Des. **136**, 1226–1230 (2018)
64. Mccarthy, K.A., et al.: The safety implications of tokamak dust size and surface area. Fusion Eng. Des. **42**(1–4), 45–52 (1998)
65. Sharpe, J.P., Petti, D.A., Bartels, H.W.: A review of dust in fusion devices: implications for safety and operational performance. Fusion Eng. Des. **63**, 153–163 (2002)
66. Smolik, G.R., et al.: Hydrogen generation from steam reaction with tungsten. J. Nucl. Mater. **258**(4), 1979–1984 (1998)
67. Furudate, M.A., Cho, S., Hagebaum-Reignier, D.: Study on chemical kinetics of HTO + H2 → H2O + HT for design of tritium breeding blanket. Fusion Eng. Des. **136**, 438–441 (2018)
68. Black, J., Taylor, H.: Equilibrium in hydrogen-water systems containing tritium. J. Chem. Phys. **11**, 395–402 (1943)
69. Cheng, W.-L., et al.: Effect of droplet flash evaporation on vacuum flash evaporation cooling: modeling. Int. J. Heat Mass Transf. **84**, 149–157 (2015)
70. Elias, E., Chambré, P.: Flashing inception in water during rapid decompression (1993)
71. Ogawa, M., Kunugi, T.: Thermohydraulic experiments on a water jet into vacuum during ingress of coolant event in a fusion experimental reactor. Fusion Eng. Des. **29**, 233–237 (2010)
72. 张强, 刘淼, and 戎玲, 非均匀加热管内单相流动传热特性数值模拟. 应用能源技术 (3), 5 (2019)
73. 崔青蓝, CFETR水冷固态包层瞬态与典型事故的热工水力分析. 中国科学技术大学 (2018)

Development and Verification of a New Depletion, Activation and Radiation Source Term Calculation Code

Xingjian Wen[1](✉), Zian Zhai[1], Songqian Tang[1], Chao Tian[1], and Zhouyu Liu[2]

[1] Science and Technology on Reactor System Design Technology Laboratory, Nuclear Power Institute of China, Chengdu, Sichuan, China
`wenxingjian35@126.com`
[2] Xi'an Jiaotong University, Xi'an Shaanxi, China

Abstract. Existing depletion and source term calculation codes lack flexible interfaces, which is difficult to meet the actual engineering design needs. Based on the Chebyshev rational approximation method, a new depletion, activation and source term calculation code TIST is developed and verified. Full-fidelity depletion library based on ENDF-VII.0 and EAF2010 contains 3837 isotopes is generated. Flexible interfaces are built-in to support cross sections from different sources for depletion and activation calculations. The EAF2010 library and the cross sections from the high-fidelity code NECP-X are adopted by TIST for the verification in this work. Based on the nuclide inventory of the depletion and activation calculation, the radiation source term calculation capability of TIST is developed, including the radioactivity, the decay heat, the neutron source and the photon source. The comparison results with NECP-X and FISPACT demonstrate good accuracy of TIST.

Keywords: TIST · NECP-X · Depletion calculation · Activation calculation · Source term calculation

1 Introduction

The radiation source term for the fuel stacks and the structure materials is one of the important inputs for the radiation shielding design. Accurate prediction of the source term could support the design of nuclear facilities and improve economic efficiency. Nuclide inventory is the basis of the source term calculation, which involves the depletion calculation of the fuel stacks and the activation of the non-fissile materials. The existing codes such as ORIGEN-2 [1] and FISPACT [2] suffer from low accuracy and bad robustness of old algorithms. Nevertheless, the in-house modules do not open interfaces to other organizations, including ORIGEN-S in SCALE [3] and son on.

In this work, a new depletion, activation and radiation source term calculation code TIST is developed and verified with the high-fidelity code NECP-X [4] and FISPACT. The content is organized as follows. In Sect. 2, the theory of TIST is presented, including the library of TIST, depletion and source term models. The accuracy demonstration of the

depletion calculation, activation calculation and the source term calculation are shown in Sect. 3. Conclusions are summarized in Sect. 4.

2   Theory

The development of depletion, activation and radiation source term calculation functions in TIST include the generation of the depletion and activation chain library, the estimation of nuclide inventories and the radiation source term calculation from different radioactive sources. This section can be divided into three parts. Firstly, the high-fidelity depletion and activation chain library is generated for TIST, and then the basic governing equation of depletion and activation calculation and its solution are introduced. Finally, the method of calculating radiation source term in TIST is described in detail.

2.1   Generation of the Depletion and Activation Chain Library for TIST

The depletion and activation chain library provides nuclides' property, transmutation and decay information for TIST, including the half-life, the energy per disintegration, transmutation paths and branching ratios, etc. A full-fidelity depletion and activation chain library is developed in TIST ENDF/B-VII.0 evaluated nuclear data library [5] and the neutron-induced activation library EAF-2010 [6] in this work. Nuclides in TIST are grouped into three categories: actinides, fission products and activations. The major characteristics of libraries of TIST are presented in Table 1, including number of three kinds of nuclides and information of transmutation and decay paths.

Table 1. Main characteristics of the depletion and activation chain of TIST

# of nuclides	# of actinides	# of fission products	# of activations	# of decay paths	# of neutron-induced paths
3837	442	1137	2258	5666	60407

2.2   The Solution of the Bateman Equations in TIST

The Bateman equations are solved for a set of time steps, which can be written in a matrix form as follows:

$$\frac{d\overrightarrow{N}}{dt} = A \cdot \overrightarrow{N}(t) \tag{1}$$

The general solution of Eq. (1) is given in Eq. (2):

$$\overrightarrow{N}(t2) = e^{tA} \cdot \overrightarrow{N}(t1) \tag{2}$$

where A is the transmutation and decay matrix, which is a large-scale and stiff system. $\vec{N}(t1)$ is the initial number densities of all nuclides of previous time step.

The Chebyshev rational approximation method (CRAM) [7] is used for calculating Eq. (2) in TIST. The eigenvalues of the coefficient matrix of Bateman equations are clustered around the negative real axis. In this situation, exponential function for the interval $(-\infty, 0]$ can adopt Chebyshev rational approximation. When the approximation is applied to the matrix exponential, Eq. (2) can be presented as following:

$$\vec{N}(t2) = \alpha_0 \vec{N}(t1) + 2\left[\operatorname{Re}\sum_{i=1}^{k/2}\alpha_i(A\Delta t + \theta_i I)^{-1}\right]\vec{N}(t1) \tag{3}$$

where α_0 is the limiting value of the approximation at infinity, α_i and θ_i is the residues and poles which depend on order k and thus they can be pre-calculated and tabulated against expansion order k in the code. $t1$ is time of the beginning of the step, $t2$ is the time of the end of the step, Δt equals $t2 - t1$.

Due to the sparse structure of the coefficient matrix, Eq. (3) can be solved accurately and efficiently with the non-zero storage function in and the Jacobian iterative method in TIST.

2.3   Radiation Source Term Calculation Methods

Based on the isotopic inventory from the transmutation calculation, and the decay constants, the radioactivity of every isotope can be explicitly tracked:

$$A_{inuc} = N_{inuc}.\lambda_{inuc} \tag{4}$$

where A_{inuc} is the radioactivity, λ_{inuc} is the decay constant of isotope $inuc$, and N_{inuc} is the number of isotope $inuc$.

The decay heat of every isotope relies on the radioactivity and the energy per disintegration can be obtained:

$$DH = \sum_{inuc}^{nnuc} A_{inuc}.E_{inuc}^{decay} \tag{5}$$

where DH is the decay heat, E_{inuc}^{decay} is the energy per disintegration of isotope $inuc$, $nnuc$ is the total number of isotopes.

The photon source term model implemented in TIST considers gammas arising from X-rays, gamma-rays, bremsstrahlung, spontaneous fission, and (α, n) reactions. ENSDF-2011 [8] is adopted to provide the photon yields. The photon source term calculation method is the same as ORIGEN'S method. When the line-energy data is transformed to multi-group photon yields, the adjusted group yield per disintegration of the emitter $inuc$ is given as following based on the conservation of energy:

$$yield(ig, inuc) = \sum_{i=1}^{n} yield_{i,inuc}.E_i/E_{ig} \tag{6}$$

where *yield* (*ig*, *inuc*) is the photon yield per disintegration of group *ig*, $yield_{i,inuc}$ is the actual photon yield at photon energy E_i, E_{ig} is the mean energy of the group and n is the total number of photon yield in the group *ig* given in ENSDF-2011.

The neutron source term of TIST includes neutrons produced from spontaneous fission and (α, n) reactions. The calculation of the neutron source term includes the calculation of strengths and the spectra. The methods are adopted from the SOURCE 4C code [9].

The spontaneous fission reaction can be considered as a decay reaction, and its strength N_{sf} can be directly calculated with the activity of the precursor A_{sf}, and the number of neutrons per fission υ.

$$N_{sf} = A_{sf} \cdot \upsilon \tag{7}$$

As for the normalized spontaneous neutron spectrum, the Watt fission spectrum [10] is applied:

$$N(E) = ce^{-E/a} \sinh \sqrt{bE} = ce^{-E/a} \frac{\left(e^{\sqrt{bE}} - e^{-\sqrt{bE}}\right)}{2} \tag{8}$$

where a and b are evaluated nuclide-dependent constants, c and E are the normalization constant and neutron energy.

The calculation of neutron source strength from the (α, n) reaction is based on the neutron yield and the activity of alpha decay. It is assumed that all alpha particles are stopped within the medium, and react with the target nuclides in the medium, not transporting to adjacent regions [9].

In the medium, the α particles have multiple origins and the (α, n) reactions happen with different target nuclides. For one specific α particle and a target nuclide *i*, the calculation of the neutron yield from (α, n) reaction requires the stopping power $S(E)$, microscopic (α, n) reaction cross-section $\sigma_i^{(\alpha, n)}(E)$ of the target nuclide *i*, and the alpha particle energy E.

The stopping power $S(E)$ is defined as the loss energy dE per unit path length dx:

$$S(E) = -\frac{dE}{dx} \tag{9}$$

The yield of the neutron production from the alpha partial with the target nuclide *i* is given as follows:

$$Y_i(E_\alpha) = \int_{E_\alpha}^{0} P_i^{(\alpha, n)}(E)dE = N_i \int_{0}^{E_\alpha} \frac{\sigma_{(\alpha, n)}(E)}{S(E)} dE \tag{10}$$

where N_i is the number density of target nuclide in the mediums, E_α is the energy of the alpha particle.

3 Numerical Results

Three cases were used to verify TIST. The results provided by TIST were compared with FISPACT and the high-fidelity code NECP-X. Firstly, the second international activation

calculation benchmark [11] was presented to demonstrate the accuracy of the activation calculation. Secondly, a pin cell problem from VERA depletion benchmark was used to test the depletion calculation in TIST. Finally, the radiation source term calculation based on the spent fuel is conducted by TIST and NECP-X, respectively.

3.1 The Second International Activation Calculation Benchmark

The activation benchmark was completed under the coordination of the IAEA Nuclear Data Section in 1994. Two problems were developed in this benchmark, including the activation of ^{50}Cr and natural Fe. Besides, a 100-group fusion flux was also provided for the calculations. FISPACT-2007 is chosen to offer the reference results, which are publicly available in the literature [12].

The results are shown in Table 2 and Table 3 for the activation of ^{50}Cr and natural Fe, respectively (T for TIST, N for NECP-X and F for FISPACT2007). It is found that the differences between FISPACT2007, TIST and NECP-X are small. The errors of nuclide inventory for all isotopes between TIST and FISPACT are within 0.7% and the maximum error is -0.63% for ^{50}V.

Table 2. Comparison results for the activation of ^{50}Cr

Nuclide	N-F diff (%)	T-F diff (%)
^{48}Ti	−0.15	−0.23
^{49}Ti	−0.12	−0.12
^{50}Ti	−0.14	−0.14
^{49}V	−0.05	−0.05
^{50}V	−0.07	−0.07
^{51}V	−0.08	−0.07
^{50}Cr	0.00	0.00
^{51}Cr	0.00	0.00
^{52}Cr	−0.13	−0.13
^{53}Cr	−0.20	−0.20
^{54}Cr	−0.27	−0.26

3.2 The VERA Depletion Benchmark

In order to assert the accuracy of the depletion capability of TIST, a pin cell problem from the VERA depletion benchmark [13] is tested.

VERA depletion benchmark problems were developed based on the VERA progression problems [14] by Oak Ridge National Laboratory in 2015. It contains detailed information, including the geometry, temperature and the materials of fuel, moderator,

Table 3. Comparison results for the activation of natural Fe

Nuclide	N-F diff (%)	T-F diff (%)
^{49}Ti	−0.13	−0.24
^{50}Ti	0.08	−0.02
^{49}V	−0.09	−0.52
^{50}V	−0.08	−0.63
^{51}V	0.04	0.04
^{50}Cr	0.05	0.05
^{51}Cr	0.11	0.11
^{52}Cr	−0.13	−0.22
^{53}Cr	0.05	0.05
^{54}Cr	0.00	−0.01
^{54}Mn	0.07	0.07
^{55}Mn	−0.01	−0.01
^{56}Mn	−0.02	−0.02
^{57}Mn	0.12	0.12
^{54}Fe	0.11	0.11
^{55}Fe	0.07	0.07
^{56}Fe	0.12	0.12
^{57}Fe	0.12	0.12
^{58}Fe	0.12	0.11
^{59}Fe	0.06	0.05
^{59}Co	−0.01	−0.01
^{60}Co	−0.06	−0.08
^{60m}Co	0.08	0.01

guide/instrument tubes and burnable poisons. Pin cell problems cove the enrichment of fuel from 2.1% to 4.6%, and fuel temperature from 565 K to 1200 K. More detailed pin cell configurations, materials, depletion options may refer to the benchmark report [13]. VERA-1C problem is chosen for the test in this work, the cross sections are provided by NECP-X and important isotopes at 60 GWd/tU are compared, which is presented in Table 4. It is found that the differences between TIST and NECP-X are small. The errors of nuclide inventory for all isotopes are within 0.4% and the maximum error is 0.37% for ^{243}Am.

3.3 Radiation Source Term of the Spent Nuclear Fuel

The accuracy of TIST for the source term calculation is asserted by comparison of code-to-code. The comparison of TIST to NECP-X is conducted here. To eliminate the errors

Table 4. Comparison results for the actinides and fission products

Actinides			
Nuclide	NECP-X	TIST	T-N diff (%)
^{235}U	7.27E–05	7.25E–05	−0.35
^{236}U	9.97E–05	9.98E–05	0.01
^{238}U	2.09E–02	2.09E–02	0.01
^{237}Np	1.90E–05	1.90E–05	0.08
^{238}Pu	1.23E–05	1.23E–05	0.19
^{239}Pu	1.73E–04	1.73E–04	0.04
^{240}Pu	7.96E–05	7.96E–05	0.08
^{241}Pu	5.55E–05	5.55E–05	0.12
^{242}Pu	3.43E–05	3.44E–05	0.27
^{241}Am	1.82E–06	1.82E–06	−0.14
^{242m}Am	3.61E–08	3.61E–08	−0.12
^{243}Am	9.00E–06	9.04E–06	0.37
^{242}Cm	8.79E–07	8.80E–07	0.16
^{243}Cm	3.41E–08	3.42E–08	0.26
^{244}Cm	6.52E–06	6.52E–06	0.06
^{245}Cm	6.24E–07	6.25E–07	0.08
^{246}Cm	9.92E–08	9.94E–08	0.23
Fission products			
Nuclide	NECP-X	TIST	T-N diff (%)
^{95}Mo	6.16E–05	6.17E–05	0.08
^{99}Tc	6.71E–05	6.70E–05	−0.24
^{103}Rh	3.65E–05	3.65E–05	0.09
^{133}Cs	7.03E–05	7.03E–05	0.08
^{147}Sm	3.32E–06	3.32E–06	−0.1
^{149}Sm	1.17E–07	1.17E–07	0.1
^{150}Sm	1.78E–05	1.79E–05	0.2
^{152}Sm	6.97E–06	6.95E–06	−0.17
^{143}Nd	4.21E–05	4.21E–05	0.08
^{145}Nd	3.81E–05	3.82E–05	0.12
^{153}Eu	7.79E–06	7.78E–06	−0.09
^{155}Gd	5.91E–09	5.90E–09	−0.26

introduced by the depletion calculation, the same compositions of SNF are provided for both codes, which come from the nuclide inventory of irradiated nuclear fuel of VERA-1C in this work. Note that '0 year' means the shut-down time.

Figure 1 and Fig. 2 present the comparison of the radioactivity and the decay heat results between TIST and NECP-X, respectively. In the figures, the results of NECP-X are taken as the reference. As shown in Fig. 1 and Fig. 2, the maximum relative difference of decay heat and radioactivity of two codes for all decay time range is less than 0.15%.

Figure 3 and Fig. 4 shows the relative difference of photon spectra and neutron spectra between TIST and NECP-X. The maximum relative difference of photon spectra and neutron spectra between TIST and NECP-X is 0.44% and -0.37%, respectively, whose strength is pretty low in this situation.
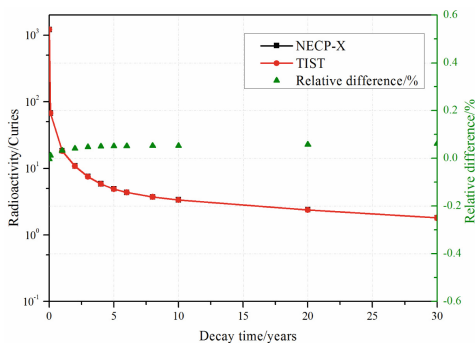
Fig. 1. Comparison of the radioactivity between TIST and NECP-X
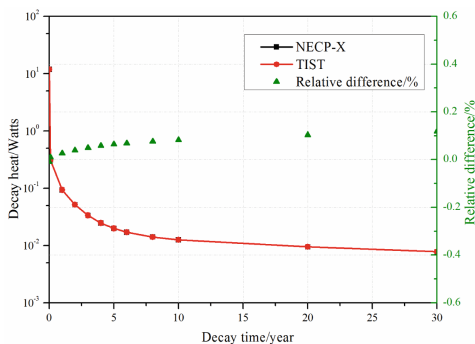
Fig. 2. Comparison of the decay heat between TIST and NECP-X
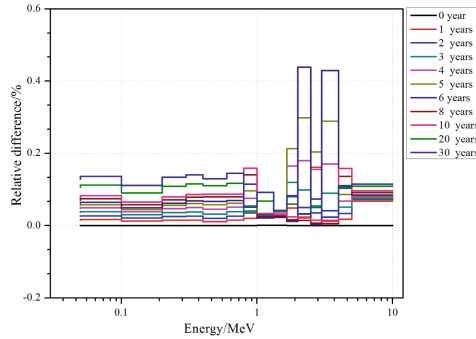
Fig. 3. Comparison of photon spectra between TIST and NECP-X
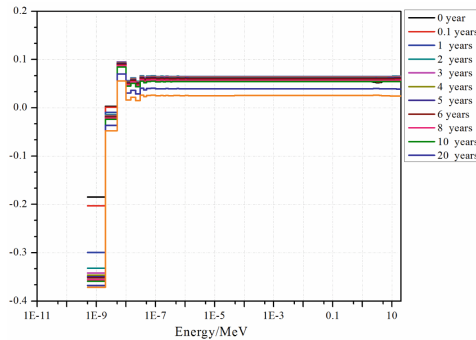
Fig. 4. Comparison of neuron spectra between TIST and NECP-X

4   Conclusions

The depletion, activation and radiation source term calculation code TIST is developed and verified in this work. The theoretical models of TIST are introduced briefly in this paper, including the depletion and activation chain library, depletion model and the source term calculation model. The accuracy of TIST for the depletion calculation, the activation calculation and the source term calculation are verified by a set of benchmarks, and the results show good consistency for TIST, FISPACT and the high-fidelity code NECP-X. More work is under going to compare the results of TIST to the measurements.

References

1. Croff, A.G.: A User's Manual for the ORIGEN2 Computer Code. Oak Ridge National Laboratory (1980)
2. Sublet, J.C., et al.: FISPACT-II: an advanced simulation system for activation, transmutation and material modelling. Nucl. Data Sheets **139**, 77–137 (2017)
3. Bowman, S.M.: SCALE 6: comprehensive nuclear safety analysis code system. Nucl. Technol. **174**(2), 126–148 (2011)

4. Wen, X.J., et al.: Development and validation of the depletion capability of the high-fidelity neutronics code NECP-X. Ann. Nucl. Energy **138**, 107096 (2020)
5. Chadwick, M.B., et al.: ENDF/B-VII.0: next generation evaluated nuclear data library for nuclear science and technology. Nucl. Data Sheets **107**(12), 2931–3060 (2006)
6. Sublet, J.-C., et al.: The European Activation File: EAF-2010 neutron-induced cross section library (2010)
7. Pusa, M., Leppänen, J.: Computing the matrix exponential in burnup calculations. Nucl. Sci. Eng. **164**(2), 140–150 (2010)
8. Bhat, M.R.: Evaluated Nuclear Structure Data File (ENSDF). United States (1991)
9. Wilson, W.B., et al.: Sources: a code for calculating (alpha, n), spontaneous fission, and delayed neutron sources and spectra. Prog. Nucl. Energy **51**(4), 608–613 (2009)
10. Cullen, D.E.: Sampling ENDL Watt Fission Spectra. United States (2004)
11. Cheng, E.T., Pashchenko, A.B. : Report Onthe Second International Activation Calculation Benchmark Comparison Study. TSI Research, Inc., Solana Beach, USA, Culham Laboratory, Culham, UK, IAEA Nuclear Data Section, Vienna, Austria (1994)
12. Zhang, J., Ma, Y., Peng, Y., Chen, Y.: ABURN: a material activation calculation code based on CRAM method. Fusion Eng. Des. **125**, 659–663 (2017)
13. Kim, K.S.: Specification for the VERA Depletion Benchmark Suite. Oak Ridge National Lab. (ORNL), Oak Ridge, TN (United States). p. 32 (2015)
14. Godfrey, A.: VERA Core Physics Benchmark Progression Problem Specifications. Revision 4, CASL Technical Report: CASL-U-2012-0131-002 (2014)

Derivation of Activity Concentration Upper Limits for Low Level Solid Radioactive Waste

Jianqin Liu$^{(\boxtimes)}$, Chao Gao, Li Zhang, and Xiang Qin

China Institute for Radiation Protection, Xuefu Street 102, Taiyuan, Shanxi, China
`565998530@qq.com`

Abstract. The derivation method of activity concentration upper limits for low level radioactive waste is put forward. The activity concentration upper limits for low level solid radioactive waste will be ascertained, on the basis of safety assessment of near surface disposal. On the premise of basic safety requirements about radioactive waste near surface disposal, taking Yaotian disposal site and Feifengshan disposal site as the reference sites, the drilling water scenario, drilling scenario, post-drilling scenario, and housing scenario after the institutional control period when the disposal sites have been closed are considered. The radionuclide transfer process and exposure pathway of various scenarios are analyzed, the conceptual model and mathematical model of radionuclide transfer are established, and the effective dose to human from various scenarios is calculated. Assuming a linear relationship between the activity concentration and the dose, the activity concentration upper limits of various scenarios are then derived for each radionuclide that meet the appropriate dose criteria. The smallest upper limit is chosen, by the approximate integer principle, the magnitude of upper limit of each radionuclide for low level solid waste is then ascertained.

Keywords: Activity Concentration Upper Limit · Safety Assessment · Near Surface Disposal

1 Introduction

In 2009, International Atomic Energy Agency (IAEA) released the latest Safety Guidelines for the Classification of Radioactive Waste (IAEA-GSG-1, 2009) [1], which provides a dispose-based classification scheme of radioactive waste, classifying radioactive waste into exempt waste, very short-lived waste, very low level waste, low level waste, intermediate level waste and high-level waste. Low level waste is defined as the waste that is above clearance levels, but with a limited amounts of long-lived radionuclides. This class of waste requires robust isolation and containment for periods of up to a few hundred years. It is suitable for disposal in engineered near-surface disposal facilities and covers a very broad range of waste. The activity concentration of short-lived radionuclides in LLW may be high, while the activity concentration of long-lived radionuclides is relatively low, but IAEA has not given a specific upper limits. Quantitative waste classification values need to be determined on the basis of safety assessment of disposal

facilities. The aim of this study is to derive the upper limits of the activity concentration of radionuclides in the low level solid waste based on the safety assessment of the near surface disposal of radioactive waste.

2 Approach to Deriving Activity Limits

Safety assessment is required in the derivation of the near-surface disposal activity concentration limits for specific radionuclides to ensure that the results of safety assessment for both operational and post-closure periods of disposal facilities meet the appropriate safety criteria [2]. The derivation process of the activity concentration limit is shown in Fig. 1. First, take a unit activity concentration of each radionuclide, consider all the potential scenarios, calculate the dose caused by each scenario, compare the peak dose of each nuclide in each scenario, that is, the maximum dose. In order to obtain the activity concentration limit, the maximum dose of each nuclide was compared with the dose limit. Assuming that there is a linear relationship between the activity concentration value and the dose, the activity concentration limit of each radionuclide can be derived in each scenario meeting the appropriate radiological protection criteria. For any given scenario, the activity concentration limits of each radionuclide in the waste can be calculated using formula (1):

$$Cp_i = \frac{Dose_{\text{lim}} \cdot C_i}{MaxDose_{iu}} \tag{1}$$

where, Cp_i is the activity concentration limit of radionuclide i in the waste (Bq/kg), $Dose_{\text{lim}}$ is the relevant dose limit (Sv/a), $maxDose_{iu}$ is the peak dose resulting from the initial activity of radionuclide i in the waste (Sv/a), C_i is the initial activity concentration of the radionuclide i in the waste (Bq/kg).

The minimum value of the activity concentration limit calculated by each scenario is selected to obtain the activity concentration upper limit of the nuclide in the waste, and the corresponding scenario is the key scenario.
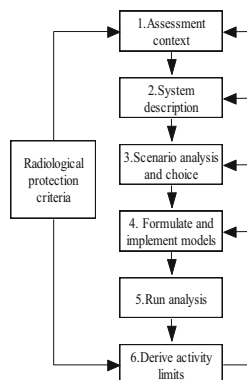
Fig. 1. Activity limits derivation process

2.1 Assessment Context

The purpose of the assessment is to derive the activity concentration limit of the radionuclide for the disposal of radioactive waste in the near surface disposal site, so as to determine the activity concentration upper limit of the low level solid waste, and to ensure that the radiation impact of low level solid waste in near surface disposal on human beings and the environment remains at an acceptable level. In the derivation of the activity concentration limit, 300 years of institutional control period was assumed. Therefore, a possible inadvertent human intrusion should occur 300 years after closure of the facility.

2.2 Dose Limit

The derivation of the activity concentration upper limit of radionuclide in radioactive waste is to consider the long-term safety of the disposal of waste, that is, to consider its potential harm to current and future human beings. The derivation of the activity concentration upper limit of radionuclide for low level solid waste follows the following dose criteria:

The annual effective dose of radionuclides released into the environment by various pathways from the near surface disposal facility to key groups of individuals in the public before the expiration of 300 years of institutional control does not exceed 0.25 mSv [3].

The annual effective dose to the individual public of radionuclides released into the environment by various pathways from the near surface disposal facility at any time after 300 years of institutional control has been released from the disposal facility does not exceed 0.01 mSv [4]. For intruders who breach engineering barriers, the annual effective dose of the radionuclides released from disposal facility to intruders through various pathways does not exceed 1 mSv.

2.3 Disposal Site and Nuclide Selection

In the derivation of the activity concentration limit of the radionuclide in waste, the Yaotan disposal site [5] and Feifengshan disposal site [6] were taken as the objects to conduct evaluation and derivation. The selected nuclides are as follows:

The nuclides with half-life of 5–30 years: ^{3}H, ^{90}Sr and ^{137}Cs. ^{3}H represents the transferable nuclide; ^{90}Sr and ^{137}Cs represent nuclides with half-lives of 30 years, which are about one-tenth of the institutional control period.

β nuclides with long half-life: ^{63}Ni, ^{14}C and ^{99}Tc.

α nuclides with long half-life: ^{239}Pu, ^{240}Pu, ^{237}Np and ^{241}Am.

2.4 Scenario Analysis and Choice

Scenario analysis is an analytical method to determine and quantify the phenomena that can facilitate the release of radionuclides from near surface repository, or influence the release rate. According to the scenarios selected for the environmental impact assessment of the disposal site, the scenarios considered in the derivation of the upper limit value of the activity concentration of low level solid waste can be divided into two categories:

Operational scenarios: in the operational scenarios (such as waste package dropping, fire and other accidents), the risk of radioactivity may be generated for a short duration. The presence of operators and government supervision agencies minimizes the release of radioactivity during operations. Therefore, when determining the limit of the activity concentration of radionuclides, this kind of scenario is of little significance, so the operational scenario is not calculated in this derivation.

Post-closure scenarios:

After the expiration of the institutional control period, the exposure scenario caused by drilling wells and drinking water at the boundary of the disposal site is mainly related to the migration of groundwater, and depends on the environmental characteristics and facility design of the specific site. As this scenario is dependent on the total activity of the whole repository, and has nothing to do with the nuclide concentration in the waste, is called the total activity scenario, the scenario can be used to calculate the total activity limit in the whole site, divided by the waste volume of the entire disposal site can be concluded that nuclide activity concentration limit related to groundwater migration mechanism [7].

After the expiration of the institutional control period, the occurrence of human intrusion scenario, that is, the exposure scenario caused by drilling on the disposal site, living after drilling, and housing. These scenario analysis results are generally less dependent on the environmental characteristics of the site and restrict the concentration level of nuclides, so they are called concentration scenarios. Because the intrusion scenario has little dependence on the characteristics of a particular site, the derived limits are of general significance.

3 Derivation and Calculation of the Upper Limit of Activity Concentration

3.1 Assessment Context

Conceptual Model

After the repository is closed, the performance of the engineering barrier will gradually deteriorate over time. Due to the effect of seepage water, the nuclides will be leached from the waste form, then released from the disposal unit floor into the unsaturated zone under the disposal unit, and then enter the aquifer and transfer along the direction of underground water flow. It is assumed that after the closure of the repository, the public dug a well at 100m downstream of the disposal site to drink the well water and use it for agricultural irrigation. The internal exposure caused by drinking the well water, ingesting the agricultural products irrigated by the well water, and ingesting the poultry and livestock products fed by the crops irrigated by well water is considered. For the drilling water scenario, the radionuclides transfer process and exposure pathways are shown in Fig. 2.
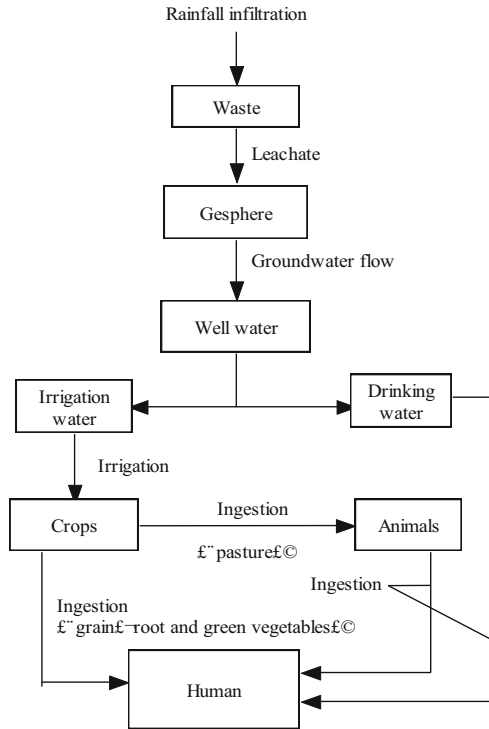
Fig. 2. Radionuclide transfer process and exposure pathway of drilling water scenario

Mathematical Model

(1) Migration of nuclides in the disposal unit

Decay, adsorption and vertical downward migration of nuclides are considered in the calculation of nuclide migration in the disposal unit. The vertical downward transfer rate ($\lambda_{inf, a-1}$) of nuclides caused by infiltration water is given by the following formula [8]:

$$\lambda_{\inf} = \frac{q_{in}}{L_w \theta_{w,1} R} \tag{2}$$

where, q_{in} is the Darcy flow rate (m/a) through the disposal unit, namely infiltration rate; L_w is the total length of radionuclide migration (m), namely the height of the disposal unit; is the effective porosity of the medium in the disposal unit; R is the retention coefficient of the media in the disposal unit for nuclides, and its value is given by the following formula:

$$R = 1 + \frac{\rho K d}{\theta_{w,1}} \tag{3}$$

where, ρ is the density of the medium in the disposal unit (kg/m^3), Kd is the distribution coefficient of nuclides in the medium in the disposal unit (m^3/kg).

(2) Migration of nuclides in unsaturated zone

The nuclides released from the bottom of the disposal unit enter the unsaturated zone, and the same model is used to calculate the migration of nuclides in the unsaturated zone. The migration process of nuclides vertically downward is shown in Eqs. (2) and (3).

(3) Migration of nuclides in aquifer

The nuclides migrate into the aquifer through the unsaturated zone. Decay, adsorption, convection and dispersion are considered in the calculation of the nuclides migration in the aquifer. It is assumed that: there is no other leakage source term; the nuclides are uniformly mixed vertically in the aquifer; ignoring molecular diffusion.

When calculating the migration of nuclides in aquifer, for convective transport, the transfer rate is $\lambda_{A,ij}$, and for dispersion, the transfer rate $\lambda_{D,ij}$ is:

$$\lambda_{A,ij} = \frac{q}{\theta_w L_i R} \tag{4}$$

$$\lambda_{D,ij} = \frac{a_x}{\Delta_x} \lambda_{A,ij} \tag{5}$$

where, q is the Darcy flow rate of groundwater, m/a; θ_w is the effective porosity of the aquifer; q/θ_w is the actual velocity of groundwater, m/a; L_i is the length of the compartment in the aquifer, m; α_x is longitudinal dispersion, m; $a_x = \frac{D_x \theta_w}{q}$; D_X is longitudinal dispersion coefficient, m^2/a; Δ_X is the migration distance of the nuclide in the medium, m.

(4) Dose estimation

The total individual dose for drinking water from drilling Wells is calculated as follows:

$$D_{well} = D_{W,P} + D_g + D_{g,1} \tag{6}$$

where, $D_{W,P}$ is annual individual effective dose from drinking well water, Sv/a; D_g is annual individual effective dose from ingestion of contaminated agricultural products, Sv/a; $D_{g,1}$ is annual individual effective dose from ingestion of poultry and livestock products, Sv/a.

The annual individual effective dose from drinking well water can be calculated by the following formula:

$$D_{W,P} = Q \times C_{W,i} \times DC_{ing} \tag{7}$$

where: Q is the amount of drinking water, m^3/a; $C_{W,i}$ is the concentration of nuclide i in well water, Bq/m^3; DC_{ing} is the dose coefficient of nuclides for ingestion, Sv/Bq.

The annual individual effective dose from ingestion of contaminated agricultural products can be calculated by the following formula:

$$D_g = DC_{ing} \times v_p \times f_p \times C_{p,i} \tag{8}$$

where, v_p is an individual's annual intake of P products, kg/a; f_p is the share of P products consumed in the relevant area, conservatively taking FP = 1; $C_{p,i}$ is the activity concentration of nuclide i in P agricultural products, Bq/kg, where $C_{p,i}$ is calculated by the following formula:

$$C_{p,i} = \frac{C_{G,i} \times B_V}{P} \times e^{-\lambda t_h} \tag{9}$$

where, B_V is the concentration factor of nuclides absorbed by the edible part of crops from soil, Bq·kg^{-1}(fresh crops)/Bq·kg^{-1}(dry soil); P is the effective surface density of soil, kg(dry soil)/m^2, P = 240; t_h is the time from harvest to consumption of crops, a; $C_{G,i}$ is the concentration of nuclides deposited on the soil surface caused by irrigation water, Bq/m^2, and its value can be calculated by the following formula:

$$C_{G,i} = \frac{C_{W,i} \times I}{\lambda_e^s} \times (1 - exp(-\lambda_e^s t_b)) \times P_p \tag{10}$$

where, I is the average irrigation rate in the growing season, m^3/(m^{2}a); t_b is the accumulation time of radionuclides on the soil surface, a; P_p is the share of well water irrigation, 0.1; λ_e^s is the effective rate constant for the removal of radionuclides from the soil surface, a^{-1}, which can be calculated by the following formula:

$$\lambda_e^s = \lambda + \lambda_s \tag{11}$$

where, λ_s is the rate constant for other removal processes of nuclide other than decay, a^{-1}.

The annual individual effective dose from ingestion of poultry and livestock products can be calculated by the following formula:

$$D_{g,1} = DC_{ing} \times v_p \times f_p \times C_{p,i,1} \tag{12}$$

where, $C_{p,i,1}$ is the activity concentration of nuclide i in animal products, Bq/kg, which can be calculated by the following formula:

$$C_{p,i,1} = F_A \times C_F \times Q_F \times exp(-\lambda t_f) \tag{13}$$

where, F_A is the average share of daily intake of radionuclides in each kilogram of animal products, d/kg; C_F is activity concentration of nuclide in animal feed, Bq/kg(dry weight); Q_F is the daily feed consumption of animals, kg(dry weight)/d; t_f is the time from the slaughter of the animal to the consumption of the animal product, a.

3.2 Drilling Scenario Calculation

Conceptual Model

It is assumed that 300 years after the closure of the repository, intruders drill above the disposal unit with a core diameter of $D = 0.1$ m, a waste length of $L = 8$ m, a uniform distribution of nuclides, a drilling operator 0.5 m away from the core and the contact time of 8 h. Consider the dose to drilling operators caused by external irradiation from the waste and internal exposure of radioactive dust inhalation. In the drilling scenario, the radionuclide transfer process and exposure pathway are shown in Fig. 3.
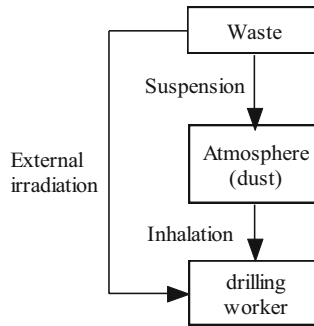
Fig. 3. Radionuclide transfer process and exposure pathway of drilling scenario

Mathematical Model

The total annual individual effective dose to a intruder caused by drilling scenario is calculated by the following formula:

$$D_{drill} = D_{ex} + D_{inh} \tag{14}$$

where, D_{ex} is the external exposure dose, Sv; D_{inh} is the dose of internal exposure due to inhalation, Sv.

(1) External exposure dose

Simplified as a line source, the operator's dose due to external exposure of a certain nuclide is calculated by the following formula:

$$D_{ex} = t \times \frac{47.4 \times A \times \Gamma}{L_{rock} \times R} \times tg^{-1} \frac{L_{rock}}{2R} \tag{15}$$

where, t is the time that the operator contacts the core containing waste, s; Γ is the exposure rate constant, $C \cdot m^2 \cdot kg^{-1} \cdot Bq^{-1} \cdot s^{-1}$, and the radionuclide of gamma rays is ^{137}Cs. L is the length of the core containing waste, m; R is the distance between the operator and the core, m; A is the activity of radionuclide in the core of 8 m long, Bq.

$$A = C_{rock} \times V_{rock} \times \rho_{waste} \tag{16}$$

where, C_{rock} is the activity concentration of the nuclide in the core, Bq/kg; V_{rock} is the volume of the core, m³; ρ_{waste} is the density of waste in the core, kg/m³.

(2) Internal exposure dose

Dose due to internal exposure of inhalation is calculated by the following formula:

$$D_{inh} = t \times \eta \times C_i \times DC_{inh} \tag{17}$$

where, η is the air respiration rate of personnel, m³/min; t is the contact time, min; DC_{inh} is the dose coefficient of nuclides for inhalation, Sv/Bq; C_i is the activity concentration of nuclides in the air, Bq/m³.

$$C_i = C_{rock} \times S \tag{18}$$

where, S is the dust content in the air (kg/m³).

3.3 Post-drilling Scenario Calculation

Conceptual Model

The post-drilling scenario refers to the drilling that occurred 300 years after the closure of the repository. The 8 m-long core brought out by the drilling scattered and contaminated the soil. Then the intruder will be engaged in farming on the contaminated soil, and will be exposure by various pathways. It is assumed that the core is evenly distributed in the soil of 2500 m² with a thickness of 0.15 m and a soil density of 2000 kg/m³. Inhalation internal irradiation through resuspension of contaminated soil, direct external irradiation through surface deposition of contaminated soil, and internal exposure through ingestion of crops and vegetables growing in contaminated soil were considered. In the post-drilling scenario, radionuclide transfer process and exposure pathways are shown in Fig. 4.

Mathematical Model

The total annual individual effective dose to an intruder caused by post-drilling scenario is calculated by the following formula:

$$D_{afterdrill} = D_{soil} + D_{inh,1} + D_{ing} \tag{19}$$

where, D_{soil} is the dose caused by surface deposition external exposure, Sv; $D_{inh,1}$ is the dose of internal exposure due to inhalation, Sv; D_{ing} is ingestion dose, Sv.

(1) External exposure dose

The annual individual effective dose due to surface deposition external exposure is calculated by the following formula:

$$D_{soil} = C_{i,soil} \times s \times DC_{ext} \times t \tag{20}$$
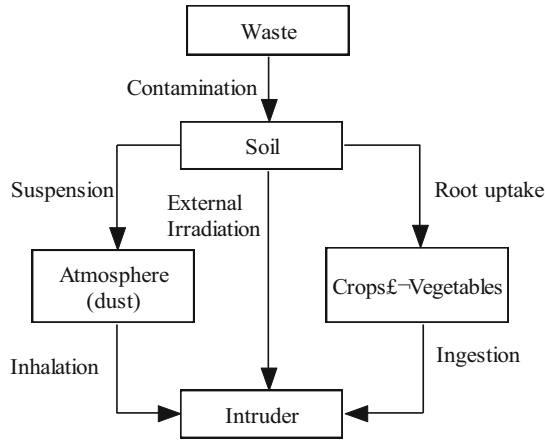
Fig. 4. Radionuclide transfer process and exposure pathway of post-drilling scenario

where, $C_{i,\ soil}$ is the surface concentration of nuclide i in the soil, Bq/m^2; $C_{i,soil} = A/S_{soil}$, A is the activity of radionuclide in the core of 8 m long, Bq; S_{soil} is the area of soil, m^2; s is the building shielding factor, s = 1; DC_{ext} is the dose coefficient for external irradiation from soil, (Sv/a)/(Bq/m^2); t is the time of exposure in a year, a.

(2)   Inhalation internal exposure dose

Inhalation internal exposure due to suspension of soil into the air. The resulting dose is calculated by the following formula:

$$D_{inh,1} = t \times \eta \times C_{i,air} \times DC_{inh} \tag{21}$$

where, η is the air respiration rate of personnel, m^3/a; t is the contact time, a; $C_{i,air}$ is the concentration of nuclide in air, Bq/m^3.

$$C_{i,air} = \frac{A}{V_{soil} \times \rho_{soil}} \times S \tag{22}$$

where, V_{soil} is the volume of soil, m^3; ρ_{soil} is soil density, kg/m^3; S is the dust content capacity in the air, kg/m^3.

(3)   Ingestion internal exposure dose

Individual dose due to consumption of crops grown on soil contaminated by scattered cores is expressed in the following formula:

$$D_{ing} = I_j \times f \times C_{i,SOIL} \times B_i \times DC_{ing} \tag{23}$$

where, I_j is the annual intake of crop type j, kg; f is the proportion of crops produced in contaminated areas in the annual crop intake, where 1 is taken; B_i is the concentration factor of crops, Bq·kg^{-1}(fresh weight)/Bq·kg^{-1} (dry soil); $C_{i,SOIL}$ is the activity concentration of radionuclide i in the soil, Bq/kg, calculated by the following formula:

$$C_{i,SOIL} = \frac{A}{V_{soil} \times \rho_{soil}} \tag{24}$$

3.4 Housing Scenario Calculation

Conceptual Model

It is assumed that the building and living above the disposal unit takes place 300 years after the closure of the repository, and there is 0.5 m concrete between the house and the waste due to the stripping of all 5 m of the covering layer by digging the foundation. The exposure pathway considered was γ external irradiation. In the housing scenario, the exposure pathway of radionuclide is shown in Fig. 5.
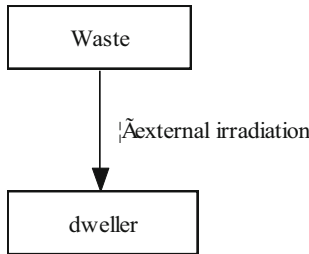
Fig. 5. Radionuclide exposure pathway of housing scenario

Mathematical Model

The waste form is regarded as an infinite flat body source with a certain thickness and uniform distribution of nuclides. After adding 0.5 m concrete shielding, the exposure rate can be calculated by the following formula:

$$X_B = B \exp(-\mu L) \frac{2\pi M \Gamma}{\mu} (1 - E_2(\mu d)) \tag{25}$$

where, X_B is the exposure rate with shielding, C·kg^{-1}·s^{-1}; M is the volume specific activity of a certain nuclide in the disposal unit 300 years after the closure of the repository, Bq/m^3; Γ is the exposure rate constant, C·m^2·kg^{-1}·Bq^{-1}·s^{-1}; μ is the attenuation coefficient of concrete to γ-ray of some energy, m^{-1}; d is the thickness of the body source, m; E_2 is a constant, looking up the table, it can be found that the value of E_2 is in the order of magnitude of 10^{-6}, which is far less than 1 and can be ignored. L is the shielding thickness, m; B is the exposure accumulation factor, $B = A\exp(-a_1\mu L) + (1 - A)\exp(-a_2\mu L)$,, A, a_1 and a_2 are constants.

The air absorbed dose rate calculated from the exposure rate is:

$$D_1 = 33.85X_B \tag{26}$$

where, D_1 is the absorbed dose rate of air, Gy/s. The radionuclide of gamma ray is ^{137}Cs. For ^{137}Cs, the ratio of effective dose rate to air absorbed dose rate is expressed by 1Sv/Gy. H is the effective dose rate, Sv/s, H = D1.

The individual dose to an intruder caused by housing scenario is calculated by the following formula:

$$D_{house} = H \times t_{juzhu} \tag{27}$$

where, t_{juzhu} is the residence time, s.

4 Determination of Nuclide Activity Concentration Upper Limit for Low Level Radioactive Waste

Based on the upper limit value of the activity concentration of each nuclide derived from the above scenarios, the minimum upper limit value was selected and the magnitude of the upper limit value of the activity concentration of each nuclide was determined by the rule for rounding of numbers. According to the rule for rounding of numbers in IAEA RS-G-1.7, that is, if $3 \times 10^x < \text{result} < 3 \times 10^{x+1}$, it is $1 \times 10^{x+1}$. The rounding result of the upper limit value is shown in Table 1.

Table 1. Activity concentration upper limits for low level solid radioactive waste

Nuclide	Half-life (a)	Activity concentration upper limit of drilling scenario (Bq/kg)	Activity concentration upper limit of post-drilling scenario (Bq/kg)	Activity concentration upper limit of housing scenario (Bq/kg)	Activity concentration upper limit of drilling water scenario (Yaotian disposal site) (Bq/kg)	Activity concentration upper limit of drilling water scenario (Feifengshan disposal site) (Bq/kg)	Activity concentration upper limit (Bq/kg)
^{3}H	12.3	7.66E+18	8.98E+17		9.92E+07	**3.78E+07**	**1E+08**
^{90}Sr	29.1	8.27E+11	2.30E+09		**4.62E+07**	4.93E+07	**1E+08**
^{137}Cs	30.0	2.47E+10	3.30E+09	**4.36E+08**	2.23E+15	2.04E+16	**1E+09**
63Ni	96	6.38E+11	**4.45E+10**		1.24E+12	3.03E+12	**1E+11**
^{241}Am	4.32E+02	**1.76E+06**	1.14E+07		9.90E+07	3.92E+06	**1E+06**
^{14}C	5.73E+03	1.86E+10	2.70E+07		**1.97E+06**	3.78E+06	**1E+06**
^{240}Pu	6.54E+03	8.96E+05	6.10E+06		4.63E+05	**3.35E+05**	**1E+05**
^{239}Pu	2.41E+04	8.75E+05	5.69E+06		9.20E+04	**5.34E+04**	**1E+05**
99Tc	2.13E+05	8.02E+09	2.59E+06		**5.93E+04**	7.25E+04	**1E+05**
^{237}Np	2.14E+06	2.08E+06	1.21E+07		9.01E+04	**1.74E+03**	**1E+03**

As can be seen from Table 1, the key scenario of ^{137}Cs is housing scenario, the key scenario of ^{63}Ni is post-drilling scenario, the key scenario of ^{241}Am is drilling scenario, and the key scenario of other nuclides is drilling water scenario.

For low level solid waste containing a variety of artificial radionuclides, the sum of the ratio of the activity concentration value of each artificial radionuclide to the upper limit value of their respective activity concentration should not be greater than 1, that is, it should satisfy Eq. (28):

$$\sum_{i=1}^{n} \frac{C_i}{C_{io}} \leq 1 \tag{28}$$

where, C_i is the activity concentration of nuclide i in low level solid waste, Bq/kg; C_{io} is the upper limit of activity concentration of nuclide i in low level solid waste, Bq/kg; n is the number of artificial radionuclides in low level solid waste.

References

1. Derivation of Activity Limits for the Disposal of Radioactive Waste in Near Surface Disposal Facilities. IAEA-TECDOC-1380. International Atomic Energy Agency, Vienna (2003)
2. National Standard of the People's Republic of China, GB9132-2018, Safe Requirements for Near Surface Disposal of Low and Medium Level Radioactive Solid Waste, Beijing (2018)
3. National Standard of the People's Republic of China, GB18871-2002, Basic Standards for Protection Against Ionizing Radiation and for the Safety of Radiation Sources, Beijing (2002)
4. China Guangdong Nuclear Power Group Co. Ltd, Yaotian Low and Medium level Radioactive Solid Waste Disposal Site Environmental Impact Assessment (Site Approval Application Stage), Guangdong (2010)
5. China Nuclear Qingyuan Environmental Technology Engineering Co. Ltd, Feifengshan Low and Medium level Radioactive Solid Waste Disposal Site Environmental Impact Assessment (Construction Application Stage), Beijing (2011)
6. Institute of Nuclear Science and Technology Information, Performance Evaluation of Low and Medium Level Radioactive Waste Disposal and Method for Derivation of Long-Life Nuclide Content Limit, Beijing (1995)
7. Safety Assessment Methodologies for Near Surface Disposal Facilities, Results of a Coordinated Research Project, vol. 2, Test Cases. International Atomic Energy Agency, Vienna (2004)
8. Pan, Z., et al.: Assessment of Radiation Environment Quality in China's Nuclear Industry in the Past 30 Years. Atomic Energy Press, Beijing (1990)

Evaluation of Uncertainty for Determination of Trace Uranium in Biology by Laser Fluorescence Method

Yajie Wang[✉], Lufeng Wang, Chuanjiang Dong, Li Li, Mengqi Tang, Weizhong Sun, and Yao Wu

Sichuan Engineering Laboratory for Nuclear Facilities Decommissioning and Radwaste Management, The Reactor Operation and Application Research Sub-Institute, Nuclear Power Institute of China, Chengdu, Sichuan, China
2277055135@qq.com

Abstract. Large amounts of uranium-containing radioactive waste are generated in reactor operation and in the research and manufacture of nuclear fuel elements. At present, there are various uranium enrichment and separation methods such as reduction precipitation method, ion exchange method, solvent extraction method, membrane filtration method, adsorption method, and microorganism method to treat the uranium-containing radioactive waste generated in the related processes of nuclear facilities. However, the airborne effluent or liquid effluent discharged after treatment may still contain radioactive uranium. It is well known that uranium is a radioactive heavy metal element, and its radioactive and chemical toxicity cannot be ignored. Uranium in the environment enters the human body through the food route, and its long half-life can make the human body suffer from continuous radioactive internal radiation damage. As an environmental medium, organisms are closely related to the entry of uranium into the human body through food. Therefore, it is of great significance to carry out accurate measurement of uranium content in environmental-grade biological samples around nuclear facilities, however, complete and accurate measurement results include measurement data and uncertainty. Laser fluorescence method is a method for rapid analysis of uranium content in environmental samples. It has the advantages of high sensitivity, simple sample pretreatment, and wide measurement range, which has been widely used in nuclear industry, environmental monitoring and scientific research. At present, there is a lack of relevant reports on the uncertainty of the measurement of total uranium content in environmental-grade biological samples by laser fluorescence method. It is of great significance to accurately measure the uranium content in biological samples by evaluating the uncertainty of this method. In this paper, the WGJ-III trace uranium analyzer was used to analyze the uncertainty source of total uranium in environmental-grade biological samples by laser fluorescence method. The uncertainty measurement model was established, the uncertainty components were quantified, and the expanded uncertainty of the measurement of total uranium content in environmental biological samples was calculated. The evaluation results showed that the expanded uncertainty of a 0.05 g environmental biological sample is 10.8% ($k = 2$) without dilution, and the dominant uncertainty component is derived from the measurement uncertainty of sample fluorescence counting.

1 Introduction

Large amounts of uranium-containing radioactive waste have been generated in reactor operation and in the research and manufacture of nuclear fuel elements. At present, there are various uranium enrichment and separation methods such as reduction precipitation method, ion exchange method, solvent extraction method, membrane filtration method, adsorption method, and microorganism method to treat the uranium-containing radioactive waste generated in the related processes of nuclear facilities. However, the airborne effluent or liquid effluent discharged from the treatment may contain radioactive uranium [1]. As a radioactive heavy metal element, uranium's radioactive toxicity and chemical toxicity cannot be ignored, uranium in the environment enters the human body through food, and its long half-life can make the human body suffer from continuous radioactive internal radiation damage [2]. As an environmental medium, organisms are closely related to the entry of uranium into the human body through food. Therefore, it is of great significance to accurately measure the total uranium content in environmental-grade biological samples around nuclear facilities, however, complete and accurate measurement results include measurement data and uncertainty.

The laser fluorescence method is famous for its rapid analysis of uranium content in environmental samples. It has the advantages of high sensitivity, simple sample pretreatment, and wide measurement range, which has been widely used in the nuclear industry, environmental monitoring and scientific research [3, 4]. As we all know, the complete measurement result of the sample should contain the measurement result data and measurement uncertainty, where the measurement uncertainty is used to indicate the reliability of the measurement result [5, 6]. After investigation, only the uncertainty evaluation method for the determination of uranium content in water, soil and uranium ore by laser fluorescence method has been reported, and there is a lack of relevant reports on the uncertainty of the measurement of total uranium content in environmental-grade biological samples. The evaluation of the uncertainty of the results obtained from the samples is of great significance for the accurate measurement of uranium content in organisms. In view of this, the laser fluorescence method has been used to measure trace uranium in organisms, and the uncertainty of the method has been evaluated in this paper.

2 Measurement Method and Measurement Model Analysis

The laser fluorescence method in the standard HJ840-2017 has been referenced to determine the total uranium content in biological samples in this paper. The determination principle is roughly as follows: first, the environmental biological samples are converted into water samples to be tested through pretreatment. Next, measure the fluorescence counts of the samples in the following order: the water sample to be tested, the water sample to be tested after adding the fluorescence enhancer, and the water sample to be

tested after adding the uranium standard solution. The fluorescence intensity is proportional to the uranium content, when the uranium content is within a certain range. The uranium content can be calculated by measuring the fluorescence intensity. The mathematical model for the determination of trace uranium content in biological samples by laser fluorescence method has been shown in Eq. (1):

$$A = \left(\frac{N_1 - N_0}{N_2 - N_1} - \frac{N_1' - N_0'}{N_2' - N_1'} \right) \times \frac{KVMC_1V_1}{V_0WY} \tag{1}$$

where A represent the uranium content in biological samples (μg/kg), N_0 represent the fluorescence intensity without adding uranium fluorescence enhancer, N_1 represent the fluorescence intensity with adding uranium fluorescence enhancer, N_2 represent the fluorescence intensity with adding uranium standard working fluid, N_0', N_1' and N_2' represent the corresponding instrument reading for reagent blank sample, C_1 represent the concentration of uranium standard solution for measuring N_2 (μg/kg), V_1 represent the volume of uranium standard solution for measuring N_2 (mL), V represent the constant volume of dissolved biological sample ash (mL), V_0 represent the volume of sample, M represent the ratio between ash content and fresh content (g/kg), K represent the dilution ratio of water sample, W represent the ash weight of biological sample, Y represent the overall recovery (%).

3   Evaluation of Uncertainty

The uncertainty of trace uranium content in organisms consists of the following nine components:

(1) Uncertainty of repeatability of sample fluorescence intensity measurement (u_{1rel});
(2) Uncertainty of concentration of uranium standard solution at 1 μg/mL (u_{2rel});
(3) Uncertainty of volume of uranium standard solution at 1 μg/mL (u_{3rel});
(4) Uncertainty of constant volume (u_{4rel});
(5) Uncertainty of sample volume (u_{5rel});
(6) Uncertainty of overall chemical recovery (u_{6rel});
(7) Uncertainty of sample quality (u_{7rel});
(8) Uncertainty of the ash/fresh ratio (u_{8rel});
(9) Uncertainty of diluted multiples (u_{9rel});

3.1   Uncertainty of Repeatability of Sample Fluorescence Intensity Measurement (u_{1rel})

The uncertainty of repeatability of sample fluorescence intensity measurement comes from 6 aspects which include uncertainty of repeatability of measurement without adding fluorescence enhancer u_{11rel}, uncertainty of measurement repeatability with adding fluorescence enhancer u_{12rel}, uncertainty of measurement repeatability with adding uranium standard solution u_{13rel}, uncertainty of repeatability of blank samples without adding

fluorescence enhancer u_{14rel}, Uncertainty of measurement repeatability of blank samples with adding fluorescence enhancer u_{15rel}, Uncertainty of measurement repeatability of blank samples with adding uranium standard solution u_{16rel}.

Six physical quantities N_0, N_1, N_2, N_0', N_1' and N_2' were measured by trace uranium analyzer, and A class evaluation method was adopted. After pretreatment of a 0.05 g biological sample and a blank sample, the fluorescence intensity of the six physical quantities mentioned above was measured repeatedly for 5 times respectively to calculate the mean value, and the standard deviation of the mean value was calculated by Bessel equation. The measured readings were shown in Table 1. The calculation equation for uncertainty is shown in Eq. (2). After calculation, the value of u_{11rel}, u_{12rel}, u_{13rel}, u_{14rel}, u_{15rel} and u_{16rel} are 2.41%, 1.27%, 1.39%, 2.77%, 2.20% and 1.52%, respectively.

$$u_{11rel} = \frac{1}{N}\sqrt{\frac{\sum_{i=1}^{n}(N_i - \overline{N})^2}{n - 1}} \tag{2}$$

Table 1. Sample measurement results of fluorescence counting

Number of repeated measurements	Fluorescence count value N_0	Fluorescence count display value $\overline{N}_0$	Standard deviation S_0
1	56	54	1.30
2	55		
3	54		
4	53		
5	53		
Number of repeated measurements	Fluorescence count value N_1	Fluorescence count display value $\overline{N}_1$	Standard deviation S_1
1	67	66	0.84
2	66		
3	66		
4	65		
5	65		
Number of repeated measurements	Fluorescence count value N_2	Fluorescence count display value $\overline{N}_2$	Standard deviation S_2
1	116	114	1.58
2	115		
3	114		
4	113		
5	112		

(*continued*)

Table 1. (*continued*)

Number of repeated measurements	Fluorescence count value N_0	Fluorescence count display value $\overline{N}_0$	Standard deviation S_0
Number of repeated measurements	Fluorescence count value $N_0{'}$	Fluorescence count display value $\overline{N_0'}$	Standard deviation $S_0{'}$
1	63	60	1.67
2	61		
3	60		
4	59		
5	59		
Number of repeated measurements	Fluorescence count value $N_1{'}$	Fluorescence count display value $\overline{N_1'}$	Standard deviation $S_1{'}$
1	61	59	1.30
2	60		
3	58		
4	58		
5	59		
Number of repeated measurements	Fluorescence count value $N_2{'}$	Fluorescence count display value $\overline{N_2'}$	Standard deviation $S_2{'}$
1	121	119	1.82
2	120		
3	121		
4	118		
5	117		

The uncertainty of repeatability of sample fluorescence intensity measurement u_{1rel} is shown as follows:

$$u_{1rel} = \sqrt{u_{11rel}^2 + u_{12rel}^2 + u_{13rel}^2 + u_{14rel}^2 + u_{15rel}^2 + u_{16rel}^2} = 4.92\% \qquad (3)$$

3.2 Uncertainty of Concentration of 1.0 µg/mL Uranium Standard Solution (u_{2rel})

The concentration of uranium standard solution added for the determination of fluorescence intensity N_2 was 1.0 µg/mL. The solution was prepared by moving 1 mL 100 µg/mL uranium standard solution into a 100 mL volumetric flask with constant

volume to the scale line through a 1 mL pipette. The concentration of diluted solution is shown in Eq. (4).

$$C_2 = \frac{C_1 V_2}{V_2} \tag{4}$$

where C_2 is the concentration of the diluted solution (μg/mL), V_2 is the volume of the diluted solution (mL), C_1 is the concentration of the solution before dilution (μg/mL), V_1 is the volume of the solution before dilution (mL).

As can be seen from Eq. (4), Uncertainty of 1.0 ug/mL uranium standard solution concentration u_{2rel} is composed of uncertainty of concentration of 100 μg/mL uranium standard solution u_{21rel}, uncertainty in the sample volume of 100 ug/mL uranium standard solution u_{22rel}, and uncertainty of diluted solution volume u_{23rel}.

3.2.1 Uncertainty of Concentration of 100 μg/mL Uranium Standard Solution $u21_{rel}$

The standard solution uncertainty was evaluated by class B method, and the extended uncertainty of standard solution was U = 0.2% ($k = 2$), u_{21rel} = U/k = 0.1%.

3.2.2 Uncertainty of 100 ug/mL Sample Volume of Uranium Standard Solution u_{22rel}

The uncertainty of 100 ug/mL sample volume of uranium standard solution u_{22rel} is composed of the uncertainty of pipette accuracy u_{221rel}, the uncertainty of temperature correction u_{222rel}, the uncertainty of solution removal repeatability u_{223rel}.

(1) Uncertainty of pipette accuracy u_{221rel}

As can be seen from the pipette surface mark, the accuracy of 1 mL pipette is 0.02 ml. Assuming rectangular distribution, take the inclusion factor $k = \sqrt{3}$ and calculate the uncertainty u_{221rel} of pipette accuracy according to the evaluation method of class B uncertainty as shown in Eq. (5).

$$u_{221rel} = \frac{U}{K} = \frac{0.02 \text{ mL}}{1 \text{ mL} \times \sqrt{3}} = 1.15\% \tag{5}$$

(2) Uncertainty of temperature correction u_{222rel}

The temperature of the laboratory varies at ±5 °C, and the liquid volume can change under the influence of the expansion coefficient. The volumetric expansion coefficient of water is 2.1×10^{-4} °C^{-1}. Assuming that the distribution of temperature change is rectangular, the calculation of the uncertainty of temperature calibration u_{222rel} is shown in Eq. (6) according to the evaluation method:

$$u_{222rel} = \frac{2.1 \times 10^{-4} {}^{\circ}C^{-1} \times 5 {}^{\circ}C}{\sqrt{3}} \times 100\% = 0.0606\% \tag{6}$$

(3) Uncertainty of solution removal repeatability u_{223rel}
    Sample removal was 1.00 mL, and 1.00 mL distilled water was absorbed with a 1 mL pipette, and weighed with a balance for 20 times. The deviations introduced by constant volume repeatability were determined experimentally, and the results were shown in Table 2.

Table 2. 1 mL pipette absorbed 1.00 mL distilled water quality change

Number	1	2	3	4	5
Quality/g	1.0153	1.0112	1.0146	1.0115	1.0122
Number	6	7	8	9	10
Quality/g	1.0150	1.0108	1.0120	1.0190	1.0173
Number	11	12	13	14	15
Quality/g	1.0131	1.0117	1.0096	1.0108	1.0144
Number	16	17	18	19	20
Quality/g	1.0127	1.0134	1.0216	1.0153	1.0117

According to the evaluation method of class A uncertainty, the uncertainty of constant volume repeatability u_{233rel} is shown in Eq. (7).

$$u_{223rel} = \frac{1}{\overline{m}}\sqrt{\frac{\sum_{i=1}^{n}(m_i - \overline{m})^2}{n-1}} = 0.30\% \tag{7}$$

Therefore, the synthesis expression of uncertainty of 100 ug/mL sampling volume of uranium standard solution u_{22rel} is shown in Eq. (8).

$$u_{22rel} = \sqrt{u_{221rel}^2 + u_{222rel}^2 + u_{223rel}^2} = 1.19\% \tag{8}$$

3.2.3 Uncertainty of Constant Volume of Diluted Solution u_{23rel}

The uncertainty of constant volume of diluted solution u_{23rel} consists of the uncertainty of volumetric flask accuracy u_{231rel}, the uncertainty of temperature correction u_{232rel} and the uncertainty of constant volume repeatability u_{233rel}.

(1) Uncertainty of volumetric flask accuracy u_{231rel}
    A 100.00 mL volumetric flask with a precision of 0.10 mL was used to volume the solution to 100.00 mL. Assuming from triangular distribution, the inclusion factor $k = \sqrt{6}$ was taken. According to the evaluation method of class B uncertainty, the volumetric flask accuracy uncertainty $u_{231rel}l$ was 0.04%.
(2) Uncertainty of temperature correction u_{232rel}
    The laboratory temperature varies at ± 5 °C, and the calculation method of uncertainty of temperature correction u_{232rel} is the same as that of temperature correction uncertainty u_{222rel} in Sect. 3.2.2 is consistent, and u_{232rel} is 0.0606%.

(3) Uncertainty of constant volume repeatability u_{233rel}

The 100.00 mL volumetric bottle was fixed volume with distilled water, and the net weight of distilled water was weighed by a balance. The number n was 20 times. The deviation introduced by the constant volume repeatability was determined in the experiment, and detailed data results were shown in Table 3. According to the evaluation method of class A uncertainty, the uncertainty of constant volume repeatability u_{232rel} was 0.15%.

Table 3. Quality change of distilled water in 100 mL volumetric bottle with constant volume

Number	1	2	3	4	5
Quality/g	99.65	99.71	99.79	100.18	100.12
Number	6	7	8	9	10
Quality/g	99.80	100.10	99.83	99.94	99.87
Number	11	12	13	14	15
Quality/g	100.13	99.79	99.91	99.83	99.94
Number	16	17	18	19	20
Quality/g	99.86	99.84	100.13	99.87	99.85

Therefore, the synthesis expression of the uncertainty of constant volume of diluted solution u_{23rel} is shown in Eq. (9).

$$u_{23rel} = \sqrt{u_{231rel}^2 + u_{232rel}^2 + u_{233rel}^2} = 0.167\% \tag{9}$$

Overall, the synthesis expression of the Uncertainty of concentration of 1.0 µg/mL uranium standard solution u_{2rel} is shown in Eq. (10).

$$u_{2rel} = \sqrt{u_{21rel}^2 + u_{22rel}^2 + u_{23rel}^2} = 1.21\% \tag{10}$$

3.3 Uncertainty of 1.0 µg/mL Uranium Standard Solution Volume ($u3_{rel}$)

The 1.0 pg/mL uranium standard solution was moved by a micro sampler, and u_{3rel} was composed of the uncertainty of measuring accuracy of micro sampler u_{31rel}, and the uncertainty of temperature correction u_{32rel}.

3.3.1 Uncertainty of Measurement Accuracy of Micro Sampler u_{31rel}

The accuracy of 10 µL micro sampler is 0.1 µL, assuming the rectangular distribution is followed, take the inclusion factor $k = \sqrt{3}$ in Eq. (11):

$$u_{31rel} = \frac{0.1\,\mu L}{5\,\mu L \times \sqrt{3}} = 1.15\% \tag{11}$$

3.3.2 Uncertainty of Temperature Correction u_{32rel}

The temperature of the laboratory varies at $\pm 5\,°C$, and the calculation method of the temperature correction uncertainty u_{32rel} is consistent with that of the temperature correction uncertainty u_{222rel} in Sect. 3.2.2, and the calculated u_{32rel} is 0.0606%.

Overall, the synthesis expression of the Uncertainty of 1.0 μg/mL uranium standard solution volume u3rel is shown in Eq. (12).

$$u_{3rel} = \sqrt{u_{31rel}^2 + u_{32rel}^2} = 1.15\% \tag{12}$$

3.4 Uncertainty of Sample Constant Volume (u_{4rel})

The uncertainty of sample constant volume u_{4rel} was composed of uncertainty of measurement accuracy of volumetric flask u_{41rel}, uncertainty of temperature correction u_{42rel} and uncertainty of constant volume repeatability u_{43rel}.

3.4.1 Uncertainty of Measurement Accuracy of Volumetric Flask u_{41rel}

A 25.00 mL volumetric bottle with a precision of 0.03 mL was used to keep the volume from 25.00 mL to 25.00 mL. Assuming from triangular distribution, the inclusion factor $k = \sqrt{6}$ was taken. According to the evaluation method of class B uncertainty, the measurement accuracy uncertainty of the volumetric bottle u_{41rel} was calculated as shown in Eq. (13):

$$u_{41rel} = \frac{0.03\,\text{mL}}{25\,\text{mL} \times \sqrt{3}} = 0.05\% \tag{13}$$

3.4.2 Uncertainty of Temperature Correction u_{42rel}

The temperature in the laboratory was changing at $\pm 5\,°C$, and the calculation method of the uncertainty of temperature correction u_{42rel} was consistent with the uncertainty of temperature correction u_{222rel} in Sect. 3.2.2. The u_{42rel} calculated was 0.0606%.

3.4.3 Uncertainty of Constant Volume Repeatability u_{43rel}

The 25.00 mL volumetric bottle was fixed volume with distilled water, and the net weight of distilled water was weighed by a balance. The number n was 20 times. The deviation introduced by constant volume repeatability was determined in the experiment, and detailed data results were shown in Table 4. According to the evaluation method of class A uncertainty, the uncertainty of constant volume repeatability u_{43rel} was 0.32%.

Overall, the synthesis expression of the uncertainty of sample constant volume u_{4rel} is shown in Eq. (14).

$$u_{4rel} = \sqrt{u_{41rel}^2 + u_{42rel}^2 + u_{43rel}^2} = 0.34\% \tag{14}$$

Table 4. Quality change of distilled water from constant volume to 25.00 mL volumetric flask

Number	1	2	3	4	5
Quality/g	24.95	24.92	25.07	24.89	24.84
Number	6	7	8	9	10
Quality/g	25.03	24.84	25.05	24.99	24.84
Number	11	12	13	14	15
Quality/g	25.06	25.03	24.97	24.98	25.05
Number	16	17	18	19	20
Quality/g	24.88	25.08	24.95	24.98	25.03

3.5   Uncertainty of Sample Volume (u_{5rel})

The uncertainty of sample volume u_{5rel} is composed the uncertainty of pipette measurement accuracy u_{51rel}, the uncertainty of temperature correction u_{52rel} and the uncertainty of transport repeatability u_{53rel}.

3.5.1   Uncertainty of Pipette Measurement Accuracy u_{51rel}

The uncertainty of pipette measurement accuracy u_{51rel} can be seen from the pipette surface mark that the accuracy of 5 mL pipette is 0.03 mL. Assuming rectangular distribution, take the inclusion factor $k = \sqrt{3}$ and calculate the uncertainty u_{51rel} of 5 mL according to the evaluation method of class B uncertainty as shown in Eq. (15):

$$u_{51rel} = \frac{0.03 \text{ mL}}{5 \text{ mL} \times \sqrt{3}} = 0.35\% \tag{15}$$

3.5.2   Uncertainty of Temperature Correction u_{52rel}

The temperature in the laboratory varies at ± 5 °C, and the calculation method of the uncertainty of temperature correction u_{52rel} is consistent with the uncertainty of temperature correction in Sect. 3.2.2, and the calculated u_{52rel} is 0.0606%.

3.5.3   Uncertainty of Transport Repeatability u_{53rel}

Sample removal was 5.00 mL, 5.00 mL water sample was absorbed with a 5 mL pipette and weighed with a balance. The number of times n = 20 was used to determine the deviation introduced by the removal repeatability. The results were shown in Table 5.

According to class A uncertainty evaluation method, u_{53rel} can be calculated according to Eq. (16):

$$u_{53rel} = \frac{1}{\overline{m}} \sqrt{\frac{\sum_{i=1}^{n} (m_i - \overline{m})^2}{n - 1}} = 0.581\% \tag{16}$$

Table 5. 5 mL pipette absorbed 5.00mL water sample quality change

Number	1	2	3	4	5
Quality/g	5.0765	5.0213	5.0036	5.0600	5.0788
Number	6	7	8	9	10
Quality/g	5.0020	5.0550	5.0624	4.9996	4.9849
Number	11	12	13	14	15
Quality/g	5.0723	5.0809	5.0139	5.0449	5.0452
Number	16	17	18	19	20
Quality/g	5.0462	5.0444	5.0525	5.0145	5.0552

Overall, the synthesis expression of the uncertainty of sample volume u_{5rel} is shown in Eq. (17).

$$u_{5rel} = \sqrt{u_{51rel}^2 + u_{52rel}^2 + u_{53rel}^2} = 0.681\% \tag{17}$$

3.6 Uncertainty of Weighing Samples is (u_{6rel})

The uncertainty of weighing sample size u_{6rel} is composed of the uncertainty of weighing accuracy u_{61rel} and uncertainty of quality weighing repeatability of the balance u_{62rel}.

3.6.1 Uncertainty of Weighing Accuracy u_{61rel}

The weighing accuracy of the electronic balance is 0.1 mg. Assuming rectangular distribution, take the factor $k = \sqrt{3}$ and weigh the balance with 0.05 g sample's weighing accuracy uncertainty u_{61rel} according to the class B uncertainty evaluation method, and as shown in Eq. (18):

$$u_{61rel} = \frac{0.1\,\text{mg}}{0.05\,\text{g} \times \sqrt{3}} = 0.11\% \tag{18}$$

3.6.2 Uncertainty of Quality Weighing Repeatability of the Balance u_{62rel}

According to the method of class A uncertainty, 0.05 g biological samples were found in measuring bottles and weighed every 10 min, n = 10. Results of weighing biological samples are shown in Table 6. After calculation, u_{62rel} equal to 0.09%.

Therefore, the synthesis expression of uncertainty of weighing accuracy u_{6rel} is shown in Eq. (19).

$$u_{6rel} = \sqrt{u_{61rel}^2 + u_{62rel}^2} = 0.11\% \tag{19}$$

Table 6. Reproducibility of mass weighing of biological samples

Number	1	2	3	4	5
Quality/g	0.0499	0.0501	0.0492	0.0507	0.0503
Number	6	7	8	9	10
Quality/g	0.0497	0.0495	0.0502	0.0504	0.0503

3.7 Uncertainty of Total Chemical Recovery(u_{7rel})

Two 0.05 g of the same biological ash samples were weighed, one was added with 0.5 µg/mL uranium standard solution, the other was not added with uranium standard solution, and the control experiment was conducted. Uranium concentration was measured after pretreatment of the two samples according to HJ840-2017, and the chemical recovery Y was calculated according to Eq. (20).

$$Y = \frac{C_2 - C_1}{C_0} \times 100\% \tag{20}$$

where C_2 represent Determination of uranium content in a standard sample (ng), C_1 represent Determination of uranium content in blank samples (ng) and C_0 represent Quantity of uranium standard sample (ng).

10 groups of control experiments were repeated (n = 10), and the total chemical recovery Y of the same biological ash sample was obtained for 10 times. The detailed data were shown in Table 7, so the total chemical recovery uncertainty u_{7rel} was calculated to be 0.58%.

Table 7. Overall chemical recovery of biological samples

Number	1	2	3	4	5
Overall chemical recovery (%)	90.4	90.4	90.0	89.0	89.8
Number	6	7	8	9	10
Overall chemical recovery (%)	90.0	89.4	90.4	89.2	89.4

3.8 Uncertainty of the Ash/fresh Ratio (u_{8rel})

The uncertainty of the ash/fresh ratio is mainly caused by mass weighing, which is composed of the uncertainty of fresh weighing u_{81rel} and ash weighing u_{82rel}. The uncertainty of fresh weighing u_{81rel} consists of the uncertainty of fresh weighing accuracy u_{811rel} and the uncertainty of fresh weighing repeatability u_{812rel}. The uncertainty of ash weighing u_{82rel}, consists of the uncertainty of ash sample weighing accuracy u_{821rel} and the uncertainty of ash sample weighing repeatability u_{822rel}.

3.8.1   Uncertainty of Fresh Weighing u_{81rel}

(1)   Uncertainty of fresh weighing accuracy u_{811rel}

According to the test certificate of platform scale, the accuracy of platform scale can be obtained as $s = 50$ g, according to rectangular distribution, including factor $k = \sqrt{3}$. The mass of typical fresh sample measured is 4.10 kg, and the mass of empty bag is 0.10 kg. The calculation of the uncertainty of weighing accuracy of fresh sample, u_{811rel}, is shown in Eq. (21):

$$u_{811rel} = \frac{\sqrt{2\left(\frac{s}{k}\right)^2}}{m - m_0} = 1.02\% \tag{21}$$

(2)   Uncertainty of fresh weighing repeatability u_{812rel}

The evaluation method of class A method was adopted, and fresh samples were weighed for 10 times. The data were shown in Table 8. According to Bessel formula, the weighing repeatability of fresh samples u_{812rel} was 0.41%.

Table 8. Results of Fresh sample weighing

Number	1	2	3	4	5
Fresh weighing/kg	4.15	4.12	4.10	4.12	4.10
Number	6	7	8	9	10
Fresh weighing/kg	4.10	4.11	4.14	4.12	4.13

Therefore, the synthesis expression of the uncertainty of fresh weighing U_{81rel} is shown in Eq. (22).

$$u_{81rel} = \sqrt{u_{811rel}^2 + u_{812rel}^2} = 1.10\% \tag{22}$$

3.8.2   Uncertainty of Ash Weighing u_{82rel}

(1)   Uncertainty of ash sample weighing accuracy u_{821rel}

According to the verification certificate, the accuracy of the balance is $s = 0.4$ mg ($k = \sqrt{3}$), the mass of the typical gray sample measured is $m = 55.7833$ g, and the mass of the empty plate is $m_0 = 0.3920$ g. The calculation of the uncertainty of the weighing accuracy of the gray sample u_{821rel}, is shown in Eq. (23):

$$u_{812rel} = \frac{\sqrt{2\left(\frac{s}{k}\right)^2}}{m - m_0} = 0.00059\% \tag{23}$$

(2)   Uncertainty of ash sample weighing repeatability u_{822rel}

The evaluation method of class A method was used, and the gray samples were weighed for 10 times. The data were shown in Table 9. The weighing repeatability uncertainty u_{822rel} was 0.001% calculated by Bessel equation.

Table 9. Results of Ash sample weighing

Number	1	2	3	4	5
Ash weighing/g	55.7833	55.7840	55.7839	55.7836	55.7842
Number	6	7	8	9	10
Ash weighing/g	55.7829	55.7827	55.7831	55.7825	55.7831

Therefore, the synthesis expression of uncertainty of ash weighing u_{82rel} is shown in Eq. (24).

$$u_{82rel} = \sqrt{u_{821rel}^2 + u_{822rel}^2} = 0.001\% \tag{24}$$

Overall, the synthesis expression of uncertainty of the ash/fresh ratio (u_{8rel}) is shown in Eq. (25).

$$u_{8rel} = \sqrt{u_{81rel}^2 + u_{82rel}^2} = 1.10\% \tag{25}$$

3.9   Uncertainty of Dilution Ratio (u_{9rel})

When the concentration of the sample is too high or the sample precipitates after adding the fluorescence enhancer, it is often necessary to dilute the solution under test.

Sample dilution usually uses pipette to remove a quantitative amount of liquid into a volumetric flask and then determine volume. The uncertainty of dilution ratio is composed of Uncertainty of sample volume u_{91rel} and the uncertainty of dilute solution volume u_{92rel}. The uncertainty of sampling volume u_{91rel} was composed of the uncertainty of pipette measurement accuracy u_{911rel}, the uncertainty of pipette temperature correction u_{912rel}, and the uncertainty of removal repeatability u_{913rel}. The uncertainty of diluted solution volume u_{92rel} was composed of the uncertainty of volumetric flask standard measurement accuracy u_{921rel}, Uncertainty of volumetric flask temperature correction u_{922rel} and Uncertainty of constant volume repeatability u_{923rel}. Taking dilution by a factor of 10.

3.9.1   Uncertainty of Sample Volume u_{91rel}

(1) Uncertainty of pipette measurement accuracy u_{911rel}.

5.00 mL pipette with accuracy of 0.03 mL was used to remove 5.00 mL original solution. Assuming rectangular distribution, the inclusion factor $k = \sqrt{3}$ was taken. According to class B uncertainty evaluation method, the pipette measurement accuracy uncertainty u_{911rel} was calculated as shown in Eq. (26).

$$u_{911rel} = \frac{0.03 \text{ mL}}{5 \text{ mL} \times \sqrt{3}} = 0.35\% \tag{26}$$

(2) Uncertainty of pipette temperature correction u_{912rel}

The temperature of the laboratory varies at $\pm 5\,°C$, and the calculation method of the temperature correction uncertainty is consistent with the calculation method of the temperature correction uncertainty u_{222rel} in Sect. 3.2.2. The calculated u_{912rel} is 0.0606%.

(3) Uncertainty of removal repeatability u_{913rel}

Sample removal was 5.00 mL, 5.00 mL water sample was absorbed with a 5 mL pipette and weighed with a balance for 20 times. The deviation introduced by the repeatability of removal was determined experimentally, and the results were shown in Table 5. According to the evaluation method of class A uncertainty, the calculated uncertainty u_{913rel} of removal repeatability is 0.581%.

Therefore, the synthesis expression of Uncertainty of sample volume u_{91rel} is shown in Eq. (27).

$$u_{91rel} = \sqrt{u_{911rel}^2 + u_{912rel}^2 + u_{913rel}^2} = 0.681\% \qquad (27)$$

3.9.2 Uncertainty of Diluted Solution Volume u_{92rel}

(1) Uncertainty of volumetric flask standard measurement accuracy u_{921rel}

A 50 mL volumetric bottle with a precision of 0.05 mL is used from constant volume to scale line, assuming trigonometric distribution is followed, and the inclusion factor $k = \sqrt{6}$ is taken. According to the evaluation method of class B uncertainty, the measurement accuracy uncertainty of the volumetric bottle u_{921rel} is calculated as shown in Eq. (28).

$$u_{921rel} = \frac{0.05\,\text{mL}}{50\,\text{mL} \times \sqrt{6}} = 0.04\% \qquad (28)$$

(2) Uncertainty of volumetric flask temperature correction u_{922rel}

The temperature of the laboratory varies at $\pm 5\,°C$, and the calculation method of the temperature correction uncertainty u_{922rel} is consistent with that of the temperature correction uncertainty u_{222rel} in Sect. 3.2.2, and the calculated u_{922rel} is 0.0606%.

(3) Uncertainty of constant volume repeatability u_{923rel}

Distilled water was used for constant volume of 50.00 mL volumetric bottle, and the net weight of distilled water was weighed by a balance, n = 20 times. The deviation introduced by constant volume repeatability was determined experimentally, and the results were shown in Table 10. According to the evaluation method of class A uncertainty, the uncertainty of constant volume reproducibility u_{923rel} was 0.21%.

Therefore, the synthesis expression of the uncertainty of diluted solution volume u_{92rel} is shown in Eq. (29).

$$u_{92rel} = \sqrt{u_{921rel}^2 + u_{922rel}^2 + u_{923rel}^2} = 0.22\% \qquad (29)$$

Table 10. 50 mL pipette absorbed 50.00 mL water sample quality change

Number	1	2	3	4	5
Quality/g	49.85	49.97	50.10	49.82	49.87
Number	6	7	8	9	10
Quality/g	50.06	50.02	49.84	49.99	49.87
Number	11	12	13	14	15
Quality/g	50.11	49.78	49.92	49.82	50.06
Number	16	17	18	19	20
Quality/g	49.88	50.09	49.86	49.98	49.89

Overall, the synthesis expression of the uncertainty of dilution ratio u_{9rel} is shown in Eq. (30).

$$u_{9rel} = \sqrt{u_{91rel}^2 + u_{92rel}^2} = 0.72\% \tag{30}$$

3.10 Total Measurement Uncertainty

Uncertainty variables u_{1rel}, u_{2rel}, u_{3rel}, u_{4rel}, u_{5rel}, u_{6rel}, u_{7rel}, u_{8rel} and u_{9rel} are independent and unrelated to each other. The uncertainty information of each is shown in Table 11. When dilution multiple is not considered, the synthesized uncertainty u_{Ar} is shown in Eq. (31):

$$
\begin{aligned}
u_{Ar} &= \sqrt{u_{1rel}^2 + u_{2rel}^2 + u_{3rel}^2 + u_{4rel}^2 + u_{5rel}^2 + u_{6rel}^2 + u_{7rel}^2 + u_{8rel}^2} \\
&= 5.39\%
\end{aligned}
\tag{31}
$$

When $k = 2$, the extended uncertainty $U_r(A) = 2 \times u_{Ar} = 10.8\%$.

When there is dilution process, take dilution of 10 times as an example, and the resultant uncertainty u_{Ar} is shown in Eq. (32).

$$
\begin{aligned}
u_{Ar} &= \sqrt{u_{1rel}^2 + u_{2rel}^2 + u_{3rel}^2 + u_{4rel}^2 + u_{5rel}^2 + u_{6rel}^2 + u_{7rel}^2 + u_{8rel}^2 + +u_{9rel}^2} \\
&= 5.54\%
\end{aligned}
\tag{32}
$$

When $k = 2$, the extended uncertainty $U_r(A) = 2 \times u_{Ar} = 10.9\%$.

Table 11. Uncertainty information table of trace uranium in organisms

Uncertainty component	Sources of uncertainty		Uncertainty	Order of sources
u_{1rel}	u_{11rel}	2.40%	4.92%	1
	u_{12rel}	1.26%		
	u_{13rel}	1.39%		
	u_{14rel}	2.77%		
	u_{15rel}	2.20%		
	u_{16rel}	1.52%		
u_{2rel}	u_{21rel}	0.10%	1.21%	2
	u_{22rel}	1.19%		
	u_{23rel}	0.167%		
u_{3rel}	u_{31rel}	1.15%	1.15%	3
	u_{32rel}	0.0606%		
u_{4rel}	u_{41rel}	0.04%	0.34%	8
	u_{42rel}	0.0606%		
	u_{43rel}	0.21%		
u_{5rel}	u_{51rel}	0.35%	0.68%	6
	u_{52rel}	0.0606%		
	u_{53rel}	0.581%		
u_{6rel}	u_{61rel}	0.11%	0.11%	9
	u_{62rel}	0.09%		
u_{7rel}	u_{7rel}	0.58%	0.58%	7
u_{8rel}	u_{81rel}	0.68%	0.72%	5
	u_{82rel}	0.22%		
u_{9rel}	u_{91rel}	1.10%	1.10%	4
	u_{92rel}	0.0001%		

4   Conclusions

Uranium content in biological samples was determined by laser fluorescence method, the sources of uncertainty of the method were analyzed, and the uncertainty components were calculated. The results showed that the uncertainty of the measurement of the total uranium content of a 0.05 g environmental biological sample is 10.8% ($k = 2$) under the condition of no dilution, and the dominant factor is the measurement of the sample fluorescence count.

References

1. Yi, Z.J., Yao, J., Chen, H.L., et al.: Uranium biosorption from aqueoussolution onto Eichhornia crassipes. J. Environ. Radioact. **154**, 43–51 (2016)
2. Jiang, C.X., Kong, Q.M., Feng, Z.G.: Heavy metal poluution in a Uranium mining ang metallurgy area in South China. China Environ. Sci. **40**, 338–349 (2020)
3. Muqrin, A.A., Sharkawy, A.E., Abdellah, W.M.: Uranium content in groundwater by laser fluorimetry; method validation and dose assessment. J. Radiol. Prot. **38**, 1140–1146 (2018)
4. Esphahani, A.G., Veselsky, J.C., Zepeda, E., et al.: Determination of Uranium in biological materials by laser fluorimetry. Radiochim. Acta **50**, 155–158 (2013)
5. Claudia, L., Costanza, M., Marco, F., et al.: ValiValidation and measurement uncertainty evaluation of a GC/MS method for the quantification of nine phthalates in tattoo and PMU inks. Accred. Qual. Assur. **26**, 249–260 (2021)
6. Mathew, C.E., Rai, V.K., Ottenfeld, C., et al.: Effect of weighing uncertainty on assay values by isotope dilution mass spectrometry. J. Radioanalytical Nucl. Chem. **328**, 1–9 (2021)

Research on Thermal-Hydraulic Model and Characteristics of Lead Cooled Traveling Wave Reactor

Yaoxiang Zhang[✉], Xue Zhang, Hongxing Yu, and Sijia Du

Science and Technology on Reactor System Design Technology Laboratory, Nuclear Power Institute of China, Chengdu 610213, China
`zhangyaoxiang2021@163.com`

Abstract. Traveling wave reactor (TWR) is an advanced nuclear power system, which can keep the total amount of fissionable nuclides constant during its lifetime through the transformation of fissionable nuclides in the reactor, so as to maintain the stability of the effective proliferation factor of the reactor core. As a coolant, lead has low neutron moderation ability and capture cross section. At the same time, it also has excellent thermal characteristics. Lead cooled traveling wave reactor is a reactor with high inherent safety and good application prospects. The research on reactor core mainly focuses on the physical calculation of the reactor, and the analysis of its thermal hydraulic model and characteristics is relatively scarce, which limits the design and safety analysis of the advanced reactor. Therefore, it is necessary to investigate the thermal hydraulic model of lead cooled traveling wave reactor. In this paper, a thermal hydraulic model suitable for the core of lead cooled traveling wave reactor is proposed. Considering the axial particularity of heat release from the core of traveling wave reactor, the model considers the axial thermal conductivity of fuel rods ignored by other thermal hydraulic models. Due to the strong thermal conductivity of core coolant, the thermal model also considers the heat transfer of fuel assemblies and the flow distribution of core flow. The research shows that the thermal hydraulic model is suitable for the analysis of thermal hydraulic characteristics of lead cooled traveling wave reactor, the thermal hydraulic characteristics are studied by using the thermal hydraulic model.

Keywords: Traveling wave reactor · Thermal hydraulic · Axial thermal conductivity · Flow distribution · Heat transfer

1 Introduction

With the increasingly energy shortage and environmental problems, and the large-scale development of nuclear power is facing challenges such as safety, economy, nuclear waste treatment and nuclear proliferation prevention, the concept of traveling wave reactor [1] has been put forward internationally. Traveling wave reactor is a self-sustaining Breed-and-Burn (B&B) reactor. Its basic concept comes from proliferation combustion

reactor. Its theoretical basis is that the reactor core starts from highly enriched fuel, the superfluous fast neutrons produced by the fission reaction convert the surrounding U-238 into Pu-239 (or Th-232 into U-233). When Pu-239 (or U-233) reaches a certain concentration, a new fission reaction is formed, that is, and the fission reaction generates superfluous fast neutrons again to realize the proliferation of nuclear fuel. In the process of proliferation and burning, the traveling wave is continuously moved along the axis throughout its life.

The coolant liquid metal lead used in lead cooled fast reactor has strong chemical inertness. Its good thermodynamic properties provide a guarantee for the full heat removal of the reactor core, which is conducive to the design of the reactor core with higher power density, and conforms to the characteristics of higher power density in the combustion zone of traveling wave reactor. At the same time, due to the small moderation and absorption of neutrons by lead, the high neutron economy in the core of lead cooled fast reactor is conducive to the long-life operation of traveling wave reactor.

In 2006, Sekimoto [2] carried out the research on the core design and safety characteristics of lead-bismuth cooled traveling wave reactor. The research shows that during the whole life of the traveling wave reactor, the neutron fluence rate or power in the core can maintain a stable shape to propagate very slowly, because of this characteristic of traveling wave reactor, Sekimoto calls axial traveling wave reactor as CANDLE. (**C**onstant **A**xial shape of **N**eutral flux nuclide, number identities and power shape **D**uring **L**ife of **E**nergy producing reactor).

In order to better understand and master the thermal phenomena of lead cooled traveling wave reactor, it is necessary to develop a more accurate thermal hydraulic calculation model. Taking the lead cooled traveling wave reactor core as the object, according to the investigation and investigation of the thermal hydraulic model of the lead based fast reactor, this paper develops a program suitable for the thermal hydraulic calculation of the lead cooled traveling wave reactor core, applies the developed thermal program to carry out the thermal hydraulic analysis of the lead cooled traveling wave reactor, and studies and analyzes the safety and temperature field distribution characteristics of the lead cooled traveling wave reactor.

2 Thermal-Hydraulic Model

2.1 Model of Coolant

Due to the closed fuel assembly used in lead cooled traveling wave reactor, the exchange of coolant momentum and mass between the assemblies is not considered.

In this paper, based on the finite volume method, the mass, momentum and energy conservation equations of coolant are established, which are solved by axial propulsion in space and implicit scheme in time.

Mass conservation equation:

$$\frac{\partial m_t}{\partial t} = \sum_{i=1}^{N} \frac{\partial m_i}{\partial t} \tag{1}$$

In the formula (1), m_t refers to the total mass flow of inlet coolant, m_i refers to the mass flow of coolant in the i channel, and N refers to the number of core channels.

Momentum conservation equation:

$$\frac{1}{A_i}\frac{\partial m_i}{\partial t} + \frac{\partial}{\partial z}\left(\frac{m_i^2}{\rho A_i^2}\right) = -\frac{\partial p}{\partial z} - \rho g$$
$$-\frac{fm_i^2}{2d_e \rho A_i^2} \tag{2}$$

In the formula (2), A_i is the area of the i channel, ρ is the coolant density, p is the coolant pressure, f is the friction coefficient, and d_e is the equivalent diameter of the channel.

Energy conservation equation:

$$\rho\frac{\partial h}{\partial t} + \frac{\partial}{\partial z}\left(\frac{w_i h}{A_i}\right) = q(t) \tag{3}$$

In the formula (3), $q(t)$ is the heat absorbed by the coolant in the control body. The first item on the left represents the increment of heat in the control body over time, the second item represents the heat of coolant flowing in and out of the control body, and the right item represents the heat absorbed by the coolant.

The core calculation program HANDF [6] and the thermal hydraulic program developed in this paper are used for code-to-code verification, and the coolant temperature and fuel temperature of each component are compared. The temperature calculated by the program in this paper is in good agreement with the calculated value of HANDF, and the maximum relative deviation is less than 0.5%, which proves that the model of the program is reliable and stable, and can be used for the thermal hydraulic analysis and calculation of the reactor core.

2.2 Model of Fuel Rod

For the heat conduction calculation of fuel rod, the circumferential heat conduction is ignored, and only the radial and axial heat conduction of fuel are considered. For the air gap and cladding, the thermal resistance model is used. The governing equation of the two-dimensional heat conduction model is:

$$\rho c_p \frac{\partial T}{\partial t} = \frac{1}{r}\frac{\partial}{\partial r}\left(\lambda \cdot r \cdot \frac{\partial T}{\partial r}\right) +$$
$$\frac{\partial}{\partial z}\left(\lambda \cdot \frac{\partial T}{\partial z}\right) + S \tag{4}$$

In the formula (4), ρ is the density of the fuel rod, c_p is the heat capacity of the fuel rod, T is the temperature of the fuel rod, λ is the thermal conductivity of the fuel rod, and S is the volumetric heat release rate.

2.3   Model of Flow Distribution

In the fuel assembly pressure drop calculation, the total pressure drop of the channel is composed of gravity pressure drop, friction pressure drops, acceleration pressure drop and local pressure drop. Set the boundary condition that the pressure of each channel at the inlet and outlet is the same. Control equation of flow dynamic distribution:

$$
\frac{L}{A_i}\frac{\partial m_i}{\partial t} = (P_{in} - P_{out}) - \int_0^L \frac{\partial}{\partial z}\frac{m_i^2}{\rho A_i^2}dz -
$$
$$
\int_0^L \frac{fm_i^2}{2d_e \rho A_i^2}dz - \int_0^L \rho g dz
\tag{5}
$$

In the formula (5), L it is the length of parallel channel, and the first term on the left represents the inertia pressure drop term, which is the additional pressure drop caused by the transient change of flow. The formula (5) can be sorted as:

$$
\frac{L}{A_i}\frac{\partial m_i}{\partial t} = (P_{in} - P_{out}) -
$$
$$
\Delta P_{a,i} - \Delta P_{f,i} - \Delta P_{el,i}
\tag{6}
$$

In the formula (6), $\Delta P_{a,i}$ is the acceleration pressure drop in the i channel, $\Delta P_{f,i}$ is the friction pressure drop in the i channel, and $\Delta P_{el,i}$ is the gravity pressure drop in i the channel.

The equations (7) are the flow distribution calculation model of parallel channels.

$$
\begin{cases}
\dfrac{L}{A_1}\dfrac{\partial m_1}{\partial t} = (P_{in} - P_{out}) - \Delta P_{a,1} - \Delta P_{f,1} \\
-\Delta P_{el,1} \\
\dfrac{L}{A_2}\dfrac{\partial m_2}{\partial t} = (P_{in} - P_{out}) - \Delta P_{a,2} - \Delta P_{f,2} \\
-\Delta P_{el,2} \\
\cdots \\
\dfrac{L}{A_i}\dfrac{\partial m_i}{\partial t} = (P_{in} - P_{out}) - \Delta P_{a,i} - \Delta P_{f,i} \\
-\Delta P_{el,i} \\
\dfrac{\partial m_t}{\partial t} = \displaystyle\sum_{i=1}^N \dfrac{\partial m_i}{\partial t}
\end{cases}
\tag{7}
$$

2.4   Model of Heat Transfer Between Assembles

The heat transfer model of thermal program assemblies developed in this paper adopts multi-layer heat conduction model, and the heat transfer coefficient between the m and

n assembly of the j layer can be expressed as:

$$\frac{1}{K_{m,n}^j} = \frac{\delta}{k_{liq}^j} + \frac{2t}{k_s^j} + \frac{1}{h_m^j} + \frac{1}{h_n^j} \qquad (8)$$

In the formula (8): $K_{m,n}^j$ is the total heat transfer coefficient between the assembly m and n in the j layer, δ is the distance between the assembly boxes, k_{liq}^j is the thermal conductivity of the coolant between the boxes, t is the thickness of the assembly box, k_s^j is the thermal conductivity of the assembly box, h_m^j is the convection heat transfer coefficient between the coolant and the wall of the m assembly box in the j layer.

Considering the calculation efficiency, the core assembly is divided into several circles. Since the power distribution of assemblies in the same circle is relatively consistent, the heat exchange between assemblies in the same circle is ignored. This paper only considers the heat exchange between fuel assemblies, not between fuel assemblies and reflector assemblies.

3 Candle

The research object of this paper is based on the lead cooled traveling wave reactor [5] designed by Chinese Academy of Sciences. With reference to its core physical design, thermal hydraulic design and analysis are carried out on this basis. The radial and arrangement of the reactor core are shown in Fig. 1. Table 1 gives the basic parameters of traveling wave reactor. The fuel is metal fuel, the coolant is liquid metal lead, and the cladding is made of HT-9 material.
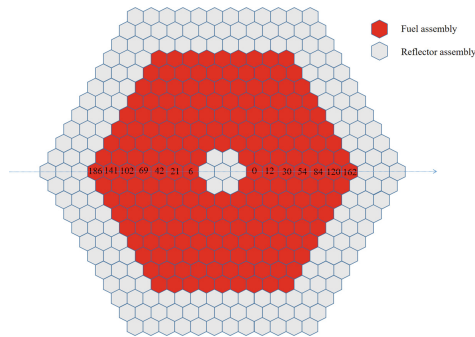
Fig. 1. Core Radial Arrangement

4 Result Analysis

4.1 Axial Heat Transfer

The core of lead cooled traveling wave reactor is divided into new fuel area, main combustion area and spent fuel area along the axial direction. The core heat is mainly

Table 1. Reactor Core Parameters

Parameters	Design values
Core power	500 MW
Fuel	Metal
Coolant	Pb
Number of assemblies	217
Height of fuel assembly	2.0 m
Material of cladding	HT-9
Number of rods in one assembly	61
Length of breeding zone	1.2 m
Length of start-up zone	0.8 m
Coolant core-inlet temperature	650 K
Coolant core-outlet average temperature	845 K

generated by the main combustion area. The power density of new fuel area and spent fuel area is low, and the axial power density difference is great.

Based on the given power distribution, Fig. 2 compares the central temperature and coolant temperature of various types of fuels. The coolant inlet temperature is 650 K. Since the axial power distribution of the fuel assembly has been given, that is, the spatial heat source distribution of the coolant, the temperature change of the coolant in the axial direction is basically the same. Because the thermal conductivity of oxide fuel is less than that of nitride, and that of nitride fuel is less than that of metal fuel, the central temperature of oxide fuel is the highest, which can reach 2350 K, and that of metal fuel is the lowest under a given power distribution. Due to the low power density in the spent fuel area ($0 <$ node number < 7), the temperature rise of the coolant in this area is slow. The power density in the main combustion zone ($7 <$ node number < 14) is high, the coolant temperature rises rapidly, and the fuel has the highest central temperature in this zone. The power density of the new fuel area ($14 <$ node number < 20) is almost zero, and the coolant temperature hardly rises.

Figure 3 compares the calculated temperature difference of fuel rods before and after considering axial heat conduction for various types of fuels. The influence ratio is defined as:

$$\Delta T / T = \frac{\left(T_{Axial\_heat\_conduction} - T_{Not\_axial\_heat\_conduction} \right)}{T_{Axial\_heat\_conduction}} \tag{9}$$

As can be shown in the Fig. 2, the middle section of the fuel rod will transfer heat to start and end of fuel. Therefore, the fuel temperature in the middle area ($7 <$ node number < 14) has decreased, and the maximum decrease ratio is 2.6×10^{-4}. It can be seen from the Fig. 3 that the metal fuel has a high thermal conductivity, so its axial heat conduction has a great effect, while the oxide fuel has a small effect on the axial heat
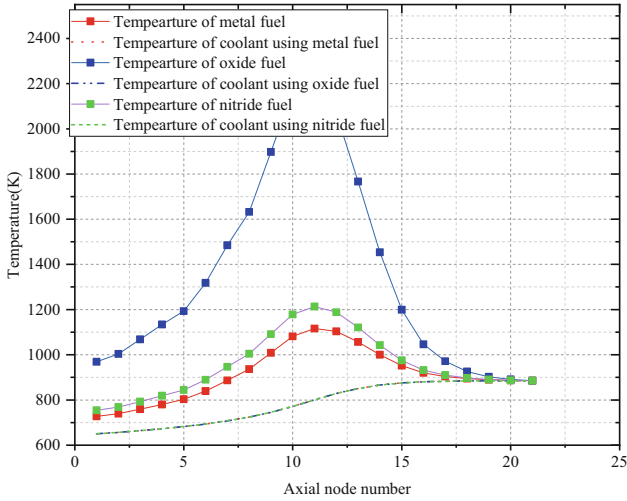
Fig. 2. Temperature of Fuel and Coolant in the Core

conduction. The axial heat conduction of all types of fuels has a proportion of $10^{-5} - 10^{-4}$ on the temperature distribution.
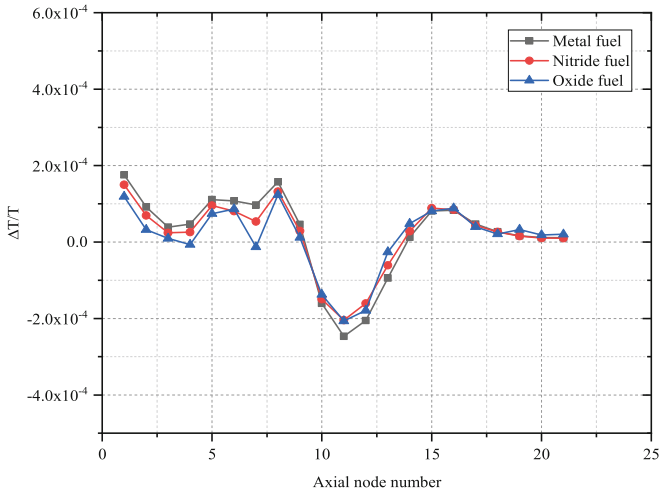
Fig. 3. Temperature of Various Types of Fuel under the Same Condition

Figure 4 compares the calculated temperature difference of coolant before and after considering axial heat conduction for various types of fuels. Axial heat transfer of the fuel rod also has a certain impact on the temperature of the coolant. As the fuel temperature in the spent fuel area ($0 <$ node number < 7) rises slightly under the action of axial heat conduction, the heat transferred to the coolant there will increase. Therefore, the coolant temperature in this area rises faster under the consideration of axial heat

conduction and is higher than the coolant temperature without consideration of axial heat conduction. However, the fuel temperature in the main combustion zone (7 < node number < 14) decreases slightly under the action of axial heat conduction, so the heat transferred to the coolant there will decrease. Therefore, under the consideration of axial heat conduction, the coolant temperature in this zone rises slowly and is lower than that without consideration of axial heat conduction. In the new fuel area (14 < node number < 20), the heat transferred to the coolant there will increase. Therefore, considering axial heat conduction, the coolant temperature in this area increases rapidly. Due to the high thermal conductivity of metal, the effect of axial heat conduction is slightly more obvious than that of other types of fuels. Therefore, the coolant using metal fuel has the largest temperature difference before and after considering axial heat conduction.
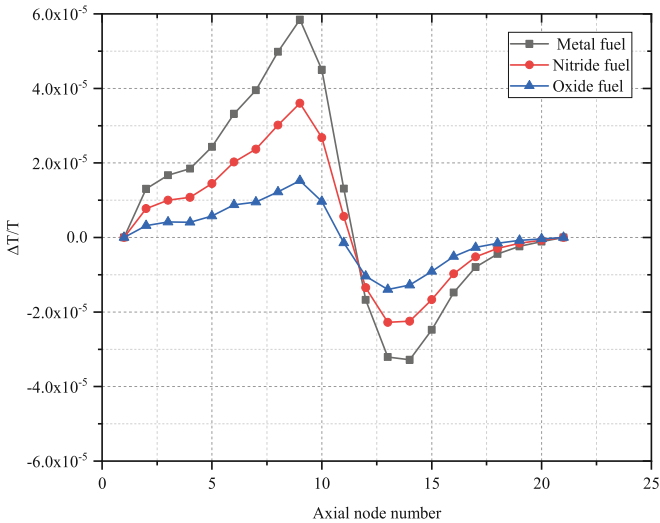
Fig. 4. Temperature of Coolant with Various Types of Fuel

The difference of fuel temperature and coolant temperature between considering axial heat conduction and not is about $10^{-5} - 10^{-4}$, which has little impact on the thermal hydraulic calculation of the core. This study shows that its influence on the temperature distribution of fuel rod is very limited, and the influence of axial thermal conductivity can be ignored to a certain extent.

4.2   Flow Distribution

In order to further analyze the core flow distribution characteristics, a group of representative assemblies are selected along the core diagonal for research and analysis. Figure 1 has 14 assemblies from 186 to 162 along the diagonal, corresponding to the serial numbers from 1 to 14.

In this paper, the normalized flow is introduced, which is defined as the ratio of the inlet flow of each assembly in the core to the average inlet flow of the core assembly.
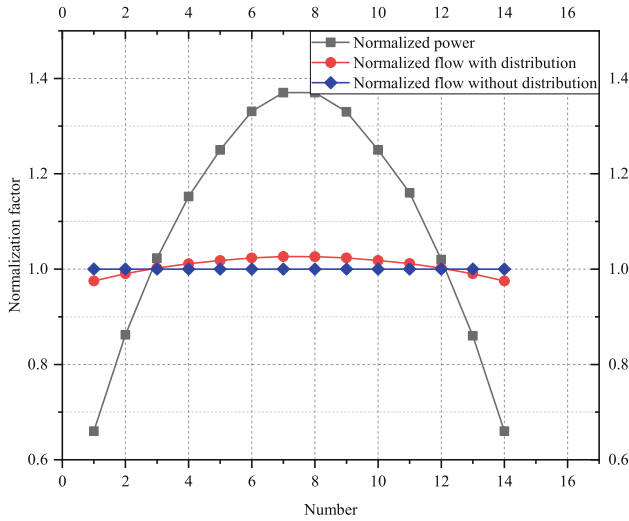
Fig. 5. Power distribution and flow distribution

Figure 5 shows the radial distribution curve of core power and the flow distribution of each assembly before and after considering flow distribution. It can be seen from the Fig. 5 that after considering the flow distribution, the flow share of the middle assemblies of the core will increase to a certain extent. Among them, the power normalization coefficient of the hottest assembly is 1.37, and its flow normalization coefficient is 1.03. The flow share of core edge assemblies will decrease, and the normalized power coefficient of the coldest assembly is 0.66, and its flow normalized coefficient is 0.98. It can be seen that the core has a certain flow distribution capacity, but there are some limitations, that is, there are "overheating" of high-power assembly and "supercooling" of low-power assembly in the core.

Figure 6 shows the coolant outlet temperature distribution of assemblies along the diagonal of the core under rated working conditions. The coolant outlet temperature in the middle of the core is extremely high, reaching 917 K. The coolant outlet temperature gradually decreases outward along the radial direction of the core, and the coolant outlet temperature of the most marginal assembly is 780 K. After considering the flow distribution, the coolant outlet temperature of the assemblies inside the core have decreased to a certain extent. Among them, the coolant outlet temperature of the intermediate assemblies in the core has decreased by about 8 K, and the coolant temperature at the edge of the core has slightly increased. This is because the automatic distribution of the core flow makes the intermediate thermal assemblies distribute more coolant flow, while the edge assemblies distribute less coolant flow, as a result, the coolant temperature of the core middle assembly decreases and the coolant temperature of the edge assembly increases.

In order to analyze the core flow distribution characteristics, this paper studies the influence of the flow channel area of assembly on the core flow distribution capacity. In order to evaluate the mismatch between the core flow and power, the non-uniformity
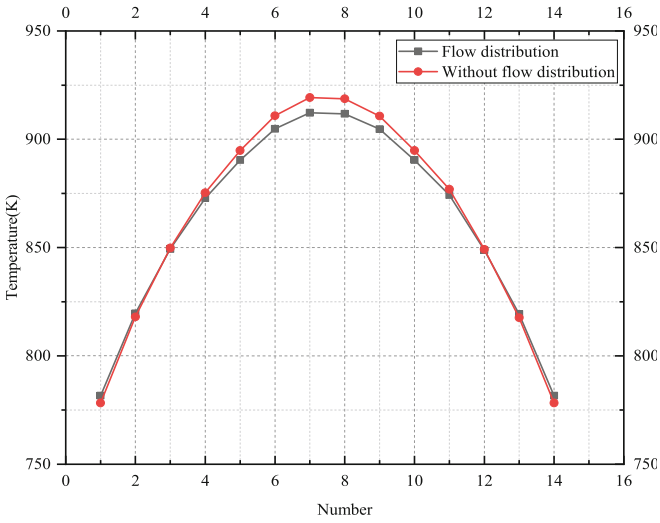
Fig. 6. Coolant temperature in the core outlet

coefficient is introduced, and its formula is defined as:

$$M = \frac{1}{N} \sum_{1}^{N} \left| \frac{f_{i,power}}{f_{i,flow}} - 1 \right| \tag{10}$$

N is the number of assemblies, $f_{i,power}$ is the power factor of the i assembly, $f_{i,flow}$ is the flow factor of the i assembly.
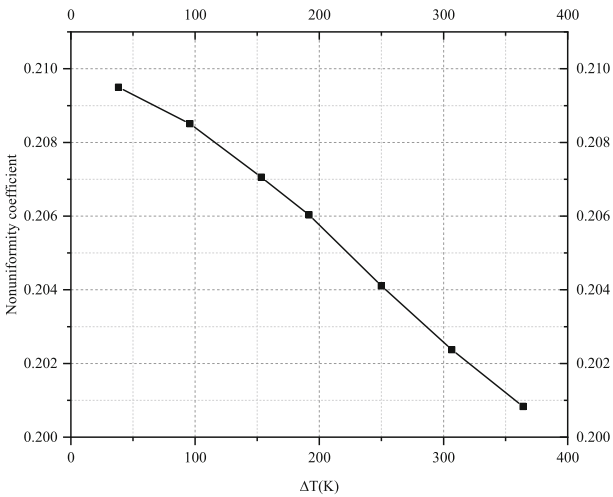
Fig. 7. Relation Curve Between Non-Uniformity Coefficient and Δ_T

Figure 7 shows the non-uniformity coefficient under different inlet and outlet temperature differences of the core. The inlet and outlet temperature of the core is changed by adjusting the total inlet flow of the core. When the inlet and outlet temperature difference increases, the power flow non-uniformity coefficient will decrease to a certain extent. When the inlet and outlet temperature difference of the core is small, as shown in the Fig. 7, the minimum temperature difference is 38 K, the non-uniformity coefficient is 0.209. When the temperature difference between the inlet and outlet of the core is large, as shown in the Fig. 8, the maximum temperature difference is 364 K, the non-uniformity coefficient is 0.201. This is because when the average inlet and outlet temperature difference of the core increases, the coolant temperature difference and density difference between the hot and cold assemblies will increase, that is, the driving force for automatic flow regulation is increased, and the flow distribution of the core is more suitable for the power distribution of the core.

4.3   Assembly Heat Transfer

The distribution of core flow is not considered in this subsection, and the basic assumption is that the coolant flow of each fuel assembly is consistent. Considering the symmetry of the core, a quarter of the core is taken as the research object. There are 7 layers of fuel assemblies in the radial direction of the reactor core. Selects 0, 12, 30, 54, 84, 120 and 162 assemblies in Fig. 1 as the research objects, which respectively correspond to No. 1–7 in the Fig. 8. Figure 8 compares the coolant outlet temperatures of the above assemblies before and after the assemblies' heat exchange is considered. After considering the heat exchange, the coolant temperature in the hot channel decreases from 918.69 K to 916.01 K, decreases by 2.68 K, increases from 778.31 K to 787.25 K, increases by 8.94 K, and the maximum coolant temperature difference at the channel outlet decreases by 11.62 K. However, the influence of assembly heat transfer on the coolant temperature distribution is limited.

Figure 9 shows the three-dimensional distribution of the heat flux transferred between the core assemblies. Considering the symmetry of the core, a quarter of the core is taken as the research object. It can be seen from the Fig. 9 that in the radial direction, the heat exchange power of the assemblies in the middle area of the core is small, and the heat exchange power gradually increases along the radial direction. This is because the difference between the normalized power of adjacent assemblies inside the core is small, so the coolant temperature difference between adjacent assemblies in this area is small, so the heat exchange power between assemblies inside the core is small. The power density of heat transfer between core edge assemblies is large, and the heat flux density at the radial edge is about 4–5 times that in the middle region.
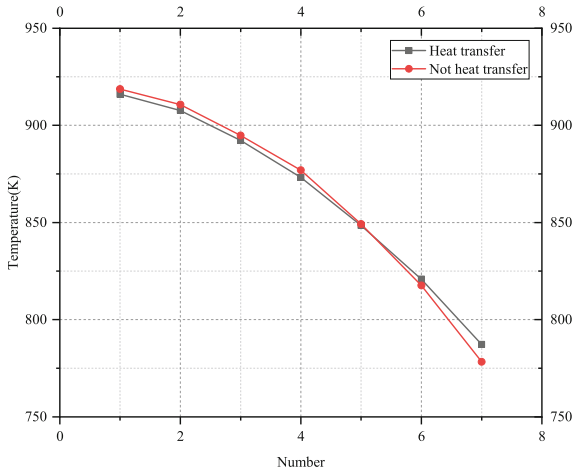
Fig. 8. Coolant Outlet Temperature Between Heat Transfer and Not Heat Transfer
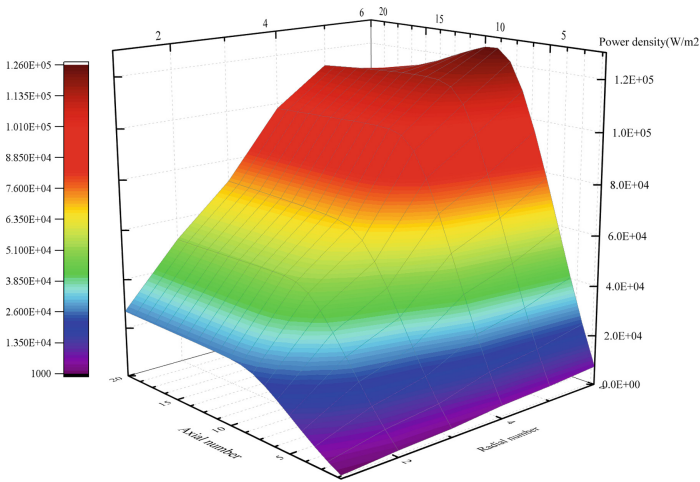
Fig. 9. C Three-Dimensional Distribution of Heat Transfer Power

5   Conclusion

Thermal-hydraulic program is developed in this paper. The thermal hydraulic program developed is used to calculate the core thermal characteristics of lead cooled traveling wave reactor. The research results show that:

1) The influence of axial heat conduction on fuel temperature and coolant temperature distribution is compared and analyzed by using the calculation program. The calculated axial thermal conductivity is about $10^{-5} - 10^{-4}$, so its influence on the

temperature distribution of fuel rod is very limited, and the influence of axial thermal conductivity can be ignored.

2) The developed thermal hydraulic program is used to study the flow distribution characteristics of the whole reactor core. The calculation results show that the reactor core has capacity of automatic flow distribution. At the same time, this paper studies the influence of inlet and outlet temperature difference on the core flow distribution capacity. When the inlet and outlet temperature difference of the core is large, the core has a large flow automatic distribution capacity. However, there is still a mismatch between the normalized flow and the normalized power of the core, that is, it is necessary to optimize the core flow distribution in the future.

3) The program was used to carry out the heat exchange calculation of the whole core assemblies. After considering the assembly heat exchange, the temperature difference at the coolant outlet between each channel decreased, from 140.38 K to 128.76 K, the change was relatively small. This is because the heat resistance of heat exchange between assemblies is large, and the coolant temperature difference in adjacent assemblies is not very significant. Therefore, the assembly heat exchange capacity is weak under this working condition.

References

1. Sekimoto, H., Ryu, K., Yoshimura, Y.: CANDLE: the new burnup strategy. Nucl. Sci. Eng. **139**, 306–317 (2001)
2. Sekimoto, H., Udagawa, Y.: Effects of fuel and coolant temperatures and neutron fluence on CANDLE burnup calculations. J. Nucl. Sci. Technol. **43**, 189–197 (2006)
3. Fomin, S., Mel'nik, Y., Pilipenko, V., Shul'ga, N.: Initiation and propagation of nuclear burning wave in fast reactor. Prog. Nucl. Energy **50**, 163–169 (2008)
4. Sekimoto, H.: Introductions of 208PB coolant to innovative fast reactors. Application of Stable Lead Isotope Pb-208 in Nuclear Power Engineering and its Acquisition Techniques, pp. 21–42 (2013)
5. Zouxiaoliang: Core physical design and neutronics characteristic analysis of lead cooled traveling wave reactor. Nucl. Sci. Eng. **4**, 590–597 (2018)
6. Wei, S.: Research on the Reactor Physics Analysis Methods and Characteristics of Traveling Wave Reactor (2015)

Design and Application of γ-Ray Energy Spectrum Survey System Based on UAV

Jiangkun Li[(✉)], Wei Zhang, Xuliang Wu, Xue Wu, Bin Wei, Leichao Wu, Yizhou Li, and Peijian Wang

Airborne Survey and Remote Sensing Center of Nuclear Industry, Shijiazhuang, Hebei, China
li_jiankgun@163.com

Abstract. Airborne γ-ray energy spectrum measurement is an effective method for radioactive mineral investigation and radiation environment monitoring. In recent years, with the gradual maturity of Unmanaged air vehicle (hereinafter referred to as UAV) technology, UAV airborne geophysical survey technology is becoming a hot research field. But the UAV has less load and space and is difficult to carry traditional aeronautical geophysical equipment. The miniaturization, intelligentization and automation of airborne geophysical survey instruments are the key technologies of airborne geophysical survey for UAVs. The γ-ray energy spectrum measurement system is designed suitable for UAV platform with load in the range of 30–180 kg, at the same time, the data acquisition control and remote monitoring software is developed. The calibration of the system is completed on the Shijiazhuang airborne standard model and Huangbizhuang dynamic belt, and the calibration parameters are obtained, the resolution of the crystal is better than 8.5%, and the peak drift is better than ±1, the sampling frequency of energy spectrum data is 1 Hz. Based on SY-120H and CH-3 UAV platforms, test flights were carried out in Karamay, Xinjiang and Erlianhot, Inner Mongolia, respectively, to find out the distribution of radioactive field in the test area and quickly delineate the specific location and range of the radioactive anomaly. The test results show that: UAV aviation γ The results of K, U and Th content measured by energy spectrum are basically consistent with those measured on the ground, which can provide a fast and efficient exploration technology and equipment for radioactive mineral investigation and radiation environment monitoring.

Keywords: UAV · γ-ray energy spectrum · survey system · design

1 Introduction

Airborne geophysical survey is a fast, economic and effective geophysical exploration method. In 1955, the nuclear industry department carried out aerial radioactivity measurement in Hunan and Xinjiang for the first time [1], which was mainly used to search for radioactive mineral resources such as uranium, thorium and potassium. After the 1980s, this method was gradually extended to oil and gas exploration, environmental radioactive pollution assessment and nuclear emergency aviation monitoring [2–5].

Airborne geophysical survey mainly takes fixed wing aircraft and helicopters as the measurement platform. In recent years, with the gradual maturity of UAV technology, UAV aerial geophysical survey technology that explores UAV carrying aerial geophysical instruments for measurement is rising. After entering the 21st century, there have been British UAV aeromagnetic measurement system (2003), Dutch aeromagnetic measurement system (2004), Finnish UAV radioactivity monitoring system (2005), Canadian UAV aeromagnetic measurement system (2009), Japanese unmanned helicopter radioactivity measurement system (2012) [6], German mgt-uas (magnetic/Electrical) measurement system (2013), American UAV nuclear radiation detector (2013) Unmanned aerial geophysical exploration and measurement equipment such as the multi rotor UAV radioactivity measurement system (2018) of the Russian company came out, and these systems have carried out application tests in geological exploration, UXO detection, radiation environment monitoring and other fields [7, 8].

In China, due to the large volume, weight, power consumption and low compatibility of data acquisition and control system of existing airborne geophysical exploration and measurement equipment, it is not suitable for UAV load and structural requirements [9]. The Chinese Center for aerial geophysical and remote sensing of land and resources, the Chinese Academy of Geological Sciences and the Chinese Academy of Sciences carried out research on the aeromagnetic measurement technology of unmanned aerial vehicles based on fixed wings or helicopters around 2010. Since 2013, the nuclear industry aerial survey and Remote Sensing Center has developed ugrs series unmanned aerial vehicles γ Energy spectrometer, and has carried out test flights and production applications at home and abroad.

2   System Design

The design and development of measurement system host, detector and measurement software are completed.

2.1   Development of Measurement System Host

Based on the reinforced computer, the host of the measurement system has developed a data interface. By optimizing the equipment structure and using low-power devices, the volume, weight and energy consumption of the system are reduced, and the miniaturization of the system is realized. It is mainly used for control, communication, acquisition of airborne emission/aeromagnetic measurement data, etc. At the same time, it realizes full duplex communication with the ground control station, sending/receiving data and instructions. See Table 1 for main technical indicators.

Table 1. Main technical indexes of ugrs system host

Parameter	Technical indicators
Input voltage	18–30VDC
Power	70 W
Dimension	240 mm × 195 mm × 76 mm
Weight	5 kg
Working temperature	−20 °C–60 °C

2.2 Development of Detector

The detector is aviation γ The core part of the spectrometer is composed of NaI (TL) crystal scintillator, photomultiplier tube (PMT), digital pulse processor, power supply, detector box and other parts. See Fig. 1 for the composition block diagram.

The scintillator of the detector adopts about 4.2L cubic NaI (Tl) crystal, with a weight of about 17 kg. Limited by the load and installation space of the UAV platform, the system can carry up to 5 crystals. This test is equipped with 1–3 4.2L NaI(Tl) detectors.

Photomultiplier tube is an important part of scintillation detector. It is a photon detector with high sensitivity and fast time response. It is composed of photocathode, input electron optical system, electron multiplier system and anode.
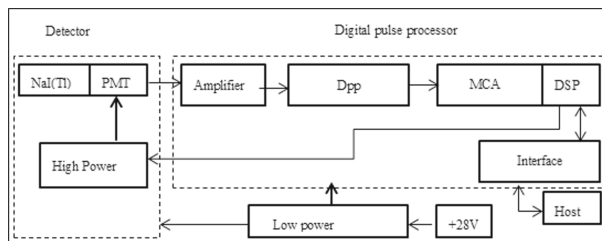
Fig. 1. Composition block diagram of detector

The high-voltage power supply provides 600–1500 V high-voltage power supply for the photomultiplier tube. The DC-DC module is used to design the high-voltage power supply control circuit. Each detector is composed of independent NaI (Tl) crystal, photomultiplier tube (PMT), digital pulse multichannel analyzer and high-voltage power supply.

2.3 Measurement Software Development

Data acquisition and control software and remote operation monitoring software are designed and developed.

2.3.1 Data Acquisition Control Software

Data acquisition and control software is used to collect and record measurement data in real time, and transmit instructions and data with ground monitoring software. The actual operation interface is shown in Fig. 2. The current interface displays eight parameters, including TC, K, u, th, RALT, balt, Galt and unmag.
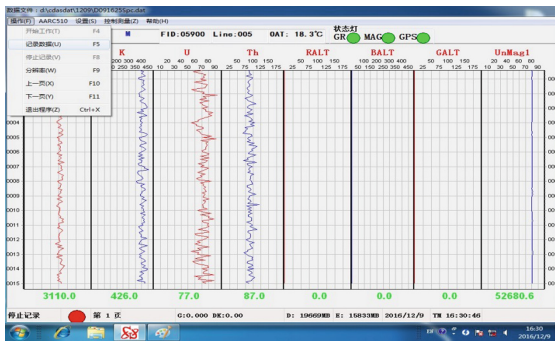
Fig. 2. Interface of data acquisition and control software

2.3.2 UAV Remote Operation Monitoring Software

With the help of the data flow of UAV Ground Control Station, the monitoring software compiles the control command set and data decoding, and realizes the real-time monitoring and control function of the aerial survey instrument by sending commands and receiving data. See Fig. 3 for the composition block diagram of the monitoring system (Table 2).
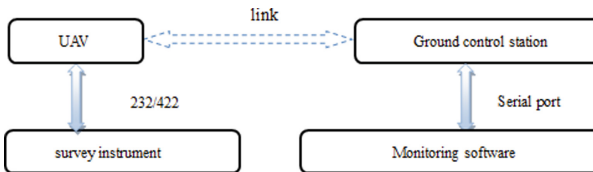
Fig. 3. Composition block diagram of ground monitoring and remote control system

2.3.3 Technical Indicators

Table 2. Main performance indexes of ugrs-10 airborne gamma spectrometry measurement system

Parameter	Technical indicators
Crystal detector volume	2–4.2L
Energy resolution	CsI:10%; NaI(Tl):8.5% (@^{137}Cs 0.662 meV)
Energy spectrum peak drift	better than ±1 (@^{208}Tl 2.615 meV)
Channels	256/1024
Energy range	0.2–3 meV, cosmic rays: 3–6 meV
Sampling frequency	1 Hz
Communication mode	Ethernet, RS232
Power supply	+28DCV
Data storage	Electronic hard disk storage
Stability	≥8 h
Working temperature	−20 °C–50 °C

3 Application

3.1 Measurement Test of Fixed Wing UAV

From 2013 to 2015, the ugrs unmanned aerial geophysical exploration and measurement system completed 9721 km of flight test, pilot production and application demonstration measurement in China, with a total of 42 flights [14]. The magnetic dynamic noise level of the system is better than 0.08nt, the total accuracy of aeromagnetic is better than 1.80 NT, the energy resolution is better than 9.5%, and the peak drift is better than ±1 channel; The endurance capacity of the system is more than 1200 km, the yaw distance is better than ±10 m, and the average operating flight altitude is about 120 m (it can fly along the topographic relief), all of which meet the design indicators. See Fig. 4 for the results of airborne geophysical and magnetic emission measurement.

By comparing and analyzing the aerial measurement results of UAV, the ground inspection results and the comprehensive survey results of aerial survey and remote sensing in 2007 (see Table 3), the data show that the system has good stability and reliability in the operation of the survey area, has achieved the effect of application demonstration, and has the foundation of popularization and application.

3.2 Rotor UAV Measurement

Two aeronautical radiation anomalies in Inner Mongolia Autonomous Region were selected as the test area to carry out the test flight. The survey line flight was 51.4 km,
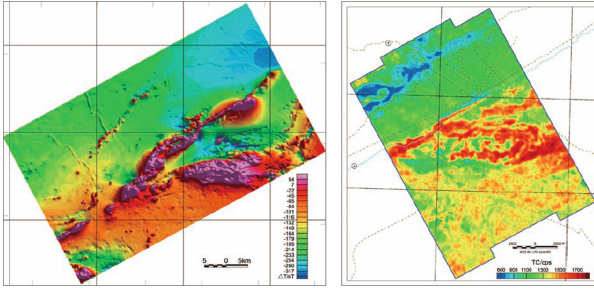
Fig. 4. Aeromagnetic (left) and airborne radiometer (right) measurement results

Table 3. Comparison and statistics of measurement results

Measurement result	K (%)	U (μg/g)	Th (μg/g)
UAV measurement results	1.66	3.31	9.57
Ground measurement results	1.80	2.97	10.94
Measurement results in 2007	1.70	2.95	9.50

the average flight altitude was 49.7 m, the average flight speed was 27.57 km/h, and the data sampling rate was 1 Hz.

According to the projection coordinates, K, u, th contents and TC of the navigation and positioning data of UAV aerial measurement in the abnormal area, the minimum curvature method is used to grid the data, and the UAV aerial measurement TC isograms and K, u, th contents isograms are obtained. Among them, the hf-09 TC contour map is shown in Fig. 5 (a). In this abnormal area, the high value of u content is mainly distributed in the northeast and southwest, with 5×10^{-6} and 10×10^{-6} delineate the abnormal area for the boundary value (see Fig. 5 (b)).
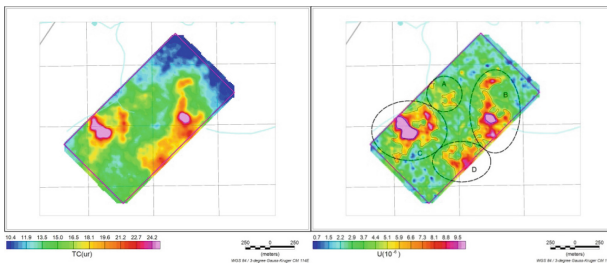
Fig. 5. (a) Tc contour map of UAV airborne radio (HF-09) (b) U abnormal range delineated (HF-09).

Pilotless aircraft aviation γ The energy spectrum measurement results are compared with the ground measurement results, as shown in Table 4:

Table 4. Data statistics of the same range measured by line 8040 UAV and ground

Measurement method	Data volume	TC(Ur)	K(%)	U(10^{-6})	Th(10^{-6})
Ground survey	14	15.5	2.6	3.1	7.7
UAV measurement	82	16.4	2.9	3.8	10.4
Relative deviation (%)	/	5.8	10.6	23.5	34.4

4 Conclusions

(1) The ugrs UAV airborne geophysical (magnetic/radio) measurement system is independently developed. Through the application test of 9721 km in different regions in China and the production of 80000 km of survey lines in Africa, it is confirmed that the instrument has stable working performance and good working condition, and meets the design index.

(2) UAV aerial survey effectively complements the regional gap that is difficult for drones to implement, realizes ultra-low altitude terrain follow-up autonomous survey and night aerial survey, and effectively improves the national airborne geophysical survey capability.

(3) The test proves that UAV aviation γ Energy spectrum measurement technology is effective in carrying out anomaly inspection, and can provide a fast and efficient exploration technology equipment for geological exploration and radioactive environment assessment in areas where it is difficult to carry out work on the ground.

References

1. Yu, B.: Aviation of China and several major countries in the world γ Review of energy spectrum measurement. Foreign Uranium Gold Geology **4**, 64–93 (1992)
2. Li, H.: Application of airborne radioactivity measurement in environmental detection. Geophys. Geochem. Explor. **28**(6), 515–517 (2004)
3. Jiangminzhong: Research on aerial survey and remote sensing oil and gas prediction in the western region of Pingle depression. Geol. Sci. Technol. Inf. **21**(4), 60–64 (2002)
4. Ni, W. : Aviation monitoring method for nuclear emergency. Uranium Geol. **19**(6), 366–373 (2003)
5. Liu, Y., Gu, R., et al.: Airborne radioactivity measurement. Geophys. Geochem. Explor. **26**(4), 250–252 (2002)
6. Li, W., Li, J., Liu, S., et al.: Research and development progress of autonomous UAV aerogeophysical (radio/magnetic) integrated station. Acta Geoscientifica Sinica **35**(4), 399–403 (2014)
7. Laliberte, J.: Carleton University Fixed Wing UAV Project. Carleton University, Canada (2013)
8. Cui, Z., Xu, G., Li, J., et al.: Current situation and prospect of research, development and application of unmanned aerial geophysical exploration technology. Geophys. Geochem. Explor. Calculation Technol. **38**(6), 740–745 (2016)

9. Li, J., Li, Y., Liu, S., et al.: Development and test application of UAV airborne radioactivity measurement system . China Nuclear Science and technology progress report, vol. 5 (2017)
10. Wang, L.: Design of digital multichannel pulse amplitude analyzer based on DSP. Nucl. Electron. Detect. Technol. **29**(4), 880–883 (2009)
11. Ge, L., Zeng, G., Lai, W., et al.: Aeronautical figures γ Development of energy spectrum measurement system. Nucl. Technol. **34**(2), 156–160 (2011)
12. Liu, S., Li, J., Li, Y.: Design of airborne gamma ray spectrum data transmission system based on UAV. Sci. Technol. Innov. Guide **12**(3), 5–6 (2015)
13. Hu, M., Zhang, J., Jiang, M., et al.: Aviation γ general calibration technology of energy spectrometer. China Nuclear Science and technology progress report, vol. 1 (2009)
14. Gao, G., Qiu, C., Wang, J., et al.: Demonstration and application of new technology for aerial measurement of UAV. Geophys. Geochem. Explor. **40**(6), 1131–1137 (2016)
15. IAEA. TECDOC-323. Airborne Gamma Ray Spectrometer Survey, Vienna (1991)

Research on the Radioactive Waste Discharge Permit Regulation

Li Huang, Ting Liu[✉], Yun Fan, Meng Chang, and Yiman Dong

Nuclear and Radiation Safety Center, MEE, Beijing, China
`liuting@chinansc.cn`

Abstract. For the release of radioactive waste, the regulatory body must establish or approve operational limits and conditions relating to public exposure, including approved discharge limits. The parties concerned must ensure that the release of radioactive waste and radioactive substances into the environment is managed in accordance with the instrument of ratification. Discharge authorization procedures, including the establishment of emission authorizations and emission allowances, the establishment and use of dose constraints, emission characteristics, and the circumstances of exposure used in the establishment of emission allowances, etc., According to the legal requirements of our country, at present, all units in the nuclear industry that produce and discharge radioactive waste gases and liquids into the Environment shall rely on the examination and approval of prior environmental impact reports or environmental impact assessment documents, the permit mode of total discharge control for the examination and approval of the designed nuclide discharge of radioactive waste gas and liquid. At present, China's radioactive contamination emissions are not included in the management of emission permits, nuclear and radiation-related key industries and units are not included in the "Fixed Source Emission Permits Classified Management Directory" management. Whether it is feasible to carry out the pollution discharge permit system in the nuclear and radiation industry of our country, in the theoretical system, there are already relevant laws and regulations of our country to guarantee or can guarantee, however, there are still some problems in the actual operation, such as insufficient research on radiation environmental quality objectives, further work is needed to promote the full implementation of the discharge permit system in the nuclear industry.

Keywords: Radioactive Waste · Discharge · Limit Value · Control Value · Permit · License

1 Introduction

The discharge of radioactive waste must be regulated and restricted by the state. Article 41 of my country's "Radioactive Pollution Prevention and Control Law" stipulates that units that generate radioactive waste gas and waste liquid discharge into the environment radioactive waste gas and waste liquid that meet the national standards for the

prevention and control of radioactive pollution, shall report to the environmental protection administrative director who has examined and approved the environmental impact assessment documents. The department applies for the discharge of radionuclides and regularly reports the discharge measurement results.

In January, China issued regulations on the management of pollution permits, 2021 that enterprises, institutions and other producers and operators under the management of pollution permits should apply for pollution permits in accordance with the regulations, no pollutants shall be discharged. According to the factors such as the amount of pollutants produced, the amount of pollutants discharged and the degree of impact on the environment, etc., the discharge units shall be subject to the classified management of discharge permits. However, the nuclear and radiation industries are not explicitly included in the current "Classified management list of emission permits for fixed sources of pollution", and there are no specific requirements for emission permits in China's current Local ordinance regulations, therefore, the industry has not implemented a licensing system.

2   Relevant Regulations of Chinese Standards

2.1   GB18871 "Basic Standard for Protection Against Ionizing Radiation and for the Safety of Radiation Source"

Article 8.6.2 stipulates that radioactive waste liquid shall not be discharged into ordinary sewers, unless it is confirmed by the review and management department that it is low-level waste liquid that meets the following conditions, it can be directly discharged into ordinary sewers with a flow rate greater than 10 times the discharge amount, and Each discharge should be recorded:

a) The total activity emitted per month does not exceed 10 ALI_{min} (ALI_{min} is the smaller of the ingestion and inhalation ALI values corresponding to occupational exposure, and the specific value can be obtained according to the provisions of B1.3.4 and B1.3.5);

b) The activity of each discharge shall not exceed 1 ALI_{min} and shall be flushed with not less than 3 times the amount of water discharged after each discharge.

2.2   GB6249 "Environmental Radiation Protection Regulations for Nuclear Power Plants"

Article 6 "Dose constraint value and emission control value in operating state" stipulates that the effective dose to any individual in the public caused by the radioactive substances released to the environment from all nuclear power reactors at any site must be less than the dose constraint value of 0.25 mSv per year.

The operating organization of the nuclear power plant shall formulate the dose management target values for airborne radioactive effluent and liquid radioactive effluent respectively according to the dose constraint value approved by the audit and management department. The nuclear power plant must implement the control of the total annual emission of radioactive effluents for each reactor. For a reactor with a thermal power of 3000 MW, the control value is as follows (Tables 1 and 2).

Table 1. Control values of airborne radioactive effluents

	Light water reactors	Heavy water reactors
Inert gas	$6 * 10^{14}$ Bq/a	
Iodine	$2 * 10^{10}$ Bq/a	
Particles (half-life > 8 days)	$5 * 10^{10}$ Bq/a	
14C	$7 * 10^{11}$ Bq/a	$1.6 * 10^{12}$ Bq/a
3H	$1.5 * 10^{13}$ Bq/a	$4.5 * 10^{14}$ Bq/a

Table 2. Control values for liquid radioactive effluents

	Light water reactors	Heavy water reactors
3H	$7.5 * 10^{13}$ Bq/a	$3.5 * 10^{14}$ Bq/a
14C	$1.5 * 10^{11}$ Bq/a	$2.0 * 10^{11}$ Bq/a
Other nuclides	$5.0 * 10^{10}$ Bq/a	(Except 3H)

3 Radioactive Waste Discharge Permits in China

At present, the discharge of radioactive pollutants in my country has not been included in the management of pollutant discharge permits for the time being, and relevant key industries and units have not been included in the "List of Fixed Pollution Source Pollutant Discharge Permit Classification Management" management.

According to the requirements of the Pollution Discharge Law, at present, all units in my country that generate and discharge radioactive waste gas and waste liquid into the environment implement a permit system based on construction permits, safety permits, mining permits, etc., with pre-environmental impact reports or environmental impact assessment documents. Based on the approval of radioactive waste gas and waste liquid, the total emission control permit mode is approved for the design of radioactive waste gas and waste liquid emission.

When submitting an environmental impact report to the ecological environment department, the unit producing radioactive waste gas and liquid should also submit an application for the estimated discharge of radioactive waste gas and waste liquid, including determining the characteristics and activities of the radionuclides to be discharged and possible discharges where and how, and the exposure doses to key populations of the public that may be caused by the planned discharge. According to the discharge situation of other facilities in the area where the emission unit is located, the ecological environment department will allocate a certain emission share to the unit according to the public dose limit standard. The approved emission limits for nuclear power plants and research reactors must be included in the operating limits and conditions. The nuclear technology utilization unit generally adopt emission and clean decontamination models that conform to national standards, while uranium mines adopt emission limits for corresponding nuclides based on environmental standards, and associated mines currently

do not have relevant standards, the corresponding limits of national sewage discharge standards can be used.

A nuclear power plant unit is a million kilowatt-class pressurized water reactor nuclear power unit. According to the approval of the original Ministry of Environmental Protection "Approval of the Environmental Impact Report of a Nuclear Power Plant (Operation Stage)" and other documents, as well as the monitoring of the effluent of the nuclear power plant, the annual emission control value and actual value of the radioactive effluent of the unit in a certain year as follows (Table 3):

Table 3. Annual emission control value and actual value of radioactive effluents from 1/2 unit of a nuclear power plant

		6249 control value (single unit)	A nuclear power plant (1/2 units control value)	A nuclear power plant (1/2 units actual value)	Proportion
Airborne effluent	Inert gas	6.00E+14	1.37E+14	4.54E+11	0.33%
	Iodine	2.00E+10	1.18E+09	1.15E+07	0.97%
	Particles	5.00E+10	1.31E+08	1.56E+06	1.19%
	14C	7.00E+11	7.81E+11	3.00E+11	38.38%
	3H	1.50E+13	9.90E+12	7.38E+11	7.46%
Liquid effluent	3H	7.50E+13	9.90E+13	4.58E+13	46.27%
	14C	1.50E+11	5.87E+10	5.87E+09	9.99%
	Other nuclides	5.00E+10	5.56E+10	6.16E+08	1.11%
	Total concentration	1000Bq/L	900Bq/L (all)	180Bq/L	–
Dose		0.25 mSv (all units)		0.000452 mSv (all units)	0.18%

The annual emissions of Airborne Carbon 14 and liquid tritium were higher than the annual control value, and the emissions of other airborne and liquid radioactive effluents were far lower than the annual control value. The annual maximum individual effective dose of effluents released to the public was $4.52 * 10^{-7}$ Sv, and the residents receiving the maximum individual dose were adults within 1–2 km north-northeast (NNE) of the plant site, about 0.18% of the dose-limiting value of 0.25 mSv/a.

For radioactive contamination, the monthly and quarterly monitoring results of the water samples near the outfall comply with the first-class Standard in Table 4 of the comprehensive wastewater discharge standard (GB8978-1996), and there is no obvious change compared with the outfall. Monthly monitoring and analysis items include dissolved oxygen, residual chlorine, conductivity, Ph value, hexavalent chromium, total chromium, orthophosphate, hydrazine. Quarterly monitoring items include Boron, iron, anions, sulphates, lithium, sodium, nickel and oils.

Table 4. Annual emission control value and actual value of radioactive effluents from 3/4 unit of a nuclear power plant

		6249 control value (single unit)	A nuclear power plant (3/4 units control value)	A nuclear power plant (3/4 units actual value)	Proportion
Airborne effluent	Inert gas	6.00E+14	9.11E+13	7.04E+11	0.77%
	Iodine	2.00E+10	6.45E+08	4.95E+06	0.77%
	Particles	5.00E+10	7.14E+07	1.00E+06	1.40%
	14C	7.00E+11	7.65E+11	2.31E+11	30.18%
	3H	1.50E+13	5.63E+12	4.98E+11	8.85%
Liquid effluent	3H	7.50E+13	6.30E+13	3.28E+13	52.11%
	14C	1.50E+11	5.62E+10	5.46E+09	9.72%
	Other nuclides	5.00E+10	4.00E+10	7.24E+08	1.81%

3.1 Nuclear Technology Utilization Units

My country's nuclear technology utilization units basically have very few waste gas emissions, and the amount is also very small. The main radioactive pollutants in the management of pollutant discharge licenses are mainly concentrated in waste liquids, and in various industries, waste liquid discharges are mainly medical-related units. Although there are many types of radionuclides used in medical institutions, most of them are of low toxicity and short half-life. However, in the investigation and research on the application status of nuclear medicine projects in Guangdong Province, it was found that the total β of the wastewater at the outlet of the decay pool of the hospital with a large amount of iodine-131 was greater than the "Water Pollutant Discharge Standard for Medical Institutions" (GB18466-2005) the specified emission limits.

3.2 Associated Minerals

At present, my country has no associated radioactive mine radiation environmental safety standard guidelines and associated mine development and utilization project effluent discharge limit. From the actual discharge situation, the discharge concentration of wastewater may be higher than the relevant limit in the "Integrated Wastewater Discharge Standard" (GB8978-1996), and the radon concentration in some places will also be higher than the limit, but the resulting dose is basically low The public individual effective dose limit for the development and utilization of mineral resources is 1 mSv/a.

3.3 Situation Analysis

After investigation, various local provinces in my country have carried out relevant explorations in the implementation of the radioactive pollutant discharge permit system.

Article 18 of the "Administrative Measures for the Prevention and Control of Radioactive Pollution in Sichuan Province" promulgated by Sichuan Province in 1999 stipulates: "Any unit that discharges radioactive waste water and waste gas into the environment must be monitored by a statutory monitoring agency; It is prohibited to discharge radioactive waste water and waste gas into the environment without a pollution discharge permit or beyond the regulations of the pollution discharge permit." But this method has been abolished at present, and there is no such relatedness in the newly issued Regulations on the Prevention and Control of Radiation Pollution in Sichuan Province in 2016. Regulation. At present, radioactive pollutant discharge permits have also been set up in the ecological environment examination and approval of Shandong and other provinces, but there has been zero application status.

Whether it is feasible to implement a pollutant discharge permit system in my country's nuclear and radiation industry, in terms of theoretical system, there are relevant laws and regulations in my country to guarantee or can be guaranteed, but in terms of practical operation, there are problems such as insufficient research on radiation environmental quality objectives.

The ultimate purpose of the implementation of the pollutant discharge permit system is to reduce the discharge of pollutants, thereby improving the quality of the environment. However, in the nuclear and radiation industry, there is a lack of relevant standards and research on how to link the allowable amount of radioactive pollutant discharge with environmental quality goals.

According to the pollution discharge permit management regulations, three modes of management are stipulated according to factors such as pollutant generation, discharge, and degree of impact on the environment, which are divided into key management, simplified management and registration management. The corresponding degree of environmental impact is divided into three categories. In the nuclear and radiation industry, it is generally based on the natural background, and the 1mSv equivalent dose limit for humans is used to control the effluent discharge of relevant units, but when it comes to the degree of environmental impact It is difficult to define the size of the industry and the impact on the ecological environment, which is also a problem that affects the determination of which mode of supervision the relevant industry should be.

4   Conclusions

In general, the conditions for implementing a pollutant discharge permit system in accordance with the requirements of the pollutant discharge permit regulations in my country's nuclear and radiation industries are not yet mature. However, in the medical and associated mining industries where management is relatively weak at present, a pilot registration management model can be considered, and It is possible to explore more scientific and reasonable emission standards and management models based on practice, laying the foundation for the comprehensive implementation of the emission permit system in the nuclear and radiation industry. At the same time, it is recommended to establish a radiation environment quality index system, improve the standard system, and strengthen the building of monitoring capabilities and professional supervision teams. Carry out research on the relationship between the discharge of radioactive pollutants

and environmental quality objectives, to provide sufficient theoretical basis for the implementation of key management, simplified management, and registration management of pollutant discharge permits, and to achieve the goal of improving environmental quality and ensuring the health of personnel with pollutant discharge permits.

References

1. Li, D., et al.: Talking about the difficulties and countermeasures of implementing the pollutant discharge permit system in my country. Environ. Manage. China (5) (2016)
2. Liang, Z., et al.: Legislative positioning and legislative demands of my country's pollutant discharge permit system—legal reflections on the establishment of pollutant discharge permit management regulations (Continued). Environ. Impact Assess. (2) (2018)
3. Li, Y., et al.: Study on the radiation environmental impact of the development and utilization of the Bayan Obo Rare Earth Mine. Rare Earths (4) (2020)
4. Jia, P., et al.: Research on the setting system of pollution discharge permit under the background of ecological civilization system reform . J. Harbin Inst. Technol. Sci. (Soc. Sci.) (1) (2020)
5. Wang, S., et al.: The experience of the management of pollutant discharge permits in the United States. Oil Gas Field Environ. Protect. (1) (2017)

Preparation and Shielding Performance of Gamma Ray Shielding Composite Materials Based on 3D Printing Technology

Yulong Li, Chengxin Li[✉], Danfeng Jiang, Feng Liu, Xiajie Liu, and Li Li

China Nuclear Power Technology Research Institute, Shenzhen, Guangdong, China
cikerlee416@163.com

Abstract. Excessive gamma-rays will be emitted when a nuclear power plant is under the refueling overhaul, leading to a certain number of hotspots. To meet the shielding requirements of these hotspots of complex components, a nylon-tungsten shielding composite material was developed by laser selective sintering 3D printing technology. The effects to shielding performance of 3D printing shielding materials were emphatically studied for two preparation processes (including mechanical mixing method and coating method) of 3D printing composite powders. Experimental results show that the nylon-tungsten shielding composite material with tungsten content of 70–85% was obtained by 3D printing technology, which realizes the manufacture of mold-free customized and bonded shielding materials. The shielding material prepared by 3D printing technology by coating method is better than that by mechanical mixing method in shielding performance. When the mass ratio of tungsten powders is 80%, the linear attenuation coefficient can reach 0.32, which is the best formula of the composite material and can be used for shielding of complex components. All these results lay a theoretical foundation for the engineering application of 3D printing shielding materials.

Keywords: 3D printing · Shielding materials · Performance study

1 Introduction

During the operation of a PWR nuclear power plant, many radiation hotspots may appear on different operating pipelines and equipments in the control area. Therefore, it is necessary to adopt certain radiation shielding measures to reduce the external dose for working staff near the radiation hotspots.

At present, it is common to use sheet lead or lead apron for radiation shielding in the domestic nuclear power plants [1, 2], but there are many problems for this shielding way. Sheet lead is messy and difficult to clean. Sheet lead and lead apron are soft, which is easy to cause deformation and affect the stability of radiation protection. This shielding method does not meet the seismic performance requirements of nuclear power plants, and hinders the operation and maintenance of instruments and valves. In addition, most of the wrapped shielding sheet lead and lead apron need to be removed when the refueling overhaul is finished for the nuclear power plant. Repeating installations and

removals not only consumes a lot of sheet lead and lead apron, but also causes high dose on the working staff. According to the management requirements of the control area of nuclear power plants, it is necessary to develop a new shielding composite material which is customized and completely fitting with the component, and innovate the traditional shielding mode of nuclear power plants.

At present, research on the new type of shielding materials has aroused more and more attention. Shin et al. [3] developed a BN/high-density polyethylene composite material with good neutron shielding performance; A kind of rubber-based flexible shielding materials has been developed by British ITW Company for radiation shielding in nuclear industry and the nondestructive testing field, which has been applied in the Size-well B nuclear power plant in Britain; Fu Ming et al. [4] developed a flexible shielding material with styrene butadiene rubber (SBR) for matrix; Zhuo Mingchuan et al. prepared PA6-tungsten shielding composites with different densities by melt extrusion method [5]; Ahmed et al. Studied the gamma-ray shielding characteristics of tungsten-silicone rubber composites, which can be used as manufacturing materials for protective clothing such as gloves and jackets [6]; Samantha et al. used 3D printing technology to prepare resin-based neutron and gamma-ray shielding materials, of which the content of functional filler Bi can reach 40% or the content of ^{10}B can reach 60% [7].

It is complex and diverse for equipment structure at radiation hotspots in nuclear power plants. Radiation protection composite materials based on polymer materials are generally produced by injection molding or compression molding. There are many disadvantages for preparing shielding materials with complex structures by traditional manufacturing method, such as a long manufacturing cycle, high mold cost, low mold utilization rate and easy to cause lead pollution. Therefore, it is necessary to develop a new gamma-ray shielding composite material based on advanced manufacturing technology, in order to meet the requirements of customized coated shielding materials for complex equipments in nuclear power plants.

3D printing technology is an additive manufacturing technology, which was born in 1980s. With this technology, rapid and free molding can be realized, and polymer materials with complex structure can be manufactured conveniently, quickly and at low cost. In this paper, a new type of nylon-tungsten shielding composite materials is prepared by 3D printing technology, in which thermoplastic nylon is used as matrix material, and tungsten is used as functional filler. Through the research of powder mixing process and shielding performance, the best material formula is obtained, and the shielding protection problem of complex components in nuclear power site is solved effectively.

2   3D Printing Radiation Protection Material Design

3D printing is a new type of additive manufacturing technologies compared with the current traditional manufacturing technologies (such as turning, milling, planning, grinding, etc.). This technology is a rapid manufacturing technology by which materials can be fusioned in one-time. Based on digital model files, it uses powdery metal or plastic and other bindable materials to construct three-dimensional objects by printing layer by layer and superimposing different shapes [8]. Compared with traditional manufacturing process, 3D printing has some advantages as followed: (1) Rapid free forming without

mold; (2) Short manufacturing cycle and low cost; (3) near net shape and even net shape of complex structure; (4) Full digitalization; (5) multi-materials arbitrary composite manufacturing.

At present, the most widely used radiation protection materials are those containing the elements with high atomic numbers such as lead and tungsten. Lead is toxic and has a "Pb weak absorption zone" for rays with energy between 40–88 keV, which is easy to produce secondary bremsstrahlung radiation. In addition, lead has poor structural strength and is not resistant to high temperature. It is commonly used as lead containers, movable screens, lead bricks, etc. Tungsten has high density and atomic number. As an ideal shielding material, it has many advantages, such as good ray shielding effect and no secondary electron radiation produced [9]. It is an environmentally friendly radiation protection material with the strong ability of ray protection. However, tungsten has the characteristics of high melting temperature, high strength, poor plasticity and toughness, so it is difficult to process it into parts with complex shapes. Nylon is one of the engineering materials with the characteristics of excellent mechanical properties, low cost, easy processing and widely used, especially commonly used as one kind of 3D printing materials. It is a practical and effective way to solve the above problems by using nylon powders as substrate and the filler of tungsten powders to prepare nylon-tungsten composite products with complex shapes, which is based on 3D printing technology. Nylon-tungsten composites belong to the environmentally friendly materials. It is particularly important that the parts with complex shapes, which are difficult to be formed with pure tungsten, can be easily produced by using 3D printing technology with nylon-tungsten composites. Based on the above analysis, a new nylon-tungsten gamma-ray shielding composite was prepared by using 3D printing technology with thermoplastic nylon as the matrix and tungsten powders as the functional filler, which can meet the customized shielding requirements of the complex components in the control area of nuclear power plant.

3   Materials and Method

3.1   Raw Materials and Forming Process

The median particle size of tungsten particles with 99.99% pure is 15–20 μm, while the median particle size of nylon powders is 50–55 μm.

Composite materials are composed of polymer materials and metal materials. 3D printing technology that can both print nonmetallic materials and metal materials mainly includes fused deposition modeling (FDM), stereo lithography apparatus (SLA) and selective laser sintering (SLS). Table 1 shows the comparison of three process types of 3D printing technology. Compared with SLA and FDM, SLS has the following advantages: (1) SLS process is applicable to a wide range of materials, and the powder laying process adopted by SLS process is more suitable for mixed materials printing with great different density such as nylon powder and tungsten powder, which can ensure the dispersion and distribution of tungsten powder particles in nylon matrix; (2) SLS process is better than SLA and FDM process in forming precision and forming speed; (3) The SLS printing environment is generally a sealed space with inert gases such as argon as the protective gas. There is no risk of toxic and harmful substances being released during

the printing process; (4) SLS does not need supporting materials, and is more suitable for the preparation of complex structural parts. Comprehensively considering material applicability, precision, forming efficiency and other factors, SLS printing process is chosen as the best one of the 3D printing process of shielding composite materials.

Table 1. Comparison of Process Types

Process	Precision/mm	Volume molding rate/cm^3·h^{-1}	Support	Applicable materials	Printing environment
SLA	±0.1	1000–2000	need	Photohardening resin	seal
FDM	±0.3	500–1000	need	Thermoplastics	open
SLS	±0.1	2000–3000	no need	Thermoplastics, Low melting point metal powder, ceramic powder	Sealing, protection gas

Figure 1 shows the molding principle of the SLS process of shielding composite materials. When the laser acts on the mixed powder of nylon and tungsten, the mixed powder absorbs heat, and its temperature gradually increases. When the temperature reaches the melting temperature (T_R) of nylon powder, the nylon powder changes from a solid state at room temperature to a liquid viscous flow state. As the temperature increases, the viscosity of the melt decreases, but its fluidity increases. It is easy to contact with the surrounding particles of tungsten powders. After cooling, the melt nylon powder solidifies and binds together. The particles of tungsten powders are uniformly dispersed in the nylon matrix without any change. The parts of the shielding material which are molded by laser selective sintering, mainly bond tungsten powder particles together through the adhesion of nylon. The adhesion value is determined by the cohesion and adhesion force of liquid nylon. Cohesion force refers to the force between the molecules of nylon binder itself, that is, the strength of nylon. Adhesion force is the force between the particles of nylon and tungsten powders, that is, the force of nylon adhering to the surface of tungsten powders.
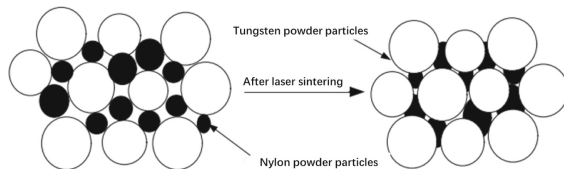
Fig. 1. SLS Forming Principle of Shielding Composites Material

Figure 2 shows the process flow of the shielding material prepared by 3D printing. The specific preparation process is as follows: Firstly, a certain quality of nylon powder

and tungsten powder are mixed according to the design ratio by the mixing process; Secondly, the fully mixed nylon and tungsten powders were put into the laser selective sintering 3D printing equipment. After preheating the mixture and parameter settings, including laser power, scanning speed, scanning spacing and scanning mode, researchers input the model size of the printing part, and start printing; Finally, the sample was taken out for post-treatment. The powder adhered to the sample surface was removed, and then the sample was polished to make its surface bright, as shown in Fig. 3. During the preparation of 3D printing composite shielding materials, the batching design, mixing process and SLS sintering process are the most important factors, which affect the shielding performance, mechanical properties and forming accuracy of the shielding material.
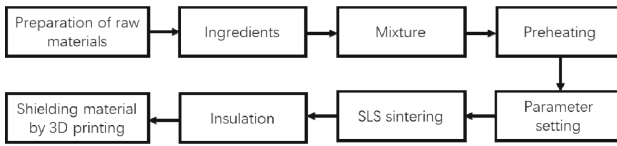
Fig. 2. 3D Printing Shielding Material Preparation Process
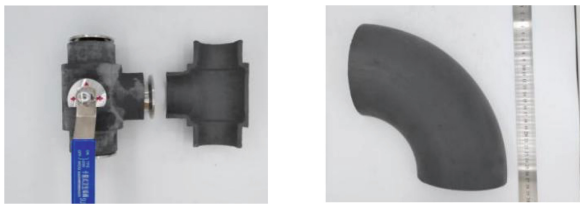
Fig. 3. 3D Printing Nylon-Tungsten Composite Shielding Material

3.2 Test and Analysis

The gamma shielding performance test of radiation protection composite materials was conducted with 137Cs (0.662 meV). The radiation decay rate of the sample was tested by standard device of γ-ray radiation amount (protection level) and dosimeter, according to GBZT 147-2002.

4 Results and Discussion

4.1 Composite Powder Mixing Process

At present, there are two main methods for preparing composite powders suitable for SLS printing, including the mechanical mixing method and the film coating method.

4.1.1 Mechanical Mixing Method

Mechanical mixing method is to mix polymer powders and filler powders mechanically in the mixer for three-dimensional movement, high speed kneading machine and other mixing equipments. The tungsten powder and nylon powder with a certain mass ratio were put into the double-motion mixer and mixed for 30 min. The surface appearance of the composite powder is shown in Fig. 4 (a). The mechanical mixing method is simple in process, low in equipment requirements, and economical. However, when the particle size of filler powders is very small (for example, less than 10 microns), or when the proportion of the filler powders (for example, metal powders) is much larger than that of polymer, it is difficult to disperse inorganic filler particles evenly in the polymer matrix by mechanical mixing method. The powder particles are easy to segregate during transportation and SLS powder laying, which leads to the existence of non-uniform distribution of filler particle aggregates in SLS formed parts, resulting in the decrease of capability of the products.

4.1.2 Film Covering Method

The coating method is to coat the polymer material on the outer surface of the filler powders to form a kind of composite powders with a polymer coating. The steps of preparing the shielding composite material powder by the film coating method are as follows: putting nylon powders, tungsten powders, coupling agent, leveling assistant into a stainless steel reaction kettle in a certain proportion, sealing and injecting nitrogen for protection, slowly heating up to about 150 °C, so that nylon powders are completely dissolved in solvent, then cooling the kettle to room temperature at a certain rate under vigorous stirring, and solid-liquid separation is carried out to obtain precipitated coated composite powders. After vacuum drying, crushing and sieving the obtained aggregates, the composite material containing nylon coated tungsten powders with suitable particle size distribution can be obtained. The surface appearance of the powder is shown in Fig. 4(b). In the coated powder, the filler and polymer matrix are mixed evenly without the segregation phenomenon in the process of transportation and powder spreading.
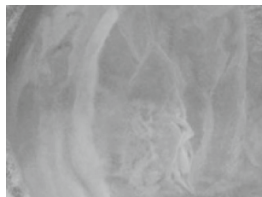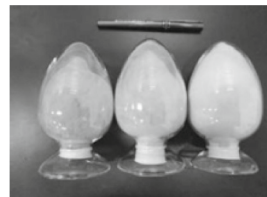
a) Preparation of powder by   b) Preparation of powder by film
mechanical mixing   coating

Fig. 4. Nylon-tungsten composite powder

According to the characteristics of the two composite powder mixing processes, nylon can be coated on the surface of tungsten powders uniformly by coating method.

The particle size of the nylon is significantly reduced during melting, coating on the surface of tungsten powder particles to achieve adhesion effect, so that the dispersion of tungsten powders in nylon matrix is more uniform.

4.2 Shielding Performance Research

4.2.1 Theoretical Shielding Efficiency of Composites

In the study of γ-ray shielding materials, the shielding performance of the materials was simulated in advance, which facilitated formulation design and adjustment. WPA1, WPA2, WPA3, WPA4, WPA5 and WPA6 were defined as different proportions of tungsten and nylon. The material proportions are listed in Table 2. The simulation of 90% (mass ratio) of tungsten powder ratio was not carried out because the sample could not be formed in the machine.

Table 2. Proportions of shielding composite materials

Material type	Raw material ratio
WPA1	60%W + 40%PA
WPA2	65%W + 35%PA
WPA3	70%W + 30%PA
WPA4	75%W + 25%PA
WPA5	80%W + 20%PA
WPA6	85%W + 15%PA

The linear attenuation coefficient model of the shielding composites was established. The theoretical shielding coefficients of the composites were calculated by MCNP (Monte Carlo N Particle Transport Code) program. MCNP is a general software package developed by Los Alamos National Laboratory (LANL) based on Monte Carlo method for computing neutrons, photons, electrons or coupled neutrons, photons, electrons transport problems in complex three-dimensional geometry. It can greatly save research funds and time by simulating shielding performance of materials with MCNP. The calculation model is shown in Fig. 5. The source is a unidirectional point source, which is 1m away from the detection point and 0.46 m away from the material surface. The material size is 20 cm (length) × 20 cm (width) × 1 cm (thickness). The attenuation of the material to 137Cs source was simulated, and the source energy was 0.662 meV. The radiation intensity before and after the material was recorded by F1 card. The linear attenuation coefficient μ of the composite material was obtained according to the formula (2).

All the test results were converted into linear attenuation coefficients in order to compare the test results of different formulations. The attenuation rate and linear attenuation coefficient were calculated as follows:

When gamma-rays pass through the shielding material, they will not be completely absorbed, but attenuated (intensity decreases). The attenuation relationship is shown in
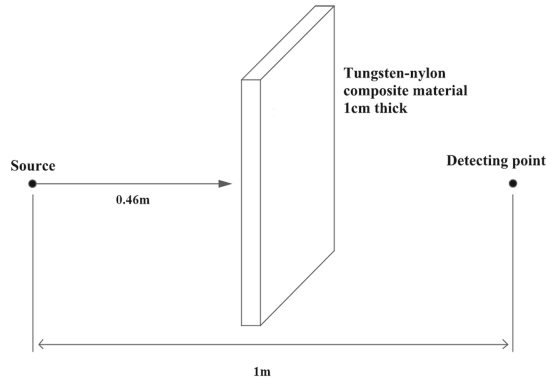
Fig. 5. Calculation model of linear attenuation coefficients of composite materials

Eq. (1):

$$R_x = R_0 e^{-\mu x} \tag{1}$$

where R_x is the dose rate after passing through a certain thickness x of shielding material;
R₀ is the dose rate before shielding;

R_0 is the dose rate before shielding;

X is the thickness of the shielding material;

and μ is the linear attenuation coefficient of the shielding material.

Formula (1) is converted to the following Eq. (2):

$$\mu = -\frac{-Ln\left(\frac{R_x}{R_0}\right)}{x} \tag{2}$$

The simulation values of linear attenuation coefficients of the shielding composites with different formulas were calculated by formula (2), which are shown in Fig. 6. The γ-ray shielding performance of composites increases exponentially with the increase of tungsten powder content. When the proportion of tungsten powders is low (<70%), the theoretical linear attenuation coefficient of the composite is low. Thus the ingredients with tungsten powder ratio between 70 and 85% were selected for 3D printing experiment.

4.2.2 Effect of Powder Ratio on Shielding Performance of Composites

According to the simulation results of linear attenuation coefficients of composite materials in Fig. 6 and combined with the powder mixing process of composite materials, the sample preparation and testing schemes of different formulas are set in Table 3. The linear attenuation coefficients of the samples with different formulas are obtained through shielding performance tests and conversion results by formula (2).

The shielding effect of the samples with different contents of tungsten powders was tested. The results are shown in Fig. 7: (1) The shielding performance of the composite is obviously improved when the mass fraction of tungsten powders increases from 70% to 80%. When the mass fraction of tungsten powders increases from 80% to 85%, the
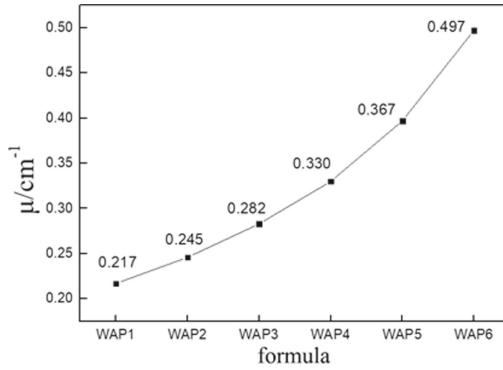
Fig. 6. Analog value of linear attenuation coefficients of composites without formula

Table 3. Test values of attenuation coefficients of samples with different formulations

Serial number	Tungsten mass fraction/%	Mixing method	γ-ray shielding rate/%	Linear attenuation coefficient/μ/cm^{-1}
1	70	Coated mixture	21.7	0.24
2	80	Mechanical mixing	21.5	0.24
3	80	Coated mixture	27.6	0.32
4	85	Coated mixture	25	0.29

shielding performance of the composite decreases. When the mass fraction of tungsten powders increases from 70% to 80%, the laser selective sintering of composites is in good condition, and there is no obvious defect in the samples. When the mass fraction of tungsten powders increases from 80% to 85%, due to the nylon content of the composite material is only 15%, cracks and warping occur in some areas of the sample during laser selective sintering, resulting in the final measured shielding performance of the composite material being lower than that of the composite material with the mass fraction of tungsten powders of 80%. (2) For mechanical mixing process, the linear attenuation coefficient of tungsten powders with 80% mass fraction is obviously lower than that of coated tungsten powders with 80% mass fraction. (3) The linear attenuation coefficient of the sample coated with film is lower than the simulation value of Monte Carlo under any tungsten powder mass ratio, which shows that there is still much room for improvement in the 3D printing process, and the uniform dispersion of tungsten powders in the matrix needs further improvement. When using the film covered mixing process, the best formula is that the mass fraction of tungsten powders and nylon matrix are 80% and 20% respectively.
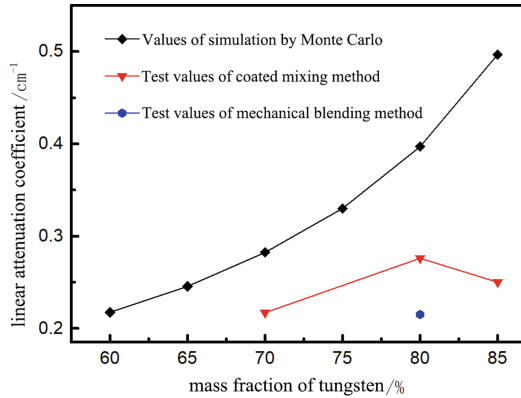
Fig. 7. Comparison of shielding capability of 3D printing shielding materials with different formulas

The main factor affecting the shielding performance of the shielding composite is the content of tungsten powders in the composite, followed by the dispersion of tungsten powders in the matrix. According to the above results, the higher the content of tungsten powders, the better the shielding performance of qualified samples. Under the condition of same mass fraction, the more uniform the dispersion of tungsten powders in matrix, the better the shielding performance of the material. The mixing process of composite powders has a great influence on the dispersion of tungsten powders in matrix.

4.2.3 Effect of Powder Mixing Process on Shielding Performance of Composite Materials

In order to further explore the reasons for the difference of shielding performance of samples under the two mixing process conditions, SEM-scan of 3D printing products of mechanical mixing and coated mixing was carried out, as shown in Fig. 8. It can be found that the macroscopic fracture surface of mechanical mixture presents obvious lines, showing typical characteristics of brittle fracture, while the microscopic fracture presents agglomeration of tungsten powders and only nylon powders in some areas (as shown in the box area in Fig. 5 (e)); In contrast, the surface of macroscopic fracture is smooth and the distribution of tungsten powder in the matrix is uniform in microstructure This also verified the results of the shielding performance experiment, and the 3D printing shielding composite products under the condition of mulching and mixing technology showed better shielding performance. The composite powder prepared by coating method has good sintering capability, high bonding strength and high forming precision, and the shielding composite powder is well coated, and almost no exposed tungsten powder is found.

The essential attribute of 3D printing radiation protection composite materials lies in its shielding performance, which is mainly reflected in the mass fraction and dispersion state of tungsten particles in the composite material. Excellent powder mixing and manufacturing process can ensure the uniform dispersion of tungsten powders in the matrix under high mass fraction and ensure the shielding performance.
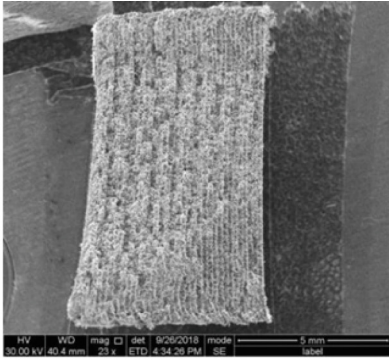
a) SEM Morphology of Macroscopic
Fracture of Mechanical Mixture
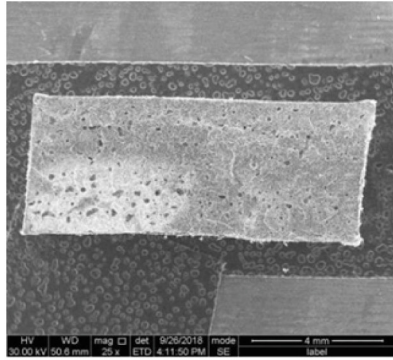
b) SEM Morphology of Macroscopic
Fracture of Coated Mixture
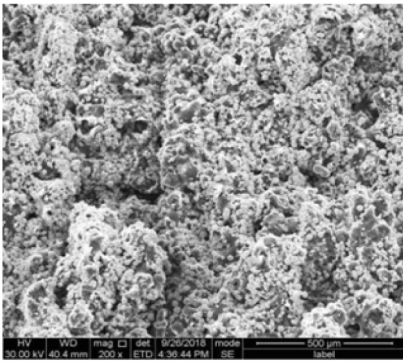
c) SEM morphology of 200 times
micro-fracture surface of mechanical mixture
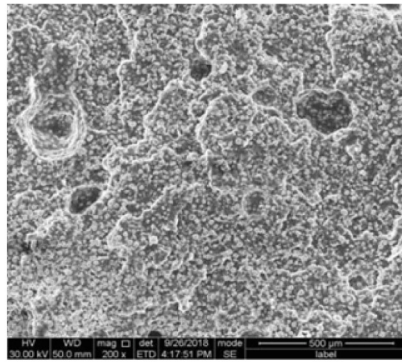
d) SEM morphology of 200 times
micro-fracture surface of coated mixture
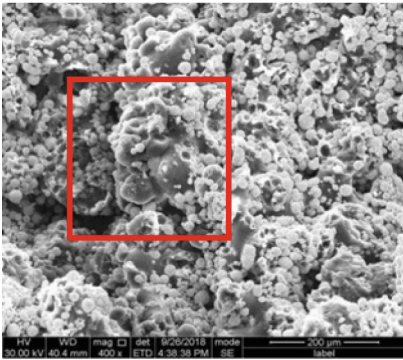
e) SEM morphology of 400 times
micro-fracture surface of mechanical mixture
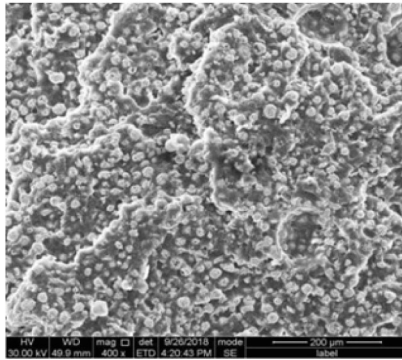
f) SEM morphology of 400 times
micro-fracture surface of coated mixture

Fig. 8. Fracture scan photo

5   Conclusions

In this paper, a nylon-tungsten gamma-ray shielding composite material was developed by using laser selective sintering 3D printing technology, and two kinds of 3D printing composite powders were prepared by mechanical mixing method and coating method, respectively. The performance of the shielding materials was studied, and the conclusions are as follows:

(1) The laser selective sintering 3D printing technology adopting the technology route of powder spreading is more suitable for the manufacture of customized and laminated shielding materials for complex components in nuclear power plants;

(2) The coating method is preferred in the mixing process of the powders of the 3D printing shielding material composite. Compared with the mechanical mixing method, the product by the former method has better shielding performance. Through 400 times SEM scanning micro-fracture morphology, tungsten powders are still uniformly dispersed in nylon matrix;

(3) By carrying out performance research on different ratios of shielding materials, the best formula of nylon-tungsten 3D printing shielding materials was obtained. By shielding performance test, the linear attenuation coefficient of the shielding material reached 0.32 at 80% of tungsten powder mass ratio, which is the best formula and can be used for shielding of complex components;

(4) 3D printing technology can conveniently, quickly and low-costly prepare customized shielding composite materials to meet the need of special-shaped parts such as valves, elbows, large and small heads in the control area of nuclear power plants. This method has practical application value, and is a powerful technical supplement to the mold manufacturing process.

 3D printing shielding composite materials can effectively solve the radiation protection problem of complex components in the control area of nuclear power plants. This study lays a theoretical foundation for the engineering application of 3D printing shielding composite materials.

References

1. Gu, H.: The effect of reasonable shielding on reducing the site radiation level. Daya Bay Nuclear Power **4**, 36–38 (2003). (in Chinese)
2. Han, Y., Yu, W., Chen, F., et al.: Investigation of temporary radiation shielding facilities in Nuclear Power Plants. Nucl. Electron. Detect. Technol. **36**(12), 1263–1267 (2016). (in Chinese)
3. Singh, V.P., Badiger, N.M., Chanthima, N., et al.: Evaluation of gamma-ray exposure buildup factors and neutron shielding for bismuth borosilicate glasses. Radiat. Phys. Chem. **98**(1), 14–21 (2014)
4. Fu, M., Wang, Y., Li, F.: Preparation of SBR rubber based flexible shield material. Nucl. Power Eng. **34**(6), 165–168 (2012). (in Chinese)
5. Zhuo, M., Li, Y., Xiao, Y., et al.: Investigation on properties of PA6/Tungsten shielding composite. Eng. Plast. Appl. **39**(3), 23 (2011). (in Chinese)
6. Ahmed, B., Shah, G.B., Malik, A.H., et al.: Gamma-ray shielding characteristics of flexible silicone tungsten composites. Appl. Radiat. Isotopes **155**, 1–7 (2019)

7. Talley, S.J., Robison, T., Long, A.M., et al.: Flexible 3D printed silicones for gamma and neutron radiation shielding. Radiat. Phys. Chem. **188**, 1–12 (2021)
8. Yang, Y., Song, C.: Technology Roadmap of Guangdong Additive Manufacturing (3D Printing) Industry. South China University of Technology Press, pp. 1–2 (2017)
9. Lin, Q., Yang, Y., He, Y.: Simulation and verification of γ-multi-layer shielding with Monte Carlo method. Nucl. Phys. Rev. **27**(2), 182–186 (2010)

Dynamic Response Analysis of Floating Nuclear Power Plant Containment Under Marine Environment

Jialin Cui[1,2], Lijuan Li[3], Meng Zhang[1(✉)], Hongbing Liu[1,2], and Xianqiang Qu[1,2]

[1] Yantai Research Institute and Graduate School, Harbin Engineering University, Yantai, China
{cuijialin001,zhangmeng}@hrbeu.edu.cn
[2] College of Shipbuilding Engineering, Harbin Engineering University, Harbin, China
[3] Nuclear Power Institute of China, Chengdu, China

Abstract. Floating nuclear containment is in a harsher environment than conventional onshore nuclear containment. In view of the Marine environment under the condition of floating nuclear power plant containment structure safety, combined water dynamics and structural mechanics, considering the containment response under random movement of hull in the Marine environment, the influence of the containment structure load calculation, thus checking containment when working in pile structure safety, provide theoretical basis for the safe operation of floating nuclear power plants. In this paper, taking a floating nuclear power plant as an example, ANSYS 2021R1, Workbench, Fluent and other software of finite element analysis are used to conduct fatigue simulation of floating nuclear power plant. The time course curve of the 6-dof motion of the ship's center of gravity is obtained, then, a remote displacement method is adopted to transfer the hull motion to the containment vessel to realize the numerical simulation of the containment vessel movement with the hull, thus to solve maximum normal stress and strain, the maximum load component of containment bearing under the action of Marine environmental load is obtained. The results show that the maximum stress and strain of the vessel increase obviously in the moving state compared with the static state of the vessel, which indicates that the random motion response of the vessel must be considered in the structural safety analysis of the floating nuclear power plant containment.

Keywords: floating nuclear power plant · Ocean circulation · containment · structural loads · Random motion response

1 Introduction

With the continuous adjustment and optimization of China's energy structure and the continuous promotion of the strategy of becoming a maritime power, traditional fossil energy and emerging energy such as wind, wave and solar energy are increasingly difficult to meet the energy needs brought about by China's coastal oil and gas resources and island development. Therefore, as a clean, efficient and flexible location of offshore

nuclear power generation technology, the national government pays more and more attention to it. Marine floating nuclear power station is a mobile floating offshore platform equipped with nuclear reactor and power generation system. It is the organic combination of mobile small nuclear power station technology with ship and ocean engineering technology. In floating nuclear power plants, a sealed steel containment structure is usually installed around the reactor and other auxiliary power generation structures to protect the normal operation of the reactor and the external environment. Compared with the traditional onshore nuclear power plant containment, the environment and load borne by the small steel containment (including support) of floating nuclear power plant at sea are very different, especially the complexity of the Marine environment leads to more complex load borne by the containment (including support). Therefore, in order to ensure the safe operation of floating nuclear power plants and protect the surrounding personnel and the external environment from nuclear radiation damage, it is urgent to carry out researches on mechanical analysis and safety evaluation technology of steel containment of floating nuclear power plants in marine environment.

The floating nuclear power plant containment vessel is not only subjected to huge vertical and horizontal loads, but also inevitably subjected to wind load, wave load and current load. Therefore, it is particularly important to analyze the dynamic response of the floating nuclear power plant containment vessel in the Marine environment. Reissner [1] studied the vibration characteristics of rigid circular foundation plate under vertical load, and proposed and verified the feasibility of elastic half-space theory in vibration research of foundation and foundation. Choprah [2] proposed the dynamic substructure method, which made numerical calculation effectively applied in this field. Lysmer et al. [3] proposed lumped parameter method, which laid the foundation for structural dynamic response analysis. Gazetas [4] and Mrakis et al. [5] proposed the calculation and analysis method of pile-soil-structure dynamic interaction, and provided empirical expressions of stiffness coefficients and damping coefficients. Fan Min et al. [6] conducted nonlinear seismic response analysis and research, and the results showed that the soil-pile-structure interaction system would affect the dynamic characteristics of the structure, resulting in the extension of the natural vibration period and the increase of damping of the system. Wang et al. [7] used hydrodynamic model to simulate the evolution of wind, wave and tide under 32 typhoon events in Bohai Bay from 1985 to 2014, and used two-dimensional Gumbel Logistic model to establish the joint distribution of wave and storm surge in Bohai Sea. De Waal and Van Gelder [8] established the joint distribution of extreme wave height and period through Copula function. Michele et al. [9] used two-dimensional Copula function to analyze the frequency of effective wave height, storm duration, storm direction and storm interval of ocean storms, and established the joint probability distribution between pairs. Xu et al. [10] established the two-dimensional joint distribution of storm surge height and effective wave height. Dong Sheng et al. [11] established the joint distribution of the annual maximum wave height and the corresponding wind speed of a jacket platform for 24 years based on Archimedean Copula function, combined with the response of the offshore platform, and found that considering the joint effect, the response of the offshore platform could be reduced in the same return period. Chen Minglu et al. [12] conducted hydrodynamic

analysis and wave load prediction for semi-submersible offshore platforms. Zhou Sulian et al. [13] studied the mooring system design of deep-water semi-submersible platform.

Due to the complex wind, wave and current environment under the action of Marine environment of floating nuclear power plant containment, the research on dynamic response characteristics of floating nuclear power plant containment is insufficient and almost no reports have been reported. Therefore, it is of great significance to carry out dynamic response analysis of floating nuclear power plant containment under Marine environment conditions, and to explore the variability and ultimate load effect of short-term time history analysis, so as to understand dynamic response characteristics of floating nuclear power plant containment under Marine environment.

The main work of this paper is to establish a hydrodynamic analysis model, using Ansys Workbench HD software module for frequency domain analysis of the platform and obtain the hydrodynamic parameters of the platform. The anchor chain model was added to the platform model to control the six degrees of freedom movement of the platform under the action of wave and flow. The HR module of Ansys Workbench software was used to conduct time-domain analysis of the platform to obtain the time-history curve of the platform motion response. The structural dynamic response analysis of the containment vessel of floating nuclear power plant under the action of wind load, wave load and current load is carried out, which provides important reference for the safe operation of floating nuclear power plant.

2 Theoretical Basis of Potential Flow

2.1 Small Scale Member

The stress of offshore floating structures in waves is studied. The stress of offshore structures is the most important topic in the field of offshore engineering, in which the wave force of piles is the basis of the stress of offshore structures. The method proposed by Morison et al. in 1950 is used to calculate wave force for small components, that is, structures whose diameter is smaller than the wavelength of the incident wave. Morison equation is basically an empirical formula, which takes wave particle velocity, acceleration and cylinder diameter as parameters to calculate the wave force in each depth of water, and then obtains the wave force along the length of the column.

Morrison et al. believed that the horizontal wave force acting on any height of the cylinder included two components:

$$f_H = f_D + f_I \tag{1}$$

Its magnitude is in the same mode as the drag force exerted on the column by unidirectional steady water flow, that is, it is proportional to the square of the horizontal velocity of the wave water point and the projection area of the unit column height perpendicular to the wave direction. The difference is that the wave water points oscillate periodically, and the horizontal velocity is positive and negative, so the drag force on the cylinder is also positive and negative:

$$f_D = \frac{1}{2} C_D \rho A u_x |u_x| \tag{2}$$

$$f_I = \rho V_0 \frac{du_x}{dt} + C_m \rho V_0 \frac{du_x}{dt} = C_M \rho V_0 \frac{du_x}{dt} \tag{3}$$

In the engineering design of floating buildings and piled offshore platforms, one of the main problems to be solved is to determine the movement, stress and deformation of these structures under the action of external forces such as wave and wind. We can regard these structures as a dynamic system, the wave action is called the input of the system, and the movement, stress and deformation of the structure are called the output of the system.

Remember this transformation as:

$$y(t) = K[x(t)] \tag{4}$$

For different systems and different inputs, the operator K may have different forms. According to the different operators, dynamic systems can be divided into linear systems and nonlinear systems. An operator is a linear system if it has the following properties, and its operator is denoted by L.

a. Superposition property

$$L[x_1(t) + x_2(t)] = L[x_1(t)] + L[x_2(t)] = y_1(t) + y_2(t) \tag{5}$$

b. The constant α can be removed from the operator

$$L[\alpha x(t)] = \alpha L[x(t)] = \alpha y(t) \tag{6}$$

therefore:

$$L\left[\sum_i \alpha_i x_i(t)\right] = \sum_i \alpha_i y_i(t) \tag{7}$$

It's called the principle of linear superposition, which means that the response of a linear system to inputs is equal to the sum of the responses of the inputs acting independently.

The following operations are linear transformations:

$$y(t) = \frac{d}{dt}x(t), \; y(t) = \int_0^T x(t)dt, \; y(t) = \varphi(t)x(t) \tag{8}$$

In Formula (1-179), $\varphi(t)$ is A non-random function. The above types are linear secondary operations. If a certain function is added, they are called linear non-secondary operations, such as:

$$y(t) = \frac{d}{dt}x(t) + \varphi(t) \tag{9}$$

Systems whose operators do not conform to the above conditions are called nonlinear systems. Linear systems are often encountered in practical work, and some nonlinear systems can be linearized within a certain range.

2.2 Large Scale Member

Ship hydrodynamic problems can be solved by frequency domain method. The frequency-domain method is based on the assumption that the wave-ship interaction has lasted for quite a long time, the initial disturbance of the incident wave and the transient influence of the initial rocking of the ship have disappeared, and the fluid motion in the field has reached a steady state. In this case, if the incident wave is harmonic, then the ship's motion is also harmonic (the encounter frequency must be the changing frequency), and the steady-state solution can be obtained in the frequency domain.

Due to the action of waves, the ship has six degrees of freedom besides constant speed forward motion. Assuming that the motion of the six degrees of freedom is small, the ship's center of gravity G point can be at. The three linear displacements (swing, roll, and heave) and the three angular displacements (roll, pitch, and yaw) around the G point in the O-XYZ coordinate system are represented. In the stable state, its displacement vector will be regarded as the harmonic quantity with the encounter frequency field as the changing frequency:

$$\{\eta(t)\} = \{\eta\}e^{i\omega t} = (\eta_1 \ \eta_2 \ \eta_3 \ \eta_4 \ \eta_5 \ \eta_6)^T e^{i\omega t} \tag{10}$$

According to rigid body dynamics, the ship motion equation with the center of gravity G as the center of moment can be expressed as:

$$[M]\left\{\ddot{\eta}(t)\right\} = \{F(t)\} = \{F\}e^{i\omega t} \tag{11}$$

For the convenience of calculation, the fluid loads acting on the hull are divided into two parts: hydrostatic loads due to changes in the position of the ship's relative hydrostatic equilibrium and hydrodynamic loads dependent on wave and ship motion. Hydrostatic load comes from the contribution of hydrostatic pressure change caused by ship movement, which can be directly given by ship statics as follows:

$$\left\{F^S(t)\right\} = -[C]\{\eta(t)\} \tag{12}$$

Among them, only 5 items of hydrostatic coefficient $C_{ij}, \ i, j = 1, 2, \cdots, 6$ are not zero, they are:

$$\begin{cases} C_{33} = \rho g A \\ C_{35} = C_{53} = -\rho g S_y \\ C_{44} = \rho g \forall h_x \\ C_{55} = \rho g \forall h_y \end{cases} \tag{13}$$

In Formula (13), A and Sy are the waterplane area of the ship and the static moment to the Y-axis, $\forall$ is the drainage volume of the ship, h_x and h_y are the transverse and longitudinal metacentric heights of the ship respectively. According to the different dimensions of the mathematical model used to solve the flow field, it can be divided into three dimensional method and two dimensional method (slice method).

The above equation shows that the free surface condition under low speed has the same form as that under zero speed.

If zero velocity radiation potential ϕ_j^0 and ϕ_j^U additional velocity potential ϕ_j^U are defined, let them satisfy continuity equation $[L]$ of the fixed solution, bottom condition $[D]$, distant radiation condition $[R]$, free surface condition and object surface condition $[S]$ defined by the following formula:

$$\begin{cases} \frac{\partial}{\partial n}\phi_j^0 = n_j, \ (j = 1, 2, ...6) \ \ It's \ on \ plane \ S \\ \frac{\partial}{\partial n}\phi_j^U = m_j, \ (j = 1, 2, ...6) \ It's \ on \ plane \ S \end{cases} \tag{14}$$

For the above fixed solution problem, the disturbance potential ϕ_j and its gradient $\nabla\phi_j (j = 1 \sim 7)$ can be determined by using appropriate numerical solution method. Introducing differential operator:

$$\frac{d}{dt} \equiv \frac{\partial}{\partial t} - U\frac{\partial}{\partial x} = i\omega - U\frac{\partial}{\partial x} \tag{15}$$

According to the linearized Bernoulli equation, the hydrodynamic pressure after deducting the change of hydrostatic pressure is as follows:

$$p(x, y, z, t) = -\rho\frac{d}{dt}\left[\phi_T(x, y, z)e^{i\omega t}\right] \tag{16}$$

3   Wave Load and Structural Response in Frequency Domain

3.1   Wave Load in Frequency Domain

A floating nuclear power plant with a total length of 229.8 m and a total weight of 83,200 tons is taken as the numerical simulation object, and the model is modeled by the APDL module in Ansys 2021R1. The finite element model of hull structure is constructed by Shell181 and BEAM188 elements. The mesh size of the bottom and supporting part of the containment is 0.1 m, the mesh size of the upper part of the containment is 0.2 m, and the mesh size of the rest of the containment is 0.8 m. The total number of the whole ship elements is about 1.56 million. The finite element model of the built floating nuclear power plant and containment vessel is shown in the figure below (Figs. 1 and 2).
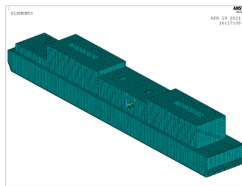
Fig. 1. Overall finite element model of floating nuclear power plant structure

In general, the hydrodynamic response of large floating body structure is a linear system. Therefore, when calculating the hydrodynamic response of the containment vessel of floating nuclear power plant under random waves, regular waves can be used
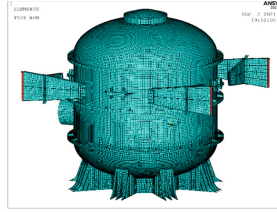
Fig. 2. Finite element model of floating nuclear power plant containment

to calculate first, and the calculated response can be divided by wave amplitude. In this way, the RAO of the floating nuclear power plant containment vessel can be obtained, which preliminarily reflects the hydrodynamic performance of the containment vessel, and then the HD module in Ansys Workbench is used for frequency domain analysis. As the floating nuclear power plant in this paper is symmetric about X-axis and Y-axis, the dynamic response caused by waves within the range of 0°–180° to the containment vessel of floating nuclear power plant is mainly analyzed. A wave direction is set every 15°, which is divided into 13 wave directions in total. The schematic diagram of wave incidence Angle is shown in the figure below (Fig. 3).
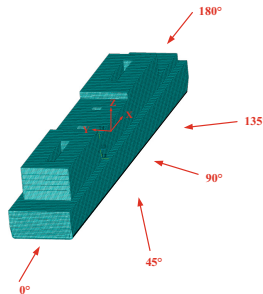
Fig. 3. Diagram of wave incidence Angle

The wave load calculation and structure analysis in this paper are based on linear theory. Under this condition, if the wave is a stationary random process, so is the alternating stress obtained by transformation. According to random process theory, the power spectral density of the above two stationary random processes has the following relationship:

$$G_{XX}(\omega) = |T(\omega)|^2 G_{NN}(\omega) \tag{17}$$

For A linear system composed of ships and waves, the stress response follows the characteristics of the linear system, and the synthetic stress can be written as $\sigma = \sigma_C + i\sigma_S$. In actual calculation, it is necessary to process the loads generated by regular waves of unit amplitude with different frequencies according to the real and imaginary parts respectively to obtain the corresponding response σ_c and σ_s, and then synthesize

it into $\sigma_A(\omega_e)$. Thus, the transfer function of stress can be written as:

$$H_\sigma(\omega_e) = \sigma_A(\omega_e) \tag{18}$$

P-m spectrum can be written as the expression of different parameters. If it is expressed by the two parameters of meaningful wave height Hs and mean zero-crossing period Tz, the expression of wave spectrum can be written as follows:

$$G_{\eta\eta}(\omega) = \frac{H_S^2}{4\pi}(\frac{2\pi}{T_Z})^2\omega^{-5}\exp(-\frac{1}{\pi}(\frac{2\pi}{T_Z})^4\omega^{-4}) \tag{19}$$

In the analysis, the actual response frequency should be the encounter frequency A, and its relationship with wave frequency A is as follows:

$$\omega e = \omega(1 + \frac{2\omega U}{g}\cos\theta) \tag{20}$$

Therefore, the response spectrum of stress can be expressed as:

$$G_{\chi\chi}(\omega_e) = |H_\sigma(\omega_e)|^2 G_{\eta\eta}(\omega_e) \tag{21}$$

3.2 Structural Response Calculation of Wave Load

In the pre-processing of AQWA, the mass information and moment of inertia information of the hull structure need to be obtained through the whole ship finite element analysis. The incident wave direction interval is 15°, the number of wet surface units of the hydrodynamic model is 20403, and the total number of units is 38559, as shown in the figure below (Fig. 4).
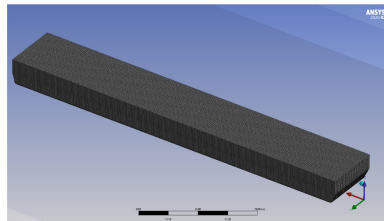
Fig. 4. Hydrodynamic model

The calculated frequencies of waves in the frequency domain were 0.01592 Hz–0.27 Hz, and 48 calculated frequency points were interpolated at equal intervals, totaling 50 calculated frequency points.

In AQWA calculating unit amplitude structural response under the action of amplitude, according to the main control parameters (RY), namely the total longitudinal bending moment, derived the relationship between the frequency and phase, and then according to the wave height (2 m), wave Angle of incidence, frequency and phase extraction wet surface wave pressure and the ship's hull acceleration, and loads it into structural response of the hull computation, as shown in the figure below (Figs. 5 and 6):
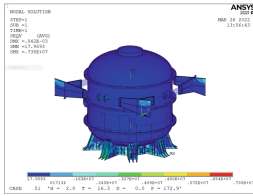
Fig. 5. Stress cloud of containment at wave frequency 0.06139 Hz
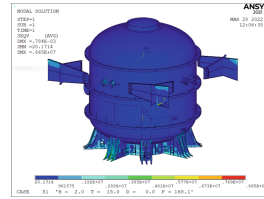
Fig. 6. Stress cloud of containment at wave frequency 0.06688 Hz

4 Wind Load and Structural Response

4.1 Wind Load

The wind load rapid loading plug-in currently in use is based on API 4F specification: "Drilling and Workover Structure Specification", 2008 edition. Typical structural analysis is derrick, fan pile leg and jacket platform. The API Wind load Quick loading plugin is limited to API 4F specification profiles and methods and is not intended for general use. Other wind codes (like ASCE 7-05/7-10) are not included in this plugin.

This plug-in has the following advantages:

(1) Suitable for different geometric types. No matter solid, shell or beam structure can take advantage of this plug-in.
(2) Enable load step selection, allowing multiple wind load conditions.
(3) Directly implement API 4F specification, allowing factor coverage.
(4) Wind load can be applied to the leeward side.
(5) The actual windward surface can be detected.

The total wind force on the structure is estimated by the vector sum of the wind force acting on individual components and accessories, as shown in the following formula:

$$F_{\mathrm{m}} = 0.00338 \times K_i \times V_z^2 \times C_s \times A \tag{22}$$

$$F_t = G_f \times K_{sh} \times \Sigma F_m \tag{23}$$

In Eqs. (3-1) and (3-2):

F_m – The force of the wind perpendicular to the vertical axis of a single member, or to the surface of the wind wall, or to the projected area of the appendage.

K_i – a factor of the inclination Angle φ between the longitudinal axis of a single member and the wind.

V_z – Local wind speed at altitude Z.

C_s – shape coefficient.

A – The projected area of A single member is equal to the length of the member multiplied by its projected width with respect to the normal wind component.

G_f – Gust effect factor, used to explain spatial coherence.

K_{sh} – the conversion factor for the total shielding of a member or accessory and the variation of airflow around the end of the member or accessory.

Ft – the vector sum of wind forces acting on each individual member or accessory throughout the drilling structure.

4.2 Structural Response Calculation of Wind Load

In this paper, the wind-loading plug-in in ANSYS Workbench is used. Firstly, the structural model of floating nuclear power plant is fixed rigidly and released inertia, and then constant Wind load is carried out on the Wind receiving surface of floating nuclear power plant (Wind speed $50.7 = 98.56$ knot, Wind direction: 13, $0°$ to $180°$ with wind direction set at $15°$ intervals), at the same time, then export the result file, and perform post-processing in classic ANSYS.

The wind speed is 50.7 m/s, and the maximum equivalent stress of the containment is 8.15 MPa. The maximum stress occurs at the junction between the upper support and the bulkhead, as shown in the figure below (Figs. 7, 8 and 9).
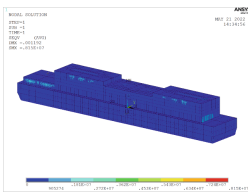
Fig. 7. Ship - wide stress cloud
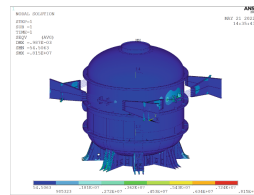
Fig. 8. Containment stress cloud map
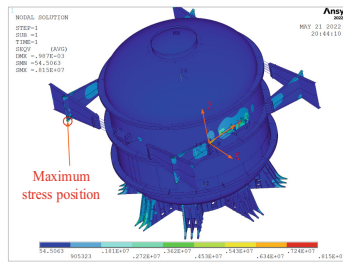
Fig. 9. Maximum stress and position of containment under wind load

5 Flow Load and Structural Response

5.1 Current Loading

Ocean currents can be caused by many factors, such as local stationary currents caused by ocean circulation, tidal currents caused by periodic changes in the gravitational pull of the sun and moon on the Earth, differences in the density of ocean water, and the action of wind. It should be pointed out that the speed of wind on the sea surface is

about 3% of the speed at 10 m above the sea surface. Tidal currents have an important influence on the flow field in some restricted waters. Tidal currents in restricted waters generally have a speed of 2–3 m/s and a maximum of 10 m/s.

For floating bodies, the flow of the ocean surface is of greatest concern to us. However, for the mooring system at sea, the distribution of water flow along the water depth is also our concern. For the designers, the maximum limit flow encountered during the operation of floating body is the most important factor affecting the design, so the actual measurement and monitoring of water flow velocity is essential. Since the velocity and direction of the water flow change slowly, we can approximately consider the water flow to be steady.

The action of water flow on floating body can be divided into the following two parts:

(1) Viscosity effect. Viscosity resistance due to frictional effects, and differential pressure resistance. For blunt body, the friction resistance can be ignored, and the pressure difference resistance is mainly.

(2) Influence of potential flow. The lift effect caused by the ring volume and the drag effect caused by the free surface effect are small in comparison.

Using flow force coefficient to estimate the flow load on the surface ship floating body:

The flow force/moment can be calculated by the following formula, in which the flow force coefficients are usually determined by model test methods.

$$\left.\begin{aligned} X_c &= \frac{1}{2}\rho v_c^2 C_{X_c}(\alpha_c) A_{TS} \\ Y_c &= \frac{1}{2}\rho v_c^2 C_{Y_c}(\alpha_c) A_{LS} \\ N_c &= \frac{1}{2}\rho v_c^2 C_{N_c}(\alpha_c) A_{LS} L \end{aligned}\right\} \tag{24}$$

Similar to the wind load calculation of ship type floating body, the key to the flow load of ship type floating body is how to obtain the flow load coefficient, which is mainly obtained by model test.

For the calculation of flow load of large oil tankers, OCIMF based on model test data gives flow force coefficient curves of two different bow forms, full load and ballast, which have good reference value and are widely used in engineering design and analysis of mooring ships.

Remery and Van Oortmerssen carried out an experimental study in the MARIN Tank to test the flow loads on tanker models of different profiles and sizes. Since ships are mostly slender bodies, the axial flow load is mainly caused by frictional resistance. If the axial flow velocity is small, this resistance is difficult to measure, and it is not accurate to predict the axial resistance of real ships from model tests, because the scale effect is very obvious.

The axial flow load is important for anchored vessels. The force can be estimated based on the frictional resistance of the plate. The following formula is recommended by ITTC:

$$X_c = \frac{0.075}{\left(\log_{10}(R_N - 2)\right)} \cdot \frac{1}{2}\rho V_c^2 \cos\alpha_c \cdot |\cos\alpha_c| \cdot S \tag{25}$$

$$\text{Re} = \frac{|\cos\alpha_c| V_c \cdot L}{\upsilon} \tag{26}$$

For tanker, it is generally not a problem to estimate the transverse force and yawing moment of the real ship. For the transverse flow of ocean current in an oil tanker, the ship can be regarded as a blunt body. Because the bilge radius of the hull is relatively small, it can be considered that the flow separation situation in the model and the real ship is consistent, and the transverse force and the bow rolling moment can be considered independent of the Reynolds number.

In MARIN pool, the lateral force and bow rolling moment are expanded into Fourier series through experiments.

$$C_{Y_c}(\alpha_c) = \sum_1^n b_n \cdot \sin(n \cdot \alpha_c) \tag{27}$$

$$C_{N_c}(\alpha_c) = \sum_1^n c_n \cdot \sin(n \cdot \alpha_c) \tag{28}$$

The above formula can be applied in deep water, but for shallow water, the lateral force and bow torque coefficients need to be multiplied by a correction factor. In practice, the free surface effect is small for deep water with flow rates of 3kn.

5.2 Structural Response Calculation of Flow Load

In this paper, Workbench Fluent and classical ANSYS 2021R1 are used to realize flow field analysis and structural response calculation. The viscous flow model, namely K-Omega (2EQN) SST model, is selected for flow field analysis. A THREE-DIMENSIONAL flow field model is established in Workbench DM module, and the flow field size is $500 \times 600 \times 27.6$ (m), as shown in the figure below (Fig. 10):
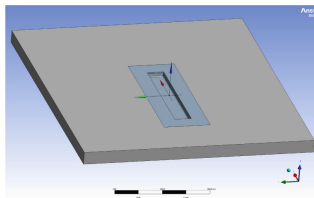
Fig. 10. 3d model of flow field

The mesh of fluid domain is divided in Workbench mesh module. The mesh size of near-field fluid domain is 1.5 m, and that of far-field fluid domain is 3.5 m. The flow field and structural stress (75° flow direction as an example) corresponding to flow velocity of 0.83 m/s are shown as follows (Fig. 11):

At a flow rate of 0.83 m/s and a flow direction of 75°, the maximum equivalent stress of the containment fourth strength is 1.15 MPa. The maximum stress occurs at the arc transition of the equipment base inside the containment vessel, as shown below (Fig. 12).

（a）Wet surface pressure cloud of hull

（b）motion pattern

（c）Ship - wide stress cloud

（d）Containment stress cloud map
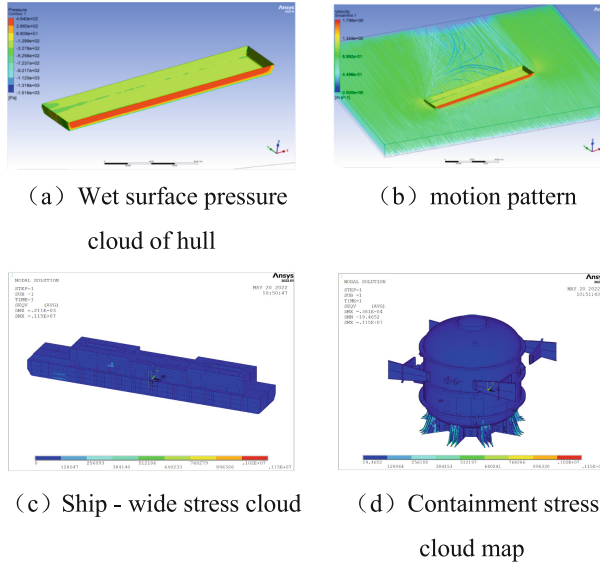
Fig. 11. Calculation results of 75° flow direction
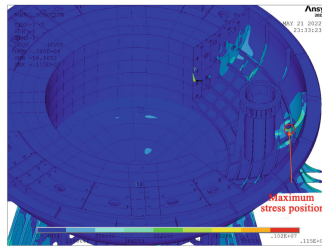
Fig. 12. Maximum stress position

6 Conclusions

(1) Under the action of wave load in the frequency domain, the maximum load component (absolute value) of the containment support is as follows: $F_X = 2.68 \times 10^5 N$ (wave direction 60°), $F_Y = 5.89 \times 10^6 N$ (wave direction 90°), $F_Z = 1.16 \times 10^6 N$ (wave direction 90°), $M_X = 3.93 \times 10^7 N \cdot m$ (wave direction 90°), $M_Y = 1.93 \times 10^6 N \cdot m$ (wave direction 75°), $M_Z = 1.13 \times 10^5 N \cdot m$ (wave direction 105°). This part of the resultant force only includes the structural response caused by waves, not the structural response caused by static equilibrium.

(2) Under the action of wave load in the frequency domain, the maximum equivalent stress of the containment vessel appears when the wave direction is 90° and the frequency is 0.09433 Hz, and the size is 98.3 MPa. The maximum stress occurs at the junction between the upper support and bulkhead.

(3) When the wind speed is 50.7 m/s and the wind direction is 75°, the equivalent stress of the fourth strength of the containment vessel is the largest, which is 8.15 MPa. The maximum stress occurs at the junction between the upper support and bulkhead.

(4) When the flow velocity is 0.83 m/s and the flow direction is 75°, the equivalent stress of the fourth strength of the containment vessel is the largest, which is 1.15 MPa. The maximum stress occurs at the arc transition of the equipment base inside the containment vessel.

(5) The wind speed and flow velocity are 50.7 m/s and 0.83 m/s respectively, and the maximum structural stress caused by wind load and flow load is 8.15 MPa and 1.15 MPa respectively, which can be almost ignored. Therefore, wind load and flow load can be ignored in the analysis of ultimate load.

References

1. Reissner, E.: Stationare, axisalsy mmetrische, dutch eine Schuttelnde Masse e,egte. chwingun-gen eines homogegen elastischen Halbranmes. Ingenianr-Archiv, Band **7**(6), 381–396 (1936)
2. Chopra, A.K., Perumalswami, P.R.: Dam foundation interaction during earthquakes. In: Proceedings of 4th WCEE, Santiago, Chile (1969)
3. Gou, M.: Pile-soil-bridge dynamic interaction in seismic response analysis of Bridges. Qingdao University of Technology, Shandong (2011)
4. Gazetas, G., Mrakis, N.: Dynamic pile-soil-pile interaction part I: analysis of axial vibration. Earthquake Eng. Struct. Dynam. **20**(2), 115–132 (1991)
5. Mrakis, N., Gazetas, G.: Dynamic pile-soil-pile interaction part II: analysis of lateral vibration. Earthquake Eng. Struct. Dynam. **21**(2), 145–162 (1992)
6. Fan, M., Xie, M.Y., Bu, R.F.: Nonlinear seismic response analysis of soil-pile-structure interaction system. Earthq. Eng. Eng. Vib. **5**(3), 6–12 (1985)
7. Wang, Y., Mao, X., Jiang, W.: Long-term hazard analysis of destructive storm surges using the ADCIRC-SWAN model: a case study of Bohai Sea, China. Int. J. Appl. Earth Obs. Geoinf. **73**, 52–62 (2018)
8. de Waal, D.J., van Gelder, P.H.A.J.M.: Modelling of extreme wave heights and periods through copulas. Extremes **8**(4), 345–356 (2005)
9. De Michele, C., Salvadori, G., Passoni, G., et al.: A multivariate model of sea storms using copulas. Coast. Eng. **54**(10), 734–751 (2007)
10. Xu, H., Xu, K., Lian, J., et al.: Compound effects of rainfall and storm tides on coastal flooding risk. Stoch. Env. Res. Risk Assess. **33**(7), 1249–1261 (2019)
11. Dong, S., Zhai, J.J., Tao, S.S.: Combined statistical analysis of wind and wave based on Archimedean Copula function. J. Ocean Univ. China (Nat. Sci. Edn.) **44**(10), 134–141 (2014)
12. Chen, M.L., Ji, C.Y., Liu, Z.: Hydrodynamic analysis and wave load prediction for semi-submersible offshore platforms. Mar. Technol. **31**(4), 68–70 (2012)
13. Zhou, S.L., Nie, W., Bai, Y.: Design and research on mooring system of deep water semi-submersible platform. Ship Mech. **14**(5), 495–502 (2010)

Research on Process Diagnosis of Severe Accidents Based on Deep Learning and Probabilistic Safety Analysis

Zheng Liu[1]([✉]) and Hao Wang[2]

[1] CNNC Key Laboratory on Severe Accident in Nuclear Power Safety, CNPE, Beijing, China
`liuzheng.2009@tsinghua.org.cn`
[2] Department of Engineering Physics, Tsinghua University, Beijing, China

Abstract. Severe accident process diagnosis provides data basis for severe accident prognosis, positive and negative effect evaluation of Severe Accident Management Guidelines (SAMGs), especially to quickly diagnose Plant Damage State (PDS) for operators in the main control room or personnel in the Technical Support Center (TSC) based on historic data of the limited number of instruments during the operation transition from Emergency Operation Procedures (EOPs) to SAMGs. This diagnosis methodology is based on tens of thousands of simulations of severe accidents using the integrated analysis program MAAP. The simulation process is organized in reference to Level 1 Probabilistic Safety Analysis (L1 PSA) and EOPs. According to L1 PSA, the initial event of accidents and scenarios from the initial event to core damage are presented in Event Trees (ET), which include operator actions following up EOPs. During simulation, the time uncertainty of operations in scenarios is considered. Besides the big data collection of simulations, a deep learning algorithm, Convolutional Neural Network (CNN), has been used in this severe accident diagnosis methodology, to diagnose the type of severe accident initiation event, the breach size, breach location, and occurrence time of the initial event of LOCA, and action time by operators following up EOPs intending to take Nuclear Power Plant (NPP) back to safety state. These algorithms train classification and regression models with ET-based numerical simulations, such as the classification model of sequence number, break location, and regression model of the break size and occurrence time of initial event MBLOCA. Then these trained models take advantage of historic data from instruments in NPP to generate a diagnosis conclusion, which is automatically written into an input deck file of MAAP. This input deck originated from previous traceback efforts and provides a numerical analysis basis for predicting the follow-up process of a severe accident, which is conducive to severe accident management. Results of this paper show a theoretical possibility that under limited available instruments, this traceback and diagnosis method can automatically and quickly diagnose PDS when operation transit from EOPs to SAMGs and provide numerical analysis basis for severe accident process prognosis.

Keywords: Process Diagnose · Process Traceback · EOP · SAMG · Deep Learning · PSA · ET · MAAP

1 Introduction

The application of the concept of defense in depth is the primary means of preventing accidents in a nuclear power plant and mitigating the consequences of accidents if they do occur [1]. If an accident occurs at a nuclear power plant, to restore safety, two types of accident management guidance documents are typically used: EOP for preventing fuel rod degradation, and SAMG for mitigating significant fuel rod degradation when a severe accident is imminent [2]. And the relationship between different components of an Accident Management Programme (AMP) is illustrated in Fig. 1. Preventive accident management EOPs integrate actions and measures needed to prevent or delay severe damage to the reactor core. Mitigatory accident management SAMGs refers to those actions or measures which become necessary if the preventive measures fail and severe core damage occurs or is likely to occur [3].
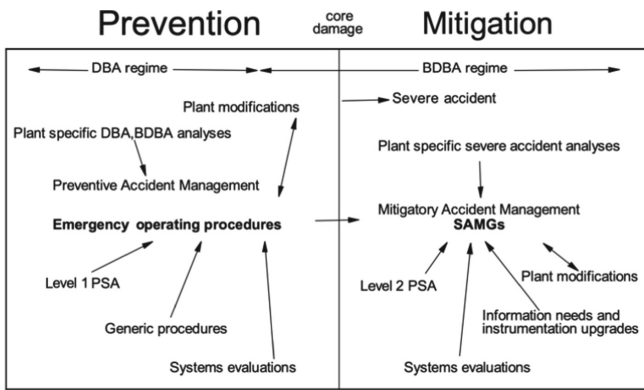
Fig. 1. Relationship between EOPs and SAMGs

Severe accident management guidelines should be comprehensively Verified and Validated [4] (V&V). Implementing and enhancing the existing SAMG program in NPPs is an important post-Fukushima activity [5]. Expert judgment, simulators, field training, tabletop exercises, emergency drill, and exercise and analysis are current practices related to SAMG V&V. Moreover, informing SAMG and actions through analytical simulation is a practical and commendable practice [5].

While numerical simulation is scenario/event based from initiating event to core damage, and even to fission product release to the off-site environment. There is a great challenge that SAMGs take an integrated, symptom-and-knowledge-based approach [5], and that means, SAMGs contain actions to be taken that are based on the values of directly measurable plant parameters [6].

SAMEX, a decision support system, is developed for use in severe accident management following an incident at a nuclear power plant [6]. Risk-informed severe accident risk database management module (RI-SARD), which is a risk-informed accident diagnosis and prognosis module of SAMEX [7], examines (a) a symptom-based diagnosis of a plant damage state (PDS) sequence in a risk-informing way and (b) a PDS sequence-based prognosis of key plant parameter behavior, through a prepared database, SARDB,

which stores the data of integrated severe accident analysis code results like MAAP and MELCOR for hundreds of high-frequency scenarios from the plant damage state event tree of a Level 2 PSA. RI-SARD predicts a series of potential severe accident sequences that match the user-specified symptom criteria, and then prioritizes and adds more symptoms to screen down scenarios for prognosis analysis.

The accident process diagnosis and prognosis method, with fast-running severe accident codes and scenario selection, used in SAMEX, fills the gap between symptom-based analysis and event-based analysis. But with the given symptom of key parameters of NPPs, a small set of initiating events and sequences may lead to a similar plant damage state, and this method is not precisely focused on one scenario, which means multiple parallel sub-section simulations should be conducted to provide information for users to select.

Numerically reproducing symptom-based scenarios and selecting a small set of accident sequences to be simulated is practical in accident process diagnosis for SAMG implementation and assessment. Ideally, the selection of scenarios to be simulated should be made from the results of both Level 1 and Level 2 PSA [5], whereas only Level 2 PSA result is used in SAMEX.

The main purpose of this paper is to: 1) a concept of risk-and-knowledge informed diagnosis and prognosis of plant damage state during the entrance of SAMG, tracing back process progression from initiating event to core damage; 2) a feasible way to select only one scenario from the result of Level 1 PSA, especially ET, for numerically decision support for SAMG implementation and assessment, with an application of advanced algorithms, deep learning, in Artificial Intelligence (AI).

2   AI Application in Accident Diagnosis of NPPs

Since the 1980s, with the field of artificial intelligence evolved, kinds of artificial intelligence methodologies are implemented for accident diagnosis in NPPs.

Jaques Reifman [8] provides a comprehensive survey of computer-based diagnostic systems using artificial intelligence techniques that have been proposed for the nuclear industry up to 1997. Two computing tools: expert systems or Artificial Neural Networks (ANNs), are used for artificial intelligence-based systems for process diagnostics. Hybrids of them and a combination of these technologies with numerical quantitative simulation programs have also been proposed.

The early diagnostic approaches were based on expert systems, and then ANNs before the 21st century, which follows chronologically the popularity of these artificial intelligence technologies.

Kinds of diagnosis systems were developed based on an expert system. REACTOR, an expert system for diagnosis and treatment of nuclear reactor accidents, was developed at the beginning of the 1980s in the U.S.A [9]. DISKET, which is based on knowledge engineering in the field of expert systems, has been developed to identify the cause and the type of abnormal transient of a nuclear power plant in the middle of the 1980s in Japan [10]. ADAM, an accident diagnostic, analysis, and management system application for severe accident simulation and management in the 2000s in the U.S.A [11]. Even in the past few years, a decision support system called SEVERA was developed in Europe [12],

aimed at supporting the decision-making team during an accident or a training exercise, using decision modeling software DEXi, which is based on if-then rules.

The ANNs method application for diagnosis in NPPs is data-driven with model training and is mainly trained with simulation data of NPPs. Diagnosis result is highly dependent on the quality of simulation results. At the early stage, numerical simulation is not quite competent for accident progression. No systemic application was built based on ANNs, only in some specific domains, ANNs were applied as a methodology basis.

But nowadays, integrated simulation code, MAAP or MELCOR, is advanced involved in the past few decades. And several diagnosis systems were developed. ADAS, using neural networks, was developed in the 2000s in Korea for accident diagnosis and support operator decision-making [13]. A severe accident diagnosis and response support system was developed in China, which uses three diagnostic methods including BP neural network method, SDG expert diagnosis, and artificial diagnosis [14].

Moreover, some other machine learning methods emerged and are applied for accident diagnosis in NPPS. A cascaded support vector regression (CSVR) model is used to predict accident scenarios, accident locations, and accident information [15]. An approach for diagnosis of multiple failures based on dynamic Bayesian networks (DBNs) is proposed to support emergency response in case of an incident [16].

Nowadays, the most popular AI technology is Deep Learning, which is a subset of machine learning and essentially a neural network with three or more layers. Related algorithms in this domain include Convolutional Neural Networks (CNN), Recurrent Neural Networks (RNN), Auto Encoder (AE), Generative Adversarial Network (GAN), etc. These algorisms greatly improve the ability to solve practical issues, such as image recognition, speech recognition, auto driving, language translation, etc. And inspires new prosperity of AI applications.

Although numerical simulation is applied to generate accident data, those AI methods mentioned above do require not a very large dataset to train the model, hundreds or even thousands of simulations may be enough. As a drawback, the diagnosis capability may be limited.

3 Traceback Accident Progression Methodology During Transition from EOP to SAMG

Following the occurrence of initiating event, EOPs are step-by-step procedures for operators in the main control room to put the NPPs into a safe state. Prevention efforts, including safety system function and human performance, with success or failure execution, direct to different branches of the progression path, which are static sets of ETs of L1 PSA. Key procedures in EOPs are simplified as header events of ETs, for example, depressurizing the primary system. This path with the uncertainty of time may produce tens of thousands of scenarios.

According to different SAMG entrance conditions, for example, core exit temperature exceeds 650 °C, TSC is formed to mitigate accident progression from large nuclide release. Plant damage state assessments are required when operation transitions from EOPs to SAMG.

With fast-running simulation code, qualitatively PDS and SAMG action assessment is conducive for accident management. But the obstacle gap between symptom-based SAMG and event-based numerical analysis needs to be filled first.

This paper promotes a traceback method for TSC, which can automatically generate an input deck of simulation code, based on chronological parameter data from initiating event occurrence time to time when SAMG entrance condition is realized. And this method is data-driven, using the good performance of deep learning algorithms to diagnose header events and their time to define a relatively reasonable scenario that confines symptoms on assessment time. It's their advantage to diagnose from big datasets for DL algorithms, while with a little number of datasets, they may diagnose with poor capability.

3.1 Traceback Methodology

The main steps are described as follows:

1) Analysis of event trees and header events selection

First, a review of event trees from publicly available Level 1 PSA is performed to select the main header events for every sequence path which causes core damage.

2) Sequences simulation and database generation

With the previously identified header events delineated for each sequence, using a simulation tool, and with the occurring time uncertainty branch, a database is produced with a large amount of CPU calculation work. The branching method will be explained in the following section. Selection of key parameters as the figure of merits is performed for simulation output.

3) Traceback model training for scenario confinement

Using DL algorithms, classification and regression models are trained with formerly generated scenarios database. This may last for weeks. Different kinds of DL algorithms are tried to be used, and hyperparameters are tuned with effort.

4) PDS diagnose with simulation and real-time instruments indicator

Put chronological real-time instrument data into DL-trained models to diagnose confined scenarios, and then generate an input deck of the simulation tool, ranging from initiating event occurrence time to the time when core exit temperature exceeds 650 °C. This defined scenario is a base scenario for the following accident simulation.

5) Prognosis and SAMG action assessment

Put SAMG action into input deck of base scenario, and following simulation code execution, which runs fast ahead of real-time, will prognosis the following accident progression with/without SAMG action.

3.2 Header Event Branches

According to step 2, header event branching is conducted in dealing with scenario uncertainties.

The third issue described in the report of OECD/NEA [5] is the treatment of simulation uncertainty for assessing SAM actions using an analytical tool. The best-estimate approach is recommended for analytical simulation because a conservative approach may not be of much help and sometimes could even lead to a wrong decision.

Despite code uncertainties, representation uncertainties, numerical inadequacies, user effects, computer/compiler effects, and plant data uncertainties for the analysis of an individual event, branching time is one important uncertainty for sequence definition. Lots of evaluation effort has been done for computer code uncertainty.

While some safety systems function automatically, there is still uncertainty between simulation and real-time accident progression. In addition, automatic safety systems may fail and manual work with delayed time may still be needed to define accident scenarios.

Besides, manual actions following up EOPs may delay branching time for diagnosis time, preparation time, and execution time.
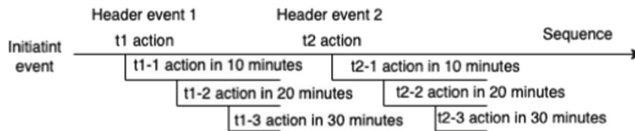
Fig. 2. Event tree branches

Kinds of breaching time for both safety systems and manual actions are simulated for scenarios, as shown in Fig. 2. For one sequence of ETs, header event 1 action should be done at time t1 as action condition is fulfilled in simulation, three branches deviated t1 time, which are 10 min after t1, 20 min after t1 and 30 min after t1. The safety system or manual actions at header event 2 is similar to header event 1, and three branches are formed with different delay times. And another three branches for t2 action are formed for a scenario with t1–2 action in 20 min. So, the permutation of delayed action time for header events makes a very large number of scenarios for one sequence of ETs.

4   Case Study – Medium Break LOCA (MBLOCA) in a Pressurized Water Reactor (PWR)

This section presents an example application of the above-referred traceback methodology to define a suitable input deck of accident progression scenario from initiating event to core exit temperature exceeding 650 °C in no more than one day, which is the basic scenario for SAMG actions implementation assessment.

The initiating event of this case study is the middle break loss of coolant accident in a pressurized water reactor. According to L1 PSA, two ETs are analyzed which differ in the position of break, one break is on one hot leg, and the other one is on one cold leg. Only hog leg ETs is analyzed in this case study.

4.1   Event Tree Analysis and Header Events Selection

The event tree of MBLOCA with a break on the hot leg is depicted in Fig. 3. There are a total of 21 sequences in this ET, 4 sequences result in bringing back to safety status (OK), and the remaining 17 sequences lead to core damage (CD), which cause different plant damage state.

Among these 17 sequences, some of them may not need to be distinguished due to their header events. For example, sequences 7, 8, and 9 are like sequences 11, 12, and 13 respectively. The difference between them is human error in safety actions or the mechanical inherent failure of these safety systems. So, 13 sequences causing CD are screened for the next steps.

Not all of the header events in Fig. 3 are used for each sequence. For example, only E01, H01, and E02 are used for scenario 2. And head events needed for each sequence are analyzed for each sequence.

Fig. 3. MBLOCA Event Trees

4.2 Event Tree Scenarios Simulation with Branches

Modular Accident Analysis Program (MAAP) is used as a numerical analysis tool for scenario simulation.

For every one of the screened 13 sequences, 10 different initiating event occurrence times, 10 break sizes, 2 break locations (near/not pressurizer), and 10 branching times for each header event are analyzed and simulated. The branching point is managed in the above-referred method. All these simulation results generate a database of knowledge on accident progression. Some parameters chosen as figure-of-merits (FOMs) are listed in Table 1.

Table 1. FOMs of simulation

No.	Parameter	Unit
1	The collapsed water level in the broken steam generator downcomer	m
2	The collapsed water level in the unbroken steam generator downcomer	m
3	Pressure in broken steam generator	Pa
4	Pressure in unbroken steam generator	Pa
5	Pressure in the primary system	Pa
6	Pressure in pressurizer	Pa
7	Pressure in accumulator	Pa
8	Core exit temperature	K
9	Boiled-up water level measured from the bottom of RPV	m
10	The collapsed water level in the cavity room	m
11	Pressure in cavity room	Pa
12	The temperature of the gas in the cavity room	K
13	The temperature of water in the cavity room	m
…	…	…

4.3 DL Models Training

1D-CNN (one-dimension convolutional neural network) algorithm is used for this modeling task. The knowledge database formally generated is used as training and testing data for classification and regression models.

The classification models include the sequence number of ETs, and break location near or not near the pressurizer.

And regression models include initiating event occurrence time, break size, and branching time for every header event in every sequence.

The result of the training models is listed in Table 2.

Due to the large scale of scenarios, weeks of training time may be needed for this task.

Table 2. Result for sequence 2 of ETs in MBLOCA

No.	Type	Description	Accuracy/Error
1	Classification	Sequence No 2	85.94%
2	Classification	If break on pressurizer side	86.09%
3	Regression	Break size	0.0262 (0.8 quantile)
4	Regression	E01 time	0.2231 (0.8 quantile)
5	Regression	H01 time	0.0944 (0.8 quantile)
6	Regression	E02 time	0.0124 (0.8 quantiles)
7	Regression	Initiating event occurrence time	0.2258 (0.8 Quantile)

4.4 Trace Back Accident Progression

Accident data from the simulator or MAAP is generated for testing 1D-CNN trained models. In the case of real implementation, parameters of instrument indicators are used for gathering chronological data of accident progression.

The task in this section is to automatically generate a defined input deck of MAAP, which relatively accurately depicts the chronological progression from initiating event to core exit temperature exceeding 650 °C. And the methodology is to input chronological data to 1D-CNN trained models and get classification and regression data for each model. These tracked back model data are written to an input deck of MAAP.

Based on this section, a basic scenario for testing accident data is confined to an input deck of MAAP.

4.5 Application of Basic Scenario for SAMG Assessment

With the above-referred tasks, TSC can diagnose plant damage state using an input deck of basic scenarios. For the prognosis of an accident, TSC personnel put related action commands for SAMG actions into this basic input deck, with the calculation result of MAAP, the negative or positive effect of these actions can be foreseeable with fast running code. And the simulation result is used for decision support of TSC.

5   Conclusions

Numerical analysis is a practical tool for SAMG assessment. But the gap between symposium-based SAMG actions and event/scenario-based numerical simulation is the first obstacle to on-time decision support. Although methods of using L2 PSA are provided, the drawback of several screened scenarios are not focused and may generate controversial calculation results.

Event trees of L1 PSA are used for scenarios database generation, and header events selection is performed to generate the skeleton of scenarios.

Uncertainty of scenarios is considered in this traceback method, with different time branching points for each header event of scenarios, and confidence is gained for the following decision-making support.

The method described in this paper is good at automatically generating an input deck for a basic scenario ranging from initiating event to core exit temperature exceeding 650 °C. And the track back result fills the gap between symposium-based SAMG actions and event-based simulations. The prognosis for SAMG assessment can be realized based on this methodology.

References

1. Safety of nuclear power plants: Design. International Atomic Energy Agency, Vienna (2016)
2. Accident management programmes in nuclear power plants. International Atomic Energy Agency, Vienna n.d.
3. Implementation of accident management programmes in nuclear power plants. International Atomic Energy Agency, Vienna (2004)
4. Accident management insights after the Fukushima Daiichi NPP accident report of the CNRA task group on accident management, p. 72 (2014)
5. Th, S.: Informing severe accident management guidance and actions for nuclear power plants through analytical simulation n.d.
6. Park, S.-Y., Ahn, K.-I.: SAMEX: a severe accident management support expert. Ann. Nucl. Energy **37**, 1067–1075 (2010). https://doi.org/10.1016/j.anucene.2010.04.014
7. Ahn, K.-I., Park, S.-Y.: Development of a risk-informed accident diagnosis and prognosis system to support severe accident management. Nucl. Eng. Des. **239**, 2119–2133 (2009). https://doi.org/10.1016/j.nucengdes.2009.06.001
8. Reifman, J.: Survey of artificial intelligence methods for detection and identification of component faults in nuclear power plants. Nucl. Technol. **119**, 76–97 (1997). https://doi.org/10.13182/NT77-A35396
9. Nelson, W.R.: REACTOR: an expert system for diagnosis and treatment of nuclear reactor accidents. In: AAAI (1982)
10. Yokobayashi, M., Yoshida, K., Kohsaka, A., Yamamoto, M.: Development of reactor accident diagnostic system DISKET using knowledge engineering technique. J. Nucl. Sci. Technol. **23**, 300–314 (1986). https://doi.org/10.1080/18811248.1986.9734987
11. Zavisca, M.J., Khatib-Rahbar, M., Esmaili, H., Adam, S.R.: An accident diagnostic, analysis and management system—applications to severe accident simulation and management. In: 10th International Conference on Nuclear Engineering, vol. 2, pp. pp. 131–136. ASMEDC, Arlington, Virginia, USA (2002). https://doi.org/10.1115/ICONE10-22195
12. Bohanec, M., Vrbanić, I., Bašić, I., Debelak, K., Štrubelj, L.: A decision-support approach to severe accident management in nuclear power plants. J Decis Syst **29**, 438–449 (2020). https://doi.org/10.1080/12460125.2020.1854426
13. Lee, S.J., Seong, P.H.: A dynamic neural network based accident diagnosis advisory system for nuclear power plants. Prog. Nucl. Energy **46**, 268–281 (2005). https://doi.org/10.1016/j.pnucene.2005.03.009
14. Chen, P., Xu, W., Yang, F., Liao, Y.: Introduction of three methods used for the nuclear accident diagnosis. In: Decontamination and Decommissioning, Radiation Protection, Shielding, and Waste Management; Mitigation Strategies for Beyond Design Basis Events, vol. 7, p. V007T11A007. American Society of Mechanical Engineers, Shanghai, China (2017). https://doi.org/10.1115/ICONE25-66433

15. Yoo, K.H., Back, J.H., Na, M.G., Hur, S., Kim, H.: Smart support system for diagnosing severe accidents in nuclear power plants. Nucl. Eng. Technol. **50**, 562–569 (2018). https://doi.org/10.1016/j.net.2018.03.007

16. Zhao, Y., Tong, J., Zhang, L., Wu, G.: Diagnosis of operational failures and on-demand failures in nuclear power plants: an approach based on dynamic Bayesian networks. Ann. Nucl. Energy **138**, 107181 (2020). https://doi.org/10.1016/j.anucene.2019.107181

Study on Calculation Method of Corrosion Product Source Term in Lead-Bismuth Fast Reactor Coolant System

Haixia Wan[✉]

China Institute of Atomic Energy, Beijing, China
`why_1022@163.com`

Abstract. In the coolant system of lead-bismuth fast reactor, the corrosion products produce great occupational radiation dose to the workers, especially in the process of maintenance and repair of nuclear facilities. Therefore, it is very important to accurately calculate the corrosion product source term caused by the reaction between coolant and structural materials. The generation, migration, decay and deposition of corrosion products are described by the corrosion characteristics of lead-bismuth alloy on stainless steel in coolant loop, and the mathematical equilibrium equation is established. The equation is used to calculate the corrosion product source term of the coolant loop in the $20MW_{th}$ lead-bismuth fast reactor and the variation laws of the corrosion product with time are obtained. The results show that the radioactivity of the corrosion products mainly comes from nuclides such as ^{51}Cr, ^{54}Mn, ^{58}Co and ^{60}Co, and the short-lived nuclides such as ^{51}Cr and ^{58}Co decay gradually after shutdown, long-lived nuclides such as 54Mn and ^{60}Co are the main sources of radioactivity.

Keywords: Corrosion Product · Coolant · Lead-Bismuth Alloy · Stainless Steel · Activity

1 Introduction

Lead-bismuth fast reactor is one of the six main types of the fourth generation reactor, which has the characteristics of safety, economy, continuity and nuclear non-proliferation. However, the corrosion ability of lead-bismuth alloy cannot be neglected, and the corrosion products caused by it should not be underestimated. Studies have shown that more than 90% of occupational exposure is caused by corrosion products deposited on the pipe wall from the coolant, which continue to decay and emit gamma rays in the pipe wall or coolant, in particular, some long-life nuclides in the shutdown for a period of time will still cause radiation damage to equipment maintenance workers. Therefore, it is important to study the generation and migration of corrosion products in the alkali metal coolant loop, predict the change and distribution of corrosion products for the radiation shielding design of lead-bismuth fast reactor, the inspection and maintenance of the reactor, and the accident analysis.

In view of the important influence of corrosion products on radiation protection, a great deal of research has been carried out at home and abroad, Such as the PWR-GALE program developed in the United States, the PACTOLE program in France, the Nuclear Power Institute, the Suzhou Thermal Engineering Institute, Tsinghua University, the North China Electric Power University Shanghai Jiao Tong University, and Harbin Engineering University. The above calculation program or method, the principle used is basically the same, but the simplification and assumptions used, as well as the specific treatment methods are not the same. The point reactor model is often used in the calculation, which does not take into account the influence of uneven distribution of neutron flux rate and coolant flow time, so its calculation precision is not high. In addition, the existing source item calculation program has some limitations; the calculation system and equipment are also specific, not universal. At present, the study on source term of corrosion products in water-cooled reactor is mainly focused in China, but there is no systematic study on source term of corrosion products for lead-bismuth coolant.

Based on the characteristics of lead-bismuth reactor coolant loop, the corrosion mechanism of lead-bismuth alloy and the corrosion rate of lead-bismuth alloy, the process of corrosion products generation, decay, migration and deposition in the loop are simulated in this paper; the mathematical equilibrium equation is established. The source term of corrosion products of lead-bismuth coolant was calculated by calculating the fast neutron reaction cross section of the reactor. This study provides reference data for related research in China.

2 Corrosion Source

2.1 Impurities in the Coolant

The impurities in the coolant mainly come from the raw materials and the impurities introduced in the operation. The lead-bismuth alloy was synthesized from lead and bismuth in the ratio of 44.5% and 55.5%, the impurities are mainly non-metallic impurities such as oxygen, carbon, and metallic impurities such as calcium. The pipelines and equipment of the reactor loop are processed, welded and cleaned in the process of manufacture, installation and maintenance, this process inevitably leaves behind some dirt, grease, gasoline, metal chips, welding slag, surface oxides and moisture, which is another major cause of contamination and impurities in the coolant system.

2.2 The Structural Material of the Coolant Channel

Lead and bismuth coolants have the characteristics of high melting point, high boiling point, chemical property inactivity and "Negative" cavitation reactivity. Lead and bismuth are chemically inert with fuels, low alloy steel, water and air. The structural material commonly used in contact with lead-bismuth alloys is stainless steel.

By analyzing the main components and impurities in stainless steel, the possible activation reaction types were determined. Finally, the radionuclide types of various corrosion products, the corresponding reaction types and the main sources of structural materials were counted; the results are shown in Table 1. The common active corrosion products in the main circuit are radionuclide as ^{24}Na, ^{51}Cr, ^{56}Mn, ^{59}Fe, ^{58}Co and ^{60}Co, and their initial nuclides are mainly Fe, Cr, Ni, Mn and Co in the structural materials.

Table 1. Source of Corrosion Products

Target Nucleus	Reaction Type	Radiation sources	Half-life	Decay constant, 1/s
^{50}Cr	^{50}Cr (n, γ) ^{51}Cr	^{51}Cr	27.72d	2.89413E−07
^{54}Fe	^{54}Fe (n, p) ^{54}Fe	^{54}Fe	312.5d	2.56721E−08
^{55}Mn	^{55}Mn (n, γ) ^{56}Mn	^{56}Mn	2.587h	7.44263E−05
^{58}Ni	^{58}Ni (n, p) ^{58}Co	^{58}Co	71.3d	1.12518E−07
^{59}Co	^{59}Co (n, γ) ^{60}Co	^{60}Co	5.26a	4.17862E−09
^{60}Ni	^{60}Ni (n, p) ^{60}Co			
^{58}Fe	^{58}Fe (n, γ) ^{59}Fe	^{59}Fe	45.1d	1.77883E−07
^{60}Ni	^{60}Ni (n, p) ^{60}Co			

3   Method of Establishment

3.1   Coolant Migration Process

When calculating the source term of corrosion products in the main loop, there are two general conditions. One is that the materials in contact with the coolant in the main circuit are first corroded and dissolved in the coolant; the other is that the material in the core is first activated by radiation, and then corroded down to dissolve in the coolant. As the coolant flows, some of the activated corrosion products in the main circuit will be deposited on the equipment or pipelines in the main circuit, most of which will be cleaned by the purification system, and some will remain in the main circuit coolant. The generation and migration of corrosion product source term in the main loop can be divided into six processes as follows:

(1) The structural material in the core is activated by irradiation;
(2) The material in contact with the coolant in the main circuit is corroded down and dissolved in the coolant to become the corrosion product;
(3) Non-radioactive corrosion products in the coolant flow with the coolant, in the main circuit migration and balance;
(4) The corrosion products in the coolant are irradiated and activated as they flow through the core;
(5) Transfer and equilibrium of radionuclide in the coolant with the coolant flow;
(6) The radionuclide in the coolant precipitates in the main circuit equipment.

3.2   Computational Model

In the coolant loop, the amount of the target radionuclide of the structural material decreases gradually with neutron irradiation.

$$\frac{dN_1}{dt} = -\overline{\sigma}_1 \overline{\phi}_1 N_1$$

$$\frac{dN_2}{dt} = \overline{\sigma}_1\overline{\phi}_1 N_1 - \lambda_2 N_2$$

In the formula, N_1 is the nuclear density of the target nucleus in the structural material; t is the time; N_2 is the nuclear density of the irradiated radionuclide; σ_1 is the average neutron activation cross section of the target nucleus; ϕ_1 is the average neutron flux rate of irradiation; λ_2 is the decay constant of the irradiated radionuclide.

The increase in radionuclide in the primary circuit due to corrosion of the reactor activated materials at constant reactor power can be calculated as follows:

$$
\begin{aligned}
R_{ci} &= \sum_l \left(\sum_j \frac{f_{ai} \cdot C_{0j} \cdot S_j \cdot N_A}{A_i} \right) \\
&= \sum_l \left(\sum_j \frac{f_{nll} \cdot f_{sIlj} \cdot C_{0j} \cdot S_j \cdot N_A}{A_i} \cdot x_i \right) \\
&= \sum_l \left[\sum_j \frac{f_{nll} \cdot f_{slj} \cdot C_{0j} \cdot S_j \cdot N_A}{A_i} \cdot \frac{-\overline{\phi} \cdot \overline{\sigma}_I}{\lambda_i} \cdot \left(1 - e^{-\lambda_i t t}\right) \right] \\
&= \frac{N_A \cdot \overline{\phi}}{A_i \cdot \lambda_i} \cdot \left(1 - e^{-\lambda_j \cdot t}\right) \sum_l \left[\overline{\sigma}_{Il} \cdot \left(\sum_j f_{nnl} \cdot f_{slj} \cdot C_{0j} \cdot S_j \right) \right]
\end{aligned}
$$

In the formula, f_{ai} is the quality share of the radionuclide in the material; C_{oj} is the material corrosion rate of module j; S_j is the corrosion area of module j; N_A is the Amado Avogadro constant; A_i is the atomic weight of radionuclide I; f_{sILj} is the mass share of the nuclide chemical element in the material composition of module j; f_{nIl} is the natural abundance of the target nucleus; λ_i is the decay constant of radionuclide i.

When the reactor power is constant, the total nucleon number of the activated corrosion products in the coolant changes with time according to the following equation:

$$
\begin{aligned}
\frac{dn_{vit}}{dt} &= R_{ci} - \lambda_i \cdot n_{vi} \\
&= \frac{N_A \cdot \overline{\phi}}{A_i \cdot \lambda_l}\left(1 - e^{-\lambda_1 \cdot t}\right) \sum_l \left[\overline{\sigma}_{ll} \left(\sum_j f_{vilf_{sllj}}C_0 S_j \right) \right] - \lambda_i \cdot n_{wt} \\
R_{ci} &= \frac{N_A \cdot \overline{\phi}}{A_1 \cdot \lambda_l} \sum_l \left[\overline{\sigma}_{ll} \left(\sum_j f_{nll}f_{sIlj}C_0 S_j \right) \right] \\
\frac{dn_{wl}}{dt} &= R_{cl}\left(1 - e^{-\lambda_i t}\right) - \lambda_l \cdot n_{wl}
\end{aligned}
$$

If $t \le t_1$, the analytical solution of the equation is:

$$ n_{wi}(t) = \frac{R_{ct}}{\lambda_t} - \frac{R_{ct}\lambda_t t + R_{ct}}{\lambda_l} e^{-\lambda_1 t} $$

if $t > t_1$, The power of the reactor has changed, the average neutron flux rate of the reactor has changed, The solution of the equation is:

$$n_{wt}(t) = \frac{R_{ci2}}{\lambda_l}\left[1 - e^{\lambda_i(t_1 - t)}\right] - R_{cc2}(t - t_1)e^{-\lambda_t t}$$
$$+ \frac{R_{ci1}}{\lambda_l}\left[e^{\lambda_l(t_1 - t)} - e^{-\lambda_l t}\right] - R_{ct1}t_1 e^{-\lambda_l t}$$

3.3 Example Description

The type of this example is a compact pool structure, as shown in Fig. 1; the main parameters are shown in Table 2. Under normal operating conditions, the circulation flow of lead-bismuth medium in the first circuit is as follows: Lead and Bismuth are heated from bottom to top by the core in the internal components of the reactor, and then enter the upper steam generator of the collector chamber through openings in the upper part of the containment vessel, After the heat transfer is completed from the top to the bottom of the primary side of the steam generator and the secondary side, the secondary side outlet is reintegrated into the lower collecting cavity of the side shield, and the inner opening of the side shield returns to the upper collecting cavity from the bottom to the top, Then flow down the annular passage between the side shield and the main vessel and enter the main pump inlet, under the pumping of the main pump, the annular passage between the lower shield and the lower head of the main vessel enters the lower collecting cavity of the core along the flow distribution mechanism, and finally returns to the core.
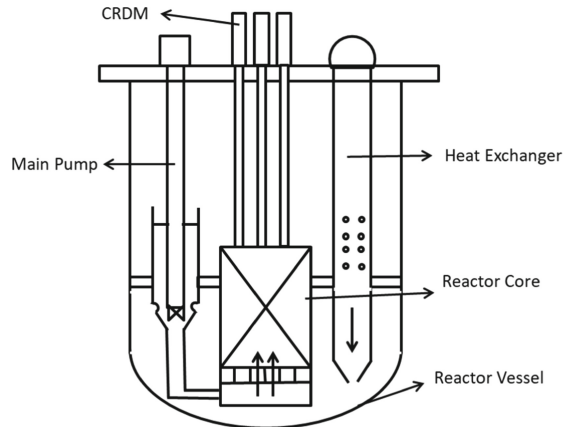
Fig. 1. Schematic Diagram of Pool-type Structure of Lead-bismuth Fast Reactor

Table 2. Main Parameters

Parameters	This Example	CLEAR-1
Thermal Power	20 MW	l0 MW
Design Life	30 years	30 years
Loop Number	2	4
Coolant Temperatures	280–485 °C	260–450 °C
Coolant Flow	660 kg/s	529.5 kg/s
Structural Materials	SS316H	SS316L

3.4 Calculation Results and Comparative Analysis

The fast neutron average reaction cross sections for various reactions were calculated using the MCNP code, as shown in Table 3. The radioactivity of the corrosion products in the model coolant is calculated using the formula in Sect. 3.2, and a comparison with the results of the same type of reactor is shown in Table 4.

Table 3. Fast Neutron Average Reaction Cross Section

	^{50}Cr-^{51}Cr	^{54}Fe-^{54}Mn	^{55}Mn-^{56}Mn	^{58}Ni-^{58}Co	^{59}Co-^{60}Co	^{60}Ni-^{60}Co	^{58}Fe-^{59}Fe	^{59}Co-^{59}Fe
barn	0.0123	0.0095	0.0753	0.0098	0.0642	0.0003	0.0019	0.0002

Table 4. Results and Comparison of Radioactive Activity of Corrosion Products

Nuclides	Half-life	This Example	CLEAR-1
		Activity, Bq	
^{51}Cr	27.72d	1.94E+13	7.40E+14
^{54}Mn	312.5d	7.69E+14	–
^{56}Mn	2.587h	1.00E+12	–
^{58}Co	71.3d	3.80E+14	2.06E+14
^{60}Co	5.26a	7.95E+14	1.25E+12
^{59}Fe	45.1d	1.04E+12	2.44E+14
Total		1.97E+15	1.19E+15

As can be seen from Table 4, the total activity of corrosion products in the lead-bismuth coolant circuit is 1.97E+15Bq. Among them, ^{51}Cr, ^{54}Mn, ^{58}Co and ^{60}Co have the largest proportion, but ^{51}Cr and ^{58}Co are short-lived nuclides, which can decay rapidly after shut down for a period of time, and ^{54}Mn and ^{60}Co have longer lifetime, which are the main contributors to the total activity.

Compared with ClEAR-1, the model has same life, but different power, temperature, flow, and structural materials. These factors cause the total amount of corrosion products to be more than ClEAR-1.

4   Conclusions

The sediment source term of corrosion products is the main source of occupational irradiation, and it is also the key and difficult point in the source term analysis of nuclear facilities. Based on the characteristics of lead-bismuth coolant system, the release, migration, decay and deposition of corrosion products in the coolant loop are fully considered, a method for calculating the source term of corrosion products in lead-bismuth coolant loop is developed, The method is used to simulate the coolant loop of lead-bismuth fast reactor, and the source term of corrosion products is calculated. The results show that the source terms of the corrosion products are mainly composed of ^{51}Cr, ^{54}Mn, ^{56}Mn, ^{58}Co, ^{60}Co and ^{59}Fe, among which the long-lived nuclides ^{60}Co and ^{54}Mn are the main contributors to the radioactive activity. The analytical methods and conclusions of this paper can provide theoretical support for relevant domestic research.

References

1. Wu, Y., et al.: Conceptual design of China lead-based research reactor CLEAR-1. Nucl. Sci. Eng. **6** (2014)
2. Chandrasekaran, T., Lee, J.Y., Willis, C.A.: Calculation of Releases of Radioactive Materials in Gaseous and Liquid Effluents from Pressurized Water Reactors. Division of Systems Integration Office of Nuclear Reactor Regulation U.S. Nuclear Regulatory Commission, Washington, D.C (1985)
3. Dacquait, F., Nguyen, F., Martean, H.: Simulations of Corrosion Product Transfer with the PACTOLE V3.2 Code
4. Zhang, C.: Source terms calculation analysis for the reactor and primary coolant system of Qinshan Phase II NPP project. Nucl. Power Eng. **24**, 73–77 (2003)
5. Ding, S., Shangguan, Z., Tao, Y.: Study on computational models of secondary source terms for normal operation of CPR1000 Nuclear Power Plants. Radiat. Protect. **29** (2009)
6. Liu, Y.: Calculation method and computer program for radionuclide concentration in primary circuit of light water reactor. Radiat. Protect. (1986)
7. Liu, Z., et al.: Source team analysis of DORAST code used in AP1000 primary and secondary coolant system. Atomic Energy Sci. Technol. **47**, 625–629 (2013)
8. Wu, M.: Study on Radiation Source Term of Main Coolant in Nuclear Power Plant. Shanghai Jiao Tong University (2005)
9. Yang, Y., et al.: Analysis of dose field in marine reactor cabin. Nucl. Sci. Eng. (2014)
10. Goorley, T., Bull, J., Brown, F., et al.: Release of MCNP 5_RSICC_1.30, Los Alamos National Laboratory (2004)
11. Gang, T.: Study on Radioactive Source Term and Dose Assessment for Lead-Bismuth Cooled Reactor (2013)

Research on ΔI Control Strategy During Rapid Power Reduction

Desheng Meng[(✉)], Rong Duan, and Zhijun Li

China Nuclear Power Technology Research Institute, Shenzhen, Guangdong, China
`rodolphe.mengdesheng@foxmail.com`, {`duanrong,`
`lizhijun`}`@cgnpc.com.cn`

Abstract. Cold source for the cooling system is provided by CRF pump in nuclear power plant. During failure of CRF pump, a rapid core power reduction to a lower power level is needed, which poses a challenge to ΔI control of the core. Based on the requirements of operating technical specifications, the influence of various factors concerned the ΔI control strategy such as cycle burn-up, low power level and power reduction methods is researched for the rapid power reduction process in a certain balance cycle. Meanwhile, sensitivity analysis is carried out on the action of the control banks for different phases during the rapid power reduction process. Based on the analysis of the main influencing factors, proposal on the rapid power reduction strategy related to the reduced power level, power reduction method and different characteristic burn-up is put forward. The match of the cooling capacity of the CRF pump and the reduced core power is realized, thus ensure the safety and economy performance of reactor core.

Keywords: ΔI · Power Reduction · Control Strategy · Operation Diagram · CRF Pump

1 Introduction

Two circulating water pumps (CRF pumps) are equipped in the three loops of the nuclear power plant in order to provide cooling water and thus to realize the heat removal [1]. During a cold source failure or CRF pump failure, a rapid core power reduction to a lower power level is demanded based on the available CRF pump cooling capacity. During the power reduction process and the stay of the low-power platform, the core axial power distribution is disturbed, and the axial power deviation of the core (ΔI) is relatively hard to control, which is likely to cause a reactor trip. Consequently, it is vital to study the ΔI control strategy in order to achieve a compromise between the CRF pump cooling capacity and ΔI control. It is also of importance for core safety and plant economics.

In the process of rapid power reduction, many problems appear in ΔI control. The power reduction methods in nuclear power plants can be divided into two types: boronization and rod insertion. As for the method of boronization, the power distribution is less perturbed. However, due to the limitation of the boronization speed, the power change rated is relatively low, which is difficult to satisfy the rapid reduce power requirements

at some time. Meanwhile, when using the boronization method to reduce power, ΔI is likely to continue increasing. As the power difference is so large until exceeding the right boundary the operation diagram. It will cause a reactor trip. The safety and economy performance of the unit are infected. As far as the way of rod insertion is concerned, the power reduction process can be realized within a short period of time by a rapid introduction of negative reactivity. Nevertheless, the rod insertion method disturbs largely the core power distribution. Meanwhile, The GN rods must be fully extracted out of the core within a certain period of time after the operating technical specifications which strictly restricts on rod insertion time. During the GN rod withdrawal, it is likely for ΔI to exceed the right boundary. In addition, during the rapid power reduction, the core ΔI is also significantly related to the core burnup and the magnitude of the power reduction, that's why the core control strategy research is challenging.

In this paper, the SCIENCE program is utilized to simulate the variation of ΔI in the process of rapid power reduction. The control strategy of ΔI, which involves fuel burnup, low-power platform, and power-reduction methods, is optimized with the help of SOPHORA program. At the same time, the control rod action sensitivity analysis is also completed in this paper. Suggestions for ΔI control strategy in the process of rapid power reduction are given.

2   Research Background of Rapid Power Reduction

Researchers have carried out a lot of explorations and researches on the problem of ΔI control strategy of the rapid power reduction process. Among them, qualitative analysis has been given from the perspective of core characteristic including burn up, burnable absorber, control rod position, fuel type and moderator temperature in a large number of literatures [2–10]. At the same time, power reduction types, such as power reduction to hot shutdown, daily power reduction or augmentation, extended low power operation (namely ELPO), stretch out operation, are also described qualitatively [5]. Nevertheless, literature related to rapid power reduction is relatively scarce, especially the quantitative analysis. The difficulty of ΔI control is mentioned [9] in a case that the reactor realize a reduction of power rapidly by a speed of 50 MW/min due to cooling source failure. Therefore, the power is forced to reduce to below 30% FP in order to prevents load rejection action due to the uncontrollable ΔI. On the basis of previous research, quantitative and in-depth research on the impact of different factors in the process of rapid power reduction is meaningful to the ΔI control and to the matching between the low-power platform and the cooling capacity of the cold source pump, thus ensuring the safety and economy performance of the reactor operation.

3   Research Methods

In order to ensure the safe operation of reactor, the operating diagram limitations on ΔI must be met. In addition, operation technical specifications are also mandatory considering the operation factors. Under the condition of meeting these limitations, SCIENCE and SOPHORA programs are utilized to study the influence of difference factors, such as burnup, low-power platform, power reduction method and control rod action on ΔI control in the process of rapid power reduction.

3.1 Operation Technical Specifications

As one of the main bases for the operator to control the reactor, the operation diagram shows the relationship between the allowable value of ΔI and the relative reactor power. During the rapid power reduction process, the operator must ensure that ΔI satisfies the operation diagram. In addition, the ΔI performance also needs to meet the operation technical specification in which the operation diagram is defined. Related operating technical specifications are listed: when $P_{\Delta Iref}$ is determined and the power of the core is reduced from high power to 50% or less, control rod insertion time is limited to 12 h in any 24 h period in region I and ΔI is limited at region I. In the case of a capacity of a quick return to high power levels, the control rod insertion limitation time can be extended to 24 h. When all the power compensation rods(GN rod) are completely drawn out, ΔI is able to leave the area I after 6 h of stable operation.

3.2 SCIENCE and SOPHORA Software

SCIENCE graphical software package, which invoked by the Copilote graphical user interface is used in this paper for calculations. SMART programs is used for 3D homogenized cores calculation. SOPHORA program is utilized for ΔI control strategy optimization.

3.3 Overall Control Strategy

Under the condition of meeting the demands of operation technical specifications, two periods related to rapid power reduction, which is the period of rapid power reduction and the low power platform is respectively considered in order to evaluate various influencing factors in this article.

Concerned the strategy of rapid power reduction period, the control of ΔI is achieved in two ways. One is to insert the GN rod according to the G9 curve, while the power decrease at a speed of 10MW/min until reaching the low power platform. The other is to increase the boron concentration of the core firstly, at the same time, the power decrease at a rate of 3 MW/min until 80%FP. Then, GN rods is inserted in order to reduce the power at a relatively high speed of 10 MW/min. As for the strategy of low power platform, the core is boronized in order to withdraw all GN rods while R rod is used to control ΔI in order to meet the requirements of operating technical specifications in Sect. 3.1 (the time limitation for rod insertion).

In order to study the ΔI control strategy of reducing power to different low-power platforms at different fuel burnup points, a certain 18-month refueling cycle was selected for research at 150 (BLX), 6000, 11000 (ΔI most negative burnup point), 14000 (MOL), 16000 (80%EOL), 18000MWd/tU and EOL. Low power platform of 50%, 60%, 65%, 70%, 80% FP are studied and the ΔI control strategy is carried out in case of reactor cold source failure.

4 Optimization Results

The ΔI control strategy optimization results of rapid power reduction is researched by mainly focusing on three factors: fuel burnup, reached low power level platform, and the

power reduction method. The comprehensive impact evaluation of the three factors is also studied. Then, this paper introduces the sensitivity analysis of the control rod action in the process of rapid power reduction, and gives the ΔI control strategy conclusion of the rapid power reduction process.

4.1 Influence of Fuel Burnup

During the reactor normal operation, the temperature of the lower part of the core is lower than that of the upper part. Due to the negative feedback of temperature, the core ΔI is generally negative. Along with the deepening of burnup, the burnup in the lower part of the core is gradually larger than that of the upper part, therefore, ΔI tends to increase due to the influence of the burnup effect. In this research, after the GN rods are extracted, a larger ΔI is unfavorable for core control. Worse, the xenon oscillation effect manifest more negative effects at EOL than BOL.

In order to study the influence of the fuel burnup effect, the GN rod is inserted to reduce the power to 50% PN during the rapid power reduction period and the ΔI variation is compared at BLX, MOL and EOL. R rod is used to control ΔI only at the low power platform. The variations of ΔI are shown in Fig. 1:
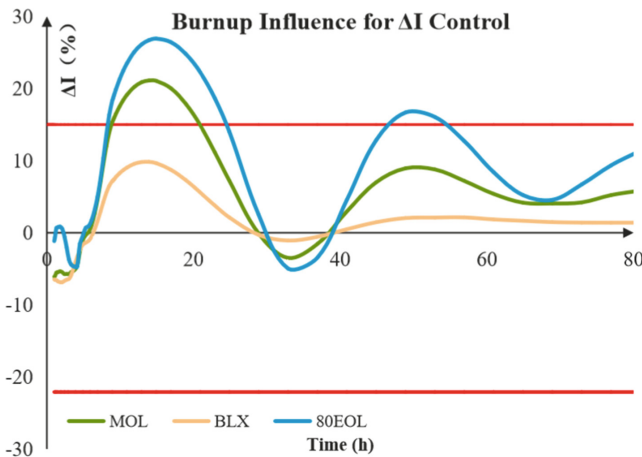
Fig. 1. Burnup influence for ΔI control

It can be seen from Fig. 1 that ΔI exceeds zone I when the GN insertion time is limited to 12h for all three burnup points. Therefore, we can draw that for the whole cycle, it's likely to exceed zone I when the power is reduced to 50%FP rapidly. We also note that ΔI will not exceed the right boundary at operation diagram at BLX; Nevertheless, at MOL and 80% EOL burnup, the xenon oscillates more violently and ΔI tends to be bigger, thus it exceeds the right boundary. ΔI control is influenced significantly by fuel burnup.

4.2 Impact of Low-Power Platforms

In addition to fuel burnup, the low power level reached by the core after a rapid power reduction also has a considerable impact on ΔI control. When the core power is reduced from 100% to 80% FP or more, ΔI is easy to control due to the small variations in power. Additionally, if the core power is reduced to 30% FP or even less, although power distribution go worse, ΔI may still be controllable thanks to the lower power levels. However, as the power is reduced to 30%–80% FP, ΔI is the most difficult to control.

ΔI variations for three low-power platforms (80%, 60% and 50%FP) is compared at burnup of 11000 MWd/tU in this section. R rod is not inserted at the power reduction period. At the low power platform, the core is boronized in order to extract GN rods. Meanwhile, R rod is inserted to control ΔI. The variation of ΔI for the three low-power platforms is shown in the Fig. 2:
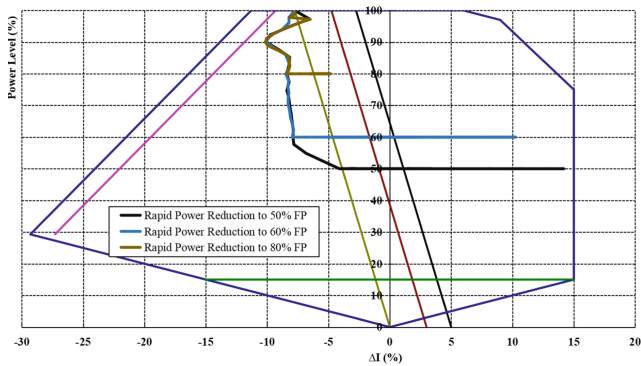
Fig. 2. Low-power platform influence for ΔI control

As shown in Fig. 2, when the power is reduced to a low-power platform which is greater than 50% PN, the greater is the power reduction, the greater is the ΔI oscillation caused by the xenon oscillation. When the power is decreased to the 80% FP, ΔI varies slightly within zone I. While the power is reduced to 60% or 80% FP, ΔI exceeds zone I. Therefore the low-power platform also affects largely the ΔI control.

4.3 Influence of Boronization and Rod Insertion

It can be obtained from Sect. 3.3. That two methods can be used for rapid power reduction: one is direct rod insertion and the other is boronization to 80%FP and then rod insertion. The power drops rapidly in the upper part of the core because of the rod insertion, and thus ΔI becomes more negative. The boronization power reduction method disturbs less to the core ΔI than rod insertion method, and it leads to a more positive ΔI. In order to compare the effects of two power reduction methods on ΔI control, the core ΔI elevation of the two cases is compared.

It can be seen from Fig. 3 that the ΔI performance is slightly improved by adopting the method of boronizing and then inserting the rod. At the same time, studies have

shown that if boronization itself is used to reduce power to 50% PN, not only the power change rate is limited, but ΔI is easy to exceeds the right boundary. The ΔI oscillation can be slightly reduced by using the rapid power reduction strategy of boronization and then insertion the control rod.
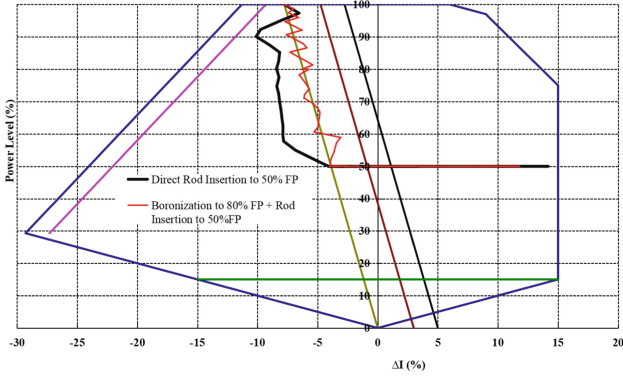
Fig. 3. Boronization and rod insertion influence for ΔI control

4.4 Comprehensive Feasibility Analysis of Fuel Burnup, Low Power Platform and Boronization

It can be drawn from Sect. 4.1–4.3 that fuel burnup, low power platform and power reduction method have major influence on ΔI control. A comprehensive analysis contains the ΔI control strategy optimization at different fuel burnups to different low-power platforms and by using different methods. We also note that the criteria of feasibility for rapid power reduction strategy is that ΔI does not exceed the operation diagram.

The power reduction analysis is based on two assumptions to facilitate the calculation. The first is that, at a higher fuel burnup, if the core power can be reduced to a certain power level without exceeding the right boundary, the core power can also be reduced to that level without exceeding the right boundary at a relatively lower burnup. The other is that, if the direct insertion of control rod method is feasible to reduce the power without exceeding the right boundary, the power reduction method of boronization and then rod insertion will also be feasible. These two assumptions correspond to the conclusions in Sects. 4.1 and 4.3, respectively. On the basis of these two assumptions, the conclusion of whether ΔI is controllable can be obtained for different fuel burnups (the unit of fuel burnup is %EOL), with different power reduction method (use direct rod insertion, boronization without stay at 80%FP and rod insertion, and finally boronization with stay at 80%FP and rod insertion) to different power platform including 80%, 70%, 65%, 60% and 50% FP. The result is shown in Fig. 4:

From Fig. 4, the boundary between controllable and uncontrollable power is obtained. When the fuel burn-up is less than about 50% EOL (about 11GWd/tU), ΔI does not exceed the operation diagram if the power is reduced rapidly to 50%. However, as the

Burnup and low-power plateform Influence
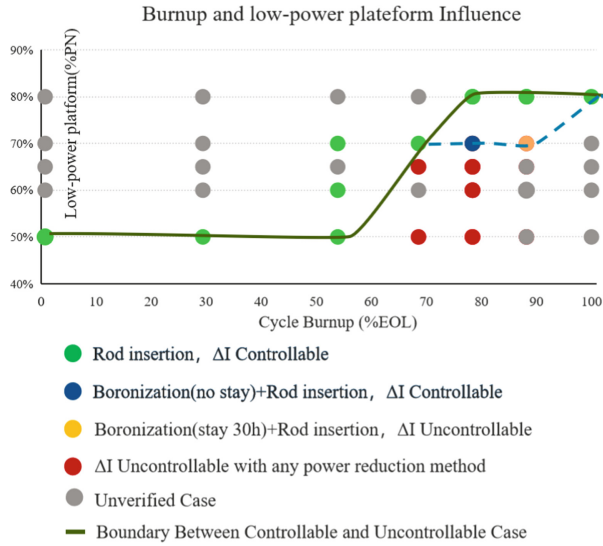
Fig. 4. Combined influence of burn-up, low power platform and power reduction method for the feasibility of rapid power reduction

fuel burn-up increases, in order to prevent ΔI from exceeding the operation diagram, the power reduction magnitude should be gradually reduced. When the fuel burn-up is high enough, a direct rod insertion to reduce the power may cause the ΔI exceeding the right boundary. In this case, the power can be reduced by boronization followed by rod insertion, and a stay of 80%FP may be necessary to avoid ΔI oscillation. The matching of cooling capacity and core power can be achieved with help of the strategy.

5   Sensitivity Analysis of Control Rod Motion

To limit ΔI oscillations during rapid power reduction, the R-rod action can be manually optimized. In addition, after reaching the low power platform, the GN rod is supposed to be raised in 12h, the GN rod action is flexible in time and in speed. Therefore, it is also of importance to carry out the analysis of the influence of the control rod action on ΔI during the rapid power reduction and the low-power platform.

Considering the power reduction method of direct insertion of control rod, according to the time and logical sequence, the sensitivity analysis of control rod action can be divided into: R rod action in power reduction process, GN rod action at low-power platform and R rod action low-power platform. The sensitivity analysis is simulated at a burnup of 80%EOL.

5.1   Sensitivity Analysis of R Rod Action During Power Reduction Process

During the power reduction process, GN rod needs to be inserted according to the known G9 curve, ΔI is generally more negative. In this process, the R rod can be properly raised

in order to leave an insertion margin for the ΔI control when the GN rod is extracted for the low-power platform. In this section, the influence of whether to extract R rod out of the core during the power reduction process so as to leave a insertion margin in the low-power platform is researched.

Two case during power reduction process, which is firstly R rod is gradually extracted out of the core during power reduction and secondly R rod keeps still, is studied. At lower-power platform, R rod is evenly inserted into the core to its lower limit. ΔI variation at low-power platform is shown in Fig. 5:
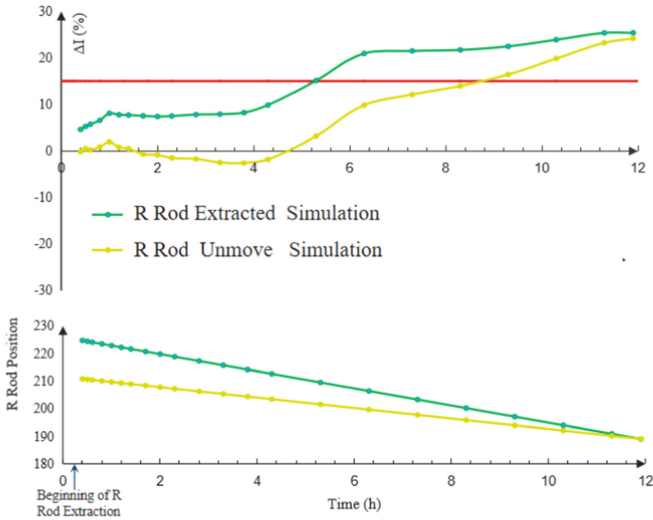
Fig. 5. Sensibility study of for the withdrawal of R bank

It can be drawn from Fig. 5 that in the process of power reduction, an extraction of R rod for more insertion margin has no significant optimization effect on the ΔI control strategy. ΔI raises as the GN rod is extracted, and finally exceeds the right boundary. The value of final ΔI is basically the same in both cases.

5.2   Sensitivity Analysis of GN Rod Motion of Low Power Platform

In order to meet the requirements of the operation technical specifications, the GN rods must be extracted of the core within 12 h. During the low-power platform, when GN rods are extracted, studies of its action include: extraction speed, beginning time and time interval of GN rod withdrawal.

For the analysis of extraction speed of GN rods, three cases of GN rod extraction at low-power platform are simulated. The result of ΔI is shown in Fig. 6:

It can be seen from the above figure that the maximum ΔI is positively correlated with the GN rod extraction rate, but both ΔI are far beyond the right boundary.

For the beginning time of the GN rod extraction, at low-power platform, due to the Xe effect, ΔI tends to decrease in the low-power platform from 0 to 10 h in which is
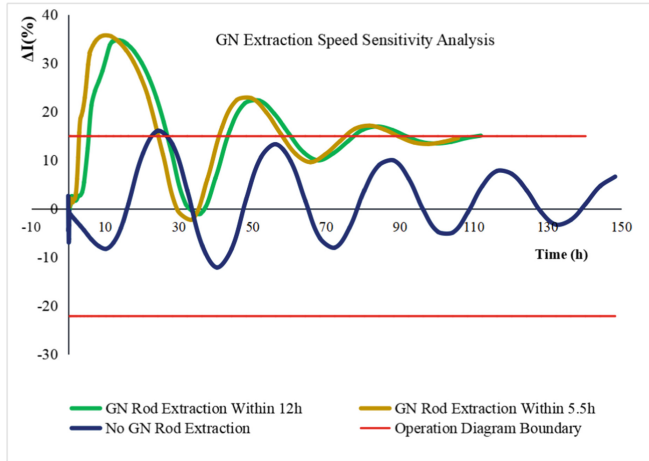
Fig. 6. Influence of the withdrawal speed of GN bank on ΔI

favorable for GN rods extraction. The GN rods are selected to be extracted at 2, 4, 6, and 8 h, and all of the cases are fully extracted at the 12th hour. The R rod keeps still, and the comparison of ΔI changes is shown in Fig. 7:
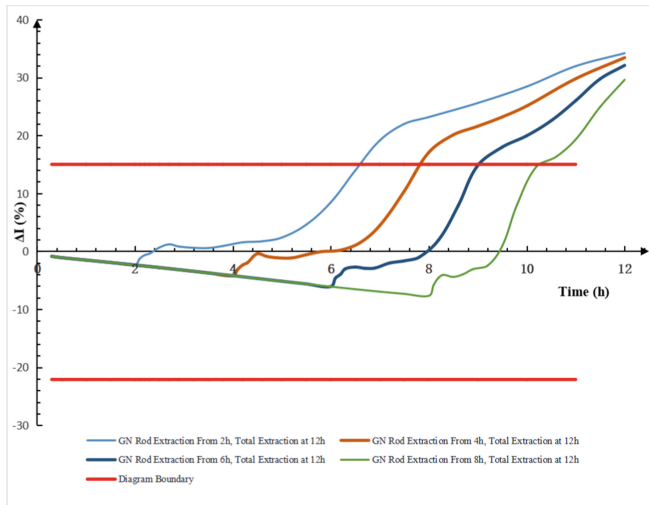
Fig. 7. Influence of the withdrawal time of GN bank on ΔI

From Fig. 7, we observe the changes of ΔI In all four cases, the xenon oscillation causes ΔI to exceed the right boundary. However, by adjusting the time of GN rod withdrawal, the peak value of ΔI can be slightly reduced and the time to exceed right boundary can be delayed.

As shown in Fig. 8, after the rapid power reduction of the core, the ΔI variation is simulated for different stay times of 2h and 6h after reaching low-power platform in a real specific case. Compared with the 2h stay condition, the maximum value of ΔI after extraction the GN rods is lower and does not exceed the I zone for 6h-stay case. The operation technical specification is obeyed. Therefore, the beginning time optimization of GN rod has a positive effect on ΔI control.
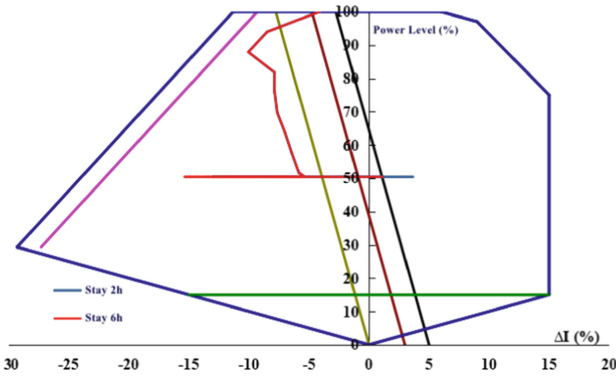
Fig. 8. Influence of the withdrawal time of GN bank on ΔI for Daya Bay unit at middle of cycle

For the sensitivity analysis of the extraction time interval of the GN rod, after the power is rapidly reduced, R rod keeps still, and GN rod is extracted at different time interval, as shown in Fig. 9:
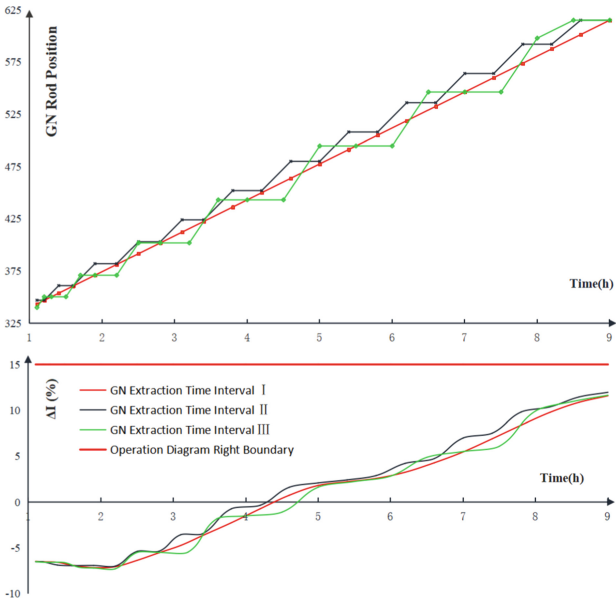
Fig. 9. Influence of the withdrawal time interval of GN bank on ΔI

From the above figure, ΔI attains the same value in the end. The extraction time interval of the GN rod does not affect greatly the variation of ΔI. Consequently, the GN rod can be evenly raised on the power platform.

5.3 Sensitivity Analysis of R-rod Motion of Low-Power Platform

In the low-power platform, during the process of the extraction of GN rod, the R rod needs to be inserted to control ΔI. The R rod can be either evenly inserted to its lower limit, or inserted once at a certain moment or inserted at different time. This section is to study the effect of the R rod action.
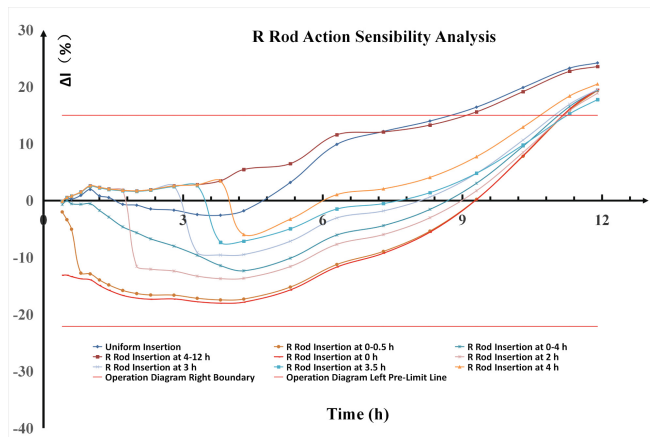
Fig. 10. Influence of the R bank action on ΔI at reduced power level

As can be seen from Fig. 10, the R rod adopts different insertion strategies, none of them can control the ΔI within the right boundary. There is no significant correlation between R rod insertion method and final ΔI value. The later is mainly affected by the final position of R rod (namely the low-low limit).

5.4 Summary of Sensitivity Analysis

In this section, at the 80% EOL burn-up point, the sensitivity analysis of the control rod action to ΔI in the process of rapid power reduction and low-power platform is carried out, including the analysis of the R rod action in the process of the GN rod insertion, the action of the GN rod and R-rod at the low-power platform. We can basically conclude that the control rod motion improves slightly the ΔI performance, but it has no decisive effect on the core control. The fuel burnup, low power platform and power reduction method keeps the main factor affecting ΔI during the rapid power reduction.

6   Conclusion

Based on SCIENCE software, this article describes the effects of different factors such as fuel burnup, low power platform, power reduction method and control rod action on

rapid power reduction. Aimed at the three main factors, the comprehensive feasibility analysis is carried out and based on a specific cycle, a rapid power reduction ΔI control strategy is given: when the fuel consumption is less than approximately 50% EOL, ΔI is controllable when the power is quickly reduced to 50% FP. As the fuel burnup deepens, in order to keep ΔI within the operation diagram, the power reduction should be gradually reduced to 70% FP. When the fuel burn-up is high enough (80% EOL), using the direct rod insertion method to reduce the power will cause the ΔI to exceed the right boundary. The power can be reduced by boronization and then rod insertion. When the fuel burnup deepens to 90% EOL, in order to quickly reduce the power to 50% FP, it is recommended to stay for a certain time after boronization. When the fuel consumption reaches EOL, if the core reduces the power rapidly to 70%PN, no matter how long it stays, ΔI is uncontrollable. At this time, it is recommended that the unit be reduced to more than 80% FP. The quantitative research of this paper is carried out between the CRF pump cooling capacity and the core power. It is of reference value for core control for rapid power reduction during CRF pump and cold source response failure.

References

1. System and Equipment of 900 MW PWR Nuclear Power Plant (In Chinese) **15**, 488. Atomic Energy Press (2005)
2. Cheng, J.: Research on axial power deviation (ΔI) control of reactor (In Chinese). Daya Bay Nuclear Power, (2000)
3. Wang, S., Zhang, Q.: Axial power deviation control in the process of reactor power rise (In Chinese). Daya Bay Nuclear Power (2008)
4. Long, S., Gao, Y.: Control of axial power deviation in daily operation of M310 nuclear power unit during load variation (In Chinese). Technol. Innov. Appl. **15**, 12–13 (2019)
5. Liao, Y., Xiao, M., Li, X., Zhu, M.: Axial power difference control strategy and computer simulation for GNPS during stretch-out and power decrease (In Chinese). Nuclear Power Engineering, pp. 297–299 (2004)
6. Duan, C., Wu, X.: Analysis of ΔI control of power reduction at the end of cycle (In Chinese). Shandong Industrial Technology, p. 276 (2016)
7. Wang, B.: Operation control strategy of nuclear power units during ELPO (In Chinese). J. Manag. Sci., 45–46 (2015)
8. Liu, Z., Pan, Y.: Control of axial power deviation during power variation (In Chinese). In: CORPHY 2006, pp. 533–542 (2006)
9. Chen, Z., Chen, C.: Core axial power deviation control at the end of life of PWR nuclear power (In Chinese). Daya Bay Nucl. Power **4**, 7–12 (2011)
10. Zhang, H.: Analysis on axial power distribution and ΔI control in pressurized water reactor

Minor Actinides Transmutation in Thermal, Epithermal and Fast Molten Salt Reactors with Very Deep Burnup

Chunyan Zou, Chenggang Yu, Jun Zhou, Shuning Chen, Jianhui Wu[(✉)], Yang Zou, Xiangzhou Cai, and Jingen Chen[(✉)]

Shanghai Institute of Applied Physics, Chinese Academy of Sciences, Shanghai, China
{zouchunyan,wujianhui,chenjg}@sinap.ac.cn

Abstract. Deep burnup and high minor actinides (MA) loading are two alluring features for molten salt reactors (MSR) to incinerate the nuclear wastes. The transmutation capability of minor actinides in MSR is tightly related with the neutron spectrum, the loading of MA and the carrier salt compositions. In this work, three MSR core designs (thermal, epithermal and fast) and two types of salt compositions (Flibe and Flinak) with different solubility limits of transuranic elements are chosen for analyzing the transmutation capability of MA. With a significant mole fraction of MA loading (4% in the Flibe salt and 10% in the Flinak salt) and the continuous MA refueling, MSR acquires an excellent transmutation rate. The specific incineration rates of MA in the thermal, epithermal and fast MSR cores with the Flibe salt are about 167, 185 and 206 kg/GWth/y, respectively. With a larger loading of MA in the Flinak salt, a higher annual incineration rate of MA can be obtained, which are about 170, 206 and 247 kg/GWth/y in thermal, epithermal and fast MSRs, respectively. On the other hand, since there is a preferred neutron economy for the Flibe salt, a higher MA incineration ratio is achieved than that for the Flinak salt. When the neutron spectrum varies from the thermal to fast region, the MA incineration ratio ranges from 0.79 to 0.82 for the Flibe salt and it ranges from 0.75 to 0.81 for the Flinak salt. The transmutation capability of MA in MSR is much higher than that in solid-fueled reactors (~20 kg/GW.y in a PWR), which can provide a feasible way for reducing the current nuclear wastes.

Keywords: Molten Salt Reactor · Minor Actinides · Transmutation Capability · Incineration Rate · Incineration Ratio

1 Introduction

Minor actinides (MA) in the spent fuel of the current pressurized water reactors (PWRs), namely neptunium (Np), americium (Am) and curium (Cm), are the main long-lived radioactive waste in the long term, which is one of the most severe issues associated with sustainable nuclear energy development [1–4]. Until now, transmutation is considered to be an effective way for nuclear waste management and tremendous works have been devoted to achieving a high transmutation capability of MA in different types

of reactors, such as PWR, Gas-cooled Fast Reactor (GFR), Lead-cooled Fast Reactor (LFR), Sodium-cooled Fast reactor (SFR) and Accelerator Driven Sub-critical System (ADS) [5–8].

Molten salt reactor (MSR) is an old concept but has been gathered many attentions in recent years due to its special features [9, 10]. One of the most alluring advantages in MSR is that it operates with a liquid fuel, which permits an arbitrary core design and a flexible reprocessing system. Furthermore, the molten salt is capable to dissolve various fissile fuels (eg. enriched uranrium, ^{233}U and transuranium elements (TRUs)), which is convenient to implement different types of fuel cycles in an MSR [11, 12]. A closed nuclear fuel cycle is expected to be realized and the utilization of nuclear fuel can be significantly improved due to the effective burning of minor actinides in an MSR. The MOlten Salt Actinide Recycler & Transmuter (MOSART) was first proposed by the Kurchatov Institute of Russia within the International Science and Technology Center project 1606 (ISTC#1606) with aims to effectively transmute TRUs [13]. A series of studies have been conducted to demonstrate the feasibility of MOSART for reducing TRU radiotoxicity. Afterwards, another fast spectrum MSR concept of the Molten Salt Fast Reactor (MSFR), which was proposed by the Centre National de la Recherche Scientifique (CNRS) to achieve a high thorium breeding ratio, was also applied to investigate the feasibility of TRU transmutation [14]. Recently, some thermal spectrum MSR concepts are also put forward to evaluate the possibility of TRU transmutation [15, 16].
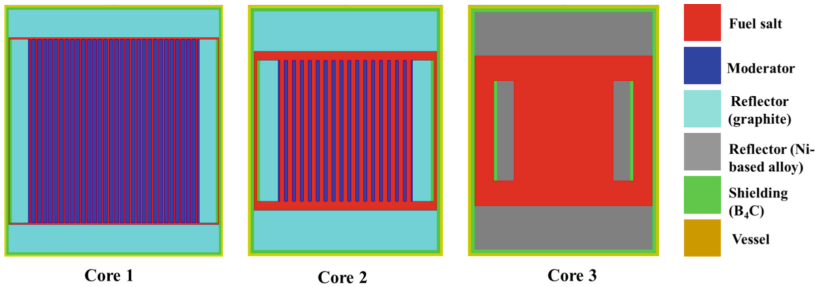
Fig. 1. Geometrical description of the three MSR cores

In an MSR, the MA transmutation capability is tightly related with the neutron spectrum and the MA loading in the core. The dominant transmutation way for MA is varied with the neutron spectrum since the fission and capture cross sections of MA have significant discrepancies with the neutron energy. In addition, different types of carrier salt compositions have various TRU solubility limits, which have a direct influence on the MA loading in MSR. In this paper, it is aimed to evaluate the transmutation behaviors of MA with different neutron spectra and various MA loadings in MSR, which can provide a reference for realizing various transmutation objects for different MA elements. Three typical MSR cores (thermal, epithermal and fast) are proposed to compare the MA transmutation capability. Meanwhile, two typical molten salt compositions (Flibe and FlinaK) which have different TRU solubility limits are selected to analyze the influence of MA loading on the transmutation capability. Furthermore, the radiotoxicity and safety parameters are also analyzed in detail.

A general description of the thermal, epithermal and fast MSRs and the calculation tools is presented in Sect. 2. In Sect. 3, the MA transmutation capabilities in the three MSR cores with two types of molten salts are first analyzed. And then the neutronic performances at different burnups in the thermal, epithermal and fast MSR cores are presented and discussed. The conclusions are given in Sect. 4.

2 General Description of the Geometry Models and Calculation Tools

2.1 Description of the Thermal, Epithermal and Fast MSRs

In the past, a series of MSR core designs ranging from the thermal to fast neutron spectrum have been conducted to achieve a high thorium breeding ratio in our research group [11, 12]. This work extends three typical reactor core configurations, corresponding to thermal, epithermal and fast spectrum cores, respectively. The geometrical descriptions for the three cores are shown in Fig. 1. In an MSR, the power density is a vital parameter to determine the main neutronic behaviors. Therefore, a constant thermal power of 2500 MWth and a constant fuel volume of about 46.2 m^3 are designed for the three cores, respectively. Therein, two thirds of the total fuel volume is located in the core salt channels, the upper and lower plena, and the other one third is located in the heat exchangers, pipes and pumps.
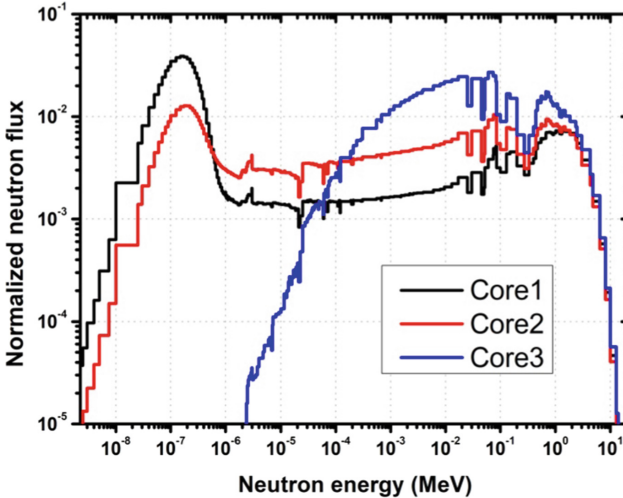
Fig. 2. Neutron spectra of the three cores

The core parameters are detailed in Table 1. For the thermal and epithermal MSR cores, the reactor core is a cylindrical geometry assembled with graphite hexagons and surround by the graphite reflectors. The radii of the fuel salt channel in each graphite hexagon are designed as 3 cm and 7.5 cm to obtain thermal and epithermal spectra,

respectively. In the fast MSR, the graphite reflector is replaced by nickel-based alloy to prevent nuclear fissions from being decentralized to reactor's borders. To maintain a constant fuel volume in the core, the dimension for the three MSRs varies from each other, which is designed by keeping the height and the diameter equivalent. The radial reflector with 0.5 m thickness and the axial reflectors with 1.3 m thickness are designed around the core for the three cores to improve the neutron economy. The neutron spectra of the three core configurations fueled with Th-232 and U-233 are shown in Fig. 2, which are shown as typical thermal, epithermal and fast neutron spectra.

Table 1. Main parameters of the three MSR cores

Parameters	Core 1	Core 2	Core 3
Thermal power (MWth)	2500	2500	2500
Fuel volume (m^3)	46.2	46.2	46.2
Fuel channel radius (cm)	3	7.5	—
Active core diameter/height (m)	8.6	4.6	3
Plena height (m)	0.09	0.3	0.75
Radial/axial reflector thickness (m)	0.5/1.3	0.5/1.3	0.5/1.3
Reflector material	Graphite	Graphite	Nickel-based alloy

2.2 Selection of Salt Compositions

The MA loading in the core is an important factor that determines the transmutation capability, which is a major restriction on achieving a high transmutation rate in solid-fueled reactors. In MSR, there is no fuel rod fabrication which extends the feasibility of MA mass loading. However, the solubility limit of TRU in the molten salt is an important restriction on the MA mass loading. Therefore, choice of the fuel salt is also one of the most important tasks for the MA transmutation since the solubility limit of TRU is tightly dependent on the molten salt compositions. In the past decades, the physico-chemical properties of various salt compositions were researched for selection of fuel and coolant compositions for MSR. Until now, there are three typical carrier salts proposed in different MSR designs, which are Flibe, Fli, and Flinak, respectively [19]. The Flibe salt with 99.995% of Li-7 enrichment has excellent neutron economy, and has been widely used in various MSRs. The PuF_3 solubility limit for the fuel compositions of 77% LiF–17% BeF_2–6% ThF_4 is 4.0%. The Fli carrier salt removes BeF_2 to accommodate a higher fraction of actinide tetrafluorides, which has been selected as the fuel compositions in the molten salt fast reactor (MSFR) (78% LiF–22% ThF_4) for Th breeding and MA transmutation. The 78% LiF–22% ThF_4 fuel salt has a worse neutron economy but has a higher solubility limit (5.2%) than the Flibe salt. Compared to the Flibe and Fli salts, the Flinak carrier salt has the highest solubility of actinides but the worst neutron economy due to the large absorptions of Na-23 and K-39. For the composition 46.5% LiF, 11.5%

NaF and 42% KF, the solubility limits for ThF_4, UF_4, PuF_3 and AmF_3 are as high as 37.5%, 45%, 30%, and 43%, respectively. In this work, the Flibe and Flinak carrier salts are selected for comparing the MA transmutation capability with different MA loadings.

The initial MA mole fraction for the Flibe salt is loaded with its limit value of 4.0% while 10% of MA is loaded for the Flinak salt in the thermal, epithermal and fast MSR cores. Th-232 and U-233 are used as the fertile and fissile fuels in the three MSR cores due to the very low TRU production. To enhance the MA transmutation rate and to ensure the stability of fuel salt simultaneously, MA including Np, Am and Cm are fed online into the core to keep the total inventory of MA and Pu constant during the entire operation. Furthermore, Th-232 and U-233 are also fed into the fuel salt continuously to maintain the criticality of reactor and keep the total heavy metal inventory in the fuel salt constant.

The MA compositions come from the spent fuel of current light water reactors (LWRs), which are mainly composed of Np-237, Am-241, Am-243, Cm-243, Cm-244 and Cm-245 in the proportions of 56.2%, 26.4%, 12%, 0.03%, 5.11% and 0.26%, respectively [4].

2.3 Calculation Tools

The SCALE6.1 code system, which has powerful functions for criticality, depletion and shielding calculations for critical reactors, was used to establish the simulation model of the MSR core [17]. Meanwhile, the molten salt reactor reprocessing system (MSR-RS) developed by our research group was applied to simulate the characteristics of online refueling and reprocessing in MSR. In this paper, the MSR-RS sequence is also used to calculate MA transmutation in MSR [18]. MA is fed continuously to enhance the transmutation rate and the feeding MA inventory is adjusted by keeping the total TRUs inventory constant to assure the TRU fraction in the fuel salt below the solubility limit. Meanwhile, the total heavy metal mass in the core is always kept constant by feeding Th-232 and U-233 during the entire operation time. The 238-group ENDF/B-VII cross section database is selected, and 388 nuclides are tracked in trace quantities in this simulation which contains most of the nuclides in the fuel cycle chain with very deep burnup.

3   Results and Discussion

To evaluate the MA transmutation capability of the thermal, epithermal and fast MSRs, the neutron spectra and fission/capture cross sections of MA varying with different MA loadings are first analyzed. Then the transmutation capability and the radiotoxicity of TRU are evaluated in detail. Finally, the related safety parameters will be discussed.

3.1 Neutron Spectra Variation with Addition of MA into the Fuel Salt

Neutron spectrum is a key core parameter which determines the MA transmutation performances mainly through the capture and fission reactions. When MA is refueled into the fuel salt, the neutron spectra in the three MSR cores will have a different shift

due to the variation of cross sections of MA in different neutron energies. In further, the neutron spectrum change will have an influence on the fission/capture cross sections of MA. The neutron spectrum variations with MA addition at the beginning of life in the three MSR cores are displayed in Fig. 3. One can be seen that the neutron spectra in the thermal, epithermal and fast MSR cores harden significantly with addition of MA into the fuel salt. Furthermore, the variation in the epithermal core is more obvious than those in the other two cores as most of MA have strong resonance absorptions. In addition, the neutron spectrum with the Flinak salt shifts to a slightly fast region due to the parasitic absorption of Na-23 and K-39.
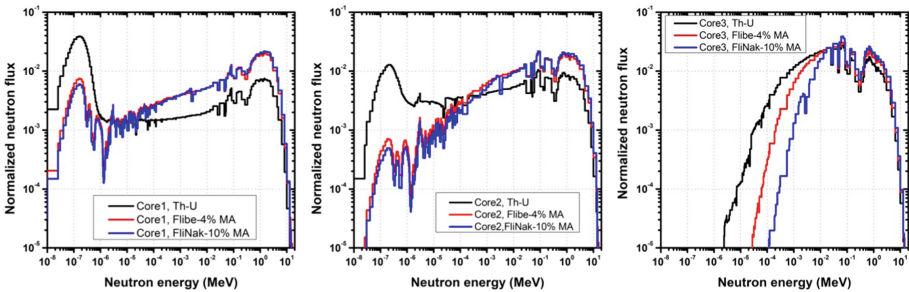
Fig. 3. Neutron spectrum variations with MA loading in the three cores

3.2 Transmutation Capability in the Three MSR Cores

To evaluate the transmutation capability of MA in an MSR, several parameters are introduced, namely the specific MA incineration consumption (SIC), the MA incineration ratio (TR) and the disappearance rate (DR) of each element in MA. The SIC is defined as

$$\text{SIC} = \frac{MA(T=0) + MA(feeding) - MA(residue) - HN(residue)}{P \times T}$$

where $MA(T=0)$, $MA(feeding)$, $MA(residue)$ and $Pu(residue)$ denote the initial MA loading, the online MA feeding and the MA residue, respectively. The HN residue in the fuel salt is the total TRU inventory except MA. P is the thermal power of MSR, while T is the entire operation time.

The TR is another important parameter for evaluating the MA incineration efficiency, which is defined as the ratio of the incinerated MA mass to the total loaded MA mass and calculated by

$$\text{TR} = \frac{MA(T=0) + MA(feeding) - MA(residue) - HN(residue)}{MA(T=0) + MA(feeding)}$$

In addition, the disappearance rate (DR) of each element in MA is also applied to evaluate the transmutation capability of Np, Am and Cm in the thermal, epithermal and fast MSR cores, which is defined as

$$\text{DR(i)} = \frac{M(i)(T=0) + M(i)(feeding) - M(i)(residue)}{(M(i)(T=0) + M(i)(feeding)) \times P \times T}$$

where $M(i)(T=0)$, $M(i)(feeding)$ and $M(i)(residue)$ represent initial loading, the online feeding and the residue inventory of element i, respectively.

Table 2. SIC and TR for two salts in the three MSR cores

scenario	Flibe			Flinak		
	Core1	Core2	Core3	Core1	Core2	Core3
MA initial loading (t)	22.0	22.0	22.0	28.9	28.9	28.9
MA feeding (t)	41.3	45.1	50.4	41.5	49.7	60
SIC (kg/GWth.y)	167	185	206	170	206	247
IR	0.79	0.81	0.82	0.75	0.78	0.81

With 4% of MA in the Flibe salt and 10% of MA in the Flinak salt, the initial MA inventories are loaded as about 22 tons and 28.9 tons for the Flibe and Flinak salts, respectively. During the whole operation, the total TRU inventory is always kept constant to maintain the TRU fraction below the solubility limit. Therefore, the incinerated MA inventory is dependent on the feeding amount of MA. During the 100-year operation, the total MA feeding inventory with the Flibe salt ranges from 41.3 to 50.4 tons in the thermal, epithermal and fast MSR cores while it varies from 41.5 to 60 tons with the Flinak salt for the three cores. The STC and TR with Flibe and Flinak salts in the thermal, epithermal and fast MSR cores during 100-year operation are presented in Table 2. As most TRU nuclides have preferred fission ability in the fast neutron spectrum, which is an efficient way for MA incineration, a preferred MA transmutation capability is achieved in the fast MSR core for both of the two salts. One can be seen that the SICs with the Flibe salt for the three MSR cores at the end life of 100-year operation are 167, 185 and 206 kg/GWth.y, respectively. Due to the higher loading of MA for the Flinak salt, higher SICs are achieved correspondingly in the thermal, epithermal and fast MSR cores, which are 170, 206 and 247 kg/GWth.y, respectively. The discrepancy of SIC for the two salt compositions is more obvious in the fast spectrum due to the fact that the core with the Flinak salt hardens the spectrum more efficiently than that with the Flibe salt, which benefits the fission ability of most TRU nuclides and facilitates the MA incineration rate. The IR is an important parameter that evaluates the transmutation efficiency of MA. The IR variances of the SIC among the three MSR cores are similar for both of the two salts. However, the IR with the Flinak salt is lower than that with the Flibe salt, especially in the thermal MSR core. This is because that there is an inferior neutron economy in the Flinak salt with significant capture cross sections of Na-23 and K-39, especially in the thermal energy region. With the high MA loading and the feasibility of online refueling, MSR can attain an alluring transmutation efficiency of MA with the TR over 0.75, which means that more than 75% of MA loaded in the core is incinerated. The DR is an important indicator to evaluate the transmutation capability of a single element, which is displayed in Fig. 4. It can be seen that Np has a higher DR than the other two MA of Am and Cm as Np has a higher fraction in MA and a larger absorption cross section than those of Am and Cm, which ranges from 120.7 to 141.9 kg/GWh.y with the Flibe salt

and from 122.1 to 163.3 kg/GWh.y with the Flinak salt in the above three cores. The DR of Am is inferior to that of Np due to a lower mass loading, a smaller absorption cross section and a significant production from Pu. In the transmutation chains, a significant amount of Cm will be accumulated by successive neutron captures and β decays from Np, Pu and Am, which impedes the DR of Cm significantly except its own low mass loading.
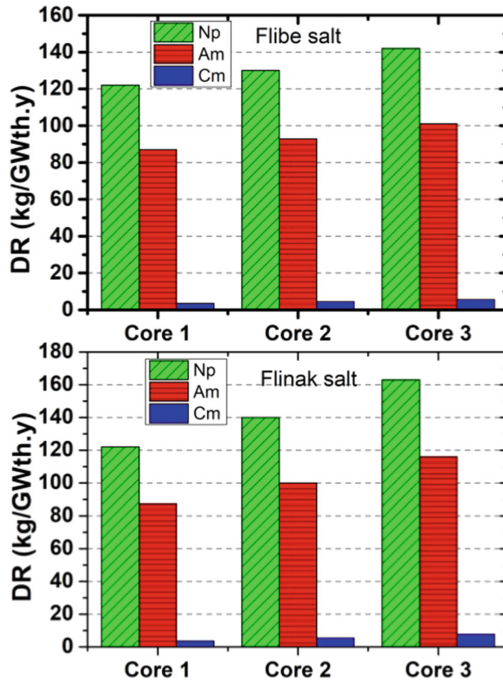
Fig. 4. DRs of Np, Am and Cm with Flibe and Flinak salts in the three MSR cores

3.3 TRU Evolution and Radiotoxicity

In the transmutation chains of MAs, the disappearance ways differ significantly in different neutron energies. Some MAs such as Np-237, Am-241 and Am-243 with larger capture cross sections than their fission ones in the thermal region are transmuted by capturing neutrons consecutively to form Pu-239, Am-242, Am-242m, and Cm-245 with very large fission cross sections. In the fast neutron spectrum, most MA can be transmuted by fissions with higher fission cross sections than the capture ones. Therefore, the TRU evolution varies significantly with the neutron spectrum, which imposes a variation on the radiotoxicity.

Figure 5 and Fig. 6 display the evolutions of the Pu isotopes and new created MA for the Flibe salt in the three MSR cores, respectively. One can find that the produced Pu isotopes are the majority of the new created nuclides, whose production rates are
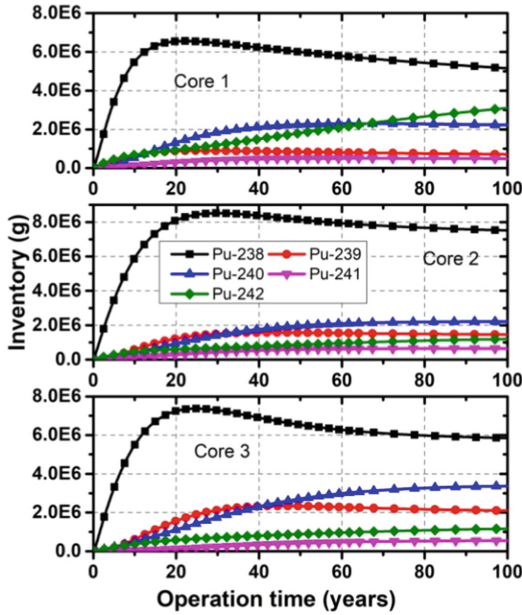
Fig. 5. Evolutions of the Pu isotopes with Flibe salt for the three cores during 100-year operation
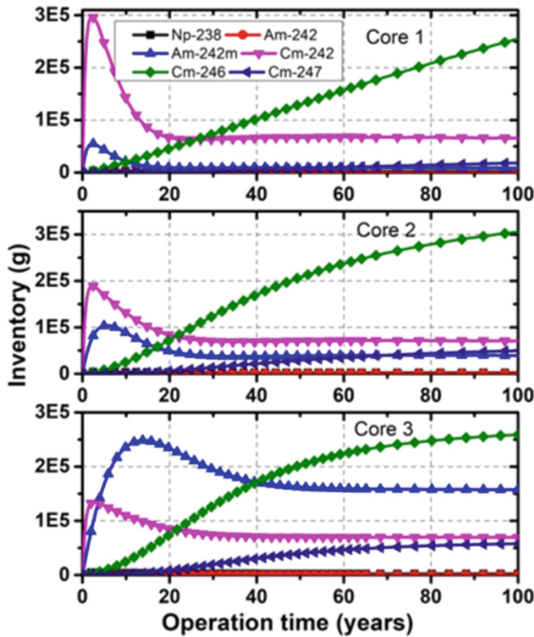
Fig. 6. Evolutions of the MA isotopes with Flibe salt for the three cores during 100-year operation

as high as about 116, 130 and 129 kg/y for the thermal, epithermal and fast cores, respectively. For the Pu isotopes, there are two main reaction chains to produce Pu-238 from Np-237 and Am-241 by successive (n, γ) and β/α decay reactions. In further, Pu-239 produced from the Pu-238 capture has a large fission cross section, which is the major disappearance way for Pu-239. Hence, the inventories of the higher Pu isotopes which are mainly produced by Pu-239 capture are much less than Pu-238. It can be seen in Fig. 5 that Pu-238 accounts for the majority of the transmuted products as the source nuclides of Np-237 and Am-241 are the main isotopes of the initial MA with the fraction of as high as about 86.2%. On the other hand, the accumulated inventory of Pu-238 in the epithermal core is higher than the other two cores due to the fact that most TRU have significant capture resonances in the epithermal region than in the fast region and the total loading of MA in the epithermal core is higher than that in the thermal core. The evolutions of the other Pu isotopes also reveal significant variations because of the different reaction cross sections and MA loadings. At the end of 100-year operation, the mass fraction of Pu-238 in the Pu isotopes is 44.4%, 57.6% and 44.9% in the thermal, epithermal and fast MSR cores, respectively, which is advantageous from the view point of non-proliferation. Similarly, the evolutions of new created MAs in the three cores reveal a significant variation which is tightly related with the MA loadings and the neutron spectrum. The production rate of the new created MA is 3.5, 4.7 and 5.5 kg/y for the thermal, epithermal and fast MSR cores, respectively, which is much lower than that of the Pu isotopes.
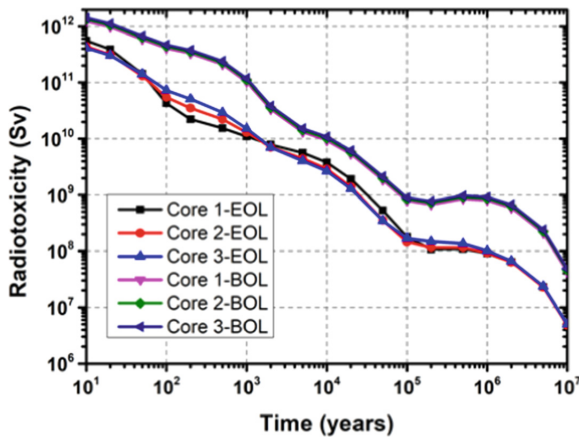
Fig. 7. Evolutions of the total radiotoxicity with Flibe and Flinak salts in the three MSR cores

The radiotoxicity is an important parameter to evaluate the effect of radionuclides to human health by ingestion or digestion, which is defined as:

$$R(t) = \sum_i R_i(t) = \sum_i r_i \lambda_i N_i(t)$$

where $R_i(t)$ represents the radiotoxicity of nuclide i at time t in unit of Sv; r_i refers to the effective dose coefficient in Sv/Bq by ingestion for the public [20], which depends on the

decay mode and the emitted energy of particles; λ_i and $N_i(t)$ represent the decay constant and atoms of nuclide i, respectively. In the SCALE6.1 software system, the ORIGEN-S module is feasible to calculate the radioactivity of each nuclide and the radiotoxicity is calculated with multiplying the effective dose coefficient by the radioactivity of each nuclide.

To evaluate the radiotoxicity of MA with different MA loadings in the thermal, epithermal and fast MSR cores, the total radiotoxicities of MA and the radiotoxicities of Np, Am and Cm at the beginning and end of lifetime are chosen for discussion. One can see from Fig. 7 that the total radiotoxicitiy of MA for the Flibe salt in the three different MSR cores after 100-year operation is reduced significantly, about 45% lower than that at the beginning of lifetime. For the total radiotoxicity of MA, the highest contribution is from Cm because of the high dose coefficients of most Cm isotopes and their daughter products even though the total Cm inventory is extremely small (as shown in Fig. 8). For this reason, the total radiotoxicity of MA for the three different cores are very similar since the difference of the MA inventory can be negligible. Due to a significant accumulation of Np-238 with a very short half-life, the radiotoxicity of Np at the end of lifetime is increased slightly in the first 100 years, which is decreased rapidly in the following decay time and is about 80% lower than that at the beginning of lifetime. Am has a significant reduction on radiotoxicity, with more than an order of magnitude lower than that at the beginning of lifetime, which is the major factor to decrease the total radiotoxicity of MA.
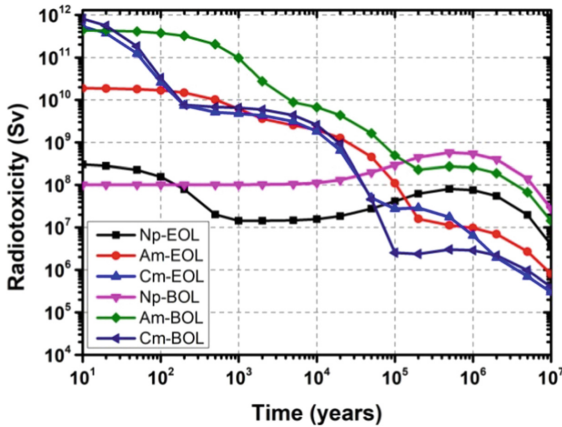
Fig. 8. Evolutions of the MA radiotoxicity with Flibe salt in the thermal MSR core

3.4   Evaluation on Safety Parameters

To evaluate the influence of MA loading on the reactor safety of the thermal, epithermal and fast MSR cores, two important parameters of the temperature feedback coefficient (TFC) and the effective delayed neutron fraction (β_{eff}) are analyzed in this work.

The TFC is an essential indicator for the inherent safety issues, which is required to be negative during the whole lifetime of the reactor. The total TFC in a reactor is calculated as the sum of the fuel TFC and the moderator TFC. In further, the fuel TFC can be broken down into the Doppler effect and the fuel salt expansion.
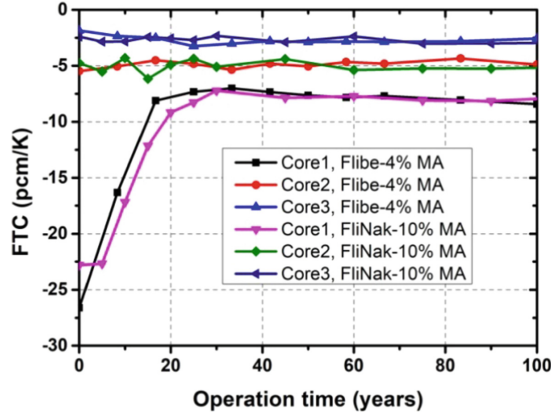
Fig. 9. Evolutions of the TFC with Flibe and Flinak salts in the three MSR cores
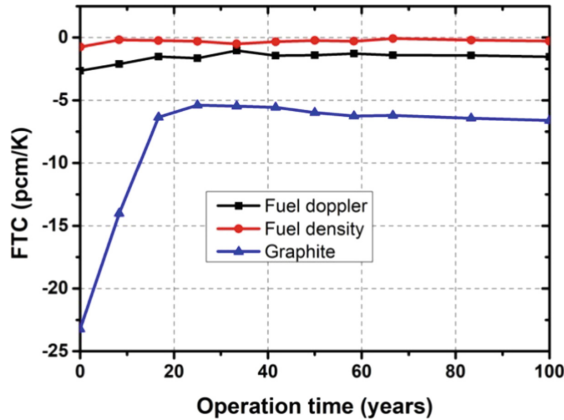
Fig. 10. Evolutions of the TFC with Flibe salt in the thermal MSR core

The evolutions of the TFC for different MA loadings in the three MSR cores are displayed in Fig. 9. One can be seen that the total TFC is significantly related with the neutron spectrum and slightly varied with the evolutions of the fuel compositions. To evaluate the contribution of TFC from fuel density, fuel Doppler and graphite, the three items of TFC for the Flibe salt in the thermal core are exampled for discussion, as shown in Fig. 10. For the MA from the spent fuel of PWR, the MA nuclides except Cm-245 (with the mole fraction in MA of 0.26%) are poisonous to reactivity, especially in a thermal region. Furthermore, Np-237 at 0.5 eV and Am-241 at 0.3 eV, 0.6 eV and 1.1 eV reveal

significant capture resonance cross sections (>1000 barns), respectively, which is benefit for decreasing the TFC as the MA captures with a Doppler broadening can counteract the increased fissions of fissile nuclides with the fuel temperature increasing. In addition, when the graphite temperature is increased, the Maxwellian spectrum shifts to a higher energy region, where it is closer to the strong capture resonance cross-sections of MA. Hence, a negative graphite TFC with the value as low as about -26.6 pcm/K is obtained at the beginning of lifetime. During operation, the thermal neutron spectrum hardens gradually as the continuous feeding of MA, which is gradually away from the capture resonances of MA and increases the graphite TFC. The total TFC for the Flibe salt in the thermal MSR core which is mainly influenced by the graphite effect varies from -26.6 pcm/K to be an equilibrium value of about -8 pcm/K. As there is a minor variation on the neutron spectrum with the Flibe salt and Flinak salt, little differences on the total TFC are caused with the two different salt compositions in the same MSR core. For the epithermal MSR core, the negative effect of the graphite TFC tends to be weakened as the neutron spectrum is far away from the capture resonances of MA. The total TFC is around -5 pcm/K during the entire operation time. As there is no moderator in the fast MSR core, the total TFC is just the sum of the fuel doppler and the fuel density effects. Therefore, the total TFC is higher than the other two cores but always keeps negative with the value of about -2.5 pcm/K.

β_{eff} is another important parameter for both kinetics reactivity controlling safety and static reactor physics experiments. It can be defined as the ratio of the average delayed neutron number and the total average fission neutron number:

$$\beta_{eff} = \frac{\sum_i \overline{\nu_D}(i) R_f(i)}{\sum_i (\overline{\nu_D}(i) + \overline{\nu_P}(i)) R_f(i)}$$

where $\overline{\nu_D}(i)$ and $\overline{\nu_P}(i)$ denote the average delayed neutron number and the average prompt neutron number per fission for actinide i, respectively. When regarding a reactor involved with various heavy nuclides, the contribution of actinide i to the total β_{eff} can be separated as:

$$\beta_{eff}(i) = \frac{\overline{\nu_D}(i) R_f(i)}{\sum_i (\overline{\nu_D}(i) + \overline{\nu_P}(i)) R_f(i)}$$

Figure 11 presents the total β_{eff} evolutions for different MA loadings in the thermal, epithermal and fast MSR cores. For all the cases, the total β_{eff} is quickly decreased in the first 20-year operation and then increased gradually during the remaining 80 years. To explore the source of the variation of β_{eff}, the separate contributions of the main actinides in the case of 4% MA in the Flibe salt for the thermal MSR are evaluated, which is listed in Fig. 12. One can see that the β_{eff} of U-233 at the beginning of the lifetime is as high as 274 pcm, which accounts for the vast majority of the total β_{eff} (287 pcm). This is because that U-233 contributes the majority of fissions in the thermal core. When the neutron spectrum hardens, more U-233 is required which increases the total β_{eff} correspondingly. Furthermore, an inferior neutron economy for the Flinak salt also requires more fissile fuels for criticality. Therefore, when the neutron spectrum ranges from thermal to fast, the initial total β_{eff} rises from 287 pcm to 298 pcm for the Flibe salt while it increases from 289 pcm to 315 pcm for the Flinak salt. During the first
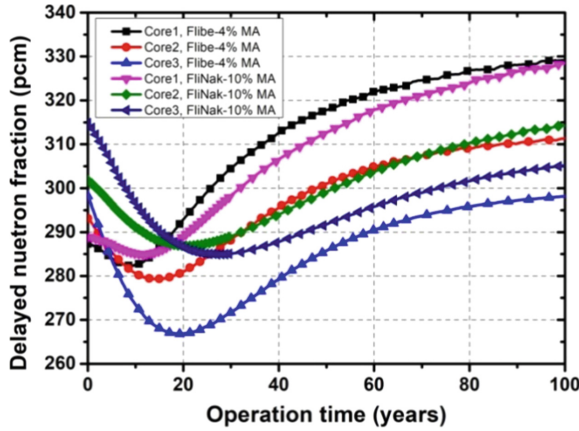
Fig. 11. Evolutions of the total β_{eff} with Flibe and Flinak salts in the three MSR cores
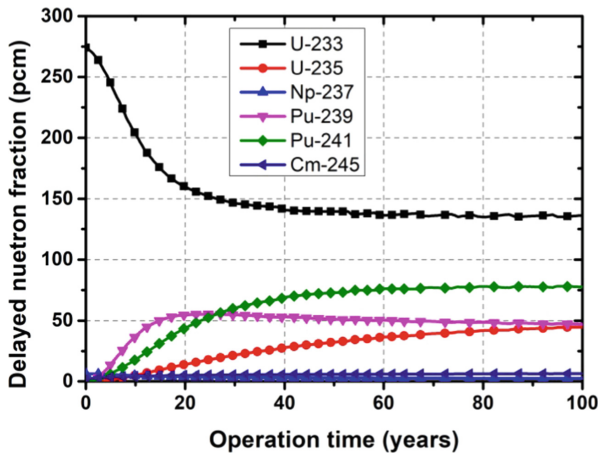
Fig. 12. Evolutions of the β_{eff} contribution of main nuclides with Flibe salt in the thermal MSR core

20-year operation, several fissile isotopes (Pu-239, Pu-241, Cm-245) transmuted from MA are quickly accumulated which weakens the requirement of U-233 significantly. As the single β_{eff} of Pu-239, Pu-241 and Cm-245 are much smaller than that of U-233, the total β_{eff} decreases correspondingly during the first decades of operation. Since most of the TRU nuclides have a higher ratio of fission to capture in a fast neutron spectrum, the requirement of U-233 is reduced in further. Hence, the total β_{eff} decreases more rapidly when the neutron spectrum hardens. The total β_{eff} increases gradually to be an equilibrium state in the remaining 80-year operation due to the accumulated fissile isotopes except U-233.

4 Conclusions

In this paper, the MA transmutation capabilities with different MA loadings for thermal, epithermal and fast MSRs are evaluated. The MA transmutation characteristics with two types of carrier salts and three neutron spectra are compared and discussed. The effects on neutron spectrum, SIC, TR, DR, radiotoxicity and safety parameters are analyzed.

With a significant amount of MA loading into the fuel salt, the thermal, epithermal and fast neutron spectra are all moved to a faster region due to the large captures of most MA. Benefiting the online refueling, MSR can attain a high MA transmutation capability. One can be concluded that the SICs with the Flibe salt (4% MA in the fuel salt) for the three MSR cores at the end life of 100-year operation are 167, 185 and 206 kg/GWth.y, respectively. With a higher loading of MA for the Flinak salt (10% MA in the fuel salt), higher SICs are achieved in the thermal, epithermal and fast MSR cores, which are 170, 206 and 247 kg/GWth.y, respectively. MSR can attain an alluring transmutation efficiency of MA with the TR over 0.75. In addition, the IR with the Flinak salt is lower than that with the Flibe salt, especially in the thermal MSR core, because that there is an inferior neutron economy in the Flinak salt with significant capture cross sections of Na-23 and K-39, especially in thermal energy region. With little production source, high mole faction and large captures, Np has the highest DR in three MA elements, which ranges from 120.7 to 141.9 kg/GWh.y with the Flibe salt and from 122.1 to 163.3 kg/GWh.y with the Flinak salt in the three different MSR cores. With an effective transmutation capability, the total radiotoxicitiy of MA after 100-year operation is reduced significantly, about 45% lower than that at the beginning of lifetime.

Two safety parameters of TFC and β_{eff} are also evaluated. The total TFC is significantly varied with different neutron spectra and MA loadings but all are located in a negative region. The total TFC in the thermal MSR is varied obviously from below -20 pcm/K to about -7.5 pcm/K during 100-year operation because the thermal neutron spectrum is tended to be a faster region with the online refueling of MA which weakens the effects of MA capture resonances. The total TFC for the epithermal MSR is kept around -5 pcm/K during the entire operation time while it is about -2.5 pcm/K for the fast MSR. The total β_{eff} is decreased firstly in the initial 20-year operation and then increased gradually to be an equilibrium state in the remaining 80-year operation. The total β_{eff} at the equilibrium state varies from about 298 pcm to 329 pcm for all cases.

In conclusion, it is feasible to transmute MA in an MSR and achieve the goals of reduction of MA long-term radioactive hazards. A higher SIC is obtained with a higher MA loading for the Flinak salt while a higher TR is achieved with a better neutron economy for the Flibe salt.

References

1. Salvatores, M., Palmiotti, G.: Radioactive waste partitioning and transmutation within advanced fuel cycles: achievements and challenges. Prog. Part. Nucl. Phys. **66**(1), 144–166 (2011)
2. Bala, A., Namadi, S.: A review of the advantages and disadvantages of partitioning and transmutation. Int. J. Sci. Adv. Technol. **5**, 11–14 (2015)
3. OECD-Nuclear Energy Agency: Status and Assessment Report on Actinide and Fission Product Partitioning and Transmutation (1999)
4. Mukaiyama, T., Gunji, Y., Ogawa, T., et al.: Minor actinide transmutation in fission reactors and fuel cycle considerations. IAEA-TECDOC-693, Vienna, Austria: IAEA 86 (1993)
5. OECD, 2014. Minor Actinide Burning in Thermal Reactors: A Report by the Working Party on Scientific Issues of Reactor Systems, Nuclear Science, OECD Publishing, Paris
6. Liu, B., Han, J., Liu, F., et al.: Minor actinide transmutation in the lead-cooled fast reactor. Prog. Nucl. Energy **119**, 103148 (2020)
7. Takeda, T.: Minor actinides transmutation performance in a fast reactor. Ann. Nucl. Energy, **95**, 48–53 (2016)
8. Zhou, S., Wu, H., Zheng, Y.: Flexibility of ADS for minor actinides transmutation in different two-stage PWR-ADS fuel cycle scenarios. Ann. Nucl. Energy **111**, 271–279 (2018)
9. Jiang, M.H., Xu, H.J., Dai, Z.M.: Advanced fission energy program-TMSR nuclear energy system. Bull. Chin. Acad. Sci. **27**, 366 (2012)
10. Zhou, B., Xiaohan, Y., Zou, Y., et al.: Study on dynamic characteristics of fission products in 2 MW molten salt reactor. Nucl. Sci. Tech. **31**(17), 1–17 (2020)
11. Zou, C.Y., Cai, X.Z., Yu, C.G., et al.: Transition to thorium fuel cycle for TMSR. Nucl. Eng. Des. **330**, 420–428 (2018)
12. Zou, C.Y., Zhu, G.F., Yu, C.G., et al.: Preliminary study on TRUs utilization in a small modular Th-based molten salt reactor (smTMSR). Nucl. Eng. Des. **339**, 75–82 (2018)
13. Ignatiev, V., Feynberg, O., Merzlyakov, A., et al.: Progress in development of MOSART concept with Th support. In: Proceedings of ICAPP, 12394 (2012)
14. Heuer, D., Merle-Lucotte, E., Allibert, M., et al.: Towards the thorium fuel cycle with molten salt fast reactors. Ann. Nucl. Energy **64**, 421 (2014)
15. Zou, C., Yu, C., Wu, J., et al.: Parametric study on minor actinides transmutation in a graphite-moderated thorium-based molten salt reactors. Int. J. Energy Res. (12) (2021)
16. Ma, K.F., Yu, C.G., Cai, X.Z., et al.: Transmutation of ^{129}I in a single-fluid double-zone thorium molten salt reactor. Nucl. Sci. Tech. **31**(1) (2020)
17. ORNL: Scale: A Comprehensive Modeling and Simulation Suite for Nuclear Safety Analysis and Design. ORNL/TM-2005/39 (2011)
18. Yu, C., Zou, C., Wu, J., et al.: Development and verification of molten salt reactor refueling and reprocessing system analysis code based on SCALE. At. Energy Sci. Technol. **52**, 2136–2142 (2018)
19. Lizin, A.A., Tomilin, S.V., Gnevashov, O., et al.: PuF$_3$, Am $_F$3, Ce$_F$3, and Nd$_F$3 solubility in LiF-NaF-KF MELT. At. Energ. **115**, 11 (2013)
20. ICRP: Compendium of dose coefficients based on ICRP publication 60. In: ICRP Publication 119. Ann. ICRP **41**(Suppl.) (2012)

Development and Preliminary Verification of a Neutronics-Thermal Hydraulics Coupling Code for Research Reactors with Unstructured Meshes

Mingrui Yang[1], Chixu Luo[1], Dan Wang[2], Tianxiong Wang[2], Xiaojing Liu[1], and Tengfei Zhang[1(✉)]

[1] Shanghai Jiao Tong University, Shanghai, China
{yangmr96,zhangtengfei}@sjtu.edu.cn
[2] Nuclear Power Institute of China, Chengdu, Sichuan, China

Abstract. To maximize their adaptability and versatility, research reactors are designed to adapt to various operational conditions. These requirements result in more complex configurations and irregular geometries for research reactors. Besides, there is usually a strong coupling of neutronics-thermal hydraulics (N-TH) fields inside the reactor. A three-dimensional N-TH coupling code has been developed named CENTUM (CodE for N-Th coupling with Unstructured Mesh). Steady-state and transient neutronic analyses are performed using a 3D triangular-z nodal transport solver with the stiffness confinement method (SCM). Meanwhile, thermal-hydraulics calculations adopt a multi-channel model. For a preliminary verification of the code, we examine CENTUM with benchmark problems including TWIGL, 3D-LMW, and NEACRP. CENTUM produces maximum power errors of -1.27% and -0.45% for the TWIGL A1 and A2 cases, respectively. For the 3D-LMW benchmark, the largest relative power error of 3.84% is observed at 10 s compared with the reference SPANDEX code. For the NEACRP N-TH coupling benchmark, CENTUM results in a 0.35 ppm error in critical boron concentration, a 2.16 °C discrepancy in the fuel average Doppler temperature, and a 0.63% overestimation in the maximum axial power. Moreover, transient results considering thermal-hydraulics feedback are in good agreement with the PARCS reference solutions, with the maximum relative power deviation being only 0.055%.

Keywords: Reactor Kinetics · Stiffness Confinement Method · Neutronics-Thermal Hydraulics Coupling · Safety Analysis · Research Reactor

1 Introduction

Research reactors have served as the workhorse for nuclear fuel and material irradiation testing, and they can also be used for secondary missions such as isotope production and electricity generation. They serve as research, development, and demonstration platforms for fuels, materials, and other critical components. To maximize their adaptability and

versatility, research reactors are designed to adapt to a variety of operational conditions. These requirements result in more complex configurations and irregular geometries for research reactors than for conventional Pressurized Water Reactors (PWRs) and Boiling Water Reactors (BWRs). Direct application of conventional reactor analysis codes to research reactors is challenging due to their complex geometrical configurations and high neutron streaming caused by frequent control rod movement. It is noted that geometry complexity is a feature shared by almost all research reactors, which limits the feasibility of conventional methods based on rectangular or hexagonal meshes. As a result, the ability to accurately model research reactors require the ability to describe unstructured meshes. Additionally, the local neutron spectrum in a research reactor varies significantly with position, and frequent control rod operation results in significant neutron flux heterogeneity. Therefore, it is required to solve the neutron transport equation that can describe the angular anisotropy and to take into account the coupling of various physical fields in order to accurately simulate the behavior of the reactor. This will surely use a lot of computational resource during the core's transient analysis. However, due to the physical nature of the reactor, the use of conventional numerical methods, such as implicit Euler method [1] and Runge-Kutta methods [2], encounters serious problems due to the "rigidity" of the set of equations. Solving with these methods requires very small time-step sizes in order to ensure the stability of the method, and thus many unnecessary information will be computed while the computation continues for long transition times, leading to a huge waste of computational resources, and may also contain large cumulative errors. The precursor concentration equation introduced stiffness into the system, so we employ the stiffness confinement method (SCM) technique to decouple the neutron flux density equation and the delayed neutron density equation, eliminating the stiffness introduced by the precursor concentration equation [3].

Due to the strong coupling between reactor neutronics and thermal hydraulics, a multi-channel model is used to describe the coolant convection and the finite difference method to calculate the thermal conductivity of the fuel rods, so as to provide feedback on the cross-section used for the neutronics calculation. CENTUM's adopts the OSSI [4] (Operator Splitting Semi-Implicit) method for coupling. Figure 1 depicts the coupling flow of the OSSI method. Each time step begins with a neutronics calculation, and the power rate for each assembly is transferred to the thermal hydraulics module. Without iterating, the process enters directly to the next time step after the thermal hydraulics calculation is finished.

This paper is organized as follows. Section 2 illustrates the steady-state triangular-z node neutron transport model, the transient SCM method and the thermal hydraulics models embedded in CENTUM. As a preliminary verification, Sect. 3 presents numerical verification results using TWIGL, LMW and NEACRP benchmark cases. Specifically, the TWIGL benchmark and the LMW benchmark are neutronics transient problems, and the NEACRP is a problem to demonstrate CENTUM's capability of modeling the N-TH coupling effect.
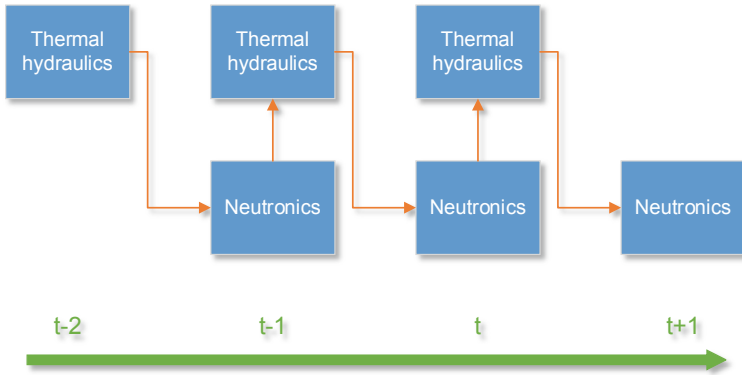
Fig. 1. The OSSI method in CENTUM

2 Methodology

2.1 Triangular-Z Node Neutron Transport Model

Considering isotropic scattering and using S_N method, the three-dimensional multigroup neutron transport equation in the triangular prism can be written as [5]:

$$\mu^m \frac{\partial \Psi_g^m(x, y, z)}{\partial x} + \eta^m \frac{\partial \Psi_g^m(x, y, z)}{\partial y} + \frac{\xi^m}{h_z} \frac{\partial \Psi_g^m(x, y, z)}{\partial z} + \Sigma_t^g \varphi_g^m(x, y, z) = \hat{Q}_g(x, y, z) \tag{2.1}$$

Here, μ^m, η^m, ξ^m are the components of the angular direction m on the x, y, z axes; m is a certain angular direction after using S_N discretization; $\hat{Q}_g(x, y, z)$ is The neutron source term includes fission sources and scattering sources ($cm^{-3} \cdot s^{-1}$); Ψ_g^m represents the neutron angular flux density of the g group in the m direction ($cm^{-2} \cdot s^{-1}$). Usually, the solved triangular node is arbitrary, and it needs to be transformed into a unified coordinate system (Fig. 2).

Using the coordinate transformation, we obtain the equation as:

$$\mu_x^m \frac{\partial \psi_g^m(x', y', z)}{\partial x'} + \eta_x^m \frac{\partial \psi_g^m(x', y', z)}{\partial y'} + \frac{\xi^m}{h_z} \frac{\partial \psi_g^m(x', y', z)}{\partial z} + \Sigma_t^g \psi_g^m(x', y', z) = Q_g(x', y', z) \tag{2.2}$$

where

$$\mu_x^m = \frac{(-y_n + y_p)\mu^m + (x_n - x_p)\eta^m}{2\Delta}$$

$$\eta_x^m = \frac{(-x_k + \frac{1}{2}x_n + \frac{1}{2}x_p)\eta^m + (y_k - \frac{1}{2}y_n - \frac{1}{2}y_p)\mu^m}{\sqrt{3}\Delta}$$

$$-2/3 \leq x' \leq 1/3, \quad -y_s(x') \leq y' \leq y_s(x'), \quad y_s(x') = (x' + 2/3)/\sqrt{3}, \quad -1/2 \leq z \leq 1/2$$
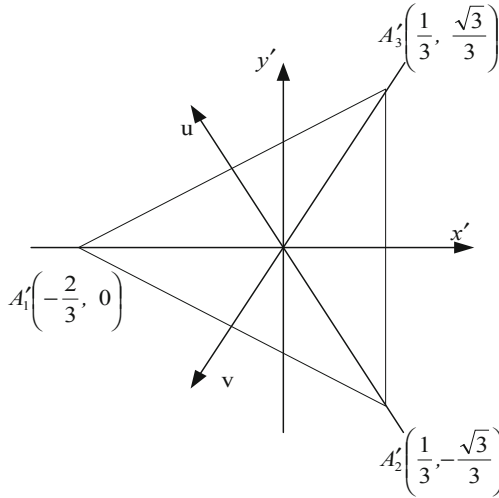
Fig. 2. Equilateral triangle in the calculated coordinate system

The nodal balance equation is given by:

$$2\mu_x^m \overline{\psi}_x^m + 2\mu_u^m \overline{\psi}_u^m + 2\mu_v^m \overline{\psi}_v^m + \frac{\xi^m}{h_z}\left(\overline{\psi}_{z+}^m - \overline{\psi}_{z-}^m\right) + \Sigma_t \overline{\psi}^m = \overline{Q} \qquad (2.3)$$

$\overline{\psi}_i^m$ is the averaged outgoing surface flux in the x, u, v directions, as is shown in Fig. 1; $\overline{\psi}_{z\pm}^m$ are the outgoing surface averaged flux of the upper and lower sides of the node; $\overline{\psi}^m$ is the averaged flux in the node. The transport computation is performed using a specific sweeping and source iteration approach.

2.2 Transient Neutronic Model

For solving transient problems, CENTUM adopts the SCM [6]. By considering that the dynamic frequency of the angular flux is isotropic:

$$\omega_g(r, t) = \frac{\partial}{\partial t} \ln \varphi_g(r, t) \qquad (2.4)$$

where $\omega_g(r, t)$ is the flux dynamic frequency of group g; $\varphi_g(r, t)$ is the scalar flux of group g.

The flux dynamic frequency can be further decomposed into the shape frequency $\omega_{s,g}(r, t)$ and the amplitude frequency $\omega_t(t)$.

$$\omega_g(r, t) = \omega_{s,g}(r, t) + \omega_t(t) \qquad (2.5)$$

Similarly, the precursor frequency of group i is defined as:

$$\mu_i(r, t) = \frac{\partial}{\partial t} \ln C_i(r, t) \qquad (2.6)$$

Inserting (2.4) and (2.6) into the 3-D multigroup time-space neutron transport equation within a triangular-z prism, the time-dependent neutron transport equation can be transformed into an equation for solving the eigenvalue problem:

$$
\mu^m \frac{\partial}{\partial x}\varphi_g^m(r,t) + \eta^m \frac{\partial}{\partial y}\varphi_g^m(r,t) + \frac{\xi^m}{h_Z}\frac{\partial}{\partial z}\varphi_g^m(r,t)
$$
$$
+\Sigma'_{t,g}(r,t)\varphi_g^m(r,t) = \frac{\chi'_g}{k_D}\sum_{g'=1}^{G}(\nu\Sigma_f)_{g'}(r,t)\varphi_g^m(r,t) \tag{2.7}
$$
$$
+\sum_{g'=1}^{G}\varphi_g^m(r,t)\Sigma_{g'\to g}(r,t)
$$

k_D is the dynamic eigenvalue; $\Sigma'_{t,g}$ is the dynamic total cross-section and χ'_g is the dynamic fission spectrum, which are respectively defined as:

$$
\Sigma'_{t,g}(r,t) = \Sigma_{t,g}(r,t) + \frac{\omega_g(r,t)}{v_g} \tag{2.8}
$$

$$
\chi'_g = \chi_g(1-\beta) + \sum_{i=1}^{M}\chi_{ig}\lambda_i\frac{\beta_i}{\mu_i+\lambda_i} \tag{2.9}
$$

Here, v_g represents the neutron velocity of the g group. The unknown quantities are the flux dynamic frequency and the precursor frequency. Solving for k_D iteratively by Eq. (2.7), combined with the secant method, we get amplitude frequency:

$$
\omega_t^{(m+1)}(t_n) = \omega_t^{(m)}(t_n) + \left[\omega_t^{(m-1)}(t_n) - \omega_t^{(m)}(t_n)\right]\frac{1-k_D^{(m)}}{k_D^{(m-1)}-k_D^{(m)}} \tag{2.10}
$$

Based on the isotropic approximation, the average scalar flux in the nodal v is used to update the node wise shape frequency:

$$
\overline{\omega}_{v,S,g}(t_n) = \frac{1}{\Delta t_n}\ln\left[\frac{\int_v dr f^T(r)\widehat{\varphi}_{v,g}(t_n)}{\int_v dr f^T(r)\varphi_{v,g}(t_{n-1})}\right] \tag{2.11}
$$

in which $\widehat{\varphi}_{v,g}$ is the flux normalized according to the neutron density; $\overline{\omega}_{v,S,g}(t_n)$ is the average shape frequency within $[t, t+\Delta t]$. Meanwhile the actual flux can be written as:

$$
\varphi_{v,g}(r,t) = \widehat{\varphi}_{v,g}(r,t)e^{\frac{\omega_T(t_n)+\omega_T(t_{n-1})}{2}\Delta t_n} \tag{2.12}
$$

Assume that the precursor concentration is uniform within each node, the analytical solution for the precursor concentration is expressed as:

$$
C_{v,i}(t_n) = C_{v,i}(t_{n-1})e^{-\lambda_i\Delta t_n} + \beta_i e^{-\lambda_i\Delta t_n}\int_{t_{n-1}}^{t_n}Q_v(t)e^{\lambda_i t}dt \tag{2.13}
$$

where β_i is the share of group i precursor, λ_i is its decay constant; Q_v is the the node-wise fission source. Combined with Eq. (2.13) the precursor frequency can be updated by:

$$
\mu_{v,i}(t_n) = \begin{cases} \beta_i\frac{Q_v(t_n)}{C_{v,i}(t_n)} - \lambda_i & C_{v,i}(t_n) \neq 0 \\ 0 & C_{v,i}(t_n) = 0 \end{cases} \tag{2.14}
$$

After obtaining the flux frequency and the precursor frequency, we can iteratively Solve k_D by adjusting dynamic total cross-section and the dynamic fission spectrum by using Eq. (2.8) and (2.9). The neutronics transient solving process is shown below (Fig. 3).
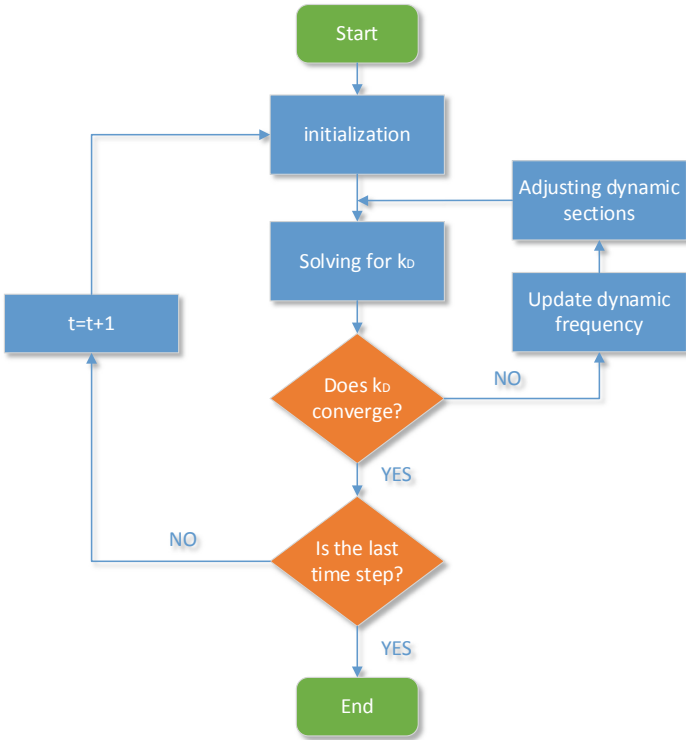
Fig. 3. Flowchart of the transient calculations with SCM

2.3 Thermal Hydraulics Model

In the N-Th coupling process, the thermal hydraulics calculation is used to obtain the thermal hydraulic parameters of the fuel rods and moderator. These parameters are then used to calculate the effect on the cross-sections used for the neutronics calculations.

2.3.1 Moderator Thermal Hydraulics Equation

CENTUM solves the thermal-hydraulics field using multi-channel models. The one-dimensional thermal hydraulics equations are expressed as follows [7]:

Moderator mass conservation equation:

$$\frac{\partial}{\partial t}(\rho)+\frac{\partial}{\partial z}(\rho u) = 0 \tag{2.15}$$

Moderator energy conservation equation:

$$\frac{\partial}{\partial t}(\rho h) + \frac{\partial}{\partial z}(\rho u h) = Q^f \tag{2.16}$$

Moderator momentum conservation equation:

$$\frac{\partial}{\partial t}(\rho u) + \frac{\partial}{\partial z}(\rho u^2) + \frac{\partial P_{fric}}{\partial z} + g\rho + \frac{\partial P}{\partial z} = 0 \tag{2.17}$$

Moderator control equations are solved using a parallel multi-channel model, the flow distribution is based on equal pressure drop in each parallel multi-channel where the inlet and outlet are at the same isobaric surface. The time derivative term is treated with the full-implicit backward difference method and the space variables are treated with the finite difference method.

2.3.2 Fuel Rod Heat Transfer Equation

In a one-dimensional cylindrical coordinate system, ignoring the effect of the axial direction, Fuel rod heat transfer equation as shown below [8]:

$$\rho c \frac{\partial T}{\partial t} + \frac{d^2 T}{dr} + \frac{1}{r}\frac{dT}{dr} + \frac{Q}{\lambda} = 0 \tag{2.18}$$

where T is the distribution of temperature; Q is the volumetric heat release rate of the fuel; λ, ρ and c are the thermal conductivity, density and heat capacity of the fuel material respectively. These properties change with temperature.

The spatial variable in the thermal conductivity equation is treated by the finite difference method. The cylindrical geometry from the inside to the outside are taken successively as the fuel zone, the air gap zone and the cladding zone. For the time discretization, the Crank-Nicholson implicit difference method is used, where θ equals 0.5 in Eq. (2.19).

$$\frac{\frac{\partial A(r,t)}{\partial t} = B(r, t)}{\frac{A(r,t+\Delta t)-A(r,t)}{\Delta t} = (1 - \theta)B(r, t + \Delta t) + \theta B(r, t)} \tag{2.19}$$

By discretization, the following tridiagonal matrix can be obtained:

$$\begin{pmatrix} b_1 & c_1 & 0 & 0 & \cdots & 0 & 0 \\ a_2 & b_2 & c_2 & 0 & \cdots & 0 & 0 \\ 0 & a_3 & b_3 & c_3 & \ddots & \vdots & \vdots \\ 0 & 0 & \ddots & \ddots & \ddots & 0 & 0 \\ \vdots & \vdots & \ddots & a_{n-2} & b_{n-2} & c_{n-3} & 0 \\ 0 & 0 & \cdots & 0 & a_{n-1} & b_{n-1} & c_{n-1} \\ 0 & 0 & \cdots & 0 & 0 & a_n & b_n \end{pmatrix} \begin{pmatrix} \overline{T_1}^{t+\Delta t} \\ \overline{T_2}^{t+\Delta t} \\ \overline{T_3}^{t+\Delta t} \\ \\ \overline{T_{n-2}}^{t+\Delta t} \\ \overline{T_{n-1}}^{t+\Delta t} \\ \overline{T_n}^{t+\Delta t} \end{pmatrix} = \begin{pmatrix} q_1 \\ q_2 \\ q_3 \\ \\ q_{n-2} \\ q_{n-1} \\ q_n \end{pmatrix} \tag{2.20}$$

in which n is the node number; a_n, b_n, c_n and q_n are constants related to the geometry, material and the temperature distribution at the previous time step.

3   Results and Discussion

The primary purpose of this section is to verify CENTUM's the transient function. TWIGL and LMW benchmark problem are mainly to verify the neutronics model of CENTUM, and NEACRP is to verify the N-Th coupling function. All results are evaluated with the angular discretization order of S_2. The triangular-z nodes are generated by Gmsh. All calculations are performed on a personal computer with a 2.90 GHz Intel i7-10700 CPU processor useing serial computation.

3.1   TWLGL Benchmark Problem

This section illustrates the preliminary verification of CENTUM using a simplified two-dimensional two-group dynamics benchmark problem with one set of precursor dynamics parameters [9, 10]. The core consists of three fuel zones forming a square core with a side length of 160 cm, and the fuel assembly size is 8 cm × 8 cm. The geometric arrangement of the core is shown in Fig. 4. The outer boundary condition of the original problem is a zero-flux density boundary, and since the transport calculations cannot handle this type of boundary, vacuum boundary conditions are used instead. The total number of triangular meshes used in the calculation is 400 as shown in Fig. 5, with one radial layer, and reflection boundary conditions are set on the upper and lower surfaces.
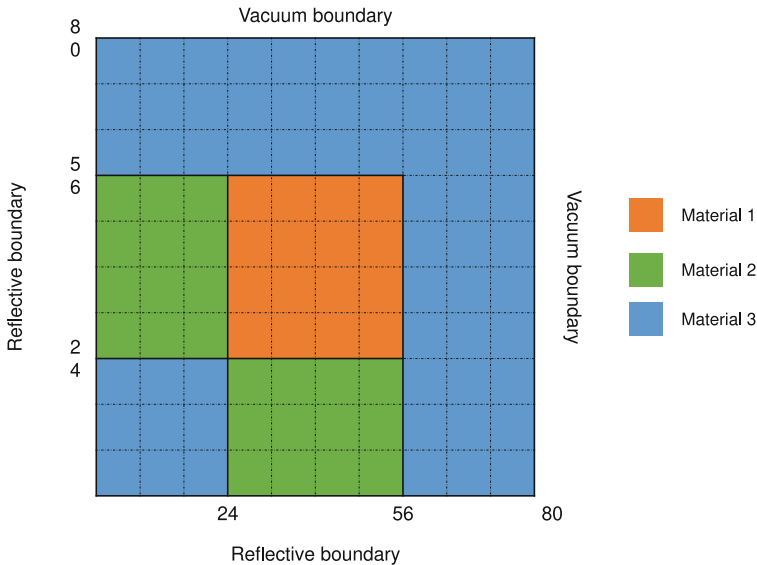
Fig. 4. Layout of the TWIGL problem

The calculation area is 1/4 of the core, and the transient process lasts for 0.5 s. The original problem includes two delayed supercritical problems, A1 and A2. The two problems introduce perturbation ramp and stepwise, respectively. For A1 and A2 problems, two sets of reference values are used, one is the transport calculation result
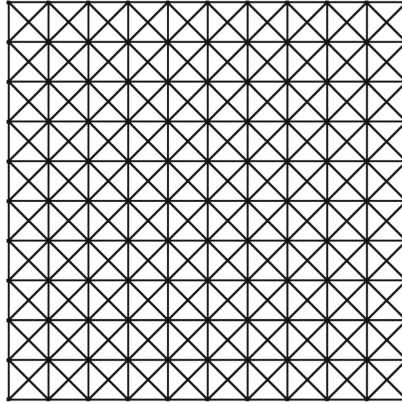
Fig. 5. Mesh of TWIGL benchmark in CENTUM

of UTK's improved quasi-static method code TDTORT; the other is the diffusion cal-culation result of the time direct discrete nodal code SPANDEX which adopts the θ method with a time-step sizes of 0.1 ms [9, 10]. As can be seen from the results in Fig. 6, the results of CENTUM (S_2) agree well with TDTORT (S_4), while the results of both transport codes are higher than the diffusion code. This discrepancy is mainly due to the zero-flux boundary condition used for the diffusion calculation, which leads to the core internal total power value being slightly smaller for the same perturbation case.

(a) A1   (b) A2
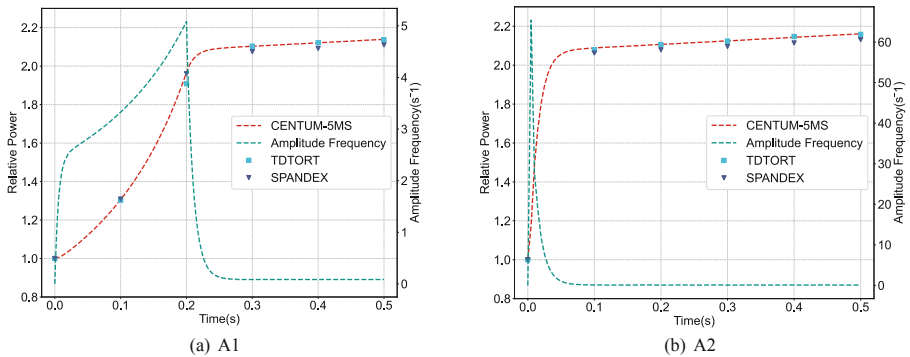
Fig. 6. Results of the TWIGL A1, A2 problem

To further compare the effect of time-step sizes on the calculation results, Table 1, Table 2 gives the normalized power values for the A1, A2 problems.

Compared with TDTORT, the results of CENTUM (20 ms) are in good agreement in both cases, the maximum deviation of the A1 case is 3.83%, and the maximum deviation of the A2 case is 0.41%. And the results obtained by CENTUM using the two time-step sizes are consistent, it show that CENTUM ensures acceptable accuracy even with large time-step sizes.

Table 1. Comparison of core relative powers for the TWIGL A1 problem

Time (s)	TDTORT	CENTUM $\Delta t = 5$ ms	CENTUM $\Delta t = 20$ ms	Err (%) Vs. $\Delta t = 5$ ms	Vs. $\Delta t = 20$ ms
0.0	1.000	1.000	1.000	0.00	0.00
0.1	1.304	1.313	1.313	0.70	0.71
0.2	1.909	1.982	1.982	3.83	3.83
0.3	2.104	2.103	2.103	−0.03	−0.03
0.4	2.122	2.121	2.120	−0.03	−0.07
0.5	2.137	2.140	2.139	0.12	0.11

Table 2. Comparison of core relative powers for the TWIGL A2 problem

Time (s)	TDTORT	CENTUM $\Delta t = 5$ ms	CENTUM $\Delta t = 20$ ms	Err (%) Vs. $\Delta t = 5$ ms	Vs. $\Delta t = 20$ ms
0.0	1.000	1.000	1.000	0.00	0.00
0.1	2.079	2.089	2.087	0.46	0.41
0.2	2.106	2.107	2.106	0.04	0.00
0.3	2.124	2.125	2.123	0.05	−0.03
0.4	2.147	2.143	2.141	−0.18	−0.26
0.5	2.158	2.161	2.160	0.15	0.10

In CENTUM, the neutron density of the core is given by Eq. (2.12). The amplitude frequency determines the overall power of the core. From Fig. 7, it can be found that the longer the time step, the more obvious the oscillation of the amplitude frequency.

When the time-step sizes is increased, the solution of the amplitude frequency will deviate more from the true value. CENTUM use the average of the amplitude frequencies at time t and $t + \Delta t$ to approximate the amplitude frequency of the time period $[t, t + \Delta t]$. Affected by this characteristic, when iteratively solves the amplitude frequency at time $t + \Delta t$, it will be affected by the amplitude frequency of the previous time step. Eventually, the amplitude frequency at large time-step sizes fluctuate around the true value. So in the end we can get accurate results as long as the average between the two time steps is close to the true value, this feature can effectively reduce the cumulative error. However, when the time-step sizes is too large and the reactivity changes sharply, the average amplitude frequency at two time points cannot reflect the real change very well.
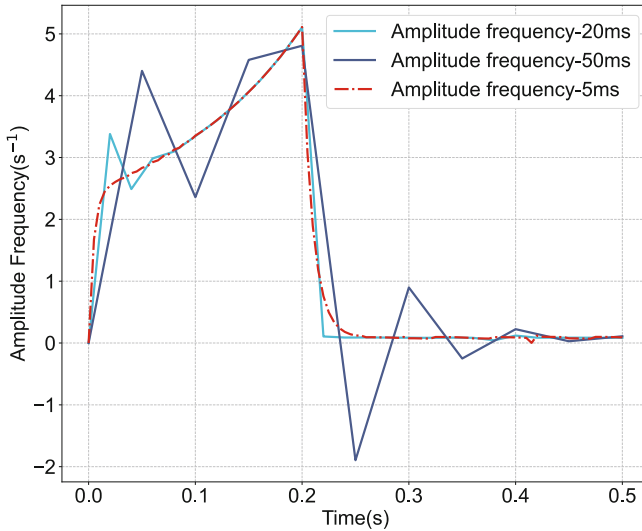
Fig. 7. Amplitude frequencies at different time-step sizes in TWIGL A1

3.2   3D-LMW Benchmark Problem

The 3D-LMW is a 3D diffusion benchmark [9, 10], which contains six sets of delayed neutron dynamics parameters, and the outer boundary is a vacuum boundary. In this paper, the calculation is performed with a quarter-core model. Figure 8 and 9 depict the problem's radial and axial geometrical arrangements, respectively. The motion of two groups of control rods is what causes the transient process: at the start of the transient, the first group of rods are inserted into the middle of the core at a height of 100 cm from the bottom, and the second group rods are withdraw from the active core; between 0.0 s and 26.666 s, the first group rods were lifted out of the active area of the core at a speed of 3.0 cm/s, and the second group rods were gradually inserted into the core from 7.5 s to 47.5 s. CENTUM uses spatial volume weights to deal with the cuspate effect of the control rods.

The size of the LMW assemblies is 20 cm × 20 cm. In CENTUM calculations, a total of 468 triangular meshes are divided radially, as shown in Fig. 10, and the axial 200 cm is divided into 10 layers. The entire transient process lasts for 60 s, and the reactivity changes during the process are slight, so a large time-step sizes of 0.5 s chosen for calculation.

The calculation results shown in Fig. 11. The two sets of reference solutions used for comparison are diffusion codes. The relative power trend of CENTUM is in good agreement with the reference solution, the largest relative power error of 3.84% occurs at 10s compared with SPANDEX [9, 10]. However, at this time step, the deviation between SPANDEX and SIMULATE is also quite significant. Likewise, this difference attributed to the discrepancy between the transport method and the diffusion method.
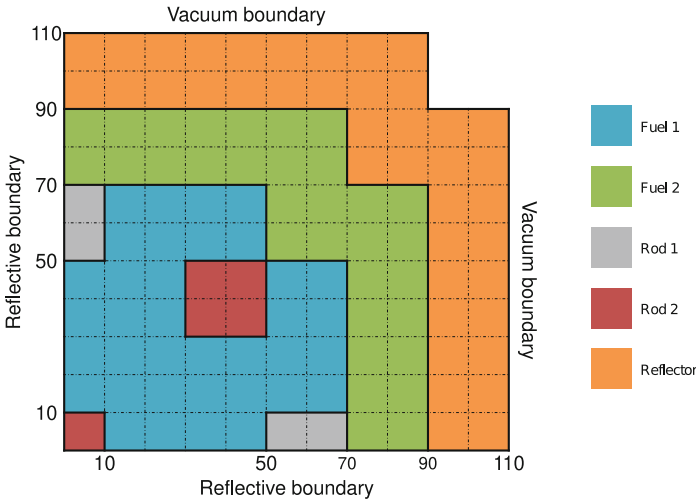
Fig. 8. Radial layout of the LMW problem
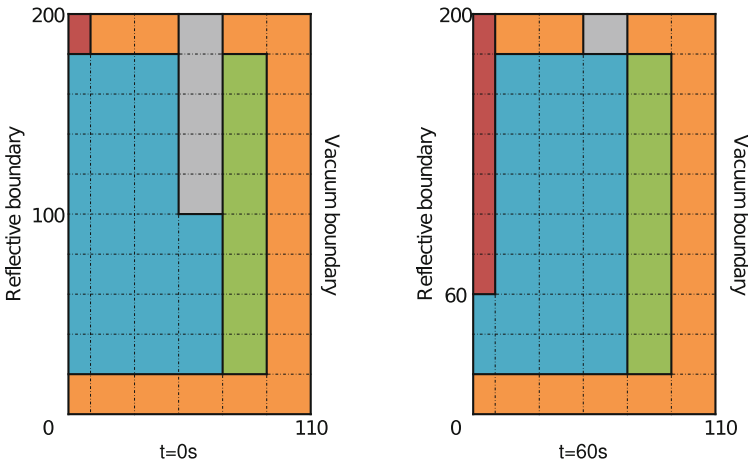
Fig. 9. Axial layout of the LMW problem

3.3 NEACRP Benchmark Problem

The NEACRP rod ejection benchmark includes two types of reactors, i. e. pressurized water reactor and boiling water reactor. It is mainly used for the verification of the neutronics-thermal hydraulics coupling codes of the light water reactor core [11]. The PWR benchmark refers to the geometric size and operating state of a typical PWR. The core consists of 157 assemblies, each measuring 21.606 cm in width. The fuel assemblies are made up of assemblies with various numbers of absorber rods and fuels with various levels of enrichment. Reflectors are set on the periphery region of the core. In the axial direction, the height of the active core is 367.3 cm. The control rod
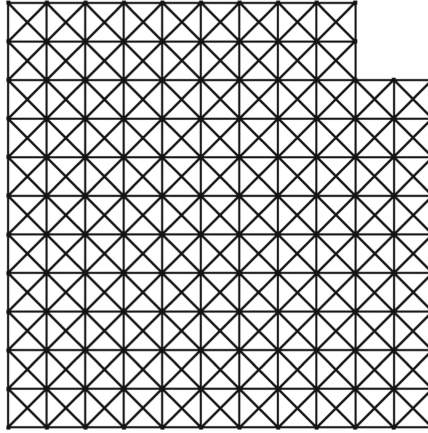
Fig. 10. Mesh of LMW benchmark in CENTUM
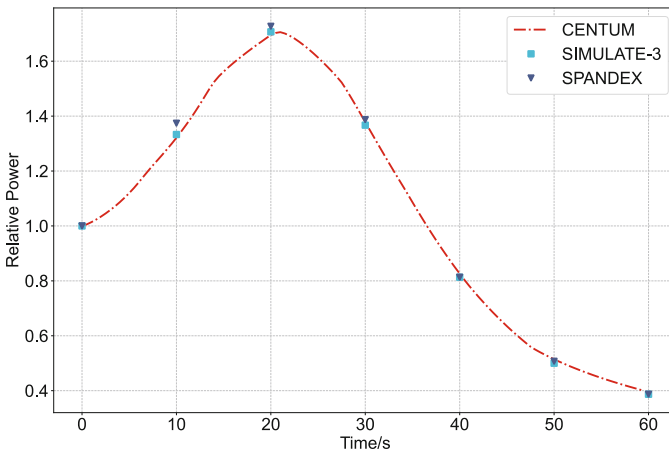
Fig. 11. LMW transient results

has a length of 363.195 cm, the height of the bottom of the absorbent rod when fully inserted is 37.7 cm, and the height when fully ejected is 401.183 cm. The cross section at a numerical node with control rod is determined by adding the cross section $\Delta\Sigma_{CR}$ contributed from the control rod to the cross sextion without control rod [11]:

$$\Sigma_{withCR} = \Sigma_{withoutCR} + p\Delta\Sigma_{CR} \qquad (3.1)$$

where p is the relative insertion in the node, i.e. $0 \leqq p \leqq 1$.

The problem contains a total of 6 operating conditions. For simplicity, we select problem A2 as an example to demonstrate the accuracy of CENTUM. Case A2 represents the HFP (hot full power, 2775 MW) condition of the reactor, and the control rods in the center position (blue area in the Fig. 13) are ejected. In case A2, the central control rod eject to the top from a height of 196.12 cm from 0 ms to 100 ms.

There are 18 layers in the axial direction, with heights of 30 cm 7.7 cm, 11 cm, 15 cm, 30 cm * 10, 12.8 cm * 2, and 8 cm, which are the same as PARCS [12] used for reference. As shown in Fig. 12, Centum is divided into a total of 790 triangular meshes in the radial direction, while PARCS is divided into 205 squares of 10.803 cm * 10.803 cm. In CENTUM's Thermal-Hydraulics Model, a fuel assembly is equivalented as a channel, Axial meshing consistent with neutronics module. The entire transient process lasts for 5 s. CENTUM sets the time-step sizes to 5 ms at 0 s–1 s and 20 ms at 1 s–5 s.
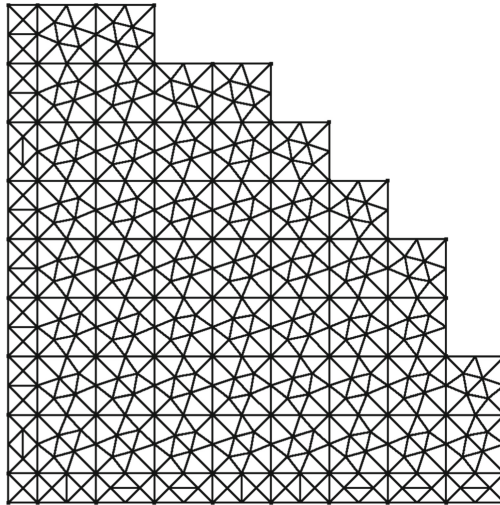
Fig. 12. Mesh of NEACRP benchmark in CENTUM
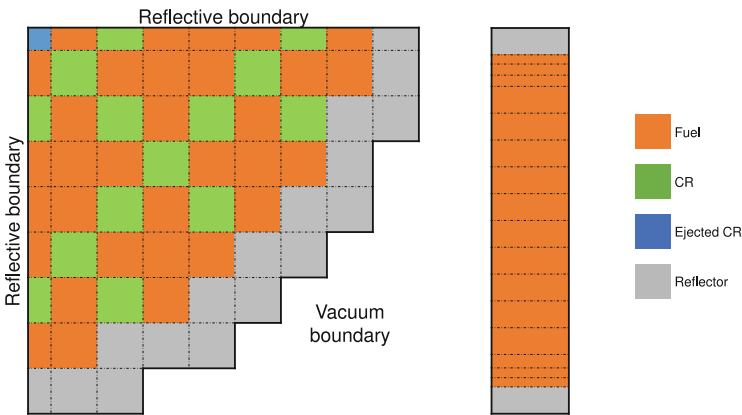
Fig. 13. The layout of case A2

For the steady-state coupling results, the critical boron concentration deviation of the two codes is 0.35 ppm, and the fuel average Doppler temperature deviation is 2.16 °C. Both of these are aggregate parameters of the core, so they match up well. The maximum fuel temperature difference is 30 °C. By comparing the axial power distribution in Fig. 14, it can be found that the maximum axial power of CENTUM is 0.63% higher. Figure 14 also shows the deviation of the radial power distribution, which is higher for the CENTUM outer assemblies compared to PARCS. The difference in power distribution is the most important reason for the difference in maximum fuel temperature. The transport method can better handle the various anisotropies of the angles, plus CENTUM uses a vacuum boundary condition, while PARCS uses a zero-flux boundary condition, all of which can lead to differences in the power distribution.
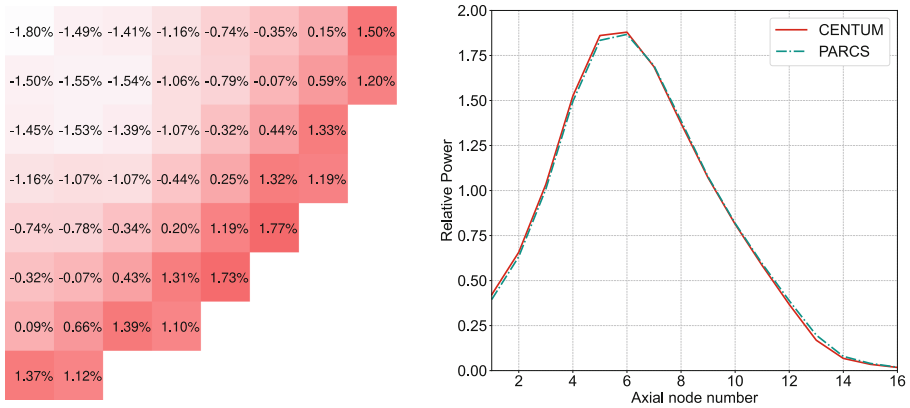
Fig. 14. Comparison of radial and axial power distribution between CENTUM and PARCS at steady-state

As can be seen in Fig. 15, the results of CENTUM are in good agreement with the PARCS reference solutions, with the maximum relative power deviation being 0.055%. Because CENTUM adopts the OSSI method, each neutronics calculation uses the thermal-hydraulic calculation results of the previous time step. This results in a delayed feedback to the neutronics calculation, which can also be observed in Fig. 15. The temperature rise curve of the coolant outlet is slightly deviated, which is mainly caused by the slightly different description of the coolant channel between the two codes (Table 3).
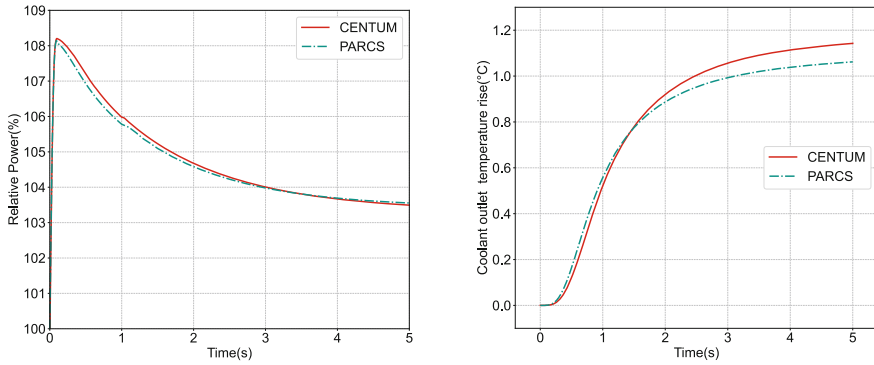
Fig. 15. Transient calculation results of CENTUM for A2

Table 3. Comparison between CENTUM and references results for case A2

Parameter	Critical boron concentration (ppm)	Fuel maximum power (at 0 s, °C)	Average Doppler Fuel Temperature (at 0 s, °C)	Time of power peak (s)	Power peak (%)	Final coolant outlet temperature (at 5 s, °C)
PARCS	1158.86	1672	546.61	0.09	108.14	325.03
CENTUM	1159.21	1702	548.77	0.1	108.20	325.80
Err	0.35	30	2.16	0.01	0.060	0.77

4 Conclusions

In this study, the CENTUM code is developed to analyses steady-state and transient neutronics problems using a 3D triangular-z nodal transport solver with the SCM. Meanwhile, the N-TH coupling calculation can be carried out using the multi-channel model. For neutron dynamics calculations, CENTUM agrees well with the references in the TWIGL and LMW benchmarks. The maximum errors with the TWIGL A1, A2 reference solution are -1.27% and -0.45%, respectively, when using a 20 ms time-step sizes. The maximum error with the LMW reference solution is 3.84%, and the time-step sizes set is 0.5 s. The results show that SCM can maintain good accuracy in longer time-step sizes, which can effectively reduce computing resources.

A preliminary comparison with PARCS shows that CENTUM can accurately simulate the core N-Th coupling process. It should be noted that all test cases are based on Cartesian geometry assemblies which cannot reflect the complex geometrical design of research reactors. We will preserve the verifications and applications of CENTUM on research reactors as an important research direction in the future work.

References

1. Zimin, V.G., Ninokata, H.: Nodal neutron Kinetics model based on nonlinear iteration procedure for LWR analysis. Ann. Nucl. Energy **25**(8), 507–528 (1998)
2. Lu, D., Guo, C., Sui, D.: A three-dimensional nodal neutron kinetics code with a higher-accuracy algorithm for reactor core in hexagonal-z geometry. Ann. Nucl. Energy **101**, 250–261 (2017)
3. Chao, Y.-A., Attard, A.: A resolution of the stiffness problem of reactor kinetics. Nucl. Sci. Eng. **90**(1), 40–46 (1985)
4. Toth, A., et al.: Analysis of Anderson acceleration on a simplified neutronics/thermal hydraulics system. Oak Ridge National Lab.(ORNL), Oak Ridge, TN (United States). Consortium for Advanced Simulation of LWRs (CASL) (2015)
5. Zhang, T., et al.: A 3D transport-based core analysis code for research reactors with unstructured geometry. Nuclear Eng. Des. **265**, 599–610 (2013)
6. Xiao, W., et al.: Application of stiffness confinement method within variational nodal method for solving time-dependent neutron transport equation. Comput. Phys. Commun., 108450 (2022)
7. Křepel, J., et al.: DYN3D-MSR spatial dynamics code for molten salt reactors. Ann. Nuclear Energy **34**(6), 449–462 (2007)
8. Ghiaasiaan, S.M., et al.: Heat conduction in nuclear fuel rods. Nucl. Eng. Des. **85**(1), 89–96 (1985)
9. Goluoglu, S.: A deterministic method for transient, three-dimensional neutron transport. The University of Tennessee (1997)
10. Ban, Y., Endo, T., Yamamoto, A.: A unified approach for numerical calculation of space-dependent kinetic equation. J. Nucl. Sci. Technol. **49**(5), 496–515 (2012)
11. Finnemann, H., et al.: Results of LWR core transient benchmarks. No. NEA-NSC-DOC-93-25. Nuclear Energy Agency (1993)
12. Joo, H.G., et al.: PARCS: a multi-dimensional two-group reactor kinetics code based on the nonlinear analytic nodal method. PARCS Manual Version **2** (1998)

Preliminary Multi-physics Coupled Simulation of Small Helium-Xenon Cooled Mobile Nuclear Reactor

Xiangyue Li, Xiaojing Liu, Xiang Chai, and Tengfei Zhang[✉]

Shanghai Jiao Tong University, Shanghai, China
zhangtengfei@sjtu.edu.cn

Abstract. For the prediction of the internal physical process of SIMONS (Small Innovative helium-xenon cooled MObile Nuclear power Systems), this research created a coupled three-dimensional high-fidelity calculation platform of the neutronics/ thermo-elasticity analysis called FEMAS (FEM based Multi-physics Analysis Software for Nuclear Reactor). This platform allows for the multi-physics coupling calculations of neutron diffusion/ transport, thermal diffusion, and thermal elasticity. It is based on the open-source Monte Carlo code OpenMC and the open-source finite element codes Dealii and Fenics. In this paper, a simplified SIMONS reactor core is analyzed using the coupling platform. The results demonstrate that the coupling platform is capable of accurately predicting the effective multiplication factor change curve, power and temperature distribution, and thermal expansion phenomenon of SIMONS. With 240 kW of thermal power, the local temperature difference of the whole reactor is 390.1 K, and thermal stress-related deformation occurs at a rate of 2.4%. The reactivity feedback caused by the monolith's heating and thermal expansion is 30.5 pcm. Leveraging the high-precision computing hardware, this platform can assess the core performance to ensure that the core design satisfies the design criteria of ultra-long life and inherent safety.

Keywords: Multi-physics Coupling · Numerical Simulation · Mobile Nuclear Power Systems · Thermal Expansion · Finite Element Method

1 Introduction

In some circumstances, a micro transportable nuclear reactor power system can function as an independent micro-grid that can offer a long-term, high-power emergency power supply. It will lessen the loss of life and property due to power outages, helping in communication, transportation, the military, medicine, natural disaster rescue and many other industries, offering a wide range of application prospects in the future.

At present, the United States has carried out projects such as the Prometheus [1], eVinci [2], and Holos reactors [3]. Reactors have been designed using a wide variety of cutting-edge technologies aiming at output powers ranging from kilowatts to megawatts. In China, Tsinghua University has designed a 200-kW gas-cooled reactor with power called IGCR-200 [4].

Designed to be packaged in an ISO container and transported by truck or train, the design of the core of the micro transportable nuclear reactor power system is particularly important. Compared with regular reactors, mobile reactors have strict restrictions for size, weight, power-density and lifetime. Besides, it has been demonstrated that the thermal expansion effect constitutes a significant portion of the reactivity feedback for micro nuclear reactors [5]. Conventional methods of research and analysis based on a single physical field and static geometry can hardly meet these needs.

In order to precisely forecast the internal physical processes of SIMONS, this research developed FEMAS (FEM-based Multi-physics Analysis Software for Nuclear Reactor), a coupled three-dimensional high-fidelity computation platform for neutronics/thermo-elasticity analysis. For neutronics, it employs a high-fidelity 3D multi-group neutron diffusion/ transport model with unstructured grids to estimate the neutron flux field and heat release distribution of the nuclear reactor core. For thermo-elasticity, it can establish a 3D thermal diffusion model and stress analysis model to accurately obtain the temperature field and deformation. This multi-physics platform enables us to carry out high-precision analysis of neutron physics, heat-conduction, deformation, providing technical assistance for the core design of the mobile nuclear reactor power system.

2 Methodology

2.1 Method

2.1.1 Neutronics

The neutronics model of FEMAS is based on the finite element method (FEM) [6] to support a high-fidelity geometrical modeling of SIMONS. The FEM is a basic strategy based on "discrete approximation", a numerical method for solving Partial Differential Equations (PDEs). As an illustration, consider the steady-state neutron diffusion equation of a two-group [7]:

$$\mathcal{L}\Phi + \mathcal{S}\Phi = \frac{1}{\lambda}\mathcal{F}\Phi \tag{1.1}$$

where

$$\mathcal{L} = \begin{pmatrix} -\vec{\nabla} \cdot \left(D_1\vec{\nabla}\right) + \Sigma_{a1} + \Sigma_{s12} & 0 \\ 0 & -\vec{\nabla} \cdot \left(D_2\vec{\nabla}\right) + \Sigma_{a2} \end{pmatrix}, \; \mathcal{S} = \begin{pmatrix} 0 & 0 \\ -\Sigma_{s12} & 0 \end{pmatrix},$$
$$\mathcal{F} = \begin{pmatrix} \nu\Sigma_{f1} & \nu\Sigma_{f2} \\ 0 & 0 \end{pmatrix}, \; \Phi = \begin{pmatrix} \phi_1 \\ \phi_2 \end{pmatrix}, \; \chi = \begin{pmatrix} 1 \\ 0 \end{pmatrix}$$

where ϕ is the neutron flux, D is the diffusion factor, Σ_s is the scattering cross section, $\nu\Sigma_f$ is the neutron production cross section, and χ is the fission spectrum. The rest notations are conventional in the reactor physics field, thus will not be elaborated here.

By introducing the finite element shape function and the Galerkin method, the steady-state neutron diffusion equation of two-group in finite element form can be obtained as follows:

$$A^\lambda \tilde{\phi}^\lambda = \frac{1}{\lambda} B^\lambda \tilde{\phi}^\lambda \qquad (1.2)$$

where

$$A^\lambda = \begin{pmatrix} L_{11} & 0 \\ S_{21} & L_{22} \end{pmatrix}, \quad B^\lambda = \begin{pmatrix} F_{11} & F_{12} \\ 0 & 0 \end{pmatrix}, \quad \tilde{\phi}^\lambda = \begin{pmatrix} \tilde{\phi}_1^\lambda \\ \tilde{\phi}_2^\lambda \end{pmatrix}$$

and the matrices elements (a, b) are given by

$$L_{11(ab)} = \sum_{c=1}^{N_c} D_1^c \int_{V_k} \vec{\nabla}\mathcal{N}_a \vec{\nabla}\mathcal{N}_b dV - D_1^c \int_{\Gamma_k} \mathcal{N}_a \vec{\nabla}\mathcal{N}_b d\vec{S} + \left(\Sigma_{a1}^c + \Sigma_{12}^c\right) \int_{V_c} \mathcal{N}_a \mathcal{N}_b dV,$$

$$L_{22(ab)} = \sum_{c=1}^{N_c} D_2^c \int_{V_k} \vec{\nabla}\mathcal{N}_a \vec{\nabla}\mathcal{N}_b dV - D_2^c \int_{\Gamma_k} \mathcal{N}_a \vec{\nabla}\mathcal{N}_b d\vec{S} + \Sigma_{a2}^c \int_{V_c} \mathcal{N}_a \mathcal{N}_b dV,$$

$$S_{21(ab)} = \sum_{c=1}^{N_c} -\Sigma_{12}^c \int_{V_c} \mathcal{N}_a \mathcal{N}_b dV,$$

$$F_{11(ab)} = \sum_{c=1}^{N_c} \nu\Sigma_{f1}^c \int_{V_c} \mathcal{N}_a \mathcal{N}_b dV,$$

$$F_{12(ab)} = \sum_{c=1}^{N_c} \nu\Sigma_{f2}^c \int_{V_c} \mathcal{N}_a \mathcal{N}_b dV.$$

where $\mathcal{N}_i$ and $\mathcal{N}_j$ are the shape functions in the finite element. Similarly, this principle can be applied to the multigroup neutron diffusion equation.

2.1.2   Thermal Conduction

The differential equation of thermal conduction in Cartesian coordinates is:

$$\rho c \frac{\partial T}{\partial t} = \text{div}(\lambda \, \text{grad}(T)) + q_v \qquad (1.3)$$

This equation can be cast into the variational form:

$$\int_\Omega \nabla T \cdot \nabla v dx = \int_\Omega \frac{q_v}{\lambda} v dx \qquad (1.4)$$

Equation (1.4) can be easily solved with the open-source finite element platform Fenics, as will be illustrated in Sect. 2.2.

2.1.3 Thermal-Elasticity

The thermal-elasticity model in FEMAS is based on a perfectly elastic isotropic body assumption. The relationship between the deformation component (strain: ε) and the stress component (stress: σ) is [8]:

$$
\begin{aligned}
\sigma_x &= \lambda\left(\varepsilon_x + \varepsilon_y + \varepsilon_z\right) + 2\mu\varepsilon_x \\
\sigma_y &= \lambda\left(\varepsilon_x + \varepsilon_y + \varepsilon_z\right) + 2\mu\varepsilon_y \\
\sigma_z &= \lambda\left(\varepsilon_x + \varepsilon_y + \varepsilon_z\right) + 2\mu\varepsilon_z \\
\tau_{xy} &= 2\mu\varepsilon_{xy} \\
\tau_{yz} &= 2\mu\varepsilon_{yz} \\
\tau_{zx} &= 2\mu\varepsilon_{zx}
\end{aligned}
\tag{1.5}
$$

where λ and μ are Lame constants. The transformation relationship between them and elastic modulus E, Poisson's ratio v is:

$$
\begin{aligned}
\lambda &= \frac{vE}{(1+v)(1-2v)} \\
\mu &= \frac{E}{2(1+v)}
\end{aligned}
$$

Therefore, the expression for stress can be written as:

$$
\sigma = \lambda \operatorname{tr}(\varepsilon)I + 2\mu\varepsilon
\tag{1.6}
$$

where I denotes the identity tensor. The expression for strain can be written as:

$$
\varepsilon_{ij} = \frac{1}{2\mu}\left(\sigma_{ij} - \frac{\lambda}{3\lambda + 2\mu}\sigma_{kk}\delta_{ij}\right)
\tag{1.7}
$$

The stress governing equation of the whole system is:

$$
-\nabla \cdot \sigma = f, \text{ in } \Omega
\tag{1.8}
$$

where $\sigma = \lambda\operatorname{tr}(\varepsilon)I + 2\mu\varepsilon$, $\varepsilon = \frac{1}{2}\left(\nabla u + (\nabla u)^T\right)$, and f is the external force per unit volume in the entire system. Similar as Sect. 2.1.2, the variational form of the stress equation is:

$$
\int_{\Omega} \sigma(u) :\in (v)\mathrm{d}x = \int_{\Omega} f \cdot v\mathrm{d}x
\tag{1.9}
$$

Temperature variations induce deformations in elastically unrestrained solids. Therefore, mechanical and thermal processes form the global strain field. In the context of the theory of linear small deformation, the total strain can be decomposed into the sum of mechanical and thermal components as:

$$
\varepsilon_{ij} = \varepsilon_{ij}^{(M)} + \varepsilon_{ij}^{(T)}
\tag{1.10}
$$

For isotropic materials,

$$
\varepsilon_{ij}^{(T)} = \alpha(T - T_o)\delta_{ij}
\tag{1.11}
$$

where α is the linear thermal expansion coefficient of the material.

Therefore, the expression for the total strain is:

$$\varepsilon_{ij} = \frac{1+\nu}{E}\sigma_{ij} - \frac{\nu}{E}\sigma_{kk}\delta_{ij} + \alpha(T - T_o)\delta_{ij} \tag{1.12}$$

Thus, the linearized thermoelastic constitutive equation can be given by:

$$\sigma_{ij} = \lambda\varepsilon_{kk}\delta_{ij} + 2\mu\varepsilon_{ij} - (3\lambda + 2\mu)\alpha(T - T_o)\delta_{ij} \tag{1.13}$$

Similar to the elasticity equation, the weak form of the thermal expansion equation can be obtained as:

$$\int_{\Omega} \sigma(u) : (v)\mathrm{d}x = \int_{\Omega} f \cdot v\mathrm{d}x \tag{1.14}$$

2.2 Coupling Framework

In order to achieve high-precision simulation of full reactor, this research developed the multi-physics calculation platform FEMAS, integrated open-source codes (OpenMC, Dealii and Fenics) based on the external coupling framework.

The iteration process goes as follows:

(1) Use OpenMC to perform neutron transport simulation and obtain a cross-section library.
(2) Based on the pre-set temperature distribution and geometric parameters in cold state, use Dealii to perform multi-group neutron diffusion calculation, thus getting the spatial distribution of power.
(3) Given the boundary conditions of the helium-xenon cooling channel and the spatial distribution of power, the temperature distribution was calculated by solving the thermal diffusion equation using Fenics.
(4) Combined with the temperature field and the mechanical boundary conditions, the structural displacement is obtained by solving the thermo-elasticity equation using Fenics.
(5) Update the geometry, density and cross sections of the model.
(6) Dealii then performs the neutron diffusion calculation again. The steps above are repeated until certain physical quantities meet the convergence criteria or the execution reaches the maximum number of iteration steps (Fig. 1).
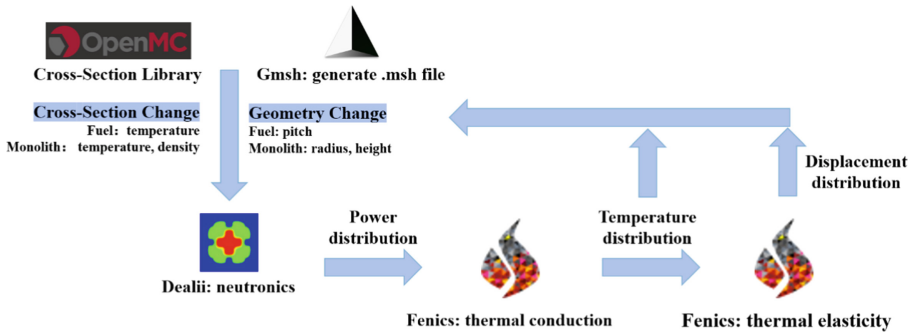
Fig. 1. Schematic view of the coupling framework

2.3 Model

2.3.1 Model

To meet the demand for terrestrial transportable nuclear reactor power supply, this research takes the overall conceptual design of SIMONS as the test case. SIMONS is designed to be an intelligent micro land-based transportable nuclear reactor featuring small size, high power density and inherent safety. Its thermal power is 20 MWe and it can operate continuously for 3300 EFPDs without refueling.

As a preliminary test of the coupling platform, a simplified scaling model of the SIMONS core is employed to reduce the computational cost. The scaled core exhibits a prismatic core design, using graphite as the monolith material. There are several holes in the monolith with a hexagonal arrangement to accommodate fuel rods and coolant. The overall height of the core is 30 cm, and the overall radius is 23 cm. The axial-radial schematic diagram of the core is shown in Fig. 2.
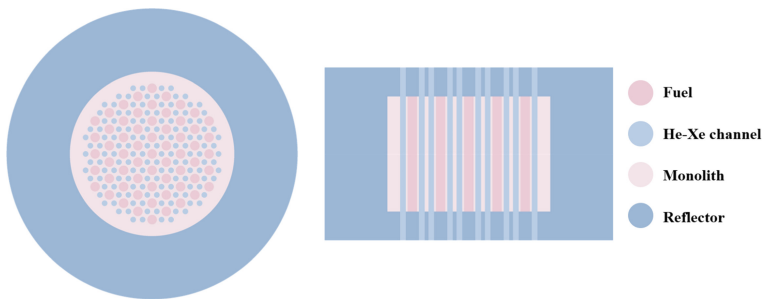
Fig. 2. Schematic diagram of the core

The operating parameters, geometric information and material selection of the simplified SIMONS modeling are shown in Table 1.

Table 1. Simplified SIMONS design parameters

Parameters	Value	Unit
Operating parameters		
Thermal power	0.24	MW
Helium-xenon volume ratio	88:12	/
Coolant channel wall temperature	1000	K
Geometry		
Fuel diameter	1.5	cm
Coolant channel diameter	0.9	cm
Fuel pitch	1.5	cm
Number of fuel rods	61	/
Number of Coolant channels	138	/
Fuel height	10	cm
Monolith radius	13	cm
Radial reflector width	10	cm
Axial reflector height	5	cm
Material		
Fuel	UC	/
Monolith	Graphite	/
Reflector	Be	/
Coolant	Helium-xenon	/

2.3.2 Neutronics

The coupling calculations employ a high-fidelity modelling approach by explicitly describing all the rods and holes using three-dimensional unstructured meshes. Homogenized cross sections are generated using two-dimensional OpenMC calculations for every material zone. This research uses a four-group structure which is divided as:

1) Group-1 (497.87 keV–20 meV)
2) Group-2 (9.11882 keV–497.87 keV)
3) Group-3 (0.625 eV–9.11882 meV)
4) Group-4 (0 eV–0.625 eV)

The cross sections are stored as data tables with considering different fuel and monolith temperatures. During the neutronics calculations, the cross sections for each material zone are updated using linear interpolation method. The cross sections of fuel are only related to the temperature, while those of monolith are dependent on both temperature and density.

Due to the simplification of the core design, setting vacuum boundary conditions will make the k_{eff} too small. Therefore, the reflective boundary condition is imposed on the outer boundaries in the calculation. Figure 3 shows the mesh used in the neutronics calculation.
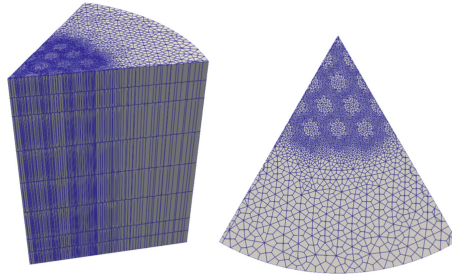
Fig. 3. Meshes used in neutronics simulation

2.3.3 Thermo-Elasticity

Figure 4 depicts the mesh used in thermo-elasticity calculations. In the heat diffusion calculation, it is assumed that the thermal conductivities of the fuel and the monolith are constant. Currently, the coolant channels are treated as Dirichlet boundaries, and subsequent work will consider the heat transfer portion of the flow in the channel. Based on the temperature distribution obtained by solving the thermal diffusion equation, the thermal expansion calculation can be performed.

3 Results

3.1 Coupling Results

In the coupling calculation, the maximum number of iterations is set to 10. In fact, between the second and third steps, the k_{eff} error dropped below the predetermined convergence threshold (1e−5). However, the iteration step is set to 10 in order to study the characteristics of the coupled calculation results in greater detail. The results of various fields of neutronics/thermos-elasticity coupling calculations are shown in the Fig. 5.

The 3D four-group neutron flux distribution is shown in Fig. 6. It can be observed that the fast neutron flux are generated in the fuel rods, while thermal neutrons presents at the periphery of the active core due to the strong thermalization effect of the Be reflectors.

For the fuel region, based on the aforementioned neutron flux distribution and the combined total power, the heat release rate then can be calculated. Through thermal diffusion calculation, the temperature distribution of the simplified SIMONS can be obtained, shown in Fig. 7. Maximum temperature difference across the whole reactor is 390.1 K.

(a) monolith

(b) Full Core
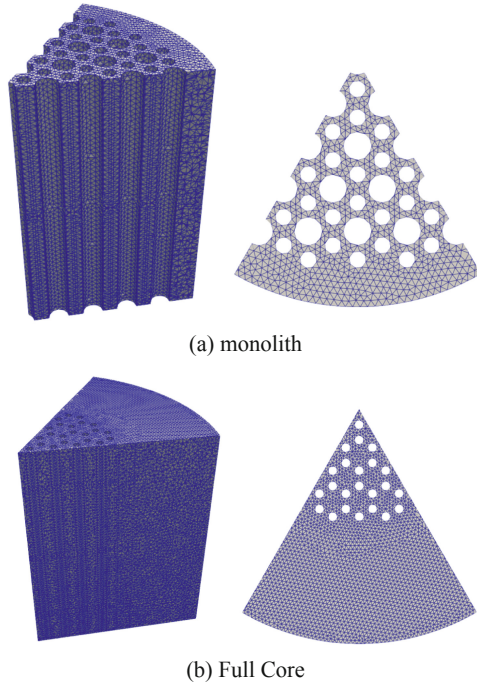
Fig. 4. Meshes used in thermos-elasticity simulation
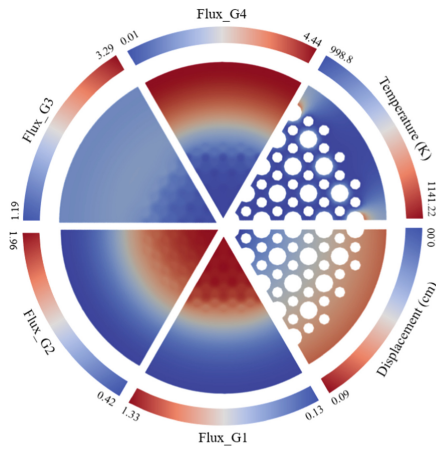
Fig. 5. 2D Results of neutronics/ thermos-elasticity coupling calculation (H = 15 cm)
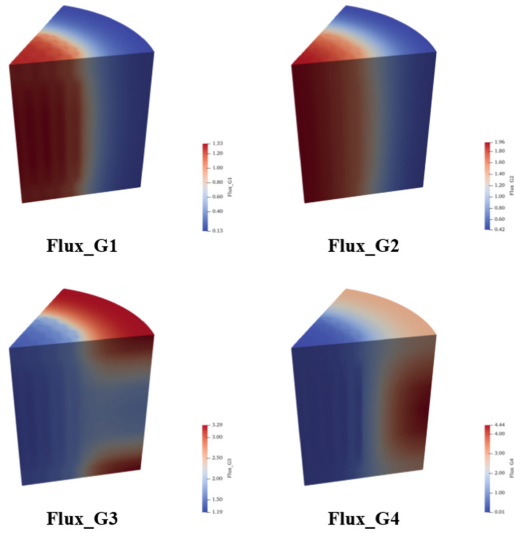
Fig. 6. Neutron flux distribution
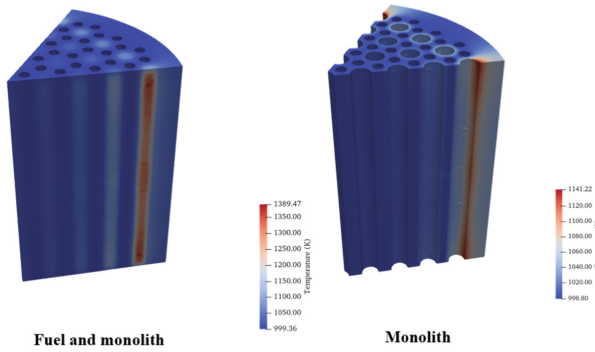
Fig. 7. Temperature distribution

According to the temperature field, the effective temperature of the fuel rod can be calculated, shown in Fig. 8. The results indicate that the fuel rods on the periphery have the highest temperatures due to the thermalization of neutrons in the reflector. Within the fuel rod, the middle of it has the highest temperature. This is because given the reflective boundary condition, the neutron fluxes of the third and fourth groups are predominantly spread outside the core, resulting in a higher power here. Moreover, The hot spot locations are also attributed to less numbers of surrounding coolant channels than other fuel locations.

Figure 9 depicts the thermal expansion calculation results. It reveals that the maximum displacement is about 0.09 cm, and the core expands radially from the center to the periphery. Graphite's linear thermal expansion coefficient is quite small, hence the
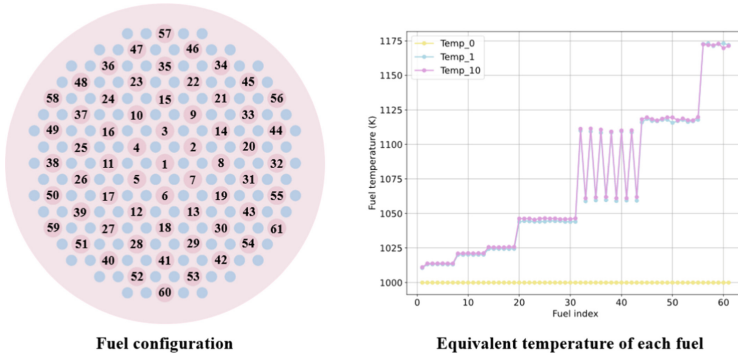
Fig. 8. Equivalent temperature of each fuel

thermal expansion impact is not as pronounced compared to other solid reactors. However, it still creates a succession of reactive feedback, geometric expansion, and other effects worthy of our consideration.
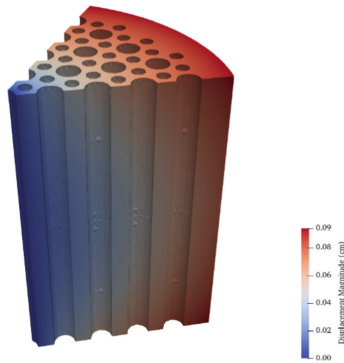
Fig. 9. Magnitude of structure displacement distribution

3.2 Thermal Results Analysis

Figure 10 illustrates the convergence diagram and monolith geometrical parameters for multi-physics calculations. At the first step, the k_{eff} is calculated by directly applying the OpenMC-generated cross section in the diffusion calculation, yielding a value of 1.65501. Meanwhile, at the last step, the value of k_{eff} is 1.65471. Comparing their k_{eff} values reveals that the adoption of thermo-elasticity calculation results in a 30.5 pcm decrease in reactivity because of the enhanced neutron leakage effect. Regarding the monolith's geometric specifications, its radius expanded from 13 cm to 13.08 cm, and its height increased from 10 cm to 10.06 cm. Consequently, its density is lowered to 97.6% of its original value.
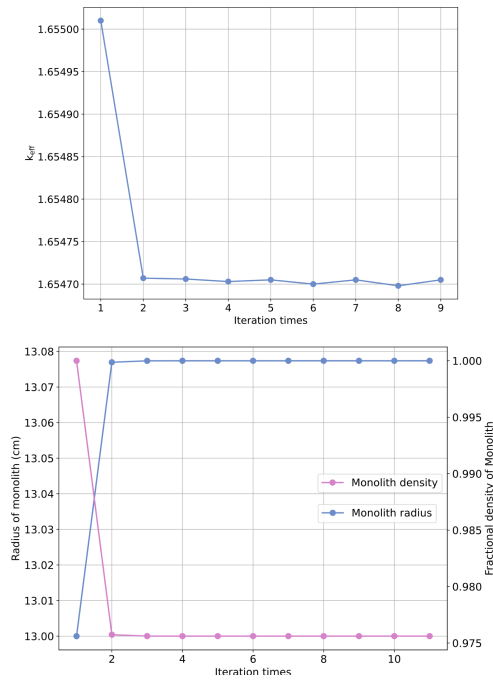
Fig. 10. Convergence diagram of k_{eff} and geometry

4 Conclusion

In response to the research and development requirements of innovative helium-xenon cooled mobile nuclear power systems, this research developed a three-dimensional high-fidelity multi-physics coupling platform FEMAS. This platform is built on the Picard iteration and incorporates the open source OpenMC, Dealii, and Fenics codes, which enables the multi-physics modeling of neutronics/ thermoelasticity.

Simultaneously, based on the scaled model of SIMONS, this research preliminarily concludes a series of simulations and analyses, including from the OpenMC cross-section generation, reactor modeling, and multi-physics simulations. The results demonstrate that the coupling platform can predict the power distribution, temperature distribution and thermal expansion of SIMONS. Given 240-kW of thermal power, the local temperature difference of the whole reactor is 390.1 K, and the deformation rate caused by thermal stress is 2.4%, and the reactivity feedback due to heat conduction and thermal expansion is 30.5 pcm.

In the era of high-precision computing, this platform can evaluate the core performance of the core to guarantee that the design of the core meets the standards for ultra-long life and inherent safety.

References

1. Wollman, M.J., Zika, M.J.: Prometheus project reactor module final report, for naval reactors information. United States: N. p. 2006. Web. https://doi.org/10.2172/884680
2. Arafat, Y., Van Wyk, J.: eVinci™ micro reactor – our next disruptive technology. Nucl. Plant J., 34–37 (2019)
3. Filippone, C., Jordan, K.: The holos reactor: a distributable power generator with transportable subcritical power modules (2017). https://doi.org/10.31224/osf.io/jzac9
4. Li, Z., Sun, J., Liu, M., et al.: Design of a hundred-kilowatt level integrated gas-cooled space nuclear reactor for deep space application. Nuclear Eng. Des. (2020)
5. Xiao, W., Li, X., Li, P., Zhang, T., Liu, X.: High-fidelity multi-physics coupling study on advanced heat pipereactor. Comput. Phys. Commun. (2022). https://doi.org/10.1016/j.cpc.2021.108152
6. Strang, G., Fix, G.J., Griffin, D.S.: An Analysis of the Finite Element Method. Prentice-Hall (1973)
7. Henry, A.F., Scott, C.C., Moorthy, S.: Nuclear reactor analysis. IEEE Trans. Nucl. Sci. **24**(6), 2566–2567 (1978)
8. Eslami, M.R., Hetnarski, R.B., Ignaczak, J., Noda, N., Sumi, N., Tanigawa, Y.: Basic equations of thermoelasticity. In: Theory of Elasticity and Thermal Stresses. SMIA, vol. 197, pp. 391–422. Springer, Dordrecht (2013). https://doi.org/10.1007/978-94-007-6356-2_16

Study on the Steady-State Performance of the Fuel Rod in M²LFR-1000 Using KMC-Fueltra

Guangliang Yang, Weixiang Wang, Wenpei Feng, Tao Ding, and Hongli Chen$^{(\boxtimes)}$

University of Science and Technology of China, Hefei, Anhui, China
hlchen1@ustc.edu.cn

Abstract. Operating conditions in the liquid metal fast reactor, like higher power density, higher temperature gradient, and higher burnup, are more severe to the fuel rod comparing to the light water reactor. The integrity and safety of the fuel rod is very essential to the reactor safety. In this study, the fuel rod designed for M²LFR-1000, which is a typical pool type lead cooled fast reactor, is evaluated using a fuel performance analysis code named KMC-Fueltra. Irradiation behaviors and material properties for the MOX fuel and T91 cladding are established and introduced into the code. The steady-state performance of the fuel rod is analyzed. Results concerning both fuel and cladding performance are discussed based on indicative design limits collected from the open literatures. This study is useful to improve the conceptual design of the M²LFR-1000.

Keywords: Conceptual design · Fuel rod performance · Lead-cooled fast reactor · M²LFR-1000 · KMC-Fueltra

1 Introduction

Ensuring the integrity and safety of the fuel rod, which is the core component in the reactor, is the most essential issue in the design of a nuclear reactor [1]. For the fast reactor, the power density, temperature gradient and burnup are higher than light water reactor. This brings a greater challenge for the fuel rod in the fast reactor.

Many materials have been developed and studied in order to meet the above characteristics of fast reactors. Material properties and irradiation behaviors are implemented into the fuel performance code to evaluate their performance in the specific reactor. Considering the transmutation and proliferation, MOX fuel has been widely used in fast reactors. The cladding material are mainly stainless steel. One is austenitic stainless steel; the other is ferritic martensitic stainless steel. Due to the better thermal creep resistance, the austenitic steel 15-15-Ti has been chosen to be the cladding material in the ALFRED, MYRRHA and ASTRID reactors [2]. Marcello extended the TRANSURANS code [3] and it is adopted for the simulation of the fuel and cladding performance covering the average and the hottest reactor conditions in the ALFRED reactor [2]. 316SS is also used

in fast reactors like JOYO and EBR-II [4], but the it has poor compatibility with lead coolant. Corrosion with lead coolant should be considered at certain coolant velocity and temperature in the lead cooled fast reactor. Benefit from the good corrosion resistance to the lead coolant, T91 is selected as the cladding in 1000Mth Medium-size Modular Lead-cooled Fast Reactor (M^2LFR-1000) [5]. In order to ensuring the safety of the reactor, the integral performance of the fuel rod design should be investigated under the operational condition in M^2LFR-1000.

In this paper, material properties and irradiation behaviors of MOX fuel and T91 cladding are incorporated into the fuel performance code KMC-Fueltra. The widely used failure mechanism and design limits of some important parameters applicable for the fast reactors are collected from the public literatures to evaluate the fuel rod design. The steady-state performance of the fuel rod in M^2LFR-1000 is studied using KMC-Fueltra. Results are discussed and some improvements are suggested.

2   Material Properties

Material properties are of great importance to the fuel performance analysis. The thermal and mechanical properties of the MOX fuel and T91 cladding implemented in the KMC-Fueltra are presented in this part. The main point is put on the basic material properties. The unique irradiation behaviors did not list but can be found in the former work.

2.1   MOX Fuel

(1)   **Thermal conductivity**

Many correlations have been proposed for MOX fuel concluded from the fresh or irradiation fuel data. A wide set of factors like fuel temperature, burnup, plutonium content, stoichiometry, and porosity have effects on the MOX fuel thermal conductivity. Magni et al. [6] assessed the most recent and reliable experimental data statistically and proposed a new correlation for the MOX fuel with above factors taking into consideration. The correlation of thermal conductivity for the fresh MOX fuel is:

$$k_0(T, x, [Pu], p) = \left(\frac{1}{A_0 + A_x \cdot x + A_{Pu} \cdot [Pu] + (B_0 + B_{Pu}[Pu])T} + \frac{D}{T^2}e^{-\frac{E}{T}} \right) \tag{1}$$
$$(1-p)^{2.5}$$

where T is the temperature, K; $[Pu]$ is the plutonium atomic fraction; p is the porosity fraction; Considering the thermal conductivity of degradation at certain burnup values, the correlation after the irradiation is:

$$k_{irr}(T, x, [Pu], p, bu) = k_{inf} + \left(k_0(T, x, [Pu], p) - k_{inf} \right) \cdot e^{-\frac{bu}{\varphi}} \tag{2}$$

where $k_0(T, x, [Pu], p)$ is the fresh MOX thermal conductivity; bu is the burnup, GWd/tHM; k_{inf} asymptotic thermal conductivity, $W/m/k$; φ is the fitted coefficient, GWd/tHM; Parameters used in this correlation is listed in the Table 1.

Table 1. Parameters in the correlation

Parameters	Value
A_0 $(m \cdot K/W)$	0.01926
A_x $(m \cdot K/W)$	1.06×10^{-6}
A_{Pu} $(m \cdot K/W)$	2.63×10^{-8}
B_0 (m/W)	2.39×10^{-4}
B_{Pu} (m/W)	1.37×10^{-13}
D $(W/m/k)$	5.27×10^9
E (k)	17109.5
k_{inf} $(W/m/k)$	1.755
φ (GWd/tHM)	128.75

(2) **Young's modulus and Poisson's ratio**

Young's modulus of MOX fuel is related to the Pu content and stoichiometric state [7]. The relation can be expressed as:

$$E = E(UO_2) \cdot (1 + 0.15 w_{Pu}) exp(-Bx) \tag{3}$$

where B is constant, 1.34 for the hyper-stoichiometric fuel and 1.75 for the hypo-stoichiometric fuel; x is the deviation from stoichiometry; w_{Pu} is the weight fraction of PuO_2; $E(UO_2)$ is the Young's modulus of UO_2 and can be denoted as:

$$E(UO_2) = 2.334 \times 10^{11}[1 - 2.752(1 - D)]\left(1 - 1.0915 \times 10^{-4}\right) \cdot T \tag{4}$$

where D is the theoretical density fraction; T is the temperature, K.

Possion's ratio of MOX fuel is given as a function of the weight fraction of PuO_2:

$$v(MOX) = w_{Pu} \cdot v(PuO_2) + (1 - w_{Pu}) \cdot v(UO_2) \tag{5}$$

$$v(PuO_2) = 0.276 + \frac{T - 300}{2800}(0.5 - 0.276) \tag{6}$$

$$v(UO_2) = 0.316 + \frac{T - 300}{2800}(0.5 - 0.316) \tag{7}$$

where $v(UO_2)$ and $v(PuO_2)$ is the Possion's ratio of UO_2 and PuO_2 respectively; T is the temperature, K; w_{Pu} is the weight factor of PuO_2.

(3) **Thermal expansion**

Thermal expansion of the MOX fuel is obtained by weight factor of different components [8].

$$\varepsilon^{th}(MOX) = (1 - w_{Pu}) \cdot \varepsilon^{th}(UO_2) + (w_{Pu}) \cdot \varepsilon^{th}(PuO_2) \tag{8}$$

where, ε^{th} is thermal expansion, %; w_{Pu} is the weight factor of PuO_2. Thermal expansion of UO_2 and PuO_2 is expressed by:

$$\varepsilon_i^{th} = K_1 \cdot T - K_2 + K_3 exp\left(-\frac{E_D}{kT}\right) \tag{9}$$

The subscript i takes 1 and 2, which represent UO_2 and PuO_2, respectively. Parameters used in this correlation is listed in the Table 2.

Table 2. Parameters used in thermal expansion model

Parameters	UO$_2$	PuO$_2$
$K_1 (K^{-1})$	9.8×10^{-6}	9.0×10^{-6}
K_2	2.61×10^{-3}	2.7×10^{-3}
K_3	3.16×10^{-1}	7.0×10^{-2}
E_D (J)	1.32×10^{-19}	7.0×10^{-20}

(4) Creep model

Creep can effectively release the stress caused by irradiation behaviors like swelling and thermal expansion in the fuel, which can protect the fuel from reaching the safety limits [9]. Creep of the MOX fuel is divided into two parts: thermal creep and irradiation creep [4]. Thermal creep is composed of diffusional creep and dislocation creep and is expressed as follows:

$$\dot{\varepsilon}_{th} = 3.23 \times 10^9 \cdot \frac{\sigma_{eff}}{a^2} \exp\left(-\frac{Q_1}{RT}\right) + 3.24 \times 10^6 \cdot \sigma_{eff}^{4.4} \cdot exp\left(-\frac{Q_2}{RT}\right) \tag{10}$$

where $\dot{\varepsilon}_{th}$ is the fuel thermal creep rate, $1/h$; a is the grain size, μm; σ_{eff} is the equivalent stress, MPa; $Q_1 = -92500$ and $Q_2 = -136800$ are activation energy; R is the universal gas constant.

Irradiation creep is denoted as;

$$\dot{\varepsilon}_{irr} = 1.78 \times 10^{-26} \sigma_{eff} \cdot \varphi \tag{11}$$

where $\dot{\varepsilon}_{irr}$ is the fuel irradiation creep rate, $1/h$; φ is the fission rate, $fission/(m^3 \cdot s)$.

2.2 T91 Cladding

(1) Thermal conductivity

Thermal conductivity of the cladding is denoted as a function of temperature as follows [10]:

$$k = 21.712 + 0.011T - 9.5483 \times 10^{-6}T^2 + 3.627 \times 10^{-9}T^3 \tag{12}$$

where T is the temperature, K.

(2) **Young's modulus and Poisson's ratio**

Young's modulus of the cladding is a function of temperature and can be expressed as [11]:

$$E = 2.11458 \times 10^5 - 21.24 \cdot T - 7.94 \times 10^{-2} \cdot T^2 \tag{13}$$

where E is Young's modulus, Mpa; T is the temperature, °C, with the range of applicability in $20 < T < 760$ °C.

Possion's ratio of the cladding is set as a constant:

$$v = 0.3 \tag{14}$$

(3) **Thermal expansion**

Thermal expansion of the cladding is expressed as [10]:

$$\varepsilon^{th} = \frac{\Delta L}{L} = -3.0942 \times 10^{-3} + 1.1928 \times 10^{-5} \cdot T - 6.7979 \times 10^{-9} \cdot T^2 + 7.9606$$
$$\times 10^{-12} \cdot T^3 - 2.546 \times 10^{-15} \cdot T^4 \tag{15}$$

where ε^{th} is thermal expansion, %; T is the temperature, K.

(4) **Creep model**

Similar to the MOX fuel, creep model of the cladding is also divided into two parts: thermal creep and irradiation creep. Thermal creep is expressed as [11]:

$$\dot{\varepsilon}_{th} = A\sigma^n exp(-Q/RT) \tag{16}$$

where $Q = 728 \pm 35\,\text{kJ/mo l}$ is the activation energy; $n = 5$.

Irradiation creep is expressed as:

$$\dot{\varepsilon}_{irr} = 1.8 \times 10^{-22}\varphi_v(t) \cdot \sigma_{eq} \tag{17}$$

where $\varphi_v(t)$ is the neutron flux rate, $n/(cm^2 \cdot s)$; σ_{eq} is the equivalent stress, Mpa; t is the time, h.

(5) **Plasticity model**

Plasticity is an important aspect in the fuel rod mechanical performance, which is related to the fuel failure highly. Plasticity model of the cladding is denoted as a function of temperature [11].

$$\sigma_y = 536.1 - 0.4878 \cdot T + 1.6 \times 10^{-3} \cdot T^2 - 3 \times 10^{-6} \cdot T^3 + 8 \times 10^{-10} \cdot T^4 \tag{18}$$

where σ_y is the yield stress, Mpa; T is the temperature, °C, with the range of applicability in $20 < T < 700$ °C.

(6) **Cumulative damage function**

Fuel rod failure time is a critical parameter to the reactor safety. Predicting this parameter as accurately as possible is one of the main tasks of fuel performance analysis. The traditional cumulative damage function (CDF) is used to evaluate the fuel rod failure.

$$CDF = \sum_{i=1}^{n} \frac{\Delta t}{t_r(\sigma_i, T_i)} \tag{19}$$

where Δt is the time step, s; $t_r(\sigma_i, T_i)$ represents time to failure at certain stress and temperature. It can be calculated by the Larson-Miller parameter (LMP) [12], defined as:

$$LMP(\sigma) = T(C + \log_{10} t_r) \tag{20}$$

For the T91 cladding, the LMP is fitted by the polynomial function.

$$LMP(\sigma) = 38387.008 - 84.880\sigma + 0.403\sigma^2 - 1.15 \times 10^{-3}\sigma^3 + 1.254 \times 10^{-6}\sigma^4 \tag{21}$$

where σ is the equivalent stress, Mpa; C is set as 33.

3 Model Implementation

3.1 Description of M²LFR-1000

The 1000MWth Medium-size Modular Lead-cooled Fast Reactor (M²LFR-1000) is a typical pool-type fast reactor developed by USTC [5]. It adopts a rod-shaped fuel element design. The pellet is MOX with Pu enrichment about 20%, the cladding is T91 stainless steel and the coolant is lead. The operating temperature is 400–480 °C. The main design parameters of the fuel rod are outlined in Table 3.

Table 3. Fuel specifications for M²LFR-1000

Property	Value
Fuel type	MOX
Cladding type	T91
Coolant type	Pb
Fuel pellet inner diameter (mm)	1.9

(continued)

Table 3. (*continued*)

Property	Value
Fuel pellet outer diameter (mm)	8.6
Cladding inner diameter (mm)	8.9
Cladding outer diameter (mm)	10.0
Fuel pellet density (% of TD)	95
Pitch (mm)	14.0
Active fuel height (mm)	1000
Average linear power (W/mm)	20.5
Average neutron flux rate (n/cm^2/s)	1.55×10^{15}
Initial gas pressure (MPa)	0.5
Plenum to fuel ratio	1.15
Oxygen-to-Metal ratio	1.97
Coolant inlet temperature (°C)	400
Coolant inlet velocity (m/s)	1.5
Coolant pressure (MPa)	0.1

3.2 Introduction of KMC-Fueltra

KMC-Fueltra is a 1.5D fuel performance analysis code designed for the liquid metal fast reactor. It is applicable for the steady-state and transient operating conditions and covers typical materials used in LMFRs [13, 14]. Figure 1 shows the flow diagram of KMC-Fueltra. It can perform the thermal, thermal migration, fission gas release, and mechanical analysis of the fuel rod. Based on the above calculation results, the fuel rod failure analysis is also performed. Irradiation behaviors considered in this code contain thermal expansion, swelling, densification, relocation, cracking-healing, restructuring, creep, and plasticity for the pellet as well as thermal expansion, swelling, creep, and plasticity for the cladding. In this article, KMC-Fueltra is used to evaluate the steady-state performance of the fuel rod in the M^{2}LFR-1000.

3.3 Indicative Design Limits

Design limits are important for the conceptual design of the fuel rod. Luzzi et al. [2] has concluded some conservative design limits for many important parameters that influence thermal and mechanical performance from the open literatures. These limits are adopted for the conceptual design of fuel rods in M^{2}LFR-1000 as well. Some limits are concluded from the view of the corrosion and erosion problem of the lead environment, others are from the material properties or irradiation experiments. Table 4 lists the conservative design limits of some important parameters.
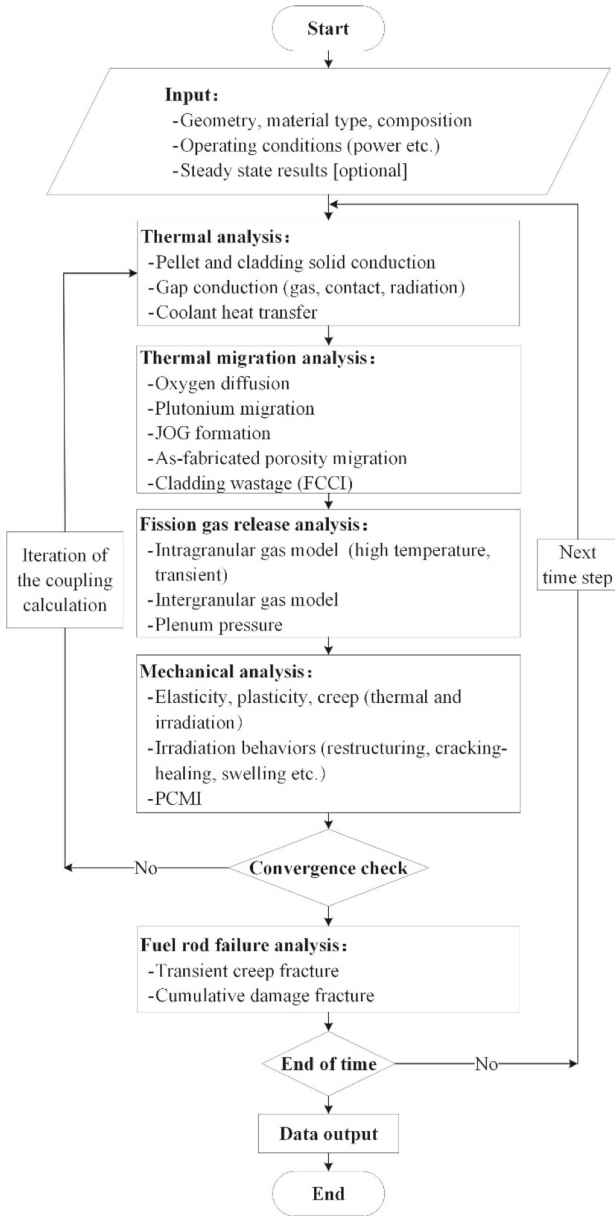
Fig. 1. Flow diagram of KMC-Fueltra.

Table 4. Indicative design limits for M^{2}LFR-1000

Quantity	Value
Peak fuel temperature	<2300 °C
Peak cladding temperature	<550 °C
Maximum coolant velocity	<2 m/s
Plenum pressure	<5 MPa
Total creep strain	<3%
Instantaneous plastic strain	<0.5%
Maximum cladding stress	<128 MPa
Cumulative damage function	<0.2/0.3

4　Results and Discussions

4.1　Thermal Performance

The change of fuel rod temperature with time is shown in Fig. 2. The maximum fuel pellet temperature is about 1314.4 °C, which appears at the half height of the fuel rod and is consistent with the axial power distribution. The maximum cladding temperature is about 529.6 °C, which appears at the top of the fuel rod. The margin to the safety limits is abundant. The maximum temperature of the fuel pellet becomes larger with time while the cladding did not show too much change. Burnup effect on the fuel rod can account for this. Thermal conductivity of the fuel pellet in Eq. 2 gets smaller with burnup and the gap conductance also decreases at a certain burnup as can be seen in Fig. 3. These factors lead to the deterioration of heat conduction in fuel rod. Gap conductance is affected by many factors including the gap with, gas temperature, plenum pressure, and gas content. Its change depends on which factor is dominant in the operational life. Due to the swelling in the fuel pellet, the gap width decreases with time, which improves the gap conduction at the initial stage. However, the gap conductance decreases later because of the increasing released fission gases.

4.2　Fission Gas Release

Figure 4 gives the change of fission gas release fraction in MOX fuel. At the initial stage, fission gases diffuse and agglomerate in the fuel matrix with the fission process, so the release fraction is almost zero. When the fission gases atoms accumulate to a certain amount in the gas bubbles, the migration process starts. These gas bubbles migrate to the intergranular and then to the gap under the temperature gradient. The released fission gases cause the plenum pressure getting larger as shown in Fig. 5. The initial gas pressure is 0.5 MPa and the maximum plenum pressure is about 1.8 MPa at the end of burnup.
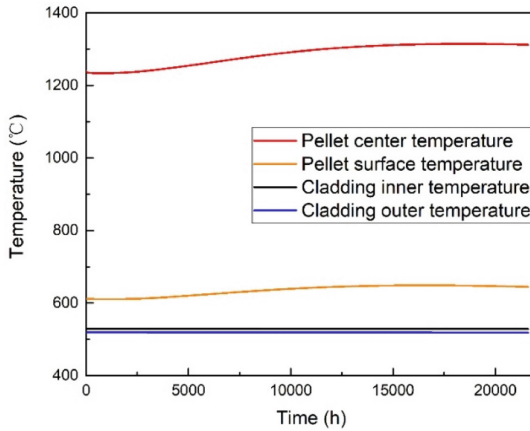
Fig. 2. Evolution of the fuel rod maximum temperature.
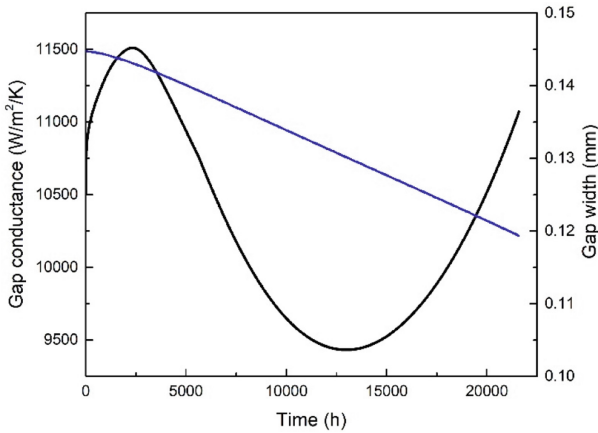
Fig. 3. Evolution of the gap conductance and gap width.

4.3 Mechanical Performance

In addition to the temperature field, the effect of irradiation behaviors on the fuel performance is also shown in the deformation of the fuel rod. Figure 6 illustrates the evolution of fuel rod size. The biggest change is the fuel pellet outer diameter. Irradiation behaviors that occur within the fuel pellet is more intense where the neutron flux is the largest. Thermal expansion and swelling contribute a lot to the expansion of the fuel pellet. Although densification can decrease the pellet deformation, its contribution is small and it ends at the initial stage quickly. The size of the cladding does not show too much change during the entire operational life. Table 5 gives the comparison results of the parameters with the design limits. The safety margin of fuel pellet temperature is very large while the cladding is only 20 °C. This should be paid attention in the later optimization of the fuel rod design. Some burnup related parameters like plenum pressure, total creep strain,
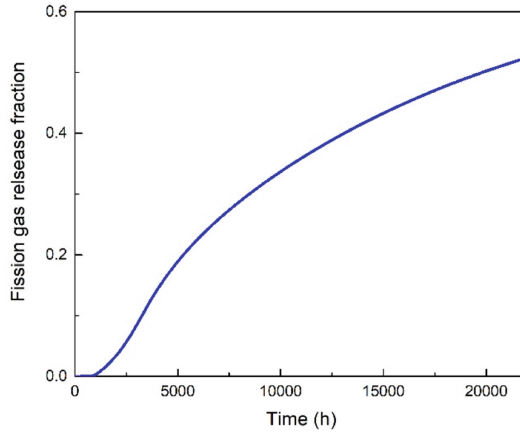
Fig. 4. Evolution of the fission gas release fraction.
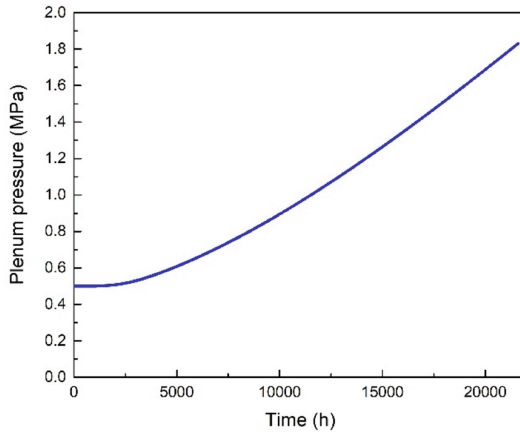
Fig. 5. Evolution of the plenum pressure.

maximum cladding stress and CDF is far from the design limits. Meanwhile, due to the low stress state, the plastic strain does not appear in the fuel rod. A major reason is that burnup of the fuel rod, as shown in Fig. 7, is not very large compared to the other fast reactors of the same type. The maximum burnup is about 4.2 at%. For better economy, it can enlarge by modifying the reactor design if needed.
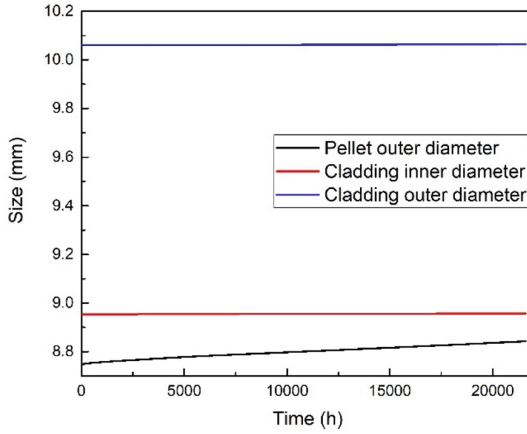
Fig. 6. Evolution of the fuel rod size.

Table 5. Comparison results of the parameters.

Quantity	Limits	Value
Peak fuel temperature	<2300 °C	1314.4
Peak cladding temperature	<550 °C	529.6
Maximum coolant velocity	<2 m/s	1.5
Plenum pressure	<5 MPa	1.83
Total creep strain	<3%	0.0565
Instantaneous plastic strain	<0.5%	0
Maximum cladding stress	<128 MPa	27.4
Cumulative damage function	<0.2/0.3	9.622×10^{-11}
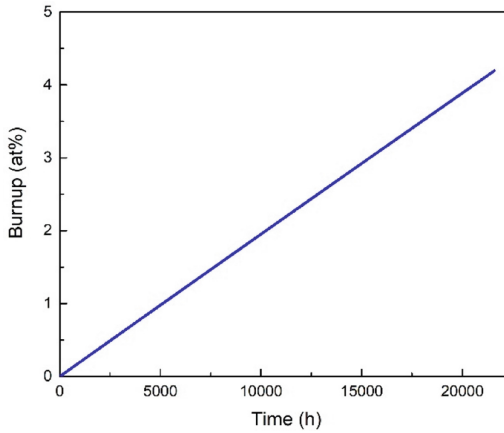
Fig. 7. Evolution of the fuel rod maximum burnup.

5   Conclusions

In this paper, the steady-state fuel rod performance in M^{2}LFR-1000 has been studied using the fuel performance code KMC-Fueltra. Material properties for the MOX fuel and T91 cladding have been incorporated into the code. An important evaluation model and some indicative design limits are collected from the open literatures to help find out the shortcoming of the fuel rod design. The corresponding thermal and mechanical parameters of the fuel rod are evaluated and discussed. Some important parameters concerning the thermal and mechanical performance of the fuel pellet and cladding do not exceed the design limits, proving the safety of the fuel rod design. Even some parameters are far from the design limits, leaving a lot of room for optimization. Burnup of the fuel rod in M^{2}LFR-1000 is about 4.2 at%, which is not very deep compared to fast reactors of the same type. It can also be optimized in the later design process.

References

1. Van Uffelen, P., Hales, J., Li, W., et al.: A review of fuel performance modelling. J. Nucl. Mater. **516**(INL/JOU-18-45934-Rev000) (2018)
2. Luzzi, L., Cammi, A., Di Marcello, V., et al.: Application of the TRANSURANUS code for the fuel pin design process of the ALFRED reactor. Nucl. Eng. Des. **277**, 173–187 (2014)
3. Di Marcello, V., Botazzoli, P., Schubert, A., et al.: Improvements of the TRANSURANUS code for FBR fuel performance analysis (2011)
4. Karahan, A., Buongiorno, J.: Modeling of thermo-mechanical and irradiation behavior of mixed oxide fuel for sodium fast reactors. J. Nucl. Mater. **396**(2–3), 272–282 (2010)
5. Chen, H., Zhang, X., Zhao, Y., et al.: Preliminary design of a medium-power modular lead-cooled fast reactor with the application of optimization methods. Int. J. Energy Res. **42**(11), 3643–3657 (2018)
6. Magni, A., Barani, T., Del Nevo, A., et al.: Modelling and assessment of thermal conductivity and melting behaviour of MOX fuel for fast reactor applications. J. Nucl. Mater. **541**, 152410 (2020)
7. Siefken, L.J., Coryell, E.W., Harvego, E.A., et al.: SCDAP/RELAP5/MOD 3.3 code manual MATPRO - a library of materials properties for light-water-reactor accident analysis. NUREG/CR-6150; INEL-96/0422, Idaho Falls (2000)
8. Luscher, W., Geelhood, K., Porter, I.: Material property correlations: comparisons between FRAPCON-4.0, FRAPTRAN-2.0, and MATPRO[R]. PNNL-19417 Rev.2, Richland (2015)
9. Yang, G., Liao, H., Ding, T., et al.: Preliminary study on the thermal-mechanical performance of the U3Si2/Al dispersion fuel plate under normal conditions. Nucl. Eng. Technol. **53**(11), 3723–3740 (2021)
10. Angelo, A.D., Casaccia, E., Torino, P., et al.: Benchmark on beam interruptions in an accelerator-driven system final report on phase II calculations. Nuclear Energy Agency, Organisation for Economic Cooperation and Development (2003). (7)
11. Agosti, F., Botazzoli, P., Marcello, V.D., et al.: Extension of the TRANSURANUS code to the analysis of cladding materials for liquid metal cooled fast reactors: a preliminary approach (2013)
12. Larson, F.R.: A time-temperature relationship for rupture and creep stresses. Trans. ASME **74**, 765–775 (1952)

13. Yang, G., Guo, Z., Wang, P., et al.: Research and validation on the numerical algorithm of mechanical module in a transient fuel rod performance code for fast reactor. Ann. Nucl. Energy **171**, 108991 (2022)
14. Yang, G.L., Liao, H.L., Ding, T., et al.: Development and validation of a new oxide fuel rod performance analysis code for the liquid metal fast reactor. Nucl. Sci. Tech. **33**, 66 (2022)

Heterogeneous Reactivity Effect Analysis of Pu Spots Considering Grain Size Distribution Based on MOC

Masato Ohara[(✉)], Akifumi Ogawa, Takanori Kitada, and Satoshi Takeda

Osaka University, Suita, Osaka, Japan
m-ohara@ne.see.eng.osaka-u.ac.jp

Abstract. In the process of Mixed Oxide (MOX) fuel fabrication, plutonium grains, called plutonium spots (Pu spots), occur in MOX fuel because uranium and plutonium cannot be mixed completely. The previous study showed that the prediction accuracy of criticality is improved by considering the heterogeneity of Pu spots in MOX fuel in the analysis of some critical experiments. The analysis of the heterogeneity has been performed by Monte Carlo calculations, to ensure that core geometry and self-shielding effects are accurately considered in nuclear calculations. However, the results of Monte Carlo calculations are obtained with the statistical errors, thus the small reactivity worth is difficult to be analyzed. Therefore, in the previous study, the heterogeneous model by using a method devised by R. Sanchez was introduced into OpenMOC that is deterministic calculation code. Although there are numerous sizes of Pu spots in MOX fuel, an only single size of the grain could be considered in the modified OpenMOC. Therefore, in this study, the modified OpenMOC code was additionally modified to consider the grain size distribution of Pu spots.

The calculation result obtained by the additionally modified OpenMOC shows that the heterogeneous reactivity effect caused by numerous grain sizes of Pu spots is evaluated at $-0.190\%\Delta k/kk'$ at highly enriched fuels. On the other hand, a heterogeneous reactivity effect by single grain size is evaluated at $-0.225\%\Delta k/kk'$. The additionally modified OpenMOC makes it possible to study the effect of considering the grain size distribution of Pu spots in MOX fuel.

Keywords: MOX fuel · Pu spots · OpenMOC · GMVP · Heterogeneous model · Grain size distribution · Heterogeneous reactivity effect

1 Introduction

MOX fuel contains plutonium oxide grains (Pu spots) within the pellet. Pu spots burn locally and cause a problem with local power distribution in the fuel. Currently, the size of Pu spots is measured and controlled to ensure that local power distribution does not occur. The previous studies showed that the accuracy of criticality predictions can be improved by considering the heterogeneity of Pu spots [1]. The analysis of considering the heterogeneity of Pu spots is performed by Monte Carlo calculations to consider

the exact core geometry and self-shielding effects. However, the results of Monte Carlo calculations are obtained with statistical errors, thus the small reactivity worth is difficult to be analyzed.

The deterministic calculation is suitable for the analysis of small reactivity worth. One deterministic approach to treating the self-shielding effect is introducing the reduced order-modeling [3–6]. Another approach is introducing the heterogeneous model by using a method devised by R. Sanchez [7–10]. In the previous study, the heterogeneous model was introduced into the MOC code OpenMOC [11]. Although there are numerous sizes of Pu spots in MOX fuel, the heterogeneous model in the modified OpenMOC could consider only a single grain size. Therefore, in this study, the modified OpenMOC code was additionally modified to consider the grain size distribution of Pu spots, and the effect of grain size distribution on criticality was investigated.

2 Calculation Method and Condition

2.1 Calculation Flow

The OpenMOC code was modified so that numerous grain sizes can be calculated to treat the grain size distribution. The calculation flow of the modified OpenMOC code is shown in Fig. 1. In Fig. 1, the input module was modified to read the numerous sizes of the grain, and the angular flux calculation function was modified to calculate the flux in each grain size. At the beginning of the calculation, the escape probabilities and transmission probabilities required to introduce the heterogeneous model are calculated.
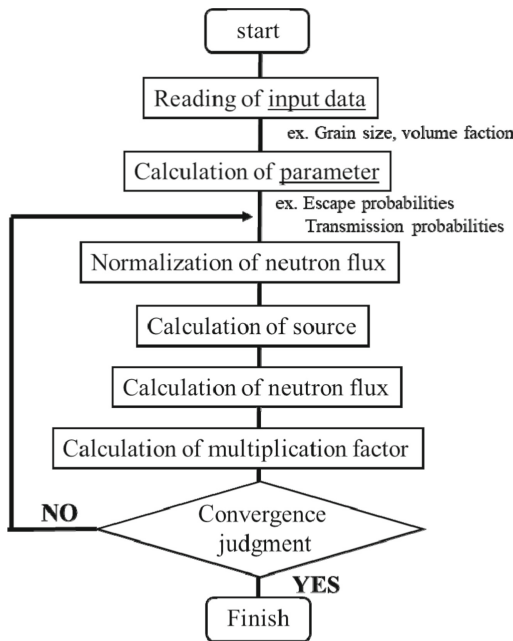
Fig. 1. Calculation flow of modified code

2.2 Calculation Condition

This section shows the calculation condition of the modified OpenMOC and additionally modified OpenMOC. The effective cross section is obtained by the collision probability method (PIJ) of SRAC2006 [12]. 107 energy group structure are used. The fast neutron energy region is divided into 61 groups, and the thermal neutron energy region is divided into 46 groups. The modified OpenMOC calculations was performed in the pin-cell model. The geometry of pin-cell model is shown in Fig. 2. The fuel temperature is 900K and moderator temperature is 600K. JENDL-4.0 is used [13]. U-235 enrichment of matrix is 0.2wt%. Pu enrichment of each region is shown in Table 1. Isotopic ratio of Pu is shown in Table 2. The calculations of the modified OpenMOC are performed under the conditions shown in Table 3.
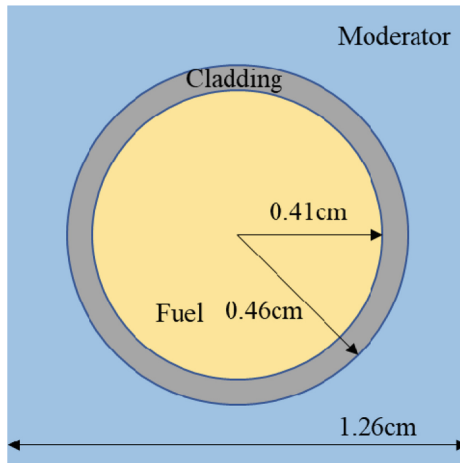
Fig. 2. Geometry of Pin-cell model

Table 1. Pu enrichment of each region

Fuel type	Entire region	Grain region	Matrix region
High enrichment	10.6%	25.0%	3.0%
Middle enrichment	6.2%		3.7%
Low enrichment	4.5%		3.0%

In this study, the calculations were performed for both the homogeneous model, in which uranium and plutonium are homogeneously mixed, and the heterogeneous model, in which Pu spots are included. The effect of Pu spots is expressed as a heterogeneity reactivity effect. The heterogeneity reactivity effect is defined as the reactivity which is obtained by changing from the homogeneous model to heterogeneous model. The effect is defined as:

$$heterogeneity\ reactivity\ effect = \frac{1}{k\,(homogenenous\,model)} = \frac{1}{k'\,(homogenenous\,model)} \quad (1)$$

Table 2. Isotopic Ratio of Pu (wt%)

Pu-238	5
Pu-239	55
Pu-240	20
Pu-241	15
Pu-242	5

Table 3. Calculation Conditions on the modified OpenMOC

number of polar angle(π)	3
number of azimuth angle(2π)	32
Track Spacing [cm]	0.01
convergence citeria	1.00E–07

2.3 Estimation of Grain Size Distribution

This section shows the conditions related to Pu spots used in the calculations. In this study, the conditions related to Pu spots are determined based on previously investigated grain size distribution [14]. The volume fraction and particle size distribution of Pu spots vary with plutonium enrichment, thus three analyses (analyses for high, middle, and low enrichment) were performed. In Table 4, the volume fractions of Pu spots at each enrichment are shown. In Tables 5, 6, and 7, the grain size distribution is expressed in terms of four grain sizes and the volume fraction of Pu spots at each grain size are shown.

Table 4. Volume fraction of Pu spots at each enrichment

Fuel type	Volume fraction of Pu
High enrichment	30.3%
Middle enrichment	10.1%
Low enrichment	5.8%

Table 5. Volume fraction of each grain size in high enrichment fuel

Grain Size	125 μm	45 μm	25 μm	10 μm
Volume fraction	23.80%	1.49%	2.59%	2.42%

Table 6. Volume fraction of each grain size in middle enrichment fuel

Grain Size	75 μm	45 μm	25 μm	10 μm
Volume fraction	6.35%	0.95%	0.97%	1.86%

Table 7. Volume fraction of each grain size in low enrichment fuel

Grain Size	65 μm	35 μm	25 μm	10 μm
Volume fraction	4.50%	0.36%	0.30%	0.68%

In addition, calculations that simulate single grain size are also carried out to investigate the effect of considering the grain size distribution. In the high, middle, and low enrichment fuels, most of Pu spots are 125, 75, and 65 μm in diameter respectively. Therefore, these grain sizes are used in the calculation of the single grain size. The single grain sizes used in the calculations are shown in Table 8.

Table 8. The single grain sizes used in the calculations at each enrichment

	single grain size
High enrichment	125 μm
middle enrichment	75 μm
low enrichment	65 μm

3   Calculation Result

The calculation results of single grain size and four grain sizes are shown in Fig. 3.

In all conditions, the results of the heterogeneity reactivity effect are negative because the ratio of Pu-239 is high and the ratio of Pu-240 is low in the Pu isotope ratio. Pu 239 has a fission resonance at 0.3 eV and the fission reaction is reduced by the self-shielding effect of Pu spots. The reason for the negative heterogeneity reactivity effect is the high proportion of Pu-239. On the other hand, the isotope ratio with the high proportion of Pu-240 is used, the heterogeneity reactivity effect shifts to the positive side. The reason is that Pu-240 has a neutron absorption resonance at 1.0eV and neutrons escaping this resonance can cause fission.

At all enrichments, the heterogeneity reactivity effect of the calculation of single grain size is larger than four grain sizes. Because the larger the grain size, the larger the self-shielding effect. In this study, the calculations of single grain size are carried out by replacing smaller grain sizes with the largest one. Therefore, the calculations of single grain size have a large proportion of Pu spots with a larger grain size than the
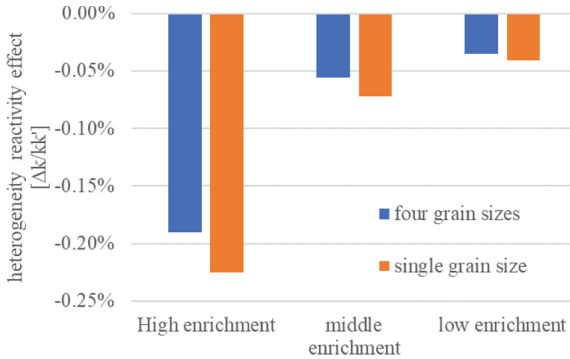
Fig. 3. Comparison of calculation results between the case of single grain size and four grain sizes

calculations of four grain sizes. As a result, the heterogeneity reactivity effect is larger in the calculation of single grain size.

At the high enrichment fuel, the difference between the calculation results of single grain size and four grain sizes was the largest. The difference is 0.035%k/kk'. When calculating a slight difference in reactivity effect by Monte Carlo calculation, a huge calculation cost is required to suppress statistical error. This study makes it possible to carry out calculations that consider the grain size distribution of Pu spots in MOX fuel, using a deterministic calculation method that does not have statistical errors.

4 Conclusions

The heterogeneous model introduced in previous studies could only consider a single grain size. In practice, there is a distribution of Pu spots sizes in MOX fuel. Therefore, the purpose of this study is to investigate the effect of the Pu spots size distribution on criticality. Initially, the modified OpenMOC was additionally modified to consider the grain size distribution, thus the effect of the grain size distribution on criticality can be evaluated without statistical errors. At high enrichment fuel, the difference between the calculation results of single grain size and four grain sizes was found to be $0.035\Delta k/kk'$. The additionally modified OpenMOC makes it possible to study the effect of considering the grain size distribution of Pu spots in MOX fuel. Further improvement of the criticality prediction accuracy in MOX fuel is expected by the additionally modified OpenMOC.

References

1. Reactor Integral Test Working Group, JENDL Committee "Compilation of the Data Book on Light Water Reactor Benchmark to Develop the Next Version of JENDL" Japan Atomic Energy Agency (2017)
2. William, B., Shaner, S., Li, L., et al.: The open MOC method of characteristics neutral particle transport code. Ann. Nucl. Energy **68**, 43–52 (2014)
3. Yamamoto, A., Endo, T., Takeda, S., et al.: A resonance calculation method using energy expansion bases based on a reduced order model. In: M&C 2019, 25–29 August 2019 (2019)

4. Yamamoto, A., Kondo, R., Endo, T., et al.: Resonance calculation using energy spectral expansion based on reduced order model: application to heterogeneous geometry. In: 2019 Transactions of the American Nuclear Society, 7–21 November 2019 (2019)
5. Kondo, R., Endo, T., Yamamoto, A., et al.: A resonance calculation method using energy expansion based on a reduced order model: Use of ultra-fine group spectrum calculation and application to heterogeneous geometry. In: PHYSOR 2020, 28 March–2 April 2020 (2020)
6. Kondo, R., Endo, T., Yamamoto, A., et al.: A new resonance calculation method using energy expansion based on a reduced order model. Nucl. Sci. Eng. **195**(7), 694–716 (2021)
7. Sanchez, R., Pomraning, G.C.: A statistical analysis of the double heterogeneity problem. Ann. Nucl. Energy **18**(7), 371–395 (1991)
8. Sanchez, R., Masiello, E.: Treatment of the double heterogeneity with the method of characteristics. In: PHYSOR 2002, 7–10 October 2002 (2002)
9. Sanchez, R.: Renormalized treatment of the double heterogeneity with the method of characteristics. In: PHYSOR 2004, 25–29 April 2004 (2004)
10. Joo, H.G., Park, T.K.: Derivation of Analytic Solution and MOC Calculation Procedure for Double Heterogeneity Treatment. Seoul National University. SNURPL-SR-001 (2007)
11. Ogawa, A.: Modification of MOC for considering double heterogeneity due to pu spots in MOX fuel. In: Proceedings of the Reactor Physics Asia 2019 Conference, pp. 86–89(2019)
12. Okumura, K., Kugo, T., Kaneko, K., Tsuchihashi, K.: SRAC2006: a comprehensive neutronics calculation code system. Japan Atomic Energy Research Institute (2007)
13. Shibata, K., et al.: JENDL4.0: a new library for nuclear science and engineering. J. Nucl. Sci. Technol. **48**(l), 1(2011)
14. Documentation of the 4th Safety Review Meeting handout 4–3. Miyagi Prefecture. Accessed 27 June 2022. [In Japanese]. https://www.pref.miyagi.jp/documents/10438/4042.pdf

Preparation and Properties of Graphite Surface Vitrification Y_2O_3 Coating

Zhen Lei$^{(\boxtimes)}$, Hongya Li, Bingzhai Yu, and Binghan Geng

The Fourth Filial Company of 404 Company Limited, CNNC, Lanzhou 732850, Gansu, China
576442476@qq.com

Abstract. The Mo-Y_2O_3 composite coating was prefabricated on the surface of the graphite crucible by plasma spraying, and then the coating surface was remelted by high-power laser. The coating was subjected to SEM analysis, X-ray diffraction, bond strength testing, and molten terbium metal corrosion test. The results show, After laser cladding treatment, the problems of pores and unmelted particles on the surface of the Mo-Y_2O_3 coating have been significantly improved, and the porosity has been reduced to less than 1.5%, Vitrified Y_2O_3 with a thickness of about 80–120 µm and columnar crystal growth was formed on the surface of the coating, and the bonding strength was increased from 2–3 MPa before treatment to 7–11 MPa, In the corrosion assessment test of molten terbium metal, the coating was intact and did not fall off, the surface of the ingot was not adhered, and there was no contamination by impurity elements, which could be easily demolded.

Keyword: Surface treatment · Laser micro-nano sintering · Performance optimization · Composite materials

1 Introduction

In recent years, industries such as nuclear energy technology, aerospace, new energy, new materials, marine ships and medical equipment have been changing rapidly. The progress in these fields is inseparable from the rapid development of high-performance special alloy materials. Such alloy materials are often active metals with a high melting point, the raw materials are precious, and are easily reacted with various gases and crucible materials at high temperatures. Therefore, solving the problem of "sticking and contamination" of melting crucibles has become a hotspot of surface engineering research. Graphite material has excellent thermal shock resistance, thermal shock resistance and ease of processing, and is the most commonly used crucible material in high melting point active metal smelting. However, at high temperature, the CO gas and free carbon vapor generated in the furnace can easily react with the smelted metal to form carbides, resulting in melt carbon pollution, which affects the properties of metal materials [1]. Xiao [2] studied the thermal shock resistance of Nb/ZrO_2(Y_2O_3), Nb/$CaZrO_3$, Mo/ZrO_2(Y_2O_3) composite coatings, and the results showed that the coatings basically cracked and peeled off at 1500 °C for 30 min. Koger J W [3] prepared a Nb/ZrO_2/Y_2O_3 composite coating, which can withstand the test of metal smelting many times, but

the process technology is harsh. Kim [4] prepared a Y_2O_3 coating that can be used for ternary alloy casting, but it is difficult to prepare. Petitbon [5] added Al_2O_3 powder when remelting the plasma sprayed zirconia coating by laser to obtain the Al_2O_3/ZrO_2 composite coating. The coating's strength, wear resistance and high temperature corrosion resistance are significantly increased Experimental materials and methods. Ahmaniemi [6] used the laser cladding method to seal the ZrO_2 coating, the lattice distortion of the ZrO_2 crystal occurred, the coating became dense, and the microhardness increased.

At present, most of the researches focus on the optimization of the plasma spraying process parameters and the repair of the coating on the surface of the crucible, and the process is complicated and tedious, while the research and application of the coating required for the smelting of special materials are very few. In order to solve the above shortcomings, this paper takes graphite/Mo/Y_2O_3 as the research system, and uses the laser micro-nano sintering method to clad the plasma sprayed Mo/ Y_2O_3 coating, and obtain the vitrified Y_2O_3 coating. The coating can withstand multiple corrosion tests of molten terbium metal. The preparation method and formation mechanism of vitrified Y_2O_3 coating on graphite surface were studied in order to provide some theoretical guidance for production practice.

2   Test Materials and Methods

High-purity graphite has the advantages of light weight, high strength and good thermal shock resistance. It is a commonly used crucible material in high-temperature smelting and high-temperature smelting of rare earth metals, niobium silicide-based superalloys and some actinide metals. However, carbon as an impurity element needs to be strictly controlled in the metallurgical processing of metal materials, and the increase of carbon content in the smelting process should be avoided as much as possible. Therefore, it is necessary to spray a layer of oxide on the surface of the crucible to prevent carbon increase. As the intermediate transition layer of the composite coating, the thermal expansion coefficient of Mo is between high-purity graphite and yttrium oxide, which can effectively prevent the coating from peeling, cracking and falling off due to high temperature melt erosion. Y2O3 is stable and does not react or wet with high temperature melts, which can ensure the purity of the melts.

The materials selected in this study and their properties are shown in Table 1.
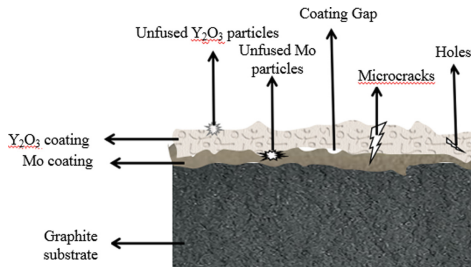
Fig. 1. Schematic diagram of plasma spray coating structure.

Firstly, the Mo-Y$_2$O$_3$ composite gradient coating was prefabricated on the surface of the graphite mold crucible by plasma spraying method, and the coating structure is shown in Fig. 1.

Table 1. Material types and their properties.

High purity graphite	Ash content (ppm)	Density (g/cm^3)	Graininess (mm)	Thermal conductivity w/(m·k)	Coefficient of thermal expansion (°C^{-1})
	≤40	≥1.8	≤0.02	≥110	4.0–4.8 × 10^{-6}
Molybdenum powder	Principal content (%)		Particle size distribution (μm)		5.2 × 10^{-6}
	≥99.90		45–96		
Yttrium powder	Principal content (%)		Particle size distribution (μm)		8.0 × 10^{-6}
	≥99.98		11–53		

Next, the graphite crucible was dried in a blast drying oven at a temperature of 50–60 °C for 30 min, again, the crucible was fixed on a special fixture after the dust on the surface was blown off by compressed air, and the equipment was turned on to perform the laser fusion treatment of the coating. The micro-nano sintering process is shown in Fig. 2.
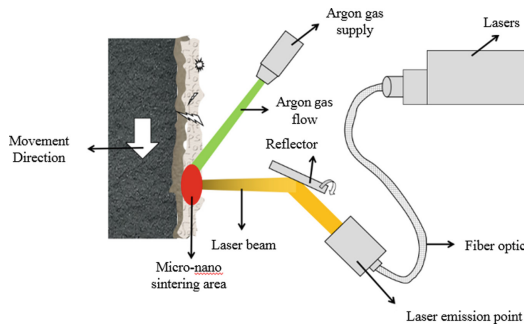
Fig. 2. Schematic diagram of laser micro-nano sintering process.

Finally, the molds after laser micro-sintering were placed in a vacuum well furnace for heat treatment to eliminate the residual stresses generated during the spraying and laser micro-sintering experiments at 400 °C for 4 h.

The process parameters of plasma spraying and laser micro-nano sintering during the experiment are shown in Table 2.

The surface morphology of the coating was characterized by a Zeiss EVO scanning electron microscope. And use Image J image processing software to calculate apparent porosity. The phase structure and composition of the coating were determined by X-ray

Table 2. Plasma spraying and laser micro-nano sintering process parameters.

Plasma spray	Voltage (V)	Current (A)	Spraying distance (mm)	Main air flow (Ar/MPa)	Auxiliary gas flow (He/MPa)
	45–55	600–750	90	2.00–3.00	0.20–0.40
Laser Micro-Nano Sintering	Overlap rate (%)	Scan speed (°/min)	Laser power (w)	Energy Density (w/mm^2)	Laser spot diameter (mm)
	50	2600–2800	105–120	145	2–3

diffractometer XRD-6100. The bond strength of the coating was tested by the pull-off method.

3   Experimental Results and Analysis

3.1   Coating SEM, XDR Analysis

The SEM micro-morphologies of the coatings before and after laser micro-nano sintering are shown in Fig. 3.
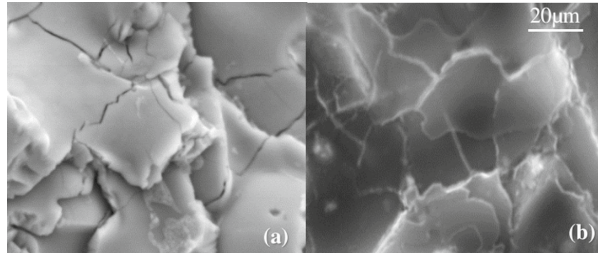
Fig. 3. Microscopic surface morphology of the coating after plasma spraying and laser micro-nano sintering.

As shown in Fig. 3, a and b indicate the microscopic morphology of the coating by plasma spraying and laser micro-nano sintering, respectively. The surface of the plasma sprayed coating is uneven, loose and porous, and has a lamellar structure. The connection between the coating and the substrate belongs to mechanical bonding. Because in the spraying process, the molten powder is not shot to the surface of the substrate at a high speed, and a porous layered coating is formed after deformation and spreading. Some powder particles that are not fully melted reach the surface of the substrate to form spherical particles of different sizes, and through layer-by-layer superposition, many holes are formed in the coating, causing defects. In addition, during the spraying process, the air in the surrounding environment absorbed by the molten particles cannot be completely eliminated during cooling and solidification, which also forms a defect.

After laser micro-nano sintering, the surface of the coating is flat and smooth, and there are no obvious holes. This shows that the coating performance is optimized, and the bonding between the coatings is closer to metallurgical bonding. After micro-nano sintering, micro-cracks can still be seen on the surface (the bright part in Fig. 3b), which is caused by the combined effect of tensile stress and compressive stress on the coating surface during the rapid heating and cooling of the coating. After laser remelting, the surface lamellar structure almost disappeared. After micro-nano sintering, the coating formed a vitrified Y_2O_3 film with a thickness of about 80–120 μm and columnar crystal growth. The defects such as pores and inclusions of the coating are greatly reduced, and the density has been greatly improved.

The XRD analysis of the plasma sprayed coating and the laser micro-nano sintered coating was carried out using an X-ray diffractometer XRD-6100, and the results are shown in Fig. 4.
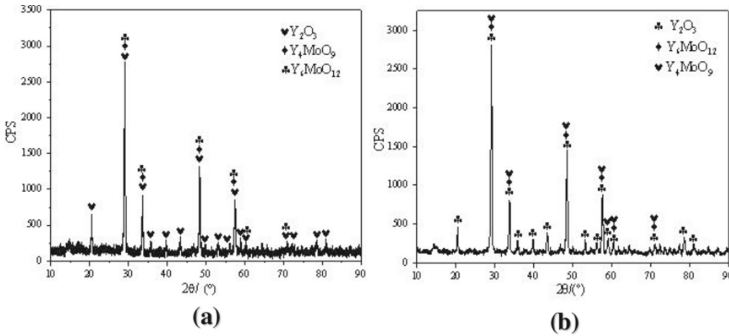
Fig. 4. XRD physical phase analysis of the coating.

As shown in Fig. 4, Figs. a and b represent the results of the physical phase analysis of the plasma spraying method and the laser micro-nano-sintering coating, respectively. It can be seen from Fig. 4a that there are mainly compounds such as Y_2O_3, Y_4MoO_9, and Y_6MoO_{12} on the surface of the plasma sprayed yttrium oxide coating. At high temperature, Y_2O_3 and MoO_3 react as follows, which is consistent with Fig. 4b.

$$2Y_2O_3 + MoO_3 = Y_4MoO_9 \tag{1}$$

$$3Y_2O_3 + MoO_3 = Y_6MoO_{12} \tag{2}$$
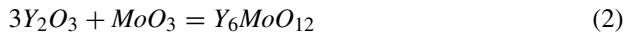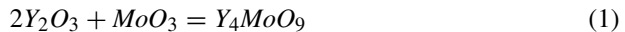
Because the plasma temperature is much higher than the sublimation temperature of MoO_2 (700 °C) during the spraying process, the coating material does not contain MoO_2. The X-ray diffraction peaks corresponding to MoO_3 are mainly at $2\theta = 13°$, $26°$ and $39°$, so it can be considered that the coating surfaces are all Y_2O_3. It can be seen that the laser micro-nano sintering process does not change the phase composition of the coating surface, nor does it introduce other impurities.

3.2   Coating Bonding Strength Score

The bonding strength of the coating was tested by the pull-off method. Three samples were prepared with different process parameters. The test results are shown in Table 3. Plasma Binding force test.

Control tests 1 and 2 show that the overall bonding force of the plasma sprayed layer is low, and the fractured part is on the surface of the substrate. Because the surface temperature of the substrate is very high after spraying, a large internal stress will be generated inside the coating, which is directly quenched in the air, and defects such as microcracks will be generated during the stress release process, which will reduce the bonding force of the coating. From experiments 1 and 3, it can be seen that laser micro-nano sintering can increase the bonding force of the coating from 2–3 MPa to 5–10 MPa, because the coating is converted from mechanical bonding to metallurgical bonding after laser micro-nano sintering. It can be seen from experiments 3 and 4 that heat treatment can further optimize the laser cladding coating, eliminate the internal stress, and further improve the bonding force of the coating.

Table 3. Plasma Binding force test.

No	Laser power/W	heat treatment	Experimental results and binding force (MPa)
1	0	-	Fractured from graphite substrate after stretching, bonding force 2–3
2	0	4 h at 700 °C	Fractured from graphite substrate after stretching, bonding force 2.5–4
3	110	-	Fractured from graphite substrate after stretching, bonding force 7–9
4	110	4 h at 700 °C	Fractured from yttrium oxide coating after stretching, bonding force 8–11

3.3   Terbium Metal Melting Test Coating Test

At 1550 °C, under 8.5×10^{-2} Pa, the metal terbium in the distilled state is smelted by an intermediate frequency induction heating furnace. Then, the liquid terbium metal was cast into Mo/Y_2O_3 graphite crucibles with two coatings (plasma spray coating and laser cladding coating) respectively, and the temperature was kept for 20 min. Finally, the bottom of the crucible is cooled, filled with inert gas, and after cooling to room temperature, it is released from the furnace and demolded.

As shown in Fig. 5 a, b, and c represent the inner wall of the crucible treated by plasma spraying, the local morphology of the coating and the appearance of the terbium ingot after demolding. d, e, and f represent the inner wall of the crucible, the partial morphology of the vitrified coating after laser micro-nano sintering, and the appearance of the terbium ingot after demolding. Terbium casting test results show that the plasma sprayed Mo/Y_2O_3 composite coating falls off after contacting with terbium melt. During
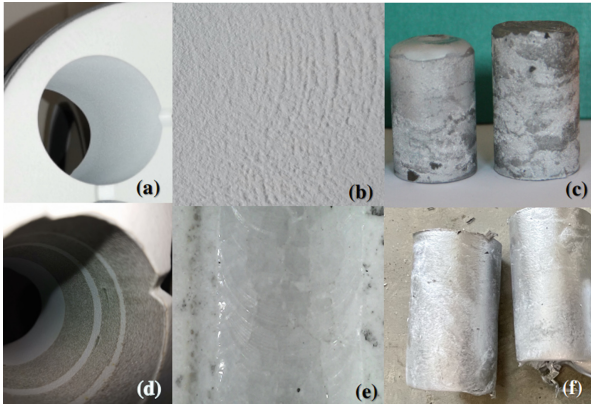
Fig. 5. Terbium metal casting test.

the solidification and shrinkage process of the terbium melt, the melt penetrates into the interior of the coating through pores and cracks, and forms a mosaic bonding structure with the coating surface. Causes the molybdenum and yttrium oxide coatings to peel off in a large area, and black and white spots appear (as shown in Figure c).

It can be seen from this: the bonding force of the plasma sprayed coating is low, and this phenomenon is consistent with the results of Test 1 in Table 3. After the Mo/Y_2O_3 composite coating is sintered by laser micro-nano, the surface of the terbium ingot is smooth and clean, and there is no "sticking to the ingot" phenomenon, as shown in Fig. f. Because the heating and cooling speeds are extremely fast during the laser cladding process, and the solidification speed is about 10^4 °C/s, the surface of the Y_2O_3 coating will be vitrified, and the voids and cracks on the coating surface will be repaired. The rapid melting makes the surface produce fine-grain strengthening, and the interfacial bonding force increases. This phenomenon is consistent with the results of Test 4 in Table 3.
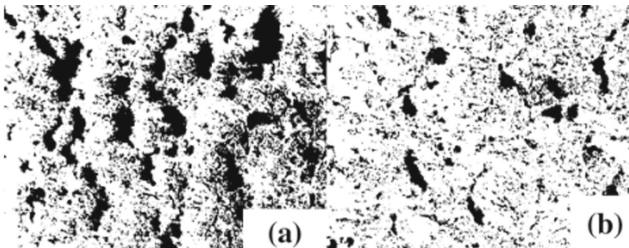
Fig. 6. Pore space on the surface of the coatin.

Apparent porosity was calculated using Image J image processing software. Eight SEM photos of the coating were randomly selected in different areas and at the same magnification, and then the apparent porosity of each photo was calculated by the gray-scale method, and the arithmetic mean was taken as the apparent porosity of the coating.

As shown in Fig. 6,a and b represent the micro-morphologies of the plasma spray coating and the laser micro-nano sintering coating after grayscale processing of the Image image, respectively. After calculation, the apparent porosity of the coating after laser micro-nano sintering decreased from 5–6% to less than 1.5%. It shows that laser micro-nano sintering can significantly reduce the surface porosity of the coating, effectively reduce the infiltration path of the melt, and alleviate the peeling of the coating.

	C	Al	Si	Na	N	Mo	Y
	148	59	1.2	0.74	22	83	0
	162	52	2.5	29.8	31	75	2.4
	178	54	3.4	35.2	37	96	4.9

Average value before meltingReflector
Average value of laser cladding coating after melting
Average value after plasma coating melting
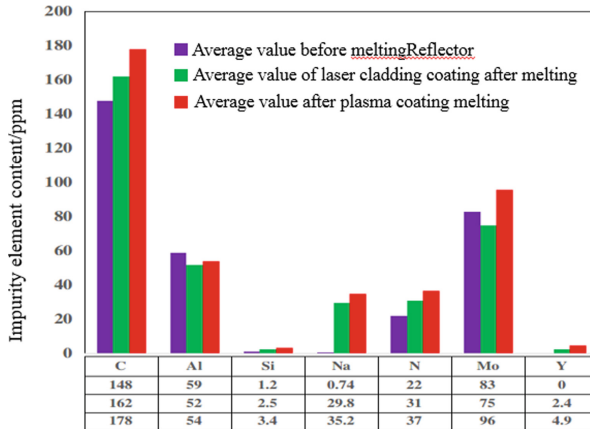
Fig. 7. Variation of impurity element content.

After After demoulding, the content of impurity elements on the surface of the ingot was analyzed. The impurity content on the surface of the ingot is shown in Fig. 7.

Compared with the terbium metal raw material, the content of each impurity element in the ingot after the plasma spray coating is smelted has increased, especially the C content exceeds the standard, which does not meet the smelting requirements. After laser cladding coating smelting, the C content of the ingot increased by 4 ppm on average, the Al, Na, Mo, N content decreased by 7 ppm, 29 ppm, 8 ppm and 9 ppm respectively, the content of Y element met the requirements. The average impurity content is within the control range, and there is no obvious carbon increase, indicating that the Mo/Y_2O_3 coating after laser micro-nano sintering has the effect of preventing carbon completely. The surface of the terbium metal ingot has no white spots attached (Fig. 5f), the interface between the coating and the terbium metal melt does not infiltrate, the coating does not adhere to the surface of the ingot, the ingot is easily demolded, and the melting target is achieved.

4 Conclusion

(1) The surface of the coating after laser micro-nano sintering is smooth and flat, the porosity is reduced to less than 1.5%, and a vitrified Y_2O_3 coating with a thickness of about 80–120 μm and columnar crystal growth is formed. It shows that laser micro-nano sintering can repair coating cracks, and can make the bonding between coatings change from mechanical bonding to metallurgical bonding.

(2) After the plasma sprayed layer is sintered by laser micro-nano, the surface of the coating has a fine-grain strengthening effect due to rapid melting, and the bonding strength of the coating is increased from 2–3 MPa before treatment to 7–11 MPa.

(3) The laser micro-nano sintering coating has the function of blocking carbon without introducing impurities and meeting the smelting requirements.

References

1. Holcombe, C.E., Banker, J.G.: Uranium/ceramic oxide and carbon/ceramic oxide interaction studies. Metall Trans. B **9**(2), 317–319 (1978)
2. Xiao, Y., Shuiyi, J.C., et al.: Research on the control of carbou pollution during metal smelting in carbon atmosphere. Cast. Technol. **24**(1), 59–60 (2003)
3. Koger, J.W., Holcombe, C.E., Banker, J.G.: Coatings on graphite crucibles used in melting uranium. Thin Solid Films **39**(none), 297–303 (1976)
4. Kim, J.H., Song, H., Kim, K.H., et al.: Protective yttria coatings of melting crucible for metallic fuel slugs. Surface Interface Anal. **47**(3), 301–307 (2015)
5. Petitbon, A.L., Delsart, B.D.: Delsart laser surface sealinand strengthening of zirconia coatings. Surface Coatings Technol. **49**, 57–61 (1991)
6. Ahmaniemi, S., Vuoristo, P., Mntyl, T.: Improved sealing treatments for thick thermal barrier coatings. Surface Coatings Technol. **151–152**, 412–417 (2002)

Numerical Study on the Mechanism of Oxygen Diffusion During Oxygen Control Process in Heavy Liquid Metals

Ying Li, Liang Guo, Chao Zhang$^{(\boxtimes)}$, Hongbo You, and Yuanfeng Zan

CNNC Key Laboratory on Nuclear Reactor ThermoHydraulics Technology, Nuclear Power Institute of China, Chengdu, Sichuan, China
zhangchao_turbo@163.com

Abstract. In order to investigate the mechanisms and characteristics of oxygen diffusion during oxygen control in Heavy Liquid Metals (HLM). Turbulence model coupling species transport model are used to predict the oxygen transport and distribution in liquid lead-bismuth eutectic (LBE) during gas oxygen control process. The oxygen mass flow coefficients are calculated under diffident LBE temperatures, inlet LBE flow rates, inlet oxygen concentrations and gas/liquid interface oxygen concentrations. A mass transfer correlation for oxygen transport is finally acquired. The simulated results indicate that oxygen transport is mainly influenced by the combined effect of convection and diffusion. Specifically, the mass flow coefficient increases with the increase of mass flow coefficient and LBE temperature. The gas/liquid interface oxygen concentration has little effect on the oxygen mass transfer coefficient in the oxygen transfer device of this study. Comparatively, the smaller inlet oxygen concentration leads to the larger average oxygen mass transfer coefficient and the effects of inlet oxygen concentration become weaker with the increase of flow rate. The numerical data presented in this study represents an essential step to reveal the mechanism of oxygen transport in flowing LBE and provides the theoretical basis for guiding the design of oxygen transfer device in HLM-cooled nuclear reactors.

Keywords: Heavy liquid metal · Oxygen diffusion · Gas oxygen control · Oxygen concentration

1 Introduction

Heavy Liquid Metals (HLM) such as liquid lead (Pb) and lead-bismuth eutectic (LBE) are considered as candidate coolants in Generation IV Nuclear Reactors thanks to their suitable thermo-physical and chemical properties. However, the oxidation of HLM and corrosion of structural steels have become major issue in the development of HLM-cooled nuclear reactors. One of the most viable methods for protection of HLM-cooled nuclear reactors is to control the oxygen content dissolved in the HLM among an appropriate range, which could guarantee the structural steels and avoid the HLM oxidation at the same time.

Several researchers have studied the characteristics of oxygen control technics based on different facilities [1–5]. Schroer et al. [1] investigated the oxygen-transfer to flowing lead alloys inside a gas/liquid transfer device in the CORRIDA loop. Marino et al. [2] acquired a mass transfer correlation for the lead oxide mass exchanger and the model was validated using experimental data from the CRAFT loop. Chen et al. [3] explored the LBE flow and oxygen transport in a simplified container under the gas oxygen control using a lattice Boltzmann simulation. However, the mechanisms and characteristics of oxygen diffusion during oxygen control are still not well understood.

In this study, a CFD model in the specific oxygen transfer device has been developed to determine the oxygen transport and distribution in flowing LBE. A mass transfer correlation for oxygen transport was obtained in terms of the Sherwood with simulation results. The numerical data presented in this study represents an essential step to reveal the mechanism of oxygen transport in flowing LBE and provides the theoretical basis for guiding the design of oxygen transfer device in HLM-cooled nuclear reactors.

2   Numerical Modeling

2.1   Geometry and Mesh

The simulated oxygen transfer device has a similar geometry with that in the CORRIDA loop [6], which has a specific inner diameter of 400 mm and a length of 1300 mm. As shown in Fig. 1, the LBE flows through vessels with a liquid level of 1/3 diameter. The control gas is pumped into the oxygen transfer device in the opposite direction through top vessels. The computational domain is simplified and depicted in Fig. 2. The minimum mesh size is set as $5 \cdot 10^{-3}$ m and the total number of the elements is about 2150977 after the mesh independence analysis [7].
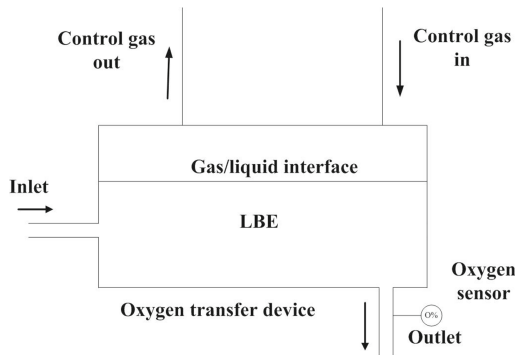
Fig. 1. Schematic diagram of the gas control apparatus
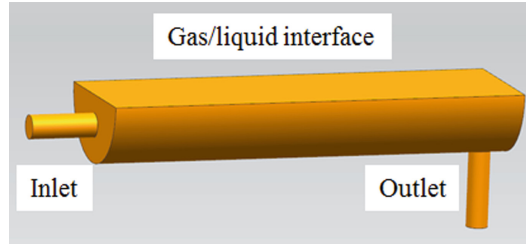
Fig. 2. Geometry of the simulated oxygen transfer device

2.2 Governing Equations and Boundary Conditions

The transport of oxygen obeys the Reynolds-averaged transport equation for turbulent flow:

$$\frac{\partial C_o}{\partial t} + \overrightarrow{u} \cdot \nabla C_o = \nabla \cdot (D + \frac{\mu_t}{Sc_t})\nabla C_o + q_o \tag{1}$$

where C_o is the oxygen concentration, u is the velocity of LBE, μ_t is the eddy viscosity, Sct is the turbulent Schmidt number, and q_o is the oxygen source, D is the diffusion coefficient of oxygen. D (cm^2·s^{-1}) is given by the following equation [8]:

$$D= 0.0239e^{-\frac{43073}{RT}} \quad 473K < T < 1273K \tag{2}$$

where R is the molar gas constant.

Based on the research in [9], the gas/liquid interface is simulated as a free-surface boundary with constant oxygen concentration.

The average dissolution rate q (kg·s^{-1}) of oxygen in the flowing LBE is described by:

$$q = m(C_{out} - C_{in}) \tag{3}$$

where C_{out} and C_{in} are the oxygen concentration at the outlet and inlet of oxygen transfer device (wt%), respectively. m is the mass flow rate.

The average mass transfer coefficient k (kg·m^{-2}·s^{-1}) of oxygen in the flowing LBE is calculated by:

$$k = \frac{q}{A(C_{g/l} - C_{ave})} \tag{4}$$

where A is the area of gas/liquid interface (m^2), $C_{g/l}$ is the oxygen concentration at the gas/liquid interface (wt%), C_{ave} is the average oxygen concentration of inlet and outlet (wt%).

The Sherwood number (Sh) representing the dimensionless form of the average mass transfer coefficient is defined by:

$$Sh = \frac{k \cdot l}{\rho \cdot D} \tag{5}$$

where l is a characteristic length and ρ is the density of LBE.

3   Results and Discussion

The simulation parameters (T_{lbe}, u_{lbe}, C_{in}, $C_{g/l}$) and calculated results (C_{out}, k, Sh) are summarized in Table 1.

Table 1. Simulated parameters

T_{lbe}/°C	u_{lbe}/m·s^{-1}	C_{in}/wt%	$C_{g/l}$/wt%	C_{out}/wt%	k/kg·m^{-2}·s^{-1}	Sh
550	2	8×10^{-7}	1×10^{-3}	1.30×10^{-5}	1.79	0.26
550	1	8×10^{-7}	1×10^{-3}	1.54×10^{-5}	1.07	0.16
550	1.5	8×10^{-7}	1×10^{-3}	1.32×10^{-5}	1.36	0.20
550	0.5	8×10^{-7}	1×10^{-3}	2.57×10^{-5}	0.92	0.13
550	2	8×10^{-7}	1×10^{-4}	2.00×10^{-6}	1.77	0.26
550	1	8×10^{-7}	1×10^{-4}	2.24×10^{-6}	1.06	0.16
550	1.5	8×10^{-7}	1×10^{-4}	2.02×10^{-6}	1.36	0.20
550	0.5	8×10^{-7}	1×10^{-4}	3.29×10^{-6}	0.93	0.14
550	2	8×10^{-7}	1×10^{-5}	9.05×10^{-7}	1.67	0.24
550	1	8×10^{-7}	1×10^{-5}	9.21×10^{-7}	0.96	0.14
550	1.5	8×10^{-7}	1×10^{-5}	9.07×10^{-7}	1.28	0.19
550	0.5	8×10^{-7}	1×10^{-5}	1.02×10^{-6}	0.86	0.13
550	2	1×10^{-8}	1×10^{-5}	1.22×10^{-7}	1.65	0.24
550	1	1×10^{-8}	1×10^{-5}	1.57×10^{-7}	1.08	0.16
550	1.5	1×10^{-8}	1×10^{-5}	1.34×10^{-7}	1.36	0.20
550	0.5	1×10^{-8}	1×10^{-5}	2.90×10^{-7}	1.04	0.15
500	2	8×10^{-7}	1×10^{-5}	1.72×10^{-6}	1.24	0.27
500	1	8×10^{-7}	1×10^{-5}	1.91×10^{-6}	0.72	0.16
500	0.5	8×10^{-7}	1×10^{-5}	9.63×10^{-7}	0.66	0.14
450	2	8×10^{-7}	1×10^{-5}	1.38×10^{-6}	0.89	0.30
450	1	8×10^{-7}	1×10^{-5}	1.67×10^{-6}	0.52	0.18
450	0.5	8×10^{-7}	1×10^{-5}	9.19×10^{-7}	0.48	0.16
400	2	8×10^{-7}	1×10^{-5}	1.19×10^{-6}	0.61	0.35
400	1	8×10^{-7}	1×10^{-5}	1.48×10^{-6}	0.36	0.21
400	0.5	8×10^{-7}	1×10^{-5}	8.84×10^{-7}	0.34	0.20
350	2	8×10^{-7}	1×10^{-5}	8.24×10^{-7}	0.38	0.41
350	1	8×10^{-7}	1×10^{-5}	8.29×10^{-7}	0.36	0.21
350	0.5	8×10^{-7}	1×10^{-5}	8.56×10^{-7}	0.23	0.24

Figure 3 depicts the distribution of oxygen concentration and velocity under the typical working condition ($T_{lbe} = 550\ °C$, $u_{lbe} = 0.5$ m/s, $C_{in} = 8 \times 10^{-7}$ wt%, $C_{g/l} = 1 \times 10^{-5}$ wt%). In the simulated model, the oxygen concentration at gas/liquid interface is considered as a constant 1×10^{-5} wt%. The oxygen concentration inside oxygen transfer device is set as 8×10^{-7} wt% in the initial condition. It can be seen from Fig. 3(a), after the transport of oxygen, the oxygen concentration inside the device increases from inlet to outlet with the flow of LBE. Especially, the oxygen distributed near inlet and outlet is obviously higher as a result of the reversed flow of LBE, as shown in Fig. 3(b).
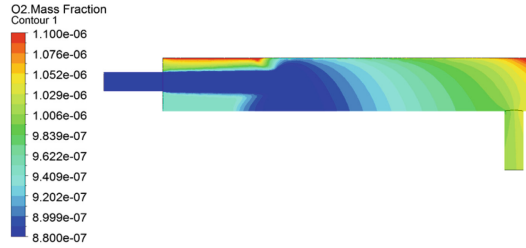
(a) Oxygen concentration distribution
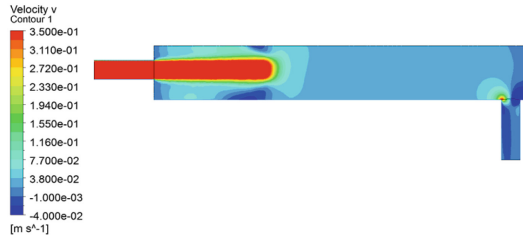
(b) Velocity distribution

Fig. 3. The distribution of oxygen concentration and velocity under the typical working condition ($T_{lbe} = 550\ °C$, $u_{lbe} = 0.5$ m/s, $C_{in} = 8 \times 10^{-7}$ wt%, $C_{g/l} = 1 \times 10^{-5}$ wt%)

Figure 4 shows the effects of the temperature and the velocity of LBE on the average oxygen mass transfer coefficient. It can be obtained that the average oxygen mass transfer coefficient increases with the increase of temperature and velocity of LBE. The reason is that the thermophysical properties such as viscosity and diffusion coefficient change with the LBE temperature and the mass transfer of oxygen is improved with the combined effect of convection and diffusion.
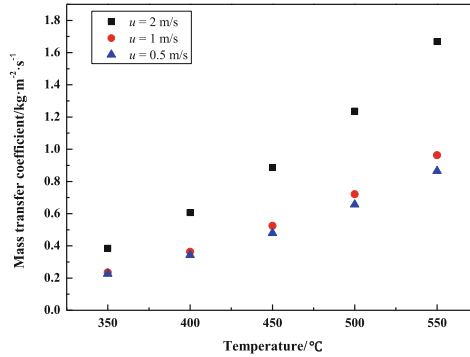
Fig. 4. The effects of the temperature and the velocity of LBE on the average oxygen mass transfer coefficient

Parameter analysis is performed for comparison of the average oxygen mass transfer coefficient k among different gas/liquid interface oxygen concentrations $C_{g/l}$ and different inlet oxygen concentrations C_{in} under different velocities of LBE at LBE temperature of 550 °C in Fig. 5(a) and 5(b), respectively. The results demonstrate that there is no obvious difference among average oxygen mass transfer coefficients on interface oxygen concentrations, as shown in Fig. 5(a). However, the average oxygen mass transfer coefficients are slightly smaller related to the higher inlet oxygen concentration (8×10^{-7}wt%) when the flow rate $u_{lbe} < 2$ m/s, as shown in Fig. 5(b). Thus, the gas/liquid interface oxygen concentration has little influence on the mass transfer coefficient of oxygen in the oxygen transfer device with specific geometry. On the other hand, the smaller inlet oxygen concentration leads to the larger average oxygen mass transfer coefficient and the effects of inlet oxygen concentration become weaker with the increase of flow rate.

Finally, a mass transfer correlation for oxygen transport was obtained in terms of the Sherwood with simulation results, as described by

$$Sh = A \cdot Pe^{B} \tag{6}$$

The corresponding coefficients A and B are listed in Table 2.

The deviations between simulated results and calculated results by (6) are shown in Fig. 6. It can be noted that the predictions of the correlation equation are all in agreement with the simulated Sh numbers in general with the maximum deviation of ± 26%.
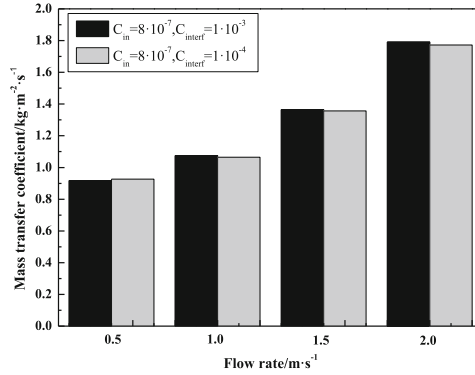
(a) The effects of the gas/liquid interface oxygen
concentration on the average oxygen mass transfer coefficient
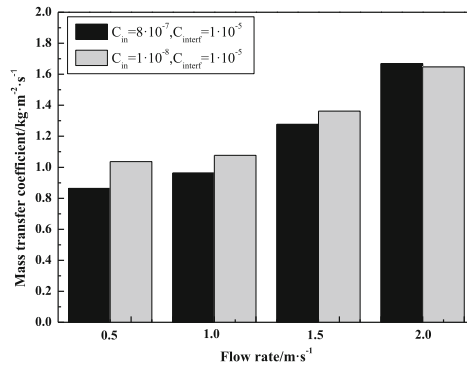
(b) The effects of the inlet oxygen concentration on the
average oxygen mass transfer coefficient

Fig. 5. Comparison of the average oxygen mass transfer coefficient k among different gas/liquid interface oxygen concentrations $C_{g/l}$ and different inlet oxygen concentrations C_{in} under different velocities of LBE at temperature of 550 °C

Table 2. Coefficients in (6)

Coefficient	Value
A	0.0169
B	0.321
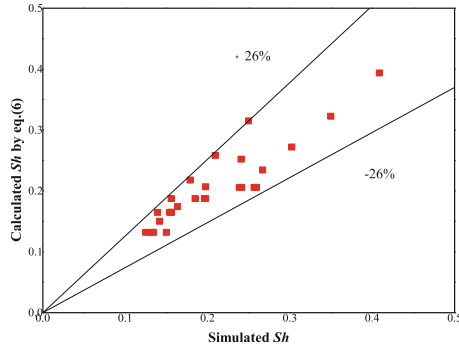
Fig. 6. The deviations between simulated results and calculated results by (6)

4 Conclusions

In this study, the oxygen transport characteristic in flowing LBE has been investigated with a turbulence model coupling species transport model in the specific oxygen transfer device. The following conclusions could be drawn:

1) The mass transfer coefficient of oxygen increases with the increase of temperature and velocity of LBE because of the combined effect of convection and diffusion.
2) The gas/liquid interface oxygen concentration has little influence on the mass transfer coefficient of oxygen in the oxygen transfer device with specific geometry. Comparatively, the smaller inlet oxygen concentration leads to the larger average oxygen mass transfer coefficient and the effects of inlet oxygen concentration become weaker with the increase of flow rate.
3) A mass transfer correlation for oxygen transport is obtained and the calculations of the correlation equation are all in agreement with the simulated results.

References

1. Schroer, C., Wedemeyer, O., Konys, J.: Gas/liquid oxygen-transfer to flowing lead alloys. Nucl. Eng. Des. **241**(5), 1310–1318 (2011)
2. Marino, A., Lim, J., Keijers, S., et al.: A mass transfer correlation for packed bed of lead oxide spheres in flowing lead–bismuth eutectic at high Péclet numbers. Int. J. Heat Mass Transf. **80**, 737–747 (2015)
3. Chen, Y., Chen, H., Zhang, J.: Numerical investigation on enhancement of oxygen transfer by forced convection in liquid lead–bismuth eutectic system. Int. J. Heat Mass Transf. **50**(11–12), 2139–2147 (2007)
4. Müller, G., Heinzel, A., Schumacher, G., et al.: Control of oxygen concentration in liquid lead and lead-bismuth. J. Nucl. Mater. **321**(2–3), 256–262 (2003)
5. Aerts, A., Gavrilov, S., Manfredi, G., et al.: Oxygen-iron interaction in liquid lead-bismuth eutectic alloy. Phys. Chem. Chem. Phys. **18**(29), 19526 (2016)
6. Brissonneau, L., Beauchamp, F., Morier, O., et al.: Oxygen control systems and impurity purification in LBE: learning from DEMETRA project. J. Nucl. Mater. **415**, 348–360 (2011)

7. ANSYS. ANSYS fluent theory guide (2016)
8. OECD, Handbook on Lead-bismuth Eutectic Alloy and Lead Properties, Materials Compatibility, Thermalhydraulics and Technologies. Organisation for Economic Co-Operation and Development (2015)
9. Wang, C., Zhang, Y., Zhang, D., et al.: Numerical study of oxygen transport characteristics in lead-bismuth eutectic for gas-phase oxygen control. Nucl. Eng. Technol. **53**, 2221–2228 (2021)

Research of Steady-State Heat Transfer Performance of Heat Pipe Inside Mobile Heat Pipe Reactor

Huaichang Lu[1,2,3], Tao Zhou[1,2,3]([✉]), Wenbin Liu[1,2,3], Shang Mao[1,2,3], Dong Wei[1,2,3], Yao Yao[1,2,3], and Tianyu Gao[1,2,3]

[1] Department of Nuclear Science and Technology, School of Energy and Environment, Southeast University, Nanjing 210096, China
`101012636@seu.edu.cn`
[2] Institute of Nuclear Thermal-Hydraulic Safety and Standardization, Beijing, China
[3] National Engineering Research Center of Power Generation Control and Safety, Nanjing 210096, China

Abstract. High-temperature heat pipe is an important element in a mobile heat pipe reactor, and the study of the steady-state heat transfer performance of the heat pipe is of great value to the design and safe application of the heat pipe. Based on COMSOL software, a three-dimensional heat pipe model is established to study the effects of the input power of the evaporative section of the heat pipe and the horizontal acceleration of the heat pipe due to its movement on the heat transfer performance of the potassium heat pipe in steady-state operation. The results show that the overall temperature of the outer wall surface of the heat pipe and the axial temperature variation of the center of the heat pipe are less affected by the horizontal acceleration and more affected by the input thermal power within the study range; the thermal resistance of the heat pipe decreases with the increase of the input power of the evaporation section of the heat pipe, and shows a trend of decreasing and then increasing with the increase of the horizontal acceleration.

Keywords: Potassium heat pipe · Heating power · Horizontal acceleration · Thermal resistance

1 Introduction

China's total energy consumption is growing, and although the rate of energy consumption growth is decreasing year by year, the overall total energy consumption [1] is still high. China plans to achieve carbon peaking by 2030 and carbon neutrality by 2060. According to Lin Boqiang [2], China's current carbon emissions are mainly concentrated in the power generation, industrial and transportation sectors, and deep decarbonization of the power sector is the key to achieving China's carbon neutrality goal. Nuclear power, as the second largest source of low-carbon electricity in the world after hydropower, will be the optimal choice to solve the problem of fossil energy depletion in the future. Heat

pipe reactors are an emerging type of reactor with the advantages of compact structure, high inherent safety, and modularity. Heat pipe reactors were initially proposed for application in space nuclear reactors [3], and heat pipe cooled reactors [4] use a solid state reactor design concept that directly exports heat from the core through high temperature heat pipes and are more suitable as a technology option for small nuclear power sources. Heat pipe reactors do not contain conventional reactor equipment such as main cooling circuits, circulation pumps, and various valves. The system design is extremely simplified compared to conventional reactors, and these features make heat pipe reactors suitable as a technology option for small mobile reactors. The mobile small reactor focus is located in islands, plateaus, polar regions and other special environments or isolated island power supply applications under major disasters, and has a strong national defense and civilian significance.

The change of conditions such as horizontal acceleration due to the movement of the heat pipe small stack has a certain effect on the heat transfer performance of the heat pipe. Tian Z X [5] et al. used a thermal resistance network model and wrote a program to study the heat transfer characteristics of a high-temperature potassium heat pipe with a liquid-absorbing core in steady-state operation, and obtained the effect of the inclination angle on the heat transfer performance of the heat pipe at different heating powers. Liu S Y [6] et al. experimentally investigated the comparison of the steady-state operating performance of loop heat pipes in an accelerated environment to provide some guidance on the design of loop heat pipes for cooling airborne electronic equipment. Xiao Lv [7] et al. studied the temperature oscillations of a double-compensated cavity loop heat pipe under acceleration conditions, and analyzed and discussed the effects of different loading modes, thermal loads, acceleration directions and amplitudes, and other control parameters on the loop temperature oscillations. Hao S [8] et al. experimentally studied the thermal behavior of a horizontal high temperature heat pipe under motion conditions. The current studies focus on the heat transfer performance during conventional heat pipe start-up and heat pipe steady-state operation, and there are still relatively few studies on the heat transfer performance of heat pipes in mobile heat pipe reactors. Therefore, the study of heat transfer performance of heat pipes in mobile heat pipe reactors under different operating conditions can provide a certain theoretical basis for the design and application of mobile heat pipe reactors.

2   Research Object

2.1   Geometric Model

The heat pipe used is shown in Fig. 1.

It can be seen from the Fig. 1 that the heat pipe from below to above is the evaporation section, adiabatic section and condensing section.
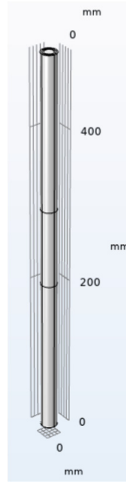
Fig. 1. Heat pipe structure

2.2 Calculation Parameters

Heat pipe structure parameters and calculation parameters are shown in Table 1.

Table 1. Calculated parameters of heat pipe

Name	Unit	Quantity
Working medium in heat pipe	-	Potassium
Evaporation section length	mm	200
Condensation section length	mm	200
Adiabatic section length	mm	100
Heat pipe outer diameter	mm	20
Pipe wall thickness	mm	2
Wick thickness	mm	2
Convective heat transfer coefficient	W/(m^2·K)	300
Environmental temperature	K	300
Heating power of evaporation section	W	150/250/350/450
Pipe wall material	-	Haynes 230

2.3 Grid Irrelevance Verification

In the simulation process, in order to ensure the accuracy of the model and at the same time improve the efficiency of the calculation, the mesh will be verified for irrelevance.

Under the premise of ensuring the mesh quality, four different cell size meshes are used to divide the model, and the mesh numbers are 151107, 222363, 277810, and 378839, respectively. the results of the axial temperature distribution at the center of the heat pipe in steady state with the four mesh numbers are shown in Fig. 2.
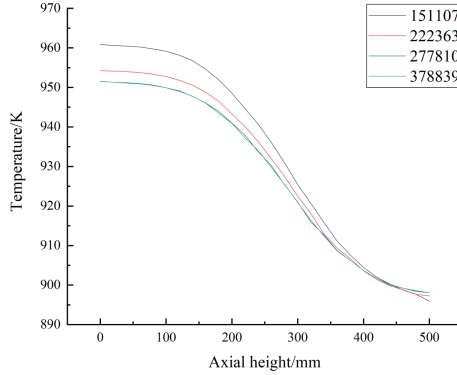
Fig. 2. Axial temperature distribution in the center of the heat pipe at steady state

From Fig. 2, it can be seen that the change of axial temperature distribution in the center of heat pipe tends to be stable with the increase of the number of grids, and the temperature difference of evaporating section of heat pipe is larger when the number of grids is 151107 and 222363, while the trend of axial temperature distribution in the center of heat pipe is almost the same when the number of grids is 277810 and 378839. Within the margin of error, 277810 meshes are appropriate considering that too many meshes will reduce the calculation efficiency.

3 Calculation Formula

(1) **Thermal conductivity model of pipe wall**

$$\rho C_p u \cdot \nabla T + \nabla \cdot q = Q \tag{1}$$

$$q = -k \nabla T \tag{2}$$

ρ is the density, kg/m^3; C_p is the constant pressure heat capacity, J/(kg·K); K is the effective thermal conductivity, W/(m·K). q_v is the heat source, W/m^3.

(2) **Thermal conductivity equation of liquid-absorbing core**

$$\rho_f C_{p,f} u \cdot \nabla T + \nabla \cdot q = Q \tag{3}$$

$$q = -k_{eff} \nabla T \tag{4}$$

$(\rho C_p)_{eff}$ is the effective volumetric heat capacity at constant pressure, J/(m^3·K); k_{eff} is the effective thermal conductivity, W/(m-K).

(3) **Vapor flow model**

$$\rho(u \cdot \nabla)u = \nabla \cdot [-\rho I + K] + F \tag{5}$$

$$\rho \nabla \cdot u = 0 \tag{6}$$

$$K = \mu\left(\nabla u + (\nabla u)^T\right) \tag{7}$$

∇ is the gradient calculation symbol; μ is the dynamic viscosity, Pa-s.

(4) **Flow model of liquid-absorbing core**

For porous medium flow, the BRINKMAN equation was used as a coupling calculation in the study

$$0 = \nabla \cdot [-\rho 2I + K] - \left(\mu\kappa^{-1} + \beta\rho|u_2| + \frac{Q_m}{\varepsilon_p^2}\right)u_2 + F \tag{8}$$

$$\rho\nabla \cdot u_2 = Q_m \tag{9}$$

where, ρ is the liquid density, kg/m^3; Q_m is the flow rate, kg/s; g is the acceleration of gravity, m/s^2; ∇ is the Laplace operator.

(5) **Equivalent thermal resistance of heat pipe**

The heat pipe heat transfer characteristics are studied using the form of calculating the overall thermal resistance of the heat pipe with the following expressions.

$$R_{sum} = \frac{T_{e,ave} - T_{c,ave}}{Q_{in}} \tag{10}$$

R_{sum} is the overall thermal resistance of the gravity heat pipe, W/K; $T_{e,ave}$ is the average temperature of the wall of the evaporating section of the heat pipe, K; $T_{c,ave}$ is the average temperature of the wall of the condensing section of the heat pipe, K; Q_{in} is the thermal power input to the evaporating section of the heat pipe, W.

4 Results and Discussion

4.1 Effect of Horizontal Acceleration on Heat Pipe Temperature

(1) **Surface temperature of outer wall**

The temperature distribution on the outer wall surface of the heat pipe when the horizontal acceleration is changed under the heat pipe evaporation section input thermal power of 450 W is shown in Fig. 3.

From Fig. 3, it can be seen that the temperature distribution of the outer wall surface of the heat pipe under different horizontal acceleration conditions has basically the same trend, and the heat pipe is in a stable working condition. The temperature change of the
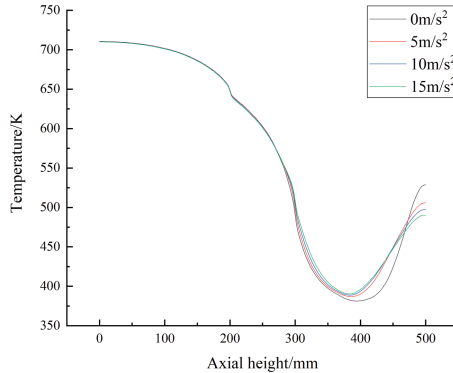
Fig. 3. Temperature distribution on the outer wall surface of the heat pipe

outer wall surface of the heat pipe shows a trend of decreasing first and then increasing. In the evaporation and adiabatic sections of the heat pipe, the change of horizontal acceleration almost does not affect the temperature of the outer wall surface, and the temperature of the outer wall surface gradually decreases along the axial direction. At the end of the condensing section of the heat pipe, the temperature of the outer wall surface increases, while the temperature increase at the end of the condensing section decreases with the increase of the horizontal acceleration, and the uniformity of the heat pipe increases. This is because with the operation of the heat pipe, the evaporating section of the heat pipe is constantly fed with thermal power, and a large amount of superheated steam gathers at the top of the steam chamber of the heat pipe, and the steam entering the suction core condenses into small liquid beads or liquid film adsorbed on the wall of the top of the heat pipe and exothermic. In addition, because the liquid beads or liquid film by gravity decline, the thickness of the liquid film from the top of the heat pipe to the bottom gradually increase, the upper part is thinner, the lower part is thicker, there is a difference in thermal resistance, making the temperature of the outer wall surface appears to rise. And with the increase of horizontal acceleration, it is equivalent to the heat pipe working under a certain inclination angle, which makes the instability of liquid phase workpiece flow inside the suction core reduced, thus offsetting part of the temperature increase of the outer wall surface.

(2) **Central axial temperature**

The axial temperature distribution at the center of the heat pipe when the horizontal acceleration is changed under the input thermal power of 450 W in the evaporation section of the heat pipe is shown in Fig. 4.

From Fig. 4, it can be seen that the trend of axial temperature distribution in the center of the heat pipe under different horizontal acceleration conditions is basically the same, and the heat pipe is in steady state. At this time, the heat pipe shows good homogeneity in the evaporation section, the adiabatic section and the beginning of the condensation section, and the temperature decreases faster at the end of the condensation section of the heat pipe, and finally stabilizes. With the increase of horizontal acceleration, the
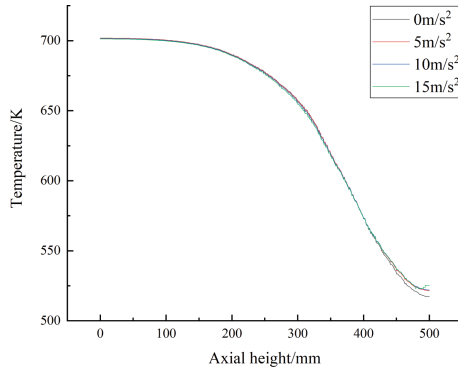
Fig. 4. Axial temperature distribution in the center of the heat pipe

temperature at the end of the condensing section increases, which indicates that the heat transfer performance of the heat pipe is improved.

4.2 Effect of Horizontal Acceleration on Heat Transfer Performance of Heat Pipes

In order to compare the heat transfer capability of potassium heat pipe easily, the equivalent thermal resistance is used to describe the heat transfer performance of the heat pipe, which can be given by Eq. (10). The trend of the equivalent thermal resistance of the heat pipe with increasing horizontal acceleration is given in Fig. 5.
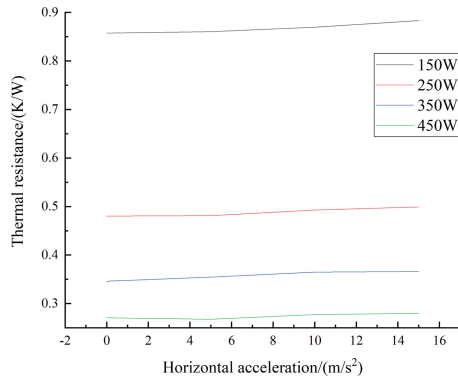
Fig. 5. Variation of equivalent thermal resistance of heat pipe with horizontal acceleration

From Fig. 5, it can be seen that the equivalent thermal resistance of the heat pipe under different input thermal power has basically the same trend, and the equivalent thermal resistance shows a trend of first decreasing and then slightly increasing with the increase of horizontal acceleration. Under the same horizontal acceleration, the equivalent thermal resistance of the heat pipe decreases with the increase of the input thermal power.

The minimum thermal resistance of the heat pipe occurs between 5 m/s^2 and 10 m/s^2 acceleration. When the heat pipe is in a smaller horizontal acceleration condition, the heat pipe moves with the heat pipe reactor, the effect of gravitational acceleration is greater than the effect of horizontal acceleration, and the heat pipe as a whole shows the form of vertical heat transfer; when the horizontal acceleration exceeds the gravitational acceleration, the effect of gravitational acceleration on the heat transfer of the mass in the heat pipe decreases, and the heat pipe gradually changes from vertical heat transfer to horizontal heat transfer, the equivalent thermal resistance increases, and the heat transfer performance of the heat pipe decreases.

4.3 Influence of Input Thermal Power on Heat Pipe Temperature

(1) **Surface temperature of outer wall**

The distribution of the temperature on the outer wall surface of the heat pipe when the input thermal power of the evaporating section of the heat pipe is changed under no horizontal acceleration is shown in Fig. 6.
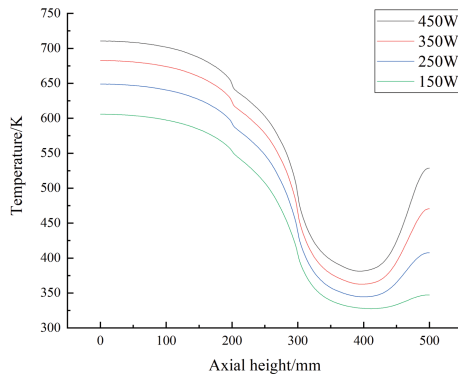
Fig. 6. Temperature distribution on the outer wall surface of the heat pipe

From Fig. 6, it can be seen that the temperature distribution of the outer wall surface of the heat pipe under different input thermal power conditions is basically the same, showing a trend of first decreasing and then increasing. The evaporation and adiabatic sections of the heat pipe show good temperature homogeneity, and the end of the condensing section also shows the phenomenon of temperature increase, and the degree of temperature increase increases with the increase of the input thermal power.

(2) **Central axial temperature**

The distribution of the axial temperature at the center of the heat pipe when the input thermal power of the evaporating section of the heat pipe is changed without horizontal acceleration is shown in Fig. 7.
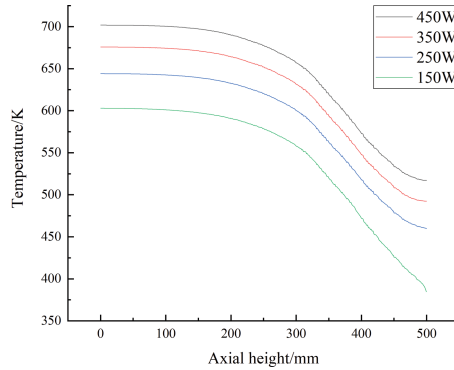
Fig. 7. Axial temperature distribution in the center of the heat pipe

From Fig. 7, it can be seen that the trend of axial temperature change in the center of the heat pipe under different input thermal power conditions is basically the same. The heat pipe is in steady-state operation, and the axial temperature difference at the center of the heat pipe decreases with the increase of the input thermal power, indicating that the overall heat transfer performance of the heat pipe can be improved by increasing the input thermal power within a certain range.

4.4 Influence of Input Thermal Power on Heat Transfer Performance of Heat Pipe

Figure 8 gives the trend of the equivalent thermal resistance of the heat pipe with increasing heating power.
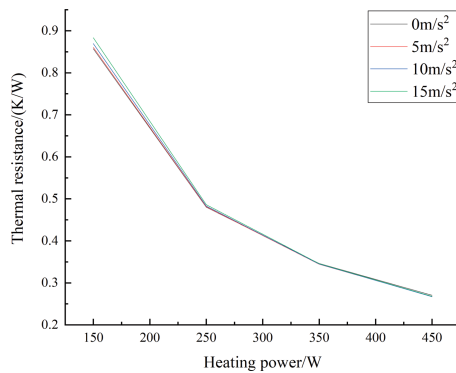
Fig. 8. Variation of equivalent thermal resistance of heat pipe with heating power

From Fig 8, it can be seen that the trend of equivalent thermal resistance of heat pipe under different horizontal acceleration conditions is basically the same. The equivalent thermal resistance shows a decreasing trend with the increase of heating power. In the

studied heating power range, when the heating power increases, the evaporation in the heat pipe evaporation section intensifies, the thermal resistance decreases, and the overall heat transfer performance of the heat pipe is improved. With the increase of heating power, the degree of thermal resistance affected by heating power gradually decreases.

5   Conclusion

Based on the multi-physics field simulation software COMSOL Multiphysics, the heat transfer characteristics of the steady-state operation of heat pipes in a mobile heat pipe stack are investigated, and the effects of horizontal acceleration and variation of input thermal power on the heat pipe center temperature, wall temperature and equivalent thermal resistance are obtained.

(1) The overall temperature variation of the outer wall surface of the heat pipe is less influenced by horizontal acceleration and more influenced by the input thermal power in the study range. The wall surface temperature increases with the increase of the input thermal power. The temperature increase existing at the end of the condensing section is suppressed by the increase in acceleration and the decrease in input thermal power.

(2) The axial temperature variation at the center of the heat pipe is less affected by the horizontal acceleration and more affected by the input thermal power in the studied range. The wall surface temperature increases with the increase of input thermal power.

(3) The equivalent thermal resistance of the heat pipe shows a trend of decreasing and then increasing with the increase of horizontal acceleration in the study range, and decreases with the increase of input thermal power, and the effect of the change of acceleration on the thermal resistance becomes smaller with the increase of input thermal power.

References

1. Jiang, H.L., Liu, Y.Q., Feng, Y.M., Zhou, B.Z., Li, Y.X.: Analysis of power generation technology trends in the context of carbon peaking and carbon neutrality in the 14th five-year plan period. Power Gener. Technol. **43**(01), 54–64 (2022). (in Chinese)
2. Lin, B.Q.: China's difficulties and the way forward towards carbon neutrality. New Finan. **07**, 26–29 (2021). (in Chinese)
3. Yan, B.H., Wang, C., Li, L.G.: The technology of micro heat pipe cooled reactor: a review. Ann. Nucl. Energy **135**, 106948 (2020)

4. Grover, G.M., Cotter, T.P., Erickson, G.F.: Structures of very high thermal conductance. J. Appl. Phys. **35**(10), 3072–3072 (1964)
5. Tian, Z.X., Liu, Y., Wang, C.L., Su, G.H., Tian, W.X., Qiu, S.Z.: Study on heat transfer characteristics of high-temperature potassium heat pipe in steady-state operation. At. Energy Sci. Technol. **54**(10), 1771–1778 (2020). (in Chinese)
6. Liu, S.Y., Xie, Y.Q., Su, J., Zhang, H.X., Li, G.G.: Comparative study of steady-state operating performance of loop heat pipe in accelerated environment. J. Aeronaut. 1–12, 28 June 2022. (in Chinese)
7. Lv, X., Xie, Y., Zhang, H., et al.: Temperature oscillation of a dual compensation chamber loop heat pipe under acceleration conditions. Appl. Therm. Eng. **198**(3), 117450 (2021)
8. Sun, H., Liu, X., Liao, H., et al.: Experiment study on thermal behavior of a horizontal high-temperature heat pipe under motion conditions. Ann. Nucl. Energy **165**, 108760 (2022)

Direct Contact Condensation Characteristics of Steam Injection into Cold-Water Pipe Under Rolling Condition

Zhiwei Wang[1], Yanping He[1(✉)], Zhongdi Duan[1(✉)], Chao Huang[1], and Shiwen Liu[2]

[1] State Key Laboratory of Ocean Engineering, Shanghai Jiao Tong University, Shanghai, China
{hyp110,duanzhongdi}@sjtu.edu.cn
[2] Science and Technology on Reactor System Design Technology Laboratory, Nuclear Power Institute of China, Chengdu, China

Abstract. Direct contact condensation (DCC) is widely occurred in nuclear power systems and leads to undesired phenomena such as condensation-induced water hammer. For ocean nuclear power ships, DCC is inevitable in the passive heat removal system and influenced by sea conditions. In this paper, the characteristics of DCC under rolling conditions are analyzed. The numerical model of DCC is established based on computational fluid dynamics approach. The VOF model, SST k–ω turbulence model and the additional inertia force model are incorporated to describe the liquid-gas two-phase flow under the rolling motion. The condensation model based on surface renewal theory (SRT) is used to simulate steam-water DCC phenomenon. The simulation results are compared with the experimental data and show reasonable agreement. The effects of rolling motion on DCC for steam injection into a horizontal pipe filled with cold water are numerically investigated. The results show that the additional inertial forces and the average condensation rate increase with the increase of the rolling angle and frequency. The reverse flow of the seawater induced by rolling motion leads to the accumulation of the steam at the lower part of the pipe, resulting in a large pressure pulse. With the increase of rolling angle and frequency, the pressure pulse induced by DCC increases.

Keywords: Ocean nuclear power ships · Direct contact condensation · Rolling motion · Average condensation rate · Pressure pulse

1 Introduction

For the ocean nuclear power ships, the direct contact condensation (DCC) phenomenon is inevitably occurred due to the efficient heat transfer characteristics [1, 2]. In addition, when the nuclear power system is working in the marine environment, it will inevitably be affected by the ocean environment and produce a series of motions, such as heaving, pitching and rolling [3, 4]. These motions will affect the two-phase flow and heat transfer characteristics in the cooling systems [5]. Therefore, the research of the transient

behaviors of the DCC phenomenon under ocean conditions is of great significance for the application of the ocean nuclear power ships.

At present, many experimental and numerical simulation researches have been conducted to focus on the DCC under static conditions [6]. Prasser et al. (2008) experimentally observed the DCC events induced by steam-water counterflow in the horizontal pipe, and focused on the number of pressure pulse and formation of steam slug [7]. Chong et al. (2020) experimentally studied the DCC phenomenon induced by steam discharged into a horizontal pipe and focused on the condensation induced water hammer induced phenomenon by the DCC [8]. Sun et al. (2020) experimentally observed the DCC phenomenon in the passive heat removal system for offshore application and analyzed the formation mechanism [9]. Wang et al. (2022) simulated the DCC phenomenon in the horizontal pipe by the ANSYS FLUENT software, and captured the formation process of DCC phenomenon by the VOF method [10].

The typical motion of the floating structures under ocean conditions, such as rolling motion, will generate various additional forces and further affect the coolant flow and heat and mass transfer. Peng et al. (2020) numerically studied the effect of rolling motion on the void distribution of subcooled flow boiling. The results indicated that the void fraction distribution is sensitive to the rolling period [11]. Wang et al. (2022) numerically investigated the flow characteristics of gas-liquid two-phase flow under rolling condition. They found that the void fraction presents periodical variation and will induce complex secondary-flow phenomenon [12]. Chen et al. (2022) numerically studied the dominant oscillation frequency of the unstable steam jet under rolling condition and indicated that the Coriolis force has a great influence on the dominant oscillation frequency [13]. Therefore, the effects of rolling motion on boiling two-phase flow and gas-liquid two-phase flow have attracted enough attention from relevant researchers.

Based on the literature review, the present study aims to study the transient behaviors of the direct contact condensation (DCC) phenomenon under rolling conditions. The DCC numerical model frame was established based on the volume of fluid (VOF) model, the condensation model and the rolling motion model. The additional inertial forces, formation process, average condensation rate, and pressure behaviors were obtained to study the effects of rolling motion on the DCC phenomenon.

2   Mathematic Model

2.1   Two-Phase Flow Mode

The direct contact condensation usually occurs at the steam-subcooled water interface, so obtaining a clear steam-subcooled water interface is the key to the numerical simulation. Previous studies indicated that the VOF model has significant advantages in tracking the gas-liquid interface [14]. Hence, the VOF model is used to describe the steam-subcooled water two-phase flow in the present study. The tracking of the steam-subcooled water interface is by solving the continuity equation for the volume fraction of each phase. The conservation of mass as follow:

$$\frac{\partial(\alpha_v \rho_v)}{\partial t} + \nabla \cdot \left(\alpha_v \rho_v \overrightarrow{u}\right) = S_m \tag{1}$$

There exists a closed equation for the volume fraction of gas phase and liquid phase:

$$\alpha_v + \alpha_l = 1 \tag{2}$$

In the VOF model, the gas and liquid phase share a set of momentum equations. The surface tension and the additional inertial forces are added to the momentum equation in the form of source terms. The momentum equation as follow:

$$\frac{\partial\left(\rho\overrightarrow{u}\right)}{\partial t} + \nabla \cdot \left(\rho\overrightarrow{u}\,\overrightarrow{u}\right) = -\nabla P + \nabla\left[\mu\left(\nabla\overrightarrow{u} + \left(\nabla\overrightarrow{u}\right)^{T}\right)\right] + \rho\overrightarrow{g} + \overrightarrow{F}_{st} + \overrightarrow{F}_{roll} \tag{3}$$

Similarly, the gas and liquid phase share a set of momentum equation, as follow:

$$\frac{\partial}{\partial t}(\rho E) + \nabla \cdot (\vec{v}(\rho E + P)) = \nabla\left(k_{eff}\nabla T - \sum_{j}h_j\vec{J}_j + \left(\overline{\overline{\tau}}_{eff} \cdot \vec{v}\right)\right) + Q_m \tag{4}$$

where: the Q_m represents the energy source term and is modeled by the UDF, the specific form refers to the Sect. 2.2.

In the present study, the SST $k - \omega$ turbulence model is used to compute the turbulence characteristics induced by the rolling motion [15]. The governing equations as follow:

The equation of turbulent kinetic energy:

$$\frac{\partial(\rho k)}{\partial t} + \frac{\partial}{\partial x_j}\left(\rho k u_j\right) = \frac{\partial}{\partial x_j}\left[\Gamma_k\frac{\partial k}{\partial x_j}\right] + G_k - Y_k + S_k \tag{5}$$

The equation of specific dissipation rate:

$$\frac{\partial(\rho\omega)}{\partial t} + \frac{\partial}{\partial x_j}\left(\rho\omega u_j\right) = \frac{\partial}{\partial x_j}\left[\Gamma_\omega\frac{\partial\omega}{\partial x_j}\right] + G_\omega - Y_\omega + D_\omega + S_\omega \tag{6}$$

where: the G_k is the turbulent kinetic energy term due to velocity gradient, Γ_k and Γ_ω represent the convective term of k and ω, Y_k and Y_ω represent the effective diffusion term of k and ω induced by turbulence, Y_k represents the cross convective term. S_k and S_ω represent the user-defined source terms.

2.2 Condensation Phase Change Model

During the process of condensation induced water hammer, only the condensation phenomenon occurs. It is assumed that condensation occurs only at the steam-subcooled water interface. The heat and mass transfer during the condensation is calculated by the UDF, and then added to the momentum and energy conservation equation [16]. The energy source term represents the heat transfer from the steam phase to the water phase at the interface, which is expressed as:

$$Q_m = HTC \cdot a_{int} \cdot (T_{sat} - T_l) \tag{7}$$

where: the *HTC* is the heat transfer coefficient, a_{int} is the interfacial area density, T_{sat} is the saturated temperature, T_l is the subcooled water temperature.

For the VOF model, the absolute value of volume fraction gradient is defined as the interfacial area density [17], which is expressed as:

$$a_{int} = |\nabla \alpha_l| = \frac{\partial \alpha_l}{\partial n} \tag{8}$$

where: α_l is the liquid volume fraction, n is the unit vectors.

Mass transfer source can be obtained on the basis of the energy transfer source, which is expressed as:

$$S_m = \frac{Q_m}{h_{lv}} \tag{9}$$

where: h_{lv} is the latent heat with a constant value of 1026 kJ/ kg

2.3 Rolling Motion Model

In the present study, the additional inertial force method is utilized to calculate the effects of rolling motion. Figure 1 shows the relationship between the non-inertial frame and inertial frame [18]. The additional inertial forces mainly include the centripetal force (F_{ce}), tangential force (F_{ta}), and Coriolis force (F_{co}).
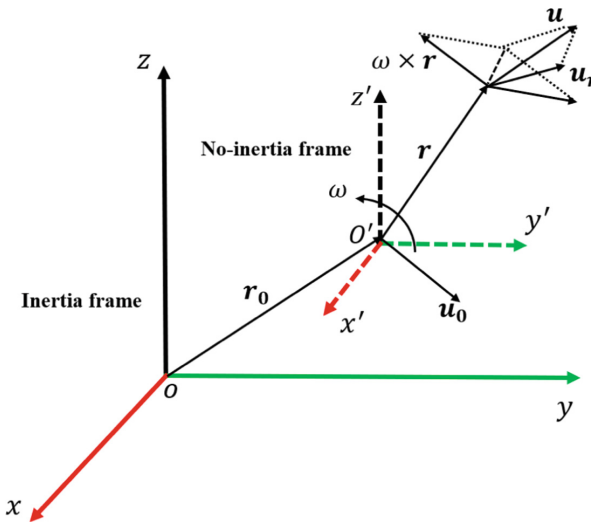
Fig. 1. Relationship between the non-inertial frame and the inertial frame.

The additional inertial force method involves two reference frames, an inertial frame and a non-inertial frame. The geometric model moves relative to the inertial frame, and

we only considered the rolling motion in the YOZ plane. Hence, the equations of rolling motion are as follows [30]:

$$\theta(t) = \theta_m \sin\left(\frac{2\pi t}{T}\right)\vec{i} \tag{10}$$

$$\omega(t) = \frac{2\pi}{T}\theta_m \cos\left(\frac{2\pi t}{T}\right)\vec{i} \tag{11}$$

$$\varepsilon(t) = -\frac{4\pi^2}{T^2}\theta_m \sin\left(\frac{2\pi t}{T}\right)\vec{i} \tag{12}$$

In conclusion, the additional inertial force can be calculated as follows:

$$\vec{F}_{roll} = -\rho(\vec{g} + \vec{\varepsilon}(t) \times \vec{r} + \vec{\omega}(t) \times (\vec{\omega}(t) \times \vec{r}) + 2\vec{\omega}(t) \times \vec{u}_r) \tag{13}$$

2.4 Defined Geometry and Mesh Generation

For marine floating structures, the nuclear reactor is usually arranged in the reactor room. The DCC events mainly occurs in the upper horizontal pipe, as depicted in Fig. 2 (a). In addition, the length and inner diameter of the geometric model is 2.0 m and 0.1 m respectively [19]. In order to ensure the calculation convergence, the structured grid was generated in the ANSYS ICEM software, and the boundary layer was densified, as shown in Fig. 2 (b).

(a) physical model

(b) structured mesh
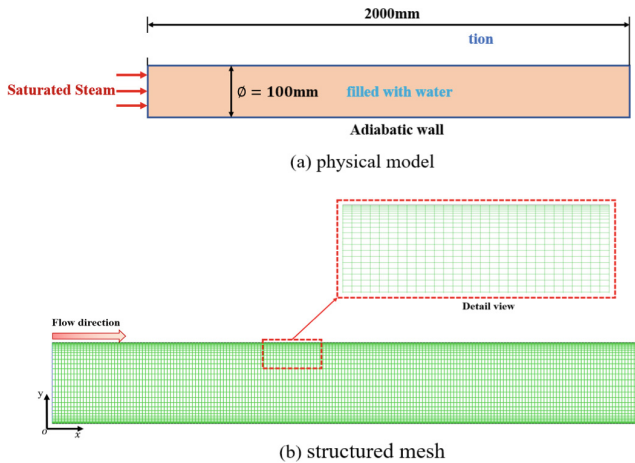
Fig. 2. Determination of geometric model and mesh generated

In this paper, the commercial CFD software Ansys Fluent 2020 has been utilized to conduct the numerical simulation. The numerical simulations adopt the pressure-based solver. The pressure-velocity coupling scheme adopts the pressure-implicit with splitting of operators (PISO). The QUICK discretization scheme is applied to the momentum and energy equations [20]. Geo-Reconstruct scheme is applied to the spatial discretization for volume fraction.

3   Results and Discussion

3.1   Mesh Independence Test

The mesh independence test was conducted with three different mesh sizes in the present study. The minimum size of the three meshes were selected 1 mm, 0.5 mm and 0.25 mm, respectively. Then, the temperature evolution and the variation of liquid volume fraction under different mesh sizes were analyzed. As depicted in Fig. 3 (a), with the decrease of the minimum size, the trend of the temperature evolution is gradually consistent. The mesh sizes also affect the variation of the liquid volume fraction. With the mesh size decreased from 0.5 mm to 0.25 mm, the variation trend of the liquid volume fraction is gradually consistent, as shown in Fig. 3 (b). Therefore, the subsequent numerical simulations are based on the mesh with the minimum size 0.5 mm.

(a) Temperature evolution   (b) Liquid volume fraction evolution
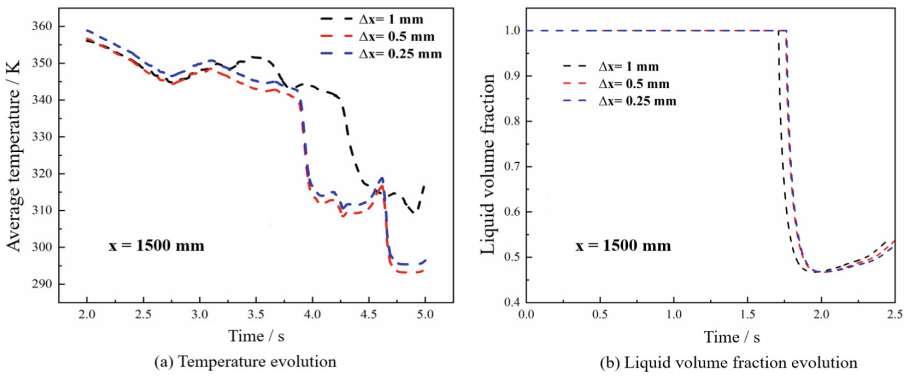
Fig. 3. The temperature evolution and variation of liquid volume fraction under different mesh sizes

3.2   Validation of DCC Numerical Model

We conducted the verification of the UDF by comparing the PMK-2 experimental results. The geometric model and boundary conditions of the PMK-2 experiment is shown in Fig. 4 (a). We selected the monitoring points T4 to compare the temperature evolution between the numerical simulation and experiment. Figure 4 (b) shows the comparison of the temperature evolution in T4 between the numerical simulation and experiment. The results indicated that the temperature step time obtained by the numerical simulation is basically consistent with the experiment. In summary, the present condensation model can effectively simulate the condensation behaviors and provide a guarantee for the subsequent numerical simulation of the DCC events.

(a) PMK-2 experimental geometric model

(b) Comparison of temperature evolution
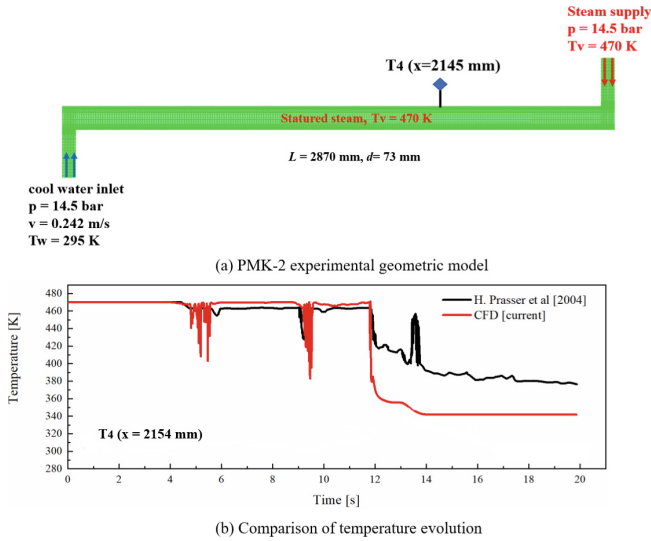
Fig. 4. PMK-2 experimental facility and temperature validation

3.3 DCC Process Under Rolling Conditions

Figure 5 shows the formation process of the CIWH phenomenon under rolling condition. Similarly, the stratified-wave flow is formed in the horizontal pipe at the early stage. From 0 to T/4, the additional inertial force accelerates the reverse flow of the subcooled water. During the process of the reverse flow, the saturated steam is continuously squeezed down the pipe until the isolated steam bubble is formed. From T/4 to T/2, the isolated steam bubble is surrounded by the subcooled water, and the steam bubble collapse quickly due to the DCC. At T/2, the condensation induced water hammer occurs. After the CIWH event, the horizontal pipe is filled with water and has a larger subcooling. Hence, from T/2 to T, the saturated steam flowing into the pipe is rapidly condensed, and the formation mechanism of the CIWH disappears. With the temperature field in the horizontal pipe increases, the saturated steam can flow into again, which in turn triggers a new CIWH event. In summary, the formation mechanism of the CIWH under static and rolling condition is basically the same. While, it is worth noting that the rolling motion complicates the reverse flow of the subcooled water and the DCC phenomenon.

3.4 Effect of Rolling Motion on Condensation Rate

The condensation rate is a key parameter to describe the DCC phenomenon. Thus, the effects of rolling motion on the condensation rate are numerically studied. The condensation rate is calculated by the UDF and recorded by the UDM function in the present study. As depicted in Fig. 6 (a) and (b), compared to the static condition, the average condensation rate under rolling conditions has a remarkable increase. The average condensation rate has a tendency to decrease as the rolling period increased, and has a tendency to increase with the rolling angle increased. This is mainly due to the larger
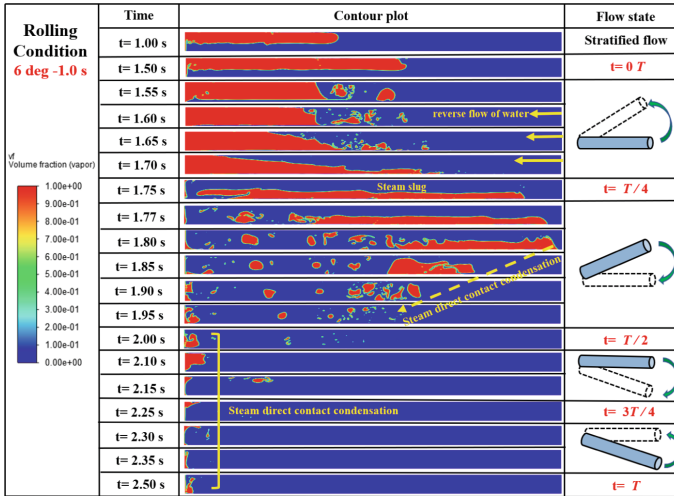
Fig. 5. The formation process of the direct contact condensation under rolling conditions.

rolling angle and high rolling frequency enhanced the contact area between the steam and subcooled water, which in turn improved the capacity of heat and mass transfer at the steam- subcooled water interface. In addition, the average condensation rate is proportional to the steam inlet velocity, as depicted in Fig. 6 (c) and (d). This is mainly due to the increase of the steam inlet velocity increased the amount of steam in the pipe, and then increased the average condensation rate.

3.5 Effect of Rolling Motion on Pressure Behaviors

Figure 7 shows the comparison of the pressure behaviors induced by the DCC events under static condition and rolling conditions. The main pressure behaviors observed in the time domain signals are as flows: (1) the pressure peak under rolling conditions is obviously greater than that under static condition. This is mainly due to the larger condensation rate and reverse flow of subcooled water under rolling condition aggravated the pressure peak. (2) the pressure behaviors under rolling conditions are more complex, which present periodic fluctuations after generating the violent pressure peak. This is mainly due to the rapid formation and collapse of the isolated steam bubbles in the early stage of the rolling motion. Then the subcooled water filled with the pipe, and the saturated steam is completely condensed at the pipe inlet due to the larger subcooling. Therefore, the periodic fluctuation is mainly induced by the subcooled water flow under the rolling motion. (3) the pressure peak decreased with the rolling period increase and increased with the rolling angle increase. This is mainly due to the high-frequency and large-angle rolling motions have aggravated the reverse flow of the subcooled water and increased the average condensation rate. In addition, we also found that as the steam inlet velocity is constant, the occurrence positions of the pressure peaks under different rolling parameters are consistent.
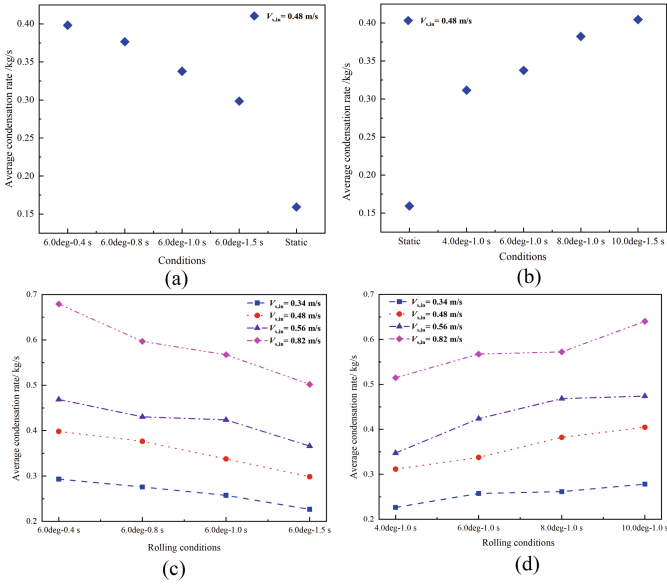
Fig. 6. Effects of rolling motion and steam inlet velocity on the average condensation rate
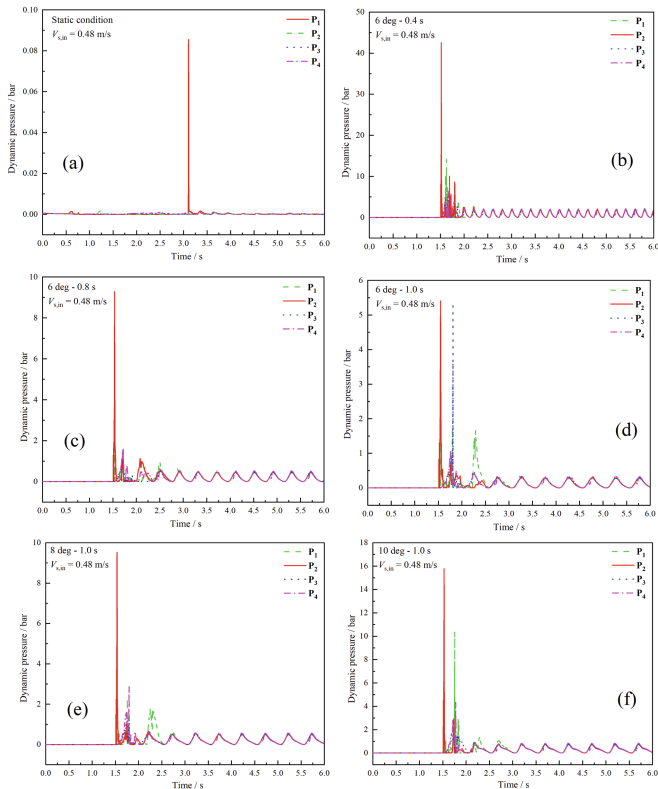
Fig.7. Comparison the pressure behaviors between the static condition and different rolling conditions

4   Conclusions

In this paper, the direct contact condensation (DCC) numerical model under rolling conditions is established based on the CFD code combined with UDFs. The effects of rolling motion on the transient behaviors of the DCC are investigated, including transient formation process, average condensation rate and pressure behaviors. The main conclusions are summarized as follows:

(1)   The rolling motion intensifies the reverse flow of subcooled water and causes the gas phase to be continuously squeezed moved down the pipe until an isolated steam slug is formed. The volume of the steam slug is significantly larger than that in the static condition, and the steam-subcooled water contact area is significantly increased.

(2)   The average condensation rate under rolling conditions is always larger than that in the static condition. This is mainly due to the large volume of isolated steam bubbles increasing the steam-subcooled water contact area. With the increase of the rolling angle and decrease of the rolling period, the average condensation rate increased.

(3)   Under rolling condition, the pressure behaviors are more complex and the pressure peak induced by the DCC is increased significantly. This is largely because the rolling motion intensifies the subcooled water reverse flow and enhances the condensation rate. Similar, the pressure peak by the DCC increases with the increasing rolling angle and rolling frequency. In addition, the location where the pressure peak occurred gradually moves towards the pipe outlet with the steam inlet velocity increased.

References

1. Zhang, Y.L., Buongiorno, J.: Safety analysis of a 300-MW (electric) offshore floating nuclear power plant in marine environment. Nucl. Tech. **203**, 129–145 (2018)
2. Sun, J.C., Ding, M.: Experimental research on reverse flow phenomenon in an equal-height-difference natural circulation system at low pressure. Nucl. Eng. Des. **370**, 110–121 (2021)
3. Chun, M.H., Yu, S.O.: A parametric study and a guide chart to avoid condensation induced water hammer in a horizontal pipe. Nucl. Eng. Des. **201**, 239–257 (2000)
4. Wang, C.Y., Peng, M.J., Xia, G.L.: Sensitivity analysis based on Morri's method of passive system performance under ocean conditions. Ann. Nucl. Energy. **137**, 107067 (2020)
5. Kim, G., Yoo, J., Lee, C.: Critical heat flux characteristics of flow boiling on a heater rod under inclined and rolling conditions. Int. J. Heat Mass Transf. **189**, 662–670 (2022)
6. Datta, P., Chakravarty, A., Ghosh, K.: Modeling and analysis of condensation induced water hammer. Num. Heat. Transf. Part A Appl. **74**, 975–982 (2018)

7. Prasser, H., Baranyai, G.: Water Hammer Tests, Condensation caused by Cold water Injection into Main Steam-Line of VVER-440-type PWR-Quick-Look Report (QLR), Technical report. 236–248 (2004)

8. Chong, D.T., Wang, L.T.: Characteristics of entrapped bubbles of periodic condensation-induced water hammer in a horizontal pipe. Int. J. Heat Mass Transf. **152**, 119–134 (2020)

9. Sun, J.C., Ding, M.: Experimental research on characteristics of condensation induced water hammer in natural circulation systems. J. Int. Commun. Heat Mass Transf. **114**, 104–112 (2020)

10. Wang, Z.W., He, Y.P., Duan, Z.D.: Numerical investigation on direct contact condensation-induced water hammer in passive natural circulation system for offshore applications. Num. Heat. Transf. Part A Appl. **63**(3), 974–985 (2022)

11. Peng, J., Chen, D.Q., Xu, J.J.: CFD simulation focusing on void distribution of subcooled flow boiling in circular tube under rolling condition. Int. J. Heat Mass Transf. **156**, 380–390 (2020)

12. Wang, Z.W., He, Y.P., Duan, Z.D.: Effects of rolling motion on transient flow behaviors of gas-liquid two-phase flow in horizontal pipes. Ocean Eng. **255**, 111–122 (2022)

13. Chen, W.X., Mo, Y.L., Wei, P.B.: Numerical study on dominant oscillation frequency of unstable steam jet under rolling condition. Ann. Nucl. Energy. **171**, 109–116 (2022)

14. Li, S.Q., Wang, P.: CFD based approach for modeling steam-water direct contact condensation in subcooled water flow in a tee junction. Prog. Nucl. Energy. **85**, 729–746 (2015)

15. Tan, H.B., Wen, N., Ding, Z.: Numerical study on heat and mass transfer characteristics in a randomly packed air-cooling tower for large-scale air separation systems. Int. J. Heat Mass Transf. **178**, 121–129 (2021)

16. Szijártó, R., Badillo, A., Prasser, H.: Condensation models for the water–steam interface and the volume of fluid method. Int. J. Multiphase Flow. **93**, 63–70 (2017)

17. Antham, R.: Condensation induced water hammer, Ph. D thesis, Chalmers University of Technology Gothenburg, Sweden (2016)

18. Liu, Z.P., Huang, D.S., Wang, C.L.: Flow and heat transfer analysis of lead–bismuth eutectic flowing in a tube under rolling conditions. Nucl. Eng. Des. **382**, 111–128 (2021)

19. Adumene, S., Islam, R., Amin, M.: Advances in nuclear power system design and fault-based condition monitoring towards safety of nuclear-powered ships. Ocean Eng. **251**, 111–126 (2022)

20. Li, M.Z., He, Y.P., Liu, Y.D.: Hydrodynamic simulation of multi-sized high concentration slurry transport in pipelines. Ocean. Eng. **163**, 691–705 (2018)

The Dynamic Response Analysis Method of Steel Containment in Floating Nuclear Power Plant

Weizhe Ren[1], Shuyou Zhang[1], Danrong Song[2], Meng Zhang[1(✉)], and Wei Wang[2]

[1] Yantai Research Institute of Harbin Engineering University, Yantai, Shandong, China
{renweizhe,zhangmeng}@hrbeu.edu.cn
[2] Nuclear Power Institute of China, Chengdu, Sichuan, China

Abstract. During the operation of the floating nuclear power plant, if the floating nuclear power plant is anchored near the shore for power generation, it may be impacted by runaway ships. If the impact causes damage to the tank of the floating nuclear power plant and water inflow, and even damage to the containment structure, it will seriously threaten the structural safety of the floating nuclear power plant and even threaten nuclear safety. This paper uses the explicit dynamics method to establish two models of dry/wet impact. It assumes that the 5000T container ship will laterally impact the reactor compartment of the floating nuclear power plant at a speed of 2 m/s, and the effects of the fluid domain (water and air domain) are ignored/counted in the calculation process. Then, comparing the effects of the above two models of dry/wet impact on the calculation duration, the damage and water ingress state of the floating nuclear power plant, the stress of the steel containment (including support). Studies have shown that if the relevant personnel do not need to understand the effect of water intrusion into the damaged cabin, the influence of water and air domain on the impact simulation results can be ignored, and the dry model can be directly used for calculation.

Keywords: Floating nuclear power plant · dry/wet impact · fluid-structure interactions

1 Introduction

Ship impact refers to the accident that ships contact and cause damage at sea or in navigable waters connected with the sea. It often leads to disastrous consequences, such as casualties, sinking of ships, and even environmental pollution. There are many reasons for ship impact accidents, and researchers in many countries are trying to find ways to avoid ship impact accidents [1]. At present, due to the influence of human factors, ship impact accidents cannot be completely eliminated. For floating nuclear power plants, it is more important to study the dynamic response of impact. Once a ship collides with a floating nuclear power plant, it will not only cause serious economic losses, but also cause more terrible harm to the environment that is difficult to evaluate [2, 3].

There are three main methods for impact analysis of ship structures: experimental method, simplified analytical method and numerical simulation method. The test

method includes actual accident investigation and real ship or ship model impact test. The results obtained by it are very intuitive and have self-evident guiding significance for the theoretical method [4, 5]. However, it often costs a lot of money. The accuracy of the simplified analytical method is relatively low. It simplifies a lot of ships in impact. Using the analytical method and some empirical data, it establishes the semi analytical/semi empirical mechanical equations of the hull or local ship structures to evaluate the impact characteristics of the hull. The advantage of numerical simulation method is that it can reproduce the real ship impact scene virtually. With the help of some finite element analysis software, various physical quantities in the process of ship impact can be output as results [6].

With the continuous upgrading and development of computer software and hardware technology and the increasing progress and maturity of finite element technology, explicit finite element numerical simulation technology has gradually received attention in the research of ship impact, and the research of ship structure impact based on full coupling technology has become gradually feasible. This paper mainly uses ANSYS-APDL software to establish the impact model, and uses the nonlinear explicit dynamics analysis software ANSYS workbench LS-DYNA to solve the analysis. Based on the comparison of dry/wet calculation results, the applicability of the two impact models is studied.

2   Modeling and Theoretical Basis

2.1   ANSYS APDL Model Parameter Settings

Container ships and floating nuclear power plants are modeled by 4-node shell181 shell element and beam188 beam element in classic ANSYS (after importing work bench LS-DYNA, it is automatically converted to LS-DYNA applicable element types: shell163 and beam161). The plate thickness is divided into 15, 18, 20, 22, 24, 26, 28, 30, etc. The grids at the bulbous bow of the container ship and the impact part on the port side of the floating nuclear power plant are densified (Figs. 1 and 2).

After the model is processed in classical ANSYS, three CBD files of stern containment, floating nuclear power plant (excluding stern containment) and container ship are written respectively, and then imported into workbench LS-DYNA module for pre impact model processing.

2.2   Contact Algorithms and Contact Types

The contact impact algorithm in LS-DYNA usually has the following methods:

(1)   Dynamic constraint method

As the contact algorithm first used in dyna program, the basic principle of dynamic constraint method is: before calculating and running each time step ΔT, retrieve those slave nodes that currently have no penetration with the master surface, and retrieve whether these slave nodes have penetration with the master surface at this time step.
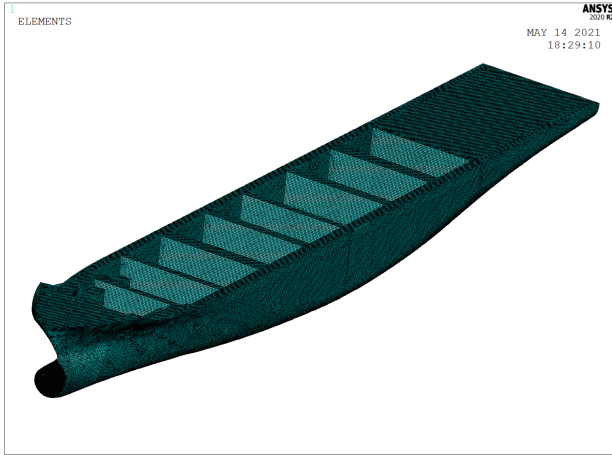
Fig. 1. Finite element model of container ship.
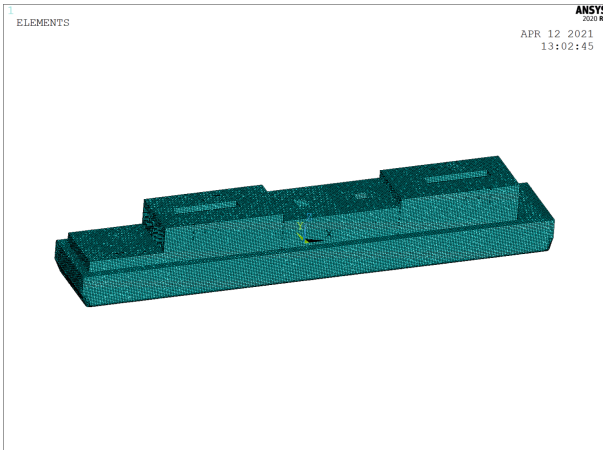
Fig. 2. Finite element model of floating nuclear power plant.

If there is penetration, reduce the time step ΔT. under the reduced time step, the slave node just contacts the main surface but does not penetrate the main surface. However, when the mesh division of the master surface is fine, some nodes on the master surface can penetrate the slave surface without constraints, which has a great impact on the accuracy of the calculation results. This algorithm will not be applicable. To sum up, this algorithm has certain limitations and is relatively complex, so it is only used for fixed connection and fixed connection disconnection contact at present.

(2) Distributive parameter method

The basic principle is: distribute half of the mass of each slave unit being contacted to the main surface being contacted, and distribute positive pressure at the same time.

Then, the principal surface acceleration is corrected. Finally, the acceleration and velocity constraints are imposed on the slave node to ensure that the slave node does not slide and avoid rebound.

(3) Penalty function method

This method is widely used in numerical calculation. The basic principle is: in each time step, check whether the slave node passes through the main surface. If not, do not deal with it. On the contrary, a larger surface is introduced between the slave node and the penetrated surface. The size of this contact surface is related to the penetration depth and the stiffness of the main surface, also known as the penalty function value. Its physical meaning is that a spring is placed between the two to limit the penetration, as shown in the following figure. The so-called symmetric penalty function method means that the program processes all master nodes according to the above steps, using the same algorithm as the slave nodes (Fig. 3).
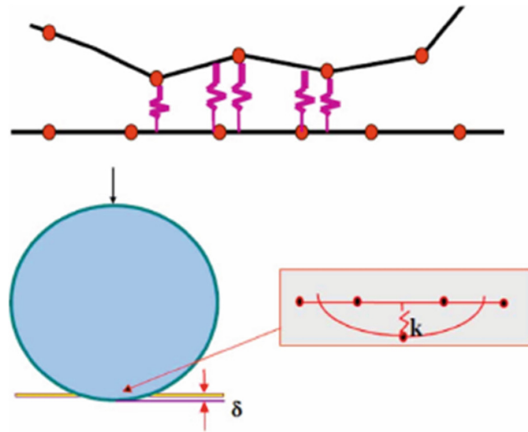
Fig. 3. Penalty function method.

The magnitude of contact force is expressed by this formula: In the above formula: k is contact interface stiffness, is penetration.

Because the symmetrical penalty function method is adopted, the calculation of this method is simple, the hourglass phenomenon in the impact process is not obvious, and there is no noise impact. The energy conservation in the system is accurate, symmetrical and the momentum conservation is accurate, and the impact conditions and release conditions are not required. If obvious penetration occurs in the calculation process, it can be adjusted by enlarging the penalty function value or reducing the time step.

Among the three algorithms, the dynamic constraint method is mainly applicable to the fixed interface, the distributed parameter method is mainly used for the sliding interface, and the symmetric penalty function method is the most commonly used method. The following problems in contact analysis should be paid attention to: first, in terms of data, try to make the material data accurate, because the accuracy of most nonlinear

dynamic problems is related to the mass density of the input data; Second, in terms of units, the definition of material properties is to coordinate units, which will cause abnormal response and even calculation problems; Third, in terms of contact, the calculation efficiency varies greatly with different contact types. It is best to use automatic contact types and be particularly cautious about complex problems; Fourth, multiple contacts should be defined in the definition process.

Contact problem is state nonlinear, and is a highly nonlinear behavior, which requires more computer resources. There are two major difficulties in simulating contact problems with finite elements: the user usually does not know the contact area until the problem is solved. Moreover, it is difficult to estimate the time when their contact surfaces are separated. Changes in the two contact surface materials, loads, boundaries, and other conditions will also change the analysis of the contact problem. In LS-DYNA, contact is not simulated by elements that are in contact with each other, but by contact surfaces that may be in contact. By setting the contact type and parameters, the contact-impact interface algorithm is used to solve the problem. Common contact types are single-surface contact, node-to-surface contact, and surface-to-surface contact.

2.3   Workbench LS-DYNA Model Preprocessing

Since the displacement of the container ship is 5000t and the ship type has been determined, the draft of the container ship is set to 8 m in this simulation. In addition, in order to reduce the simulation time, the distance between the container ship and the floating nuclear power plant is adjusted to about 0.1 m, and the impact position is the port side in the middle of the stern bunker. The three-dimensional and finite element models are shown in the following (Figs. 4, 5 and 6):
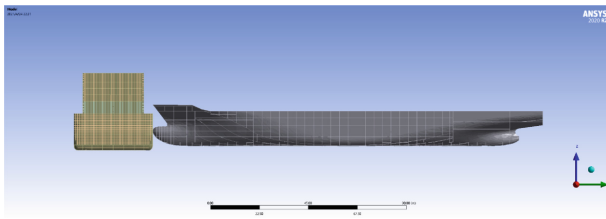
Fig. 4. Three dimensional model of impact between two ships.
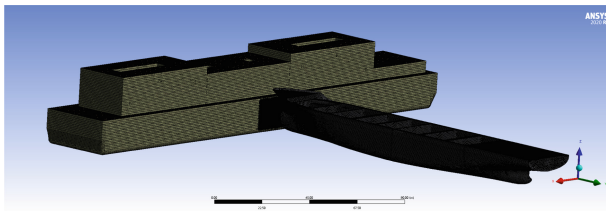
Fig. 5. Finite element model of two ship impact.
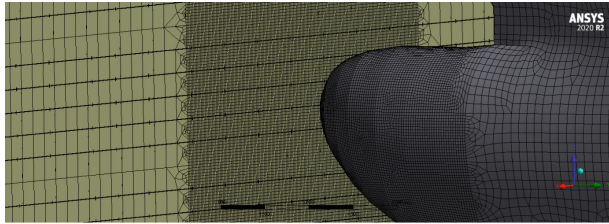
Fig. 6. Local finite element mesh refinement model of two ship impact.

Define the material properties. The material of the floating nuclear power plant (except the stern containment) is defined as nonlinear structural steel, Poisson's ratio is set to 0.3, elastic modulus is set to 2.06×10^{11}Pa, tangent modulus is set to 1.45×10^9Pa, and yield strength is set to 3.55×10^8Pa. In order to make the floating nuclear power plant have the possibility of damage, it is necessary to add a plastic strain failure criterion, and its maximum equivalent plastic failure criterion is set to 0.0035, according to the young's modulus.

Connection relationship settings. The single surface only type suitable for the beam shell hybrid model in the body interaction is adopted, and the constraint for forming contact algorithm with high accuracy is adopted for the flexible constraint algorithm. In addition, the contact and connection between the stern containment and the floating nuclear power plant are realized by using body to body fixed, and the coupling point is set as flexible coupling (Fig. 7).
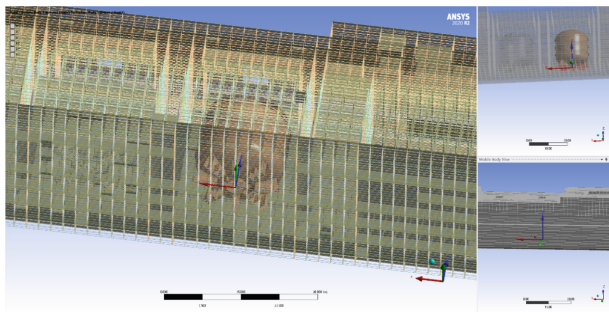
Fig. 7. Connection between containment and floating nuclear power plant.

Loads, boundary conditions and analysis settings of workbench LS-DYNA. Fix the bow and stern surfaces of the floating nuclear power plant rigidly, as shown in Figs. 8 and 9. Set the end time to 3.5 s, and the calculation accuracy is double precision. Set the speed of the container ship to 2 m/s and the direction to $-y$, and conduct body tracking for the container ship, the floating nuclear power plant and its containment, so as to check the contact force later. In addition, it can provide data for subsequent fatigue analysis and ultimate bearing capacity analysis.
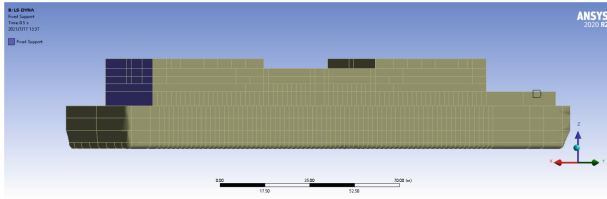
Fig. 8. Rigid fixed surface 1.
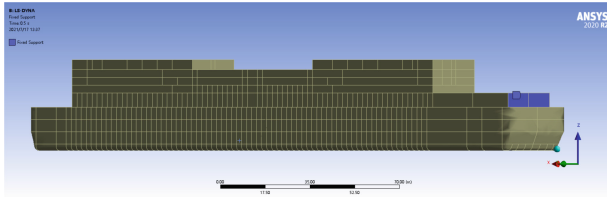
Fig. 9. Rigid fixed surface 2.

3   Comparison of Simulation Results

3.1   Equivalent Stress During Impact

For dry impact, the time history curve of the maximum equivalent stress of the whole ship is shown in Fig. 10. The maximum equivalent stress is 360 MPa, which occurs in 0.471 s, as shown in Fig. 11. The degree of damage is shown in Fig. 12. The simulation results show that the damage range of the hull outer plate is small, and the deformation of the bulkheads is small and undamaged.
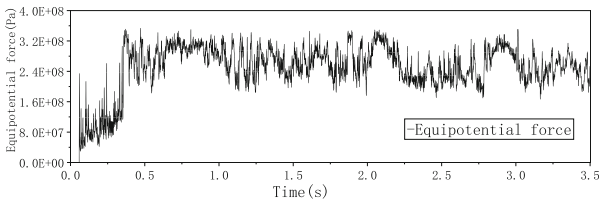
Fig. 10. The time history curve of the maximum equivalent stress of the whole ship

For dry impact, the maximum equivalent stress of the containment is 331.7 MPa, which occurs at 0.319 s as shown in Fig. 13.

For wet impact, the maximum equivalent stress of the whole ship is about 360 MPa, which occurs at 0.48 s, as shown in Fig. 14. The degree of damage is shown in Fig. 15. Figure 16 shows the details of the water ingress of the damaged tank. The maximum equivalent stress of the containment is 304.3MPa, which occurs at 0.320 s, as shown in Fig. 17.
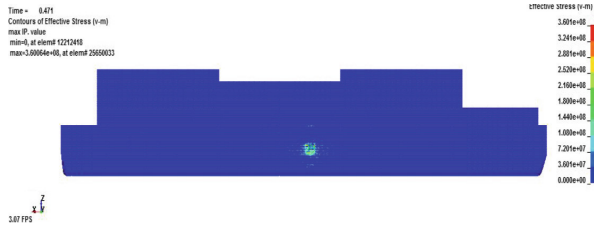
Fig. 11. Equivalent stress cloud diagram of the whole ship at 0.471 s
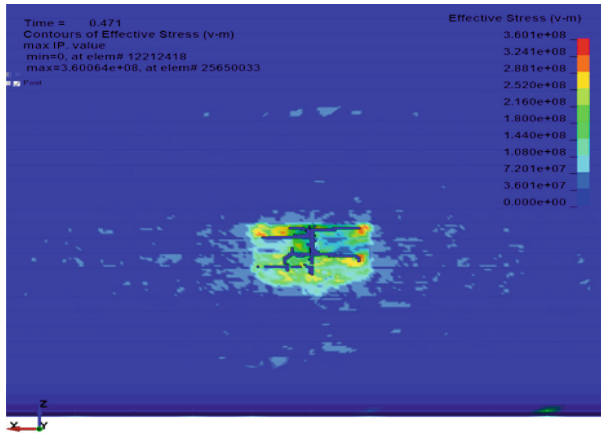
Fig. 12. Damage diagram of the whole ship at 0.471 s
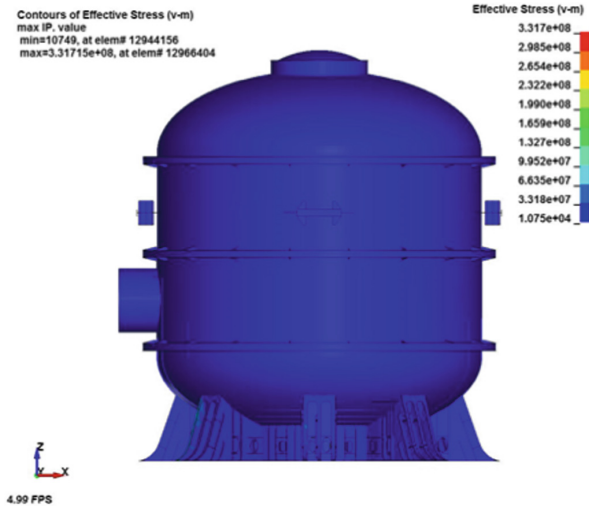
Fig. 13. Equivalent stress cloud diagram of containment at 0.319 s

Fig. 14. Equivalent stress cloud diagram of the whole ship at 0.48 s
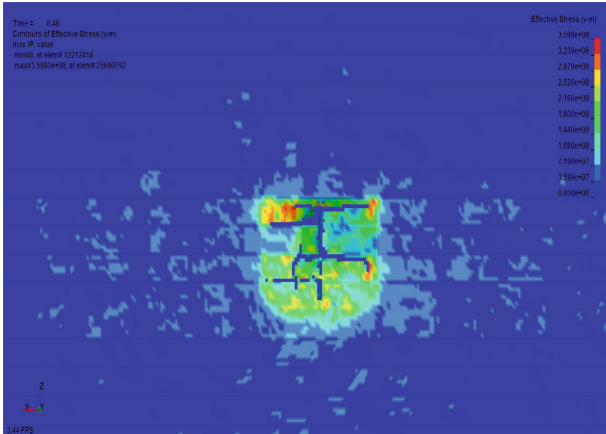
Fig. 15. Damage diagram of the whole ship at 0.48 s
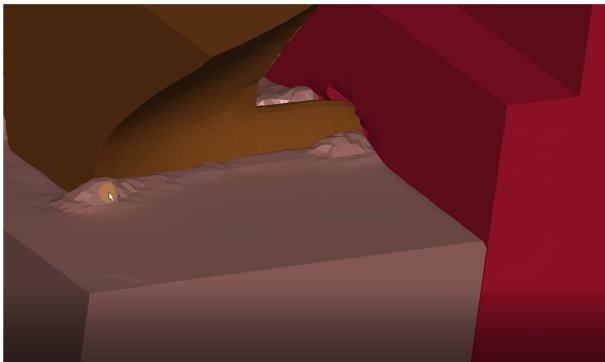
Fig. 16. The water ingress of the damaged tank.

3.2 Force Analysis of Supports During Impact

For dry impact, the time history curve of the horizontal force on the containment support is shown in Fig. 18–20. The maximum translational force of the containment support in the X direction is $1.04 \times 10^6 N$, which occurs in 0.655 s; The maximum translational force
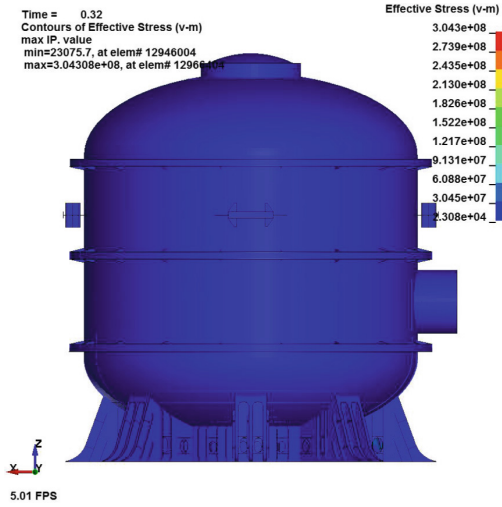
Fig. 17. Equivalent stress cloud diagram of containment at 0.320 s
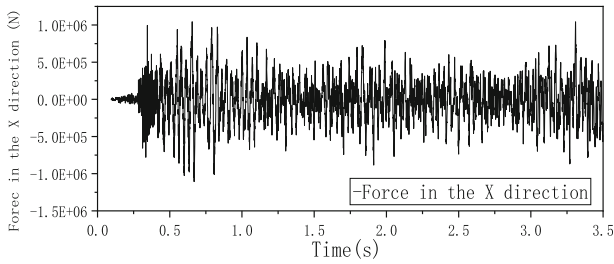
Fig. 18. The time history curve of the horizontal force on the bearing in the X direction
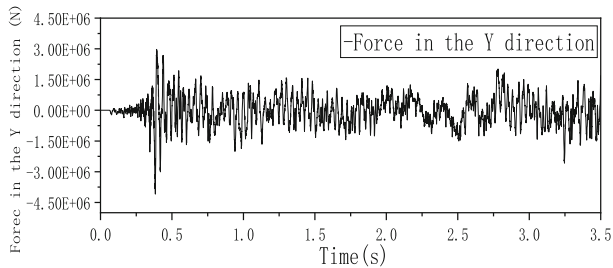
Fig. 19. The time history curve of the horizontal force on the bearing in the X direction

in the Y direction is $4.09 \times 10^6 N$, which occurs in 0.384 s; The maximum translational force in the Z direction is $2.25 \times 10^6 N$, which occurs in 0.453 s.
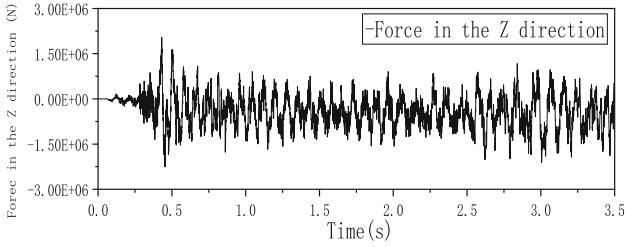
Fig. 20. The time history curve of the horizontal force on the bearing in the Z direction

For wet impact, the maximum translational force of the containment support in the X direction is $1.03 \times 10^6 N$, which occurs in 0.659 s; The maximum translational force in the Y direction is $4.09 \times 10^6 N$, which occurs in 0.388 s; The maximum translational force in the Z direction is $2.25 \times 10^6 N$, which occurs in 0.456 s.

For dry impact, the time history curve of the rotating force on the containment support is shown in Fig. 21–23. The maximum rotation force of the containment support around the X direction is $2.10 \times 10^7 N \cdot m$, which occurs in 2.753 s; The maximum rotation force around the Y direction is $7.78 \times 10^6 N \cdot m$, which occurs in 0.396 s; The maximum rotation force around the Z direction is $1.11 \times 10^7 N \cdot m$, which occurs in 0.384 s.
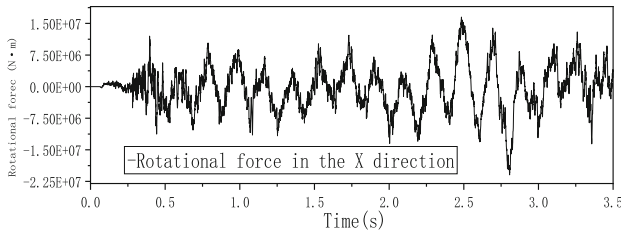
Fig. 21. The time history curve of the rotating force on the bearing in the X direction
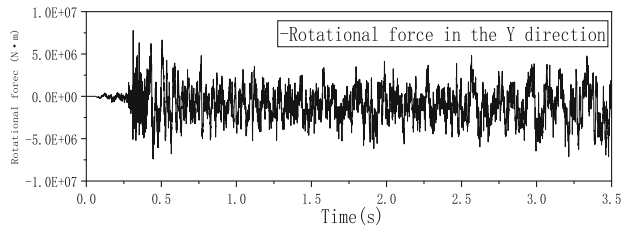
Fig. 22. The time history curve of the rotating force on the bearing in the Y direction

For wet impact, the maximum rotation force of the containment support around the X direction is $2.09 \times 10^7 N \cdot m$, which occurs in 2.807 s; The maximum rotation force around the Y direction is $7.78 \times 10^6 N \cdot m$, which occurs in 0.409 s; The maximum rotation force around the Z direction is $1.11 \times 10^7 N \cdot m$, which occurs in 0.384 s.
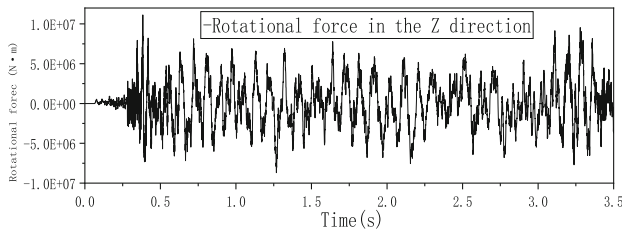
Fig. 23. The time history curve of the rotating force on the bearing in the Y direction

4 Conclusion

The simulation time of wet impact is 2.5 times that of dry impact, and the equivalent stress of the whole ship, the equivalent stress of the containment, the damage degree of the hull and the force of the support are not much different. So, if the relevant personnel do not need to understand the effect of water intrusion into the damaged cabin, the influence of air and water on the impact simulation results can be ignored, and the dry mode can be directly used for calculation.

References

1. Li, C., Wang, J.: Correlation analysis of ship collision accidents. J. Shanghai Marit. Univ. **42**(02), 70–74 (2021)
2. Wen, X., W., Lu, J., Cui, Z.: Numerical simulation and experiment research of ship collision process. J. Zhejiang Ocean Univ. Nat. Sci. **30**(1), 71–76 (2011)
3. Liu, K., L., Zhang, Y., Wang, Z.: Study on the influence of bow shape to the side structure during ship collision. Ship Eng. **32**(2), 12–14 (2010)
4. Zhang, W.: Numerical simulation research of ship collision analogue rule. Chin. J. Ship Res. **4**(3), 38–41 (2009)
5. Travanca, J., Hao, H.: Dynamics of steel offshore platforms under ship impact. Appl. Ocean Res. **47**, 352–372 (2014)
6. Oshieo, R.E., Alves, M.: Scaling of cylindrical shells under axial impact. Int. J. Impact Eng **34**, 89–103 (2007)

Three-Dimensional Pin-by-Pin Transient Analysis for PWR-Core

Junwei Qin and Yunzhao Li$^{(\boxtimes)}$

School of Nuclear Science and Technology, Xi'an Jiaotong University, Xi'an 710049, China
`yunzhao@xjtu.edu.cn`

Abstract. To ensure the safety of PWR-core operation, three-dimensional whole-core transient analysis needs to be carried out for the sake of the pin-power distribution. For this purpose, this paper presents "Bamboo-Transient 2.0", a three-dimensional pin-by-pin transient analysis program. The program adopts a fully-implicit backward method with finite difference for time variable discretization, a method of exponential function expansion nodal (EFEN) SP$_3$ for the neutron transport calculation, and a multi-channel model for the thermal feedback calculation. In addition, Picard iteration is used to couple the neutronics with thermal-feedback, which is intended to guarantee the convergence of coupling iteration at each time step. Moreover, the program can perform parallel computing based on Message Passing Interface (MPI) for the whole-core pin-by-pin transient analysis. This developed program has been applied to two commercial PWRs, viz. AP1000 and CNP1000. Numerical results of this application demonstrate that Bamboo-Transient 2.0 can yield much more refined results than the traditional legacy coarse-mesh neutron-diffusion programs based on assembly homogenization. Its pin-wise distributions of state parameters are reliable and thus can satisfactorily meet the requirements and purpose of safety analysis.

Keywords: PWR · NECP-Bamboo · Pin-by-pin · Transient analysis

1 Introduction

Compared with the steady-state operation process, the reactor core is more dangerous in transient processes. For PWR, only by determining the hot spots and heat pipes at the core can its safe operation be ensured and the ultra-high temperature-caused core melting be prevented. To find the hot spots and heat pipes at the core, the transient analysis is supposed to be accurate in the fuel rod scale and be capable of providing various state parameters. Thus, it is necessary to track and predict the changes in the key parameters of the core to prevent accidents and reduce the harm after accidents if there is any. As the traditional transient analysis method is based on the diffusion calculation of assembly homogenization, only information in the assembly scale can be retained whereas other relevant information in the pin scale is ignored. Therefore, in order to obtain the power distribution of fuel rod scale, it is necessary to carry out the power reconstruction based on a series of approximations and assumptions. Consequently, the calculation accuracy of the traditional method is far from desirable [1].

It is against such a background that fast and accurate transient analysis methods for nuclear reactors are becoming increasingly important and should be designed and developed. In recent years, a pin-by-pin transient analysis method based on pin homogenization has attracted extensive attention. With the pin transport calculation accomplished, this method can directly homogenize the calculation area and retain all kinds of information in the pin scale. As a result, in the core calculation, the core information in the pin scale can be obtained directly without introducing the error caused by the power reconstruction [2]. In addition, the channel of thermal feedback should be accurate in the rod scale so as to match with neutronics. Additionally, the transient process of PWR is a process of coupling neutronics with thermal-hydraulics [3]. This paper presents how the coupling of neutronics with thermal-feedback is calculated, which is to be suitable for the pin-by-pin transient analysis. In addition, due to the significantly increased number of computational meshes, it is urgent to improve the efficiency of whole-core pin-by-pin transient analysis. In this paper, the parallel technology is also discussed.

The rest of the paper is organized as follows. Section 2 introduces each method in detail. Section 3 introduces the numerical verification and analysis. Section 4, the last part of this paper, sums up the study and concludes the paper.

2 Theoretical Models

The fully implicit method and EFEN method are specially employed to solve the neutron kinetics equation, whereas a multi-channel model in the pin scale is employed to treat the heat transfer and flow process of coolant, and a 1D cylindrical heat conduction model is employed to treat the heat conduction process in fuel rods. Picard iteration is utilized at each time step to guarantee the convergence between neutronics and thermal-feedback. Using MPI of distributed memory, the same spatial domain decomposition is performed for both neutronics and thermal-feedback calculation for parallel computing, which can significantly shorten the computing time needed by transient analysis.

2.1 Calculation of Neutron Dynamics

In the transient process of PWR, considering the influence of delayed neutrons and adopting multi-group approximation, the neutron flux distribution at the core meets the spatiotemporal neutron transport equations, which is shown in Eq. (1). Where, v_g is the neutron velocity of group g/cm·s^{-1}, r the spatial location, Φ_g the neutron angular flux of group g/(cm3·s)$^{-1}$, $\boldsymbol{\Omega}$ the neutron motion direction, t the time/s, $\Sigma_{t,g}$, $\Sigma_{f,g}$ the total, fission cross sections of group g/cm^{-1}, $\Sigma_{s,g' \to g}$ the scattering cross section from group g' to group g/cm^{-1}, $\chi_{p,g}$ and $\chi_{d,g,i}$ the prompt neutron fission spectrum of group g and the delayed neutron fission spectrum of group g, delayed group i, v the number of neutrons per fission, C_i the precursor concentration of delayed group i, λ_i the decay constant of precursor delayed group i/s^{-1}, β_i the delayed neutron fractions of group i/pcm, $g = 1, 2, …, G$; $i = 1, 2, …, $Nd the neutron energy group index and the delayed

neutron precursor group index.

$$
\begin{cases}
\dfrac{1}{\upsilon_g(\mathbf{r})}\dfrac{\partial \Phi_g(\mathbf{r}, \mathbf{\Omega}, t)}{\partial t} = -\mathbf{\Omega}\cdot\nabla\Phi_g(\mathbf{r}, \mathbf{\Omega}, t) - \Sigma_{t,g}(\mathbf{r}, t)\Phi_g(\mathbf{r}, \mathbf{\Omega}, t) \\
\qquad + \displaystyle\int \Sigma_{s,g'\to g}(\mathbf{r}, \mathbf{\Omega}' \to \mathbf{\Omega}, t)\Phi_g(\mathbf{r}, \mathbf{\Omega}', t)d\mathbf{\Omega}' \\
\qquad +(1-\beta(\mathbf{r}))\dfrac{\chi_{p,g}(\mathbf{r})}{4\pi}\displaystyle\sum_{g'=1}^{G}\int \nu(\mathbf{r})\Sigma_{f,g'}(\mathbf{r}, t)\Phi_{g'}(\mathbf{r}, \mathbf{\Omega}', t)d\mathbf{\Omega}' \\
\qquad\qquad +\dfrac{1}{4\pi}\displaystyle\sum_{i=1}^{Nd}\chi_{d,g,i}(\mathbf{r})\lambda_i C_i(\mathbf{r}, t) \\
\dfrac{\partial C_i(\mathbf{r},t)}{\partial t} = \beta_i(\mathbf{r})\displaystyle\sum_{g'=1}^{G}\int \nu(\mathbf{r})\Sigma_{f,g'}(\mathbf{r}, t)\Phi_{g'}(\mathbf{r}, \mathbf{\Omega}', t)d\mathbf{\Omega}' - \lambda_i C_i(\mathbf{r}, t)
\end{cases}
\tag{1}
$$

As Eq. (1) cannot be solved straightforwardly, it has to be discretized. First, the fully implicit backward difference method is used for the time term [4] to obtain the equation of the angular flux at t_{n+1}, which is shown in Eq. (2):

$$
\begin{aligned}
&\mathbf{\Omega}\cdot\nabla\Phi_g(\mathbf{r}, \mathbf{\Omega}, t_{n+1}) + \overline{\Sigma}_{t,g}(\mathbf{r}, t_{n+1})\Phi_g(\mathbf{r}, \mathbf{\Omega}, t_{n+1}) = \\
&\sum_{g'=1}^{N}\int \Sigma_{s,g'\to g}(\mathbf{r}, \mathbf{\Omega}' \to \mathbf{\Omega}, t_{n+1})\Phi_g(\mathbf{r}, \mathbf{\Omega}', t_{n+1})d\mathbf{\Omega}' \\
&+\frac{1}{4\pi}\overline{\chi}_g(\mathbf{r})\sum_{g'=1}^{N}\int \nu(\mathbf{r})\Sigma_{f,g'}(\mathbf{r}, t_{n+1})\Phi_{g'}(\mathbf{r}, \mathbf{\Omega}', t_{n+1})d\mathbf{\Omega}' + Q_g(\mathbf{r}, \mathbf{\Omega})
\end{aligned}
\tag{2}
$$

where,

$$
\overline{\Sigma}_{t,g}(\mathbf{r}, t_{n+1}) = \Sigma_{t,g}(\mathbf{r}, t_{n+1}) + \frac{1}{\upsilon_g(\mathbf{r})\Delta t}
$$

$$
\overline{\chi}_g(\mathbf{r}) = (1-\beta(\mathbf{r}))\chi_{p,g}(\mathbf{r}) + \sum_{i=1}^{Nd}\chi_{d,g,i}(\mathbf{r})\beta_i(\mathbf{r}) - \sum_{i=1}^{Nd}\chi_{d,g,i}(\mathbf{r})\frac{\beta_i(\mathbf{r})}{1+\lambda_i\Delta t}
$$

$$
Q_g(\mathbf{r}, \mathbf{\Omega}) = \frac{1}{4\pi}\sum_{i=1}^{Nd}\chi_{d,g,i}(\mathbf{r})\lambda_i\frac{C_i(\mathbf{r}, t_n)}{1+\lambda_i\Delta t} + \frac{1}{\upsilon_g(\mathbf{r})}\frac{\Phi_g(\mathbf{r}, \mathbf{\Omega}, t_n)}{\Delta t}
$$

Next, the P_1 approximation is used for the angle to obtain the diffusion fixed source equation as shown in Eq. (3):

$$
-D\nabla^2\psi_g^0(x) + \overline{\Sigma}_{t,g}\psi_g^0(x) = S_g
\tag{3}
$$

The SP_3 approximation is used for the angle to obtain the SP_3 fixed source equations as shown in Eq. (4):

$$
\begin{cases}
-D\nabla^2[\psi_g^0(x)+2\psi_g^2(x)] + \overline{\Sigma}_{r,g}[\psi_g^0(x)+2\psi_g^2(x)] = S_g + 2\overline{\Sigma}_{r,g}\psi_g^2(x) \\
-\frac{27}{35}D\nabla^2\psi_g^2(x) + \overline{\Sigma}_{t,g}\psi_g^2(x) = S_2 + \frac{2}{5}(\overline{\Sigma}_{r,g}\psi_g^0(x) - S_g)
\end{cases}
\tag{4}
$$

The derivation process is described in detail in Reference [4]. Equation (3) and (4) can be solved by using EFEN method, whose process is described in detail in Reference [5]. By solving the diffusion or SP$_3$ fixed source equation at each time step, the neutron dynamics is calculated.

2.2 Calculation of Thermal Feedback

The transient analysis of PWR entails that the coupling of neutron dynamics with transient thermal feedback is calculated. The solution to the neutron dynamics equation requires the cross-sections of all materials in the core. To obtain these cross-sections, the state parameters at the core are needed. Thus, thermal feedback calculation should provide the distributions of these state parameters. Calculation of the thermal feedback of the reactor core consists of two parts, viz. Fluid calculation of the coolant and heat conduction calculation of the fuel rod, in which the fluid calculation is 1D calculation in the axial direction of the flow area and the heat conduction calculation is 1D calculation in the radial direction of the cylindrical rod.

Fluid Model
Transient mass and energy conservation equations of the coolant are shown in Eq. (5) and (6). Where, ρ is the density of coolant/kg·cm^{-3}, h the enthalpy of coolant/J, u the velocity of coolant/cm·s^{-1}, A$_c$ the circulation area/ cm^{-2}, q_c the heat release in fuel and q_w the fuel surface heat flux.

$$\frac{\partial \rho(z, t)}{\partial t} + \frac{\partial (\rho(z, t)u(z, t))}{\partial z} = 0 \tag{5}$$

$$\frac{\partial (\rho(z, t)h(z, t))}{\partial t} + \frac{\partial (\rho(z, t)u(z, t)h(z, t))}{\partial z} = P_h \frac{q_w(z, t)}{A_c} + q_c(z, t) \tag{6}$$

The two equations are discretized by θ difference in time to obtain the equation of the nodal enthalpy rise. Given the parameters of the coolant at the channel inlet, the heat flux can be obtained via the heat conduction calculation. Hence, the temperature of the coolant can be solved in the axial direction from the inlet to the outlet.

Heat Conduction Model
1D transient heat conduction model of cylinder is shown in Eq. (7). Where, c_p is the specific heat capacity at constant pressure/(J/kg·K), k the thermal conductivity/(W/m·K), and T the temperature/K.

$$\rho(r, t)c_p(r, t)\frac{\partial T(r, t)}{\partial t} = \frac{1}{r}\frac{\partial}{\partial r}\left(k(r, t) \cdot r \cdot \frac{\partial T(r, t)}{\partial r}\right) + q(r, t) \tag{7}$$

In the radial direction, the fuel pellet is divided into n meshes, the gas gap divided into 1 mesh, and the clad divided into 3 meshes. Equation (7) is discretized by finite difference in space and θ difference in time. The radial temperature distribution of the fuel is obtained by Gauss-Seidel iterative calculation.

2.3 Coupling of Neutronics with Thermal-Hydraulics

As the mesh size of the whole-core pin-by-pin neutron dynamics calculation can be either that of a fuel rod, or a control rod or a water tunnel, the corresponding thermal feedback adopts multi-channels in pin scale division to simulate the coolant flow between the rods. The channel is the coolant area between fuel rods and guide tubes. The channels along the axis can be divided into several meshes, which can exchange mass and energy with each other, ignoring the exchange of momentums and the exchange between the radial channels. In addition, different physical fields adopt various meshing methods while the neutron and thermal fields uses rod-centered meshing methods and the flow field uses channel-centered meshing method. The various methods are shown in Fig. 1.

(a) neutron and thermal fields   (b) flow field
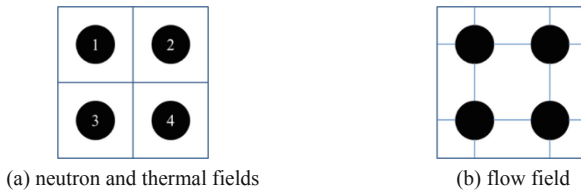
Fig. 1. Various meshing methods of physics fields

As the mapping relationships across neutron field, thermal field and flow field are complicated, five types of conversion relationships are considered for different physical fields as follows, which is shown in Fig. 2 as follows:

1) conversion from the nodal power of neutron field to the channel power of flow field;2) conversion from the coolant temperature of flow field to the cladding surface temperature of thermal fields;3) conversion from the nodal power of neutron field to the mesh power of thermal field;4) conversion from the coolant temperature of flow field to the nodal average coolant temperature of the neutron field;5) conversion from the fuel temperature of thermal field to the nodal effective fuel temperature of neutron field.
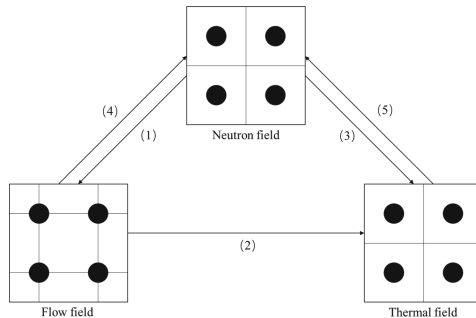
Fig. 2. Conversion of various physical fields

Traditional transient analysis calculation programs mostly use explicit coupling method. This method can solve the neutronics equation and thermal feedback calculation separately, but cannot perform the iteration between them. Thus, the convergence of the coupling cannot be guaranteed. To ensure the convergence, a shorter time step is needed for this method. However, due to lack of iteration, the cost of calculation at each time step is also low. However, implicit coupling, or rather, Picard iteration, solves the neutronics and thermal-feedback separately. In essence, Picard iteration is intended to solve the various physical fields in different ways through operator splitting, and then iterates between the two physical fields to converge the coupled parameters. However, it takes a longer time step and more convergence than the explicit coupling. In view of this, the current study employs Picard iteration to calculate the coupling of neutronics with thermal-feedback to accurately calculate the coupling. The neutron dynamics and thermal feedback are calculated at each time step. Only when the neutronics and thermal-hydraulics coupling iteration are converged can the next time step be calculated. The iterative process is shown in Fig. 3.
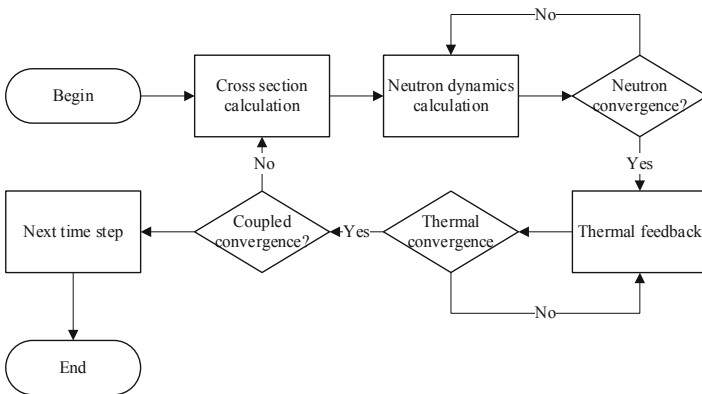
Fig. 3. Neutronics and thermal-hydraulics coupling iteration.

2.4 Parallel Calculation

The parallel efficiency is mainly affected by the following factors. 1) Communication overhead. As different threads need to communicate, it takes longer time. Thus, the longer communication lasts, the lower the parallel efficiency. 2) Parallel computing may degrade the iterative format, and as a result, increase the amount of computation. 3) Multithreading may cause worthless waiting to the processes caused by load imbalance. 4) Redundant computation can be caused by parallel algorithm per se.

Given the factors above, the parallelization of whole-core pin-by-pin transient calculation consists of the following aspects:

1) Broadcast of input parameters. To prevent multiple CPUs from using the same input channel at the same time, a designated CPU reads the input file and then uses the broadcast function of sending multiple data of the same type in batch at one time to send the input information to all CPUs.

2) Domain decomposition. The whole area on average is divided according to the number of CPUs and the scale of calculation problems to keep the load balance across different CPUs. Each CPU stores only the area information responsible for calculation.

3) Node sweep and communication. To improve the parallel efficiency, the Red-Black Gauss-Seidel node sweep method [6], which is suitable for parallel computing, is selected to avoid the degradation in iterative format caused by parallel computing. In addition, the fractional neutron currents only need to communicate once after the red and black node sweep to reduce the communication overhead.

4) Post-processing of calculation results. To prevent multiple CPUs from using the same output channel at the same time, the calculation results of all CPUs are exported uniformly by the designated CPU.

2.5   Interim Summary

Based on the theoretical models mentioned above, a pin-by-pin program called "Bamboo-Transient 2.0" is developed for the 3D whole-core transient analysis. This program can be automatically coupled with both the lattice-calculation program "Bamboo-Lattice 2.0" and the 3D whole-core pin-by-pin steady-state calculation program "Bamboo-Core 2.0". This strongly suggests that Bamboo-Transient 2.0 can improve the function of the software package called "NECP-Bamboo 2.0" and enables the software package to perform Pin-by-pin transient analysis for PWR-core. The calculation flow chart of Bamboo-Transient 2.0 is shown in Fig. 4. The multi-physical coupling iteration is shown in detail in Fig. 3.
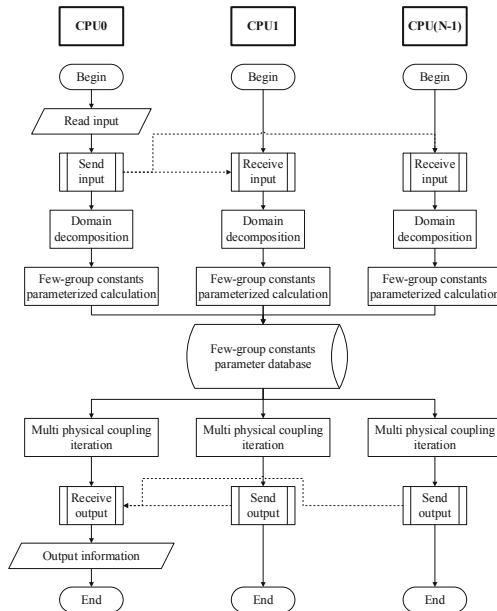
Fig. 4. The calculation flow chart of Bamboo-Transient 2.0.

3   Numerical Verification and Analysis

To verify the accuracy and the analytical ability of Bamboo-Transient 2.0, the program is applied to the transient analysis of two commercial PWRs. This section will show the numerical verification and analysis of CNP1000 and AP1000 reactor core by using Bamboo-Transient 2.0.

3.1   CNP1000

The rated power and the rated operating pressure of CNP1000 are 2895MWt and 15.5 MPa, respectively. There are 157 boxes of fuel assemblies at the reactor core and 57 control rod assemblies in the first cycle. The reactor core is divided into 9 groups according to the needs of the problem. The control rods are 362.49 cm in length, which is divided into 225 steps. The grouping of the control rods is shown in Fig. 5. The program calculates the rod ejection in the following case: the initial power level of the core is 1%. The control rods of the ninth group are fully inserted while the rest are all lifted. The control rods of the ninth group are all ejected in 0–0.1 s. It takes 0.4 s to accomplish the transient process, and the time step is divided into 0.001 s.
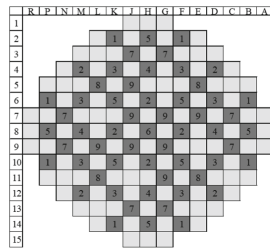
Fig. 5. The grouping of the control rods in CNP1000

The normalized power is shown in Fig. 6. As the control rods are gradually ejected from the core, the normalized power of the core increases rapidly. When all the control rods are ejected from the core, the core enters a stable state. The 3D distribution of power, the effective temperature of fuel and the temperature of coolant are shown in Fig. 7. At the beginning, due to the insertion of control rods, the power is distributed precipitously, and the distribution is high outside but low inside the core. With the control rods ejected, the power distribution is flattened. While the temperature distributions show the same regularity, the effective temperature of the fuel and the temperature of the coolant are more uniform than at the beginning in the radial direction after the rod ejection.

3.2   AP1000

AP1000 is the third-generation advanced passive PWR designed by Westinghouse. Compared with the traditional PWR nuclear reactor, AP1000 adopts a passive safety system, which further simplifies the structure of the power station and improves the safety of the
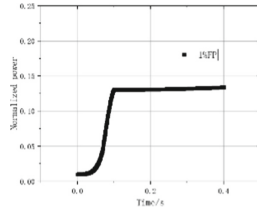
Fig. 6. Normalized power of CNP1000
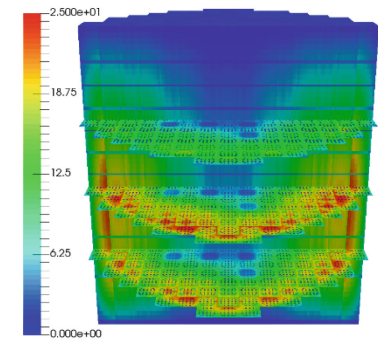
(a) power distribution at the beginning
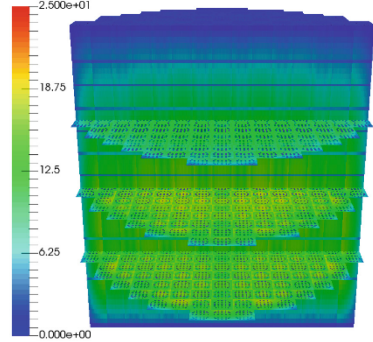
(b) power distribution at the end
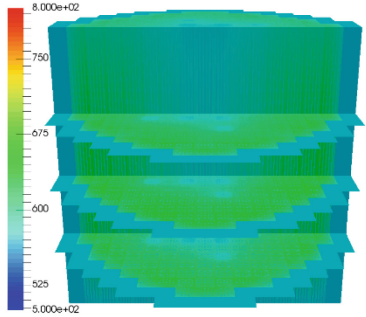
(c) effective temperature of fuel at the beginning
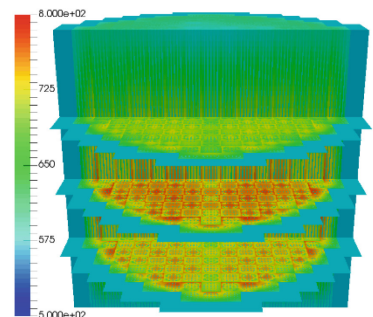
(d) effective temperature of fuel at the end
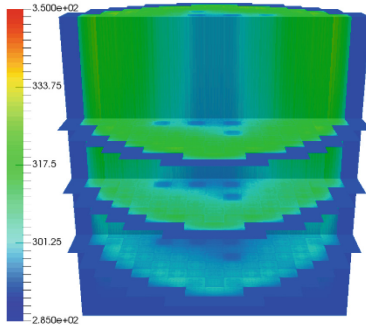
(e) temperature of coolant at the beginning
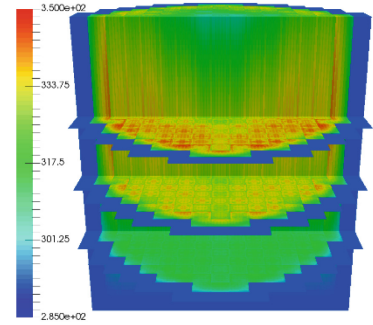
(f) temperature of coolant at the end

Fig. 7. Three-dimensional distribution at different time

reactor. There are 69 groups of control rods in AP1000, including 53 groups of black rods and 16 groups of gray rods. Some of the grey rods and black rods are employed to form the MSHIM system of the core, which controls the reactivity and power distribution of the core with the boron containing coolant, while the remaining black rods are employed to form the shutdown rod group [7]. The pattern of the control rods is shown in Fig. 8.
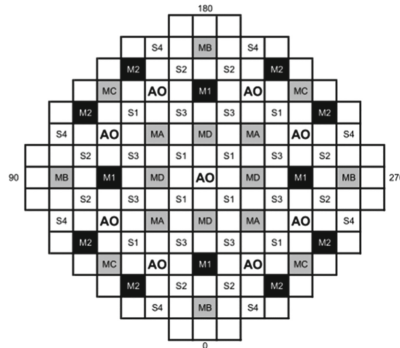
Fig. 8. The pattern of the control rods of AP1000
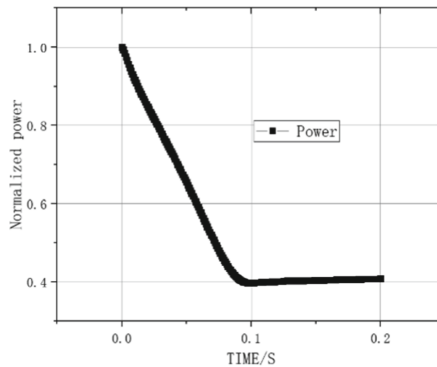
Fig. 9. Normalized power of AP1000

AP1000 has designed a rapid power reduction system (RPR system). To analyze the system, this study calculates the simulation of rod drop working condition of M1 and S2 rod groups under full power. M1 and S2 rod groups simultaneously fall into the core within 0.1 s while the program simulates the transient process within 0.2 s. The normalized power of the core is shown in Fig. 9. It can be seen that the core power decreased rapidly due to the insertion of control rods into the core. At 0.1 s, the normalized power is reduced to 40% of that at the initial time. Then, the core power increases slowly as the fuel temperature decreases. The 3D distribution at the beginning and at the end is

shown in Fig. 10. The figure shows that the power distribution is distorted by the insertion of the control rod and that the power around the control rod is significantly decreased. Besides, the effective fuel temperature also shows this regularity. At the same time, the axial distribution of power and the fuel temperature become increasingly uneven while the temperature of the coolant changes little and decreases slightly.
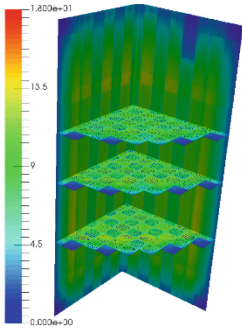
(a) power distribution at the beginning
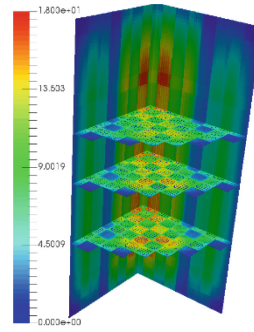
(b) power distribution at the end
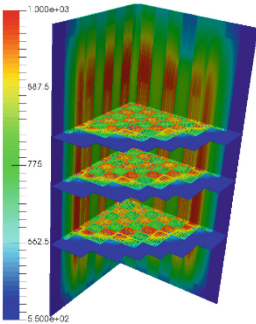
(c) effective temperature of the fuel at the beginning
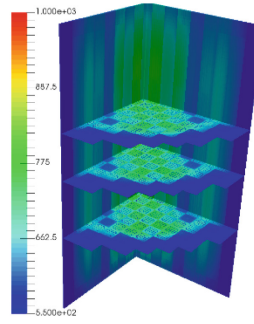
(d) effective temperature of the fuel at the end
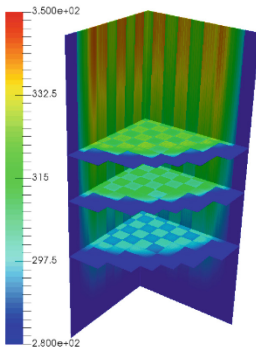
(e) the temperature of coolant at the beginning
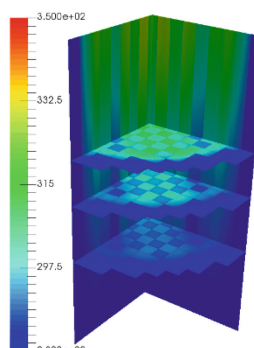
(f) the temperature of coolant at the end

Fig. 10. Three-dimensional distribution at different time

4   Conclusion

In order to perform the 3D whole-core pin-by-pin transient analysis, the theoretical model of the transient analysis is established in this study as follows:

1) The pin-by-pin neutron dynamics is calculated by using the fully implicit method and the exponential function expansion nodal method;
2) The model of 3D whole-core pin-by-pin transient thermal feedback is established by using multi-channel in the pin scale to simulate the heat transfer and flow process of coolant, and by using a 1D cylindrical heat conduction model to simulate the heat conduction process in fuel rods;
3) In each time step, Picard iteration is used to perform the iterative calculation of the coupling of neutronics with thermal-feedback;
4) Based on MPI, the parallel calculation of the 3D whole-core pin-by-pin transient analysis is accomplished, which significantly shortens the calculation time.

To sum up, in this study, the program system that couples the pin-by-pin transient neutronics with thermal-feedback is applied to the PWR-core transient analysis of the second-generation nuclear power CNP1000 and the third-generation nuclear power AP1000. Both the condition for rapid rod drop power reduction and that for rod ejection accident are analyzed. The rod power distribution and fuel temperature distribution are more refined than the traditional diffusion program of assembly homogenization. Bamboo-transient 2.0 makes full use of the ability of pin-by-pin transient analysis and calculation, which is more accurate than the traditional program. The working conditions of the reactor core under transient conditions are simulated and speculated finely, which provides a guarantee for the safe operation of PWR.

References

1. Li, Y., He, T., Liang, B., et al.: Development and verification of PWR-core nuclear design code system NECP-Bamboo: Part III: Bamboo-Transient. Nuclear Eng. Design **359** (2018)
2. Yang, W., Wu, H., Li, Y., et al.: Development and verification of PWR-core fuel management calculation code system NECP-Bamboo: Part II Bamboo-Core[J]. Nucl. Eng. Des. **337**, 279–290 (2018)
3. Grahn, A., Kliem, S., Rohde, U.: Coupling of the 3D neutron kinetic core model DYN3D with the CFD software ANSYS-CFX. Annals Nuclear Energy. **84**, 197–203 (2015)
4. Xie, W., Cao, L., Li, Y.: Study on Pin-by-pin Neutron Kinetics Calculation based on EFEN-SP$_3$ Method. Atomic Energy Sci. Technol. **53**(2), 7 (2019)
5. Yang, W., Wu, H., Li, Y., et al.: Acceleration of the exponential function expansion nodal SP 3 method by multi-group GMRES algorithm for PWR pin-by-pin calculation. Annals Nuclear Energy, **120**, 869–879 (2018)
6. Palmiotti, G., Carrico, C.B., Lewis, E.E.: VARIANT: Variational anisotropic nodal transport for multidimensional Cartesian and hexagonal geometry calculation. Technical Report Archive & Image Library (1995)
7. Li. X., Du, C.: Study on selection of rapid power reduction system banks for load rejection for AP1000 NPP. Nuclear Power Eng. (S02), 4 (2019)

S3R Advanced Training Simulator Core Model: Implementation and Validation

Jeffrey Borkowski[1], Lotfi Belblidia[2], and Oliver Tsaoi[3($\boxtimes$)]

[1] Studsvik Scandpower, Idaho Falls, Idaho, USA
[2] Studsvik Scandpower, Gaithersburg, MD, USA
[3] Studsvik Scandpower, Beijing, China
`oliver.tsaoi@studsvik.com`

Abstract. Modern training simulators core models are required to replicate plant data for neutronic response. Replication is required such that reactivity manipulation on the simulator properly trains the operator for reactivity manipulation at the plant. This paper discusses advanced models which perform this function in real-time using S3R, the real-time, time-dependent core model of the Studsvik Core Management System (CMS). This paper also discusses the coupled multi-physics of the Reactor Coolant System (RCS) model, using RELAP5 as a prototype. Finally, this paper discusses the implementation of S3R under the control of a server-based executive environment and instructor station, essential for training simulator applications.

Keywords: Operational Training · Real-Time Simulation · Cycle Specific · Just-Time Training · Reactivity Management

1 Introduction

The Studsvik nuclear reactor analysis code, SIMULATE-3, has been extended to transient applications for both engineering analysis and real-time operator training. The physics models used in S3R are much the same as those used for steady-state core design/safety analysis, except that no core design or depletion calculation are done, and some simplifications are introduced to run in real-time under the control of real-time executive.

S3R has become the standard in 3D real-time core models for training simulator. It has been installed in more than 90 sites worldwide. The neutronics model of S3R has been coupled to several real-time thermal hydraulic models, including RELAP5, used in training simulators.

2   Neutronic Model Description

2.1   Features

The neutronics model used in S3R solves the 3-D, two-energy group, neutron diffusion equation with one radial node to represent each fuel assembly. In the axial direction, 24–25 nodes are typically used to represent the active portion of each fuel assembly, and one node is used to represent the upper and lower reflectors.

The S3R core model uses a fourth-order flux expansion to represent the neutron flux distribution within each node (in each of the three directions), and the spatial gradient of the flux can then be taken analytically (a third-order function, rather than the traditional first-order function). This results in a much more accurate representation for the flux than that of simpler methods.

The S3R core model uses explicit nodes (both radially and axially) to model the PWR baffle/reflectors. This permits direct solutions for the fluxes and leakages into the reflectors, without need for introduction of albedos (which are often used in simpler models) to treat the leakage out of the core. The baffle/reflector nodes are treated like any other node in the S3R core model.

2.2   Nuclear Data

Accuracy of the S3R core model depends not only on detailed 3-D neutronic and thermal-hydraulic modeling, but also on accurate representation of feedback parameters. These parameters include:

- Two-Group Macroscopic Cross Sections
- Fission Product Yields and Microscopic Cross Sections
- Assembly Discontinuity Factors (ADFs)
- Kinetics Data (Betas, Lambdas, Velocities)
- Spontaneous Fission/Alpha-n Neutron Sources
- Decay Heat Data (Fission Fractions by Isotope)
- Pin Power Distributions
- Detector Data

The functional dependence of the nuclear parameters is expressed as "base cross-section" and several "delta cross-sections" in the form:

$$NP^{S3R}\left(\rho, \sqrt{TF}, N_{xe}, N_{sm}, N_{Bo}, wfct_2, wfct_3\right) =$$
$$= NP_{Base}(\rho)$$
$$+ \frac{\partial NP}{\partial \sqrt{TF}}(\rho) \cdot \left(\sqrt{TF} - \sqrt{TF^{REF}}\right) +$$
$$+ \frac{\partial NP}{\partial N_{Bo}}(\rho) \cdot \left(N_{Bo} - N_{Bo}^{REF}\right) +$$
$$+ \frac{\partial NP}{\partial CR2}(\rho) \cdot wfct_2 + \frac{\partial NP}{\partial CR3} \cdot wfct_3 +$$
$$+ \delta NP(Xe) + NP(Sm)$$

For a given core life, all the history effects are frozen and only the instantaneous effects are input to S3R. The only instantaneous dependence is due to the moderator density, fuel temperature, control fractions, and boron. By freezing all history dependence, the calculation of the base cross-section is reduced to a set of 1D interpolations in density.

2.3   Decay Heat

Following a fission event in the fuel, about 93% of the heat of fission is immediately released, and the remaining 7% is released slowly over time. Modeling of this decay heat is very important in transients which have large changes in power level (e.g., Reactivity excursions, SCRAMs, and LOCAs). The fission product heat generation in S3R is modeled by using the ASNI/ANS-5.1, 23-group data. The decay heat sources are initialized as part of the steady-state solution in S3R by assuming infinite-time operation at constant power. It can be reset at any time after shutdown (see example in Sect. 5.1).

The predominant isotopes that contribute to decay heat are U-235, U-238, Pu-239, and Pu-241. The split among these isotopes varies from node to node with exposure. Effect of neutron capture in fission products and contributions from heavy elements (U-239 and Np-239) are also included.

2.4   Detectors

For in-core detectors, the detector responses are predicted as the power average from the surrounding nodes. The geometrical weighting factors account for the axial position of the detector. The detector constants are specified individually for each detector string and its surrounding channels and are obtained from the data library. Their radial locations as well as the number of axial strings and axial locations at each radial location are provided in the S3R input file. Flux data at these locations will be accessible from the instructor station and process computer.

In the case of ex-core detectors, top and bottom detector signals are constructed based on weighted sums of the flux at the core boundary and reflect accurately power imbalances and flux tilts. Detector response is based on flux value at the location of the detectors. A weighting is used to relate the ex-core detector response to the powers of the bundles contributing to it. Changes in the downcomer density cause changes in the attenuation of neutron escaping from the core and reaching the detectors and its effect is accounted for by using an empirical function of downcomer density.

3   Coupling to System Code

This section describes the algorithm and software used to expand thermal-hydraulic data from an RCS model, such as RELAP5, to S3R and collapse nodal powers from S3R to RELAP5-3D. RELAP5-3D is used as an example herein; however, the coupling algorithm may be applied to any system code which can model core channels. The RELAP5-3D model uses a coarser nodalization in the active core regions than S3R and a method for expanding the RELAP5-3D data from this coarse nodalization to the fuel assembly wise data needed for S3R is needed. The axial nodalization may also be different between the models and this is addressed by the algorithm.

For a 3-loop PWR, typically RELAP5 groups the assemblies into 4 active channels (each representing 39¼ assemblies). The channels assignment is illustrated in the figure below. S3R uses 5 radial power zones. The fifth zone receives the average properties from the 4 RELAP5 channels. This is illustrated below.
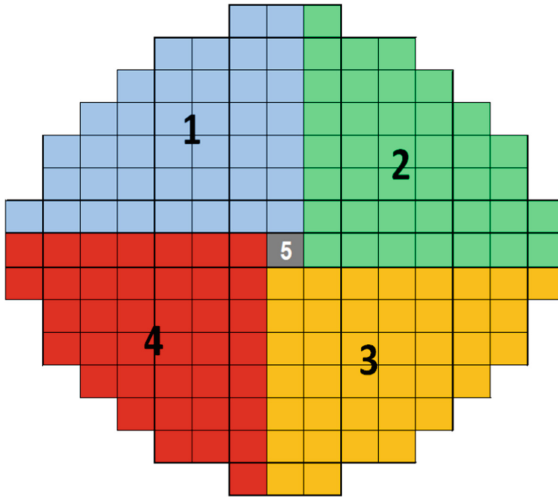
In the axial direction, a possible nodalization used in RELAP5 is:

– 6 hydraulic cells per channel
– 24 heat structures per channel

S3R uses 24 axial levels per assembly (see illustration below).

A mapping scheme that takes the RELAP5 data and expands it from the RELAP5 geometry to the S3R nodalization and collapses the S3R data for use in RELAP5 has been implemented in S3R.

The algorithm is comprised of three parts. The first part takes the thermal-hydraulic data and expands it to S3R axial nodalization utilizing an axial power weighting scheme in each thermal-hydraulic channel. The second part uses a power-weighting scheme to expand the fuel temperatures in the radial direction using the last time step 3D power distribution. The third part uses a simple enthalpy rise model and last time step 3D power distribution to calculate the nodal moderator densities.
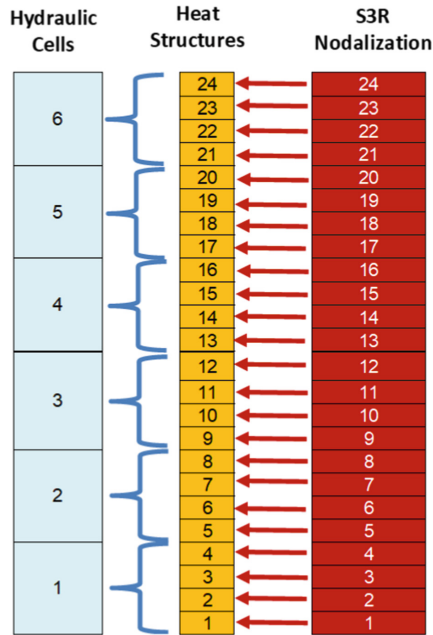
A few assumptions are made:

- The number of axial subdivisions in the RELAP5 volumes and/or heat structures for the active fuel shall be such that an integer multiple of S3R axial nodes are bound by a volume or heat structure height.
- The number of axial subdivisions in the RELAP5 volumes and/or heat structures shall not be greater than the S3R axial nodalization.
- The number radial flow paths used in the RELAP5 model shall only include full assemblies, assemblies may not be subdivided.
- Thermal-hydraulic data shall be provided for the lower and upper plenum regions of the RELAP5 model for use in the reflector cross-section calculations.

4 Interfface with Executive

S3R is used as a library used during the generation of the load regardless of the real-time executive used on the simulator. There are basically two interface routines used to transfer data back-and-forth between S3R and the rest of the simulator. An illustration of what is exchanged at each time step is shown here.
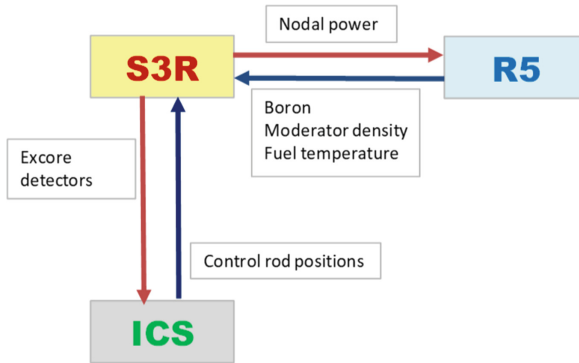
5 Cycle Update and Initial Conditions

The key factor in updating the core data on the training simulator for S3R is that all the information needed for such an update is contained in the SIMULATE nuclear data library and restart files. The transfer of data from core depletion calculations to the simulator is automatic and does not require any intermediate program or additional data manipulation.

To update the core model with data for a new cycle, the following information needs to be supplied by the organization that maintains the CASMO/SIMULATE model:

a) Nuclear data library for the new cycle from Studsvik's CMS system.
b) Restart file(s) for the new cycle with enough exposure points to be able to model all core lives of interest (e.g., BOC, MOC, EOC, etc.).
c) Input and output files from the S3 core depletion calculations. This is needed to conveniently determine the conditions used at each depletion point and the exposure points saved on the restart file.
d) The boron concentration used during the core depletion calculations for the core lives of interest.
e) Updated S3R input files (essentially only the 'RES' and 'LIB' cards) to provide names of the new data files and point to the exposure of interest.

The process of updating ICs with new core data is straightforward and includes the following steps:

• Acquire the nuclear data files (S3 restart and library files) for the new cycle
• Edit the S3R input file to point to the new nuclear data files
• Reset to an existing IC
• Set the boron concentration
• Snap to a temporary location
• Reset to snapped IC to reinitialize (this step accesses the new core data)

- Run until steady state has been established at the desired power level, while using the fast xenon flag to force xenon to equilibrium.
- Snap IC. Process completed.

Depending on the real-time executive, it may be possible to automatize this process using scripts. An example from one site includes the different parts in which the conditions of the existing ICs are used to generate an IC-specific restart file to be used in updating the ICs with the new cycle core data. This is illustrated below.
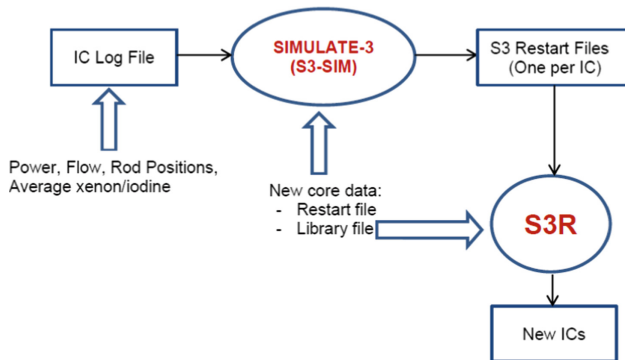
6 Physics Testing

The S3R core model has been validated against CMS results, vendor codes, and plant data when available. As part of the implementation of S3R on a training simulator, standalone physics testing is conducted to compare, in the case of PWRs, power distributions, critical boron concentrations, boron coefficients, temperature coefficients, bank worths, and xenon and samarium worths.

This is done by running S3R (with its own internal TH model) and compare it to the design code (SIMULATE-3 or SIMULATE5). Results from the vendor's code, typically available in the Nuclear Design Report, are also used to validate the S3R model.

Finally, S3R predictions are validated against plant data, such as data collected during the Low-Power Physics Tests conducted during the plant startup and flux maps when these are generated.

Examples of comparison results are show below for boron letdown, temperature coefficient, and bank worths.
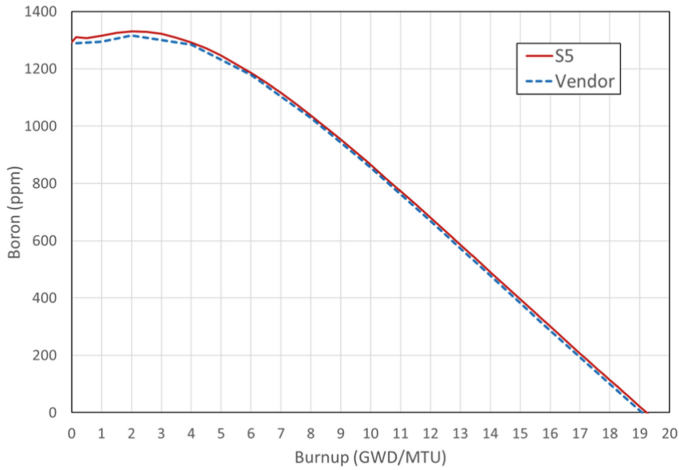
Core Condition	S5 (pcm/C)	S3R (pcm/C)	S3R-S5 (pcm/C)
ZBC	-2.38	0.00	2.38
BOC	-1.71	0.52	2.23
MOC	-11.84	-11.03	0.81
EOC	-30.47	-29.81	0.67

Configuration	S5	S3R	Measured
CA	1268	1309	1131
CB	270	286	294
CC	1180	1224	1241
CD	731	762	678
SA	789	819	775
SB	1320	1361	1252

7   Core Monitoring

Many LWRS use a core monitoring system in the plant control room. These core monitor systems combine measured data and physics calculations to provide operations assistance information. For a variety of reasons, these systems are frequently not available in the simulated control room or are available only via a simplified emulation.

Although conceptually simple, there have been obstacles to implementing core monitoring in the simulator control room. Besides cost and hardware, one important issue from a training point of view is accuracy. The simulator core models take the place of measured data in the plant. The core monitoring system takes measured data and performs calculations to predict things that are not measured. If the simulator is generating inaccurate "plant data," the simulator core monitoring system will generate an inconsistent plant state, and the predicted results will be unusable.

Since S3R is an engineering-grade core model and replicates closely design calculations, it can be used to provide data to a core monitoring system in lieu of the process computer in the plant. This has been demonstrated in several sites which use the simulator version of the Studsvik Core Monitoring product GARDEL. This version, called GARDEL-SIM, runs on its own server (PC, Linux, or Unix) and responds consistently to executive commands such a run, init, freeze, etc. It also responds to numbered Initial Conditions (ICs) or backtracks and gets "plant data" directly from the simulator database.

The data requirement for GARDEL-SIM is the same data required by S3R. No additional data is required.

8 Additional Items

8.1 Decay Heat Reset

S3R includes several fast flags to advance the fission products (Xe and Sm) solution or the decay heat solution faster than real time. One option for decay heat is to be able to reinitialize to a representative decay heat at a given time after shutdown. An example is shown below. This figure shows three curves:

- The base case in red with the expected decrease of decay heat after shutdown
- The case with multiple reinitialization in blue with:

  (1) Reinitialization to 10 days after shutdown
  (2) Reset to about 52 s after shutdown
  (3) Reset to about 17 s after shutdown
  (4) Reinitialization to 1 day after shutdown

- Verification that time behavior after reset to 52 s after shutdown is preserved (broken green line)

This code feature makes the control of the amount of decay heat after shutdown and its impact on the response of the system very straightforward alleviating any need for guessing or tuning.
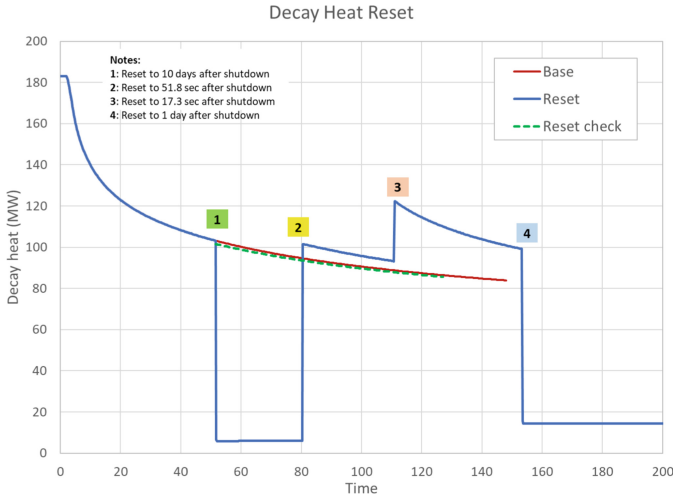
8.2 Xenon Worth

In most cases, the calculation of xenon worth edit is assumed to be proportional to the average xenon concentration. This is a valid assumption in typical LWRs and is one of the methods used in S3R. Not this is only used for providing a xenon.

One case where this assumption shows its limitation is when the core uses mixed UO2 and MOX assemblies. The MOX fuel assemblies have higher initial (equilibrium) Xenon number density due to larger yield and smaller absorption cross section, which dominates the total xenon in the core. On the other hand, the Xenon worth is larger in UO2 fuel (due to softer spectrum) than MOX, and this dominates the core reactivity. Therefore, the time to peak differs between MOX and UO2.

The figure below show change in xenon concentration (red) and the change in xenon worth (blue) following a scram. The largest xenon worth change occurs about one hour later than the peak xenon.

Xenon Response
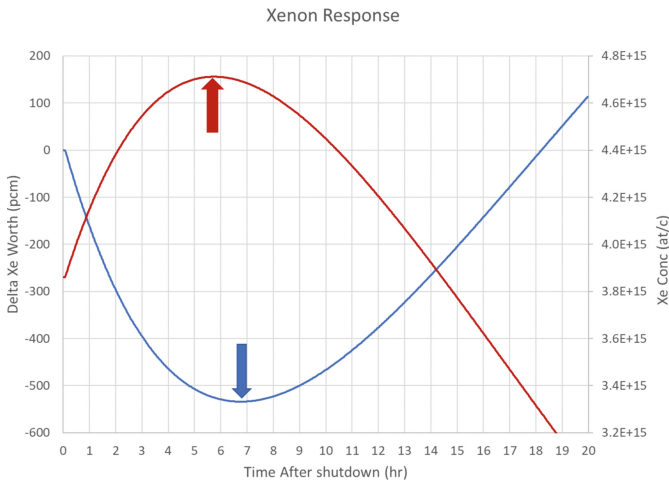
9 Conclusions

S3R and its connection to the design methods of Studsvik has been demonstrated as the go-to tool for training simulators. Since it can directly take data from the depletion calculations, it makes the cycle update automatic and the process of generating new ICs fast and easy. With S3R, training anywhere in the cycle or performing just-in-time training, is readily available.

References

1. Borkowski, J.: SIMULATE-3K Models and Methodology. SOA-98/13 Rev 0 (1998)
2. Borkowski, J.: Core monitoring applications in the simulator control room. In: Power Plant Simulation Conference, San Diego, California (2007)

Study of Stress Analysis Method for Floating Nuclear Power Plant Containment Under Combined Multiple Loads

Jiyue Li, Donghui Wang, Meng Zhang[✉], Hongbing Liu, and Xianqiang Qu

Harbin Engineering University, Harbin, Heilongjiang, China
{lijiyue,zhangmeng}@hrbeu.edu.cn

Abstract. Floating nuclear power plants (FNPP) are a combination of small nuclear reactors and hull structures. The applicable design codes and simulation analysis methods of floating nuclear power plants are nearly seldom, especially for the ultimate strength of containment considering multi loads. In order to analyze the structural strength of the steel containment of a floating nuclear power plant under the combined action of multiple loads, the structural response is analyzed in ANSYS considering the external hull loads and internal containment loads such as wave loads, wind loads, current loads, hull impact loads, internal pressure and temperature of the containment. The structural response result from wind, wave, current, internal pressure and temperature loads are calculated, separately, to obtain the stress field of the containment. Finally, the stress fields of the containment generated by each load are superimposed to obtain the stress distribution characteristics of the containment, and then strength assessment and stress analysis are performed.

Keywords: Floating nuclear power plant · combined multi-load action · quasi-static equivalence · containment · stress analysis

1 Introduction

As small reactor technology continues to develop, the advantages of using nuclear reactors on offshore floating platforms to provide energy such as electricity for areas such as offshore oil extraction or remote areas are emerging. In addition, offshore nuclear power plants can also meet a variety of needs such as heat supply and desalination. As a combination of small nuclear reactors and offshore vessels, offshore floating nuclear power plants are becoming a hot spot for engineering research applications. How to ensure the safety of reactors and floating platforms under various accidental operating conditions and extreme loads has become the focus of technical research on offshore floating nuclear power plants [1].

At present, the most mature floating nuclear power plant is the Russian "Lomonosov", which is a large unpowered barge carrying two "KLT-40" type nuclear reactors [2]. In the USA, MIT has designed and developed a new offshore cylindrical floating nuclear power plant that combines an advanced light water reactor with a floating platform,

similar in structure to an offshore oil and gas plant [3]. South Korea and France have each developed concepts for the safe design of floating nuclear power plants by submerging them underwater [4].

The safety of floating nuclear power plants is a central factor in their structural design. Because floating nuclear power plants have a nuclear reactor compartment that houses the containment and support structures that encase the reactor, the safety requirements for the containment structure during the design phase are higher than those for conventional nuclear reactors and conventional marine platforms. Under the unique accident conditions of a nuclear power plant and the superposition of multiple accident loads in the sea, both the internal steel structure of the containment and the external support elements are subject to material yielding or structural failure. Therefore, we need to take into account the external hull loads and internal containment loads in various typical marine environments, such as wave loads, wind loads, current loads, hull impact loads, internal pressure in the containment and temperature.

In this paper, the structural response to the combined effects of multiple loads is analyzed in ANSYS, and the structural response to the wave, hydrostatic, internal pressure and temperature loads are calculated separately to obtain the stress field of the containment under the individual effects of the above loads.

2 Materials and Methods

2.1 Study Subjects

The finite element analysis software ANSYS is used to build the overall analysis model of the floating nuclear power plant including the hull and the containment (including support) structure, in which the hull part uses shell cells, the bone part uses beam or shell cells, and the steel containment (including support) uses solid cells.

The hull structure finite element model is constructed using shell181 and beam188 cells, the mesh size of the containment and support part is 0.1 m, the mesh size of the support and hull transition part is 0.2 m, and the rest of the mesh size is 0.8 m. For the pressure vessel structure which is the focus of analysis, the shell cell is used to simplify the analysis. Steel containment shells and internal components such as multi-layer platforms, core shells and pressure suppression pools were established. The geometric model is shown in Fig. 1.
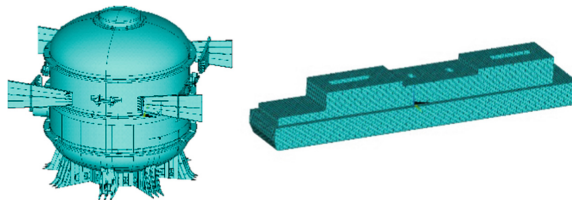
Fig. 1. Geometric model of vessel structure and FNPP

Because of the special characteristics of the nuclear reactor in the containment compartment, the steel plate material used for the containment structure cannot be traditional

marine steel, but needs to be high strength steel. In this paper, SA738GrB steel is chosen as the material strength standard. The material properties are shown in the table below (Table 1).

Table 1. SA738GrB steel material properties

Material properties	SA738GrB
Young's modulus(MPa)	2.06E5
Poisson's ratio	0.3
Density(kg/m^3)	7850
Yield limit(MPa)	415
Tensile limit(MPa)	585

2.2 Combination of Working Conditions

The containment structure needs to meet the strength requirements of the load combinations under different categories of operating conditions. Combined with the design provisions of the MC class components in the ASME Code [5], the containment loads are divided into several categories of operating conditions such as A, B, C and D.

Referring to the onshore nuclear power plant containment analysis model, the floating reactor will focus on the marine environmental loads, and the design wave is selected as the ultimate wave load in this paper, replacing the onshore nuclear power plant seismic load. In addition, there are external loads caused by man-made events, such as ship collisions, as accidental load conditions for floating reactor containment. Therefore, the design conditions and load combinations for the containment are shown in Table 2. In the table, I to VIII denote gravity, hydrostatic pressure, ultimate wave load, operating pressure, abnormal pressure, accident pressure, thermal load under accident conditions, and collision load respectively.

Table 2. Combination of loads and working conditions

Load	Working conditions	A	B	C	D
Fixed load	I	✓	✓	✓	✓
	II	✓	✓	✓	✓
Environmental loads	III		✓	✓	✓
Working load	IV	✓	✓		
Design accident load	V			✓	
	VI				✓
	VII			✓	✓
Artificial event load	VIII				✓

2.3 Internal Pressure Loads and Temperature Loads

Nuclear power platforms with a range of design basis accidents based on regulatory or accident analysis assumptions are a fundamental requirement for system design to be met. For reactors, the design basis accident for floating nuclear power plant containment can be modelled on that for land-based nuclear power plants. It is generally accepted that the most serious baseline accident is the Loss of Coolant Accident (LOCA), which causes an increase in containment pressure and temperature [6], and the containment design should meet the structural integrity under this condition.

In the event of a LOCA accident, the pressure inside the containment rises rapidly from 0.1 MPa to 0.8 MPa, and under containment pressure suppression measures the pressure drops to about 0.6 MPa and the temperature drops to about 150 °C.

Combined with the operating conditions of a floating nuclear power plant, the maximum vessel temperature of the containment for accidental operation is 300 °F (148.89 °C) according to the US onshore AP1000 nuclear power plant containment design control document. In the workbench steady state thermal module, the temperature field of the containment and the floating nuclear power plant as a whole can be simulated, and the thermal stresses in the containment structure can then be calculated (Fig. 2).
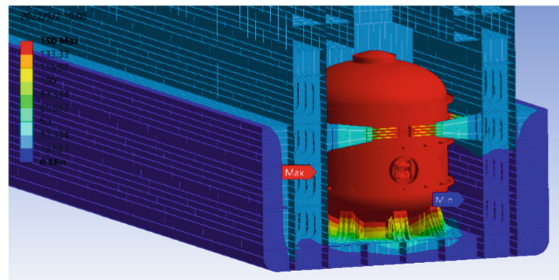
Fig. 2. Temperature field of part of the structure

It is therefore considered that the containment abnormal pressure is 0.6 MPa and the accident pressure is 0.8 MPa. The accidental service heat load can be calculated indirectly by importing the.rth whole ship temperature field in ANSYS to calculate the whole ship temperature stress.

2.4 Wave Load

The principle of design waves is to replace randomly distributed waves with a series of regular wave equivalents. In order to be able to reflect the maximum force on the platform, the equivalent design waves should put the platform in the most dangerous wave loading condition. The design wave method can simplify the calculation process of wave loads and is widely used by the engineering community. At present, it is mainly divided into deterministic methods, stochastic methods and long-term forecasting methods.

The stochastic design wave method is a short-term forecast of the platform through the wave spectrum, which is more informative than the deterministic design wave method as it reflects the random nature of waves.

Firstly, the overall hydrodynamic characteristic response and load transfer function RAO are determined, then the appropriate wave spectrum $Sw(\omega)$ is selected based on the meaningful wave height in the short-term sea state, and the response spectrum $SR(\omega)$ of the wave load is calculated, i.e. $SR(\omega) = [RAO(\omega)]^2 Sw(\omega)$.

Finally, the maximum load response value R and the corresponding load transfer function are selected to calculate the design wave amplitude. The design wave amplitude, A, for stochastic design wave forecasting can be calculated by the following equation: $A = (Rmax/RAO)$. The process is shown in the diagram below (Fig. 3).
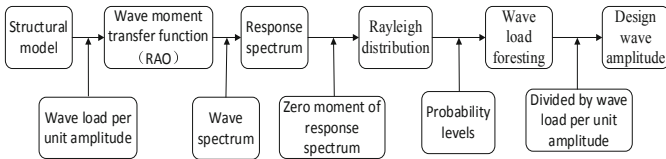
Fig. 3. Design wave calculation flow chart

2.4.1 Frequency Domain Wave Transfer Loads

Regarding the analysis of the load-bearing characteristics of the structural system of floating nuclear power plants under wave action, firstly, based on the overall analysis model of floating nuclear power plants established by ANSYS, the overall hydrodynamic analysis model of floating nuclear power plants can be established using ANSYS-AQWA in combination with the weight of the reactor of the floating nuclear power plant, the center of gravity and other parameters, and further carry out the overall hydrodynamic analysis of floating nuclear power plants under all-round wave incidence angle to obtain the relevant The wave load distribution characteristics of the overall structure of the floating nuclear power plant in the relevant sea area were obtained.

In this project, the waves are divided into 13 directions for analysis, with wave directions set at 15° intervals from 0° to 180°. Load them into the hull to calculate the structural response, the structural response is the corresponding structural under the action of unit wave amplitude, extract the combined force acting on top of the floating nuclear power plant containment, the transfer function is the modulus square of the extracted combined force, thus the transfer function obtained.

2.4.2 Wave and Response Spectra

Due to the shallow depth of the marine structures analyzed in this project and the combined distribution of effective wave height and spectral peak period, the improved JON-SWAP spectrum is recommended for the prediction of wave loads in different wave directions. The improved JONSWAP spectrum is expressed in the following form.

$$S(f) = \beta_J H_{\frac{1}{3}}^2 T_P^{-4} f^{-5} \exp[-\frac{5}{4}(T_P f)^{-4}]\gamma^{\exp[-(\frac{f}{f_P}-1)^2 / 2\sigma^2]} \tag{1}$$

Wave loads on ships are forecast using spectral analysis. Short-term forecasts are generally within a few hours, so short-term waves can be considered as a smooth normal

stochastic process with zero mean, where the response of the ship to the waves can be considered as a linear relationship, so the wave load response is also a smooth normal stochastic process with zero mean. The response spectrum of a ship's wave load can be expressed as the product of the wave spectrum and the transfer function squared, i.e.

$$S_w(\omega) = |H_w(\omega)|^2 \cdot S_\xi(\omega) \tag{2}$$

Considering the diffusion effect of the wave, a diffusion function can be introduced, which is the angle between the combined wave and the main wave direction. The diffusion function can generally be taken as:

$$fs(\theta) = \frac{2}{\pi} \cos^2 \theta \tag{3}$$

Calculating the nth order spectral moment of the response spectrum yields a range of response values.

$$m_n = \int_0^\infty \int_{-\frac{\pi}{2}}^{\frac{\pi}{2}} \omega_n \cdot f_s(\theta) \cdot S_w(\omega) d\theta d\omega \tag{4}$$

where is the spectral moment of order of the response spectrum; is the angle between the combined wave and the main wave direction.

It has been shown that the short-term response of the ship's wave load amplitude follows a Rayleigh distribution with a probability distribution function F(x) of

$$F(x) = 1 - \exp(\frac{-x^2}{2m_0}) \tag{5}$$

$m0$ is the 0th order moment of the response spectrum. The amplitude of the wave load response of the ship corresponding to any exceeded probability level in a certain sea state can be obtained. The design value of wave load R for a ship at a certain number of fluctuations N is:

$$R = \sqrt{2m_0 \cdot \ln N} \tag{6}$$

2.4.3 Determination of Design Wave Parameters

The maximum meaningful wave height for a floating nuclear power plant in the vicinity of the operating sea is 5.2 m with a spectral peak period of 7.8 s. The wave load design calculates the wave bending moment at a probability level of 10^{-8} for a 500 years event. The design wave amplitude is calculated by taking the maximum load response value R and the corresponding load transfer function per unit wave amplitude. The design wave amplitude, A, for a stochastic design wave forecast can be calculated by the following equation:$A = (Rmax/RAO)$.

From this the design wave height corresponding to the wave bending moment at the 10^{-8} probability level can be calculated, as shown in the table below (Table 3).

Table 3. Design waves at the 10^{-8} probability level

Wave (°)	Wave moment forecasting(N*m)	RAO(N*m/m)	Design wave amplitude(m)
0	6.83E + 08	6.19E + 08	1.1
15	7.21E + 08	6.00E + 08	1.2
30	8.90E + 08	5.42E + 08	1.7
45	1.46E + 09	4.84E + 08	3.0
60	2.30E + 09	4.32E + 08	5.3
75	1.39E + 09	2.02E + 08	6.9
90	3.24E + 08	5.63E + 07	5.8
105	1.26E + 09	1.87E + 08	6.7
120	2.16E + 09	4.13E + 08	5.3
135	1.44E + 09	4.75E + 08	3.1
150	8.67E + 08	5.43E + 08	1.6
165	6.80E + 08	6.02E + 08	1.2
180	6.38E + 08	6.21E + 08	1.1

2.5   Crash Load

Collision simulation and quasi-static equivalence in the workbench LS-DYNA module. A container ship with a displacement of 5000 T was selected for this artificial accident load. Lateral collision stresses were calculated to simulate the most dangerous external accident. The impact site is the middle port side of the transom hold.

The dynamic forces of the collision need to be converted into equivalent static forces so as to superimpose with other physical field stresses, there are relevant international codes to simplify the calculation of ship collision forces, among which the European code and the American code are more commonly used and accurate. 1999 European code gives the ship collision force calculation formula to consider the ship navigation waters. The formula given in the 1999 Eurocode takes into account the impact of the ship's speed and tonnage on the collision force and is more applicable to this case.

The simplified Eurocode formula for ship collision force is shown below.

$$P = v\sqrt{Km} \tag{7}$$

where P is the collision force (N), v is the ship impact velocity, K is the ship equivalent stiffness, for sea area ships can be taken as 15×106 N/m, m is the collision ship mass (kg).

Through the formula calculation, 2m/s impact of 5000 tons ship equivalent collision static force is 1.73x107N.

2.6 Stress Analysis Methods

Based on the ASME Code, we use the Analytical method to carry out stress intensity checks. We classify the stresses at each check point along the thickness direction to obtain the corresponding membrane stress, bending stress and peak stress.

The membrane stress is the average of the target stresses integrated in the thickness direction and the bending stress is the total stress at the point of integration in the thickness direction minus the membrane stress, i.e. the sum of the membrane stress and bending stress is the stress on the surface of the shell unit. According to the stress intensity calculation method specified in the ASME Code, the stress intensity value of the target node is the Tresca stress value.

For a node connected to different units, the magnitude of the stress value extrapolated to the node by each unit is not necessarily the same. The FEA software usually uses the arithmetic mean of the above extrapolated stress values as the equivalent of the stress value at the node. However, in the case of a discontinuous structure or a local structure with a non-uniform distribution of stress levels, the stress values extrapolated to the node vary considerably and the use of arithmetic averaging to estimate the stress level at the node is not desirable. Therefore, when calibrating the strength of the containment, the extrapolated stress value of the unit in the region with the higher stress level should be used as the stress value at the node.

3 Results

3.1 Stress Evaluation

Different levels of service have different stress limits in the elastic analysis, for the design condition and the limits specified for the operational condition, as shown in the table below (Table 4).

Table 4. Limits and stress limits for different operating conditions during elastic analysis of pressure vessels

Restrictions	P_m(MPa)	P_L(MPa)	$P_m + P_b$(MPa)
Design constraints	$\leq S_m$	$\leq 1.5 S_m$	$\leq 1.5 S_m$
A	–	–	–
B	$\leq 1.1 S_m$	$\leq 1.65 S_m$	$\leq 1.65 S_m$
C	$\leq Min(S_y, 2/3S_n)$	$\leq Min(1.5S_y, S_n)$	$\leq Min(1.5S_y, S_n)$
D	$\leq 0.7 S_n$	$\leq S_n$	$\leq S_n$

where S_y, S_m, S_n are the yield strength, design strength and tensile strength respectively.

3.2   Individual Load Conditions

The stress response of the whole vessel under the above loads acting separately and independently was calculated in ANSYS and the maximum stresses in the pressure vessel structure under each load were extracted. The results are shown in the Table 5 and Fig. 4.

Table 5. Stress strength assessment and calibration for each individual load condition

Load	P_L Max (MPa)	Stress limits (MPa)	$P_L + P_b$ Max (MPa)	Stress limits (MPa)
Design wave	96.2	390	99.53	585
0.8MPa	244.16	409.5	246.65	585
0.6MPa	170.95	409.5	171.64	585
0.1MPa	28.78	202.3	33.5	303.4
Hydro pressure	143.44	183.9	177.72	275.9
Collision	21.02	390	247.8	585
Thermal stress	415.45	409.5	441.7	585

After analysis, the film and bending stresses of all load components except thermal stresses meet the stress limits.
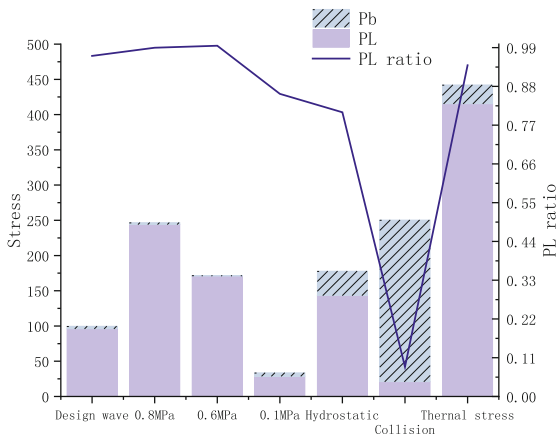
Fig. 4. Individual load stress analysis

Only one node exceeds the stress limit under thermal stress, the maximum stress occurs at the bottom support of the containment shell, the film stress at the node at the maximum stress location is 415.45MPa, the maximum film stress plus bending stress is 441.70MPa, the maximum stress occurs locally. The other locations of the bottom support

are all less than 400MPa, the maximum stress at the containment shell is 85.63MPa and the maximum stress at the pressure suppression pool is 274.15MPa, both of which meet the stress limits.

3.3 Combined Load Conditions

The stress field results are calculated individually and obtained as rst results files, after which the stress field results are superimposed according to the combination of conditions to obtain the superimposed stress field and then analyze the structural stress distribution. The superimposed stress field for the whole ship and the containment stress field (Fig. 5).
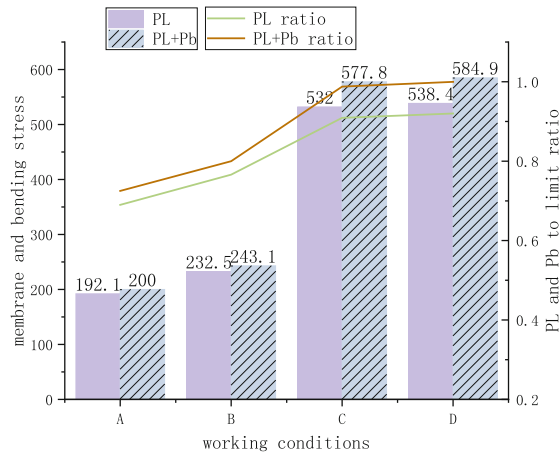
Fig. 5. Combined load conditions stress analysis

4 Discussion

Comparing the structural response of the hull under each condition individually, it can be seen that hydrostatic pressure, temperature load and internal pressure have a greater influence on the stresses of the whole ship and the containment structure.

Comparing the elastic stress composition of each condition, the stresses caused by internal pressure are primary stresses; the temperature load, design wave and other conditions belong to the stresses generated by the containment structure to meet the displacement restraint conditions or the continuous requirements of its own deformation after being subjected to displacement loads, which are secondary stresses. The internal pressure, hydrostatic pressure, thermal stress and design wave conditions are mainly composed of film stress, and bending stress is small; while the bending stress accounts for a large proportion of the stress in the collision condition.

For the composition of the combined working condition stress: for the maximum stress point at the bottom support, mainly the high temperature thermal stress and hydrostatic pressure have a large force on it. For the internal structure of the containment,

especially the relatively high stress parts of the ground floor platform and the outer shell, are mainly affected by internal pressure and thermal stresses.
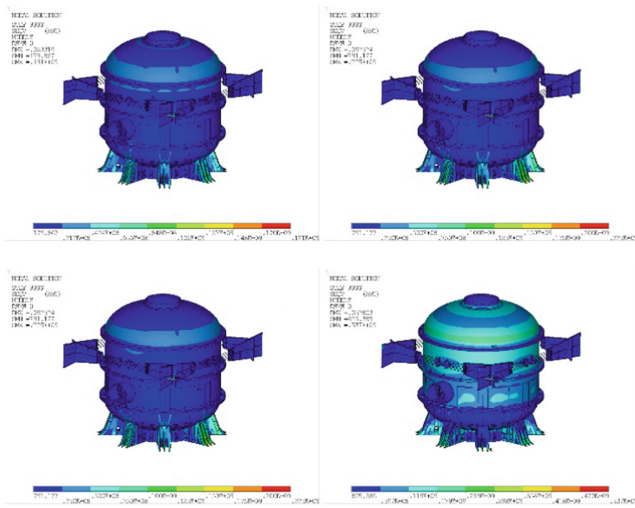
Fig. 6. Pressure vessel mises stress clouds for operating conditions A, B, C and D

The stresses on the containment structure are calculated to be lower in conditions A and B and higher in conditions C and D under extreme loads. The stress distribution of the pressure vessel mises under working conditions A, B, C and D is shown in Fig. 6. The maximum stresses occurred at the bottom support and the inner base plate weld, while the maximum film stress in accident condition D was 538 MPa, reaching 92% of the stress limit, and the sum of the maximum film stress and bending stress was 584.9 MPa, reaching 99.6% of the limit. These are local stress and the overall maximum film stress in the bottom support is approximately 254MPa, which is below the ASME Nuclear Code and Standard Stress Strength Assessment Value, and below the Offshore Mobile Platform Entry Code Allowable Strength and Material Yield Value. This indicates that the design of the structure satisfies the containment and floating nuclear power plant limits for self-sustainability.

References

1. Qiu, C.F., Deng, J., Chen, H.H., Li, F., Yu, N., Wu, P., et al.: Modular small reactor overpressure risk and design optimization study. Atomic Energy Sci. Technol. **50**(1), 5 (2016)
2. Dowdall, M., Standring, W.: Floating nuclear power plants and associated technologies in the northern areas. Norwegian Radiation Protection Authority (2008)
3. Kindfuller, V., Todreas, N., Buongiorno, J., et al.: Overview of security plan for offshore floating nuclear plant. In: International Conference on Nuclear Engineering, V005T15A076 (2016)
4. IAEA. Nuclear Technology Review. Section B, Advanced Fission And Fusion (2014)

5. American Society of Mechanical Engineers. ASME BPVC-III rules for construction of nuclear facility components. Volume 1 NE Sub-volume: MC-class components. 2004 Edition. Shanghai Science and Technology Press, Shanghai (2007)
6. Tan, M,. Li, P.F., Guo, J., et al.: Design of floating nuclear power plant containment under marine environment conditions. Chin. J. Ship Res. **15**(1), 107–112, 144 (2020)

Analytical Method to Study the Ultimate Bearing Capacity of Containment for Floating Nuclear Power Plants Considering Wave Loads

Shuo Mu[1,2], Lijuan Li[3], Meng Zhang[1(✉)], Hongbing Liu[1,2], and Xianqiang Qu[1,2]

[1] Yantai Research Institute and Graduate School, Harbin Engineering University, Yantai, China
{mushuo,zhangmeng}@hrbeu.edu.cn
[2] College of Shipbuilding Engineering, Harbin Engineering University, Harbin, China
[3] Nuclear Power Institute of China, Chengdu, China

Abstract. In floating nuclear power plant (FNPP), important equipment such as nuclear pressure vessel, pressure pipeline and pressurizer are installed in the containment, which is the last safety barrier of the reactor primary circuit of FNPP. The ultimate bearing capacity of containment is one of the important safety indexes of FNPP. In this study, considering the wave load, internal pressure load and their corresponding combination conditions in the sea area of FNPP, the overall finite element model of FNPP and the local finite element model of containment are established by using ANSYS software. The ultimate bearing capacity of containment structure is analyzed by nonlinear method. The ultimate internal pressure that the containment can bear is analyzed based on the wave load. Two methods are used to analyze the ultimate internal pressure that the containment can withstand. One is direct analysis method to directly carry out nonlinear analysis of the whole ship model. The other, called indirect analysis method, first makes a linear analysis of the whole ship model to calculate the input load transmitted from the marine environment to the containment through the containment support, and then uses the nonlinear method to analyze the ultimate internal pressure that the containment can withstand. The analysis results of the above two methods show that the ultimate bearing capacity of the containment is basically consistent, while the efficiency of the indirect analysis method is higher. In addition, the ultimate bearing capacity of the containment is far beyond the design requirements considering the wave load.

Keywords: floating nuclear power plant · containment · ultimate bearing capacity · direct analysis method · indirect analysis method

1 Introduction

At present, the research on the ultimate strength of offshore platform structures has become a hot topic in the field of international offshore engineering. For the structural design of offshore platforms, the limit state based design method has been introduced [1]. Through the calculation of the ultimate strength of the platform, the dangerous

component parts can be predicted, and the local strengthening of the components can timely control the degree of damage and reduce the potential crisis. Up to now, scholars have put forward different research methods for the ultimate strength of ship structures, and several of them have been widely recognized and gradually improved. At present, the ultimate strength analysis methods of hull structures mainly include: direct calculation method, nonlinear finite element method, progressive collapse method, ideal structural element method and model test method.

The direct calculation method is also called Caldwell method. In 1965, Caldwell [2] first proposed the plastic behavior of the total longitudinal strength of surface ships, and derived the analytical formula of the total longitudinal ultimate strength. In view of the limitations of Caldwell method, Smith [3] proposed a relatively simple method based on Caldwell method, taking into account the reduction of strength after the member reaches the ultimate strength, and thus the progressive collapse method is also called Smith method. Another simple method for progressive failure analysis of hull beams is the ideal structural element method (ISUM) proposed by Japanese scholar Ueda et al. [4] in the 1980s. With the general improvement of computer hardware level, the finite element method (FEM) has been applied more often to engineering problems. Compared with the above analysis methods, the physical test can more directly reflect the collapse process of the ship structure and measure the ultimate strength of the structure. Dow [5] established a hull beam model of a frigate at a scale of 1/3 and conducted ultimate strength tests. Nishihara [6] conducted a series of collapse tests under pure bending load on a box beam model similar to the corresponding ship structure. The phenomena and results observed in the experiment also have high reference value for theoretical calculation and numerical simulation.

2 Nonlinear Analysis Method

Chen [7] et al. proposed a finite element method for hull ultimate bearing analysis, which is applicable to any loading type and structural model. This method introduces three element types: beam element, plate element and orthotropic plate element, which can analyze the limit state of the structure under static or dynamic loads, and It can also analyze the overall response of a single member (deck, side, bulkhead, longitudinal girder, etc.) and consider the response of the hull under the combined action of bending moment, torque and shear force. Kutt [8] et al. used nonlinear analysis method to analyze the longitudinal ultimate strength of four hulls, reflecting the interaction between various local and overall failure modes and the interaction between the elastic−plastic, buckling and post buckling effects of materials.

With the development of calculation technology and nonlinear finite element, many large general finite element programs, such as NASTRAN, ANSYS, ABAQUS, Marc, have been applied to the ultimate strength calculation of ship structures. Based on the nonlinear finite element method, this chapter will use the finite element software ANSYS to study the solution method.

2.1 Arc length method

The arc length method is a static analysis method based on the Newton Raphson iterative solution of the nonlinear static equilibrium equation of the structure [9]. Its basic idea is to set a parameter (arc length l) to control the incremental iteration and convergence of the equilibrium equation.

$$\{P\} - \{I\} = 0 \tag{1}$$

$$[K_T]\{\Delta u\} = \{\Delta P\} - \{R\} \tag{2}$$

where $[K_T]$ is tangent stiffness matrix, $\{\Delta u\}$ is the displacement increment, $\{\Delta P\}$ is load increment, $\{R\}$ is residual force.

When using the arc length method, let the $i-1$ load step converge to (x_{i-1}, P_{i-1}), for the i load step, j iterations are required to reach the new convergence point (x_i, P_i). Step i iterates the true load size $\{\Delta P\}$ acting on the structure, which is determined by the load increment factor $\Delta\lambda_i$ and the input external load $\{P_{ref}\}$,

$$\{\Delta P\}_i = \Delta\lambda_i\{P_{ref}\} \tag{3}$$

By introducing Eq. (3) into Eq. (2), the incremental form of iteration i of arc length method can be obtained:

$$[K_T]\{\Delta u\}_i = \Delta\lambda_i\{P_{ref}\} - \{R\}_i \tag{4}$$

The position of the equilibrium point in step i is obtained by Newton Raphson iteration with the equilibrium point calculated in step $i-1$ as the center of the circle and the arc length increment Δi as the radius, as shown in Fig. 1. The arc length increment Δl_i, load increment factor $\Delta\lambda_i$ and displacement increment $\{\Delta u\}_i$ of each step satisfy the governing equation of Eq. (5).

$$\Delta l_i^2 = |\{\Delta u\}_i|^2 + \left|\Delta\lambda_i\{P_{ref}\}\right|^2 \tag{5}$$
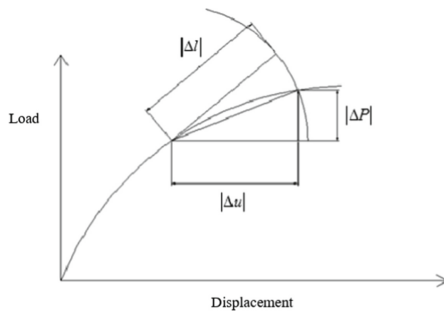
Fig. 1. Load displacement curve

Through iteration, until the residual force is within the tolerance {R}, when the iteration of step i is completed, there are:

$$\text{Load array } \{P\}i = \sum_i \{\Delta P\}_i = \sum_i \Delta\lambda_i\{P_{ref}\} \tag{6}$$

$$\text{Displacement array } \{u\}_i = \sum_i \{\Delta u\}_i \tag{7}$$

$$\text{arc length } l_i = \sum_i \Delta l_i \tag{8}$$

The arc length increment Δl contains the information of load increment and displacement increment at the same time. As long as the appropriate iteration step is selected, the arc length method can track the load displacement equilibrium path of the structure in the process of loading and unloading, and effectively solve the 'step' problem in the limit equilibrium path.

2.2 Quasi Static Method

In essence, the quasi−static analysis method is a dynamic solution process of structure. The basic idea of the quasi−static method is to simulate the static problems with the dynamic analysis of slow loading, which is based on the explicit solution of the structural nonlinear motion equation (central difference method).

The central difference method is used to perform explicit time integration for the structural nonlinear motion Eq. (9). The dynamic conditions of the next incremental step are calculated from the dynamic conditions of the previous incremental step until the end of the solution time.

$$[M]\{\ddot{u}\} = \{P\} - \{I\} \tag{9}$$

where $\{P\} - \{I\}$ is the mass matrix, $\{\ddot{u}\}$ is the acceleration array, $\{P\}$ is the load array, and $\{I\}$ is the internal force array.

The key to the solution of quasi−static method is to set a reasonable loading rate. Too fast loading rate leads to severe local deformation of the solution results, which makes the calculation results deviate from the requirements of "quasi−static", and the load displacement curve oscillates. However, too slow loading rate increases the calculation time greatly, which means a long loading time. Therefore, we usually take several different loading rates for comparison and analysis, and then select the appropriate loading rate when analyzing.

By studying the various energies in the model, we can evaluate whether the simulation produces the correct quasi−static response.

$$E_{KE} + E_{FD} + E_I + E_V - E_W = E_{total} \tag{10}$$

where E_{KE} is the structural kinetic energy, E_{FD} is the energy dissipated and absorbed by friction, E_I is the internal energy, including plastic and elastic strain energy, E_V is the energy dissipated and absorbed by viscosity, E_W is the work done by external forces, and E_{total} is the total energy in the system, which is a constant.

If the finite element simulation is quasi−static, the internal energy of the system is almost equal to the work done by the external force. Generally, the viscous dissipation energy is very small, unless material damping, viscoelastic materials or discrete shock absorbers are used. Therefore, we can determine that the inertia force is ignored according to the small flow velocity of the material in the model in the quasi−static process. It can be inferred from these two conditions that the kinetic energy is also very small. In most processes, the ratio of kinetic energy to strain energy of the structural model is an important criterion to judge whether the loading rate is appropriate. As a general rule, the general quasi−static requirement is that the ratio of kinetic energy to strain energy is less than 5%.

The applied loads are required to be as smooth as possible for accurate and efficient quasi−static problems. Stress waves arise from sudden, rapid movements that will cause oscillations or inaccurate results. The loading method shall be as smooth as possible, and the acceleration between two incremental steps shall only change by a small amount. If the acceleration is smooth, the varying velocity and displacement are smooth.

Since the central difference method is a conditionally stable algorithm, the time step Δt must be less than the stability limit Δt_{stable} to ensure the stability of the solution:

$$\Delta t_{stable} = 2/\omega_{\max} \geq \Delta t^e \tag{11}$$

where $\omega_{\max}$ is the highest natural frequency of the structure, Δt^e is the stable time step of the element with the smallest size in the structural model, Δt^e is related to the characteristic scale L^e, elastic modulus E and material density of the element ρ Is the upper bound of the stability limit Δt_{stable}:

$$\Delta t^e = L^e/\sqrt{E/P} \tag{12}$$

In the calculation, since the highest order frequency $\omega_{\max}$ of the structure is not easy to obtain, the time step Δt is taken as Δt^e.

Compared with the arc length method, the quasi−static method has no convergence problem because the central difference method is used for explicit integration, and can solve more complex structural collapse problems such as material failure and structural self−contact. Because the time step Δt is often small, the quasi−static loading is slow and the solution time is very long when solving the limit state problem, which can be adjusted by means of mass amplification.

3 Calculation of Ultimate Bearing Capacity Under Different Working Conditions

According to the classification of marine environmental conditions and the guide for buckling strength assessment of offshore engineering structures, the load distribution characteristics of the hull under different marine conditions are calculated respectively. The finite element model of the floating nuclear power plant is established based on ANSYS software, and then the load borne by the hull is applied to the finite element analysis model of the floating nuclear power plant to calculate and analyze the stress and displacement response of the overall structure of the floating nuclear power plant and

the steel containment, and carry out the calculation of the ultimate bearing capacity of the containment of the floating nuclear power plant under different working conditions.

The finite element model of the hull structure is constructed with shell181 and beam188 elements. The mesh size of the bottom and supporting parts of the containment is 0.1 M, the mesh size of the upper part of the containment is 0.2 m, and the mesh size of the rest is 0.8 m. The total number of elements on the whole ship is about 1.56 million (Figs. 2 and 3).
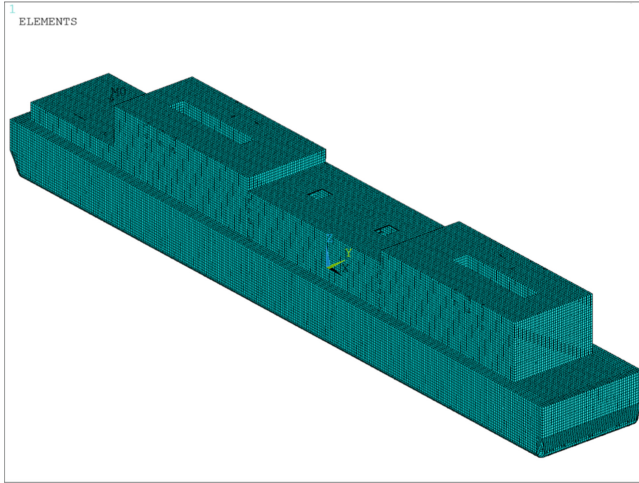
Fig. 2. Overall finite element model of ship structure
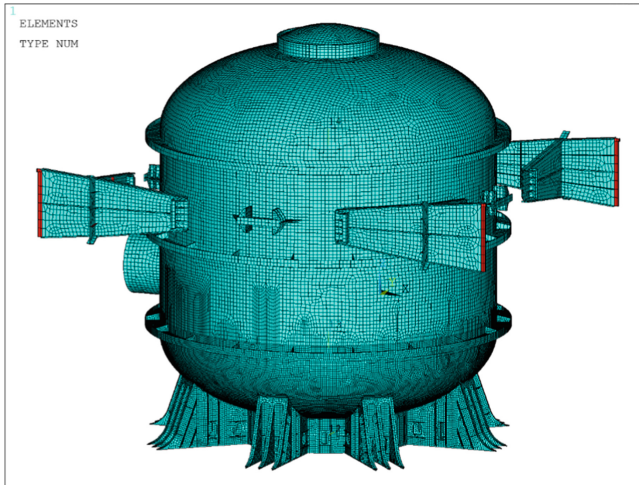
Fig. 3. Finite element model of containment

3.1 Calculation and Analysis of Ultimate Bearing Capacity Under Internal Pressure Condition of Containment

The internal pressure load is loaded inside the containment by uniformly distributing the load in the element, and the fixed support constraint is added at the bottom node of the compartment where the containment is located. Considering the influence of material hardening on the ultimate strength of the structure, the material constitutive relationship is set as shown in the figure below (Fig. 4).
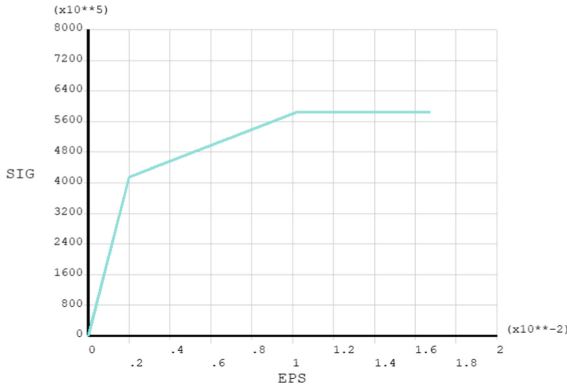
Fig. 4. Constitutive relation of material model

Sort out the calculation results, and select the top with the largest deformation and change rate as the analysis point. The load displacement curve is shown in the figure below (Fig. 5).
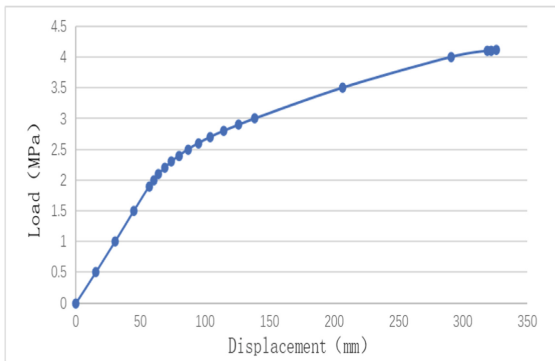
Fig. 5. Load displacement relationship of steel containment top node

The analysis shows that when the internal pressure load is below 2 MPa, the slope of the curve does not change, showing a linear growth trend, indicating that the structure is still in the elastic deformation order, and the equivalent plastic strain is 0; When the

internal pressure load increases from 2 MPa, the curvature in the load displacement curve begins to change, indicating that the structure begins to enter the plastic deformation stage.

(1) Double limit method

The double elastic slope method is used to determine the limit load in ASME VIII−2. In this method, the origin of load displacement curve is taken as the starting point to draw the straight line of elastic slope in the elastic stage, and then another straight line is drawn to meet the elastic slope whose slope is equal to twice. The load value projected on the vertical coordinate by the intersection of the straight line and the load displacement curve is the limit load value [10] (Fig. 6).
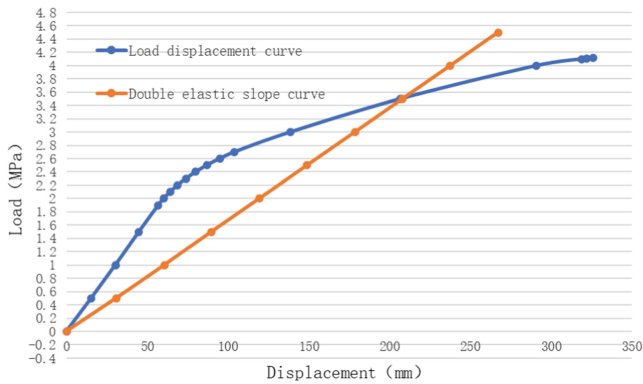
Fig. 6. Load displacement relation of double limit method

It can be seen from the figure that the limit load value determined by this model based on the more accurate load displacement curve after reducing the load increment step and using the double elastic slope method is about 3.442 MPa. This method is an artificial regulation and is greatly affected by human factors. The determined limit load value may have great dispersion and error.

(2) Double tangent intersection method

The double tangent intersection method is the method for determining the limit load in the European standard EN 13445. Based on the load displacement curve, the tangent lines of elastic stage and plastic stage are drawn respectively. The tangent of the plastic section adopts the first−order fitting function obtained from the plastic section data processed by the least square method, and the load value projected on the longitudinal coordinate by the intersection of the two tangents is the limit load value [11] (Fig. 7).

It can be seen from the figure that the limit load value determined by the model based on the load displacement curve and the double tangent intersection method is about
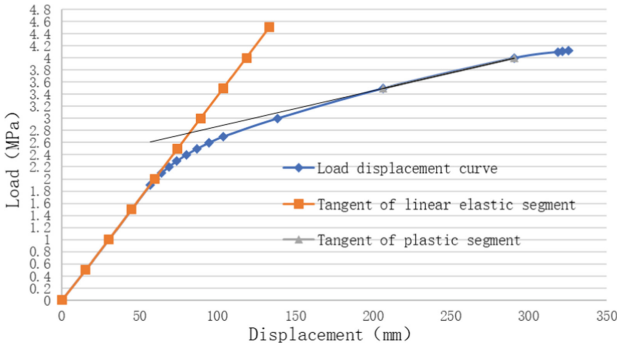
Fig. 7. Load displacement relationship of double tangent intersection method

2.755 MPa, which is completely determined by the curve itself, and is less affected by human factors than the double elastic slope method.

3.2 Calculation and Analysis of Ultimate Bearing Capacity of Containment Vessel Under Combined Wave Load and Internal Pressure

Taking the 100 year return period sea conditions, set the wave height as 9 m, calculate the loading of the finite element model of the whole ship of the floating nuclear power plant, and analyze the waves in 13 directions. Set a wave direction every 15° from 0° to 180°. The schematic diagram of wave incidence angle is shown in the following figure (Fig. 8):
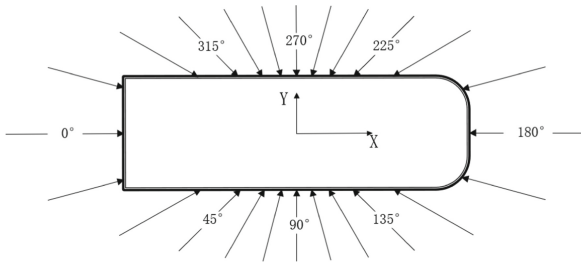
Fig. 8. Schematic diagram of wave incidence angle

In order to improve the calculation efficiency, the displacement structure response in the overall finite element model under wave load is calculated, and then the node displacement of the containment support in the overall model is extracted and loaded at the corresponding node of the containment finite element model as a boundary condition. Take the nodes with the stress value greater than 50 MPa in the containment, and compare the stress value of the containment nodes in the finite element model of the whole ship with the corresponding node stress value on the separate containment model. Some results are shown in the table below (Table 1).

Table 1. Comparison of node stress (zero degree wave load as an example)

NODE	Full ship model	Containment model		
	S1(Pa)	deformation and acceleration	deformation	acceleration
12200162	5.50E+07	3.24E+07	3.35E+07	4.22E+04
12200163	5.52E+07	2.76E+07	2.86E+07	5.25E+04
12200783	5.01E+07	2.69E+07	2.76E+07	−3.67E+04
12200822	5.45E+07	2.64E+07	2.72E+07	5.30E+04
12200823	5.52E+07	3.18E+07	3.28E+07	4.30E+04
12201023	6.81E+07	3.87E+07	4.03E+07	−5.00E+04
12201214	5.52E+07	3.20E+07	3.30E+07	−4.04E+04
12201215	5.56E+07	2.67E+07	2.75E+07	−4.80E+04
12202276	6.24E+07	3.65E+07	3.76E+07	4.21E+04
12202277	6.19E+07	3.05E+07	3.14E+07	5.21E+04
12202354	5.37E+07	2.75E+07	2.83E+07	5.24E+04
12202355	5.75E+07	3.29E+07	3.37E+07	4.51E+04
12202382	6.10E+07	3.50E+07	3.68E+07	−4.15E+04
12202768	5.67E+07	3.29E+07	3.46E+07	56786
12202798	5.31E+07	2.72E+07	2.79E+07	−52338
12202799	5.65E+07	3.19E+07	3.27E+07	−38352
12203178	5.43E+07	2.92E+07	3.01E+07	−39267
12203179	5.43E+07	3.03E+07	3.12E+07	−46813
12204241	6.28E+07	3.63E+07	3.74E+07	41805
12204242	6.28E+07	3.10E+07	3.19E+07	51568
12204764	5.35E+07	2.69E+07	2.75E+07	−49527
12204765	5.53E+07	3.06E+07	3.14E+07	−35320
12204954	6.82E+07	3.89E+07	4.05E+07	−49907
12205145	5.51E+07	3.20E+07	3.30E+07	−40471
12205146	5.54E+07	2.67E+07	2.75E+07	−47568
12206147	5.70E+07	3.09E+07	3.18E+07	45327
12206174	5.57E+07	3.29E+07	3.46E+07	−39438
12206543	6.30E+07	3.52E+07	3.67E+07	55582
12206573	5.78E+07	2.90E+07	2.96E+07	−50465
12206574	6.15E+07	3.39E+07	3.46E+07	−38538

(*continued*)

Table 1. (*continued*)

NODE	Stress ratio (containment node stress value/whole ship node stress value)		
	deformation and acceleration	deformation	acceleration
12200162	58.98%	60.99%	0.08%
12200163	50.02%	51.80%	0.10%
12200783	53.54%	55.00%	0.07%
12200822	48.50%	49.89%	0.10%
12200823	57.69%	59.37%	0.08%
12201023	56.93%	59.25%	0.07%
12201214	57.97%	59.77%	0.07%
12201215	48.10%	49.47%	0.09%
12202276	58.49%	60.21%	0.07%
12202277	49.23%	50.74%	0.08%
12202354	51.26%	52.67%	0.10%
12202355	57.09%	58.63%	0.08%
12202382	57.40%	60.28%	0.07%
12202768	58.00%	60.94%	0.10%
12202798	51.23%	52.56%	0.10%
12202799	56.37%	57.84%	0.07%
12203178	53.72%	55.38%	0.07%
12203179	55.83%	57.41%	0.09%
12204241	57.88%	59.53%	0.07%
12204242	49.37%	50.84%	0.08%
12204764	50.21%	51.41%	0.09%
12204765	55.37%	56.76%	0.06%
12204954	57.07%	59.38%	0.07%
12205145	58.11%	59.91%	0.07%
12205146	48.26%	49.65%	0.09%
12206147	54.21%	55.83%	0.08%
12206174	58.99%	62.17%	0.07%
12206543	55.80%	58.22%	0.09%
12206573	50.10%	51.16%	0.09%
12206574	55.13%	56.33%	0.06%

It is known from the data that the acceleration has little effect on the node stress, and the node stress on the containment mainly comes from the deformation of the structure. In order to simulate the structural response under the wave load in the separate containment model, compare the stress values of the corresponding nodes in the whole ship model and the separate containment model, and load twice the displacement structural response of the containment support node to the corresponding node of the separate containment, As the initial displacement boundary condition, the ultimate bearing capacity of wave load under the combined action of internal pressure is analyzed. The internal pressure loading method is the same as above.

The double limit method is used to analyze the ultimate bearing capacity of the structure as follows (Fig. 9).
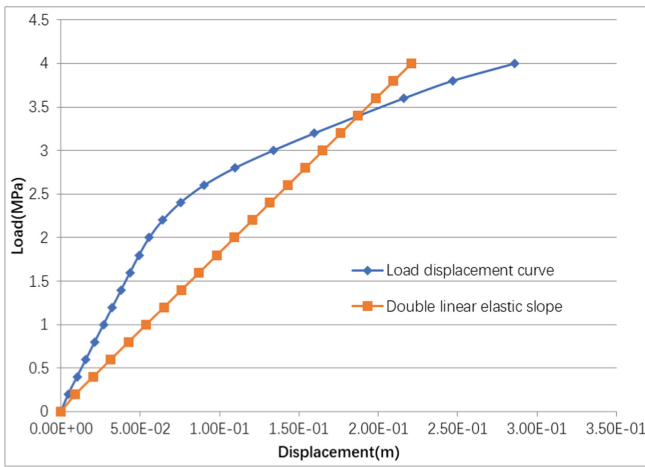
Fig. 9. Load displacement relation of double limit method

It can be seen from the figure that the limit load value determined by the model based on the more accurate load displacement curve after reducing the load increment step and using the double elastic slope method is about 3.45 MPa.

The ultimate bearing capacity of the structure is analyzed by the double tangent intersection method as follows (Fig. 10).

It can be seen from the figure that the limit load value determined by the model based on the load displacement curve and the double tangent intersection method is about 2.56 MPa.

According to the constitutive characteristics of the material, when the stress of the material exceeds the tensile strength of 585 mpa, it is considered that the strength failure of the material occurs there. According to the finite element analysis, when the internal pressure of the structure is 3.1 Mpa, the maximum value of the maximum stress point is 584 mpa. Therefore, it is considered that the structure has strength failure at 3.1 Mpa (the stress nephogram is shown in the figure below) (Fig. 11).
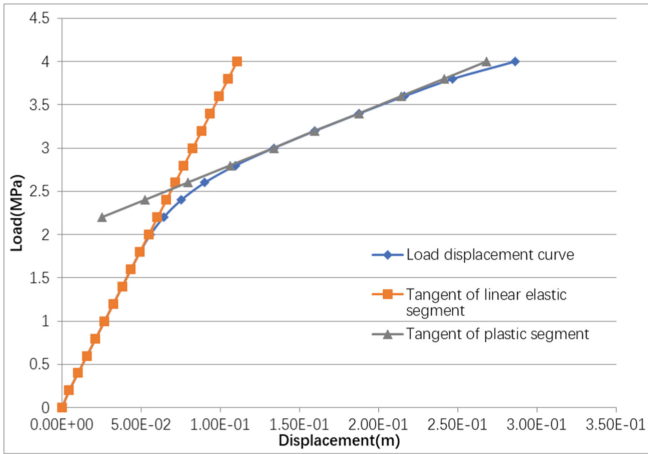
Fig. 10. Load displacement relationship of double tangent intersection method
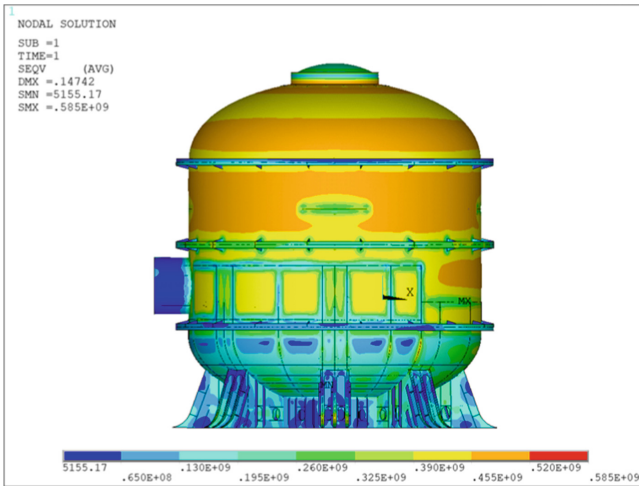
Fig. 11. Stress nephogram of steel containment in case of strength failure

4   Conclusions

Based on an engineering example model, this paper studies the analysis method of the ultimate bearing capacity of the containment of a floating nuclear power plant, and draws the following conclusions.

1. Based on the finite element analysis software, the stress−strain nephogram and load displacement curve are accurately calculated, and the limit load can be judged and determined by the double elastic slope method and the double tangent intersection method. In terms of the accuracy of determining the limit load value, the double

tangent intersection method is within an acceptable range due to the difficult determination of the tangent in the plastic stage, and the double elastic slope method is susceptible to human factors, so the accuracy is conservative.

2. Considering the wave load, compared with the finite element nonlinear analysis of the whole ship model, the method of extracting the load at the containment support in the overall model for linear calculation and loading it on the corresponding node of the local model of the containment is adopted to ensure the accurate load loading, shorten the calculation time and improve the calculation efficiency.

3. In the method of indirect loading, the impact of wave load on the containment of floating nuclear power plant is divided into two parts: the impact of structural deformation and the impact of structural acceleration. Compared with the impact of structural deformation on the ultimate bearing capacity of the containment, the impact of structural acceleration is relatively small and can be ignored.

References

1. Veritas, D.N.: Design of Offshore Steel Structures - General (lrfd Method) (2004)
2. Caldwell, J.B.: Ultimate longitudinal strengt. trans rina (1965)
3. Smith, C.S.: Influence of local compressive failure on ultimate longitudinal strength of a ship's hul. In: Proceedings of International Symposium on Practical Design in Shipbuilding, Tokyo, Japan (1977)
4. Ueda, Y., Rashed, S.M.H., Paik, J.K.: Plate and stiffened plate units of the idealized structural unit method (1st Report) under in plane loading. J. Soc. Naval Arch. Jpn. (1984)
5. Dow, R.S.: Testing and analysis of 1/3-scale welded steel frigate model. In : Proceedings of the International Conference on Advances in Marine Structures, pp. 749–773 (1991)
6. Nishihara, S., Engineering, O.: Ultimate longitudinal strength of mid-ship cross section. Naval Arch. **22**, 200–214 (1984)
7. Chen, Y.K., Kutt, L.M., Piaszezyk, C.M., et al.: Ultimate strength of ship structures. Trans. SNAME, pp. 149–168 (1983)
8. Kutt, L.M., Piaszczyk, C.M., Yung-Kuang, C., et al.: Evaluation of the longitudinal ultimate strength of various ship hull configurations. Trans.-Soc. Naval Arch. Marine Eng. **93**, 33–53 (1985)
9. Peng, D., Zhang, S.: Study on three finite element methods for structural ultimate strength analysis. China Offshore Platform **2**, 5 (2010)
10. Li, J.: Mechanical basis of pressure vessel design and its standard application (2004)
11. Spraragen, W.: Unfired pressure vessels. Indengchem **23**(2), 220–226 (1931)

Decoupling and Coupling Simulation Analysis in Small Nuclear Power Plant

Peiyu Tian[1]([✉]), Yi Li[1], Tianyang Xing[2], Tiebo Liang[1], and Changshuo Wang[1]

[1] Science and Technology on Reactor System Design Technology Laboratory, Nuclear Power Institute of China, Chengdu, Sichuan, China
805656155@qq.com
[2] School of Energy and Environment, Southeast University, Nanjing, Jiangsu, China

Abstract. As the development of computer science technology and the requirement of thorough research, more researchers are setting their eyes on coupling method because of the tight coupling in NPP (nuclear power plant) system. However there were few researches studying the difference between decoupling and coupling methods and the importance of coupling method. This research respectively establishes the primary and secondary loop decoupling models and the two loops coupling model based on the small NPP by APROS. Then the differences between the decoupling and coupling models is studied under the steady state and dynamic state which contains the ramp load variation and load shedding. The results show that there are small differences between these models in the main parameter values under the steady state. But the differences between decoupling models and coupling model are large. Therefore the NPP system needs be modeled by coupling method as to study its dynamic characteristic.

Keywords: Small NPP · Decoupling simulation · Coupling simulation · APROS · Ramp load variation · Load shedding

Nomenclatures

A heat transfer area, m^2
$C(t)$ delayed neutron precursor concentration for each period
c_p specific heat capacity, kJ/(kg °C)
G mass flow, kg/s
h specific enthalpy, kJ/kg
K heat transfer coefficient, W/(m2 °C)
M mass, kg
$n(t)$ neutron number for each period
T temperature, °C
t time, s
V volume, m^3
β delayed neutron fraction
λ disintegration constant, s
$\rho(t)$ reactivity for each period, $\Delta k/k$

ρ	density, kg/m^3
Λ	neutron generation time, s
	Subscript
a	average
c	coolant
fw	feed water
i	ith delayed neutron group
m	metal material
s	saturation
st	steam
w	water

1 Introduction

Simulation technique has been the main method used to study the reactor engineering field since the late 1960s because of the objective factors limitation such as measurement and manufacture level, the danger of test involving accident conditions, and the high price of the test. Then when there are more NPP systems with higher capacity and parameter value designing and application, researchers and engineers pay more attention to the simulation technique aftthe er accidents at Three-Mile Island and Chernobyl. But most of the research was decoupling simulation because the NPP system contains many subsystems which make the modeling difficult and there were few simulation softwares that amid at both the primary loop and secondary loop. For instance, Guo Liang [1], etc. used the C++ Builder to study the dynamic characteristic of the Daya Bay NPP's secondary loop system. Huo Binbin [2] etc. used Matlab/Simulink software to model the reactor coolant system of Daya Bay NPP under the positive signal disturbance.

And with the rapid development of computer techniques and the requirement of thorough research in the system characteristic, more and more researchers want to study the NPP system by coupling simulation model because of the tight coupling in the NPP system and think it's necessary to study the system by coupling model which is more complex and time-consuming than decoupling model. For example, LIN Meng [3] etc. expanded RELAP5 by C++ language to achieve the real-time simulation of a nuclear power plant. Xiao Kai [4] etc. coupled RELAP5, 3KEYMASTER and Matlab/Simulink to establish multi-reactors and multi-turbines nuclear power systems and simulated the dynamic condition. Nianci Lu [5] etc. studied the nuclear power system dynamic response under reactor trip by the Gsuite simulation platform. Pack J [6] etc. proposed a coupling model between RELAP5 and LABVIEW to model and simulate the whole nuclear power system.

However although Pack J compared the coupling model with the RELAP5 decoupling model under the LOCA event which showed that the coupling model agreed well with the RELAP5 decoupling model, the paper didn't talk about the necessity and importance of the coupling method. Besides in that paper, the second model in LABVIEW was simplified where the steam generator was calculated by the thermal equilibrium equation and there was no control system, so the comparison between decoupling and coupling models had limitations.

Therefore this research respectively established decoupling system models and coupling system models based on a small NPP. Then on basis of it, steady state and transient state are simulated to compare the coupling method and decoupling method, which direct the difference between the two methods and under what circumstances the decoupling method could be used.

2   Model

This small NPP system is configured with one reactor, double circuits, and double turbine generators. And the primary loop system contains a reactor coolant system and pressure safety relief system. The secondary loop system contains the main steams system, exhausted steams system, two turbine generator units, condensate extraction system and feed water system, and so on. According to the system configuration and flow, this paper establishes respectively the primary and secondary loop decoupling models and the whole system coupling model based on the APROS simulation software.

2.1   Primary Loop Decoupling Model

It supposes that the secondary side of the steam generators is a boundary condition in this decoupling model. So the user should give the steam mass flow value when the dynamic process is simulated. And the feed water temperature is constant during the simulation.

In this case, the steam mass flow is controlled by the control valve which is on the main steam pipe as Fig. 1 showed. And the control schematic diagram is shown in Fig. 2. Then the feed water mass flow is mainly controlled by the flow deviance between the
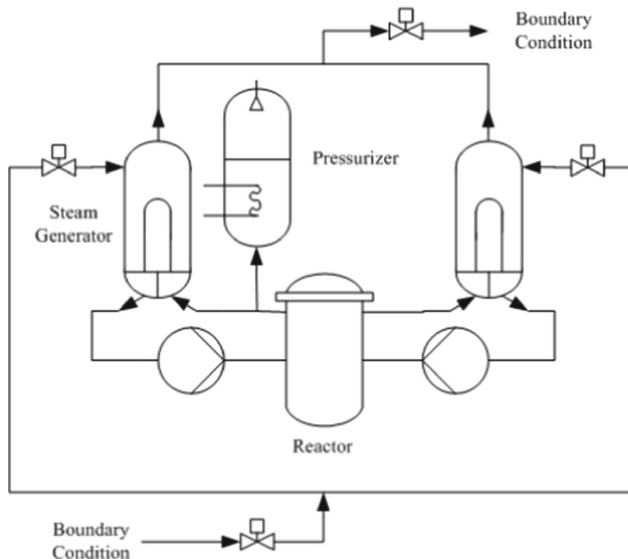
Fig. 1. The Schematic Diagram of the Primary Loop Decoupling Model

steam and feed water, whose control schematic diagram is shown in Fig. 3. It is also controlled by the control system of the steam generator water level, which consists of the feed water control valve control module and the feed water pump control module. And Fig. 4 is the water level control system's schematic diagram. Besides, there is the reactor power control system as Fig. 5 shows.
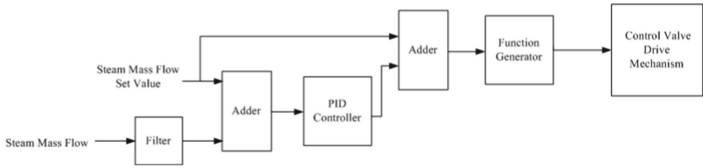
Fig. 2. The Control Schematic Diagram of the Steam Mass Flow
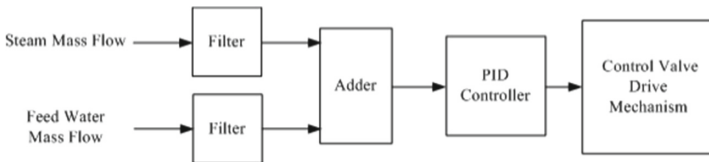
Fig. 3. The Control Schematic Diagram of the Feed Water Mass Flow
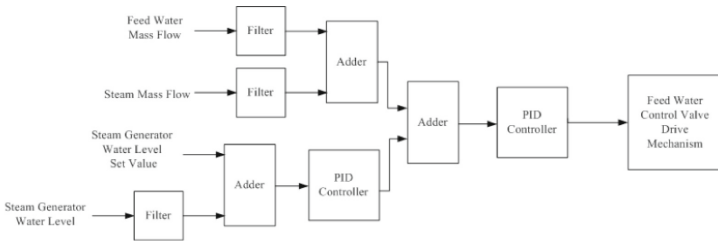
a. The Control Schematic Diagram of the Feed Water Control Valve
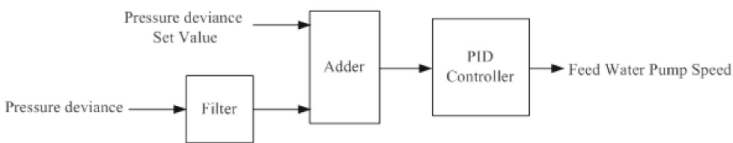
b. The Control Schematic Diagram of the Feed Water Pump Speed

Fig. 4. The Control Schematic Diagram of the Steam Generator Water Level
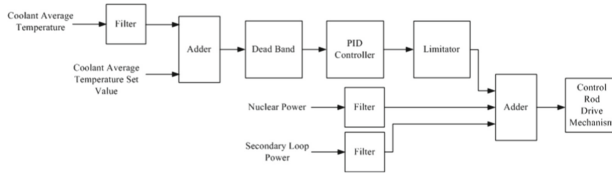
Fig. 5. The Control Schematic Diagram of the Reactor Power

2.2 Secondary Loop Decoupling Model

Although the secondary loop decoupling model usually doesn't consist of the steam generator, in this paper the steam generator is contained in the secondary loop decoupling model because the steam generator is a vital link connecting the primary and secondary loop and contrast to the primary loop decoupling model, the primary side of the steam generator is a boundary condition. Figure 6 is this decoupling system schematic diagram. If the dynamic process is simulated, the coolant enthalpy of the primary side inlet needs to be given. And the primary inlet and outlet pressure are constant during the simulation.
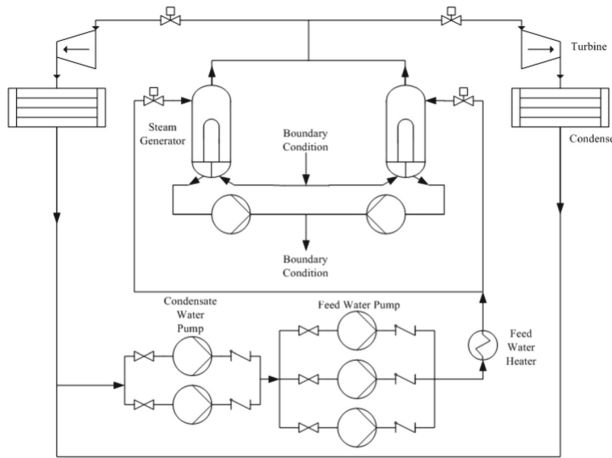
Fig. 6. The Schematic Diagram of the Secondary Loop Decoupling Model
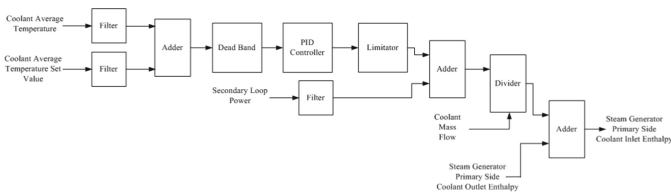
Fig. 7. The Control Schematic Diagram of the Reactor Power
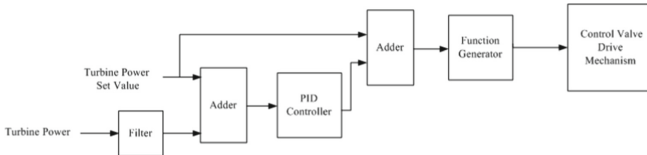
Fig. 8. The Control Schematic Diagram of the Turbine Power

The steam generators' primary side coolant inlet enthalpy is calculated and controlled by the reactor power control module which is shown in Fig. 7. And the feed water mass flow is mainly controlled by the control system of the steam generator water level in this secondary loop decoupling model, whose schematic diagram is the same in Fig. 4 Besides, the turbine generator power control system is established as Fig. 8 shows. So the steam mass flow is dependent on the turbine valve opening.

2.3 Primary and Secondary Loop Coupling Model
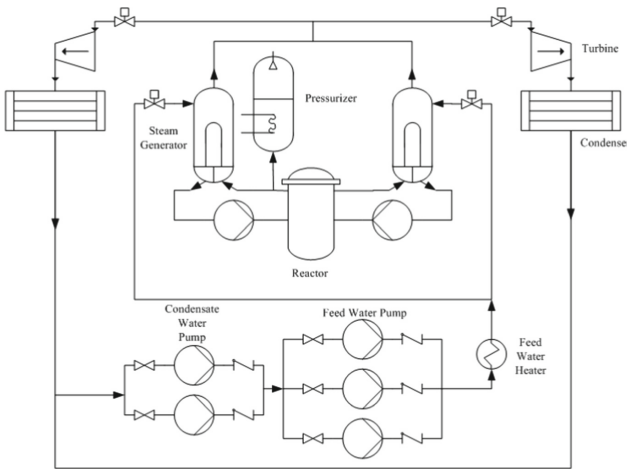
Fig. 9. The Schematic Diagram of the Two Loops Coupling Model

According to the decoupling models, the whole system coupling model is established which is no boundary condition. During the dynamic simulation, the steam mass flow is dependent on the turbine power target whose control schematic diagram is the same as Fig. 8. And the steam generator's primary side inlet temperature is dependent on the heat transfer process in the steam generator and the reactor power which is influenced by the nuclear physical temperature effect and the control rods that are controlled by the reactor power control system under the reactor following the generator mode. The reactor power control system is shown in Fig. 5. And the feed water mass flow is controlled by the steam generator water level control system as Fig. 4 shows (Fig. 9).

3   Simulation Analyses

3.1   Model Verification

The system's nominal design values are used to verify the coupling simulation model's accuracy. And the comparison results are in Table 1. And all the values are normalized by the nominal design values.

Table 1. Comparison of Nominal Steady Simulation Results

Parameter	Design Value	Simulation Value	Relative Error
Reactor Power	1.00000	0.99827	−0.173%
Coolant Mass Flow	1.00000	1.00001	0.001%
Coolant Average Temperature	1.00000	1.00002	0.002%
Pressurizer Pressure	1.00000	0.99493	−0.507%
Feed Water Temperature	1.00000	1.00135	−0.014%
Feed Water Mass Flow	1.00000	0.99986	−0.934%
Steam Mass Flow	1.00000	0.99066	0.065%
Steam Pressure	1.00000	1.00065	−0.013%
Steam Generator Water Lever	1.00000	0.99987	−0.121%
Turbine Power	1.00000	0.99879	0.038%
Condenser Pressure	1.00000	0.99968	−0.042%

The steady state simulation accuracy requirement is selected as 5%. And it shows that the simulation results' absolute relative errors are less than 5%, which meets the precision requirement. Therefore this model is available.

3.2   Steady Simulation Comparison

The full power condition and 20% of full power condition are simulated in order toe difference in steady condition analysis between these models. The main parameters' steady simulation results of these models and their relative errors based on the nominal design values are listed in Table 2. And all the values are normalized by nominal design values.

According to Table 2a, there are apparent differences between these models in the reactor power, feed water mass flow, steam mass flow, and steam pressure under the 20% FP steady condition. And Table 2b shows that the differences between these models in all parameters are small under the nominal steady condition.

There are some reasons accounting for the difference between these models. Firstly, the secondary loop decoupling model doesn't consider the heat caused by the coolant pumps and the heat capacity of the pipes' wall in the reactor coolant system. Secondly,

the primary system decoupling model doesn't consider the heat caused by the condensate pumps and the feed water pumps.

However, the relative errors of these models in all parameter values listed in Table 2 are all less than 5%, which meets the simulation precision requirement. And it shows that the decoupling method can be used to study the steady characteristic of the small NPP, which is more convenient and simple than the coupling method.

3.3 Dynamic Simulation Comparison

To study the difference in dynamic analysis between the decoupling method and the coupling method, the ramp load variable condition and the load shedding condition are simulated in different models. And the main system parameters, for instant reactor power, steam mass flow, steam pressure, and so on, are monitored and recorded. Figure 10 is the system dynamic response in these models under the load ascension and Fig. 11 is the system dynamic response in these models under the load reduction. Besides, Fig. 12 is the system dynamic response in these models under the load shedding to 15%FP. All the values are normalized by the nominal design values.

According to Fig. 10 and Fig. 11, it is obvious that there are differences between the coupling system and decoupling system under ramp load variation. But Fig. 11 shows that the differences in steam mass flow and coolant average temperature dynamic response curves are small. Besides it can be found through these figures that the dynamic response of the primary loop decoupling model isn't similar to the secondary loop decoupling model.

And the difference between these models is more apparent under the load shedding in the main parameters.

The reasons that the simulation results of these models aren't similar under different conditions are following:

(1). According to formulas (3-1) and (3-2) called the point reactor model [7], nuclear power mainly depends on the reactivity and delayed neutron precursor concentration which are related to time. So nuclear power is a non-linear parameter. Besides, the most significant feature of the reactor is the temperature effect. But in the secondary loop decoupling model, there is no reactor, and the reactor power is calculated according to the steam mass flow and the coolant temperature operation scheme, which neglects the temperature effect and the control rods that impact the change rate of nuclear power because of the control dead band, its limited moving speed, and its integrated worth. Therefore the differences between the secondary loop decoupling model and the coupling model are larger than primary loop decoupling in reactor power and coolant average temperature.

$$\frac{\mathrm{d}n(t)}{\mathrm{d}t} = \frac{\rho(t) - \beta}{\Lambda} n(t) + \sum_{i=1}^{6} \lambda_i C_i(t) \tag{3-1}$$

$$\frac{\mathrm{d}C_i(t)}{\mathrm{d}t} = \frac{\beta_i}{\Lambda} n(t) + \lambda_i C_i(t) \ i = 1, 2, \ldots 6 \tag{3-2}$$

Table 2. Steady Simulation Results Comparison

a. 20%FP Condition

Parameter	Primary Loop Decoupling	Secondary Loop Decoupling	Two Loops Coupling
Reactor Power	0.198	0.208	0.205
Coolant Mass Flow	1.003	1.004	1.004
Coolant Average Temperature	0.954	0.956	0.954
Pressurizer Pressure	0.999	0.997	1.002
Feed Water Temperature	1.000	0.997	0.998
Feed Water Mass Flow	0.198	0.206	0.207
Steam Mass Flow	0.200	0.208	0.205
Steam Pressure	1.290	1.302	1.284
Steam Generator Water Lever	1.000	0.998	1.001
Turbine Power	/	0.096	0.096
Condenser Pressure	/	0.293	0.293

b. 100%FP Condition

Parameter	Primary Loop Decoupling	Secondary Loop Decoupling	Two Loops Coupling
Reactor Power	0.997	1.000	0.998
Coolant Mass Flow	1.000	1.000	1.000
Coolant Average Temperature	1.000	1.000	1.000
Pressurizer Pressure	0.997	0.997	0.998
Feed Water Temperature	1.000	0.999	0.999
Feed Water Mass Flow	0.990	0.991	1.000
Steam Mass Flow	1.000	1.001	0.998
Steam Pressure	1.000	1.000	0.999
Steam Generator Water Lever	1.000	1.001	1.003
Turbine Power	/	1.001	1.000
Condenser Pressure	/	1.002	1.002
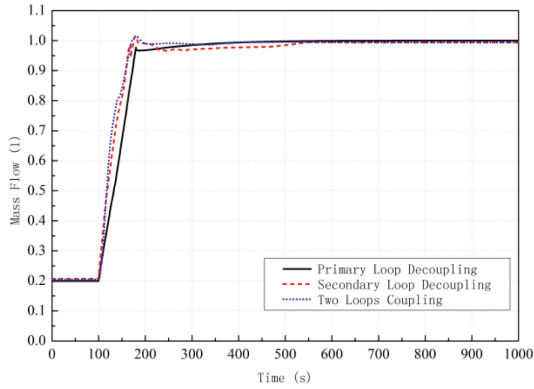
a. Steam Mass Flow Dynamic Response Curve
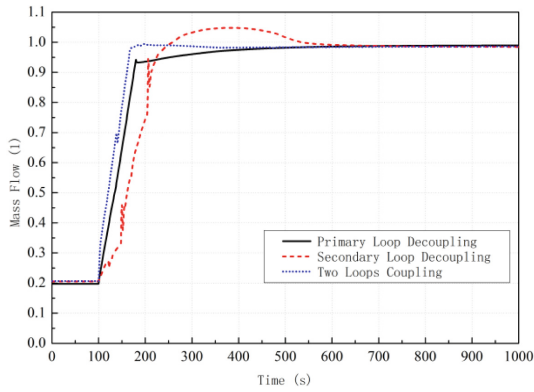
b. Feed Water Mass Flow Dynamic Response Curve
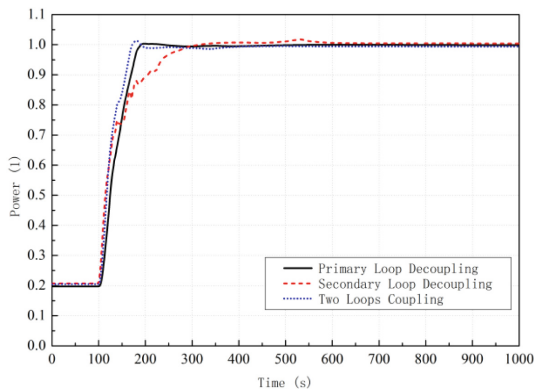
c. Reactor Power Dynamic Response Curve

Fig. 10. System Dynamic Response under the Load Ascension
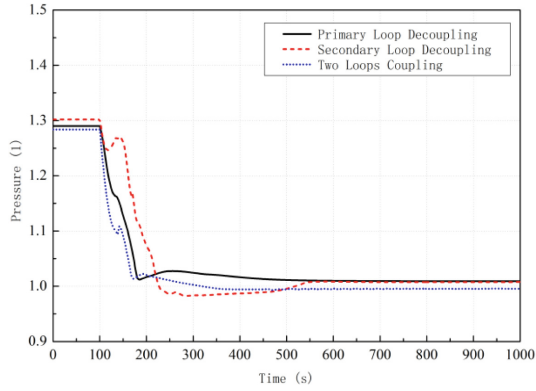
d. Steam Pressure Dynamic Response Curve
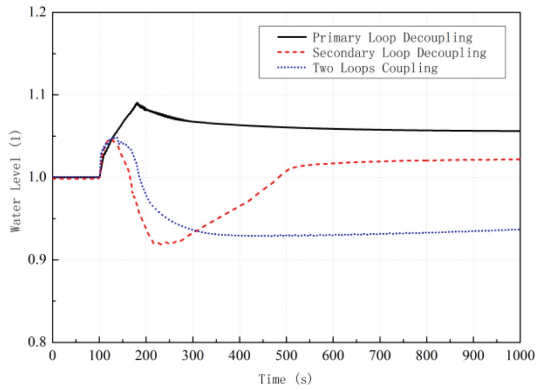
e. Steam Generator Water Level Dynamic Response Curve
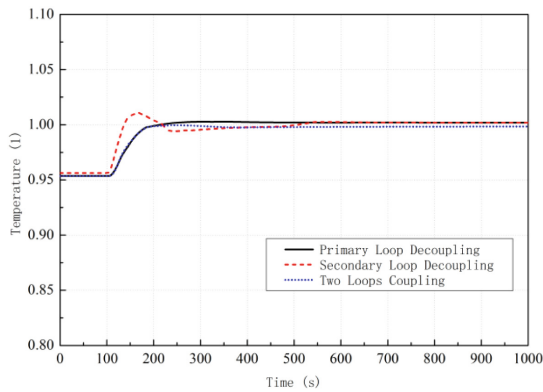
f. Coolant Average Temperature Dynamic Response Curve

Fig. 10. (*continued*)
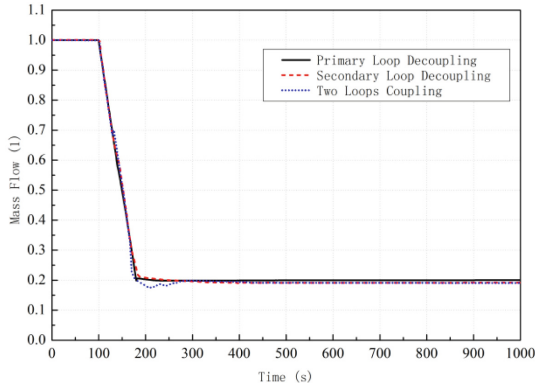
a. Steam Mass Flow Dynamic Response Curve
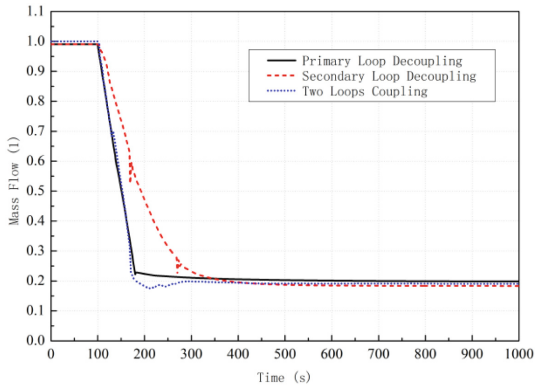
b. Feed Water Mass Flow Dynamic Response Curve
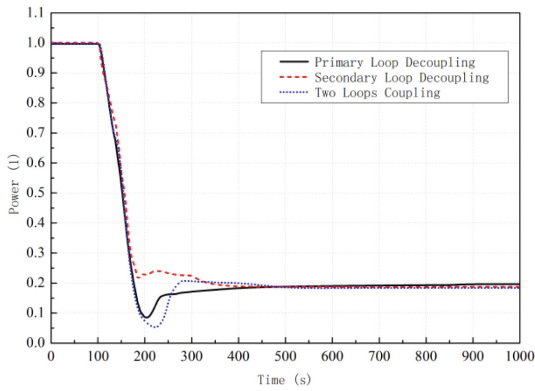
c. Reactor Power Dynamic Response Curve

Fig. 11. System Dynamic Response under the Load Reduction
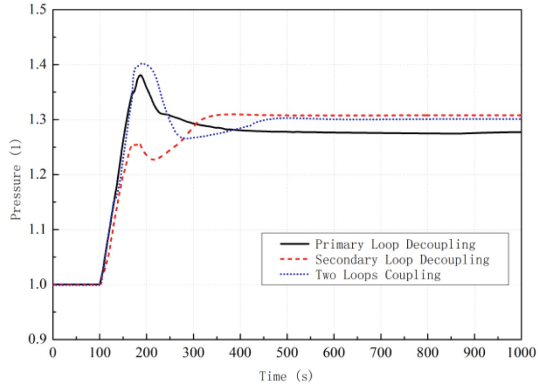
d. Steam Pressure Dynamic Response Curve
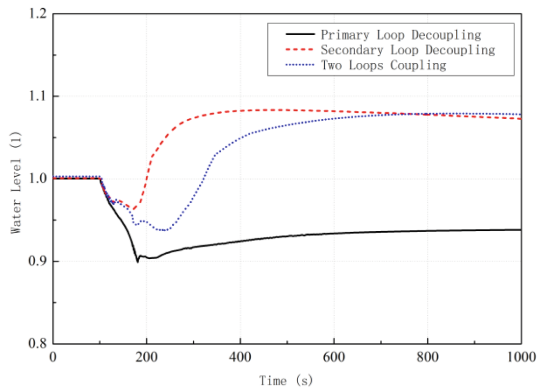
e. Steam Generator Water Level Dynamic Response Curve
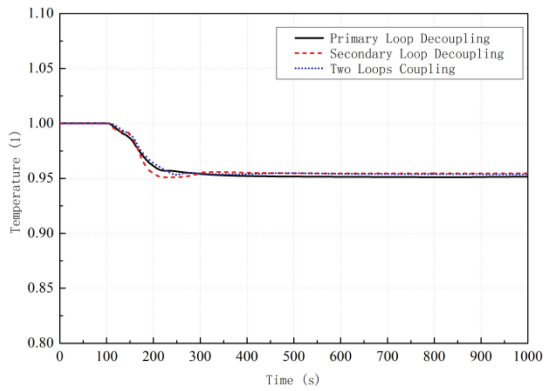
f. Coolant Average Temperature Dynamic Response Curve

Fig. 11. (*continued*)
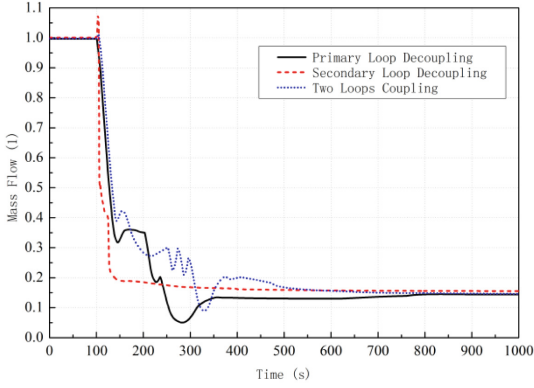
a. Steam Mass Flow Dynamic Response Curve
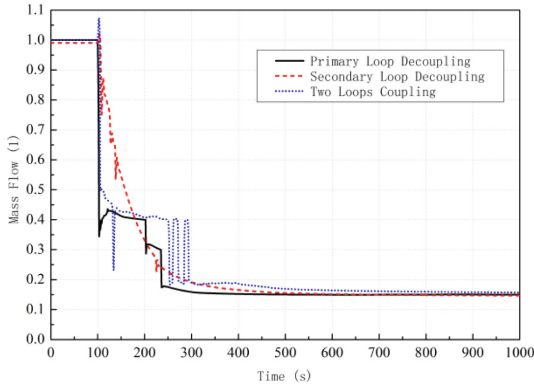
b. Feed Water Mass Flow Dynamic Response Curve
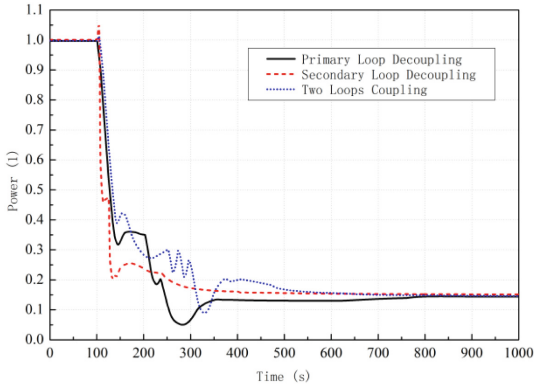
c. Reactor Power Dynamic Response Curve

Fig. 12. System Dynamic Response under the Load Shedding
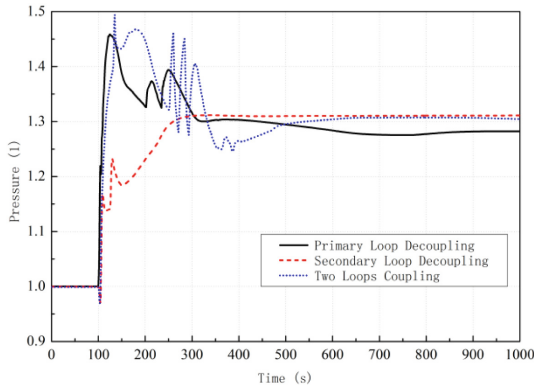
d. Steam Pressure Dynamic Response Curve
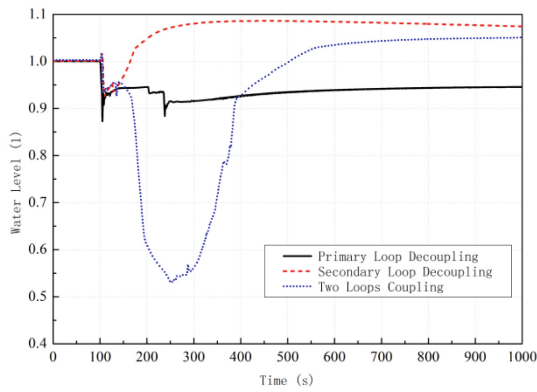
e. Steam Generator Water Level Dynamic Response Curve
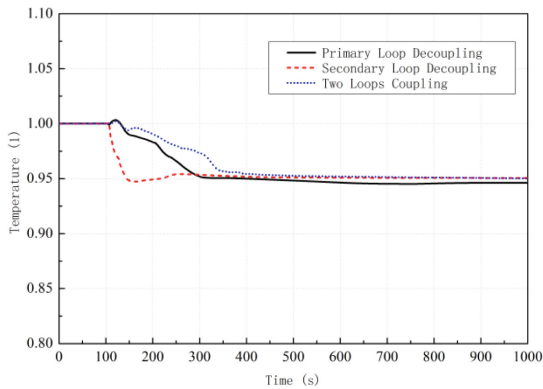
f. Coolant Average Temperature Dynamic Response Curve

Fig. 12. (*continued*)

(2). In the real NPP system, the steam mass flow mainly depends on the turbine power under normal operating conditions. And there are other steam users, like gas ejectors and steam-driven pumps. So the steam mass flow is also related to the other users. However, in the primary loop decoupling model, the steam generator's secondary side is regarded as a boundary condition, which means that there is only one steam user. Thus, the steam mass flow is given by the researcher and it is an ideal curve during the simulation. But in the secondary loop decoupling model or coupling model, the steam mass flow is influenced by the steam users' requirements during the simulation and the value is the coupling calculated results.

(3). Steam generator is the most important pivot in the NPP system which connects the primary loop and secondary loop. In the light of the steam generator's dynamic equations [8] which are deduced by lumped parameter technique as the formula (3-3) and (3-4) show, at first the steam mass flow changes under load variation conditions with the reactor following the turbine operational mode, then heat transfer required for the secondary side changes, which cause the steam saturation pressure changed because the heat transfer coefficient and the coolant temperature are nearly constant at that moment. Then the coolant average temperature changes. Meanwhile, nuclear power starts to change thanks to the temperature effect and the control rods' moving that is controlled by the reactor power control system. Thus the heat cooled by the coolant in the reactor changes, which changes the average temperature and the heat transfer to the secondary side again. Therefore the steam pressure's dynamic characteristic is related to the nuclear power dynamic curve.

$$M_c c_{p,c} \frac{\mathrm{d}T_{c,a}(t)}{\mathrm{d}t} = G_c c_{p,c}\left(T_{c,2}(t) - T_{c,1}(t)\right) - \\ K(t) \cdot A \cdot \left(T_{c,a}(t) - T_s(t)\right) \tag{3-3}$$

$$K(t) \cdot A \cdot \left(T_{c,a}(t) - T_s(t)\right) + G_{f_w} h_{f_w} - G_{st}, h_{s,st} \\ = \frac{d}{dt}\left[\rho_{s,w} V_w h_{s,w} + M_m c_{p,m} T_s(t) + \rho_{s,st}(V_w + V_{st})h_{s,st}\right] \tag{3-4}$$

Besides it shows that the heat transfer will change if the feed water mass flow and its enthalpy change in formula (4), which means that when the feed water mass flow or feed water temperature dynamic curve is different, the steam saturation temperature will be different whose trend of changes is consistent with the steam pressure.

(4). Feed water mass flow variation mode. The feed water is related to the feed water pumps, the pressure drop of the feed water pipeline, and the steam pressure. The feed water pump often is a variable speed pump, so the flow it could provide is different under different speeds. Meanwhile, the speed is controlled by the steam generator water level control system. But in the primary loop decoupling model, the feed water pumps models don't establish and the feed water mass flow is mainly controlled through the mass flow deviance. Besides, during operation, the numbers of operating pumps relate to the secondary loop power and current feed water mass flow.

To sum up, because many assumptions neglect the system coupling and the internal disturbances in the decoupling model, its results are more ideal. Besides the nuclear power which is influenced by the moderator and fuel temperature is one of the most important parameters in the nuclear system, so compared with the primary loop decoupling model, the secondary decoupling model is less accurate.

4 Conclusions

The ramp load variation and load shedding simulation in two-power loop a small NPP system is analyzed in this paper based on APROS software. And the main parameter's dynamic response curves are compared in different models, such as steam mass flow, nuclear power, steam pressure, and so on. According to the simulation results, the following results are obtained.

1) Difference between the coupling method and the decoupling method is small in steady-state simulation, so the system's steady characteristic feature could be studied by the decoupling method.
2) Differently observed between the coupling method and decoupling method in dynamic simulation. Therefore the coupling method should be used to study the dynamic characteristic feature of the system.
3) Because the assumptions aren't similar, the simulation results of the primary loop decoupling model and secondary loop decoupling model are different. But compared with the secondary loop decoupling model, the results of the primary loop decoupling model are more close to the coupling model.

These conclusions are crucial and could significantly refer to the system simulation analysis.

References

1. Guo, L., Sun, B., Song, Z., et al.: Modeling and real-time simulation of secondary circuit thermal system for nuclear power station based on C++ builder. Electric Power Constr. **34**(6), 1–6 (2013)
2. Huo, B., Xu, F., Liu, S., et al.: Nuclear power plant reactor coolant system principle simulation based on matlab. J. Nanjing Inst. Technol. (Nat. Sci. Ed.) **12**(2), 55–58 (2014)
3. Lin, M., Yang, Y.-H., Zhang, R.-H., et al.: Development of nuclear power plant real-time engineering simulator. Nucl. Sci. Tech. **16**(3), 177–180 (2005)
4. Kai, X., Liao, L., Zhou, K., et al.: The modeling and simulation research on control scheme of multi-reactor and multi-turbine nuclear power plant. J. Univ. South China (Sci. Technol.) **31**(3), 13–20 (2017)
5. Lu, N., Li, Y., Pan, L., et al.: Study on dynamics of steam dump system in scram condition of nuclear power plant. IFAC-PapersOnLine **52**(4), 360–365 (2019)
6. Pack, J., Fu, Z., Aydogan, F.: Modeling primary and secondary coolant of a nuclear power plant system with a unique framework (MCUF). Prog. Nucl. Energy **3**, 197–211 (2015)
7. Xie, Z.: Nuclear Reactor Physical Analysis. Xi'an Jiaotong University Press, Xi'an (2004)
8. Pang, F., Peng, M.: Marine Nuclear Power Device. Harbin Engineering University Press, Harbin (2000)

Development of Heat Pipe Modeling Capabilities in a Fully-Implicit Solution Framework

Guojun Hu(✉)

University of Science and Technology of China, Heifei Anhui, China
`huguojun@ustc.edu.cn`

Abstract. One key aspect in analysis of heat pipe microreactors is the efficient modeling of heat pipes and its coupling with the solid reactor core. Various options exist for modeling of heat pipes. Most models require an explicit coupling between the vapor core, which brings in an additional layer of coupling when the heat pipe model is integrated into a system-level safety analysis model. This additional layer of coupling causes both convergence concern and computational burden in practice. This article aims at developing a new heat pipe modeling algorithm, where the heat pipe wall, wick, and vapor core are discretized and coupled in a monolithic fully-implicit manner. The vapor core will be modeled as a one-dimensional compressible flow with the capability of predicting sonic limit inherently; a two-dimensional axisymmetric heat conduction model will be used to model the heat pipe wall and wick region. The heat pipe wick and vapor core are coupled through a conjugate heat transfer interface. Eventually, the coupled system will be solved using the Jacobian-Free Newton-Krylov (JFNK) method. It is demonstrated that the new coupled system works well. Consideration of the vapor compressibility in the two-equation model allows more detailed representation of the vapor core dynamics while remains light-weight in terms of computational complexity. The new model is verified by an approximate analytical solution to the heat pipe vapor core and is validated by a sodium heat pipe experiment.

Keywords: Microreactor · JFNK · Heat Pipe

1 Introduction

The heat pipe cooled MicroRx reduces most moving parts in the reactor design and provides an autonomous operation capability with passive safety systems. Its applications in remote area power stations, space nuclear power supplier, and other non-commercial fields attract much attention from governments, military, and nuclear industry in recent years. The heat pipe cooled MicroRx had been designed and demonstrated in several space exploration projects, KRUSTY [1] for example. Recently, several MWe-scale heat pipe cooled MicroRx were designed for terrestrial applications as well, including the eVinci reactor of Westinghouse and Aurora reactor of Oklo [2]. Before the demonstration and eventual construction of this new type of reactor technology, substantial effort is required in the safety analysis of this type of reactor and the associated modeling and

simulations work. One key aspect in this analysis work is the efficient modeling of heat pipes and its coupling with the solid reactor core.

It is necessary to know the liquid and vapor flow phenomena occurring within a heat pipe to determine the heat removal capacity and heat pipe performance. Many analytical and numerical models were proposed for predicting heat pipe operation limits, startup phenomena, steady-state operation, and transient behaviors. Faghri [3] proposed a two-dimensional incompressible vapor flow model for prediction of an annular heat pipe steady-state operation. Later, Faghri and Pavani [4] considered the compressibility of vapor and derived analytical axial pressure drop within the heat pipe. Chen and Faghri [5] studied the importance of conjugate heat transfer within the heat pipe wall and wick by the coupling of a two-dimensional compressible vapor flow model and a two-dimensional heat conduction model. This study showed that the compressible vapor flow model gave more reasonable results than incompressible vapor flow model. Cao and Faghri [6] proposed a two-dimensional transient analysis model which considered the vapor compressibility and coupled the vapor flow with wall and wick. They confirmed that the heat conduction model was sufficient for modeling the heat transfer in the wick when the thermal conductivity of working fluid is high, especially for high-temperature heat pipes where alkali metals are used as the working fluid. Cao and Faghri [7] also proposed a transient model for modeling of nonconventional heat pipes where a one-dimensional compressible vapor flow model is coupled to the multi-dimensional heat conduction model for the wall and wick. A comprehensive review of heat pipe analysis model is referred to Faghri's paper [8].

In this work, the target application of heat pipe analysis model is the transient safety analysis of heat pipe cooled MicroRx. Targeting the nuclear applications, several heat pipe analysis models were proposed, ranging from the simpler superconductor model to the more complex two-phase flow model. The ANL's SAM code implemented a so-called superconductor model where the heat transfer through vapor core was modeled with heat conduction using an extremely high effective thermal conductivity [9]. This heat pipe model was eventually used in a full-core multi-physics simulations of a 5 MWt heat pipe cooled MicroRx with great success. Wang et. al [10] developed a heat pipe heat transfer model based on the quasi-steady compressible one-dimensional laminar flow model and applied it to performance analysis of heat pipe radiator unit for space nuclear power reactor. A more complex heat pipe analysis model was proposed in the Sockeye code based on a two-phase flow model for the vapor core and porous medium flow model for the wick [11].

There are two critical issues when integrating a heat pipe analysis model into a system-level safety analysis model. The first issue is the balance between accuracy and computational complexity of heat pipe analysis model. The simplest thermal resistance model requires user inputs of vapor core thermal resistance and brings in significant uncertainties if without support from experiments. The more detailed multi-dimensional flow model of the vapor core is not applicable to system-level safety analysis due to its computational complexity. From the author's point of view, the balance lies in the one-dimensional vapor flow model. The second issue is the tight coupling between the heat pipe wall and the vapor core models. The fully-implicit technique is best fit for resolving this tight-coupled problem.

This work aims at developing the heat pipe modeling capability in a fully-implicit code framework, named RETA. RETA is a modern object-oriented system thermal-hydraulics analysis software developed in C++ by the author. It aims at providing the capabilities for modeling and simulation (M&S) of advanced reactors. Its underline solution scheme is the Newton-Krylov algorithm developed for the solution of system of nonlinear equations. The heat pipe analysis model is one key module of RETA code for the next-step development of transient safety analysis model of heat pipe cooled MicroRx.

2 Models

This work considers at first the conventional cylindrical heat pipes consisting of heat pipe wall, wick, and vapor core regions.

2.1 Vapor Flow Model

Various models and governing equations were formulated for modeling of the flow field in the vapor core region, including the simple thermal resistance network model, one-dimensional flow model, and three-dimensional flow model. This work follows the transient compressible one-dimensional vapor flow model, as was originally proposed by [7]. The one-dimensional vapor flow model will be coupled to a cylindrical two-dimensional heat conduction model for the heat pipe wall and wick. The major difference is that explicit coupling between the wick and vapor core is avoided in this newly developed model.

The conservation equations for vapor flow with negligible body forces were formulated using mass and momentum equation, i.e., a two-equation model. The conservation of mass is formulated as,

$$\frac{\partial \rho}{\partial t} + \frac{\partial \rho u}{\partial z} - \Gamma = 0 \tag{1}$$

In which Γ is the mass generation rate per unit volume. The conservation of momentum equation is,

$$\frac{\partial \rho u}{\partial t} + \frac{\partial \rho u^2}{\partial z} + \frac{\partial p}{\partial z} + \frac{\lambda}{2D_h} \rho u |u| = 0 \tag{2}$$

In which D_h is the hydraulic diameter of the vapor core region, and λ is the dimensionless friction coefficient. This work considers the compressible vapor flow model with potential Mach number as high as 1. The ideal gas law is used to describe the vapor equation of state, i.e.

$$p = \rho R T \tag{3}$$

In which T is vapor temperature and R is the specific gas constant. In the current formulation, the vapor is assumed to be in saturated condition, and the Clausius-Clapeyron equation is used to determine the vapor saturation temperature from the vapor pressure,

$$\frac{dp}{p} = \frac{h_{fg}}{R} \frac{dT}{T^2} \tag{4}$$

In which h_{fg} is the specific enthalpy of vaporization. In practice, given the reference temperature T_c and reference pressure p_c, the saturation temperature can be obtained by

$$\frac{1}{T} = \frac{1}{T_c} - \frac{R}{h_{fg}} \ln \frac{p}{p_c} \tag{5}$$

Equation (1), (2), (3), and (5) gives the closed set of governing equation for the one-dimensional vapor flow.

Equation (3) and (5) serve as an algorithmic correlation, and there are 2 partial differential equations (PDEs) for solution of 2 nonlinear variables, yet to be selected. This work aims at developing the heat pipe modeling capability in a fully-implicit solution framework, the first important task is the selection of nonlinear variables. It is natural to use vapor velocity u as the first nonlinear variable to be solved by the momentum Eq. (2). We have the freedom to solve the mass equation using vapor temperature T or vapor pressure p as the nonlinear variable. These two choices should be equivalent mathematically. Using pressure p is more straightforward because the pressure gradient is an important term in the momentum equation. We implemented and tested this choice, however it was observed that the resulting nonlinear system of equations was quite unstable, as minor density perturbation causes significant change in pressure. In contrast, a temperature formulation was found to be much more stable and was selected in this work.

Using the Clausius-Clapeyron equation, the pressure gradient term is transformed into,

$$\frac{\partial p}{\partial z} = \frac{dp}{dT} \frac{\partial T}{\partial z} = \frac{\rho h_{fg}}{T} \frac{\partial T}{\partial z} \tag{6}$$

With vapor temperature as the dependent variable, the vapor density is formulated as

$$\rho = \frac{p_c}{RT} \exp\left[\frac{h_{fg}}{R} \left(\frac{1}{T_c} - \frac{1}{T} \right) \right] \tag{7}$$

Finally, Eq. (1), (2), (6), and (7) are the closed set of governing equations for modeling the one-dimensional vapor flow.

2.2   Heat Conduction Model

This work considers primarily high temperature heat pipe with liquid metal (e.g., Sodium) as the working fluid. Because the thermal conductivity of the liquid metal working fluid is quite high, and wick thickness is thin, the effect of liquid flow in the wick can be neglected without causing significant modeling error in terms of macroscopic average temperature in the wick structure [6]. We will ignore the liquid flow in the wick structure and model the wick structure as a solid heat conduction region, with an effective thermal conductivity evaluated based on wick structure porosity, fluid thermal conductivity, and wick material conductivity. Currently, this effective thermal conductivity is specified as a user-input, which could be a temperature and porosity dependent function.

The heat pipe wall and wick regions are modeled as a two-dimensional axisymmetric solid heat structure. The governing equation for solid temperature is

$$\rho_s c_{p,s} \frac{\partial T_s}{\partial t} - \frac{1}{r}\frac{\partial}{\partial r}\left(rk_s\frac{\partial T_s}{\partial r}\right) - \frac{\partial}{\partial z}\left(k_s\frac{\partial T_s}{\partial z}\right) - q_s''' = 0 \tag{8}$$

In which subscript s represents solid. Note that solid density ρ_s, specific heat capacity $c_{p,s}$, and thermal conductivity k_s are all temperature dependent. The nonlinearity due to this dependency is resolved by the fully-implicit solution scheme.

2.3   Heat and Mass Transfer Model

The heat pipe vapor core is coupled with the heat pipe wick inner surface through a convection-like formulation. A user-specified effective heat transfer coefficient h_v is used to couple the vapor core temperature T and solid temperature T_s by

$$q_s'' = -k_s\frac{\partial T_s}{\partial r} = h_v(T_s - T) \tag{9}$$

In which q_s'' is the heat flux at wick-core interface. For the heat pipe, the heat transfer at the wick-core interface is in fact through the evaporation/condensation of working fluid. The mass generation rate per unit volume Γ is thus modeled as

$$\Gamma = \frac{a_w q_s''}{h_{fg}} \tag{10}$$

In which a_w is the heat transfer surface area density per unit volume.

2.4   Friction Model

A closed form friction coefficient correlation is required to correctly predict the flow field in the vapor core region. The friction coefficient λ in Eq. (2) depends on the Reynolds number. In this study, the friction coefficient is modeled as

$$\lambda = \begin{cases} \frac{64}{\mathrm{Re}} & \mathrm{Re} \leq 2200 \\ \frac{0.316}{\mathrm{Re}^{0.25}} & \mathrm{Re} > 3000 \end{cases} \tag{11}$$

This corresponds to the classical friction correlation for pipe flow in laminar and turbulent situation. An interpolation is performed for Reynolds number between 2200 and 3000. The effect of friction pressure drop will be seen clearly in the following verification and validation cases.

3   Numerical Scheme

3.1   Discretization Scheme

Finite Volume Method (FVM) is used to solve the one-dimensional vapor flow equations. A one-dimensional staggered grid is used, as is shown in Fig. 1. This work considers

the implicit Backward Euler discretization of temporal terms and upwind discretization of the convection terms. Extension to higher-order temporal and spatial discretization schemes are possible, which will not be discussed in this article. Wall boundary conditions are applied at both ends of the vapor core region. Velocity magnitude and temperature gradient are set to be zero at both ends.
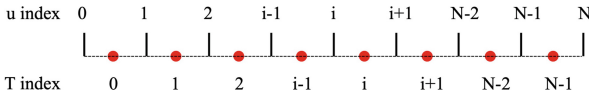
Fig. 1. One-dimensional staggered grid for vapor flow simulation

The final discretized vapor mass and momentum equations are summarized as:

$$R_{1,i} = \Delta x_i \frac{\rho_i - \rho_i^n}{\Delta t} + \left(u_{i+1}\rho_i^+ - u_i\rho_i^-\right) - \Delta x_i \Gamma_i \tag{12}$$

$$R_{2,i} = \Delta x_i \frac{\rho_i u_i - \rho_i^n u_i}{\Delta t} + \left(\rho_i \frac{u_i + u_{i+1}}{2} u_i^+ - \rho_{i-1} \frac{u_{i-1} + u_i}{2} u_i^-\right) + \frac{\rho(\overline{T}) \cdot h_{fg}(\overline{T})}{\overline{T}} (T_i - T_{i-1}) + \Delta x_i \frac{\lambda_i}{2D_h} \rho(\overline{T}) \cdot u_i |u_i| \tag{13}$$

Let $\mathcal{U}(u, a, b)$ be the operator for selecting the upwind value based on the velocity, which is defined as

$$\mathcal{U}(u, a, b) = \begin{cases} a \ u \geq 0 \\ b \ u < 0 \end{cases} \tag{14}$$

In Eq. (12) and (13), ρ_i^+ and ρ_i^- are evaluated based on the upwind concept as

$$\rho_i^+ = \mathcal{U}(u_{i+1}, \rho_i, \rho_{i+1}), \ \rho_i^- = \mathcal{U}(u_i, \rho_{i-1}, \rho_i) \tag{15}$$

u_i^+ and u_i^- are evaluated based on the upwind concept as

$$u_i^+ = \mathcal{U}\left(\frac{u_i + u_{i+1}}{2}, u_i, u_{i+1}\right) \tag{16}$$

$$u_i^- = \mathcal{U}\left(\frac{u_{i-1} + u_i}{2}, u_{i-1}, u_i\right) \tag{17}$$

$\overline{T}$ is vapor temperature evaluated at velocity cell center

$$\overline{T} = \frac{T_{i-1} + T_i}{2} \tag{18}$$

The heat conduction equation of wall and wick region is also solved with FVM in an orthogonal two-dimensional grid. This discretization is rather straightforward and is thus ignored in this article, except for two notes. The first note is that non-uniform mesh size is allowed in both radial and axial directions. This flexibility is quite useful in distinguishing the wall and wick regions in radial direction; or in distinguishing the evaporator, adiabatic, and condenser regions in axial direction. The second note is

that solid density, specific heat capacity, and thermal conductivity are all temperature dependent. The nonlinearity is resolved by the fully-implicit solution scheme.

The discretized vapor flow equations and heat conduction equations are combined to form a monolithic system of nonlinear algebraic equations. The vapor temperature and solid temperature are coupled using the conjugate heat transfer Eq. (9). This coupling is achieved internally with respect to nonlinear degree of freedom (DOF), which avoids the explicit boundary data exchange, as in the case where the vapor flow equations and solid heat conductions equations are solved separately.

3.2 Jacobian-Free Newton-Krylov Method

The system of nonlinear algebraic equations will be solved with the JFNK method, with an approximate Jacobian matrix serving as the preconditioner. Let $\mathbf{U}$ the vector of nonlinear DOFs and $\mathbf{R}$ be the system residual vector generated from the discretized vapor flow equations and solid heat conduction equations. The system of nonlinear algebraic equations is expressed as

$$\mathbf{R}(\mathbf{U}) = 0 \tag{19}$$

The JFNK method is based on the Newton's method, which solves the nonlinear algebraic equation iteratively by

$$\mathbb{J}\left(\mathbf{U}^k\right) \cdot \delta\mathbf{U} = -\mathbf{R}\left(\mathbf{U}^k\right) \tag{20}$$

$$\mathbf{U}^{k+1} = \mathbf{U}^k + \alpha \cdot \delta\mathbf{U} \tag{21}$$

In which $\mathbb{J}$ represents the system Jacobian matrix and α is a relaxation parameter in [0, 1] to improve the stability of Newton's iteration. In this work, α is calculated with a line-search algorithm. In the JFNK algorithm, the linear Eq. (20) is solved with the Krylov subspace method. The Krylov subspace method tries to find the iterative solution of the linear equation using the truncated Krylov subspace defined as

$$\mathcal{K}_m(\mathbb{J}, \mathbf{v}) := \left\{ \mathbf{v}, \mathbb{J}\mathbf{v}, \mathbb{J}^2\mathbf{v}, \cdots, \mathbb{J}^{m-1}\mathbf{v} \right\} \tag{22}$$

The fundamental operation in constructing the Krylov subspace is the matrix-vector product. The essential idea of the JFNK method is that the matrix-vector product in Eq. (22) is approximated using a finite difference scheme by

$$\mathbb{J}\mathbf{v} \approx \frac{\mathbf{R}(\mathbf{U} + \varepsilon\mathbf{v}) - \mathbf{R}(\mathbf{U})}{\varepsilon} \tag{23}$$

In which ε is a small scalar parameter. In this work, the JFNK scheme is implemented with the open-source scientific toolkit PETSc [12] developed by Argonne National Laboratory. The generalized minimum residual (GMRES) Krylov subspace linear solver is used.

It is well-known that the Krylov subspace linear solver in general needs a good preconditioner for better and faster convergence behavior. In this work, an approximate

system Jacobian matrix is provided to serve as the preconditioner. The complexity and computational burden of constructing an approximate system Jacobian matrix could be significantly reduced compared with constructing the exact system Jacobian matrix as required in the conventional Newton's method. In practice, one approximate system Jacobian matrix is constructed for each time step. If deemed necessary and efficient, this JFNK method can be converted to the Newton's method in a rather simple way, specified by an end user.

4   V & V Tests

4.1   Heat Conduction Model Verification

A simple cylinder with uniform internal heating power density and constant solid properties is used to verify the two-dimensional axisymmetric heat conduction model. Dimensionless heat conduction equation is solved. The radius of the cylinder is set to be 1. The radial outer surface is fixed at a boundary value of 0 and the axial boundaries are adiabatic. The density, specific heat capacity, and thermal conductivity is set to 1. A uniform heating power density of 50.0 is applied in the cylinder. The verification is shown in Fig. 2. Additional verifications of the heat conduction model were conducted but ignored here for brevity.
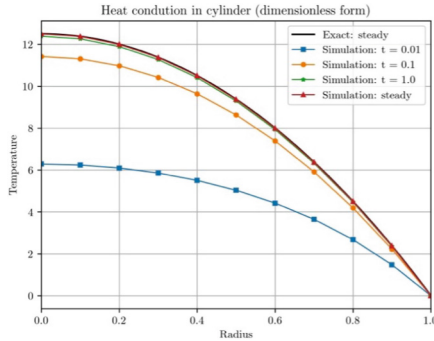
Fig. 2. Verification of two-dimensional axisymmetric heat conduction model in dimensionless form

4.2   Vapor Flow Model Verification

The verification of vapor flow model is performed using a heat pipe with uniform heating at the evaporator wall surface and a fixed temperature at the condenser wall surface, as is shown in Fig. 3.

We at first derive an approximate analytical solution of vapor for verification purposes. The following assumptions are made:
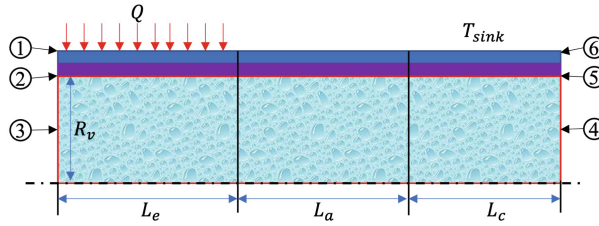
Fig. 3. Heat pipe verification model

- Heat flux at the interface between wick inner surface and vapor core is uniform in both evaporator and condenser section.
- The specific enthalpy of evaporation is a constant value.
- Heat removal rate in the vapor core is low, the pressure and temperature variation in the vapor core are thus small, vapor density is approximated to be a constant value.
- Friction coefficient is a constant value. This is in general not a valid approximation in practical simulations but should not be a problem in a verification test.

Let $M = \rho u$ be the mass flux of vapor flow. At steady-state, with the assumption that Γ is a piecewise uniform function of axial location z, the mass flux and pressure drop are found to be:

$$M = \int_0^z \Gamma dz \tag{24}$$

$$\Delta p = -\frac{1}{\rho_c}\left(M^2 + \frac{\lambda}{2D_h}\int_0^z M^2 dz\right) \tag{25}$$

The vapor temperature can be calculated with Eq. (25) and the Clausius-Clapeyron Eq. (4). Physical and boundary conditions for this verification test are listed in Table 1.
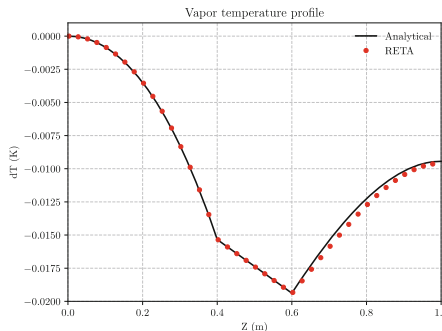
Fig. 4. Verification of vapor temperature

The total heat removal rate in this verification test is 10 W, which is relatively low such that the vapor speed is low. The maximum Mach number in this test is about

Table 1. Physical and boundary conditions of heat pipe verification test cases

Parameters	Value
$k_{s,wall}$	20.0 W/(m-K)
$k_{s,wick}$	60.0 W/(m-K)
L_e, L_a, L_c	0.4 m, 0.2 m, 0.4m
$\delta_{wall}, \delta_{wick}$	0.001 m, 0.001 m
R, h_{fg}	361.66 J/(kg-K), 4.0E + 06 J/kg
R_v, D_h	0.005 m, 0.01 m
λ, h_v	0.032, 1.0E + 06 W/(m^2-K)
Q, T_{sink}	10 W, 800 K
p_c, T_c, ρ_c	1157 Pa, 800 K, 0.004 kg/m^3

0.015, thus the incompressible assumption is valid. The verification results for vapor temperature, vapor pressure, and vapor mass flux are shown in Fig. 4, Fig. 5, and Fig. 6. The simulation results agree very well with the analytical solutions in the evaporator and adiabatic sections. Minor difference is seen in the condenser section, which is caused by the non-uniform heat flux distribution (and thus vapor condensation rate) in this section. The heat conduction model in the heat pipe wall and wick considers two-dimensional effect. While uniform heat flux is added at the evaporator outer wall, the heat flux at the interface of wick and vapor core still contains non-uniform profile. In the evaporator section, vapor pressure drops due to both evaporation of working fluid and friction; in the adiabatic section, vapor mass flux is a constant value, vapor pressure drops linearly due to friction; in the condenser section, the condensation of vapor brings in pressure recovery, but because of the frictional losses, only partial pressure recovery is achieved. Similar trend is seen in vapor temperature. Overall, there is a positive pressure and temperature drop in the vapor core from the evaporator end to the condenser end, as required by the thermodynamics law.
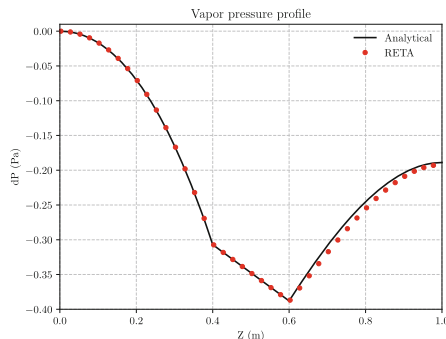
Fig. 5. Verification of vapor pressure
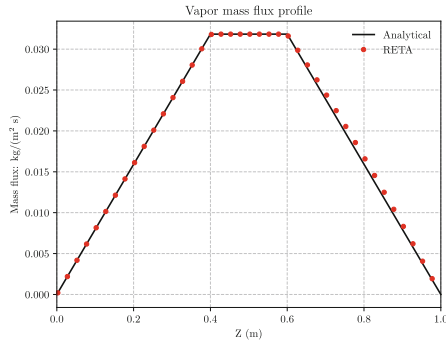
Fig. 6. Verification of vapor mass flux

A temperature drop analysis is also conducted for this verification test. The results are shown in Table 2. The subscript number is corresponding to location as labeled in Fig. 3. The simulation results match analytical results very well. The newly implemented fully-implicit model is thoroughly verified.

Table 2. Temperature drop analysis results

Variable	Analytical: K	Simulation: K	Error: K
$T_1 - T_2$	4.28E-2	4.16E-2	-1.2E-3
$T_2 - T_3$	7.95E-4	7.96E-4	1.0E-6
$T_3 - T_4$	9.44E-3	9.59E-3	1.5E-5
$T_4 - T_5$	7.95E-4	8.58E-4	6.3E-5
$T_5 - T_6$	4.28E-2	4.30E-2	2.0E-4

4.3 Validations

In this subsection, we will conduct two steady-state validation studies using experimental data and reference results from other codes available in literatures. The validation cases are based on cylindrical sodium heat pipe experiments conducted by Ivanovskii et al. [13], where vapor temperatures were measured and reported. Besides the experimental data, simulation results from Chen and Faghri [5] are also used as reference results for a code-to-code comparison, which includes results from both incompressible and compressible models.

Two cylindrical sodium heat pipes are modeled, the details of physical and boundary conditions are listed in Table 3. In the evaporator wall surface, a uniform heat flux is applied as the boundary condition; in the condenser wall surface, a convective boundary condition is applied with a sink temperature (T_{sink}) of 300 K. For this model, the thermal resistance due to convective heat transfer in the condenser wall surface is much larger
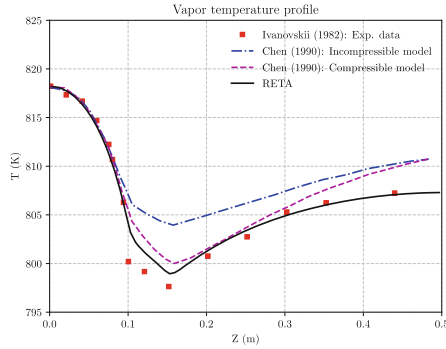
Fig. 7. The axial vapor temperature profile for sodium heat pipe with Q = 560 W

than that of the heat pipe. The heat pipe working temperature is very sensitive to the heat transfer coefficient (h_{sink}) at this surface. For this study, h_{sink} is iteratively calibrated such that the vapor pressure and temperature at the evaporator end match the reference values. The heating power in these two test cases are 560 W and 1000 W, respectively. An axial mesh size of 6.25E-03 m is used in the simulations. Steady-state results are obtained and compared with experimental/reference values.

Table 3. Physical and boundary conditions of heat pipe validation test cases

Parameters	Case 1	Case 2
Fluid	Sodium	Sodium
p_c: Pa	1300	2476
T_c: K	818	856
$k_{s,wall}$: W/(m-K)	19.0	19.0
$k_{s,wick}$: W/(m-K)	66.2	66.2
L_e, L_a, L_c: m	0.1, 0.05, 0.35	0.1, 0.05, 0.55
δ_{wall}: m	0.001	0.001
δ_{wick}: m	0.0005	0.0005
h_{fg}: J/kg	4.182E + 06	4.182E + 06
μ_v: Pa s	1.80E-05	1.80E-05
R_v: m	0.007	0.007
h_v: W/(m^2-K)	1.0E + 06	1.0E + 06
Q: W	560	1000
h_{sink}: W/(m^2-K)	59.6	62.6
T_{sink}: K	300	300
Axial elements	80	112

Figure 7 shows the comparison between numerical results from this study and reference results, including experiment data and simulation results, for the vapor temperature for Case 1. The results from RETA match the experimental data well, with a maximum deviation of about 4 K near the evaporator-adiabatic interface. Similar order of deviation was observed in the reference simulation results as well. This deviation is acceptable considering that uncertainty in vapor temperature measurement can be quite big.
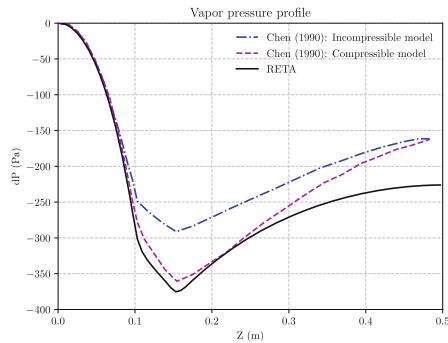
Fig. 8. The axial vapor pressure profile for sodium heat pipe with Q = 560 W
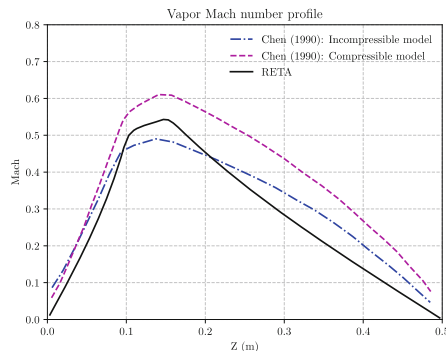
Fig. 9. The axial vapor Mach number profile for sodium heat pipe with Q = 560 W

Figure 8 shows the vapor pressure profile for Case 1. It is seen that results from RETA match the reference results and is closer to the reference compressible model results. This is expected because the current model considers the compressibility as well. Figure 9 shows the Mach number profile for Case 1. The maximum Mach number, happening at the adiabatic section, is around 0.55 from RETA prediction. In general, results from RETA match the reference results well in the evaporator section but shows deviation in the condenser section. This is determined by the difference in the vapor flow model (e.g., one-dimensional vs two-dimensional) and the difference in the friction model, etc.

Figure 10 shows the comparison between numerical results from RETA and reference results for the vapor temperature for Case 2. The results from RETA match the
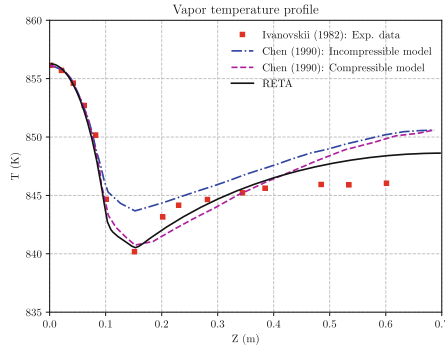
Fig. 10. The axial vapor temperature profile for sodium heat pipe with Q = 1000 W

experimental data well, especially in the evaporator section. The maximum deviation of about 3 K is observed near the end of condenser section. Similar order of deviation was observed in the reference simulation results as well. In general, the newly developed model can predict the various physics in a cylindrical heat pipe reasonably well but with future work to be done for improvements.

5   Conclusions

This work proposed a fully-implicit solution algorithm for simulations of cylindrical heat pipes in the RETA code. To better predict the temperature profile of the working fluid in the vapor core, a compressible one-dimensional vapor flow model is developed and discretized in the finite volume manner. An axisymmetric two-dimensional heat conduction model is developed, which is then coupled to the one-dimensional vapor flow model through conjugate heat transfer at the interface. The fully-coupled vapor flow and heat conduction models form a monolithic system of nonlinear equations, which are solved with Newton's method in combination with a Krylov sparse linear solver.

Several numerical tests are conducted to verify and validate the newly developed model. An approximate analytical solution for the vapor flow is derived based on a few assumptions. The excellent agreement of RETA simulation results with analytical solution confirms the model setting, derivation, and code implementation of the newly developed model. Two steady-state validation tests are conducted. Comparison of vapor temperature with experimental data and reference simulation results shows that the newly developed model has a good prediction accuracy. It is observed that the prediction accuracy is worse in the condensation section, likely caused by the rather simple friction factor correlations. Future work is needed to improve this.

To conclude, this new model considers the vapor flow with a compressible one-dimensional flow model in the vapor core. Compared with other simpler models, for example thermal resistance model, this new model can predict the vapor pressure, temperature, and velocity with good accuracy, which should help reduce the uncertainty in predicting the performance of a heat pipe. It is expected that this new heat pipe model will play an important role in the design and safety analysis of heat pipe cooled microreactors.

There are several future works for improvement of the newly developed model, including but not limited to:

- Transient simulation capability is available in the current code; however, it requires more verification and validation tests.
- Development and implementation of various heat transfer limits of heat pipe operation.
- Improvement of heat pipe solution algorithms for simulation of vapor flow at higher Mach number. At a test study, the solution algorithm is found to be struggle at supersonic conditions where discontinuities exist in vapor region.
- Development of heat pipe microreactor modeling capabilities by coupling of heat pipe models with heat conduction model of the reactor core, system loop model of the heat pipe heat exchangers, etc.

References

1. McClure, P.R., et al.: Kilopower project: the KRUSTY fission power experiment and potential missions. Nucl. Technol. **206**(sup1), S1–S12 (2020)
2. Mueller, C., Tsvetkov, P.: A review of heat-pipe modeling and simulation approaches in nuclear systems design and analysis. Ann. Nucl. Energy **160**, 16 (2021)
3. Faghri, A.: Vapor flow analysis in a double-walled concentric heat pipe. Numerical Heat Transf. **10**(6), 583–595 (1986)
4. Faghri, A., Parvani, S.: Numerical analysis of laminar flow in a double-walled annular heat pipe. J. Thermophys. Heat Transf. **2**(2), 165–171 (1988)
5. Chen, M.-M., Faghri, A.: An analysis of the vapor flow and the heat conduction through the liquid-wick and pipe wall in a heat pipe with single or multiple heat sources. Int. J. Heat Mass Transf. **33**(9), 1945–1955 (1990)
6. Cao, Y., Faghri, A.: Transient two-dimensional compressible analysis for high-temperature heat pipes with pulsed heat input. Numerical Heat Transf. **18**(4), 483–502 (1991)
7. Cao, Y., Faghri, A.: Transient multidimensional analysis of nonconventional heat pipes with uniform and nonuniform heat distributions (1991)
8. Faghri, A.: Review and Advances in Heat Pipe Science and Technology. J. Heat Transfer-Trans. Asme, **134**(12) (2012)
9. Hu, G., et al.: Multi-physics simulations of heat pipe micro reactor (2019)
10. Wang, C.L., et al.: Performance analysis of heat pipe radiator unit for space nuclear power reactor. Ann. Nucl. Energy **103**, 74–84 (2017)
11. Hansel, J.E., et al.: Sockeye theory manual. Idaho National Lab.(INL), Idaho Falls, ID (United States) (2020)
12. Balay, S., et al.: PETSc users manual (2019)
13. Ivanovski, M., Sorokin, V., Yagodkin, I.: Physical principles of heat pipes (1982)

Analysis and Qualification Control of Welding Defects of Coated 15-15Ti Cladding Tube

Junling Han[1,2(✉)], Guannan Ren[1,2], Limei Peng[1,2], Hongyu Tian[1,2], and Pengbo Ji[1,3]

[1] CNNC Key Laboratory on New Materials Research and Application Development, Baotou, Inner Mongolia, China
`hanjunling0805@163.com`
[2] China North Nuclear Fuel Co., Ltd., Baotou, Inner Mongolia, China
[3] CNNC Key Laboratory on Fabrication Technology of Reactor Irradiation Special Fuel Assembly, Baotou, Inner Mongolia, China

Abstract. Physical property test fuel rod is used for the engineering test and thermal comprehensive experimental verification of lead-cooled reactors. Preliminary electron beam welding (EBW) trials showed that the welding quality of coated 15-15Ti tube and 316L end plug were significantly affected by welding defects. By studying the welding defects with optical microscopy (OM) and scanning electron microscopy (SEM), it is showed that the inclusions in the coating of the cladding tube enter the welding line during EBW, increasing the tendency to form cracks and leading to welding cracks; the excessively long mating surface between the cladding tube and end plug results in welding gas expansion. Through the design of orthogonal tests with influential parameters including the length of the mating surface of the end plug, the removal amount of the inner wall of the cladding tube and the interference amount on the quality characteristics, the comprehensive effects of these parameters were studied and the best matching structure was determined, which breaks through the difficulty in the welding between 316L end plug and coated 15-15Ti tube, and the welding qualification has been verified to be improved.

Keywords: fuel rod · electron beam welding (EBW) · welding with coating material · welding defect · orthogonal experiment qualification control · 15-15Ti cladding tube

1 Introduction

The lead-based reactor is one of six fourth-generation reactors recommended by the International Forum on Energy Systems (GIF), it has significant advantage in safety, miniaturization and feasibility. Therefore, the research on Physical property test fuel rod promotes the progress of ADS transmutation system and related technology of lead based reactor, and lays a solid foundation for the engineering of lead based reactor in China. Physical characteristics fuel rod welding is completed by ring welding of upper end plug, lower end plug and clad tube. The upper and lower end plugs are machined from 316L stainless steel and the coated tube is 15-15Ti material.

The main defects of fuel rod welding are incomplete penetration, porosity, gas expansion and crack, etc. Porosity is one of the commonly occurring welding defects in welding, it exists inside or on the surface of the weld metal, and its defect form is round porosity, columnar porosity and round dense porosity. The harmfulness of porosity is mainly manifested as a reduction in the load-bearing capacity of the welded joints, resulting in increased probability of local corrosion perforation. Incomplete penetration is the incompletely penetration of root or interlayer of the joint during welding. Stress concentration is easily generated at the incomplete ends and gaps, which may lead to cracking under external forces. Cracks are gaps that exist inside or on the surface of the weld or heat-affected zone, and there is a significant stress concentration at the sharp root. When the stress level exceeds the strength limit of the sharp root, the crack will expand, which will aggravate fatigue failure and stress corrosion failure.

2   Statistics and Analysis of Welding Defects

2.1   Statistics of Qualification Rate

According to the statistics of welding test results in the early stage of the test, the average welding qualification rate was 81.9%, and the batch welding qualification rate was shown in Fig. 1. The welding defects leading to unqualified fuel rods in the above experimental batches include gas expansion, crack, incomplete penetration, porosity, non-fusion and unqualified appearance, as shown in Fig. 2.
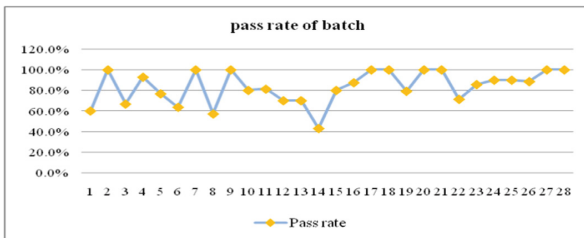
Fig. 1. Fuel rod welding batch pass rate statistics during the experimental phase Statistics
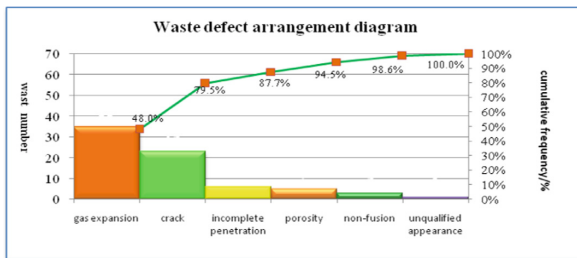
Fig. 2. Experimental phase fuel rod welding failure statistics

Analysis of the arrangement in Fig. 2 shown that the cause of the passing rate plummeting is the generation of gass expansion and cracks; By the statistical date, it was found that gas expansion and cracking accounted for 79.5% of the total number of defects, through the theoretical calculations, if we reduce the number of gas expansion and cracking defects of 85.1%; Though the analysis of two kinds of defects, take the corresponding control measures, and improve the welding pass rate.

2.2 Defect 1-Crack Analysis

In the welding experiments, the fuel rods that are not qualified in NDT were examined by means of penetration test, metallurgical inspection, scanning electron microscopy and energy spectrum analysis, and the welds were further analyzed.
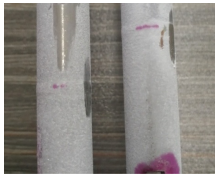
Fig. 3. Penetration testing-crack
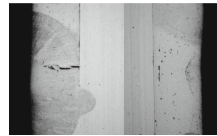
Fig. 4. Metallographic testing-crack

For the analysis of the test welded fuel rods for the experimental process generated by the X-ray inspection failed fuel rods, and targeted further destructive testing of the welding seam is carried out to analyze the root cause of its generation. Figure 3 shows the penetration test, and the test results shown that there was a crack about 5 mm in the lower plug ring welding area on the left side of the fuel rod, and there was a crack about 2 mm in the upper plug ring welding area on the right side of the fuel rod. The metallographic test specimens were prepared for the penetration detection cracks; Fig. 4 shown the metallographic test at the corresponding cracks, and the figure shown that the cracks were found in the metallographic test corresponding to the welding cracks of the fuel rod on the left, and no cracks were found at the welding cracks of the fuel rod on the, right, but one crack was found in the cladding matrix material.

Figure 5 shown the scanning electron microscopy analysis of the crack at the welding, combined with the energy spectrum analysis can be obtained, the crack is mainly composed of C, O and Si elements, and the C is the highest content of elements. Figure 6 shown the scanning electron microscopy analysis of the crack at the substrate, combined with the energy spectrum analysis, it can be seen that in addition to the high content of C and O elements, Ti, Mn and Cr elements with high composition were been detected (Fig. 7).

In view of the metallographic results founded cracks from the cladding matrix, though the cladding analysis, it is founded that the fuel rod cladding is a kind of coated 15-15Ti cladding tube, combined with the analysis about scanning electron microscopy and energy spectrum of cladding tube coating in Fig. 9, it was obtained the inner wall coating C, O, Ti, Mn, Cr elements on the high side. It is inferred that the inner wall coating of the tube is mainly composed of oxides and carbides of Mn, Ti and Cr etc.
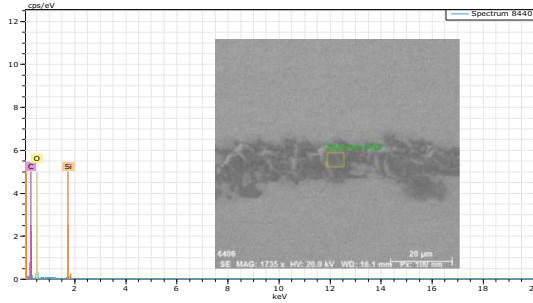
El	AN	Series	unn. C [wt.%]	norm. C [wt.%]	Atom. C [at.%]	Error (1 Sigma) [wt.%]
O	8	K-series	32.76	32.76	26.93	12.41
C	6	K-series	66.35	66.35	72.65	15.37
Si	14	K-series	0.89	0.89	0.42	0.16
		Total:	100.00	100.00	100.00	

Fig. 5. The results of electron microscopy detection crack at the welding scanning

Referred to the relevant literatures, it was known that the cracking mechanism can be divided into hot cracks and cold cracks; Hot cracking is generated during the transition of the weld metal from liquid to solid state, such as sulfur and phosphorus in the weld is prone to thermal cracking. Cold cracking is generated during the cooling process of the weld, such as higher carbon content or more alloy elements is prone to cold cracking. When the carbon equivalent of the material is less than 0.4%, the basic will not produce cracks, while the carbon equivalent of the material is greater than 0.6%, it is difficult to completely avoid the cracks.

Combined with the analysis of the above test results could be obtained, the inclusions of inner coating lead to the cracks; the oxides and carbides of inner coating enter the weld increases the cracking tendency during the welding, so that the cracks were occured to some welds, at the same time, the high content of C elements in the coating can lead to the formation of saturation at the grain boundaries, further formation of carbon precipitation, increased the cracking tendency of the weld.

2.3   Defect 2-Gas Expansion Analysis

Selected X-ray detection of the failed fuel rod, the further analysis of metallurgical testing about the weld, the results were shown in Fig. 8, the cavity between the weld and the substrate is the gas expansion.

Reference to the relevant literatures [4] can be seen, gas expansion mainly occurs in the heat-affected zone close to the fusion zone, a slight gas expansion lead to the mating surface of the end plug and the inner wall to form a small gap along the circumferential direction of the clad tube, a serious gas expansion can make the wall thickness of the clad tube thinning.
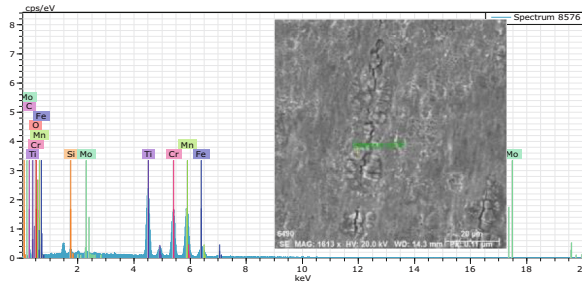
El	AN	Series	unn. C [wt.%]	norm. C [wt.%]	Atom. C [at.%]	Error (1 Sigma) [wt.%]
Ti	22	K-series	16.92	19.09	11.54	0.50
Mn	25	K-series	20.55	23.19	12.22	0.59
Cr	24	K-series	16.52	18.64	10.38	0.48
O	8	K-series	25.56	28.83	52.18	3.46
Fe	26	K-series	4.42	4.99	2.59	0.16
C	6	K-series	3.86	4.36	10.51	0.81
Si	14	K-series	0.37	0.42	0.43	0.05
Mo	42	L-series	0.43	0.49	0.15	0.05
		Total:	88.64	100.00	100.00	

Fig. 6. The results of scanning electron microscopy at the matrix crack

During the vacuum electron beam welding process, Due to the rapid crystallization of metal, electron beam welding seam is usually very narrow, rapid cooling and solidification, litter chance of gas overflow from the weld, thus increased the possibility of porosity and gas expansion. The analysis of gas expansion in electron beam welding was complicated, the main reasons include: 1) the cleanliness of workpiece is not enough; 2) The coating tube and the end plug are not properly matched; 3) The gas generated during the welding process without drainage channels; 4) Excessive heat input during welding.

Through the observation of a lot of X-ray photos found that gas expansion has the following characteristics: 1) the gas expansion and porosity produced at the same time, different batches of ring welds, the probability and size of gas expansion and porosity fluctuates greatly; 2) the location of gas expansion is fixed, it is that the fusion zone near the end plug side, the end plug and the clad tube with the gap area, as shown as Fig. 9.

In view of relevant research and tests has been carried out in the experimental stage, the best welding parameters had been developed, and the welding heat input could be well controlled; In order to eliminate the porosity and gas expansion, the measures were be taken as followed: Strictly cleaning into and drying for the clad tube and end plug before welding, maintaining the cleanliness of the welding area; Choose a qualified end plug interference structure to reduce the residual gas in the mating gap.
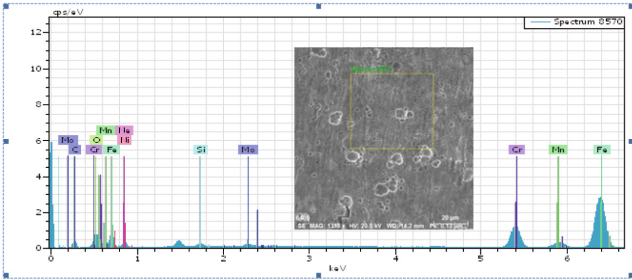
El AN	Series	unn. C [wt.%]	norm. C [wt.%]	Atom. C [at.%]	C Error (1 Sigma) [wt.%]
Fe 26	K-series	51.85	55.20	36.83	1.42
Cr 24	K-series	11.92	12.69	9.10	0.36
Ni 28	K-series	11.84	12.61	8.00	0.37
O 8	K-series	5.88	6.26	14.59	0.95
Mn 25	K-series	1.82	1.94	1.31	0.09
C 6	K-series	8.25	8.78	27.24	1.51
Mo 42	L-series	0.91	0.97	0.38	0.07
Si 14	K-series	0.56	0.59	0.79	0.06
Ne 10	K-series	0.90	0.96	1.77	0.25
	Total:	93.93	100.00	100.00	

Fig. 7. The scanning electron microscopy detection results of cladding coating

Fig. 8. The defect of gas expansion
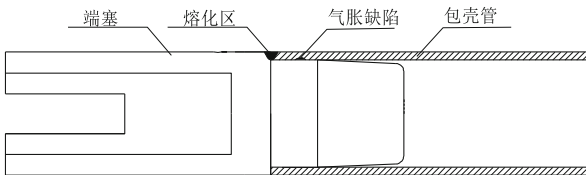
Fig. 9. Schematic diagram of fuel rod gas expansion defect

3   Test Program

Summarize above statistics can be shown that the main reason for the low welding pass rate is cracks and gas expansion, the main reason affecting the generation of cracks in the weld is the inner wall coating of the casing tube; The gas expansion during the welding process is caused by the longer surface between the end plug and the casing tube contact.

Therefore, the impact of welding defects is the inner wall removal amount of cladding tube, end plug and clad mating surface length., The amount of interference fit between them will be changed, when the clad and end plug structure changes at the same time.

Select orthogonal table of $\mathbf{L}_9(3^4)$, makes the factor level Table 1.

Table 1. Factor level table of welding test

levels	Factors		
	Removal amount of inner wall of cladding(mm)	Interference between end plug and the tube(mm)	Length of mating surface between end plug and cladding(mm)
1	0	0.02	3.5
2	0.02	0.03	2.0
3	0.04	0.04	0.8

According to the above three influencing factors, orthogonal experiments were designed, and 10 fuel rod welding tests were carried out according to different test groups. As the X-ray inspection, penetration detection and weld appearance detection results for judge reference, it was shown in Table 2.

Table 2. Test criteria items

Record	Item		
	X-ray result	penetration detection	weld appearance detection
1	pass	flawless	pass
0	defects of porosity and gas expansion	crack	defects of rough weld, obvious fish-lock lines, appearance holes

Analysis of test data can be obtained, the crack defects could been effectively controlled by removed the internal coating, the generation of gas expansion defects could been effectively suppressed for the length about 0.8 mm of mating surface. The best test scheme is to remove the internal coating of the cladding tube about 0.04 mm, the mating surface length between the cladding tube and end plug is 0.8 mm, and the interference fitting amount of the cladding tube and end plug is 0.03 mm.

4   Verification of Process Parameters

4.1   Experimental Data Verification

In order to further verify the feasibility of the orthogonal test results, experimental verification was carried out for the above parameters. The cladding tube with 0.04 mm removal of the inner wall coating, re-processed the end plug contact surface with 0.8 mm, and the interference amount of 0.03 mm were used to carry out welding tests, The welding of 10 fuel rods were completed, and the helium leak detection of welding seam, X-ray inspection, metallographic testing and penetration testing were carried out.

The helium leak detection results were all passed, the test results of X-ray inspection of the weld shown that 9 roots qualified, while one root had small pores, Which may be caused by the uncleaned pores before welding; Combined with the analysis of the results of metallographic testing and penetration testing, it can be found that there is no welding cracks. Figure 10 shown the metallographic testing results of a few randomly selected welds, metallographic testing results shown that no cracks and no gas expansion; Fig. 11 shown the results of penetration testing of the weld, It was could be seen no cracks from the figure.
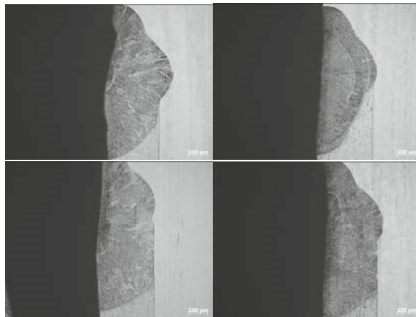
Fig. 10. Weld metallographic result

Fig. 11. Weld penetration result

In order to further confirm whether there were cracks in the above-mentioned weld seam with qualified test results, 1 fuel rod with qualified test results was randomly selected for metallographic layer grinding test, and the grinding was carried out and photographed according to the grinding volume of 0.15 mm each time, and the test results were shown in Fig. 11. Through the layer grinding metallographic inspection photos can be seen, there was no cracks in the welding area (Fig. 12).

(a) the first layer grinding (b) the second layer grinding

(c)the third layer grinding (d)the fourth layer grinding

(e)the fifth layer grinding (f) the sixth layer grinding
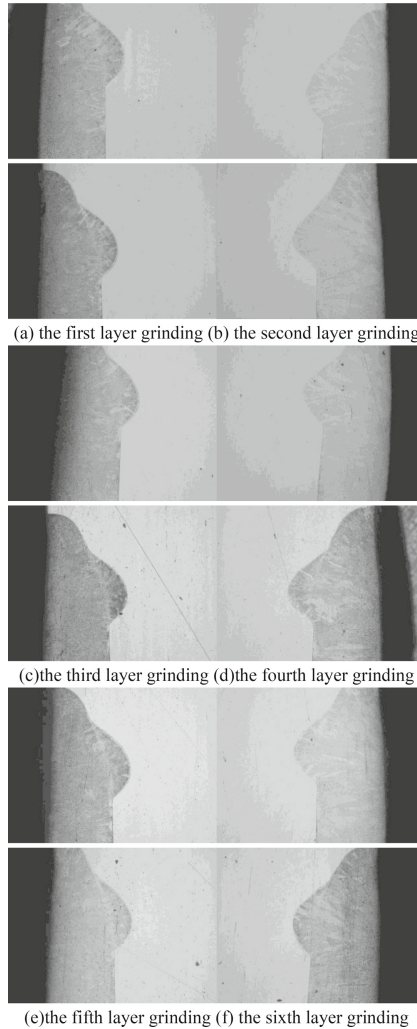
Fig. 12. Layer grinding test metallographic test results

4.2 Production Data Verification

The process program was carried out to subsequent welding work, the welding about 876 fuel rods had no helium leak detection and penetration testing failed fuel rods. The quality data of the production phase was analyzed, the qualification rate of fuel rods reached 94.1%, and the qualification rate statistics were shown in Fig. 13. IF the influence of fuel rod surface non-quality (pitting, scratching, etc.)was excluded, the fuel rod welding pass rate would be reach 95.9%.
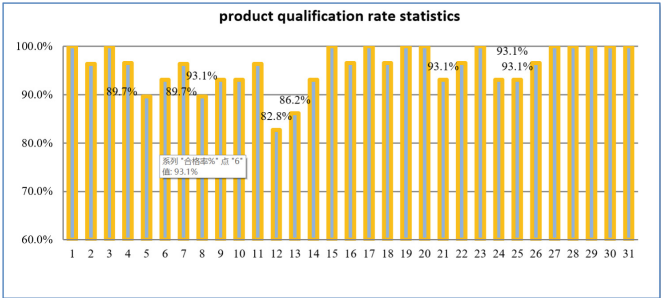
Fig. 13. Fuel rod batch pass rate

The non-conforming products was counted during the welding process, and the quality trends, were shown in Fig. 14, the distribution of non-conforming product types shown, that no gas expansion defects caused by the award of the scrap, and the crack award of the fuel rod occupied a very small proportion of the scrap, achieved a better result.
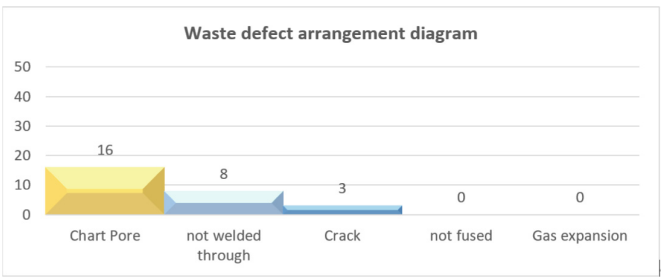
Fig. 14. Welding seam failed to award the statistical trend chart

5 Conclusions

(1) Cracking and gas expansion is the root cause of the fuel rod welding quality degradation on the welding between 316L end plug and coated 15-15Ti tube, the inner wall coating of the clad tube is the root cause of cracking, end plug mating surface length is the root cause of gas expansion.

(2) The best process parameters for the inner wall coating removal amount of 0.04 mm, end plug mating surface length with 0.8 mm and the amount of overfill is 0.03 mm. It could effectively reduce the generation of cracks and gas expansion defects, the pass rate of fuel rod welding increase to 95.9%.

References

1. Yang, J.: Exploring the defects and prevention measures in the welding press of metallic materials. Management and others 125–126 (2021)
2. Jia, Z., Jiang, Z., Li, Y., Wang, F.: Analysis of welding defects and prevention of austenitic stainless steel tubes. Weld. Technol. **47**(9), 26–29 (2018)
3. ASTM Technical Committee: ASTM B338. Standard Specification for Seamless and Welded Titanium and Titanium Alloy Tubes for Condensers and Heat Exchangers. ASTM International, United States (2010)
4. Ma, C.: Analysis of welding defects and prevention measures of austenitic stainless steel. Heat Process. Technol. **44**(17), 243–246 (2015)
5. Liu, Y.: Using orthogonal tests to optimize the welding process parameters of Gr2 titanium tube (T0.5 mm). 05, 8 (2014)
6. Zhang, J.: Selection of welding parameters for the bottom frame floor based on the orthogonal test method. Des. Res. **43**(04), 12–16 (2016)

Experimental Study on the Intrusion/Erosion Behavior of GMZ Bentonite Considering Fracture Aperture Effects

Libo Xu, Weimin Ye[✉], Qiong Wang, and Hewen Luo

Tongji University, Shanghai, China
{xulb,ye_tju}@tongji.edu.cn

Abstract. Intrusion/erosion will cause mass loss of bentonite, resulting in endangering the operation safety of the repository for disposal of high-level radioactive waste. In this work, intrusion/erosion tests were conducted on GMZ bentonite specimens with a fracture aperture of 0.1, 0.5, 0.75 and 1.0 mm, as well as a duration of 60 days. Images were regularly captured with a digital camera. The intrusion distance and width of accessory-mineral ring were obtained. The erosion rate was determined by a turbidimeter. Meanwhile, parallel tests with a fracture aperture of 0.5 and 1.0 mm were repeated with a duration of 5, 15 and 30 days. After tests stopped, dry weight of specimens was measured. Results show that the intrusion distance increased with increasing fracture apertures, resulting in the increase of accessory-mineral-ring width, which will in turn restrict intrusion and erosion. Actually, the erosion rate in the early period decreased obviously with increasing accessory-mineral-ring widths, due to its filtration effects. However, when erosion reached stabilization, the erosion rate increased with increasing fracture apertures and intrusion distances but not independent of the accessory-mineral ring. The majority part of specimen mass loss ratio in the early period was from intrusion. But when intrusion reached stabilization, the mass loss ratio of specimen will be mainly contributed by erosion and would keep on increasing. Moreover, the mass loss ratios of specimens after 60 days by intrusion and erosion both increased with increasing fracture apertures. Meanwhile, the difference between the mass loss ratio by intrusion and erosion increased with increasing fracture apertures.

Keywords: Bentonite · Intrusion/erosion · Accessory-mineral ring · Fracture aperture · Mass loss

1 Introduction

Deep geological disposal is considered as an effective way to solve the problem of safe disposal of high-level radioactive waste (HLW). According to the concept of this method, high-level radioactive waste is designed to store in a natural geological body (500–1000 m below the ground surface), in order to isolate it from the ecological environment for a long time or permanently. In this regard, compacted bentonite has been considered as a candidate buffer material for sealing the gaps and fractures in the repository

[1–4]. Researches reveal that numerous fractures with various sizes would be inevitably encountered in the surrounding rock including those naturally originated or generated during construction activities, etc. [1, 13, 16]. Theses fractures could serve as channels for groundwater flow. Once compacted bentonite in the core area contacted with groundwater in the fractures, it will expand and squeeze into the fractures. Meanwhile, when the cation concentration in the groundwater is below the critical coagulation concentration (CCC) [8, 15], bentonite colloidal particles could be generated at the clay/water interface and carried away, resulting in bentonite erosion by flowing groundwater. The phenomenon that bentonite buffer material hydrated into fractures in the surrounding rock and then eroded away by groundwater was defined as bentonite intrusion/erosion. This intrusion/erosion behavior may cause significant mass loss of bentonite during the long-term operation of the repository, especially for the fractures with larger sizes. Therefore, it is of great importance to figure out the intrusion/erosion behavior of bentonite with consideration fracture aperture effects.

During past decades, numerous work has been conducted on the intrusion/erosion process of montmorillonite in artificial fractures. A two-dimension fracture formed by two transparent plates is designed and the intrusion/erosion tests were performed to investigate effects of the types of montmorillonite, water velocity and slope angle of the fracture on the intrusion distance and erosion rate. Vilks et al. (2010) found that the intrusion distance and erosion rate of Na-rich montmorillonite was significantly higher than Ca-rich montmorillonite [14]. Schatz et al. (2013) found that there was not enough test data to prove the relationship between the intrusion distance and flow velocity [12]. While the erosion rate of Na-rich montmorillonite increased with the increase of the flow velocity under the most dilute conditions (ionic strength < 1 mM). Subsequently, with the same apparatus, the influence of fracture angles on the intrusion distance and erosion rate was investigated by Schatz et al. (2016) [11]. It was observed that the intrusion distance was larger in the bottom half than that in the upper one, with the fracture angle of 45° and 90°. Moreover, an increase in erosion rate of Na-rich montmorillonite was observed with an increasing fracture slope angle from 0° to 90°.

In comparison with montmorillonite materials, the intrusion/erosion process of bentonite also has attracted much attention. The intrusion/erosion behavior of MX-80 bentonite with a naturally varying fracture aperture was investigated by Reid et al. (2015) [10]. It was found that an accessory-mineral ring, mainly composed of accessory minerals (such as quartz, felspar, etc.) was generated at the intrusion edge during the process of erosion. A two-stage cyclic intrusion/erosion mechanism was derived, that confirms the mitigating effects of accessory-mineral ring on the intrusion and erosion.

Previous studies have focused on the intrusion/erosion behavior with one single fracture aperture. However, the variability of the fracture aperture may play an important role in the development of the accessory-mineral ring, which may in turn inhibit intrusion and erosion [10]. Moreover, research of influence of intrusion/erosion on mass loss of bentonite has rarely been reported, which is necessary for assessing the deterioration process of buffer materials with fractures.

In this study, tests on intrusion/erosion of GMZ bentonite into artificial fractures were carried out with a fracture aperture of 0.1, 0.5, 0.75 and 1.0 mm, as well as a duration of 60 days, in order to evaluate the influence of fracture apertures on bentonite intrusion

and erosion. Meanwhile, parallel tests with a fracture aperture of 0.5 and 1.0 mm were repeated with a duration of 5, 15 and 30 days. After tests stopped, the mass loss of specimens for each test could be determined. Based on these results, influences of the intrusion/erosion behavior and on the mass loss of bentonite were analyzed.

2 Methodlogy and Test Procedures

2.1 Apparatus

In this study, an experimental apparatus was developed (Fig. 1) for conducting intrusion/erosion tests. By inserting stainless-steel gasket into two transparent acrylic plates, a flow-through cell was generated between the two plates. Then, fractures with different sizes could be formed by adjusting the thickness of the gasket. Meanwhile, a hole for placing the specimen was set in the center of the apparatus. A cross-type counterforce frame was mounted on the upside of the acrylic plate (Fig. 1), to restrict the vertical deformation of the acrylic plate due to the specimen swelling. Finally, with a high-precision camera fixed above the test apparatus, the bentonite intrusion process could be monitored by taking images automatically at given time intervals.
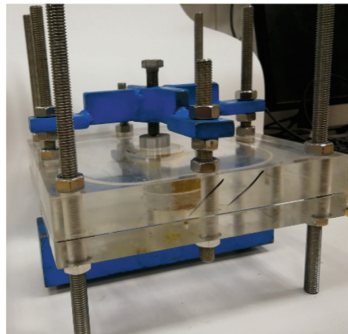
(a) Image of the test apparatus
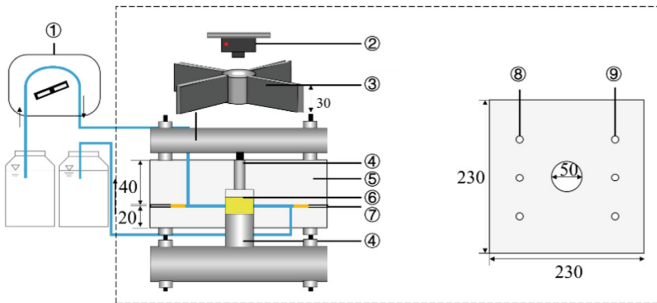
(b) Schematic diagram of the test apparatus

① Peristaltic pump;   ② Camera;   ③ Counterforce frame;
④ Piston;   ⑤ Acrylic plate;   ⑥ Specimen;
⑦ Crack;   ⑧ Inlet;   ⑨ Outlet

Fig. 1. Setup for conducting the intrusion/erosion test

2.2 Materials and Specimen Preparation

1) Materials

Gaomiaozi (GMZ) bentonite was tested in this study, which was extracted from Inner Mongolia autonomous region of northern China [5, 6]. Its basic properties are listed in Table 1.

2) Specimen preparation

For specimen preparation, 77.5 g of GMZ bentonite powder with an initial water content of 10.0% and filtrate conductivity below 10 μs/cm was statically compacted into a cylindrical specimen with a target height of 20 ± 0.5 mm, a diameter of 50.4 mm and a dry density of 1.70 ± 0.05 Mg/m^3.

Table 1. Basic properties of GMZ bentonite [5]

Properties	Description
Specific gravity of soil grain	2.66
Mesh	200
Liquid limit (%)	276
Plastic limit (%)	37
Total specific surface area (m^2/g)	570
Cation exchange capacity (mmol/g)	0.773
Main minerals	Montmorillonite (75.4%), Quartz (11.7%), Cristobalite (7.3%), Feldspar (4.3%)

Table 2. Specifications of the tests conducted

Tests	Fracture aperture (mm)	Test termination time (day)
T1	0.1	60
T2-5	0.5	5, 15, 30 and 60
T6	0.75	60
T7-10	1.0	5, 15, 30 and 60

2.3 Test Procedures

In order to investigate the influence of fracture apertures on intrusion/erosion behavior, as well as the intrusion/erosion process on the mass loss of buffer materials, a total of 10 tests were conducted (Table 2).

First of all, after installation of the compacted bentonite specimen into the central compartment, a peristaltic pump was used to provide deionized water injected into the three inlets. A constant velocity of 8.3×10^{-5} m/s could be produced. Then, the camera was activated and images were regularly obtained. According to the relationship between the circular area and the radius, the intrusion distance (l) or width of the accessory-mineral ring (l_1) could be derived,

$$l = \left(\sqrt{\frac{2(S_1 + S_2)}{\theta} + r^2} \right) - r \tag{1}$$

$$l_1 = l - \left[\left(\sqrt{\frac{2S_1}{\theta} + r^2} \right) - r \right] \tag{2}$$

where, S_1 and S_2 are the circular area of non-accessory and accessory-mineral ring, θ is the angle of fan-shape area and r is the radius of specimen. (Fig. 2).
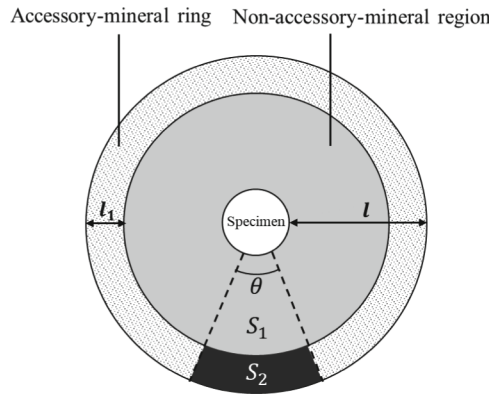
Fig. 2. A bird view of the test apparatus with bentonite intruded

Meanwhile, with a portable turbidimeter (TN-100 from Eutech Instruments), the turbidity of outlet effluent was measured every 24 h. Then, according to the calibration curve shown in Fig. 3, erosion rate could be determined [2]. After the test, the specimen was pushed out and its dry mass was weighed.

New specimens were installed and procedures above were repeated. Until all the 10 specimens with respect to the various fracture apertures and test termination time were tested corresponding to their own specifications (Table 2), all the tests were completed.

3 Results

3.1 Intrusion Behavior

The intrusion stage with a fracture aperture of 1.0 mm during 60 days is presented in Fig. 4. As shown in Fig. 4, a ring of layered material (accessory-mineral ring) was
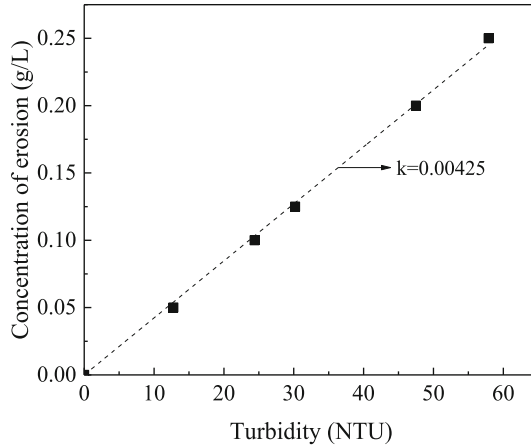
Fig. 3. Calibration curve for the turbidity and concentration of erosion
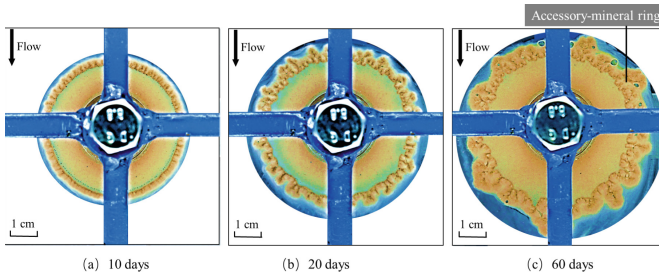
Fig. 4. Scenarios after different intrusion times for the test with a fracture aperture of 1.0 mm

formed and developed at the clay-water interface. This observation is consistent with the research by Reid et al. (2015) [10].

According to the ImageJ software, evolutions of intrusion parameters (intrusion distance and width of accessory-mineral ring) are obtained in Figs. 5 (a) and (b). It clearly shows that the intrusion distance and width of accessory-mineral ring both increased significantly in the early stage. Then, the two intrusion parameters increased more gradually and reached stability after 60 days. Moreover, for one given day, the two intrusion parameters increased with increasing fracture apertures.

3.2 Erosion Behavior

The erosion curve in terms of erosion rate versus time is shown in Figs. 6 (a). Results in Fig. 6 (a) show that the erosion rates with a fracture aperture of 1.0, 0.75, 0.5 and 0.1 mm decreased rapidly before 5 days. Then the erosion rates increased and reached a second peak value after 10, 9, 8 and 9 days, with a fracture aperture of 1.0, 0.75, 0.5 and 0.1 mm, respectively. Finally, their corresponding erosion rates decreased and kept stable around after 60 days.
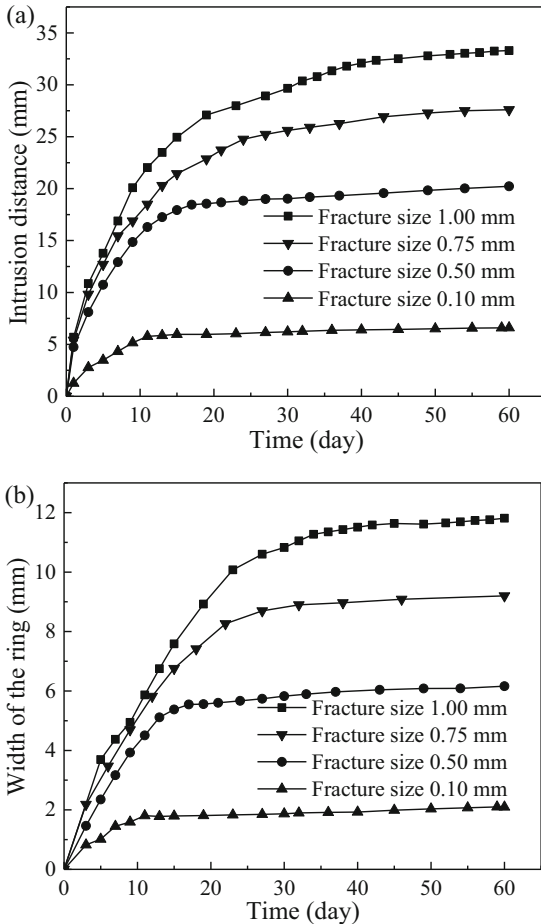
Fig. 5. Evolutions of intrusion distance (a) and width of accessory-mineral ring (b) with time

Meanwhile, the evolutions of the accumulated erosion mass with time are depicted in Fig. 6 (b). It can be observed that the accumulated erosion mass increased significantly in the early period. Then, an obvious turning point of the erosion curve was observed. Moreover, for one given day, the accumulated erosion mass increased obviously with increasing fracture apertures.

3.3   Mass Loss Ratio of Specimens

With tests stopped, the specimens were pushed and weighed to obtain the dry mass. Then, for tests with a fracture aperture of 0.5 and 1.0 mm, the evolutions of mass loss ratio of specimens with time are obtained in Fig. 7. It appears in Fig. 7 that once the intrusion/erosion occurred, the mass loss ratios of specimens both increased rapidly and then followed by an obvious reduction in the increase rate after about 15 days.
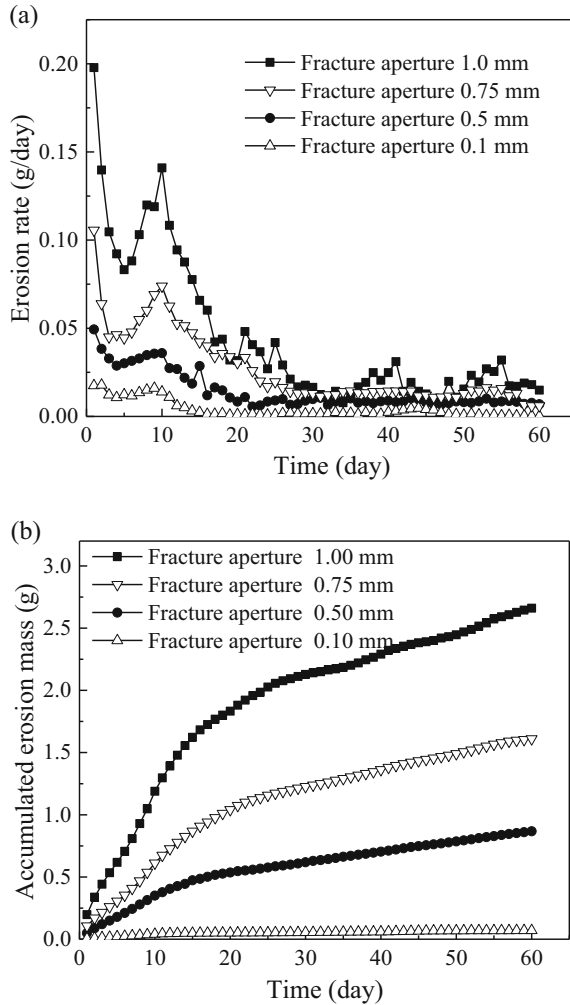
Fig. 6. Evolutions of erosion rate (a) and accumulated erosion mass (b) with time

Subsequently, the mass loss ratio of specimens after 60 days is plotted versus the fracture aperture in Fig. 8. It can be observed in Fig. 8 that the mass loss ratio of specimens increased significantly with increasing fracture apertures.

4 Discussion

4.1 Influences of Fracture Apertures on Bentonite Intrusion

According to the intrusion model by Svobody (2013) [13], the sidewall friction factor decreases with increasing fracture apertures. Therefore, the intrusion distance in the steady state is proportional to the fracture aperture. Meanwhile, based on this theory and
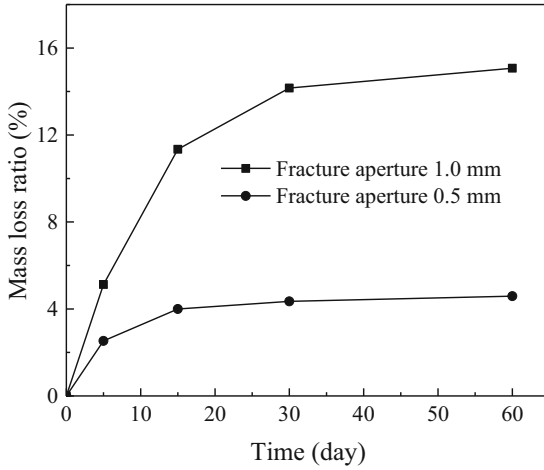
Fig. 7. Evolutions of mass loss ratios of specimens with time for tests with a fracture aperture of 0.5 and 1.0 mm
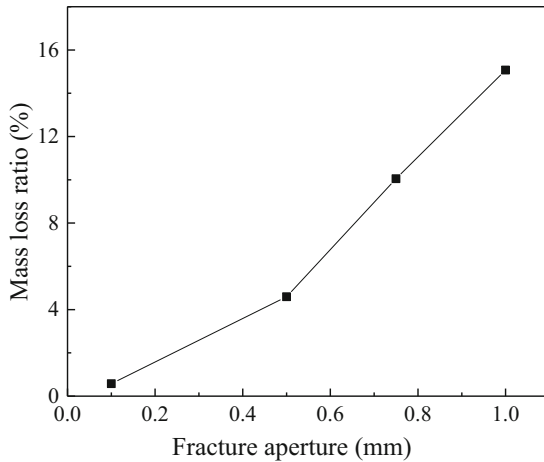
Fig. 8. Relationship between mass loss ratios of specimens and fracture apertures after 60 days

the test result with fracture aperture of 0.1 mm, the predicted intrusion distance after 60 days versus fracture apertures could be obtained in Fig. 9. However, it appears in Fig. 9 that the predicted value was obviously larger than the measured one, especially for tests with a larger fracture aperture. This observation could be due to the mitigating influence of the accessory-mineral ring on intrusion (Reid et al., 2015) [10] and its explanation could be given as follows. According to the research by Moreno et al. (2011) [7], the erosion rate would increase with increasing intrusion distances, leading to more accessory minerals left at the clay/water interface. Accordingly, the width of accessory-mineral ring would increase correspondingly with increasing intrusion distances and more significantly with a larger fracture aperture. Indeed, according to Figs. 5 (a) and (b),

the relationship between the width of accessory-mineral ring and intrusion distance could be obtained in Fig. 10. The width of accessory-mineral ring increased with increasing intrusion distances and was larger with increasing fracture apertures, which confirmed the conclusion above. Therefore, as the fracture aperture and intrusion distance increase, the larger width of accessory-mineral ring may lead to the more restrictive effects on intrusion. In this regard, the intrusion model proposed by Svobody (2013) [13] could not be used for simulating the intrusion behavior in this study, especially with a larger fracture aperture.
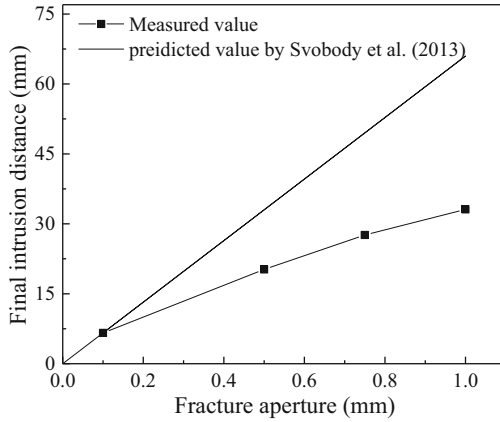
Fig. 9. Relationship between the final intrusion distance and fracture aperture after 60 days
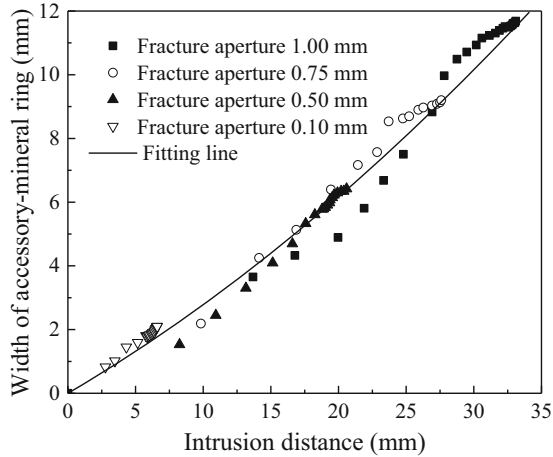
Fig. 10. Relationship between width of the accessory-mineral ring and intrusion distance

4.2 Influences of Fracture Apertures on Bentonite Erosion

According to research by Neretnieks et al. (2017) [9], the erosion rate ($N_{erosion}$) could be calculated as,

$$N_{erosion} = 4\rho_s \delta \phi_c \sqrt{Du(l+r)} \qquad (3)$$

where, ρ_s is the density of montmorillonite, δ is the fracture aperture, ϕ_c is the volume fraction of montmorillonite at the intrusion front, D is the diffusion coefficient, u is the flow velocity, l is the intrusion distance and r is the radius of specimens.

For one given fracture aperture, based on this erosion model (Eq. (3)), the erosion rate will increase with the increase of the diffusion coefficient and intrusion distance. However, according to Figs. 5 (a) and Fig. 6 (a), it is clear that the erosion rate in the early stage decreased significantly with the increase of the intrusion distance and accessory-mineral-ring width, indicating that the development of the accessory-mineral ring would lead to the reduction in the diffusion coefficient [10]. After the intrusion distance reached stabilization, the erosion rate basically remained unchanged. According to Eq. (3), it can be concluded that the diffusion coefficient would also keep constant in the steady state. Meanwhile, according to Figs. 5 (a) and Fig. 6 (b), the relationship between the final average erosion rates after 60 days and $\delta\sqrt{(l+r)}$ can be derived in Fig. 11. Results in Fig. 11 show that the erosion rate is proportional to $\delta\sqrt{(l+r)}$. It can be drawn from Eq. (3) that the diffusion coefficient in the steady state is equal to the slope of this curve in Fig. 11 and keeps constant with any fracture aperture. In other words, the diffusion coefficient is independent of facture aperture and thus, the erosion rate in the steady state would only increase with increasing fracture apertures and intrusion distances.
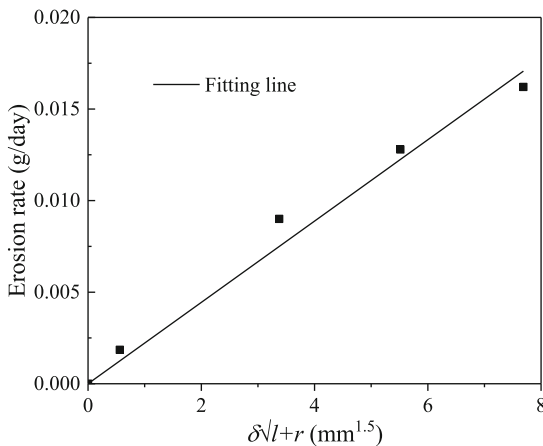
Fig. 11. Relationship between final erosion rate between and $\delta\sqrt{(l+r)}$ after 60 days

4.3 Influences of Intrusion/erosion on the Mass Loss of Specimens

According to Fig. 6 (b), the mass loss ratio of specimens by erosion could be calculated and was plotted versus time in Fig. 12. It appears in Fig. 12 that the mass loss ratio by

erosion with a fracture aperture of 0.5 and 1.0 mm increased quickly but then followed by an obvious reduction in the increase rate after 15 days, which has a good agreement with that in the erosion curve (Fig. 6 (b)). Meanwhile, the evolution of mass loss ratio of specimens by intrusion with time could also be determined by the difference between total mass loss ratio of specimens (Fig. 7) and that by erosion (Fig. 12). Results in Fig. 12 show that the mass loss ratio by intrusion with a fracture aperture of 0.5 and 1.0 mm both started with a significant increase and then reached a stable value after 15 and 30 days, respectively. The turning points are consistent with that in the intrusion curve (Fig. 5 (a)). Moreover, it could also be observed in Fig. 12 that the mass loss ratios of specimens with a fracture aperture of 0.5 and 1.0 mm were mainly contributed by intrusion before 15 and 30 days, respectively. Subsequently, the specimen mass loss ratios kept on increasing and would be only dependent on the erosion rate. Indeed, as long as time for erosion is enough, the mass loss ratios of specimens by erosion may exceed that by intrusion.
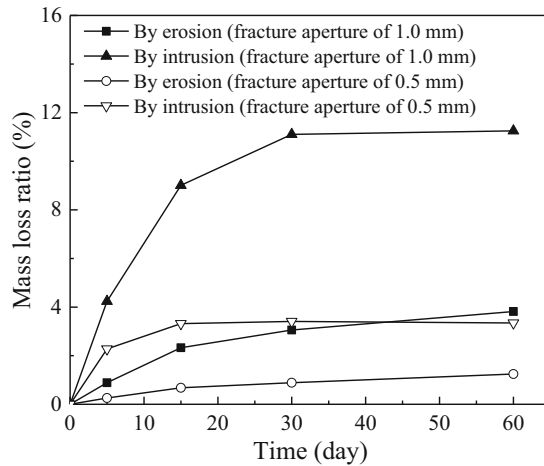
Fig. 12. Evolutions of mass loss ratio of specimens by erosion or intrusion with time foe tests with a fracture aperture of 0.5 and 1.0 mm

According to Fig. 6 (b), the mass loss ratio of specimens by erosion after 60 days could be calculated and was plotted versus the fracture aperture in Fig. 13. Results in Fig. 13 shows that the mass loss ratio by erosion increased with increasing fracture apertures. Meanwhile, according to Figs. 8 and 13, mass loss ratio of specimens by intrusion could also be determined. Then, the relationship between mass loss ratio of specimens by intrusion and fracture aperture after 60 days was depicted in Fig. 13. It could be observed in Fig. 13 that the mass loss ratio after 60 days by intrusion increased with increasing fracture apertures. Moreover, the difference between the mass loss ratio by intrusion and erosion increased with increasing fracture apertures.

References

1. Bian, X., Cui, Y.J., Zeng, L.L., Li, X.Z.: State of compacted bentonite inside a fractured granite cylinder after infiltration. Appl. Clay Sci. **186**, 105438 (2020)
2. Birgersson, M., Boergesson, L., Hedstroem, M., Karnland, O., Nilsson, U.: Bentonite erosion. Final report (No. SKB-TR-09-34). Swedish Nuclear Fuel and Waste Management Co (2009)
3. Cui, L.Y., Ye, W.M., Wang, Q., Chen, Y.G., Chen, B., Cui, Y.J.: Investigation on gas migration in saturated bentonite using the residual capillary pressure technique with consideration of temperature. Process Saf. Environ. Protect **125**, 269–278 (2019)
4. Nguyen, T.S., et al.: A case study on the influence of THM coupling on the near field safety of a spent fuel repository in sparsely fractured granite. Environ. Geol. **57**(6), 1239–1254 (2008)
5. Xu, L.B., Ye, W.M., Liu, Z.R., Wang, Q., Chen, Y.G.: Extrusion behavior of bentonite-based materials considering pore size and sand content effects. Constr. Build Mater. **347**, 128580 (2022)
6. Luo, H.W., Ye, W.M., Wang, Q., Chen, Y.G., Chen, B.: Pore fluid chemistry effects on the swelling behavior of compacted GMZ bentonite with an artificial annular gap. Bull. Eng. Geol. Env. **80**(7), 5633–5644 (2021)
7. Moreno, L., Liu, L., Neretnieks, I.: Erosion of sodium bentonite by flow and colloid diffusion. Phys. Chem. Earth, Parts A/B/C **36**(17–18), 1600–1606 (2011)
8. Missana, T., Alonso, Ú., Turrero, M.J.: Generation and stability of bentonite colloids at the bentonite/granite interface of a deep geological radioactive waste repository. J. Contam. Hydrol. **61**(1–4), 17–31 (2003)
9. Neretnieks, I., Moreno, L., Liu, L.: Clay Erosion: Impact of Flocculation and Gravitation. Svensk kärnbränslehantering AB. Swedish Nuclear Fuel and Waste Management Company (2017)
10. Reid, C., Lunn, R., El Mountassir, G., Tarantino, A.: A mechanism for bentonite buffer erosion in a fracture with a naturally varying aperture. Mineral. Mag. **79**(6), 1485–1494 (2015)
11. Schatz, T., Akhanoba, N.: Bentonite buffer erosion in sloped fracture environments (No. POSIVA-2016-13). Posiva Oy (2017)
12. Schatz, T., et al.: Buffer erosion in dilute groundwater (No. POSIVA-12-44). Posiva Oy (2013)
13. Svoboda, J.: The experimental study of bentonite swelling into fissures. Clay Miner. **48**(2), 383–389 (2013)
14. Vilks, P., Miller, N.H.: Laboratory bentonite erosion experiments in a synthetic and a natural fracture. NWMO Technical Report TR-2010-16 (2010)
15. Xu, L.B., Ye, W.M., Wang, Q., Chen, Y.G., Chen, B.: Investigation on intrusion of bentonite–sand mixtures in fractures with consideration of sand content andseepage effects. Bull. Eng. Geol. Environ. **81**(1), 1–16 (2022)
16. Ye, W.M., Xu, L.B., Wang, Q., Chen, Y.G., Chen, B.: Bentonite-sand mixture intrusion process and its model in rock fissures with consideration of lateral wall friction. Chin. J. Geotech. Eng. **44**(4), 613–621 (2022). (in Chinese)

Research on Ultra High Flux Research Reactor

Xue Zhang, Hongxing Yu[(✉)], Bangyang Xia, Wenjie Li, and Xilin Zhang

Science and Technology on Reactor System Design Technology Laboratory, Nuclear Power Institute of China, Chengdu 610213, China
`Yuhong_xing@126.com`

Abstract. The lack of fast neutron irradiation test equipment is a key practical factor that restricts the development of the new generation nuclear energy technology with fast reactor as the core in China. Scarce isotopes such as californium 242, which are urgently needed in industry and medicine, are also highly dependent on imports. In order to provide a fast reactor material irradiation environment and isotope production environment, significantly accelerate the development of fast reactor fuel and structural material technology, and improve the efficiency of rare isotope production, this paper proposes a multifunctional inherently safe ultra-high flux reactor design with fast/thermal neutron flux levels up to 10^{16} n/(cm^2.s), namely UFR-10^{16}. The neutron energy spectrum covers fast spectrum, superheat spectrum and thermal spectrum; several material irradiation test orifices, isotope production orifices and test loop orifices are arranged in the core, and the test loop supports many new reactor coolants such as H_2O, Na, He, He-Xr, molten salt, etc., and supports the simulation of typical transient processes and accident conditions. This paper discusses the overall construction scheme of the reactor, and the current construction scheme shows that each performance index can meet the target requirements and achieve the expected functions while ensuring the safety performance of the reactor. This study can provide a basis for the development of ultra-high flux reactors and provide strong support for the cause of nuclear energy, nuclear technology, and nuclear medicine in China.

Keywords: Ultra-high flux · Research reactor · Fast reactor · UFR

1 Introduction

The research and development of cleaner, more efficient, and safer new nuclear energy systems is of great significance to the sustainable development of nuclear energy, and the performance of nuclear fuel and structural materials, especially their irradiation performance, has always been an important basis for the development of new nuclear energy systems. The irradiation experiment of materials is mainly carried out in the research reactor. The irradiation test ability of the research reactor is mainly determined by the neutron flux level. The higher the neutron flux level, the faster the irradiation test of materials and shorten the research and development cycle of materials.

The construction of high-flux reactors is of great benefit to the entire nuclear energy field. In the 1960s, thermal spectrum and fast spectrum research reactors were built and

put into use in various countries around the world. In terms of thermal spectrum research reactors, Russia and Belgium have built high-flux research reactors SM-2 [1] and BR-2 [2] respectively, and the United States has built HFIR [3] and ATR [4]. Among them, the HFIR thermal neutron flux is about 2.5×10^{15} cm^{-2}s^{-1}, which is one of the research reactors with the highest steady-state thermal neutron flux. Most of the 252 Cf in the world comes from here; the ATR thermal neutron flux is about 1×10^{15} cm^{-2}s^{-1}, with a power level of 250 MW, is one of the research reactors with the highest power level and has a strong material irradiation capability. In terms of fast-spectrum research reactors, Russia's BOR-60 [4] has not yet been retired, and the United States' EBR-II [6] and FFTF [7] were retired in the 1990s for political and economic reasons, but also has left quite a wealth of experience and relatively mature technology to American fast-spectrum reactors (especially sodium-cooled fast reactors). The development of high flux research reactors in China is relatively late compared to other countries. The thermal spectrum research reactor HFETR [8] was critical in 1979, and the fast spectrum research reactor CEFR [9] was critical in 2010.

In 2002, the International Forum on Generation IV Nuclear Energy Systems proposed six priority development of Generation IV nuclear energy systems, most of which are fast reactors. The development of fast reactors is inseparable from the corresponding material irradiation experiments. However, the existing thermal spectroscopy research reactors have limited irradiation capabilities, and it is difficult to match the development and research speed of fast reactors. France started construction of the water-cooled research reactor JHR [10] in 2007, Russia started the construction of the sodium-cooled research reactor MBIR [11] in 2015, and the U.S. sodium-cooled fast reactor VTR [12] has also been put on the agenda. It can be seen that the overall development trend of foreign research reactors is to develop towards high-flux fast reactors. At the same time, more advanced irradiation methods are required, such as independent coolant circuits, on-line monitoring equipment in the reactor, and particle beam pipelines, etc.

Among the fourth-generation advanced nuclear power systems, fast reactor is one of the most promising reactor types. At present, there is an extreme lack of data on fast neutron irradiation of reactor materials in China, and there is also a lack of fast neutron irradiation research reactor. In addition, scarce isotopes such as californium 242, which are urgently needed in industry and medicine, are also highly dependent on imports. In order to provide fast reactor material irradiation environment and isotope production environment, greatly accelerate the research and development of fast reactor fuel and structural materials technology, and improve the production efficiency of scarce isotopes, this paper proposes a multifunctional intrinsically safe ultra-high flux reactor design with fast/thermal neutron flux level up to 10^{16} n/(cm^2.s), namely UFR-10^{16}, and discusses the overall construction scheme.

2   The Design Goals of the Ultra-high Flux Reactor

According to the current demand for research reactors, the overall design goal of UFR is to cover the fast spectrum, super thermal spectrum and thermal spectrum with fast/thermal neutron flux up to 10^{16} n/(cm2.s); A number of material irradiation test channels, isotope production channels and test circuit channels are arranged in the core.

Table 1. Comparison of key parameters

	VTR	MBIR	JHR	PIK	UFR
Power/MW	150–300	150	100	100	200
Type	SFR	SFR	LWR	LWR	LFR
Neutron spectrum	Fast	Fast	Thermal	Thermal	Fast
Neutron Flux n/cm^2.s	4.0×10^{15}	5.3×10^{15}	1.0×10^{15}	4.5×10^{15}	1.0×10^{16}
Coolant	Na、He 、Pb-Bi、Pb 、molten salt	Na、He 、Pb-Bi、Pb 、molten salt	light water, gas	light water, gas	Na、Pb-Bi 、Pb、molten salt、light water、CO$_2$ 、He
Loop Number	3	3	3	/	3

The test circuit supports many new reactor coolants such as H_2O, Na, he, He-Xr, molten salt, etc., supports the simulation of typical transient processes and accident conditions, and meets the strong needs of radiation test and performance test of nuclear fuel and materials, transient and typical accident simulation. The ultra-high-flux multi-function reactor is facing the frontier of world science and technology, and aims to surpass the comprehensive research facilities such as the VTR under construction in the United States and the MBIR under construction in Russia. The key parameters are shown in Table 1.

3   Ultra-high Flux Reactor Construction Scheme

The overall construction plan of the research reactor includes: a key system, namely, ultra-high flux inherently safe nuclear reactor system; Three large-scale test loop systems, namely, advanced nuclear fuel and material steady-state test loop (coolant could be Na, Pb, Pb Bi, CO_2, He, H_2O, etc.), reactor transient behavior simulation test loop (through radial movement, realize rapid and controllable adjustment of fuel power, and carry out research on transient characteristics of fuel elements under the conditions of power jump, load follow, reactivity introduction, etc.) and accident simulation test circuit (meet the functional requirements of operating condition simulation, triggering of the accident condition, accident mitigation, fuel failure and fission product monitoring); A neutron science experiment platform, which can provide horizontal channels of neutron beams with different energies; Carry out experimental research on irradiation and neutron activation of small-size materials. Figure 1 shows the general layout of ultra-high flux reactor. The construction schemes of these systems will be discussed below.
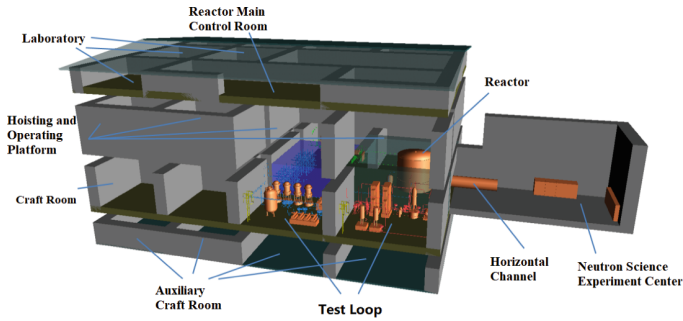
Fig. 1. Schematic diagram of Ultra-high flux reactor

3.1   Inherent Safety Nuclear Reactor System Scheme of Ultra-high Flux Reactor

Table 2 shows the overall design parameters and design choices of the intrinsically safe nuclear reactor system of ultra-high flux reactor. The rated thermal power of the reactor is set at 200 MW, and the refueling cycle is 90 days. Lead-bismuth eutectic (LBE) is selected as the core coolant, which has good neutron physical properties, thermophysical properties and chemical properties. The reactor core is arranged as an atmospheric pool with a height of 450 mm, a temperature of 165/350 °C at the inlet and outlet of the core, and a maximum coolant flow rate of 4.0 m/s. As for the selection of the fuel, considering the characteristics of the core, such as high fast neutron flux, hard neutron energy spectrum and high power density, the U-Zr metal fuel with high U density, few moderating elements and good heat conduction is selected, zirconium alloy with excellent neutron property, mechanical property and irradiation property is a good choice as cladding material.

Table 2. Overall design parameters

Parameters	Value
Rated Power	200 MW
Core arrangement	atmospheric pool
Coolant	LBE
Fuel	U-Zr metal fuel
Cladding	Zirconium alloys
Height of active zone	450 mm
Core Inlet Temperature	165 °C
Coolant max velocity	4.0 m/s
Reload cycle	90 EFPD

The natural circulation of coolant in the circuit is sufficient to cool the reactor without the risk of residual heat export from the reactor core, and the reactor protection vessel is

arranged in the passive heat conduction system tank filled with water. The primary circuit system mainly includes: reactor core, steam generator module, main pump, and internal radiation shielding, which is located in the reactor vessel. The secondary circuit system mainly includes: steam generator module, feedwater and steam pipelines, steam-water separator, and independent cooler. The LBE coolant is heated by the core, enters the core outlet chamber and flows out laterally, enters the steam generator from the bottom of the primary circuit, and is cooled by the secondary loop at the same time. When the coolant reaches the top of the primary side of the steam generator, it turns over and enters the main pump, and then the coolant is transported by the main pump from top to bottom to the reactor inlet chamber. The protective gas system mainly includes: gas system condenser, membrane safety device, pressure relief device and pipeline. The coolant process system mainly includes: LBE filling and discharging system, purification system and real-time online monitoring system, which are used to maintain the quality of LBE in the system during operation. The safety system mainly includes reactive accident protection system, steam generator leakage suppression system, independent cooling system and passive residual heat removal system. In addition, the refueling system needs to be set up.

Among them, the reactor core is the key part. The layout of the reactor core is shown in Fig. 2. The high-power density standard fuel assembly is located in the central area, and the periphery is the shielding assembly. In order to improve the reactivity control ability and reliability, two kinds of control rod systems with different principles are set up. The holes for the irradiation test of advanced nuclear fuel and materials are located in the central zone of the core with ultra-high neutron flux. The holes for the nuclear reactor transient test and the typical accident simulation test are located in the reflector area of the core. And several material irradiation test holes are set in the high-power density fuel area and emitter area of the core. Several horizontal and vertical experimental channels are set in the radial direction of the reactor (mainly used for neutron scattering experiments, neutron photography and other basic research of Neutron Science).
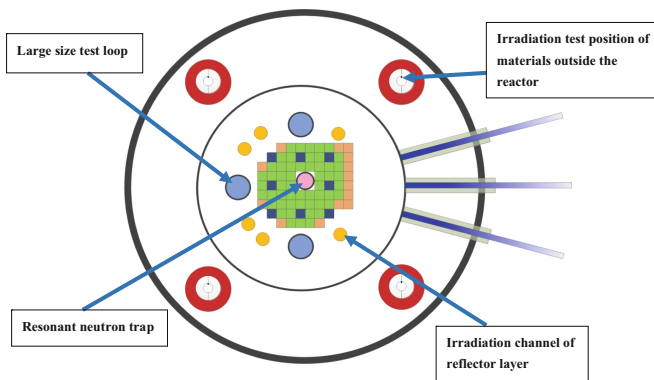
Fig. 2. Schematic diagram of the core layout

In order to improve the power density of the reactor core and reduce the problem of fuel core, considering the swelling of fuel elements caused by axial and radial temperature differences, irradiation and other factors, and referring to the design ideas of fuel

elements of European JHR, China's HFETR and other test reactors, the standard fuel assemblies in the high-power density area of the reactor core initially adopt the narrow rectangular fuel elements shown in Fig. 3. The core adopts high-performance U-10Zr metal fuel with an U235, enrichment of 64.4%., and the cladding material adopts T91.
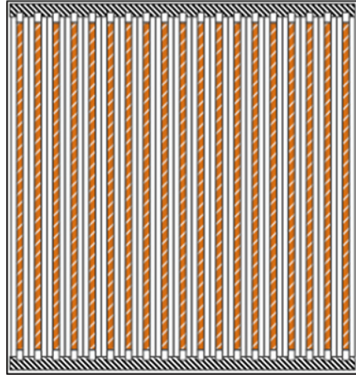
Fig. 3. Narrow rectangular fuel assembly

In terms of thermal design criteria, due to the high boiling point of LBE, it is very difficult to boil, and the design criteria related to boiling threshold do not need to be considered. It is only necessary to consider operating temperature limits of the core and integrity requirements design limits of the cladding.

For narrow rectangular fuel elements, there is usually no gap to contain fission gas. In order to avoid the fission gas causing the fuel rod to swell and burst, the temperature of the fuel is usually limited to a certain range.

For U-Zr alloy fuel, the fuel temperature should be lower than 560 °C. In order to maintain the integrity of the cladding, the coolant flow rate outside the fuel cladding and the maximum temperature on the outer surface of the cladding shall be limited. Among them, considering the heat carrying capacity of lead bismuth per unit volume, the coolant flow rate limit is relaxed to 4 m/s. The maximum temperature of the outer surface of the cladding is still limited to below 550 °C. In the design process, the flow heat transfer model of the coolant channel refers to the previous research results [13–15].

Based on the overall design objectives and criteria, after repeated demonstration, the core design parameters are shown in Table 3, and the results show that it meets the core neutron flux requirements.

3.2 Advanced Nuclear Fuel and Material Irradiation Test Loop System

In order to speed up the research on the radiation mechanism of advanced nuclear fuels and materials, three forms of nuclear fuel and material irradiation tests can be carried out on ultra-high flux reactors, including static container irradiation test, instrumented irradiation test and loop irradiation test. Among them, the loop irradiation test can accommodate nuclear materials or fuels with large heat release and scaled fuel components

Table 3. Core design parameters

	Value	Units
Power	200	MW
Fuel Assembly number	56	
Diameter	954.33	mm
Active height	450.00	mm
Pitch	83.70	mm
Power density	1132.87	MW/m^3
Uranium quality	400.16	kg
U-235 quality	279.83	kg
Upper reflector	400.00	mm
Lower reflector	400.00	mm
Total length	1450.00	mm
Flow direction	upward	
Coolant velocity	4.00	m/s
Coolant flow rate	10609.91	kg/s
Inlet temperature	165.00	°C
Outlet temperature of active zone	293.84	°C
Maximum fast neutron flux	$\geq 1.0 \times 10^{16}$	n/cm^2.s

and cladding materials requiring irradiation under actual operating conditions. The most significant advantage is that it can simulate the actual thermal hydraulic environment and hydro chemical environment, and accurately monitor and control irradiation parameters. This is one of the most complex and important test devices. The loop device is located in the center of the nuclear reactor and has ultra-high fast neutron flux. According to the different test tasks, the coolant can choose Na, Pb, Pb Bi, CO2, he, etc., and the inlet and outlet temperature can be adjusted according to the coolant type to meet the requirements of rapid screening and performance testing of advanced nuclear energy materials and nuclear fuel samples.

The loop device has an independent coolant circuit, which can independently control the coolant parameters in the device, such as pressure, temperature, flow rate, chemical composition, etc., and take away the heat generated by the test piece. By connecting with the computer control system, the emergency control and alarm functions are realized, and a variety of irradiation parameters are monitored online, including flow, temperature, pressure, differential pressure, fission products and water chemistry. The loop irradiation device needs to occupy multiple core cells, and the empty cell space outside the irradiation device is filled with special-shaped components (Fig. 4).
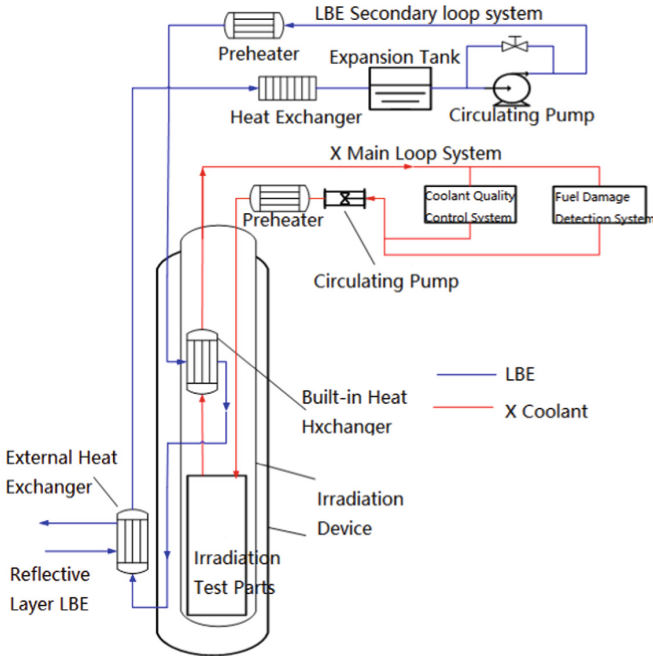
Fig. 4. Advanced nuclear fuel and material irradiation test device

3.3 Nuclear Reactor Transient Behavior Simulation Test Loop System

In order to study the structural integrity and material irradiation behavior of fuel elements in advanced nuclear power system under transient conditions, the transient behavior simulation test of nuclear fuel with fast power up and down can be carried out on ultra-high flux reactor. The loop device is located in the reactor core reflector area and is mainly used for the power jump experiment in the irradiation environment to realize various hypothetical irradiation operating conditions for new fuel elements or irradiated fuel elements, such as power increase experiment, fuel rod internal pressure overpressure experiment, fuel rod free gas elimination experiment, fuel core melting experiment, etc. Rapid changes in neutron flux are achieved using device translation and/or He-3 loops, which in turn rapidly regulate the heat release rate of the test fuel element and its axial distribution. The loop device also has a separate coolant loop so that the coolant parameters in the device, such as pressure, temperature and flow rate, chemical composition, etc., can be controlled individually and take away the heat generated by the test piece. The connection to the computer control system enables emergency control and alarm functions, and online monitoring of a variety of irradiation parameters, including flow rate, temperature, pressure, differential pressure, fission products and water chemistry. The coolant circuit also features fission gas collection and is capable of on-line analysis of gas composition, taking into account the leakage of radioactive material after the breakage of the fuel cladding in transient tests. A fully automatic quick-disassembly joint is located above the unit to enable remote disassembly and assembly of fuel elements and to avoid high dose irradiation to the operator.

3.4   Accident Simulation Test Loop System

This loop device is located in the core reflector region and is mainly used for LOCA experimental simulations of LWRs to test the thermal-mechanical behavior of fuel elements and their cladding, and the radioactive consequences in case of breakage in the event of a LOCA accident at LWRs nuclear power plants.

The loop device is divided into two parts: the internal system and the external system (compartment). The internal reactor system is partially installed in the channel of the reflective layer (210 mm in diameter), and the internal reactor system is moved by the moving device (which can be moved radially by about 0.5 m). Its nuclear power is controlled by the distance between the fuel rod of the reactor system and the ultra-high flux multifunctional reactor vessel (close to the reactor system, the power is high, far away from the reactor vessel, the power is low) and by increasing or reducing the blocks between them. At the same time, the minimum distance between the mobile device and the reactor vessel and the blocks are limited to limit the maximum nuclear power. In addition, the anti-fly-out system is installed on the top of the reactor system and fixed on the mobile system to prevent the axial movement of the reactor system.

The reactor system is located in a double-layered bottle body made of stainless steel. The inner layer bottle is a pressure bottle body, which is used to bear the internal pressure. An air gap is formed between the inner and outer bottle bodies, which is filled with helium gas for thermal insulation. The flow separation tube is located in the inner bottle, forming two concentric channels, the hot channel surrounding the fuel sample, and the cold channel between the separation tube and the inner bottle. Thus, thermosiphon can be established to ensure fuel rod cooling before LOCA transient starts. The flow separation tube is integrated with the surrounding heater to form an adiabatic condition for the fuel in the adiabatic stage. The gap between the support structure of the in-reactor system and the outer bottle body forms a cooling channel, and the pump is used to provide forced circulation. The neutron shield (hafnium) is fixed on the inner side of the support structure of the in-reactor system to flatten the axial neutron flux. The test instruments are used to measure temperature and pressure.

The external reactor system (compartment) is connected to the internal system by cables. The main function of the external system is to ensure the initial structure of the internal system loop to control the emptying and re-flooding phases. The in-reactor system is connected to the fission product laboratory, where the contaminated fluid will be contained, analyzed and partially sampled during the final phase of the test. The sampling line at the bottom will be for water, while the top is for gas. The external reactor system (compartment) are also used to store contaminated gases and liquids (from the fission product laboratory), and the fluids will be stored in different containers depending on the level of contamination.

3.5   Neutron Science Experiment Platform

The device is located in the external area of the reactor, which is mainly used for neutron photography of highly reflective nuclear fuel elements, materials and large-scale equipment, analyzing its internal organization structure, and providing basic data for material performance evaluation and modification. The reactor horizontal channel provides neutron sources to the device.

The cooling pool outside the reactor provides a measurement environment that is closer to the operating parameters for the study of the behavior of nuclear materials in the reactor. Under this condition, the camera platform for highly radioactive materials has its unique advantages. Due to the difference in the interaction characteristics of neutrons and photons with matter, neutrons are sensitive to light materials, fissile materials and strong absorbing materials, while photons are sensitive to heavy materials; the attenuation of neutrons in matter is much smaller than that of photons, which is beneficial to Photography of heavy samples. Therefore, the neutron photography platform and the photon photography platform complement each other and have good complementarity in material detection.

The platform is located in the reactor pool and is used for neutron photography of new fuel and irradiated nuclear fuel with strong radioactivity. In order to achieve the neutron detection of large samples, indirect neutron imaging based on wedge-shaped neutron beam is adopted, and water provides effective neutron shielding for the photography platform. The underwater neutron and photon photography platform can meet the load-bearing requirements of most samples, which can not only realize rapid imaging of short-lived nuclides in irradiated samples, but also grasp the distribution of nuclides in the samples (such as distribution of special nuclides in fuel rods). Under the three-degree-of-freedom spatial motion adjustment of the sample holding mechanism, γ-ray passive tomography imaging of samples of any shape can be realized. In order to achieve different scanning effects, various shapes and types of gamma-ray front-end collimators are preset. Since the collimator penetrates the reactor pool wall, it is necessary to set up a shielding structure at the corresponding position outside the pool wall to achieve effective protection for devices and staff.

4   Conclusion

This paper proposes an ultra-high flux research reactor and discusses the reactor construction scheme, including the nuclear reactor system scheme and the design of each test loop. After demonstration and design, on the premise of ensuring the safety performance of the reactor, each performance index can meet the target requirements and achieve the expected functions:

1) It can build a high-intensity, fast neutron spectrum and high-energy neutron field irradiation testing environment for the research and development of nuclear fuels and materials for the next generation and future advanced nuclear power systems, fusion reactors and other new reactors;
2) It can significantly shorten the irradiation test time of nuclear fuel and nuclear materials, and improve the research and development efficiency of new nuclear fuel and nuclear materials; It can realize the deep depletion of nuclear fuel, and effectively meet the basic theoretical data required by researches such as closed fuel cycle and nuclear fuel transmutation theory;
3) It can significantly improve the industrial production capacity and efficiency of 238 Pu, 252 Cf and other high value-added or scarce isotopes;
4) It can provide a more powerful, stable, continuous horizontal neutron beam that can be used for neutron scientific research;

5) It can provide the super-strong neutron field required by the fuel element to realize the step change of power for simulation experiments such as transient behavior and typical accidents of nuclear power plants.

References

1. Tsykanov, V.A., Korotkov, R.I., Kormushk, Y.P.: Some Physical Features of SM-2 Reactor, and Comparison of SM-2 with Other High-Flux Reactors. Meeting Abstract (1971)
2. Ponsard, B.: The BR2 high-flux reactor. ATW **57**(10):, 612–613 and 583 (2012)
3. Cheverton, R.D., Sims, T.M.: Hfir Core Nuclear Design (1971)
4. O'Kelly, D.S.: The Advanced Test Reactor. Reference Module in Earth Systems and Environmental Sciences (2020)
5. Izhutov, A.L., Krasheninnikov, Y.M., Zhemkov, I.Y., et al.: Prolongation of the BOR-60 reactor operation. Nucl. Eng. Technol. **47**(3), 253–259 (2015)
6. Koch, L.J.: Experimental Breeder Reactor-II (EBR-II) (1967)
7. Tobin, J.C.: FFTF and the ASME Code (1978)
8. Hong, Y., Bu, Y., Lin, J. : 10 Years Safety Operation of the High Flux Engineering Test Reactor(HFETR). Nuclear Power Engineering (1990)
9. Gu, C.X., Liu, et al.: Progress in China Experimental Fast Reactor. Annual Report of China Institute of Atomic Energy **00**, 46–49 (2014)
10. Gilles, B., Christian, C., Jocelyn, P., et al. : The Jules Horowitz Reactor Research Project: A New High Performance Material Testing Reactor Working as an International User Facility – First Developments to Address R&D on Material. EPJ Web of Conferences **115**, 01003-(2016)
11. Tuzov, A.: MBIR International Research Center: Current Progress and Prospects (2015)
12. Pasamehmetoglu, K.: Versatile Test Reactor Overview. Advanced Reactors Summit VI (2019)
13. Jaeger, W.H.W.L. : Liquid metal thermal hydraulics in rectangular ducts: Review, proposal and validation of empirical models: International Conference on Nuclear Engineering, Japan, JSME (2015)
14. Ushakov, P.A., Zhukov, A.V., Matyukhin, N.M. : Heat transfer to liquid metals in regular arrays of fuel elements. High Temp. (USSR)(Engl. Transl.); (United States) **15**(5) (1978)
15. Mikityuk, K. : Heat transfer to liquid metal: Review of data and correlations for tube bundles. **239**(4), 680–687 (2009)

Numerical Simulation of Convective Heat Transfer of CO_2 in a Tube Under Supercritical Pressure at Low Reynolds Numbers

Zhihui Li[✉]

State Power Investment Corporation Research Institute, Beijing, China

Abstract. The supercritical carbon dioxide (S-CO_2) Brayton cycle has the advantages of compact layout, simple structure, high thermal efficiency, clean working quality, its application in lead-cooled fast reactor power conversion system helps the miniaturization and modularization of the whole system. The development of an efficient and compact supercritical CO_2 heat exchanger has important reference significance for improving the thermal efficiency of the system of lead-cooled fast reactor. Supercritical CO_2 can operate in high Reynolds number turbulence and low Reynolds number turbulence in heat exchanger. The convective heat transfer of supercritical pressure CO_2 flowing upward and downward in a vertical circular tube (d = 2 mm) at low inlet Reynolds number (Re_{in} = 1970) was numerically simulated by different turbulence models to study the effects of variable properties, buoyancy and thermal acceleration on wall temperature and turbulent kinetic energy. The results showed that the heat transfer deterioration and enhancement occurred at the entrance of the heating section during the upward flow, which was mainly attributed to the influence of buoyancy and heat acceleration on the turbulent kinetic energy distribution. The LB turbulence model was used to simulate the heat transfer phenomenon, which was occurred in the downward flow.

Keywords: Supercritical Pressure · Buoyancy · Thermal Acceleration · Heat Transfer Deterioration · The Numerical Simulation

1 Introduction

In recent years, researchers at home and abroad have proposed to use supercritical CO_2 Brayton cycle in the power cycle system of the fourth generation reactor (lead-cooled fast reactor) and the energy production of solar energy system [1, 2]. The advantage of this cycle is that the whole cycle will not undergo phase change. Compared with supercritical water, supercritical helium and other circulating refrigerants, supercritical CO_2 has the advantages of high density and large specific heat, which helps to simplify the cycle process and reduce the size of the whole cycle. The development of a high efficiency and compact supercritical CO_2 heat exchanger has important reference significance for improving thermal efficiency of the lead-cooled fast reactor power cycle system.

Supercritical CO_2 can operate in high Reynolds number turbulence and low Reynolds number turbulence in heat exchanger. Domestic and foreign scholars have carried out a lot of experimental research and theoretical analysis on the turbulent flow of supercritical pressure fluid at high Reynolds number [3–7], but there are few studies on the turbulent mixed convection heat transfer in this small structure heat exchanger at low Reynolds number. Therefore, in this paper, the turbulent mixed convective heat transfer of supercritical CO_2 under the condition of low Reynolds number in a tube with an inner diameter of 2 mm is numerically simulated and compared with the experimental results. The effects of variable physical properties, buoyancy and thermal acceleration on flow and heat transfer are analyzed to provide theoretical guidance for the design of supercritical CO_2 heat exchanger.

2 Physical Model and Governing Equation

The physical model and coordinate system are shown in Fig. 1. The origin of the coordinates is the center point of the supercritical pressure CO_2 at inlet section. The axial coordinate x axis is the same as the flow direction, and the radial coordinate r axis is perpendicular to the flow direction and points to the pipe wall. The physical model used for numerical calculation is the same as the material and size of the experimental section in the experiment [8]. The experimental section has an inner diameter of 2.0 mm, an outer diameter of 3.14 mm and a length of 500 mm. In the middle is a heating section that is directly energized, with a length of 290 mm. As the resistivity changes with temperature during the experiment, the local heat flux density is not completely uniform, but its unevenness does not exceed 1%. Therefore, in the process of numerical calculation, it can be regarded as a uniform internal heat source q_v. There are 105 mm long inlet and outlet sections at both ends of the heating section. The material of the experimental section is stainless steel, and the thermal conductivity constant is 16.38 W/m.k. This is a coupled problem of heat conduction and convection. Since the convection heat transfer of supercritical pressure CO_2 in a vertical circular tube is symmetrical, in the process of numerical calculation, half of the circular tube is taken for two-dimensional calculation for convenience. The whole flow is axisymmetric two-dimensional steady flow.

Governing equations in cylindrical coordinates are as follows:

Heat conduction equation:

$$\frac{1}{r}\frac{\partial}{\partial r}(\lambda r \frac{\partial T}{\partial r}) + \frac{1}{x}(\lambda \frac{\partial T}{\partial x}) + \dot{\phi} = 0 \tag{1}$$

Continuity equation:

$$|\frac{1}{r}\left\{\frac{\partial}{\partial x}(prU) + \frac{\partial}{\partial r}(rpV)\right\} = 0 \tag{2}$$

Momentum equation in U direction:

$$\frac{1}{r}\left\{\frac{\partial}{\partial x}(prU^2) + \frac{\partial}{\partial r}(prVU)\right\} = -\frac{\partial p}{\partial x} + pg + \frac{1}{r}\left\{ \begin{array}{l} 2\dfrac{\partial}{\partial x}\left[r\mu_e\left(\dfrac{\partial U}{\partial x}\right)\right]+ \\ \dfrac{\partial}{\partial r}\left[r\mu_e\left(\dfrac{\partial U}{\partial r} + \dfrac{\partial V}{\partial x}\right)\right] \end{array}\right\} \tag{3}$$

Momentum equation in V direction

$$\frac{1}{r}\left\{\frac{\partial}{\partial x}(\rho rUV) + \frac{\partial}{\partial r}(\rho rV^2)\right\} = -\frac{\partial p}{\partial r} +$$
$$\frac{1}{r}\left\{\frac{\partial}{\partial x}\left[r\mu_e\left(\frac{\partial U}{\partial r} + \frac{\partial V}{\partial x}\right)\right] + 2\frac{\partial}{\partial r}\left[r\mu_e\left(\frac{\partial V}{\partial r}\right)\right]\right\} \tag{4}$$
$$-2\frac{\mu_e V}{r^2}$$

Energy equation:

$$\frac{1}{r}\left\{ \begin{array}{l} \dfrac{\partial}{\partial x}(\rho C_p rUT)+ \\ \dfrac{\partial}{\partial r}(\rho C_p rVT) \end{array}\right\} = \frac{1}{r}\left\{ \begin{array}{l} \dfrac{\partial}{\partial x}\left[rC_p\left(\dfrac{\mu}{\text{Pr}} + \dfrac{\mu_T}{\sigma_T}\right)\dfrac{\partial T}{\partial x}\right]+ \\ \dfrac{\partial}{\partial r}\left[rC_p\left(\dfrac{\mu}{\text{Pr}} + \dfrac{\mu_T}{\sigma_T}\right)\dfrac{\partial T}{\partial r}\right] \end{array}\right\} \tag{5}$$

The control equations are discretized by the control volume integral method using the ANSYS FLUENT software for numerical calculation. In discretizing the equations, the fluid region and the solid wall region adopt the uniform grid in the axial direction, the non-uniform grid in the radial direction, and the pressure velocity coupling is carried out by the SIMPLEC algorithm. The momentum equation and the energy equation first adopt the first-order upwind scheme, and then change to the second-order upwind scheme after reaching convergence, and then iterate until convergence. For the numerical turbulence models, LB, LS and RNG, standard and realizable turbulence models with enhanced wall function method are used in this paper. Due to the drastic changes in physical properties, relaxation factors in the range of 0.1–0.3 are used for all independent variables. In order to ensure the grid independence, a relatively precise grid is divided near the wall during the calculation process. Through adaptive grid adjustment, the condition $y+ < 0.6$ is satisfied to obtain an approximate grid independent solution. When all variables meet the following criteria, the numerical solution is considered to be convergent.

$$\left|\left(\phi^{i+1} - \varphi^i\right)/\phi^i\right| \le 10^{-6} \quad \phi, U, V, T, \varepsilon$$

Figure 2 shows the physical properties change of supercritical CO_2 at the pressure of 8.8 MPa. Because the pressure difference between the inlet and outlet of the vertical circular pipe is very small, the change of CO_2 physical properties with pressure has little impact on the results. Therefore, the physical properties of CO_2 in the circular pipe are selected as the corresponding physical properties under different inlet pressures, and the change of physical properties with temperature is processed by piecewise linear
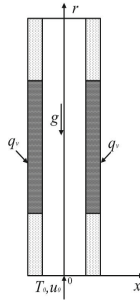
Fig. 1. Physical model and coordinate system

interpolation. After verification, the maximum deviation between the processing method and the physical property value calculated by NIST is not more than 1%.

The boundary conditions of numerical calculation are selected according to the boundary conditions of experimental conditions. The boundary conditions at the inlet are the velocity inlet boundary conditions of uniform incoming flow. At the same time, given the inlet temperature, the boundary conditions at the outlet are the pressure outlet boundary conditions. The heating section of the experimental section is a solid wall with internal heat source, and the boundaries of the rest are adiabatic boundary conditions. Coupled solution of heat conduction in solid wall and convection heat transfer in fluid region.
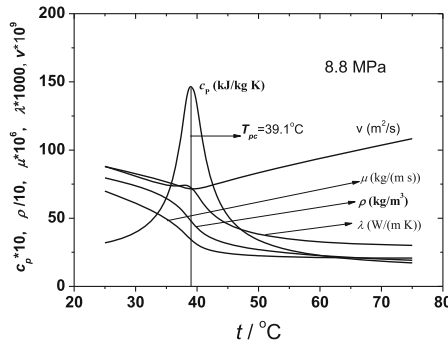
Fig. 2. CO_2 Physical properties at the pressure of 8.8 MPa

3 Effects of Buoyancy and Thermal Acceleration on Flow and Heat Transfer

In this paper, Bo* number proposed by Jackson hall [5] is used to evaluate the effect of buoyancy on flow and heat transfer. The experimental conditions taken in this paper are calculated as Bo* $> 8 \times 10^{-6}$, indicating that the buoyancy force has a great influence

and are located in the area where the turbulent kinetic energy is enhanced. See literature [9]. The effect of thermal acceleration on flow and heat transfer is evaluated by the k_V number proposed by McElicott [10]. Murphy [11] believes that when $Kv > 9.5 \times 10^{-7}$, the turbulent kinetic energy is restrained and the heat transfer is deteriorated due to thermal acceleration. Through calculation, the experimental conditions calculated in this paper are greater than this value at the entrance of the heating section, indicating that the thermal acceleration has a great impact.

4 Calculation Results and Analysis

For the convenience of verification, the conditions of numerical calculation are exactly the same as those of experiment. The inlet pressure is 8.8 MPa, the inlet temperature is 25 °C, the mass flow is 0.77 kg/h, and the inlet Re is about 1970.

Figure 3 shows the comparison between the numerical calculated outside wall temperature and the experimental results for upward flow under three heat flux conditions. Different turbulence models are used in the calculation. It can be seen from the figure that local wall temperature peaks and valleys occur at the inlet of the pipe when flowing upward, that is, local heat transfer deterioration and heat transfer enhancement occur, and this phenomenon becomes more obvious with the increase of heat flux. The heat transfer enhancement and heat transfer deterioration at the inlet of the tube are mainly attributed to the changes of thermal physical properties and turbulent kinetic energy caused by buoyancy and thermal acceleration. The later part of this paper will be explained in detail as shown in Figs. 5 and 6. The maximum deviation between the experimental results and the calculated results is 5.6%, 15%, 10% respectively.

The LB turbulence model with low Reynolds number can simulate this kind of heat transfer phenomenon well. At the same time, the wall temperature calculated by the turbulence model at the inlet of the pipe is in good agreement with the experimental results, indicating that the flow at the inlet has been in a turbulent state.

Figure 4 shows the comparison between the numerical calculated outer wall temperature and the experimental results when flowing downward under similar conditions. Due to the limitation of convergence, RNG, realizable and standard turbulence models are used in the calculation. It can be seen that the calculated results using RNG turbulence model are in good agreement with the experimental results when the heat flux is low. While the calculated results using realizable and standard turbulence models are in good agreement with the experimental results at the rear half of the pipe when the heat flux is high. It may be that the choice of turbulence model is related to heat flux which needs to be further studied. The wall temperature rises continuously along the flow direction, and there is no abnormal distribution phenomenon in the upward flow. The maximum deviation between the experimental results and the calculated results is less then 2%.

(a)

(b)

(c)
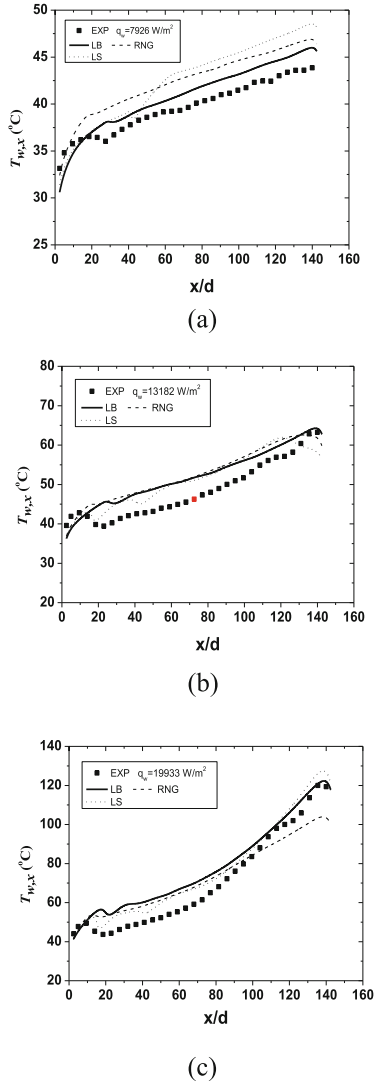
Fig. 3. Comparison of calculated and experimental outside wall temperatures on upward flow. q_w, W/m^2: (a)—7 926; (b)—13182; (c)—19933 ■—Experimental values; Solid line—LB; Dashed line—RNG; Dot line—LS

Figure 5 shows the comparison of turbulent kinetic energy at r/R = 0.9 calculated by LB model with and without buoyancy under the three heat flux conditions on upward flow and downward flow. It can be seen from the figure that: (1) the turbulent kinetic energy of upward flow and downward flow with buoyancy considered is higher tha**n that w**ithout buoyancy considered, indicating that buoyancy enhances the turbulent kinetic energy of upward flow and downward flow, which is consistent with the experimental results; (2) The turbulent kinetic energy of downward flow is significantly higher than
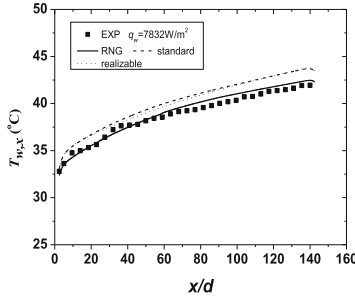
(a)
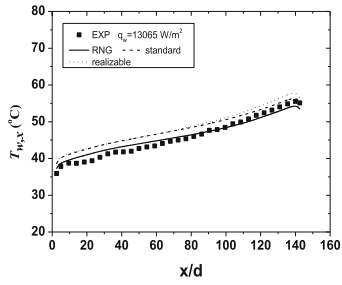
(b)
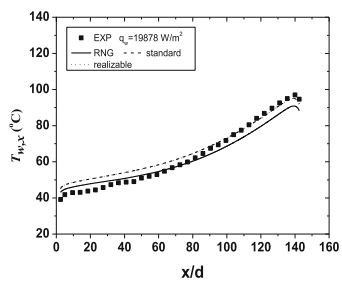
(c)

Fig. 4. Comparison of calculated and experimental outside wall temperatures on downward flow. q_w, W/m^2: (a)—7 832; (b)—13065; (c)—19878. ■—Experimental values; Solid line—RNG; Dashed line—Standard; Dot line—Realizable

that of upward flow (except for local positions), indicating that the buoyancy force has a stronger effect on heat transfer enhancement of downward flow than upward flow; (3) When flowing upward, the turbulent kinetic energy begins to decrease to 0 at the inlet of the tube for a short distance, and the heat transfer deteriorates. This may be because the physical property change and thermal acceleration lead to the weakening effect of the turbulent kinetic energy being greater than the enhancement of the turbulent kinetic energy caused by the buoyancy, which will be discussed further below. Later, due to the physical property change and the weakening of the thermal acceleration effect, the buoyancy force changed the flow from laminar flow to turbulent flow again. At a certain

position of the pipe, the turbulent kinetic energy increased sharply, and the corresponding wall temperature appeared a valley as shown in Fig. 5, that is, the heat transfer appeared local enhancement; (5) The turbulent kinetic energy in downward flow rises continuously along the path, and there is no abnormal change in upward flow. This may be because the effect of buoyancy on the enhancement of turbulent kinetic energy is stronger than that caused by variable physical properties and thermal acceleration.
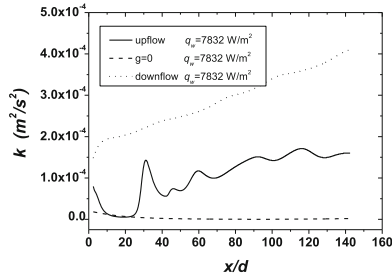
(a)
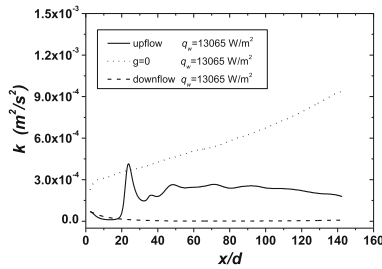
(b)
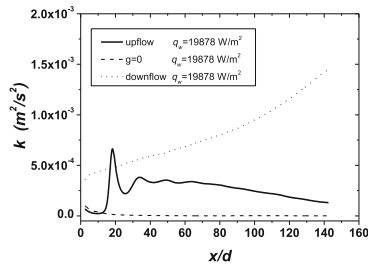
(c)

Fig. 5. The change of turbulent kinetic energy under the action of upward, downward and no gravity (R/R = 0.9). q_w, W/m^2: (a)—7 832; (b)—13065; (c)—19878 Solid line—LB(upward); Dashed line—LB(g = 0); Dot line—LB(downward)

Figure 6 shows the axial distribution of turbulent kinetic energy at the radial position r/R = 0.9 obtained by considering the density change and all physical parameters without considering the buoyancy force. LB turbulence model is used in the calculation. It can be
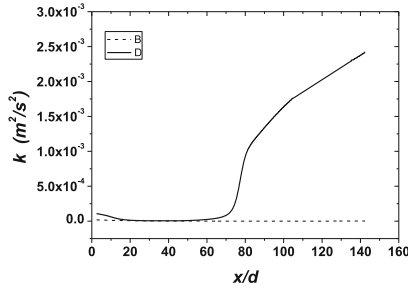
(a)
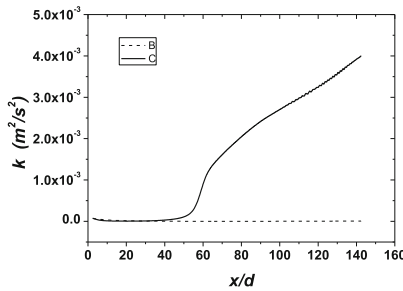
(b)
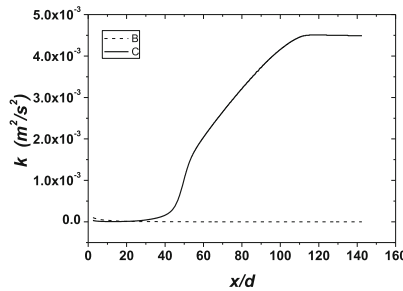
(c)

Fig. 6. Variation of turbulent kinetic energy without buoyancy (r/R = 0.9) q_{w}, W/m^2: (a)—7926; (b)—13182; (c)—19933 Solid line—Consider only changes in density; Dashed line—Change of all physical parameters

seen that at the inlet of the pipe, the change trend of turbulent kinetic energy obtained by considering only the change of density and all physical parameters basically coincides, and both decrease to 0, That is, laminar fluidization occurs in turbulence. We know that the thermal acceleration is mainly caused by the axial fluid density difference, which can further explain that the heat transfer deterioration at the pipe inlet in the upward flow

is mainly caused by the thermal acceleration, which is also in good agreement with the experimental results.

5 Conclusions

(1) LB turbulence model can better simulate the local wall temperature peaks and valleys of upward flow at low Reynolds number, while RNG turbulence model can better simulate the wall temperature of downward flow.

(2) The enhancement effect of buoyancy on downward flow heat transfer is greater than that of upward flow.

(3) The local heat transfer deterioration and enhancement in the upward flow and the heat transfer enhancement in the downward flow are mainly due to the influence of buoyancy and thermal acceleration on the turbulent kinetic energy.

(4) For the design of supercritical CO$_2$ heat exchanger of lead-cooled fast reactor, the subsequent research on convective heat transfer under higher pressure and temperature will be carried out in the future.

References

1. Huang, Y., Wang, J.: Applications of supercritical carbon dioxide in nuclear reactor system. Nuclear Power Engineering **33**(3), 21–27 (2012)
2. Li, M.J., Zhu, H.H., Guo, J.Q.: The development technology and applications of supercritical CO$_2$ power cycle in nuclear energy, solar energy and other energy industries. Applied Thermal Engineering **126**, 255–275 (2017)
3. Shitsman, M.E.: Impairment of the heat transmission at supercritical pressures. High Temp. **1**, 237–244 (1963)
4. Krasnoshchekov, E.A., Protopopov, V.S.: Experimental study of heat exchange in carbon dioxide in the supercritical range at high temperature drops(in Russian). Teplofizika Vysokikh Temperature **4**(3), 389–398 (1963)
5. Jackson, J.D., Cotton, M.A., Axcell, B.P.: Studies of mixed convection in vertical tubes. Int. J. Heat Fluid Flow **10**(1), 2–15 (1989)
6. Kurganov, V.A., Kaptilnyi, A.G.: Flow structure and turbulent transport of a supercritical pressure fluid in a vertical heated tube under the conditions of mixed convection. Int. J. Heat Mass Transfer **36**(13), 3383–3392 (1993)
7. Jiang, P.X., Zhang, Y., Xu, Y.J., Shi, R.F.: Experimental and numerical investigation of convection heat transfer of CO$_2$ at supercritical pressures in a vertical tube at low Reynolds numbers. Int. J. Thermal Sciences **47**, 998–1011 (2008)
8. Zhi-hui, L., Pei-xue, J., Chen-ru, Z., et al.: Experimental Investigation of Convection of Heat Transfer of CO$_2$ at supercritical pressures in vertical circular tube. J. Engineering Thermophysics **29**(3), 461–464 (2008)
9. McEligot, D.M., Jackson, J.D.: "Deterioration" criteria for convective heat transfer in gas flow through non-circular ducts. Nucl. Eng. Des. **232**, 327–333 (2004)
10. McEligot, D.M., Coon, C.W., Perkins, H.C.: Relaminarization in tubes. Int. J. Heat Mass Transfer **13**, 431–433 (1970)
11. Murphy, H.D., Chambers, F.W., McEligot, D.M.: Laterally converging flow. I. Mean flow. J. Fluid Mech **127**, 379–401 (1983)

Verification of Solver for Coupled Simulation of Fluid and Fuel Pin in LFR Based on Openfoam

Wenlan Ou, Zhengyu Gong, Qiwen Pan, Ling Zhang, Jianing Dai, and Zhixing Gu[✉]

College of Nuclear Technology and Automation Engineering, Chengdu University of
Technology, Chengdu, Sichuan, China
`guzhixing17@cdut.edu.cn`

Abstract. The Computational Fluid Dynamics (CFD)-based thermal-hydraulics
and safety analyses of Lead-based Fast Reactor (LFR) have attracted great atten-
tions in recent years. Commercial CFD tools have been widely used in the 3D
simulations of pool-type reactors owing to their powerful abilities in geometric
modeling and meshing. Compared with the commercial CFD tools, OpenFOAM
is a free open-source CFD code, which is more flexible to perform multi-physics
coupling activities. In this paper, in order to develop a solver for simulating the
coupled flow and heat transfer behaviors of fluid (coolant) and fuel pin in LFR,
the fuel pin Heat Conduction (HC) model was coupled to the modified icoFoam
solver of OpenFOAM. Verifications were conducted by the steady-state coupled
simulation of fluid and fuel pin heat transfer behaviors, comparing with the MPC-
LBE code which has been verified by the benchmarks for LFR fuel pin channel.
The results simulated by the coupled solver proposed in this paper agreed well
with the ones provided by the MPC-LBE code. This study lays a foundation for
the further development of transient safety analysis code for LFR in our future
work.

Keyword: OpenFOAM · IcoFoam · LFR · Multi-physics coupling · Benchmark

1 Introduction

As one of the Generation-IV advanced nuclear energy systems, Lead-based Fast Reactor
(LFR), has appealed to many international research institutions owing to its excellent
inherent safety and nuclear sustainability [1]. The Lead Bismuth Eutectic (LBE) coolant
employed in LFR with special characteristics (such as better heat conduction) different
from the water (conventional coolant), as well as its integrative pool-type configuration
may give rise to complicated three-dimensional thermal hydraulic phenomena in the
large space plenum, such as thermal stratification and coolant mixing [2], making the
thermal-hydraulics and safety problems of LFR always the research highlights. Com-
putational fluid dynamics (CFD)-based commercial programs for simulating, owing to
its mature technologies (plentiful models and algorithms) as well as the powerful pre-
processing (modeling and mesh generation of complex geometric structures) capability,

is considered as an effective method to overcome the multi-dimensional complicated thermal hydraulic problems involved in the liquid metal pool-type reactors [3].

At present, some commercial CFD tools, such as ANSYS Fluent, Star-CCM + , ABAQUS, have been widely used for simulations of liquid metal pool-type reactors, particularly the multi-scale coupling simulations with other reactor core physical models. For example, Gu Z. developed an advanced two-dimensional fuel pin heat transfer model, then integrated it with the self-developed PK model into ANSYS Fluent to conduct multi-physics coupling [4]. Deng J. developed a three-dimensional transient nuclear thermal coupling solution program based on OpenFOAM platform [5]. Narayanan developed the numerical models that deal with lead thermal hydraulics and solidification with ANSYS Fluent and Star-CCM + software [2].

As we summarized above, CFD tools are popularly used for multi-physics coupling simulation on liquid-metal-cooled reactors, but such commercial CFD programs are incapable to conduct the advanced coupling algorithms due to their closed source codes. OpenFOAM, as a free open-source CFD code, has a unique advantage of direct contact with the source code of existing solvers, making it relatively convenient for us to develop a new solver by modifying its source code from existing solver to vitally design its core computing functions.

In order to conduct the multi-physics coupling simulation with a high degree of customization based on complex coupling algorithms, a solver for simulating the coupled flow and heat transfer behaviors of fluid (coolant) and fuel pin in LFR was developed, and the fuel pin HC model was coupled to the modified icoFoam solver of OpenFOAM in this study. Verifications were conducted by the steady-state coupled simulation of coolant and fuel pin heat transfer behaviors, comparing with the MPC-LBE code which has been verified by the benchmarks for LFR fuel pin channel [6]. The simulation results agree well with the results provided by the MPC-LBE code, which shows the feasibility and accuracy of the solver.

2   Coupling of HC Code with Modified IcoFoam Solver

For LFR, the fuel pin channel consists of a slender cylindrical fuel pin and LBE coolant. Especially, the fuel pin constitutes of a centra hole, pin fuel pellet made of mixed oxides of uranium and its proliferator plutonium, gas plenum filled with Helium (under high pressure) and cladding mainly made of Zr-4 alloy. All the features above can be found in the benchmark reports [7].

2.1   CFD-Based Modifications of IcoFoam Solver

The new solver developed in this paper is based on the icoFoam solver of OpenFOAM, which can simulate the laminar flow by solving the incompressible Newtonian fluid N-S equations shown in Eq. (1) with the finite volume method.

$$\frac{\partial \rho \boldsymbol{U}}{\partial t} + \nabla \cdot (\rho \boldsymbol{U}\boldsymbol{U}) = \rho \boldsymbol{g} - \nabla p + \nabla \cdot (\mu \nabla \boldsymbol{U}) \tag{1}$$

In icoFoam, the fluid flow model is simplified by the neglect of gravity as well as the assumption of constant fluid density and kinematic viscosity. As shown in Fig. 1, the

coupling solution of velocity and pressure, based on the simplified N-S equations and continuity equations, is obtained by using the transient PISO algorithm.
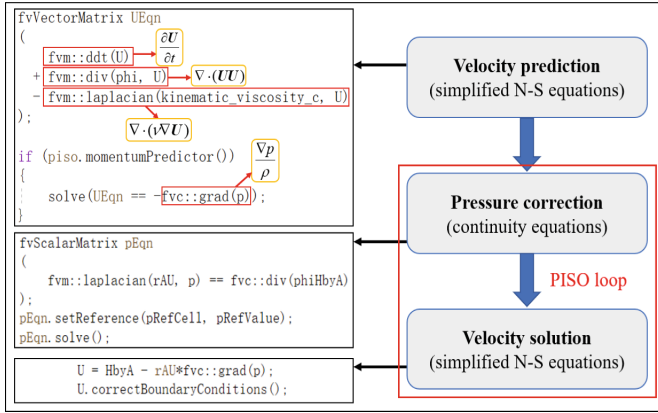
Fig. 1. Coupling solution of velocity and pressure

However, icoFoam is incapable of simulating the heat transfer phenomena in fluid (coolant) region due to the neglecting of energy conservative equation for fluid. To conduct the simulation coupled flow and heat transfer behaviors in coolant region, corresponding energy equation containing the heat source term, shown as Eq. (2), is added to icoFoam source code.

$$\frac{\partial \rho_{LBE} c_{p,LBE} T_{LBE}}{\partial t} + \nabla \cdot \left(\rho_{LBE} c_{p,LBE} T_{LBE} U \right) = \nabla \cdot \left(\lambda_{LBE} \nabla T_{LBE} \right) + q_V \qquad (2)$$

The velocity-based solution of energy conservative equation using the existing solver in OpenFOAM, is carried out after the coupling solution of velocity and pressure, as shown in Fig. 2.
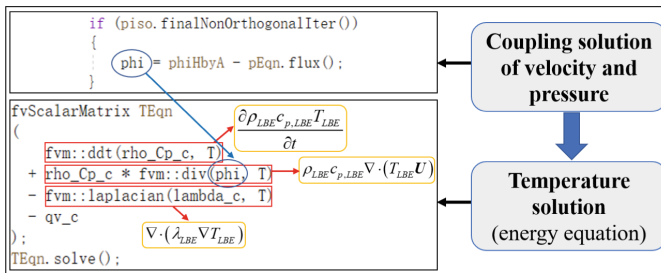
Fig. 2. Velocity-based solution of temperature

What's more, the new variables involved in this new equation, such as temperature, specific heat, conductivity etc., indispensably need to be added to the solver as mesh-based variable fields just, which is similar to the pressure and velocity. Meanwhile, these

newly added variable fields should be defined and initialized in include files, source code and running environment, including internal meshes and boundary conditions.

In particular, with the consideration of temperature changes caused by the energy change in coolant channel, it should be noted that most of the coolant parameters (density, conductivity, kinematic viscosity) are no longer constants as before but variables changing with temperature, whose calculation formulas can be obtained in detail from the benchmark reports [7]. Consequently, it is necessary to calculate then update these variables as feedbacks to corresponding mesh-based variable fields after the temperatures are solved in each time-step. In this paper, as shown in Fig. 3, only the kinematic viscosity (involved in N-S equations), density and conductivity (involved in energy equation) are regarded as variables with the feedbacks from continuous update.
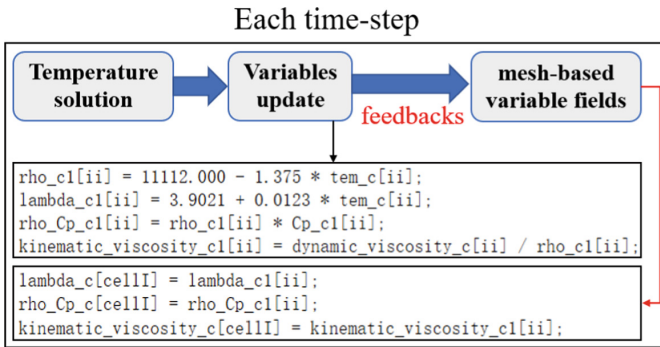
Fig. 3. Mesh-based variable fields update

2.2 Coupling Strategies with HC Code and Modified IcoFoam Solver

The modified icoFoam can simulate both the flow and heat transfer phenomena in coolant region, a three-dimensional mesh system based on OpenFOAM, after the works we did in the last section. As for the fuel pin region, its heat conduction process can be described by using the fully implicit finite volume method to discretize then solve the Heat-Conduction Equation in fuel pin sub-mesh system based on two-dimensional cylindrical coordinate system, which is already in our previous research work [4].

Through the convective heat transfer process at the interface (cladding outer surface) between fuel pin and LBE coolant, the heat transfers in these two regions are coupled as each other's dynamic boundary conditions with the explicit calculating strategy as shown in Fig. 4.

Firstly, the average convective heat transfer coefficient and average coolant temperature at specific axial position are provided to the fuel pin heat transfer module within the same axial position after the temperatures are solved in each time-step. Especially, the calculations of these two average variables are conducted by modifying icoFoam source code.

After that, the fuel pin region gives a heat source to coolant region in return. Generally, this heat source is transferred in the form of heat flux as a boundary condition,
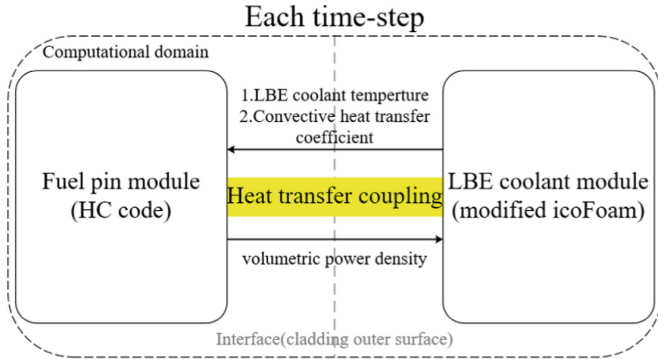
Fig. 4. Heat transfer explicit coupling strategy

nevertheless, in this study we tried a new method to conduct this transfer. By the heat flux calculated in fuel pin region, the power transferred from cladding outer surface to LBE coolant can be also obtained, which is applied to the meshes at the inner wall of coolant channel as its volume power density (external heat source). Many mesh related parameters need to be obtained then used for calculations above.

Importantly, the fuel pin heat transfer module (HC code) is added after the coolant module to icoFoam source code based on the integral coupling framework shown in Fig. 5, so as to realize the coupling calculations in each time-step. These two modules use the same time-step size (0.02s) to coupled calculate, which has been already proved that this size of time-step can guarantee numerical stability. In each time-step, the temperatures of fuel pin module and coolant module are calculated iteratively, until the calculated time-steps meet the steady-state establishment.
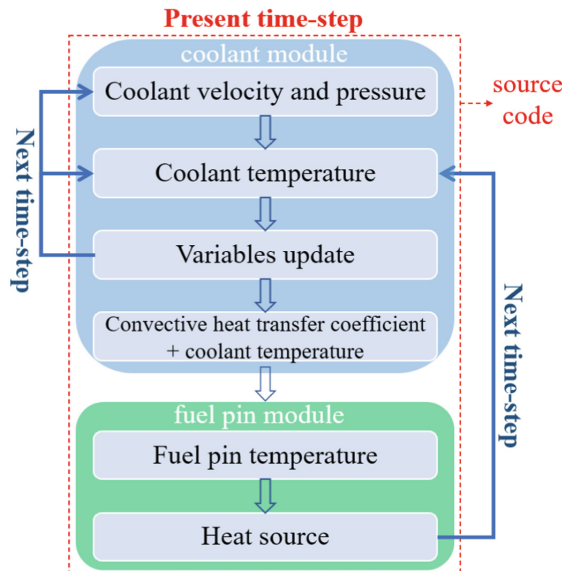
Fig. 5. Integral coupling framework

3   Verifications on Coupled Solver

3.1   Description and Mesh Generation for Computational Domain

In this paper, only a single fuel pin channel model is considered as the computational domain, whose composition is shown in Fig. 6 [6].
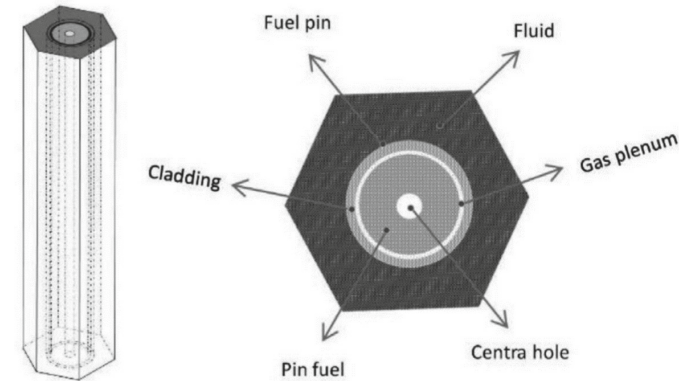
Fig. 6.   Model of fuel pin channel [6]

The computational domain is treated as a hexagon prism by its symmetrical characteristic. For the convenience of calculations of steady-state process, the inlet coolant temperature and velocity are constantly equal to the initial value, and the heat decay power is neglected. The geometry data and material properties of the fuel pin channel can be found with details in the benchmark report [6].

The fluid region in fuel pin channel is only the coolant channel, which is a complex digging hexagonal prism with a central hole. Therefore, such complicated channel is meshed by ANSYS instead of the existing meshing tool (blockMesh) of OpenFOAM. Then, this three-dimensional mesh system, shown in Fig. 7, is imported into OpenFOAM, whose quality analysis meets the service conditions.

3.2   Computation Results and Code Verification Compared with the MPC-LBE

The steady state of the fuel pin channel is simulated by using the HC-coupled modified icoFoam solver code (coupled solver) developed in this paper. In Figs. 8 and 9, the coolant temperature spatial distributions, both at the mid-plane and outlet of the coolant channel, occur the thermal stratification, and the high-temperature heat ring on the inner wall of coolant channel is thicker, owing to the better heat transfer performance of LBE (liquid metal) coolant compared with other general coolants (such as water). And it is obvious that the overall level of the outlet temperature is higher than that of the mid-plane, and the trend of the former gradually decreasing outward along the radial direction is slower than that of the latter.

What's more, as shown in Fig. 10, four axial distribution related temperature curves, representing the fuel pellet inner surface, fuel pellet outer surface, cladding outer surface
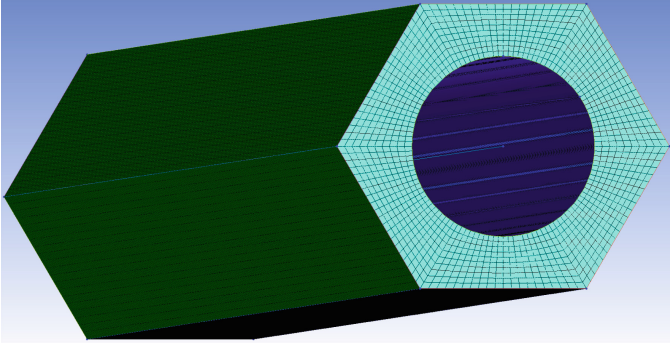
Fig. 7. Mesh generation of coolant channel

and coolant temperatures (arranged from high to low), are drawn and compared with the ones by the MPC-LBE code whose feasibility and accuracy have already been verified [4]. Since the power generated from fuel pellet will heat the coolant channel around with coolant continuously flowing through the channel, the coolant temperature will gradually rise during the process from inlet to outlet. Obviously, such good agreements are achieved in terms of both the trends and values among the results provided by the HC-coupled modified icoFoam solver code and by the MPC-LBE code [4] in Fig. 10.
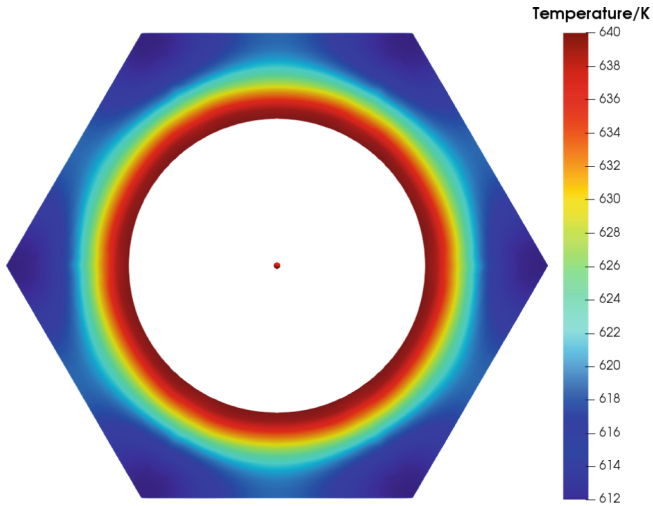
Fig. 8. Temperature spatial distribution at mid-plane of coolant channel
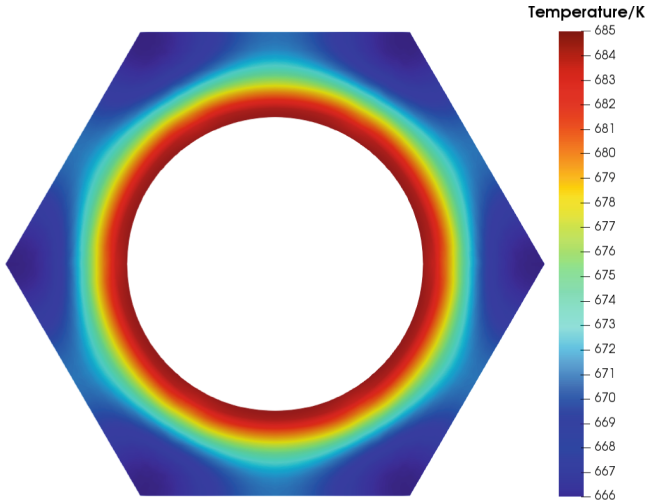
Fig. 9. Temperature spatial distribution at outlet of coolant channel
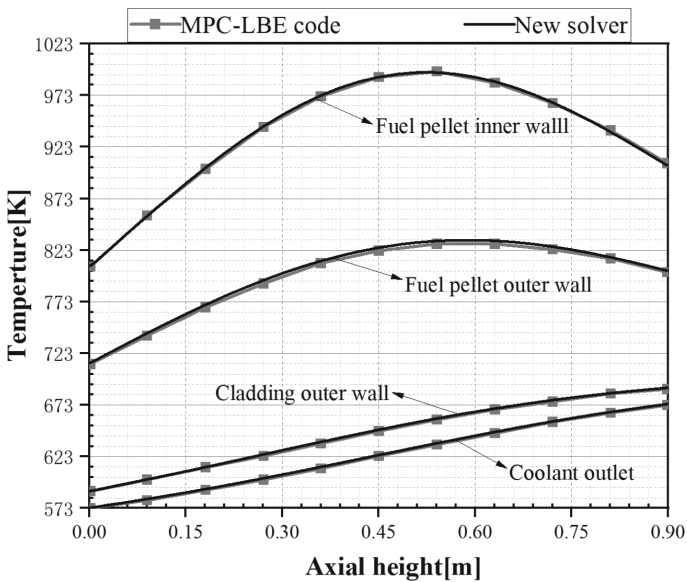
Fig. 10. Material axial temperature distribution of fuel pin channel at steady state

4   Conclusions

In this paper, a single fuel pin channel model is established for the reactor core of LFR, so as to analyse the coupled flow and heat transfer behaviors in coolant and fuel pin. Multi-physics simulation system is built by coupling the fuel pin heat transfer model

(two-dimensional HC module) to the three-dimensional open-source CFD code Open-FOAM by its icoFoam. This coupled simulation system for reactor thermal-hydraulics and safety analyses is abbreviated as the HC-coupled modified icoFoam solver code (coupled solver), which copes with the key data transmission problems of multi-physics coupling strategy within the framework of OpenFOAM platform. Mathematics models and methods as well as the coupling strategy of two modules are elaborated.

Verifications were conducted by the steady-state coupled simulation of flow and heat transfer behaviors between coolant and fuel pin regions in fuel pin channel of LFR, including the comparison with the benchmarks-verified MPC-LBE code [4]. The results simulated by the HC-coupled modified icoFoam solver code proposed in this paper agreed well with the ones provided by benchmarks-verified MPC-LBE code. It is testified that the HC-coupled modified icoFoam solver code is capable to perform the multi-physics simulations involved in thermal-hydraulics and safety analyses of LFR with enough accuracy.

However, only a simple single fuel pin model is considered to preliminarily verify the basic coupling strategies and schemes of reactor core heat transfer behaviors. Therefore, the coupling simulation of the whole fuel assembly channel of reactor core should be further studied in the future work, which can describe the reactor core more carefully and comprehensively. Meanwhile, for the heat transfer calculation coupled with coolant and fuel pin regions, the implicit iteration can be considered instead of the explicit calculating strategy used in this study. All in all, this study already verified the initial steady state, laying a foundation for the further development of transient safety analysis code to conduct transient simulation for LFR in our future work.

References

1. 罗晓, 张喜林, 陈红丽, 王帅, 郭超 & 王驰（2021）. 铅冷快堆多物理耦合分析方法及三维瞬态特性研究. 核动力工程(S1), 11–16.
2. Achuthan, N., et al.: Computational fluid dynamics modelling of lead natural convection and solidification in a pool type geometry. Nuclear Engineering and Design, p. 376 (2021).
3. Tenchine, D.: Some thermal hydraulic challenges in sodium cooled fast reactors. Nucl. Eng. Des. **240**(5), 1195–1217 (2010)
4. Gu, Z., Li, F., Ge, L., et al.: Verification of a HC-PK-CFD coupled program based a benchmark on beam trip transients for XADS reactor. Ann. Nucl. Energy **133**, 491–500 (2019)
5. Deng, J., Deng, J., Li, Z., et al.: Study on transient characteristics of nuclear ramjet reactor based on three-dimensional nuclear thermal coupling method. Nucl. Sci. Eng. **42**(01), 18–27 (2022)
6. Gu, Z.-X., et al.: Verification of a self-developed CFD-based multi-physics coupled code MPC-LBE for LBE-cooled reactor. Nucl. Sci. Tech. **32**(5), 1–17 (2021). https://doi.org/10.1007/s41365-021-00887-x
7. D'Angelo, A., Arien, B., Sobolev, V., et al.: Benchmark on Beam Interruptions in an Accelerator-Driven System Final Report on Phase I Calculations, Technical Report NEA/NSC/DOC(2003)17, NEA (2003)
8. Behar, C.: Technology roadmap update for generation IV nuclear energy systems. In: OECD Nuclear Energy Agency for the Generation IV International Forum, accessed Jan. 2014, 17, 2014–03

9. Alemberti, A., Smirnov, V., Smith, C.F., et al.: Overview of leadcooled fast reactor activities. Prog. Nucl. Energy **77**, 300–307 (2014)

10. Chen, H., Chen, Z., Chen, C., et al.: Conceptual design of a small modular natural circulation lead cooled fast reactor SNCLFR100. Inter. J. Hydrog. Energy **41**(17), 7158–7168 (2016)

11. Chen, H., Zhang, X., Zhao, Y., et al.: Preliminary design of a medium-power modular lead-cooled fast reactor with the application of optimization methods. Inter. J. Hydrog. Energy **42**(11), 3643–3657 (2018)

12. Zou Zeren et al. (2020). 3D thermal hydraulic characteristics analysis of pool-type upper plenum for lead-cooled fast reactor with multi-scale coupling program. Nuclear Engineering and Design, pp. 370 110892-

13. 魏诗颖, 王成龙, 田文喜, 秋穗正 & 苏光辉 (2019). 铅基快堆关键热工水力问题研究综述. 原子能科学技术(02), 326-336.

14. 雷洲阳 (2021). 基于 CFD 物理热工耦合的池式快堆 UTOP 事故不确定性分析研究(硕士学位论文, 南华大学)

15. 李尚卿, 王伟民 & 李玉同 (2022). 基于 OpenFOAM 的磁流体求解器的开发和应用. 物理学报(11), 424–433.

16. T.H. Fanning, A.J. Brunett, T. Sumner, The SAS4A/SASSYS-1 Safety Analysis Code System, Version 5 (Argonne national lab. (ANL), argonne, IL United States, 2017)

17. Mesina, G.L.: A history of RELAP computer codes. Nucl. Sci. Eng. **182**(1), v–ix (2016)

18. Lerchl, G., Austregesilo, H., Glaeser, H., et al.: ATHLET Mod 3.0— Cycle A. Validation. Gesellschaft fu¨r Anlagen-und Reaktorsicherheit (GRS) gGmbH, Garching bei Mu¨nchen, Germany, Report No. GRS-P-1, 2012, 3

19. Fanning, T.H., Thomas, J.W.: Advances in Coupled Safety Modeling Using Systems Analysis and High-Fidelity Methods (Argonne national lab. (ANL) argonne, IL United States (2010)

20. Pialla, D., Tenchine, D., Li, S., et al.: Overview of the system alone and system/CFD coupled calculations of the PHENIX natural circulation test within the THINS project. Nucl. Eng. Des. **290**, 78–86 (2015)

21. Bandini, G., Polidori, M., Gerschenfeld, A., et al.: Assessment of systems codes and their coupling with CFD codes in thermal– hydraulic applications to innovative reactors. Nucl. Eng. Des. **281**, 22–38 (2015)

22. Chen, Z., Chen, X.N., Rineiski, A., et al.: Coupling a CFD code with neutron kinetics and pin thermal models for nuclear reactor safety analyses. Ann. Nucl. Energy **83**, 41–49 (2015)

Research of Helium Thermal Power System Based on Lead-Cooled Fast Reactor

Zhihui Li[✉]

State Power Investment Corporation Research Institute, Beijing, China

Abstract. The Helium Brayton cycle with re-compression has the advantages of compact layout, simple structure, thermal high efficiency, good heat transfer characteristics and small friction characteristics, its application in the power conversion system of the lead-cooled fast reactor and the high temperature gas-cooled reactor helps the miniaturization of the whole system. In this paper, the mathematical model was established for Helium Brayton cycle with re-compression and the 100 MWt lead-cooled fast reactor power system was calculated. The effects of several key factors such as the turbine inlet temperature, the turbine outlet pressure, the high pressure compressor outlet pressure, the low pressure compressor outlet pressure and the recuperator outlet temperature were analyzed. The results show that the turbine outlet pressure, the turbine inlet temperature and the high/low pressure compressor outlet pressure have remarkable effects on thermal efficiency of the system. Thermal efficiency of the system increases first and then decreases with the turbine outlet pressure increasing as well as increases with turbine inlet temperature. The research results of this paper could provide important theoretical reference both for thermal cycle parameters for 100 MWt lead-cooled fast reactor and system design of power cycle based on the lead-cooled fast reactor.

Keywords: LEAD-COOLED FAST REACTOR · HELIUM · RE-COMPRESSION · BRAYTON CYCLE

1 Introduction

In the traditional nuclear reactor, the Rankine steam cycle is used in the energy conversion system. Because the reactor can only provide saturated steam at about 320 °C, it can not provide superheated steam at a higher temperature to meet the need of Rankine cycle to improve efficiency, so the efficiency is relatively low. The lead-cooled fast reactor gas turbine cycle combines the gas turbine with the modular lead-cooled fast reactor, and uses the high-temperature gas generated by the lead- cooled fast reactor to directly drive the gas turbine to do work for high-efficiency power generation. It can break through the temperature limit of the steam cycle, and use intermediate cooling and regenerative technologies to improve efficiency, thus becoming an important direction for the study of high-efficiency power generation of the lead-cooled fast reactor.

The earliest gas-cooled reactor power cycle device combined with helium turbine began to develop in the late 1960's. From 1968 to 1981, Germany cooperated with

the United States and Switzerland to complete the HHT (HTR with helium turbine) experimental program for the helium turbine power conversion system [1]. The purpose of the plan was to study the technology of high temperature gas-cooled reactor power generation with helium turbine, including turbine, compressor, hot gas duct, materials, heat exchanger and other component technologies.

In the early 1990's, with the support of the U.S. Department of energy, MIT carried out the research on modular high temperature gas-cooled reactor (MGR) helium turbine cycle power plant [2], and proposed two technical schemes, namely direct helium turbine cycle scheme (MGR-GT) and indirect helium turbine cycle scheme (MGR-GTI). Necsa of South Africa has carried out research on PBWR of pebble bed modular high temperature gas-cooled reactor [3]. PBWR adopts standard Brayton cycle with closed water-cooled precooler and intercooler. The United States and Russia cooperated in the research of GT-MHR [4] and adopted the design of closed Brayton cycle power conversion system.

In recent years, foreign scholars have carried out a lot of theoretical research on the scheme and system characteristics of helium turbine cycle system [5–12]. Professor Wang Jie from the Institute of nuclear energy technology design and research, Tsinghua University, China [13–15] respectively carried out thermodynamic analysis and optimization calculation for the direct helium cycle, open air cycle and indirect nitrogen cycle of the high temperature gas-cooled reactor, and carried out aerodynamic design for the turbine compressor. The results show that helium direct circulation is an ideal choice, but it is difficult based on the existing technical level. The closed indirect circulation of helium or nitrogen is a relatively realistic scheme at present, which can realize the idea of gas turbine circulation and accumulate technology for the direct circulation in the future. State power corporation research institute are carrying out the research on 100 MW lead-cooled fast reactor (BLESS-D) to meet the public's demand for a safer, more economical and more environmentally friendly nuclear power system [16–19]. It is a pool-style reactor with LBE (lead and bismuth eutectic alloy) as the coolant. It is mainly used to study the key problems and technologies of lead cooled fast reactor, verify and demonstrate relevant solutions. Among, The thermal power cycle system adopts different working fluid scheme, such as water, supercritical carbon dioxide, Helium.

In this paper, the thermodynamic calculation of helium re-compression Brayton cycle is carried out for 100 MW_t lead-cooled fast reactor. The effects of core outlet temperature, turbine outlet pressure, high-pressure compressor outlet pressure, low pressure compressor outlet pressure and recuperator outlet temperature on thermal efficiency of the system are analyzed. The design parameters of helium re-compression Brayton cycle for 100 MWt lead-cooled fast reactor are optimized, which can provide an important theoretical reference for the design of power cycle system of lead-cooled fast reactor.

2 Helium Brayton Cycle Introduction

2.1 Thermophysical Properties of Helium

Table 1 shows the comparison of thermophysical properties between helium and other working fluids under standard conditions. It can be seen from Table 1 that, compared

with other working fluids, helium has the following physical properties: strong thermal conductivity, large specific heat, small gas density and large is entricity index.

The effects of these special thermophysical properties of helium on the helium Brayton cycle are as follows:

(1) The gas density is small, so a high circulating pressure is required to increase its density;
(2) The isentropic index is large, so under the same temperature difference, the pressure ratio is small, so it is difficult to compress;
(3) The specific heat is large, so under the same temperature difference, the cycle specific work is large, and the expansion work of the turbine and the compression work of the compressor are larger than those of other gases.

Helium is very close to ideal gas in the range of 0–1000 °C, 0.1–10 MPa, and its specific heat and adiabatic index are almost constant. Compared with air, helium has a higher specific heat (about 5 times that of air), so the compression ratio of helium is small under the same temperature difference, and the mass flow of helium is small under the same output power. Helium also has good heat transfer characteristics and small friction characteristics, which is conducive to improve the efficiency of the heat exchanger and reduce the volume of the heat exchanger.

Table 1. THE COMPARISON OF THERMO PHYSICAL PROPERTIES BETWEEN HELIUM AND OTHER WORKING FLUIDS (1ATM, 0 °C)

Fluids	Thermal conductivity (W/(m.K))	Density (kg/m^3)	Specific heat (kJ/(kg.K))	Isentri-ity index
He	0.14	0.17	5.19	1.67
N_2	0.02	1.25	1.04	1.4
Air	0.02	1.29	1.06	1.4
CO_2	0.01	1.64	0.82	1.3
Ar	0.01	1.78	0.52	1.67
H_2	0.16	0.08	14.19	1.41
O_2	0.02	1.42	0.92	1.34

2.2   Helium Closed Re-compression Brayton Cycle Process

There are many specific circulation modes in the helium turbine circulation scheme. From the point of view of improving power generation efficiency, helium turbine direct circulation is an ideal choice. In other words, the high-temperature and high-pressure gas produced by the reactor core is used to directly drive the turbine to generate electricity.

Figure 1 shows the flow chart of helium closed re-compression Brayton cycle [14] which is the scheme to realize the direct cycle of helium turbine. This cycle scheme adopts

recuperator and intermediate cooling of gas flow in the process of compression to improve thermal efficiency of the system. The system is composed of turbine, recuperator, high-pressure compressor, low-pressure compressor, intercooler, precooler, generator and corresponding pipelines.

The working process is as follows: 1-2a refers to the isentropic compression process of low-temperature and low-pressure helium in the low-pressure compressor; 2a-2b refers to the constant pressure heat release process of helium in the intercooler (ICL); 2b-2 refers to the isentropic compression process of cooled helium in the high-pressure compressor; 2–3 shows the heat absorption process of high pressure helium at the high pressure side of the recuperator (RPT); 3–4 refers to the constant pressure heat absorption process of high temperature and high pressure helium in the reactor; 4–5 refers to the isentropic expansion process of high-temperature helium in the turbine. The expansion work is used to drive the high-pressure compressor, low-pressure compressor and generator. 5–6 shows the constant pressure heat release process of helium at the low pressure side of the recuperator (RPT). 6–1 shows the constant pressure heat release process of cooled helium in the precooler (PCL). Finally, the low-temperature and low-pressure helium enters the low-pressure compressor for isentropic compression to complete the whole cycle.
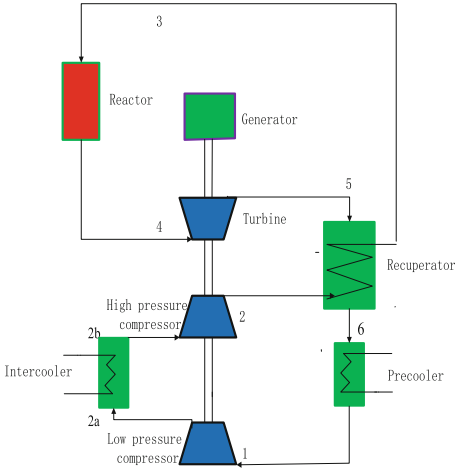
Fig. 1. HELIUM BRAYTON CYCLE WITH RE-COMPRESSION

3   Influence of Key Parameters on Thermal Efficiency of the System

The mathematical model of helium closed recompression Brayton cycle of 100 Wt lead cooled fast reactor is established by using MATLAB software. Thermal efficiency of the system is expressed by the following formula:

$$\eta = f\left(\tau, \gamma, \overline{\theta}, \overline{\eta}_c\right)$$

where, τ refers to the circulating temperature ratio which is the ratio of the absolute temperature of the high-temperature heat source to the low-temperature heat source of the system; γ refers to the circulating pressure ratio which is ratio of the inlet pressure to the outlet pressure of high-pressure compressor and low-pressure compressor; The physical property vector $\overline{\theta}$ is composed of the ratio of the specific heat at constant pressure for the compression process and the endothermic process, the ratio of the specific heat at constant pressure for the expansion process and the endothermic process, and the isentropic index. For helium, the specific heat at constant pressure and specific heat at constant volume are constant, the ratio of specific heat at constant pressure is 1, and the isentropic index is 1.67. Component efficiency vector is composed of recuperator efficiency, turbine efficiency, compressor efficiency and pressure loss. Limited by today's manufacturing level, after taking a group of reasonable values according to literature [13], as shown in Table 2, the component efficiency vector becomes a constant vector. The whole cycle is steady-state calculation. Therefore, thermal efficiency of the system is mainly determined by the circulating temperature ratio and circulating pressure ratio.

Table 2. COMPONENT EFFICIENCY AND RESSURE LOSS

Component parameters	Values
Turbine efficiency	90%
High-pressure Compressor efficiency	89%
Low-pressure Compressor efficiency	89%
Generator efficiency	98%
Recuperator efficiency	95%
Pressure loss	5%

3.1 Influence of the Core Outlet Temperature

Figure 2 shows the influence of different core outlet temperature on the thermal efficiency of the system under the conditions of high-pressure compressor outlet pressure of 5.6 MPa, low-pressure compressor outlet pressure of 4.9 MPa and recuperator outlet temperature of 80 °C. With the increase of core outlet temperature, thermal efficiency of the system increases. When the core outlet temperature increases from 400 °C to 500 °C, thermal efficiency of the system increases by 86%. Therefore, under the conditions of reactor thermal conditions and core materials, increasing the core outlet temperature can increase the output power of the system.
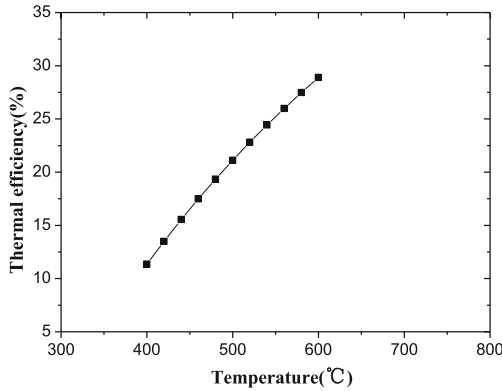
Fig. 2. VARIATION OF THERMAL EFFICIENCY OF THE SYSTEM WITH CORE OUTLET TEMPERATURE

3.2 Influence of the Turbine Outlet Pressure

Figure 3 shows the influence of turbine outlet pressure on thermal efficiency of the system under the conditions of high-pressure compressor outlet pressure of 5 MPa, reactor core outlet temperature of 400 °C and low-pressure compressor outlet pressure of 3.5 MPa. With the increase of the turbine outlet pressure, thermal efficiency of the system first increases and then decreases. The reason is that with the increases of turbine pressure, the power consumption of the low-pressure compressor decreasing and the net power of the system increasing. However, with the further increase of the pressure, the output power of the turbine decreases rapidly, resulting in the decrease of the net output power and the decrease of thermal efficiency of the system. That is, there is an optimal turbine outlet pressure, which well matches the turbine output power and compressor power consumption, so as to maximize thermal efficiency of the system.
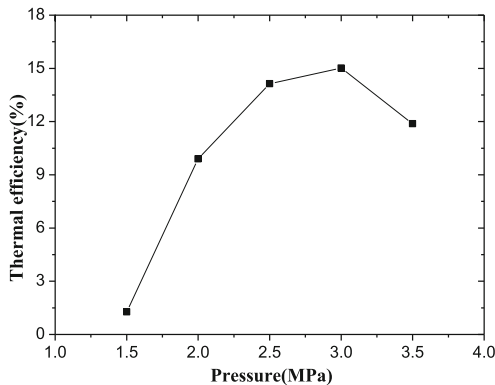
Fig. 3. VARIATION OF THERMAL EFFICIENCY OF THE SYSTEM WITH TURBINE OUTLET PRESSURE

3.3   Influence of the High-Pressure Compressor Outlet Pressure

Figure 4 shows the influence of high-pressure compressor outlet pressure on thermal efficiency of the system under the conditions of low-pressure compressor outlet pressure of 4.18 MPa, reactor core outlet temperature of 500 °C and recuperator outlet temperature of 142.5 °C. With the increase of the high-pressure compressor outlet pressure, thermal efficiency of the system increases. Therefore, increasing the high-pressure compressor outlet pressure can improve thermal efficiency of the system, but subject to the current technical conditions, the high-pressure compressor outlet pressure is usually lower than 7 MPa.
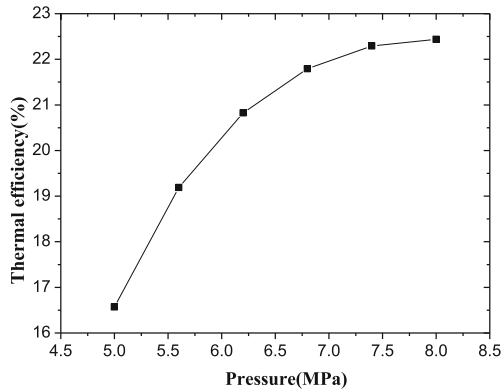
Fig. 4. VARIATION OF THERMAL EFFICIENCY OF THE SYSTEM WITH HIGH-PRESSURE COMPRESSOR OUTLET PRESSURE

3.4   Influence of the Low-Pressure Compressor Outlet Pressure

Figure 5 shows the influence of low-pressure compressor outlet pressure on thermal efficiency of the system under the conditions of high-pressure compressor outlet pressure of 5 MPa, reactor core outlet temperature of 400 °C and recuperator outlet temperature of 167.5 °C. With the increase of low-pressure compressor outlet pressure, thermal efficiency of the system decreases. The reason is that the specific capacity at the inlet of the low-pressure compressor is large. Under the same pressure ratio, the compression work is much greater than that of the high-pressure compressor. At the beginning, with the increase of the low-pressure compressor outlet pressure, the power consumption of the low-pressure compressor increases relatively slowly, which is less than the power consumption reduced by the high-pressure compressor, resulting in the increase of thermal efficiency of the system. When the low-pressure compressor outlet pressure is continuously increased, although the power consumption of the high-pressure compressor decreases, the power consumption of the low-pressure compressor increases faster, resulting in the decline of thermal efficiency of the system.
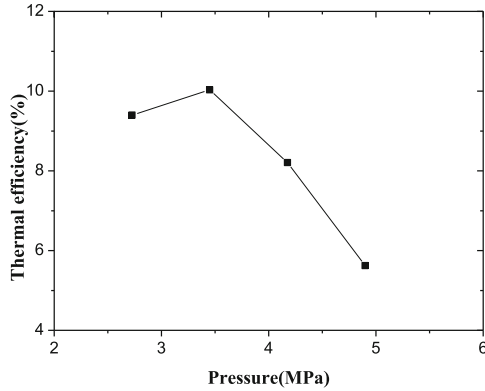
Fig. 5. VARIATION OF THERMAL EFFICIENCY OF THE SYSTEM WITH LOW-PRESSURE COMPRESSOR OUTLET PRESSURE.

3.5 Influence of the Recuperator Low-Pressure Side Outlet Temperature

Figure 6 shows the influence of the recuperator outlet temperature at low-pressure side on thermal efficiency of the system under the conditions of high-pressure compressor outlet pressure of 5.6 MPa, reactor core outlet temperature of 400 °C and low-pressure compressor outlet pressure of 4.9 MPa. With the increase of the recuperator outlet temperature at low-pressure side, thermal efficiency of the system decreases. The reason is that after the outlet temperature at low-pressure side increases, the regenerative degree of the recuperator decreases, the cooling capacity of the precooler increases, and the high-temperature heat generated by the compressor is not fully utilized, resulting in the increase of heat absorption of the system and the decrease of thermal efficiency of the system.
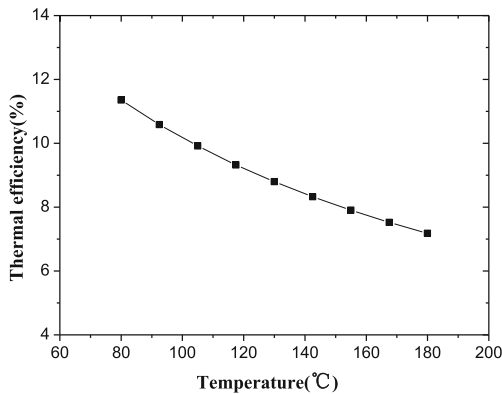
Fig. 6. VARIATION OF THERMAL EFFICIENCY OF THE SYSTEM WITH RECUPERATOR OUTLET TEMPERATURE AT LOW-PRESSURE SIDE

To sum up, in order to improve the thermal efficiency of the helium Brayton cycle, the reactor core outlet temperature should be increased as much as possible, the design scheme of the recuperator should be reasonably optimized, the system regenerative efficiency should be increased, the compression ratio should be reasonably distributed in combination with the characteristics of the high and low pressure compressor, and the of the high pressure compressor outlet pressure should be increased as much as possible.

4 Optimization Results of He Closed Re-compression Brayton Cycle

Through the analysis of the influence of different key parameters on helium closed re-compression Brayton cycle, it can be concluded that the turbine inlet temperature can be taken as 400–600 °C, the low-pressure compressor inlet temperature is taken as 35 °C for lead-cooled fast reactor. Considering that the maximum pressure limit of the system is 7.0 MPa, the high-pressure compressor outlet pressure is set as 5.0 MPa. Table 3 shows the optimization results of he closed re-compression Brayton cycle of lead-cooled fast reactor with thermal power of 100 MW under three different working conditions. Thermal efficiency of the system. When the core outlet temperature reaches 600 °C,Thermal efficiency of the system reaches 34.8%.

Table 3. OPTIMIZATION RESULTS OF HE CLOSED RE-COMPRESSION BRAYTON CYCLE

Cycle category	He (Condition 1)	He (Condition 2)	He (Condition 3)
Initial parameters	$t_{min} = 35$ °C $t_{max} = 400$ °C	$t_{min} = 35$ °C $t_{max} = 500$ °C	$t_{min} = 35$ °C $t_{max} = 600$ °C
Restrictions	$P_{max} = 7.0$MPa	$P_{max} = 7.0$MPa	$P_{max} = 7.0$MPa
High-pressure compressor outlet ressure (MPa)	5.0	5.0	5.0
Optimal pressure ratio of high-pressure compressor	1.44	1.44	1.44
	1.73	1.73	1.73
Mass flow (kg/s)	153.4	133.6	118.4
Thermal efficiency of the system (%)	16.03	26.6	34.8
Heat absorption per unit mass (kJ/kg)	651.8	748.4	844.9
Turbine power (MW)	98.55	98.48	98.42
Turbine inlet volume flow (m^3/s)	43.2	43.2	43.2
Turbine outlet volume flow (m^3/s)	64.8	64.8	64.9
Low-pressure compressor power (MW)	36.42	31.72	28.1
High-pressure compressor power (MW)	46.01	40.16	35.5

5   Conclusions

(1)   Thermal efficiency of helium re-compression Brayton cycle system increases with the increase of high-pressure compressor outlet pressure, increases with the increase of core outlet temperature, decreases with the increase of recuperator outlet temperature and increases first and then decreases with the increase of turbine outlet pressure.

(2)   The optimized parameters of helium re-compression Brayton cycle system of lead-cooled fast reactor with thermal power of 100 MW under three different core outlet temperatures are obtained, which provides an important theoretical reference for the design of power cycle system of lead-cooled fast reactor. When the core outlet temperature reaches 600 °C, thermal efficiency of the system reaches 34.8%.

(3)   At present, the technical level of helium re-compression Brayton cycle still has some limitations. The research on the materials of helium turbine device, the deposition of radioactive products on turbine blades and the integrated layout are still need to be carried out in the future.

References

1.   Weibrodt, I.A.: Summary Report on Technical Experiences from High-temperature Helium Turbomachinery Testing in Germany. In: Proceedings of a Technical Committee Meeting, IAEA-TECDOC-899. Beijing (1995)

2.   Brey, H.L.: Historical background and Future Development of the High Temperature Gas-cooled Reactor[A]. In: Proceedings of the Seminar on HTGR Application and Development. Beijing (2001)

3.   Nicholls.: Pebble Bed Modular Reactor. In: Proceedings of Seminar on HTGR Application and Development Beijing, China (2001)

4.   Ball, S.: Status of the Gas Turbine Modular Helium Reactor for Plutonium Disposition. In: Proceedings of Seminar on HTGR Application and Development, Beijing, China (2001)

5.   Forsberg, C.W., Peterson, P.F., Pickard, P.S.: Study on characteristic of helium turbine with the high temperature gas-cooled react0r. Nucl. Technol. **144**(3), 289–302 (2003)

6.   Fujikawa, S., Hayashi, H., Nakazawa, T., et al.: Achievement of reactor-outlet coolant temperature of 950° C in HTTR. J. Nucl. Sci. Technol. **41**(12), 1245–1254 (2004)

7.   Yari, M., Mahmoudi, S.M.S.: Utilization of waste heat from GT-MHR for power generation in organic Rankine cycles. Appl. Therm. Eng. **30**(4), 366–375 (2010)

8.   Kunitomi, K., Yan, X., Nishihara, T., et al.: JAEA's VHTR for hydrogen and electricity cogeneration: GTHTR300C. Nucl. Eng. Technol. **39**(1), 9–20 (2007)

9.   Meyer, M.K., Fielding, R., Gan, J.: Fuel development for gas-cooled fast reactors. J. Nucl. Mater. **371**(1), 281–287 (2007)

10. Kissane, M.P.: A review of radionuclide behaviour in the primary system of a very-high-temperature reactor. Nuclear Eng. Design **239**(12), 3076–3091 (2009).

11. El-Genk, M.S., Tournier, J.M.: Noble gas binary mixtures for gas-cooled reactor power plants. Nucl. Eng. Des. **238**(6), 1353–1372 (2008)

12. Talamo, A., Gudowski, W., Venneri, F.: The burnup capabilities of the deep burn modular helium reactor analyzed by the Monte Carlo continuous energy code MCB. Ann. Nucl. Energy **31**(2), 173–196 (2004)

13. Verfondern, K., Nabielek, H., Kendall, J.M.: Coated particle fuel for high temperature gas cooled reactors. Nucl. Eng. Technol. **39**(5), 603–616 (2007)
14. Jie, W.: Preliminary study on thermal features for high temperature gas-cooled reactor gas turbine cycle. Chinese High Technology Letters **12**(9), 91–95 (2002)
15. Wang, J., Gu, Y.: Study on fundamental features of helium turbo machine for high temperature gas-cooled reactor. Chinese J. Nuclear Sci. Eng. **24**(3), 218–223 (2004)
16. Wang, J., Yihua, G.: Parametric studies on different gas turbine cycles for a high temperature gas-cooled reactor. Nucl. Eng. Des. **235**, 1761–1772 (2005)
17. Mian, X., Linsen, L., Gang, Z., et al. Preliminary Transient Analysis for LBE-cooled Fast Reactor BLESS-D. In: Proceedings of the ICONE28 international Conference on Nuclear Engineering, August4–6, 2021, Virtual Conference (2021)
18. Wang, Z.G., Zhang, L.Y., Yeoh, E.Y., et al.: Pre-conceptual core design of a LBE-cooled fast reactor (BLESS). In: Proceeding of International Conference on Mathematics & Computational Methods Applied to Nuclear Science & Engineering (M&C 2017), Jeju, Korea, April 16–20, (2017)
19. Wang, Z., Li, L., Yeoh, E.Y., et al. Research on accumulation of high level radioactive waste for a LBE-cooled fast reactor. Atomic Energy Sci. Technol. **51**(12), 2294−2299 (2017)
20. Yeoh, E.Y., Li, L., Chen, X., et al.: Calculation of DPA in the main components of a LBE-cooled fast reactor (BLESS-D). Nuclear Techniques **43**(6), 37–42 (2020)

Study on the 3-D Natural Circulation Characteristics of LFR Under Steady State by Using Ansys Fluent

Jianing Dai, Yulin Yan, Erhao Li, Zhengyu Gong, Ling Zhang, and Zhixing Gu[(✉)]

College of Nuclear Technology and Automation Engineering, Chengdu University of
Technology, Chengdu, Sichuan, China
`guzhixing17@cdut.edu.cn`

Abstract. As one of the Generation IV reactors, Lead-based Fast Reactor (LFR) has been considered to be great promising owing to its advantages in nuclear safety, sustainable development of nuclear energy and nuclear waste disposal. Owing to the excellent thermal expansion characteristics of Lead-based coolant materials, the primary cooling system of LFR can operate in natural circulation driven mode. The CFD (Computational Fluid Dynamics)-based thermal-hydraulics and safety analyses of nuclear reactors, especially liquid metal pool-type reactors have attracted great attentions in recent years. In this paper, the entire 3-D geometric model of a 10 MWth natural circulation driven LFR primary cooling system was established and simulated by ANSYS Fluent, in which the mesh was partitioned by utilizing structured meshing technology, and the porous medium model was utilized to fine the reactor core simulation. The results showed that the above LFR can operate safely in natural circulation mode, and has excellent natural circulation characteristics for the primary cooling system.

Keywords: Natural Circulation · LFR · CFD · ANSYS Fluent · Structured meshing technology

1 Introduction

As one type of the much anticipated fourth generation reactors, Lead or Lead-bismuth cooled Fast Reactor (LFR) was developed rapidly, its excellent capabilities in miniaturization, modularization and waste transmutation made it has great prospects in district heating, electricity and accelerator driven sub-critical system (ADS). Numerous of research institutes have great enthusiasm for LFRs, and a lot of experimental and teaching LFRs were developed, such as ELSY [1], SSTAR [2], SNCLFR [3], CLEAR-I [4] and MYRRHA [5]. Owing to the large thermal expansion coefficient and stable physical properties of Lead-based materials, LFRs have well natural circulation capability. At the same time, natural circulation capacity also guaranteed forced circulation passive security. Therefore, it is important to study the natural circulation thermal-hydraulic characteristics. With the development of computer hardware and software, computational fluid dynamics (CFD) methods was recognized as an accurate and efficient way,

and it had been utilized widely. Nowadays, numerous of thermal-hydraulic programs or codes were developed. On the one hand, 1-D system analysis codes, such as RELAP5 and ATHLET, had been applied extensively. These codes can simulate the entire reactor system rapidly and precisely. However, system analysis codes were not good at reflecting thermal-hydraulic phenomena elaborately in LFRs, such as thermal stratification and flow details. On the other hand, numerous of CFD programs were adopted, the popular ones are ANSYS FLUENT, STAR-CCM . Through the simulation by these programs costs higher than system analysis codes, they can show heat transfer and flow characteristic details. In recent years, CFD programs became more and more extensive in investigating the thermal-hydraulic characteristics of LFRs.

In the past decades, a great deal of 2-D and 3-D simulations were carried out. In 2012, Jin [6] built a quarter 3-D model of CLEAR-I, carried out 3-D simulations by using ANSYS FLUENT to investigate the natural circulation capacity and thermal-hydraulic characteristics of CLEAR-I under steady state and loss of heat sink (LOHS) accident condition. In2013, in order to study the thermal stratification phenomena in CLEAR-I, Zhao [7] established a 2-D axisymmetric model and carried out 2-D simulations by utilizing ANSYS FLUENT, in which different power density was given based on the neutronics analysis. From the result, apparent thermal stratification appeared in the regions of the hot pool below the inlet window of heat exchanger under reactor scram conditions, but it never stopped the natural circulation of the primary circuit. In 2015, a self-developed CFD code namely NTC-2D was utilized by Gu [8] to investigate CLEAR-I under steady state, unprotected loss of heat sink (ULOHS) and unprotected transient overpower (UTOP) conditions. NTC-2D is a 2-D CFD code coupled with neutron transport kinetics model. The results demonstrated that the nice natural circulation capabilities contributed to the accident mitigation process. In 2015, to investigate the natural circulation characteristics of a small modular natural circulation LBE (Lead-Bismuth Eutectic) cooled fast reactor, 3-D simulations was conducted by using ANSYS FLUENT [9], in which a 3-D quarter reactor model was established, and the core power distribution was realized by UDF tools according to the reactor core layout. In 2015, to study the thermal-hydraulic characteristics of SNCLFR under UTOP accident, Chen [10] performed a 2-D simulation by using FLUENT coupled with neutron kinetics and pin thermal transfer models. In 2016, 3-D FLUENT simulations which aimed to evaluate two types of cooling systems, RVACS (reactor vessel air cooling system) and PHXs (primary heat exchangers), was conducted by Wang [11]. The results showed that both two cooling systems have excellent heat exchange capability, while PHXs is stronger than the RVACS. In 2017, Martelli [12] developed a RELAP5-ANSYS FLUENT coupling code to investigate the thermal-hydraulic characteristics of NACIE experimental loop. Natural circulation condition, isothermal gas enhanced circulation and unprotected loss of flow (ULOF) accident were simulated, in which the fuel pin was simulated by FLUENT while other parts were simulated by RELAP5. In 2020, aimed to study the hydraulic phenomena in M2LFR-1000 reactor, Zou [13] performed the simulations of steady state and ULOF accident conditions by using coupling ATHLET with Open-FOAM, in which a 3-D 1/8 model of hot pool was adopted. In 2021, Achuthan [14] studied the natural circulation characteristics of SESAME facility in steady state and several transient conditions.

At present, on the one hand, most researches on thermal-hydraulic characteristics of LFRs in the whole reactor scale did not consider the core power distribution. One the other hand, simulations with considerations of core power distribution were restricted to 2-D or symmetrical 3-D scales. Comparing with the above scales, the whole 3-D simulations can reveal the thermal-hydraulic characteristics more elaborately and precisely. In this paper, a 3-D CFD model of a pool type LFR primary cooling system was established, and the mesh was structured by using block-structed strategy. The steady state simulation which considered power distribution in the core was performed, and the evaluation and discussion of velocity and temperature distribution were also conducted.

2   Calculation Model

2.1   Geometry Model

The geometry model was established based on a typical 10 MW$_{th}$ pool type experimental reactor. To guarantee the simulation efficiency and enhance the visuality of the simulation, some subordinate parts and unnecessary details were removed or simplified. After abundant rational consideration, the concrete components of interior structure in heat exchangers and subassemblies in reactor core was simplified. The CFD simulation geometry includes hot pool, cold pool, core, above core structure (simplified based on control rod driven system) and HXs. The hot pool and the cold pool were separated by a heat barrier. Four inlets and four outlets of each HX were located in the side of them. The geometry model was showed in Fig. 1.
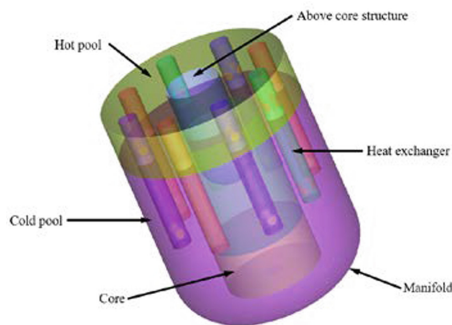
Fig. 1. The calculated geometry model of the primary cooling system

2.2   Mesh Construction and Sensitivity Analysis

To guarantee the accuracy of results and reduce simulation cost, the mesh was established by utilizing block-structed strategy. Specifically, mesh at the hot pool and core were more dense than other parts. To make the simulation results independent with the mesh quantity, the mesh sensitivity analysis was also carried out. Three mesh sizes, including 1.5 million, 5 million and 8 million were selected. Three cases distinguished by different mesh quantity were simulated, and the corresponding temperatures of core outlet were interpolated linearly and plotted in Fig. 2. Obviously, it can be found from this figure that the 1.5 million mesh agreed bad with the two others, while the result of 5 million mesh had tiny difference with the 8 million mesh ones. Therefore, 5 million mesh was selected for the subsequent simulations.
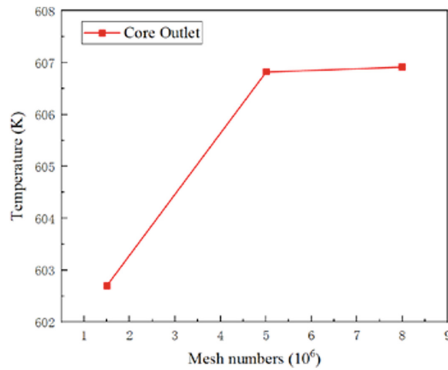
Fig. 2. The temperatures of core outlet for three cases

2.3   Construction of Reactor Core Model

Limited to the simulation cost and complexity, the reactor core was divided into eleven annular sections instead of simulating all the sub-assemblies, which was illustrated in Table 1. Each section contained certain number of sub-assemblies which had similar characteristics, such as power density. Considering the existence of sub-assembly walls, the internal boundary conditions were used to prevent above sections from heat and mass transfer. For each section, the porous medium model was employed in ANSYS FLUENT to simulate the reactor core configuration, in which the volume fraction for structures was set to be 0.7, and the volume fraction of fluid was set to be 0.3. As the detail configuration for sub-assembly was not considered, the viscous resistance in the x and y direction was set to be extremely large to ignore the cross flow of fluid. Moreover, the power density distributions in each annular section was considered by using the UDF techniques of Fluent [15].

2.4   The HXs Model

The HX is one of the significant components of LFR to establish the natural circulation, it determined the temperature level of primary cooling system. In HXs, the porous medium

Table 1. Radial distribution of the reactor core

Layer Number	Radius of loops (m)	Zone
1	0.0761	Neutron source zone
2	0.2014	Neutron source zone
3	0.3318	fuel zone
4	0.4239	fuel zone
5	0.4439	Control rod zone
6	0.5646	fuel zone
7	0.5897	Control rod zone
8	0.7342	fuel zone
9	0.8374	reflecting zone
10	0.9355	reflecting zone
11	1	Shielding zone

model was also used to simulate the primary coolant and heat transfer tube and prevent the coolant from flowing along the horizontal direction. As there are Eight HXs installed in the primary cooling system, meaning that each HXs needs to remove 1.25 MW. Fluid Inlets and outlets of HX were located at the side of two HXs ends. Average coolant temperature at HXs outlet was 573K. Just as demonstrated below, therefore, a volumetric heat source term model was used in each HX [11].

$$Q = \frac{1.25\,\text{MW}}{0.73} \times \frac{T_{LBE} - 573}{119} \tag{1}$$

2.5 Physical Properties

Density difference provided the driving force of natural circulation. The temperature dependent lead properties equations referred to the lead or lead-alloy properties handbook edited by OECD/NEA (2007) was used here. The equation of LBE density was given as Eq. (2). And other 2 key physical properties, conductivity and viscosity were also given. UDF tools were utilized to realize these items.

$$\rho_{LBE} = 11065 - 1.293 * T \tag{2}$$

$$C_{pLBE} = 164.8 - 0.0394 * T + 0.0000125 * T^2 - 4.56 \tag{3}$$

$$\mu_{LBE} = 0.000494 * e^{\frac{754.1}{T}} \tag{4}$$

3   Results and Discussion

Aiming to obtain the velocity field and temperature distribution under full power conditions, the steady state analysis was implemented. For evaluating and discussing the simulation results, a plane y = 0 m, which crossed hot pool, cold pool, two HXs, above core structure and core was established, as shown in Fig. 3.
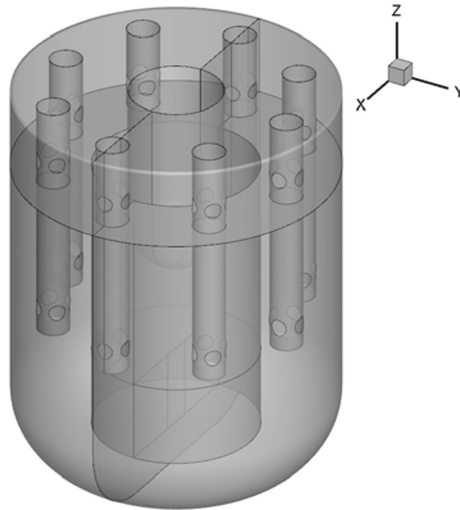
Fig. 3. The schematic diagram of the plane

3.1   Discussion of Velocity Field

The velocity field was given in Fig. 4, it can be seen that a stable natural circulation was established in the primary cooling system. In hot pool, hot coolant raised perpendicularly until arrived at the bottom of above core structure, then it dispersed around, flow upward and entered HXs inlets at last. The larger velocity along wall of above core structure and swirl at the upper part of hot pool promoted coolant mixing. The maximum velocity in the core was 0.127 m/s presented at ring 4 (fuel zone). Figure 5 showed the velocity field approaching a HX. Obvious swirl can be seen near the right HX inlet, and velocities near inlets and outlets of HXs were significantly larger, the maximum velocity in primary cooling system was 0.44060713 m/s, located in a HX. However, velocities at two ends of HXs were slightly small, that may lead poor heat transfer capability in these areas. In cold pool, velocity in upper part of cold pool was relatively small, and occurred swirl that promoted coolant mixing. While at the lower part, owing to the reduction of flowing area at lower part of cold pool, the velocity increased obviously. In addition, it can be seen that velocity vectors above and below the core were extremely intensive, this was due to the slender shape of mesh blocks and big nodes number.
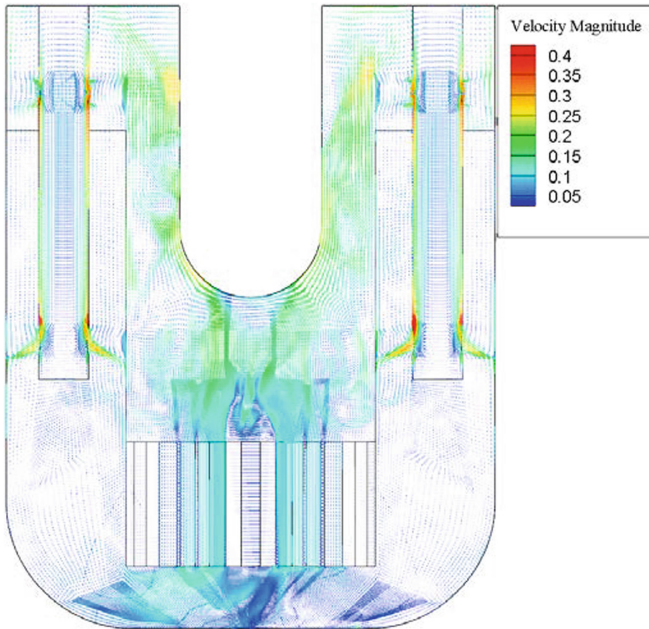
Fig. 4. Velocity field of the reactor system
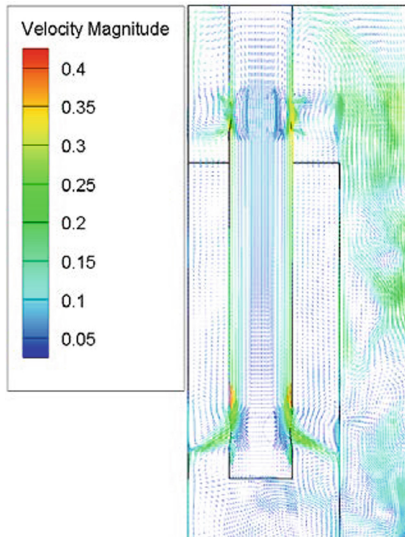
Fig. 5. Velocity field at HXs

3.2 Discussion of Temperature Distribution

Temperature distributions under steady state at y = 0 m was illustrated in Fig. 6. In hot pool, the temperature of coolant reached maximum value of 710.51K at ring 8 (fuel zone). Owing to the heat exchange in reactor core, it can be seen apparent thermal stratification in vertical direction. In radial direction, the figure indicated that temperature at fuel rings was significantly higher than other parts. However, the temperature at lower parts of fuel zones was relatively small, the reason can be concluded combing with Fig. 7. The figure indicated that velocity at fuel zones was much higher than other parts, means that the temperature and density changed most drastically, and caused the mass flow rate at these zones was larger than other parts. In the upper part of hot pool, owing to the reasonable arrangement of subassemblies and hot pool structure, no obvious thermal stratifications can be observed. In cold pool, the temperature distribution was more homogeneous than in hot pool ones, and the maximum temperature was 578.323K occurred at an outlet of HX. However, the symmetry of temperature distribution was imperfect. In the preliminary analysis, this was due to the mesh was not symmetrical entirely.
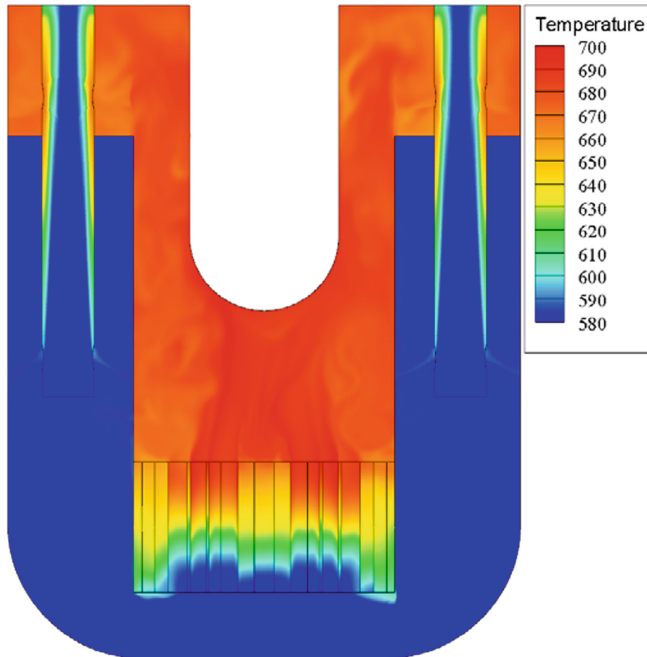
Fig. 6. The temperature distribution of the reactor system
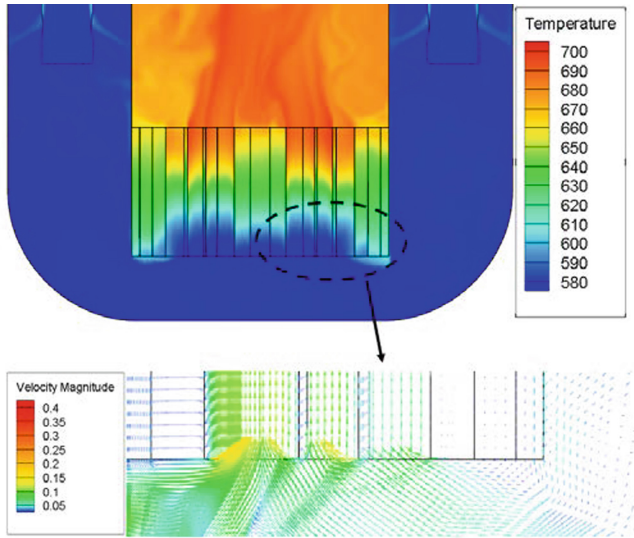
Fig. 7. The velocity vector at inlet of core (right side)

4   Conclusion

In this paper, a 3-D global CFD simulation which aims to study the thermal-hydraulic characteristics of LFR under steady state was implemented. In the core, power distribution in both vertical and radial direction were realized by utilizing UDF tools. Basing on velocity field and temperature distribution, discussion and evaluation of natural circulation.

were carried out. From the simulation results and discussion, the following results had been obtained:

(1) Lead-bismuth fast reactors have good thermal-hydraulic characteristics under natural circulation conditions. Under steady state conditions, decay heat generated by the core can be removed welly by HXs to establish an ideal steady state. At the same time, maximum temperatures of the reactor, temperature in the center of reactor core were also lower than the safety limits, which also shows that the lead-bismuth reactor has good natural circulation capability.

(2) Based on the analysis of the velocity field, it can be concluded that the coolant generated some swirls, and clear thermal stratification phenomena was occurred in many parts of the primary cooling system. It is recommended that structural design optimization or material reinforcement be carried out, such as decrease cavity volume between end face and inlets or outlets of HXs.

(3) Referred to other relevant literature, the simulation results in this paper were accurate generally. However, under the condition that the mesh quality was acceptable, the mesh symmetry and mesh shape may still lead obvious difference of simulation results.

In our future work, a more detailed model will be established, a more regular and symmetrical mesh partition strategy will be utilized. Furthermore, point kinetic model in core will be considered.

References

1. Alemberti, A., et al.: European lead fast reactor—ELSY. Nucl. Eng. Des. **241**(9), 3470–3480 (2011)
2. Smith, C.F., Halsey, W.G., Brown, N.W., Sienicki, J.J., Moisseytsev, A., Wade, D.C.: SSTAR: the US lead-cooled fast reactor (LFR). J. Nucl. Mater. **376**(3), 255–259 (2008)
3. Chen, H., et al.: Conceptual design of a small modular natural circulation lead cooled fast reactor SNCLFR-100. Int. J. Hydrogen Energy **41**(17), 7158–7168 (2016)
4. Wu, Y., Bai, Y., Song, Y., Huang, Q., Zhao, Z., Hu, L.: Development strategy and conceptual design of China Lead-based Research Reactor. Ann. Nucl. Energy **87**, 511–516 (2016)
5. Hamid, A.A., Baeten, P., De Bruyn, D., Fernandez, R.: MYRRHA – a multi-purpose fast spectrum research reactor. Energy Conv. Manag. **63**, 4–10 (2012)
6. Jin, M., Chen, Z., Chen, H., Zhou, T., Bai, Y.: Natural circulation characteristics of China lead alloy cooled research. In: The 9th International Topical Meeting on Nuclear Thermal-Hydraulics, Operation and Safety (NUTHOS-9), Kaohsiung, Taiwan (2012)
7. Zhao, P., Chen, Z., Zhou, T., Chen, H.: CFD analysis of thermal stratification of China lead alloy cooled research reactor (CLEAR-I). In: Proceedings of the 2013 21st International Conference on Nuclear Engineering (2013)
8. Gu, Z., Wang, G., Wang, Z., Jin, M., Wu, Y.: Transient analyses on loss of heat sink and overpower transient of natural circulation LBE-cooled fast reactor. Prog. Nucl. Energy **81**, 60–66 (2015)
9. Pengcheng, Z., Shuzhou, L., Zhao, C., Jie, Z., Hongli, C.: Natural circulation characteristics analysis of a small modular natural circulation lead–bismuth eutectic cooled fast reactor. Prog. Nucl. Energy **83**, 220–228 (2015)
10. Chen, Z., Chen, X.-N., Rineiski, A., Zhao, P., Chen, H.: Coupling a CFD code with neutron kinetics and pin thermal models for nuclear reactor safety analyses. Ann. Nucl. Energy **83**, 41–49 (2015)
11. Wang, X., Jin, M., Wu, G., Song, Y., Li, Y., Bai, Y.: Natural circulation characteristics of lead-based reactor under long-term decay heat removal. Prog. Nucl. Energy **90**, 11–18 (2016)
12. Zhao, P., Shi, K., Li, S., Feng, J., Chen, H.: CFD analysis of the primary cooling system for the small modular natural circulation lead cooled fast reactor SNRLFR-100. Sci. Technol. Nucl. Install. **2016**, 1–12 (2016)
13. Zou, Z., Shen, C., Zhang, X., Wang, S., Chen, H.: 3D thermal hydraulic characteristics analysis of pool-type upper plenum for lead-cooled fast reactor with multi-scale coupling program. Nucl. Eng. Design **370**, 110892 (2020)
14. Achuthan, N., Melichar, T., Profir, M., Moreau, V.: Computational fluid dynamics modelling of lead natural convection and solidification in a pool type geometry. Nucl. Eng. Des. **376**, 111104 (2021)
15. Incorporated, A.: ANSYS Fluent UDF Manual15 (2013)

Multi-physics Coupling Analyses of Nuclear Thermal Propulsion Reactor

Wenbin Han[1,2], Zechuan Guan[1,3], Shanfang Huang[1(✉)], and Jian Deng[2]

[1] Department of Engineering Physics, Tsinghua University, Beijing, China
sfhuang@mail.tsinghua.edu.cn
[2] Science and Technology on Reactor System Design Technology Laboratory, Nuclear Power Institute of China, Chengdu, China
[3] China Institute of Atomic Energy, Beijing, China

Abstract. Nuclear thermal propulsion (NTP) reactors have high-temperature solid-state characteristics and significant thermal expansion, which therefore require multi-physics coupling analyses. In this paper, the framework of Neutronics, Thermal-Hydraulics and Mechanics coupling (N/T-H/M) of nuclear thermal propulsion reactor is developed, and the typical reactor XE-2 is analyzed with this method. The results show that the N/T-H/M coupling will bring -1049 pcm negative reactivity, of which the thermal expansion effect accounts for 22%, indicating that the nuclear thermal propulsion reactor has a certain capacity for self-regulation. However, thermal expansion will lead to 0.88 mm peak deformation and 233 MPa peak stress, which will severely threaten the mechanical tolerance of the materials. Therefore, there is a trade-off between the advantages and disadvantages of the high-temperature solid-state core while designing NTP reactors.

Keywords: Nuclear Thermal Propulsion Reactor · Neutronics and Thermal-Hydraulics Coupling · Neutronics · Thermal-Hydraulics and Mechanics Coupling

1 Introduction

Deep space exploration and interstellar travel are the persistent pursuits of humankind. The propulsion system is the key to further investigation of the universe. Currently, the chemical propulsion system have been widely used in rockets and spacecraft, but its low energy density and small specific impulse makes it difficult to be applied in deep space exploration and interstellar navigation. Nuclear Thermal Propulsion (NTP) uses nuclear fission energy to heat the working medium flowing through the core to high temperature, and then the hot propellant flows through the nozzle, expands and accelerates to provide thrust for the rockets. NTP has advantages of high specific impulse, high thrust, and long service life, therefore is the preferred propulsion choice for deep space exploration.

The concept of nuclear thermal propulsion could date back to the "space race" between the United States and the Soviet Union in the 1950s [1]. From the 1950s to 1970s, the US successively carried out ROVER and NERVA programs. The US built

and tested more than 20 NTP reactors, including KIWI, Phoebus, Pewee, NRX, and XE series, generating more than 100,000 technical reports and memos [2]. The achievements in ROVER/NERVA program laid the foundation for later NTP research and designs.

Although there are also liquid and gaseous designs [3], the solid-core nuclear thermal propulsion reactor is the most general design, of which the typical structure is shown in Fig. 1. The specific impulse I_{sp} is a key performance of a rocket engine, which is determined by the operation conditions, propellant properties and exhaust nozzle geometry according to Eq. (1).

$$I_{sp} = \frac{1}{g}\sqrt{\frac{2\gamma}{\gamma-1}\frac{RT}{M}\left(1-\left(\frac{P_e}{P_i}\right)^{\frac{\gamma-1}{\gamma}}\right)} \tag{1}$$

where i and e represent the inlet and exit conditions, γ is the specific heat ratio, R is the universal gas constant, T is the inlet temperature of the nozzle, P is the pressure of the propellant, g is the gravitational acceleration, and M is the molecular weight of the propellant.

To increase the specific impulse as much as possible, a NTP reactor needs high operation temperatures (usually ~ 3000 K in solid-state core) and small propellant molecular weight (usually hydrogen). Therefore, a typical NTP reactor is actually a high-temperature hydrogen-cooled reactor.

Compared with traditional light water reactors, NTP reactors have mainly the following features:

(1) Solid-state core design. Except for the hydrogen coolant, the body of the reactor is in a solid state, including fuel and moderator elements.
(2) High operation temperature. The operation temperature can reach 3000 K.
(3) Hard neutron energy spectrum. To reduce the size of the reactor, the loading of the moderator is limited, thus the reactor is generally designed with a hard neutron energy spectrum.

The high-temperature solid core can experience significant thermal expansion, which will bring in negative reactivity feedback and thermal stress. The hard spectrum design and small core size lead to the tight coupling of different physical fields.

In light water reactors, the effect of thermal expansion is usually negligible, only the neutronics and thermal-hydraulics (N/T-H) coupling is considered. However, for high-temperature solid-state reactors, such as heat pipe cooled reactors and NTP reactors, thermal expansion is non-negligible. Previous studies show that in the heat pipe cooled reactor KRUSTY, the thermal expansion accounts for ~ 90% of the reactivity feedback [5]. Therefore, the neutronics, thermal-hydraulics and mechanics (N/T-H/M) coupling analyses are needed for core design and safety analysis in high-temperature solid-state reactors.

For the heat pipe cooled reactor, the coolant is replaced by heat pipes, so it should consider neutronics, thermal-mechanics and heat pipe (N/T-M/HP) coupling analysis [6, 7]. However, for NTP reactors, the operation temperature is much higher, and there is a
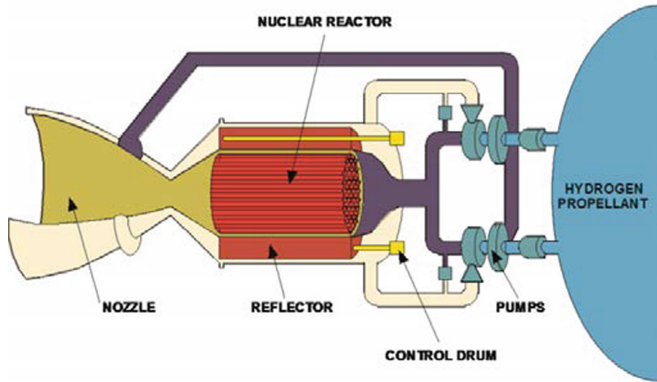
Fig. 1. Schematics of a typical NTP system [4]

hydraulic effect of hydrogen propellant. Therefore, a new coupling code is needed for NTP reactor analysis.

In this work, a neutronics, thermal-hydraulics and mechanics coupling method is developed to analyze the NTP reactor. The Reactor Monte Carlo code (RMC) [8] and the commercial finite element analysis software ANSYS Mechanical are used for the neutronic and thermal-mechanical analyses, respectively. A single channel code is developed for the hydrogen flow and heat transfer analysis.

2 Methodology

2.1 Computational Methods

RMC (Reactor Monte Carlo code) is a Monte Carlo neutron and photon transport code developed by the Department of Engineering Physics at Tsinghua University [8], which has been validated for criticality calculation, burnup calculation, neutron and photon coupled transport calculation, full-core refueling simulation, randomly dispersed fuel calculation, and neutronic-thermal-mechanical coupling analysis [6, 7, 9–13].

ANSYS Mechanical is a commercial finite element mechanical analysis software that includes structural mechanics analysis, thermal analysis, and coupling analysis. APDL, also known as ANSYS parametric design language, enables users to organize ANSYS commands and write parametric user-defined programs.

A single channel code is developed for the hydrogen hydraulic analysis, which will be described detailly in Sect. 2.5.

2.2 Coupled N/T-H/M Framework

The neutronic, thermal-hydraulic and mechanical coupling framework is shown in Fig. 2. An outer iteration strategy is used to schedule different codes with a main scheduling routine. The Picard iteration method is used to couple the various physical fields. The main pipeline in the iteration is as follows:

(1) RMC reads the initial input file and simulates the neutron transport to get the criticality result and power distribution.

(2) A data processing script reads the power distribution file from RMC, converts it into absolute power density and builds an ANSYS input command file with the power density as the heat source.

(3) ANSYS Mechanical reads the input commands then executes thermal-mechanical coupling analyses with initial wall temperatures of every coolant channel. Once finished, the heat flux into each coolant channel is calculated.

(4) The single-channel hydraulic analysis routine updates the wall temperature distributions with heat flux from ANSYS results as boundary conditions.

(5) Steps (3) and (4) are repeated until T-H/M coupling converges in a sense. Afterwards, the final T-H/M result is written into files, including temperature, deformation, density and stress distributions.

(6) A data processing script reads the T-H/M result and builds new geometry, and sets new densities and new temperatures for the RMC input file.

(7) RMC reads the new input file, updates the cross-sections, geometry and material properties, and starts new neutronic calculations.

(8) Steps (1)–(7) are repeated until the N/T-H/M coupling convergence criteria are satisfied.
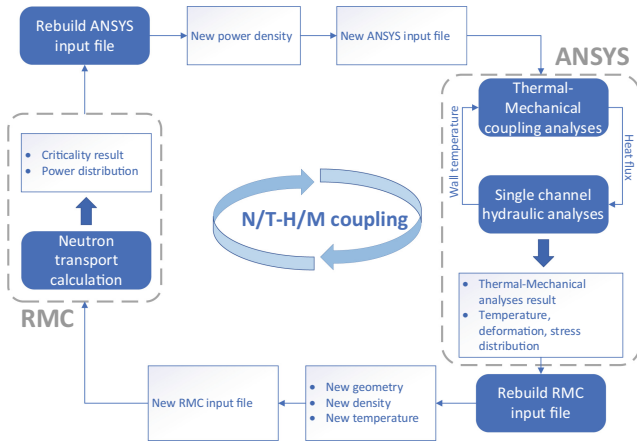
Fig. 2. Coupled N/T-H/M framework

2.3 Neutronic Model

To improve the computing efficiency, a 1/6 model of the XE-2 reactor core is built with RMC constructive solid geometry as shown in Fig. 3. The geometry, materials and nuclide compositions mainly refer to the XE-2 reactor design manual [14]. The fuel element is a 19-channel hexagonal prism dispersed with UC_2 particles. To tally the

power distribution and receive T-H/M feedbacks, the active core is axially divided into 26 segments.

In criticality calculations, the simulations use 100,000 particles per cycle with 30 inactive cycles and 270 active cycles, resulting in a standard error of k_{eff} less than 0.0002.
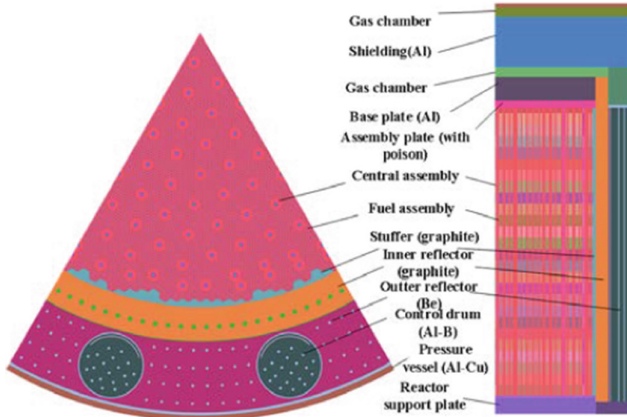
Fig. 3. 1/6 core model of RMC

2.4 Thermal-Mechanical Model

A 1/6 core finite element model is constructed with ANSYS Mechanical APDL as shown in Fig. 4. The thermal-mechanical properties refer to the NERVA material manual [15]. The triangular mesh is used in the radial direction and then sweeping in the axial direction. For thermal boundary conditions, the outer boundary is set to be adiabatic and the walls of each channel are set to be in constant temperatures given by the single-channel analysis code, which will be updated every T-M/H iteration. For mechanical boundary conditions, the center line and the bottom are set to be fixed, while the others can expand freely.

2.5 Hydraulic Model

There are numerous coolant channels in the XE-2 reactor. In the 1/6 model, 500 ~ 600 coolant channels can transfer heat with the fuel. Because the channels are independent without any coolant mixing, they can be treated one by one with single channel analysis. Therefore, a single-channel hydraulic analysis code for hydrogen is developed with APDL. The main correlations used in this algorithm comes from the thermal hydraulic calculation program ELM [16] developed by NASA for nuclear thermal propulsion reactors.
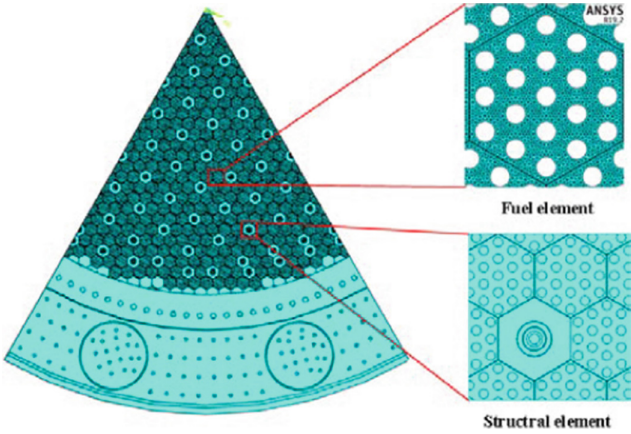
Fig. 4. 1/6 core model of ANSYS Mechanical

As shown in Fig. 5, given the cooling channel length L and hydraulic diameter D, a channel is divided into N control volumes with individual inlet and outlet temperatures and pressures. The inlet temperature T_{in} and pressure P_{in} are given. The heat flux into each control volume $Q_1 \sim Q_N$ is known from ANSYS T-M coupling results. The flow rate is known as W_{CH}. The outlet pressure of the nth control volume is assumed as Eq. (2).

$$P_n = \frac{P_N - P_{n-1}}{N - n + 1} + P_{n-1} \tag{2}$$
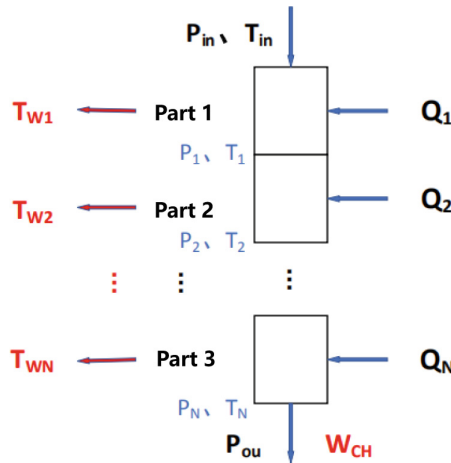
Fig. 5. Single channel boundary conditions and control volume partition schematics

From the inlet control volume on, the calculation proceeds in sequence, and the outlet temperature and pressure obtained from the previous control volume are used as the inlet condition of the next control volume. When the calculation arrives at the last volume, according to the known outlet pressure, the outlet temperature and mass flow are calculated. The iteration continues until convergence. The detailed process is as follows:

(1) The density of hydrogen ρ_{n-1} is looked up in the hydrogen property table according to P_{n-1} and T_{n-1}.

(2) H_n and ρ_n are obtained iteratively by trial and error with Eq. (3) and referring to the hydrogen physical properties look-up table.

$$H_{n-1} + \frac{\left(\frac{4W_{CH}}{\pi D^2 \rho_{n-1}}\right)^2}{2} + \frac{Q_n}{W_{ch}} = H_n + \frac{\left(\frac{4W_{CH}}{\pi D^2 \rho_n}\right)^2}{2}. \tag{3}$$

(3) Determine the qualitative temperature and pressure:

$$T_b = \frac{T_{n-1} + T_n}{2} \tag{4}$$

$$P_b = \frac{P_{n-1} + P_n}{2}. \tag{5}$$

(4) According to T_b and P_b, look up the hydrogen physical property table and get μ_b, ρ_b, C_{pb}, C_{vb}, λ_b.

(5) Calculate the Reynolds number and Prandtl number:

$$Re_b = \frac{v_b D \rho_b}{\mu_b} = \frac{4W_{CH}}{\pi D \mu_b} \tag{6}$$

$$Pr_b = \frac{C_{pb}\mu_b}{\lambda_b} \tag{7}$$

(6) Find the fluid resistance coefficient:

$$f = \left(\frac{T_b}{T_{wn}}\right)^{0.5} \left(0.0014 + \frac{0.125}{Re_b^{0.32}}\right)(1.85 \times 10^{-5} Re_b + 0.73)^{0.5} \tag{8}$$

(7) If it is the $1^{st} \sim (N\text{-}1)^{th}$ control volume, update the outlet pressure:

$$P_n = P_{n-1} - \left(\frac{4W_{CH}}{\pi D^2}\right)^2 \frac{fL}{ND}\left(\frac{1}{\rho_{n-1}} + \frac{1}{\rho_n}\right) - \left(\frac{4W_{CH}}{\pi D^2}\right)^2 \left(\frac{1}{\rho_n} - \frac{1}{\rho_{n-1}}\right) \tag{9}$$

If it is the Nth control volume, skip.

(8) Solve the Nusselt number Nu_D with Eq. (10)–(14).

$$E_t = \left(1.82 \times \log_{10} Re_b - 1.64\right)^2 \tag{10}$$

$$K_1 = 1 + 3.4 E_t \tag{11}$$

$$K_2 = 11.7 + 1.8 \times Pr_b^{-\frac{1}{3}} \tag{12}$$

$$Nu_0 = E_t Re_b Pr_b / 8 \Big/ \left(K_1 + K_2 \left(\frac{E_t}{8} \right)^{0.5} \left(Pr_b^{\frac{2}{3}} - 1 \right) \right) \tag{13}$$

$$Nu_D = Nu_0 \left(\frac{T_w}{T_b} \right)^{-0.31 \times \ln(T_w - T_b) - 0.36} \tag{14}$$

(9)   Solve the convection transfer coefficient:

$$h = \frac{Nu_D \lambda_b}{D} \tag{15}$$

(10)   Update wall temperature T_{wn} according to Eq. (16)–(19):

$$T_{AW} = T_b \times \left(1 + 0.5 \times Pr_b^{\frac{1}{3}} (\gamma_b - 1) M_b^2 \right) \tag{16}$$

$$\gamma_b = \frac{C_{pb}}{C_{vb}} \tag{17}$$

$$M_b = \frac{v_b}{(\gamma_b R T_b)^{0.5}} \tag{18}$$

$$T_{Wn} = \frac{NQ}{h \pi D L} + T_{AW} \tag{19}$$

(11)   Iterate and update the channel mass flow:

$$W_{CH} = \frac{\pi D^2}{4} \times \sqrt{\frac{P_{n-1} - P_n}{\frac{fL}{2D\rho_b} + \frac{1}{\rho_n} - \frac{1}{\rho_{n-1}}}} \tag{20}$$

3   Performance Analyses

3.1   Neutronic Performance

To study the significant influence of thermal expansion, the results of N/T-H coupling and N/T-H/M coupling are compared. The variation of k_{eff} with iterations is shown in Fig. 6. There is a sharp decrease of k_{eff} in both N/T-H coupling and N/T-H/M coupling. The k_{eff} without feedback is 1.00792. After several iterations, the k_{eff} converges. The k_{eff} is 1.00035 with N/T-H coupling, and 0.99737 with N/T-H/M coupling. The reactivity feedbacks are summarized in Table 1. Both the doppler effect and thermal expansion effect can lead to a negative reactivity feedback, in which the thermal expansion counts for 22%. This result reveals the fact that in high-temperature solid state reactors, thermal expansion is a significant source of negative reactivity feedback, which enables the reactor certain self-regulating characteristics.

Table 1. Reactivity feedbacks in N/T-H/M coupling

	Doppler effect	Expansion effect	Total effect	Expansion fraction
Reactivity feedback (pcm)	−821	−228	−1049	22%
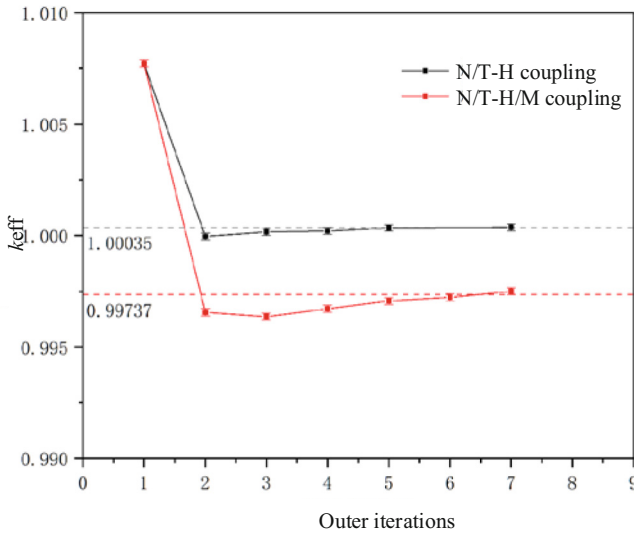
Fig. 6. The variation of k_{eff} with N/T-H and N/T-H/M coupling iterations

3.2 Thermal Performance

The fuel average and peak temperature converge during the coupling iterations as shown in Fig. 7 and Fig. 8. The temperatures gradually decrease from the initial value and tend to be stable. After convergence, the difference in fuel average temperature between N/T-H/M and N/T-H is very small, while the difference in peak temperature is much more. The peak temperature decreases by 164 K with N/T-H coupling, and 175 K with N/T-H/M coupling. The final temperature distribution is shown in Fig. 9.

3.3 Mechanical Performance

The thermal expansion will lead to displacement and thermal stress. The linear expansion variation with iterations is shown in Fig. 10. The final average linear expansion reaches 0.293%. The displacement and stress distributions are shown in Fig. 11 and Fig. 12. The maximum displacement is 0.882 mm. The stress peaks near the wall of coolant channels with the peaking stress as 233 MPa, which will threaten the strength of structural materials.
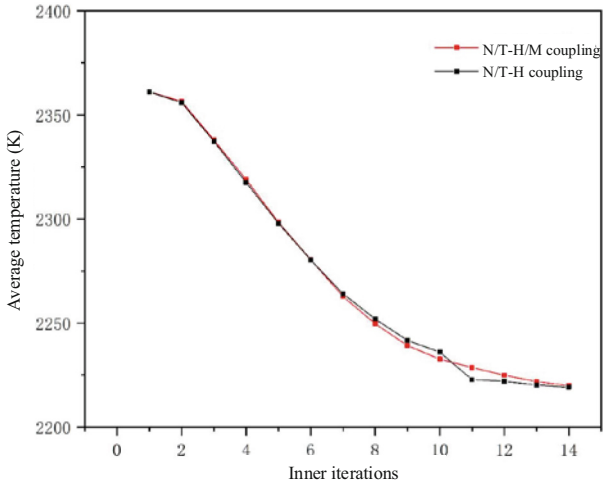
Fig. 7. The variation of fuel average temperature with N/T-H and N/T-H/M coupling iterations
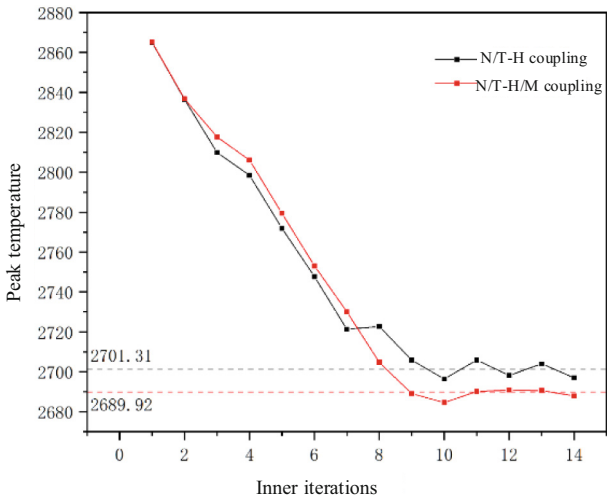
Fig. 8. The variation of fuel peak temperature with N/T-H and N/T-H/M coupling iterations
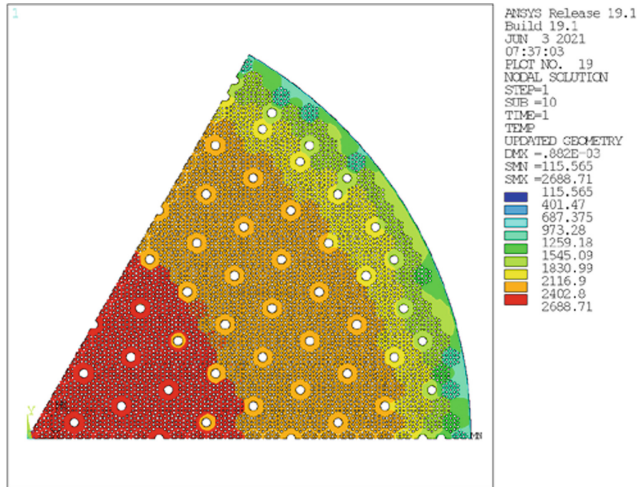
Fig. 9. The temperature distribution after N/T-H/M coupling
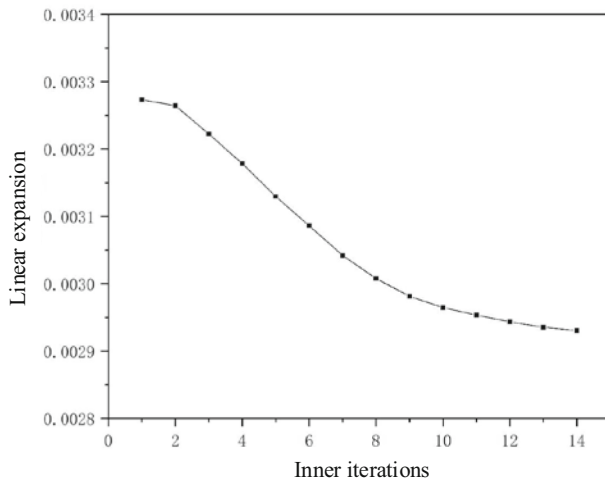
Fig. 10. The variation of expansion with N/T-H/M iterations
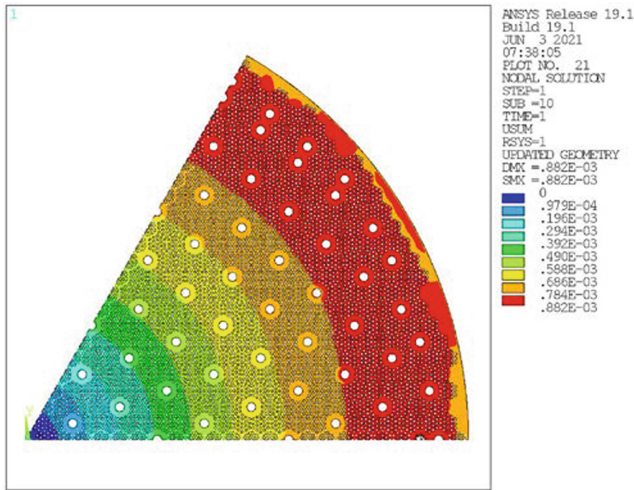
Fig. 11. The displacement distribution after N/T-H/M coupling
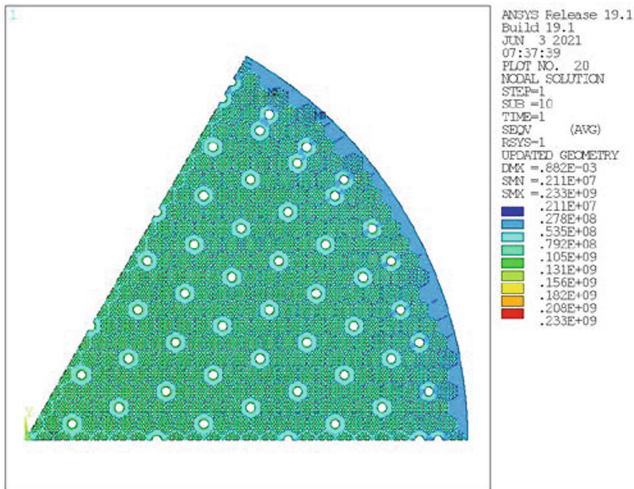
Fig. 12. The stress distribution after N/T-H/M coupling

4   Conclusions

In this work, a neutronic, thermal-hydraulic and mechanical coupling framework is developed for typical thermal propulsion reactors with RMC and ANSYS Mechanical. The XE-2 reactor is analyzed with this method. The effects of multi-physics coupling on analysis results are summarized in Table 2. The results show that the N/T-H/M coupling will bring -1049 pcm negative reactivity, of which the thermal expansion effect accounts for 22%, which indicates that the nuclear thermal propulsion reactor has a certain capacity of self-regulation. However, thermal expansion will lead to 0.88 mm peak deformation

and 233 MPa peak stress, which will severely threaten the mechanical tolerance of the materials. Therefore, there is a trade-off between the advantages and disadvantages of the high-temperature solid-state core while designing NTP reactors.

Table 2. Effects of multi-physics coupling on analysis results

	Without coupling	With N/T-H coupling	With N/T-H/M coupling
k_{eff}	1.007918	1.00035	0.99737
Peaking temperature (K)	2865	2701	2690
Peaking stress (MPa)	–	–	233
Peaking displacement (mm)	–	–	0.88

References

1. Zhang, W., et al.: Technical research on nuclear thermal propulsion ground tests. Astron. Syst. Eng. Technology **2**, 10 (2019)
2. Robbins, W.: An historical perspective of the NERVA nuclear rocket engine technology program. In: Conference on Advanced SEI Technologies (1991)
3. Gabrielli, R.A., Herdrich, G.: Review of nuclear thermal propulsion systems. Prog. Aeros. Sci. **79**, 92–113 (2015)
4. Houts, M.: High Performance Nuclear Thermal Propulsion NASA (2020)
5. Poston, D.I., et al.: KRUSTY reactor design. Nucl. Technol. **206**(sup1), S13–S30 (2020)
6. Ma, Y., et al.: Neutronic and thermal-mechanical coupling analyses in a solid-state reactor using Monte Carlo and finite element methods. Ann. Nucl. Energy **151**, 10792 (2021)
7. Ma, Y., et al.: Coupled neutronic, thermal-mechanical and heat pipe analysis of a heat pipe cooled reactor. Nucl. Eng. Des. **384**, 111473 (2021)
8. Wang, K., et al.: RMC–A Monte Carlo code for reactor core analysis. Ann. Nucl. Energy **82**, 121–129 (2015)
9. Wang, K., et al.: Analysis of BEAVRS two-cycle benchmark using RMC based on full core detailed model. Prog. Nucl. Energy **98**, 301–312 (2017)
10. Liu, S., et al.: BEAVRS full core burnup calculation in hot full power condition by RMC code. Ann. Nucl. Energy **101**, 434–446 (2017)
11. Ma, Y., et al.: RMC/CTF multiphysics solutions to VERA core physics benchmark problem 9. Ann. Nucl. Energy **133**, 837–852 (2019)
12. Liu, S., et al.: Random geometry capability in RMC code for explicit analysis of polytype particle/pebble and applications to HTR-10 benchmark. Ann. Nucl. Energy **111**, 41–49 (2018)
13. Wu, Y., et al.: Monte Carlo simulation of dispersed coated particles in accident tolerant fuel for innovative nuclear reactors. Int. J. Energy Res. **45**(8), 12110–12123 (2021)
14. Hill, D.J.: XE-2 nuclear subsystem thermal and nuclear design data book. No. WANL-TME-1805. Westinghouse Electric Corp., Pittsburgh, Pa.(USA). Astronuclear Lab (1975)
15. Hladdun, K.R., et al.: Materials properties data book. Volume II. Ferrous alloys. Environ. Toxicol. Chem. **32**, 2584–2592 (2013)
16. Walton, J.T.: Program ELM: a tool for rapid thermal-hydraulic analysis of solid-core nuclear rocket fuel elements (1992)

Effects of Inlet Conditions on the Two-Phase Flow Water Hammer Transients in Elastic Tube

Zixiang Zhao[1], Zhongdi Duan[1(✉)], Hongxiang Xue[1], Yuchao Yuan[1], and Shiwen Liu[2]

[1] State Key Laboratory of Ocean Engineering, Shanghai Jiao Tong University, Shanghai, China
`duanzhongdi@sjtu.edu.cn`

[2] Science and Technology on Reactor System Design Technology Laboratory, Nuclear Power Institute of China, Chengdu, China

Abstract. Two-phase flow water hammer events occur in the pipelines of the nuclear power systems and lead to transient and violent pressure shock to tube structures. For the sake of operation safety, the occurrence and severity of the two-phase water hammer should be carefully assessed. This paper presents a parameter analysis of the inlet conditions on the two-phase flow water hammer transients, with considering the elastic effect of the tube walls. A numerical model is established for the vapor-liquid two-phase flow based on the two-fluid six-equation modelling approach, with incorporating correlations and criterions for two-phase flow regime, interfacial interactions and heat transfer. The governing equations are transformed to matrix form expressed by characteristic variables, and solved using the splitting operator method and the total variation diminishing scheme. The accuracy of the model is verified against the experimental data in open literature. Then, the model is applied to investigate the effect of inlet velocity and inlet water temperature on the two-phase flow water hammer transients. The simulation results show that the increase of inlet velocity increases the pressure peak values and brings forward the onset of water hammer, and the increase of inlet temperature decreases the pressure shock. A comparison of the water hammer results between the elastic tube and rigid tube is further presented, and the effect of the elastic modulus on the water hammer is analyzed. The results also show that the pressure peak is largely affected by the tube diameter.

Keywords: nuclear power plants · condensation induced water hammer · fluid-structure-interaction · direct contact condensation · shock wave

1 Introduction

The passive heat removal system is one of the important systems to ensure the safety of ocean nuclear power plants. While using seawater as the infinite heat sink to cool the reactor, it also suffers the risk of reverse flow of subcooled seawater into the steam tube, which gives rise to the direct contact between the steam and subcooled water, and triggers condensation-induced water hammer (CIWH), resulting in high peak pressure pulses and consequently pipeline damage. CIWH is a common phenomenon in nuclear

power plants, steam power plants, and other energy power plants, and has received widespread attention from domestic and international research institutions and scholars.

Regarding CFD numerical simulation methods for CIWH, there are three main types of representative models: one is the use of surface renewal theory to calculate condensation heat transfer, such as Tiselj [1], Strubelj [2], and Ceuca [3], which established a large interface model for direct contact condensation based on surface renewal theory, which considered the turbulence effect between the vapor-liquid phase and showed that the model can predict the transient temperature change better by comparing with the PMK-2 experimental data. Second, the temperature gradient of the vapor-liquid phase is calculated directly, and the vapor condensation is calculated based on the thermal conductivity heat transfer [4], and this method can also predict the fluid temperature variation of the direct contact condensation process better. Third, a traditional evaporative condensation model is used for the calculation, such as Pham et al. [5], who obtained the CIWH pressure wave at the MPa level through Lee model simulations. In addition, the two-fluid model used by Höhne et al. [6] and the Large Eddy Simulation (LES) method used by Li et al. [7] also allow the simulation of direct contact condensation processes with a good agreement with experiments. These method give visual access to two-phase flow and phase interface information, however, most of the results obtained by commercial CFD software are not very satisfactory in the calculation of CIWH pressure waves, and it is difficult to capture the peak pressure.

For the prediction of condensation-induced water hammer pressure waves, several research institutions and scholars have developed computational models specifically for CIWH, and representative ones include the WAHA3 numerical computational program developed by Barna [8] and Tiselj [9] based on the WAHALoads project, as well as the computational program ATHLET [10]. The above models use a one-dimensional, two-fluid, six-equation model, and a surge capture algorithm for pressure wave prediction of CIWH. Hibiki [11] also computationally captured the transient process of CIWH based on the RELAP5 code, but the validity of this approach is controversial. Milivojevic et al. [12] developed a one-dimensional, three-equation single fluid model based on the HEM (Homogeneous Equilibrium Model) model that captured the steam-filled CIWH phenomenon in a vertical pipe. However, this method has not been applied in CIWH calculations for stratified flow in horizontal pipes because it cannot characterize the heat mass transfer relationship between the gas and liquid phases.

2 Mathematical Model Development

2.1 Basic Control Equations

For the vapor-liquid two-phase flow model, the basic idea for establishing the control equation is that regard the two-phase mixed flow as two single-phase flow, and their characteristics in terms of continuity, momentum and energy are examined separately, and then the inter-phase effects of mass exchange, momentum exchange and energy exchange are taken into account to form the basic control equation of the two-phase flow.

    The mass, momentum and energy balance equations for both phases are the following:

$$\frac{\partial A\alpha_l\rho_l}{\partial t} + \frac{\partial A\alpha_l\rho_l v_l}{\partial x} = A\Gamma_l \tag{1}$$

$$\frac{\partial A\alpha_v\rho_v}{\partial t} + \frac{\partial A\alpha_v\rho_v v_v}{\partial x} = A\Gamma_v \tag{2}$$

$$\frac{\partial \alpha_l\rho_l}{\partial t} + \alpha_l\rho_l K\frac{\partial P}{\partial t} + \frac{\partial \alpha_l\rho_l v_l}{\partial x} + \alpha_l\rho_l v_l K\frac{\partial P}{\partial x} = \Gamma_l \tag{3}$$

$$\frac{\partial \alpha_v\rho_v}{\partial t} + \alpha_v\rho_v K\frac{\partial P}{\partial t} + \frac{\partial \alpha_v\rho_v v_v}{\partial x} + \alpha_v\rho_v v_v K\frac{\partial P}{\partial x} = \Gamma_v \tag{4}$$

$$\alpha_l\rho_l\frac{\partial v_l}{\partial t} + \alpha_l\frac{\partial P}{\partial x} - P_i\frac{\partial \alpha_v}{\partial x} + \alpha_l\rho_l v_l\frac{\partial v_l}{\partial x} - VM$$
$$= F_D + \Gamma_l(v_i - v_l) + \alpha_l\rho_l g\sin\theta - F_{l,\text{ wall}} \tag{5}$$

$$\alpha_v\rho_v\frac{\partial v_v}{\partial t} + \alpha_v\frac{\partial P}{\partial x} + P_i\frac{\partial \alpha_v}{\partial x} + \alpha_v\rho_v v_v\frac{\partial v_v}{\partial x} + VM$$
$$= -F_D + \Gamma_v(v_i - v_v) + \alpha_v\rho_v g\sin\theta - F_{v,\text{ wall}} \tag{6}$$

where index l refers to the liquid phase and index v to the vapor phase. α is volume fraction, Γ is mass transfer rate, P_i is interfacial pressure, F_D is inter-phasic drag force and F_{wall} is wall friction force.

    To consider the geometric deformation of the pipe cross-section under pressure pulses, the cross-sectional area term A in Eqs. (1)–(2) is considered as a function of time and space, i.e., the elasticity of the pipe is considered. The cross-sectional area is of the form

$$A(x,\ t) = A(x) + A_{el}[P(x,\ t)] \tag{7}$$

where $A(x)$ is the nominal cross-sectional area of the pipe, and A_{el} represents the amount of change in cross-sectional area produced by a pressure pulse acting on the elastic pipe. The radial movement of the pipe wall is considered free in this paper. The study of Wylie and Streeter [13] gives the relationship between A_{el} and pressure

$$\frac{dA_{el}}{A(x)} = KdP \tag{8}$$

where $K = D/E\chi$, D is the tube cross-sectional diameter (m), E is the modulus of elasticity of the pipe material (N/m^2), χ is the pipe wall thickness (m). Combining Eqs. (1)–(2) and (7)–(8), the mass equation for two-phase flow in an elastic pipe can be written as

$$\frac{\partial \alpha_l\rho_l}{\partial t} + \alpha_l\rho_l K\frac{\partial P}{\partial t} + \frac{\partial \alpha_l\rho_l v_l}{\partial x} + \alpha_l\rho_l v_l K\frac{\partial P}{\partial x} = \Gamma_l \tag{9}$$

$$\frac{\partial \alpha_v\rho_v}{\partial t} + \alpha_v\rho_v K\frac{\partial P}{\partial t} + \frac{\partial \alpha_v\rho_v v_v}{\partial x} + \alpha_v\rho_v v_v K\frac{\partial P}{\partial x} = \Gamma_v \tag{10}$$

    The Eqs. (3)–(6),(9)–(10) are still not closed equations and the unknown variables in them need to be determined by supplementary equations.

2.2   Closure Models for Control Equations

2.2.1   Equation of State

There is a differential relationship between the density of the workpiece and the pressure, internal energy and temperature as follows

$$d\rho_k = \left(\frac{\partial \rho_k}{\partial P}\right)_{u_k} dP + \left(\frac{\partial \rho_k}{\partial u}\right)_P du_k \tag{11}$$

where the subscript k represents the vapor phase (v) or liquid phase (l). The thermodynamic coefficients involved in the above equation are constant volume compressibility k_k, constant pressure specific heat capacity C_{Pk}, constant pressure volume thermal expansion coefficient β_k. Differential form written as

$$k_k = -\frac{1}{\forall_k}\left(\frac{\partial \forall_k}{\partial P}\right)_{T_k} \tag{12}$$

$$C_{Pk} = \left(\frac{\partial h_k}{\partial T_k}\right)_P \tag{13}$$

$$\beta_k = \frac{1}{\forall_k}\left(\frac{\partial \forall_k}{\partial T_k}\right)_P \tag{14}$$

where $\forall_k = 1/\rho_k$. The partial differential term of density with respect to pressure and internal energy can be further written as

$$\left(\frac{\partial \rho_k}{\partial u_k}\right)_P = \frac{\beta_k}{(C_{Pk} - \forall_k \beta_k \rho_k)\forall_k} \tag{15}$$

$$\left(\frac{\partial \rho_k}{\partial P}\right)_{u_k} = \frac{C_{Pk}k_k - T_k\beta_k^2\forall_k}{(C_{Pk} - \forall_k\beta_k P)\forall_k} \tag{16}$$

2.2.2   Two-Phase Flow Regime Criteria

Two-phase flow at different flow rates and vapor-liquid ratios exhibit different inter-phase interactions and interactions between the fluid and the pipe wall. The two characteristic factors, vapor volume fraction α_v and relative velocity $v_r = v_v - v_l$ are selected to classify the two-phase flow regime, as shown in Fig. 1. The flow is divided into five states, including dispersed bubbly flow, dispersed droplet flow, horizontal stratified flow and transition flow, covering the main flow characteristics of horizontal pipeline two-phase flow.

When the relative velocity is low, the vapor-liquid two phases exhibit horizontal stratified flow regardless of the vapor volume fraction. When the relative velocity is higher than the critical velocity, the velocity difference between the two phases is larger and shows the characteristics of dispersed flow; at a lower vapor volume fraction, the liquid phase dominates and the flow process is diffusive bubble flow; at a higher vapor volume fraction, the vapor phase dominates and the flow process is diffusive droplet flow. There is a mutual transformation between these flow types.
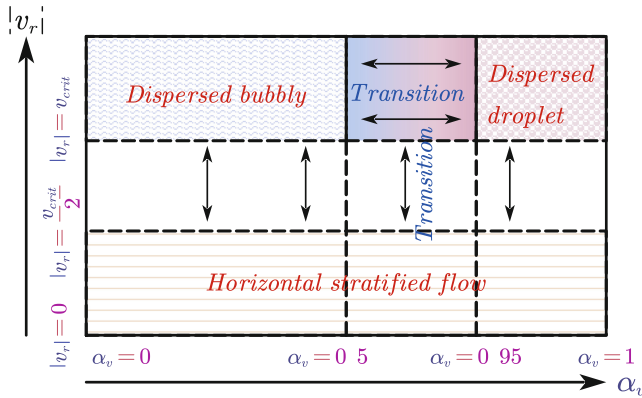
Fig. 1. Two-phase flow regime diagram

The flow regime parameter R is also one of the indicators describing the flow characteristics, reflecting the degree of stratification and dispersion of the two-phase flow, proposed and validated by Tiselj [15], and contains five factors

$$R = R_{K-H} R_\theta R_{\rho v} R_v R_\alpha \tag{17}$$

where R_{K-H} 1 is Kelvin–Helmholtz instability factor, which is assumed to be the primary reason for the transition of flow regime in CIWH phenomenon.

2.2.3 Virtual Mass

During the flow process, forces exist between the phases due to the spatial and temporal variation of the relative velocities of the two phases. For the part of the interphase force caused by the acceleration of the vapor or liquid phase, the virtual mass is used to characterize it. The virtual mass of a solid sphere (bubble or droplet) in an ideal fluid has a theoretical analytical solution, but the form of the virtual mass term in a real two-phase flow is not known. In the WAHA3 method, the virtual mass term in the momentum equation takes the form given by Drew [16]

$$VM = C_{VM} \left(\frac{\partial v_v}{\partial t} + v_l \frac{\partial v_v}{\partial x} - \frac{\partial v_l}{\partial t} - v_v \frac{\partial v_l}{\partial x} \right) \tag{18}$$

where C_{VM} is the virtual mass coefficient, which is determined by the flow regime parameters, mixture density, and vapor volume fraction

$$C_{VM} = \begin{cases} C_1 \frac{1+2\alpha_v}{2\alpha_l} & \alpha_v \le 0.4 \\ C_1[1.5 - 10(\alpha_v - 0.4)(\alpha_v - 0.6)] & 0.4 < \alpha_v < 0.6 \\ C_1 \sqrt{\left(\frac{3-2\alpha_v}{2\alpha_v} \right)^2 + \frac{\alpha_l(2\alpha_v - 2)}{\left(\alpha_l + \frac{\alpha_l \rho_v}{\rho_l} \right)^2}} & \alpha_v \ge 0.6 \end{cases} \tag{19}$$

2.2.4 Heat Transfer Correlations

The heat transfer at the phase interface in the two-phase energy equation is

$$Q_{ik} = H_{ik}(T_s - T_k) \tag{20}$$

where T_s is the saturation temperature, which is only related to the work substance and pressure. H_{ik} is the volumetric interfacial heat transfer coefficient, which is calculated by the method proposed by Brucker [14].

3 Numerical Solution Method

3.1 Splitting Operator Method

The basic governing equations of mass, momentum and energy for individual phases can be transformed to the following matrix form

$$A\frac{\partial \Phi}{\partial t} + B\frac{\partial \Phi}{\partial x} = S \tag{21}$$

where ϕ represents a vector of the variables for solving $\phi = (P\alpha_v v_l v_v u_l u_v)^\top$ and A, B are 6-times-6 matrices and S is the source vector. Depending on the time scale of the source term, the source is split into a non-relaxation source and a relaxation source

$$S = S_{NR} + S_R \tag{22}$$

Non-relaxation source, which contains friction and volume force terms, is closely related to the convective term of the model. The relaxation source, which establishes the heat and mechanical equilibrium between two phases, reflects the heat, mass and momentum transfer between the phases.

$$A = \begin{pmatrix}
G_l\left(\frac{\partial \rho_l}{\partial P}\right)_u + \rho_l K & -\frac{\rho_l}{\alpha_l} & 0 & 0 & 0 & 0 \\
G_v\left(\frac{\partial \rho_v}{\partial P}\right)_u + \rho_k K & \frac{\rho_v}{\alpha_v} & 0 & 0 & 0 & 0 \\
0 & 0 & \rho_l + \frac{C_{VM}}{\alpha_l} & -\frac{C_{VM}}{\alpha_l} & 0 & 0 \\
0 & 0 & -\frac{C_{VM}}{\alpha_v} & \rho_v + \frac{C_{VM}}{\alpha_v} & 0 & 0 \\
PK & -\frac{P}{\alpha_l} & 0 & 0 & \rho_l & 0 \\
PK & \frac{P}{\alpha_v} & 0 & 0 & 0 & \rho_v
\end{pmatrix}
\qquad
G_k = \frac{1}{1 - \frac{P}{\rho_k^2}\left(\frac{\partial \rho_k}{\partial u_k}\right)_P}$$

$$B = \begin{pmatrix}
v_l\left[G_l\left(\frac{\partial \rho_l}{\partial P}\right)_u + \rho_l K\right] & -\frac{\rho_l v_l}{\alpha_l} & \rho_l & 0 & 0 & 0 \\
v_v\left[G_v\left(\frac{\partial \rho_v}{\partial P}\right)_u + \rho_k K\right] & \frac{\rho_v v_v}{\alpha_v} & 0 & \rho_v & 0 & 0 \\
1 & -\frac{P_i}{\alpha_l} & \rho_l v_l + \frac{C_{VM}}{\alpha_l}v_v & -\frac{C_{VM}}{\alpha_l}v_l & 0 & 0 \\
1 & \frac{P_i}{\alpha_v} & -\frac{C_{VM}}{\alpha_v}v_v & \rho_v v_v + \frac{C_{VM}}{\alpha_v}v_l & 0 & 0 \\
Pv_l K & -\frac{Pv_l}{\alpha_l} & P & 0 & \rho_l v_l & 0 \\
Pv_v K & \frac{Pv_v}{\alpha_v} & 0 & P & 0 & \rho_v v_v
\end{pmatrix}$$

$$
S_R = \begin{pmatrix} \frac{G_l}{\alpha_l}\left\{\Gamma_l - [Q_{il} + \Gamma_l(h_l - u_l)]\frac{1}{\rho_l}\left(\frac{\partial \rho_l}{\partial u_l}\right)_P\right\} \\ \frac{G_v}{\alpha_v}\left\{\Gamma_v - [Q_{iv} + \Gamma_v(h_v - u_v)]\frac{1}{\rho_v}\left(\frac{\partial \rho_v}{\partial u_v}\right)_P\right\} \\ \frac{1}{\alpha_l}F_D + \frac{1}{\alpha_l}\Gamma_l(v_i - v_l) + \rho_l g \sin\theta \\ -\frac{1}{\alpha_v}F_D + \frac{1}{\alpha_v}\Gamma_v(v_i - v_v) + \rho_v g \sin\theta \\ \frac{1}{\alpha_l}[Q_{il} + \Gamma_l(h_l - u_l)] \\ \frac{1}{\alpha_v}[Q_{iv} + \Gamma_v(h_v - u_v)] \end{pmatrix}
\quad
S_{NR} = \begin{pmatrix} -v_l F_{l,\,\text{wall}}\,\frac{G_l}{\rho_l \alpha_l}\left(\frac{\partial \rho_l}{\partial u_l}\right)_P \\ -v_v F_{v,\,\text{wall}}\,\frac{G_v}{\rho_v \alpha_v}\left(\frac{\partial \rho_v}{\partial u_v}\right)_P \\ -\frac{1}{\alpha_l}F_{l,\,\text{wall}} \\ -\frac{1}{\alpha_v}F_{v,\,\text{wall}} \\ \frac{1}{\alpha_l}v_l F_{l,\,\text{wall}} \\ \frac{1}{\alpha_v}v_v F_{v,\,\text{wall}} \end{pmatrix}
$$

3.2 Two-Step Iterative Algorithm

The final model with all the control and closure equations is

$$
A\frac{\partial \Phi}{\partial t} + B\frac{\partial \Phi}{\partial x} = S_{NR} + S_R \tag{23}
$$

After applying the operator splitting method, the solution of Φ is iterated in two steps, as shown in Fig. 2.

$$
\Phi_j^{(n)} \quad \overset{\Delta t_{NR}}{\Longrightarrow} \quad \Phi_j^{*\,(n)} \quad \overset{\Delta t_R}{\Longrightarrow} \quad \Phi_j^{(n+1)}
$$
$$
S_{NR}\ works\ as\ source \qquad S_R\ works\ as\ source
$$
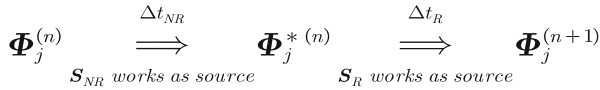
Fig. 2. Schematic of the two-step iterative method

The superscript n in $\Phi_j^{(n)}$ indicates the time node where Φ is currently located, and the subscript j indicates the spatial node where Φ is currently located. The iteration of a time step is split into two parts, and the variable $\Phi_j^{(n)}$ at a certain spatial position needs to experience an intermediate time *(n) when crossing from time (n) to time (n + 1).

3.2.1 Convective Iterative

Only consider the effect of non-relaxation sources in the convection step, Eq. (23) can be re-written as

$$
\frac{\partial \Phi}{\partial t} + C\frac{\partial \Phi}{\partial x} = A^{-1}S_{NR} \tag{24}
$$

where the Jacobain matrix $C = A^{-1}B$ can be diagonalized in terms of its eigen vector V and eigen value matrix Λ as follows

$$
C = V\Lambda V^{-1} \tag{25}
$$

Applying the diagonalization result to Eq. (23) and setting s $R_F = -V^{-1}S_{NR}$ yields

$$
V^{-1}\left(\frac{\partial \Phi}{\partial t} + V\Lambda V^{-1}\frac{\partial \Phi}{\partial x} + R_F\right) = 0 \tag{26}
$$

Introduce the characteristic variable $W_{6\times 1}$, which is related to the original variable Φ as

$$\partial W = V^{-1}\partial\Phi + \Lambda^{-1}V^{-1}R_F \partial x \tag{27}$$

Equation (26) can be expressed by the characteristic variables

$$\frac{\partial W}{\partial t} + \Lambda\frac{\partial W}{\partial x} = 0 \tag{28}$$

The TVD [17] (Total Variation Diminishing) format with restriction factors is used to differential Eq. (28) in the space of eigenvariables

$$\frac{W_j^{*(n)} - W_j^{(n)}}{\Delta t_{NR}} + \Lambda^+\frac{W_j^{(n)} - W_{j-1}^{(n)}}{\Delta x} + \Lambda^-\frac{W_{j+1}^{(n)} - W_j^{(n)}}{\Delta x} = 0 \tag{29}$$

where the eigenvalue diagonal array in Eq. (29) splits into two parts, and the split Λ is still a diagonal array, and its relationship in spatial location is shown in Fig. 3.

$$\Lambda_j^{(n)} = \Lambda_{j-1/2}^{(n)} + \Lambda_{j+1/2}^{(n)} = \Lambda^+ + \Lambda^- \tag{30}$$
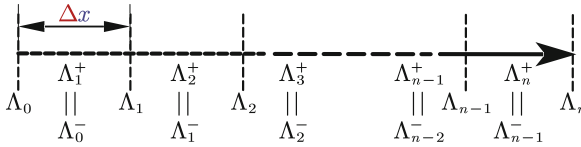
Fig. 3. Spatial discrete schematic

Replacing the characteristic variables with the original variables Φ, $\Phi_j^{*(n)}$ can be deduced from Eq. (28) as

$$\Phi_j^{*(n)} = \Phi_j^{(n)} - \Delta t_{NR}\cdot\left(V\Lambda^+\Lambda^{-1}V^{-1}R_F + V\Lambda^-\Lambda^{-1}V^{-1}R_F\right.$$
$$\left. + V\Lambda^+V^{-1}\frac{\Phi_j^{(n)} - \Phi_{j-1}^{(n)}}{\Delta x} + V\Lambda^-V^{-1}\frac{\Phi_{j+1}^{(n)} - \Phi_j^{(n)}}{\Delta x}\right) \tag{31}$$

The time step size Δt_{NR} is evaluated based on the CFL [18] (Courant-Friedrichs-Levy) criterion as follows

$$\Delta t_{NR} \leq \frac{\Delta x}{\max|\lambda_t|} \tag{32}$$

3.2.2 Relaxation Iterative

In the relaxation step only consider the relaxation source. The velocity terms in the variables (corresponding to the momentum equation) are calculated from the assumptions on the relative and mixed velocities. In the calculation of the other variables, momentum transfer is not considered, but only the effects of heat and mass transfer at the phase interface.

$$A_T \frac{\partial \psi}{\partial t} = S_{R-HMT} \tag{33}$$

$$A_T = \begin{pmatrix} \left(\frac{\partial \rho_l}{\partial P}\right)_{T_l} + \rho_l K & -\frac{\rho_l}{\alpha_l} & \left(\frac{\partial \rho_l}{\partial T_l}\right)_P & 0 \\ \left(\frac{\partial \rho_v}{\partial P}\right)_{T_v} + \rho_v K & \frac{\rho_v}{\alpha_v} & 0 & \left(\frac{\partial \rho_v}{\partial T_v}\right)_P \\ PK + \rho_l \left(\frac{\partial u_l}{\partial P}\right)_{T_l} & -\frac{P}{\alpha_l} & \rho_l \left(\frac{\partial u_l}{\partial T_l}\right)_P & 0 \\ PK + \rho_v \left(\frac{\partial u_v}{\partial P}\right)_{T_v} & \frac{P}{\alpha_v} & 0 & \rho_v \left(\frac{\partial u_v}{\partial T_v}\right)_P \end{pmatrix}$$

$$S_{R-HMT} = \begin{pmatrix} \frac{G_l}{\alpha_l}\left\{\Gamma_l - [Q_{il} + \Gamma_l(h_l - u_l)]\frac{1}{\rho_l}\left(\frac{\partial \rho_l}{\partial u_l}\right)_P\right\} \\ \frac{G_v}{\alpha_v}\left\{\Gamma_v - [Q_{iv} + \Gamma_v(h_v - u_v)]\frac{1}{\rho_v}\left(\frac{\partial \rho_v}{\partial u_v}\right)_P\right\} \\ \frac{1}{\alpha_l}[Q_{il} + \Gamma_l(h_l - u_l)] \\ \frac{1}{\alpha_v}[Q_{iv} + \Gamma_v(h_v - u_v)] \end{pmatrix} \quad \psi = \begin{pmatrix} P \\ \alpha_v \\ T_l \\ T_v \end{pmatrix}$$

The time step of the relaxation iterative is related to the relative rate of change of the variable ψ

$$\frac{\partial \psi}{\partial t} = A_T^{-1} S_{R-HMT} = \left(\dot{P} \ \dot{\alpha}_v \ \dot{T}_l \ \dot{T}_v\right)^\top \tag{34}$$

The relaxation time step is evaluated as follows

$$\Delta t_R = 0.01 \min(t_1, t_2, t_3, t_4) \tag{35}$$

$$\begin{cases} t_1 = \frac{P}{\max(\epsilon, |\dot{P}|)} \\ t_2 = \frac{\max(0.01, \min(\alpha_v, \alpha_l))}{\max(\epsilon, |\dot{\alpha}_v|)} \\ t_3 = \frac{\max(|T_l - T_s|)}{\max(\epsilon, |\dot{T}_l|)} \\ t_4 = \frac{\max(|T_v - T_s|)}{\max(\epsilon, |\dot{T}_v|)} \end{cases} \tag{36}$$

The relative velocity is iterated in the relaxation step as

$$v_r^{(n+1)} = \frac{v_r^{*(n)}}{1 - \Delta t_R S_{vr}} \tag{37}$$

where

$$
S_{vr} = \begin{cases} \dfrac{-C_i|v_r|\rho_m + \alpha_v\rho_v\Gamma_v}{\alpha_v\alpha_l\rho_l\rho_v + C_{VM}\rho_m} & \Gamma_v < 0 \\[3mm] \dfrac{-C_i|v_r|\rho_m - \alpha_l\rho_l\Gamma_v}{\alpha_v\alpha_l\rho_l\rho_v + C_{VM}\rho_m} & \Gamma_v > 0 \end{cases} \tag{38}
$$

4   Results and Discussions

4.1   Verification with Benchmark Problem (Two-Phase Shock Tube Case)

The one-dimensional Riemann two-phase shock wave tube problem is a typical benchmark problem for condensation-induced water hammer, reflecting the ability of the model to capture discontinuous physical states and millisecond pressure transients.

A straight tube of length 1 m is filled with vapor-liquid mixture, the diameter of the tube is 19 mm, the wall thickness is 1.6 mm, and the modulus of elasticity of the tube material is 760 MPa, as shown in Fig. 4. In the initial state, a thin film at the center of the tube divides the tube into two parts, both with an initial vapor volume fraction of 0.3. The densities of the left and right side of the mixture are 998.64 and 998.23 kg/m^3.
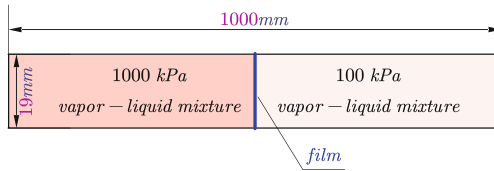
Fig. 4. Schematic of the initial state of the shock wave tube
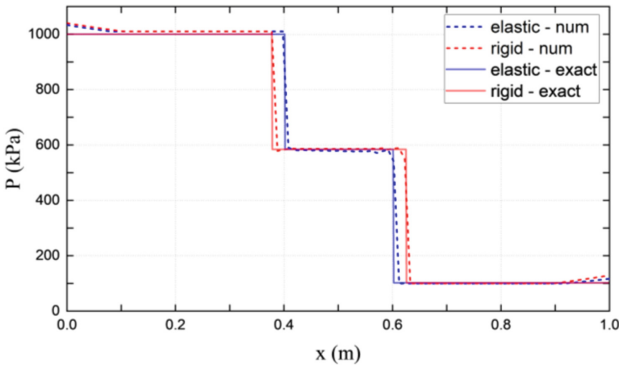
Fig. 5. Numerical solution of the Riemann shock wave tube problem for pressure in elastic and rigid tubes (at 0.42 ms)

The test starts after the film is completely ruptured and the vapor-liquid mixture diffuses from high to low pressure, forming a surge inside the tube. The surge tube is

discretized into 100 nodes, and the calculated results are shown in Fig. 5, reflecting the pressure distribution inside the tube at 0.42 ms after the vapor-liquid mixture with different pressure starts to contact. The calculated results show good agreement with the analytical values.

4.2 Verification with Experimental Results of PMK-2

In order to study the CIWH phenomenon that occurs during the entry of cold water into steam-filled pipes in the water circuit of a nuclear power facility, the Hungarian KFKI Institute constructed a model steam pipe and conducted the PMK-2 test.

The test section of the PMK-2 test is a tube with a length-to-diameter ratio of about 39. The pipe is filled with saturated water vapor at a pressure of 1.45 MPa at the initial moment, and the saturation temperature of the water vapor at this pressure is 470 K. The pipe and boundary conditions can be simplified as shown in Fig. 6. The volume of the steam kettle at the end is sufficiently large that the outlet pressure can be considered to be approximately constant.
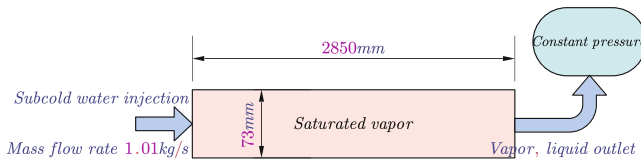
Fig. 6. PMK-2 test section tube schematic

The numerical solution method of this paper is used to calculate the PMK-2 test conditions, and the pipeline is divided into a total of 10 intervals (11 nodes), and the occurrence of pressure pulses is successfully captured. A comparison of the calculation results in this paper with the PMK-2 test results is shown in Fig. 7.
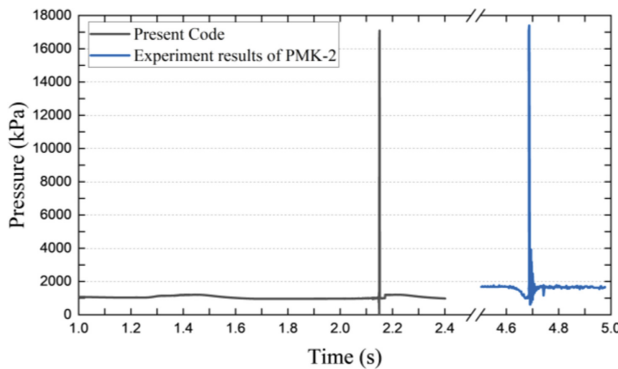
Fig. 7. Comparison of pressure time history between PMK-2 test and the results calculated in this paper

In terms of peak pressure, the pressure pulse amplitude of 17.1 MPa obtained by the calculation method in this paper, compared with the highest value of 17.4 MPa recorded in the test, the relative error is 1.7%, indicating that the calculation method can be more accurate in forecasting the impact pressure when water hammer occurs under the test conditions.

4.3   Analysis of the Effect of Inlet Velocity on CIWH

The temperature and pressure parameters of the PMK-2 test are applied, and the injection velocity of subcooled water is varied (0.1 m/s–0.4 m/s) to investigate the effect of subcooled water flow rate on the CIWH phenomenon in the tube. A total of five velocities are numerically calculated for the model with the modulus of elasticity of the pipe material set to 206 GPa, the model discretization are 10 nodes, the velocity boundary condition at the left inlet and the pressure boundary condition at the right outlet (Figs. 8, 9 and Table 1).

Table 1. Parameters used in the analysis of inlet velocity

Parameter	Value
Tube diameter	73 mm
Saturated steam temperature	470 K
Initial pressure	1450 kPa
Inlet water temperature	295 K
Elastic modulus	206 GPa
Inlet velocity	0.1–0.4 m/s
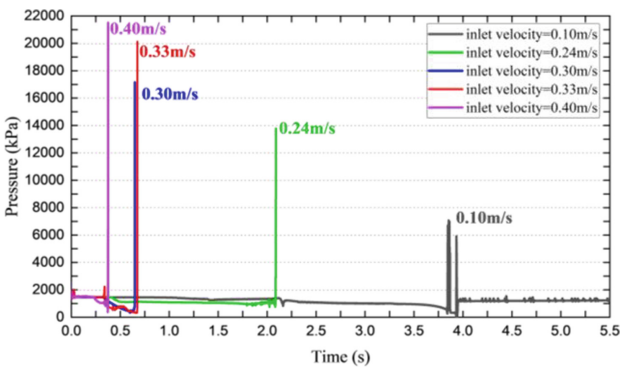
Fig. 8. Effect of subcooled water inlet velocity on CIWH

With the increasing flow rate of subcooled water (0.1 m/s to 0.4 m/s), the peak pressure of condensate water hammer is growing, but the growth rate is gradually slowing
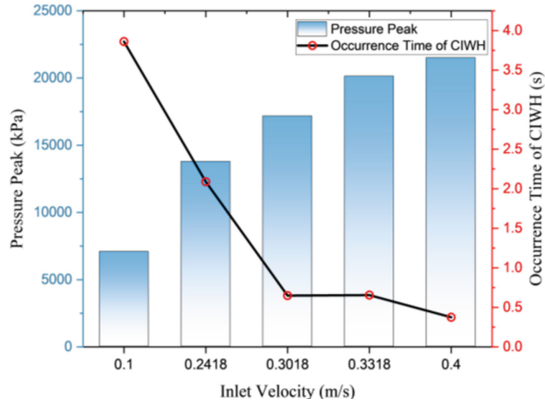
Fig. 9. Effect of subcooled water inlet velocity on peak pressure and time of CIWH occurrence

down; the occurrence time of water hammer is constantly in advance, but when the flow rate is greater than 0.3 m/s, the change of the occurrence time is no longer obvious and is maintained at 0.5 s or less.

4.4 Analysis of the Effect of Inlet Water Temperature on CIWH

Following the calculation conditions in Sect. 4.3, the injection velocity of subcooled water remains unchanged at 0.24 m/s, and only the liquid phase temperature is changed from 285 K to 325 K, every 10 K for a grade, for a total of 5 water temperature conditions (Figs. 10 and 11).
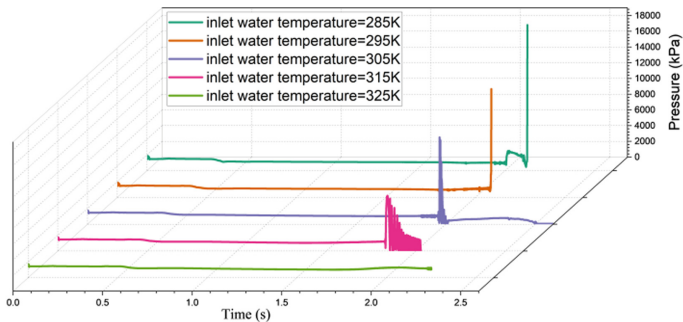
Fig. 10. Effect of subcooled water temperature on CIWH

Except for the liquid phase temperature of 325 K, the sudden pressure change occurs about 2 s after the cold water starting inject. The condensate water hammer pressure peak is the largest at 285 K, reaching 18.5 MPa, and the lowest at 315 K, 7.0 MPa, and enter a state of continuous oscillation after the water hammer occurs. The obvious pressure pulse phenomenon is no longer observed when the temperature increased to 325 K.
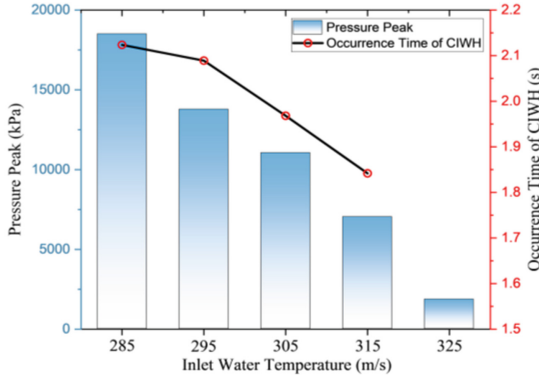
Fig. 11. Effect of subcooled water temperature on peak pressure and time of CIWH occurrence

4.5 Analysis of the Effect of Elastic Modulus on CIWH

Using the numerical algorithm of this paper, a computational study of CIWH phenomenon occurring in pipes with different modulus of elasticity (E) is done. The injection velocity and temperature of the supercooled water are kept constant at 0.24 m/s and 295 K.
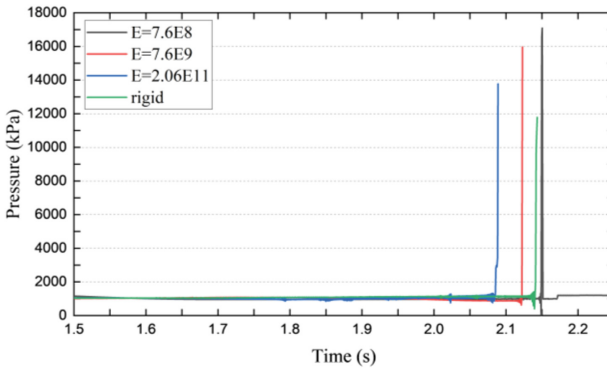
Fig. 12. Effect of tube elasticity modulus on CIWH

    The change in the elasticity of the pipe structure does not have a significant effect on the time of occurrence of CIWH, and the peak pressure occurs within 2.1 ± 0.05 s for several conditions in Fig. 12. The change of the pressure peak is mainly related to the deformation of the pipe cross-section. In the pipe with greater stiffness, the smaller the growth of the cross-sectional area caused by the pressure pulse, the smaller the cavitation area formed after gas condensation, and the smaller the stroke of the bubble collapse effect, which shows a lower pressure peak.

    As shown in Fig. 13 and Fig. 14, comparing the cross-sectional area before and after the water hammer, we can see the extent of the deformation of the pipe caused by the
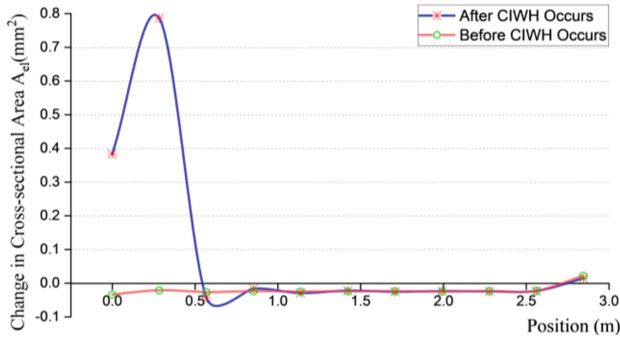
Fig. 13. Comparison of changes in tube cross-sectional area before and after the occurrence of CIWH (E = 760 MPa)
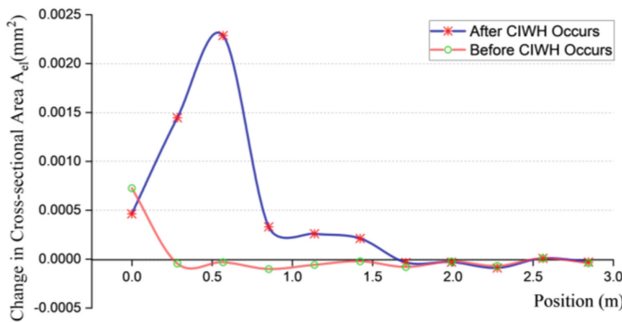
Fig. 14. Comparison of changes in tube cross-sectional area before and after the occurrence of CIWH (E = 206 GPa)

pressure pulse. For the pipe with E = 206 GPa, although the deformation of the pipe cross-section is much smaller than the former, the pressure pulse has a broader impact on the pipe deformation.

4.6 Analysis of the Effect of Tube Diameter on CIWH

The tube diameter is directly related to the mass flow rate of subcooled water injection and the contact area between the two phases, and also has an impact on the peak pressure and occurrence time of condensate hammer. The numerical model of this paper is used to calculate the pressure time history of the same temperature of subcooled water with the same flow rate into different diameter pipes, the modulus of elasticity is taken as 206 GPa, and the diameters are taken as 63 mm, 68 mm, 70.5 mm, 73 mm, 75.5 mm, 78 mm and 80.5 mm.

As shown in Fig. 15, in the diameter range of 70.5 to 80.5 mm, with the increase of pipe diameter, the peak pressure of condensate hammer increases up to 20.3 MPa, but the time of pressure pulse occurs backward, the peak pressure occurs at 1.96 s under 70.5 mm pipe diameter, and this moment is delayed to 2.44 s under 80.5 mm pipe diameter. When the pipe diameter is less than 70.5 mm, the peak pressure will be When

the pipe diameter is less than 70.5 mm, the pressure peak will be much smaller than the result recorded in PMK-2 test.
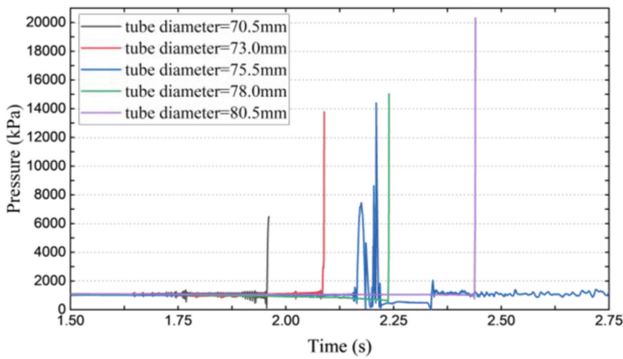
Fig. 15. Effect of tube diameter on CIWH

5   Conclusions

The computational results of the Riemann two-phase surge problem confirm the accuracy and sensitivity of the computational method in this thesis, demonstrating that the compressible two-fluid six-equation control model is capable of capturing pressure and velocity transients on the millisecond scale. Numerical simulations of the important experimental PMK-2 for condensation-induced water hammer are also performed on top of the benchmark problem, and a good match is achieved in terms of pressure pulse amplitude prediction and location of occurrence.

Based on the test equipment conditions, this paper also calculates the subcooled water flow rate and subcooled water temperature factors, which are of interest in this research area. The results show that as the inlet flow rate increases, the peak pressure pulse rises and CIWH occurs earlier; as the subcooled water temperature increases, the peak pressure falls and no longer triggers CIWH if the subcooled water temperature decreases to a certain extent. The pressure peak of CIWH is largely affected by the tube diameter. When the pipe cross-sectional area increases by 7.2% from an initial diameter of 70.5 mm, the pressure peak increases up to 2.1 times if the original, while CIWH is not be observed when the pipe diameter turns to be small.

References

1. Zouhri, L., Smaoui, H., Carlier, E., et al.: Modelling of hydrodispersive processes in the fissured media by flux limiters schemes (Chalk aquifer, France). Math. Comput. Model. **50**(3–4), 516–525 (2009)
2. Strubelj, L., Ezsöl, G., Tiselj, I.: Direct contact condensation induced transition from stratified to slug flow. Nucl. Eng. Des. **240**(2), 266–74 (2010)
3. Ceuca, S.C., Macián-Juan, R. : CFD simulation of direct contact condensation with ansys cfx using locally defined heat transfer coefficients. In: Proceedings of the International Conference on Nuclear Engineering, Proceedings, ICONE, F (2012)
4. Datta, P., Chakravarty, A., Ghosh, K., et al.: Modeling of steam–water direct contact condensation using volume of fluid approach. Numer. Heat Transf. Part A: Appl. **73**(1), 17–33 (2018)
5. Pham, T.Q.D., Choi, Sanghun: Numerical analysis of direct contact condensation-induced water hammering effect using OpenFOAM in realistic steam pipes. Int. J. Heat Mass Transf. **171**, 121099 (2021). https://doi.org/10.1016/j.ijheatmasstransfer.2021.121099
6. Höhne, Thomas, Gasiunas, Stasys, Šeporaitis, Marijus: Numerical modelling of a direct contact condensation experiment using the AIAD framework. Int. J. Heat Mass Transf, **111**, 211–222 (2017). https://doi.org/10.1016/j.ijheatmasstransfer.2017.03.104
7. Li, S.Q., Wang, P., Lu, T.: CFD based approach for modeling steam–water direct contact condensation in subcooled water flow in a tee junction. Prog. Nucl. Energy **85**, 729–746 (2015)
8. Barna, I.F., Imre, A.R., Baranyai, G., et al.: Experimental and theoretical study of steam condensation induced water hammer phenomena. Nucl. Eng. Des. **240**(1), 146–150 (2010)
9. Tiselj, I., Petelin, S.: Modelling of two-phase flow with second-order accurate scheme. J. Comput. Phys. **136**(2), 503–521 (1997)
10. Ceuca, S.C., Laurinavicius, D. : Experimental and numerical investigations on the direct contact condensation phenomenon in horizontal flow channels and its implications in nuclear safety. In: Proceedings of the Kerntechnik (2016)
11. Hibiki, T., Rassame, S., Liu, W., et al.: Modeling and simulation of onset of condensation-induced water hammer. Prog. Nucl. Energy **130**, 103555 (2020)
12. Milivojevic, S., Stevanovicv, D., Maslovaric, B.: Condensation induced water hammer: numerical prediction. J. Fluids Struct. **50**, 416–436 (2014)
13. Wylie, E.B., Streeter, V.L., Wiggert, D.C.: Fluid transients. J. Fluids Eng. **102**(3), 384–385 (1980)
14. Brucker, G.G., Sparrow, E.M.: Direct contact condensation of steam bubbles in water at high pressure. Int. J. Heat Mass Transf. **20**(4), 371–381 (1977)
15. Tiselj, I., Horvat, A., Černe, G., et al.: WAHALoads-two-phase flow water hammer transients and induced loads on materials and structures of nuclear power plants: WAHA3 code manual (2004)
16. Drew, D., Cheng, L., Lahey, R.T.: The analysis of virtual mass effects in two-phase flow. Int. J. Multiph. Flow **5**(4), 233–242 (1979)
17. Glaister, P.: Flux difference splitting for the Euler equations in one spatial co-ordinate with area variation. Int. J. Numer. Meth. Fluids **8**(1), 97–119 (1988)
18. Datta, P., Chakravarty, A., Ghosh, K., et al.: Modeling and analysis of condensation induced water hammer. Numer. Heat Transf. Part A: Appl. **74**(2), 975–1000 (2018)

Study on Coupling Effect and Dynamic Behavior of Double Bubbles Rising Process

Lanxin Gong, Changhong Peng[✉], and Zhenze Zhang

School of Nuclear Science and Technology, University of Science and Technology of China, Hefei, Anhui, China

{lenovomax,desolate}@mail.ustc.edu.cn, pengch@ustc.edu.cn

Abstract. Gas-liquid two-phase flow widely exists in nuclear energy engineering, in which bubble movement and deformation are critical problems. Because the activity of bubbles in the fluid is a very complex physical process, and the movement process is a flow field-bubble coupling process, which has strong non-linearity and unsteady, the relevant research is usually based on experiments and simulation.

We built a medium-sized experimental device to generate double bubbles with different sizes and characteristic numbers and recorded the motion trajectory with a high-speed camera. We developed and improved the image processing method to obtain high-quality bubble motion information and realized a good capture of bubble shape and rotation.

The experimental results show that in the two bubbles rising successively, the trailing bubble is affected by the trailing field of the leading bubble, and the bubble velocity, relative distance, deformation rate, and other parameters change accordingly. In addition, through simulation, we get the interaction mechanism of the bubbles under experimental conditions. The results show that the coupling leads to flow field velocity and pressure changes, which explains the experimental results. The research results are helpful for a thorough understanding of the law of bubble movement and provide empirical data support for developing a thermal-hydraulic model.

Keywords: Bubble rising experiment · Bubble coupling · Gas-liquid two-phase flow

1 Introduction

Since the last century, researchers have carried out a lot of research on bubble motion from the aspects of theory, experiment, and numerical simulation [1–3].

There are various forms of bubble movement. For the free bubble, if it is affected by the rigid wall, it will not only deform the bubble interface but also change its original motion state, mainly including the movement of the bubble away from the wall, the movement of the bubble close to the wall, and the bounce movement of the bubble along the wall. For free-space bubbles, it is relatively simple, mainly showing a zigzag and spiral rise. Predecessors have also carefully studied the rise of single bubble and bubble

chains and obtained the laws of bubble terminal velocity, bubble deformation, and other motion parameters in some cases.

Generally speaking, in the presence of a wall, bubbles are affected laterally by the wall attraction (lift pointing towards the wall) and the wall repulsion (lift pointing away from the wall). When bubbles are affected by repulsive force and attraction, they appear in a zigzag motion. In the longitudinal direction, bubbles are usually affected by lift, drag, additional mass force, and film-induced force, regardless of whether the wall exists. Because the growth and movement of bubbles are very complex, involving the mass conversion between two phases and the energy transfer between three phases, the growth and movement mechanism of bubbles have not been fully understood. In addition, as a unique flow field boundary, bubbles have an important influence on the dynamics of other bubbles around them, making the problem more complex. When two bubbles rise in parallel, the smaller spacing will lead to bubble fusion; When bubbles rise one after another, the wake of the leading bubble will cause the bubbles that follow to rise faster. These coupling effects significantly change the bubble distribution and two-phase contact area and affect the heat and mass transfer performance.

Clift et al. [1] studied the change of bubble shape and drew the bubble phase diagram. It was found that bubbles with a diameter of less than 1.3 mm remained spherical, and the shape of large bubbles would be the oval and spherical cap. Duineveld [4] studied the floating characteristics of bubbles with a diameter of 0.33–1 mm in purified water, explored the equilibrium velocity and shape coefficient obtained by bubbles and the relationship between Weber number We, and found that the maximum Weber number that can float in a stable shape and velocity does not exceed 3.2. Raymond and Rosant [5], Zenit [6], and Magnaudet [6] use different liquids or add different proportions of chemicals to the water to change the density, viscosity, surface tension coefficient, and other parameters of the fluid and explore the changing laws and internal relations of physical quantities such as bubble resistance coefficient, shape, and buoyancy under different We and Re. Wu and Gharib [7] found that the bubbles with a diameter of 0.1–0.2 cm were spherical or ellipsoidal in the floating process. When the bubble volume was constant, the bubbles with high rising velocity were generally ellipsoidal; In addition, the upward floating path of bubbles with a diameter less than 1.5 mm is a straight line. When the bubble size is larger, the upward floating path of bubbles will be Z shaped or spiral-shaped.

As for the interaction between two bubbles, Duineveld's experimental research shows that if the horizontal approach velocity of bubbles is the characteristic velocity when We are less than 0.18, the two bubbles will become a single bubble. When the bubble radius is less than 0.7 mm, the impact velocity of the two bubbles is always tiny, so the possibility of bubbles fusion is high. When We are less than the critical value, the two bubbles after springing could collide again. Sanada et al. [8] conducted an experimental study on the interaction between two horizontal bubbles and found that when re exceeds a specific range, the two bubbles attract each other. After the collision, there may be two cases of fusion or bounce-off. If the bounce-off occurs, the bubble floating speed will be reduced by about 50% due to vortex shedding and other reasons. The occurrence of different phenomena is related to Re and We. It is pointed out that the critical We are about 2, and the critical Re is related to the Morton number Mo.

As for the terminal velocity, it depends on the bubble shape and is related to the Eotvos number, Reynolds number, and Morton number. Wallis [9], Grace [10], Jamialahmadi [11], Bozzano [12], Sung-Hoon Park [13], and others proposed a series of correlations based on experiments. As for the application of final velocity, it is widely used in system analysis programs (such as RELAP5 [14]) to determine the selection of flow patterns, heat transfer correlations, etc.

2 Experimental Equipment

The central part of the experimental device is a $30 \times 30 \times 40$ cm acrylic water tank. In the tank, the rubber tube and Ruhr joint are connected with the flat head stainless steel needle tube; Outside the tank, the micro air pump and the gas pipe are connected with the flow regulating valve and the micro syringe. When bubbles need to be generated, open the air pump, control the gas flow rate by adjusting the flow regulating valve, and change the bubble size by changing the diameter of the syringe needle in the cylinder. As shown in Fig. 1, when recording bubbles from the front, a strip-shaped parallel light source is set at the back of the cylinder; When shooting bubbles on the left side, place a rectangular light source on the right side of the cylinder, as shown in Fig. 1. The high-speed camera is supported by stable support and is connected to the computer, which can process the captured images in real-time. To simplify the subsequent image processing, we record the bubbles in the dark environment and keep the white LED light source so that the captured image has a white background and the bubble itself is black. In the experiment, we set the camera to shoot at the frame rate of 500 fps.

Table 1. Experimental group and needle diameter

Serial number	1	2	3	4	5	6
OD/mm	2.42	1.86	1.29	3.46	2.78	4.00
Number of experiments	21	23	17	14	16	12

(a) front view   (b) left view
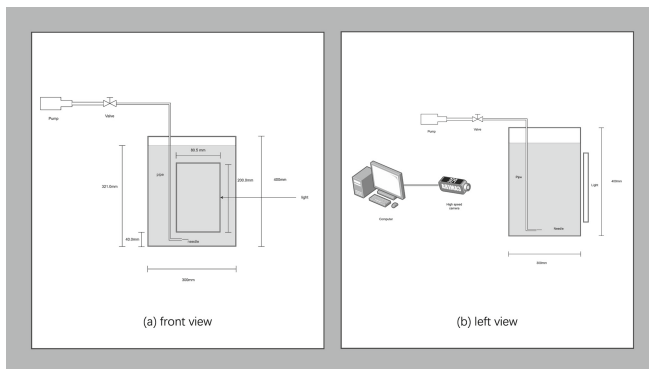
Fig. 1. Schematic diagram of the experimental device

Under the above experimental conditions, we generated a free-rising single bubble and a continuous rising double bubble. It is noted that it is difficult for parallel bubbles to combine into a single bubble due to the influence of initial needle diameter and spacing. Several experiments were carried out under each working condition to generate single and double bubbles repeatedly, and the rising motion of bubbles was photographed with a camera. The bubble video with high contrast, slight noise, and within the width of the light source is selected to study the law of motion and deformation. We used the following diameter needles to generate bubbles of different sizes (Table 1).

3   Image Processing

We use mature image processing technology, and the Python program and OpenCV library are selected to develop the corresponding image processing program. Image processing mainly includes four steps: preprocessing, image segmentation, contour clustering, and feature extraction.

3.1   Preprocessing

Preprocessing includes image frame clipping, keyframe interval selection, gray level processing, binarization processing, Gaussian filtering, etc. The image frame is cut to retain the image of the experimental section, and the width is slightly wider than the width of the light source. Keyframe interval selection mainly selects the video interval of the bubble rising process. Gray processing prepares for binarization, and binarization processes the image into a two-color image according to the threshold. Gaussian filtering can filter out part of the image noise.

3.2   Image Segmentation

Image segmentation is mainly to identify bubbles and the surrounding environment. The Canny operator processes the image to obtain the bubble boundary, and then the contour data is obtained using the *findcontours* function in OpenCV.

3.3   Contour Clustering

For some single bubble cases, due to the uniformity of the light source and the light refraction caused by the bubble movement, the bubble contour is divided into several parts. For the double bubble case, the attribution relationship of the bubble contour needs to be considered, so the contour clustering analysis code needs to be developed. The sub-function is used to calculate the center of a single outline and the number of data points. Then the center points representing each contour are divided according to the distance (such as Manhattan distance, Euclidean distance, etc.), which are mainly divided into two categories, namely, the corresponding leading bubble and the trailing bubble (for the case of a single bubble, it can be considered that the top bubble and the trailing bubble overlap), as shown in Fig. 2. In addition, it is often necessary to eliminate interference

profiles. The elimination of the interference profile depends on the shape factor, which is defined as follows.

$$K = \frac{P^2}{4\pi S} \tag{1.1}$$

where P is the contour perimeter and S is the contour area.

3.4 Feature Extraction

According to the results of segmentation and clustering, the feature parameters such as bubble centroid are extracted, and the saved data are output for subsequent data processing. The pictures processed in four steps are shown in Fig. 2.
   We define the center of mass and velocity of the bubble as follows,

$$X = \frac{\sum\limits_{i=1}^{i=N} x_i}{N} \tag{1.2}$$

$$Y = \frac{\sum\limits_{i=1}^{i=N} y_i}{N} \tag{1.3}$$

$$v_x^t = \frac{X^{t+1} - X^t}{\Delta t} s \tag{1.4}$$

$$v_y^t = \frac{Y^{t+1} - Y^t}{\Delta t} s \tag{1.5}$$

where x_i, y_i are coordinates of all pixels within the bubble contour. X and Y are obtained bubble centroid coordinates. s is the ratio of true distance to unit pixel. Δt is the time difference between two frames.

(a) segmentation clustering   (b) image processing
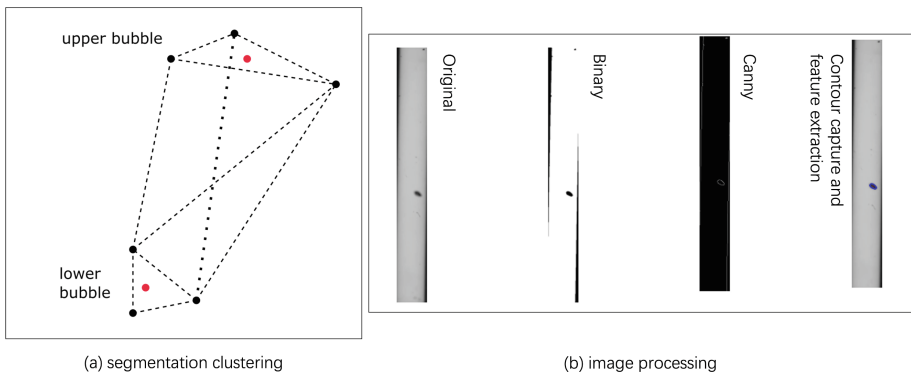
Fig. 2. Schematic diagram of segmentation clustering algorithm and image processing flow

The deformation degree and equivalent volume diameter are related to the long-axis b and short-axis a (assuming the bubble shape is elliptical). The deformation degree of the bubble can also be expressed by the aspect ratio, while the volume diameter could be defined as,

$$E = \frac{b}{a} \tag{1.6}$$

$$d_e = \sqrt[3]{b^2 a} \tag{1.7}$$

During the experiment, we also extracted dimensionless parameters, which are defined as follows,

$$\mathrm{Re} = \frac{\rho v d_e}{\mu} \tag{1.8}$$

$$Eo = \frac{d_e^2 (\rho_l - \rho_g) g}{\sigma} \tag{1.9}$$

$$We = \frac{v^2 d_e \rho_l}{\sigma} \tag{1.10}$$

where ρ is the density, v is the velocity of the bubble, g is the gravitational acceleration, σ is the surface tension.

4 Result and Analysis

4.1 Trajectory and Deformation

The trajectory of bubble motion is different under different equivalent volume diameters. As shown in Fig. 3, the captured trajectory shows that almost all bubbles are zigzagging or spiraling. When the equivalent diameter is less than 5 mm, the bubble is easier to twist.

Generally speaking, the larger the equivalent diameter, the more serious the deformation. Generally speaking, the larger the equivalent diameter, the more serious the deformation. According to the definition, when K and E are large, the deviation from the circle is big, and the deformation is large.

We get the deformation coefficients under different diameters, as shown in Fig. 4. It can be seen that when K is used as a parameter to characterize deformation, it conforms to the previous discussion. However, when E is taken as a parameter, the deformation relationship of the leading bubble is broken. This is because the ratio of long and short axes can only reflect the length relationship in the direction of the two main axes. Therefore, we propose to use K instead of E to represent the degree of deformation. In addition, we can also see that the deformation degree of the lower bubble increases under the influence of the flow field behind the forward bubble.

(a) 4.9 mm   (b) 6.17 mm
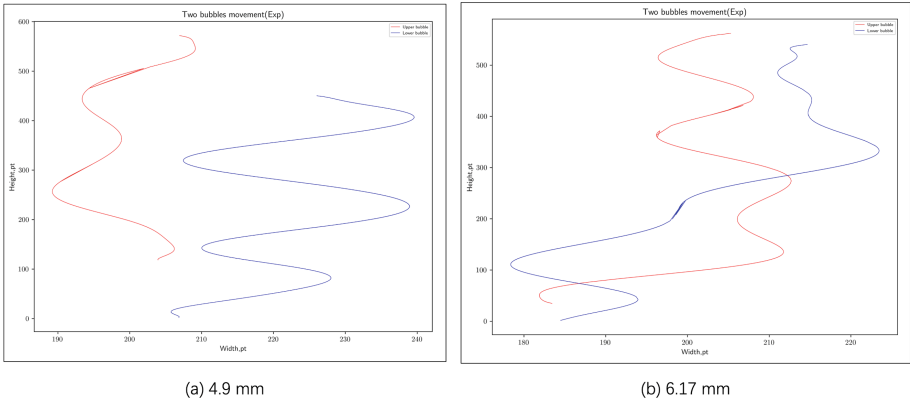
Fig. 3. Centroid locus (red line: top bubble blue line: bottom bubble)

(a) E ratio   (b) K ratio
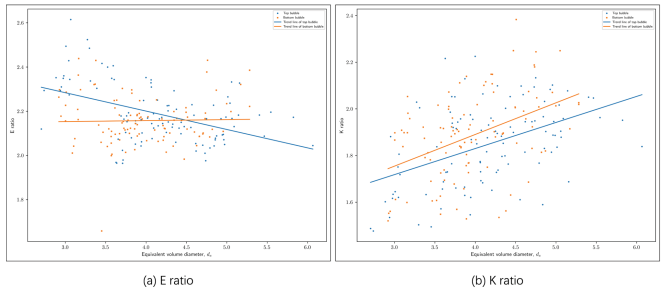
Fig. 4. K and E under different equivalent diameters(E on the left, K on the right)

4.2 Instantaneous Parameters

We place the light source in the middle and rear part of the bubble movement and record the changes in velocity, relative distance, and dimensionless number with time. As shown in Fig. 5 and Fig. 6, the speed in the x-direction under different equivalent diameters presents periodic variation characteristics. The speed in the y-direction fluctuates up and down in the mean value.

It is observed that the x-direction distance between the two bubbles fluctuates around the mean value, while the y-direction distance may fluctuate or decrease. This is related to the relative velocity of the two bubbles. The dimensionless parameters also present periodic fluctuations, mainly related to the changes in equivalent diameter and speed.

4.3 Terminal Velocity

In the field of nuclear engineering, people are concerned about the change of terminal velocity with equivalent diameter.

(a) Velocity in *y* direction(upper bubble)   (b) Velocity in *x* direction(upper bubble)

(c) Velocity in *y* direction (lower bubble)   (d) Velocity in *x* direction (lower bubble)
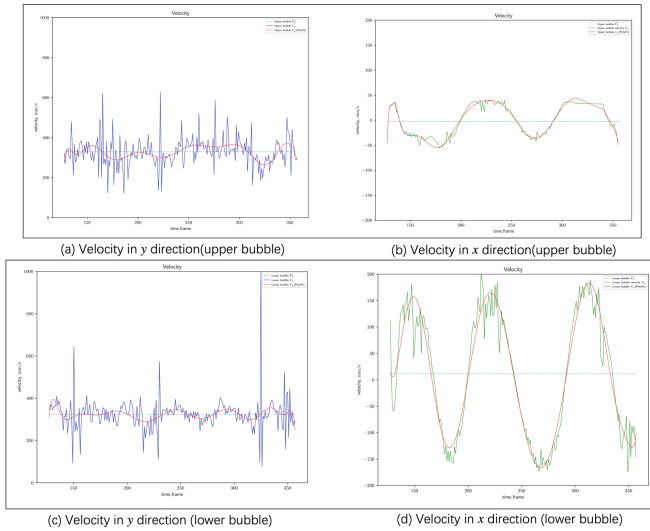
Fig. 5. Bubble velocity in ***x-y*** direction

(a) Reynolds number (b) Eötvös number (c) Relative distance(4.9 mm) (d) Relative distance(6.17 mm)
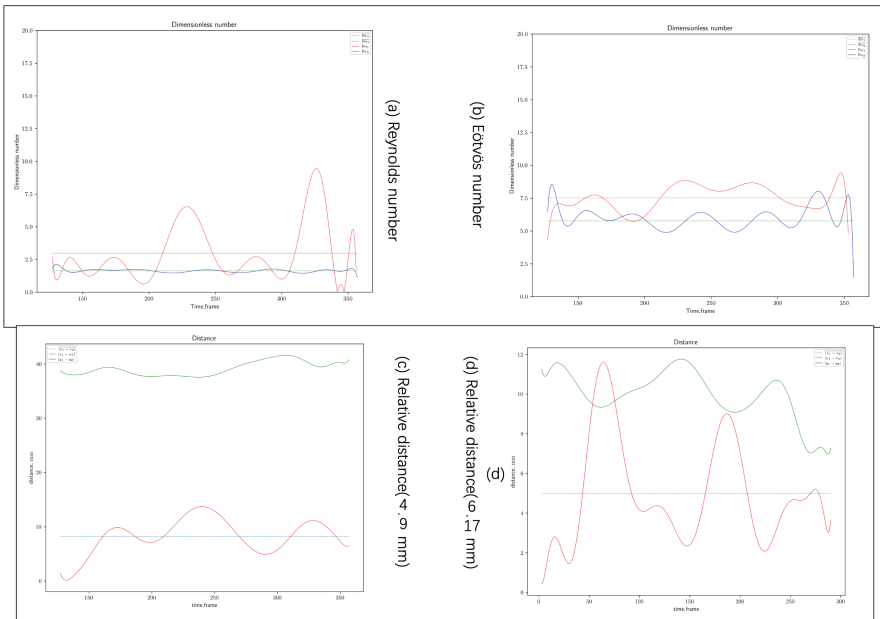
Fig. 6. Schematic diagram of time variation of dimensionless parameters and relative distance under different equivalent diameters

As shown in Fig. 7, we used a series of correlations for prediction and found that the Wallis correlation had a significant error, Davis and Taylor[15, 16] correlation were slightly better, and Park correlation and Clift[1] correlation were close in trend. We
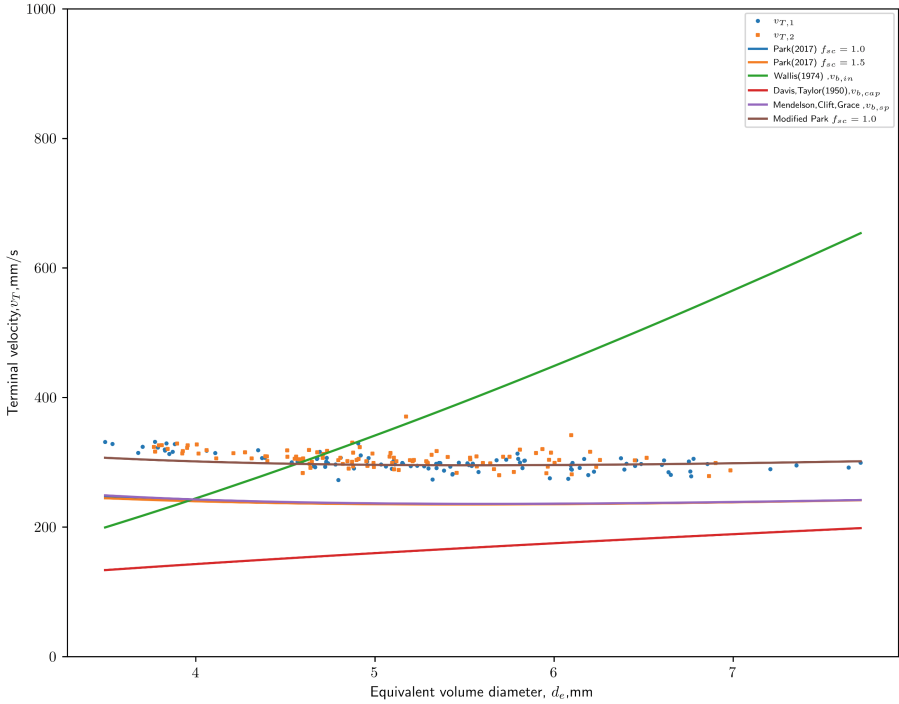
Fig. 7. Bubble terminal velocity under different equivalent diameters and fitting correlations

corrected the Park[13] correlation by adding a velocity offset term $v_{offset} = 0.06\,\text{m/s}$, and found that the predicted results were in good agreement with the experiment.

$$v_{b,in} = 0.14425g^{5/6}\left(\frac{\rho_L}{\mu_L}\right)^{2/3}d_e^{3/2} \tag{1.11}$$

$$v_{b,\,sp} = \sqrt{\frac{2.14\sigma_L}{\rho_L d_e} + 0.505gd_e} \tag{1.12}$$

$$v_{b,\,cap} = 0.721\sqrt{gd_e} \tag{1.13}$$

$$v_{b,park} = \frac{1}{\sqrt{\dfrac{1}{v_{b,sp}^2} + \dfrac{1}{v_{b,\,non\text{-}sp}^2}}} = \frac{1}{\sqrt{f_{sc}^2\left(\dfrac{144\mu_L^2}{g^2\rho_L^2 d_e^4} + \dfrac{\mu_L^{4/3}}{0.14425^2 g^{5/3}\rho_L^{4/3}d_e^3}\right) + \dfrac{1}{\dfrac{2.14\sigma_L}{\rho_L d_e}+0.505gd_e}}} \tag{1.14}$$

4.4   Numerical Simulation

In this paper, the VOF multiphase flow model in Fluent software is used to simulate the bubble flow field. A rectangular space of 10×40 cm is taken, the two sides of the surface boundary are set as symmetry surfaces, the top is set as a pressure outlet, and the surface tension coefficient of water at room temperature and pressure is taken using Harkins' empirical formula. The flow field was obtained by simulating the forward bubble with an equivalent diameter of 5 mm as shown in Fig. 8 and Fig. 9. It can be seen that under the influence of bubble-field coupling, the transverse velocity of the flow field (x-direction) changes significantly, and the fluid's transverse velocity and the flow field's longitudinal velocity (y-direction) increases, which will affect the next bubbles. We can see that the change in the transverse velocity of the flow field will strengthen or limit the transverse movement of the next bubbles (depending on the direction of the bubble movement), and the increase in the longitudinal velocity of the flow field will accelerate the next bubbles.
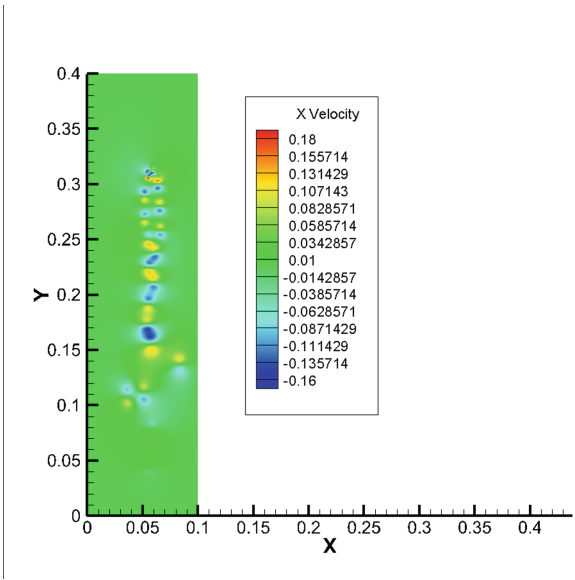
Fig. 8. Bubble flow field velocity (x direction)
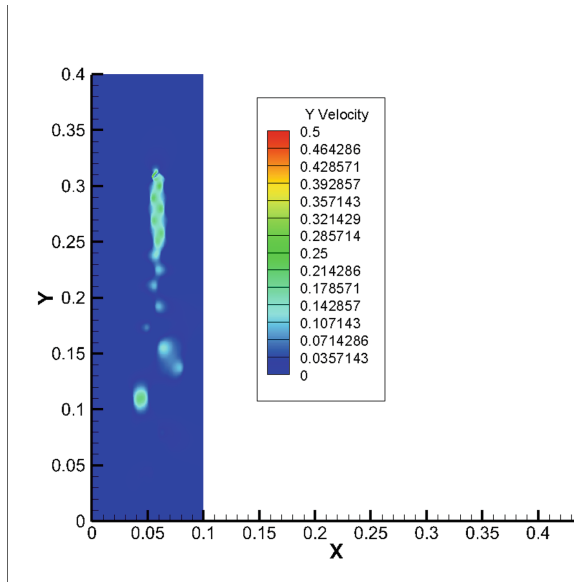
Fig. 9. Bubble flow field velocity (*y* direction)

5   Conclusions

To sum up, by generating double bubbles in different states, we developed an image processing program based on OpenCV to study the motion and deformation law of double bubbles with varying diameters of equivalent. We get the following conclusions: 1) the shape coefficient K can better reflect the shape change during bubble rising than the aspect ratio E. 2) The instantaneous parameters of two bubbles show periodic characteristics. 3) Both simulations and experiments show that the change of the tail flow field caused by the movement and deformation of the first bubble will affect the subsequent bubble and then change its movement. 4) The bottom bubbles were slightly accelerated by the flow field behind the top bubbles. We modified the Park correlation and achieved a good prediction of the terminal velocity of the experiment.

References

1. Clift, R., Grace, J.R., Weber, M.E.: Bubbles, Drops, and Particles. Dover Publications (2005)
2. Feng, Z.G., Michaelides, E.E.: Interparticle forces and lift on a particle attached to a solid boundary in suspension flow. Phys. Fluids **14**(1), 49–60 (2002)
3. Zhang, A.M., Cui, P., Cui, J., Wang, Q.X.: Experimental study on bubble dynamics subject to buoyancy. J. Fluid Mech. **776**, 137–160 (2015)
4. Duineveld, P.C.: The rise velocity and shape of bubbles in pure water at high Reynolds number. J. Fluid Mech. **292**, 325–332 (1995)
5. Raymond, F., Rosant, J.M.: A numerical and experimental study of the terminal velocity and shape of bubbles in viscous liquids. Chem. Eng. Sci. **55**(5), 943–955 (2000)

6. Zenit, R., Magnaudet, J.: Path instability of rising spheroidal air bubbles: a shape-controlled process. Phys. Fluids **20**(6), 061702 (2008)

7. Wu, M., Gharib, M.: Experimental studies on the shape and path of small air bubbles rising in clean water. Phys. Fluids **14**(7), L49–L52 (2002)

8. Sanada, T., Sato, A., Shirota, M., Watanabe, M.: Motion and coalescence of a pair of bubbles rising side by side. Chem. Eng. Sci. **64**(11), 2659–2671 (2009)

9. Wallis, G.B.: The terminal speed of single drops or bubbles in an infinite medium. Int. J. Multiphase Flow **1**(4), 491–511 (1974)

10. Grace, J.R.: Shapes and velocities of bubbles rising in infinite liquids. Trans. Inst. Chem. Eng. **51**, 116–120 (1973)

11. Jamialahmadi, M., Müuller-Steinhagen, H.: Effect of superficial gas velocity on bubble size, terminal bubble rise velocity and gas hold-up in bubble columns. Dev. Chem. Eng. Miner. Process. **1**(1), 16–31 (1993)

12. Bozzano, G., Dente, M.: Shape and terminal velocity of single bubble motion: a novel approach. Comput. Chem. Eng. **25**(4–6), 571–576 (2001)

13. Park, S.H., Park, C., Lee, J., Lee, B.: A simple parameterization for the rising velocity of bubbles in a liquid pool. Nucl. Eng. Technol. **49**(4), 692–699 (2017)

14. Fletcher, C., Schultz, R.: RELAP5/MOD3 code manual. Nuclear Regulatory Commission, Washington, DC (United States) (1992)

15. Davis, R.E., Acrivos, A.: The influence of surfactants on the creeping motion of bubbles. Chem. Eng. Sci. **21**(8), 681–685 (1966)

16. Davies, R.M., Taylor, G.I.: The mechanics of large bubbles rising through extended liquids and through liquids in tubes. Proc. Roy. Soc. Lond. Ser. A Math. Phys. Sci. **200**(1062), 375–390 (1950)

Monte Carlo Simulation and Analysis of Specified Element Samples by Nuclear Resonance Fluorescence Detection

Chen Zhang, Yu-Lai Zheng$^{(\boxtimes)}$, Qiang Wang, Yong Li, and Zi-Han Li

China Institute of Atomic Energy, P.O. Box 275-3, Beijing 102413, China
1059463405@qq.com, mczyl@sina.com

Abstract. The detection of explosives and drugs in large cargo distribution centers such as customs and logistics stations has a great effect on preventing smuggling crimes and terrorist incidents. However, the relatively thick shielding of container cargo makes the material composition information obtained by conventional detection methods such as X-ray transmission detection and imaging technology very limited. Nuclear Resonance Fluorescence (NRF) is an emerging nondestructive assay technology that uses the specific resonance energy of nuclides to identify unknown nuclides, which can be used to detect and analyze the isotopic composition of the inspected cargo. In this paper, according to the theoretical analysis of NRF, Geant4 is used to build the NRF backscatter detection model, the collimator structure of the electron accelerator and the background shield of the NRF signal are optimized and calculated, and the NRF process with ^{12}C as the target element is simulated and calculated. The results show that the simulated characteristic energy spectrum of NRF signal is consistent with the theory, the designed background shielding scheme meets the needs of NRF signal identification and detection, and the simulated signal-to-noise ratio data provides the basis for the experiment.

Keywords: Nondestructive Assay · Backscatter · Nuclear Resonance Fluorescence · Genat4 · Nuclear Safeguards

1 Introduction

In recent years, the transportation of cargo through customs containers and land trucks has become a major part of world trade. At the same time, illegal event such as smuggling commercial contraband, explosives, and special nuclear materials (SNM) through borders and customs are also rampant. According to the International Atomic Energy Agency's Illicit Trafficking Database (ITDB), between 1993 and 2021, countries reported a total of 3,928 nuclear safety incidents. In 2021 alone, 32 countries reported 120 incidents to the ITDB [1].

NRF has developed rapidly in the fields of explosives detection, container security inspection and nuclear weapons inspection in recent years. It describes that the nucleus absorbs a photon through resonance and is excited to a specific excited state, and then

de-excited by emitting one or more photons, as shown in Fig. 1. For each isotope (Z > 2), the gamma-ray energy spectrum produced by NRF is different. If the gamma-ray beam is adjusted to a specific energy, specific nucleons can be detected by nuclear resonance fluorescence, and the isotopic composition of the cargo can be analyzed. In addition, the emitted NRF photon energy is several MeV, which can penetrate most materials and boxes.
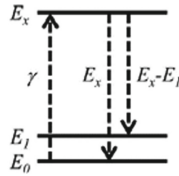
Fig. 1. NRF excitation-de-excitation process

In this paper, an optimization scheme is designed for NRF detection based on an electron accelerator. The influence of different shield thicknesses and different target thicknesses on the NRF count rate is studied from theoretical calculations and Monte Carlo analysis, and a target with ^{12}C as the target element is simulated and calculated. The optimized simulation scheme and the characteristic energy spectrum of the NRF process of the target were obtained.

2   Physical Background

NRF is a typical $X(\gamma, \gamma')X$ reaction, which includes two basic processes: transition by absorbing energy; decay by releasing energy. At absolute zero T = 0K, when a photon with energy E is incident, the target atom absorbs energy through isolated resonance to reach the energy level E_r, and then decays to the energy level E_j, and its cross section follows the single-level Breit-Wigner profile [2]

$$\sigma^{NRF}(E) = \pi \frac{2J_1 + 1}{2(2J_0 + 1)} (\frac{\hbar c}{E})^2 \frac{\Gamma_{r,0}\Gamma_{r,j}}{(E - E_r)^2 + (\Gamma_r/2)^2} \tag{1}$$

where J_0 and J_r are the nuclear spins at the ground state and resonance level, respectively. The terms $\Gamma_{r,0}$ and $\Gamma_{r,j}$ denote the partial widths of decay from E_r to ground state and from E_r to E_j, while Γ_r is the total width of the energy level transition. At non-absolute zero degrees (T ≠ 0K), the energy level broadening of the NRF reaction cross-section will decrease the NRF cross-section, but compared with the cross-section values of other electromagnetic interaction processes such as photoelectric effect, Compton scattering and electron pair effect, the NRF cross-section still comparable to or even exceeding [3], so even a small amount of special nuclear material can be detected with high sensitivity of the detection system. Due to the conservation of energy and momentum, free nuclei undergoing NRF will recoil with kinetic energy. The recoil energy E_{rec} is determined by the following Compton-like formula [4]

$$E_{rec} = E[1 - \frac{1}{1 + E(1 - cos\chi)/Mc^2}] \cong \frac{E^2}{Mc^2}(1 - cos\chi) \tag{2}$$

where χ is the photon scattering angle relative to the incident direction. For bound nuclei in the atomic lattice, E_{rec} may be large enough to overcome the lattice displacement energy E_d, in which case the kinetic energy transfer is $E_{rec} - E_d$. For unbound nuclei $E_{rec}E_{rec}$ less than E_d, the recoil is transferred across the entire lattice and recoilless NRF is achieved. For outgoing photons, the energy decreases accordingly by $E_{rec} \gg \Delta E_{rec}$, but the energy of photons emitted in the backward direction will be much lower than the resonance energy E_r and it is highly unlikely that another NRF interaction will occur in the same target atom. According to the definition of the angle integral, the differential angular cross-section of the NRF outgoing photon is defined as

$$\frac{d\sigma_r^{NRF}(E)}{d\Omega} = \frac{W(\chi)}{4\pi}\sigma_r^{NRF}(E) \tag{3}$$

The angular correlation function [5] $W(\chi)$ is symmetric around $\chi = \pi/2$, so $W(\chi)$ = $W(\theta)$, where the emission angle θ is relative to the back-beam direction. Then, the angular correlation function $W(\theta)$ is shown in formula (4)

$$W(\theta) = 1 + (R/Q)cos^2\theta + (S/Q)cos^4\theta \tag{4}$$

The constants (R/Q) and (S/Q) represent the contributions of dipole and quadrupole transitions, respectively, and are determined by the sequence of spins $J_0 \rightarrow J_r \rightarrow J_j$. In most experiments, it was roughly isotropically distributed. According to formula (4), the scattering angle of the NRF of ^{12}C is calculated in the order of $0^+ \rightarrow 2^+ \rightarrow 0^+$. The parameters and calculation results are shown in Table 1.

Table 1. Resonance excitation-de-excitation parameters, NRF cross section and scattering angle of ^{12}C

Isotope	$E_r[MeV]$	$\Gamma_r[MeV]$	$\int \sigma_r^{NRF}(E)[eV \cdot b]dE$	(R/Q) (S/Q)	θ
^{12}C	4.438	10.8	6.939	0,4	90°

3   Simulation Setup

Figure 2 is a schematic of the constructed Geant4 simulation model. The model is as follows: the backscattering method is adopted as a whole, a high-energy electron beam is generated by an electron accelerator, electron beam produces X-rays via bremsstrahlung, the collimator confines X-rays to a certain angle range, then high-energy X-rays bombard the target to generate an NRF reaction. The HPGe detector located at 110° relative to the main beam direction receives the NRF photon signal. The detector is provided with a low-energy background shielding lead on the axial end face, and a thick shielding lead facing the accelerator to block the X-Rays from the accelerator.

Figure 3 shows the design structure of the collimator. The overall design is a cylinder. The radius of the inlet end and the outlet end of the cylinder are different, so that the
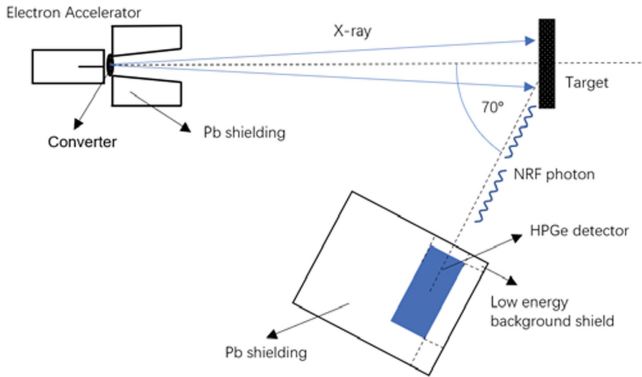
Fig. 2. NRF detection design structure

X-ray with the second highest dose at the scattering angle of 3° –7° is not shielded, and the lifting device overall efficiency. The tungsten alloy converter is placed at the exit of the accelerator beam and at the entrance of the collimator. The inner diameter of the inlet end of the collimator is 0.5 cm, the outer diameter is 5 cm, the inner diameter of the outlet end is 1.2 cm, the outer diameter is 5 cm, and the overall axial length is 10 cm. The diameter of the inlet end of the collimator completely fits the diameter of the converter.
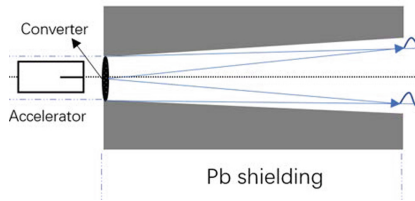
Fig. 3. Collimator structure diagram

The target material is graphite with ^{12}C as the target element. The target shape is a square thick sheet, the width is 10.2 cm $\times$ 10.2 cm, and the target thickness is 1.25 cm. The count rate of the NRF peak corresponds to the mass thickness ρD of the measurement object. As thickness increases, NRF photon yield increases according to a power function variant relationship; the NRF photons emitted forward in the thick target have no recoil energy reduction, and the emitted photons can also cause NRF reactions. The thin lead shielding layer of the detector entrance window is 1.25 cm, which can reduce the low-energy background from the target and improve the NRF count rate of the detector. The detector faces the accelerator lead shield of 25 cm, which shields the background photons from the accelerator and other scatterers.

According to the NRF photon exit angle of ^{12}C, it can be seen that the optimal setting angle of the detector is 90°. However, the interrogation system needs to inspect various explosives and nuclear materials. Combined with the 125° scattering angle set for the

nuclear material ^{238}U and the approximate isotropic NRF scattering angle characteristics, this design adopts a 110° scattering angle design.

The isotope contained in nuclear materials include ^{238}U, ^{235}U, and the isotope contained in explosives include ^{12}C, ^{14}N, ^{16}O, etc. The NRF energy levels of ^{238}U and ^{235}U are concentrated in 1.5 MeV–2.5 MeV, while the NRF energy levels of ^{12}C, ^{14}N, and ^{16}O are concentrated in 4 MeV–7.5 MeV, the photons in this energy range can easily penetrate the planar and coaxial HPGe detectors with low relative efficiency, and NRF requires excitation at higher incident energy. Therefore, this paper chooses the coaxial HPGe detector with a relative efficiency of 95%, the axial length of the crystal is 80.5 mm, and the radius is 79.5 mm.

4   Simulation Results

The simulation setup for the electron accelerator is as follows: the angular distribution is a Gaussian distribution with a one-dimensional 5° broadening, the energy is a Gaussian distribution with a center value of 10 MeV and a 0.001 MeV broadening, and the number of incident γ particles is 2×10^7. Figure 4 is a thermal diagram of the X-ray count rate at a distance of 20 cm from the converter without a collimator, bright colors indicate high counts, cold colors indicate low counts, and the horizontal and vertical coordinates indicate distances in millimeters. It can be seen that the X-ray count at the central position is higher, and the count rate gradually decreases with the increase of the distance from the central axis.
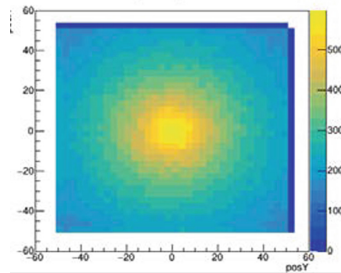
Fig. 4. X-ray energy spectrum generated by converter and count distribution at 20 cm

The selection of the distance between the target and the collimator is constrained by the beam diffusion angle of the collimator and the limitation of the target area; at the same time, the target and the detector have a linkage relationship, that is, if the target is too close to the collimator, the detector will move, increasing its background value. In order to make the X-rays completely incident on the target, the X-ray count rate distributions on the target were measured at distances of 40 cm and 50 cm from the target and the collimator, respectively, as shown in Fig. 5.

It can be seen from the Fig. 5 that as the distance increases, the count rate distribution area on the target increases. When the distance is 50 cm, the counted area ratio can reach 65.6%, and no X-rays escape from the target, which can provide the highest NRF signal
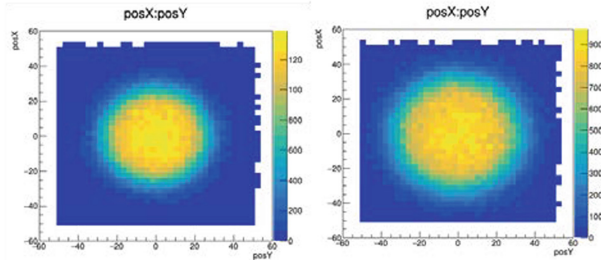
Fig. 5. Count distribution on target Left: Distance 40 cm; Right: Distance 50 cm

rate, which meets the experimental requirements. The purpose of masking is to obtain a clearer NRF peak, and the evaluation factor is introduced accordingly

$$Y_0 = n_{E_r}/n_{off}$$

where n_{E_r} is the NRF photon count generated at a specific resonance energy level when the incident energy is E, n_{off} is the total count of scattered X-rays (background part) received on the detector from the electron accelerator when the source term is unchanged, Its significance is to test the ability of lead shielding to block the corresponding background when generating quantitative target counts (NRF photons). The NRF photons is recorded by the detector, contributing η_n. Then

$$\eta_n = \begin{cases} 1 & \text{Record} \\ 0 & \text{not recorded} \end{cases}$$

To count the number of all NRF photons recorded by the detector as N_1, the approximate probability of generating an NRF signal is $\widehat{P}_N^{(1)}$, when the confidence coefficient is 1-α = 0.95, the error of $\widehat{P}_N^{(1)}$ is

$$\left| \widehat{P}_N^{(1)} - P \right| < 1.96 \sigma_\eta / \sqrt{N}$$

σ_η is the mean square error of η. Since η obeys the binomial distribution, according to the simulation analysis, P is 10^{-6}. If the relative error is required to be less than 5%, The magnitude of N is 10^9. A bias factor of 10 is applied to the physical process of bremsstrahlung of electrons, and the simulation result with a detector shielding thickness of 25 cm is counted as 3. This count can be considered to be no statistically. At this time, the evaluation factor Y_0 can meet the design requirements.

In addition, comparing the X-ray energy spectrum before and after adding the shield on the side of the detector facing the accelerator is helpful to evaluate the performance of the shield. Figure 6 shows the X-ray energy spectrum of the shielded entrance end of the detector when the incident particle is 2×10^7. The number of X-ray particles can be statistically 1.5×10^5, while the statistical particle number on the target is 3.3×10^5. According to the calculation of the shielding effect, when the incident particle is 10^9, the shielding ability of X-rays is 7.5×10^6, and it is 1.6×10^7 on the main beam, so the shielding effect of this thickness can at least reach 1.6×10^7 particles (the shielding
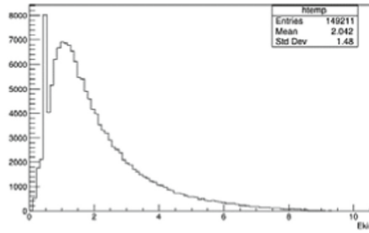
Fig. 6. Detector shield entrance window energy spectrum

effect is at least 6.3×10^{-8}) on the main beam, the detector will receive the background from the electron accelerator.

The source term of the NRF simulation adopts a Gaussian distribution with an energy center of 4.438 MeV and a spread of 0.001 MeV. The surface source is 0.5 mm × 0.5 mm, the length and width are spread by 0.1 mm, and the angular distribution is spread by 0.5° along the axial direction facing the target. The incident particle is γ, and the number is 2 × 10^7. When the distance between the target and the detector is 20 cm, the thickness of the target is 1.25 cm, 2.5 cm, 3.75 cm, 5.0 cm respectively, and the simulation is carried out without adding a thin lead shielding layer on the axial plane of the detector, as shown in Fig. 7 for the detector energy spectrum.
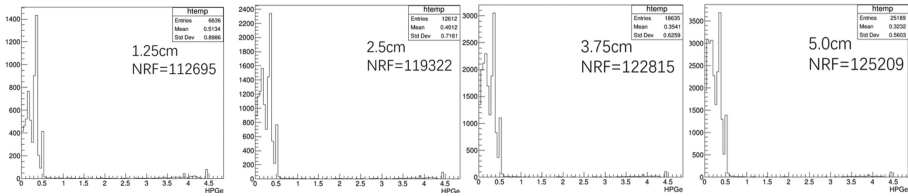
Fig. 7. Detector energy spectrum when the target thickness is 1.25 cm, 2.5 cm, 3.75 cm and 5.0 cm

It can be seen from Fig. 7 that the change of target thickness has no significant effect in the energy spectrum of the signal generated by the target, and the shape of the energy spectrum after normalization has no significant difference. Secondly, in the experimental measurement, the thickness of the sample is expected to be as thin as possible. The purpose of thinning is to reduce the absorption of the γ-ray by the sample material when it is transported in the sample, which is commonly referred to as "self-absorption" [6], thin sample thickness can weaken the count stacking of the detector.

Adding a thin lead shield to the detector entrance window can reduce the low-energy background from the target, thereby increasing the detector's NRF count rate. When the distance between the target and the detector is 20 cm, and the source term is set as above, compare the NRF counts before and after adding a thin lead layer and with different lead layer thicknesses (1.25 cm, 2.5 cm, 3.75 cm lead layer thickness), as shown in the Fig. 8. It can be known that adding a thin lead layer to the detector entrance window, with the increase of lead layer thickness, the shielding effect on the low-energy background from the target becomes more and more significant. For low

background counts, 1460.75 keV of low-background nuclide ^{40}K, which is common in the laboratory, is used as the counting threshold, and those below this threshold are counted into statistics. The significance of this evaluation factor is to select the maximum relative NRF photon rate to obtain a clearer energy spectrum through long-term measurement in the experiment. The calculation results based on this evaluation factor are listed in Table 2.
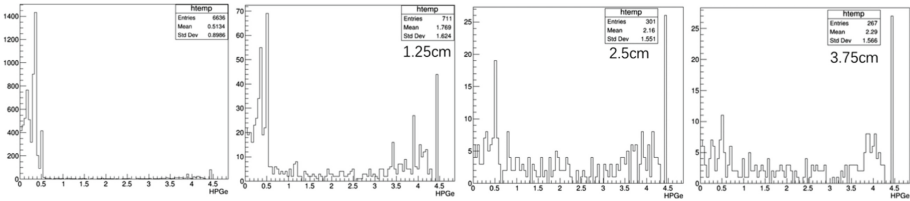
Fig. 8. The order from top to bottom and left to right is lead-free layer, 1.25 cm, 2.5 cm, 3.75 cm lead layer thickness

Table 2. Thin lead layer thickness and count

Target thickness [cm]	NRF count rate	Low background count	Evaluation factor Y	Total count
0	81	6144	0.013	6636
1.25	44	400	0.110	711
2.5	26	129	0.202	301
3.75	27	105	0.257	267

Note: When the thickness is 3.75 cm, the number of incident particles is 3×10^7.

It can be seen from the Table 2 that as the thickness of the thin lead layer increases, the low background count decreases rapidly, and the low background count changes weakly after the lead shielding thickness reaches 2.5 cm; considering that the resonance energy peak region of ^{238}U and ^{235}U is 1.5 MeV–2.5 MeV, the attenuation amplitude should not be too large, and the thickness of the thin lead layer of 2.5cm is suitable.

5   Conclusion

In this paper, by analyzing the relationship between the physical process of X-ray excited NRF process and setting different target parameters, shield thickness and detection efficiency, the following conclusions can be drawn: (1) The yield of NRF photons is ~ 10^6/An incident particle under the calculation conditions in this paper, which requires long-time detection. Optimizing the parameters of the shielding material can improve the despectral efficiency; (2) Optimized lead shield thickness for X-rays from accelerators. At a thickness of 25 cm, the shielding effect can be improved. The main beam/background

is ~ 6.3×10^{8}; (3) The thickness of the target has a weak influence on the detection efficiency, and the computational performance can be reduced in order to reduce "self-absorption" and prevent wasted computing performance of emitted recoilless NRF photons.

This paper provides a design method of an NRF backscatter detection scheme. The advantages of this structure design are: on the basis of ensuring the NRF detection efficiency, the design reduces the thickness of the shield, reduces the overall weight of the equipment, and improves the feasibility and practicality of technology application.

References

1. Incident and Trafficking Database (ITDB). 2022 Factsheet. https://www.iaea.org/resources/databases/itdb,2022-01
2. Jordan, D.V., Warren, G. A.: Simulation of nuclear resonance fluorescence in Geant4. In: 2007 IEEE Nuclear Science Symposium Conference Record, pp. 1185–1190 (2007)
3. Huang, W., Yang, Y., Li, Y., et al.: Research on SNM detection technology based on LINAC. In: The fifteenth Proceedings of the National Academic Annual Conference on Nuclear Electronics and Nuclear Detection Technology, pp. 505–511 (2010)
4. Vavrek, J.R., Henderson, B.S., Danagoulian, A.: High-accuracy Geant4 simulation and semi-analytical modeling of nuclear resonance fluorescence. Nucl. Instrum. Methods Phys. Res. Sect. B **433**, 34–42 (2018)
5. Hamilton, D.R.: On directional correlation of successive quanta. Phys. Rev. **58**, 121–131 (1940)
6. Zhu, C., Chen, Y., Guo, H., et al.: Research on detection efficiency of high-purity germanium detectors. Nucl. Electron. Detect. Technol. **26**(2), 191–194 (2006)

Research on Public Communication of Small Reactor

Rongxu Zhu[✉], Feng Zhao, Xiaofeng Zhang, Jiandi Guo, and Meng Zhang

Suzhou Nuclear Power Research Institute, Suzhou, Jiangsu, China
zrx441@163.com

Abstract. Based on the conclusions of small reactor environmental impact assessment and social stability risk assessment of small reactors, this paper conducts a special study on the public communication of small reactors. This article discusses the work content, scope and form of public communication of small reactor, and give suggestions on the scope and form of public publicity, public participation and information disclosure. It is matched with small reactor public communication theoretical system and operation manual.

The research on the public communication work of small reactor can provide necessary theoretical basis and technical support for the specific public communication work of small reactor. Provide decision support for local policies and construction departments to implement public communication. It is hoped that this study can provide some reference for the public communication of small reactors in the exploratory stage.

Keywords: small reactor · public communication · NIMBY · EIA · SSRA

Nomenclature

EIA	Environmental Impact Assessment
SSRA	Society Stability Risk Assessment
MEE	Ministry of ecological environment of the people's Republic of China
NDRC	National Development and Reform Commission of the People's Republic of China
PWR	Pressurized Water Reactor
PAZ	Precautionary Action Zone

1 Introduction

In order to expand the application scope of nuclear energy, ensure energy security and meet the needs of low-carbon energy development, China has invested a lot of human and material resources in the development of small reactors in recent years, and has achieved a series of results. The natural avoidance effect of nuclear related projects and the particularity of the utilization of small reactors, such as being close to cities and residents, bring new challenges to public communication. If we simply copy the guidelines

for public communication of nuclear power projects to carry out public communication of small reactors, it is difficult for enterprises and local governments to bear such a huge workload and resource investment, Therefore, it is necessary to study the public communication of small reactors.

2   Relevant Background

In 2012, in order to promote scientific decision-making, democratic decision-making and legal decision-making, prevent and resolve social contradictions, NDRC issued the notice of the national development and Reform Commission on the Interim Measures for social stability, risk assessment of major fixed asset investment projects, requiring NDRC to approve or report to the State Council for approval. Fixed asset investment projects constructed and implemented within the territory of the people's Republic of China shall be subject to SSRA.

The measures for public participation in environmental impact assessment issued by MEE stipulates that the construction departments of reactor facilities and commercial spent fuel reprocessing plants with a core thermal power of more than 300 MWth shall listen to the opinions of citizens, legal persons and other organizations within a radius of 15 km of the facilities or reprocessing plants; The construction departments of other nuclear facilities and uranium mining and metallurgy facilities shall listen to the opinions of citizens, legal persons and other organizations within a certain range according to the specific conditions of environmental impact assessment[1].

The guidelines for public communication of nuclear power projects issued by MEE stipulates that public communication of nuclear power projects should pay attention to the public within a certain range around the plant site (usually 30 km radius of the plant site) that may be directly or indirectly affected by the project construction and operation, and focus on the public within 5 km radius of the plant site [2].

In 2017, the national nuclear accident emergency office issued the guidance on nuclear emergency work of onshore small PWR, which clearly put forward that "the recommended range of small PWR emergency planning area shall not be greater than 3 km, and the specific range shall be proposed by the operating unit after systematic demonstration and scientific calculation, and determined according to the specified procedure".

In the draft for comments on the principles and requirements for the division of nonresidential areas and planning restricted areas of small nuclear power plants, for light water reactors with a single reactor thermal power of less than 300 MWth, the boundary of nonresidential areas can generally be consistent with the plant boundary of nuclear facilities, and the distance from the reactor is generally not less than 100 m; The distance between the boundary of the planned restricted area and the reactor shall not be less than 1 km.

Arrangements for preparedness for a nuclear or radiological emergency (IAEA GS-G-2.1) recommends that the PAZ with reactor thermal power of 100–1000 MWth is 0.5–3 km away from the plant site [3].

3 Small Reactor SSRA

The 6 × 200 MWth small reactor project is planned and arranged at one time and implemented by stages. Phase I project construction 2 × 200 MWth small reactor. The social stability risk investigation scope of the project includes the interest related groups directly and indirectly affected by the project, mainly including: residents, heating enterprises, relevant heat users and other social organizations directly affected by the siting, construction and operation of the project within 5 km of the project site, sensitive objects around the project, including planters, farms, industrial and mining enterprises, schools, hospitals, etc. And government departments in the project location and village committees in the area around the plant site; Mass media and online new media in the project site; Pay due attention to the opinions, suggestions and demands of non-local residents on the project.

The personal questionnaire survey is mainly organized within 5 km around the plant site and the urban area where the project is located. A total of 720 questionnaires were distributed and 720 questionnaires were collected, of which 687 were valid questionnaires (invalid questionnaires were mainly due to lack of ID number, incorrect contact information or incorrect information, etc.). The respondents are mainly men. The main reason is that the household survey is generally filled in by men. The age distribution is mainly middle-aged and young people, taking into account the actual situation of many lefts behind elderly people in rural areas. The occupation is mainly farmers, taking into account the distribution of enterprise and institution employees, individual industrial and commercial households and other professionals. The education level is mainly from junior high school to senior high school, which can effectively reflect the real opinions and demands of the respondents. At the same time, there are a small number of highly intelligent elements, which are representative and extensive. The main findings are as follows [4] (Table 1).

Table 1. Classified statistics outcome of public's attitude to project

Question	Outcome	Proportion	Remarks
Do you understand that this project is a nuclear project	YES	62.6%	1 person did not fill in
	NO	37.3%	
How well do you know the project	Very well	8.2%	2 persons did not fill in
	Basic	28.4%	
	A little	38.4%	
	NO	24.7%	

Table 1. (*continued*)

Question	Outcome	Proportion	Remarks
Channels of understanding of the project	meeting	4.7%	This topic is multiple choice, and 3 persons did not fill in
	Notice	4.8%	
	Public discussion	76.6%	
	TV	0.9%	
	website	1.3%	
	Nuclear science popularization activities	8.2%	
	micro-blog	0.6%	
	WeChat	11.6%	
	other	1.6%	
Issues most concerned about project construction	environmental effect	39.7%	This topic is multiple choice
	Land requisition compensation	56.6%	
	Providing employment opportunities	57.2%	
Issues most concerned about project construction	conserve energy, reduce emissions	3.5%	This topic is multiple choice
	Nuclear safety issues	40.5%	
	Economic drive	23.0%	
	Safety and quality during construction	11.8%	
	Stability of heating	24.0%	
	other	0.4%	

The construction departments has carried out a small amount of popular science publicity before this questionnaire survey, but the coverage is limited. According to the questionnaire survey, more than half of the respondents understand that the project is a nuclear power project, most of the respondents have a certain understanding of the project, and a few respondents do not understand the project. The respondents understand the project mainly through public discussion, WeChat and nuclear science popularization activities; Respondents focused on land acquisition compensation, employment opportunities, environmental impact, nuclear safety issues, stability of heating, etc.

4 Small Reactor EIA

The environmental impact assessment of the small reactor shows that the radioactive waste gas generated during normal operation is discharged into the atmospheric environment through the chimney after being treated to meet the annual total emission limit

specified in GB6249. The radioactive waste liquid generated is reused after being treated to meet the radioactivity level and annual total emission limit specified in GB6249. If it cannot be reused completely, it is discharged into the atmospheric environment through carrier evaporation. The maximum individual effective dose caused by the discharge of airborne effluent is less than 0.25 mSv, which meets the provisions of GB6249 and the safety review principles of small pressurized water reactor nuclear power plant. At the same time, it meets the public individual effective dose constraint value (0.02 mSv/a) caused by two small reactors, and its radiation impact on the environment is acceptable [5].

Within the duration of the site selection accident, the effective dose of public individuals (adults) at the site boundary is less than 10 mSv, and the thyroid equivalent dose is less than 100 mSv, which meets the safety review principles of small PWR nuclear power plant.

The emergency planning area is preliminarily divided into a small reactor centered area with a radius of 1 km of the plant site. The feasibility analysis results of implementing emergency plan at the plant site show that there are no insurmountable difficulties in implementing off-site emergency plan for nuclear accidents.

5   Small Reactor Public Communication

According to the conclusions of EIA and SSRA of small reactor, special research on public communication of small reactor is carried out, discussing the work content, scope and form of public communication of small reactor, and suggesting on the scope and form of public publicity, public participation and information disclosure. So Finally, a complete theoretical system of small pile public communication is developed..

5.1   Work Scope

The public communication scope of small reactor includes the public, enterprises, institutions and social organizations that may be directly or indirectly affected by the project construction and operation within 5 km of the plant site, focusing on the public, enterprises and institutions within 3 km. For nuclear heating reactors, attention should also be paid to the residents around the heating pipeline and end users (relevant residents and enterprises, etc.).

5.2   Work Content

The contents of public communication include public publicity, public participation, information disclosure and public opinion response. The public communication work should be guided by the local government, the construction company shall provide relevant resource guarantee, and the professional technical company shall be responsible for the whole process of technical consultation.

The public publicity shall be based on increasing the public's understanding of nuclear energy and the project, with the purpose of improving the public's acceptability. A combination of visits, exhibition halls, expert lectures and other means shall be adopted

to ensure the full coverage of the public publicity objects. Before the publicity work is carried out, the publicity objects should be reasonably and scientifically classified, so as to make the publicity work more targeted, so as to achieve twice the result with half the effort. At the same time, in combination with the social conditions and historical contradictions of the project location, the local public's acceptance of publicity contents and methods should be fully considered, so as to achieve the purpose of both publicity and risk control.

In principle, public participation should include questionnaire survey and symposium. The questionnaire shall be designed according to the project impact and public concerns to ensure easy to understand and comprehensive content. The questionnaire survey shall be determined according to the distribution of the resident population of the public near the plant site and the impact of stakeholders. Generally, the individual questionnaire shall be distributed by household. The questionnaire survey shall include stakeholders, especially direct stakeholders (residents of land acquisition and demolition, enterprises and institutions affected by the project construction), and shall include expert representatives of relevant government departments and professional institutions. When selecting the respondents, we should consider the selection of individuals and organizations with certain professional knowledge background and social level, and also pay attention to the wide representation of the respondents in terms of age, gender, educational background, occupation, etc. The specific number of individual questionnaires shall be decided based on the number of resident households around the project site. Generally, it should not be less than 300.

Information disclosure shall be implemented with reference to the measures for public participation in environmental impact assessment, guidelines for public communication of nuclear power projects and other relevant documents. It needs to be carried out in the form of newspapers, websites and paper posts. The scope of paper posting suggestions is the scope of public communication of the project. The posting place is the bulletin board of relevant administrative village committee and township government, and the postings last for 10 working days.

The construction company and local government shall establish a stability maintenance linkage mechanism and a public opinion response system. Carry out daily public opinion monitoring, conduct 24-h supervision during the information announcement, study and judge the public opinion of the project as soon as possible, and report the negative public opinion as soon as possible. During the publicity period, increasing the update cycle and amount of information of government official websites, microblogs, forums and popular science news can strengthen the effect of online popular science publicity.

5.3 Work Suggestion

(1) Strengthen public publicity

Strengthen the popularization and publicity of the basic knowledge of nuclear energy utilization, reduce and eliminate the public's anxiety and fear about nuclear safety. In view of the public's doubts and concerns about nuclear safety and the impact of

radiation on the environment, take the government as the leading role and cooperate with enterprises, do a good job in the publicity, education and public opinion guidance on nuclear safety and the impact of nuclear radiation, and constantly strengthen the communication with the residents near the plant site. Carry out popular science publicity in a way acceptable to the local public. Pay attention to further strengthen popular science publicity for heat users, carefully listen to the opinions of the public, answer questions or questions in time, and improve the public's understanding of nuclear heating reactor. The public's awareness and acceptability of nuclear heating will be improved through visits and field visits. Strengthen information disclosure, ensure the public's right to know and participate in the safe production of nuclear heating reactors, and strive for the public's understanding and trust.

(2)   Strengthen public opinion information monitoring

Strengthen the monitoring of public opinion information, especially pay attention to the possible cross regional avoidance effect and a wide range of public opinion risks; Reduce the dissemination and diffusion of negative public opinion of relevant projects through the supervision and guidance of media public opinion.

(3)   Mutual trust and benefit sharing among the three parties

Strengthen public relations management. Strengthen mutual communication and consultation with the government, groups affected by the project construction and surrounding residents. Strengthen the publicity of nuclear safety knowledge, optimize the ways of information disclosure, improve the efficiency of information disclosure, and enhance the public's cognitive trust in the project. The construction company shall actively fulfill its corporate social responsibility, strengthen the development assistance of villages near the plant site, and try to localize the employment as much as possible, so as to make the development benefits more benefit the surrounding people. On the premise of law and regulation, local governments take the initiative to communicate and exchange with construction units, timely inform public needs, and promote the construction of benefit sharing mechanism among the government, enterprises and the public; We will promote the reemployment of landless farmers and ensure that the quality of life of landless farmers does not decline.

6   Conclusion

Through the research on the public communication work of small reactors, we can provide necessary theoretical basis and technical support for the specific public communication work of small reactors, also provide specific support for the implementation of public communication work by local policies and construction company, and give opinions and suggestions for the follow-up public communication work of small reactors.

References

1. MEE. Measures for public participation in environmental impact assessment (2018). (in Chinese)
2. National Nuclear Safety Administration. Guideline of public communication for nuclear power projects (2015). (In Chinese)
3. Arrangements for preparedness for a nuclear or radiological emergency ,IAEA GS-G-2.1
4. Project social stability risk assessment report. SNPI (2021)
5. Regulations for environmental radiation protection of nuclear power plant. GB6249 (2011)

Study on a Non-collecting Atmospheric Radon Concentration Measurement System

Chuanfeng Tang[1], Liangquan Ge[2], Shengliang Guo[3(✉)], Zhipeng Deng[1], and Jin Li[1]

[1] College of Nuclear Technology and Automation Engineering, Chengdu University of Technology, Chengdu, Sichuan, China
[2] College of Nuclear Technology and Automation Engineering, Applied Nuclear Technology in Geosciences Key Laboratory of Sichuan Province, Chengdu University of Technology, Chengdu, Sichuan, China
[3] Chengdu Newray Technology Technology Co., Ltd., Chengdu, Sichuan, China
gsl33@qq.com

Abstract. Radon in the atmosphere is an important tracer in meteorology and geology and an important index of environmental radioactivity level evaluation. In this paper, NaI (Tl) scintillator detector was developed to directly measure radon concentration in the atmosphere, and a mathematical model of atmospheric radon gamma measurement was proposed, which solved the technical problem of online real-time monitoring of atmospheric radon concentration. It has important scientific and practical value.

In this paper, the characteristic gamma peaks of radon daughters ^{214}Bi (609.31 keV) and ^{214}Pb (351.92 keV) are respectively selected to calculate the radon concentration in the atmosphere. During the measurement period, the variation trend of radon concentration is the same as the theory, which suggests a higher concentration in the morning and a lower in the evening. Finally, the experimental measurement results were compared with the RAD7 radon measuring instrument. The error range of this detection system is 79.73% smaller than that of RAD7 on average, and its detection limit reaches 0.29 Bq/m^3 with a 30-min-measurement at room temperature. This paper proves that it is feasible to directly measure the activity concentration of radon in the atmosphere. The atmospheric radon measurement method proposed in this paper can accurately obtain the concentration of atmospheric radon and has the advantages of convenience, large measuring range, low detection limit, and online measurement.

Keywords: Radon concentration · Online measurement · Gamma-ray measurement · Radioactivity of the atmosphere · Radon-in-air

1 Introduction

Radon and its daughters are members of the natural radioactive uranium and thorium series and are one of the main sources of human natural radiation. According to a report by the United Nations Scientific Committee on the Effects of Radiation, exposure doses to radon and its daughters are about 1.3 mSv per year and are 54% of natural radiation. The U.S. Environmental Protection Agency (EPA) lists radon and its daughters as the

only major causes of lung cancer other than smoking. In 2005, R. Williamsfield et al., and David Hilld et al., reported that radon inhalation is directly related to lung cancer [1, 2]. In recent years, with the improvement of people's working and living environment, the harm of radon and its daughters has naturally become a hot issue, which is concerned by all sectors of society. At the same time, radon in the atmosphere is also an important tracer in many related research fields such as meteorology and geology. In particular in seismology, earthquakes and similar geological activities such as volcanic eruptions can affect the concentration of radon in the atmosphere, and the concentration of it is commonly used for earthquake prediction [3]. The time scale and scope of these effects are often unclear, so rapid responses and long-term continuous measuring of radon concentration in the atmosphere are also required. There are many kinds of measurement methods of radon in the atmosphere, which can be classified into continuous sampling method, instantaneous sampling method, and passive sampling method by sampling method. For example, passive cumulative sampling is generally used for long-term measurement of radon gas, whereas the active continuous sampling method is used for continuous monitoring of radon concentration changes. And the measurement methods also can be divided into thermoluminescence method, solid nuclear track method, electret method, scintillation chamber method, electrostatic collection method, and activated carbon box method by measuring principle.

In terms of the general situation, the thermoluminescence measurement method has the advantages of being cheap, small-in-volume, no-radiation-source, and it's easy to read data, but the result obtained by this method is greatly affected by ambient temperature and wind speed. The attenuation of thermoluminescence over time and the trace radionuclides contained in the encapsulated or fluorescent material will further reduce the accuracy and reliability of the measurement results [4].

The solid track method has the advantages of low cost, small volume, and no-radiation-source. It is generally suitable for large-scale radon measurement. However, the disadvantage is also very obvious. In a low concentration area, the tracking number will be easier to generate errors because of the small detecting area [5, 6].

The electret method has the advantages of low cost, small volume, and weight, reusable and wide application range [6]. However, special care should be taken in the storage and use of electret, and the natural background should be corrected before measurement.

The scintillation chamber method has the advantages of a low lower limit of detection, ease to use, and high accuracy [7]. However, the detector is large in size and heavy in mass, and it is difficult to remove radon daughters deposited in the scintillation chamber. Therefore, it must be corrected before carrying out a continuous measurement.

The electrostatic collection method has a low lower limit of detection and it's easy to integrate [8]. However, its collection efficiency is greatly affected by air humidity, it must be equipped with a drying tube during measurement, and the drying tube must be replaced frequently in the humid air. It is not suitable for long-term continuous and unattended measurement.

The advantages of the activated carbon box method are that it is easy to use, can be continued after cleansing, and can be used for large area radon measurement in batches. The disadvantage is that the adsorption of radon by activated carbon is greatly affected

by atmospheric conditions, and the radon concentration before the end of collection contributes more to the measurement results by this measurement method [9].

The above measurement methods cannot meet the requirements of outdoor continuous measurement in situ because of the response time, measurement residues, or measurement environmental conditions. This paper introduces a new field measurement system of radon concentration in the atmosphere, which consists of a NaI (Tl) detector and directional detector, and can realize the field and continuous measurement of radon concentration in the atmosphere. Calibration experiment and field measurement are also carried out. In this paper, the working principle and performance of the system are introduced in detail, and some field measurement results are given.

2   Materials and Methods

2.1   Measurement System
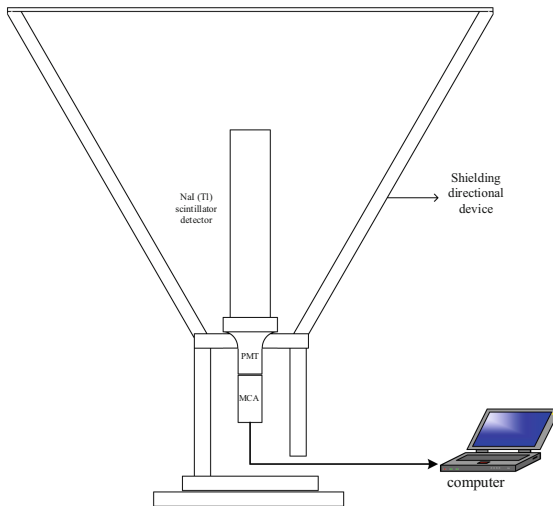
Fig. 1. Radon concentration measurement system for the atmosphere

As shown in Fig. 1, the whole measurement system is roughly composed of a detection part and a directional shielding part. The detection part uses a NaI(Tl) scintillator detector, which is generally composed of three main components: NaI(Tl) scintillator, photomultiplier tube, and pre-amplifier Circuit. NaI(Tl) scintillation detector workflow is as follows:

(1) Produce fluorescence. After gamma-ray enter NaI(Tl) scintillator, it will generate the photoelectric effect, Compton scattering, and electron pair effect with NaI(Tl) scintillator, resulting in secondary charged particles. These charged particles can ionize the atoms of the NaI(Tl) scintillator. When the excited atoms deactivate, they will emit fluorescent photons.

Fig. 2. Photos of measurement system entities

(2) Photoelectric conversion. The photoconductive materials and optical coupling agents are used to transfer the fluorescent photons to the photocathode of the photomultiplier tube, and then the photocathode will emit photoelectrons when the photoelectric effect is generated.

(3) Electron multiplication. After passing through the photomultiplier tube, the number of photoelectrons is changed from 1 to 10^4–10^9, so that a huge flow of electrons is collected at the anode of the photomultiplier tube.

(4) Pulse shaping. The flow of electrons at the anode further forms an electrical pulse signal on the load, which is then output through a pre-circuit.

Then the resulting pulse signal is analyzed by a single-channel pulse analyzer or multi-channel pulse analyzer to form a gamma-ray spectrum.

Another part is the directional shielding device, the function of it is to shield and exclude gamma-rays from the ground and surrounding building materials. Figure 3 shows the comparison between the spectrums after shielding and those without shielding, it can be seen that the directional shielding device is effective in shielding gamma-rays from most of the ground and surrounding building materials, such as the characteristic peak of 40K shown in Fig. 1 can be blocked 75.78%, so the shielding effect of the directional shielding is very obvious.

2.2 Principle

The most important step in calculating the detecting volume is to determine the 95% attenuation thickness of the characteristic energy selected for calculating radionuclide in air. Manjunatha et al. gave the following empirical formula for the mass attenuation
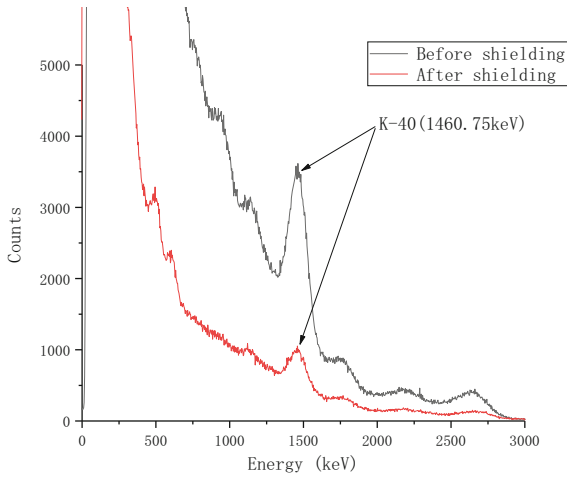
Fig. 3. Comparison of gamma spectrums between the spectrums after shielding and that without shielding with 8000 s measurement

coefficients of the gamma-ray with the energy of 0.1 meV to 20 meV penetrating different substances [10]:

$$\frac{\mu}{\rho_{0.1-20MeV}} = \begin{cases} \frac{1}{\Delta_1 E^{\Delta_2}+\Delta_3}(1 < Z < 17) \\ (\rho_1 E + \rho_2)\rho_3(18 < Z < 24) \\ \frac{1}{\xi_1 \ln(E)+\xi_2}(25 < Z < 30) \\ \frac{\eta_1}{E+\mu_2} + \mu_3(31 < Z < 37) \\ \psi_1 E^{\frac{\psi_2}{E}}(38 < Z < 53) \\ \chi_1 \exp(\frac{\chi_2}{E+\chi_3})(54 < Z < 92) \end{cases} \tag{1}$$

In Formula 1, Z is the atomic number of the materials penetrated by gamma photon. Δ, ρ, ξ, η, Ψ, and χ are nonlinear fitting parameters corresponding to the penetrated substances with different atomic numbers, and some values of them can be found in Table 1.

Shao Qiwei gave the transformation formula of the mass attenuation coefficient of different media when studying the variation rule of point source gamma spectrum in the air [11]:

$$\mu = (\frac{\rho}{\rho_i}) \cdot [\mu_i + (C^3 - 1) \cdot \tau_i + (C - 1) \cdot \kappa_i] \tag{2}$$

In the type $C = \frac{z}{z_i}$, ρ_i is the known density of the elemental substance of an element; μ_i, τ_i, κ_i is the total attenuation coefficient, photoelectric effect attenuation coefficient,

Table 1. Nonlinear fitting parameters of mass attenuation coefficients with the energy of 0.1–20 meV and atomic number of 1–17

Z	Δ_1	Δ_2	Δ_3	R_2
1	0.047982133	0.691880705	2.238642389	0.99
2	0.107417393	0.675949755	4.312357789	0.99
3	0.140243972	0.659953864	4.814931496	0.99
4	0.154706411	0.643613157	4.514027117	0.99
5	0.169836414	0.626296457	4.128023198	0.99
6	0.182339125	0.607519221	3.591093182	0.99
7	0.2128311	0.588115345	3.324194141	0.99
8	0.254511573	0.566099072	2.980792844	0.99
9	0.328662042	0.541807911	2.694584435	0.99
10	0.391679834	0.515722504	2.045656896	0.99
11	0.516585414	0.487557871	1.453406302	0.99
12	0.649524818	0.457794714	0.618606405	0.99
13	0.887895087	0.42549067	−0.380992808	0.99
14	1.169847578	0.391521387	−1.589755847	0.99
15	1.678263885	0.356046899	−3.219101428	0.99
16	2.311611291	0.319734571	−5.060422121	0.99
17	3.459415953	0.283349367	−7.809427731	0.99

and electron pair effect attenuation coefficient of an element elemental with the incident gamma-ray of a particular energy, If $K = (\frac{\rho}{\rho_i}) \cdot (C^3 - 1)\tau_i + (C - 1) \cdot \kappa_i \ K = (\frac{\rho}{\rho_i}) \cdot (C^3 - 1)\tau_i + (C - 1) \cdot \kappa_i$, it can be formulated as:

$$\mu = K \cdot \frac{\rho}{\rho_i} \cdot \mu_i \tag{3}$$

When calculating the air attenuation coefficient in this method, the atomic number of the converted elemental substance must be as small as possible, so this paper adopts the mass attenuation coefficient of Al $(Z = 13)$ for conversion calculation.

In the case of the same elemental substance, the attenuation coefficient μ of the material has the following relationship with 95% attenuation thickness d:

$$\mu = \frac{\ln 20}{d} \tag{4}$$

According to the above formula, the 95% attenuation thickness of gamma rays of given energy in air can be calculated.

Because the 95% attenuation thickness of gamma rays in the air is much larger than the detector size, the detector can be regarded as a point detector. The detection volume of

the detector is the volume of a spherical cone with a height of 95% attenuation thickness and the apex angle of the directional shielding device is taken as the apex angle of the detection volume. Thus, the characteristic energy air attenuation coefficient and 95% attenuation thickness of the nuclides that may be detected are calculated, as shown in Table 2.

Table 2. Air attenuation coefficient and 95% attenuation thickness of the corresponding radionuclide characteristic energy

Radionuclide species	Characteristic energy (keV)	Attenuation coefficient of air (μ, $\times 10^{-5}$)	Attenuate 95% thickness (d, cm)
^{214}Bi	609.31	9.67	33175.64
^{214}Pb	351.92	12.30	26065.98
^{7}Be	477.59	10.80	29815.23
^{208}Tl	2614.53	5.13	62483.13
^{40}K	1460.75	6.60	48559.32

MC method is used to simulate the detection efficiency of each characteristic energy detector, as shown in Table 3:

Table 3. The detection efficiency of each characteristic energy detector is obtained by MC method

Radionuclide species	Characteristic energy (keV)	Detection efficiency of the detector (ε, $\times 10^{-9}$)
^{214}Pb	351.92	7.52
^{214}Bi	609.31	4.27
	1764.49	1.85
^{40}K	1460.75	2.24
^{7}Be	477.59	6.29
^{208}Tl	2614.53	1.52

The detected effective volume can be regarded as a spherical cone, and the formula of gamma-ray measurement for atmospheric radon is established as follow:

$$AC = \frac{S}{\varepsilon \eta V t} \qquad (5)$$

In formula 5, AC is the activity concentration of ^{214}Bi or ^{214}Pb in the atmosphere, and its value is equal to the activity concentration of ^{222}Rn in the atmosphere after equilibrium. S is a net area of the selected characteristic peak; ε is the detection efficiency of

the detector for the selected characteristic energy; η is the branching ratio of characteristic gamma rays; V is the detecting volume of the detector; t is the measurement time. In formula 5, V can be obtained from formula 6:

$$V = \frac{2\pi(1 - \sin\theta)d^3}{3} \tag{6}$$

In formula 6, θ is half of the apex angle of the directional shielding device. d is the thickness of the characteristic gamma-ray exposure rate in the air attenuates to 5% of the incidence.

According to formulas 5 and 6, the activity concentration of radon and its daughters in the atmosphere can be calculated by measuring the gamma spectrum.

2.3   In Situ Measurements

First, a fully enclosed lead chamber was built to measure the background gamma spectrum, and the lower limit of detection of the system was calculated. When the measured radionuclide radioactivity level is close to the background, and the confidence level is 95%, the probability of the first- and second-class errors is 5% ($K_\alpha = K_\beta = 1.645$), and the background and measurement time are the same, the lower limit of detection of radionuclide activity concentration measured by gamma energy spectrum, L_D, can be approximated as:

$$L_D = \frac{4.65}{\varepsilon\eta V}\sqrt{\frac{n_b}{t}} \tag{7}$$

In formula 7, η is the branching ratio of characteristic gamma rays, V is the volume of the sample to be analyzed, ε is the detection efficiency of the gamma-ray omnipotent peak, n_b is the background counting rate in the selected peak region measured within the measurement time t, It includes the unshielded nuclides in the measurement system and its surroundings, the counting rate of interference peak caused by high-energy cosmic rays and the contribution of the continuous spectrum of other high-energy gamma rays in the sample [12].

Subsequently, on-site measurement was carried out. The site selection of this experiment needed to eliminate the influence of tall buildings around the measuring device as far as possible, so the open-air parking lot of a university in Chengdu was selected as the experimental measurement site. There are no tall buildings around the parking lot, and the surrounding environment is empty. In this experiment, the activity concentration of ^{222}Rn in the atmosphere, the atmospheric conditions, temperature, and humidity were measured continuously for 10 days.

Preliminary analysis of the measured spectral line is mainly to check the nuclide belonging to the obvious peak that can be detected in the spectral line, and the results are shown in Fig. 4. From the gamma energy spectrum detected, it can detect ^{214}Pb (351.92 keV), ^{214}Bi (609.31 keV, 1764.49 keV), ^{40}K (1460.75 keV), ^{208}Tl (2614.53 keV), However, the content of ^{7}Be (477.59 keV) is low and cannot be clearly displayed on the spectrum line due to the limitation of NaI(Tl) detector's energy resolution. The measured radionuclides include ^{222}Rn and its daughters to be measured in

this paper, as well as uranium-series, thorium-series, and non-series radionuclides ^{40}K that enter the atmosphere in the form of aerosols due to human production and life, land dust suspension, etc. As can be seen from Fig. 4, in addition to the characteristic energy peaks of ^{214}Pb and ^{214}Bi of ^{222}Rn's daughters, the characteristic energy peaks of 1460.75 keV of nonseries radionuclide ^{40}K and 2614.53 keV of thorium daughter ^{208}Tl can be obtained by this spectrum line measurement.
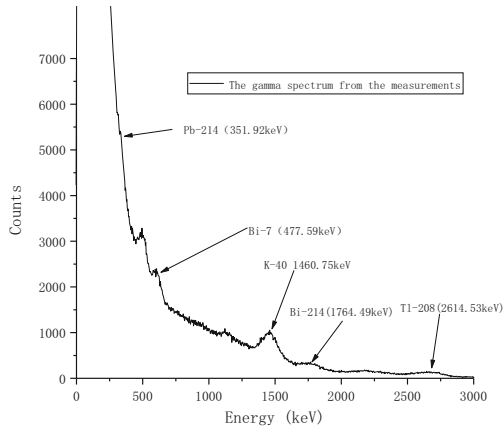
Fig. 4. The measured gamma spectrum line and the characteristic energy peaks of the main nuclides in 1 h

Then the spectra were solved and the activity concentration of ^{222}Rn in the atmosphere was calculated. The RAD7 was used to measure the activity concentration of ^{222}Rn at the same time to compare the results.

The source terms of the uncertainty of the measurement system mainly come from the uncertainty of the counts of gamma photons, the uncertainty of the detecting efficiency, the uncertainty of the detecting volume, the uncertainty of the branching ratio of gamma rays and the uncertainty of the measurement time. As shown in Table 4:

Table 4. The source terms of the uncertainty of the measurement system

The source term of the uncertainty	Counts	Detecting efficiency	Detecting volume	Branching ratio	Measurement time
The value of the uncertainty	$1/\sqrt{S}$	0.005	0.005	0.013	0.00001

The uncertainty formula of radon activity concentration in the atmosphere of this measurement system can be calculated according to the error transfer formula, as shown in formula (8):

$$\mu = \sqrt{(\frac{\partial AC}{\partial S})^2 \delta_S^2 + (\frac{\partial AC}{\partial \varepsilon})^2 \delta_\varepsilon^2 + (\frac{\partial AC}{\partial \eta})^2 \delta_\eta^2 + (\frac{\partial AC}{\partial V})^2 \delta_V^2 + (\frac{\partial AC}{\partial t})^2 \delta_t^2} \quad (8)$$

3   Results and Discussion

The lower limit of detection of the measurement system is 0.29Bq/m^3 with a measurement time of 30 min, and it can be lower as the measurement time increases. At different measuring times, the results of the measurement system and RAD7 radon detector are drawn into a change curve, as shown in Fig. 5.
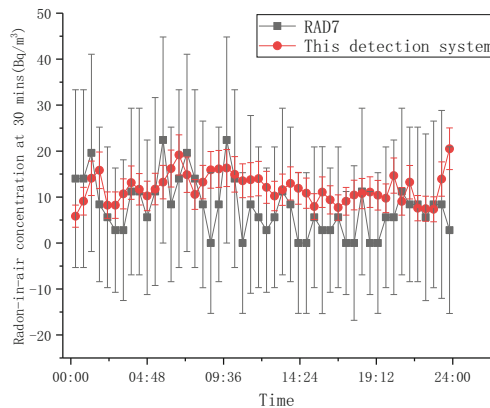
Fig. 5. The measurement data of RAD7 and this measurement system with a measurement time of 30 min

As can be seen from the comparison results in Fig. 5, the radon concentrations measured by this measurement system and the RAD7 have the same variation trend, showing a high concentration at sunrise and a low concentration at sunset. The error range of measurement results is 79.73% smaller on average than that of RAD7. From the above results, it can be seen that this measurement system can realize online measurement and has the advantages of being more convenient and faster.

Draw a line chart of the measurement data obtained by using this measurement system for 3 days, and Fig. 6 is obtained:

In The Sichuan Basin, the inversion layer will form after sunset, and its thickness will continue to accumulate before dawn. When the accumulation of the inversion layer reaches the maximum, atmospheric turbulence will be inhibited, which weakens the mixing effect of radon on the surface in the vertical direction, so the radon concentration reaches the highest point at 6 to 8 o'clock. After sunrise, the sun makes the earth's
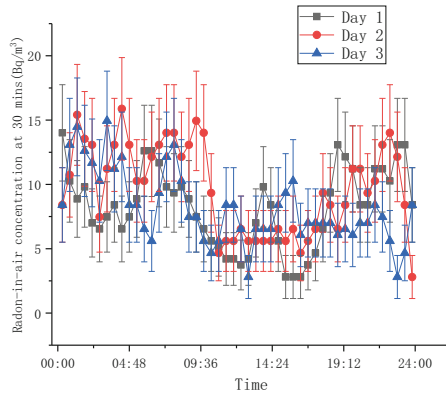
Fig. 6. Radon concentration change curve during 3 days

surface temperature rise faster than the air temperature, which let the inversion layer to be disturbed, and let the mixing and vertical convection of the atmospheric turbulence increase, so in the sunset time (17 to 18 o'clock) meet minimum atmospheric radon concentration near the ground [13, 14]. We can be seen from Fig. 6, that the variation trend conforms to the theory of radon concentration in one day. It shows that the detection system is highly feasible.

4   Conclusions

In this paper, NaI(Tl) detectors were used to measure and calculate the concentration of radon and its daughters in the atmosphere based on the radioactive decay equilibrium principle and gamma-ray attenuation law. Compared with the traditional activated carbon box method using a gamma spectrometer to measure radon and its progeny, the time of collecting activated carbon or filter membrane is saved, which is more convenient and faster.

In order to shield the gamma-rays from the surrounding soil and buildings, we developed a custom lead shielding device with a rotatable direction. Then the effective atmospheric volume of the detector is estimated, and the MC method is used to simulate the detector to obtain the characteristic gamma detection efficiency of the detector for the selected radionuclides. Finally, the atmospheric radon concentration was measured in an open-air parking lot of a university in Chengdu, and the atmospheric radon concentration was calculated according to the established mathematical model of atmospheric radon measurement. The daily variation of the measured radon concentration was preliminarily analyzed, and the theoretical variation trend was consistent with the measured data, which proved the feasibility of the measurement system.

The measured values of low radon concentration in the environment obtained by this measurement system are compared with those obtained by the RAD7 detector. The variation trend of the measured data is basically consistent, and the error range of this method is 79.73% smaller than that of the RAD7 detector on average, which further confirms the feasibility of this measurement system. This measurement system can be

used for on-line monitoring of atmospheric radon concentration. Compared with other measurement methods, its detection limit is lower, its measurement process is shorter, more convenient, and faster.

References

1. Field, R.W., Steck, D.J., Smith, B.J.: Residential radon gas exposure and lung cancer the iowa radon lung cancer study. Am. J. Epidemiol. (2005)
2. Darby, S., Hill, D., Auvinen, A., Barros-Dios, J.M., Baysson, H., Bochicchio, F., et al.: Radon in homes and risk of lung cancer: collaborative analysis of individual data from 13 European case-control studies. BMJ **330**, 223 (2005). https://doi.org/10.1136/bmj.38308.477650.63
3. Iwata, D., Nagahama, H., Muto, J., Yasuoka, Y.: Non-parametric detection of atmospheric radon concentration anomalies related to earthquakes. Sci. Rep. **8**(1) (2018). Accessed 1 July 2022
4. Quanlu, G.: A brief introduction to measurement methods of radon and its daughters. Radiat. Prot. Bull., 35–41 (1994)
5. Ranjbar, A.H., Durrani, S.A.: Scintillator-filled etch-pit method of counting radon-decay alpha tracks, and calibration in a diffusion chamber. Radiat. Meas. **25**(1–4), 757–760 (1995)
6. Nikezic, D., Krstic, D., Savovic, S.: Response of diffusion chamber with LR115 detector and electret to radon and progeny. Radiat. Meas. **44**(9–10), 783–786 (2009)
7. Maozhi, W., Jianliang, Z., Xiaoping, Q., Tao, Y.: The relationship between detection efficiency and setting of instruments for 222Rn, 220Rn measurements with scintillation cell. Nucl. Electron. Detect. Technol., 514–516 (2008)
8. Tan, Y., Tokonami, S., Hosoda, M.: On the calibration of a radon exhalation monitor based on the electrostatic collection method and accumulation chamber. J. Environ. Radioact. **144**, 9–14 (2015)
9. Lian, F., Meng, J.: Research on affecting factors of measuring radon by active carbon box method. Guangdong Trace Elem. Sci. **17**(8), 51–54 (2010). https://doi.org/10.3969/j.issn.1006-446X.2010.08.008
10. Manjunatha, H.C., Seenappa, L., Sridhar, K.N., Sowmya, N., Hanumantharayappa, C.: Empirical formulae for mass attenuation and energy absorption coefficients from 1 keV to 20 MeV. Eur. Phys. J. D **71**(9), 1–22 (2017). https://doi.org/10.1140/epjd/e2017-70679-7
11. Qiwei, S.: Study on the variation of point source γ spectrum in the air (2009)
12. Du, Y.-w., Xiao-dong, X., Qian, W.: Sensitivity analysis of detection limit of atmospheric aerosol nuclide activity concentration by gamma ray spectrum. Sichuan Environ. **35**, 32–37 (2016)
13. Li, L., Ge, L., Cheng, F., Tian, L., Jing, B.: Study on the temporal change of radon concentration. Radiat. Prot., 13–18 (2007)
14. Singh, K., et al.: Variation of radon (222Rn) progeny concentrations in outdoor air as a function of time, temperature and relative humidity. Radiat. Meas. **39**(2), 213–217 (2005)

Numerical Simulation of Flow Boiling Heat Transfer in Helical Tubes Under Marine Conditions

Leqi Yuan[1], Kun Cheng[2(✉)], Haozhi Bian[1], Yaping Liao[1], and Chenxi Jiang[1]

[1] Fundamental Science on Nuclear Safety and Simulation Technology Laboratory, Harbin Engineering University, Harbin, Heilongjiang, China
[2] Science and Technology on Reactor System Design Technology Laboratory, Nuclear Power Institute of China, Chengdu, Sichuan, China
chengkunhrbeu@sina.com

Abstract. Lead-based cooled reactors in most countries and some small reactors at sea use helical tube steam generators. Compared with U-tubes, the convection heat transfer coefficient in the spiral tube is higher, the structure is more compact, and the secondary flow is generated under the action of centrifugal force and gravity, which can achieve the effect of wetting the inner wall of the tube. However, due to the importance of the steam generator in the reactor and the complexity of the flow and boiling in the helical tube, the aggregation behavior of bubbles, the distribution of the two-phase interface and the secondary flow in the tube will significantly affect the heat transfer characteristics, so the gas-liquid phase in the tube is studied. Distribution, changes in heat transfer coefficients, and fluid flow characteristics are very important.

In order to study the boiling heat transfer characteristics of helical once-through steam generators under static and marine conditions to provide safe and reliable energy supply for offshore facilities such as marine floating, this study uses STAR-CCM+ software, VOF method and Rohsenow boiling model to study the heat transfer capacity and flow characteristics of flow boiling in a helical tube under swaying and tilting conditions. The gas-liquid phase distribution characteristics, secondary flow variation characteristics and convective heat transfer coefficient of the fluid under different swing functions and inclined positions are obtained by numerical calculation, and the law of physical parameters changing with the cycle is found. The research results show that the secondary flow and heat transfer capacity in the tube change with the cycle, and the change is most obvious at the tube length of 0.8m. 5% of the normal condition; when the inclination angle is 45°, the maximum increase of the convection heat transfer coefficient is 16.8%, and the maximum decrease is 6.6%.

Keywords: Helical tubes · Ocean conditions · Flow boiling · Secondary flow · Computational fluid dynamics

1 Introduction

The once-through steam generator (OTSG) is a bridge for heat transfer in the primary and secondary circuits of the reactor, which can generate superheated steam, and the

pressure stabilization does not require dehumidification. And compared with the natural circulation steam generator, the structure is more compact, suitable for small spaces such as ships, and has higher maneuverability to achieve rapid power change. Helical tube once-through steam generators are used in many lead-based cooling reactors. Compared with U-shaped tubes, the convection heat transfer coefficient in the spiral tube is higher and the structure is more compact. More importantly, the fluid in the tube produces secondary flow under the action of centrifugal force and gravity, which can achieve the effect of wetting the inner wall of the tube [1–3].

In recent years, with the continuous development of two-phase computational fluid dynamics (CFD) technology, there are more and more studies on the heat transfer model of helical tube once-through steam generators. Kumar V et al. [4] studied the laminar flow of the fluid in the helical tube, and found the non-uniform distribution of the flow velocity in the tube, and obtained its influence on the heat transfer characteristics by changing the placement method of the helical tube. Niu X J et al. [5] used the VOF model to study the fluid flow and heat transfer characteristics of the helical tube under full-side and half-side heating conditions.Chung Y J et al. [6] studied the relationship between the pressure in the helical tube and the dryout, and found that the centrifugal force caused the liquid film to move to the outside of the tube wall and the secondary flow effect was obvious at higher mass flow rates. And the heat transfer coefficient increases with the increase of pressure, but it is not obvious at low mass flow rate. The experimental results are consistent with the experimental results obtained by Styrikovich et al.Yang Yupeng et al. [7] used the fluid-structure interaction model of computational fluid dynamics to simulate the flow and heat transfer characteristics of the helical tube once-through steam generator. The obtained results are compared with Bartolomei's straight-tube boiling experiment and Santini's spiral-tube boiling experiment, and the errors of both are within 25%. And the numerical simulation of the liquid metal on the shell side is verified with the lead-bismuth liquid metal heat transfer experiment of Xi'an Jiaotong University, the Kalish-Dwyer relation and the Schad relation.

Due to the importance of the steam generator in the reactor and the complexity of flow boiling in the helical tube, the aggregation behavior of bubbles, the distribution of the two-phase interface, and the secondary flow in the tube can significantly affect the heat transfer characteristics. So, it is very important to study the gas-liquid phase distribution in the tube, the change of the heat transfer coefficient and the fluid flow characteristics. Under ocean conditions, the force of the fluid in the pipe will change significantly, which may have a significant impact on the heat transfer characteristics. At present, there is a lack of research on the law of fluid flow and boiling in the spiral pipe under ocean conditions. Therefore, based on the CFD method, this paper simulates the heat transfer characteristics of the uniformly heated helical tube under the conditions of swaying and tilting, and studies the variation law of the secondary flow and convection heat transfer coefficient by changing the swaying function and the inclination angle of the helical tube. The parameters such as flow and convective heat transfer coefficients are analyzed to provide a reference for the subsequent research on the heat transfer of spiral tubes under ocean conditions.

2 Numerical Computation Model

2.1 VOF Model

In this paper, the VOF model is used to simulate the fluid. The VOF method is an interface tracking method based on Euler grid. The immiscible fluids use the same set of governing equations. By defining the phase volume fraction α, two or more Simulation of a variety of immiscible fluids, tracking interphase interfaces. Typical applications include the movement of large air bubbles in liquids, jet breakup phenomena, the flow of liquids in the event of a dam break, and transient and steady-state simulations of any gas-liquid interface [8]. The main assumptions of the model are:

(1) Each component fluid is immiscible, incompressible and does not undergo chemical reaction;
(2) Each component fluid flows at the same speed, ignoring interphase slip;
(3) Each component fluid is in a state of thermal equilibrium.

For the VOF model, the fluid flow and energy transfer process follow specific governing equations. These equations are mathematical expressions of the physical properties of the fluid, which determine the simulation process of the CFD software. The following governing equations are used:

(1) Continuity Equation:

$$\frac{\partial\left(\alpha_q\rho_q\right)}{\partial t} + \nabla \cdot \left(\alpha_q\rho_q\vec{V}_q\right) = S_\alpha \tag{1}$$

S_α—quality source term.

(2) Momentum Equation:

$$\frac{\partial(\rho\vec{V})}{\partial t} + \nabla \cdot (\rho\vec{V}\vec{V}) = -\nabla\rho + \nabla \cdot (\overline{\overline{\tau}}) + \rho\vec{g} + \vec{F} \tag{2}$$

where: $\vec{V}$ is the mass average velocity, which satisfies the following relationship:

$$\vec{V} = \frac{\alpha_l\rho_l\vec{V}_l + \alpha_v\rho_v\vec{V}_v}{\rho} \tag{3}$$

(3) Energy Equation:

$$\frac{\partial(\rho h)}{\partial t} + \nabla \cdot (\rho h\vec{V}) = \frac{\partial p}{\partial t} + \nabla \cdot (k_t\nabla T) + (\overline{\overline{\tau}} \cdot \nabla)\vec{V} + S_h \tag{4}$$

The physical parameters such as density, viscosity and specific heat at constant pressure used in the process of solving the steam-water interface in the VOF model

should be the volume-weighted average value, which can be calculated by the following relationship:

$$\rho = \sum_i \rho_i \alpha_i \tag{5}$$

$$\mu = \sum_i \mu_i \alpha_i \tag{6}$$

$$C_p = \sum_i (C_p)_i \alpha_i \rho_i / \rho \tag{7}$$

2.2 Turbulence Model

Considering that the flow in the helical tube is turbulent with high Reynolds number and the possible secondary flow, the realizable K-Epsilon two-layer model is adopted in this paper. The Realizable K-Epsilon Two-Layer Model is a combination of the Realizable K-Epsilon model and the two-layer method, which improves the calculation of swirl and separation flows compared to the standard K-Epsilon model, using two layers The method can significantly improve the calculation accuracy in the low Reynolds number region, and reduce the calculation error caused by the large difference between the viscous bottom layer and the mainstream physical properties in the standard K-Epsilon model [9].

The turbulent kinetic energy and turbulent dissipation rate in this model can be calculated by:

The formula for calculating turbulent kinetic energy:

$$\frac{d}{dt} \int_V \rho k dV + \int_A \rho k(v) \cdot da = \int_A \left(\mu + \frac{\mu_t}{\sigma_k} \right) \nabla k \cdot da \\ + \int_V \left[G_k + G_b - \rho(\varepsilon - \varepsilon_0 + \gamma_M) + S_k \right] dV \tag{8}$$

Calculation formula of turbulent dissipation rate:

$$\frac{d}{dt} \int_V \rho \varepsilon dV + \int_A \rho \varepsilon(v) \cdot da = \int_A \left(\mu + \frac{\mu_t}{\sigma_\varepsilon} \right) \nabla \varepsilon \cdot da \\ + \int_V \left[C_{\varepsilon 1} S \varepsilon + \frac{\varepsilon}{k} (C_{\varepsilon 1} C_{\varepsilon 3} G_b) - \frac{\varepsilon}{k + \sqrt{v\varepsilon}} + S_\varepsilon \right] dV \tag{9}$$

2.3 Boiling Model

In this paper, the Rohsenow boiling model is used to simulate the flow boiling in the tube. The Rohsenow boiling model in STAR CCM+ is combined with the liquid film boiling model, so that the model is suitable for the nucleate boiling stage where the wall temperature is only slightly higher than the liquid saturation temperature. It is also suitable for The high wall temperature results in a liquid film boiling stage in which a continuous film of vapor covers the heated surface. Its empirical relationship is as follows [10]:

$$q_{bw} = \mu_l h_{lat} \sqrt{\frac{g(\rho_l - \rho_v)}{\sigma}} \left(\frac{C_{pl}(T_w - T_{sat})}{C_{qw} h_{lat} Pr_l^{np}} \right)^{3.03} \tag{10}$$

q_{bw} is the wall heat flux in boiling heat transfer, w/m^2;

μ_l is the hydrodynamic viscosity, $Pa \cdot s$;

h_{lat} is the latent heat of vaporization, J/kg;

ρ_l is the liquid density, kg/m^3;

ρ_v is the steam density, kg/m^3;

σ is the liquid surface tension, N/m, The size of the surface tension will affect the shape of the bubble. In the three-dimensional space, the bubble is not strictly a sphere, and the surface tension will reduce the area of the bubble and become closer to a sphere. In this paper, the following relationship is used to calculate the surface tension [10]:

$$\sigma = 0.09537 - 2.24 \times 10^{-6}T - 2.56 \times 10^{-7}T^2 \tag{11}$$

The total correlation coefficient of this formula is 0.9999, which has good correlation with the data and is applicable in a wide temperature range.

C_{pl} is the specific heat of liquid, $J/(kg \cdot K)$;

T_w is the wall temperature, K;

T_{sat} is the Saturation temperature, K;

C_{qw} is the The empirical coefficient determined by the combination of liquid type and wall surface, this paper takes 0.008;

Pr_l is the liquid Prandtl number;

n_p is the Prandtl number index, depends on the working fluid, this paper takes 1.

The steam mass production rate $\dot{m}_{ew}$ at the vaporization core is calculated by the following relation:

$$\dot{m}_{ew} = \frac{C_{ew}q_{bw}}{h_{lat}} \tag{12}$$

C_{ew} is the Model constant for the amount of heat flux required to generate bubbles.

Since the Rohsenow relation does not depend on the fluid temperature and the heat in the computational domain is independent of the fluid temperature, exceeding its applicable range may result in an unrealistically high heat flux, causing the fluid temperature to be higher than the wall temperature. To prevent this, multiply the calculated heat flux by:

$$\max\left[0, \min\left(\frac{T_w - T}{T_w - T_{sat}}\right), 1\right] \tag{13}$$

T is the Fluid temperature near the heated wall.

2.4 Swaying Model Under Ocean Conditions

The equations of motion and dynamics for swaying in ocean conditions are as follows:

$$\begin{aligned} x &= \theta_0 + \theta_m \sin\left(\frac{2\pi t}{T}\right) \\ \omega &= \theta_m \frac{2\pi}{T} \cos\left(\frac{2\pi t}{T}\right) \\ \beta &= -\theta_m \frac{4\pi^2}{T^2} \sin\left(\frac{2\pi t}{T}\right) \end{aligned} \tag{14}$$

where x, ω, β is the distance, angular velocity and angular acceleration, respectively. The centrifugal acceleration of the fluid in the tube is determined by the following relationship:

$$a = \beta \cdot h \tag{15}$$

Among them, a and h are the additional centrifugal acceleration of the fluid and the height of the fluid element from the rotation axis, respectively.

Figure 1 is a schematic diagram of the swing motion under ocean conditions. The main parameters affecting the swing of the spiral tube are the swing cycle, swing height and maximum swing angle.
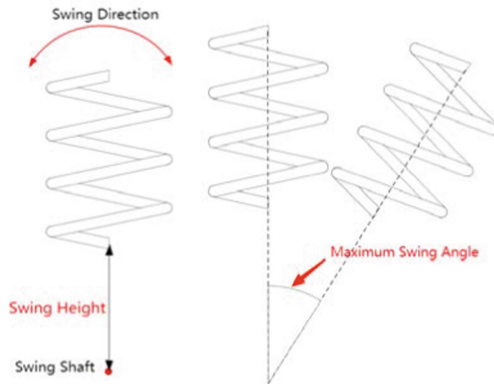
Fig. 1. Swing Motion Model Diagram

3   Validation of Numerical Models

3.1   Boiling Model Validation

Bartolomei (1980) used a vertical circular tube to conduct in-tube flow boiling experiments, and there are perfect experimental data [11], which are easy to use for the verification of the flow boiling model. As shown in the figure below, a model with a pipe diameter of 12.03 mm and a height of 1m is established. The cold water flows through the round pipe from bottom to top and is heated by the pipe wall. The feasibility of the boiling model is verified by comparing the simulated data and experimental data of this model (Fig. 2).

In this paper, two experimental conditions are selected from Bartolomei's experiments, and thermal parameters such as working pressure, inlet temperature and inlet flow rate are determined for simulation to ensure the accuracy of the boiling model. The parameters are shown in the table below.

After verifying the grid independence of the simulated pipe section, the working conditions A1 and A2 in Table 1 are simulated, and the obtained data curve is compared
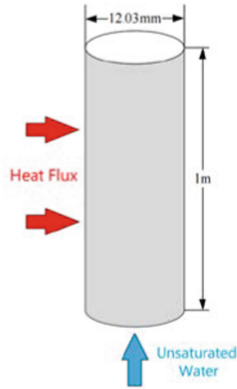
Fig. 2. Schematic Diagram of Test Piece Geometry

Table 1. Bartolomei's Experimental Parameter Table

Condition	P (MPa)	T_{in} (K)	q (MW/m^2)	G_{in} [kg/(m^2·s)]
A1	6.89	495	1.2	1500
A2	6.89	519	0.8	1500

with the circular pipe boiling experiment conducted by Bartolomei. The results are shown in Fig. 3.

The cross-sectional cavitation fraction along the height direction is selected as the monitoring quantity. From the results, it can be seen that the error between the simulated data and the experimental data is larger at 0.65m under the A1 working condition, and the errors at the other positions are smaller; under the A2 working condition, the error before 0.7m is small, and there is a certain error after 0.86m. In general, considering that the current boiling flow formulas in the tube have large errors and cannot obtain very accurate simulation results, it can be considered that the boiling model is reliable for simulating the flow boiling in the spiral tube.

3.2 Helical Tube Mesh Independence Verification

In order to make the used helical tube model have good accuracy and fast calculation speed, the grid-independent verification must be carried out. Taking the operating conditions of a small lead-bismuth fast reactor helical once-through steam generator as the calculation condition [12], and taking it as a modeling reference, the specific thermal parameters are shown in Table 2 below.

The cross-sectional mesh of the spiral tube model used for verification is shown in Fig. 4. The polyhedral mesh generator and the prism layer mesh generator are used. The thickness of the prism layer is 1 mm, the extension of the prism layer is set to 1.5, and the number of prism layers is set to 7, change the base size to change the number of
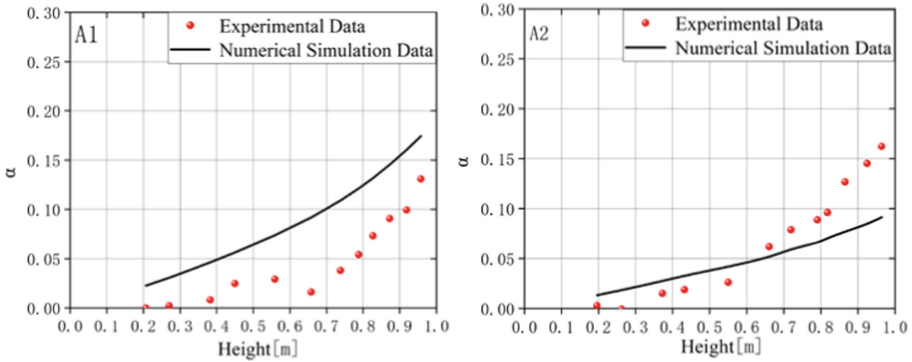
Fig. 3. Comparison between Simulation and Bartolomei's Experimental Data

Table 2. Thermal Boundary Conditions used in the Simulation

Physical Parameters	Symbol	Unit	Value
System Pressure	P	MPa	5.0
Import Temperature	T_{in}	°C	210
Import Speed	v_{in}	m/s	0.665
Heat Flux	q	MW/m^2	0.5

meshes. Monitor the convective heat transfer coefficient at 0.8 m and the cross-section gas content α at the cross-section, and draw the curve of the two with the number of grids, as shown in Fig. 5.

It can be found that when the number of grids is greater than 3×10^6, more stable results can be obtained, and the basic grid size is 0.7 mm.
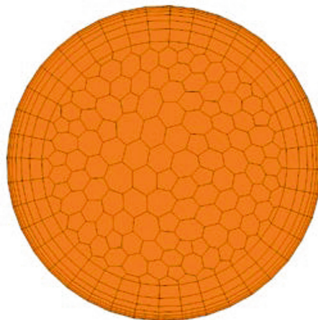
Fig. 4. Grid Schematic
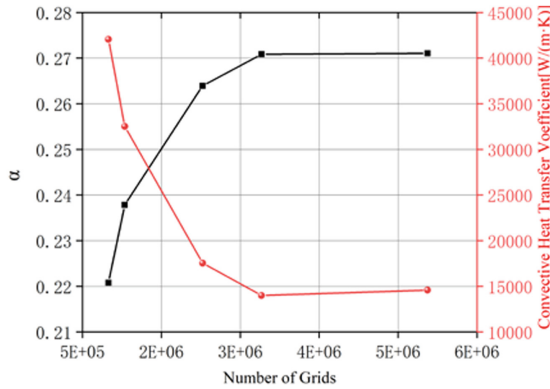
Fig. 5. Mesh Independence Verification of Helical Tubes

4 Analysis of Calculation Results

4.1 Analysis of the Change of Flow Heat Transfer Characteristics with Time

Taking the operating conditions of a small lead-bismuth fast reactor spiral-tube once-through steam generator as the calculation condition, the specific thermal parameters are shown in Table 2 above. The specific motion parameters of the simulated swing motion are shown in Table 3.

Table 3. Swing Motion Parameter Table

Physical Parameters	Symbol	Unit	Value
Swing cycle	T	s	7.0
Maximum Swing Angle	ϕ_m	deg	30
Swing Height	H	m	5.0

In order to avoid the possible instability of the calculation results of the first cycle, take the time cycle from the swing motion to the second cycle to study. Draw the change of the convection heat transfer coefficient of the spiral tube with time under ocean conditions, as shown in the Fig. 6.

It can be found that the three convective heat transfer coefficients change most obviously at about 0.8 m, and the fluctuation range is large. The convective heat transfer coefficient here shows a significant increase and decrease with time. This is because the displacement effect of the liquid phase on the gas phase under the action of the secondary flow is not obvious when the gas content is small, and the secondary flow is less affected by the swing motion when the gas content is large. The gas content here is relatively moderate, which can make the secondary flow change more violently, so the influence of the secondary flow is obviously different.
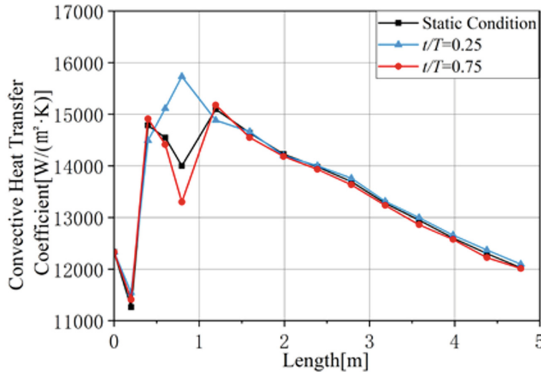
Fig. 6. Convective Heat Transfer Coefficient Curves at Different Times

When t/T is 0.25, the secondary flow is strengthened under the action of swing acceleration, so the convective heat transfer coefficient increases significantly compared with the static state, and the increase range is 12.4%; similarly, when t/T is 0.75, the secondary flow weakened, the convective heat transfer coefficient decreased by 5.0%. At the same time, it can be seen that the convective heat transfer coefficient does not change significantly after the tube length is 2 m, which is because the gas content is higher after 2 m, and the impact of the swing acceleration on the secondary flow is small.

Several circular sections were taken at a pipe length of 0.8 m to observe the change of the secondary flow with the swing motion. As shown in Fig. 7 below, the ratio of the motion time t to the swing cycle T in the second cycle is 0, Secondary flow cloud images at 0.25, 0.5, 0.75 and 1.0:

It can be found from the figure that the secondary flow is the strongest when t/T is 0.25, and the weakest when t/T is 0.75. This is because the acceleration generated by the former's swing motion is in the same direction as the acceleration generated by the fluid's circular motion in the tube, and the combined action of the accelerations strengthens the secondary flow.

In order to further illustrate that the convective heat transfer coefficient and the secondary flow are affected by the ocean conditions, the time-dependent curves of the two at a pipe length of 0.8 m are drawn, as shown in Fig. 8:

In order to observe the effect of the swing motion on the temperature at different times, the pipe wall surface and circular section near the pipe length of 0.8 m were taken. The temperature distributions of the wall temperature and fluid were observed when t/T was 0.25 and 0.75, respectively, as shown in Fig. 9 and Fig. 10 show.

It can be found that the position of the maximum wall temperature at different times has a certain deviation, and the peak position is closer to the upper part when t/T is 0.75. However, the maximum temperature values of the two are basically the same. The maximum temperature of the pipe wall at a pipe length of 0.8 m is 637 °C when the t/T is 0.25 and 0.75, while the minimum temperature of the wall is significantly different, which are 560 °C and 570 °C, respectively.

The temperature cloud map of the fluid circular section shows that the temperature of the fluid does not change much in value, but its spatial distribution changes significantly.
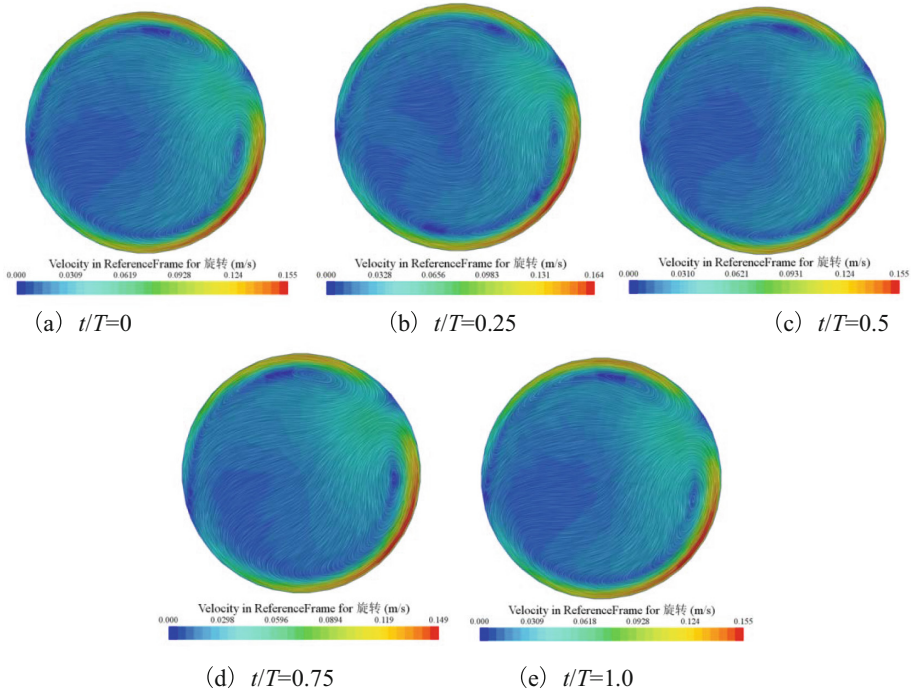
Fig. 7. Cloud Map of Secondary Flow with Time
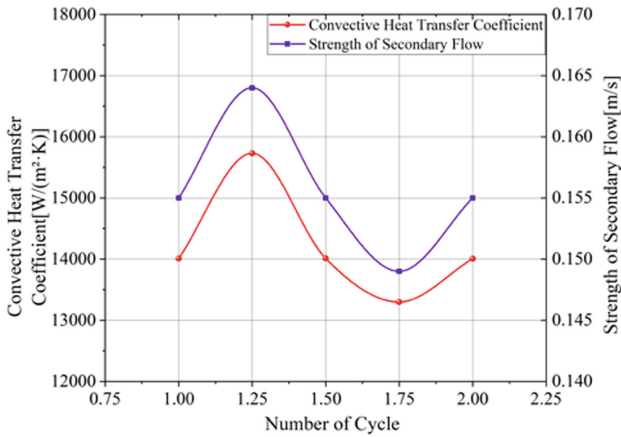
Fig. 8. Convective Heat Transfer Coefficient and Secondary Flow Curve with Time at Pipe Length of 0.8 m

When t/T is 0.75, it is closer to the upper part. This law is consistent with the distribution law of the secondary flow and the peak temperature of the wall.

Draw the curve of the average wall temperature along the length of the pipe with time and its partial magnification, as shown in Fig. 11.

(a) $t/T=0.25$ (b) $t/T=0.75$
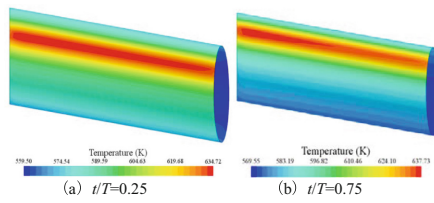
Fig. 9. Cloud Map of Wall Temperature at Different Times

(a) $t/T=0.25$ (b) $t/T=0.75$
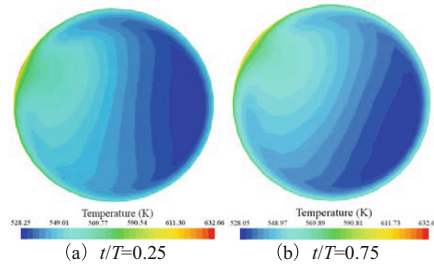
Fig. 10. Cloud Map of Fluid Temperature at Different Times
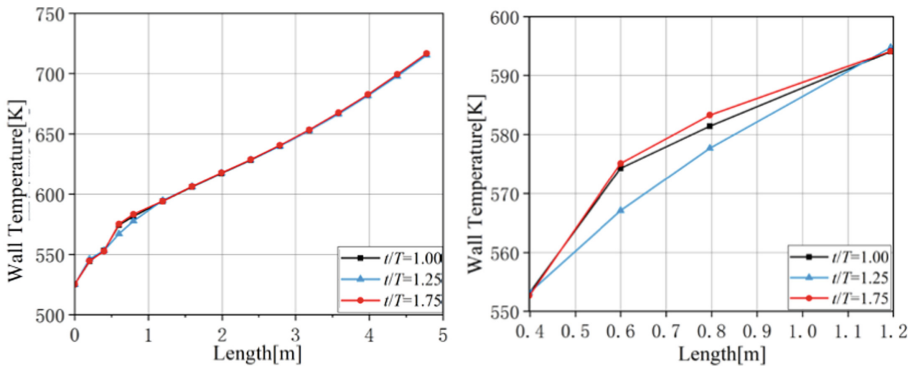
Fig. 11. Wall Temperature Change Curve and Its Partial Magnification

From the laws of Figs. 9, 10 and 11, it can be found that the maximum value of the wall temperature does not change much with time, but the average temperature fluctuates to a certain extent with time. This is because the highest temperature of the pipe wall is located in the secondary flow stagnation zone, and the secondary flow changes have little effect on it. The wall at the lower wall temperature is under the scouring of the secondary flow, and the change of the secondary flow has a significant impact on it, and the temperature change in the lower temperature region is also more obvious. In the

range of tube length from 0.4 m to 1.2 m, when the secondary flow is strong, the wall temperature is lower, and the average temperature drops by 5 °C; when the secondary flow is weak, the average wall temperature is higher, and the average temperature increases by 1 °C.

4.2   Influence of Ocean's Inclination Condition on Heat Transfer Characteristics

The helical tube may be inclined for a long time in marine conditions, and when the spiral tube is inclined, the centrifugal force in some positions will be strengthened by the gravitational component, and some positions will be weakened. This will lead to changes in the secondary flow, which in turn changes the heat transfer performance. As shown in Fig. 12 below, the centrifugal force on the left is weakened by gravity, while the right is enhanced.

The spiral tube was simulated at an inclination angle of 20° and 45°, and the spatial distribution of gas and liquid phases was observed along the circular section of the tube under some working conditions. As shown in Fig. 13 below.
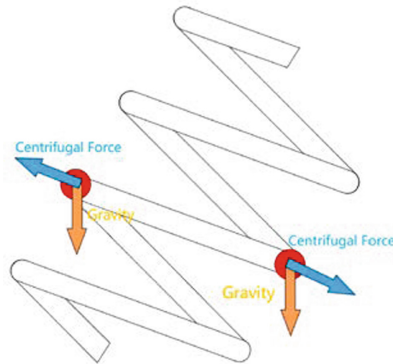
Fig. 12. Force Analysis of Fluid in Spiral Tube in Inclined State

It can be found from the figure that the gas phase of the first section in the state of tilting 45° is carried by the secondary flow, and the gas phase accumulation area is closer to the horizontal axis of symmetry of the tube than the first section without tilt. This is because the swing acceleration at this position is strengthened by the gravitational acceleration component, so the secondary flow is stronger, and the gas phase is carried by the secondary flow to approach the horizontal axis of symmetry.

In the same way, the swing acceleration is weakened by the gravitational acceleration component at the second section position in the state of tilting 45°, and the gas phase is closer to the upper part of the circular section. On the third and fourth sections, the effect of the secondary flow on the distribution of the gas and liquid phases is not obvious due to the high content of the gas phase. The convective heat transfer coefficient distribution curve along the tube length in the inclined state is made, as shown in Fig. 14:

It can be found that at the tube length of 0.8 m, the convective heat transfer coefficient is larger than that of the no-tilt condition due to the enhanced secondary flow due to the

(a) No Tilt

(b) Tilt 45°
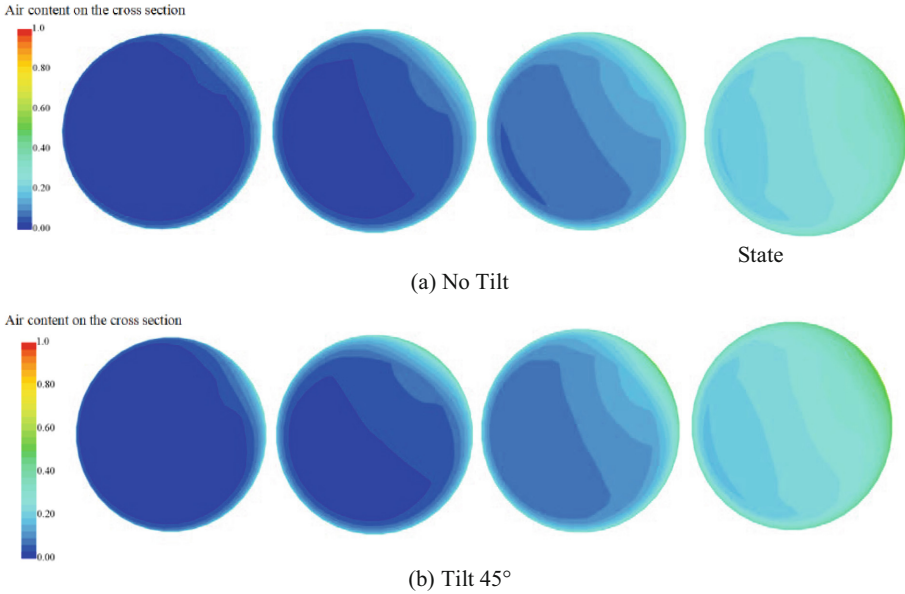
Fig. 13. Gas-liquid Phase Distribution in Inclined State
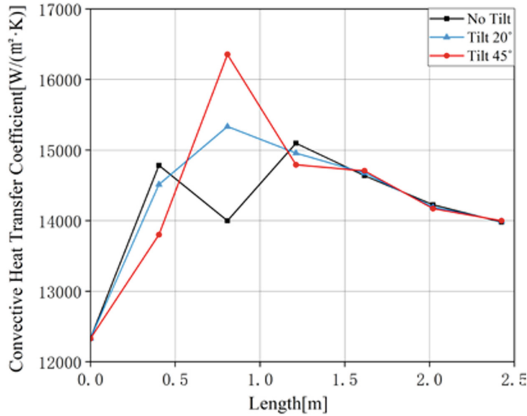
Fig. 14. Convective Heat Transfer Coefficient Curve of Spiral Tube in Inclined State

gravitational acceleration component. Similarly, the reduction of convection heat transfer coefficient can be seen at the tube lengths of 0.4 m and 1.2 m.

And it can be clearly found that the increase or decrease of the convective heat transfer coefficient increases with the increase of the inclination angle. When the inclination angle is 20°, the maximum increase of convection heat transfer coefficient is 9.5%, and the maximum decrease is 1.8%. When the inclination angle is 45°, the maximum increase of convection heat transfer coefficient is 16.8%, and the maximum decrease is 6.6%.

5   Conclusions

In order to study the specific influencing factors of the swing motion on the heat transfer characteristics of the helical tube, simulations were carried out under different swing cycles, maximum swing angles and swing heights, and the exact effects of the three on the heat transfer of the helical tube were verified.

For the inclined working condition, this paper mainly carries out the simulation under the inclined angle of 20° and 45°, and draws certain conclusions according to the distribution of cross-section gas content and the change of convective heat transfer coefficient.

The main conclusions are as follows:

(1) When the swing motion is a sinusoidal function, the curve of the secondary flow intensity at the local position in the pipe also presents a sinusoidal relationship, reaching a maximum value in 1/4 cycle and a minimum value in 3/4 cycle. At the same time, the distribution of gas content in the cross-section also shifted to a certain extent.

(2) The convective heat transfer coefficient of the spiral tube under the swing motion fluctuates with time, and the change is most obvious at the position where the tube length is 0.8 m. However, the convective heat transfer coefficient of the middle and rear pipe sections has little change. This is because the secondary flow is not significantly affected by the swing acceleration when the gas holdup is high, and the convective heat transfer coefficient at the rear position changes less than 1%.

(3) The fluctuation of the secondary flow intensity and the convective heat transfer coefficient with time under the swing motion shows a high degree of consistency, and the increase of the convective heat transfer coefficient at 0.8 m can reach 12.4% of the normal condition, and the reduction is 5% of the normal condition.

(4) The peak value of the wall temperature under the swing motion basically does not fluctuate, but the value at the lower wall temperature fluctuates greatly. When the secondary flow is strong, the average wall temperature is low, and conversely, the wall temperature is high. The main change positions of the wall temperature are concentrated in the tube length of 0.4 m to 1.2 m, and the maximum change temperature reaches 10 °C. At the same time, the position of the wall temperature peak will shift cycleically with the swing motion.

(5) Under the inclined condition, the secondary flow at different positions of the spiral tube is strengthened and weakened respectively, and the convective heat transfer coefficient also changes accordingly. When the inclination angle is 20°, the maximum increase of convective heat transfer coefficient is 9.5%, and the maximum decrease is 1.8%; when the inclination angle is 45°, the maximum increase of convective heat transfer coefficient is 16.8%, and the maximum decrease is 6.6%. When the inclination direction of the spiral tube changes, the change of the convection heat transfer coefficient may also change accordingly.

References

1. Wang, Z.: IEA releases new edition of world energy outlook report.Foreign Nucl. News (12), 2 (2013)
2. Chen, Z.: Thermal-hydraulics Design and Safety Analysis of a 100MWth Small Natural Circulation Lead Cooled Fast Reactor SNCLFR-100. University of Science and Technology of China (2015)
3. Li, Z.Y.: Development and military application of lead-bismuth reactors abroad. Foreign Nucl. News (07), 29–31 (2020)
4. Kumar, V., Nigam, K.D.P.: Numerical simulation of steady flow fields in coiled flow inverter. Int. J. Heat Mass Transf. **48**(23–24), 4811–4828 (2005)
5. Niu, X., Luo, S., Fan, L.L., et al.: Numerical simulation on the flow and heat transfer characteristics in the one-side heating helically coiled tubes. Appl. Therm. Eng. **106**, 579–587 (2016)
6. Chung, Y.J., Bae, K.H., Kim, K.K., et al.: Boiling heat transfer and dryout in helically coiled tubes under different pressure conditions. Ann. Nucl. Energy **71**, 298–303 (2014)
7. Yang, Y.P.: Numerical study of liquid metal helical coil once-through tube steam generator. Atomic Energy Sci. Technol. **55**(07), 1288–1295 (2021)
8. Wu, T.T.: Numerical Simulation of Cross Flow in Microstructure of Gas Diffusion Layer in Proton Exchange Membrane Fuel Cell. TianJin University (2014)
9. Shih, T.H., Liou, W.W., Shabbir, A., et al.: A new k-ϵ eddy viscosity model for high reynolds number turbulent flows. Comput. Fluids **24**(3), 227–238 (1995)
10. Rohsenow, W.M.: A method of correlating heat transfer data for surface boiling of liquids. MIT Division of Industrial Cooporation, Cambridge (1951)
11. Ustinenko, V., Samigulin, M., Ioilev, A., et al.: Validation of CFD-BWR, a new two-phase computational fluid dynamics model for boiling water reactor analysis (2008)
12. Ding, X.Y.: Athermal Hydraulic Model for a Helical Coiled Tube Once Through Steam Generator of Lead Cooled Fast Reactor, pp. 196–206. China Academic Journal Electronic Publishing House (2019). https://doi.org/10.26914/c.cnkihy.2019.047767
13. Wongwises, S., Polsongkram, M.: Evaporation heat transfer and pressure drop of HFC-134a in a helically coiled concentric tube-in-tube heat exchanger. Int. J. Heat Mass Transf. **49**(3–4), 658–670 (2006)
14. Yang, Y., Wang, C., Zhang, D., et al.: Numerical study of liquid metal helical coil once-through tube steam generator. Atomic Energy Sci. Technol. **55**(7), 1288 (2021)
15. Zaman, F.U., Qureshi, K., Haq, I., et al.: Thermal hydraulics analysis of a helical coil steam generator of a small modular reactor. Ann. Nucl. Energy **109**, 705–711 (2017)

Numerical Simulation of the Transient Flow Characteristics and Thermal Stratification Phenomena in the Passive Residual Heat Removal System of NHR-200-II

Yiwa Geng and Xiongbin Liu[✉]

Institute of Nuclear and New Energy Technology (INET), Tsinghua University, Collaborative Innovation Center of Advanced Nuclear Energy Technology, Key Laboratory of Advanced Reactor Engineering and Safety of Ministry of Education, Beijing, China
lxb@mail.tsinghua.edu.cn

Abstract. The NHR-200-II nuclear heating reactor is a multi-purpose small integral pressurized water reactor (iPWR) developed by the Institute of Nuclear and New Energy Technology (INET) of Tsinghua University. The design of NHR-200-II features a reactor core with thermal power of 200MW, in-vessel hydraulically-driven control rods and passive residual heat removal (PRHR) systems, et.al. Passive residual heat removal experiments were conducted in a scaled integral test facility for NHR-200-II. The PRHR experiments in the scaled facility were simulated by a layered RELAP5 system model to study the flow characteristics of the PRHR system in different primary fluid temperatures and different valve states. The phenomenon of reversed flow occurred in some primary heat exchangers in the numerical simulations when the primary fluid temperature was higher than certain level, which was consistent to the experiments. The simulated uneven outlet temperature distribution of the primary heat exchangers was also consistent with the experimental data when the isolation valves for the steam generator was kept open. Thermal stratification effect in the headers of the PRHR system played an important role in the phenomenon of uneven outlet temperature distributions, and the layered RELAP5 model was proven to be an efficient method for preliminary estimation of thermal stratification effect in the headers.

Keywords: NHR-200-II · Passive Residual Heat Removal System (PRHRS) · RELAP5 · Natural Circulation

1 Introduction

Various advanced small modular reactors (SMRs) are currently under development in the worldwide, including the Westinghouse Small Modular Reactor (W-SMR) [1], NuScale [2], SMART (System-integrated Modular Advanced Reactor) [3], mPower [4] and IRIS [5]. NHR-200-II is also a new type of advanced SMR designed by the Institute of Nuclear and New Energy Technology (INET) of Tsinghua University, the NHR-200-II reactor can be a safe, clean, affordable, and less carbon-footprint choice of nuclear power generation

[6, 7], and the reactor can be used for district heating, power generation, process heat, desalination, et al.

NHR-200-II has several engineered safety systems [7]. The passive residual heat removal (PRHR) systems are key part of the safety features of the reactor. A series of passive residual heat removal experiments have been conducted in a scaled integrated test facility for NHR-200-II by INET [8, 9]. To explain the flow phenomenon in the experiments, it was necessary to establish a detailed numerical model to analysis the transient characteristics of the PRHR system in the scaled integral test facility of NHR-200-II.

In this paper, a layered RELAP5 model of the PRHR system was established, numerical simulations with different primary fluid temperatures were carried out, and the simulation results were discussed and compared to the experiments.

2 Design of the PRHRS Test Facility of NHR-200-II

The NHR-200-II reactor has two parallel intermediate circuits, and two parallel PRHR columns are connected to each intermediate circuit. For the sake of simplicity, only one of the PRHR columns was chosen for modeling. The schematic of the PRHR column was shown in Fig. 1. The PRHR column consists of seven primary heat exchanger (PHE) branches, a residual heat exchanger (RHE) branch and a steam generator (SG) branch. A hot header and a cold header that connecting all the branches are arranged above the top of reactor pressure vessel. The seven PHEs are placed inside the reactor pressure vessel, and the RHE is a finned tube heat exchanger that is installed in the air-cooling tower of NHR-200-II. PHEs are connected asymmetrically to the hot header and the cold header by T-shaped junctions, and the steam generator (SG) is connected to the headers by low resistance Y-shaped junctions. The RHE is connected between the hot leg and cold leg of the SG. The pressurizer (PRZ) is placed at the highest location of the loop.

The PRHR column removes heat from the core by three coupled natural circulation loops. The first natural circulation loop is the natural circulation of the primary fluid inside the reactor pressure vessel, the second natural circulation loop is the fluid circulation in the PRHR loop (Fig. 1), and the third loop is the natural circulation of air in the air-cooling tower.

An integral test facility was built to study the characteristics of the PRHR system of NHR-200-II. Design of the test facility was similar to the original PRHR system of NHR-200-II with some exceptions due to site and equipment limitations. The main differences between PRHR system in the integral test facility and the PRHR system of NHR-200-II were:

(1) The PRHR system in the integral test facility was a scaled model, the height ratio is about 1:5, the hydraulic diameter ratio is about 1:3 for most pipes, the system volume ratio is about 1:50, and the thermal power ratio of the integral test facility is about 1:20 to that of the prototype.
(2) Temperature and pressure of the PRHRS of the integral test facility were slightly lower than those of the prototype due to site limitations.
(3) The heat sink of the residual heat exchanger (RHE) in the test facility was water, instead of air in the prototype.
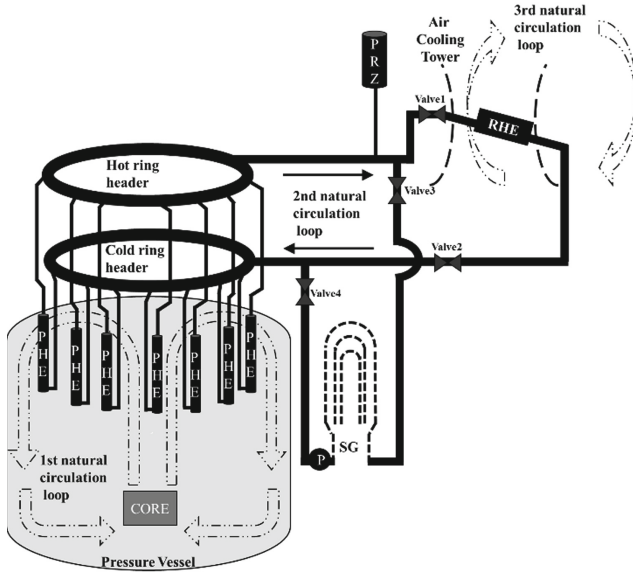
Fig. 1. Schematic Diagram of a PRHR system.

(4) The RHE was a smooth tube-array heat exchanger in the test facility, while the RHE was a finned-tube air cooler in the prototype.

(5) The number of PHE was six for the test facility due to space constraints, while there are seven PHE in the prototype.

The geometry information of key components of the integral test facility is summarized in Table 1.

Table 1. Geometry Information of Key Components in the integral Test Facility of NHR-200-II

Components name	SG	PHE	RHE	Cold ring header	Hot ring header
Elevation (m)	3.05 (center) (951P-953P)	0 (center)	1.427 (center)	2.198	2.432
Hydrulic diameter (mm)	118.0	60.0	76.0	92.0	92.0
Heat transfer area (m2)	9360	39.8	8.09	/	/
Tube/Pipe length (m)	3.79785 (length of heat transfer tubes)	1.6 (length of heat transfer tubes)	2.76 (length of heat transfer tubes)	8.69 (length of the circular pipe)	8.69 (length of the circular pipe)

In the PRHR system of Fig. 1, there are four valves to switch branches, i.e. Valve1 at hot leg of RHE branch, Valve2 at cold leg of RHE branch, Valve3 at hot leg of SG branch, and Valve4 at cold leg of SG branch. The pump of intermediate circuit was located behind the SG outlet, and the pump was used only on normal operating conditions. The PRHR system can be triggered by opening isolation Valve1–2 and closing the Valve3–4. However, possible failure in closing the Valve3–4 should be considered.

A series of scaled PRHR experiments were conducted with the primary fluid temperature kept constant during each experiment. This was achieved by controlling the reactor core at a low but constant fission power, and the core fission power was balanced by adjusting the cooling capacity of the PRHR system, so the primary fluid temperature was kept constant during each experiment.

The following conclusions were made depend on the experiment data:

(1) Reverse flow may occur in some PHE branches, and the heat removal capacity of the PRHR system was significantly lower when reverse flow occurred.
(2) The outlet temperatures of PHE branches were significantly different once the SG branch was not isolated.
(3) The outlet temperature of PHE branches were near equal if the SG branch was isolated.

To explain those observations, transient flow characteristics of the PRHR system was simulated with different combination of valve states (opening or closing) and different primary fluid temperatures.

3 Numerical Model of the PRHRS Test Facility

A REALP5 model was setup according to the geometry and hydraulic parameters of the PRHR system of the scaled integral test facility. The node diagram of the RELAP5 model was shown in Fig. 2. In this diagram, the six primary heat exchangers (PHEs) were named with starting numbers of 1–6, and the cold header and hot header were named starting with numbers 7 and 8 correspondingly.

Unlike other pipe components, the hot and cold headers in the test facility were closed circular pipes, and the pipe diameter of the headers was significantly larger than other pipe components, so possible local recirculation and thermal stratification may occur in the hot and cold headers. To capture the secondary flow phenomena in the headers, a layered model was used for the headers. The layered header model composed of three layers that arranged vertically, and the center layer was connected to its neighborhoods to simulate vertical flow mixing at low flow rates. The schematic diagram of layered model for the headers was shown in Fig. 3.
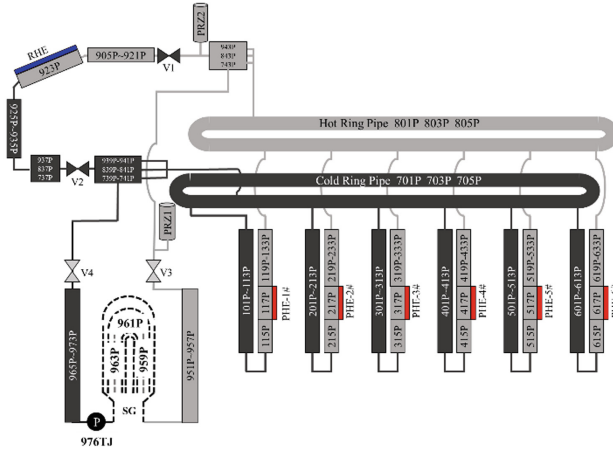
Fig. 2. The Overall Figure of Node Diagram of PRHRS.
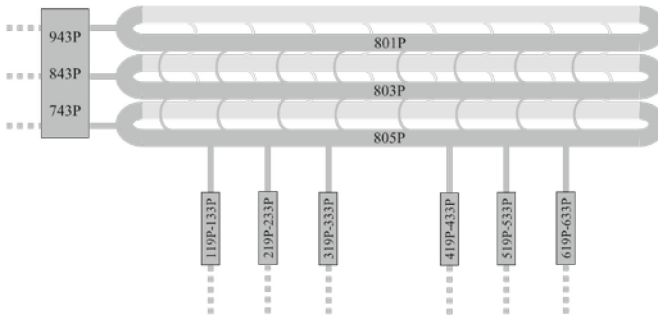
(a) Schematic of the hot header.
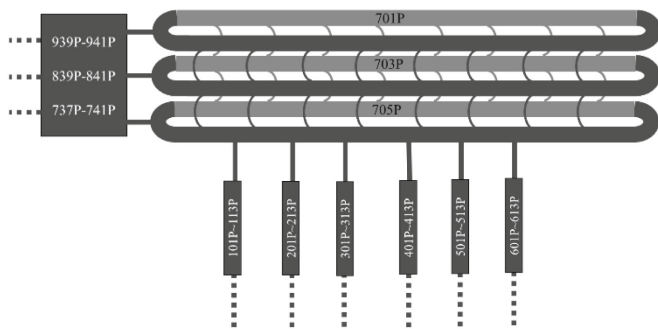
(b) Schematic of the cold header.

Fig. 3. Node Diagram of Hot and Cold Header with Layered Model.

4 Numerical Simulations and Analysis of Results

All numerical simulations were divided into four stages through the control of the target flow rate of pump (976TJ) and the control of the valves of V1 ~ V4.

(1) In the first stage (0–100 s), the PHE and SG branches were put into operation, where the valves of V1 and V2 were closed and the valves V3 and V4 were opened. The SG branch and PHE branches were driven by the pump 976TJ. The mass flow rate of the pump was ramped from zero to a maximum of approximately 32 kg/s. At this stage the pressurizer PRZ1 was put into operation.

(2) In the second stage (100–600 s), the pump 976TJ was gradually stopped but the RHE branch was failed to put into operation (the valves of V1 and V2 were failed to open). The loop was in natural circulation mode between the six PHE branches and the SG branch.

(3) In the third stage (600–2700 s), the RHE branch was successfully put into operation by opening the valves of V1 and V2, however, the isolation valves of V3 and V4 were assumed failing to close in this stage. In this stage, the PHE branches, the PHE branch and the SG branch were all running. The purpose of this stage was to simulate the case of isolation failure of the SG branch.

(4) In the fourth stage (2700–5000 s), the SG branch was switched off by closing the valves of V3 and V4. In this stage, the loop was in natural circulation mode between the six PHE branches and the RHE branch.

The temperatures were set to 298.15 K for the RHE secondary fluid, and 453.15 K for the SG secondary fluid.

15 different primary fluid temperatures in PHEs were set in 15 cases. The primary fluid temperatures simulated were 327.15 K, 353.15 K, 368.15 K, 383.15 K, 398.15 K, 413.15 K, 427.15 K, 443.15 K, 458.15 K, 473.15 K, 488.15 K, 503.15 K, 522.15 K and 527.15 K.

The mass flow rates of each branch during different stage were shown in Fig. 4. The flow directions in Fig. 4 were specified as follows. For PHE branches, the flow rates were positive when fluid flows from cold header to hot header. For the RHE branch and SG branch, the flow rate was positive when the fluid flows from hot header to cold header.

In the first stage (0–100 s), due to the existence of hot and cold headers, the steady-state flow rates of each PHE branch were slightly different (Fig. 5).

In the second stage (100–600 s), as primary fluid temperature increased, the temperature difference between PHE and SG decreased gradually, so the flow rates of each branch decreased gradually (Fig. 6). The stability behavior of the PRHR system depended on the primary fluid temperature. The loop was stable when the primary fluid temperature was lower than 458.15 K, i.e. the SG secondary fluid temperature. The flow rates of PHE branch and SG branch oscillated and gradually decayed to zero when the primary fluid temperature was higher than 458.15 K.

In the third stage (600–2700 s), all the branches of the PRHR system were running, including the SG branch, the RHE branch and the PHE branches.

The PRHR system in this stage was found to be stable as the primary fluid temperature were between 327.15 K and 383.15 K. Steady flow rates of each branch under different primary fluid temperatures were shown in Fig. 7.

The flow rates in each branch of the PRHR system oscillated with decreasing magnitude when the primary fluid temperature is 458.15 K.

The flow rates of each branch of the PRHR system became steady after an initial unstable period for the primary fluid temperature range from 473.15 K to 533.15, and the flow rates of 2#PHE, 3#PHE, 4#PHE and RHE branches were positive, while flow rates of other PHE branches, i.e. 1#PHE, 5#PHE, 6#PHE, were negative (Fig. 8).

In the fourth stage (2700–5000 s), the steam generator was isolated from the PRHR system. The PRHR system became stagnated when the primary fluid temperature was in the range of 327.15 K to 458.15 K. In the primary fluid temperature of 473.15 K to 527.15 K, the flow in the PRHR system became steady-state with reverse flow in some PHE branches (Fig. 9), and the reverse flow occurred in the 1#PHE, 4#PHE, 5#PHE and 6#PHE. The flow rates of each branch increased with primary fluid temperature. The flow rates in the reversed PHE branches were basically the same value, while the flow rates in the positive PHE branches were different (Fig. 9).

Thermal stratification effect in the hot and cold ring headers and corresponding Y-junctions was shown in Fig. 10 and Fig. 11, where the temperature contours of the headers and the Y-junctions were plotted for primary fluid temperature of 522.15 K. It was clearly shown in Fig. 10 and Fig. 11 that the layered header model can capture some detail of local flow phenomena in the headers and Y-junctions, such as thermal stratification or local recirculation.

It was observed in the scaled PRHR experiments that the outlet temperatures of the six PHE branches were significantly uneven if the SG branch was not isolated, while the outlet temperatures were nearly equal if the SG branch was isolated. In the numerical simulations, the phenomenon of uneven outlet temperatures of PHE branches were successfully captured in the third stage (600–2700 s in Fig. 12), and the outlet temperatures of PHE branches were nearly equal in the fourth stage (2700–5000 s in Fig. 12). The numerical simulations agreed the experimental data quantitively.

(a) 327.15K   (b) 353.15K
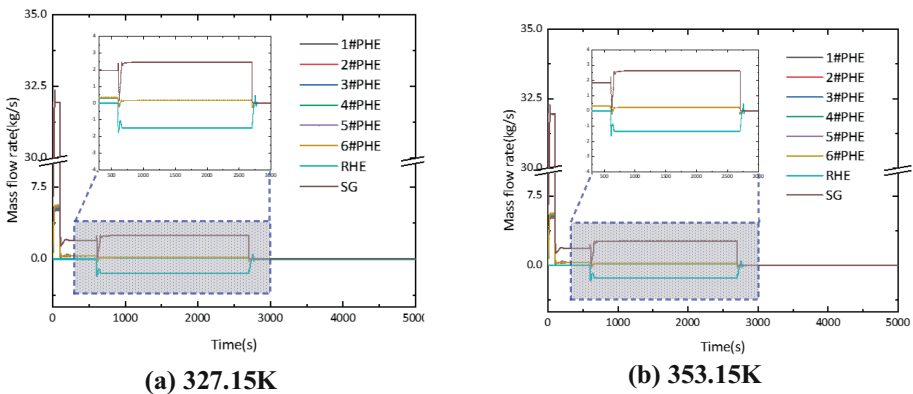
Fig. 4. Mass Flow Rate of Each Branch at Different Primary Fluid Temperature.
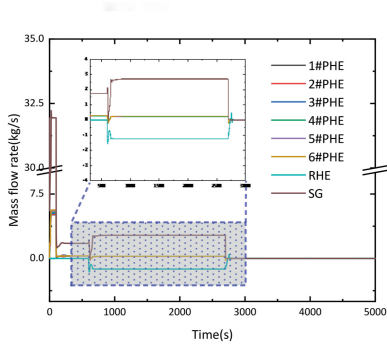
(c) 368.15K
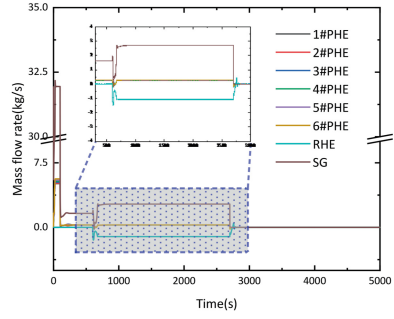
(d) 383.15K
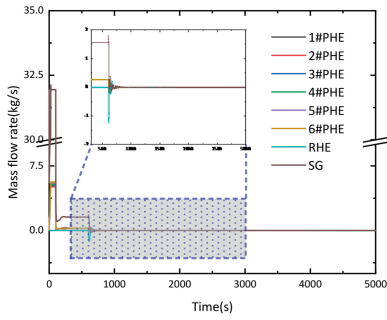
(e) 398.15K
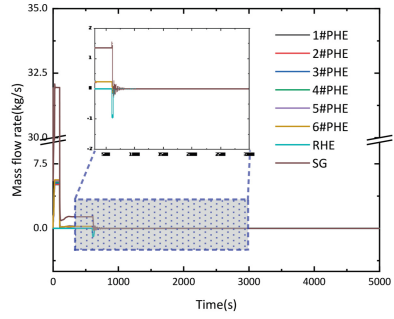
(f) 413.15K
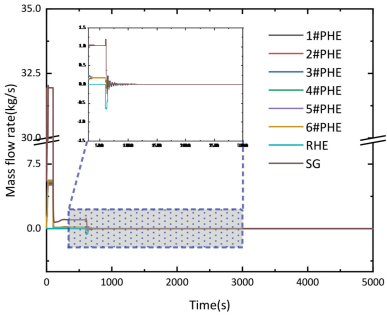
(g) 427.15K
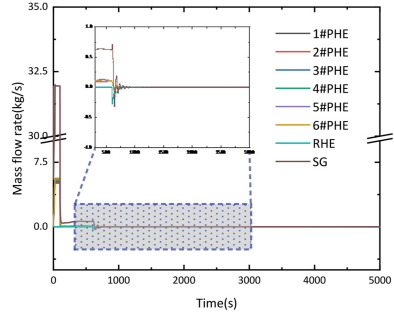
(h) 443.15K

Fig. 4. (*continued*)
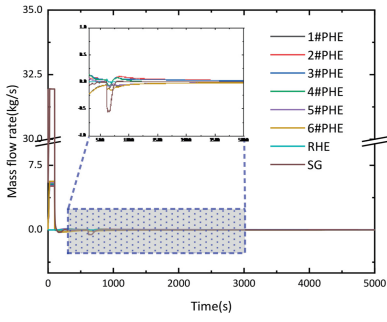
(i) 458.15K
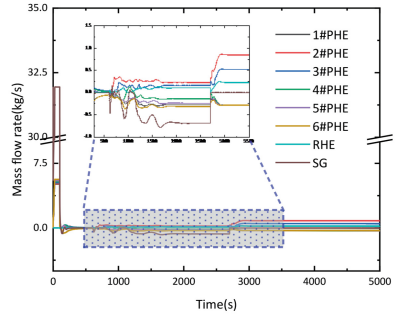
(j) 473.15K
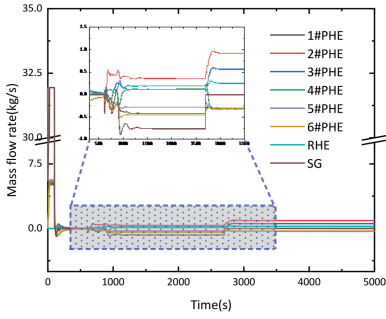
(k) 488.15K
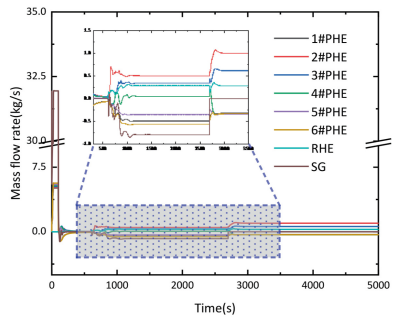
(l) 503.15K
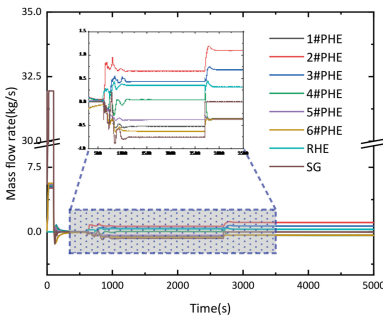
(m) 522.15K
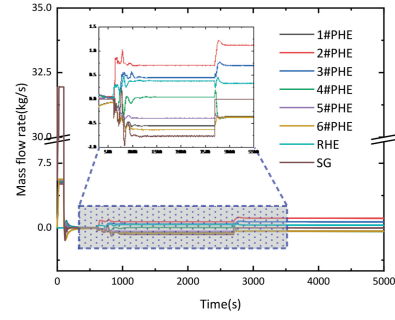
(n) 527.15K

Fig. 4. (*continued*)
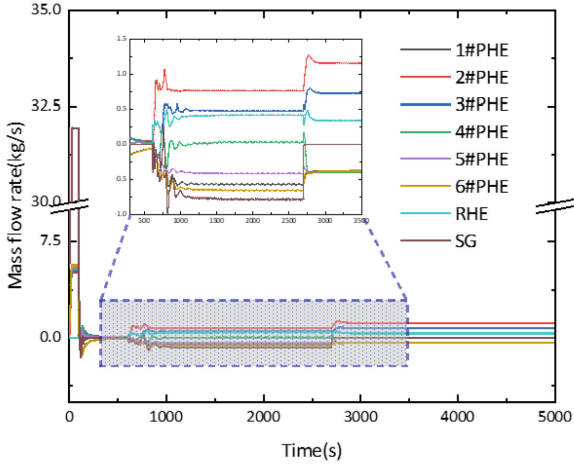
(o) 533.15K

Fig. 4. (*continued*)
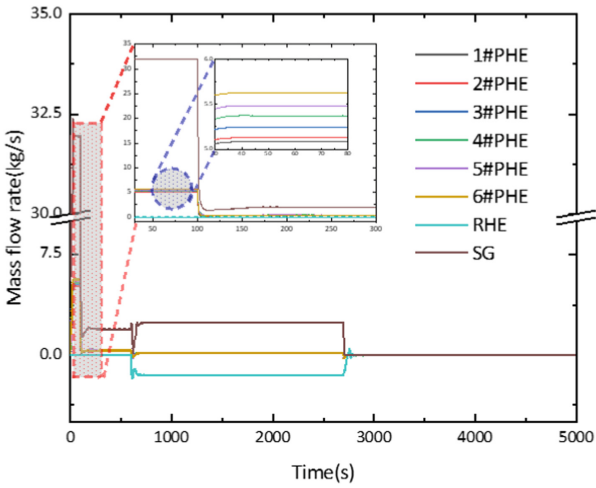
Fig. 5. Mass Flow Rate of Each Branch at Primary Fluid Temperature of 327.15 K.
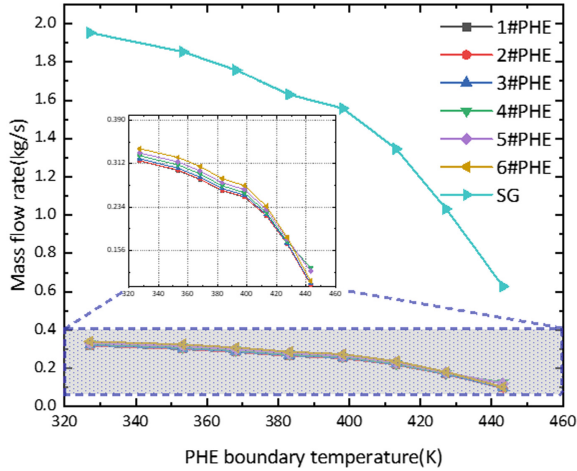
Fig. 6. Steady Mass Flow Rate at the Second Stage (PHE 327.15–443.15K, t = 500.0 s).
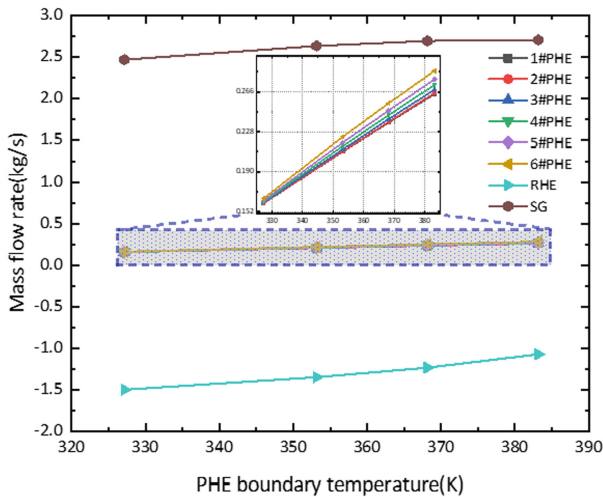
Fig. 7. Steady Mass Flow Rate at the Third Stage (PHE 327.15–383.15 K, t = 2000.0 s).

The uneven outlet temperatures of the PHE branches in the third stage can be explained by the reverse flow in some PHE branches and the thermal stratification effects in the headers. Significant thermal stratification occurred in the third stage, since the fluid from SG branch can flow into the lower part of the cold header or hot header through the low-resistance Y-junctions in the headers. In the fourth stage, since the valves of the SG branch closed, the thermal stratification phenomenon in the headers became insignificant, and the outlet temperatures of PHE branches became the same value.
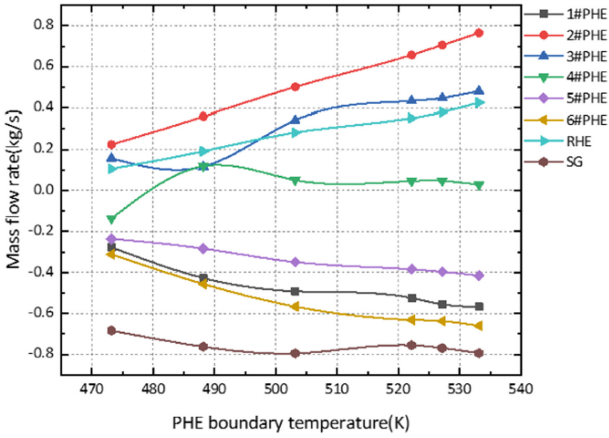
Fig. 8. Steady Mass Flow Rate at the Third Stage (PHE 473.15–533.15 K, t = 2000.0 s).
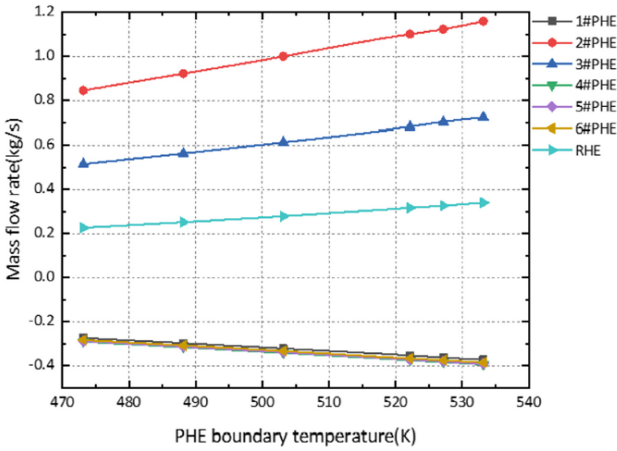
Fig. 9. Steady Mass Flow Rate at the Fourth Stage (PHE 473.15–533.15 K, t = 4000.0 s).
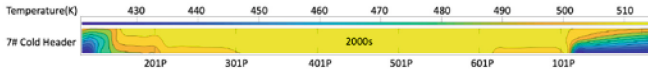
(a)   Temperature of Cold Header -2000s.
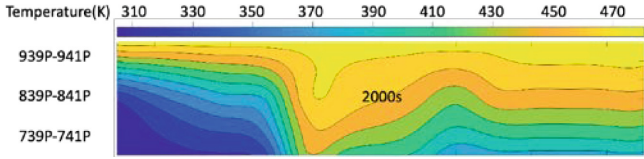
(b) Temperature of Y-Junction of Cold Header
(939P-941P/839P-841P/739P-741P) -2000s.

Fig. 10. Thermal Stratification of Cold Header and Y-Junction.
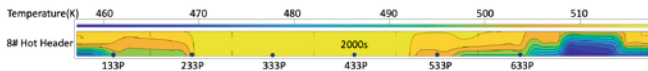
(a) Temperature of Hot Header -2000s.
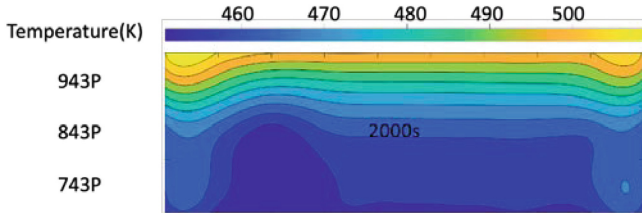
(b) Temperature of Y-Junction of Hot Header
(943P/843P/743P) -2000s.

Fig. 11. Thermal Stratification of Hot Header and Y-Junction.

5   Conclusions

In this paper, a layered RELAP5 model was developed for the PRHR system of a scaled test facility for the NHR-200-II reactor. Numerical simulations were carried for both the PRHR scenario of SG branch isolated and the PRHR scenario of SG branch not isolated. The main conclusions include:

(1) For the case of SG branch not isolated, the numerical simulations shown that the outlet temperatures of all PHE branches were significantly uneven (600–2700 s in Fig. 12), and for the case of SG branch isolated, the outlet temperatures of PHE branches were nearly equal (2700–5000 s in Fig. 12). In both cases, the numerical results were qualitatively consistent with the experimental observations.

(2) The primary fluid temperature has a significant impact on the PRHR system. The phenomenon of reversed flow occurred in some PHE branches when the primary
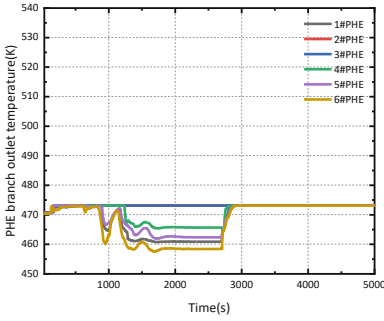
(a) 473.15K
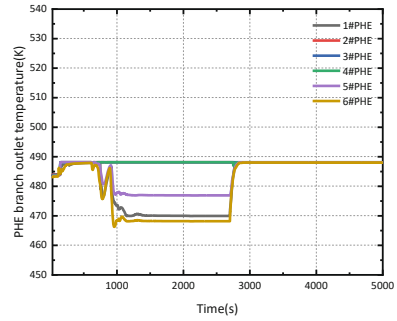
(b) 488.15K
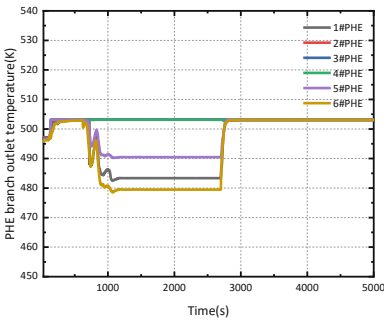
(c) 503.15K
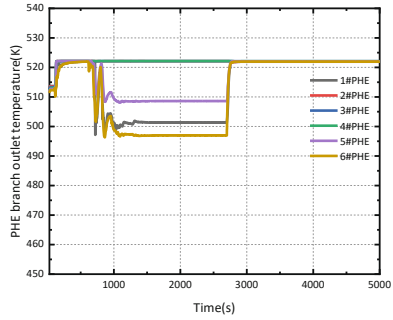
(d) 522.15K
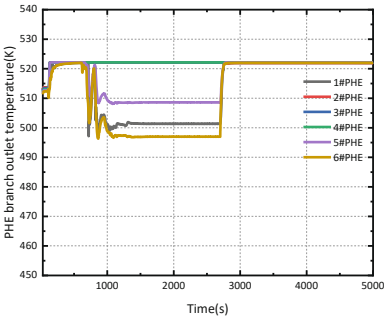
(e) 527.15K
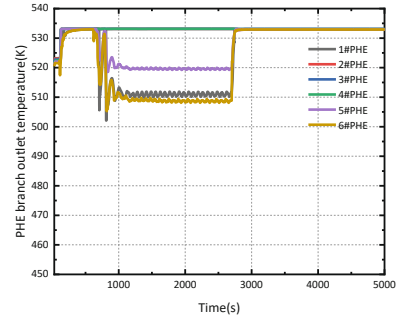
(f) 533.15K

Fig. 12. PHE Branch Outlet Temperature Dispersion (PHE 473.15–533.15 K).

fluid temperature was higher than 473.15 K (Fig. 8 and Fig. 9), which was also consistent with the experiment observations.

(3) The uneven outlet temperatures of the PHE branches when the SG branch was not isolated can be explained by the reverse flow in some PHE branches and the thermal stratification effect in the headers. The layered RELAP5 nodalization for

the hot and cold headers can be used as a preliminary estimation method of the thermal stratification effect, however, detailed 3-dimensional CFD methodology is still necessary to accurately capture the phenomenon of thermal stratification in the hot and cold headers of the PRHR system.

References

1. W (2013) http://www.westinghousenuclear.com/SMR/index.htm
2. IAEA.: Status of Small Medium Sized Reactor Designs. IAEA (2011a)
3. Park, K.B.: SMART design and technology features. In: Interregional Workshop on Advanced Nuclear Reactor Technology for Near Term Deployment, Austria (2011c)
4. IAEA (2011b) http://www.iaea.org/NuclearPower/Downloads/Technology/meetings/2011-Jul4-8-ANRT-WS/3_USA_mPOWER_BABCOCK_DELee.pdf
5. Carelli, M.D., Conway, L.E., Oriani, L.: The design and safety features of the IRIS reactor. In: ICONE11e36564, 11th International Conference on Nuclear Engineering, Tokyo, Japan (2003b)
6. Dazhong, W.A.N.G., Jiagui, L.I.N., Changwen, M.A., et al.: Design of 200MW nuclear heating station. Nucl. Power. Eng. **14**(4), 289–295 (1993)
7. Zhang, Z., Gao, Z., Wang, Y., et al.: Inherent safety of 200MW nuclear heating reactor. Nucl. Power. Eng. **03**, 227–231+255 (1993)
8. Test of Passive Residual Heat Removal System for Low-Temperature Reactor (Internal Technical Report), Institute of Nuclear and New Energy Technology (INET), Tsinghua University, Beijing, China (2018)
9. Xu, Z., Wu, X.: Dynamic analysis of passive residual heat removal system of 200 MW low-temperature nuclear heating reactor. Nucl. Power. Eng. **02**, 61–65 (2008)

Fatigue Analysis Method of Steel Containment of Floating Nuclear Power Plant

Mingxuan Liu[1], Xinyang Fan[1], Danrong Song[2], Bin Zheng[2], and Meng Zhang[1(✉)]

[1] Yantai Research Institute and Graduate School, Harbin Engineering University, Yantai, Shandong, China
zhangmeng@hrbeu.edu.cn
[2] Nuclear Power Institute of China, Chengdu, Sichuan, China

Abstract. Floating nuclear power plant (FNPP) is a movable nuclear power plant built on the floating platform, which can provide clean and stable power for remote coastal areas, and are currently a hot research topic in the field of nuclear power. The steel containment is located in the reactor compartment of the FNPP and it is an important safety guarantee structure. Fatigue and fracture have been an important issue for ship and offshore structures for a long time. Fatigue failure of containment will have serious consequences.

In order to research the fatigue life analysis method of steel containment of the first FNPP in China, the paper adopts miner linear cumulative damage theory and spectral analysis method, based on the American Society of Mechanical Engineers (ASME) standards and relevant standards of China Classification Society (CCS), and uses AQWA to analyze Wave load of FNPP. The hydrodynamic calculation results are imported into finite element model to analyze the structural response of each point of containment, and calibrate the transfer function data of each key point by using the linear system theory and regular wave periodic evaluation method. The fatigue analysis of each point is carried out according to the transfer function and the wave dispersion diagram drawn by the forty years monitoring sea conditions of the working sea area of the FNPP. The result shows that the fatigue life of steel containment is superior and meets the service requirements.

Keywords: Floating nuclear power plant · Containment vessel · Fatigue analysis · Transfer function · Regular wave simulation method

1 Introduction

With the continuous adjustment and optimization of China's energy structure and the continuous promotion of the strategy of strengthening the country through the sea, it is increasingly difficult for traditional fossil energy sources as well as emerging energy sources such as wind, wave and solar energy to meet the energy demand brought by the development of coastal oil and gas resources and islands. Offshore floating nuclear power plant refers to a movable floating marine platform equipped with nuclear reactor and power generation system, which is a product of the organic combination of mobile small nuclear power plant technology and ship and marine engineering technology. As

early as in the 1970 s, researchers in the United States proposed the idea of floating nuclear power plants [1], and the world's first floating nuclear power plant 'Akademik Lomonossov' was also launched in Russia in 2016 [2]. In floating nuclear power plants, a sealed steel containment structure is usually installed to wrap around the reactor and other auxiliary power generation equipment structures to protect the reactor from normal operation as well as to protect the external environment. Compared to traditional onshore containment, the environment and loads on the small steel containment and support structure of an offshore floating nuclear power plant are very different, especially because the complexity of the marine environment leads to more complex loads on the containment and support structure.

The alternating loads caused by these complex sea conditions may cause fatigue damage to the structure and generate cracks, which in turn threaten the safety of the floating nuclear power plant structure and cause the structure to fracture when the cracks expand to a certain extent, resulting in serious accidents. Floating nuclear power plants. However, there are few studies on the fatigue of floating nuclear power plant containment. Therefore, in order to ensure the operational safety of floating nuclear power plants and protect the surrounding personnel and external environment from nuclear radiation, it is important to carry out research on the fatigue assessment method of floating nuclear power plant steel containment in marine environment to ensure the safe operation of floating nuclear power plants during the design life and reduce economic losses.

The current fatigue assessment methods for marine structures can be divided into, simplified algorithm [4], design wave method [5] and direct calculation of spectral analysis method, among which spectral analysis method has the advantages of high accuracy and can reflect the specific structural details of the ship is widely used in the field of marine engineering, previously Hadi and Yang et al. used spectral analysis method for fatigue reliability analysis of marine platforms [6, 7], Zhang et al. used the spectral analysis method to evaluate the fatigue strength of a small waterline surface catamaran [8]. In contrast, in the study of nuclear power system pressure-bearing equipment, the transient method is usually used to assess its fatigue damage because its stress response time course is easily accessible [9, 10].

In this paper, based on the above research, the fatigue reliability study of a type of floating nuclear power plant containment is carried out by combining the spectral analysis method commonly used in marine engineering with the fatigue strength analysis of floating nuclear power plant containment, while referring to ship-related codes and ASME-related codes [11], using the regular wave simulation method.

2 Fatigue Strength Spectrum Analysis Method

2.1 Spectrum Analysis Method

The FNPP has a complex working environment and is subjected to the combined action of wind, wave and current. The main part of the fatigue load that causes the fatigue failure of the containment structure of the FNPP is the wave load. The key points of evaluating the fatigue strength of the containment of FNPP are the selection of wave spectrum, the calculation of transfer function and the calculation of fatigue damage.

Spectrum analysis method is a commonly used method in ship and ocean engineering to study load and structural response. Its theoretical basis is the linear system transformation in random process theory. The method firstly obtains the power spectral density function (PSD) of the structural stress response, after that establishes the relationship between the stress response power spectral density function and the rain flow stress range distribution, and then selects a suitable S-N curve and Miner cumulative damage theory to calculate the fatigue damage of the structure (Fig. 1).
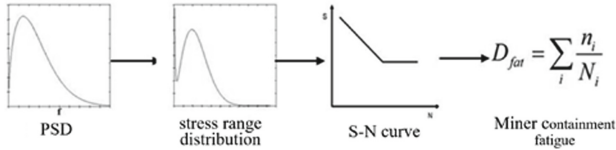
Fig. 1. Fatigue analysis flow

The FNPP can be regarded as a typical dynamic system in ships and offshore engineering structures. The wave process a acting on the hull is the input of the system, and the alternating stress B caused by the wave action in the structure is the response of the containment. In general, the relationship between the response process of the containment and the wave load input process of the FNPP can be written as:

$$X(t) = L[\eta(t)] \tag{1}$$

where, B represents the operator that transforms C into D. When e is a linear operator, the system is linear.

In the fatigue analysis of ship structure, the calculation of wave load and structural response are based on linear theory. Under this condition, if the wave is a stationary random process, the alternating stress obtained by transformation is also a stationary random process. According to the random process theory, there is the following relationship between the power spectral density functions of two stationary random processes:

$$G_X(\omega) = |H(\omega)|^2 \cdot G_\eta(\omega) \tag{2}$$

In function (2), $H(\omega)$ is a transfer function or frequency response function of linear dynamical system. $|H(\omega)|^2$ is response amplitude operator (RAO).

The physical meaning of $H(\omega)$ is the ratio of the amplitude of the response process to the amplitude of the input process when the linear dynamic system vibrates with a circular frequency of ω.

2.2 Wave Spectrum

For the spectral analysis method for fatigue assessment of ship structures, since the FNPP is located in a shallow water depth and the wave dispersion diagram is the joint distribution of meaningful wave height and spectral peak period, the improved JONSWAP spectrum is selected for analysis, and its expression is as follows:

$$S(f) = \beta_J H_{\frac{1}{3}}^2 T_P^{-4} f^{-5} \exp[-\frac{5}{4}(T_P f)^{-4}]\gamma^{\exp[-(\frac{f}{f_P}-1)^2 / 2\sigma^2]} \tag{3}$$

In function (3):

$$B_J = \frac{0.06238}{0.23 + 0.0336\gamma - 0.185(1.9 + \gamma)^{-1}}[1.094 - 0.01915 \ln \gamma]$$

γ is the crest factor, mean value is 3.3.

σ is the peak shape parameter. When the frequency is on the left side of the maximum value point, it is taken as 0.07, and when the frequency is on the right side of the maximum value point, it is taken as 0.09.

2.3 Regular Wave Simulation Method

The transfer function is determined by the system through experiments under the action of rule input or random input, or by the system's theoretical analysis of rule input. Based on the regular wave test method in the pool test, we propose the regular wave simulation method, that is, using the wave load calculation program to obtain the response of the ship motion and external hydrodynamic pressure of a series of regular waves arranged according to a certain initial phase interval under the heading angle and circular frequency. The external hydrodynamic pressure and various inertial forces related to the motion of the hull are applied to the finite element model of the hull structure to obtain the stress response. For the stress response of a series of regular waves under the heading angle and circular frequency, the maximum stress response at the point is fitted by Fourier transform, and the stress amplitude of the heading angle and circular frequency can be obtained. The value of the transfer function under the heading angle and circular frequency can be obtained by comparing the obtained stress amplitude with the wave amplitude.

2.4 Fatigue Cumulative Damage Calculation and S-N Curve

After obtaining the damage caused by each cycle, the selection of a suitable fatigue accumulation damage theory is also one of the core elements of fatigue calculation. The S-N curve and the fatigue cumulative damage analysis method of linear cumulative damage theory are commonly used to evaluate the fatigue of structures in the codes of classification societies of various countries.

When the fatigue load spectrum is expressed as a continuous probability density function corresponding to a certain period of time, the fatigue cumulative damage degree can be expressed as

$$D = \int_L \frac{dn}{N} = \int_0^\infty \frac{N_L f_S(S) dS}{N} = N_L \int_0^\infty \frac{f_S(S) dS}{N} \tag{4}$$

S is the stress range, is the probability density function of the stress range distribution, is the number of cycles required to achieve fatigue failure under a single cyclic load with a stress range of, is the total number of cycles of the internal stress range during the whole time period considered, is the number of cycles of the included stress range, and represents the integral of the whole time interval considered. According to the cumulative damage theory, when the damage degree is accumulated, the fatigue failure of the structure will occur.

The S-N curve is often used to reflect the relationship between the stress range S and the number of cycles required for the structure to achieve fatigue failure under a single cyclic load at the level of the stress range, i.e. the fatigue life n. It is generally obtained by fitting the fatigue test results. A large number of research results show that under a given stress range s, the discrete type of the parameter m is small and can be regarded as a certain value, the fatigue life n and parameter a should be treated as random variables, and it is generally considered that n obeys lognormal distribution. Expressed as

$$NS^m = A \tag{5}$$

Take logarithm on both sides of the equation

$$\lg N + m \lg S = \lg A \tag{6}$$

Equation (6) is a commonly used double log-linear model of the S-N curve. The small steel containment material studied in this paper is Steel-SA-738Gr.b. Therefore, the parameters are referred to the appendix of ASME BPVC Volume III [11].

The tensile strength of Steel-SA-738Gr.b is 585-705mpa. According to the S-N curves, the S-N curve of the material can be obtained by interpolation. The curve is transformed into a double logarithmic linear form, taking m = 3 and a = 11.464.

3   Containment Fatigue Strength Analysis

3.1   Hydrodynamic Analysis

The structural hydrodynamic model is shown in Fig. 2. The right-hand rectangular coordinate system is used. The origin is taken at the intersection of the intersection line of the longitudinal section and the middle transverse section of the platform and the base plane. The X axis is the longitudinal axis, and the point from the tail to the head is positive; Y-axis is the transverse axis, and it is positive from the centerline to the port; The z-axis is the vertical axis, and upward from the base is positive.

For model hydrodynamic analysis, AQWA software is used for hydrodynamic analysis of FNPP. During frequency domain hydrodynamic calculation, the minimum frequency of each wave direction is set at 0.01592 Hz and the maximum frequency is set at 0.27 Hz, with a total of 50 frequency points.

The frequency response curve of the longitudinal bending moment of the middle hull cross-section (x = 0.328 m cross-section) of the reactor bay at 0° wave incidence angle is shown in the following Fig. 3:
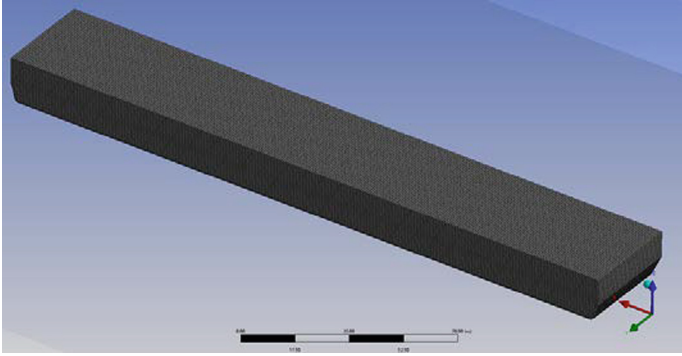
Fig. 2. Hydrodynamic model of FNPP.
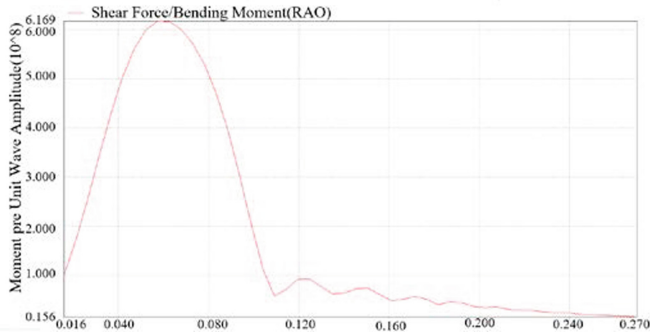
Fig. 3. Frequency response curve of longitudinal bending moment (0° wave incidence angle)

Taking 0° wave incidence angle as an example, it can be seen from the calculation results that the peak longitudinal bending moment in the transverse section of the hull in the middle of the stack is about $6.169*10^8$ N*m under 0° wave incidence angle and unit wave amplitude, and the corresponding wave frequency is 0.0574 Hz. Another longitudinal bending moment value at the waistline is $3.425*10^8$ N*m corresponding to the wave frequency of 0.03147 Hz, and the longitudinal bending moment value is $3.035*10^8$ N*m corresponds to a wave frequency of 0.0937 Hz.

3.2 Selection of Fatigue Damage Assessment Points

The finite element model of the FNPP structure is constructed with shell181 and beam188 elements. The mesh size of the bottom and supporting parts of the containment is 0.1 M, the mesh size of the upper part of the containment is 0.2 m, and the mesh size of the rest parts is 0.8 m. The total number of elements on the ship is about 1.56 million. The finite element model of the containment is shown in Fig. 4.
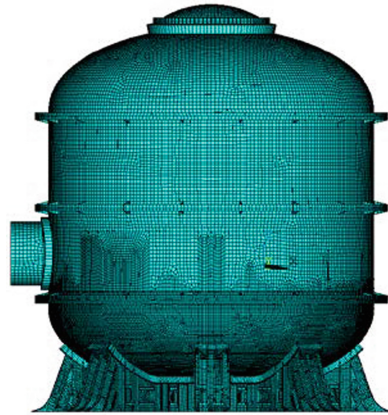
Fig. 4. Structural finite element model.

Since the spectrum analysis method needs to superimpose all working conditions and the number of structural finite element nodes is very large, according to the hydrodynamic calculation results and the longitudinal bending moment diagram, the wave load files of 0.03147 Hz, 0.0574 Hz and 0.0937 Hz in all wave directions are selected to be loaded on the whole ship finite element model of the FNPP without preload and hydrostatic pressure, and the calculation results are obtained. Select the stress concentration node as shown in Table 1:

A local refinement of the grid near the evaluation point of the model is shown in Fig. 5.

3.3   Fatigue Life of Containment

Wave scatter diagram is a common method to describe the marine environment in ship and ocean engineering. Table 2 shows the monitoring data of the nearby platform in the sea area where the floating nuclear power plant works. In the table, H_s denotes the meaningful wave height and T_p denotes the spectral peak period.

The long-term distribution of the stress range within the design life of the FNPP containment can be obtained from the short-term distribution combined with the distribution of various sea conditions that may be encountered in operation. In a given sea state, the ship may sail in any course. In the calculation, several courses are divided, and it is assumed that the probability of each course is equal.

The FNPP can set a course every 15° from 0° to 360° in the marine environment. There are 24 courses in total, and the probability of each course angle is 1/24. In order to simplify the calculation, the FNPP, as a symmetrical structure, can simplify the structural response caused by the symmetrical course. Therefore, in the actual calculation, take a course every 15° from 0° to 180°, a total of 13 courses, of which the probability of 0° and 180° is 1/24, and the probability of other courses is 1/12 (Fig. 6).

Therefore, in the regular wave experimental simulation method, AQWA software is used to calculate the response of hull motion and external hydrodynamic pressure

(a)Refined finite element mesh at point 1

(b)Refined finite element mesh at point 2

(c)Refined finite element mesh at point 3

(d)Refined finite element mesh at point 4

(e)Refined finite element mesh at point 5

(f)Refined finite element mesh at point 6
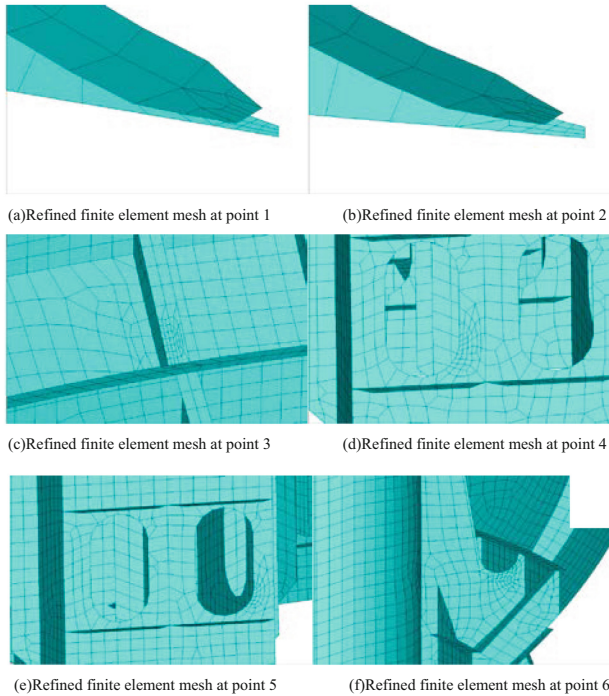
Fig. 5. Finite element refinement mesh
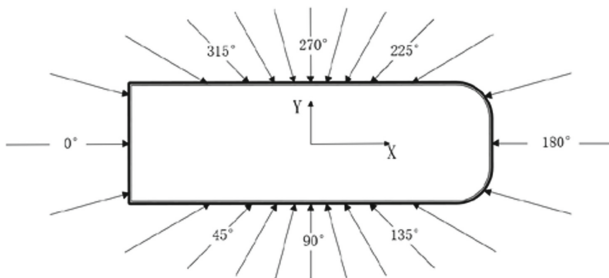
Fig. 6. Schematic diagram of wave incidence angle.

of a series of regular waves with unit wave amplitude of 1 at each heading angular circular frequency arranged at a certain initial phase interval, the phase is taken as 0° to 360° with 45° interval, 8 regular waves at each wave direction frequency, and the wave load file is extracted. The wave load is the wave surface pressure, and the wave surface pressure is mapped to the wet surface of the hull to calculate the structural response. The structural response is the response of the structure under the action of unit wave amplitude. The maximum stress value at each calculation point acting on the top of the FNPP containment is extracted and fitted using the fast Fourier transform (Fig. 7), and

the stress response transfer function is obtained by dividing the magnitude of the two trigonometric functions.

Since the unit wave amplitude is 1, the fitted resulting amplitude is the stress response transfer function.
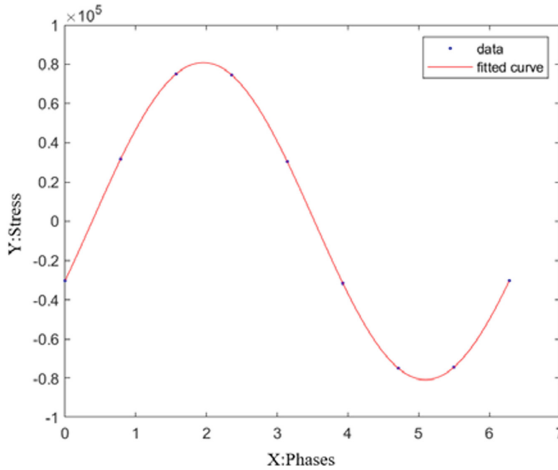
Fig. 7. Fitted curve of stress response of evaluation point 4 at 0° wave direction 0.26451 Hz.

Under the above conditions, the long-term distribution of the stress range can be expressed as a weighted combination of short-term distributions, and its distribution function is Eq. (7)

$$F_S(S) = \frac{\sum\limits_{i=1}^{n_s} \sum\limits_{j=1}^{n_H} v_{ij} \cdot p_i \cdot p_j \cdot F_{s\theta ij}(S)}{\sum\limits_{i=1}^{n_s} \sum\limits_{j=1}^{n_H} v_{ij} \cdot p_i \cdot p_j} = \sum\limits_{i=1}^{n_s} \sum\limits_{j=1}^{n_H} r_{ij} \cdot p_i \cdot p_j \cdot F_{s\theta ij}(S) \qquad (7)$$

In Eq. (7),n_S is the total number of sea states in the sea state distribution data, n_H is the total number of divided courses, p_i is the probability of occurrence of the i-th sea state, which can be obtained according to the frequency of occurrence of each sea state in Table 3;p_j is the frequency of occurrence of the j-th heading. v_{ij} is the average zero crossing rate of stress alternating response under the i-th sea state and the j-th heading.v_0 is the total average zero crossing rate of stress response considering all sea conditions and heading.

$$v_0 = \sum\limits_{i=1}^{n_s} \sum\limits_{j=1}^{n_H} v_{ij} \cdot p_i \cdot p_j \qquad (8)$$

Table 1. Fatigue damage point calculation number and location.

Evaluation point	Location
1	Containment bottom support
2	Containment bottom support
3	T-section at bottom of containment
4	Containment bottom support
5	Containment bottom support
6	Containment pressurizer reinforcing rib

3.4 Containment Fatigue Life Correction

In addition to the influence of marine environmental load on the structure, the marine environmental conditions also have a great impact on the fatigue performance of materials, mainly in the form of corrosion. *Fatigue strength guide for hull structures (2021)* of CCS [12] stipulates that for the normal bending stress of hull girder during simplified stress analysis and the hot spot stress under overall load conditions during finite element stress analysis, the corrosion correction factor $f_{cl} = 1.05$;

For the bending normal stress under lateral load in simplified stress analysis and the hot spot stress under local load in finite element stress analysis, the corrosion correction factor $f_{cl} = 1.1$.

In the direct calculation method of fatigue assessment, the fatigue safety factor needs to be superimposed for calculation. In this regard, *GUIDELINES FOR FATIGUE STRENGTH ASSESSMENT OF OFFSHORE ENGINEERING STRUCTURES (2013)* of CCS provides relevant provisions [13].

Fatigue failure criteria can be based on fatigue damage or fatigue life. When based on fatigue damage, the fatigue strength of the calculated point shall meet Eq. (9)

$$D \leq \frac{1.0}{S_{ftg}} \tag{9}$$

D-- Fatigue damage degree;

S_{ftg}-- Fatigue strength safety factor.

The fatigue safety factor of the small steel containment of the FNPP is selected by reference to the fixed floating structure. The fatigue damage assessment location is accessible for inspection and maintenance in a dry environment, and the failure consequences are serious. Considering the special nature of the small steel containment of FNPP, we select 5 as the fatigue safety factor. Therefore $D \leq 0.2$.

See Table 4 for the cumulative fatigue damage degree and the corrected fatigue life of the final six fatigue assessment points of the containment.

T_1 is fatigue life considering corrosion correction factor/year.

T_2 is the fatigue life considering the fatigue safety factor and corrosion.

Table 2. Wave Dispersion

	Spectral Peak period – Tp(s)														
Hs(m)	0–1	1–2	2–3	3–4	4–5	5–6	6–7	7–8	8–9	9–10	10–11	11–12	12–13	13–14	14–15
0.0–0.5	0.094 (1)	1.836(2)	6.383(3)	11.998(4)	1.508(5)	0.665(6)	0.290(7)	0.018(8)	0.005(9)	0.002(10)	0.005(11)	0.012(12)	0.014(13)	0.018(14)	0.026(15)
0.5–1.0	0	0	0	7.584(16)	27.675(17)	4.405(18)	1.220(19)	0.144(20)	0.003(21)	0	0	0	0	0	0
1.0–1.5	0	0	0	0.193(22)	6.793(23)	10.673(24)	2.290(25)	0.043(26)	0.008(27)	0.001(28)	0	0	0	0	0
1.5–2.0	0	0	0	0.005(29)	0.119(30)	3.580(31)	4.138(32)	0.248(33)	0.003(34)	0	0	0	0	0	0
2.0–2.5	0	0	0	0	0.020(35)	0.112(36)	2.874(37)	0.933(38)	0.002(39)	0	0	0	0	0	0
2.5–3.0	0	0	0	0	0	0.021(40)	0.452(41)	1.566(42)	0.028(43)	0	0	0	0	0	0
3.0–3.5	0	0	0	0	0	0	0.012(44)	0.740(45)	0.253(46)	0	0	0	0	0	0
3.5–4.0	0	0	0	0	0	0	0	0.132(47)	0.426(48)	0.012(49)	0	0	0	0	0
4.0–4.5	0	0	0	0	0	0	0	0.004(50)	0.164(51)	0.135(52)	0	0	0	0	0
4.5–5.0	0	0	0	0	0	0	0	0	0.008(53)	0.054(54)	0.004(55)	0	0	0	0
5.0–5.5	0	0	0	0	0	0	0	0	0	0.013(56)	0.024(57)	0	0	0	0
5.5–6.0	0	0	0	0	0	0	0	0	0	0.002(58)	0.009(59)	0	0	0	0
6.0–6.5	0	0	0	0	0	0	0	0	0	0	0.001(60)	0.001 (61)	0	0	0
6.5–7.0	0	0	0	0	0	0	0	0	0	0	0	0	0		0

Table 3. Fatigue cumulative damage results.

Evaluation point	Cumulative fatigue damage	Fatigue life/years
1	0.009708	4120
2	0.003918	10209
3	0.02289	1747
4	0.08070	496
5	0.01025	3903
6	0.05275	758

Table 4. Fatigue cumulative damage results after correction.

evaluation point	Cumulative fatigue damage	T_1/years	T_2/years
1	0.01292	4120	619
2	0.005215	7670	1534
3	0.03047	1747	263
4	0.1074	496	74
5	0.01364	3903	587
6	0.07021	758	114
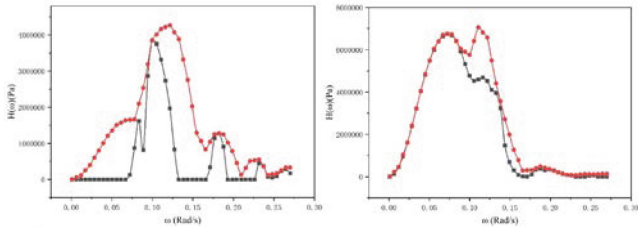
(a) evaluation point 4   (b) evaluation point 6

Fig. 8. Comparison of transfer function results

4 Conclusion

Based on the spectral analysis method and regular wave simulation method, this paper analyzes the small steel containment vessel of FNPP. It is concluded that the maximum fatigue cumulative damage is at No. 8 calculation point, the fatigue cumulative damage degree is 0.1074, and the fatigue life is 74 years. It is located at the bottom support, which meets the design requirements of FNPP. At the same time, the parameters are conservative and the fatigue life is short.

For the regular wave simulation method, take the evaluation point 4 and evaluation point 6 with short fatigue life as an example. Figure 8 shows the transfer function plots of evaluation point 4 and evaluation point 6 at 45° wave direction. The black curve is the simplified theoretical analysis method, and the red curve is the regular wave experimental simulation method. It can be concluded from the figure that the regular wave simulation method has a smoother and more accurate curve, although the calculation is more complex.

References

1. Thangam Babu P.V., Reddy, D.V.: Existing methodologies in the design and analysis of offshore floating nuclear power plants. Nucl. Eng. Des. **48**(1), 167–205 (1978)
2. Arctic's first offshore floating nuclear power plant on the verge of completion. Ship Eng. **39**(04), 9 (2017)
3. Guo, X., Kong, F., Zhu, C., Zhu, G.: Study on safety guidelines in the design of floating nuclear power plants. Nucl. Power Eng. (2021)
4. Liu, Y., Ren, H., Feng, G., et al.: Simplified calculation method for spectral fatigue analysis of hull structure. Ocean Eng. **243**, 110204 (2022)
5. Lin, I.: Study on fatigue strength of large container ships based on design wave method. Ship Eng. **37**(S2), 31–34 (2015)
6. Yang, P., Li, J., Zhang, W., et al.: Analysis on statistical uncertainties of wave loads and structural fatigue reliability for a semi-submersible platform. Ocean Eng. **237**, 109609 (2021)
7. Moghaddam Nia, H., Aghakouchak, A.A.: Evaluating frequency domain methods for fatigue analysis of fixed jacket type offshore platform. Ocean Eng. **246**, 110233 (2022)
8. Zhang, H., Li, Y., Wu, T., et al.: Fatigue strength assessment of small waterline surface catamarans based on spectral analysis method. China Shipbuilding **60**(03), 105–112 (2019)
9. Guihe, Z.: Fatigue analysis method for nuclear level pressure-bearing equipment. Nucl. Power Eng. **30**(S2), 54–59 (2009)
10. Wen, J., Fang, Y., Lu, Y., Zou, M., Zhang, Y., Sun, Z.: Methods and steps for fatigue analysis of nuclear safety equipment. At. Energy Sci. Technol. **48**(01), 121–126 (2014)
11. ASME Boiler and Pressure Vessel Code: SECTION III (2004)
12. CCS. Guidelines for fatigue strength assessment of offshore engineering structures (2013)
13. CCS. Guidelines for fatigue strength of ship structure (2021)

Correlating IASCC Growth Rate Data to Some Key Parameters for Austenitic Stainless Steels in High Temperature Water

Caibo Xie, Songhan Nie, Yiqi Tao, and Zhanpeng Lu[(✉)]

Shanghai University, Shanghai, China
zplu@t.shu.edu.cn

Abstract. Austenitic stainless steels have been widely used for fabricating reactor core-internal components in PWRs due to its high strength, ductility and fracture toughness. The accelerated failure or degradation of austenitic stainless steel represented by IASCC has become one of the key problems affecting the safe and efficient operation of reaction core-internal in PWR nuclear power plants. IASCC is generally divided into three stages: crack initiation, crack propagation and instable fracture. Among the three stages, the crack initiation stage would occupy the major service time, the crack growth stage is featured by quasi-steady crack propagation at a certain rate, and the instable fracture stage should be avoided. Stress intensity factor K at the crack tip is often used to represent the mechanical driving force for SCC as well as IASCC.

In this paper, SCC crack growth rate (CGR) data of austenitic stainless steels irradiated in high temperature water were compiled and reanalyzed to evaluate the influence of key parameters such as radiation dose and mechanical properties on IASCC sensitivity and crack growth rate of these materials in PWR nuclear power plant environment. The CGR-K curves of the irradiated materials were also analyzed. The effects of low, medium and high doses of neutron irradiation are compared, and the analysis process is illustrated with examples. In the research process, abnormal CGR and K of materials under a specific irradiation dose was found, so this phenomenon was analyzed. The CGR data and irradiation dose of austenitic stainless steel in different K range were analyzed. And proposed a way to judge the type of change:type I, type II and type III. Finally, the yield strength of the material under the same irradiation dose was found, and combined with other research data, it was further demonstrated that the neutron irradiation dose had a significant effect on the crack growth rate.

Keywords: Austenitic stainless steel · Irradiation assisted stress corrosion cracking · Crack growth rate · High temperature water

1 Introduction

There are pressurized water reactor (PWR), boiling water reactor, heavy water reactor and other types of commercial nuclear power plants. PWR is the most widely used because

of its mature technology and rich operation experience, accounting for more than half of the operating nuclear power plants in the world. Prolonged neutron irradiation leads to the changes of mechanical properties due to irradiation induced hardening effect, the changed of local chemical compositions due to radiation-induced segregation effect, the increase of physical defects such as dislocation loops, and the water decomposition due to radiolysis, and finally affects the SCC in high temperature water.

IASCC is generally divided into three stages: crack initiation, crack propagation and instable fracture [1]. At the initial stage of crack initiation, the surface of sensitive materials begins to produce microcracks under the coupling effect of environmental and mechanical factors, and these microcracks are invisible under the light microscope. Over time, the microcracks merge with each other to form an initial crack with a length of 10 μm. In the crack growth stage, the crack expands at a certain rate, which is affected by environmental and mechanical factors. The laboratory usually studies the process by introducing the stress intensity factor K at the crack tip. In the instable fracture stage, the crack expands rapidly until the material fracture.

It is well known that SCC of materials in high temperature and high pressure water depends on three factors: materials, environment and relatively high stress is shown in Fig. 1. The key parameters affecting IASCC mainly include the material itself (such as microstructure, microchemistry and yield strength, etc.) and environmental parameters (such as hydrochemistry, irradiation temperature and irradiation dose, etc.). The key parameters such as irradiation temperature and irradiation dose have great influence on the crack growth rate of austenitic stainless steel IASCC. There are also many studies on the influence of material factors such as microstructure, microchemistry and yield strength on IASCC sensitivity of austenitic stainless steel.
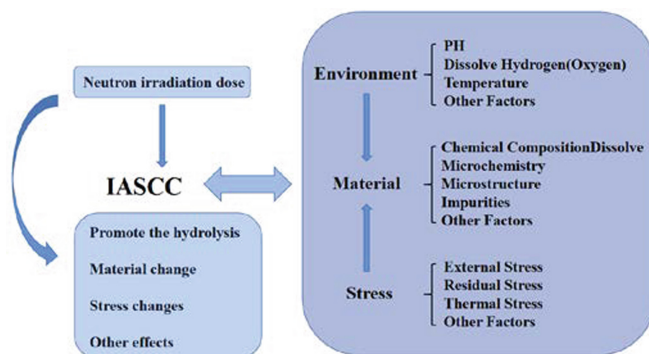
Fig. 1. The main influencing factors of IASCC

The study of IASCC behavior of austenitic stainless steel needs to pay attention to three stages: crack initiation, crack propagation and instable fracture. The crack propagation stage is the most important. Stress corrosion cracking promoted by irradiation is affected by material itself, medium environment, irradiation temperature and irradiation dose, etc. The research process is complicated and uncertain. The relationship between CGR and K is the key parameter in IASCC process of austenitic stainless steel.

SCC or IASCC is used for the study of materials. There are many types of specimens, such as compact tension (CT) specimen [2], four-point bending specimen [3], round compact tension (RCT) specimen [4] and so on. In this paper, the advantages and disadvantages of sample types are not discussed too much, and only the experimental results are concerned.

2   Compiling IASCC Data of Austenitic Stainless Steels in Simulated PWR Primary Water

Austenitic stainless steels can be divided into many types, among which 304 and 316 based austenitic stainless steel is widely studied, so here only around 304 and 316 based austenitic stainless steel is discussed.

The stress corrosion cracking experiment promoted by neutron irradiation needs special equipment, and the experimental difficulty exists objectively due to the limitation of equipment and other conditions. Radiation doses can range from a few percent of dPa to more than 100 dPa. Experimental data on crack growth rate of 0.06–47.0 dPa austenitic stainless steel were collected in this paper.

The CGR data of irradiated austenitic stainless steel in simulated BWR or PWR environments were obtained from CT samples, RCT samples or four-point bending samples. In the experiment, factors such as irradiation temperature, material type and water environment should be controlled, and the irradiation dose should be reasonably controlled. The CGR data of the sample should be matched with K one by one, and the relation data between CGR and K should be obtained.

Based on 304 and 316 austenitic stainless steel, the materials were irradiated in the light water reactor environment, and the data of researchers were summarized to obtain Fig. 2 [4–12].

Figure 2 is a summary of the relationship between CGR and K of irradiated austenitic stainless steel in a pressurized water reactor environment sorted by irradiation dose. Due to the limitation of experimental data conditions of many researchers, it is difficult to unify the irradiation temperature, which is controlled at 288–340 °C. The influence of irradiation temperature on CGR is very complex and limited by space, so the irradiation temperature will not be discussed too much in this paper. Instead, data analysis and problems will be found dialectically.

The parameter stress intensity factor K is introduced here, which essentially reflects the mechanical changes in the microstructure. Microcracks exist in the microstructure of irradiated austenitic stainless steel. If two cracks have the same strain and stress in a region near the crack tip, then they have the same K. Since the crack tip scale is small, K represents the stress and strain at the crack tip.

As shown in Fig. 2, as a whole from the reference curve, CGR generally shows an increasing trend with the increase of K. However, we found that after data integration, each data was not strictly linear and was greatly affected by the radiation dose.

The CGRs of SCC of unirradiated austenitic stainless steel is lower than that of IASCC of irradiated austenitic stainless steel under the same conditions, and the difference may be several times. Taking the CGRs data of austenitic stainless steel under 3 dpa irradiation dose as an example, the CGR of unirradiated austenitic stainless steel

is about 3×10^{-10} m/s [2–5] while the CGR of irradiated austenitic stainless steel can reach 9×10^{-10} m/s or 1×10^{-9} m/s. The difference is about three times. This indicates that neutron irradiation can promote the crack growth rate (CGR) of austenitic stainless steel IASCC to a certain extent. The effect of irradiation dose on CGR of austenitic stainless steel IASCC in PWR is complicated. From the figure, we can roughly divide the radiation dose into low dose, medium dose and high dose. Low radiation dose mainly refers to 0–9 dpa. Under this condition, the change of CGR is not obvious compared with that without radiation. K is mainly between 12 and 20 MPa $m^{0.5}$. Based on literature review and PWR experience, 3 dpa is the threshold of material irradiation. In the case of 0–3 dpa irradiation dose, the CGR of the material will not change with the increase of the irradiation dose, but still maintain the original growth rate. Under the irradiation dose of 3–9 dpa, irradiation promoted the CGR of austenitic stainless steel. For example, the CGR of 3 dpa was higher than that of 6.3 dpa and 8.0 dpa. K remained in a certain range, while CGR changed abnormally. It is speculated that the CGR is affected by the changes of microstructure defects, dislocation loops and radiation dose.
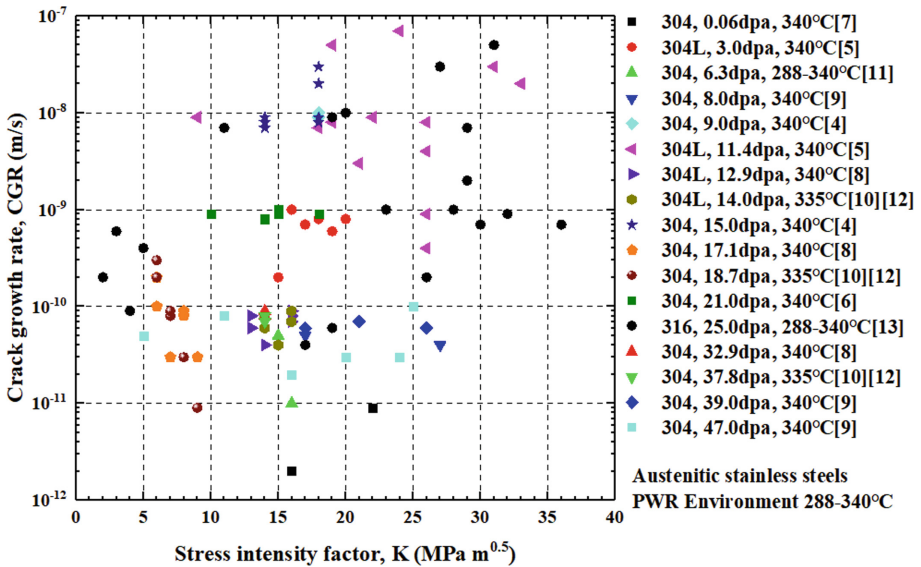
Fig. 2. Relationship between CGR and K of austenitic stainless steel at 0.6–47.0 dpa in pressurized water reactor [4–12]

The radiation dose here refers to the radiation dose of approximately 11.4–25.0 dpa. In the case of medium irradiation dose, CGR and K maintain a positive correlation. At 17.1 and 18.7 dpa, the data are mainly concentrated at the lower left of the figure near the reference curve. At 21.0, 12.9 and 14.0 dpa, the data mainly concentrated in the center of the graph near the curve. Although the data at 11.4, 15.0, and 25.0 dpa are mainly distributed in the upper right of the graph, they generally follow the trend of increasing CGR as K increases. In these data, the phenomenon of 25.0 dpa is worth separate discussion and will be carried out in the future.

High radiation dose refers to radiation dose above approximately 25.0 dpa. As can be seen from the figure, although the CGR of austenitic stainless steel under high irradiation dose is still higher than that of non-irradiated stainless steel, compared with medium irradiation dose, the CGR of austenitic stainless steel is abnormally reduced, mainly between 1×10^{-11} m/s and 1×10^{-10} m/s. These results indicate that high irradiation dose is not conducive to the acceleration of the growth rate of austenitic stainless steel IASCC in PWR, but has a certain inhibitory effect.

The relationship between CGR and K of austenitic stainless steel in pressurized water reactor remains relevant, and CGR increases with K in most cases. However, with the increase of irradiation dose, CGR and K of austenitic stainless steel do not increase simultaneously, but atrophy occurs. It may be caused by the excessive damage to the material caused by neutron irradiation.

It is worth noting that although the CGR and K relationship data of irradiated austenitic stainless steel were partially dispersed, CGR and K still showed a positive correlation. It should be pointed out that the 316 based austenitic stainless steel material under the neutron irradiation dose of 25 dpa in Fig. 2 has abnormal conditions. At lower K, that is, when K is less than or equal to 5 MPa $m^{0.5}$, the CGR of the material is more than 9×10^{-11} m/s. The appearance of abnormal data points in Fig. 2 caught our attention and thought.

3   Effect of Irradiation Dose on SCC Growth Rates

The CGR of austenitic stainless steel in high temperature water is affected not only by stress intensity factor K, but also by neutron irradiation dose, which is indispensable in the process of stress corrosion cracking promoted by irradiation. In order to study the effect of neutron irradiation dose on CGR of austenitic stainless steel in high temperature water, temperature and K must be controlled within a certain range to make the data reasonable and reliable.

Firstly, the temperature was selected between 335 and 340 °C, which could remove the interference of temperature factors on crack growth rate. Through Fig. 2, we summarized the CGR data of 0.06, 3.0, 8.0, 9.0, 11.4, 12.9, 14.0, 15.0, 17.0, 18.7, 21.0, 32.9, 37.8, 39.0, 47.0 dpa irradiation dose, as shown in Fig. 3 [4–9, 11].

Here we classify K as 5–10 MPa $m^{0.5}$, 10–15 MPa $m^{0.5}$, 15–20 MPa $m^{0.5}$ and 20–27 MPa $m^{0.5}$. The CGR and K data of austenitic stainless steel at 335–340 °C were processed to obtain the CGR and neutron irradiation dose of austenitic stainless steel under different normalized K conditions.

When K is normalized to 5–10 MPa $m^{0.5}$, as shown in Fig. 4 [5–9, 11], the CGR of the material is the highest at 11.4 dpa, close to 1×10^{-8} m/s. When K is 5–10 MPa $m^{0.5}$, CGR of all irradiation dose data is greater than 9×10^{-12} m/s. At 17.1 dpa and 18.7 dpa, the CGR values of the materials are close to each other, basically within the range of 10^{-11} m/s and 10^{-9} m/s. At 21.0 dpa, the CGR of the material increased slightly to about 10^{-9} m/s. CGR at 47 dpa was basically within the data range of 17.1 dpa and 18.7 dpa irradiation dose.

As shown in Fig. 5 [4–9, 11], when K is in the range of 10–15 MPa $m^{0.5}$, CGR of all data in the figure is greater than 4×10^{-11} m/s. CGR data under 3.0 dpa were higher than
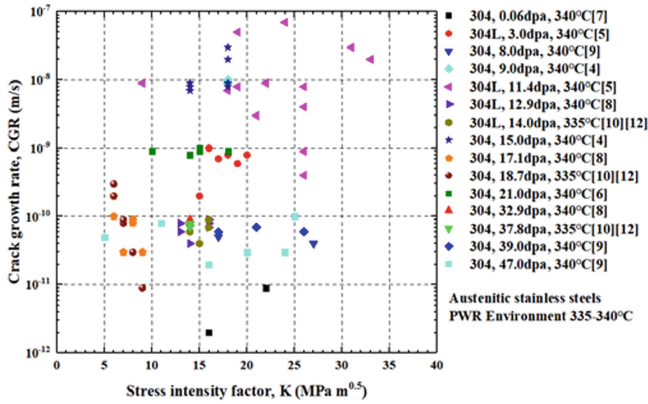
Fig. 3. CGR and K of materials with different neutron irradiation doses at 335–340 °C [4–9, 11]
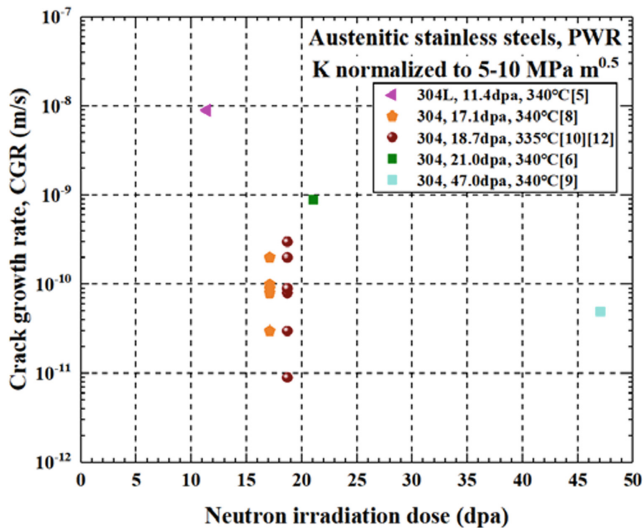
Fig. 4. CGR and neutron irradiation dose of austenitic stainless steel under normalized K 5–10 MPa m$^{0.5}$ [5–9, 11]

10^{-10} m/s. The CGR data range of 12.9 dpa and 14.0 dpa irradiation doses were similar. The CGR at 15.0 dpa was two orders of magnitude higher than that at 12.9 dpa and 14.0 dpa. The CGR data at 21.0 dpa irradiation dose were about 1 order of magnitude higher than those at 12.9 dpaand 14.0 dpa irradiation dose. The CGR data of 21.0 dpa irradiation dose was about 0.1 times that of 15.0 dpa irradiation dose. When the neutron irradiation dose increased from 32.9 dpa to 37.8 dpa and from 37.8 dpa to 47.0 dpa, the CGR data at these three irradiation doses were close to 10^{-10} m/s (between 5x10^{-11} m/s and 1x10^{-10} m/s). The CGR data at these three irradiation doses are not sensitive to the neutron irradiation dose.
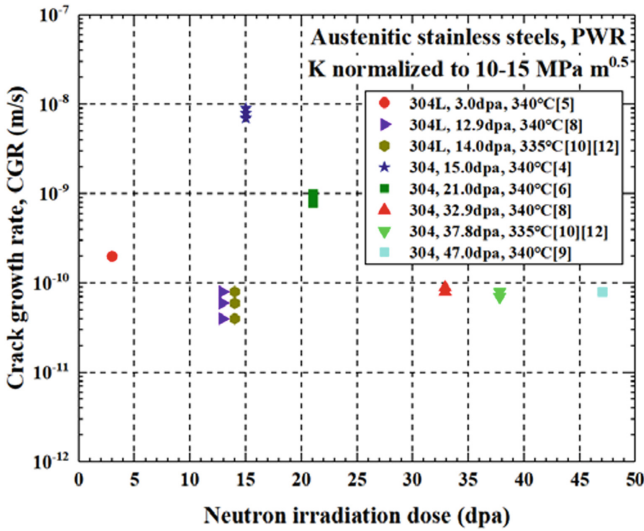
Fig. 5. CGR and neutron irradiation dose of materials under normalized K 10–15 MPa m$^{0.5}$ [4–9, 11]
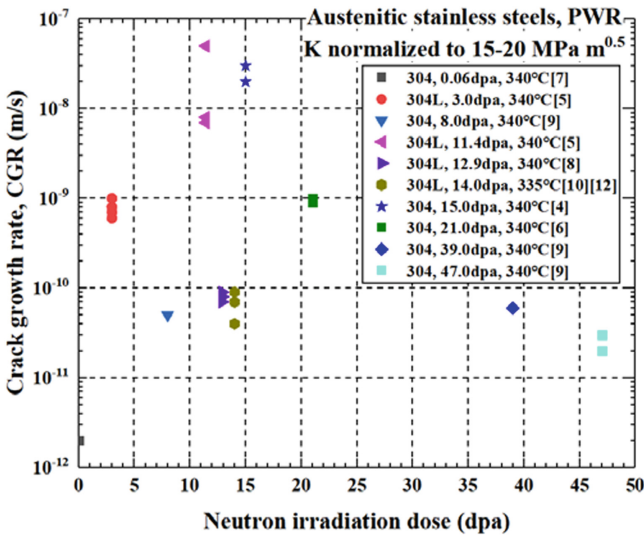
Fig. 6. CGR and neutron irradiation dose of materials under normalized K 15–20 MPa m$^{0.5}$ [4–9, 11]

CGR (3.0 dpa) < CGR(21.0 dpa) < CGR(15.0 dpa) > CGR(12.9 dpa, 14.0 dpa, 32.9 dpa, 37.8 dpa and 47.0 dpa). The peak value of CGR data with neutron irradiation dose of 15 dpa in Fig. 5 has aroused our concern. As for the reason of the peak value? What causes the spike remains to be studied and solved.

As shown in Fig. 6 [4–9, 11], when K is 15–20 MPa m$^{0.5}$, CGR at 0.06 dpa, a very low irradiation dose, is very low, about 2x10^{-12} m/s. However, when the irradiation dose reached 3.0 dpa, the CGR data directly reached nearly 10^{-9}, with a significant increase. When the irradiation dose was higher than 8.0 dpa, the CGR of the material increased significantly, and the CGR was greater than 2x10^{-11} m/s. The CGR data range of 11.4 dpa was close to that of 15.0 dpa, up to about 10^{-8} m/s. CGR data at 12.9 dpa and 14.0 dpa are close in range, but are still two orders of magnitude lower than CGR data at 11.4 dpa and 15.0 dpa. The CGR data at 21.0 dpa was between 12.9 dpa and 14.0 dpa and 11.4 dpa and 15.0 dpa, with a value of about 10^{-9} m/s.

On the whole, it shows that when the neutron irradiation dose is greater than or equal to 15 dpa, the crack growth rate decreases with the increase of the dose. At the same time, the irradiation dose of 11.4 dpa and 15.0 dpa showed two similar peak values. Similar to the situation where K is 10^{-15} m/s as shown in Fig. 5, the phenomenon of peak value arouses concern. The two can be compared and further studied.
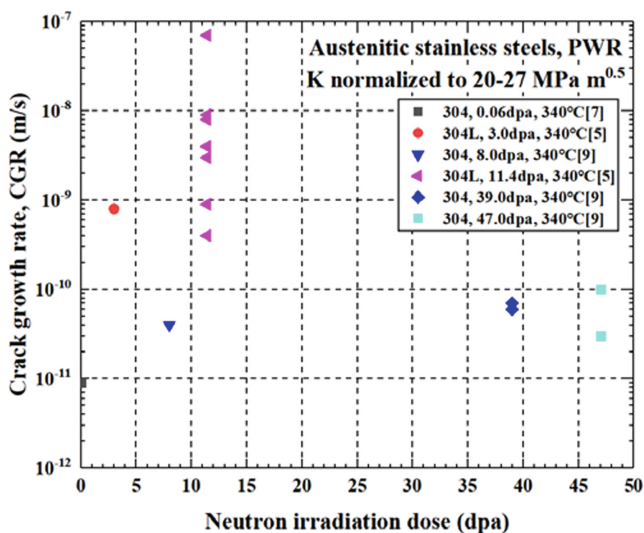
Fig. 7. CGR and neutron irradiation dose of materials under normalized K 20–27 MPa m$^{0.5}$ [5, 6, 8]

As shown in Fig. 7, when K is in the range of 20–27 MPa m$^{0.5}$, the range of CGR data fluctuates greatly. The main reason is that the CGR data of 0.06 dpa is small and that of 11.4 dpa is large. When the irradiation dose increased from 0.06 dpa to 3.0 dpa, the CGR increased by about 2 steps. From 3.0 dpa to 8.0 dpa, its CGR decreased by more than one order of magnitude, but it was still about four times the CGR data at 0.06 dpa. CGR data at 11.4 dpa fluctuated from 4x10^{-10} m/s to nearly 10^{-7} m/s, with a fluctuation range of more than 2 orders of magnitude. Compared with the CGR data at 8.0 dpa, the CGR data at 39.0 dpa was 1.5 or 1.75 times higher, and the CGR data at 47.0 dpa was 2.5 or 0.75 times higher.

Among them, CGR data at 11.4 dpa fluctuated from 4×10^{-10} m/s to nearly 10^{-7} m/s, with a fluctuation range of more than 2 orders of magnitude. In the same range of K, why is there such a high CGR data, and why is there such a large fluctuation range of CGR data in the same radiation dose? These questions remain to be explored.

Based on the above data, we propose a method to judge the phase of CGR data varying with neutron irradiation dose.

$$\frac{\delta_{CGR}}{\delta_{Dose}} > 0: \text{type I,}$$

$$\frac{\delta_{CGR}}{\delta_{Dose}} = 0: \text{type II}$$

$$\frac{\delta_{CGR}}{\delta_{Dose}} < 0: \text{type III}$$

Each type is divided into three categories: type I for increasing, type II for nearly not changing, and type III for decreasing of crack growth rate with increasing dose. There are −S for strongly, −M for moderately, and −W for weakly. As shown in Table 1, the change rate of CGR and irradiation dose in different K ranges is shown.

Table 1. Classification of CGR and radiation dose changes in different K ranges

Stress intensity factor, K (MPa m$^{0.5}$)	Neutron irradiation dose (dpa)	Type
5–10	11.4–17.1,18.7	type III-S
5–10	17.1,18.7–21.0	type I-S
5–10	21.0–47.0	type III-S
10–15	3.0–12.9,14.0	type III-M
10–15	12.9,14.0–15.0	type I-S
10–15	15.0–32.9	type III-S
10–15	32.9–47.0	type II
15–20	0.06–3.0	type I-S
15–20	3.0–8.0	type III-S
15–20	8.0–11.4	type I-S
15–20	11.4–12.9,14.0	type III-S
15–20	12.9,14.0–15.0	type I-S
15–20	15.0–47.0	type III-S
20–27	0.06–3.0	type I-S
20–27	3.0–8.0	type III-S
20–27	8.0–11.4	type I-S
20–27	11.4–39.0	type III-S
20–27	39.0–47.0	type II

4   Verification of Effect of Irradiation Doses on SCC Growth Rate

Bosch [13] et al. recently studied the correlation between neutron irradiation and mechanical properties of 316 material cold worked processed in pressurized water reactor environment, which provided reference value for our paper. He studied the relationship between neutron irradiation and stress-strain, tensile strength, yield strength and other mechanical properties, and we only take the yield strength related content.
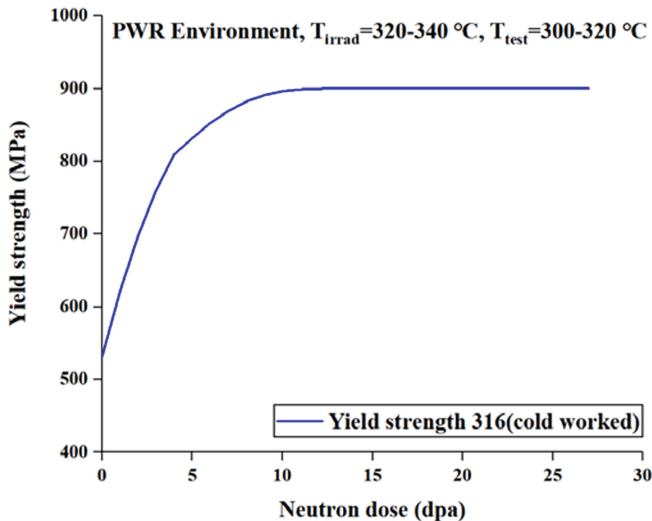
Fig. 8. Variation of yield strength of cold worked 316 material with neutron irradiation dose in pressurized water reactor [13]

Figure 8 shows the change of yield strength of 316CW material in PWR environment with neutron irradiation dose under the irradiation temperature of 320–340 °C and the test temperature of yield strength of 300–320 °C.

In Fig. 9 we can see the CGR distribution of 316CW material at 25 dpa. Through the study of Terachi [14] et al., Castano [15] et al., Shoji [16] et al., Toloczko [17] et al. and Donghai Du [18] et al., we can find the CGR situation of 316CW materials without irradiation under different yield strengths of K is 30 MPa $m^{0.5}$. It can be clearly seen that the CGR of about 800 MPa yield strength is between 10^{-10} m/s and 10^{-9} m/s, which is nearly 2 orders of magnitude lower than the CGR after irradiation at the same K. CGR with yield strengths of 500 MPa and more than 200 MPa is between 10^{-11} m/s and 10^{-10} m/s, which is nearly 3 orders of magnitude lower than CGR after irradiation.

We can obviously score that the CGR of the cold worked 316 material after neutron precipitation is much higher than that of the cold worked 316 material without neutron irradiation. This shows that neutron irradiation has a great influence on the change of material CGR. In addition, the microstructure defects and dislocations of materials may be increased due to the influence of neutron irradiation on the microstructure and mechanical properties of materials.
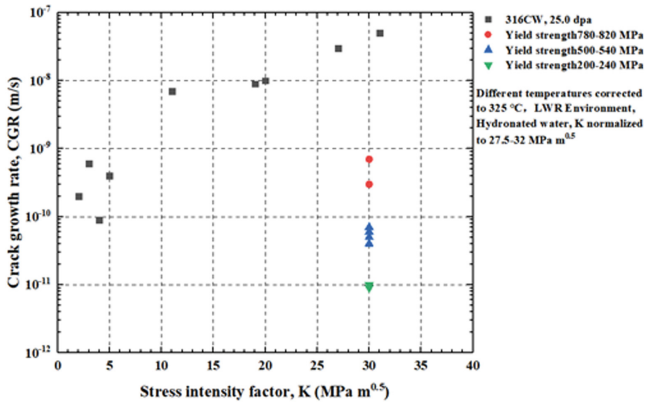
Fig. 9. CGR and K of 316CW material irradiated at 25.0 dpa, CGR of the material at different yield strengths when K is 30 MPa m$^{0.5}$ [14–18].

5   Conclusions

The CGR and K relationship data of 304 and 316 austenitic stainless steels under different neutron irradiation doses in high temperature water were summarized. The effect of irradiation dose on the crack propagation rate of irradiated SCC was analyzed and verified:

The CGR and K of austenitic stainless steel under high temperature water environment show positive correlation. The CGR of unirradiated CGR was lower than that of irradiated CGR under the same condition, and the difference was several times. There is a certain degree of dispersion in the relation data between CGR and K.

In the range of different K, the relationship between CGR data and irradiation dose of austenitic stainless steel is different. Peak data points of CGR appear at some irradiation doses, and the specific reasons need to be studied. We propose a classification method for CGR and radiation dose variation trend and apply it to the data presented in this paper.

Finally, the significant effect of neutron irradiation on CGR of austenitic stainless steel was verified based on yield strength.

References

1. Chen, W.: Modeling and prediction of stress corrosion cracking of pipeline steels. Trends Oil Gas Corros. Res. Technol. 707–748 (2017)
2. Du, D., Song, M., Chen, K., et al.: Effect of deformation level and orientation on SCC of 316L stainless steel in simulated light water environments. J. Nucl. Mater. **531**, 152038 (2020)
3. Dd, A., Kai, S.B., Gswa, B.: IASCC of neutron irradiated 316 stainless steel to 125 dpa-ScienceDirect. Mater. Charact. **173**, 110897 (2021)
4. Chen, K., Ickes, M.R., Burke, M.A., et al.: The effect of potassium hydroxide primary water chemistry on the IASCC behavior of 304 stainless steel (2021)
5. Chopra, O.K., Rao, A.S.: A review of irradiation effects on LWR core internalmaterials-ASCC susceptibility and crack growth rates of austenitic stainless steels. J. Nucl. Mater. **409**, 235–256 (2011)
6. Materials reliability program: corrosion testing of decommissioned PWR vessel internals material samples (MRP-222), EPRI, Palo Alto, CA, 1015478 (2007)
7. Materials Reliability Program: A Review of the Cooperative Irradiation Assisted Stress Corrosion Cracking Research Program (MRP-98)-EPRI Report 1002807 (2003)
8. Karlsen, T.M., Espeland, M., Horvath, A.: Summary Report on the PWR Crack Growth Rate Investigation, IFA-657. OECD Halden Reactor Project, Report HWR-773, May 2005
9. Chen, Y., Alexandreanu, B., Natesan, K., Rao, A.S.: Stress corrosion cracking and fracture toughness tests of irradiated Type 304 stainless steel. In: 19th International Conference on Environmental Degradation of Materials in Nuclear Power Systems-Water Reactors, 18–22 August 2019
10. Karlsen, T.M., Espeland, M., Horvath, A.: HWR-773, OECD Halden Reactor Project, May 2005
11. Jenssen, A., Stjarnsater, J., Pathania, R.: Proceedings of 14th International Conference on Environmental Degradation of Materials in Nuclear Power Systems – Water Reactors, American Nuclear Society, Lagrange Park, IL, 2009
12. Nakano, J., Karlsen, T.M., Espeland, M.: HWR-843, OECD Halden Reactor Project, August 2008
13. Davis, R.B., Andresen, P.: Cooperative IASCC Research (CIR) Final Report, EPRI 1007378, October 2002
14. Bosch, R.W., Renterghem, W.V., Dyck, S.V., et al.: Microstructure, mechanical properties and IASCC susceptibility of stainless steel baffle bolts after 30 years of operation in a PWR. J. Nucl. Mater. **543**, 152615 (2021)
15. Terachi, T., Yamada, T., Miyamoto, T., et al.: SCC growth behaviors of austenitic stainless steels in simulated PWR primary water. J. Nucl. Mater. **426**(1–3), 59–70 (2012)
16. Marin, M.C.: Crack Growth Rate of Hardened Austenitic Stainless Steels in BWR and PWR Environments (2003)
17. Shoji, T., Li, G.F., Kwon, J.H., et al.: Quantification of yield strength effects on IGSCC of austenitic stainless steels in high temperature waters. In: Proceedings of 11th International Conference on Environmental Degradation of Materials in Nuclear Power Systems-Water Reactors (2003)
18. Toloczko, M.B., Andresen, P.L., Bruemmer, S.M.: SCC crack growth of cold-worked type 316 SS in simulated bwr oxidizing and hydrogen water chemistry conditions. Proceedings of 13th International Conference on Environmental Degradation of Materials in Nuclear Power Systems-Water Reactors (2007)

Research on the Optimization of Commercial PWR'S Financial Evaluation Model

Meifang Bo[1], Baojun Zheng[2], Shengli Zhang[1], Zhengxu Ren[3], and Bojie Liu[1(✉)]

[1] China Nuclear Power Engineering Co., Ltd., Beijing, China
`liubja@cnpe.cc`
[2] CHINERGY Co., Ltd., Beijing, China
[3] CNNP Rich Energy Co., Ltd., Beijing, China

Abstract. Considering industry standards, policies, market environment, actual costs of nuclear power plants (NPPs) and technical characteristics of nuclear power, and combining with industrial circumstances when these industry standards were published, we analyzed the limitations of current commercial PWR's fianancial evaluation methods. Taking HPR1000 as a case study, we deeply estimated the generation cost and cash flow. Moreover, optimization direction of the financial evaluation model after comparative analysis was proposed. This research aims to provide reference to similar NPPs'financial evaluation and basis of investment decision-making for investors, owners and general contractors.

Keywords: Commercial PWR · Financial Evaluation · Optimization of Model

1 Introduction

In China, the nuclear power plant (NPP) is regarded as an independent legal entity in the economic evaluation of commercial NPPs, and the on-grid electricity price, an important indicator of the economic feasibility of the NPPs, is calculated on the basis of investment in total capital cost, power generation cost and benchmark internal return rate. The economic evaluation is based on the *Economic Evaluation Guidelines of the Nuclear Power Plant Construction Project* (NB/T20048–2011) (hereinafter referred to as the "NB"), which was released in 2011. Nevertheless, significant changes have taken place in domestic power market policy, actual operating cost of NPPs, the business environment of the external nuclear power market, the safety standards and the technical approach of NPPs since its release 10 years ago. Therefore, the gaps open up the room for research on how can current economic evaluation further contribute to the scientific decision-making in investment, rational resource allocation, and sound development in the whole chain of nuclear power industry.

In addition, the industry standard *NB* focuses on guiding studies on the economic feasibility of NPPs. However, with regard to the commercial NPPs, the shareholders,

shareholders of listed companies with the long-term development plan at heart in particular, are more concerned about the internal rate of return of all parties involved, while the general contractors pay more attention to the investment of total capital cost per kilowatt and the construction units lay emphasis on whether the project can be approved. The analysis on different schemes can be conducted through scientific economic evaluation, serving as solid data support for all parties, and the results can provide insight in understanding the gap between the theoretical and actual benefits of the project, the allocation options for subsequent development, and the range of maximum total capital cost per kilowatt within the project budget.

2   Limitations of the Current Economic Evaluation Model for Pressurized Water NPPs

On the one hand, *NB* was officially released in 2011, and the calculation parameters, criterion parameter and boundary conditions in its appendix were in consistent with the market environment and industry expectations before finalization. However, the capital cost and expected revenue based on the market environment at that time is vastly different from the current one. On the other hand, *NB* was compiled mainly based on the data of Generation 2+ NPPs that were widely built and operated in China, without taking into account the advanced design, the differences in generation costs between the Generation 2+ and Generation 3 NPPs and the actual cost of NPPs in recent years. Furthermore, the existing *NB* model lacks the in-depth research and analysis on the cash flow planning including financing, loan repayment, and corporate dividend of the whole project, and the evaluation system takes the on-grid electricity price measured by the capital benchmark rate of return as the main indicator, excluding the rate of return of the investment of all parties, which is more closely related to the investors.

2.1   The Background of *NB* Release

China's electricity pricing mechanism has undergone a series of changes since the reform and opening up, evidenced by a number of relevant policies implemented, such as the repayment of capital with interest (RCI pricing), "price pegged to the increase in transportation" and "operating price" since 1985. Before 2013, nuclear power on-grid electricity price varies among different generating sets based on compensation costs and reasonable revenue, and against which background the *NB* was compiled and released.

2.2   The Applicable Analysis of *NB* to the PWR Reactor Types

The *NB* regulates that it is suitable for the economic evaluation of PWRs and the economic evaluation of other nuclear facilities could refer to this standard. However, this standard does not clearly indicate the reactor types which are applicable to this standard and there is also no content stating about the relationship between the evolvement of PWR nuclear technology and its applicability to this standard.

The formulation of *NB* is mainly based on the economic parameters and data of the Generation 2+. The effects of technical innovation on economic evaluation methods and

parameters are not considered in current *NB*. Therefore, the methods and parameters in this *NB* could not objectively and comprehensively meet the demands of economic evaluation for current PWRs, especially for the third generation PWRs.

2.3 Analysis of Macro-economic Environment Change for Nuclear Power Enterprises

Compared with the year 2011 when the *NB* was published, the market environment regarding the fund cost and expected returns has changed significantly. From 2010 to 2019, the interest rate under macro-economy had been declined obviously. Under the current economic environment, the internal rate of returns for the capital fund could decrease to 7%–8% while the rate of returns for investors could decrease to 6%–7%.

2.4 Analysis of Business Environment Change for Nuclear Power Enterprises

Compared with the year 2011, the business environment of nuclear enterprises has changed obviously. Due to the higher safety requirement, the project cost of the third generation PWRs has increased. Meanwhile, against the backdrop of benchmark tariff reduction, power market revolution, weakened fiscal and tax support, the nuclear power enterprises are under huge business difficulties. For instance, the power generation capability of some nuclear reactors is compared with their full capacity, posing risks to the business operation of nuclear enterprises. Moreover, with the successive increase of transected electricity, NPPs in certain regions participate in the annual bidding transaction, monthly bidding transaction, straight-powered protocol for large users and trans-provincial and trans-regional power transaction, facing dual pressure from both declined planned electricity and market bidding.

Economic evaluation based on the *NB* would deviate from actual circumstances. The actual operation time of Generation 2+ far exceed 7000 h and operation costs are much higher than the regulations in *NB*, resulting in higher electricity price. Moreover, actual fiscal and tax policies also have minor differences with *NB*. As for the third generation, its economics are facing risks in terms with both power generation and electricity price. Thus, to accurately evaluate the economics of the Generation 3 NPPs, it is imperative to focus on the rationality and accuracy of economic evaluation methods. Under the background of declined interest rate, the return rate could be further decreased. *NB* regulates that the pre-tax benchmark return rate before financing is 7% and the after-tax benchmark return rate after financing is 9%. The above-mentioned return rates could be lowered. Besides, more concentration could be paid to financial internal return rate of investors, which is the core concern of investors. The financial internal return rate of investors is advocated as a core parameter in this study and it could be further optimized to 8%–10%.

2.5 Limitations of Current Financial Evaluation for PWRs

(1) Economic indicators

Based on the financial evaluation of PWRs with different Under the hypothesis of identical internal return rate, the on-grid electricity price of PWRs with different power show large disparity. Moreover, there is no significantly linear relationship between power generation cost and on-grid electricity. Focusing on the on-grid electricity price and capital internal return rate in economic evaluation would result in the overlook of other economic indicators. Therefore, apart from the internal return rate and on-grid electricity price, we should also concentrate on the power generation cost and payment schedule, achieving more precise and comprehensive economic analysis.

(2) Cost control in the whole life period

According to the feedback from NPPs, the actual operation cost has increased, exceeding the parameters regulated in *NB*. Specifically, cost from uranium mining, conversion and separation is higher than the international market, resulting in high cost of nuclear fuels. The increase of nuclear fuel cost and operation and maintenance cost counteract the advantages of investment decline brought by the batch production of Generation 2+ and design maturation of HPR1000. Therefore, apart from the investment control, we should focus on the cost from the period of both construction and operation. Operation and maintenance cost as well as nuclear fuel cost should be supplemented as auxiliary indicators in the future economic evaluation of PWRs.

(3) Indicator discordance with practice

In financial evaluation, the table of capital cash flow is formulated based on designated either on-grid electricity price or capital internal return rate. Common practice is to designate capital internal return rate as 9% and evaluate the on-grid electricity price, thus evaluating the feasibility of the on-grid electricity price of specific NPPs. However, investors pay more attention to dividend distribution and there exists large uncertainty with capital internal return rate as the only economic indicator.

3   Optimization of Economic Evaluation Model

In the future, the financial evaluation of NPPs should be transformed from the single indicator to multi indicators. Currently, focusing only on the on-grid electricity price and capital internal return rate would lead to incomplete analysis of economics of NPPs and simultaneously controlling multiple indicators is conducive to achieving comprehensive economic evaluation of NPPs. For instance, cost control should be expanded from construction to the whole life period of NPPs, including operation and maintenance. Table shows advocated multi indicators in future economic evaluation of NPPs (Table 1).

Table 1. Proposed multiple indicators for optimized model

Indicator type	Indicator name	Indicator standard
Key project cost indicator	Overnight cost per kilowatt	Absolute value
Key project cost indicator	Total capital cost per kilowatt	Absolute value
Auxiliary project cost indicator	Overnight cost	
Auxiliary project cost indicator	Total capital cost	
Key cost indicator	Average power generation cost	Absolute value
Key cost indicator	Operation and maintenance cost	Absolute value
Key cost indicator	Fuel cost	Absolute value
Key return indicator	Financial internal return rate of investors	6%–7%
Auxiliary return indicator	Capital financial internal return rate	
Auxiliary return indicator	Financial internal return rate of total investment (after tax)	
Other auxiliary indicators	Profitability and other indicators	

4 Preliminary Research on the Cost of Power Generation of HPR1000

Cost of power generation is the basis of on-grid electricity price evaluation. Because the FOAK reactor of HPR1000 has only operated for 2 years, the data for the cost of operation and maintenance is not thorough. Thus, this study only conducts preliminary research on the cost of power generation of HPR1000. Differences of operation and maintenance cost between HPR1000 and the Generation 2+ result from their technical differences.

Cost of materials consumed during operation includes expense from nuclear fuels, chemicals, water and electricity. Water consumption difference between HPR1000 and the Generation 2+ is clear but the quantity of other materials consumed in the operation of HPR1000 is still unclear. Standard of material expenses for HPR1000 should be identified based on the practice of the Generation 2+ and the in-service HPR1000. The cost for each staff of HPR1000 and the Generation 2+ should be the same, but the staff quota of HPR1000 should be modified based on actual situation. Maintenance of NPPs includes general overhaul and routine operation and maintenance. General overhaul planning is related with the type of nuclear reactors. Correspondingly, the expense of general overhaul is also different for each type of reactor. With the progress of science and technology as well as the management of power plants, the repair fee rate should be declined. Boasting with higher design standard, the repair fee rater of HPR1000 could be decreased from 1.35% to 1.2%.

Life period is one of major differences between the Generation 2+ and the HPR1000. The life period of the HPR1000 is 60 years, which mainly influences the design of major equipments. Since the capital cost is low in today's market, a shorter payback period is

conducive to sustainable bonus distribution. Therefore, adopting 20 years as depreciation period is still feasible in the economic evaluation of HPR1000.

Based on the comparative analysis and advanced design concept, we estimated the power generation cost of HPR1000 after optimization of depreciation period and repair fee rate. We estimated the power generation cost and on-grid electricity price based on the total capital cost of 37.75 billion RMB and the capital internal return rate of 9% (Table 2).

Table 2. Cost composition of HPR1000

	Cost item	Cost value (RMB/MWh)	Percentage(%)
1	**Investment cost**	**106.6**	**45%**
1.1	Depreciation	75.4	71%
1.2	Amortization	4.0	4%
1.3	Financial expense	27.2	25%
2	**Fuel cost**	**68.7**	**30%**
2.1	Nuclear fuel procurement	46.3	67%
2.2	Reprocessing cost	22.4	33%
3	**Operation and maintenance cost**	**52.6**	**22%**
3.1	General overhaul cost	26.5	50%
3.2	Wages and welfare	10.7	20%
3.3	Other expenses	6.6	13%
3.4	Material cost	5.4	10%
3.5	Water cost	0.4	1%
3.6	Medium and low radioactive waste treatment and disposal cost	0.5	1%
3.7	Other operation and maintenance cost	2.6	5%
4	**Decommissioning Funds**	**7.5**	**3%**
	合计	**235.5**	**100%**

5 Financial Evaluation of HPR1000

Based on the above-mentioned optimization clue, we formulated 8 schemes to analyze the economics of HPR1000 under each condition.

5.1 Scheme Estimation

(1) Original Scheme (Option 1)

The power generation cost, on-grid electricity price, and the rate of return for all parties were calculated at the total capital cost of 37.75 billion RMB, 1.35% rate of general overhaul cost, depreciation period of 25 years and capital return rate of 9%. The long-term loan is reimbursed by deducted VAT, refunded VAT, depreciation, amortization, and undistributed profits for repayment in order, and cash for circulation will be used to repay short-term loans annually. Dividend will be distributed under the condition of guaranteed loan repayment in the form of cash. The dividend distribution ratio is as follows (Table 3).

Table 3. Average dividend distribution ratio of option 1

No	Year after operation	Average ratio of cash dividends to distributable net profit
1	1–5	0%
2	6–10	15%
3	11–15	65%
4	16–20	98%
5	After 20	100%

As seen from the table, in the first five years after the unit is put into commercial operation, the ratio of cash dividends to distributable net profit is 0, suggesting that there will be no dividend in the first 5 years, and the trend continue till the 6th year; from the 6th to 10th years after the operation, the average distribution ratio of annual dividend is 15%, which is still far below the value proposed by the listed company (30%); from the 11th to 15th years, the average distribution ratio of annual dividend is 65%, and the full allocation can't be achieved until 17th year. The dividend distribution is so conservative that the listed company's investment in new projects and its rolling development get impeded.

(2) Base Case (Option 2)

The total capital cost, power generation cost, and investment return of all parties were retrodicted with 1.35% general overhaul rate, depreciation period of 25 years, capital return rate of 9%, and the on-grid electricity price, which was calculated according to that of the benchmark local thermal power desulfurization and denitrification. The arrangement of cash flow and dividend is similar to the Option 1 in nature with comparable annual dividend distribution ratio.

(3) General overhaul Scheme (Option 3)

The total capital cost, power generation cost, investment return of all parties were retrodicted with 1.2% general overhaul rate, adjusted from 1.35% according to the estimated quota of annual overhaul expense and fixed assets, depreciation period of 25 years, capital return rate of 9%, and the on-grid electricity price calculated according to that of

benchmark local thermal power desulfurization and denitrification. The arrangement of cash flow and dividend is similar to the previous case in nature with comparable annual dividend distribution ratio.

(4) Depreciation Scheme (Option 4)

The total capital cost, power generation cost, investment return of all parties were retrodicted with 1.2% general overhaul rate, depreciation period of 20 years, capital return rate of 9%, and the on-grid electricity price calculated according to that of benchmark local thermal power desulfurization and denitrification. The arrangement of cash flow and dividend is similar to the previous case in nature with comparable annual dividend distribution ratio.

(5) Rate of return Scheme I (Option 5)

The option 5 is to adjust the order of cash flow, the dividend distribution and repayment scheme. The total capital cost and power generation cost were retrodicted with 8% of capital return rate and 9% of return rate of all parties, considering low loan interest rate for the rolling development of the company. Combining the study of the dividend distribution of the listed companies with the research on the dividend of NPPs, the arrangement of cash flow is as follows.

Cash dividends for shareholders are guaranteed at a certain amount, and the rest is repaid to long-term loans in the order of deducted VAT, refunded VAT, depreciation, amortization, and undistributed profits remained after dividend. The short-term loan will be used to compensate for the long-term loan that could not be covered by dividend and repayment. The corresponding dividend distribution plan is that there will be no dividend in the first two years after commercial operation, 860 million RMB per year from the 3rd to 7th year, 1.2 billion RMB per year from the 8th to12th year, and full percent of the profit from the 13th year onwards through the subsequent operation.

(6) Rate of return Scheme II (Option 6)

The dividend distribution and loan repayment scheme is adjusted in option six, while other parameters remain the same as Option 4. The total capital cost and power generation cost were retrodicted with 8% of capital return rate and 10% of return rate of all parties. The slight changes in the cash flow and the corresponding dividend distribution can be found in comparison with Option 5. There will be no dividend in the first two years after commercial operation, 1.08 billion RMB per year from the 3rd to 7th year, 1.66 billion RMB per year from the 8th to 12th year, and full percent of the profit from the 13th year onwards through the subsequent operation.

(7) Rate of Return Scheme III (Option 7)

The dividend distribution and loan repayment scheme is adjusted in option seven, while other parameters remain the same as Option 4. The total capital cost and power generation cost were retrodicted with 7% of capital return rate and 9% of return rate

for shareholders. The slight changes in the cash flow and the corresponding dividend distribution can be found in comparison with Option 5. There will be no dividend in the first two years after commercial operation, 1.03 billion RMB per year from the 3rd to 7th year, 1.4 billion RMB per year from the 8th to 12th year, and full percent of the profit from the 13th year onwards through the subsequent operation.

(8) Rate of Return Scheme IV (Option 8)

The dividend distribution and loan repayment scheme is adjusted in option eight, while other parameters remain the same as Option 4. The total capital cost and power generation cost were retrodicted with 7% of capital return rate and 10% of return rate for shareholders. The slight changes in the cash flow and the corresponding dividend distribution can be found in comparison with Option 5. There will be no dividend in the first two years after commercial operation, 1.31 billion RMB per year from the 3rd to 7th year, 1.6 billion RMB per year from the 8th to 12th year, and full percent of the profit from the 13th year onwards through the subsequent operation.

5.2 Results and Comparative Analysis

(1) Estimation results

Table 4 shows the results of power generation cost and its composition for each scheme while Table 5 demonstrates main indicators.

Table 4. Estimation of power generation cost

Item	Option 1	Option 2	Option 3	Option 4	Option 5	Option 6	Option 7	Option 8
Investment cost	**106.6**	**104.2**	**105.3**	**106.3**	**115.9**	**118.4**	**124.1**	**127.5**
Depreciation	75.4	73.7	74.4	75.2	76.8	75.9	79.5	78.3
Amortization	4.0	3.9	3.9	4.0	4.0	4.0	4.2	4.1
Financial expense	27.2	26.6	26.9	27.1	35.1	38.6	40.4	45.0
Fuel cost	**68.7**	**68.7**	**68.7**	**68.7**	**68.7**	**68.7**	**68.7**	**68.7**
Nuclear fuel procurement	46.3	46.3	46.3	46.3	46.3	46.3	46.3	46.3
Reprocessing cost	22.4	22.4	22.4	22.4	22.4	22.4	22.4	22.4
Operation and maintenance cost	**52.6**	**52.0**	**49.4**	**49.1**	**49.7**	**49.4**	**50.6**	**50.2**

(*continued*)

Table 4. (*continued*)

Item	Option 1	Option 2	Option 3	Option 4	Option 5	Option 6	Option 7	Option 8
General overhaul cost	26.5	25.8	23.2	23.4	23.9	23.7	24.8	24.4
Wages and welfare	10.7	10.7	10.7	10.7	10.7	10.7	10.7	10.7
Other expenses	6.6	6.6	6.6	6.6	6.6	6.6	6.6	6.6
Material cost	5.4	5.4	5.4	5.4	5.4	5.4	5.4	5.4
Water cost	0.4	0.4	0.4	0.4	0.4	0.4	0.4	0.4
Medium and low radioactive waste treatment and disposal cost	0.5	0.5	0.5	0.5	0.5	0.5	0.5	0.5
Other operation and maintenance cost	2.6	2.5	2.6	2.1	2.1	2.1	2.2	2.2
Decommissioning funds	**7.5**	**7.4**	**7.4**	**7.5**	**7.7**	**7.6**	**8.0**	**7.8**

Table 5. Estimation of main indicators

Item	Unit	Option 1	Option 2	Option 3	Option 4	Option 5	Option 6	Option 7	Option 8
On-grid electricity price	RMB/MWh	400.2	393.2	393.2	393.2	393.2	393.2	393.2	393.2
Average power generation cost	RMB/MWh	235.5	232.2	230.8	231.6	242.0	244.1	251.4	254.3
Total capital cost per kilowatt	RMB/kilowatt	15573	15207	15369	15518	15856	15665	16415	16177
Return rate of investors	%	6.9	6.9	6.9	6.9	9.0	10.0	9.0	10.0
Capital return rate	%	9.0	9.0	9.0	9.0	8.0	8.0	7.0	7.0

(2) Comparative Analysis

Based on the results of the above options, it can be concluded that the rate of return of shareholders from all parties and the total capital cost per kilowatt increase by modification of power generation cost of the base case in the model and optimization of cash flow with current low interest rate under the condition that the on-grid electricity price and energy being the same, i.e. the same revenue from electricity sales.

The model enables shareholders to prepare for the rolling development of the company and invest in new projects from a long-term perspective. In addition, as the total capital cost of projects gradually increase, the general contractor can better allocate its resources against background of mounting investment in the Generation 3 NPPs by diverting premium resources to design, construction and procurement, which will in turn benefit the owner. The optimization that attaches more importance to the whole life cost of the project rather than limited to the investment in the total capital cost can be more conducive to the sustainable development of the entire nuclear power industry.

It can be concluded that the yield of the plant can be further increased with the same construction investment. Meanwhile, the project can endure higher construction investment under the condition of the same or even higher yield, urging relevant units to apply higher safety standards to improve the safety and reliability of the plant. Based on the current market environment and operating practice of dividend strategy of groups including China National Nuclear Corporation (CNNC), it is recommended that Option 6 can generate stable shareholder yield and total capital cost per kilowatt. Finally, the risk resisting capability of nuclear units is lifted.

6   Conclusions

Considering the current market and the experience practice of in-service NPPs, we optimized the economic evaluation model of NPPs. Since in listed nuclear power companies, investors pay more attention to dividends and the long-term development of the company, the optimized capital internal return rate, internal return rate of investors and total capital cost could be obtained via optimized capital flow and bonus allocation. This research provides viable investment strategies for decision makers.

The flexible arrangement of cash flows and allocating bonus to investors in priority would significantly enhance the debt risk compared with the baseline scenario. Moreover, if the interest rate increases with the change of financial market, the debt rate of the proposed scenarios would increase, posing debt risks to the project. However, the asset liability under current circumstances could meet the requirements. It is noted that our research is based on the current market environment and the variance of power market and financial market would influence the results of optimization.

References

1. National Development and Reform Commission. Ministry of Housing and Urban-Rural Development of the People Republic of China. Methods and Parameters of economic evaluation for construction projects (3rd edn.). Beijing: China Planning Press (2006)
2. Wei, X.Y.: Problems and suggestions in economic evaluation of infrastructure projects. Constr. Econ. **42**(S1), 74–75 (2021)
3. Qin, H.: Construction of The Project Economic Evaluation Research. Master thesis (2015)
4. Peng, F., Luo, D.K., Yin, C.F., et al.: Bibliometric study on economic evaluation of fossil energy exploration and development articles and its visualization. Pet. Sci. Bull. **5**(1), 132–140 (2020)

1084   M. Bo et al.

Design of Radioactive Waste Classification and Detection System for Nuclear Facility Decommissioning

Kang Chang[1(✉)], Guangming Cheng[2], Jinwei Zeng[2], Wenzhang Xie[1], Chenyu Shan[1], Qingxin Lei[1], Jia Huang[1], Feng Liu[1], Xiajie Liu[1], and Li Li[1]

[1] China Nuclear Power Technology Research Institute Co., Ltd., Shenzhen, China
changkang@cgnpc.com.cn
[2] Guangxi Fangchenggang Nuclear Power Co., Ltd., Fangchenggang, China

Abstract. The most important indicator of the radioactive waste classification and detection system is its identifiable minimum activity of low level radioactive waste, that is, the lower detection limit. In order to design a low level and very low level waste classification and detection system that can perform large-scale and rapid measurement, and explore the influence of various factors on the low limit of detection, this paper establishes the layout model of the detection unit of the classification detection system by Monte Carlo method to simulate the number of NaI crystals, the density of the detected object, the distance between the detection crystal and the detected object, the distance between the adjacent measured waste and the measurement time, etc. Meanwhile this paper analyzes the characteristics of the low limit of detection, and performs operations research analysis based on the principle of being able to detect radioactive waste with specific activity of not less than 0.1 Bq·g^{-1}, maximizing the shielding effect and optimizing the shielding weight, and designs a low level and very low level waste classification and detection system that can measure radioactive waste which density is not less than 0.25 g/cm^3 and which specific activity is not less than 0.1 Bq·g^{-1}.

Keywords: Monte carlo · Low limit of detection · Radioactive waste · Classification

1   Introduction

During the decommissioning of nuclear facilities, a large amount of radioactive waste will be generated, covering different types of waste such as medium, low and very low level radioactive and clearance level waste. According to Chinese current radioactive waste classification standard, different types of radioactive waste need to adopt different disposal methods. Timely and accurate classification of decommissioned nuclear facilities is one of the key links in radioactive waste management, and it is also an important means to minimize waste and reduce disposal and supervision costs [1–5].

When using physical measurement techniques such as radiation detection to classify radioactive waste, especially when classifying clearance level waste (EW), very low-level

waste (VLLW) and low-level waste (LLW), due to the very low level of radioactivity of the first two types of waste, the low limit of detection of instrument used has higher requirements. Therefore, this paper refers to other classification detection devices (e.g. box-type waste detecting device and waste barrel gamma scanning device) and uses Monte Carlo calculation software to simulate the low limit of detection of the module of a low-very low radioactive waste classification detection system, and studies relationship between the different detection crystal volume and crystal arrangement, different measurement time, different shielding thickness around the detection crystal, the distance between the detection crystal and the upper surface of the waste, and the density with the low limit of detection, and optimizes the detection module of the low-very low radioactive waste classification detection system.
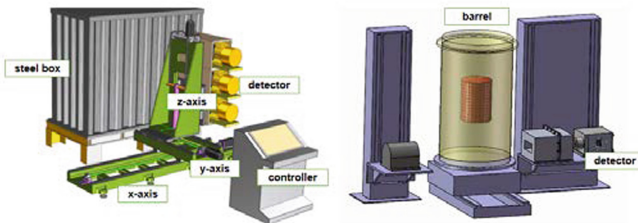
Fig. 1. Box-type waste detecting device and waste barrel gamma scannig device

2   Materials and Methods

2.1   Detector Source Response Coefficient

The detector source response coefficient K of the classification detection system is an important design parameter of the detector, that is, the counting rate generated by the radioactive source per unit specific activity in the measurement chamber of the classification detection system in the detector. In the development phase, we uses the F8 counting card in the MCNP program and SCORE card in the FLUKA program to simulate the calculation to obtain the pulse count rate produced in the detector in the measurement chamber of the specific activity of the waste in the detector. Detector source response coefficient.

$$K = Tally_{FB} \times V \times 1 \tag{1}$$

where K is the detector source response coefficient of the classification detection system, cps·Bq^{-1}·m^{-3}; $Tally_{F8}$ is counting rate (energy range of 100 keV ~ 3 meV), cps; V is the volume of waste to be measured in the simulation calculation, m^3; I is the decay branch ratio of gamma rays produced by radionuclides in the waste to be measured.

2.2 Minimum Detectable Concentration

Minimum detectable concentration ($M_{in}DC$, MDC) [4–6] represents the minimum activity concentration value that the classified detection system can analyze for specific nuclides in the measured waste. It is an important indicator of the sensitivity of the classification detection system when it is applied in a given situation. The premise that the waste to be tested can be reliably detected is that the activity concentration of the waste to be measured is greater than the minimum detectable concentration.

$$M_{in}DC = \frac{2.706/t + 4.65\sqrt{l_b/t}}{K} \tag{2}$$

where: $M_{in}DC$ is the minimum detectable concentration, Bq·m^{-3}; l_b is the environmental background count rate, cps; t is the given measurement time, s.

2.3 Model of Simulation

As shown in Fig. 2, this paper establishes the detection module model in the above-mentioned radioactive waste classification detection system in the Monte Carlo simulation software MCNP and FLUKA. In the calculation model, the size of a single NaI crystal is 40 cm × 10 cm × 5 cm; the size of the waste detection box (stainless steel) is 65 cm × 65 cm × 10 cm; the radioactive source term is divided into two parts. One is the environmental background, and it is considered that the environmental dose rate in the working area of the detection system is the upper limit of the white area's dose rate, and it is equivalent to a uniform spherical shell surrounding the whole detection device. The spherical shell is a source of air uniformly distributed with Cs-137 sources. The other part is the radioactive waste contained in the detection box, which is set as a cuboid source in the simulation.
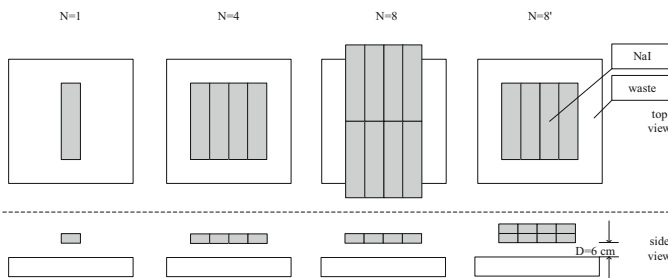
Fig. 2. Lay-out of the detectors and waste box

3 Results and Discussion

3.1 Effect of Crystal Arrangement on the Low Limit of Detection

According to the Nuclear Safety Guidelines HAD401/04 "Radioactive Waste Classification", the level of Cs-137 control is 0.1 Bq·g^{-1}, that is, the classification detection system for requirements of Cs-137.

Usually, the larger the crystal volume or the number of crystals are, the smaller the low limit of detection is. However, due to the high volume NaI crystal price, this paper selects several different NaI detection crystal arrangement and quantity as shown in Fig. 1 to simulate the detection of the lower limit change, in order to choose the most cost-effective crystal arrangement and quantity. As shown in Fig. 3(a), when the background count rate is 5 cps·cm^{-3} and when the detection time is 30 s, no detection scheme can meet 0.1 Bq·g^{-1}; when the detection time is 60 s, at least 4 NaI detection crystals should be selected to meet 0.1 Bq·g^{-1}; as shown in Fig. 3(b), when the background count rate is 0.5 cps·cm^{-3}, there is no limit to the number of NaI detection crystal blocks; in Fig. 3(a)(b), it shows that the detection efficiency of the 8 NaI crystal tiling type is better than the detection efficiency of the two-layer superposition form, mainly because the gamma ray energy is low, and the radiation energy can be deposited by selecting one layer of crystal, and the two-layer superposition form increases the lower limit of background influence detection caused by the crystal itself.

(a) background : 5 cps/m^3

(b) background : 0.5 cps/m^3
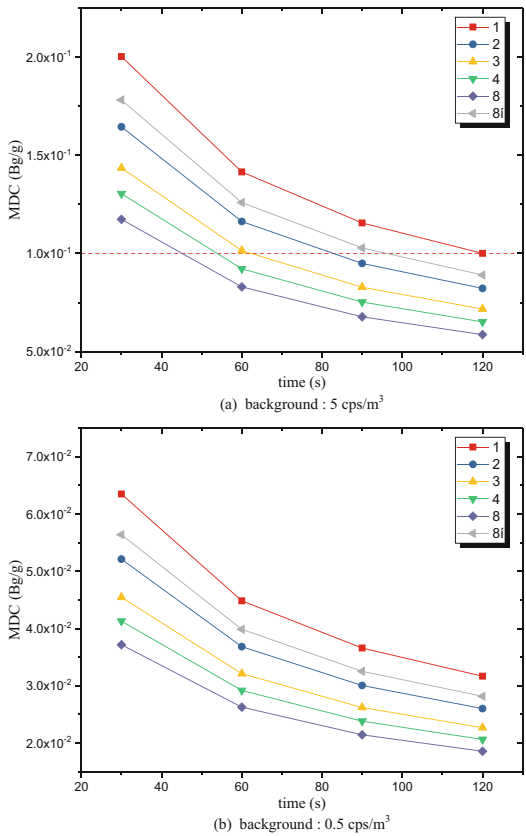
Fig. 3. Difference in the mdc with the volume of NAI crystals in different environment background

3.2 Effect of Average Distance Between Detector and Waste Upper Surface on Low Limit of Detection

In the actual measurement process of the radioactive waste classification detection system, the average distance between the detector and the waste surface is required to be adjustable, so as to avoid the overflow of the waste to be detected and the detector can achieve the best detection effect, so different source distances are used to simulate the change of the low limit of detection. As shown in Fig. 4, it can be seen that the low limit of detection increases as the average distance between the detector and the upper surface of the waste increases. Figure 4(a), when the NaI background count rate is 5 cps·cm^{-3} and when the measurement time is 60 s, the average distance between the NaI detector and the upper surface of the waste should not exceed 10 cm, even if the measurement time is relaxed to 120 s, the average distance should not exceed 20 cm. And when the NaI background count rate is 0.5 cps·cm^{-3}, the average distance between the NaI detector and the upper surface of the waste should not exceed 50 cm.

3.3 Influence of the Density of Waste to be Measured on the Low Limit of Detection

In addition, the types of waste of the decommissioning of nuclear facilities are various and the density varies greatly, including metal materials such as steam generators in nuclear power plant, waste gas masks, and radioactive medical waste. In order to explore the impact of waste density on the low limit of detection and avoid discomfort to the detection system due to excessive or small waste density, different waste densities are used to simulate changes in the low limit of detection.

As shown in Fig. 5, under the same measurement conditions, the low limit of detection decreases with increasing waste density. Figure 5(a) when the measurement time is 60 s, if the NaI background count rate is 5 cps·cm^{-3}, the waste density should not be less than 0.25g·cm^{-3}. Figure 5(b) when NaI background count rate is 0.5 cps·cm^{-3} there are no restrictions on waste density.

3.4 Effect of Shielding on the Low Limit of Detection

The background count rate in the NaI detection crystal mainly comes from the noise of the NaI crystal, the environmental background of the area where the detection system is located, and the adjacent waste box to be tested. From the above analysis, it can be seen that the background count rate of different levels also has an important impact on the detection lower limit, so shielding must be set around the detector. Since the noise of the NaI crystal itself cannot be eliminated by shielding, and the background count rate in the NaI detection crystal with different intervals of the waste box to be detected is not shielded. The result is shown in Table 1. The environmental background is much lower than the influence of the adjacent waste box to be detected on the background of the NaI detection crystal, so the following only simulates the waste box to be detected at different intervals, changes in the lower limit of detection under different shielding thicknesses.
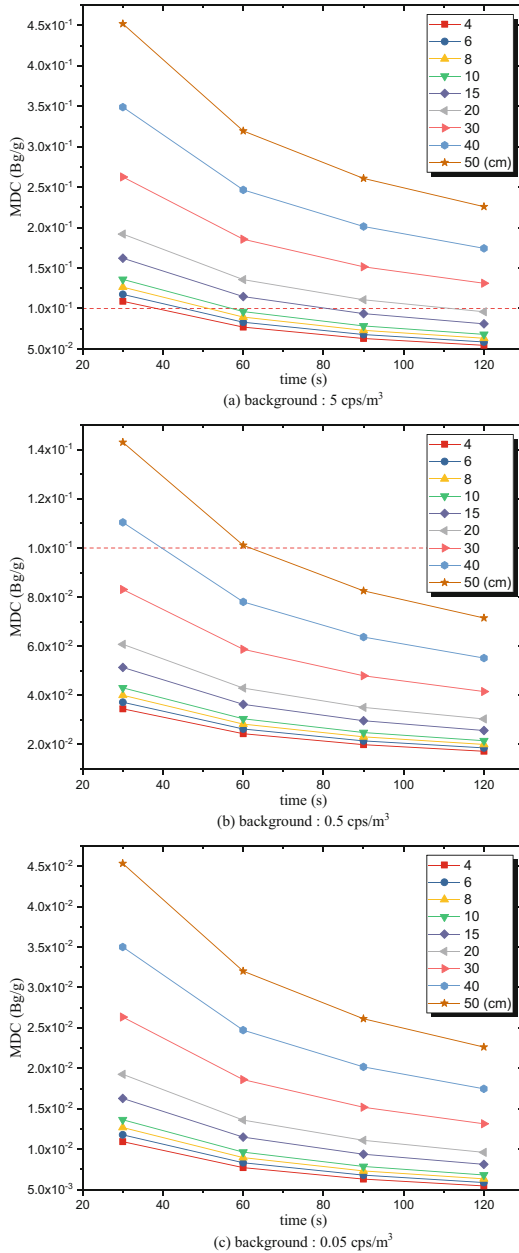
Fig. 4. Difference in the mdc with the average distance between the detector and the upper surface of waste in different environment backgrounds

(a) background : 5 cps/m³

(b) background : 0.5 cps/m³
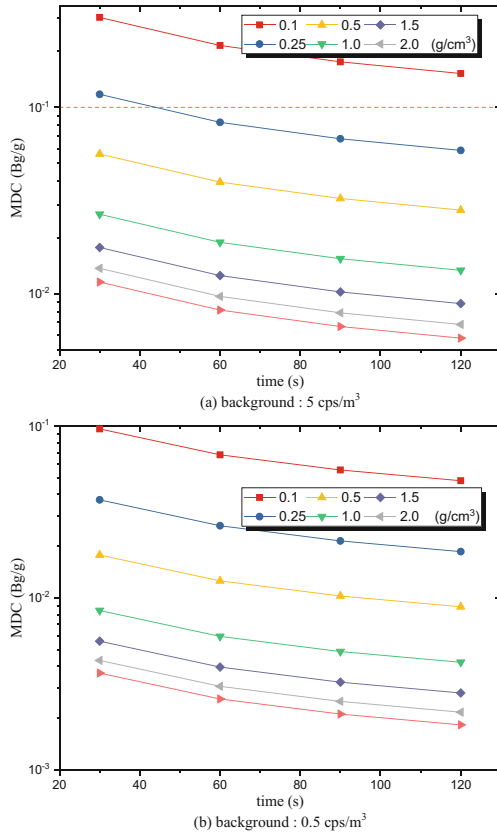
Fig. 5. Difference in the mdc with the density of waste in different environment backgrounds

As shown in Fig. 6(a), when the spacing between adjacent waste boxes is 1 m, the thickness of the shielding lead layer is 2 cm and 4 cm, respectively, the background count rate can be reduced to 5 cps·cm^{-3} and 0.5 cps·cm^{-3} as shown in Fig. 6(a) and (b), when the spacing between adjacent waste boxes is 1.5 m or more, the background count rate can be reduced to 5 cps·cm^{-3} and 0.5 cps·cm^{-3} when the thickness of the shielding lead layer is 1 cm and 3 cm, respectively. As shown in Table 2, for a conservative estimate, when the distance between adjacent waste boxes is selected for 1 m, the background count rate is reduced to 5 cps·cm^{-3} and 0.5 cps·cm^{-3}, respectively. The weight of lead shielding is about 139.3 kg and 303.1 kg, because the aging lead used for shielding is expensive, so it is proposed to use 2 cm thickness lead shielding.

Table 1. Background count rate in NAI without sheilding

Background type		NaI count rate response/CPS·Bq^{-1}
Regional environmental background		3.74E-05
Waste box to be tested	Distance 1.0 m	6.52E-03
	Distance 1.5 m	3.14E-03
	Distance 2.0 m	1.56E-03
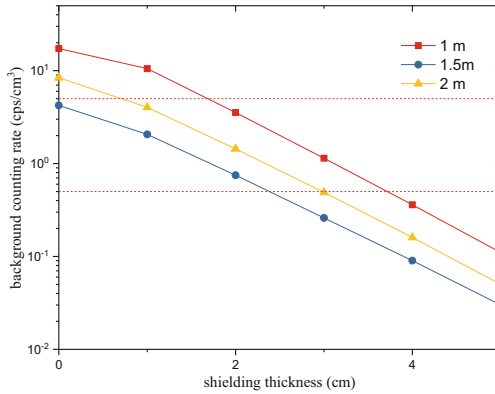
Fig. 6. Difference in the MDC with the distance between adjacent wastes to be detected

Table 2. Parameters after shielding

Shield lead layer thickness/ cm	Background count rate/ cps·Bq^{-1}	Number of crystals	Minimum source distance/ cm	Waste minimum density/ g·cm^{-3}	Lead shield weight/ kg
2	5	4	20	0.25	139.3
4	0.5	Unlimited	50	Unlimited	303.1

4   Conclusions

In this paper, Monte Carlo software MCNP and FLUKA are used to simulate the influence of the number of NaI crystals, the composition of the measured object, the distance between the detection crystal and the measured object, and the measurement time on the lower limit of detection. The results show that:

1) In the case of the same arrangement method, the lower limit of detection varies with the increase in the number of detected crystals; the low limit of detection of the

tiling type is better than the two-layer superposition form; it is expected to use 8 NaI crystal tiling type arrangement method in engineering.

2) The low limit of detection deteriorates as the average distance between the detector and the upper surface of the waste increases;

3) The low limit of detection increases with increasing waste density;

Taking into account the weight and shielding effect of lead shielding, it is proposed to use 2 cm thickness lead shielding to reduce the background count rate to 5 cps·cm^{-3} below, at the same time, the average distance between the NaI detector and the upper surface of the waste should be controlled at 20 cm, and the waste density should be controlled not less than 0.25 g·cm^{-3}.
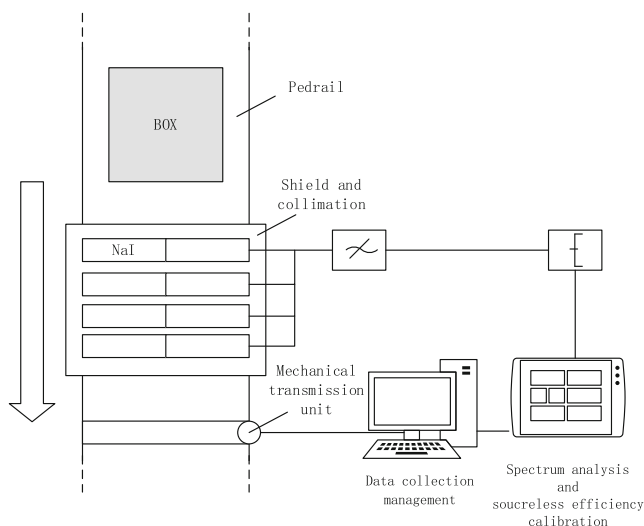
Fig. 7. Device schematic

Based on the above research contents, this paper designs the device as shown in the Fig. 7. The conveyor transports the detection cassettes containing the radioactive waste into the detection chamber with shielding and collimation through the pedrail. The source-less efficiency and energy spectrum analysis program completes the calibration and measurement of the waste, according to which the radioactive of the waste is judged and classified, and the transmission device is controlled to continue to move.

References

1. Ministry of Environmental Protection, Ministry of Industry and Information Technology, National Defense Science and Industry Bureau. Classification of Radioactive Waste (2017)
2. Ren, X., Liu, W.: Radwaste management for nuclear facility decommissioning. Radiat. Prot. Bull. **28**(4), 1–7 (2008)

3. Wang, P., Liao, Y., Wei, G., et al.: The requirement of radioactive waste clearance level. Nucl. Saf. **14**(2), 6–11 (2015)
4. Teng, Y., Zuo, R., Wang, J.: Technical methods of evaluation of nearsurface disposal of very low level radioactive waste. Bull. Mineral. Petrol. Geochem. **30**(1), 59–64 (2011)
5. Xie, Y.: Summarization of safety assessment on disposal of low level radioactive wastes. Sichuan Environ. **30**(5), 54–58 (2011)
6. Hao, R.: Practical formulae for the detection limit in low-level radioactivity measurement. Acta Metrologica Sinica **4**(4), 303–310 (1983)
7. Sha, L., Wei, W., Xuan, Y.: Study on processing method of data near the lower limits of detection for radiation environmental monitoring. Admin. Technique Environ. Monit. **18**(1), 38–43 (2006)
8. Huang, N.: Concept and calculation of detection limit in low level radioactive sample measurement. Radiat. Prot. Bull. **24**(2), 25–32 (2004)

Hot-Pressing Sintering and Analytical Characterization of Coated Particle-Dispersed Fuel Pellets

Wentao Liu[1,2(✉)], Zongyi Shao[1,2], Ying Meng[2], Zongshu Li[1,2], and Zheng Sui[1,2]

[1] CNNC Key Laboratory of Fabrication Technology of Reactor Irradiation Special Target, Baotou 014035, China
838280916@qq.com

[2] China North Nuclear Fuel Co., Ltd., Baotou 014035, China

Abstract. Coated particle-dispersed fuel pellets have the characteristics of high thermal conductivity and multilayer protection against fission products, which are an important component of ATF fuel. In this paper, by carrying out research on the dressing process of TRISO particles, it is realized that SiC powder completely encapsulates TRISO particles. The hot-pressing sintering method was used to study the influence of different sintering aids, different hot-pressing sintering holding time, different hot-pressing sintering temperature, different hot-pressing sintering pressure and different powder particle size on the density of pellets. The power with a particle size of 10nm is sintered at 3% sintering aid, 1690 °C, 1.5h holding time, 80 MPa vacuum hot pressing, and a full ceramic micro-encapsulated fuel core with a relative density of 95% or more is prepared, and the internal particle structure is complete.

Keywords: Coated particle-dispersed fuel pellets · TRISO · Hot press sintering

1 Introduction

The purpose of research and development of advanced reactor systems is to meet the economic, environmental and social development needs of the 21st century. Its technical goals involve four aspects: sustainability, economy, safety and reliability, nuclear non-proliferation and physical protection. Specifically, it contains eight technical goals, covering various technical directions related to the design and implementation of reactors, energy conversion systems and fuel cycle facilities.

The nuclear fuel element is the core component of the reactor, and its advanced nature and safety are the important basis for the advanced nature and safety of the reactor. ATF (Accident Tolerant Fuel) fuel that can tolerate accidents to a certain extent and has inherent safety, is an important development direction in the field of nuclear fuel in the world. As an important part of ATF, the coated particle-dispersed fuel obtained from TRISO particle-dispersed silicon carbide matrix is aimed at the weakness of the traditional UO_2-Zr alloy fuel system, and combines the mature TRISO (Tri-Structural Isotropic) particles with the tolerance of fission products. As well as the advantages of

good thermal performance and thermal stability of SiC matrix, it is a more promising development direction in advanced accident-resistant nuclear fuel.

The coated particle-dispersed fuel is based on a fuel pellet with three-dimensionally isotropic TRISO-coated particles embedded in a SiC matrix. The structure of the pellets and the internal TRISO particles is shown in Fig. 1. Such pellets feature high thermal conductivity, multiple layers of protection against cracking products, and high burnup, which facilitates normal and transient operability of the reactor.
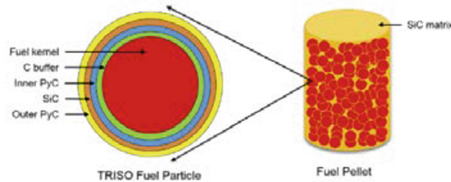
Fig. 1. Schematic diagram of TRISO particle and coated particle dispersion fuel

After the concept of coated particle dispersion fuel in which TRISO particles are dispersed in a silicon carbide matrix was proposed, researchers from the United States, South Korea and other countries have conducted in-depth research in this direction, and prepared products with good thermal conductivity. All-ceramic microencapsulated die with uniform phase distribution.

In this paper, the effect of binder on the dressing of TRISO granules and the effect of pre-compression molding pressure on the green density were studied through mixing, molding and hot-pressing sintering experiments. After the SiC matrix and TRISO particles were uniformly mixed and molded, the effects of different sintering aid contents, different hot-pressing holding times, different hot-pressing sintering temperatures, different hot-pressing sintering pressures, and different powder particle sizes on the properties of pellets were studied.

2   Materials and Methods

2.1   Materials

The TRISO particles used in the study are fuel particles with spherical UO_2 as the core. The outer layer of the core is sequentially coated with loose pyrolytic carbon, inner dense pyrolytic carbon, silicon carbide and outer dense pyrolytic carbon. The SiC powder used is β phase and its purity is greater than 99.9%. The particle size distribution of the raw material powder is relatively uniform, but the deviation between the median value and the average value is small, and the powder particle size as a whole presents a normal distribution centered on the median value.

Due to the poor sintering performance of SiC powder, in the process of preparing by NITE liquid phase sintering method, adding a small amount of sintering aid for co-sintering can improve the sintering performance of the material to a certain extent. The sintering aids used in the test are Al_2O_3 and Y_2O_3 powders with a purity > 99.9%.

2.2 Methods

Put SiC powder with a particle size of 10nm and 3wt% sintering aid (the mass ratio of nano-scale Al_2O_3 and Y_2O_3 is 7:3) into a ball mill jar, with anhydrous ethanol as the dispersant, stainless steel balls as the grinding balls, The ratio is 3:1, and the ball milling time is 4 h. After ball milling, the powder is dried, crushed and sieved; the sieved mixed powder is evenly wrapped on the surface of the TRISO particles; the TRISO particles after uniformly wrapping the base powder and the base powder are mixed uniformly according to a certain volume ratio, and then pre-compressed and formed; finally Vacuum hot pressing sintering, heating rate 10 °C·min-1, sintering temperature 1650 ~ 1750 °C, 1 ~ 2.5 h holding time, 65 ~ 90 MPa.

3 Results and Discussion

3.1 Influence of Binder on Dressing Effect of TRISO Particles

In order to improve the compatibility of SiC and TRISO particles during the green forming process of the coated particle-dispersed fuel pellets, and at the same time prevent the TRISO particles from contacting each other, it is necessary to coat a layer of SiC on the surface of the TRISO particles.

Due to the large difference in particle size between TRISO particles and SiC powder, it is difficult for SiC to directly coat the surface of TRISO particles without binder, as shown in Fig. 2(a). After investigation and test, use glycerol as binder, absolute ethanol as diluent, configure 10% glycerol-absolute ethanol as binder, and use glue tip dropper to evenly wrap the surface of TRISO particles with a layer of adhesive. Then, it is dispersed into the matrix powder (SiC + sintering aid) to realize the bonding of a layer of matrix powder on the surface of the TRISO particles. As shown in Fig. 2(b), the surface of the TRISO particles is completely covered and the dressing effect is good.

(a)   (b)

Fig. 2. Mixture macro effect diagram:(a) The effect of dressing without binder.(b) The effect of dressing without binder

3.2   Influence of Pre-press Forming Pressure on Green Density

The weight of the TRISO particles and the SiC powder after adding the sintering aid are calculated and weighed according to the volume fraction, and the ingredients are mixed, and then loaded into the pre-compression mold, and the floating female mold is pre-compressed using a micro-controlled pressure testing machine to determine the molding pressure and raw material. The relationship between blank density and TRISO particle integrity is shown in Fig. 3. It can be seen from Fig. 3 that the higher the pressing pressure, the higher the green density of the pellets. The higher the green density, the better the density of pellets after sintering, so the molding pressure should be raised as high as possible. It was observed in the experiment that when the pressure was lower than 2.0 KN, the TRISO particles were not damaged, and when the pressure reached 2.5 KN, the surface layer of some TRISO particles appeared to fall off, and there was abnormal noise during the pressing process.
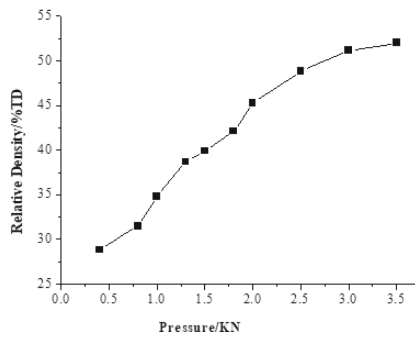
Fig. 3. Variation curve of green density with pressure

3.3   Effects of Different Hot Pressing Sintering Processes on the Properties of Pellets

Table 1 shows the density changes of pellet fuel pellets covered by pressureless sintering under different additions of sintering aids. When the addition of sintering aids is less than 3wt%, the density of pellets increases with the addition of sintering aids., when the addition amount of sintering aid is greater than 3wt%, the increase in the density of pellets is no longer obvious.

Table 2 shows the change results of the density and phase of the pellets at different hot pressing sintering temperatures. It can be seen from the results that as the sintering temperature increases, the density of the pellets increases, and the β-SiC in the pellets will be partially converted into α-SiC, when the sintering temperature is higher than 1710 °C, obvious α-SiC diffraction peaks appear in the pellet phase.

Table 1. Effect of Sintering Aid Additives on the Density of Pellets

Addition of sintering aid	Relative density of pressureless sintered pellets
0wt%	58.32%T.D
1wt%	67.24%T.D
3wt%	78.92%T.D
5wt%	78.95%T.D
7wt%	78.86%T.D
10wt%	78.97%T.D

Table 2. Influence of sintering temperature on the density and phase of pellets

Hot pressing sintering temperature	Pellets relative density	Pellets phase
1660 °C	89.77%T.D	Pure β-phase
1690 °C	92.14%T.D	No obvious α-phase diffraction peaks
1710 °C	95.31%T.D	obvious α-phase diffraction peaks
1760 °C	96.58%T.D	obvious α-phase diffraction peaks

Table 3 shows the change results of the density of pellets under different hot pressing and holding time. With the prolongation of holding time, the diffraction peak of α-SiC phase in the pellets gradually increased; when the holding time was 1h, the inner and outer layers of the pellets appeared Phenomenon, the pellets are not burned through, and after the holding time exceeds 2h, the density of the pellets does not increase significantly.

Table 3. The effect of holding time on the density of pellets

Holding time	Pellets relative density
1 h	The pellets are not fully burned, and the phenomenon of internal and external delamination occurs
1.5 h	95.31%T.D
2 h	95.89%T.D
2.5 h	95.81%T.D

Table 4 is divided into the change results of the density of pellets under different hot-pressing pressures. The analysis results show that with the increase of hot-pressing pressure, the density of pellets gradually increases. When the hot-pressing pressure is in

the range of 75 ~ 80 MPa, the The increase in density decreases. When the hot pressing pressure reaches 90 MPa, the punch on the die breaks.

Table 4. The effect of sintering pressure on the density of pellets

Hot pressing pressure	Pellets relative density
65 MPa	92.69%T.D
70 MPa	93.92%T.D
75 MPa	94.89%T.D
80 MPa	95.26%T.D
90 MPa	The punch on the die breaks

Table 5 shows the experimental results of SiC powder with different particle sizes. It can be seen from the results that with the decrease of powder particle size, the density of pellets gradually increases.

Table 5. Effect of Powder Particle Size on Pellets Density

Powder particle size	Sintering parameters	Pellets relative density
500 nm	3wt% sintering aid/1690 °C/80 MPa	94.89%T.D
100 nm		95.34%T.D
10 nm		96.23%T.D

3.4   Performance Characterization of Coated Particle-Dispersed Fuel Pellets

Using SiC matrix powder with a particle size of 10nm, vacuum hot-pressing sintering at 3wt% sintering aid addition, 1690 °C hot-pressing sintering temperature, 1.5 h holding time, and 80 MPa hot-pressing sintering pressure, the obtained all-ceramic micro-encapsulated dispersed fuel pellets were prepared. The real thing is shown in Fig. 4.

Fig. 4. Coated particle dispersion fuel pellets

The SEM of the SiC matrix is shown in Fig. 5, the second phase composed of sintering aids exists inside the SiC matrix, and the distribution is uniform. The metallographic photos of TRISO particles can clearly see that the outer layer of the particles has 4 layers of cladding layers, the particle structure is complete, and there is no damage during the molding and sintering process. After core sintering, the thickness and element distribution of each layer of TRISO particles are still comparable to those of the original particles, and the thickness of the outer dense pyrolytic carbon layer is 19 μm.
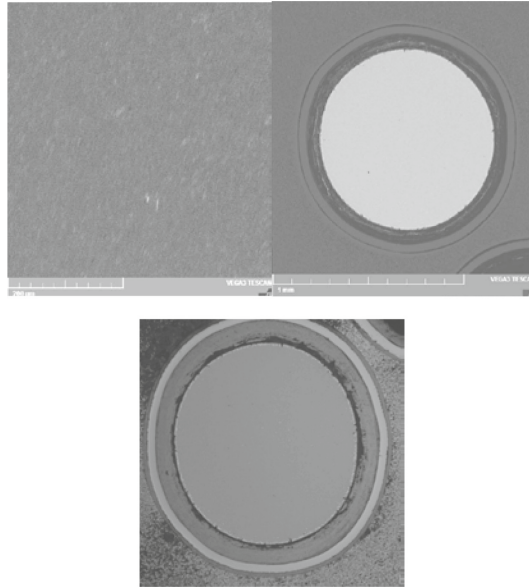
Fig. 5. SEM image of coated particle-dispersed fuel pellets

It can be seen from Fig. 6(a) that the thermal diffusivity of the coated particle-dispersed fuel core gradually decreases with the increase of temperature, and the thermal diffusivity at each temperature point is lower than that of the base SiC. The addition of TRISO particles reduces the core to a certain extent. The thermal diffusivity is still significantly higher than that of the traditional UO_2 fuel core. It can be seen from Fig. 6(b)that the thermal expansion coefficient of the fuel core increases gradually with the increase of temperature, and the change trend is linear. As the content of TRISO particles increases, the thermal expansion coefficient of the core decreases slightly. In the range of 0 – 1000 °C, the thermal expansion coefficient of the coated particle-dispersed fuel core is significantly lower than that of the traditional UO_2 core.

(a)   (b)
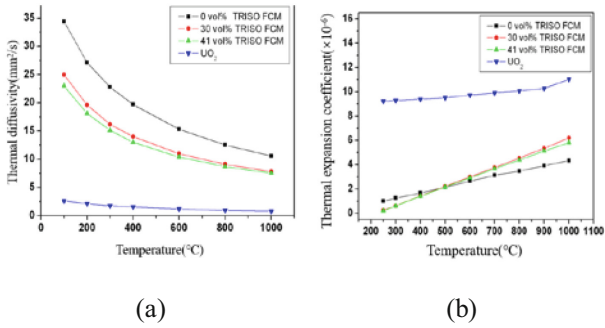
Fig. 6. Thermophysical properties vary with temperature:(a) Thermal diffusivity. (b) Thermal expansion coefficient

4   Conclusions

(1) Through the research on the dressing process of TRISO granules, TRISO granules with complete surface coating and good dressing effect were prepared.

(2) The hot-pressing sintering process of all-ceramic micro-encapsulated pellets was established, and the coated particle-dispersed fuel pellets with a relative density of 96% T.D. were prepared, and the SiC matrix phase was β-SiC, and the TRISO particles inside the pellets were evenly distributed.

(3) The thermal diffusivity of the coated particle-dispersed fuel pellets obtained under the optimal process is higher than that of the conventional UO_2 pellets, and the thermal expansion coefficient is lower than that of the conventional UO_2 pellets.

References

1. Terrani, K.A., Kiggans, J.O., Silva, C.M., et al.: Progress on matrix SiC processing and properties for fully ceramic microencapsulated fuel form. J. Nucl. Mater. **457**, 9–1 (2015)
2. Lee, H.G., Kim, D., Lee, S.J., et al.: Thermal conductivity analysis of SiC ceramics and fully ceramic microencapsulated fuel composites. Nucl. Eng. Des. **311**, 9–15 (2017)
3. Sonat Sen, R., Pope, M.A., Ougouag, A.M., et al.: Assessment of possible cycle lengths for fully encapsulated microstructure fueled light water reactor concepts. Nucl. Eng. Des. **255**, 310–320 (2013)
4. Terrani, K.A., Kiggans, J.O., Katoh, Y., et al.: Fabrication and characterization of fully ceramic microencapsulated fuels **426**, 268–276 (2012)
5. 刘荣正，刘马林，刘兵，等.碳化硅基新型包覆燃料颗粒的设计及制备[J].原子能科学技术 p. 7 (2016)
6. 许多挺，刘彤，任启森，等.事故容错燃料芯块热学性能分析[J].核动力工程 **37**(2), 82–86 (2016)
7. 刘荣正，刘马林，邵友林，等.碳化硅材料在核燃料元件中的应用[J].材料导报**29**(1), 1–5 (2015)
8. 邵友林，朱钧国，杨冰，等.包覆燃料颗粒及应用[J].原子能科学技术**39**, 117–121 (2015)
9. 李满仓，刘仕倡，秦冬，等. 全陶瓷微封装燃料压水堆弥散可燃毒物中子学分析[J].原子能科学技术**53**(7), 1188–1194 (2019)
10. 黄智恒，贾德昌，杨治华，等.碳化硅陶瓷的活化烧结与烧结助剂[J].材料科学与工艺**12**(1), 103–107 (2004)
11. 武安华，曹文斌，李江涛，等.SiC烧结的研究进展[J].粉末冶金工业**12**(3), 28–32 (2002)

12. 王静，张玉军，龚红宇.无压烧结碳化硅研究进展[J].陶瓷 **4**, 17–19 (2008)
13. Liu, F.B.: Properties and manufacturing method of silicon carbide ceramic new materials. Appl. Mech. Mater. **416–417**, 1693–1697 (2013)
14. 王坤.碳化硅技术陶瓷无压烧结工艺研究[J]. 陶瓷 **6**, 43–53 (2019)
15. 陈巍，曹连忠，张向军等. SiC陶瓷无压烧结工艺探讨兵器材料科学与工程**27**(5), 35–37 (2004)

Study on Capiliary Characteristics of Stainless Steel Wire Mesh Wick of Alkali Metal Heat Pipe

Yiru Zhu, Luteng Zhang[✉], Zhiguo Xi, Zaiyong Ma, Wan Sun, Longxiang Zhu, and Liangming Pan

Chongqing University, Chongqing, China
`ltzhang@cqu.edu.cn`

Abstract. The capillary characteristics of the wicks are of great significance to the normal operation of the heat pipe,and this study carried out the wick experiment of vertical reel stainless steel wire mesh in liquid sodium working medium and the visual observation experiment of sodium film in the wire mesh wick. The experimental results show that when the temperature of liquid sodium is about 400 °C, the capillary phenomenon of stainless steel wire mesh occurs more obviously, and after 450 °C, the evaporation of sodium is gradually obvious and accompanied by the mass fluctuation of the wire mesh wick. The visual observation experiment of sodium liquid film in the wire mesh found that the wetting and transition point of sodium on the surface of the stainless steel wire mesh was about 410 °C, which was a good verification of the occurrence of the more obvious capillary phenomenon of the wick at about 400 °C.

Keywords: Alakali metal heat pipe · Wick · Capillary characteristics · Contact angle

1 Introduction

Heat pipe is an efficient heat transfer component that uses working medium to transfer heat at different parts of the phase change. The heat pipe principle was first proposed by Gaugler [1] in 1944. In 1965, Cotter [2] first proposed a relatively complete theory of thermal management. Because of their superiority, Heat pipes are also used for cooling abyssal sea reactors and abyssal sea reactors. However, the heat transfer capacity of the heat pipe is limited by its own heat transfer limit. When the heat transfer limit of the heat pipe occurs, the heat of the reactor core cannot be exported in time, which leads to a reactor safety accident. The capillary limit is due to the fact that the capillary indenter produced by the evaporation and condensation sections of the heat pipe is not enough to overcome the pressure drop caused by the return of the working medium. The working fluid cannot flow back to the evaporation section normally. It will cause the evaporation section to dry up, and cause the wall temperature of the evaporation section to rise rapidly, and even burnout the heat pipe wall. Since the heat pipes are all operating at high temperatures in the heat pipe cooling reactor. The heat pipes must use high temperature heat pipes. The working medium of high-temperature heat pipes

is generally lithium, sodium, potassium and other alkali metals, so high-temperature heat pipes are often referred to as alkali metal heat pipes. Because of the high viscosity and density of alkali metals, a greater driving force is required in the reflux of the wick. Therefore, exploring the capillary force of the high-temperature heat pipe wick can guide the selection of the operating conditions of the heat pipe, so as to avoid the occurrence of the capillary limit of the high-temperature heat pipe and ensure the safety of the operation of the space reactor.

The most commonly used methods for testing capillary characteristics in the wick are the bubble method [3] and the capillary rising method. Shufeng Huang [4] tested the capillary characteristics of a new type of stainless steel fiber-powder composite wick with the capillary rise method and compared it with a composite wick with a single structure and other structures. Guanghan Huang [5] used an infrared camera to set up a capillary rise rate test device that measured the capillary characteristics of the axial channel wick of the alkaline corrosion treatment. Yong Tang [6] used an infrared camera combined with capillary rise method to measure the capillary performance of the sintered groove composite wick, sintered wick and groove wick with ethanol as the working medium. The results show that the sintered powder wick has better capillary characteristics than the single structure wick. Heng Tang [7] measured the capillary characteristics of a new micro-V-shaped channel wick using the capillary ascending method and acetone as the working medium. Daxiang Deng [8] used a new infrared thermal imaging method to test the capillary characteristics of the sintered groove wick with ethanol as the working medium. Daxiang Deng [9] also tested the capillary characteristics of the micro-V-channel wick with ethanol and acetone for the working medium. Li [10] calculated the capillary characteristics of different porosity wicks in acetone using the mass change curve assessment recorded by the electronic balance.

Most of the above scholars are experiments on the capillary characteristics of sintered wicks, groove wicks and composite wicks with ethanol and acetone as working medium. Due to the reactive chemical properties of the alkali metal working medium, there are fewer test experiments for the capillary core performance of alkali metal heat pipes. In this paper, 304 stainless steel is used as the material of the wire mesh wick, sodium is used as the working medium, and the capillary characteristics of the wire mesh wick is studied by the capillary rising method, and the capillary characteristics of the sodium heat pipe are preliminarily explored. The sodium film in the screen was photographed, and the spread of liquid sodium at different temperatures on the stainless steel wire mesh was obtained, and the law of the capillary ability of the wire mesh wick changed with temperature was verified.

2 Experimental Methods and Principles

2.1 Experiment on Capillary Ability of the Wire Mesh Wick

The capillary ability experiment of the wick is measured by the capillary rise method and the quality change process of the wick is recorded with an electronic balance. Figure 1 shows the entire experimental setup and schematic. The experimental principle is that when the wire mesh wick sample is extended into a stainless steel test tube containing liquid sodium, the liquid sodium will be sucked into the wick due to the influence of
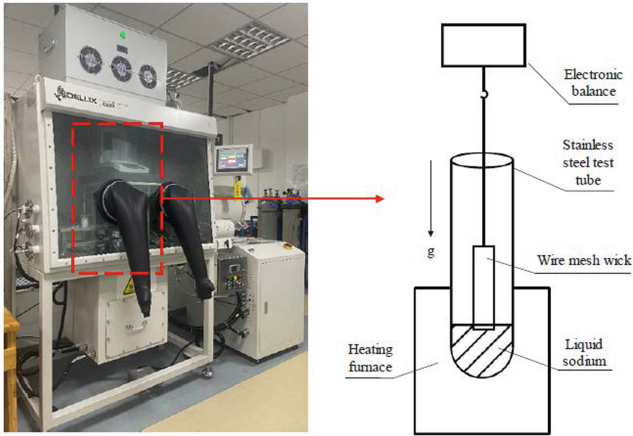
Fig. 1. Capillary ability test equipment diagram

capillary force and can reach a certain height. When the rise of sodium in the wire mesh wick reaches stability, the following relationship is satisfied:

$$h = \frac{2\sigma \cos\theta}{\rho g r_p} = \frac{2\sigma}{\rho g r_{eff}} \tag{1}$$

wherein θ is the contact angle between sodium and the wire mesh wick, the σ is the surface tension of liquid sodium, r_p is the liquid sodium density, r_{eff} is the effective capillary radius of the wick, and r_p is the pore radius. The experimental equipment includes glove box, well-type heating furnace, electronic balance and so on. The glove box provides an inert gas environment with its own dehydration and deaeration functions, which can avoid the contamination of the sodium working medium by oxygen and water vapor during the experiment. Both the well furnace and the electronic balance are placed inside the glove box in the argon atmosphere. The electronic balance has a maximum range of 220 g, an accuracy of 0.2 mg, and can be connected to the computer segment to output real-time quality changes. The test tube contains a K-type thermocouple for internal liquid sodium temperature measurement, and the XSR21A series paperless recorder is used to implement the output temperature data, and the paperless recorder error is 0.2%· F, which F is the set range.

2.2 Sodium Membrane Spreading Observation Experiment

The spreading observation experiment of liquid sodium on the surface of stainless steel wire mesh is based on a heating stage and a microscope, and the experimental equipment diagram is shown in Fig. 2. The hot stage contains platinum electric heating material and crucibles inside and can be heated at a maximum heating temperature of up to 1500 °C. Cold water circulation devices and inert gas runners are provided around the hot stage. Cooling circulation units are used to cool hot stage materials, and inert gases can reduce air pollution to sodium during experiments. The microscope has a maximum magnification of 1000X and can observe samples in the micron range.
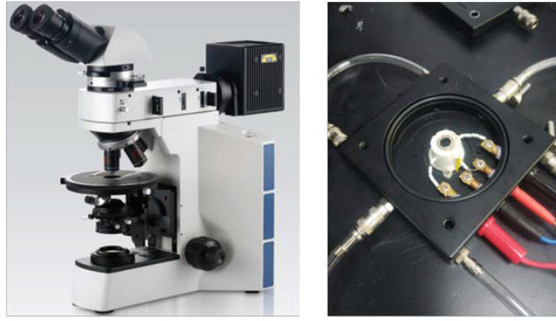
Fig. 2. Hot stage experimental equipment diagram

During the experiment, argon gas is continuously pumped in the crucible of the hot stage, and then the sodium block is placed inside the crucible of the hot stage, and then the cleaned stainless steel wire mesh is covered on the surface of the sodium block. Close the hot stage cover and place under the microscope and select multiples of the microscope objective, focusing until the mesh structure is clearly visible. Then turn on the chiller and turn on the heating to photograph the screen at the set temperature.

3   Analysis of Experimental Processes and Results

The experiment adopted 800 mesh 304 stainless steel wire mesh wick as the material, and it was fixed by three-layer rolling. The wick was cleaned in absolute ethanol and acetone successively using an ultrasonic cleaner. Samples of the cleaned wick was sent to the inside of the glove box through the glove box transition chamber. Removed the sodium from the kerosene in the glove box and cut off the surface oxide layer of sodium with a knife. Weigh 120 g of sodium on a balance and place in a stainless steel test tube. The balance indication was adjusted and zeroed, and the wick was weighed and fixed with a hook under the balance, resulting in an initial mass of 44.847 g. The tube clamping height was adjusted by the motor, and the initial liquid sodium infiltration depth was calculated to be about 1.2 cm. The experimental heating temperature program was set to rise first and then fall. When the water content and oxygen content in the gloves dropped below 0.5 ppm and 1 ppm, respectively, and the balance indication was no longer significantly changed, the well furnace was opened and the experiment began. The experimental results of the 800 mesh 3-layer wire mesh aspiration core are shown in Fig. 3.

As can be seen from the Fig. 3, the mass of the wick remains essentially unchanged when heated to 300 °C at the initial temperature. At 300 °C, the stepper motor is driven to move the wick sample downward so that it comes into contact with the liquid sodium, so there is a turning point of mass degradation at 300 °C. In the temperature range of 300–400 °C, the mass of the wick increases only slightly, and is accompanied by small mass fluctuations, and the analysis may be due to the combined effect of sodium flow and sodium evaporation. After the temperature reaches 400 °C, the mass of the wick as shown in Fig. 3 increases significantly and basically reaches the initial level. When
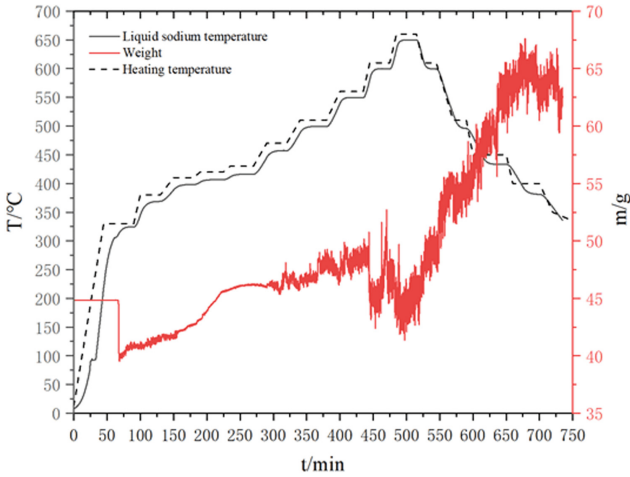
Fig. 3. 800 mesh wick experimental result diagram

heated from 400 °C to 450 °C, the mass of the wick changes are small and there are no significant mass fluctuations. When the liquid sodium temperature reaches 450 °C, the evaporation of metallic sodium is significantly enhanced, which directly leads to significant fluctuations in the quality of the wick in the range of temperature 450 °C to 650 °C. When heated to around 520 °C at 450 °C, the mass of the wick increases slightly. Bader [11] shows that the contact angle of sodium on the 304 stainless steel wire varies with temperature as shown in Fig. 4, which shows that sodium has a wetting transition point near about 400 °C. Therefore, the quality of the wick changes significantly at 400 °C in the experiment, because the contact angle of liquid sodium on the surface of stainless steel is suddenly reduced, so that the capillary ability of the wick is enhanced. The experimental results are basically consistent with the results of the contact angle change given in the literature. And after 500 °C, the liquid sodium and stainless steel have basically been completely wet, the mass change of the wick is not as obvious as when it is 400 °C, and the violent sodium evaporation phenomenon makes the quality of the wick fluctuate greatly.

However, during heating from 520 °C to 650 °C, the quality of the wick decreases slightly. However, in the cooling stage after 650 °C, due to the increase in surface tension of liquid sodium, the capillary effect is enhanced, the suction effect of the wick on sodium is enhanced, the quality of the wick continues to rise, and the quality of the wick reaches stability after the cooling reaches 400 °C. Figure 5 shows the results of the wick, which shows that the sample has been basically completely infiltrated at the end of the experiment, and the highest infiltration height of sodium measured with a ruler is about 15 cm, and the final wick weighing mass has reached 49.378 g.
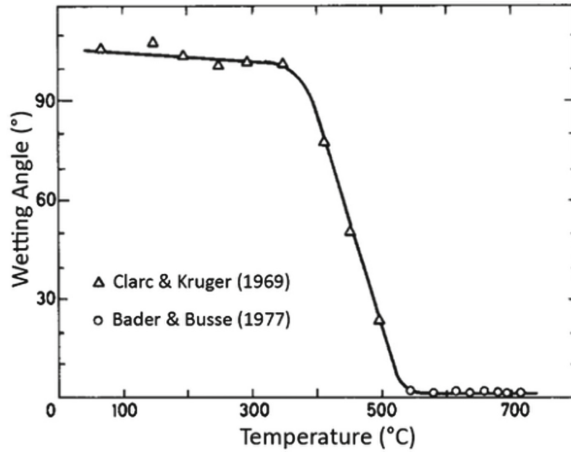
Fig. 4. The contact angle between liquid sodium and stainless steel changes with temperature
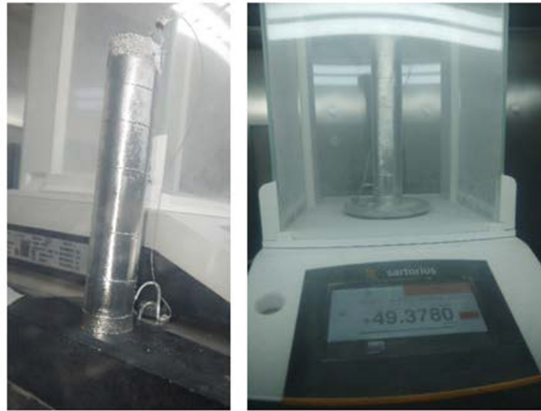
Fig. 5. wire mesh wick sodium aspiration experimental result diagram.

The results of the wire mesh wick sodium liquid film observation experiment are shown in the following figure. Figure 6 shows the microstructure diagram of the wick in the initial state, and the surface of the wire mesh shows a silvery-white luster. At a heating temperature of 400 °C, the wire mesh surface loses its original luster, producing yellow and green corrosive products. One of the corrosion products contains a Cr_2O_3 oxide layer on the surface of stainless steel that reacts with sodium to form a $NaCrO_2$ ternary oxide. At this time, a clear metallic luster appears inside the wire mesh, and liquid sodium begins to be gradually sucked onto the surface of the wire mesh wick Fig. 7.

When the heating temperature reaches 500 °C, liquid sodium is sucked onto the surface of the wire mesh due to capillary force, and the experimental results are shown in Fig. 8. When the heating temperature reaches 550 °C, the objective lens is contaminated
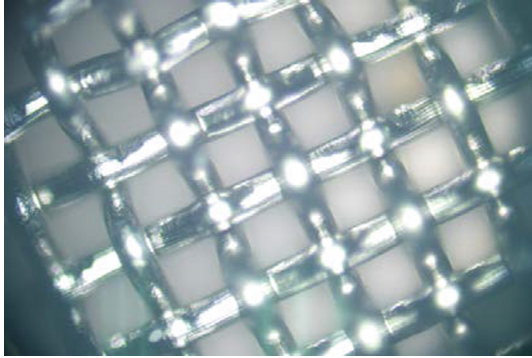
Fig. 6. Mesh structure diagram in the initial state

with sodium vapor due to the evaporation of sodium, resulting in a decrease in the brightness of the picture as shown in Fig. 9. At 600 °C, due to the evaporation of sodium, the reason for the reduction of the sodium film inside the wire mesh and the reason why the sodium vapor covers the lens cannot be observed significantly metallic. The observation experiment of sodium film spreading in the wire mesh is a good verification of the results of the increase of the capillary capacity of the 800 mesh wire mesh wick with the increase of temperature, and the increase of sodium suction of the wick leads to the increase of its own quality. During the experiment, a momentary temperature transition point was captured, it was about 410 °C. Since the argon gas flow has been passed through during the experimental process, the temperature on the surface of the wire mesh will be slightly lower than the temperature of the heating wire, so the temperature transition point should be before 410 °C.
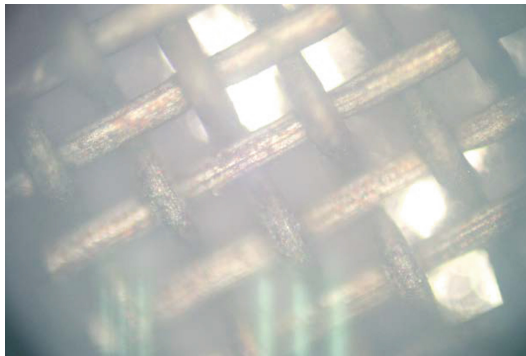
Fig. 7. Spread of sodium film in the wick at 400 °C
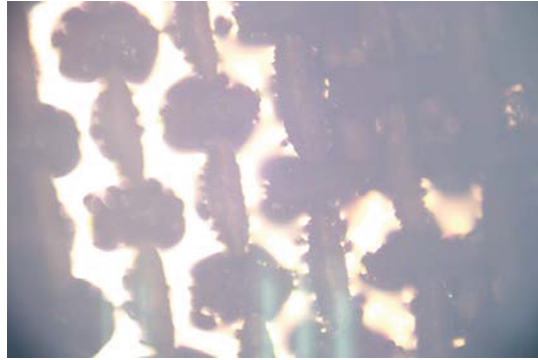
Fig. 8. Spread of sodium film in the wick at 500 °C

Fig. 9. Spread of sodium film in the wick at 600 °C

4 Conclusion

In the capillary ability experiment of the wick, when heated from 300 °C to 450 °C, the quality of the wick increased to a certain extent, and the increase of sodium vapor after 450 °C made the quality of the suction core fluctuate significantly. In the temperature range of 520–650 °C, the quality of the wick is slightly reduced. The magnitude of the fluctuations also increases as the temperature increases. And in the process of cooling down by 650 °C for the first time, with the increase of the surface tension of liquid sodium, the wick has a significant increase in mass. Before and after the experiment, the sodium infiltration height of the 800-mesh wick increased from 1.2 cm to 15 cm, and the mass increased from 44.847 g to 49.378 g. The observation experiment of the spread of sodium film in the wire mesh proved that when near 410 °C, there is a transition point of liquid sodium and stainless steel wetting, and the capillary ability increases more obviously, and more sodium is sucked on the suction core, which is mutually verified with a strong growth when the quality of the wick is about 400 °C in the capillary experiment. And at 500 °C, liquid sodium has good wetting properties on the surface of

stainless steel wire mesh, and liquid sodium has been better spread on the surface of the wire mesh wick.

References

1. Gaugler, R.S.: Heat transfer device: Google Patents (1944)
2. Cotter, T.: Theory of heat pipes. Los Alamos Scientific Laboratory of the University of California (1965)
3. Adkins, D.R., Dykhuizen, R.C.: Procedures for measuring the properties of heat-pipe wick materials[R]. Sandia National Labs., Albuquerque, NM (United States) (1993)
4. Huang, S., Wan, Z., Zhang, X., et al.: Evaluation of capillary performance of a stainless steel fiber–powder composite wick for stainless steel heat pipe. Appl. Therm. Eng. **148**, 1224–1232 (2019)
5. Huang, G., Yuan, W., Tang, Y., et al.: Enhanced capillary performance in axially grooved aluminium wicks by alkaline corrosion treatment. Exp. Thermal Fluid Sci. **82**, 212–221 (2017)
6. Tang, Y., Deng, D., Lu, L., et al.: Experimental investigation on capillary force of composite wick structure by IR thermal imaging camera. Exp. Thermal Fluid Sci. **34**(2), 190–196 (2010)
7. Tang, H., Tang, Y., Yuan, W., et al.: Fabrication and capillary characterization of axially micro-grooved wicks for aluminium flat-plate heat pipes. Appl. Therm. Eng. **129**, 907–915 (2018)
8. Deng, D., Tang, Y., Huang, G., et al.: Characterization of capillary performance of composite wicks for two-phase heat transfer devices. Int. J. Heat Mass Transf. **56**(1–2), 283–293 (2013)
9. Deng, D., Tang, Y., Zeng, J., et al.: Characterization of capillary rise dynamics in parallel micro V-grooves. Int. J. Heat Mass Transf. **77**, 311–320 (2014)
10. Li, J., Zou, Y., Cheng, L.: Experimental study on capillary pumping performance of porous wicks for loop heat pipe. Exp. Thermal Fluid Sci. **34**(8), 1403–1408 (2010)
11. Bader, M., Busse, C.A.: Wetting by sodium at high temperatures in pure vapour atmosphere. J. Nucl. Mater. **67**(3), 295–300 (1977)

Analytical Method Research of Source Term for Steam Generator Tube Rupture Accident of Small Modular Reactor

Ming-ming Xia(✉), Jun-long Wang, Jian-ping Zhu, Chao Tian, and Jia-jia Liu

Science and Technology on Reactor System Design Technology Laboratory, Nuclear Power Institute of China, Chengdu, Sicuan, China
xiamingmin@gmail.com

Abstract. Based on the full reference to the existing engineering practice and safety review experience, and considering the actual design characteristics of the small modular reactor ACP100, a set of source term analysis method suitable for ACP100 of the steam generator tube rupture (SGTR) accident is proposed, and the source term analysis and consequence evaluation of ACP100 SGTR accident was carried out using this method. The analysis shows that the radiological consequences of the accident source term calculated by this method meet the acceptance criteria of small modular reactor. The analysis results of this article can provide support for the follow-up review of accident source term of ACP100.

Keywords: Small modular reactor · SGTR · Source term analysis method

1 Introduction

The steam generator tube rupture (SGTR) is one of the design basis accidents with high frequency and great impact during the life of the pressurized water reactor nuclear power plant, and it is also the focus of domestic nuclear safety supervision and review agencies. After SGTR, the water and steam in secondary coolant were radioactively polluted due to the release of primary coolant containing radionuclides to the secondary coolant through the break in the tube of steam generator. The radioactively polluted secondary coolant steam is released to the environment through the condenser extraction or the safety valve of the steam generator, resulting in radioactive contamination of the environment [1]. Therefore, it is great significance to carry out the SGTR source term analysis conservatively and reasonably.

This study fully investigates the SGTR source term analysis methods of M310 and Hualong 1 (ACP1000). By comparing the design differences of M310, ACP1000 and ACP100, according to the calculation assumptions and parameters of M310 and ACP1000, combined with the design characteristics of ACP100, proposed the SGTR source term analysis method of ACP100, and an ACP100 nuclear power unit SGTR source term analysis and radiological consequence evaluation are carried out using this method.

2   Calculation Assumptions and Parameters

In this study, the calculation assumptions and parameters of M310, ACP1000 and ACP100 regarding the primary coolant activity and the iodine carryover coefficient in the steam generator were compared and analyzed.

2.1   Primary Coolant Activity

In the accident condition, the primary coolant activity will have an activity peak phenomenon. At this time, the primary coolant activity is in a transient value, and transient assumptions is related with steady state value before the accident.

2.1.1   Primary Coolant Activity in Steady State

SGTR source term analysis of M310, the primary coolant activity in steady state is normalized at 4.44 GBq/t in I-131 equivalent, it is the maximum value of 200 reactor-year operations in a French nuclear power plant [2]. This value is not conservative enough to be lower than the operating limit of primary coolant activity [3]. SGTR source term analysis of ACP1000, the primary coolant activity in steady state is normalized at 37 GBq/t DE I-131, it is assumed that the fuel element cladding failure rate is 0.25%. This value corresponds to the technical specification the maximum radioactivity limit condition is conservative enough [4]. Therefore, ACP100 refers to assumption of ACP1000, and the primary coolant activity in steady stat is assumed that the fuel element cladding failure rate is 0.25%, and the calculation results are normalized at 7.4 GBq/t DE I-131, as shown in Table 1.

2.2   Primary Coolant Activity in Transient State

2.2.1   Primary Coolant Noble-Gas Activity in Transient State

Primary coolant noble-gas activity in transient state of M310 and ACP1000 are the steady state value multiplied by the crest factor, the crest factor is taken from the operating experience of the French nuclear power station. The main factors affecting the crest factor are the reactor power and operating pressure. M310, ACP1000 and ACP100 have different reactor power, but the fuel assemblies used are of the same type, the mechanism of fission products released from damaged fuel rods to the primary coolant is the same, and the primary coolant system pressure is similar, so the primary coolant noble-gas activity in transient state calculation of ACP100 can use the same crest factor as that of M310 and ACP1000. The crest factor is shown in Table 1.

2.2.2   Primary Coolant Iodine Activity in Transient State

For M310, the primary coolant iodine activity in transient state is the steady state value multiplied by the crest factor. ACP1000 considers two case of preaccident iodine spike and concurrent iodine spike, referring to the assumptions in RG1.183 [5]. For preaccident iodine spike case, primary coolant iodine concentration to the maximum value (typically 60 μCi/gm DE I-131) peimitted by the technical specification. For concurrent iodine

spike, the increase in primary coolant iodine concentration is estimated using a spiking model that assumes that the iodine release rate from the fuel rods to the primary coolant increases to a value 335 times greater than the release rate corresponding to the iodine concentration at the equilibrium value (typically 1.0 μCi/gm DE I-131) specified in technical specifications, the assumed iodine spike duration should be 8 h. Through comparative analysis, the iodine peak release phenomenon in the SGTR source term analysis of M310 considers the transient state before the accident, which is similar to the preaccident iodine spike case of ACP1000, but the M310 does not consider the peak release phenomenon similar to concurrent iodine spike case of ACP1000.

According to the stipulations in Analysis criterion of the design basis accident source terms for pressurized water reactor nuclear power plant(NB/T 20444-2017RK) [6], the SGTR source term analysis in new pressurized water reactor nuclear power plants should consider the preaccident iodine spike case and concurrent iodine spike case, SGTR preaccident iodine spike case accident is a limit accident, and SGTR concurrent iodine spike case accident is a rare accident. Therefore, the ACP100 SGTR accident source term analysis intends to consider preaccident iodine spike case and concurrent iodine spike case.

1) Primary coolant activity in preaccident iodine spike
   If ACP100 directly refers to the assumption of RG1.183, it is obviously too conservative to increase primary coolant activity in preaccident iodine spike to 2220 GBq/t DE I-131. Therefore, for the SGTR preaccident iodine spike, the primary coolant activity in preaccident iodine spike calculation method is proposed in this paper of ACP100.

   Referring to ACP1000, the iodine peak assumes that the primary coolant activity in preaccident iodine spike increases from 37 GBq/t DE I-131 to 2220 GBq/t DE I-131, that is, the primary coolant activity in preaccident iodine spike increases to 60 times steady state value. Therefore, assuming SGTR preaccident iodine spike of ACP100, the primary coolant activity in preaccident iodine spike also increases to 60 times the steady state value(7.4 GBq/t DE I-131), that is, 444 GBq/t DE I-131. Under this assumption, primary coolant activity in preaccident iodine spike of ACP100 is shown in Table 1.

2) Primary coolant activity in concurrent iodine spike

   For SGTR concurrent iodine spike accident analysis of ACP100, referring to the assumption of RG1.183, assuming that the iodine release rate from the fuel rods to the primary coolant increases to a value 335 times greater than the release rate corresponding to the iodine concentration at the equilibrium value (7.4 GBq/t DE I-131) specified in technical specifications, that is, the leakage rate from the fuel element into the primary coolant is 335 times the normal leakage rate, the assumed iodine spike duration should be 8 h.

The leakage rate of iodine from the fuel element into the primary coolant in transient state:

$$L_i = \frac{C \cdot R_i}{I_i \cdot f_i \cdot \eta} \tag{1}$$

L_i is the leakage rate of the nuclide from the fuel element into the primary coolant in transient state, 1/s;
C is the iodine concentration increase times in transient state;
R_i is the equilibrium iodine release rate of nuclide, Bq/s;
I_i is the inventory of the nuclide in core, Bq;
f_i is the nuclide fraction in the fuel pellet-cladding gap;
η is the fuel cladding damage fraction, 0.25%.

Table 1. Primary coolant activity

Nuclides	Primary coolant activity in steady state (GBq/t)	Crest factor	primary coolant activity in preaccident iodine spike (GBq/t)	Leakage rate of iodine from the fuel element into the primary coolant in transient state (1/s)
Kr-85m	1.37E + 01	2.38	3.25E + 01	/
Kr-85	4.57E-01	1.00	4.57E-01	/
Kr-87	2.00E + 01	2.34	4.69E + 01	/
Kr-88	3.27E + 01	2.28	7.46E + 01	/
Xe-133m	5.31E + 00	2.22	1.18E + 01	/
Xe-133	1.56E + 02	1.89	2.96E + 02	/
Xe-135	1.13E + 02	1.35	1.52E + 02	/
Xe-138	3.59E + 01	2.84	1.02E + 02	/
I-131	4.94E + 00	/	2.97E + 02	5.63E − 04
I-132	4.74E + 00	/	2.84E + 02	1.60E − 03
I-133	7.47E + 00	/	4.48E + 02	5.59E − 04
I-134	1.44E + 00	/	8.64E + 01	1.01E − 03
I-135	4.04E + 00	/	2.43E + 02	5.86E − 04
DE I-131	7.4	/	444	/

2.3   Iodine Carrying Coefficient in Steam Generator

The design of the once-through steam generator used in ACP100 is quite different from the U-tube steam generator used in M310 and ACP1000 [7]. The U-tube steam generator

is a saturated steam generator. The heat transfer tube of the steam generator is completely immersed in water. The iodine of primary coolant leaking to the secondary coolant through the break of the steam generator tube enters the secondary coolant. The iodine of liquid phase is carried into the gas phase on the secondary coolant with the steam, and then released to the environment through the safety valve of the steam generator.

For the once-through steam generator, the secondary coolant is divided into a pre-heating section, an evaporation section and a superheating section according to the characteristics of the boiling phase change of the secondary coolant. In the superheat section, the iodine in the liquid flashes quickly into the vapor phase and is released to the environment through the steam generator safety valve. Compared with the U-tube steam generator, the iodine in the once-through steam generator is more easily carried by the vapor from the liquid phase to the vapor phase. Therefore, the carry coefficient is obviously not conservative enough if ACP100 directly refers to the iodine of M310 or ACP1000 on the secondary coolant of the steam generator. Since the liquid on the wall of the heat transfer tube will evaporate to dryness in the superheating section of the once-through steam generator, during this process, the iodine in the secondary coolant liquid phase will flash into the secondary coolant vapor phase. So it can be conservatively assumed that iodine carryover factor on the secondary coolant of steam generators is 1.

3   SGTR Source Term Analysis and Radiological Consequence Evaluation of ACP100

3.1   Source Term Analysis Results

Using the calculation assumptions and parameters in Sect. 2, the cumulative source term to the environment after SGTR accident calculated using the ASTA program are shown in Table 2. ASTA is a program independently developed by nuclear power institute of china for calculating the release of radionuclides to the environment under accident conditions.

3.2   Analysis Results of Radiological Consequences

The individual dose limits in the "Principles for Safety Review of Modular Small Pressurized Water Reactor Nuclear Power Plant Demonstration Projects (Trial version) in Chinese" are respectively determined as: The effective dose that the public individual (adult) may receive in each rare accident should be controlled below 5 mSv, and the thyroid equivalent dose should be controlled below 50 mSv; In each extreme accident, the effective dose that the public (adult) may receive should be controlled below 10 mSv, and the thyroid equivalent dose should be controlled below 100 mSv.

Using the site meteorological data of an ACP100 nuclear power plant, the radioactive consequences outside the factory were calculated for the source term of preaccident iodine spike case and concurrent iodine spike case are shown in Table 3, meet the acceptance criteria.

Table 2. Activities released to the environment after SGTR accident

Nuclides	Activities released to the environment after SGTR (Bq)	
	Preaccident iodine spike case	Concurrent iodine spike case
Kr-85m	1.59E + 11	1.59E + 11
Kr-85	2.40E + 09	2.40E + 09
Kr-87	1.95E + 11	1.95E + 11
Kr-88	3.52E + 11	3.52E + 11
Xe-133m	6.18E + 10	6.16E + 10
Xe-133	1.55E + 12	1.54E + 12
Xe-135	7.88E + 11	7.73E + 11
Xe-138	1.87E + 11	1.87E + 11
I-131	1.23E + 12	1.32E + 11
I-132	1.05E + 12	1.27E + 11
I-133	1.83E + 12	2.38E + 11
I-134	2.66E + 11	9.51E + 10
I-135	9.62E + 11	1.67E + 11

Table 3. Consequence of SGTR accident

Consequence	Effective dose (mSv)	Thyroid equivalent dose (mSv)
Preaccident iodine spike case	5.99	80.3
Concurrent iodine spike case	0.7	9.14

4   Conclusions

In this paper, on the basis of fully learning from the existing nuclear power projects, combined with the actual design characteristics of ACP100, a set of source term analysis methods for SGTR preaccident iodine spike case and concurrent iodine spike case suitable for ACP100 are proposed, and this method is used to analyze the SGTR accident source term of an ACP100 nuclear power plant has been identified, and its radiological consequences also meet the radiological consequences acceptance criteria in "Principles for Safety Review of Small Modular Pressurized Water Reactor Nuclear Power Plant Demonstration Projects (trial version) in Chinese".

References

1. Fan, Y., et al.: Calculation and analysis of steam generation tube rupture accident source term in PWR. Nucl. Tech. **43**(06), 31–36 (2020). (in Chinese)

2. Chen, Y., et al.: Analysis of radiological consequence of SGTR accident at PWRS. Radiat. Prot. Bull. **31**(006), 1–5 (2011). (in Chinese)
3. Chen, Y., et al.: Comparison of SGTR accident source terms for AP1000 and CPR1000. Radiat. Prot. **31**(003), 129–133 (2011). (in Chinese)
4. Tao, J., et al.: SGTR accident source term analysis methodology for HPR1000. Nucl. Sci. Eng. **39**(02), 267–273 (2019). (in Chinese)
5. NRC. Alternative radiological source terms for evaluating design basis accidents at nuclear power reactors[R]. RG1.183 (2000)
6. National Energy Administration. Analysis criterion of the design basis accident source terms for pressurized water reactor nuclear power plant. NB/T 20444–2017RK (2017). (in Chinese)
7. Song, D., Qin, Z.: Progress of LING LONG SMR technology and demonstration project. China Nucl. Power **11**(1), 21–25 (2018). (in Chinese)

Research on the Alarm Threshold for Steam Generator Tube Leak Monitoring of Small Modular Reactor

Ming-ming Xia[✉], Jun-long Wang, Tao Xu, Bo-chen Huang, Jian-ping Zhu, Yi-rui Wu, Jian-xin Miao, and Xin Chen

Science and Technology on Reactor System Design Technology Laboratory, Nuclear Power Institute of China, Chengdu, Sicuan, China

`xiamingmingmail@163.com`

Abstract. On the basis of fully learning from the existing principles of leak monitoring alarm thresholds setting of the steam generator tube in pressurized water reactor nuclear power plants, the principle of setting for N-16 leak monitoring alarm thresholds of steam generator tube in small modular reactors is proposed, and the N-16 monitoring alarm thresholds are given. The calculation method for total gamma count rate of steam generator tube leak monitoring alarm thresholds of the small modular reactor is established, and the total gamma count rate under the condition of the leak corresponding to the N-16 monitoring alarm thresholds is calculated to guide the leak monitoring total gamma alarm thresholds set.

Keywords: Small modular reactor · Steam generator tube leak monitoring · Alarm thresholds

1 Introduction

The steam generator tube is the weakest part of the pressure boundary of the primary circuit [1]. If the tube is ruptured, the radioactive nuclides will leak from the primary circuit to the secondary circuit and cause pollution of the secondary circuit, and the leak of the secondary circuit itself will lead to the release of radioactivity into the environment, which will seriously affect the safe operation of the pressurized water reactor nuclear power plant and pollute the environment, causing harm to equipment and personal safety. In the design of the leak monitoring system for the steam generator tube of the nuclear power plant in my country, two strategies are usually used to monitor the total gamma count rate and N-16 activity in the secondary circuit [2]. The two strategies are redundant with each other and are suitable for different working conditions: the N-16 activity monitor is the main measurement and supplemented by the total gamma count rate when the reactor power is higher than 20%; the N-16 activity monitor is no longer representative when the nuclear power level is lower than 20% [3]. And the rationality of the monitoring alarm threshold directly affects whether the monitoring system can run stably and effectively, so choosing a reasonable alarm threshold is the key to the design [4].

At present, VVER, M310 and ACP1000 units are typically set for leak monitoring alarm thresholds of steam generator tube in domestic nuclear power plants. Small modular reactors are different from the steam generator types of VVER, M310 and ACP1000 units, and the reactor power is also quite different, so the alarm threshold settings for steam generator tube leak monitoring of VVER, M310 and ACP1000 units cannot be directly used. Therefore, in this study, on the basis the principle of setting the leak monitoring alarm threshold for the steam generator tube of the VVER, M310 and ACP1000 units, and according to the design characteristics of the small modular reactor, the leak monitoring alarm threshold of the small modular reactor steam generator tube is carried out.

2   Setting of the Steam Generator Tube Leak Monitoring Alarm Thresholds in Domestic Nuclear Power Plants

2.1   VVER Unit

VVER determines that 1 kg/h is the normal design basis leak rate according to a large number of operating data of the units, and the N-16 first-level alarm threshold of steam generator tube leak monitoring is 2 kg/h, which is twice the normal design basis leak rate. The second-level alarm threshold of 5 kg/h is the safe operation limit of the primary side to the secondary side leak rate. The Russian side did not give the specific calculation process in the setting value report.

The total gamma first and second level alarm thresholds of the steam generator tube leak monitoring of VVER units are 1×10^{-6} Gy/h and 2×10^{-6} Gy/h respectively. There is no specific calculation method in the alarm threshold list provided by the Russian side. The speculation should be mainly based on the following aspects: the primary coolant source term, the secondary coolant radioactivity limit and the damage of the tube.

2.2   M310 Unit

For M310, the N-16 first-level alarm threshold of steam generator tube leak monitoring is 5 L/h, and the second-level alarm threshold is 70 L/h. The method does not give the basis for selecting the alarm threshold. It is speculated that the first-level alarm threshold is about 3 times the design basis leak rate under normal operating conditions, and the second-level alarm threshold of 70 L/h is derived from the operating regulations. The M310 steam generator tube leak monitoring total gamma first and second level alarm thresholds are 200 cps and 300 cps respectively. The French side does not give a specific calculation method, and it is speculated that the design idea is similar to that of the VVER.

3   Leak Monitoring Alarm Thresholds for Steam Generator Tube of Small Modular Reactor

3.1   Small Modular Reactor Design Features

The small modular reactor adopts once-through steam generator, a total of 16 units [5], of which 4 units are in a group, and each group is connected together and shares

a main steam pipeline. In the small modular reactor, one N-16 monitor and one total gamma monitor are respectively set on each main steam pipeline, and the two devices are mutually redundant. Under the normal operating conditions of the small modular reactor, the total leak rate of the primary coolant to the secondary coolant is 3.6 kg/h, so the total leak rate of the steam generator corresponding to one main steam pipeline is 1.8 kg /h under normal operating conditions.

3.2   Leak Monitoring N-16 Alarm Thresholds for Steam Generators Heat Transfer Tubes

Due to the N-16 alarm threshold for the leak monitoring design for the steam generator tube of the VVER and M310 units, a consensus has been reached between the review, design department and the owner. In the absence of extensive operational data to support, the practice of linking normal leak rates to operational thresholds is easier to interpret and sufficiently conservative. Therefore, this study attempts to determine the N-16 first and second level alarm thresholds from the following two aspects:

(1) Determine the alarm threshold based on the review of similar nuclear power plants, the consensus reached between the design department and the owner on the monitoring alarm threshold.
(2) The threshold setting is linked to the normal leak rate. Therefore, the first-level alarm threshold of the steam generator leak monitoring of the small modular reactor is to be considered to be twice the normal design basis leak rate, which is 3.6 kg/h; the second-level alarm threshold is 9 kg/h that set to be 5 times the normal design basis leak rate.

3.3   Total Gamma Alarm Threshold Setting for Leak Monitoring of Steam Generator Tube

Referring to the VVER and M310 units, the setting of total gamma alarm threshold setting for leak monitoring of steam generator tube should be determined by the primary coolant source term, the secondary coolant radioactivity limit and the size of the damage to the tube. Since there is currently no relevant specification for the secondary coolant radioactivity limit, this study only considers two factors, the primary coolant source term and the size of the damage to the tube. Since the N-16 monitor and the total gamma monitor are redundant with each other, the first and second level alarm thresholds of the two should correspond to each other, indicating the same leak level of the steam generator tube under different working conditions. Therefore, according to the N-16 alarm threshold value of steam generator tube leak monitoring, the total gamma of leak monitoring under 20% power level can be calculated through theoretical analysis, so as to guide the setting of the total gamma alarm threshold value of steam generator tube leak monitoring.

(1)   Total gamma count rate calculation

The calculation formula of the count rate is as follows:

$$C = \sum_i k_i \times \eta_i \times A_{vi} \tag{1}$$

$$A_{vi} = \frac{A_{pi} \times q \times \rho_v \times e^{-\lambda_i t}}{Q \times \rho_p} \tag{2}$$

where C is the total gamma count rate, cps;
k_i is the detection efficiency of the nuclide i in the Monte Carlo model, cps/(Bq/m^3);
η_i is the carrying coefficient of the nuclide i;
A_{vi} is the radioactive concentration of the nuclide i in the steam at the probe, (Bq/m^3);
A_{pi} is the radioactive concentration of the nuclide i in the primary coolant, Bq/kg;
q is the leak rate, L/h;
ρ_v is the steam density of the main steam pipeline at 20% power level, kg/m3;
λ_i is the decay constant of the nuclide i, 1/s;
t is the transit times between leak location and probe at the 20% power level, s;
Q is the steam flow rate at the 20% power level, L/h;
ρ_p is the average density of the primary coolant, kg/m^3.

(2)   Calculation of detection efficiency factor

The efficiency factor of the detector is related to the structure of the detector, the structure of the pipeline, and the relative position of the detector and the pipeline. Small modular reactor steam generator monitoring uses NaI detector. The steam pipe is filled with secondary side steam, the steam density is 19.07 kg/m^3, and the steam pipe is wrapped with a layer of thermal insulation material. The MCNP calculation result is a normalized result, and the result needs to be processed:

$$k_i = F8_i \times V_{source} \times I_i \tag{3}$$

where, $F8_i$ is the output result of pulses number of the MCNP that emits gamma-rays by the nuclide i, cps/γ;

V_{source} is the volume of the steam pipe, m^3;
I_i is the probability that the nuclide i emits gamma-rays.

(3)   Analysis of the effect of N-16 on the total gamma count rate

For M310 and VVER units, the transit time from the leak location and probe at low power is longer than that at full power, the N-16 decay share is large, and the contribution to the total gamma count rate is small. However, the transit time from the leak location to the outlet of the once-through steam generator tube at low power is still shorter than the half-life of N-16, and the transit time is shown in Table 1. The total gamma count rate still has a large contribution.

Table 1. N-16 transit times between leak location and outlet

Transit times between leak location and outlet (s)		Half-life of N-16(s)
20% Nuclear power level	100% Nuclear power level	
2.14	0.53	7.13

(4) Retention of radionuclides on the secondary side of steam generator

For radioactive gas nuclides, such as N-16 and nobla-gas, due to their insolubility in water, 100% of the gas nuclides leaking from the primary coolant to the secondary coolant are instantly released into the vapor phase of the secondary side. For iodine and particle-type fission product nuclides, after leaking to the secondary side of the steam generator, they will be retained by the water on the secondary side. The water on the secondary side of the steam generator evaporates in the form of water vapor and droplets. Iodine and particulate fission product nuclides are entrained into the vapor phase. For iodine, due to the once-through steam generator used in small modular reactor, the once-through steam generator has to go through the process from supercooled water to hot steam in the secondary side working medium. According to the characteristics of the boiling phase change of the working medium on the secondary side, the secondary side is divided into a preheating section, an evaporation section and a superheating section. In the superheating section of the once-through steam generator, the iodine in the water will flash quickly into the gas phase, so it is conservatively assumed that the iodine carrying coefficient on the secondary side of the steam generator is 1. The droplet entrainment fraction for particulate nuclides is equal to the water content level in the steam, i.e. 0.25%.

(5) The total gamma count rate corresponding to the leak rate of the steam generator tube

In summary, according to formula (1), under low power, when the leak rate is 3.6 kg/h, the total gamma count rate is about 35.8 cps; the leak rate is 9 kg/h, and the total gamma count rate is 89.6 cps.

(6) Environmental background

The energy response range of the total gamma monitoring channel for leak of the steam generator tube is wide, and it is easily disturbed by the environmental background. The selection of the threshold value needs to consider this aspect. In this study, the environmental background count rate was considered to be 5 cps

(7) The total gamma alarm threshold for leak monitoring of the steam generator tube.

Considering the environmental background, and considering the design margin of −20% from an engineering point of view, it is recommended that the total gamma count

rate is 50 cps as the first-level alarm threshold and 110 cps as the second-level alarm threshold.

4   Conclusions

In this study, referring to the setting of the leak monitoring alarm threshold of the VVER and M310 steam generator tube, and combined with the design value of the leak rate of the small modular reactor steam generator tube, the leak monitoring of the small modular reactor steam generator tube is proposed. Based on the principle of threshold setting, the N-16 alarm threshold for leak monitoring of the steam generator tube is given. The first-level alarm threshold is 3.6 kg/h, and the second-level alarm threshold is 9 kg/h. The calculation method of the total gamma count rate in the case of the small modular reactor for steam generator tube leak monitoring is established. According to the leak rate level of the leak monitoring N-16 alarm threshold, the total gamma alarm threshold of leak monitoring is set through theoretical analysis and calculation. The first-level alarm threshold is 50 cps, and the second-level alarm threshold is 110 cps.

References

1. Li, R., Ling, Q.: ^{16}N transmission analysis for steam generator tube leak monitoring in nuclear plant. J. Univ. South China (Sci. Technol.) **24**(03), 6–9 (2010). (in Chinese)
2. Xing, H., et al.: The study of online ^{16}N detecting system for marine nuclear power plant. Nucl. Electron. Detect. Technol. (01), 48–51+66 (2005). (in Chinese)
3. Xu, H., et al.: Research of Alarm Threshold Value of Steam Generator Tube Leak Total Gamma Monitoring Channel of Nuclear Power Plant. Zhongguo Fushe Weisheng **26**(03), 351–356 (2017). (In Chinese)
4. Jia, J., et al.: Alarm threshold value of SG sewerage radiation monitoring channel in nuclear power plant. J. Wuhan Univ. Technol. (Inf. Manag. Eng.) **35**(01), 52–55 (2013). (in Chinese)
5. Song, D., et al.: Researsh and development for ACP100 small modular reactor in china. China Nucl. Power **10**(02), 172–177+187 (2017). (in Chinese)

Thermodynamic Equilibrium Analysis of Steam Reforming Reaction of Radioactive Waste Oil

Xuan Wu[✉], Wenyu Li, Li Lin, Yi Liang, Jiaheng Zhang, Wenlu Gu, Jiheng Fan, EnWei Shen, and KouHong Xiong

Nuclear Power Institute of China Chengdu, Sichuan, China
`wx139x@139.com`

Abstract. At present, there are much radioactive waste oil temporarily stored in nuclear fuel processing plants, nuclear industry research institutes and operating nuclear power plants in China, which brings great storage pressure and safety risks to the operating nuclear facilities. In this paper, the components analysis of 40# waste oil used in nuclear facilities was carried out, and the elemental composition and chemical composition of the waste oil were obtained. The analysis showed that the main elements in the waste oil were C and H, and the main chemical components were alkanes, alkenes, aromatic hydrocarbons and alcohols with carbon chain length of 10–40. Using Aspen Plus software, the process flow model of waste oil's steam reforming treatment was established. Based on the components analysis results of the waste oil, organic mixtures such as ethanol, ethane and propane were selected as the model components, and the element composition close to waste oil was obtained by adjusting the proportion of each component. The mixture was used as the source input of Aspen Plus to achieve good simulation results. The experimental results obtained under Pt catalyst at 400 °C were in good agreement with the simulation results, which confirmed the validity of the model. The thermodynamic equilibrium analysis of waste oil steam reforming reaction was carried out by using the verified model. The influence of reaction temperature (350–1150 °C), pressure (0.01–100bar) and water to carbon ratio (0.01–100) on reforming reaction and off gas components in balanced state was studied. The conclusions are as follows: (1) The steam reforming reaction of waste oil has no obvious inhibition when the reaction pressure is less than 1bar, so the reforming reaction should be carried out under the condition of negative pressure less than 1bar; (2) The temperature should be maintained above 750 °C to ensure the complete steam reforming reaction; (3) Carbon deposition can be completely eliminated when the water/carbon ratio is higher than 1, and when the water/carbon ratio is higher than 10, the product components do not change with the water/carbon ratio.

Keyword: WASTE OIL STEAM REFORMING ASPEN

1 Introduction

In the process of operation, maintenance and decommissioning of nuclear facilities, radioactive nuclides such as ^{137}Cs, ^{90}Sr and ^{60}Co will be mixed into industrial oil to form radioactive waste oil [1]. The steam reforming treatment process developed by Studsvik is suitable for a variety of radioactive organic wastes, including waste oil, and has many advantages including high volume reduction ratio, stable solid products, and less environmental pollution [2]. Previously, Lin Li et al. from Nuclear Power Institute of China carried out a simulation on the steam reforming of waste resin and analyzed the balance products. They obtained the reaction parameters and operating gas velocity suitable for the treatment of radioactive waste resin [3–5]. However, there are few researches on steam reforming treatment of radioactive waste oil.

In the steam reforming process of waste oil, more hydrogen production is preferred, which is conducive to the subsequent off gas oxidation. Pressure, temperature and water-carbon ratio are the key parameters affecting the balanced off gas composition. A lot of experiments are needed to determine the appropriate reaction pressure, temperature and water-to-carbon ratio. But we can save a lot of effort by simulating the reaction process on the computer. Some researchers have carried out thermodynamic analysis on steam reforming of methanol [6, 7], ethanol [8–10], glycerol [11, 12] and other organic compounds, and obtained reforming reaction temperature, pressure and other operating parameters.

In this paper, Aspen Plus, a chemical process simulation software, was used to build a process model for oil steam reforming. In order to select the most suitable operating parameters for the oil steam reforming test, and to provide reference for the future engineering application of steam reforming process in the treatment of other radioactive wastes, the thermodynamic analysis of the oil steam reforming reaction was carried out and the effects of reaction temperature, pressure and water-carbon ratio on reforming reaction and off gas components was studied.

2 Oil Characterization

The feed composition is needed for thermodynamic analysis using Aspen Plus. 40# lubricating oil is widely used in various domestic nuclear facilities, thus we carried out the analysis of 40# oil from the aspects of elemental composition and chemical composition to provide input for Aspen Plus.

2.1 Elemental Composition

X-ray Fluorescence Spectrometer, Inductively Coupled Plasma Emission Spectrometer and electronic balance were used elemental composition analysis of 40# oil, and the mass fractions of carbon, hydrogen, oxygen, nitrogen, phosphorus and sulfur in the oil were measured. The results were shown in Table 1.

According to the analysis results, the elemental composition of the oil is approximately $C_{35}H_{66.8}$, omitting the very low content of N, O, P and S.

Table 1. Elemental composition of 40# oil.

Elements	Content/wt%	Measurement Method
C	85.06	NB/SH/T 0656–2017
H	13.53	NB/SH/T 0656–2017
N	0.033	SH/T 0657–2007
O	1.179	Substraction
P	0.021	GB/T 17476–1998
S	0.198	GB/T 11140–2008

2.2 Chemical Composition

In this study, Agilent 7890–5977 GC/MSD was used to analyze the chemical composition of the oil. The chromatographic peak signal was compared with the NIST17 spectral database by computer to obtain the chemical composition. The results indicate that the oil is a mixture of various organic compounds, and its main chemical components are alkanes, alkenes, aromatic hydrocarbons and alcohols containing 10–40 carbon atoms. The main elements in waste oil are C and H, indicating that alkanes, alkenes, aromatic hydrocarbons and other hydrocarbons account for a relatively high proportion.

According to the above analysis results, the mixture of ethanol, ethane, propane, ethylene, benzene and toluene was selected as the feedstock, and the ratio (mole ratio) of each component of the mixture was 1:20:25:10:10:10. The mixture has an elemental and chemical composition similar to waste oil, and is suitable for the analysis of waste oil steam reforming reaction.

3 Simulation Modeling

The Aspen Plus model for waste oil steam reforming, as shown in Fig. 1, consists of three main operating units, PYRCT, CARBFLIT, ONSHT and RFRCT, along with some mixers and separators.
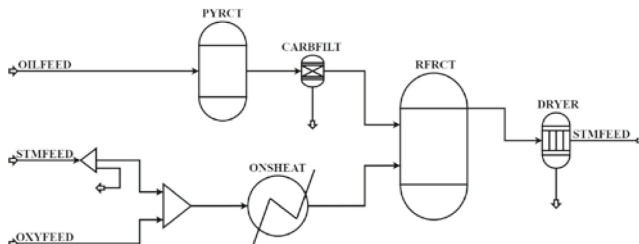
Fig. 1. Simulation scheme of oil steam reforming.

ONSHT is used to simulate steam generator and superheater. It preheats water vapor to reaction temperature and feeds the vapor into the reforming reactor RFRCT. RFRCT

adopts the RGibbs reactor as the reactor model, which can calculate the product com-
position when the system reaches chemical equilibrium and phase equilibrium. PYRCT
reactor is used to simulate the pyrolysis process of waste oil. The waste oil reaches
pyrolysis equilibrium in the reactor to generate small-molecular-weight organic matter,
hydrogen and carbon.

4 Results and Discussion

4.1 Effect of Reaction Pressure

Figure 2 presents the variations of product concentrations versus reaction pressure. The
reaction was carried out in 750 °C and steam/carbon ratio of 1.
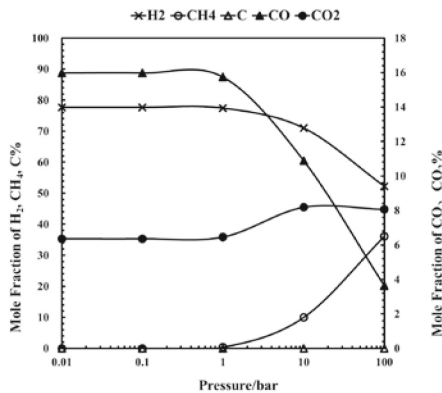
Fig. 2. Effect of pressure at T = 750 °C, S/C = 1.

At T = 750 °C and S/C = 1, methane steam reforming reaction and water gas conver-
sion reaction are the main factors that affect the product composition. The concentration
of H_2 decreases with the increase of pressure. The composition of the product remains
constant when the pressure is lower than 1 bar. However, methane steam reforming reac-
tion is a reaction in which the number of gas molecules increases, and according to Le
Chatelier's principle, when a system at equilibrium is subjected to a change in temper-
ature, volume, concentration, or pressure, the system readjusts to partially counter the
effect of the change, resulting in a new equilibrium. Therefore, as the pressure increases,
methane steam reforming balance moves in the opposite direction, consuming CO and
H_2 to form CH_4. When the pressure is higher than 1bar, the composition of the product
is significantly affected by the pressure change. The concentration of CH_4 in the product
increases with the increase of water pressure, while the concentration of H_2 and CO
decreased respectively.

4.2 Effect of Reaction Temperature

The influence of temperature can be seen from Fig. 3. Simulation is carried out at
pressure of 1 bar and steam/carbon ratio of 1. Under these conditions, the mole fraction

of hydrogen has significantly increased with increasing temperature up to 750 °C. The increasing temperature shifts the reaction equilibrium toward the products side and thus producing more hydrogen.

The concentration of CO_2 in reforming products tends to increase first and then decrease with the increase of temperature. When the temperature rises to 550 °C, the concentration of CO_2 reaches the peak. This is because the production of CO_2 is mainly affected by the water-gas shift reaction, which is endothermic. Therefore, the rise of temperature has an inhibitory effect on the production of CO_2. At low temperature, the reaction is weakly inhibited, and the mole fraction of CO also increases because the rise of temperature promotes the methane steam reforming reaction, which then shifts the equilibrium of the water-gas shift reaction to the direction of CO_2 production. While above 550 °C, the inhibition of high temperature on the water-gas conversion reaction is more obvious, so the content of CO_2 gradually decreases with the increase of temperature.
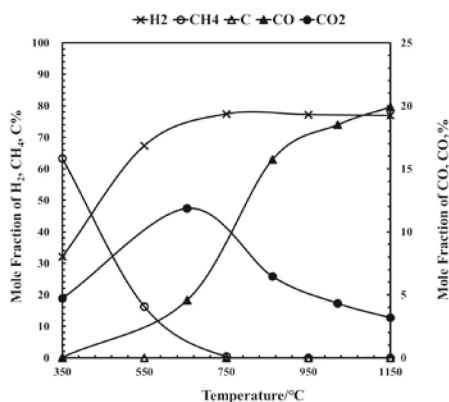
Fig. 3. Effect of temperature at P = 1 bar, S/C = 1.

4.3 Effect of Steam/carbon Ratio

The influence of steam/carbon ratio can be seen from Fig. 4. The operation temperature and pressure are fixed as 750 °C, and 1 bar, respectively. The effect of steam/carbon ratio was investigated in the range of 0.01–100.

There is a large amount of carbon and no methane in the product at low steam/carbon ratio, which is the result of methane decomposition reactions. The water-gas shift reaction mainly occurs when the water-carbon ratio is between 0.01 and 1. Therefore, with the increase of the water-carbon ratio, the carbon decreases continuously until the ratio reaches 1, during which the H_2 content also keeps rising. When the water-carbon ratio is higher than 0.1, the water-gas conversion reaction is encouraged, and the carbon dioxide content keeps rising, while the CO content reaches the peak when the water-carbon

ratio is 1. Subsequently, as carbon is completely consumed, the increasing water vapor content will consume CO and generate CO_2, and concentration remains constant when the water-carbon ratio is above 10.
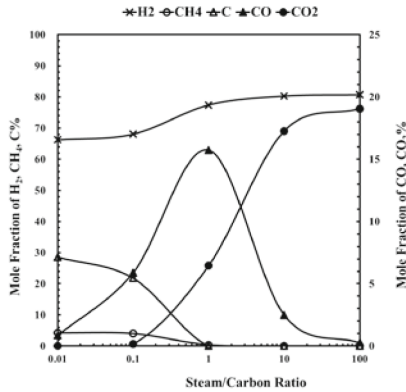
Fig. 4. Effect of steam/carbon ratio at P = 1 bar, T = 750 °C.

5   Conclusions

In this paper, the waste oil was analyzed from the aspects of elemental composition and chemical composition. The analysis shows that the main elements of radioactive waste oil is C and H, and the contents of O, N, S and P are very low. Then Aspen Plus software was used to simulate the waste oil steam reforming reaction, and the thermodynamic equilibrium analysis of the reaction was carried out. The changes of product distribution in the reforming reaction were investigated when the reaction pressure was in the range of 0.01–100 bar, the temperature in 350–1150 °C, and the water carbon ratio in 0.01–100. The following conclusions are drawn:

(1) When the reaction pressure is less than 1bar, there is no obvious inhibition on the steam reforming reaction of waste oil, so the reforming reaction should be carried out under a negative pressure less than 1bar;
(2) The temperature should be maintained above 750 °C to ensure the complete steam reforming reaction;
(3) Carbon can be completely eliminated when the water/carbon ratio is higher than 1, and when the water/carbon ratio is higher than 10, the product components do not change with the water/carbon ratio.

References

1. Zhang, L., Xiong, Y.: Electrochemical advanced oxidation treatment of simulated radioactive waste oil . Southwest University of Science and Technology (2019)

2. Neeway, J.J., Jantzen, C.M., Brown, C.F., et al.: Radionuclide and contaminant immobilization in the fluidized bed steam reforming waste product. INTECH Open Access Publisher (2012)
3. Lin, L., Zhang, H., Li, W., et al.: Numerical simulation analysis on radioactive spent resin steam reforming fluidization based on VOF model. Sci. Technol. Eng. **20**(30), 12657–12663 (2020)
4. Lin, L., Zhang, H., Li, W., et al.: Equilibrium product analysis of steam reforming waste resin based on gibbs free energy minimum principle. Sichuan Environ. **39**(05), 170–174 (2020)
5. Lin, L., Chen, X., Li, W., et al.: Coupled numerical simulation of flow field reaction in a vertical tube for steam reforming of radioactive waste. Sci. Technol. Eng. **16**(04), 200–204 (2016)
6. Amphlett, J., Evans, M., Jones, R., et al.: Hydrogen production by the catalytic steam reforming of methanol part 1: the thermodynamics. The Canadian J. Chem. Eng. **59**(6), 720–727 (1981)
7. Faungnawakij, K., Kikuchi, R., Eguchi, K.: Thermodynamic evaluation of methanol steam reforming for hydrogen production. J. Power Sources **161**(1), 87–94 (2006)
8. Garcia, E., Laborde, M.A.: Hydrogen production by the steam reforming of ethanol: thermodynamic analysis. Int. J. Hydrogen Energy **16**(5), 307–312 (1991)
9. Rossi, C., Alonso, C., Antunes, O., et al.: Thermodynamic analysis of steam reforming of ethanol and glycerine for hydrogen production. Int. Jo.f hydrogen energy, **34**(1), 323–332 (2009)
10. Fishtik, I., Alexander, A., Datta, R., et al.: A thermodynamic analysis of hydrogen production by steam reforming of ethanol via response reactions. Int. J. Hydrogen Energy **25**(1), 31–45 (2000)
11. Chen, H., Zhang, T., Dou, B., et al.: Thermodynamic analyses of adsorption-enhanced steam reforming of glycerol for hydrogen production. Int. J. Hydrogen Energy **34**(17), 7208–7222 (2009)
12. Adhikari, S., Fernando, S., Gwaltney, S.R., et al.: A thermodynamic analysis of hydrogen production by steam reforming of glycerol. Int. J. Hydrogen Energy **32**(14), 2875–2880 (2007)

Simulation Study of the Neutron Scattering Camera Based on Plastic Scintillator and MPPC

Ji Li[1(✉)] and Qing Shan[2]

[1] Nuclear Power Institute of China, Chengdu, Sichuan, People's Republic of China
liji2615@163.com

[2] Department of Nuclear Science and Engineering, College of Material Science and Engineering, Nanjing University of Aeronautics and Astronautics, Nanjing, Jiangsu, People's Republic of China

Abstract. Nuclear safety has always been the lifeline of the development of the nuclear industry, and the supervision and management of special nuclear materials is a very important part of nuclear safety. By measuring fission neutron generated by the special nuclear materials, the type and position of special nuclear materials can be determined. In this paper, a neutron scattering camera (NSC) based on plastic scintillator and MPPC was designed to detect the fission neutron in the n-γ mixed field, and then to realize the localization and discrimination of fission materials. The designed NSC contains two layers of detector arrays. The first and second layers are consisted of five and nine detection units, respectively. In order to discriminate neutrons and gamma-rays, EJ-276 plastic scintillator is chosen as the detection medium because of its PSD performance. At the same time, MPPC was used to collect the fluorescence generated in the scintillator. For optimizing the NSC, the Geant4 Monte Carlo simulation toolkit is used to study the whole detection process of the NSC. In the simulation, the factors affecting image reconstruction in neutron source image reconstruction have studied by simulation. The influences of the thickness and radius of the detection units in two layers, the distance between two layers on the image reconstruction were studied in detail. According to the simulation results, the thickness of front detector unit, radius of detector unit, thickness of back detector unit and distance between two layers were determined to be 3 cm, 5 cm, 8 cm and 50 cm, respectively.

Keywords: Neutron Scattering Camera · Plastic Scintillator · Image Reconstruction · MPPC · TOF

1 Introduction

Special nuclear measurement is a very important part of nuclear material supervision and management. In order to safely use and transport these special nuclear materials, it is usually necessary to add corresponding shielding structures on the outside. The energies of characteristic gamma-rays emitted from the radionuclides in special nuclear materials are rather low. For example, the energy of characteristic gamma-rays of ^{235}U is 185.7 keV, which has limited penetration in high Z materials. So, it is difficult to

measure special nuclear materials by detecting gamma-rays directly. Since uranium and transuranic elements can release fission neutrons through spontaneous fission or induced fission, it is possible to measure special nuclear materials in the shielding structure by detecting fission neutrons [1].

Neutron scattering camera (NSC) can detect the fission neutron, combined with the image reconstruction algorithm, the localization and discrimination of special nuclear materials can be realized [2–5]. It can provide an important means for the supervision of special nuclear materials and plays a very important role in nuclear security, non-proliferation, customs inspection and counter-terrorism. At present, it is mainly used liquid scintillator coupled photomultiplier tube (PMT) as detection unit to detect neutrons in NSC. Liquid scintillator has certain toxicity and is not easy to package. Besides, the use of PMT also makes the NSC has larger volume, which is not conducive to the portable improvement of NSC system.

EJ-276 plastic scintillator not only has the same n-γ discrimination ability as liquid scintillator, but also has the advantages of non-toxic and not easy to leak. Compared to the liquid scintillator, EJ-276 has many advantages, such as more convenient to use, safer operation and more stable physical properties. At the same times, multi-pixel Photon Counter (MPPC) has strong anti-magnetic field interference ability and smaller volume. In this paper, the NSC based on EJ-276 plastic scintillator and MPPC is studied, and the Geant4 [6] Monte Carlo method is used to optimize the NSC.

2 Principle and Performance Index of Neutron Scattering Camera

2.1 Principle of Neutron Scattering Camera

The schematic diagram of NSC was shown in Fig. 1. NSC is consisted of two layers of organic scintillator detector arrays. The incident neutron was firstly interacted with the hydrogen nucleus through the elastic scattering in the front detector array layer, and the recoil proton and the scattered neutron were generated. The scattered neutron entered the back detector array layer and may occur another elastic scattering. If there is only one scattering event occurs in the front and the scattered neutron is detected by the back detector layer, then this is an effective detection event for the neutron scattering camera.

Since the recoil proton has a large mass, its energy can be completely deposited in the front detector, so the recoil proton energy Ep can be measured by the response of the front detector layer. The scattered neutron energy $E'n$ can be calculated by the time of flight method. Then, the incident neutron energy can be acquired by adding Ep and $E'n$. According to the conservation of kinetic energy and momentum in the elastic scattering process, the neutron scattering angle θ and the incident neutron energy En can be calculated as follows:

$$\tan^2 \theta = \frac{E_p}{E'_n} \tag{1}$$

$$E_n = E_p + E'_n \tag{2}$$
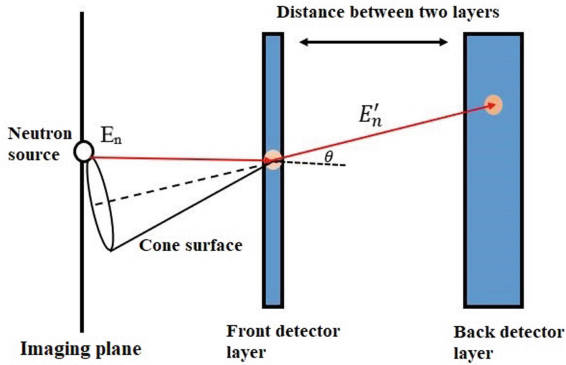
Fig. 1. The schematic diagram of NSC

According to the interaction position of elastic scattering of neutrons in the two detector array layers and neutron scattering angle θ, a cone can be reconstructed, and any position on the conical surface may be the position of the neutron source. But, one cone surface cannot accurately determine the position of the neutron source, the position of the neutron source can be determined by intersection area of multiple cone surfaces.

Simplified Back projection is a common image reconstruction algorithm for neutron scattering camera. The plane where the neutron source is located is called imaging plane X_b. The projection of the reconstructed cone from each neutron scattering event on X_b is an ellipse. X_b is divided into M × N pixel grids of the same size. When any one, two or three of the four vertices of the grid are fallen into the ellipse, it can be determined that the grid is passed through by the ellipse. The entire imaging plane is traversed to judge the grid passed through by the ellipse, and the pixel value of the grid passed through by the ellipse is added by one until the determination of all conforming events. The region with the largest pixel value is the location of the neutron source.

2.2   Performance Index of Neutron Scattering Camera

The performance indexes of NSC include position resolution of neutron source, primary scattering ratio, coincidence ratio of primary scattering and detection efficiency. The details of them are as follows.

(1) The grid with the largest pixel value in the reconstructed image is the reconstructed position of the point source. By intercepting the pixel value distribution of the point source position along the Y or Z direction, the one dimensional distribution of the neutron source direction can be obtained. Using Gaussian fitting to fit the one dimensional distribution, and the full width at half maximum (FWHM) of the fitting curve is the position resolution of the neutron source.

(2) The primary scattering ratio refers to the ratio of the number of neutrons that have only one elastic scattering in the front detector to the number of neutrons that have elastic scattering in the front detector, and is related to the size of the front detector. The coincidence ratio of primary scattering refers to the ratio of number of effective

detection events to the number of coincidence neutrons detected by the front and back detector layers. It is a performance indicator of the NSC system and is related to the geometric parameters of the NSC.

(3) The detection efficiency is defined as the ratio of detected neutrons to the number of neutrons emitted from neutron source. In Geant4 simulation, in order to improve the simulation efficiency, the cone angle of neutron emission is set as 2θ, and the absolute detection efficiency is given as following

$$\varepsilon = \frac{N_c}{N_{2\theta} \times \frac{4\pi}{\Omega}} \tag{3}$$

where EC is the number of effective detection events, $E2\theta$ is the total number of neutrons emitted from neutron source when the emission cone angle is 2θ, Ω represents the solid angle of cone angle and is calculated as following:

$$\Omega = 2\pi(1 - \cos\theta) \tag{3}$$

3 Simulation

The structural schematic diagram of designed NSC was shown in Fig. 2. There are five and nine detector units in front and back detector layer, respectively. In the front detector array, the distance between adjacent detector units is 20 cm, and the fifth detector unit is located in the center position. In the back detector array, the distance between adjacent detector units is also 20 cm.
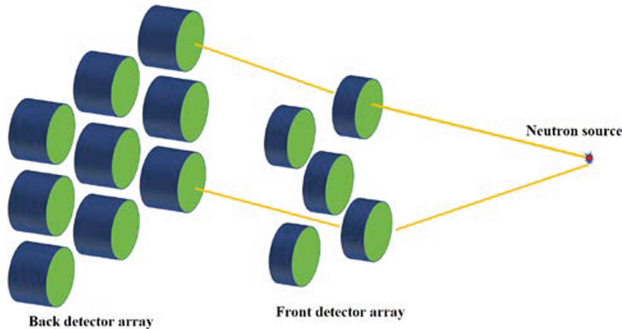
Fig. 2. The structural schematic diagram of NSC

The uranium and plutonium are special nuclear materials, and both of them can generate fission reaction with the neutrons. ^{252}Cf neutron source is spontaneous fission neutron source, and its fission neutrons energy range is similar to that of uranium and plutonium. So, the neutron sources used in Geant4 simulation is chosen to ^{252}Cf neutron sources. In Geant4 simulation, the ^{252}Cf point source was set at the center of the imaging plane which is 2m away from the front detector array, and the cone angle of emission

neutrons was 90°. The neutron emission spectrum of the ^{252}Cf neutron source was defined according to the probability density function of the emission neutron energy, as shown in Fig. 3.
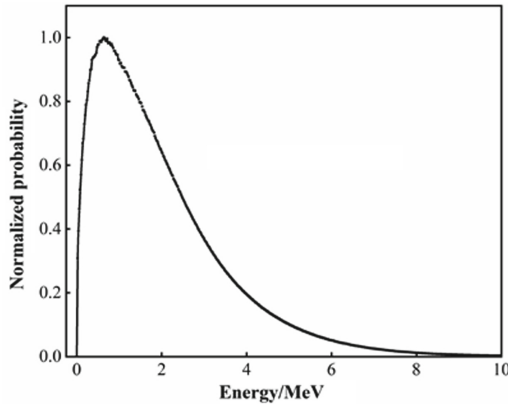
Fig. 3. The spectrum of the ^{252}Cf neutron source [6]

Using Geant4 simulation toolkit, the influences of the thickness and radius of the front and back detector unit and the distance between front and back detector on the image reconstruction were studied. Based on simulation results, the structural parameters of the neutron scattering camera were optimized.

3.1 The Thickness of the Front Detector Unit

The thickness of the front detector will not only introduce the scattering point position error to affect the resolution of neutron source of the reconstructed image, but also affect the primary scattering ratio, coincidence ratio of primary scattering and the absolute detection efficiency. The thickness range of the front detector unit was set from 1 to 8 cm with an interval of 1 cm in the simulation. At the same time, the thickness of the back detector unit was set to 8 cm, the radius of the detector units was set to 5 cm, and the distance between two layers was set to 50 cm.

The influences of thickness of front detector unit on primary scattering ratio and coincidence ratio of primary scattering were shown in Fig. 4. As the thickness of the front detector unit increases, both the primary scattering ratio and coincidence ratio of primary scattering were decreased. This may be caused by the increasing of probability of multiple scattering of neutrons in the front detector layer when the thickness of the front detector unit increases. When the thickness increases from 1 to 8 cm, the primary scattering ratio decreases from 96.5% to 85.6%, and the coincidence ratio of primary scattering decreases from 98.3% to 92.9%, indicating that the thickness of front detector unit has a great influence on the primary scattering ratio and the coincidence ratio of primary scattering.
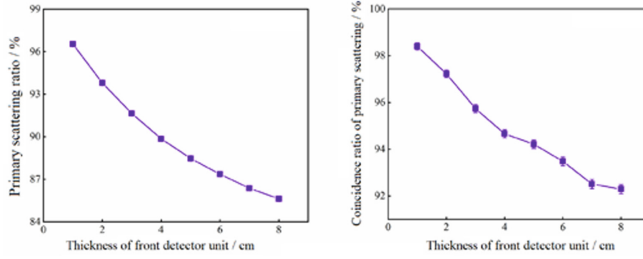
Fig. 4. The thickness of front detector unit Vs. Primary scattering ratio and coincidence ratio of primary scattering

The influences of thickness of front detector on absolute detection efficiency were shown in Fig. 5. The absolute detection efficiency increases with the increase of the thickness. When the thickness of front detector is about 7cm, the absolute detection efficiency basically reaches saturation at about 2.6×10^{-6}.
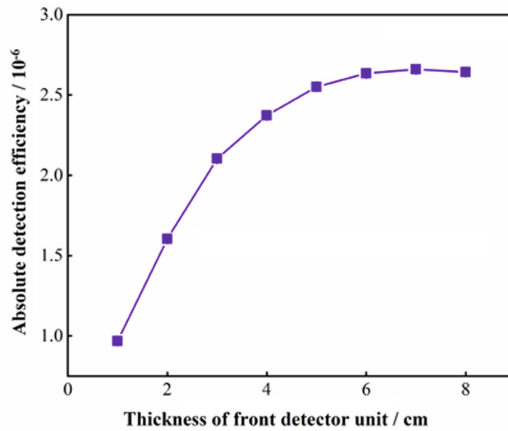
Fig. 5. The thickness of front detector unit Vs. Absolute detection efficiency

The influences of thickness of front detector unit on position resolution of neutron source were also studied and shown in Fig. 6. The position resolution was slightly deteriorated with the increase of thickness. When the thickness increases from 1 to 8 cm, the position resolutions were remained between 500 and 600 mm. Although with the increase of the thickness of front detector unit, the error of scattering point position is introduced to impact the position resolution, but this effect is very limited because the thickness of the front detector unit is quite small when compared to 50 cm distance between two layers.

Considering the simulation results comprehensively, the thickness of the front detector unit is selected as 3 cm. At this circumstance, the primary scattering ratio is bigger than 90%, and the absolute detection efficiency is about 2.2×10^{-6}.
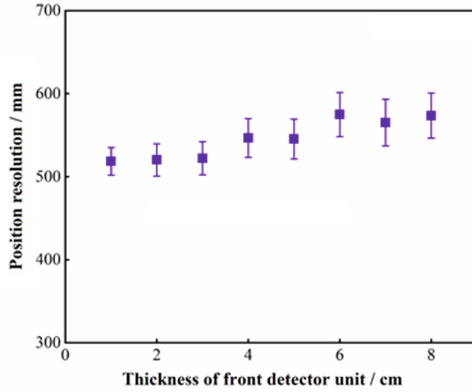
Fig. 6. Front detector thickness unit Vs. Position resolution

3.2 The Radius of the Detector Unit

The radius of detector unit was set from 2 to 8 cm, with interval of 1 cm. At same time, the thickness of the front and back detector units were set to 3 cm and 8 cm, respectively. The distance between the two layers was 50 cm. The relationships of radius of detector unit and primary scattering ratio and coincidence ratio of primary scattering were shown in Fig. 7. With the increase of the radius of detector unit, the primary scattering ratio was continuously decreased. This is because the increasing of the radius increases the probability of multiple scattering of neutrons in the front detector array. The coincidence ratio of primary scattering increases with the increasing of the radius and tends to be saturation at about 5 cm. When the radius increases from 2 to 8 cm, the primary scattering ratio only decreases from 93.5% to 91%, while the coincidence ratio of primary scattering increases from 73.7% to 95.5%, indicating that increasing of the radius has a small effect on the primary scattering ratio, but has a significant effect on the coincidence ratio of primary scattering.
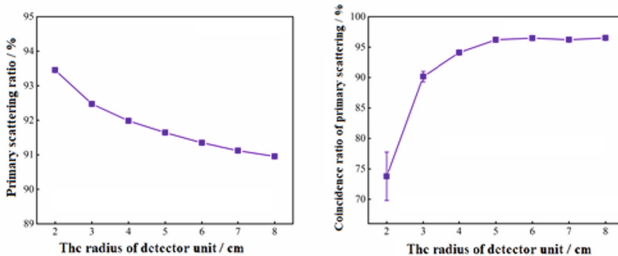
Fig. 7. The radius of detector unit Vs. Primary scattering ratio and coincidence ratio of primary scattering

The absolute detection efficiency under different radius was shown in Fig. 8. It can be seen that the absolute detection efficiency increases with the increasing of radius. When

the detector radius increases from 2 cm to 8 cm, the absolute detection efficiency was increased from 1.78×10^{-8} to 1.07×10^{-5}, which were increased about 600 times. This indicates that the radius has a significant influence on the absolute detection efficiency.
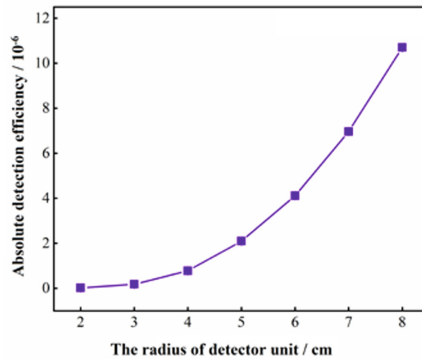
Fig. 8. The radius of detector unit Vs. Absolute detection efficiency

The influence of radius on position resolution of neutron source was shown in Fig. 9. With the increasing of the radius, the position resolutions of neutron source were got worse and worse. When the radius increases from 3 cm to 8 cm, the position resolution of neutron source was increased from 305 mm to 766 mm, indicating that the radius has a significant effect on the position resolution.
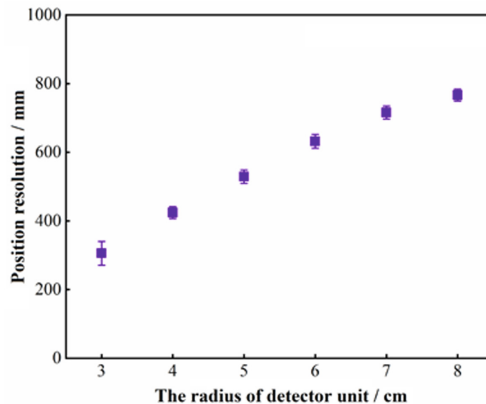
Fig. 9. The radius of detector unit Vs. Position resolution

Considering the simulation results comprehensively, when the radius of the detector unit was 5 cm, the better absolute detection efficiency and coincidence ratio of primary scattering can be obtained. Besides, the NSC also has better position resolution of neutron source. So, the radius of the detector unit was determined to be 5 cm.

3.3 The Thickness of the Back Detector Unit

In the simulation, the thickness of the back detector unit was from 5 to 20 cm with the interval of 1 cm, while the thickness of front detector unit was set as 3 cm, the radius of the detector units in two layers was set as 5 cm, and the distance between two layers was set as 50 cm. Figure 10 shows the influences of the thickness of the back detector unit on the coincidence ratio of primary scattering. The coincidence ratio of primary scattering was increased slightly with the increasing of the thickness of back detector unit. When the thickness was increased from 5 to 20 cm, the coincidence ratio of primary scattering was located between 95.7% and 96.4%, indicating that the thickness of the back detector unit has little influence on the coincidence ratio of primary scattering.
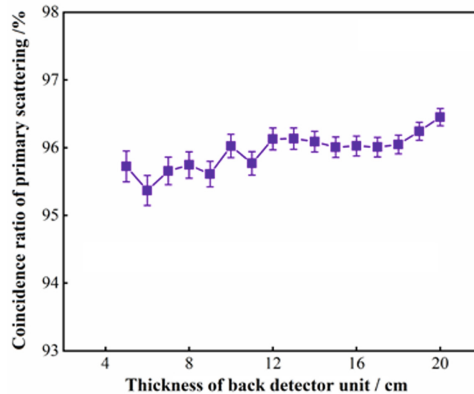
Fig. 10. The thickness of back detector unit Vs. Coincidence ratio of primary scattering

The influence of thickness of back detector unit on absolute detection efficiency was shown in Fig. 11. The absolute detection efficiency was increased linearly with the increase of the thickness of the back detector unit. When the thickness increases from 5 to 20 cm, the absolute detection efficiency was increased from 1.14×10^{-6} to 3.12×10^{-6}, indicating that the thickness of the back detector unit has a certain influence on the absolute detection efficiency.

Figure 12 illustrates the influence of thickness on point source position resolution. With the increase of the thickness of the back detector unit, the position resolutions of neutron source were maintained between 500 and 600 mm. This indicates that the increase of the thickness of the back detector unit has little influence on the position resolutions.

In conclusion, the thickness of the back detector unit mainly affects the detection efficiency. As the thickness of the back detector unit increased, the detection efficiency increases linearly. Considering the absolute detection efficiency and economic cost, the thickness of the detector is determined to be 8 cm.
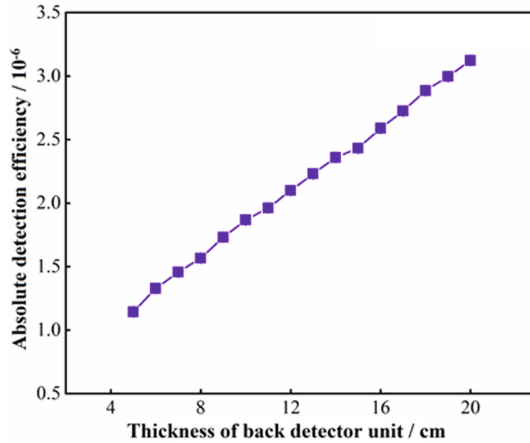
Fig. 11. The thickness of back detector unit Vs. Absolute detection efficiency
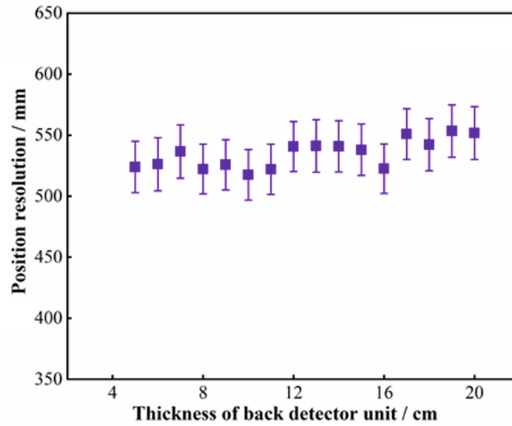
Fig. 12. The thickness of back detector unit Vs. Position resolution

3.4 The Distance Between the Two Layers

The distance between two detector layers was ranged from 30 to 100 cm with interval of 10 cm, while the thickness of the front and back detector unit were 3 and 8 cm, and the radius of the detectors unit was 5 cm. The influence of distances on the coincidence ratio of primary scattering was simulated and shown in Fig. 13. With the increasing of distance, the coincidence ratio of primary scattering was always decreased. When the distance increased from 30 to 100 cm, the coincidence ratio of primary scattering was decreased from 96.8% to 90.2%, indicating that the distance has a great influence on the coincidence ratio of primary scattering.
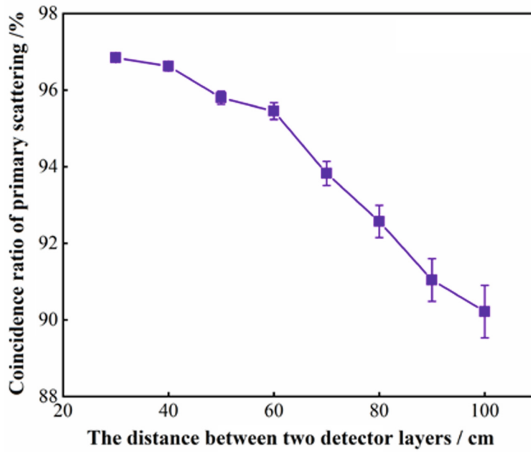
Fig. 13. The distance between two layers Vs. Coincidence ratio of primary scattering

The relationship between distance and absolute detection efficiency was given in Fig. 14. The absolute detection efficiency was decreased with the increasing of distance. With the increasing of distance, the absolute detection efficiency decreases from 5.13×10^{-6} to 2.74×10^{-7}, indicating that the distance has a great influence on the absolute detection efficiency.
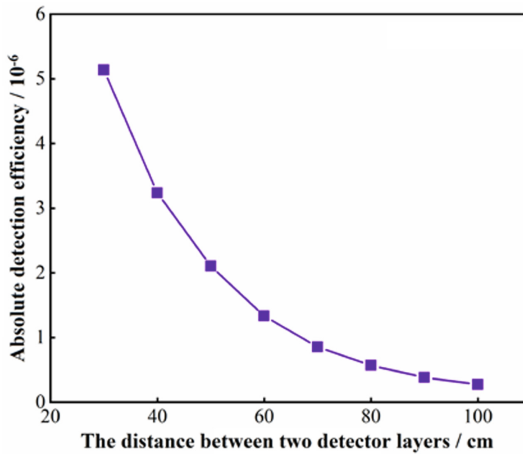
Fig. 14. The distance between two layers Vs. Absolute detection efficiency

The influence of distance between two layers on position resolution of neutron source was given in Fig. 15. With the increase of distance, the position resolution becomes better and better. When the plane distance was increased to 100 cm, the position resolution was changed from 750 to 300 mm, indicating that the plane distance has an obvious influence on the position resolution.
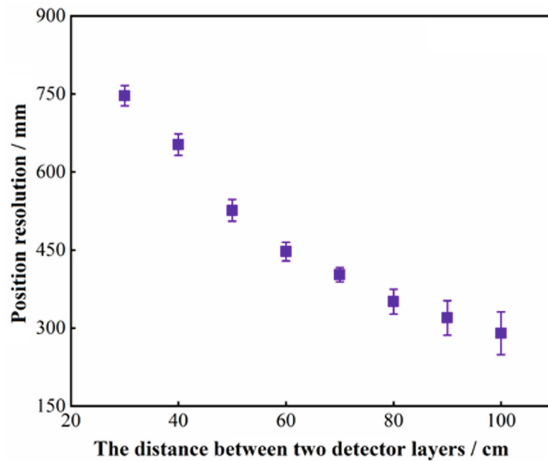
Fig. 15. The distance between two layers Vs. Position resolution

Based on the simulations, it can be seen that the distance mainly affects the coincidence ratio of primary scattering, absolute detection efficiency and point source position resolution. When the distance was 50 cm, the NSC not only has a high coincidence ratio of primary scattering and absolute detection efficiency, but also has a good position resolution. So, the distance was determined to be 50 cm.

4 Conclusions

In this paper, the effects of the thickness and radius of detector units and distance between two layers on image reconstruction were studied by the Geant4 to optimize the geometric parameter of the NSC. The simulation results show that the thickness of front detectors mainly affects the primary scattering ratio and the coincidence ratio of primary scattering, the radius of detector unit and distance between two layers mainly affect the first scattering coincidence ratio,

detection efficiency and position resolution of neutron source. Based on the simulation results, the thickness of the front detector, the radius of the detector, the thickness of the back detector and the distance between two layers were determined to be 3 cm, 5 cm, 8 cm and 50 cm, respectively.

References

1. Steinberger, W.M., Ruch, M.L., Giha, N., et al.: Imaging special nuclear material using a handheld dual particle imager. Sci. Rep. **10**(1), 1–11 (2020)
2. Bravar, U., Woolf, R.S., Bruillard, P.J., et al.: Calibration of the fast neutron imaging telescope (FNIT) prototype detector. Trans. Nucl. Sci. **56**(5), 2947–2954 (2009)
3. Pirard, B., Woolf, R.S., Bravar, U., et al.: Test and simulation of a fast neutron imaging telescope. Nucl. Instrum. Methods Phys. Res. **603**(3), 406–414 (2009)

4. Mascarenhas, N., Brennan, J., Krenz, K., et al.: Results with the neutron scatter camera. IEEE Trans. Nucl. Sci. **56**(3), 1269–1273 (2009)
5. Brennan, J., Brubaker, E., Cooper, R., et al.: Measurement of the fast neutron energy spectrum of an am-241-Be source using a neutron scatter camera. IEEE Trans. Nucl. Sci. **58**(5), 2426–2430 (2011)
6. Agostinelli, S., et al.: GEANT4—a simulation toolkit. Nucl. Inst. Methods Phys. Res. Sect. A: Accel. Spectr. Detect. Assoc. Equip. **506**(3), 250–303 (2003)

The Design of the Robust Controller for Active Magnetic Bearings on Active Disturbance Rejection Technology

Qian Shi[1], Yichen Yao[2], and Suyuan Yu[2(✉)]

[1] China National Intellectual Property Administration, Beijing, China
[2] Department of Energy and Power Engineering, Tsinghua University, Beijing, China
`suyuan@mail.tsinghua.edu.cn`

Abstract. Active magnetic bearings (AMBs) have advantages of no friction, no lubrication or sealing requirements, long lifespan, low maintenance cost, and, especially, active controllability of dynamic characteristics. Thus, AMBs are now widely used in helium-turbine circle of the high temperature gas-cooled reactor and many other high-speed rotating machinery. The design of controller is the core problem of AMBs. The AMB force has high nonlinearity and the AMBs-rotor system may be influenced by external disturbance during operation, which increase the threshold of the controller robustness and make it hard to design. Based on the AMB-rigid rotor system model, this paper adopts lumped uncertainties to describe nonlinear error and external load disturbance and then the plant model of the decentralized controller is obtained. Then, a linear active disturbance rejection controller (LADRC) is designed to compensate the model error. The LADRC contains a proportional-differential controller and a three-order external state observer. The adjustable parameters of the LADRC can be selected according to pole assignment. In order to verify the effectiveness of the LADRC, levitation experiments, rotation experiments, and re-levitation experiments are carried out with traditional PID controller as comparison.

Keywords: active magnetic bearings · active disturbance rejection controller · lumped uncertainty

1 Introduction

Active magnetic bearings (AMBs) have the advantages of no friction, no lubrication or sealing requirements, long lifespan, low maintenance and active vibration control and have widely application in helium-turbine circle of the high temperature gas-cooled reactor and many other high-speed rotating machinery [1, 2]. In fact, the dynamic characteristics of AMBs mainly depend on the controller. A suitable controller is the core problem of AMBs design. As a matter of fact, the AMB-rotor system is open-loop unstable because of the high nonlinearity of electromagnetic bearing force. Besides, the AMBs-rotor system is always influenced by external disturbance, which makes it harder

to design a suitable controller to achieve moderate rotor displacement response during normal operation.

In order to solve this problem, many researches have been carried out. The proportional-integral-differential (PID) controller is widely used in industrial applications because of its simplicity and robustness. Markus Hutterer designed PID controller through linear quadratic regulator method and validated the controller on a turbomolecular pump [3]. Tianhao Zhou proposed a robust PD control via eigenstructure assignment and evaluated the closed-loop sensitivity to change of the bias current [4]. Sun zhe applied a PID controller on a prototype of a 27000 rpm/150 kw blower and analyzed the nonlinearity of the system [5]. Chenzi Liu proposed a simple lead-lag controller, which parameters were determined through backprogation neural network [6].

Moreover, many advanced controllers have also been developed. Alexander presented a μ-synthesis-based controller to robustly minimize the difference between the tool reference and the estimated tool position in tooltip tracking spindle [7]. Syed Muhammad amrr proposed a robust control law based on high-order sliding mode control scheme, and carried out numerical analysis [8]. Xuan Yao proposed a dual-loop neural network sliding mode control to achieve large-motion rotor tracking, and validated its effectiveness through simulations [9].

These advanced controllers show better performance compared with PID controllers, but they have more complex structure and may have difficulties in parameter adjustment. Besides, they are model-based controller and may have deteriorated performance on an imprecise model.

Nowadays, linear active disturbance rejection controllers (LADRCs) have been attractive because it can achieve robust performance on an imprecise model and can simply realize parameter adjustment [10–14].

In this paper, a plant model of the decentralized controller is established based on the AMB-rigid rotor system model. This model adopts lumped uncertainty to describe nonlinear error and external load disturbance. Furthermore, a LADRC is designed, which can attenuating the impact of model nonlinear and external disturbance. The LADRC contains a proportional-differential controller and a three-order external state observer. The adjustable parameters of the LADRC can be selected according to pole assignment. In order to verify the effectiveness of the LADRC, levitation experiments, rotation experiments, and re-levitation experiments are carried out with traditional PID controller as comparison.

This paper is organized as follows. First, in Sect. 2, the plant model of the decentralized controller is established. Then, the LADRC is designed in Sect. 3. Experiments are developed in Sect. 4. Finally, Sect. 5 concludes this paper.

2 Description of the AMB-rotor System

2.1 The Rotor Model

The structure of the AMB-rigid rotor system is shown in Fig. 1. x_c, y_c denote the displacement of the centroid of rotor; α, β are the angular displacement of the rotor around x and y axes. l_{bA}, l_{bB}, l_{sA}, l_{sB} show the distance between the A/B bearing/sensor and the
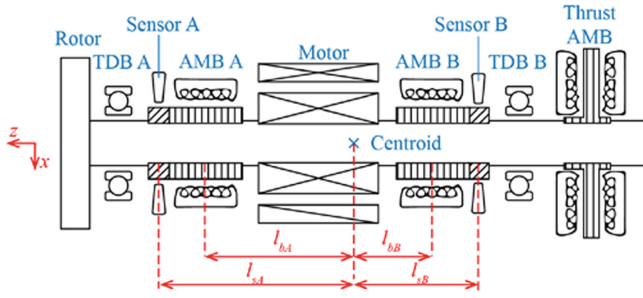
Fig. 1. AMB-rotor system

centroid. In AMB-rigid rotor system, the coupling between the axial DOF and radial DOF is negligible. Thus, axial DOF is not mentioned in this model and merely radial 4 DOF and axial angle γ are considered. There are three popular coordinates to illustrate the motion of rotor, which are centroid coordinate $\mathbf{y}^c = \begin{bmatrix} x_c & \alpha & y_c & \beta \end{bmatrix}^T$, sensor coordinate $\mathbf{y}^s = \begin{bmatrix} y_{Ax}^s & y_{Ay}^s & y_{Bx}^s & y_{By}^s \end{bmatrix}^T$ and bearing coordinate $\mathbf{y}^b = \begin{bmatrix} y_{Ax}^b & y_{Ay}^b & y_{Bx}^b & y_{By}^b \end{bmatrix}^T$. $\mathbf{y}^c$ describes the displacement of rotor centroid, $\mathbf{y}^s$ and $\mathbf{y}^b$ are rotor displacement at sensor/bearing. The relation between them can be expressed as $\mathbf{y}^s = \mathbf{T}_s^{sc}\mathbf{y}^c$, $\mathbf{y}^s = \mathbf{T}_b^{cb}\mathbf{y}^b$, in which

$$
\mathbf{T}_b^{cb} = \begin{bmatrix} 1 & 0 & 1 & 0 \\ 0 & -l_{bA} & 0 & l_{bB} \\ 0 & 1 & 0 & 1 \\ l_{bA} & 0 & -l_{bB} & 0 \end{bmatrix}, \quad \mathbf{T}_s^{sc} = \begin{bmatrix} 1 & 0 & 0 & l_{sA} \\ 0 & -l_{sA} & 1 & 0 \\ 1 & 0 & 0 & -l_{sB} \\ 0 & l_{sB} & 1 & 0 \end{bmatrix}
$$

Define bearing force as $\mathbf{f}_b^b = \begin{bmatrix} f_{bAx} & f_{bAy} & f_{bBx} & f_{bBy} \end{bmatrix}^T$ under bearing coordinate, and then define external disturbance as $\mathbf{f}_g^c = \begin{bmatrix} f_{gx}^c & f_{g\alpha}^c & f_{gy}^c & f_{g\beta}^c \end{bmatrix}^T$ under rotor centroid coordinate. The equation of motion of the rotor can be written as:

$$
\begin{cases}
m\ddot{x}_c = f_{bAx} + f_{bBx} + f_{gx}^c \\
J_r\ddot{\alpha} + J_z\dot{\gamma}\dot{\beta} = -l_{bA}f_{bAy} + l_{bB}f_{bBy} + f_{g\alpha}^c \\
m\ddot{y}_c = f_{bAy} + f_{bBy} + f_{gy}^c \\
J_r\ddot{\beta} + J_z\dot{\gamma}\dot{\beta} = l_{bA}f_{bAx} - l_{bB}f_{bBx} + f_{g\beta}^c
\end{cases}
\tag{1}
$$

Transform Eq. (1) to sensor coordinate, it gives:

$$
\begin{cases}
\ddot{y}_{Ax}^s = -\dfrac{J_z\Omega l_{sA}}{J_r(l_{sA}+l_{sB})}\left(\dot{y}_{Ay}^s - \dot{y}_{By}^s\right) + \left(\dfrac{1}{m}+\dfrac{l_{bA}l_{sA}}{J_r}\right)f_{bAx} \\
\qquad + \left(\dfrac{1}{m}-\dfrac{l_{sA}l_{bB}}{J_r}\right)f_{bBx} + f_{gAx}^s \\[2pt]
\ddot{y}_{Ay}^s = -\dfrac{J_z\Omega l_{sA}}{J_r(l_{sA}+l_{sB})}\left(\dot{y}_{Bx}^s - \dot{y}_{Ax}^s\right) + \left(\dfrac{1}{m}+\dfrac{l_{bA}l_{sA}}{J_r}\right)f_{bAy} \\
\qquad + \left(\dfrac{1}{m}-\dfrac{l_{sA}l_{bB}}{J_r}\right)f_{bBy} + f_{gAy}^s \\[2pt]
\ddot{y}_{Bx}^s = -\dfrac{J_z\Omega l_{sB}}{J_r(l_{sA}+l_{sB})}\left(\dot{y}_{By}^s - \dot{y}_{Ay}^s\right) + \left(\dfrac{1}{m}-\dfrac{l_{bA}l_{sB}}{J_r}\right)f_{bAx} \\
\qquad + \left(\dfrac{1}{m}+\dfrac{l_{bB}l_{sB}}{J_r}\right)f_{bBx} + f_{gBx}^s \\[2pt]
\ddot{y}_{By}^s = -\dfrac{J_z\Omega l_{sB}}{J_r(l_{sA}+l_{sB})}\left(\dot{y}_{Ax}^s - \dot{y}_{Bx}^s\right) + \left(\dfrac{1}{m}-\dfrac{l_{bA}l_{sB}}{J_r}\right)f_{bAy} \\
\qquad + \left(\dfrac{1}{m}+\dfrac{l_{bB}l_{sB}}{J_r}\right)f_{bBy} + f_{gBy}^s
\end{cases}
\tag{2}
$$

For slender rotor, the rotor shape usually satisfies $\left|\dfrac{1}{m}+\dfrac{l_{bA}l_{sA}}{J_r}\right| \gg \left|\dfrac{1}{m}-\dfrac{l_{sA}l_{bB}}{J_r}\right|$, $\left|\dfrac{1}{m}+\dfrac{l_{bB}l_{sB}}{J_r}\right| \gg \left|\dfrac{1}{m}-\dfrac{l_{sB}l_{bA}}{J_r}\right|$, and $J_r \gg J_z$. Then, Eq. (2) can be simplified as

$$
\ddot{y}^s = k_{stru}f_b + f_g^s
\tag{3}
$$

where $k_{stru} = \dfrac{1}{m}+\dfrac{l_{bA}l_{sA}}{J_r}$ in AMB A and $k_{stru} = \dfrac{1}{m}+\dfrac{l_{bB}l_{sB}}{J_r}$ in AMB B.

2.2 The AMB Model

The AMB always works under differential-driven mode, shown in Fig. 2. There are two electromagnets placed in one direction, since each electromagnet can only achieve attractive force. The electromagnetic force generated by the single electromagnet can be expressed as

$$
f_p = k\frac{i_a^2}{s^2}, k = \frac{\mu_0 A N^2}{4}\cos\theta
\tag{4}
$$

where i_a is the current, s is the gap, μ_0 is the magnetic field constant in vacuum, N is the number of coils turns, A is the cross-section area of the pole and θ is the angle of the electromagnet. Then, the net AMB force in one direction is the differential force of a pair of electromagnets. The net force can be linearized around the neighborhood of the operating point [1, 15], and can be expressed as

$$
f_b = k_i i_c + k_s y^s
\tag{5}
$$

where $i_c = i_{a1} - i_{a2}$, k_i and k_s are the current-force factor (in N/A) and the displacement-force factor (in N/m) respectively.
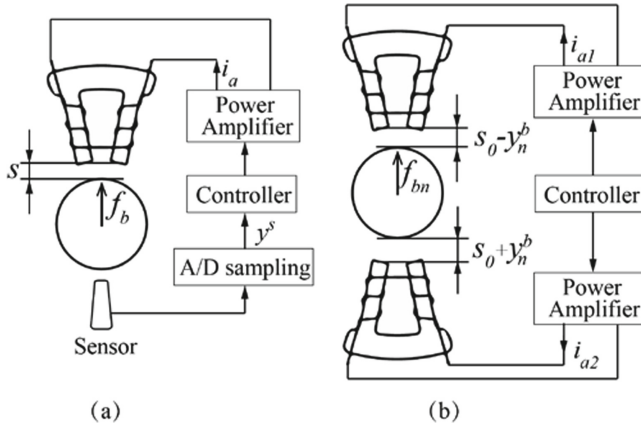
Fig. 2. Differential-driven mode in AMBs. (a) AMB force of a radial magnet. (b) AMB force of a pair of magnets.

2.3 The AMB-rotor Model

Substituting Eq. (5) into (3), the decentralized AMBs-rotor model can be written as:

$$\ddot{y}^s = k_{stru}k_i i_c + k_{stru}k_s y^s + f_g^s \tag{6}$$

It is noticed that the precise position of the rotor centroid is hard to determine due to its complex shape and its heterogeneous material, which indicate k_{stru} has uncertainty. This parameter variation can be described as $k_{stru} = (1 + \lambda)k_{stru,0}$. Then, Eq. (6) can be rewritten as

$$\ddot{y}^s = k_{x0}(1 + \lambda)\left(i_c + \frac{k_s}{k_i}y^s\right) + f_g^s \tag{7}$$

where $k_{x0} = k_i k_{stru,0}$.

3   LADRC Design
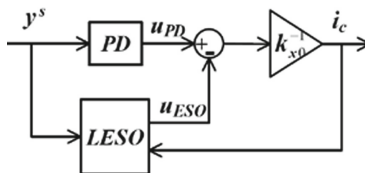
Fig. 3. The structure of LADRC.

The structure of LADRC is shown in Fig. 3. The LADRC contains a proportional-differential controller and a three-order external state observer. The transfer function

of the proportional-differential (PD) controller and the linear extended state observer (LESO) in LADRC can be written as

$$u_{PD}(s) = -k_c \frac{\alpha s + \omega_c}{s + \omega_c} y^s(s)$$

$$u_{ESO}(s) = \frac{\omega_0^3 s^2 y_r(s) + k_{x0} i_c(s)}{(s + \omega_0)^3} \tag{8}$$

where ω_0 is the bandwidth of the LESO, k_c, ω_c, α are parameters of the PD controller.

Thus, the transfer function of LADRC can be obtained as

$$G_c(s) = \frac{i_c(s)}{y^s(s)} = -\frac{k_c(\alpha s + \omega_c)(s + \omega_0)^3 + \omega_0^3 s^2 (s + \omega_c)}{k_{x0} s(s + \omega_c)(s^2 + 3\omega_0 s + 3\omega_0^2)}. \tag{9}$$

The transfer function of the closed-loop system can be written as

$$G_{cl}(s) = \frac{y^s(s)}{f_g^s(s)} = \frac{k_i}{k_i s^2 - k_{x0}(1 + \lambda)[k_i G_c(s) - k_s]}. \tag{10}$$

Therefore, the closed-loop system can achieve robust stability through proper pole assignment. If designing $\omega_0 = 50$, $\omega_c = 500$, $\alpha = 3.25$, $k_c = 25$ with nominal parameter $k_{x0} = 20$, the root locus of the closed-loop system with parameter variation can be calculated. Consider that the range of λ is $\lambda \in [0.5, 1.5]$. The roots of the closed-loop system (10) is shown in Fig. 4. The designed LADRC shows good robustness. The mapping from $f_g^s(s)$ to $y^s(s)$ under the LADRC is shown in Fig. 5. This demonstrates the capability of the LADRC to suppress the disturbance $f_g^s(s)$ under the plant with
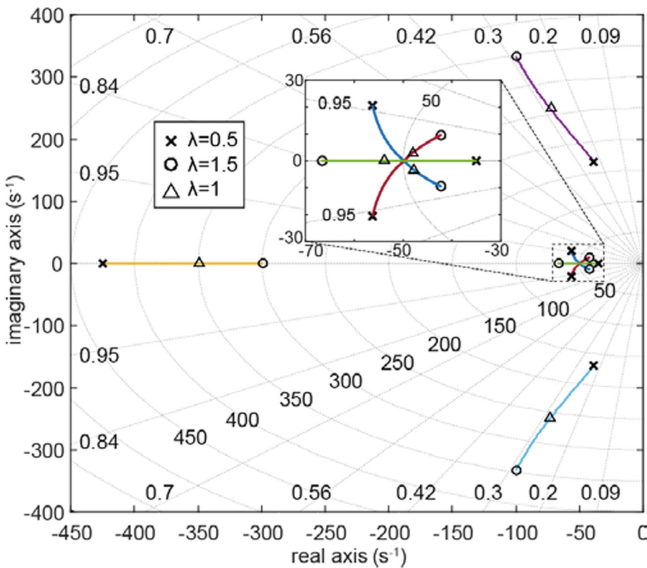
Fig. 4. The root locus diagram of the closed-loop system under LADRC.
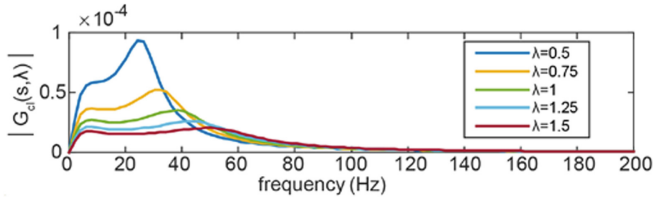
Fig. 5. The mapping from f_g^s to y^s under LADRC.

lumped uncertainty. In fact, $f_g^s(s)$ mainly contains a static load and unbalanced force. Unbalanced force causes an auto-balance effect after rigid critical speed; thus, it does not require compensation within a high-frequency range. The peak is larger when λ is smaller.

4 Experimental Results

This section contains two type of experiments, levitation experiments, and rotation experiments. In levitation experiments, the transient responses are analyzed. In rotation experiments, the analysis of rotor displacement responses within working speed range are given.

4.1 Description of the Experimental Platform

In order to verify the effectiveness of the LADRC, verification experiments are carried out on the AMBs-supported permanent magnet synchronous motor platform at Tsinghua University [16], pictured in Fig. 6. The rotor of the platform is 0.4866 m long with a total mass of 13.98 kg and is horizontally supported by two radial AMBs and one axial AMB. The radial clearance of the AMBs is 0.4 mm and the clearance of touchdown bearings (TDBs) is 0.2 mm. Radial and axial displacements of the rotor were measured by five inductive sensors. Ten pulse width modulated amplifiers power the magnet coils to generate the expected bearing force.

For comparison, a traditional PID controller, the most popular controller in industrial practice, is involved in this section. This PID controller is well-designed and performs well in various working conditions.

4.2 Levitation Experiments

The transient response at AMB A of levitation experiments are shown in Fig. 7 and Fig. 8 since AY channel has the worst results of the four. Sub-figure (a) gives the rotor trajectory. In this sub-figure, the transient response is divided into 3 phases. The first phase ends when the differential signal reaches its maximum. In this phase, the proportional signal plays the most important role. It starts at its maximum absolute value and its proportion in the total control signal gradually reduce. This phase is very short and the end position of the rotor during this phase mostly depends on the PD controller. The PID and LADRC nearly have similar displacement response in this phase. The second phase ends when the
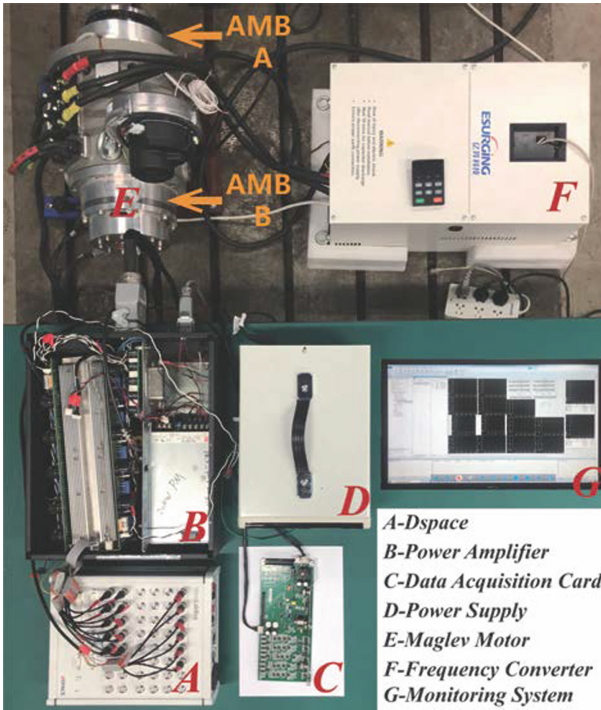
Fig. 6. The experimental platform.

proportional signal line intersects with the compensation signal line (I in PID and ESO in LADRC) at the first time. During this phase, the compensation signal increase gradually and cannot be ignored. The displacement response of the rotor results from the combined influence of three signals and is more complex. Under PID, this phase is about 0.042 s and the rotor trajectory in Fig. 7(a) displays fluctuation. Under LADRC, this phase is 0.012 s and there is less fluctuation in rotor trajectory because ESO signal has faster response. The third phase ends when the displacement response remains within 5% of the radial clearance of the TDBs (0.2 mm). The compensation signal plays important role in this phase. Since ESO signal has faster response, this phase is shorter under LADRC controller. The total startup period is 0.14 s under PID and is 0.05 s under LADRC, which shows LADRC have better performance in transient response. This indicator is significant for AMB controllers.

4.3   Rotation Experiments

Rotation experiments are of great significance not only due to being the most common working conditions but also because synchronous excitation caused by residual unbalance can help to analyze the frequency domain characteristics of the system and the control strategy.

The displacement response of rotation experiments from 0–200 Hz (up to 12000 r/min) under PID and LADRC are given in Fig. 9. During the rigid rotation speed range,
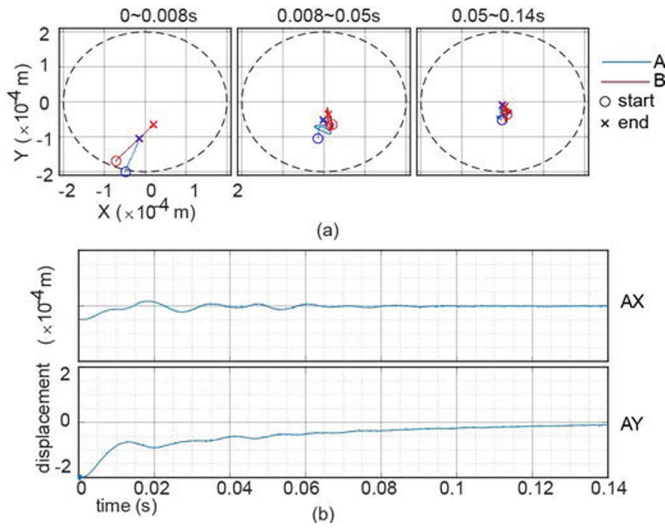
Fig. 7. The transient response in levitation experiments under PID controller
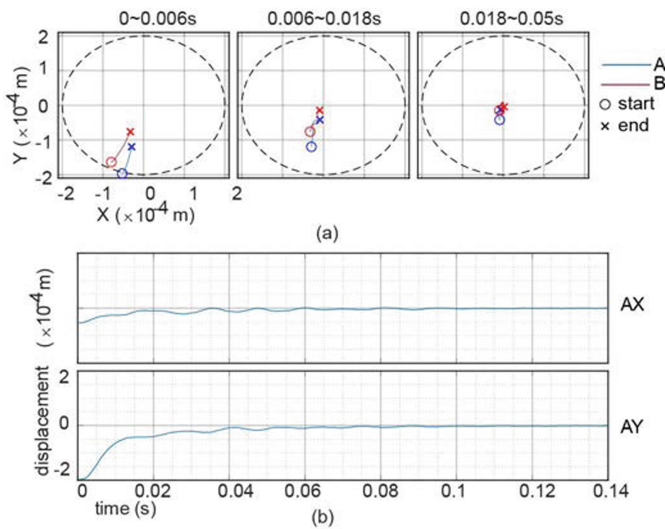
Fig. 8. The transient response in levitation experiments under LADRC

both of the two controllers show good displacement response. The amplitude of vibration remains within half of the TDBs clearance. There are four peaks within the speed range, shown in Fig. 9 (a), which correspond to the four vibration modes of the system.

However, LADRC shows better performance at the four peaks and under 100 Hz. It seems that the proposed LADRC have better damping property. When it comes to low rotating speed range, it indicates that ESO signal shows better performance in isolation of low-frequency vibration. There is a feedback loop in ESO, so that ESO signal has
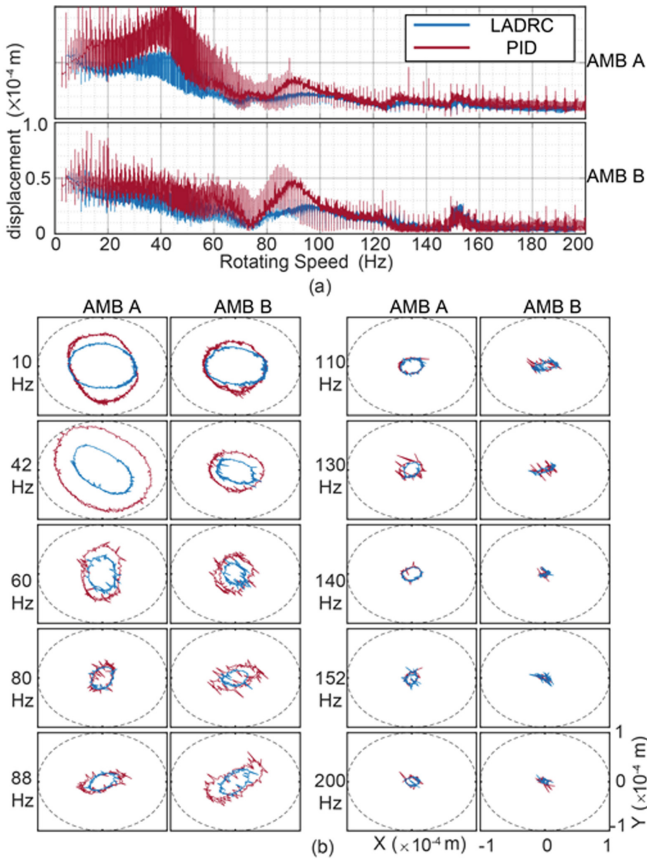
Fig. 9. The displacement response in rotation experiments under PID and LADRC controller

a more specific frequency truncation characteristic than integral signal. In fact, integral signal shows obvious synchronous fluctuations until 60 Hz while it vanishes at 20 Hz in ESO signal. Besides, the integral signal always has phase lag, which further suppress the effect of differential signal and make the AMBs show less damping than designed.

5   Conclusions

In view of the high nonlinearity, parameter perturbation and external disturbance existing in AMB-rotor system, a LADRC is designed in this paper to suppress the rotor displacement response while attenuating the impact of uncertainties. A plant model of the decentralized controller is established with lump uncertainties including the model error of the AMB force, the external load, and related parametric perturbation. Then, a LADRC is designed. The LADRC contains a proportional-differential controller and a three-order external state observer. The adjustable parameters of the LADRC can be selected according to pole assignment. In order to verify the effectiveness of the LADRC,

levitation experiments and rotation experiments are carried out with traditional PID controller as comparison.

References

1. Schweitzer, G., Maslen, E.H.: Magnetic Bearings: Theory, Design, and Application to Rotating Machinery. Springer, Heidelberg (2009)
2. Shi, Z., Yang, X., et al.: Design aspects and achievements of active magnetic bearing research for htr-10gt. Nucl. Eng. Des. **238**, 1121–1128 (2008)
3. Hutterer, M., Wimmer, D., Schrödl, M.: Stabilization of a magnetically levitated rotor in the case of a defective radial actuator. IEEE Trans. Mechatron. **66**(12), 9383–9393 (2019)
4. Zhou, T., Zhu, C.: Robust proportional-differential control via eigenstructure assignment for active magnetic bearings-rigid rotor systems. IEEE Trans. Ind. Electron. **69**(7), 6572–6585 (2022)
5. Zhang, X., Sun, Z., et al.: Nonlinear dynamic characteristics analysis of active magnetic bearing system based on cell mapping method with a case study. Mech. Syst. Signal Process. **117**, 116–137 (2019)
6. Liu, C., Deng, Z., Xie, L., Li, K.: The design of the simple structure-specified controller of magnetic bearings for the high-speed srm. IEEE/ASME Trans. Mechatron. **20**(4), 1798–1808 (2014)
7. Pesch, A.H., Smirnov, A., Pyrhonen, O., Sawicki, J.T.: Magnetic bearing spindle tool tracking through mu-synthesis robust control. IEEE/ASME Trans. Mechatron. **20**, 1448–1457 (2015)
8. Amrr, S.M., Alturki, A.: Robust control design for an active magnetic bearing system using advanced adaptive smc technique. IEEE Access **9**, 155662–155672 (2021)
9. Yao, X., Chen, Z., Jiao, Y.: A dual-loop control approach of active magnetic bearing system for rotor tracking control. IEEE Access **7**, 121760–121768 (2019)
10. Dong, S.: Comments on active disturbance rejection control. IEEE Trans. Ind. Electron. **54**(6), 3428–3429 (2007)
11. Han, J.: From pid to active disturbance rejection control. IEEE Trans. Ind. Electron. **56**(3), 900–906 (2009)
12. Huang, Y., Xue, W.: Active disturbance rejection control: methodology and theoretical analysis. ISA Trans. **53**(4), 963–976 (2014)
13. Zhao, Z.-L., Guo, B.-Z.: A novel extended state observer for output tracking of mimo systems with mismatched uncertainty. IEEE Trans. Autom. Control **63**(1), 211–218 (2018)
14. Zhang, X., Sun, L., Zhao, K., Sun, L.: Nonlinear speed control for pmsm system using sliding-mode control and disturbance compensation techniques. IEEE Trans. Power Electron. **28**(3), 1358–1365 (2013)
15. Chen, M., Knospe, C.R.: Feedback linearization of active magnetic bearings: current-mode implementation. IEEE/ASME Trans. Mechatron. **10**(6), 632–639 (2005)
16. Yao, Y.C., Sha, H.L., Su, Y.X., Ren, G.X., Yu, S.Y.: Identification of system parameters and external forces in amb-supported pmsm system. Mech. Syst. Signal Process. **166**, 18 (2022)

Author Index